SF2A 2019
P. Di Matteo, O. Creevey, A. Crida, G. Kordopatis, J. Malzac, J.-B. Marquette, M. N'Diaye, O. Venot (eds)

Proceedings of the annual meeting of the French Society of Astronomy & Astrophysics Nice, May 14-17, 2019

Crédit: Design du poster: Eva Rouland, photographie originale: Erick Bondoux

Contents

Foreword

As the president of the French Society of Astronomy and Astrophysics (*Société Française d'Astronomie et d'Astrophysique* - SF2A), it is an honour for me to write this foreword. Even if the president says this every year, I want to underline again that the annual meeting of the SF2A is a very important moment for our French community, the only place where permanent, doctoral and post-doctoral researchers can exchange their ideas and present to the whole community their new discoveries.

The 2019 edition took place from May 14th to May 17th in Nice, having been efficiently prepared by members of the *Laboratoire Lagrange, Observatoire de la Côte d'Azur.* As every year, this meeting included the general assembly of our society, plenary sessions aimed at a large audience of professionals, workshops dedicated to various scientific issues, the young researcher and thesis prize ceremony, events for schools and the public, discussions concerning societal subjects. The audience was the most important ever.

The programme of the plenary sessions was, as usual, very rich, with several high-quality presentations proposed by the various *Programmes Nationaux* and *Actions Spécifiques* of INSU-CNRS, covering a broad range of astrophysical topics, including Virtual Observatory, laboratory expriments, XMM-Newton, plasmas, stellar physics, planetology, astrobiology, numerical methods, new results with SPHERE and GRAVITY and current and future observing facilities such as SPIRou/CFHT and ELT. Representatives of institutions (G. Perrin for INSU, P. Laudet for CNES), the CNU (V. Buat), and the "*sections*" of CNRS (B. Mosser) and CNAP (H. Wozniak) presented us a detailed view of the French research situation with crucial informations for the career. Our colleague T. Montmerle presented the history and the role of IAU, for which the SF2A is the link with the French community. The last talk of the plenary session was given by T. Mondavaine on behalf of the Société Astronomique Française presenting the status of the fruitful amateur-pro collaborations. A parralel session about Professionals-amateurs collaborations was held for the second year on the last day. Like every year, SF2A had invited a "foreign" astronomical society. Dr A. Mastichiadis presented the Hellenic Astronomical Society.

The impact of Astrophyics on the global warming that our planet is unfortunately experiencing is non-negligible and our community has slowly begun some introspection. The SF2A meeting was an excellent opportunity to discuss it for the first time. P. Martin, on behalf of several persons, was presenting during the plenary sesssion a study conducted among our community and existing actions. A passionate debate followed.

Afternoons were dedicated to parallel workshops covering all branches of astronomy. These workshops were selected among propositions from the *Programmes Nationaux* and *Actions Spécifiques*, but also from individual members of the society. These workshops thus covered the interests of our whole community, in good accordance with the topicality of the field.

Finally, the SF2A journées were concluded by our general assembly where the moral and financial reports were presented. A vote from the members has complemented these presentations in July 2019.

Several special moments usually illuminated the SF2A meeting. The first one was the "outreach" conference by A. M. Lagrange about exoplanets. The second one was the SF2A prize ceremony. The laureate of the Thesis prize was Martin Turbet who presented his brilliant work concerning planet habitability, applied to early Mars. The laureate of the young researcher prize was Sébastien Deheuvels for his work on stellar physics using asterosismology. This ceremony was followed by a dinner-cocktail. An important moment of the week was also the School project prize called "Découvrir l'Univers". Last but not least, we spent a wonderful thursday evening at the historical site Mont Gros of Obseravatoire de Nice with an impressive dinner and an unforgettable concert of the Wathermelons, led by our vice-president!

Several sponsors made this meeting possible. The organizers and myself are very grateful for the financial help of INSU-CNRS, CNES, the *Service d'Astrophysique du CEA/DSM/IRFU*, the *Observatoire de la Côte d'Azur*, the *Laboratoire Lagrange*, the Université de Côte d'Azur, the Région Sud Provence Alpes Côte d'Azur and the PN and AS of INSU-CNRS that have supported the organization of the workshops. We acknowledge the help of the *Laboratoire Lagrange* and the Observatoire de la côte d'Azur for the global organization and the *Université Côte d'Azur* for its conference site at Campus de St Jean d'Angely. I would like to thank all the members of the SF2A board who were all very active for

preparing the meeting, and end with the local organizing committee:
Eric Lagadec (chair)
Benoît Carry
Aurélien Crida
Orlagh Creevey
Christine Delobelle
Patrick de Laverny
Clémence Durst
Vanessa Hill
Georges Kordopatis
Héloïse Méheut
Mamadou N'Diaye
Sophie Rousset.
They all made this meeting a success. In addition to the rich program mentioned above (and somewhat detailed in these proceedings), embracing all of the astronomy research performed in France, the work of the LOC has also offered to all the participants many opportunities to meet and discuss beyond the limits of their own field of expertise.

See you next year in Paris!

Fabrice Herpin, President of the SF2A

List of participants

ABDI Shahin e-mail: Shahin.abdi@obspm.fr
ABE Lyu e-mail: Lyu.Abe@oca.eu
ACEF Ouali e-mail: ouali.acef@obspm.fr
ADAMCZYK Paul e-mail: paul.adamczyk@lam.fr
AGUICHINE Artem e-mail: artyomaguichine@gmail.com
ALEXANDROVA Alexandra e-mail: sasha.alexandrova@gmail.com
ALEON Jérôme e-mail: jerome.aleon@mnhn.fr
AMARD Louis e-mail: l.amard@exeter.ac.uk
ANDERSON Sarah e-mail: saraheanderson@protonmail.com
ARISTIDI Eric e-mail: eric.aristidi@oca.eu
ATEK Hakim e-mail: hakim.atek@gmail.com
ATTEIA Jean-luc e-mail: jean-luc.atteia@irap.omp.eu
BABUSIAUX Carine e-mail: carine.babusiaux@univ-grenoble-alpes.fr
BAGUET Daniel e-mail: daniel.baguet@utinam.cnrs.fr
BARJOT Kevin e-mail: kevin.b.94@hotmail.fr
BAUDOZ Pierre e-mail: pierre.baudoz@obspm.fr
BEAULIEU Mathilde e-mail: mathilde.beaulieu@oca.eu
BELLOMI Elena e-mail: bellomi.elena@gmail.com
BENDJOYA Philippe e-mail: bendjoya@oca.eu
BENOIST Christophe e-mail: benoist@oca.eu
BERIO Philippe e-mail: philippe.berio@oca.eu
BETHERMIN Matthieu e-mail: matthieu.bethermin@lam.fr
BEUZIT Jean-Luc e-mail: Jean-Luc.Beuzit@lam.fr
BIGOT Lionel e-mail: lbigot@oca.eu
BOCCALETTI Anthony e-mail: anthony.boccaletti@obspm.fr
BOGDANOSKA Jana e-mail: jana.bogdanoska@lam.fr
BOILEAU Guillaume e-mail: guillaume.boileau@oca.eu
BOISSE Isabelle e-mail: isabelle.boisse@lam.fr
BOISSIER Samuel e-mail: samuel.boissier@lam.fr
BONAL Lydie e-mail: lydie.bonal@univ-grenoble-alpes.fr
BONFAND Melisse e-mail: bonfand@mpifr-bonn.mpg.de
BONNEAU Daniel e-mail: daniel.bonneau@oca.eu
BORGNIET Simon e-mail: simon.borgniet@obspm.fr
BOSSION Duncan e-mail: duncan.bossion@umontpellier.fr
BOUCHAUD Kévin e-mail: kevin.bouchaud@obspm.fr
BOUGHELILBA Margot e-mail: margot.boughelilba@gmail.com
BOUQUET Alexis e-mail: alexis.bouquet@lam.fr
BOURET Jean-Claude e-mail: jean-claude.bouret@lam.fr
BRAGA-RIBAS Felipe e-mail: felipe.ribas@obspm.fr
BRANCHEREAU Quentin e-mail: quentin.branchereau@oca.eu
BRETON Sylvain e-mail: sylvain.breton@polytechnique.edu
BREUVAL Louise e-mail: louise.breuval@obspm.fr
BRIOT Danielle e-mail: danielle.briot@obspm.fr
BUAT Véronique e-mail: veronique.buat@lam.fr
BUGNET Lisa e-mail: lisa.bugnet@cea.fr

BURDULLIS Todd e-mail: burdullis@cfht.hawaii.edu
CAILLEAU Antoine e-mail: acracing@hotmail.fr
CAMBRESY Laurent e-mail: laurent.cambresy@astro.unistra.fr
CARBILLET Marcel e-mail: marcel.carbillet@unice.fr
CARLOTTI Alexis e-mail: alexis.carlotti@gmail.com
CARRIERE Jean-Sébastien e-mail: jcarriere@irap.omp.eu
CARRY Benoit e-mail: benoit.carry@oca.eu
CASAMIQUELA Laia e-mail: laia.casamiquela-floriach@u-bordeaux.fr
CEAU Alban e-mail: alban.ceau@oca.eu
CELLINO Alberto e-mail: alberto.cellino@inaf.it
CHABE Julien e-mail: chabe@oca.eu
CHARBONNEL Corinne e-mail: Corinne.Charbonnel@unige.ch
CHARLET Arthur e-mail: arthur.charlet@ens-lyon.fr
CHARLOT Patrick e-mail: patrick.charlot@u-bordeaux.fr
CHARNAY Benjamin e-mail: benjamin.charnay@obspm.fr
CHATY Sylvain e-mail: chaty@cea.fr
CHAUVINEAU Bertrand e-mail: chauvineau@oca.eu
CHAVEROT Guillaume e-mail: guillaume.chaverot@edu.univ-fcomte.fr
CHELLI Alain e-mail: Alain.Chelli@oca.eu
CHIAVASSA Andrea e-mail: andrea.chiavassa@oca.eu
CLAVEL Maïca e-mail: maica.clavel@univ-grenoble-alpes.fr
CLENET Yann e-mail: yann.clenet@obspm.fr
COLEIRO Alexis e-mail: coleiro@apc.univ-paris-diderot.fr
COMBES Francoise e-mail: francoise.combes@obspm.fr
CONJAT Matthieu e-mail: mconjat@free.fr
CONTURSI Gabriele e-mail: Gabriele.CONTURSI@oca.eu
CORBARD Thierry e-mail: thierry.corbard@oca.eu
CORNU David e-mail: david.cornu@utinam.cnrs.fr
CORRE Julien e-mail: astroram.parsec@gmail.com
COTTALORDA Eric e-mail: cottalorda76@gmail.com
CREEVEY Orlagh e-mail: orlagh.creevey@oca.eu
CRIDA Aurélien e-mail: crida@oca.eu
CRUZALEBES Pierre e-mail: pierre.cruzalebes@oca.eu
CUELLO Nicolas e-mail: cuellonicolas@gmail.com
CUILLANDRE Jean-Charles e-mail: jc.cuillandre@cea.fr
CVETOJEVIC Nick e-mail: nick.cvetojevic@oca.eu
D'HENDECOURT Louis e-mail: ldh@ias.u-psud.fr
DAIFFALLAH Khalil e-mail: dfkhalil@gmail.com
DE ALMEIDA Elisson e-mail: Elisson.Saldanha@oca.eu
DE FOUQUIERES Louis-AimÃ© e-mail: louis-aime@calendriermilesien.org
DE LAVERNY Patrick e-mail: laverny@oca.eu
DEBRAS Florian e-mail: florian_debras@hotmail.com
DEHEUVELS Sébastien e-mail: sebastien.deheuvels@irap.omp.eu
DELCAMP Simon e-mail: simon.delcamp@etu.u-bordeaux.fr
DELCROIX Marc e-mail: delcroix.marc@free.fr
DELDEM Marc e-mail: marc.deldem@free.fr
DELL'OVA Pierre e-mail: pierre.dellova@ens.fr
DEMYK Karine e-mail: karine.demyk@irap.omp.eu
DERAM Pierre e-mail: pierre.deram@geoazur.unice.fr
DESMARS Josselin e-mail: josselin.desmars@obspm.fr
DESMONS Nathalie e-mail: nathalie.desmons@osupytheas.fr
DEVOST Daniel e-mail: devost@cfht.hawaii.edu
DI MATTEO Paola e-mail: paola.dimatteo@obspm.fr
DOMICIANO DE SOUZA Armando e-mail: armando.domiciano@oca.eu
DOUGADOS Catherine e-mail: catherine.dougados@univ-grenoble-alpes.f

DOUTE Sylvain e-mail: sylvain.doute@univ-grenoble-alpes.fr
DREVON Julien e-mail: julien.drevon@wanadoo.fr
DUBREUIL Pierre e-mail: pierre.dubreuil@gmail.com
DUC Pierre-Alain e-mail: pierre-alain.duc@astro.unistra.fr
DUCHAUFOUR Quentin e-mail: quentin.duchaufour@oca.eu
DUCOURANT Christine e-mail: christine.ducourant@u-bordeaux.fr
DUCROQUET Marie-Hélène e-mail: marylene.ducroquet@gmail.com
DUPRAT Jean e-mail: Jean.Duprat@csnsm.in2p3.fr
DURRET Florence e-mail: durret@iap.fr
DVORKIN Irina e-mail: irina.dvorkin@aei.mpg.de
EDME Florian e-mail: florian.edme@oca.eu
ELENA Lega e-mail: elena@oca.eu
ELLIEN Amael e-mail: ellien@iap.fr
EPINAT Benoît e-mail: benoit.epinat@lam.fr
FARISSIER Pierre e-mail: farissier@cala.asso.fr
FAURE Alexandre e-mail: alexandre.faure@univ-grenoble-alpes.fr
FAUROBERT Marianne e-mail: marianne.faurobert@oca.eu
FAUVAUD Stéphane e-mail: sfauvaud@gmail.com
FENSCH Jérémy e-mail: jeremy.fensch@gmail.com
FERAUD Géraldine e-mail: geraldine.feraud@upmc.fr
FERNANDEZ TRINCADO Jose gregorio e-mail: jfernandez@obs-besancon.fr
FERNANDEZ-ALVAR Emma e-mail: Emma.Fernandez-Alvar@oca.eu
FERRARI Chiara e-mail: chiara.ferrari@oca.eu
FERREIRA Joao e-mail: jferreira@oca.eu
FIENGA Agnès e-mail: agnes.fienga@oca.eu
FIGUEIRA Miguel e-mail: miguel.figueira@ncbj.gov.pl
FLAGEY Nicolas e-mail: flagey@cfht.hawaii.edu
FOLCHER Jean-Pierre e-mail: JEAN-PIERRE.FOLCHER@OCA.EU
FOUCHET Thierry e-mail: thierry.fouchet@obspm.fr
FOUREZ Julien e-mail: julien.fourez@fr.thalesgroup.com
FREUNDLICH Jonathan e-mail: jonathan.freundlich@mail.huji.ac.il
FRISCH Helene e-mail: frisch@oca.eu
FUSCO Thierry e-mail: thierry.fusco@onera.fr
FÉGHALI Christian e-mail: christian.el-khoury@laposte.net
GAGNIER Damien e-mail: damien.gagnier@irap.omp.eu
GALLET Florian e-mail: florian.gallet1@univ-grenoble-alpes.fr
GARDE Olivier e-mail: o.garde@wanadoo.fr
GATINEAU Nicolas e-mail: parsec@astrorama.net
GATTANO César e-mail: cesar.gattano@u-bordeaux.fr
GAUDEL Mathilde e-mail: mathilde.gaudel@cea.fr
GAVET Jean-Claude e-mail: mmjcgavet@gmail.com
GENOVA Françoise e-mail: francoise.genova@astro.unistra.fr
GIACINTI Gwenael e-mail: giacinti@mpi-hd.mpg.de
GILLIER Christophe e-mail: gillier.christophe@free.fr
GIORDANO Christophe e-mail: cgiordano@oca.eu
GONCALVES Ivan e-mail: ivan.goncalves@oca.eu
GONZALEZ Jean-François e-mail: Jean-Francois.Gonzalez@ens-lyon.fr
GOUVRET Carole e-mail: carole.gouvret@oca.eu
GRANIER Camille e-mail: camille.granier@etu.u-bordeaux.fr
GRITON Léa e-mail: lea.griton@obspm.fr
GROUSSIN Olivier e-mail: olivier.groussin@lam.fr
GUILLEMOT Lucas e-mail: lucas.guillemot@cnrs-orleans.fr
GUILLOT Sébastien e-mail: sebastien.guillot@irap.omp.eu
GUILLOT Tristan e-mail: tristan.guillot@oca.eu
GUITTON Florence e-mail: guitton@oca.eu

HABART Emilie e-mail: emilie.habart@ias.u-psud.fr
HADJARA Massinissa e-mail: massinissa.hadjara@raig.uchile.cl
HAHN Oliver e-mail: oliver.hahn@oca.eu
HAJIAGHAZADEH ROODSARI Maryam e-mail: maryam.h-roodsari@oca.eu
HAMMER Francois e-mail: francois.hammer@obspm.fr
HARDER Thomas e-mail: Thomas.Harder@oca.eu
HASSELMANN Pedro Henrique e-mail: pedro.hasselmann@obspm.fr
HEARNE Thomas e-mail: thomas.hearne@univ-rennes1.fr
HERPIN Fabrice e-mail: fabrice.herpin@u-bordeaux.fr
HERTLE Anton e-mail: anton.hertle@wanadoo.fr
HERVET Olivier e-mail: ohervet@ucsc.edu
HILL Vanessa e-mail: Vanessa.Hill@oca.eu
HIRSH Kieran e-mail: kieran.hirsh@univ-lyon1.fr
HOCDE Vincent e-mail: vincent.hocde@oca.eu
IANA Astafeva e-mail: iana.astafeva@oca.eu
JACQUEMIN IDE Jonatan e-mail: jonatan.jacquemin@univ-grenoble-alpes.fr
JAVANMARDI Behnam e-mail: behnam.javanmardi@obspm.fr
JOSSELIN Eric e-mail: eric.josselin@obs-mip.fr
KAPOOR Anand Utsav e-mail: Anand-Utsav.Kapoor@oca.eu
KERVELLA Pierre e-mail: pierre.kervella@obspm.fr
KLEIN Baptiste e-mail: baptiste.klein@irap.omp.eu
KLEIN Karl-Ludwig e-mail: ludwig.klein@obspm.fr
KLUSKA Jacques e-mail: jacques.kluska@kuleuven.be
KOKOULINA Elena e-mail: elena.kokoulina@oca.eu
KORDOPATIS Georges e-mail: gkordo@oca.eu
KOULOUMVAKOS Athanasios e-mail: athkouloumvakos@gmail.com
KRAVCHENKO Kateryna e-mail: kateryna.kravchenko@eso.org
KRISHNAN Ananya e-mail: ananya.krishnan@oca.eu
KROGAGER Jens-Kristian e-mail: krogager@iap.fr
LAGADEC Eric e-mail: elagadec@oca.eu
LAGARDE Nadège e-mail: Nadege.Lagarde@utinam.cnrs.fr
LAGRANGE Anne-Marie e-mail: anne-marie.lagrange@univ-grenoble-alpes.
LAI Olivier e-mail: olai@oca.eu
LALLEMENT Rosine e-mail: rosine.lallement@obspm.fr
LAMBERTS Astrid e-mail: Astrid.lamberts@oca.eu
LAU Ryan e-mail: ryanlau@caltech.edu
LAUDET Philippe e-mail: philippe.laudet@cnes.fr
LAUGIER Romain e-mail: romain.laugier@oca.eu
LAVALLE Julien e-mail: lavalle@in2p3.fr
LAYCHAK Mary e-mail: laychak@cfht.hawaii.edu
LE CONTEL Olivier e-mail: olivier.lecontel@lpp.polytechnique.fr
LE DU Pascal e-mail: ledu@shom.fr
LE GAL Romane e-mail: romane.le_gal@cfa.harvard.edu
LE SAUX Arthur e-mail: arthur.lesaux@cea.fr
LEBRE Agnès e-mail: agnes.lebre@umontpellier.fr
LEE Yueh-Ning e-mail: lee.yuehning@gmail.com
LEKIC Anica e-mail: anica.lekic@ipsa.fr
LEMOINE Martin e-mail: lemoine@iap.fr
LESAFFRE Pierre e-mail: lesaffre.pierre@gmail.com
LESEIGNEUR Guillaume e-mail: gleseigneur@oca.eu
LEUCCI Ludovic e-mail: ludoleucci@gmail.com
LEVESQUE Maëva e-mail: maeva.levesque@hotmail.fr
LEYRAT Cedric e-mail: cedric.leyrat@obspm.fr
LIBOUREL Guy e-mail: libou@oca.eu
LIGI Roxanne e-mail: roxanne.ligi@inaf.it

LINAN Luis e-mail: luis.linan@obspm.fr
LIQUE François e-mail: francois.lique@univ-lehavre.fr
LOMBARDO Simona e-mail: simona.lombardo@lam.fr
LOMBART Maxime e-mail: maxime.lombart@ens-lyon.fr
LONGOBARDI Alessia e-mail: alessia.longobardi@lam.fr
LOPEZ Bruno e-mail: bruno.lopez@oca.eu
LOUVET Fabien e-mail: fabien.louvet@cea.fr
MACQUET Adrian e-mail: adrian.macquet@oca.eu
MADATHODIKA Junais e-mail: junais.madathodika@lam.fr
MAIA Julia e-mail: julia.maia@oca.eu
MALZAC Julien e-mail: julien.malzac@irap.omp.eu
MAMON Gary e-mail: gam@iap.fr
MANCILLAS Brisa e-mail: brisa.mancillas@obspm.fr
MARCOTTE Florence e-mail: marcotte@irphe.univ-mrs.fr
MARCOTTO Aurélie e-mail: aurelie.marcotto@oca.eu
MARCOWITH Alexandre e-mail: almarcowith@gmail.com
MARQUETTE Jean-Baptiste e-mail: jean-baptiste.marquette@u-bordeaux.fr
MARQUEZ Jeremy e-mail: j.marquez101298@gmail.com
MARSHALL-LEE Andrew e-mail: andrew.marshall-lee@oca.eu
MARTIN Jean-Luc e-mail: j-luc.martin@laposte.net
MARTIN Nicolas e-mail: nicolas.martin@astro.unistra.fr
MARTIN Pierrick e-mail: pierrick.martin@irap.omp.eu
MARTINACHE Frantz e-mail: frantz.martinache@oca.eu
MARTINEZ Patrice e-mail: patrice.martinez@oca.eu
MARTINS Fabrice e-mail: fabrice.martins@umontpellier.fr
MARY David e-mail: david.mary@unice.fr
MASSON Sophie e-mail: sophie.masson@obspm.fr
MASTICHIADIS Apostolos e-mail: amastich@phys.uoa.gr
MATHIAS Philippe e-mail: Philippe.Mathias@irap.omp.eu
MATTER Alexis e-mail: Alexis.Matter@oca.eu
MATTHEW Pieri e-mail: matthew.pieri@lam.fr
MAUROGORDATO Sophie e-mail: Sophie.Maurogordato@oca.eu
MEHEUT Heloise e-mail: heloise.meheut@oca.eu
MEHEUT Heloise e-mail: heloise.meheut@oca.eu
MEILLAND Anthony e-mail: ame@oca.eu
MEKARNIA Djamel e-mail: mekarnia@oca.eu
MERLIN Frédéric e-mail: frederic.merlin@obspm.fr
MICHAUT Claire e-mail: claire.michaut@oca.eu
MICHAUX Michaël e-mail: michael.michaux@oca.eu
MICHEL Alisson e-mail: alisson.michel@oca.eu
MICHEL Patrick e-mail: michelp@oca.eu
MIDAVAINE Thierry e-mail: thierrymidavaine@sfr.fr
MIGNON-RISSE Raphaël e-mail: raphael.mignon-risse@cea.fr
MILLOUR Florentin e-mail: fmillour@oca.eu
MINAZZOLI Olivier e-mail: ominazzoli@gmail.com
MIRABEL Felix e-mail: felix.mirabel@cea.fr
MONTAIGUT Romain e-mail: romain.montaigut@hotmail.fr
MONTARGES Miguel e-mail: miguel.montarges@kuleuven.be
MONTMERLE Thierry e-mail: thierry.montmerle@iap.fr
MORAUX Estelle e-mail: estelle.moraux@univ-grenoble-alpes.fr
MORBIDELLI Alessandro e-mail: morby@oca.eu
MOSSER Benoît e-mail: benoit.mosser@observatoiredeparis.psl.eu
MOUILLET David e-mail: David.Mouillet@univ-grenoble-alpes.fr
MOURRE Sophie e-mail: sophie.mourre@oca.eu
MUNAIBARI Edhah e-mail: Edhah.Munaibari@oca.eu

MUNOZ Robyn e-mail: robyn.munoz@oca.eu
N'DIAYE Mamadou e-mail: mamadou.ndiaye@oca.eu
NAAR Joseph e-mail: joseph.naar@ens.fr
NARDETTO Nicolas e-mail: Nicolas.Nardetto@oca.eu
NARI Marco e-mail: Marco.Nari@oca.eu
NEHME Cyrine e-mail: cyrine.nehme@gmail.com
NEICHEL Benoit e-mail: benoit.neichel@lam.fr
NEZRI Emmanuel e-mail: emmanuel.nezri@lam.fr
NICCOLINI Gilles e-mail: nicolin@oca.eu
NIEMIEC Anna e-mail: anna.niemiec@hotmail.fr
NOLL Anthony e-mail: anthony.noll@irap.omp.eu
NONY Thomas e-mail: thomas.nony@univ-grenoble-alpes.fr
NOULLEZ Alain e-mail: alain.noullez@oca.eu
NOUVEL Bernard e-mail: bernardnvl@bbox.fr
NOYELLES Benoît e-mail: benoit.noyelles@univ-fcomte.fr
NUNEZ-CASTINEYRA Arturo e-mail: arturo.nunez@lam.fr
PANTIN Eric e-mail: eric.pantin@cea.fr
PARIAT Etienne e-mail: etienne.pariat@obspm.fr
PASSOT Thierry e-mail: thierry.passot@oca.eu
PATRU Fabien e-mail: fabien.patru@oca.eu
PAVIOT Romain e-mail: romain.paviot@lam.fr
PEIRANI SÃ©bastien e-mail: speirani@oca.eu
PEPINO Raphaël e-mail: raphael.pepino@univ-cotedazur.fr
PERDIGON Jérémy e-mail: jeremy.perdigon@oca.eu
PERRAUT Karine e-mail: karine.perraut@univ-grenoble-alpes.fr
PERRIN Guy e-mail: guy.perrin@cnrs-dir.fr
PESQUEIRA Alba e-mail: Alba.PESQUEIRA@student.isae-supaero.fr
PETIT Jean-Marc e-mail: jean-marc.petit@normalesup.org
PETITDEMANGE Ludovic e-mail: ludovic.petitdemange@upmc.fr
PHILIDET Jordan e-mail: jordan.philidet@obspm.fr
PICHIERRI Gabriele e-mail: gabriele.pichierri@oca.eu
PICHON Bernard e-mail: Bernard.Pichon@oca.eu
PITOUT Frédéric e-mail: frederic.pitout@irap.omp.eu
PLOTNIKOV Illya e-mail: iplotnikov@irap.omp.eu
POTIN Sandra e-mail: sandra.potin@univ-grenoble-alpes.fr
POUILLY Kim e-mail: kim.pouilly@univ-grenoble-alpes.fr
PREIS Olivier e-mail: olivier.preis@oca.eu
PRIETO Eric e-mail: eric.prieto@lam.fr
PROVOST Janine e-mail: provost@oca.eu
PUECH Mathieu e-mail: mathieu.puech@obspm.fr
RAFALIMANANA Alohotsy Jean-Pierre e-mail: alohotsy.rafalimanana@oca.eu
RAYNAUD Raphaël e-mail: raphael.raynaud@cea.fr
REBOUL-SALZE Alexis e-mail: alexis.reboul-salze@cea.fr
RECIO-BLANCO Alejandra e-mail: arecio@oca.eu
REESE Daniel e-mail: daniel.reese@obspm.fr
REGIMBAU Tania e-mail: regimbau@lapp.in2p3.fr
RENAUD Catherine e-mail: renaud@oca.eu
RETINO Alessandro e-mail: alessandro.retino@gmail.com
REYLE Céline e-mail: celine@obs-besancon.fr
RICHARD Thibaud e-mail: thibaud.richard@ens.fr
RICHARDSON Thomas e-mail: thomas.ag.richardson@gmail.com
RIVET Jean-Pierre e-mail: jean-pierre.rivet@oca.eu
ROBBE-DUBOIS Sylvie e-mail: robbe@unice.fr
ROBERT Clément e-mail: clement.robert@oca.eu
ROBERT Vincent e-mail: vincent.robert@obspm.fr

ROBIN Annie e-mail: annie.robin@obs-besancon.fr
RODRIGUEZ Jérôme e-mail: jrodriguez@cea.fr
ROGGERO Noemi e-mail: noemi.roggero@univ-grenoble-alpes.fr
RONNET Thomas e-mail: thomas.ronnet@astro.lu.se
ROUAN Daniel e-mail: daniel.rouan@obspm.fr
ROUBEAU-TISSOT Amaël e-mail: amael.roubeau-tissot@oca.eu
ROUILLARD Alexis e-mail: arouillard@irap.omp.eu
ROUSSELOT Philippe e-mail: phil@obs-besancon.fr
ROYER Frédéric e-mail: frederic.royer@obspm.fr
REGALDO-SAINT BLANCARD Bruno e-mail: bruno.regaldo@lra.ens.fr
REVILLE Victor e-mail: victorreville@gmail.com
SALOMON Jean-Baptiste e-mail: jean-baptiste.salomon@utinam.cnrs.fr
SALSI Anthony e-mail: anthony.salsi@oca.eu
SANCHEZ-CANO Beatriz e-mail: bscmdr1@le.ac.uk
SANTERNE Alexandre e-mail: alexandre.santerne@lam.fr
SANTOS Pablo e-mail: Pablo.Santos-del-Peral@oca.eu
SCHMIDER François-xavier e-mail: schmider@oca.eu
SCHULTHEIS Mathias e-mail: mathias.schultheis@oca.eu
SESTITO Federico e-mail: federico.sestito@astro.unistra.fr
SIELLEZ Karelle e-mail: ksiellez@gmail.com
SIMONS Douglas e-mail: simons@cfht.hawaii.edu
SLEZAK Eric e-mail: slezak@obs-nice.fr
SOUBIRAN Caroline e-mail: caroline.soubiran@u-bordeaux.fr
SPANG Alain e-mail: alain.spang@oca.eu
SPOTO Federica e-mail: fspoto@oca.eu
STEE Philippe e-mail: philippe.stee@oca.eu
STRUGAREK Antoine e-mail: antoine.strugarek@cea.fr
SUAREZ Olga e-mail: olga.suarez@oca.eu
SULEM Pierre-Louis e-mail: sulem@oca.eu
SULIS Sophia e-mail: Sophia.Sulis@oeaw.ac.at
SYLVESTRE Melody e-mail: melody.sylvestre@bristol.ac.uk
TAGGER Michel e-mail: michel.tagger@cnrs-orleans.fr
TANGA Paolo e-mail: paolo.tanga@oca.eu
TARRICQ Yoann e-mail: yoann.tarricq@u-bordeaux.fr
TASSI Emanuele e-mail: etassi@oca.eu
THUILLET Florian e-mail: fthuille@oca.eu
THUILLOT William e-mail: thuillot@imcce.fr
TRAHIN Boris e-mail: boris.trahin@obspm.fr
TRAVERSE Pierre e-mail: pierre.traverse@orange.fr
TRESSE Laurence e-mail: laurence.tresse@univ-lyon1.fr
TUCKEY Philip e-mail: philip.tuckey@obspm.fr
TURBET Martin e-mail: martin.turbet@unige.ch
TURC Lucile e-mail: lucile.turc@helsinki.fi
VAKILI Farrokh e-mail: vakili@oca.eu
VALLEE Malcolm e-mail: valleemalcolm@gmail.com
VALLS-GABAUD David e-mail: david.valls-gabaud@obspm.fr
VAN DER SWAELMEN Mathieu e-mail: mathieu@arcetri.astro.it
VANNIER Martin e-mail: mvannier@oca.eu
VARNIERE Peggy e-mail: varniere@apc.univ-paris7.fr
VEILLET Christian e-mail: cveillet@lbto.org
VENOT Olivia e-mail: olivia.venot@lisa.u-pec.fr
VERICEL Arnaud e-mail: arnaud.vericel@univ-lyon1.fr
VERLIAT Antoine e-mail: antoine.verliat@cea.fr
VERNAZZA Pierre e-mail: pierre.vernazza@lam.fr
VILLA VELEZ Jorge Andres e-mail: jorge.villa@lam.fr

VILMER Nicole e-mail: nicole.vilmer@obspm.fr
WALDER Rolf e-mail: Rolf.Walder@ens-lyon.fr
WEBB Natalie e-mail: Natalie.Webb@irap.omp.eu
WEGG Chris e-mail: chris.wegg@oca.eu
WOZNIAK Hervé e-mail: herve.wozniak@umontpellier.fr
WULLAERT Patrick e-mail: wullaert_chatillon@hotmail.com
YECHE Christophe e-mail: christophe.yeche@cea.fr
YU Louise e-mail: louise.yu@irap.omp.eu
ZAMBRANA PRADO Natalia e-mail: natalia.zambranaprado@ias.u-psud.fr
ZIAD Aziz e-mail: ziad@unice.fr

Session SF2A

Session Plénière

SF2A 2019
P. Di Matteo, O. Creevey, A. Crida, G. Kordopatis, J. Malzac, J.-B. Marquette, M. N'Diaye, O. Venot (eds)

EXPLORING THE HIGH-REDSHIFT UNIVERSE WITH ALMA

M. Béthermin[1]

Abstract. The Atacama Large Millimeter Array (ALMA) is now observing the (sub-)millimeter sky for more than half a decade. Thanks to its unprecedented sensitivity, it has dramatically improved our understanding of the high-z dusty Universe. In this review, I present a short summary of the main ALMA results about z>3 galaxies. I will first discuss the star formation history with a focus on the contribution of the early massive and dusty systems. I will then explain how we obtained first constraints on their interstellar medium using (sub-)millimeter lines. Finally, I will present some of the most spectacular objects that ALMA has identified.

Keywords: ALMA, galaxy formation and evolution, high-redshift galaxies, star formation, dust, gas, interstellar medium

1 Why is ALMA important to understand the formation of massive galaxies at high redshift?

Understanding the early assembly of massive galaxies remains a challenge for modern astrophysics. We still do not well know how gas is accreted by galaxies, cool down, and is finally used as fuel for star formation. For instance, very massive galaxies have been found extremely early in the Universe (e.g., Riechers et al. 2013). Some of these objects are an order of magnitude more massive than the Milky Way less than a gigayear after the recombination and the mechanisms leading to their incredibly fast assembly are poorly known. Of course, the bulk of stars at high redshift are not form in these monsters. However, at these early times (z>3), a significant fraction of the stars were formed in already massive galaxies ($>10^{10}\,M_\odot$) hosting very high star formation rates (SFR>10 $M_\odot$/yr and even >100 $M_\odot$/yr for the most massive ones, e.g., Schreiber et al. 2015).

How can we explain that the stellar mass of these galaxies was assembled so early and so fast? The major mergers were the first explanation proposed. Indeed, in the local Universe, the highest SFRs are found in major mergers (Sanders & Mirabel 1996; Di Matteo et al. 2007) and the merger rate increases with redshift (e.g., Le Fèvre et al. 2000). However, the discovery of a correlation between the assembled stellar mass and the SFR (e.g., Noeske et al. 2007; Elbaz et al. 2011) and the quickly increasing gas fraction from z=0 to z=3 (e.g., Magdis et al. 2012; Tacconi et al. 2013; Dessauges-Zavadsky et al. 2015) contributed to the emergence of a new scenarii, where the intense star formation in these objects is driven mainly by cosmic accretion of cold gas onto early-assembled dark matter halos (e.g., Dekel & Birnboim 2006). This scenario is compatible with the strong clustering (typical of host halo mass of a few $10^{12}\,M_\odot$) of the dusty star formation measured up to z$\sim$3 using the anisotropies of the cosmic infrared background, i.e. the relic emission of the dust from all galaxies across cosmic times (e.g., Béthermin et al. 2013; Maniyar et al. 2018). Recently, zoom-in hydrodynamical simulation found that high-redshift star-forming structures could be even more complex with a strong contribution from both accretion, minor, and major mergers (e.g., Narayanan et al. 2015).

Until recent years, most of our constraints on the star formation at z>3 were essentially coming from the UV light from young stars escaping the galaxies (e.g., Madau & Dickinson 2014) and we had very few information on the UV light absorbed by dust and re-emitted at long wavelength or the galaxy gas content, except in bright lensed quasars and extreme starbursts. However, the stacking of *Herschel* data showed us that the most massive galaxies had a very high dust attenuation (Heinis et al. 2014). Having access to long-wavelength observations

[1] Aix Marseille Univ, CNRS, CNES, LAM, Marseille, France

at z>3 is thus one of the keys to understand the formation of the early massive galaxies.

ALMA is a (sub-)millimeter array of 66 antennae built on the Chajnantor plateau at an elevation of 5 000m in one of the driest places on Earth (Fig. 1). It contains 50 12-meter antennae in the main array used to observe the compact sources and/or trace the small scales, 12 7-meter antennae used to reconstruct the intermediate scales, and 4 12-meter total power antennae used measure the large scales. Since ALMA has reached its final unprecedented capabilities, a new era is opening, and we can finally detect the dust emission of dusty star-forming galaxies and their cold gas reservoirs at these early times.

Fig. 1. ALMA antennae on the Chajnantor plateau (private picture).

2 ALMA and the obscured star formation history

The star formation history in the Universe, usually defined as the evolution of the sum of all the star formation per unit of comoving volume (SFR density or ρ_{SFR}), can be measured by combining the UV light from young stars both escaping the galaxies and absorbed by dust reprocessed in the infrared (8-1000 μm rest-frame).

One of the best ways to measure this SFR density is to use deep fields data. However, they need to be sufficiently deep to detect the galaxy populations responsible for the bulk of the star formation activity and sufficiently wide to detect a statistically significant number of objects. Unfortunately, despite its incredible sensitivity, the small field of view of ALMA (only one antenna beam) does not allow us to map efficiently large area. The 4.5 arcmin^2 of Dunlop et al. (2017) in the *Hubble* ultra deep field detected only one source at z> 4, while the ALMA-GOODS survey (69 arcmin^2 but shallower, Franco et al. 2018) detected two z>4 objects. Due to scheduling problems, these surveys were not observed in slightly extended configuration and their sensitivity to extended galaxies was limited. Better results should be obtained in the future from deep fields observed in compact configuration only (re-observation of ALMA-GOODS has been completed). However, it shows how hard it is even at ALMA era to probe the high-z dusty Universe in a volume-complete way.

Another possible approach is to target with ALMA galaxy samples selected at shorter wavelength. For instance, the ALPINE large program targeted 122 4<z<6 objects selected using optical spectroscopy (PI: Le Fèvre et al.). Only 23 of these objects are detected in continuum (Béthermin et al. in prep.), but we can use stacking to estimate the properties of the fainter ones as a function of various proxies (UV luminosity, stellar mass...) and reconstruct the contribution of known galaxy populations to the SFRD at z>4. This analysis shows that at least half of the SFR density is still dust obscured at z∼5.5 (Khusanova et al. in prep.).*

In extended configuration, ALMA can spatially resolve the dust emission. These observations revealed important differences between the UV and dust morphologies (Elbaz et al. 2018), suggesting that the dust attenuation and probably the presence of dust and metals can dramatically vary inside an object. One of the most extreme case is the Jekyll&Hyde systems, where a component is bright with *Hubble* and invisible with ALMA, while it is the exact opposite for the other one (Schreiber et al. 2018).

*Note also the work of Wang et al. (2019) published after the oral presentation, which shows an important contribution of massive dusty galaxies not seen by *Hubble*.

3 ALMA to probe the cold interstellar medium in the teenager Universe

The mass of the cold gas reservoirs of high-z galaxies is a crucial constraint to understand their impressive star formation rate. Observations at intermediate redshifts (1<z<2) showed that normal star-forming galaxies follow a correlation between gas mass (or gas surface density) and SFR (or SFR surface density), while the starbursting systems have a significantly higher SFR for the same gas mass (Daddi et al. 2010; Genzel et al. 2010). Where does z> 3 systems lies in this diagram? *Herschel* stacking suggested that massive systems have in average large gas reservoirs and tend to follow the "normal" relation (Béthermin et al. 2015). Using the Rayleigh-Jeans dust continuum, Schinnerer et al. (2016) and Scoville et al. (2017) confirmed this results with ALMA by measuring individual gas masses and found that most of the objects were on the "normal" gas mass-SFR relation.

At z>3, it is really hard to detect lines in normal star-forming systems. However, the 158 μm [CII] line is particularly bright and is conveniently redshifted to the atmospheric sub-millimeter windows at z>3. Paradoxically, the higher the redshift, the easier its detection is. Initially, [CII] was not detected in some of the first targeted high-redshift systems (e.g., Ouchi et al. 2013). Models suggested that high-redshift galaxies could have a lower [CII] luminosity than what could be expected from the local [CII]-L_{IR}. This would be caused by a lower metallicity and/or higher interstellar radiation field (Vallini et al. 2015; Lagache et al. 2018). No [CII]-deficit has been found for the statistical ALPINE sample (see previous section, Schaerer et al. in prep.). The faint [CII] observed in the first targeted systems could be explained by a bias towards particularly metal-poor Lyman α-emitters or a quick transition above z=6.

To perform finer diagnostics of the interstellar medium (ISM) of z>3 galaxies, we need much more lines, but their detection usually request tens of hours of integration times. However, we can use the assistance of gravitational lensing magnifying the flux of some high-z galaxies. For instance, the South Pole Telescope (SPT) identified ~70 high-redshift dusty star-forming galaxies magnified by intermediate-z elliptical galaxies and their spectroscopic redshifts were measured by ALMA (Vieira et al. 2013; Strandet et al. 2016). ALMA and NOEMA detected a large variety of lines in this type of systems: CO (e.g., Aravena et al. 2016; Yang et al. 2017), H_2O (e.g., Yang et al. 2016; Jarugula et al. 2019), [NII] (e.g., Béthermin et al. 2016; Cunningham et al. 2019), [CI] (e.g., Bothwell et al. 2016; Nesvadba et al. 2019), HCN/HNC/HCO^+ (e.g., Béthermin et al. 2018), CH^+ (Falgarone et al. 2017)...

Each of these lines probes a different phase of the ISM (Fig. 2) and provides much more powerful diagnostic than just the total gas mass. For instance, using tracers of the dense molecular gas (HCN and HCO^+), we can show that the most extreme star-forming systems (SFR>1000 $M_\odot$/yr) have both a high dense-gas fraction and a high star-formation efficiency. Combined with their large gas reservoirs, this could explain the impressive star formation they host. However, Zhang et al. (2018) suggest using CO isotopes that their actual SFR could be lower because of a top-heavy initial mass function. Using several lines and ISM models, various studies showed that the lensed dusty star-forming galaxies contain dense gas excited by an intense radiation field (e.g. Bothwell et al. 2016; Yang et al. 2017). The [NII]/[CII] ratio can also be used to obtain a rough estimate of their metallicity and we found lots of systems compatible with solar abundances (e.g., Nagao et al. 2012; Béthermin et al. 2016), suggesting a very quick enrichment in these early-assembled massive objects.

4 ALMA: a powerful tool to find the most extremes galaxies and (proto)cluster in the young Universe

Thanks to its incredible sensitivity in spectroscopy, ALMA is perfectly suited to determine the redshift of very dusty objects, which could not be measured with optical spectroscopy. SPT0311-58 was one of the reddest objects of the SPT SMG sample. The ALMA spectral scan campaign confirmed a redshift of 6.9 (Strandet et al. 2017). This is the record for an object selected purely in the millimeter, which could have never been found using lower-wavelength data because of its dustiness. SPT0311-58 has a SFR of ~2900 $M_\odot$/yr, which is fueled by $\sim 2.7 \times 10^{11}$ $M_\odot$ gas reservoir. ALMA follow-up at higher resolution revealed its kinematics. It has two distinct components, including one possibly rotation dominated (Marrone et al. 2018). The dark-matter halo mass of such a system can be estimated to be a few 10^{12} $M_\odot$ and is probably the progenitor of a cluster.

ALMA can also measure spectroscopic redshift of even higher redshift candidates selected using the Lyman break technique. The bright 158 μm [CII] and 88 μm [OIII] fine-structure lines are particularly suited for this

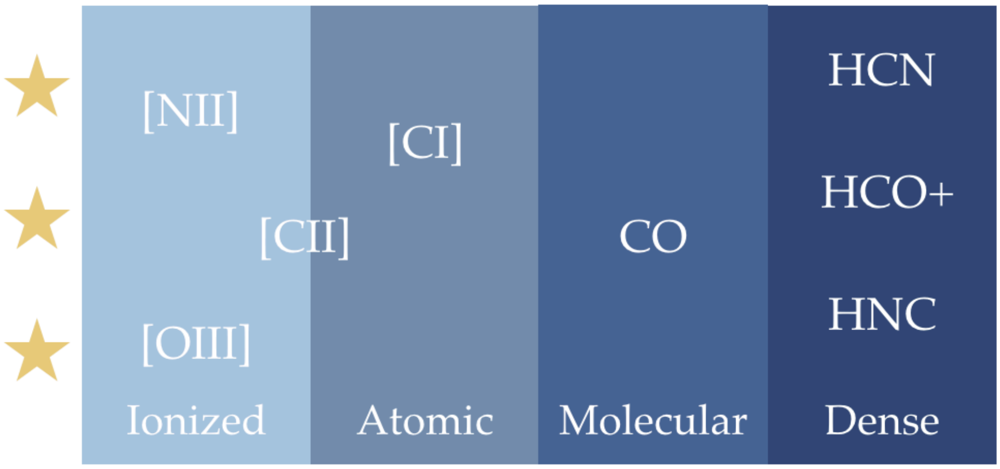

Fig. 2. (Very) simplified cartoon showing in which phase of the interstellar medium the various lines detected by ALMA are emitted.

task, since their observed frequency is lower at higher redshift and the atmosphere is thus more transparent. In addition, according to models, [OIII] has the convenient property to be bright in early low-metallicity systems (Inoue et al. 2014). This approach leads to the discovery of two consecutive record holders for spectroscopically-confirmed redshift: z=8.38 by Laporte et al. (2017) and z=9.11 by Hashimoto et al. (2018). Before the launch of JWST, ALMA is probably the best tool to determine spectroscopic redshifts at z>8.

ALMA is also particularly suited to detect the early stage of cluster formation, when their most massive galaxies were still star forming. As for field galaxies, massive cluster galaxies produced early an impressive amount of dust and are very bright in the (sub-)millimeter. Wang et al. (2016) confirmed the membership of 11 objects in a z=2.5 X-ray cluster by detecting CO with ALMA. At higher redshift, progenitors of even more massive structures can be found. Miller et al. (2018) found an overdensity of 17 galaxies with SFR>100 $M_\odot$/yr at the same spectroscopic redshift of z=4.3. The mass of such a system was estimated to be $\sim 10^{13}\,M_\odot$/yr, which corresponds to a progenitor of a Coma-like cluster. Another similar system was also identified by Oteo et al. (2018). A more systematic search for these overdensities of high-z dusty galaxies using the *Planck* is on-going (Planck Collaboration et al. 2015; Martinache et al. 2018; Kneissl et al. 2019).

5 Conclusions

Since its first observations, ALMA has dramatically changed our understanding of the high-redshift Universe. It is now clear that very dusty systems exist up to very high redshifts. These systems are already very massive, contain gigantic gas reservoirs fueling an intense star formation, and have already produced a large amount of metals and dust. They are probably the progenitor of the most massive galaxies.

However, many questions remain open and ALMA should be able to address them during the next decade:

- When were the very first massive and dusty systems assembled?
- Which fraction of these systems are in clusters or collapsing massive structures?
- Do we still miss a fraction of the star formation because of dust at very high redshift?
- How different is the physics of the star formation in high-z gas-rich galaxies fed by an intense accretion and affected by mergers compared to the local Universe?
- What is the metallicity of these early massive systems? How have they produced so quickly metals and dust?

This review is only a short summary of ALMA results, since cycle 0. It is thus highly incomplete and voluntarily biased towards the contribution of the french community.

MB acknowledges the PNCG and the SF2A for giving him the opportunity to present this review.

References

Aravena, M., Spilker, J. S., Bethermin, M., et al. 2016, Monthly Notices of the Royal Astronomical Society, 457, 4406
Béthermin, M., Daddi, E., Magdis, G., et al. 2015, A&A, 573, A113
Béthermin, M., De Breuck, C., Gullberg, B., et al. 2016, Astronomy and Astrophysics, 586, L7
Béthermin, M., Greve, T. R., De Breuck, C., et al. 2018, Astronomy and Astrophysics, 620, A115
Béthermin, M., Wang, L., Doré, O., et al. 2013, A&A, 557, A66
Bothwell, M. S., Maiolino, R., Peng, Y., et al. 2016, MNRAS, 455, 1156
Cunningham, D. J. M., Chapman, S. C., Aravena, M., et al. 2019, arXiv e-prints, arXiv:1906.02293
Daddi, E., Elbaz, D., Walter, F., et al. 2010, ApJ, 714, L118
Dekel, A. & Birnboim, Y. 2006, MNRAS, 368, 2
Dessauges-Zavadsky, M., Zamojski, M., Schaerer, D., et al. 2015, A&A, 577, A50
Di Matteo, P., Combes, F., Melchior, A. L., & Semelin, B. 2007, Astronomy and Astrophysics, 468, 61
Dunlop, J. S., McLure, R. J., Biggs, A. D., et al. 2017, Monthly Notices of the Royal Astronomical Society, 466, 861
Elbaz, D., Dickinson, M., Hwang, H. S., et al. 2011, A&A, 533, A119
Elbaz, D., Leiton, R., Nagar, N., et al. 2018, Astronomy and Astrophysics, 616, A110
Falgarone, E., Zwaan, M. A., Godard, B., et al. 2017, Nature, 548, 430
Franco, M., Elbaz, D., Béthermin, M., et al. 2018, Astronomy and Astrophysics, 620, A152
Genzel, R., Tacconi, L. J., Gracia-Carpio, J., et al. 2010, MNRAS, 407, 2091
Hashimoto, T., Laporte, N., Mawatari, K., et al. 2018, Nature, 557, 392
Heinis, S., Buat, V., Béthermin, M., et al. 2014, MNRAS, 437, 1268
Inoue, A. K., Shimizu, I., Tamura, Y., et al. 2014, The Astrophysical Journal, 780, L18
Jarugula, S., Vieira, J. D., Spilker, J. S., et al. 2019, The Astrophysical Journal, 880, 92
Kneissl, R., del Carmen Polletta, M., Martinache, C., et al. 2019, Astronomy and Astrophysics, 625, A96
Lagache, G., Cousin, M., & Chatzikos, M. 2018, Astronomy and Astrophysics, 609, A130
Laporte, N., Ellis, R. S., Boone, F., et al. 2017, The Astrophysical Journal, 837, L21
Le Fèvre, O., Abraham, R., Lilly, S. J., et al. 2000, Monthly Notices of the Royal Astronomical Society, 311, 565
Madau, P. & Dickinson, M. 2014, ARA&A, 52, 415
Magdis, G. E., Daddi, E., Béthermin, M., et al. 2012, ApJ, 760, 6
Maniyar, A. S., Béthermin, M., & Lagache, G. 2018, Astronomy and Astrophysics, 614, A39
Marrone, D. P., Spilker, J. S., Hayward, C. C., et al. 2018, Nature, 553, 51
Martinache, C., Rettura, A., Dole, H., et al. 2018, Astronomy and Astrophysics, 620, A198
Miller, T. B., Chapman, S. C., Aravena, M., et al. 2018, Nature, 556, 469
Nagao, T., Maiolino, R., De Breuck, C., et al. 2012, A&A, 542, L34
Narayanan, D., Turk, M., Feldmann, R., et al. 2015, Nature, 525, 496
Nesvadba, N. P. H., Cañameras, R., Kneissl, R., et al. 2019, Astronomy and Astrophysics, 624, A23
Noeske, K. G., Weiner, B. J., Faber, S. M., et al. 2007, ApJ, 660, L43
Oteo, I., Ivison, R. J., Dunne, L., et al. 2018, The Astrophysical Journal, 856, 72
Ouchi, M., Ellis, R., Ono, Y., et al. 2013, The Astrophysical Journal, 778, 102
Planck Collaboration, Aghanim, N., Altieri, B., et al. 2015, Astronomy and Astrophysics, 582, A30
Riechers, D. A., Bradford, C. M., Clements, D. L., et al. 2013, Nature, 496, 329
Sanders, D. B. & Mirabel, I. F. 1996, Annual Review of Astronomy and Astrophysics, 34, 749
Schinnerer, E., Groves, B., Sargent, M. T., et al. 2016, ApJ, 833, 112
Schreiber, C., Labbé, I., Glazebrook, K., et al. 2018, Astronomy and Astrophysics, 611, A22
Schreiber, C., Pannella, M., Elbaz, D., et al. 2015, A&A, 575, A74
Scoville, N., Lee, N., Vanden Bout, P., et al. 2017, The Astrophysical Journal, 837, 150
Strandet, M. L., Weiss, A., De Breuck, C., et al. 2017, The Astrophysical Journal, 842, L15

Strandet, M. L., Weiss, A., Vieira, J. D., et al. 2016, ApJ, 822, 80
Tacconi, L. J., Neri, R., Genzel, R., et al. 2013, ApJ, 768, 74
Vallini, L., Gallerani, S., Ferrara, A., Pallottini, A., & Yue, B. 2015, The Astrophysical Journal, 813, 36
Vieira, J. D., Marrone, D. P., Chapman, S. C., et al. 2013, Nature, 495, 344
Wang, T., Elbaz, D., Daddi, E., et al. 2016, The Astrophysical Journal, 828, 56
Wang, T., Schreiber, C., Elbaz, D., et al. 2019, Nature, 572, 211
Yang, C., Omont, A., Beelen, A., et al. 2017, A&A, 608, A144
Yang, C., Omont, A., Beelen, A., et al. 2016, Astronomy and Astrophysics, 595, A80
Zhang, Z.-Y., Romano, D., Ivison, R. J., Papadopoulos, P. P., & Matteucci, F. 2018, Nature, 558, 260

SF2A 2019
P. Di Matteo, O. Creevey, A. Crida, G. Kordopatis, J. Malzac, J.-B. Marquette, M. N'Diaye, O. Venot (eds)

CHARACTERIZATION OF EXOPLANETARY ATMOSPHERES WITH VLT-SPHERE

B. Charnay[1], M. Bonnefoy[2], A. Boccaletti[1], G. Chauvin [2,3], S. Lacour[1], M. Nowak[1] and VLT-SPHERE Consortium

Keywords: exoplanets, atmospheres, direct imaging, planetary formation

1 Introduction

Around 4000 exoplanets have been confirmed during the last 20 years and thousands of other planets should be discovered during the next decade by the Gaia,TESS, CHEOPS and PLATO missions. The analysis of exoplanetary atmospheres provides clues on their formation and evolution, allowing to understand their diversity and ultimately to place the Solar System in context with respect to all other known planetary systems. There are currently two main ways to analyse the atmosphere of an exoplanet. First in the case of very short periods taking advantage of the transit depth modulation in time and wavelength, and second for young massive ($\sim$10 Mjup) giant planets at large orbital separations (10-100 au) using high contrast direct imaging. In this context, the SPHERE (Spectro Polarimetric High contrast Exoplanet REsearch) instrument installed at the VLT (Beuzit et al. 2008, 2019) is a new generation high-contrast imaging instrument dedicated to the detection and spectroscopy of young giant exoplanets. First light was obtained in May 2014 and the instrument is on operation since February 2015. In section 2, we briefly described some characteristics of physics and chemistry of young giant planets. In section 3, we present the SPHERE instrument and results obtained during 5 years of operation. In section 4, we detail perspectives for the futur SPHERE upgrade its complementarity with GRAVITY.

2 Physics and chemistry of young giant planets

Planets are believed to originate from disks of gas and dust which surround young stars. Two main theoretical frameworks are proposed for planet formation. In the Core Accretion model (CA), solids made of the aggregation of dust and ice settle in the mid-plane of the disk to form solid cores which can attract the surrounding gas from the disk and create a giant planet. The Gravitational Instability (GI) considers instead that part of the disk can fragment and collapse to form a giant planet. The reality may be more complex, with potentially both mechanisms occuring in parallel. The thermal evolution of planets may be impacted by the formation mechanism, leading to differences for the luminosity and radius of young giant planets. Moreover, the atmospheric composition (i.e. metallicity and C/O) of planets formed by CA is expected to be different from the host star, depending on the mass of the core relative to the envelope, where the planet formed in the disk and how it interacted with it (Öberg et al. 2011). Probing the luminosity, radius and atmospheric composition of exoplanets therefore allows to test formation mechanisms.

Brown dwarfs are very useful to understand of the atmospheres of young giants. We expect that the physics and chemistry are very similar, the main difference being the mass so the gravity. The surface gravity of known young giant planets is typically one to two order of magnitude as low as that of field brown dwarfs. A key feature of the photometry of field brown dwarfs is the L-T transition. L dwarfs which are CO dominated appear

[1] LESIA, Observatoire de Paris, Université Paris Sciences et Lettres, CNRS, Université Paris Diderot, 5 Place Jules Janssen, 92190 Meudon, France
[2] IPAG, Grenoble, France
[3] Unidad Mixta Internacional Franco-Chilena de Astronomía, CNRS/INSU UMI 3386 and Departamento de Astronomía, Universidad de Chile, Casilla 36-D, Santiago, Chile

redder than T dwarfs which are CH4 dominated (see Fig. 1). The favored explanation for the L-T transition is linked to silicate and iron clouds. These clouds form in the photosphere of L dwarfs, blocking spectral windows and making these object red. However for colder objects as T dwarfs, they form below the photosphere and do not impact the emission spectra and colors. Young giant planets appear close to field brown dwarfs in color-magnitude diagram, but redder and the L-T transition seem to occur at a lower effective temperature (see Fig. 1). That could be due to the lower gravity making cloud optically thicker and delaying the L-T transition (Charnay et al. 2018). Photmetric observations are too limited to constrained the atmospheric properties of directly imaged planets. Spectra obtained by high contrast imaging instruments are required to make progresses.

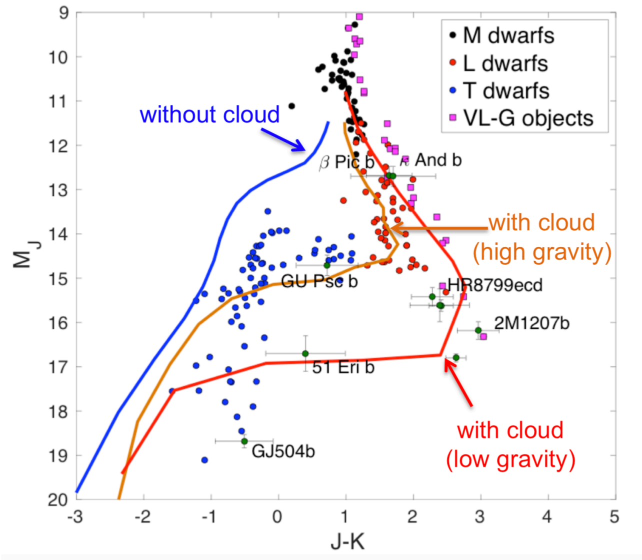

Fig. 1. Color–magnitude diagram of M, L, and T dwarfs with J - K colors plotted against the absolute J magnitude (MKO). M dwarfs are plotted as black dots, L dwarfs as red dots, T dwarfs as blue dots, low-gravity brown dwarfs as purple squares, and directly imaged substellar companions as green dots. The blue line was computed with spectra from Exo-REM assuming no clouds, log(g)=5, with Teff evolving from 400 to 2000 K. The orange (red) line was computed with silicate and iron clouds and log(g)=5 (4). Figure adapted from Charnay et al. (2018).

3 Five years of observations with VLT-SPHERE

3.1 Instrument SPHERE and SHINE program

Four last generation high-contrast instruments are currently operating: SPHERE at VLT, GPI on Gemini South, SCExAO on Subaru and MagAO on the Giant Magellan Telescope. Among them, SPHERE (Beuzit et al. 2008, 2019) can reach constrast lower than 10^{-5} by combining extrem adaptative optics with coronography (apodized-Lyot or four-quadrant coronograph). The instrument has three science subsystems:
- the infrared dual-band imager and spectrograph (IRDIS) in YJHK
- an integral field spectrograph (IFS) in Y-J with a spectral resolution R=30-50
- an imaging polarimeter (ZIMPOL).

IRDIS and IFS can be used simultaneously enabling angular differential and/or spectral imaging technics to improve the contrast. The SPHERE consortium Guaranteed Time Observations consists of 260 observing nights over 5 years. The SpHere INfrared survey survey for Exoplanets (SHINE) is the main program of the SPHERE GTO and includes 200 observing nights to conduct a large near-infrared survey of 400-600 young, nearby stars. The science goals are to characterize known planetary systems (architecture, orbit, stability, luminosity, atmosphere), to search for new planetary ones, ultimately to determine the occurrence and orbital and mass function properties of the wide-orbit, giant planet population as a function of the stellar host mass and age.

3.2 Results for the characterization of exoplanetary atmospheres

SHINE observing program led to the discovery of two new exoplanets:
- HIP 65426b (Chauvin et al. 2017), a massive (6-12 Mjup) and warm (Teff$\sim$1600 K) giant planet orbiting at a wide distance of a young star ($\sim$14 Myr). It spectral type correspond to a mid-L dwarf, intermediate between β Pictoris b and HR8799bcde. This object is quite red and its spectral fitting requires thick clouds (see Fig. 2).
- PDS 70 b (Keppler et al. 2018; Müller et al. 2018), a protoplanet discovered in the cavity of a transition disk around PDS 70 ($\sim$5 Myr, see Fig. 3). Atmospheric models have difficulties to reproduce the red spectrum of this very young object which must be surrounded by thick clouds. They predict an unphysically large radius (1.4-3.7 Rjup). The high luminosity of this young object might be due to on-going accretion and/or emission from a circumplanetary disk. A luminosity peak in Hα at the position of PDS 70 b has been detected with MagAO (Wagner et al. 2018), suggesting hydrogen accretion at a rate of $\sim 10^{-8}$ Mjup/yrs. Observations with VLT-SINFONI also suggests the possible presence of a circumplanetary disk (Christiaens et al. 2019). PDS 70 is an outstanding system for testing theories of planetary formation and planet-disk interaction.

In addition to these two new planets, SPHERE obtained photometry and spectra for a dozen of already known exoplanets and brown dwarfs companions, including HR8799 bcde (Zurlo et al. 2016; Bonnefoy et al. 2016), β Pictoris b (Lagrange et al. 2019), GJ504b (Bonnefoy et al. 2018), 51 Eri b (Samland et al. 2017) and HD206893b (Delorme et al. 2017). A common feature of young exoplanets is that they appear redder and have weaker water spectral features than field brown dwarfs, likely due to the presence of thicker clouds.

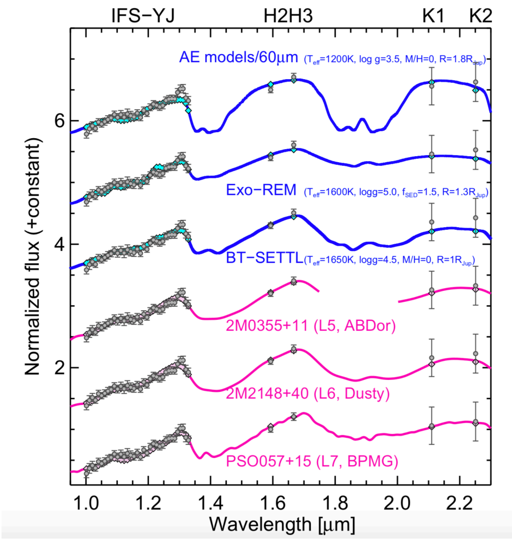

Fig. 2. SPHERE near-infrared spectrum of HIP 65426 b compared with (i) the best-fit empirical spectra in pink, and (ii) the best-fit model atmosphere from the Exo-REM, PHOENIX BT-Settl-2014 and thick AE cloud atmospheric models in blue. Figure from (Chauvin et al. 2017).

4 Perspectives

4.1 Complementarity with GRAVITY/VLTI

GRAVITY consortium recently achieved the first detection of an exoplanet (HR8799e) by optical interferometry using VLTI (GRAVITY Collaboration et al. 2019a). They obtained very accurate astrometry (0.1 mas precision) and a spectrum in K band at R=500, a resolution typically 10 times higher than GPI and SPHERE. This spectrum revealed the presence of thick clouds and CO in the atmosphere of HR8799e. GRAVITY observations were also performed for β Pictoris b (GRAVITY Collaboration et al. 2019b) providing a high quality K spectrum, showing several CO features (see Fig 4). Atmospheric retrieval from these data suggests a substellar C/O value, favoring a formation by core accretion. GRAVITY clearly is a powerful instrument for atmospheric characterization in K band. It is very complementary to SPHERE which covers YJH for spectroscopy, and which is less time-consuming and more efficient for exoplanet detection.

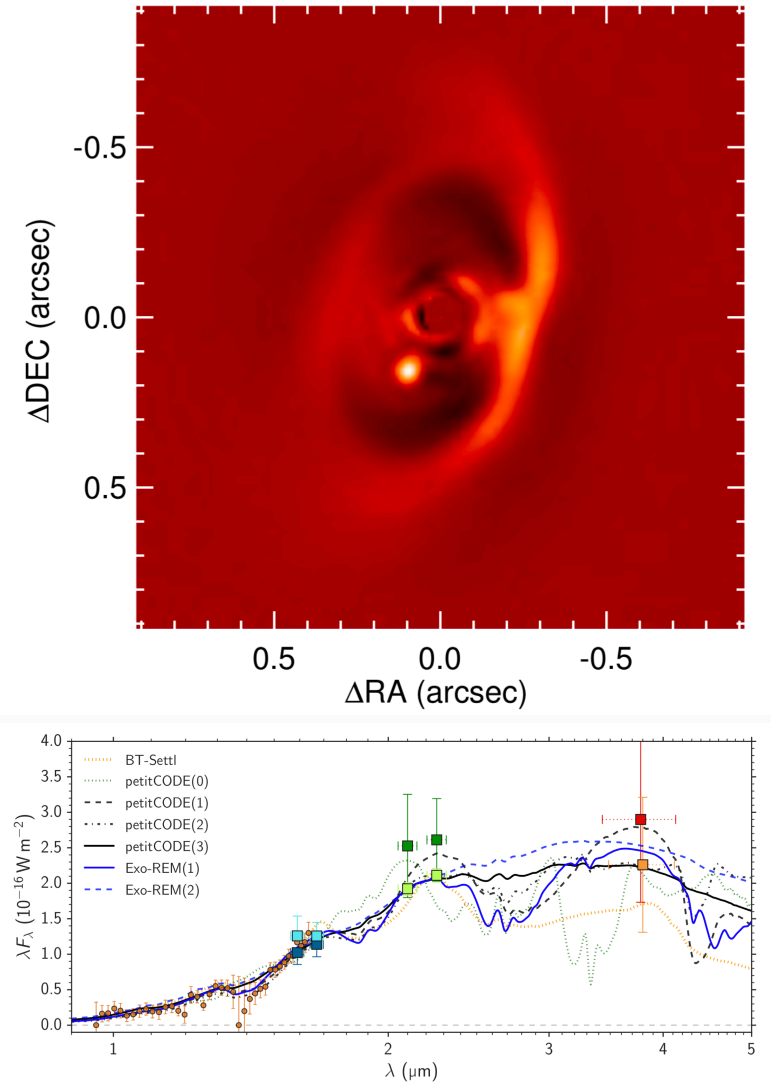

Fig. 3. Top panel: IRDIS combined K1K2 image of PDS 70 showing the planet inside the gap of the disk around PDS 70. Bottom panel: spectral energy distribution of PDS 70 b as a function of wavelength constructed from IFS spectra (orange points), IRDIS (light/dark blue and green), NaCo (red), and NICI (orange). Plotted are best model fits. Figures from (Müller et al. 2018).

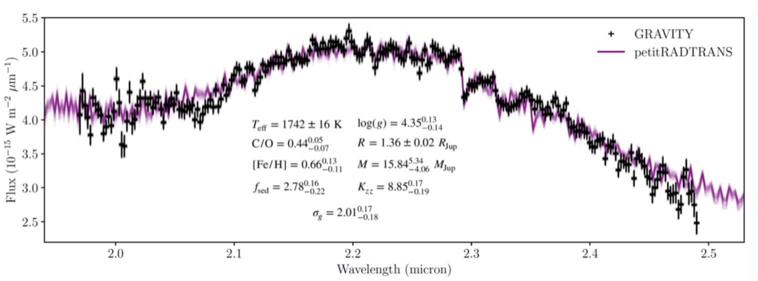

Fig. 4. K spectrum of β Pictoris b from GRAVITY data compared with the best-fit spectrum from PetitRADTRANS. Figure from (GRAVITY Collaboration et al. 2019b).

4.2 SPHERE upgrades

Upgrades of SPHERE (named SPHERE+) are considered in order to decrease the inner working angle and to look at fainter objects. There is also the possibility to add a new medium resolution spectrometer, which would increase the detection and characterization capabilities. Finally, the project HiRISE (PI: A. Vigan) aims at coupling SPHERE to CRIRES+ (both on UT3). This would allow to combine high constrast imaging and high-resolution spectroscopy to characterize exoplanetary atmospheres.

5 Conclusion

The instrument SPHERE has been in operation since five years, leading to more than 80 refereed publications young giant planets, disks and solar system bodies. It detected two new exoplanets, including PDS 70 b, which is a unique case to test models of planetary formation and planet-disk interactions. A catalogue of atmospheric spectra of young giant planets has now been collected from SPHERE and other high-constrast instruments. These observations allow to cover the equivalent of the L-T sequence of brown dwarfs. A key feature for most of young giant exoplanets is the presence of quite thick clouds. Clouds also constitute a major issue for the characterization of transiting exoplanets, limiting our ability to measure molecular abundances. Two main strategies are favored to probe cloudy atmospheres with futures instruments: either by looking at longer wavelengths where clouds are optically thinner (this will be the case with JWST and ARIEL) or by doing medium/high resolution spectroscopy to separate molecular lines. This last option will be done for direct imaging by SPHERE+ and the ELTs.

References

Beuzit, J.-L., Feldt, M., Dohlen, K., et al. 2008, in Proc. SPIE, Vol. 7014, Ground-based and Airborne Instrumentation for Astronomy II, 701418

Beuzit, J. L., Vigan, A., Mouillet, D., et al. 2019, arXiv e-prints, arXiv:1902.04080

Bonnefoy, M., Perraut, K., Lagrange, A. M., et al. 2018, Astronomy and Astrophysics, 618, A63

Bonnefoy, M., Zurlo, A., Baudino, J. L., et al. 2016, Astronomy and Astrophysics, 587, A58

Charnay, B., Bézard, B., Baudino, J. L., et al. 2018, The Astrophysical Journal, 854, 172

Chauvin, G., Desidera, S., Lagrange, A.-M., et al. 2017, A&A, 605, L9

Christiaens, V., Casassus, S., Absil, O., et al. 2019, Monthly Notices of the Royal Astronomical Society, 486, 5819

Delorme, P., Schmidt, T., Bonnefoy, M., et al. 2017, Astronomy and Astrophysics, 608, A79

GRAVITY Collaboration, Lacour, S., & et al. 2019a, Astronomy and Astrophysics, 623

GRAVITY Collaboration, Nowak, M., & et al. 2019b, submitted

Keppler, M., Benisty, M., Müller, A., et al. 2018, Astronomy and Astrophysics, 617, A44

Lagrange, A. M., Boccaletti, A., Langlois, M., et al. 2019, Astronomy and Astrophysics, 621, L8

Müller, A., Keppler, M., Henning, T., et al. 2018, Astronomy and Astrophysics, 617, L2

Öberg, K. I., Murray-Clay, R., & Bergin, E. A. 2011, The Astrophysical Journal, 743, L16

Samland, M., Mollière, P., Bonnefoy, M., et al. 2017, A&A, 603, A57

Wagner, K., Follete, K. B., Close, L. M., et al. 2018, The Astrophysical Journal, 863, L8

Zurlo, A., Vigan, A., Galicher, R., et al. 2016, Astronomy and Astrophysics, 587, A57

SF2A 2019
P. Di Matteo, O. Creevey, A. Crida, G. Kordopatis, J. Malzac, J.-B. Marquette, M. N'Diaye, O. Venot (eds)

X-RAYS FROM THE GALACTIC CENTER AND ACTIVITY OF THE CENTRAL SUPERMASSIVE BLACK HOLE

M. Clavel[1]

Abstract. Relics of intense past activity have been revealed by the X-ray observations covering the inner regions of our Galaxy provided by *XMM-Newton* and *Chandra* observatories. On the one hand, there is a non-thermal emission tracing the echoes of outbursts from the supermassive black hole, Sagittarius A*, that happened in the last centuries and whose light is currently propagating in the central molecular zone. On the other hand, and on even longer timescales, the activity of our Galactic nucleus shaped lobes and chimneys of hot gas extending on both sides of the Galactic plane. The exact origin of these structures is rather uncertain, but they could be the channel through which matter and energy is transported from the inner regions of our Galaxy into the large *Fermi* bubbles seen in γ-rays.

Keywords: Galaxy: center - X-rays: general.

1 Introduction

At about 8 kpc, the Galactic center is the closest galactic nucleus and it is therefore an excellent laboratory to study the complexity of these inner regions and, in particular, the interactions between a supermassive black hole and its environment. Since their respective launch about two decades ago, *XMM-Newton* and *Chandra* have been revealing an increasing number of X-ray features in the central degrees of our Galaxy, including numerous point and extended sources, such as X-ray binaries, stellar clusters or supernova remnants, but also more diffuse emission having thermal or non-thermal origins (see e.g. Ponti et al. 2015). Radio and sub-millimeter observations of this exact same region show that it also contains dense molecular gas and this is why it has been named the Central Molecular Zone (CMZ, Morris & Serabyn 1996).

At the very center, there is the supermassive black hole, Sagittarius A*, which is one of the very faint point sources seen in X-rays. Indeed, the $4 \times 10^6\,\mathrm{M}_\odot$ black hole Sgr A* is the least luminous known supermassive black hole. While its quiescent X-ray luminosity is around $L_X \sim 10^{33}\,\mathrm{erg\,s^{-1}}$, the X-ray counterpart of Sgr A* also experiences daily flares having a timescale of about an hour and during which the X-ray luminosity can increase by up to two orders of magnitude (e.g. Neilsen et al. 2013; Haggard et al. 2019, and references therein). This means that, since the advent of X-ray astronomy, the emission of Sgr A* has remained at least eight orders of magnitude lower than its Eddington luminosity: it is presently a dormant supermassive black hole.

Therefore, the current feedback from Sgr A* onto the Galactic center environment is expected to be extremely weak. Nevertheless, detailed studies of its surroundings have revealed signatures of important feedback, attesting to a higher level of activity from the Galactic nucleus in the past, with different tracers probing timescales from centuries to million years ago. We review the observations of the corresponding features detected in X-rays, namely: light echoes tracing the most recent past (Section 2) and bipolar outflows generated over much longer timescales (Section 3). The constraints obtained on the past activity of Sgr A* are then summarized in Section 4, along with relics seen at other wavelengths.

2 X-ray echoes tracing several short outbursts in the last centuries

The past X-ray emission from Sgr A* is propagating in the inner region of our Galaxy, where it is reflected by the dense molecular clouds of the CMZ, creating light echoes. The X-ray spectrum of the reflecting clouds is then

[1] Univ. Grenoble Alpes, CNRS, IPAG, F-38000 Grenoble, France

characterized by a continuum component created by the Compton scattering of the incident signal, absorbed at low energy, and on top of which there are fluorescent emission lines, including a strong Fe Kα line at 6.4 keV (see e.g. Sunyaev & Churazov 1998). This fluorescent line is therefore a powerful tool to trace the echoes of Sgr A*'s past outbursts in the CMZ and the extent of this region combined with the sensitivity of the current instruments allows to probe the brightest events that occurred in the last thousand years.

The 6.4 keV emission correlated with molecular clouds has been detected across the whole CMZ and, in particular, towards the main molecular complexes: Sgr A, Sgr B and Sgr C (see Figure 1; Terrier et al. 2018, and references therein). Several attempts were made to constrain Sgr A*'s past light curve from the Fe Kα flux measured in individual molecular clouds but, due to the lack of constraints on the line-of-sight position of these clouds, this technique led to divergent results in terms of age and duration of the corresponding events (e.g. Ponti et al. 2010; Capelli et al. 2012; Ryu et al. 2013). The next step was then to use the variability of the echoes, also detected in an increasing number of molecular structures (e.g. Inui et al. 2009; Ponti et al. 2010; Clavel et al. 2013, 2014; Zhang et al. 2015; Chuard et al. 2018; Terrier et al. 2018), to better constrain Sgr A*'s past light curve. This alternative technique consists in studying the fine X-ray variations to spotlight the simultaneity in the illuminated cloud behaviors. Using *Chandra* high spatial resolution, two different time behaviors were identified among the brightest clouds of the Sgr A complex (Clavel et al. 2013). The constraints implied on both the density and the distribution of the clouds make these two behaviors no longer compatible with one single illuminating event. The conclusion of this work is that at least two distinct outbursts, having a luminosity of a few 10^{39} erg s^{-1} and a duration of about 2 and more than 10 years, are currently propagating in the inner region of our Galaxy (Clavel et al. 2013). To have more information about these events, a similar systematic analysis was performed making use of the light curves obtained across the whole CMZ with *XMM-Newton* from 2000 to 2012. This study concludes that all bright clouds are significantly varying over the 12-year period (see Figure 1), so the existence of a putative bright event lasting for several decades and currently propagating in this region is excluded. Moreover, all variations observed are compatible with the two time behaviors described previously and can therefore be explained by the same short events (Terrier et al. 2018).

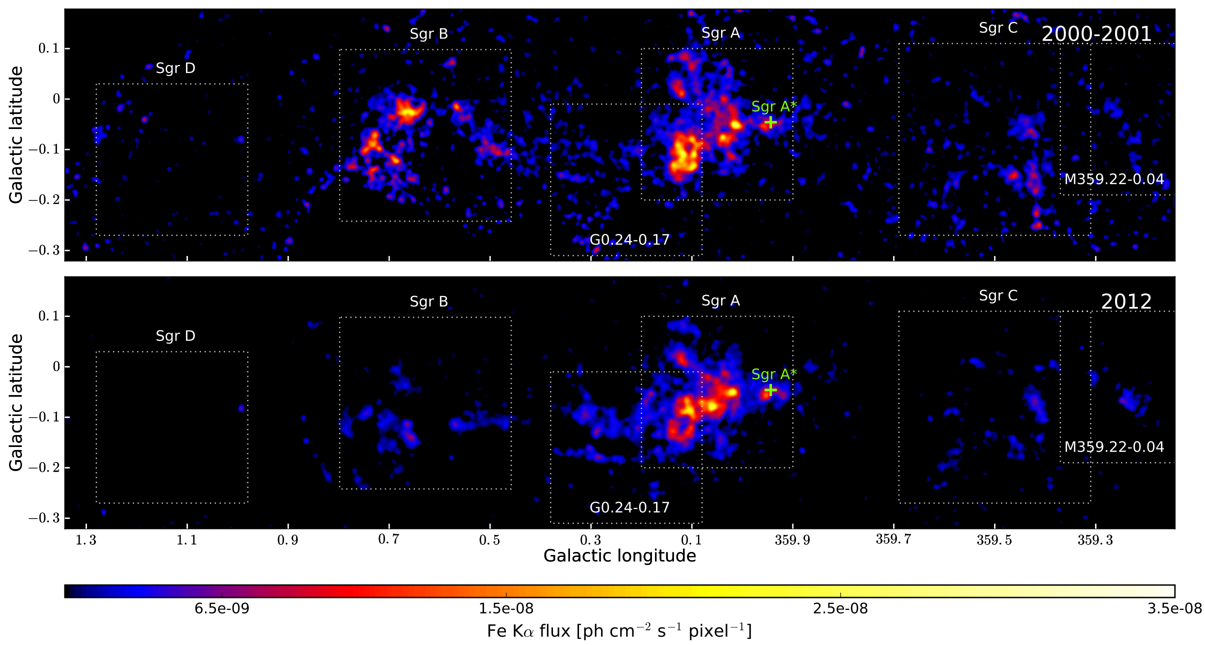

Fig. 1. Background- and continuum-subtracted intensity maps of the central molecular zone measured by *XMM-Newton* at 6.4 keV in 2000–2001 (**Top**) and 2012 (**Bottom**). The dotted square regions highlights areas where significant variations were detected. Figure published by Terrier et al. (2018).

Since the spectral shape of the reflected emission depends on the line-of-sight position of the reflecting clouds, dedicated spectral modeling can provide the age of the events identified through variability studies. The reflected spectra expected for different geometries were computed using Monte Carlo simulations and then used to fit the spectra observed in Sgr B and Sgr C (Walls et al. 2016; Chuard et al. 2018). This technique provided the line-of-sight position of several clumps. The 3D distribution obtained is only compatible with the presence of at least two different past events from Sgr A*, in full agreement with the results described in the previous paragraph. Furthermore, all slow varying features are compatible with being illuminated by the older event occurring about 240 years ago, while the ones seeing faster variations could be illuminated by a more recent, and probably shorter event, occurring about 140 years ago (Chuard et al. 2018). These results rule out the single-event scenario assumed to derive the line-of-sight position of the reflecting features from alternative techniques (see e.g. Churazov et al. 2017), but it does not exclude the existence of a putative third event that would be propagating in more distant portions of the CMZ than the ones investigated by Chuard et al. (2018).

As a summary, the X-ray signal reflected within the CMZ attests than the illuminating source experienced more than one order of magnitude variations over few years only, and several short events producing hard X-rays that are at least a million times brighter than Sgr A*'s quiescent state are needed to explain this variability. Possible alternatives to the supermassive black hole to produce such outbursts have been discussed and discarded based on the energetic involved and the spectral shape required for these events (see Terrier et al. 2010; Clavel et al. 2013; Mori et al. 2015; Zhang et al. 2015; Krivonos et al. 2017, for more details, including spectral constraints derived from *INTEGRAL* and *NuSTAR* hard X-ray observations). Therefore, there is strong evidence that Sgr A* has been brighter in the last centuries but the origin of these past outbursts remains uncertain. Several scenarios have been proposed (e.g. involving partial or full tidal disruptions of stars, planets, asteroids or gas clouds, Yu et al. 2011; Zubovas et al. 2012; Czerny et al. 2013), but a theoretical model matching all the constraints recently derived from the observations, in terms of recurrence, duration, luminosity and spectrum of Sgr A*'s past events has not yet been published.

3 X-ray lobes and chimneys carved by an enhanced level of activity in the last million years.

Periods of intense activity from the supermassive black hole are also expected to generate outflows that could possibly carve high-energy features in the Galactic nucleus environment, visible as an excess of thermal emission.

The first possible such signature has been detected close to Sgr A* and is known as the X-ray lobes (Baganoff et al. 2003; Morris et al. 2003; Markoff 2010; Heard & Warwick 2013; Ponti et al. 2015). They are 15-pc bipolar lobes extending from Sgr A* towards the Galactic north and south, with a plasma temperature $kT \sim 0.7{-}1$ keV, and are showing a strong pressure gradient (see Figure 2, left). Due to their apparent symmetry about the Galactic plane, these structures have been interpreted as outflowing gas originating from the central few parsecs of our Galaxy. This region contains the supermassive black hole and a young cluster of massive stars, as well as dense molecular gas forming the so-called circumnuclear disk (CND, see Genzel et al. 2010, for a review). The location and shape of the CND is such that it could have collimated an isotropic outflow emanating from Sgr A* itself or from its immediate vicinity, creating the bipolar lobes of hot plasma (see e.g. Morris et al. 2003). Assuming that the X-ray gas is filling the whole volume of the lobes, and considering an outflow velocity comparable to the speed of sound set by the gas temperature, the thermal energy of each lobe is $\sim 6 \times 10^{50}$ erg and they have a sound-crossing time $t_s \sim 3 \times 10^4$ yr (Ponti et al. 2019). The average power of the outflow is therefore allowing for several possible origins.

Over the time scale needed for the X-ray lobes to form, two continuous processes can be considered. First, winds from massive stars in the central parsec could be an important contribution in terms of energetic since their velocities are high enough to produce X-rays when they interact with the interstellar medium. However, the stellar cluster being several million years old and the lobes only $\sim 3 \times 10^4$ years old, this scenario does not allow to reproduce the morphology of the X-ray lobes and in particular their pressure gradient (e.g. Markoff 2010). The second possible continuous process is a putative outflow generated by the current level of accretion onto Sgr A*. Indeed, only a very small fraction of the material captured at the Bondi radius is expected to be effectively accreted onto Sgr A* (Wang et al. 2013), so the rest could be converted into outflows sculpting the environment of the black hole. If the energy budget could match the one needed to produce the lobes, again, the shape of the X-ray features is not in favor of this second continuous scenario but is rather pointing to explosive or outbursting events (e.g. Ponti et al. 2015).

Therefore, episodic scenarios have also been proposed. For instance, the X-ray lobes could be a supernova remnant (SNR). Indeed, the central cluster is expected to produce between one and ten supernova explosions every 10^5 years, so these events could contribute to power the lobes (e.g. Ponti et al. 2015). In this case, the compact object created during this event could be one of the known X-ray sources in the vicinity of Sgr A*. Several candidates have been proposed and a hydrodynamic simulation taking into account the complexity of

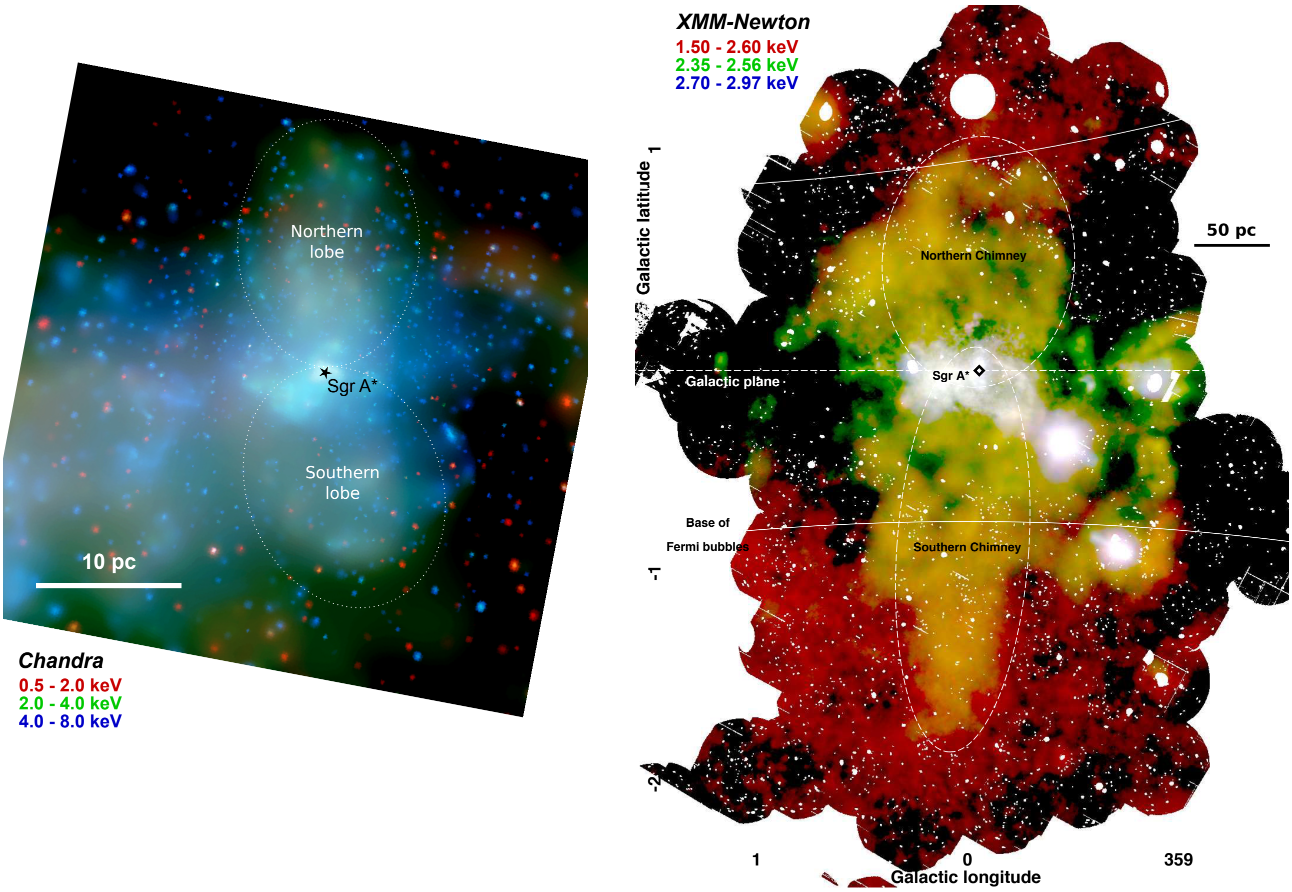

Fig. 2. Left: *Chandra* observation of the 15-pc X-ray lobes. Figure adapted from Muno et al. (2004). **Right:** *XMM-Newton* survey of the 160-pc X-ray chimneys. Figure published by Ponti et al. (2019). Both panels are displayed in Galactic coordinates. In each image, the three colors are tracing different X-ray energies soft (red) to hard (blue, see the corresponding inserts in each panel). These two bipolar structures are roughly symmetric about the Galactic plane, with the X-ray lobes nested at the base of the X-ray chimneys (in the right panel, the 15-pc lobes are the white tiny features surrounding Sgr A*). The slight asymmetry in the shape of the X-ray lobes can be explained by foreground absorption (Ponti et al. 2015), while the differences between the northern and southern chimneys could result from asymmetries in the dense interstellar medium distribution (Ponti et al. 2019).

the Galactic center environment has been able to reproduce the morphology of the X-ray lobes with a SNR that would be associated with the young magnetar SGR J1745–2900 (Yalinewich et al. 2017). From the X-ray point of view, this scenario is robust. However, no non-thermal radio counterpart of the lobes has been detected and this would be a major puzzle if the young supernova origin is confirmed (e.g. Ponti et al. 2015). This is why past outbursts from Sgr A* are also considered as a relevant hypothesis. The estimated age of the X-ray lobes is the same order of magnitude as the recurrence time computed for tidal disruptions of stars by the supermasssive black hole at the Galactic center ($1\!-\!2 \times 10^4$ yr, Alexander 2005), so one tidal disruption event, with a luminosity close to the Eddington one, could be responsible for the corresponding outflow. Nevertheless, less luminous but more frequent outbursts, such as the ones characterized from the X-ray echoes (see Section 2), can also be considered as a viable scenario. If we further assume that more prominent outbursts happened every 5000 years or so, such a collection of past events would also provide an explanation for the brighter knots observed within both lobes (Markoff 2010; Ponti et al. 2015). So the 15-pc X-ray lobes could be tracing Sgr A*'s past activity over the last $\sim 3 \times 10^4$ years.

Furthermore, all the energetic processes, either continuous or episodic, that have been described in the previous paragraphs are also expected to occur over much longer time scales, and could therefore have shaped even more extended structures. The first hint of such signatures has been an excess of soft X-ray emission detected by *Suzaku* to the south of the Galactic center. Its X-ray spectrum is consistent with a recombining plasma, its absorption indicates that it is located in the inner regions of our Galaxy and a past starburst activity or an episode of enhanced activity from Sgr A* have been proposed as most plausible origins (Nakashima et al. 2013). More recently, a similar excess interpreted as a magnetized hot gas outflow from the Galactic center was also detected by *Suzaku* towards the Galactic north (Nakashima et al. 2019). The high-latitude survey performed by *XMM-Newton* in 2016–2018 confirms the existence of these brighter regions and revealed that they are part of a 160-pc bipolar structure connected to the central region and extending on both sides of the Galactic plane (see Figure 2, right). These features, called the X-ray chimneys, have a plasma temperature $kT \sim 0.7$ keV and no pressure gradient is detected within them, which means that they are likely close to hydrostatic equilibrium. Their thermal energy is about 4×10^{52} erg and their sound crossing time $t_s \sim 3 \times 10^5$ yr, so the average power of the corresponding outflow is possibly only about a factor five greater than the one derived for the 15-pc lobes (Ponti et al. 2019). The energetic events shaping the X-ray chimneys could therefore be very similar to the ones discussed as possible origins of the X-ray lobes, and the lobes could even trace the most recent episode of energy injection into the chimneys.

However, the base of the chimneys is likely not limited to the X-ray lobes but could instead correspond to a $\sim$ 50-pc region surrounding Sgr A*. So, outflows from past energetic events, such as supernova explosions, occurring in this wider region could also be injected into the chimneys. Furthermore, Ponti et al. (2019) suggested that the X-ray chimneys could have transported powerful outflows from the Galactic center into the Halo, so the total energy conveyed by this channel could be greater than the one still radiating today. This scenario is supported by *ROSAT*, *Suzaku*, *Chandra* and *XMM-Newton* detections of X-ray emission at even higher latitudes, forming what could be the base of the *Fermi* bubbles (see Figure 2, right; Ponti et al. 2019, and references therein). If confirmed the power transported by the chimneys could be up to four orders of magnitude greater than the one computed from their X-ray emission (e.g. Su et al. 2010). Such powerful outflows could be associated with star formation processes at the Galactic center in the last few million years, and the contribution from Sgr A* could be limited. Nevertheless, scenarios involving the most extreme events such as tidal disruptions of stars by the supermassive black hole or periods of intense accretion transforming the Galactic center into an active galactic nucleus (AGN) cannot be excluded (see also Section 4).

4 Conclusions

By studying the X-ray features present in the inner regions of our Galaxy, it is possible to constrain the duty cycle of our dormant supermassive black hole.

The X-ray light emitted by Sgr A* in the last centuries is still propagating in the central molecular zone, generating X-ray echoes. The variability and the spectral properties of this reflected emission reveals the existence of several short outbursts from Sgr A* over the corresponding period. Despite an increasing precision in the description of these past events, their exact nature is still unknown.

The outflows generated by the past activity of our Galactic nucleus are also expanding away from the center, carving X-ray thermal features. The lobes and chimneys detected in the central degrees suggest periods of enhanced activity from the central region over the last million years. However, the link with Sgr A*'s past activity is uncertain as processes associated with stellar formation and supernova explosions have also been proposed. So, the energy levels derived from these X-ray structures can be considered as upper limits on the past luminosity of the supermassive black hole.

This review focused only on X-ray features and is therefore not exhaustive since relics of past activity from our Galactic nucleus have also been detected at other wavelengths. This is for instance the case of the *Fermi* bubbles already mentioned in Section 3. These large bubbles detected in γ-rays extend over ~ 10 kpc towards the Galactic poles and were likely generated by an important injection of energy in the last ten million years, such as could have been produced by past accretion events onto Sgr A* or a nuclear starburst (Su et al. 2010). If these two scenarios are able to reproduce the γ-ray emission, it is not the case of the Hα emission detected along the Magellanic Stream. The latter is too bright to be the result of stellar formation and favors an AGN-like activity of the supermassive black hole, with an intense UV radiation emitted few million years ago (Bland-Hawthorn et al. 2013). Therefore, it is likely that the gaseous accretion disk that triggered the formation of the central stellar cluster about six million years ago also significantly increased the accretion rate onto Sgr A*, creating a period of intense past activity that likely contributes to the large X-ray and γ-ray relics detected in the Galactic environment.

MC acknowledges financial support from the French National Research Agency in the framework of the "Investissements d'avenir" program (ANR-15-IDEX-02) and from CNES.

References

Alexander, T. 2005, Phys. Rep., 419, 65
Baganoff, F. K., Maeda, Y., Morris, M., et al. 2003, ApJ, 591, 891
Bland-Hawthorn, J., Maloney, P. R., Sutherland , R. S., & Madsen, G. J. 2013, ApJ, 778, 58
Capelli, R., Warwick, R. S., Porquet, D., Gillessen, S., & Predehl, P. 2012, A&A, 545, A35
Chuard, D., Terrier, R., Goldwurm, A., et al. 2018, A&A, 610, A34
Churazov, E., Khabibullin, I., Sunyaev, R., & Ponti, G. 2017, MNRAS, 465, 45
Clavel, M., Soldi, S., Terrier, R., et al. 2014, MNRAS, 443, L129
Clavel, M., Terrier, R., Goldwurm, A., et al. 2013, A&A, 558, A32
Czerny, B., Kunneriath, D., Karas, V., & Das, T. K. 2013, A&A, 555, A97
Genzel, R., Eisenhauer, F., & Gillessen, S. 2010, Reviews of Modern Physics, 82, 3121
Haggard, D., Nynka, M., Mon, B., et al. 2019, arXiv e-prints, arXiv:1908.01781
Heard, V. & Warwick, R. S. 2013, MNRAS, 434, 1339
Inui, T., Koyama, K., Matsumoto, H., & Tsuru, T. G. 2009, PASJ, 61, S241
Krivonos, R., Clavel, M., Hong, J., et al. 2017, MNRAS, 468, 2822
Markoff, S. 2010, Proceedings of the National Academy of Science, 107, 7196
Mori, K., Hailey, C. J., Krivonos, R., et al. 2015, ApJ, 814, 94
Morris, M., Baganoff, F., Muno, M., et al. 2003, Astronomische Nachrichten Supplement, 324, 167
Morris, M. & Serabyn, E. 1996, ARA&A, 34, 645
Muno, M. P., Baganoff, F. K., Bautz, M. W., et al. 2004, ApJ, 613, 326
Nakashima, S., Koyama, K., Wang, Q. D., & Enokiya, R. 2019, ApJ, 875, 32
Nakashima, S., Nobukawa, M., Uchida, H., et al. 2013, ApJ, 773, 20
Neilsen, J., Nowak, M. A., Gammie, C., et al. 2013, ApJ, 774, 42
Ponti, G., Hofmann, F., Churazov, E., et al. 2019, Nature, 567, 347
Ponti, G., Morris, M. R., Terrier, R., et al. 2015, MNRAS, 453, 172
Ponti, G., Terrier, R., Goldwurm, A., Belanger, G., & Trap, G. 2010, ApJ, 714, 732
Ryu, S. G., Nobukawa, M., Nakashima, S., et al. 2013, PASJ, 65, 33
Su, M., Slatyer, T. R., & Finkbeiner, D. P. 2010, ApJ, 724, 1044
Sunyaev, R. & Churazov, E. 1998, MNRAS, 297, 1279
Terrier, R., Clavel, M., Soldi, S., et al. 2018, A&A, 612, A102
Terrier, R., Ponti, G., Bélanger, G., et al. 2010, ApJ, 719, 143
Walls, M., Chernyakova, M., Terrier, R., & Goldwurm, A. 2016, MNRAS, 463, 2893
Wang, Q. D., Nowak, M. A., Markoff, S. B., et al. 2013, Science, 341, 981
Yalinewich, A., Piran, T., & Sari, R. 2017, ApJ, 838, 12
Yu, Y.-W., Cheng, K. S., Chernyshov, D. O., & Dogiel, V. A. 2011, MNRAS, 411, 2002
Zhang, S., Hailey, C. J., Mori, K., et al. 2015, ApJ, 815, 132
Zubovas, K., Nayakshin, S., & Markoff, S. 2012, MNRAS, 421, 1315

SF2A 2019
P. Di Matteo, O. Creevey, A. Crida, G. Kordopatis, J. Malzac, J.-B. Marquette, M. N'Diaye, O. Venot (eds)

MOLECULAR COLLISIONAL EXCITATION: THEORY, EXPERIMENT AND OBSERVATIONS

A. Faure[1]

Abstract.
For half a century, astrophysical molecules have been used as a proxy to understand both the chemistry and the physics of astronomical environments, from comets to star forming regions and external galaxies. In the last decade, significant progress has been made in our description of collisional excitation, thus contributing to the design of new molecular line diagnostics. In this article, we review a number of recent results in the field of molecular collisional excitation. Comparison between theory and experiment is presented for the benchmark CO molecule. We also illustrate through radiative transfer calculations that a good knowledge of (de)excitation rates allows to model strongly non-thermal spectra and to potentially detect new molecules. Finally, upcoming exciting perspectives in the field are evoked.

Keywords: ISM: abundances, ISM: molecules, astrochemistry, molecular data, molecular processes.

1 Introduction

The first extraterrestrial molecule, C_2, was discovered in 1864 in comet Temple by Donati (1864). This was only a few years after the identification of atomic lines in the solar spectrum and well before the advent of quantum mechanics. The first interstellar molecules, CH and CN, were identified much later in the diffuse interstellar medium (ISM) (McKellar 1940). However, the realization that molecules are ubiquitous in the Universe started only in the late 1960s and early 1970s with the opening up of other wavelengths than the visible and the discovery of CO, H_2O, NH_3, etc. Microwave and infrared observations then revealed the unanticipated presence of a variety of diatomic and polyatomic molecules, molecular ions and radicals in the ISM, both in the gas-phase and on the surface of submicron-sized solid particles (dust grains). To date, more than 200 different interstellar molecules (not including isotopologues) have been detected in the gas-phase, mainly organics i.e. carbon-bearing, and containing up to 13 atoms. In addition, larger molecules with 50-100 atoms known as polycyclic aromatic hydrocarbons (PAHs) and fullerenes have been identified. Dozens of molecules are also identified in the atmospheres of cool stars, planets and comets and in proto-planetary disks. The direct analysis of carbonaceous meteorites has finally revealed that these contain an amazing variety of complex organics, including prebiotic molecules such as amino acids.

The identification of interstellar molecules entirely relies on spectroscopy. In the gas-phase, molecular lines can appear in emission or absorption, depending on the wavelength of the transition and on the physical conditions along the line of sight. The translation of the observed intensities to the molecular column density (i.e. the integration of the abundance over the line of sight) requires to understand the transport of radiation through the astronomical source. A general property of astronomical spectra is that the molecular energy level populations are rarely at local thermodynamical equilibrium (LTE). At LTE, the molecular excitation i.e. the relative number of molecules in different energy levels is described by a single temperature through the Boltzmann equation. In interstellar space, the density is usually so low that the frequency of inelastic collisons is insufficient to maintain LTE. Deviations from LTE, including strong deviations like maser phenomena, are thus very natural in star-forming regions. In these conditions, analyzing a spectrum requires to solve simultaneously the radiative transfer equation and a set of statistical equilibrium equations. Solving the statistical equilibrium in turn necessitates the avaibility of the relevant molecular data. In addition to spectroscopic parameters,

[1] Univ. Grenoble Alpes, CNRS, IPAG, F-38000 Grenoble, France

the state-to-state rate coefficients for collisional (de)excitation by the most abundant species (H, H_2 and free electrons for the ISM) are of critical importance. These coefficients are extremely difficult to measure in the laboratory and astronomical models rely almost exclusively on theoretical calculations.

The present article is concerned with recent advances that have occurred in the field of molecular excitation. These studies were highly motivated by the rapid progress in astronomical instrumentation and, in particular, the recent opening of the submillimetre and far-infrared spectral domain by the Herschel Space Observatory (HSO) and the Atacama Large Millimetric Array (ALMA). The need for accurate collisional data has indeed become all the more acute with the improvements in sensitivity, spectral and angular resolution achieved with the new instruments. As we show below, similarly rapid progress has been made in molecular collision studies. In Section 2, CO is used as a benchmark molecule to illustrate the very good agreement reached between theoretical results and experimental measurements. Section 3 presents two case studies (CN and CH_2NH) where the knowledge of collisional data provides new chemical diagnostics. Conclusions are given in Section 4, including problems to be studied in the future.

2 Theory and experiment in harmony

2.1 *Theory of molecular scattering*

The quantum theory of scattering of a spherical atom by a rigid linear rotor has been formulated in the 1950s (Arthurs & Dalgarno 1960). It was however extensively developed and generalized to larger systems, including open-shell radicals, only in the 1970s and 1980s (Green 1976; Alexander & Corey 1986). Advances in this topic have been indeed closely linked with the progress in computer science. The standard scattering theory takes place within the Born-Oppenheimer approximation for the separation of electronic and nuclear motions. Scattering cross sections are obtained by solving for the motion of the nuclei on an electronic potential energy surface (PES), which is independent of the masses and spins of the nuclei. The process thus consists of two main steps. First, the electronic Schrödinger equation is solved using quantum chemistry methods for collision partners in their ground electronic states (in general). The nuclear motion is solved separately, in a second step, using quantum or (semi)classical scattering methods. A detailed description of the calculation of collisional rate coefficients from first principles can be found in the recent book edited by Lique & Faure (2019) (see Chapter 5 by Tennyson & Faure and Chapter 7 by Dagdigian).

2.2 *The case of CO-H_2*

For a given PES, the most exact approach is the quantum time-independent close-coupling method whose convergence can reach about 1%, depending in practice on the total number of channels involved. The accuracy of the numerous PESs for the interaction between CO and H_2 (the two most abundant molecules in the Universe) has been extensively checked against experiment. Comparisons include bound-states of the CO-H_2 complex, dissociation energies, second virial coefficients, pressure broadening parameters, state-to-state cross sections and even state-to-state rate coefficients. The different measurements are very complementary as they probe different parts of the PES. They have all confirmed that the *ab initio* coupled-cluster theory can provide an intermolecular potential accurate to about 1% in the well depth and long-range interaction regions. The latest PES for CO-H_2 was published by Faure et al. (2016). It was computed in full-dimensionality (6D) using the coupled-cluster method with up to perturbative quadruple excitations, CCSDT(Q), and very large basis sets.

The most sensitive scattering experiments are those at the lowest collisional energy/temperature where subtle details of the PES, especially at long-range, can lead to strong quantum effects. In this respect, cross sections in the vicinity of a rotational threshold provide very sensitive tests. Indeed sharp features in the cross sections are predicted by theory at low energy. These are referred as scattering *resonances* and they arise from purely quantum effects. Observing these resonances experimentally has remained elusive until the recent work of Michel Costes, Christian Naulin and Astrid Bergeat and their colleagues in Bordeaux (France). This group has reported the first high-resolution crossed-beam experiments on state-to-state inelastic cross sections in the cold regime using a variable crossing angle. Their experimental data are presented in Fig. 1 for the CO excitation $j = 0 \to 1$ by para-$H_2(j_2 = 0)$ (Chefdeville et al. 2015). Although the many theoretical resonances (upper panel) have been smeared out by the experimental convolution, three peaks are resolved experimentally, which are well reproduced by theory, both in position and amplitude (lower panel) (see Faure et al. (2016) for details). This very good agreement definitely confirms the high accuracy of the CO-H_2 PES. A review of recent theoretical and experimental progress in molecular scattering at very low energy can be found in the book edited by Dulieu & Osterwalder (2018) (see in particular Chapters 1-3).

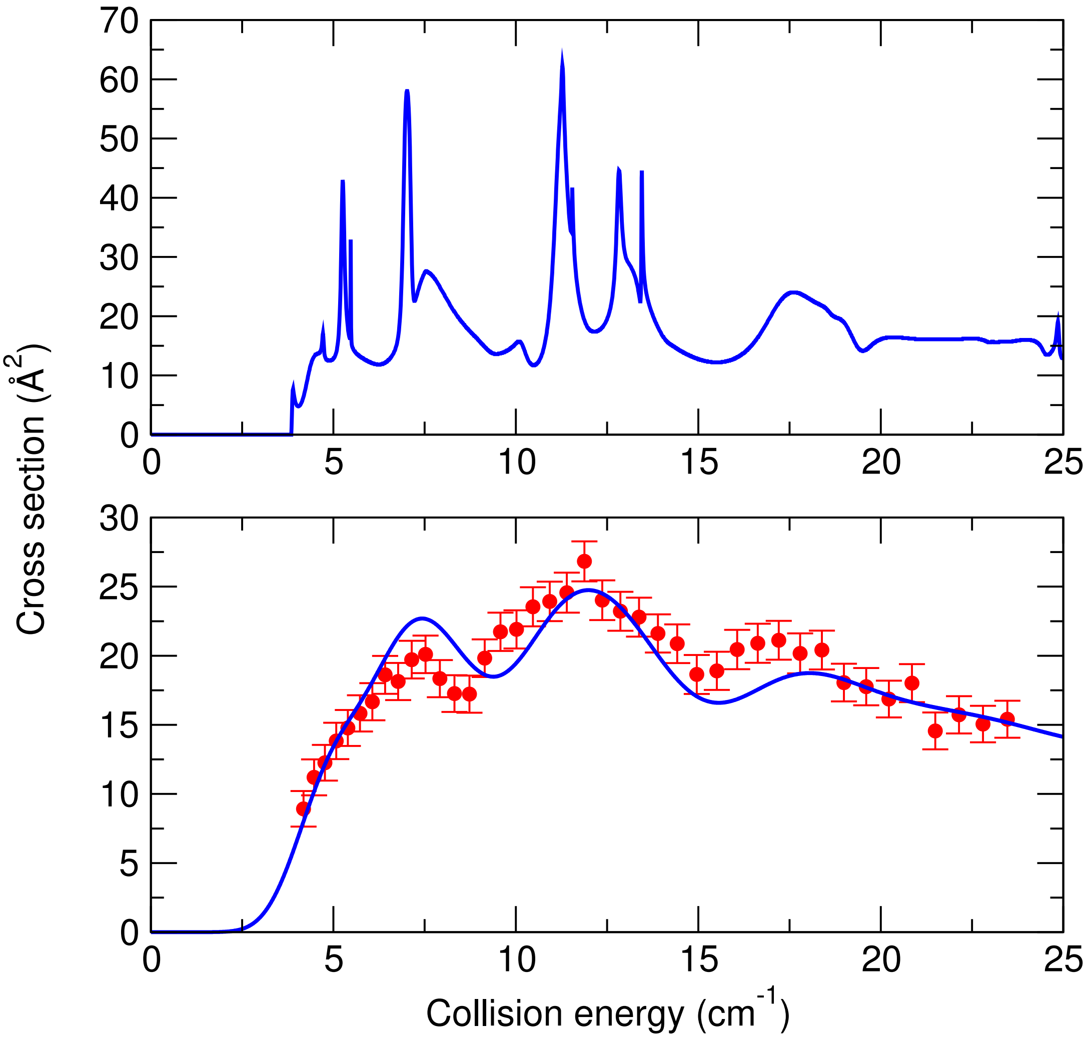

Fig. 1. Cross section for the CO excitation $j = 0 \to 1$ by para-H_2($j_2 = 0$), as function of the collisional energy. The upper panel gives the theoretical CC cross section computed with the PES of Faure et al. (2016). The lower panel gives the experimental data (red circles) and the theoretical data of the upper panel convoluted with the experimental energy spread (blue line).

3 Molecular excitation studies

3.1 The rotational excitation of interstellar CN

In diffuse interstellar clouds, where the hydrogen density is lower than 10^4 cm^{-3}, the rotational temperature of optically detected molecules such as CN is generally close to that of the cosmic microwave background (CMB) radiation temperature ($T_{\rm CMB}$=2.73 K). In the past, optical absorption-line measurements of interstellar CN have thus been used to estimate the temperature of CMB radiation at 2.6 and 1.3 mm, the wavelengths of the two lowest CN rotational transitions*. It was soon realized, however, that the accuracy of this indirect method was hampered by local excitation effects. Now that we know the CMB temperature with high precision,

*It is instructive to note that the CMB was almost discovered in 1950 by the chemist Gerhard Herzberg who wrote about the excitation of interstellar CN that it implied "a rotational temperature of 2.3 K which has of course only a restricted meaning" (Herzberg 1950). This was 15 years before the discovery by Penzias & Wilson (1965).

$T_{\rm CMB} = 2.72548 \pm 0.00057$ K (Fixsen 2009), CN can be actually used as a probe of the local excitation. This probe however requires the knowledge of collisional rate coefficients for the rotational excitation of CN. This data has recently become available for both CN-H_2 (Kalugina & Lique 2015) and CN-electron (Harrison et al. 2013) collisions. The close-coupling method was employed by Kalugina & Lique (2015) while the **R**-matrix theory combined with the adiabatic-nuclei-rotation (ANR) approximation was employed by Harrison et al. (2013).

Observationally, the most recent CN optical absorption line measurements have provided a weighted mean value of T_{01}(CN) $= 2.754 \pm 0.002$ K for a sample of diffuse clouds (Ritchey et al. 2011), where T_{01} is the excitation temperature between the two lowest rotational levels of CN $N = 0$ and $N = 1$. This implies an excess over the CMB temperature of $T_{\rm loc} = 29 \pm 0.3$ mK. In the case of the diffuse cloud towards the star HD 154368, in addition to the optical absorption lines, the weak CN rotational emission $N = 1 \rightarrow 0$ at 2.6 mm was also detected. Since the physical conditions (hydrogen density and kinetic temperature) and the CN column density in this source are well constrained, it was possible to estimate the electron density. Thus, Harrison et al. (2013) have found that the intensity of the 2.6 mm transition could be reproduced for an electron density of ~ 0.03 cm^{-3}, corresponding to an electron fraction of $\sim 2 \times 10^{-4}$, as expected from the elemental carbon abundance (C^+ is the main source of electrons in diffuse clouds). We show in Fig. 2 that for this electron density, the predicted excitation temperature is $T_{01} = 2.75$ K, in very good agreement with the weighted mean value of 2.754 K determined by Ritchey et al. (2011). We finally note that this electron density is typically 3 times larger than that of the general ISM where the hydrogen density is ~ 1 cm^{-3}.

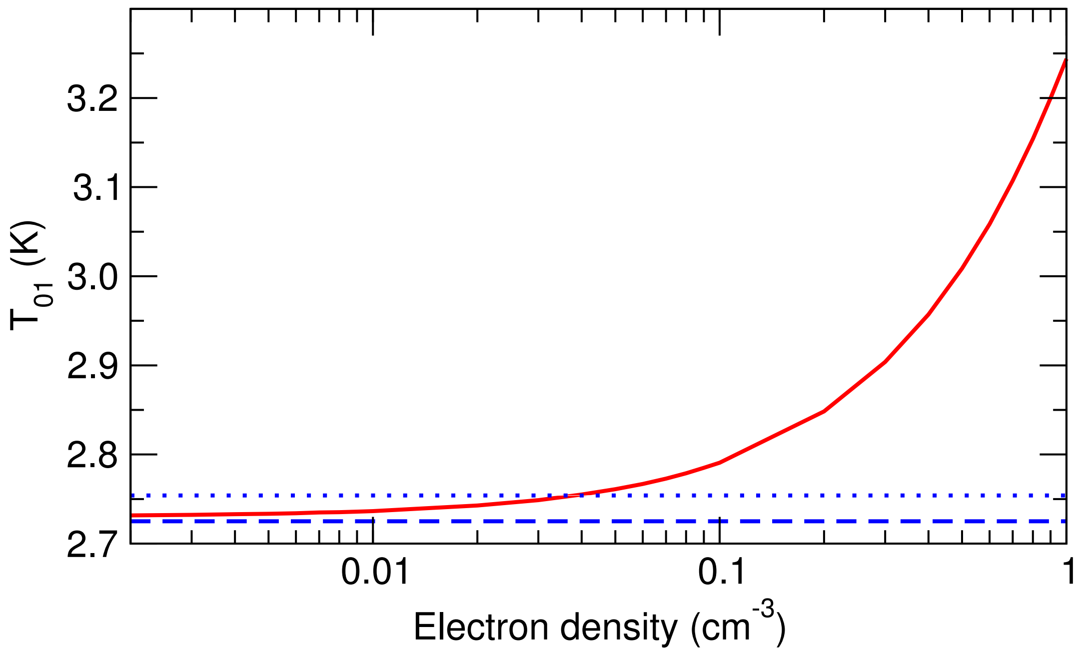

Fig. 2. Excitation temperature T_{01}(CN) as a function of electron density for the physical conditions towards HD 154368 (T=20 K, n=150 cm^{-3}) and for a column density N(CN)=2.7×10^{13} cm^{-2}. Here the dashed line represents the CMB at 2.725 K while the dotted blue line gives the measured average excitation temperature at 2.754 K (Ritchey et al. 2011).

3.2 The weak maser action of interstellar methanimine

Among the variety of interstellar organic molecules, imines are of special interest because they are possible precurors of amino acids. Amino acids are the building blocks of proteins and the study of simpler precursors in space may help to decipher the origin of life on Earth and elsewhere in the Universe. Methanimine (CH_2NH), the simplest imine, was discovered in the ISM in 1973 towards the giant molecular cloud Sgr B2 *via* the hyperfine multiplet structure of the $1_{10} \rightarrow 1_{11}$ rotational line at 5.29 GHz (Godfrey et al. 1973). Since then, CH_2NH has been detected in many galactic and even extragalactic sources from centimetric to millimetric wavelengths. In order to elucidate the chemistry of CH_2NH in the ISM, it is important to derive reliable column densities and therefore to perform non-LTE radiative transfer calculations. In particular, the strong emission of the intrinsically weak $1_{10} \rightarrow 1_{11}$ line towards Sgr B2 was soon attributed to a population inversion, rather than an anomalously high abundance. The knowledge of collisional data, however, was missing until recently.

The first rotational rate coefficients for CH_2NH were determined by Faure et al. (2018) by combining an *ab initio* CH_2NH-H_2 PES with close-coupling scattering calculations. Moreover, new observations were performed towards Sgr B2(N) (the north core of Sgr B2) with the Green Bank Telescope (GBT). The multiplet of the 5.29 GHz line was detected with a high signal-to-noise ratio, as shown in Fig. 3. It should be noted that two velocity components are resolved in this spectrum, which correspond to two different molecular clouds lying surimposed along the same line of sight, in front of the strong continuum emission produced by Sgr B2(N). Radiative transfer calculations were performed with the non-LTE `RADEX` program (van der Tak et al. 2007). The kinetic temperature and density of H_2 for both molecular clouds were fixed at T=30 K and $n_{H_2} = 10^4$ cm^3, respectively, as derived by Faure et al. (2014) from their modeling of the weak $HCOOCH_3$ masers. The column density of CH_2NH was adjusted for each cloud to best fit the observational spectrum. Other details can be found in Faure et al. (2018). A very good agreement between the observation and the model is observed in Fig. 3. As anticipated, the $1_{10} \to 1_{11}$ line was found to be inverted with an excitation temperature of -0.48 K. This inversion, by amplifying the strong background continuum radiation, is thus critical here to produce the emission of the otherwise undetectable 5.29 GHz multiplet. As a result, searching for maser lines could be very fruitful to detect new chemical species with intrinsically low abundance.

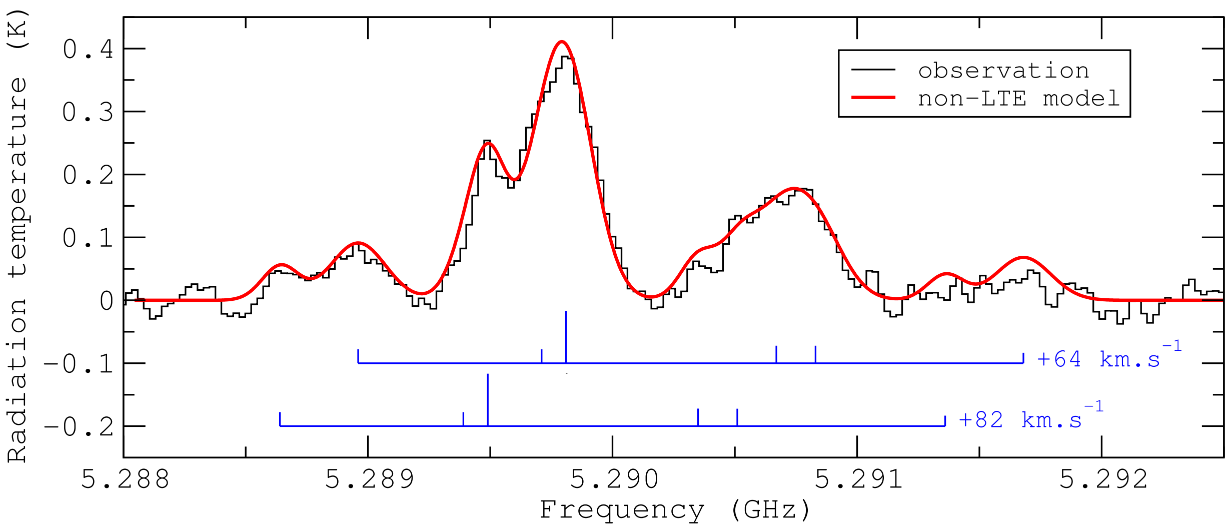

Fig. 3. Observational and model spectra of methanimine $1_{10} \to 1_{11}$ transition at 5.29 GHz towards Sgr B2(N). Relative intensities of the (partially resolved) hyperfine structure in the optically thin limit are shown at the bottom. The nominal source velocity is +64 km.s^{-1}. A second velocity component is resolved at +82 km.s^{-1}. The non-LTE model predicts a population inversion with a negative excitation temperature $T_{ex} = -0.48$ K.

4 Conclusions

Recent years have seen impressive theoretical and experimental progress regarding the description of inelastic molecular collisions involving small, non-reactive and vibrationally cold molecules. Thus, current theoretical data for rotational excitation can reach a precision of $\sim$ 10-20% that fully matches the astrophysical requirements for the modelling of both rotational spectra and cooling. This has remarkably contributed to improve the diagnostic power of rotational lines. The next step is to extend the current level of accuracy *i)* to large molecules, *ii)* to ro-vibrational excitation and *iii)* to other projectiles such as H_2O or CO (important in comets and planetesimals). Recent examples include the work by Faure et al. (2019), Stoecklin et al. (2019) and Loreau et al. (2018), respectively. Another requirement concerns *reactive* species which are both excited and destroyed by H, H_2 or free electrons. A recent example can be found in Faure et al. (2017) for the molecular ion CH^+. Guided by the enhanced sensitivity of new telescopes (JWST, E-ELT, etc.) and the prospect to detect molecular lines from Earth-like exoplanets and the early Universe, we are confident that the study of molecular collisional excitation has a bright future.

The support by the Programme National Physique et Chimie du Milieu Interstellaire (PCMI) of CNRS/INSU with INC/INP cofunded by CEA and CNES and the Agence Nationale de la Recherche, contract Hydrides (ANR-12-B505-0011-02) is acknowledged. Special thanks go to my colleagues from the ANR Hydrides project.

References

Alexander, M. H. & Corey, G. C. 1986, J. Chem. Phys., 84, 100

Arthurs, A. M. & Dalgarno, A. 1960, Roy. Soc. London Proc. Ser. A, 256, 540

Chefdeville, S., Stoecklin, T., Naulin, C., et al. 2015, ApJ, 799, L9

Donati, G. B. 1864, Astronomische Nachrichten, 62, 375

Dulieu, O. & Osterwalder, A. 2018, Cold Chemistry: Molecular Scattering and Reactivity Near Absolute Zero (The Royal Society of Chemistry), 92–149

Faure, A., Dagdigian, P. J., Rist, C., et al. 2019, ACS Earth and Space Chemistry, 3, 964

Faure, A., Halvick, P., Stoecklin, T., et al. 2017, MNRAS, 469, 612

Faure, A., Jankowski, P., Stoecklin, T., & Szalewicz, K. 2016, Scientific Reports, 6, 28449

Faure, A., Lique, F., & Remijan, A. J. 2018, J. Phys. Chem. Lett., 9, 3199

Faure, A., Remijan, A. J., Szalewicz, K., & Wiesenfeld, L. 2014, ApJ, 783, 72

Fixsen, D. J. 2009, ApJ, 707, 916

Godfrey, P. D., Brown, R. D., Robinson, B. J., & Sinclair, M. W. 1973, Astrophys. Lett., 13, 119

Green, S. 1976, J. Chem. Phys., 64, 3463

Harrison, S., Faure, A., & Tennyson, J. 2013, MNRAS, 435, 3541

Herzberg, G. 1950, Molecular spectra and molecular structure. Vol.1: Spectra of diatomic molecules (New York: Van Nostrand Reinhold, 1950, 2nd ed.)

Kalugina, Y. & Lique, F. 2015, MNRAS, 446, L21

Lique, F. & Faure, A. 2019, Gas-Phase Chemistry in Space; From elementary particles to complex organic molecules (IOP Publishing, Bristol, UK)

Loreau, J., Faure, A., & Lique, F. 2018, J. Chem. Phys., 148, 244308

McKellar, A. 1940, PASP, 52, 187

Penzias, A. A. & Wilson, R. W. 1965, ApJ, 142, 419

Ritchey, A. M., Federman, S. R., & Lambert, D. L. 2011, ApJ, 728, 36

Stoecklin, T., Denis-Alpizar, O., Clergerie, A., et al. 2019, J. Phys. Chem. A, 123, 5704

van der Tak, F. F. S., Black, J. H., Schöier, F. L., Jansen, D. J., & van Dishoeck, E. F. 2007, A&A, 468, 627

SF2A 2019
P. Di Matteo, O. Creevey, A. Crida, G. Kordopatis, J. Malzac, J.-B. Marquette, M. N'Diaye, O. Venot (eds)

THE ACTION SPÉCIFIQUE OBSERVATOIRES VIRTUELS FRANCE (VIRTUAL OBSERVATORY FRANCE SPECIFIC ACTION) IN THE OPEN SCIENCE CONTEXT

F. Genova[1]

Abstract. Astronomy has been, and continues to be, a pioneer of Open Science. It has established and maintains a disciplinary data sharing framework, the astronomical Virtual Observatory, which enables astronomers to discover the data useful for their research, to access them, and to use them with interoperable tools. Thanks to the work of the data producers and of the VO developers, astronomical data are FAIR (Findable, Accessible, Interoperable, Reusable). The *Action Spécifique Observatoires Virtuels France* (France Virtual Observatory Specific Action - ASOV) was created in 2004 by the CNRS-INSU, with CNES support, as the French chapter of the International Virtual Observatory Alliance (IVOA), which defines the Virtual Observatory standards at the international level, and a co-ordination structure at the national level. The ASOV supports French participation to the IVOA and technical exchanges between the French astronomical data and service centres. Its role and impact are described in the Open Science national and international context.

Keywords: Virtual Observatory, Open Science

1 Introduction

This paper was the contribution of the *Action Spécifique Observatoires Virtuels France* (France Virtual Observatory Specific Action - ASOV) to the 2019 meeting of the French Astronomical Society SF2A, which was held in Nice 14-17 May 2019. It describes the current Open Science context at the international and European levels, and the situation in France, with in particular the publication of the National Strategic Plan for Open Science in 2018 (Section 1). Section 2 addresses why astronomy is generally considered as one of the pioneers of Open Science. Section 3 describes how the ASOV fits into this landscape, and its impact at the national and international levels.

2 The Open Science context at the international, European and national level

Open Science has already had a long history at the political level. OCDE was mandated in 2004 to work on access to data from publicly funded research. They produced in 2007 their *Principles and Guidelines for Access to Research Data from Public Funding* (OECD 2007). The G7/G8 Ministries in charge of research published strong statements in 2013 on the transformation of the way to make research following the Open Data paradigm*. They continued since then to work together on the subject and to publish statements, with in particular the mention of the FAIR principles in 2017†. The FAIR Principles, which state that data should be Findable, Accessible, Interoperable and Reusable, were published in 2016 (Wilkinson et al. 2016). Their mention in an international ministerial statement in 2017 demonstrates how fast they became known and endorsed world-wide. In Europe, Carlos Moedas, Commissioner for Research, Science and Innovation, promoted in 2015 *Open Science, Open Innovation, Open to the World* as a vision for Europe (Directorate-General for Research and Innovation 2016).

---

[1] Université de Strasbourg, CNRS, Observatoire astronomique de Strasbourg, UMR 7550, 11 rue de l'Université, F-67000 Strasbourg, France

*`https://www.gov.uk/government/news/g8-science-ministers-statement`, Section 3 Open Scientific Research Data
†`http://www.g7italy.it/en/science-ministerial-meeting/`

In France, the Law for a Digital Republic, published on 8 October 2016, provides a legal framework to favour opening and circulation of data and knowledge. Another top-down incentive has been the questions about data policies and management among those which should be answered by Research Infrastructures candidates to the National Research Infrastructure Roadmap since its 2016 update (the same has been true at the European level for the ESFRI Roadmap questionnaire, also since its 2016 update). Several data infrastructures, such as the *Centre de Données astronomiques de Strasbourg* (Strasbourg astronomical Data Centre CDS), and the National Humanities Data Infrastructure *Huma-Num* (previously ADONIS and CORPUS), have been included in the National Roadmap since its inception in 2008, with the more recent addition of the *Earth System Research Infrastructure*, which is now called *Data Terra*. Recenly, the Ministry of Higher Education, Research and Innovation (MESRI) installed the *Comité pour la Science Ouverte* (Open Science Committee) in 2018, with 4 Colleges, *Publications*, *Research Data*, *Europe and international*, and *Skills and training*, with "Project Groups" on *Evaluation*, *Open and open Source software*, *Observatory of informational practices*, and *Building bibliodiversity*.

The MESRI published in July 2018 the National Strategic Plan for Open Science[‡], with three commitments: generalise open access to publications, structure research data and make it available through open access, and be part of a sustainable European and international Open Science dynamics. Among the measures concerning data, the following particularly resonnate with what we do in astronomy:

- Make open access dissemination mandatory for research data resulting from government-funded projects,
- Create the conditions for and promote the adoption of an Open Data policy for articles published by researchers,
- Among the structuring measures, develop subject-based and discipline-specific data repositories.

Two other structuring measures have to be noted because they impact the research and data provider communities:

- Generalise the implementation of data management plans in calls for research projects,
- Implement a certification process for data infrastructures.

Among recent progresses, one should also have in mind the rapid take-up of the FAIR Guiding Principles for Scientific Data Management. Since their publication in 2016, the principles have become the "normal" way to refer to the concepts which underline data sharing. An Expert Group set up by the European Commission published in 2018 a reference report and action plan *Turning FAIR into Reality* (Hodson et al. 2018). The rapid emergence and growth of the Research Data Alliance[§], an international organisation created in 2013 which aims at building technical and sociological bridges to facilitate the open sharing and reuse of data, is another sign of the world-wide interest for open science. At a more technical level, persistent identifiers such as DOIs (Digital Object Identifiers) and ORCID for identifying people facilitate the publication, attribution and citation of data.

3 Astronomy and Open Science

Open Science concerns all research fields, but they are not all at the same evolution stage. The cross-disciplinary usage of data is often put forward in the open science context, but it requires lots of work at the disciplinary level, since one needs to know the data to make it FAIR. Also, as demonstrated by what happened in astronomy, science data sharing enables a change in paradigm in the way science is done, first at the disciplinary level, by allowing one to discover data, and to access, reuse and combine them.

Open Science has somehow a "long" history over more than a decade, as explained, but astronomy begun to practice it long before. The *Centre de Données astronomiques de Strasbourg* was created in 1972, with the mission to "collect useful information concerning astronomical objects that is available in computerized

[‡]French version: `http://cache.media.enseignementsup-recherche.gouv.fr/file/Actus/67/2/PLAN_NATIONAL_SCIENCE_OUVERTE_978672.pdf`, English version `http://cache.media.enseignementsup-recherche.gouv.fr/file/Recherche/50/1/SO_A4_2018_EN_01_leger_982501.pdf`

[§]`https://rd-alliance.org`

form; upgrade these data by critical evaluations and comparisons; distribute the results to the astronomical community; conduct research, using these data", that it continues to fulfil nowadays. The database of the *International Ultraviolet Explorer* IUE was also heavily used in early times: the satellite was in operation from 1978 to 1996, and the data in the database had been downloaded in average 5 times in 1994 (Wamsteker & Griffin 1995). These early successes were only the beginning, because data reuse is at the core of astronomical research, allowing combination of data from different instruments to understand the physical phenomena at work in the objects - multi-wavelength/multi-messenger astronomy - and studies of temporal variations.

Another strong asset of astronomy in the Open Science context is its capacity to develop and maintain standards through co-operation at the international level, like we do to develop facilities and instruments in international collaborations. The FITS format was published in 1981 (Wells Greisen & Harten), and the paper cites discussions at a "Workshop on Standards for Image Pattern Recognition" held in 1977. The standard is maintained under the aegis of the International Astronomical Union. FITS integrates data and metadata providing information about the observation, enabling data reuse. It allows the sharing of telescopic observations and the development and sharing of common tools to use the data. Although FITS is not perfect and often criticized, all the developments which came next have been made possible by the fact that astronomy shares a common data format.

The key next step for the "FAIRisation" of astronomical data has been the development of the Astronomical Virtual Observatory (VO), the disciplinary framework of interoperability standards and tools. The activity began around 2000, with the first funded projects in Europe, France, UK and USA starting in 2001. The interoperability standards are developed and maintained by the International Virtual Observatory Alliance¶ (IVOA), which was created in 2002. The IVOA standards enable interoperability of data and of tools - one can for instance navigate seamlessly from images to tables to spectra when using VO-enabled applications and data services. This is an essential element for success: Genova et al. (2017), who compare interoperability frameworks established by different disciplines to identify commonalities and differences, states that "it is essential, for community uptake of data sharing, that data producers are enabled to share their data as well as users enabled to use the shared data."

Thanks to the data providers and VO developers, most astronomical data are open and FAIR, and they were so before the FAIR principles were defined. Data from most observatories are openly available, often after an embargo ("proprietary") period during which they are reserved to the team which proposed the observation. Data producers use FITS, which makes data Reusable, and provide their data in the VO. The VO enables astronomers to Find, Access and Interoperate data. As explained, applications are also interoperable. Other formats proposed as alternatives to FITS will have to reach the same maturity level to preserve existing capabilities.

4 The Action Spécifique Observatoires Virtuels France

The CDS had been involved in the VO development from the beginning, leading the first international *Interoperability Working Group* (2001-2002) under the aegis of the OPTICON network. This Working Group developed the first VO standard, VOTable (a standard to represent a table), which was finalised in April 2002. The IVOA was created in May 2002, and it took up the task of developing, agreeing on and maintaining interoperability standards.

The first INSU/Astronomy-Astrophysics (INSU/AA) strategic planning exercise (*Exercice de Prospective CNRS/INSU Astronomie Astrophysique*) organised after the creation of the IVOA was held in 2003. The importance of the Virtual Observatory was already well understood, which led to two recommendations:

- Create a coordination structure at the national level
- Begin to study the inclusion of modelling data in the VO

As a result, the *Action Spécifique Observatoires Virtuels France* ASOV was created by CNRS-INSU in 2004, with support from CNES. It has been regularly evaluated and renewed since then. With respect to the second recommendation, an IVOA Interest Group was set up in 2004 to work on requirements to include modelling data in the IVOA. The first assessment of this inclusion was taken up in the framework of the Euro-VO Data Centre Alliance (Euro-VO DCA) project. The project (project RI031675), coordinated by CDS on behalf of

¶ `http://www.ivoa.net`

CNRS, was funded by the European Commission for 28 months from 2006 to 2008. French teams, led by Frank Le Petit and Hervé Wozniak, played an essential role in the definition of IVOA theory standards during and after EuroVO-DCA.

The ASOV has kept the same structure since its inception: the Scientific Council is composed of members designated by the Programmes and the other Actions Spécifiques, plus a handful of specialists. The Scientific Council chairperson represents France at the IVOA Executive Board[‖]. The ASOV role is to coordinate VO activities at the national level, and to disseminate knowledge and good practices about VO standards and tools. Following a recommendation of the 2014 Astronomy-Astrophysics strategic planning exercise, the ASOV mandate was expanded to include the coordination of technical exchanges between the teams which are engaged in data management, in particular for the ANO5 services[**], when it was renewed in 2016. This additional mandate was making explicit a function that ASOV already fulfilled.

The ASOV funds travel. It organises an annual call for proposals to support travels to IVOA meetings and to similar meetings of other sub-disciplines, and collaboration, thematic and regional meetings. The travels of the people who have responsibilities in the IVOA, with also travels from representatives of the main laboratories involved, are covered as far as possible. The ASOV also organises an annual meeting, which has been complemented since 2016 by a *Semi-Hack-a-Thon* for technical exchanges.

ASOV has been having a structuring role at the national level, and enabled the French community to be very active and visible in the IVOA. The CDS has been the ASOV starting point, and remains a cornerstone. But the VO community is now country-wide, as demonstrated by the fact that the six-monthly IVOA meeting was held at Paris Observatory in May 2019. Staff working in Besançon, Bordeaux, Grenoble, Marseille, Montpellier, Nice, Paris, Paris-Sud, Strasbourg and Toulouse participated in the ASOV 2019 meeting. There are currently a number of data services in France, many of them organised in Regional Expertise Centres, some of them labelled as ANO5 Observation Services. The ANO5 evaluation committee requires that data dissemination by the services is VO-enabled. Thanks to ASOV, knowledge of how to implement the VO framework is now widespread in the services and Regional Expertise Centres. French data services implement the VO standards and share good practices. The ASOV also encouraged regional exchanges when appropriate, in particular in the South-West (Bordeaux, Montpellier, Toulouse), as a precursor of the Regional Expertise Centre which was labelled in 2013.

The strong impact of the French community in the IVOA can be quantified: in May 2019, there were 45 IVOA standards. 27 of them have at least one author from a French laboratory/observatory (CDS/Observatoire Astronomique de Strasbourg, Paris Observatory, Grenoble, Montpellier and Toulouse), among which 17 have at least one editor from a French laboratory/observatory. French teams also develop key VO tools, in particular Aladin and Cassis, and Paris Observatory provides tools to validate standards, which play an essential role in the VO framework.

One important aspect of ASOV is that it covers all the sub-disciplines of the Section 17 of the *Comité National de la Recherche Scientifique*, namely astronomy, the study of the planets, the Sun and the heliosphere, space plasma physics, the astronomy facet of astroparticle physics, and atomic and molecular physics of astronomical interest. This enabled early dissemination of the astronomical VO concepts and tools, and the French community has been leading, or very active in, the development of disciplinary interoperability layers in European projects and at the international level in the nearby disciplines. One can cite the ASTERICS Cluster (2015-2019) with its *Data Access, Discovery and Interoperability* Work Package (Genova et al. 2019), which includes CTA, KM3Net, EGO-VIRGO, and was extended to EST at the end of the project, and its successor ESCAPE (2019-2023) with its *Connecting ESFRI projects to EOSC through VO framework* work package, which has a task on FAIRisation; Europlanet and VESPA (Virtual European Solar and Planetary Access) (Erard et al. 2018); and VAMDC, the Virtual Atomic and Molecular Data Centre (Dubernet et al. 2016). The other subdisciplines reuse or customize the standards developed for the astronomical Virtual Observatory for their own needs.

5 Conclusions

Astronomy is cited as an example in the context of Open Science and FAIR, for instance in Hodson et al. (2018). It created an international framework for FAIR data sharing, which is widely used by the community

[‖]The IVOA is composed of VO initiatives from countries, including France, plus the European Virtual Observatory collaboration and the inter-governmental organization ESA.

[**]ANO5 (ANO for *Action National d'Observation*) covers the centres in charge of data processing, archival and dissemination.

in its daily research work, and fully open: anyone can declare a service in the Virtual Observatory, or develop and share a tool to access VO-enabled data. Many current large projects provide their data in the Virtual Observatory. For instance, Gaia data was only made available in the VO by ESA, CDS, and other data centres which participate in the project data dissemination. The data from all ESA missions are VO-enabled, and VO standards are implemented in the new ESO programmatic interface (Romaniello et al. 2018). LSST staff participate in the IVOA, and contact with CTA, ELT, EST, Km3Net, SKA is well establisehd, in particular through ASTERICS and ESCAPE. Several space and ground-based observatories implement VO building blocks in their data pipelines. And in any case, all the data made available at CDS, including VizieR collection of catalogues and other data attached to publications and Aladin reference image archive, are available in the VO.

The ASOV enabled the creation of a national community of people engaged in the development of data services, and supported the community to influence and actively participate in the VO development. This was made possible because the national strategic planning exercises understood early the potential value of the Virtual Observatory and renewed their support, and the funding agencies, CNRS-INSU/AA and CNES, have been providing funds on the long term. Data is one of the research infrastructures of astronomy (Genova 2018), and like all research infrastructures, they require sustainable support.

The ASOV is grateful to INSU/AA and CNES, and to its community, for their continuous support along the years.

An earlier description of astronomy and the VO in the Open Science context was presented at the *Library and Information Services in Astronomy* (LISA VIII), held in Strasbourg 6-9 June 2017 (Genova 2018).

The author warmly thanks Franck Le Petit for his careful reading of the manuscript and his very relevant suggestions.

References

OECD 2007, Principles and Guidelines for Access to Research Data from Public Funding, OECD Publications, Paris

Wilkinson, M.D., Dumontier, M., IJsbrand, J.A., et al. 2016, Scientific Data, 3, 16001

Directorate-General for Research and Innovation (European Commission) 2016, Open innovation, open science, open to the world, Luxembourg: Publications Office of the European Union

Hodson, S., Jones, S., Collins, S., et al. 2018, Turning FAIR into reality, Luxembourg: Publications Office of the European Union

Wamsteker, W., & Griffin, R.E.M. 1995, Ap&SS, 228, 385

Wells, D.C., Greisen, E.W., & Harten, R.H., A&AS, 44, 363

Genova, F., Arviset, A., Almas, B.M., et al. 2017, Data Sci. J., 16, 16

Genova, F., Allen, M.G., Boisson, C, et al. 2019, PoS, à paraître.

Erard, S, Cecconi, B., Le Sidaner, P., et al. 2018, P&SS, 150, 65

Dubernet, M.L, Anthony, B.K., Ba, Y.A., et al. 2016, J.Phys.B, 49, 7/7/074003

Romaniello, M., Zampieri, S., Delmotte, N., et al., Proc. SPIE, 10704, 1070416

Genova, F. 2018, EPJ Web Conf., 186, 01001

SF2A 2019
P. Di Matteo, O. Creevey, A. Crida, G. Kordopatis, J. Malzac, J.-B. Marquette, M. N'Diaye, O. Venot (eds)

A DECADE OF FAST RADIO BURST OBSERVATIONS

L. Guillemot[1, 2]

Abstract. Fast Radio Bursts (FRBs) are extremely short and highly-dispersed bursts of radio emission, likely of extragalactic origin. The first FRB was discovered in 2007 in a 1.4 GHz observation conducted with the Parkes radio telescope in Australia. Since then, several tens of FRBs have been observed, over a wide range of radio frequencies. While most known FRBs have never been detected again, a few sources, dubbed "repeaters", are regularly re-detected with consistent emission properties. A little more than a decade since the first FRB detection was reported (that of the so-called "Lorimer burst"), much is still to be learned about the precise origin of these events and the underlying phenomenology. In this talk I presented an overview of FRB observations since their discovery, and of their main properties.

Keywords: Fast Radio Bursts, radio astronomy, transient phenomena

1 The discovery of fast radio bursts

Recognizing that, at the time, the radio sky was 'relatively unexplored for transient signals', McLaughlin et al. (2006) conducted searches for isolated bursts of radio emission in archival data taken with the Parkes radio telescope between 1998 and 2002, and discovered 11 new sources emitting bright ms-duration bursts. Analysis of the burst arrival times revealed periodicities (with periods in the range 0.4 − 7 s) in the majority of the sources. The periodicities suggested that the new sources, dubbed rotating radio transients (RRATs), were a subset of the radio pulsar population.

Motivated by this discovery, Lorimer et al. (2007) searched archival Parkes radio telescope data taken in 2001 and found a single bright pulse with an initially-estimated peak flux density of more than 30 Jy, in a direction 5° away from the Small Magellanic Cloud. The burst was not re-detected in 90 hours of additional observations of the same sky direction with the Parkes telescope. As can be seen from Figure 1, the radio signal from the burst is "dispersed", that is, the pulse is delayed by the cold ionized plasma along the line of sight, by an amount:

$$\Delta t = \frac{\mathrm{DM}}{k \times f^2},$$

where f is the frequency, $k = 2.41 \times 10^{-4}$ MHz^{-2} pc cm^{-3} s^{-1}, and DM is the dispersion measure, given by:

$$\mathrm{DM} = \int_0^d n_e(l)\ \mathrm{d}l.$$

In the above expression, d is the distance to the source and $n_e(l)$ is the electron number density at the path length l. Lorimer et al. (2007) found that the burst had a DM of 375 pc cm^{-3}, which is several times larger than the expected contribution from free electrons in the Milky Way in this sky direction, thus suggesting an extragalactic origin. This bright burst, known as the "Lorimer burst", is now referred to as FRB 010724.

[1] Laboratoire de Physique et Chimie de l'Environnement et de l'Espace – Université d'Orléans / CNRS, F-45071 Orléans Cedex 02, France
[2] Station de radioastronomie de Nançay, Observatoire de Paris, CNRS/INSU, F-18330 Nançay, France

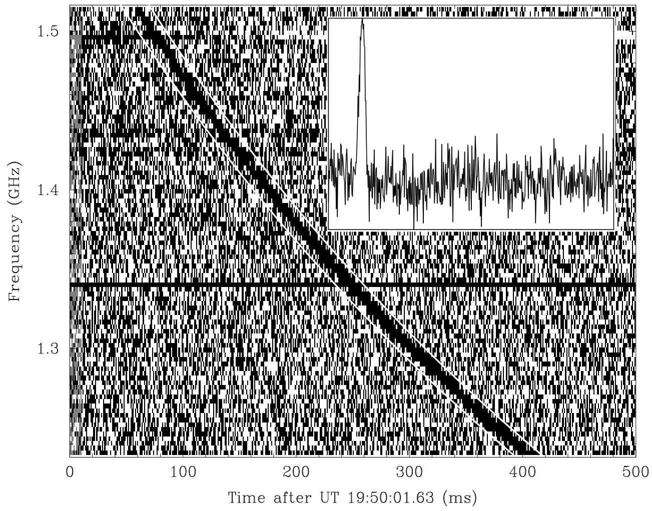

Fig. 1. Signal intensity as a function of radio frequency and time, for the fast radio burst FRB 010724 (the "Lorimer burst") as seen with the Parkes radio telescope. The inset shows the signal integrated in frequency, correcting for the dispersive delay caused by the ionized plasma on the line of sight. Figure taken from Lorimer et al. (2007).

A second FRB candidate was reported by Keane et al. (2011). The burst, known as the "Keane burst" or FRB 010621, was found in a search for pulses in data from the Parkes Multibeam Pulsar Survey. The DM value of this 7-ms burst was again large (about 745 pc cm^{-3}) and in particular larger than the expected DM contribution from the Milky Way (expected to be 533 pc cm^{-3}, according to the NE2001 model of Cordes & Lazio 2002), but because of the small fractional DM excess it was unclear whether the burst had an extragalactic origin. The discovery by Thornton et al. (2013) of a population of four short-duration and high-DM bursts in data from the High Time Resolution Universe survey at the Parkes radio telescope established FRBs as a class of radio transients, likely to be of extragalactic origin. Following these first discoveries, many FRBs were then detected in data from other radio telescopes than Parkes: for instance, FRB 121102 detected with the Arecibo radio telescope (Spitler et al. 2014), or FRB 110523 seen with the Green Bank radio telescope (Masui et al. 2015). Very recently, searches for fast transients with wide field of view instruments such as the Upgraded Molonglo Synthesis Telescope (UTMOST, see e.g. Caleb et al. 2016), the Australian Square Kilometre Array Pathfinder (ASKAP, e.g. Shannon et al. 2018) or the Canadian Hydrogen Intensity Mapping Experiment (CHIME, e.g. CHIME/FRB Collaboration et al. 2019b) have increased the sample of known FRBs dramatically. At the time of writing, the FRB Catalogue* (Petroff et al. 2016) lists the properties of 90 FRBs. Many more will likely be announced and discovered in the coming months and years. Additionally, currently unknown FRBs are likely awaiting discovery in existing radio data from many telescopes.

The vast majority of FRBs detected so far have never been observed to repeat, in spite of deep follow-up observations in some cases, such as those of the Lorimer and Keane bursts mentioned above. Initial follow-up observations of FRB 121102 (Spitler et al. 2014), known as the "Spitler burst", failed to detect additional bursts. However, new observations with Arecibo in May 2015 found ten new bursts, some of which were brighter than the original one (Spitler et al. 2016). Since then, additional bursts from this source have been detected at several radio telescopes around the world (see e.g. Michilli et al. 2018). Periodicity searches have so far failed to find an underlying periodic signal in the burst arrival times. Interestingly, because of its repeating nature, FRB 121102 cannot be caused by a cataclysmic event. In addition, repeating pulses make it possible to study the FRB in much greater details than non-repeating events. So far, no persistent high-energy emission associated with the radio bursts has been detected (see e.g. Scholz et al. 2017). On the other hand, radio interferometric observations of the FRB allowed Chatterjee et al. (2017) to associate it with a low-luminosity galaxy. Optical imaging and spectroscopy by Tendulkar et al. (2017) showed that the host galaxy is a low-metallicity and low-mass dwarf galaxy at a redshift of ~ 0.193. The discovery of a second FRB, FRB 180814.J07422+73, was reported in early

*See http://frbcat.org/ .

2019 by the CHIME collaboration (CHIME/FRB Collaboration et al. 2019a). Spectra of FRBs 121102 and 180814.J07422+73 are displayed in Figure 2. Complex time and frequency sub-structures are observed in both repeating FRBs, indicating strong similarities between the two sources. Finally, the CHIME collaboration very recently reported the discovery of eight new repeating FRBs, substantially increasing the known population of repeaters (The CHIME/FRB Collaboration et al. 2019). Extensive studies of these new repeating FRBs will enable more detailed comparisons of the properties of repeaters, such as their emission properties or host galaxy properties.

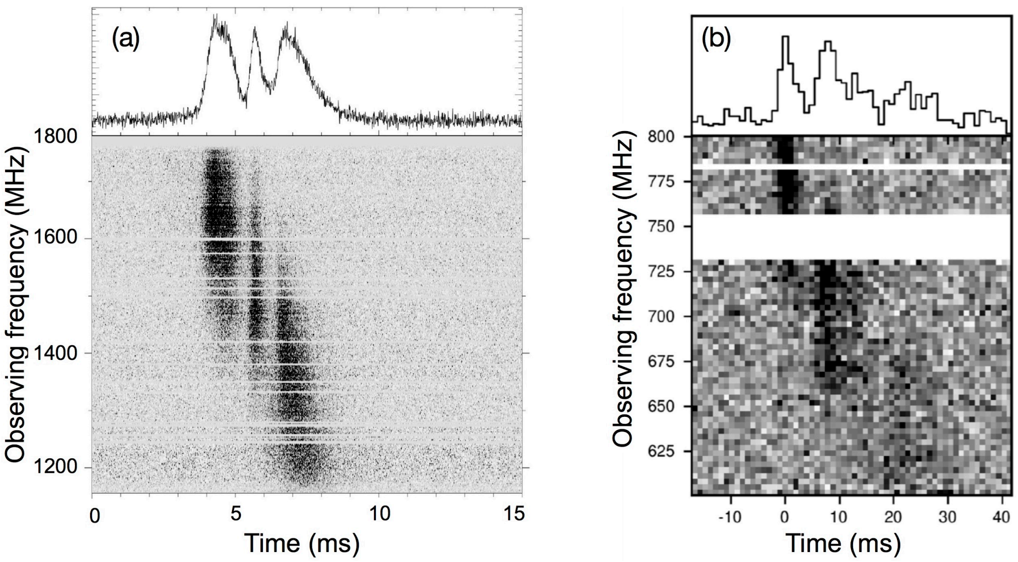

Fig. 2. Intensity as a function of radio frequency and time for the repeating FRB 121102 as seen at 1.4 GHz with Arecibo (left) and for FRB 180814.J07422+73 as seen with CHIME at 0.7 GHz (right). Spectra were corrected for the dispersive delay caused by free electrons on the line of sight of the two FRBs. Figure adapted from Petroff et al. (2019). Both bursts exhibit complex time and frequency structures. See e.g. Hessels et al. (2019) for an analysis of the sub-structures in FRB 121102.

2 FRB properties

In this section, some general properties of the population of FRBs detected so far are briefly presented. We refer the interested reader to the recent comprehensive reviews by e.g. Petroff et al. (2019) or Cordes & Chatterjee (2019) for more exhaustive descriptions of the properties of the FRB population, which are beyond the scope of these proceedings.

Plotted in Figure 3 are the DMs of published FRBs and of known radio pulsars relative to the expected DM contribution from the Milky Way along the line of sight, and as a function of Galactic latitude. A majority of published FRBs have DM values well above the maximum line of sight DM from the Galaxy, indicating extragalactic origins. As is also the case for radio pulsars, DMs can be used to estimate the distances. A DM excess can be defined as follows:

$$\mathrm{DM_E} = \mathrm{DM_{FRB}} - \mathrm{DM_{MW}} = \mathrm{DM_{IGM}} + \left(\frac{\mathrm{DM_{Host}}}{1+z}\right).$$

In the above expression, $\mathrm{DM_{FRB}}$ is the measured DM of the FRB, $\mathrm{DM_{MW}}$ is the DM contribution from the Galaxy over the line of sight, $\mathrm{DM_{IGM}}$ and $\mathrm{DM_{Host}}$ are the DM contributions from the intergalactic medium and the host galaxy, and z is the source's redshift. Although several terms (namely, $\mathrm{DM_{MW}}$, $\mathrm{DM_{IGM}}$, and $\mathrm{DM_{Host}}$) are typically uncertain, the above equation can be used to find a relationship between DMs and redshifts of FRBs. With a much increased sample of FRB DMs and redshifts it may eventually become possible to study the distribution and density of free electrons in the intergalactic medium (see Keane 2018, for more examples of IGM and cosmological studies using FRB DMs and redshifts).

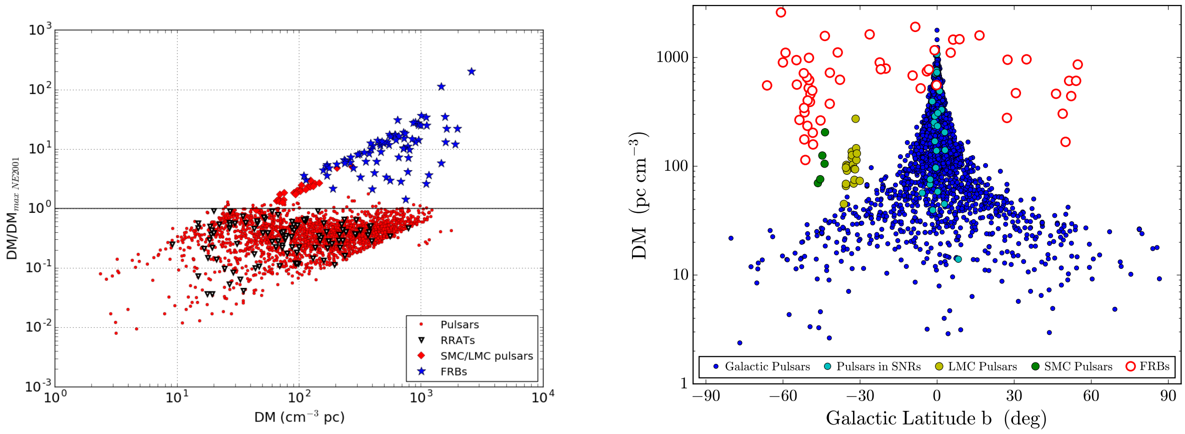

Fig. 3. *Left:* DM value of known Galactic radio pulsars, Galactic RRATs, radio pulsars in the SMC and in the LMC, and of FRBs, relative to the expected DM contribution along the corresponding lines of sight from the Galaxy, according to the NE2001 model. Figure taken from Petroff et al. (2019). *Right:* DM values as a function of Galactic latitude for known pulsars and FRBs. Figure adapted from Cordes & Chatterjee (2019).

With a larger sample of detected FRBs it will also be possible to study their sky distribution, and for instance search FRB directions for clustering (*e.g.*, around galaxy clusters) or anisotropies. Bhandari et al. (2018) analyzed the sky positions of 15 FRBs and found no significant deviation of the positions from an isotropic distribution. Figure 4 shows the distribution of measured fluences and inferred excess dispersion measures for a sample of published FRBs. Significant scatter can be seen in the measured fluences; therefore, it seems unlikely that FRBs could be used as standard candles. For a population of FRBs at different distances (and thus at different excess DMs) one would expect varying fluences; for the currently known sample of FRBs, evidence for such a dependence is seen, as expected. The different selection and observational biases between the various telescopes and surveys that found FRBs appear very clearly in this diagram.

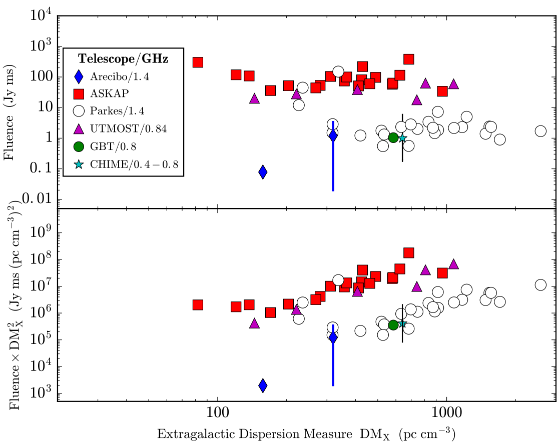

Fig. 4. Fluence – excess DM distribution for known FRBs. The blue line represents the range of fluence values measured for the repeating FRB 121102. Figure from Cordes & Chatterjee (2019).

A number of studies have attempted to estimate the rate of FRBs over the sky. Thornton et al. (2013)

estimated the all-sky rate of FRBs at 1.4 GHz to be of about 10^4 FRBs sky^{-1} day^{-1}. Recent analyses typically converged on rates at 1.4 GHz of a few 10^3 FRBs sky^{-1} day^{-1} with fluences larger than 1 Jy ms (see e.g. Champion et al. 2016; Bhandari et al. 2018). The rates estimated so far correspond to observable FRBs only; indeed, it is not clear at present whether FRB emission is beamed or not. If FRB radio emission is beamed (as in radio pulsars), then the true FRB rate is necessarily larger than estimated from survey detections. In the future, finer estimates of the all sky FRB rate along with a clearer view of the emission (including polarization) properties of FRBs may provide crucial constraints on the progenitor(s) of FRBs.

Among the main unknowns about FRBs are their progenitor(s), and over the past few years a large number of progenitor theories have been proposed. The FRB Theory Wiki[†] (Platts et al. 2018) tabulates proposed FRB theories, and summarizes some of their main features: type of progenitor(s), repeating or non-repeating, emission mechanism, presence of radio, X-ray or gamma-ray counterparts or not, presence of gravitational wave or neutrino counterparts or not, *etc.* In most FRB progenitor theories, FRBs are generated by neutron stars; either isolated neutron stars, neutron stars interacting with their environment or colliding neutron stars. Other theories invoke black hole, white dwarf or more exotic progenitors. As for the other properties of FRBs mentioned above, with a much larger sample of FRBs characterized in detail, more redshift measurements and host galaxy associations, more multi-wavelength and multi-messenger observations (and perhaps, detections), it may eventually become possible to discriminate between FRB progenitor theories. In turn, a better understanding of the origin of FRBs would likely be useful for optimizing FRB search strategies.

3 Prospects

In a little more than a decade, the population of known FRBs has grown from a single event to several tens, including one-off events and repeating FRBs. For some of them, the temporal, frequency, and polarization properties of the burst have been characterized with exquisite details. Yet, as fantastic FRB detectors such as CHIME, ASKAP, FAST, MeerKAT, the Square Kilometre Array (SKA[‡]), *etc.*, are starting to operate or will become available in the future, we could expect that the FRB discovery rate will continue to increase in the coming years, possibly reaching hundreds or thousands of FRB detections every year.

As mentioned in the previous sections, much is still to be learned about FRBs, although enormous progress has been made since the first FRB was found. Examples of open questions for the coming years are: what is the all-sky rate of FRBs? What is their sky distribution? Are there different classes of FRBs? To what extent are repeating FRBs different from non-repeating ones? What are the progenitors of FRBs and what is the emission mechanism? Can we detect them at lower frequencies than 400 MHz, *e.g.* with LOFAR or NenuFAR (see Zarka & Mottez 2016, for simulations of FRB observations with NenuFAR) and at higher frequencies than a few GHz? Could we detect high-energy (X-ray or gamma-ray) emission, neutrinos or gravitational wave emission associated with the radio bursts? What can we learn from FRB radio polarization? Can we obtain better localizations and redshift measurements for more FRB events, including non-repeating ones? Can we identify more host galaxies, and if so, what are their types? Could we clarify the relationship between FRB DMs and redshifts? Can FRBs be used as tools for astrophysics and cosmology? FRB science has so far been extremely exciting, and there is no doubt that even more impressive achievements are yet to come.

I would like to thank the scientific council of the Action Spécifique SKA-LOFAR[§] for the invitation to give this review on its behalf.

References

Bhandari, S., Keane, E. F., Barr, E. D., et al. 2018, Monthly Notices of the Royal Astronomical Society, 475, 1427
Caleb, M., Flynn, C., Bailes, M., et al. 2016, Monthly Notices of the Royal Astronomical Society, 458, 718
Champion, D. J., Petroff, E., Kramer, M., et al. 2016, Monthly Notices of the Royal Astronomical Society, 460, L30
Chatterjee, S., Law, C. J., Wharton, R. S., et al. 2017, Nature, 541, 58

[†]https://frbtheorycat.org/index.php/Main_Page
[‡]https://www.skatelescope.org/
[§]http://as-ska-lofar.fr/

CHIME/FRB Collaboration, Amiri, M., Bandura, K., et al. 2019a, Nature, 566, 235
CHIME/FRB Collaboration, Amiri, M., Bandura, K., et al. 2019b, Nature, 566, 230
Cordes, J. M. & Chatterjee, S. 2019, astro-ph/1906.05878
Cordes, J. M. & Lazio, T. J. W. 2002, astro-ph/0207156
Hessels, J. W. T., Spitler, L. G., Seymour, A. D., et al. 2019, The Astrophysical Journal, 876, L23
Keane, E. F. 2018, Nature Astronomy, 2, 865
Keane, E. F., Kramer, M., Lyne, A. G., Stappers, B. W., & McLaughlin, M. A. 2011, Monthly Notices of the Royal Astronomical Society, 415, 3065
Lorimer, D. R., Bailes, M., McLaughlin, M. A., Narkevic, D. J., & Crawford, F. 2007, Science, 318, 777
Masui, K., Lin, H.-H., Sievers, J., et al. 2015, Nature, 528, 523
McLaughlin, M. A., Lyne, A. G., Lorimer, D. R., et al. 2006, Nature, 439, 817
Michilli, D., Seymour, A., Hessels, J. W. T., et al. 2018, Nature, 553, 182
Petroff, E., Barr, E. D., Jameson, A., et al. 2016, PASA, 33, e045
Petroff, E., Hessels, J. W. T., & Lorimer, D. R. 2019, Astronomy and Astrophysics Review, 27, 4
Platts, E., Weltman, A., Walters, A., et al. 2018, arXiv e-prints, arXiv:1810.05836
Scholz, P., Bogdanov, S., Hessels, J. W. T., et al. 2017, The Astrophysical Journal, 846, 80
Shannon, R. M., Macquart, J. P., Bannister, K. W., et al. 2018, Nature, 562, 386
Spitler, L. G., Cordes, J. M., Hessels, J. W. T., et al. 2014, The Astrophysical Journal, 790, 101
Spitler, L. G., Scholz, P., Hessels, J. W. T., et al. 2016, Nature, 531, 202
Tendulkar, S. P., Bassa, C. G., Cordes, J. M., et al. 2017, The Astrophysical Journal, 834, L7
The CHIME/FRB Collaboration, :, Andersen, B. C., et al. 2019, arXiv e-prints, arXiv:1908.03507
Thornton, D., Stappers, B., Bailes, M., et al. 2013, Science, 341, 53
Zarka, P. & Mottez, F. 2016, in SF2A-2016: Proceedings of the Annual meeting of the French Society of Astronomy and Astrophysics, 347–351

SF2A 2019
P. Di Matteo, O. Creevey, A. Crida, G. Kordopatis, J. Malzac, J.-B. Marquette, M. N'Diaye, O. Venot (eds)

ACHILLES: ASTRONOMICAL HETERODYNE IN INFRARED-OPTICAL WITH MULTIAPERTURES

M. Hadjara[1], F. Besser[1], N. Ramos[1], P. Zorzi[1], O. Arias[1], M. Cadiz[1], B. Cornejo[1], D. Corvaln[1], K. Espinoza[1], R. Jara[1], N. Henriquez[1], C. Guerrero[1], B. Guo[1], J. Ocaranza[1], G. Pereira[1], M. Pina[1], D. Pollarolo[1], C. Rearte[1], I. Reyes[1], A. Rodriguez[1], J. Rojas[1], T. Rojas[1], J. Rubio[1] and E. A. Michael[1]

Abstract. We present a low-cost heterodyne near-IR interferometry instrument (H-band), which is being largely made only by Chilean students. It is aimed to work with kilometric baselines to allow further detailed studies of the stars of our galaxy (including exoplanets), as well as finally widen the field of action of the Optical Long-Baseline Interferometry (OLBI) to extragalactic objects. As this instrument is obviously of great technical complexity, this paper can only outline the main parts that it is composed of and how it basically works.

Keywords: instrumentation: interferometers, instrumentation: high angular resolution, techniques: interferometric, infrared: stars

1 Introduction

ACHILLES is an interferometer prototype based on commercial 1.55 μm fiber components. As the most crucial component of it we characterized a novel sub-shot noise correlation detection system for two receivers, and are about to extend it to three receivers. To accomplish this, we acquired a 2^{nd} Generation Reconfigurable Open Architecture Computing Hardware (ROACH2) platform for the correlator with the capacity to digitize four parallel 1.25 GHz bandwidth receivers, so that phase closure measurements will be possible. We extend the stabilization of the local oscillator (LO) phase between the telescopes to cover the whole acoustic perturbation range. For the telescope to single-mode fiber coupling under atmospheric perturbation, we develop a fiber actuator lock-loop for small telescopes and good seeing, and test an adaptive optics approach for mediocre seeing and/or larger telescopes. We constructed also a frequency comb based laser synthesizer system to include tests on multi-frequency band measurements towards ultra-broad band dispersed heterodyne detection systems finally useful for the Planet Formation Imager (PFI; Monnier et al. 2018b,a).

We develop this concept with the motivation to reach kilometric baselines for larger groups of telescopes. Indeed, as a comparison example, a single telescope with a diameter $D = 40cm$ at a wavelength $\lambda \approx 1.55\mu m$ offers an angular resolution $\theta \approx 10^3\,mas$, where, at the same λ, the Very Large Telescope Interferometer (VLTI) at Paranal/Chile with its maximum baseline $B_{max} \approx 200\,m$ offer $\theta \approx 1.5\,mas$, while the PFI with its expected $B_{max} \approx 10\,\mathrm{km}$ could reach (always at the same λ) a $\theta \approx 3 \times 10^{-2}\,mas$. In addition, the noise temperature of a cross-correlation heterodyne detection system may be under the quantum limit (Michael & Besser 2018).

2 General concept

Based on commercial 1.55μm-fiber technology, ACHILLES works in the H-band (λ =1.4-1.8μm) with more than 95% of transmission through the earth's atmosphere. Conceived as a mobile instrument, it may be connected to any group of existing less-used medium size optical telescopes (e.g. at La Silla, Las Campanas or Tololo, Chile). Our instrument is designed for high-precision phase control for kilometric baselines and nulling interferometry; e.g. using the $14'$ Goto-Dobsonians with the ALMA buried fibers to run a demonstration experiment. As well as ACHILLES could be used as development-platform forwards Planet Formation Imager (PFI) relevant techniques (Broadband heterodyne detection, Phase tracking). Figure 1 below depicts our current scheme of a static two-telescope interferometer.

[1] Astrophotonics group laboratory. University of Chile, Av. Tupper 2007, Santiago, Chile

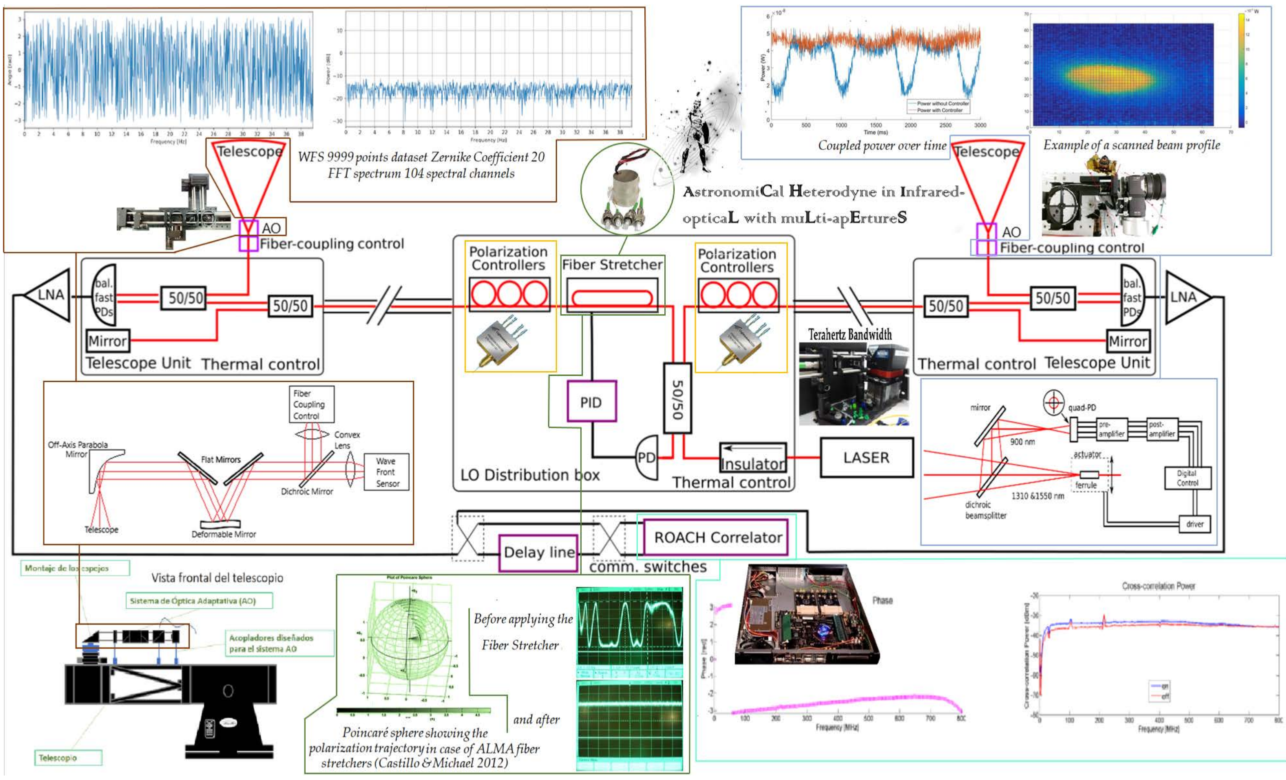

Fig. 1. Actual test setup of a static two-telescope interferometer (Besser et al. 2016, 2018). We added some real pictures and plots of main components of ACHILLES, where farmed; in brown the Adaptive Optics (AO), in blue the Coupling Control (Ramos et al. 2017), in green the Fiber Stretcher (Castillo & Michael 2012), in cyan ROACH (Besser et al. 2016) and in yellow the Polarization Control. Note that two opposite waves don't influence each other in a linear medium, which is the case at the low intensities we have in the fibers (superposition principle). LO-power distribution limit for the heterodyne interferometer: $PL \leq 500$ Wm, i.e. 1000W for 5m and 100mW for 5 km.

2.1 *Main components of ACHILLES*

ACHILLES is mainly composed of:

2.1.1 Adaptive Optics

For a better coupling efficiency we use a lens and mirror arrangement to have a "CLEAN" wavefront to be coupled to the fiber, a piezoelectric deformable mirror DMP40M-P01, which counteracts in real time the effects of Earth's atmosphere, and a wavefront sensor WFS20-14AR/M.

2.1.2 Fiber Coupling Control and Tip-Tilt Correction

Our fiber coupling controller is an amateur guiding camera for telescope coarse auto-guiding and fine guiding through an original control design. Indeed, our small telescope (35 cm diameter) needs only tip-tilt correction under good seeing, where the tip-tilt correction is done with a CD pick-up actuator, thanks to a Digital control based on dsPIC33EP device (Ramos et al. 2017).

2.1.3 Fiber Stretcher and Polarization Control

In order to keep the same phase between the two receivers, we use a fiber stretcher and a PID (Proportional-Integral-Derivative) controller. While, we correct the polarization affected by the stretching of the fiber, to ensure a constant polarization at the telescope, especially maintain parallel polarizations at all telescopes and so maximize the cross-correlations (Castillo & Michael 2012).

2.1.4 Terahertz Bandwidth

This important optional component consists in a comb-generator-based LO-system for future experiments to introduce a spectral LO step-tunability over a bandwidth of a terahertz, while fine-tuning is provided over the thermal control of the Koheras fiber laser. Additionally, it is planned for future experiments where signal and comb lines will be spectroscopically dispersed in special photonics to multiple parallelized receivers.

2.1.5 ROACH-based Correlator

The current ROACH-board is a Xilinx FPGA-board with two 3 GSPS iADC cards. It allows us a compilation of open-source correlator models with Xilinx Simulink in Matlab/Linux environment, and development of own improved models. It has also its own extension of the correlator model by a second integration block, enabling chopped ON/OFF measurements (so-called Dicke-switching in radio-astronomy).

3 Conclusions

Our short-term goals are: To obtain "first light" on a star; by finish improving the control frequency of the coupling control loop and the adding an adaptive optics system to correct higher mode turbulences. As well as to finish developing a heterodyne dispersed receiver based on an optical comb, without forgetting to manage the polarization control of the electromagnetic waves. Then proceed to the next step of implementing a 3-telescope interferometer to get closure phase. While our aims at long term are: to run tests at the ISI (Infrared Spatial Interferometer; Townes et al. 1998; Hale et al. 2000) or at the VLTI interferometer, and to achieve a test bench for mid-infrared receivers for the PFI.

Special thanks go to the project grants ESO-MIXTO funds 2018, CONICYT-ALMA funds N^o 31090018/31140025, QUIMAL N^o 150010 and CATA-Basal PFB-06.

References

Besser, F. E., Ramos, N., Rates, A., et al. 2018, in Society of Photo-Optical Instrumentation Engineers (SPIE) Conference Series, Vol. 10701, Proc. SPIE, 107012L

Besser, F. E., Rates, A., Ortega, N., et al. 2016, in Society of Photo-Optical Instrumentation Engineers (SPIE) Conference Series, Vol. 9907, Proc. SPIE, 99072L

Castillo, J. A. & Michael, E. A. 2012, IEEE Photonics Journal, 4, 2390

Hale, D. D. S., Bester, M., Danchi, W. C., et al. 2000, ApJ, 537, 998

Michael, E. A. & Besser, F. E. 2018, IEEE Access, 6, 45299

Monnier, J. D., Ireland, M., Kraus, S., et al. 2018a, in Society of Photo-Optical Instrumentation Engineers (SPIE) Conference Series, Vol. 10701, Proc. SPIE, 1070118

Monnier, J. D., Kraus, S., Ireland, M. J., et al. 2018b, Experimental Astronomy, 46, 517

Ramos, N., Ortega, N. M., Michael, E. A., Rates, A., & Besser, F. E. 2017, in 2017 CHILEAN Conference on Electrical, Electronics Engineering, Information and Communication Technologies (CHILECON), 1–5

Townes, C. H., Bester, M., Danchi, W. C., et al. 1998, in Society of Photo-Optical Instrumentation Engineers (SPIE) Conference Series, Vol. 3350, Proc. SPIE, ed. R. D. Reasenberg, 908–932

SF2A 2019
P. Di Matteo, O. Creevey, A. Crida, G. Kordopatis, J. Malzac, J.-B. Marquette, M. N'Diaye, O. Venot (eds)

THE INTERSTELLAR MEDIUM IN SILICO

P. Lesaffre[1]

Abstract.
I will review the contributions of numerical simulations to our understanding of the physics and chemistry of the interstellar medium.

1D simulations make justice to the rich microphysics of astrophysical gases. They can afford large chemical networks, detailed microscopic transport (viscosity, resistivity, ambipolar and chemical diffusion...), complex radiative transfer or can accommodate the multiple facets of dust grains physics. Although they remain in a constrained geometrical framework, they often are our primary link to observations.

Direct multi-dimensional simulations thrive on our national computing capabilities and trigger efforts for innovation in data analysis. They can be dedicated to isolated objects, or attempt to render statistical properties of the morphology or dynamics uncovered by observational surveys. Sometimes, statistical models themselves can be used to synthesise multidimensional observations: they help disentangle large scale structures from smaller scale turbulence and resolve observational biases.

These experiments "in Silico" help us to make the most of the interpretation of observational results and allow us to calibrate future instruments thanks to observational synthesis. I will brush some of the great challenges faced by these numerical experiments within the next few years: how to best extract dynamical information from the line shapes, how to master crucial dust physics ingredients (e.g. coagulation and rotation), and how we are going to need the help of engineers to go through the exascale transition.

Keywords: ISM, simulations, statistics

1 Introduction

The interstellar medium (ISM) is a *multi-phase* gaseous system where various phases have been obervationnally shown to coexist (hot ionised medium, warm ionised medium, warm neutral medium, cold neutral medium, diffuse and dense molecular media). These phases are in approximate pressure equilibrium, while their density and temperature span about six orders of magnitude. The characteristic scales of observed structures within these phases range from about 100pc (the galactic disc scale-height) down to shearing scales of a few mpc, and may range down to dissipative scales (viscous scales are on the order of 10^{-6} pc for diffuse gas): the ISM is a hugely *multi-scale* system. Finally, various forms of energy (thermal, internal, magnetic, gravitational, radiative, cosmic-rays) are observed to be in rough equipartition: the ISM is *multi-physics*.

The life of ISM modelers is hence as exciting as it is challenging... I am going to present here some of the tricks which numerical physicists of the ISM have resorted to in order to circumvent some of these difficulties. This review does not intend to be exhaustive, and I apologise to those who wished their work had been mentionned here. It is organised from the largest scales down to microphysics aspects, and illustrations ought to be found in the pdf presentation of my talk, so that the present text is going to be figure-less.

2 Global simulations of the ISM

Galactic scale simulations of the ISM include at least one pressure-scale height of the galaxy and attempt to resolve as much as they can the scales of the molecular clouds. The main physics ingredients are cooling, magnetic fields and gravitation (including both the galactic potential and self-gravitation).

[1] Laboratoire de Physique de l'ENS, ENS, Université PSL, CNRS, Sorbonne Université, Université Paris-Diderot, Paris, France

Hennebelle (2018) use the zoom technique to get the most of the adaptive mesh refinement of the code RAMSES (Fromang et al. 2006). The principle is to set a main regular “background” grid over the full extent of the computational domain (here a thousand pc), and decide on a choice region where the resolution needs to be pushed to the extreme (here a cubic region of 100 pc side-length, where the adaptive mesh capability of RAMSES is released to a maximum resolution of 4×10^{-3} pc). The focused region is embedded in several buffer zones with decreasing resolution to avoid sharp resolution jumps.

The resulting simulation allows to bridge the gap between galactic scales and a few mpc (a range of 260000 in scales !), thus providing access to small dense clumps in their natural environment for a relatively low cost compared to the resolution achieved (one such simulation is about 10 million CPU hours, and was awarded time by PRACE under the FRIGG project, PI P. Hennebelle). Statistical measurements reveal that resolution effects and sticky self-gravitating zones still remain to be better controlled, but the technique bears a huge potential for the future.

3 Local simulations of the ISM

On the contrary, one can focus on a local patch of the ISM, assuming statistically homogeneous properties (such as density, turbulent forcing, or r.m.s. velocity). The assumption of homogeneity requires to perform parameter studies, made possible by the lower computational cost compared to global simulations which are usually 'one shot'.

These simulations are more classic, less costly (about 100 000 CPU hours each), and allow to include more physics ingredients (such as radiative transfer González et al. (2015); Valdivia et al. (2016), minimal chemistry Valdivia et al. (2016), or dissipation physics Masson et al. (2016); Momferratos et al. (2014)).

For example, in the framework of the ERC MIST (PI E. Falgarone), we study dissipative structures and their observational signatures, in the hope of shedding light on the surprising molecular fertility of violent and dilute media. ERC funding allows a small team to own a machine with an available 2-3 million CPU hours per year which will later be incorporated in a meso-scale computational center (such as mesoPSL). These simulations have so far allowed us to show the unexpected weight of incompressible motions in the total dissipation budget. We show most of the dissipative structures have a sheet-like topology and we suspect these sheets project onto the plane of sky as sharp structures which can be identified as filaments by observers.

4 Link to observations

There are thousands of ways to look at a painting and convey what we've seen to another human being. One can simply take a high resolution picture of it, but the human eye can be stroke by colors, textures, contour shapes and their relative size or orientations, or more personal memories the painting brings back to us. Similarly, there are many statistical tools to assess an observational image: Fourier spectrum, filaments / clumps statistics, principal component analysis and variants (Gratier et al. 2017; Bron et al. 2018), intermittency statistics (increments statistics, structure functions or multi-fractal properties), and more recently wavelet scattering coefficients (Mallat 2012). A new version of the latter technique (Allys et al. 2019) which condenses the relative orientations between scales into a reduced set of coefficients has been recently shown to characterise very efficiently the non-linearities of the column-density maps of turbulent simulations.

The link to observations can also be realised by “painting” back observational properties on simplified simulations which are missing some of the necessary microphysics. For instance, Levrier et al. (2012) reproduced line-of-sights of a two-phase simulation of the ISM by using the Meudon PDR code (Le Petit et al. 2006) on the simulation density profiles to compute the column-density of observable tracers. Another approach can be to replay the thermodynamic history of lagrangian tracers with an extensive chemical network (Ruaud et al. 2018). This emphasises the need for sub-grid models in multi-dimensional simulations.

5 Low-dimensional models

Multi-dimensional simulations thus require calibration using 1D or 0D tools which allow to investigate an extensive range of the microphysics processes at play in the ISM (radiative transfer, detailed chemistry, grain physics using size by size bins etc..). These models (Meudon PDR code, Dustem, Paris-Durham shock code, TDR model...) capitalise on their simplified geometry to run very efficiently (a few CPU minutes on a laptop) and hence allow huge grids of parameters to be computed. These grids require new tools to be processed efficiently and the ISM database (ISMDB, see `http://ism.obspm.fr/`) provides efficient ways to inquire the huge variety of observables produced by these models and match them with actual observed data.

6 Microphysics rates

Finally, these low-dimensional models need refined collisional rates and atomic and molecular data to produce accurate predictions for the chemistry and line emission of observable tracers. Numerical computation for these rates span a huge range of computational needs depending on the degree of approximation used. The recent development of a versatile collection of computational platforms (from personal laptops, via meso-scale centers, to national computational capabilities) has allowed huge progress in the comparison between theory and experiments (Kashinski et al. 2017).

7 Prospects

To conclude, I will lay out three of the main ways of investigations which seem to be necessary for the near future in ISM computations.

7.1 Grain physics

Dust acts everywhere in the galactic matter cycle. It controls the amount of energy radiated away during protostellar collapse. It is the main catalyst for the formation of the most common molecule H_2. Icy grains surface chemistry is arguably one of the major paths towards molecular complexity. Feed back through AGB winds rely on the understanding of grains radiative properties. Grains often control the ionisation degree and the mass loading of magnetic fields. Polarisation measurements require dust polarisation models to test the interplay between magnetic fields and ISM dynamics. Anomalous emission from grains confirmed by Planck measurements hints at the importance of grains disruption by spinning (Hoang & Tram 2019; Tram et al. 2019). Many observational problems of the ISM seem to be linked to grain physics, which will likely be the focus of many ISM modelers in the next few years.

7.2 Line shapes

Until now, numerical simulations of the ISM have mainly focused on global emission properties (such as total line of sight column-densities or emission, or centroid velocities). But the advent of wide-field spectroscopy bears a wealth of dynamical information yet to be mined. Orkisz et al. (2017) have shown how to use statistically part of the velocity information by using its first and second moments. Tram et al. (2018) and Neufeld et al. (2019) have shown how detailed modeling of the line shape emission can lead to much refined diagnostics from shock emission, including the best proof of the existence of C-shocks to date. But I believe there is still a lot to be gained by understanding how chemistry, excitation and dynamics conspire to shape emission lines.

7.3 New hardwares

New generations of hardwares are motivated mainly by smart phones and video games, and are now more focused on the efficiency of energy consumption rather than sheer computational power. The future architectures are going to be more and more hybrid, extending the symbiosis between GPUs and CPUs which we have witnessed in the last two decades. This requires us to hire good computational engineers with a tight communication between them and the researchers. The development of DUMSES on GPUs by M. Joos is a nice example of the good practice which we should be aiming at.

This presentation was made in consulation with A. Faure, J. Pety, P. Hennebelle, B. Godard, F. Levrier, E. Falgarone, F. Le Petit, E. Allys and V. Wakelam, all of whom I thank for providing me material for my slides as well as comments.

References

Allys, E., Levrier, F., Zhang, S., et al. 2019, arXiv e-prints, arXiv:1905.01372

Bron, E., Daudon, C., Pety, J., et al. 2018, A&A, 610, A12

Fromang, S., Hennebelle, P., & Teyssier, R. 2006, A&A, 457, 371

González, M., Vaytet, N., Commerçon, B., & Masson, J. 2015, A&A, 578, A12
Gratier, P., Bron, E., Gerin, M., et al. 2017, A&A, 599, A100
Hennebelle, P. 2018, A&A, 611, A24
Hoang, T. & Tram, L. N. 2019, ApJ, 877, 36
Kashinski, D., Talbi, D., Hickman, A., et al. 2017, The Journal of chemical physics, 146, 204109
Le Petit, F., Nehmé, C., Le Bourlot, J., & Roueff, E. 2006, ApJS, 164, 506
Levrier, F., Le Petit, F., Hennebelle, P., et al. 2012, A&A, 544, A22
Mallat, S. 2012, Communications on Pure and Applied Mathematics, 65, 1331
Masson, J., Chabrier, G., Hennebelle, P., Vaytet, N., & Commerçon, B. 2016, A&A, 587, A32
Momferratos, G., Lesaffre, P., Falgarone, E., & Pineau des Forêts, G. 2014, MNRAS, 443, 86
Neufeld, D. A., DeWitt, C., Lesaffre, P., et al. 2019, ApJ, 878, L18
Orkisz, J. H., Pety, J., Gerin, M., et al. 2017, A&A, 599, A99
Ruaud, M., Wakelam, V., Gratier, P., & Bonnell, I. A. 2018, A&A, 611, A96
Tram, L. N., Hoang, T., Soam, A., Lesaffre, P., & Reach, W. 2019, arXiv e-prints, arXiv:1907.10654
Tram, L. N., Lesaffre, P., Cabrit, S., Gusdorf, A., & Nhung, P. T. 2018, MNRAS, 473, 1472
Valdivia, V., Hennebelle, P., Gerin, M., & Lesaffre, P. 2016, A&A, 587, A76

SF2A 2019
P. Di Matteo, O. Creevey, A. Crida, G. Kordopatis, J. Malzac, J.-B. Marquette, M. N'Diaye, O. Venot (eds)

STATUS OF THE AMATEUR-PROFESSIONAL COLLABORATIONS

T. Midavaine[1] and F. Herpin[2]

Abstract. Amateur-professional collaboration is a very vivid field in astronomy. The Société Astronomique de France (SAF) is very active with dedicated commissions gathering amateurs and professionals in specialized fields. In 2018 we organized a first workshop during the "Journées de la SF2A" to share the status of collaborations. Following the success of this meeting with several proposed actions, SAF and SF2A agreed on the development of a partnership to share the realization of several tasks, including a second workshop during the "Journées de la SF2A 2019", introduced by this plenary session paper. The vision is to build an array of amateur observers networking with professionals proposing topics and/or targets for campaign survey. Thus we are able to review the latest results of such collaborations, the new projects to be launched and the means (hardware, software, web sites, and organizations) required to support and develop such projects. Furthermore SAF and SF2A are working on the implementation of an annual dedicated prize awarding best practices in pro-am collaborations. A review of recommendations are shared to be implemented in the coming year.

Keywords: citizen science, amateur-professionnal, pro-am collaborations, astronomy

1 Introduction

Thanks to the very successful workshop hold during the "Journées de la SF2A 2018" in Bordeaux, SF2A and SAF decided to build a partnership. A dedicated group in SAF was created in September 2018 to develop several tasks proposed during the first workshop. A meeting between SF2A and SAF allowed to agreed on several decisions. One of them was to prepare a second workshop and a talk for the plenary session during the *Journées de la SF2A 2019* organized in Nice 14-17 May 2019 synthesized in this paper.

2 SAF and SF2A strength for this partnership

SAF is a 132 years old Society, funded by Camille Flammarion, gathering more than 2000 members and *L'Astronomie* magazine[*] subscribers. Within the Society, twelve commissions are supporting dedicated fields, with member and observer coordination, organizing meetings and publications: Astronautic and Space Technologies, Comets, Cosmology, Double Stars, History, Instruments, Meteors, Planet Observations, Planetology, Radioastronomy, Sun, Sundials.

SAF edits several publications: *L'Astronomie* (monthly), *Observations & Travaux*[†] (twice a year), Ephemerides Astronomiques[‡] (annual), astronomical books, and *SAF On Line Web*[§] site with a Pro-Am dedicated field introduced last year. Lectures, conferences, astronomical tutorials, are organized all the year long. Every year in May or June, Astronomical prizes and Medals, Janssen Prize are awarded with the annual national meeting of the commissions reporting their related activities. Astronomical event gatherings (Eclipse, Day of the Sun, abroad travels) are coordinated, and "Astrociel" a two weeks star party is organized every year in August at

[1] Société Astronomique de France, 3 rue Beethoven, 75016 Paris, France
[2] Société Française d'Astronomie et d'Astrophysique

[*]Mensual magazine published by Société Astronomique de France, Patrick Baradeau Head of Publications, Fabrice Mottez succeeded to Janet Borg Editor

[†]ISSN 0004-6302, technical review of the SAF Commissions, Patrick Baradeau Head of Publications, Pierre Durand Editor.

[‡]an annual publication realized by Jean Meeus

[§]https://saf-astronomie.fr/collaboration_pro_am/

Valdrome in the Alps. Three observatories (Sorbonne, Juvisy, Belesta) are managed both for public observations and amateur projects. SF2A is a 40 years old Society gathering more than 400 professional members and 1400 newsletter subscribers. SF2A is organizing an annual event, “Journées de la SF2A”, gathering the French professional community, and including some foreign participants, in 4 days dedicated to french astronomical research with plenary sessions and 16 parallel workshops. The Prize of the young researcher, and best PhD are awarded every year. On behalf the Académie des Sciences, SF2A is the French interface to IAU.

Fig. 1. Covers of L’Astronomie (mai 2009) and Ciel & Espace Hors Serie (octobre 2014) issues left and right respectively

3 Pro-Am Collaborations

These collaborations are very active and produce papers and lectures spread over a large number of meetings and conferences. This is one of the oldest field of citizen science and one of the pillars of history of science. L’Astronomie and Ciel et Espace published in 2009 and 2014 respectively (cf. Fig.1) dedicated issues reviewing the most active topics in France. In addition, amateur-professional collaboration is very active to maintain and promote legacy instruments either for the above activities and to allow public and school access to astronomical heritage. Some amateur astronomers are retired industry technicians or engineers able to maintain old instruments relying on previous generation technologies (old telescopes, electro-mechanics, old computers, refurbished equipmentsÉ). In addition, new instrument and software developments involve such Am-Pro collaborations too (sensitive CMOS cameras, spectrograph, image processing suite, etc).

4 The Amateur-Professional Topics Table

Fiveteen years ago T. Midavaine consolidated a database in an Excel file gathering the panorama of astronomical topics for amateurs willing to do science. It was first published on the Club Eclipse web site (http://astrosurf.com/club_eclipse). This data base classifies amateur activities breakdown in five headlines:

- object discovery: the most fascinating task for amateurs is the ability to discover new objects,
- object surveillance: one amateur strength, thanks to the number of observers spread over all the longitudes,
- observation campaign : mobilization of observers on astronomical events for data acquisition,
- data gathering: thanks to methodologies, digital imaging and processing, amateurs can provide reliable metrological data in astrometry, photometry, polarimetry, spectroscopy, time and datation,
- exploitation of data base: this is a growing up field, thanks to dedicated web site gathering the overwhelming data collected by robotic instruments or space probes.

The Amateur-Professional Topics Table Version X, updated in 2019 following this workshop, is shown in Fig.2 Through the lines in column A, you have a review of all the potential topics from the closest like shooting stars, up to the farthest related to quasars or even cosmology! The columns are organized according to the above activity breakdown. It covers all the topics spread over a large range of required skillness from the beginners to start to do science up to the amateur experts, including the thema for amateur professional collaborations from data acquisition, up to scientific publishing. Here are some comments on the column contents:

A	B	C	D	E	F	G	H	I	J	K	L	M	N	O	P	Q	R
Objets	Découverte	Suivi	Evenement	Métrologie	Astromètrie	Photomètrie	Polarisation	Spectroscopi	Rés Tempore	Exploitation	Point Focal France	Organisation	site web	e mail	Conférence		
Unités	Mag min				arcsec	Précision	Taux de Pola	P Résolution	seconde	sur Internet			astro-proam.com				
Météorites		Vigie Ciel									Brigitte Zanda	Fripon	https://www.fripon.org/		Commission des météores SAF		
Météores	-4	Fripon	Fragmentation	Orbite, Impac	60				1		Karl Antier	REFORME	www.boam.fr	reformemeteor.net	International Meteor Conference		
Essaims d'étoiles filantes	1	Orbite	Sursaut	ZHR Radian	240				60		J. Vaubaillon	IMO	www.imo.net		International Meteor Conference		
Cratères d'impact terrestre										Google Earth	David Baratoux						
Aurores Boréales													www.spaceweather.com	wagner.d@uni-jena.de			
Night Glow																	
Sprite																	
Rayons Cosmiques																	
Lune			TLP	Occultation Rasante			0,1	10	0,1	Moon zoo		ALPO, IOTA	users.aber.ac/atc/tlp/tlp.htm				
Impacts sur la Lune			flash								Sylvain Bouley	IMCCE	http://uranoscope.free.fr				
Lumière Cendrée								10			Luc Arnold						
Lumière Zodiacale										Stardust							
Planètes		Météorologie	Tempète, Occultation					100	1		SAF commission des planètes	ALPO	www.astrosurf.com/planetessaf/	delcroix.marc@free.fr	European Planetary Science Congress		
Venus		Akatsuki									Christophe Pellier	Akatsuki		coordinatewithakatsuki@gmai	European Planetary Science Congress		
Mars		Météorologie	Tempete, nuages							planet four	Christophe Pellier	ISMO	http://www.mars.dti.ne.jp/~cmo/ISMO.html	chrispellier@sfr.fr	European Planetary Science Congress		
Jupiter		Junocam	Impact							missionjuno.swri.edu	Marc Delcroix	SAF	www.missionjuno.swri.edu/junocam/	delcroix.marc@free.fr	Commission des observations planétaires SAF		
Jupiter		Météorologie	évolutions formations atmosphèriques								Christophe Pellier	Jupos, IOPW	http://jupos.privat.t-online.de/index.htm http://www.astrosurf.com/planetessaf/doc/project_detect.php	chrispellier@sfr.fr	European Planetary Science Congress		
Saturne		Météorologie	Tempete								Marc Delcroix	SAF, IOPW	http://pvol2.ehu.eus/pvol2/	delcroix.marc@free.fr	European Planetary Science Congress		
Uranus, Neptune		Météorologie	Tempete								Marc Delcroix	SAF, IOPW	http://pvol2.ehu.eus/pvol2/	delcroix.marc@free.fr	European Planetary Science Congress		
Impacts sur les Planètes géantes			Impacts						1		Kévin Baillié	IMCCE	https://www.imcce.fr/recherche/campagnes-	kevin.baillie@observatoiredeparis.psl.eu			
Satellites de Planètes	21		Occultation	Phemu	0,04	0,1			1		Jean-Eudes Arlot, Bruno Sicardy	IMCCE	www.imcce.fr/phemu09	Jean-Eudes.Arlot@obspm.fr			
Astéroides (orbites)	19	Position	Occultation		0,2	0,1			0,1	http://www.asteroidz	Jerome Berthier	MPC	www.minorplanetcenter.net/iau/	mpc@cfa.harvard.edu		http://m1p.fr/sof/	
Astéroides (objets)		CdR	Occultation			0,05		10	0,1	Asteroids@home	Benoit Carry, Eric Frappa	EAON, IOTA,	www.euraster.fr		ESOP		
Astéroides longues périodes		CdR		14		0,1					Stephane Fauvaud		http://asteroids.2614536-0.web-hosting.es/	sfauvaud@mail.com			
Satellites d'astéroides	CdR ou Occu	CdR	Occultation			0,01			0,1		Raoul Behrend	CdR-CdL	http://obswww.unige.ch/-behrend/page_cou.html				
Géocroiseurs AAA	19			Orbite, Impact				10	0,1	orbit@home	Mirel Birlan	EURONEAR	http://www.minorplanetcenter.org/iau/NEO/TheNEOPage.html				
Objets Trans Neptuniens	20		Lucky Star		0,2	0,2		10	10		Bruno Sicardy	LESIA	http://lesia.obspm.fr/lucky-star/predictions/	Bruno.Sicardy@obspm.fr			
Objets de la bande de Kuiper				Myosotis				10			Francoise Roque						
Planète 9										Backyard Worlds: Planet 9							
Comètes	14		Sursaut, Fragmentation		0,2	0,2		100	1	Soho	Nicolas Biver	CBAT	www.cfa.harvard.edu/iau/mpc.html	cbatiau@eps.harvard.edu	Commission Comètes SAF		
Comete 67P Tchouri			CdR								David Romeuf						
Soleil Taches		Nbre Wolf					0,05	1000	0,1	Soho	Didier Favre	GEFOS	http://solardatabase.free.fr		Commission du Soleil SAF		
Soleil Protubérances			Eruption, Eclipse				0,05	1000	0,1	Solar stormwatch	Franck Vessière	Observateurs	www.climso.fr		liste astrosoleil		
Soleil Couronne			Eclipse Totale										http://rosetta.jpl.nasa.gov/rosetta-ground-based-campaign				
Etoiles			Alertes GAIA	Temp Classe Spectrale				10		CDS VizieR	Alertes GAIA		http://cdsportal.u-strasbg.fr/				
Etoiles à record				Mouvement p	0,1	0,1		10	10000	DASCH	CDS	D. Gray modèle des atmosphères					
Jumelles du Soleil	9																
Etoiles Doubles	11				0,1	0,1		10	100000		David Valls Gabaud	WDS USNO	http://ad.usno.navy.mil/wds		Commission des étoiles doubles SAF		
Binaires Spectroscopiques								1000			Daniel Bonneau						
Binaires à éclipses EA EW	12	Photometrique				0,01	0,1	10000	1000	VSX	Laurent Corp	AAVSO/VSX	Gerry Samolyk	astro.laucorp@orange.fr			
Etoiles Variables	10	CdL				0,1			100		Dominique Proust	AFOEV	http://astro.u-strasbg.fr/afoev	afoev@astro.u-strasbg.fr			
Céphéides		0	Maxima pulsa	Spectres				10000	300-3600	aavso.org/vsx	Denis Gillet, Philippe Mathias	GRRR	http://www.aavso.org/vsx/index.php?view=s	Philippe.Mathias@irap.omp.eu			
RR Lyrae	14	GRSS	Maxima pulsa	Spectres		0,1		10000	300-900		Jean-Francois Leborgne	GEOS	http://rr-lyr.irap.omp.eu/		Workshop annuel à l'OHP		
Delta Scuti						0,1								denis.gillet@osupytheas.fr			
Etoiles Be, Eruptives	12		Sursaut			0,1		1000	10000	BeSS	Coralie Neiner	ARAS	http://basebe.obspm.fr/basebe		Stages Spectro OHP Aude		
Etoiles OB actives											Christian Buil	ARAS	www.astrosurf.com/buil/index.htm				
Etoiles Cataclismiques											Etienne Morelle		http://cbastro.org				
Etoiles Symbiotiques											Francois Teyssier	AAVSO		francois.teyssier@dbmail.com			
Nouvelles classes variables						0,001			100		Denis Gilet	GRE	Pulsating star		OHP		
Pulsars	10					0,1			0,01	einstein@home	Fabrice Mottez		http://einstein.phys.uwm.edu/				
Trous Noirs Galactiques																	
Disques Stellaires										diskdetective.org		satellite WISE	http://www.diskdetective.org				
Planètes Extra Solaire		Vitesse radia	Transit			0,01		10000	10	planethunters.org	Alexandre Santerne	transitsearch.	http://var2.astro.cz/ETD	http://brucegary.net	http://var2.astro.cz/ETD/		
Super-Terres										Kepler	Jean-Philippe Beaulieu		http://exoplanet.eu				
Satellites de Planètes Extra Solaire						0,01			10		Jean Schneider, David Kipping						
Vie extraterrestre										seti@home		SETI	seti@home				
Novae de la Voie Lactée	6,2					0,05			10000			CBAT	http://www.cbat.eps.harvard.edu/index.html	cbatiau@eps.harvard.edu			
Super Novae Voie Lactée	0	ASAS-SN									Emmanuel COnseil		http://www.cfa.harvard.edu/iau/cbat.html	skypub.com/supernovarace			
Remanents de SN					1		0,1	1000	100000		Agnés Acker						
Nébuleuses Planétaires	16			étoile centrale			0,1	600		HASH Database	Pascal Le Dû	Deep Sky Hu	http://planetarynebulae.net/	pascal.le.du@shom.fr	https://apn7.com/		
Nebuleuse de Wolf-Rayet										Digital Sky Survey	Agnés Acker			agnes.acker@astro.unistra.fr			
Nébuleuses								1000									
Bulles cosmiques										Milky way project			www.milkywayproject.org				
Amas d'étoiles et asterismes	9					0,01		10		Milky way project	Jose Peña Institut d'Astronomie Mexico						
Amas Globulaires																	
Voie Lactée										MilkyWay@Home			http://milkyway.cs.rpi.edu/milkyway/				
Galaxies naines																	
Galaxie d'Andromède	Novae									PHAT			http://www.andromedaproject.org/				
Novae galaxies voisines	16	photométrique			0,1	0,1					Emmanuel Conseil		http://econseil.blogspot.com/	econseil@gmail.com			
Amas d'etoiles galaxies voisines										http://www.projectstardate.org/							
Galaxies	green peas	Classification								Galaxy zoo :3D			www.galaxyzoo.org				
Galaxies à noyaux actifs				Variabilité AGN													
Micro Quasars											Katherine Blundell	Oxford					
Quasars	15		Sursaut			0,1		10	10000		Jean Schneider	Surveillance du Quasar Triple					
Supernovae	14 - 21	photométrie/s	Discontinuité		0,1	0,1		10	10000	http://tarot.obs-hp.fr	Emmanuel Conseil	www.rocheste	http://www.astronomerstelegram.org/	econseil@gmail.com			
Gamma Ray Burst	18	contrepartie o	SVOM			0,1			10000		Bertrand Cordier	CEA	http://gcn.gsfc.nasa.gov				
Ondes Gravitationnelles	17	contrepartie o	GRANMA								Sarah Antier	IN2P3	https://grandma-kilonovacatcher.lal.in2p3.fr/	antier@apc.in2p3.fr			
Amas de Galaxies	22			Mesure de Z		0,5		10			Vincent Boucher			aapeteam@protonmail.com			
Filaments extragalactiques											David Valls Gabaud	GEPI OBSPM					
Contres parties Neutrinos																	
Lentilles Gravitationnelles										space_warps	Alain Klotz		https://www.zooniverse.org/project/space_warps				
Autres Objets																	
Matière Noire											David Martinez-Delgado Max Plack Institute						
Energie noire																	
Cosmologie						0,1		10		cosmology@home	Jean-Pierre Martin	SAF	http://www-cosmosaf.iap.fr/		SAF Commission Cosmologie		
										www.zooniverse.org					Les Rencontres du Ciel et de l'Espace		
Code Couleurs Sujets Coll Amateurs-Pro			Facile		Exigeant		Difficile		Challenge	boinc.berkeley.edu							
V2.8 Avril 2019 Thierry Midavaine Club Eclipse										scistarter.com							
Pour tous complements et corrections adresser un mail à			thierrymidavaine@sfr.fr								Thierry Midavaine			thierrymidavaine@sfr.fr			
Publications de reference	L'Astronome n°16 Mai 2009		Ces astronomes amateurs qui font aussi de la science				Collectif										
	Hors-Série 22 Ciel et Espace		Guide Pratique de la Science Participative en Astronomie					www.afanet.fr/sciences-participatives-afa.pdf/									
	Olivier Mousis	http://arxiv.org/pdf/1305.3647v1.pdf															

Fig. 2. Amateur-Professional Topics Table Version

- Column B: minimum magnitude to reach to be able to perform the respective object discovery. You may notice this magnitude start from 6 with Nova discovery easily done every year with Digital Single Lens Reflex (DSLR) Camera with standard high aperture lens.
- Column C: surveillance program name or reference.
- Column D: event for dedicated campaign to acquire data.
- Column E: Does the topic requires metrology ? These metrologies are quoted in the five following columns with the minimum useful accuracy required from the instrument.
- Column F: expected accuracy in arc second for Astrometry.
- Column G: relative accuracy for Photometry.
- Column H: useful accuracy of Polarimetric ratio.
- Column I: expectedSpectral resolution.
- Column J: time accuracy (datation and sampling) in second for the above measurements or surveillance and event detection.
- column K: on-line data base reference where amateur or citizen contribution is expected.

- Column L : name of the active focal point in France or abroad.
- Column M: name of an organisation or Society coordinating the topic.
- Column N: web site dedicated to the topic.
- Column O: e-mail address, this is often the e-mail address of the focal point or of the organisation.
- Column P: name of the conference gathering the actors on the field.

This table could be used in several ways. One of the purposes is to allow amateur astronomers, amateur observatories, amateur societies and scolarship projects to choose a topic and to define the fitted instrument setup. Colors of the table cells allow a quick access to the project: blue for the easiest topics for the beginner with small instrument, green for topics relying on a dedicated process methodology, orange for topics requiring large telescope 500mm aperture class with sensitive and accurate instruments, purple for very challenging topics requiring heavy hardware. The known amateur-professional collaborations are quoted in this table. Some topics meet strong interest without professional involvement for its historical perspective or pedagogic purpose.

Another way to use this table is to take empty cells to wonder whether it could become a new active topic. Thanks to the papers and lectures, from the communities, given all along the years, the file is updated at least once a year. An English worldwide version could be prepared through multi-country partnerships and with IAU as it was proposed in Bruxelles during the Amateur day of the 100th year IAU Symposium[¶].

5 Workshop program

A large number of oral and poster proposals have been received for the two workshops in 2018 and this year in 2019, (see http://sf2a.eu/semaine-sf2a/2019/index.php?lang=fr). More than 70 people registered for the workshop well balanced between the amateur and professional communities, giving one of the largest attendances to the "Journées SF2A" workshops.

The two workshops conclude with a round table and a debate with some of the key actors of such collaborations and to allow attendance to give feedbacks and proposals for the future. The purposes are to review the action proposals for new collaborations and to develop this field of activities. The involvement of the attendance including the involvement of SF2A and SAF in a partnership process are welcome. The major actions decided are presented below.

6 Creation of a web portal

As a first step Maria Curlin created end of 2018 a new webpage in SAF website to promote astronomical event observations. The first events were: November December 2018 Comet Wirtanen campaign, January 2019 the Antiope (double asteroid) star occultation, January February 2019 Eros close opposition, May 2019 the Quaoar TNO star occultation.

Beyond this first step, a SAF working group gathering Maria Curlin, Patrick Duchemin, Roger Ferlet, Jean Guerard, Anica Lekic, Thierry Midavaine and Stéphane Neveu, is preparing a web portal allowing, on one side, the registration of amateur describing their observation means and skills and, on the other side, the link with professionals introducing projects or astronomical targets for campaigns. The purpose is to embed an engine to allow the smart interface between amateur observers and professionals. The process may include, if required, an amateur observer obligation to act under a non disclosing agreement to keep the covertness of astronomical targets and collected data, up to the publication. It ends with publications made with contributing observers as coauthors. Several other tools are scheduled to allow quick mobilization of observatories fitted to the event. The fitting assessment of the instrument to the campaign is given by the following criteria : limiting magnitude of the instrumental set up, magnitude/as2 darkness of the sky, Long Lat Alt of the locations, SNR for a given target magnitude and sampling rate, Seeing and other key requirements coming from the collaboration topics.

[¶]Th. Midavaine, F. Herpin : Status of the Amateur Professional Collaborations. IAU 100 Years, Amateur Day, April 14th 2019 Bruxelles Belgium.

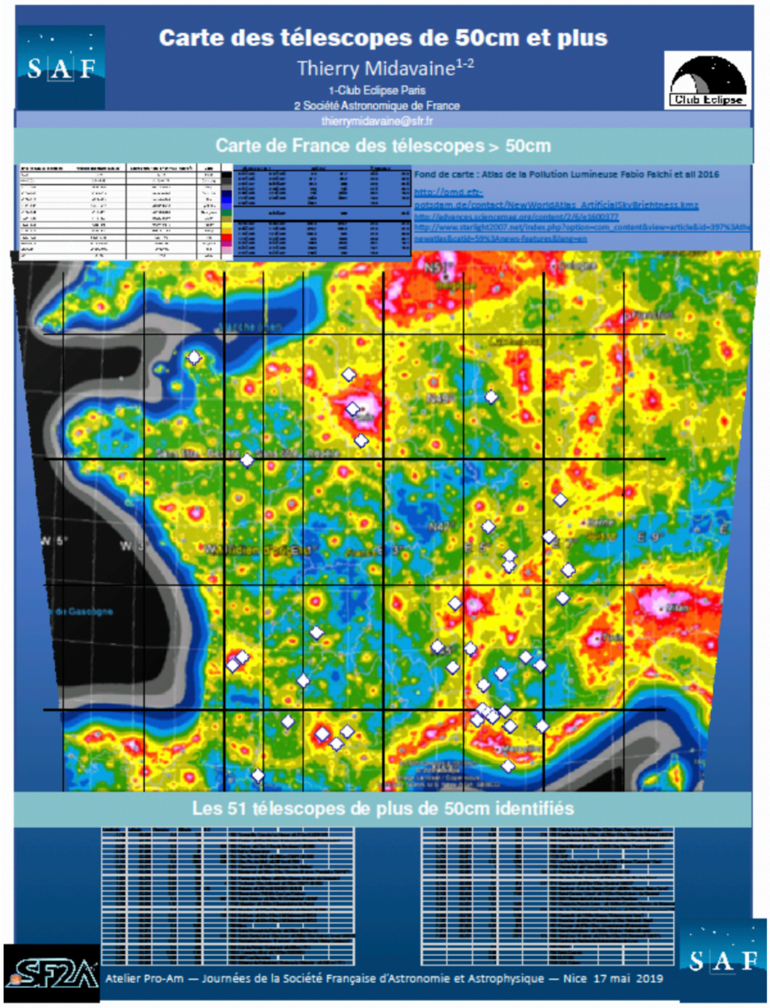

Fig. 3. 2019 consolidated map of the location of 500mm and above class telescopes (white losanges) in front of the 2016 ISTIL Fabio Falchi zenithal sky luminance map for France ((Falchi F, Cinzano P, et al, Sci Adv 2016 jun 10, 2(6)).

7 The French map of the observatories networking

One of the key function to propose to professionals is to give them an access to the network of observers including the most sensitive observatories. As a first step a poster presented this year during the workshop shows the more than 50cm diameter telescopes available in France (Fig. 3). This first map is not exhaustive and gathered about 51 observatories. Thanks to this workshop 64 telescopes are today identified. We may assume about 100 instruments available in France or in the neighbourhood, and much more in gathering smaller telescopes which may bring in addition nomad flexibilities. Collecting the location of the observers and amateur accessible telescopes is an important input for several projects where several parallel and independent collected data is worth for multi longitudes, latitudes or altitudes and to deal with cloud coverage and sky pollution background. Moreover, some projects, like asteroid occulting star events, require the identification of observer locations and to propose to nomad observers useful tactical additional locations (http://www.iota-es.de/). In addition the millisecond class (or even better) accurate time sampling and stamping of data brings by GPS receivers, allows intelligent data processing of synchronized multi recordings.

Fig. 4. Participant to the Photometry School hold the 17th-19th of may 2019 at Nice Observatory.

8 Campaign Calendars and Meetings

An important output of the workshop is to share and update our calendars. The first agenda is dedicated to coming astronomical events and campaigns. The second calendar is dedicated to symposium and meetings about amateur professional collaboration topics. These two calendars will be be updated and share on the web site (https://saf-astronomie.fr/collaboration_pro_am/) and then on the coming portal.

9 Photometry School

During the 2018 workshop we agreed on the necessity for several collaboration programs to held a dedicated school to photometry. This have been organized by Benoit Carry at Nice Observatory with the support of Raoul Behrend, Stephane Fauvaud, Romain Montaigu and CALA members to give talks and tutorials on software processings. Two topics was retained for this 1st school : Rotation Curves on asteroids and Exoplanet transit.

10 Conclusions

The SAF SF2A partnership is now on the way. For the coming years the following tasks have been retained:

- to organise the Prize award of the best Amateur Professional Collaboration through a call for candidates for the end of 2019,
- to develop the V1 of the collaboration web portal,
- to propose a third Amateur Professional Workshop during the next Journées de la SF2A in June 2020 in Paris,
- to prepare a second Photometry School.

We thank Christian Buil, Benoit Carry, Pierre Farissier, Eric Lagadec, Alexandre Santerne accepting to join the Scientific Organizing Committee and their contributions to the success of this 2nd workshop. Patrick Baradeau, Maria Curlin, Patrick Duchemin, Roger Ferlet, Jean Guérard, Anica Lekic, Stéphane Neveu, joining The Société Astronomique de France amateur professional working group for their active contributions.

SF2A 2019
P. Di Matteo, O. Creevey, A. Crida, G. Kordopatis, J. Malzac, J.-B. Marquette, M. N'Diaye, O. Venot (eds)

THE INTERNATIONAL ASTRONOMICAL UNION (IAU): A YOUNG CENTENARIAN (1919-2019)

T. Montmerle[1]

Abstract. The International Astronomical Union (IAU) has turned 100 this year. After a difficult and painful beginning in the aftermath of WWI, establishing itself as a leading international scientific union and solidifying at its first General Assembly in Rome (1922) with 207 individual members representing 19 countries, it has experienced a quasi-exponential growth since then, even accelerating during the "space race" era, to reach over 13,500 members today, representing 107 countries. This paper highlights some important steps in this evolution, the role of France within the IAU, and concludes with a brief outline of present and future projects.

Keywords: IAU: history, IAU: growth, IAU: Commissions, IAU: Divisions, IAU: Offices

1 Introduction: Before the IAU

On Nov.11, 1918, at 5:15 am, in a train parked on a discreet track in a forest near Compiègne, about 100 km north of Paris, an armistice was signed between the Allied forces and the new German government having been appointed just two days before, following the abdication of the German Emperor Wilhelm II. This event put an end to the tragic World War I, the first war in which science and technology played an important role in the conduct of the murderous battles that took place –although, after the initial army moves, the western front lines themselves, in Belgium and France, never changed in four years by more than a few tens of kilometers over a length of more than 500 km. An estimated one billion bombshells were fired, ten million casualties resulted directly from the war, followed by perhaps up to fifty million more resulting from the Spanish flu worldwide in the period 1918-1919. The world had changed irreversibly.

It was in the aftermath of this tragedy that the *International Astronomical Union*, the IAU, was born in Brussels, on July 28, 1919. [For detailed accounts of the history of the IAU, see the books by Blaauw 1994, Andersen et al. 2019, Sterken et al. 2019. This last book is referred to here as "S349", mentioned after the name of authors of selected individual articles: e.g., "Montmerle, S349".]

But the IAU was not created out of nothing. Long before WWI, astronomers had recognized the necessity of establishing international cooperation -one would say today "astronomy without borders". At least, that was the hope (Trimble, S349).

It is commonly admitted that two major initiatives paved the way to the future IAU. Chronologically, the first one was the *Carte du Ciel* project, launched in 1887 by the then Director of the Paris Observatory and Academician Ernest Amédée Mouchez (1821-1892). This project (see Lamy 2008) consisted in eventually obtaining 22,000 photographic plates of 2° on a side, by gathering the collaboration and coordination of over 20 observatories worldwide, lasting an estimated fifteen years. Due to various, not-too-unexpected difficulties (political as well as technical), the project dragged on until 1970, but was still considered as a priority for astronomy in 1919, with a special "Standing Committee" taking over at the birth of the IAU (see also below).

The second initiative, also a scientific one, albeit more institutional, was the foundation in 1904 by George Ellery Hale, an American solar spectroscopist and then Professor at the University of Chicago, of the *International Union for Cooperation in Solar Research*. The start of WWI put an end to the Union activities, but, as an active internationalist (De Vorkin, S349; remarkably, he had been a PhD student in Berlin, 1893-1894), Hale was instrumental in the creation of the *International Research Council* (IRC) in 1916, i.e., a year before the US entered the war: one of the offsprings of the IRC was the IAU.

[1] Institut d'Astrophysique de Paris, France; IAU General Secretary, 2012-2015

Once the Americans were on board, and recognizing the role (positive and negative) that science and technology had played in the conflict, three “Inter-Allied Conferences” were organized, with the aim to discuss “The Future of International Organization in Science”. The first two, under the auspices of the Royal Society and the Académie des Sciences, took place before and just after the armistice was signed (London, Oct.9-12, 1918; Paris, Nov.26-29), in preparation for the “founding meeting” of the IRC, which subsequently took place in the Palais des Académies in Brussels (July 18-28, 1919), i.e., one month after the Versailles Treaty, which had put an official end to WWI (but, as we know, already contained the germs of WWII...).

2 The creation of the IAU (1919-1922)

The Third “Inter-Allied Conference” in Brussels, following the preparations of the previous conferences, was actually the first General Assembly of the IRC. It had two main objectives: (*i*) to approve its statutes, submitted by its Executive Committee previously appointed in Paris (with Emile Picard, mathematician and Permanent Secretary of the Académie des Sciences, as President, and George Hale as one of its Vice-Presidents), mentioning a possible revision after 12 years; (*ii*) to create and approve the statutes of its founding Unions, among them the IAU,[*] which was already so well structured (thanks to Hale) that it appeared very much as a model for the other Unions, inluding the IRC itself. The last day of the Conference (July 28, 1919), when the IRC statutes were finally approved, is thus taken as the birth date of the IAU.

For a number of participants, especially astronomers, the Brussels conference missed a key point: all the Unions created were termed “International”, but by construction, it was an “Inter-Allied Conference”, which meant that the Central Powers, which had lost the war (mainly Germany, perhaps the most prominent scientific country at the time, and Austria-Hungary) were exluded from it –and were explicitly excluded by the statutes from membership[†]. Also, the neutral countries were to be admitted on a case-by-case basis. France and Belgium, which saw the war destructions on their own soil, were particularly vocal against the admission of the Central Powers. For the IAU, these restrictions were progressively lifted (for instance via the possibility of inviting colleagues individually at scientific meetings), to be terminated in 1926, in part considering also the admission in the League of Nations (which had taken effect in 1920). But the real, official change did not happen until 1931, when the IRC changed its statutes to become ICSU –the *International Council of Scientific Unions*.[‡]

These major issues notwithstanding, at the end of the Brussels conference the IAU was in perfect standing. Not only were its statutes approved and its first Executive Committee established, with Benjamin Baillaud, Academician and then Director of the Paris Observatory (and also having been responsible for the first high-altitude telescope dome at the Pic-du-Midi Observatory in 1908), as President[§], but 32 scientific “Standing Committees” (the ancestors of the IAU Commissions; see Montmerle, S349) were created, covering all fields of astronomy at the time –even Relativity (“Standing Committee” No 1, chaired by Arthur Eddington, a strong supporter of Einstein, who had just returned from his famous successful solar eclipse expedition).

It is also worthy of note that two additional astronomy-related international organizations were also created in Brussels, independently of the IAU: the *Bureau International de l'Heure* (International Time Commission) and the *International Bureau for Astronomical Telegrams* (with their own organizational and political status; in parallel there were two scientific IAU Standing Committees on “Time” and on “Astronomical Telegrams”).

The main task of this Executive Committee was then to organize the first IAU General Assembly (GA), to be held in Rome three years later at the invitation of A. Abetti. At its foundation (1919, with ratification by governments in 1920), the IAU comprised 7 countries (Belgium, Canada, France, Greece, Japan –then a member of the Allied Powers–, UK and USA); Italy and Mexico joined in 1921. There were no individual “IAU members” yet, they would have to apply in time to be officially accepted at the Rome GA.

The GA convened in the prestigious Accedemia dei Lincei in Rome, on May 2, 1922, to be adjourned on May 10. The three-year cycle of the IAU activities (the “triennium”) had begun for good: interval between GAs, renewal of the Executive Committee, financial report, assessment of the Commissions, admission of new

[*]The other Unions were: the International Union of Geodesy and Geophysics, the International Union for Radio Science, the International Union of Pure and Applied Chemistry, and the International Union of Biological Sciences.

[†]The Federal Republic of Germany eventually joined the IAU only in 1951, and the Democratic Republic of Germany was a member from 1962 until the reunification in 1990 (Wielen, S349). Austria joined in 1955.

[‡]now forming, with the *International Social Sciences Council*, the *International Science Council* (ISC) since 2018.

[§]See Bougeret, S349. The other members were: Alfred Fowler, UK, General Secretary, and as Vice-Presidents William W. Campbell (USA), Frank Dyson (UK), Georges Lecointe (Belgium), and Antonio Abetti (Italy).

individual members and national members (countries; with initially the restrictions mentioned above), etc. The next GA was scheduled to meet in Cambridge (UK) in 1925.

The Rome GA was attended by 83 participants (out of 207 individual members at the time); six women appear on the well-known group photograph (Blaauw 1994; also Montmerle 2019). Ten new countries (including neutral countries like the Netherlands) were admitted (the others were Australia, Brazil, Czechoslovakia, Denmark, Norway, Poland, Romania, South Africa and Spain), bringing the total to 17, already sampling, in spite of the international political situation, a wide distribution across the continents. Mussolini would be called to power by King Vittorio Emmanuele II just a few months after the GA, but it was a very successful meeting and the IAU was already firmly on track.

3 Growth of the IAU

A century after its creation, the IAU now has over 13,500 individual members, representing 107 countries (visit the IAU website: `https://www.iau.org/`): a 65-fold increase in its astronomers (compared with a 3.8-fold increase in the world population, from 1.9 billion in 1919, to 7.3 billion in 2015), and a 15-fold increase in the number of (vastly different) member countries. How, and why, did this happen ?

There is no space here just to even summarize the various episodes that took place (including the difficult WWII and post-WWII years), but adopting a more global approach and considering major events in the history of astronomy during this period, it is possible to draw a number of interesting conclusions.

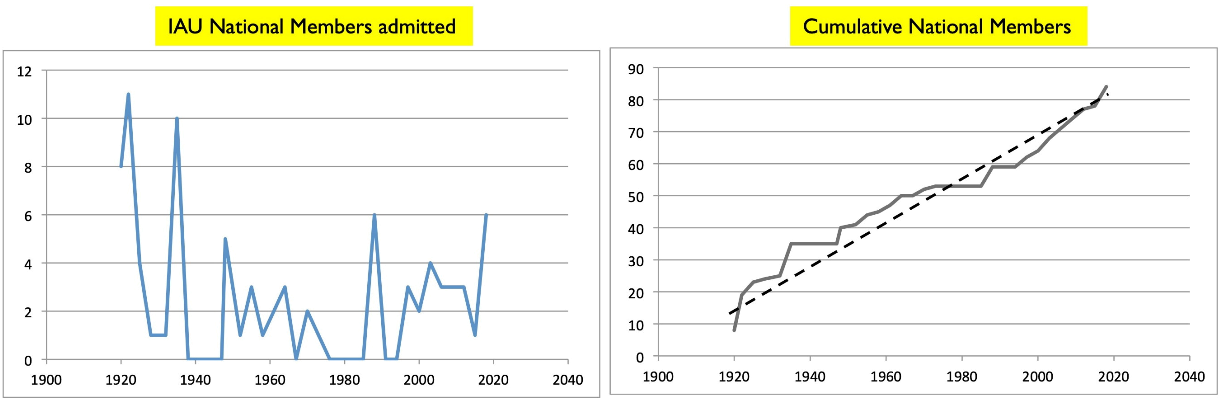

Fig. 1. Statistics of IAU "National Members" (i.e., adhering countries). *Left:* Number of countries admitted at each GA; *Right:* Cumulative number. See text for comments.

Let's consider first Fig.1 (left): the histogram shows the number of "national members" (i.e., adhering countries)¶ admitted at each GA (thus, every three years, except during WWII and on one occasion after WWII for political reasons). After the initial peak of 1922, one had to wait until 1935 (Paris GA) to see a second peak, with the arrival of China and of the Soviet Union (more precisely, of several Republics of the USSR). Then only a few national members (2-6, sometimes none) were admitted on average. Integrating this data, we obtain Fig.1 (right), which shows the corresponding cumulative distribution: this distribution is roughly linear, with ~ 10 times more national members in 2018 than in 1919: if the number of astronomers were simply proportional to the number of adhering countries, the IAU would comprise today no more than $\sim 2,000$ astronomers, i.e. ~ 6 times less that the actual number.

So let's turn to the actual distribution of individual members (astronomers) as a function of time, GA after GA. This is shown on Fig.2, along with a (personal) selection of the most important events in the history of astronomy over the past century (for details, see Montmerle, S349). First, there is a "background" exponential growth, with an e-folding time of about 20 years, which means that, averaged over countries, the population of astronomers is growing faster than the overall population itself; at this scale, WWII itself didn't have any influence (in fact, there were only about 500 astronomers worldwide at that time). However, the astronomers

¶not to be confused with "countries represented", as these include non-adhering countries with too few members, in that case admitted on an individual basis. The IAU currently has 84 national members.

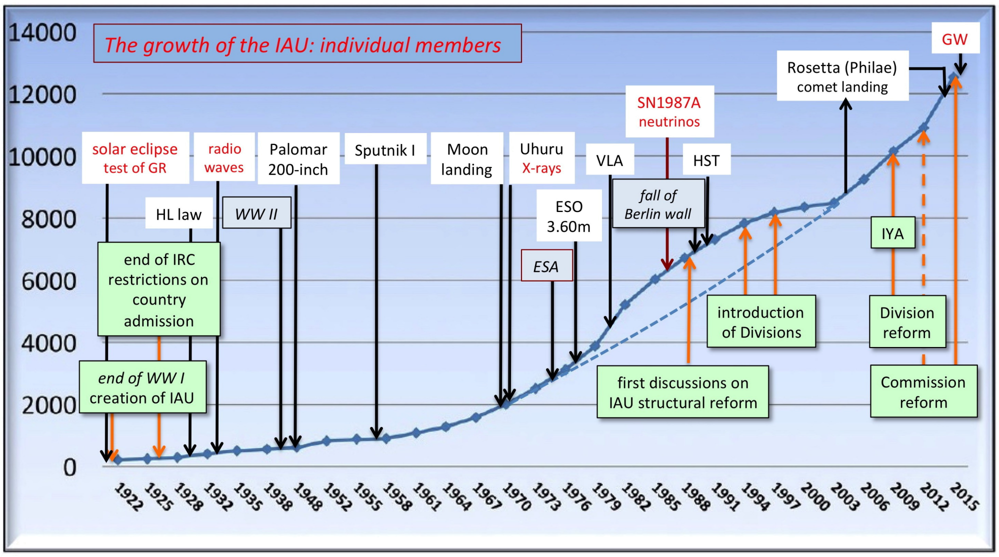

Fig. 2. Growth of the IAU over a century. See text for comments, and details in Montmerle, S349.

population started to pick up after WWII, with the important technological advances made during the war, like radars and, even more importantly, rockets and the resulting access to space (launch of the first Earth satellite, the Soviet satellite *Sputnik I* on Oct.4, 1957; IAU GA in Moscow, Aug.12-20, 1958).

Indeed, another feature is apparent in Fig.2: a "bump", which is superimposed on the "background" exponential growth curve, starts to appear at the time of the Moon landings (*Apollo 11* to *Apollo 17*: July 16, 1969 –50 years ago– to Dec. 7, 1972). The first events later known as "γ-ray bursts" were discovered by the *Vela* military satellites in the period 1963-1970, and the first astronomical satellite to explore the (non-solar) "X-ray universe" was *Uhuru*, launched on Dec.12, 1970. At the same time, important developments took place on the ground (creation of ESO in 1962, and of ESA, 1975; 4m-class telescopes, VLA, underground neutrino detectors, etc.), but it seems that, with the end of the Cold War (fall of the Berlin wall, 1989), and the resulting decline in the East-West competition, the "additional increase" in the number of astronomers started to decline as well, to merge with the exponential growth experienced previously. But the numbers were already very high, with $\sim$ 7,000 astronomers at the time of the launch of *HST* (1990). Yet, thirty years later, this number has doubled !

While a more detailed interpretation of the growth of the IAU shown on Fig.2, especially in comparison with other scientific fields, remains to be done, the features described above are so clear that they demonstrate that astronomers worldwide (and the IAU itself) have been extremely successful in organizing themselves, both in their own countries (number growing faster than the population), and as a transnational community (for instance, via large European organizations or multinational collaborations) –and also, as discussed below, via their involvement in public activities at large.

4 France within the IAU

As we saw above, French astronomers have played a key role in the IAU since its inception. A century later, because of the IAU growth just described, in relative terms the influence of France has somewhat decreased. However, as shown in Table 1, it has one of the largest number of IAU members (in fact, the largest in Europe and the second largest in the world after the USA), ranking 6th in the number of astronomers per capita (out of 84 countries; after Switzerland, Denmark, Finland, the Netherlands, and Sweden).

Also, as shown on Table 2, its role at the Executive level (and also within Commissions and Divisions) remains strong. In particular, it is worthy of note that three major "firsts" in the IAU executive happened with French astronomers: first President (B. Baillaud, 1919), first Assistant General Secretary (J.-C. Pecker, 1961 –to become General Secretary at the following triennum), and first female President (C. Cesarsky, 2006). In addition, considering the Division Presidents and Commission chairs, over the last ten years (2009-2019) 144 French astronomers (nearly 20% of France's total membership) have held executive positions for at least three years within the IAU.

Table 1. France's IAU membership in relation with selected other countries[1] (census of 2018, Vienna GA)

Country	IAU Members (2018)	Population (Mcitizens)	Ratio (Number/100kc)
Europe: EU			
France	**888**	**66**	**1.35**
UK	747	65	1.09
Germany	728	81	0.90
Italy	707	61	1.16
Spain	397	47	0.85
Netherlands	272	17	1.61
Europe: non-EU			
Switzerland	146	8.4	1.74[2]
Rest of the world			
USA	3023[3]	316	0.96
Japan	767	127	0.60
China/Nanjing[4]	737	1400	0.05

NOTES. (1) Ranked by number of individual members (membership). IAU data from its web site, population data from Wikipedia. (2) Highest ratio of astronomers per capita. (3) For the USA, the number of professional astronomers is actually significantly higher, but due to US policy those with non-renewable positions (post-docs...) cannot be IAU members. (4) For the IAU, China is considered a single country, but represented by two entities: "China/Nanjing" (mainland China), and "China/Taipeh" (Taiwan). For the historical context, see Liu (S349).

Table 2. French members of the IAU Executive Committee (1919-2018)

President	General Secretary	Vice-President
B. Baillaud (1919-1922)[1]	J.-C. Pecker (1964-1967)[2]	H. Deslandres (1922-1928)
E. Esclangon (1935-1938)	J. Bergeron (1991-1994)	C. Fabry (1928-1935; 1938-1944)
A. Danjon (1955-1958)	T. Montmerle (2012-2015)	A. Danjon (1944-1952)
C. Cesarsky (2006-2009)[3]		A. Couder (1952-1958)
		C. Fehrenbach (1973-1979)
		C. Cesarsky (1997-2000)

NOTES. (1) First President of the IAU. (2) First Assistant General Secretary (1961-1964). (3) First female President.

5 Conclusions: The IAU today and tomorrow

The exponential growth of the IAU depicted in Fig.2 started to create problems in the late 80's, when the 7,000 members mark was passed. Indeed, Commissions were the backbone of the activities of the IAU, but they had barely evolved, totalling ~ 40 at that time, compared with 32 in 1919, and most of them unchanged since then. However, the average number of members had exploded, from ~ 10 in 1919 to ~ 175 around 1990, some being even much more numerous,[‖] raising the question of the significance of Commissions. Reflections about restructuring the Commissions started, but the discussions, led by the Executive Commitee, were difficult. Finally, a new structure level, the *Divisions*, was introduced by L. Wolter in 1994 while he was IAU President-elect, and officially approved at the Kyoto GA in 1997. (See the whole story in Montmerle, S349.)

The central idea was to gather the Commissions, without changing them, into a dozen large thematic groups (the Divisions), with the hope that they would evolve within them –by merging, changing, terminating, etc. Of course this didn't change the arithmetic (some Divisions would have more than 1,000 members), but at least this reform brought some broad visibility to the activities of the IAU. In the end, however, not much happened to the Commissions. At the same time, the field of astronomy was evolving increasingly fast (think of exoplanets, discovered in 1995, now numbering over 4,000), independently of the IAU, some areas being even totally outside of the scope of its Commissions and Divisions (think of "multi-messenger astronomy", now including gravitational waves).

[‖] At that time, registration to at least one Commission was mandatory for all IAU members

In parallel with science, the IAU had started to develop "societal" activities, i.e., activities involving a direct contact with the public at large, especially in developing countries. As early as 1964, an original Commission was created: "Commission 46, *Astronomy Education & Development*". The goal of this Commission was to support dedicated astronomers –at first only a handful– willing to promote astronomy as widely as possible in the public worldwide, at all levels (see Hearnshaw, S349). It eventually grew to gave birth to several offsprings, like NASE, the *Network for Astronomy School Education* (2010), and, on a broader scale and in cooperation with South Africa, the OAD, *Office of Astronomy for Development* (endorsed by the 2009 GA in Rio de Janeiro). The interest of the IAU for education and outreach activities climaxed with the organization in 2009 of the *International Year of Astronomy*, under the auspices of the United Nations (UNESCO), which reached out to over 800 million people from 148 countries.

The IAU was then at the crossroads: (*i*) scientifically, new horizons were looming in astronomy and astrophysics, and (*ii*) more priority was given to education, outreach, and also astronomical heritage activities. The time was ripe for a fundamental reform of the IAU structures, which started in 2009 (see Montmerle 2015).

In essence, the three-tier structure in force since 1997 (i.e., Divisions, Commissions, and their Working Groups), was kept, but with a radical move: *the decision by the Executive Committee to terminate them all*, in two steps. First, introduce *ab initio* a new set of thematic Divisions (including one on Education and other activities, for better visibility), in cooperation with the Presidents of the existing Divisions, to be approved at the 2012 GA Beijing; second, set up a Call for Proposals to submit new Commissions to a joint Steering Committee composed of the Executive Committee and the Presidents of the new Divisions endorsed in Beijing, the selected Commissions being approved at the following GA (Honolulu, 2015). In the process, the number of Divisions was reduced to nine (from twelve), and that of Commissions to 35 (from 41). As a result, the activities of the IAU are now more in line with the most recent developments in astronomy (think of Commission D1 on *Gravitational Wave Astrophysics*, created before their actual discovery), as expressed by the community.

In parallel with this structural reform of Divisions, a second structure has been introduced: that of the *IAU Offices*, based not in Paris (the seat of the IAU Secretariat), but in other cities in the world. Following the example of the OAD (based in Cape Town, South Africa), two new "foreign" Offices have been created: the *Office for Astronomy Outreach* (OAO: based in Tokyo, founded in 2012), and the *Office for Young Astronomers*(OYA: based in Oslo, set up in 2015 to support and extend the activities of ISYA, the *International School of Astronomers*, itself founded by Commission 46 in 1967; Gerbaldi, S349). A fourth Office, the *Office for Astronomy Education* (OAE) is in the process of being created (ongoing selection of the site). The involvement of IAU astronomers in worldwide education and outreach has recently been praised (Entradas and Bauer 2019).

What about the future ? Based on these recent developments, an ambitious *Strategic Plan* (2020-2030) has been devised, which I encourage all astronomers to become familiar with (`https://www.iau.org/static/education/strategicplan-2020-2030.pdf`). Beyond the current $\sim$ 3,000+ celebrations of the IAU centenary (see `https://www.iau-100.org/`), the IAU certainly appears as a very healthy, young international organization (van Dishoek, S349). *En route* for the next 100 years !

6 References

History of the IAU

Andersen, J., Baneke, D., Madsen C. 2019, *The International Astronomical Union, Uniting the Community for 100 years* (Cham, Switzerland: Springer), 376 pp.

Blaauw, A. 1994, *History of the IAU: The Birth and First Half-Century of the International Astronomical Union* (Dordrecht: Kluwer), 296 pp.

Sterken, C., Hearnshaw, J., Valls-Gabaud D. (Eds.) 2019, IAU Symposium 349, *Under One Sky: the IAU Centenary Symposium* (Cambridge: Cambridge University Press) [S349], 542 pp.

In IAU Centenary Symposium Proceedings [S349; 2019]

Bougeret, J.-L.: 139-146; De Vorkin, D.: 153-160; Gerbaldi, M.: 445-451; Hearnshaw, J.: 374-387; Liu, Xiaowei: 222-227; Montmerle, T.: 289-324; Trimble, V.: 228-233; van Dishoek, 523-530; Wielen, R.: 205-213

Other references

Entradas, M., Bauer, M.W. 2019, *Nature Astronomy*, 3, 183-187

Lamy, J. (Ed.) 2008, *La Carte du Ciel* (EDP Sciences, Les Ulis, France), 250 pp.

Montmerle, T. (Ed.) 2015, *Reports on Astronomy: Commission Legacy Reports*, Transactions of the IAU, Volume 29A (Cambridge University Press), 549 pp.

Montmerle, T. 2019, *L'Astronomie*, vol.133, 126, 35-38

SF2A 2019
P. Di Matteo, O. Creevey, A. Crida, G. Kordopatis, J. Malzac, J.-B. Marquette, M. N'Diaye, O. Venot (eds)

TWENTY YEARS OF XMM-NEWTON

N. A. Webb[1]

Abstract. *XMM-Newton*, a large X-ray observatory launched by the *European Space Agency* (ESA), will be 20 years old in 2019. This cornerstone mission from ESA's *Horizon 2000 programme* continues to make ground breaking discoveries twenty years after its launch. Thanks to its sensitivity and wide field of view, *XMM-Newton* has studied hundreds of thousands of stars and active galactic nuclei (AGN), as well as rarer objects such as galaxy clusters, supernova remnants, X-ray binaries, ultra luminous X-ray sources (ULXs), exoplanets and even the aurora on planets within our solar system. Since the conception of *XMM-Newton*, France has played an important role in this flagship mission, initially in developing the instruments carried on board and since 1996 in the ground segment activities (*XMM-Newton Survey Science Centre*). Here we will review some of the more notable results from this observatory and discuss the outlook for the future with *XMM-Newton* and the next ESA large X-ray observatory, *Athena*.

Keywords: X-rays: general, Telescopes, Surveys, Catalogs

1 Introduction

XMM-Newton is the *European Space Agency's* second cornerstone mission from the *Horizon 2000 programme* (Jansen et al. 2001). *XMM-Newton* was launched on 10th December 1999 and as result, will celebrate its twentieth birthday in 2019. It has the largest effective area of any X-ray satellite (Longinotti 2014), thanks to its three X-ray telescopes observing in the 0.2-12.0 keV domain, each with $\sim$1500 cm^2 of geometric effective area. The field of view (FOV) is 30' and provides an angular resolution of arcseconds. Behind each of the X-ray telescopes is one of the three *European Photon Imaging Cameras* (EPIC) (Strüder et al. 2001; Turner et al. 2001), built by a collaboration of Italian, British, French and German scientists. The three detectors are a pn camera and two Metal Oxide Semi-conductor (MOS) cameras, spectro-imagers which can reach a time resolution of tens of microseconds. Only half of the X-ray flux falls on the MOS cameras, where the other half is directed towards the Reflection Grating Spectrographs (RGS, den Herder et al. 2001), built by a Dutch, British, American and Spanish collaboration. These provide high spectral resolution (from 100 to 500, FWHM) X-ray spectroscopy in the energy range 0.33-2.5 keV or 5-38 Å. In addition there is a complimentary ultra-violet and optical telescope called the *Optical Monitor* (OM Mason et al. 2001), built by a British, American and Belgian collaboration, that covers 17', and is centred on the same point as the X-ray telescopes. The observatory is open to all through yearly calls for proposals. Data is accessed via the XMM-Newton Science Archive[*].

The *XMM-Newton Survey Science Centre*[†] (SSC), a consortium of ten European Institutes (Watson et al. 2001) led by *IRAP* in Toulouse, was selected by ESA in 1996 to ensure that the scientific community can exploit the data accumulated by *XMM-Newton*. The SSC has developed much of the *XMM-Newton Science Analysis Software* (SAS) (Gabriel et al. 2004) for reducing and analysing *XMM-Newton* data and created pipelines to perform standardised routine processing of the *XMM-Newton* science data. The XMM-SSC also produces catalogues of detections made with the *EPIC* cameras and the OM. These catalogues are excellent resources that can be used for a wide variety of astrophysical research such as for accessing source data and products, finding new objects, studying homogeneous populations of objects and for cross-correlation with multi-wavelength data.

In this short review we will discuss results stemming from both the French and the international X-ray community. These will cover a wide variety of objects observed with *XMM-Newton*, from exoplanets to galaxy clusters. The salient points of the *XMM-Newton* catalogues will also be presented, before looking to the future with both *XMM-Newton* and *Athena*.

[1] IRAP, Université de Toulouse, CNRS, CNES, Toulouse, France
[*]`https://nxsa.esac.esa.int/`
[†]`http://xmmssc.irap.omp.eu/`

2 Highlights from the past twenty years

2.1 Stars and planets

Young, low-mass stars are X-ray bright due to considerable magnetic activity. X-rays are emitted by high temperature plasma which is heated during magnetic reconnection events (e.g. Ozawa et al. 2005). The great sensitivity and wide field of view makes XMM-Newton the ideal satellite to observe nearby active star forming regions as a significant part of the area can be observed in a single pointing. The star forming region ρ Ophiuchi was one of the first such fields to be pointed during the first month of observations with *XMM-Newton*. 87 X-ray sources were detected including 25 previously unknown X-ray sources (Ozawa et al. 2005). 15 of these were classified as class III (weak-lined T Tauri stars) sources, doubling the population of these objects known at the time of the observations. During this short pointing of only 30 ks, one of the two brown dwarfs detected was shown to be flaring, where this is likely to be due to solar-like magnetic activity.

XMM-Newton has been used to observe many solar system objects, such as the aurora on Jupiter (e.g. Dunn et al. 2017), or solar wind charge exchange on Mars (e.g. Koutroumpa et al. 2012) or even various comets (e.g. Schulz et al. 2006), but it is now also being used to understand exoplanets (King et al. 2018). A planetary transit of a hot Jupiter in the system HD 189733 was observed with *XMM-Newton* (Poppenhaeger et al. 2013). Marin & Grosso (2017) propose that a direct detection in X-rays of the exoplanet would not be possible, but the ultra-violet domain using the OM offers further possibilities to observe planets/transits (King et al. 2018).

2.2 Supernova remnants

The high collecting area and wide field of view are particularly well suited to studying supernova remnants, for example the 439 ks good time interval observations of the supernova remnant SN 1006 (Li et al. 2015). From this dataset, Li et al. (2015) extracted and analysed spectra from 3596 tessellated regions, each with at least 10^4 counts (0.3-8 keV band). This high signal to noise ratio data enabled them to map out multiple physical parameters, such as the temperature, electron density, ionization parameter, ionization age and metal abundances and allowed them to deduce an asymmetric metal distribution across the remnant. They suggested that this implies either an asymmetric explosion of the supernova or an asymmetric distribution of the interstellar medium, amongst other results.

The good angular resolution also allowed Acero et al. (2017) to measure the expansion of the supernova remnant RX J1713.73946 using *XMM-Newton*. RX J1713.73946 is the brightest supernova remnant at TeV energies and is often thought of as the prototypical cosmic ray accelerator. From the measurements they determine both the current density at the shock and the age of the remnant.

2.3 The Galactic centre

Almost 600 observations have been consecrated to the understanding of the Galactic centre region, and 8% of the detections in 3XMM-DR8 (or $\sim$62000 detections) are found in this high density region. A lot of work has gone into identifying these sources. Using 26 of the observations below a Galactic latitude of 20°, 1319 sources were detected (Nebot Gómez-Morán et al. 2013), of which 316 sources were identified thanks to multi-wavelength data. Many of these sources are not actually in the Galactic centre but are late-type active stars situated at less than 1 kpc from the Sun. The population includes 2 cataclysmic variables, 3 T Tauri stars, Herbig-Ae stars, γ-Cas-like objects, 3 X-ray binaries as well as 37 extra-galactic sources at the higher latitudes.

The supermassive black hole at the centre of our galaxy Sgr A* is extremely faint compared to other supermassive black holes in other galaxies (10^{-9} of the Eddington luminosity). A lot of effort has been invested in understanding the low luminosity, as well as the frequent X-ray flares observed (e.g. Mossoux & Grosso 2017). These could be due to a shock produced by the interaction between orbiting stars and a hot accretion flow, a Rossby instability producing magnetised plasma bubbles in a hot accretion flow, an additional heating of electrons near the black hole due to processes such as accretion instability or magnetic reconnection, an increase of the accretion rate when material reaches the close environment of the black hole, or even tidal disruption of asteroids (see Mossoux & Grosso 2017, and references therein), but their origin remains to be demonstrated.

In order to make headway in understanding the luminosity of Sgr A*, Terrier et al. (2018); Ponti et al. (2015); Clavel et al. (2013) and others showed that temporal variability observed in X-ray luminosity of molecular clouds near the Galactic centre were evidence for previous irradiation from Sgr A* during active periods in its past, when it showed flares at least one hundred times brighter than today over the last few hundred years. This is evidence that Sgr A* may have been significantly brighter during its past.

2.4 The growth of supermassive black holes

Supermassive ($\sim 10^{6-10}$ M$_\odot$) black holes (e.g. Lynden-Bell 1969) like Sgr A* are present in the cores of massive galaxies. Whilst hundreds of thousands are known, it is not yet clear how supermassive black holes (SMBH) are formed and evolve. It is unlikely that they form from stellar mass black holes, as even continuously accreting at the Eddington limit, it is difficult to reach masses as high as $\sim 10^9$ M$_\odot$ observed in a massive quasar at z$\sim$7.1 (Mortlock et al. 2011) or the 8×10^8 M$_\odot$ black hole found at z=7.54 (0.69 Gyr, Bañados et al. 2018). Different theories propose that smaller, intermediate mass black holes (IMBH, 10^{2-5} M$_\odot$) would either merge and/or accrete to create SMBH (see Volonteri 2012; Greene 2012; Mezcua 2017, for reviews). This may be at or above the Eddington rate, although the physical mechanism for super-Eddington accretion is still to be elucidated. In order to validate these mechanisms, it is necessary to find intermediate mass black holes and/or determine the mechanism for prolonged super-Eddington accretion.

The *XMM-Newton* catalogue revealed the first good IMBH candidate 2XMM J011028.1-460421, more commonly known as Hyper Luminous X-ray source 1 (HLX-1, Farrell et al. 2009; Godet et al. 2009; Webb et al. 2010). It has a mass of $\sim 10^4$ M$_\odot$ (Godet et al. 2012) and is thought to be accreting periodically by tidally stripping a companion star at periastron in a highly elliptical orbit (Lasota et al. 2011; Godet et al. 2014; Webb et al. 2014), thus making it an exceptional system. However, IMBH can also exist in the centres of lower mass galaxies, but these are often faint and difficult to detect. Nonetheless, they can tidally disrupt a passing star, causing the system to become brighter by several decades in luminosity in X-rays and at other wavelengths, making them easier to locate. These tidal disruption events (TDEs) can also go periods of super-Eddington accretion, making them interesting to study to help understand the formation of supermassive black holes. Many TDEs have been identified through exploring *XMM-Newton* data, e.g. Lin et al. (2011); Saxton et al. (2015); Lin et al. (2017a); Saxton et al. (2017); Lin et al. (2018). Some show evidence for IMBHs, i.e. the black hole in the centre of the inactive galaxy IC 4765-f01-1504 which showed a TDE in 2006. The mass of the black hole has been estimated to be 6×10^4 - 4×10^6 M$_\odot$ (Lin et al. 2011). Another TDE occurred around the massive black hole in a dwarf galaxy orbiting 6dFGS gJ215022.2-055059. The mass of this black hole has been estimated to be $5.3 \times 10^4 < M_{BH} < 1.2\times 10^5$ M$_\odot$ (Lin et al. 2018). Another TDE was identified showing super-Eddington accretion over more than 10 years (Lin et al. 2017b), demonstrating that it is possible to fuel supermassive black holes at high rates for long periods.

2.5 Galaxy clusters

Galaxy clusters are the largest bound gravitational structures in the Universe. They group together to form the large scale structure of the Universe. They are also known to contain significant amounts of dark matter, the nature of which is still unknown. In order to understand how matter is structured across the Universe and get an insight into the nature of dark matter, and constrain cosmological models, it is necessary to identify galaxy clusters across time. In order to do this a very large programme was initiated (the *XMM-Newton Large Scale Structure Survey*, XMM-LSS Pierre et al. 2004). This programme was then enlarged to become the XXL programme (Pierre et al. 2016) which was composed of 542 *XMM-Newton* observations, each of at least 10ks, totalling 6.9 Ms, as well as complimentary multi-wavelength data. This mapped two extragalactic regions of $25^{\circ 2}$. The main goal of the project is to constrain the Dark Energy equation of state using clusters of galaxies. More than 26000 sources have been found in the survey, where the majority are AGN (Chiappetti et al. 2018). Including other publicly available observations, XCLASS (Clerc et al. 2012), has examined 4200 observations at high latitudes in which 1500 galaxy clusters have been identified.

Other surveys based on public *XMM-Newton* observations, include the one based on Stripe 82 (Takey et al. 2016) which also has a wide range of multi-wavelength data. Of the 54 clusters with spectroscopic redshifts they find two strong candidates for newly discovered cluster mergers at redshifts of 0.11 and 0.26. Further, since 2018, the 3 Ms over three years XMM heritage cluster project has started. This programme is focused on the products of structure formation in mass and time: a large, unbiased, signal-to-noise limited sample of 118 galaxy clusters detected by Planck via their Sunyaev-Zel'dovich effect. The project aims are[‡] (i) obtain an accurate vision of the statistical properties of the local cluster population, and in the highest mass regime; (ii) uncover the provenance of non-gravitational heating; (iii) measure how their gas is shaped by the collapse into dark matter haloes and the mergers that built today's clusters; (iv) resolve the major uncertainties in mass determinations that limit cosmological inferences; (v) build the foundation for cluster science with next-generation surveys.

[‡] http://xmm-heritage.oas.inaf.it/

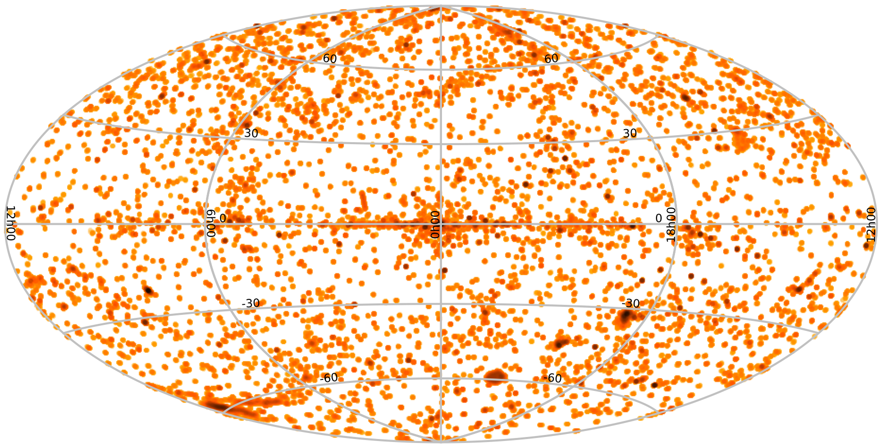

Fig. 1. The detections in the 3XMM-DR8 catalogue shown in a Hammer-Aitoff projection. The darker the colour, the greater the number of observations.

3 The XMM-Newton catalogues

3.1 The catalogue of detections

The catalogues of EPIC detections have been designated 1XMM, 2XMM and 3XMM (Watson et al. 2009; Rosen et al. 2016), with incremental versions of these catalogues indicated by successive data releases, denoted -DR in association with the catalogue number. The most recent version of the catalogue is 3XMM-DR8. It was released in May 2018[§]. It contains 775153 X-ray detections, where objects have been detected as many as 59 times over 17 years from Feb. 2000 to Nov. 2017. 332 columns of information are provided for each detection, including coordinates, observation date, time and mode, exposure and background information, counts, fluxes and rates in 7 energy bands, maximum likelihoods of detection, quality and variability flags, as well as multi-band images, lightcurves and spectra. The distribution of X-ray detections on the sky can be seen in Fig. 1.

3.2 The stacked catalogue

The SSC also produces stacked catalogues of sources. The first of these was 3XMM-DR7s[¶] (Traulsen et al. 2019), released in July 2018. For each source identified from the stacked sources, information regarding the source (similar to that given in the catalogue of detections) is provided, along with a long term lightcurve, allowing easy access to the long term variability of sources. 3XMM-DR7s was compiled from 1789 overlapping good-quality XMM-Newton observations and it contains 71951 unique sources and almost 11000 new sources compared to the single fields used in 3XMM-DR7, thanks to the deeper images obtained through stacking. The effects of stacking and the improvement in the depth of the flux can quite clearly be seen in Fig. 2.

3.3 The OM catalogue

The OM catalogue called the Serendipitous Ultraviolet Source Survey (SUSS) with successive versions designated SUSS-1 - SUSS 4, with SUSS4 the latest version containing 8.17 million detections or 5.5 million unique sources. More than a million of these sources have been detected at least twice. Data is given for the six optical and ultra-violet filters (U, B, V, UVW1, UVM2 and UVW2, Page et al. 2012).

[§] `http://xmmssc.irap.omp.eu/Catalogue/3XMM-DR8/3XMM_DR8.html`

[¶] http://xmmssc.irap.omp.eu/Catalogue/3XMM-DR7s/3XMM_DR7stack.html

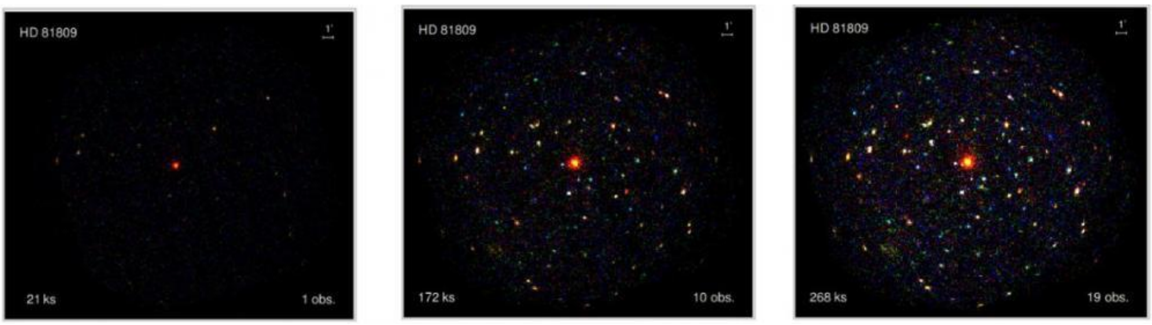

Fig. 2. An example from the stacked catalogue. Left, a single 6 hour observation, middle, 10 observations combined from the same sky region (total of 48 hours of observation), right, 19 observations combined (more than 3 days of data).

4 Future observations

4.1 XMM-Newton

XMM-Newton continues to function nominally, with very little degredation over the last 20 years. *XMM-Newton* has sufficient fuel to continue to function in a similar manner for another ten years. This will allow a larger region of the sky to be surveyed and provide time for deeper observations of sources of particular interest, especially through the new heritage programmes. Building on the current joint programmes, *XMM-Newton* will benefit from joint (and follow-up) observations associated with new space missions and ground facilities, for example, *eROSITA, Euclid*, the *Cherenkov Telescope Array* (CTA), the *Transiting Exoplanet Survey Satellite* (TESS), the *Extremely Large Telescope* (ELT) and the *James Webb Space Telescope* (JWST).

As 2019 comes to a close, we are in the final stages of producing 4XMM-DR9 (the latest release of the EPIC detections catalogue) and 4XMM-DR9s (the latest release of the stacked catalogue). These catalogues benefit from a re-reduction of the all the 14041 observations taken since the beginning of the mission using the latest software, improved calibration and innovative ideas. As with previous versions of 3XMM, these catalogues will be updated on a yearly basis. Improved SUSS catalogues will also be provided in the years to come, taking advantage of improved calibration and new observations.

4.2 Athena

Looking to the future, *Athena* (Advanced Telescope for High ENergy Astrophysics) is the next Large X-ray observatory to be launched by ESA, in the framework of its Cosmic Vision programme. It is expected to be launched in 2032 and has two main science goals, to study the *hot* and the *energetic* Universe. *Athena* will study how hot baryons assemble into groups and clusters of galaxies, determine their chemical enrichment across time, measure their mechanical energy and characterise the missing baryons which are expected to reside in intergalactic filamentary structures. *Athena* will also study the physics of accretion onto compact objects, find the earliest accreting supermassive black holes and trace their growth even when in very obscured environments, and show how they influence the evolution of galaxies and clusters (Nandra et al. 2013).

Athena will consist of a single large-aperture grazing-incidence X-ray telescope, using silicon pore optics. The 12m focal length will provide 5" on-axis angular resolution (half energy width). The focal plane contains two instruments. One is the Wide Field Imager (WFI) which will provide spectro-imaging in the 0.2-15 keV energy band over a 40' $\times$ 40' field of view (Rau et al. 2016). The other is the innovative X-ray Integral Field Unit (X-IFU). The X-IFU is a cryogenic X-ray spectrometer, based on a large array of Transition Edge Sensors (TES), offering 2.5 eV spectral resolution, with 5" pixels, over a field of view of 5' (Barret et al. 2018).

The sensitivity gain of more than a factor of ten, coupled with excellent spectral resolution and wide field of view will revolutionise our understanding of objects that we know of today and discover many new ones besides.

NW acknowledges support from the CNES.

References

Acero, F., Katsuda, S., Ballet, J., & Petre, R. 2017, A&A, 597, A106

Bañados, E., Venemans, B. P., Mazzucchelli, C., et al. 2018, Nature, 553, 473

Barret, D., Lam Trong, T., den Herder, J.-W., et al. 2018, in Society of Photo-Optical Instrumentation Engineers (SPIE) Conference Series, Vol. 10699, Proc. SPIE, 106991G

Chiappetti, L., Fotopoulou, S., Lidman, C., et al. 2018, A&A, 620, A12

Clavel, M., Terrier, R., Goldwurm, A., et al. 2013, A&A, 558, A32

Clerc, N., Pierre, M., Pacaud, F., & Sadibekova, T. 2012, MNRAS, 423, 3545

den Herder, J. W., Brinkman, A. C., Kahn, S. M., et al. 2001, Astronomy and Astrophysics, 365, L7

Dunn, W. R., Branduardi-Raymont, G., Ray, L. C., et al. 2017, Nature Astronomy, 1, 758

Farrell, S. A., Webb, N. A., Barret, D., Godet, O., & Rodrigues, J. M. 2009, Nature, 460, 73

Gabriel, C., Denby, M., Fyfe, D. J., et al. 2004, in Astronomical Society of the Pacific Conference Series, Vol. 314, Astronomical Data Analysis Software and Systems (ADASS) XIII, ed. F. Ochsenbein, M. G. Allen, & D. Egret, 759

Godet, O., Barret, D., Webb, N. A., Farrell, S. A., & Gehrels, N. 2009, ApJ, 705, L109

Godet, O., Lombardi, J. C., Antonini, F., et al. 2014, ApJ, 793, 105

Godet, O., Plazolles, B., Kawaguchi, T., et al. 2012, ApJ, 752, 34

Greene, J. E. 2012, Nature Communications, 3, 1304

Jansen, F., Lumb, D., Altieri, B., et al. 2001, A&A, 365, L1

King, G. W., Wheatley, P. J., Salz, M., et al. 2018, MNRAS, 478, 1193

Koutroumpa, D., Modolo, R., Chanteur, G., et al. 2012, A&A, 545, A153

Lasota, J.-P., Alexander, T., Dubus, G., et al. 2011, ApJ, 735, 89

Li, J.-T., Decourchelle, A., Miceli, M., Vink, J., & Bocchino, F. 2015, MNRAS, 453, 3953

Lin, D., Carrasco, E. R., Grupe, D., et al. 2011, ApJ, 738, 52

Lin, D., Godet, O., Ho, L. C., et al. 2017a, MNRAS, 468, 783

Lin, D., Guillochon, J., Komossa, S., et al. 2017b, Nature Astronomy, 1, 0033

Lin, D., Strader, J., Carrasco, E. R., et al. 2018, Nature Astronomy

Longinotti, A. L. 2014, XMM-Newton Users Handbook, Tech. Rep. 2.12, ESA: XMM-Newton SOC

Lynden-Bell, D. 1969, Nature, 223, 690

Marin, F. & Grosso, N. 2017, ApJ, 835, 283

Mason, K. O., Breeveld, A., Much, R., et al. 2001, A&A, 365, L36

Mezcua, M. 2017, International Journal of Modern Physics D, 26, 1730021

Mortlock, D. J., Warren, S. J., Venemans, B. P., et al. 2011, Nature, 474, 616

Mossoux, E. & Grosso, N. 2017, A&A, 604, A85

Nandra, K., Barret, D., Barcons, X., et al. 2013, arXiv e-prints, arXiv:1306.2307

Nebot Gómez-Morán, A., Motch, C., Barcons, X., et al. 2013, A&A, 553, A12

Ozawa, H., Grosso, N., & Montmerle, T. 2005, A&A, 429, 963

Page, M. J., Brindle, C., Talavera, A., et al. 2012, MNRAS, 426, 903

Pierre, M., Pacaud, F., Adami, C., et al. 2016, A&A, 592, A1

Pierre, M., Valtchanov, I., Altieri, B., et al. 2004, J. Cosmology Astropart. Phys., 2004, 011

Ponti, G., Morris, M. R., Terrier, R., et al. 2015, MNRAS, 453, 172

Poppenhaeger, K., Schmitt, J. H. M. M., & Wolk, S. J. 2013, ApJ, 773, 62

Rau, A., Nandra, K., Aird, J., et al. 2016, in Society of Photo-Optical Instrumentation Engineers (SPIE) Conference Series, Vol. 9905, Proc. SPIE, 99052B

Rosen, S. R., Webb, N. A., Watson, M. G., et al. 2016, A&A, 590, A1

Saxton, R. D., Motta, S. E., Komossa, S., & Read, A. M. 2015, MNRAS, 454, 2798

Saxton, R. D., Read, A. M., Komossa, S., et al. 2017, A&A, 598, A29

Schulz, R., Owens, A., Rodriguez-Pascual, P. M., et al. 2006, A&A, 448, L53

Strüder, L., Briel, U., Dennerl, K., et al. 2001, A&A, 365, L18

Takey, A., Durret, F., Mahmoud, E., & Ali, G. B. 2016, A&A, 594, A32

Terrier, R., Clavel, M., Soldi, S., et al. 2018, A&A, 612, A102

Traulsen, I., Schwope, A. D., Lamer, G., et al. 2019, A&A, 624, A77

Turner, M. J. L., Abbey, A., Arnaud, M., et al. 2001, A&A, 365, L27

Volonteri, M. 2012, Science, 337, 544
Watson, M. G., Augères, J.-L., Ballet, J., et al. 2001, A&A, 365, L51
Watson, M. G., Schröder, A. C., Fyfe, D., et al. 2009, A&A, 493, 339
Webb, N. A., Barret, D., Godet, O., et al. 2010, ApJ, 712, L107
Webb, N. A., Godet, O., Wiersema, K., et al. 2014, ApJ, 780, L9

Session 01

Atelier général PCMI

SF2A 2019
P. Di Matteo, O. Creevey, A. Crida, G. Kordopatis, J. Malzac, J.-B. Marquette, M. N'Diaye, O. Venot (eds)

MODELING THE COMPLEX CHEMISTRY OF HOT CORES IN SAGITTARIUS B2-NORTH: INFLUENCE OF ENVIRONMENTAL FACTORS

M. Bonfand[1], A. Belloche[1], R. T. Garrod[3 2], K. M. Menten[1], E. R. Willis[3], G. Stéphan[3] and H. S. P. Müller[4]

Abstract. Sagittarius B2(N) is host to several hot cores (HCs) in the early stage of star formation, where complex organic molecules (COMs) are detected in the gas phase. Given its exposure to the extreme environment of the Galactic center region, Sgr B2(N) is an excellent target to study the impact of environmental factors on the production of COMs. We combined the analysis of 3mm ALMA data and chemical models to characterize and compare the physical structure and chemical composition of Sgr B2(N)'s HCs. We investigated how the cosmic-ray ionization rate (CRIR) and the minimum dust temperature during the prestellar phase ($T_{\rm min}$) influence the production of COMs. We used COM abundances to constrain the CRIR and $T_{\rm min}$ by comparing the results of chemical models with the observations. Chemical models with $T_{\rm min}$=15 K and a CRIR of 7×10^{-16} s^{-1} best reproduce the abundances observed toward Sgr B2(N)'s HCs.

Keywords: ISM: molecules, astrochemistry, molecular processes, cosmic rays, stars:formation

1 Introduction

The Sagittarius B2 (Sgr B2) molecular cloud is one of the most prominent regions forming high-mass stars in our Galaxy. Located at a projected distance of ~100 pc from Sgr A*, Sgr B2 is exposed to the extreme environment of the Galactic center (GC) region. A strong interstellar radiation field (1000 G_0, Clark et al. 2013) is expected toward the GC region. Le Petit et al. (2016) derived a cosmic-ray ionization rate (CRIR) in the diffuse gas component of the line of sight to the GC of ζ^{H_2} ~1–11×10^{-14} s^{-1}, two to three orders or magnitude higher than the standard CRIR (ζ^{H_2} ~1.3×10^{-17} s^{-1}, Spitzer & Tomasko 1968). Dust continuum measurements carried out with *Herschel* indicate higher temperatures toward the GC region than in the rest of the Galactic disk. Longmore et al. (2012) derived a minimum dust temperature of 19 K toward the GC cloud G0.253+0.016 which shows no strong evidence of star-formation activity. Due to its exceptional characteristics and its proximity to the GC, Sgr B2 provides us with an interesting case study to investigate the influence of environmental factors on the high-mass star formation process and the associated chemistry. In particular, Sgr B2(N), one of the major sites of star formation in Sgr B2, exhibits a rich molecular inventory, including a great variety of complex organic molecules (COMs, see, e.g. Belloche et al. 2017, 2019). For this reason, Sgr B2(N) appears to be an excellent target to improve our understanding of the complex interstellar chemistry.

2 Five hot cores embedded in the same parent cloud

Sgr B2(N) is fragmented into multiple dense and compact objects. On the basis of the 3 mm imaging line survey Exploring Molecular Complexity with ALMA (EMoCA, Belloche et al. 2016), we reported the detection of three new hot cores (HCs), Sgr B2(N3), N4, and N5 (Bonfand et al. 2017, Paper I), in addition to the two already known HCs, Sgr B2(N1) and N2. Ginsburg et al. (2018) later identified 11 star-forming cores at 3 mm within a region of 0.4 pc centered on Sgr B2(N1).

[1] Max-Planck-Institut für Radioastronomie, Auf dem Hügel 69, Bonn, Germany
[2] Departments of Astronomy, University of Virginia, Charlottesville, VA 22904, USA
[3] Departments of Chemistry, University of Virginia, Charlottesville, VA 22904, USA
[4] I. Physikalisches Institut, Universität zu Koöln, Zülpicher Str. 77, 50937 Köln, Germany

By analyzing the EMoCA survey we derived the chemical composition of Sgr B2(N3-N5), identifying 24 distinct species of which about half are complex (Paper I). Figure 1a shows the abundances relative to methanol (CH_3OH) of ten COMs measured toward Sgr B2(N3-N5), as well as Sgr B2(N2) for comparison. The overall chemical composition of Sgr B2(N3) is similar to that of Sgr B2(N5). The abundances of O- and S-bearing species relative to CH_3OH are higher toward Sgr B2(N4) compared to the other HCs, except for NH_2CHO. The chemical composition of Sgr B2(N2) differs significantly from that of Sgr B2(N3-N5). In order to explain the differences in the chemical composition of these four HCs expected to originate from the same cloud material, chemical models are required. In particular we want to derive the CRIR and minimum dust temperature that best characterize the chemical history of Sgr B2(N).

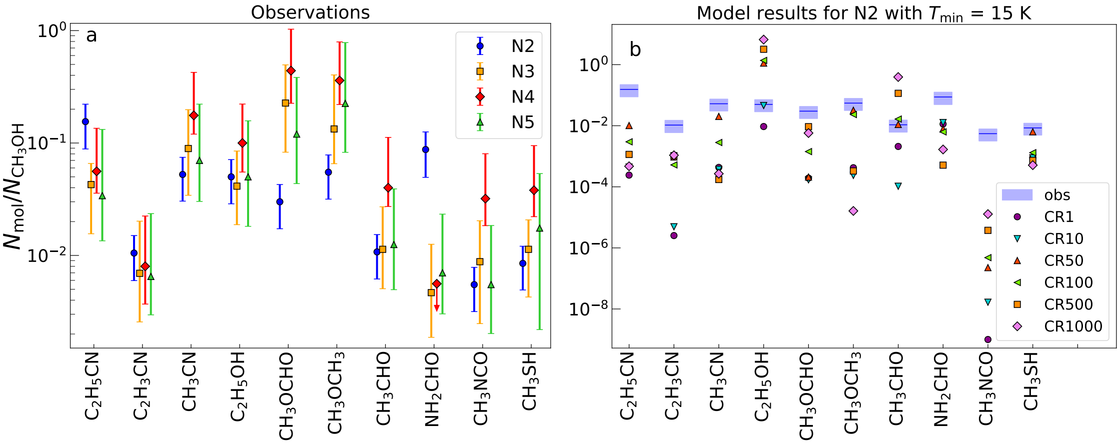

Fig. 1. a: Abundances with respect to CH_3OH of ten COMs detected toward Sgr B2(N2-N5) (Papers I and II). **b:** Abundances with respect to CH_3OH of ten COMs calculated for Sgr B2(N2) by models T15 with different CRIR values. CR1 corresponds to the standard CRIR. The observational values are indicated for comparison with horizontal blue lines and blue boxes represent the 1σ uncertainty.

3 A physical model for high-mass star formation in Sgr B2(N)

Modeling the time-dependent chemical evolution of Sgr B2(N2-N5) requires knowledge of their physical structure and its evolution. We built up a simplified physical model divided into two stages, a prestellar phase followed by the protostellar phase. During the prestellar phase the source undergoes quasi-static contraction at low densities and temperatures. Assuming that all HCs come from the same cloud material, we use the same initial conditions. The protostellar phase starts with the ignition of the central protostar which heats up its free-falling envelope. Our physical model describes the evolution of density and temperature in the envelope of the sources as they evolve from the cold prestellar phase to the present time (Bonfand et al. 2019, Paper II). During the cold, low density phase preceeding the warm up of the envelope, the dust temperature in the outermost layers of the envelope decreases as the density increases. In order to keep the model physically meaningful and to account for the somewhat high dust temperatures expected toward the GC region (see Sect. 1), we defined an arbitrary minimum temperature, $T_{\rm min}$, as the lowest temperature that is allowed in the chemical simulations. Once the central protostar has formed, the temperature in the envelope increases as the protostar's luminosity rises. Based on the estimated time-dependent evolution of the sources' luminosity (Paper II) and the excitation temperatures derived for the HCs at the radius of the COM emission (Paper I), we derived the time-dependent evolution of the dust temperature in the envelope of the sources during the free-fall collapse (Paper II). Given the high densities (Paper I), dust and gas temperatures are assumed to be well coupled during the protostellar phase.

4 Chemical modeling

We used the chemical code MAGICKAL (Model for Astrophysical Gas and Ice Chemical Kinetics and Layering, Garrod 2013) to compute chemical abundances in the envelopes of Sgr B2(N2-N5) (Paper II). We ran for each HC a grid of chemical models varying the minimum dust temperature as follows, $T_{\rm min}$= 10 K (models T10), 15 K (T15) and 20 K (T20); and the CRIR, ζ^{H_2} from 1.3×10^{-17} s^{-1} (CR1) to 1.3×10^{-14} s^{-1} (CR1000).

4.1 Production of COMs: influence of environmental factors

Figure 2b shows the evolution of the fractional abundances of six COMs during the warm up phase of model T15-CR1 for Sgr B2(N2). The solid-phase abundances of the investigated COMs directly determine their final gas-phase abundances, except for C_2H_3CN. This suggests that the COM gas-phase abundances observed in the warm envelope of Sgr B2(N2) are dominated by the thermal desorption of dust-grain ice mantles. The production of these COMs involves surface reactions between molecules accreted onto dust grains during the earlier, cold prestellar phase, followed by the subsequent sublimation of the dust-grain ice mantles. CH_3OH and C_2H_5OH are already present on the grains with significant abundances before the warm-up phase (*i.e.* at T=15 K, Fig. 2b). This suggests that they mostly form during the earlier cold phase. For instance, CH_3OH form on the grains during the prestellar phase via successive hydrogenation of the CO accreted from the gas phase. The production of CH_3CHO, CH_3OCH_3, and C_2H_3CN is still efficient on the grains up to 30–50 K.

The minimum dust temperature during the prestellar phase has an impact on the production of the main ice constituents (H_2O, CO, CO_2, and CH_3OH), essential to the production of COMs, such that the final gas-phase abundances of the investigated COMs are higher in model T10-CR1 than T15-CR1 (Fig. 2a). The CRIR value has an impact on both the solid- and gas-phase abundances of COMs during the warm-up stage (Fig. 2c). The CRIR influences the dissociation rate of surface species and thus the amount of radicals that can react to form COMs. In the gas phase, the CRIR controls the density of ions and thus the frequency of ion-molecule reactions and electronic recombinations, which both act to form but also destroy COMs.

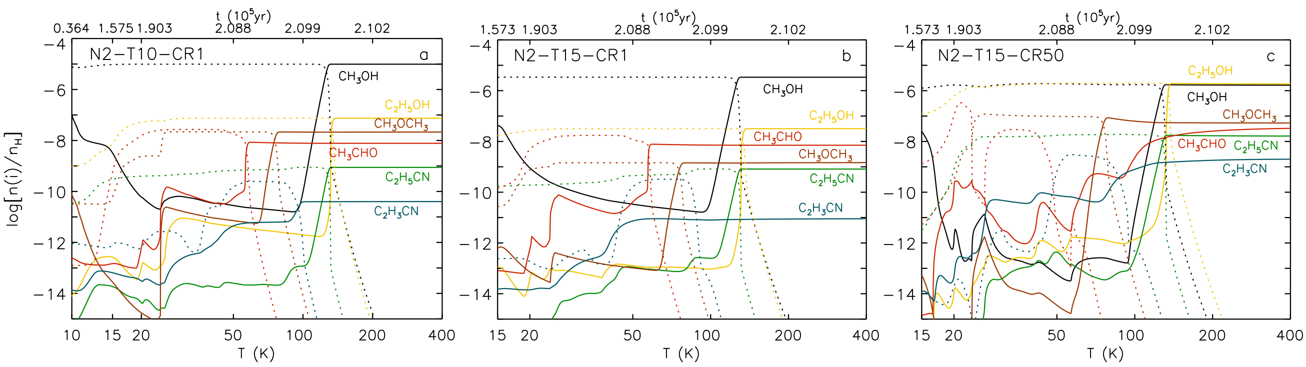

Fig. 2. Fractional abundances (with respect to total hydrogen) of six COMs as a function of the temperature in the envelope of Sgr B2(N2) during the free-fall collapse (Paper II). Results are shown for the chemical models **a:** T10-CR1, **b:** T15-CR1, and **c:** T15-CR50. The solid lines show the fractional abundances in the gas phase while the dotted lines show the abundances on the grains.

4.2 Constraining the environmental factors

Figure 1b compares the gas-phase abundances with respect to CH_3OH observed toward Sgr B2(N2) with the abundance ratios calculated by models T15 with different CRIR values. The [CH_3NCO]/[CH_3OH]] ratio is largely underestimated by all chemical models, suggesting that the binding energy used for CH_3NCO in our chemical models is most likely underestimated (Belloche et al. 2019). For this reason we ignore CH_3NCO in the rest of our analysis. By comparing the observed and calculated abundances it is possible to constrain $T_{\rm min}$ and $\zeta^{\rm H_2}$ that best characterize Sgr B2(N)'s HCs. Given the uncertainties on the observed abundances and the results of chemical models, we consider the agreement between model and observations to be reasonable when the calculated abundances are within one order of magnitude from the observed values. Figure 3a shows the matrix of confidence levels computed for nine COMs relative to CH_3OH, for Sgr B2(N2-N5) taken together. A confidence level of 32% indicates that the calculated abundances lie one order of magnitude lower/higher than the observed ones (Paper II). Given that all HCs should be exposed to the same cosmic-ray flux and probably shared a similar thermal history during the prestellar phase, our analysis shows that, with a confidence level of 37.5%, models T15-CR50 (*i.e.* $\zeta^{\rm H_2} = 6.5{\times}10^{-16}$ s^{-1} and $T_{\rm min}$ = 15 K) best match the observations. In Fig. 3b we examine in more detail how the abundance ratio of two chemically linked species, the cyanides C_2H_3CN and C_2H_5CN, is affected by the CRIR. [C_2H_5CN]/[C_2H_3CN] decreases by several orders of magnitude as the CRIR increases. The observed ratio is best reproduced by model CR50, which is consistent with the result derived overall for the nine COMs from the matrix of confidence level.

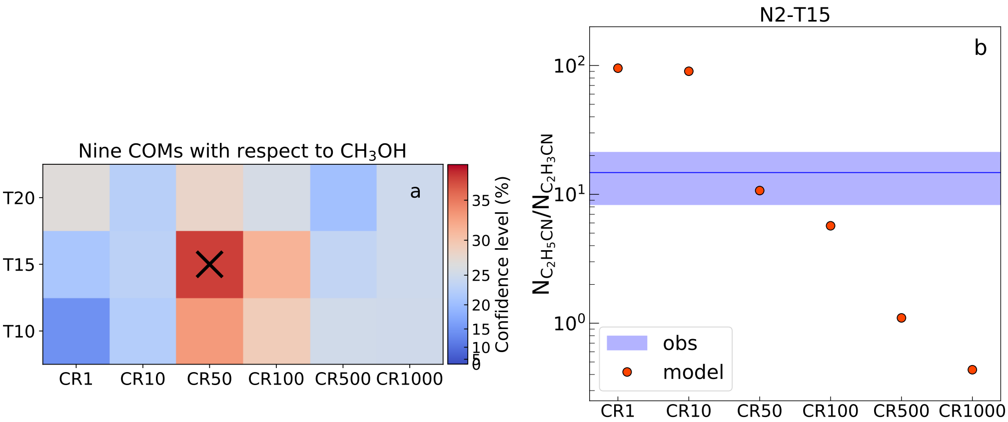

Fig. 3. a: Matrix of confidence level of the chemical models with the observations, for Sgr B2(N2-N5) taken together, and for the abundances of nine COMs with respect to CH_3OH (Paper II). The black cross shows the best-fit model. **b:** Abundances of C_2H_5CN with respect to C_2H_3CN as a function of the CRIR for model N2-T15 (Paper II). The horizontal blue line shows the ratio observed toward Sgr B2(N2) with the blue box that represents the 1σ uncertainty.

5 Conclusion

We combined the analysis of the 3 mm imaging line survey EMoCA and the chemical modeling of Sgr B2(N)'s HCs to present the first detailed comparative study of four HCs evolving in the same environment. We investigated the influence of cosmic-ray ionization and minimum dust temperature during the prestellar phase on the production of selected COMs. In the chemical simulations all investigated COMs mainly form on the surface of dust grains, followed by later desorption into the gas phase. While the production of CH_3OH and C_2H_5OH mostly relies on the cold prestellar phase, CH_3CHO, CH_3OCH_3, and C_2H_3CN still form efficiently on the grains up to 30–50 K. We used COMs as indirect probes to constrain Sgr B2(N)'s environmental conditions by comparing the observations with the results of chemical models. It showed that a minimum temperature of 15 K, higher than the low values used in previous studies ($\leq$10 K, see, e.g., Belloche et al. 2017; Garrod et al. 2017) and closer to the lowest temperature measured toward the GC region (19 K, Sect. 1), leads to an efficient production of COMs roughly consistent with the abundances measured in Sgr B2(N)'s HCs. For models with $T_{\rm min}$ = 20 K signs of disagreement emerge between models and observations, but it could be that models with $T_{\rm min}$ =17–18 K produce COMs in amounts that are still consistent with the observations. Furthermore, the coldest dust grains in the GC region may be masked by warmer outer layers and thus have been missed by *Herschel* because of its limited angular resolution. Therefore, it is likely that the constraint we derived on $T_{\rm min}$ from the COM abundances is consistent with the thermal properties of the GC region. Finally, the best match between chemical models and observations is obtained for $\zeta^{\rm H_2} = 6.5{\times}10^{-16}$ s^{-1}, which is a factor 50 higher than the standard CRIR. This is somewhat lower than extreme values expected toward the diffuse medium in the GC region (see Sect. 1). This difference may reflect the attenuation of cosmic rays in denser gas.

References

Belloche, A., Garrod, R. T., Müller, H. S. P., et al. 2019, Astronomy and Astrophysics, 628, A10
Belloche, A., Meshcheryakov, A. A., Garrod, R. T., et al. 2017, A&A, 601, A49
Belloche, A., Müller, H. S. P., Garrod, R. T., & Menten, K. M. 2016, A&A, 587, A91
Bonfand, M., Belloche, A., Garrod, R. T., et al. 2019, Astronomy and Astrophysics, 628, A27
Bonfand, M., Belloche, A., Menten, K. M., Garrod, R. T., & Müller, H. S. P. 2017, A&A, 604, A60
Clark, P. C., Glover, S. C. O., Ragan, S. E., Shetty, R., & Klessen, R. S. 2013, ApJ, 768, L34
Garrod, R. T. 2013, ApJ, 765, 60
Garrod, R. T., Belloche, A., Müller, H. S. P., & Menten, K. M. 2017, A&A, 601, A48
Ginsburg, A., Bally, J., Barnes, A., et al. 2018, ApJ, 853, 171
Le Petit, F., Ruaud, M., Bron, E., et al. 2016, A&A, 585, A105
Longmore, S. N., Rathborne, J., Bastian, N., et al. 2012, ApJ, 746, 117
Spitzer, J. L. & Tomasko, M. G. 1968, ApJ, 152, 971

SF2A 2019
P. Di Matteo, O. Creevey, A. Crida, G. Kordopatis, J. Malzac, J.-B. Marquette, M. N'Diaye, O. Venot (eds)

DEEP LEARNING FOR THE SELECTION OF YOUNG STELLAR OBJECT CANDIDATES FROM IR SURVEYS

D. Cornu[1] and J. Montillaud[1]

Abstract. The robust identification of YSOs is an important step for characterizing star-forming regions. Such classification is commonly performed with infrared suveys using straight cuts in CMD diagrams. However, Machine Learning algorithms may outperform these methods with adaptive and non-linear separations in any number of dimensions. In this paper we present our methodology to implement a supervised deep neural network for YSO classification with various datasets built from well-known regions. We detail the tuning of the network parameters, taking into account the specificities of this classification. Then we focus on the reliability of the classification and address difficulties due to the strong dilution of YSOs against contaminants.

Keywords: Young Stellar Objects, Spitzer, Infrared, Machine Learning, ANN, Classification, Protostars

1 Introduction

Observing Young Stellar Objects (YSOs) in stellar clusters can be used to characterize star-forming regions. Their presence testifies the star-formation activity and allow one to quantify its efficiency. They can also be a probe of cloud density which can be combined with astrometric surveys like Gaia to recover the 3D structure and motion of star forming clouds (Grossschedl et al. 2018). They are often identified with a classification method that mainly rely on their Spectral Energy Distribution (SED) in the infrared (IR). One can also separate them in evolutionary steps from the star-forming phase to the main sequence (class 0 to III), granting even more information on the structure and evolution of star-forming regions.

In this context we aim to design a classification method for YSOs, relying on large surveys and taking advantage of modern statistics analysis. We choose to use Artificial Neural Networks (ANN) which are popular supervised machine learning methods, and have shown strong performance on a wide variety of problems. Since it belongs to supervised methods we rely on an original classification that provides targets for the training phase. For this we use the popular method by Gutermuth et al. (2009) which describes a multi-step classification scheme using the *Spitzer* space telescope (Werner et al. 2004) surveys (using 5 bands between 3 and 24 μm) . In this study we focus on bright star-forming regions observed with Spitzer whose physical properties are well constrained. In this paper we show results based on a combination of three different dataset, namely, Orion (Megeath et al. 2012), NGC 2264 (Rapson et al. 2014), and a sample of clouds nearer than 1 kpc that exclude the two previous regions (Gutermuth et al. 2009). We briefly describe our implementation of a Multi Layer Perceptron (MLP), a kind of ANN, with a special emphasis on how to properly link the physical problem to the network. Therefore, we detail common good practices for the data preparation and a proper representation of results.

2 Deep Learning method

2.1 *Deep Artificial Neural Network : Multi Layer Perceptron*

The core element of ANN is a mathematical model of neuron (McCulloch & Pitts 1943) that performs the weighted sum h of an input vector. It is then given to an activation function $g(h)$ which usually resembles a

[1] Institut UTINAM - UMR 6213 - CNRS - Univ Bourgogne Franche Comté, France, OSU THETA, 41bis avenue de l'Observatoire, 25000 Besançon, France - email : david.cornu@utinam.cnrs.fr

binary activation. One usual activation function is the Sigmoïd : $a = g(h) = 1/(1 + \exp(-\beta h))$, where a is the result of the activation and β an hyperparameter of the network. One neuron alone only performs a linear separation. Therefore, they can be added in the form of a *deep* ANN. For this, neurons can be added in two different ways. The first one is by adding neurons independently in a layer. Each neuron is then fully connected to the input layer with no connection between neurons of the same layer. The second one is to add multiple layers on top of each other. In this case a layer will take as its own input vector the result of the activation of the neurons from the previous layer.

Such an ANN is a universal function approximator (Cybenko 1989), called a Multi Layer Perceptron (MLP) (Rumelhart et al. 1986), which is able to perform classification, regression, clustering, time series prediction, compression, image recognition, ... ANN are supervised machine learning methods, therefore they need to be trained on previously labeled data. To learn, the network will compare its own output with the expected output using an error function and will modify its weights accordingly. To do so one has to propagate the error from the output layer back to the input layer by using the well-known "Back-Propagation" algorithm. The general formula of this gradient computation is described as follows:

$$\omega_{ij} \leftarrow \omega_{ij} - \eta \frac{\partial E}{\partial \omega_{ij}} \qquad \frac{\partial E}{\partial \omega_{ij}} = \frac{\partial E}{\partial h_j}\frac{\partial h_j}{\partial \omega_{ij}} \qquad \delta_l(j) \equiv \frac{\partial E}{\partial h_j} = \frac{\partial E}{\partial a_j}\frac{\partial a_j}{\partial h_j}. \tag{2.1}$$

The indices i and j go through the input dimensions and the neurons respectively, for the current layer. These equations are the same for each layer with adjustment to the size of the corresponding layer and associated inputs. δ_l is a local error term that can be defined for each layer. The η parameter is a learning rate, that must be fine tuned to allow both fast convergence and precision of the generalization. The final network contains only one hidden layer with 25 hidden neurons and a learning rate $\eta = 7 \times 10^{-5}$. These numbers are found based on performance criteria (Cornu et. al in prep.).

2.2 Classification with ANN

The problem we want to solve is a YSO classification. Therefore, the output layer is set with one neuron per class. The expected output for a 3-class example would be in the form of : *A: (1, 0, 0), B: (0, 1, 0), C: (0, 0, 1).* Combined with an appropriate activation function it allows one to recover a membership probability (based on the network knowledge) for each class. We use the common Softmax function : $a_k = g(h_k) = exp(h_k)/(\sum_{k=1}^{N} exp(h_k))$, where k is the number of neurons in the output layer. The result of each neuron will always be between 0 and 1, and the sum of all the output neurons will always equal 1. The object is then classified regarding the neuron with the maximum output. An example of results given by the network is: (0.1, 0.05, 0.85) for a rather clear class C, and (0.3, 0.4, 0.3) for a way more confuse object still considered as class B. This brings the network in the range of Probabilistic Neural Network (PNN) (Specht 1990).

3 Data preparation and network settings

3.1 Definition of the classes and labeled sample

We construct our training sample based on a simplified version of the method by Gutermuth et al. (2009) (hereafter G09), where only Spitzer data are used. We use the $3.6, 4.5, 5.8, 8$ μm bands from IRAC and the 24 μm band from MIPS combined with their respective uncertainty as input features. The G09 method performs a multi-step extraction based on straight cuts in color-color and color-magnitude diagrams (CMDs), which allows one to extract objects that are likely contaminants and to recover YSO candidates (Fig. 1). YSO classes range from class 0, that are the youngest one, up to class III that are near the main sequence (Allen et al. 2004). However, using the previous bands we are only able to recover class I (protostars) and class II (pre-main sequence with thick disk) YSOs. For the sake of simplicity we adopt only 3 categories in our classification : YSO CI, YSO CII, and Other/Contaminants.

To get the maximum generalization capacity out of our network we need to ensure the diversity of our training sample. For that we choose to use well-known and well constrained star forming regions observed with Spitzer : Orion (Megeath et al. 2012), NGC2264 / Mon OB1 (Rapson et al. 2014), and a sample of many regions nearer than 1 kpc (Gutermuth et al. 2009). This is a major point since different star forming regions cover the input feature space differently and we want our network to be able to make predictions on various regions. We define our "labeled sample" by applying the G09 method on these catalogs (Table 1).

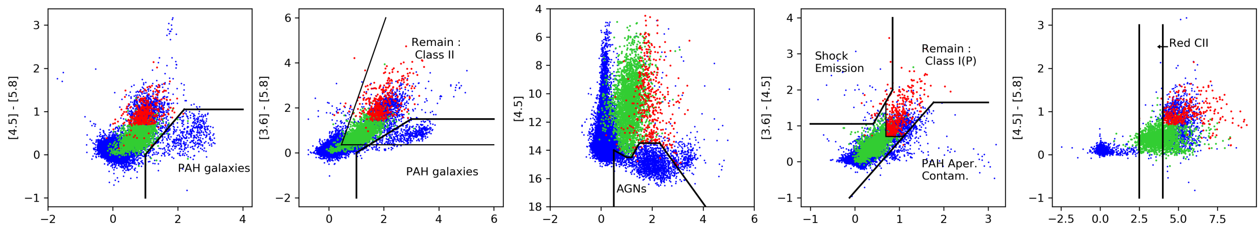

Fig. 1. Usual CMDs used for this classification. Retrieved class II candidates in green, class I candidates in red and others in blue for the Orion cloud.

Dataset	Pre-selection		Detailed contaminants					Output classes		
	Total	Selected	Gal.	AGN	Shocks	PAH	Stars	YSO CI	YSO CII	Other
Labeled sample	311407	29074	522	1448	34	89	21799	784	4396	23897
Test		5377	104	278	6	17	4359	82	531	4764
Train γ_i:			0.5	0.7	0.05	0.15	4.0	1.0	6.3	
Train		6286	331	463	27	70	2648	662	2085	3539

Table 1. Result of the application of our simplified G09 method. The third category of columns give the labels in use in the learning phase with the last "Other" column being the sum of all the detailed contaminants. The bottom lines shows the test and training sets distribution, along with the γ_i corresponding values for the train set.

3.2 Data separation : training and test sets

Most of the labeled dataset must be used for the learning process (training set), but we also need to keep aside a smaller part of it to assess the quality of the prediction of our network with objects it has never seen before (test set). This test set must be as representative as possible of the true problem we want to solve. It means that it must preserve observational proportions. Without this precaution, the results would only represent a numerical performance and not the capacity of the network to generalize a problem. We define a parameter θ so that for each subclass the number of objects kept away in the test set is $N_i * \theta$. For the results in this paper $\theta = 0.2$.

In contrast, the training set does not need to have observational proportions. Actually, re-balancing the number of objects given for each subclass is a way to force the network to give more representative strength to some subclass. It is especially important due to the strong dilution of our labeled sample. With observational proportions, contaminants (especially more evolved stars) would be so numerous than YSOs would be considered as noise. We then have to reduce the number of contaminants in our training sample, but we can not choose an equal ratio. Doing so would not take into account that some subclass of contaminants cover a larger input feature space than the YSOs, or require a more complex separation to be distinguished. Moreover, we need to keep the majority of our representative strength for the most dominant subclass as they will be the main factor of contamination of the other classes (as illustrated by the results in Sect. 4). Still, there are no exact best solutions for those proportions as it depends on what one wants to recover. We choose to put the emphasis on class I YSO candidates, since they are not recovered by many other methods, but with the objective of preserving the quality of class II candidates. It means that the number of class I YSOs in the training sample has to be maximized. The other objects are proportional to the number of class I which defines a proportion factor γ_i for each of them. The proportions we found to provide good results are presented in the bottom of Table 1. More details on this selection in Cornu et al. (in prep.).

4 Results

After the training, we can apply our network on the test set to recover the predicted result for each object for which we also have the expected answer. But to assess the quality we need a proper way to represent them. For classification it is recommended to use a Confusion Matrix. It is defined as a two dimensional table with rows corresponding to the original class distribution (labels/targets), and columns corresponding to the classes given to the same objects by our network classification (output). The "recall" represents the proportion of

		Predicted			
	Class	YSO CI	YSO CII	Other	Recall
Actual	YSO CI	75	3	4	91.5%
	YSO CII	6	515	8	97.0%
	Other	8	42	4714	99.0%
	Precision	84.3%	92.0%	99.7%	98.6%

	CI	CII	Gal	AGN	Shock	PAH	Stars
YSO CI	75	6	0	2	2	2	2
YSO CII	3	515	2	2	4	3	31
Other	4	10	101	274	0	12	4327

Table 2. Left: Confusion matrix for the test set (observational proportions). **Right:** Subclass distribution from the G09 original attribution for each of the output of the network.

objects from a given class that were recovered as expected and is given at the end of each line. The "precision" represents the fraction of correctly classified objects in a class as predicted by our network and is given at the bottom of each column. And finally a global "Accuracy" quantity that gives the proportion of objects properly classified over the total number of objects given at the bottom right corner of the matrix. The corresponding matrix for our trained network applied on our test set in observational proportions is presented in Table 2.

These results show that we get more than 90% recall on the class I YSO candidates, but also by preserving a 97% recall on the class II candidates. The precision drops at 84% for class I. Looking at the detailed subclass results in Table 2, we can see that the contamination for class I is mainly due to the confusion with class II, while contamination for class II is mainly coming from the more evolved stars that are the vastly dominant class in the sample. Those results are highly competitive with previous studies (Marton et al. 2016; Miettinen 2018), especially regarding the precision that is greatly improved, due to our more detailed analysis and management of the training proportions.

5 Conclusions

We showed that, using a rather simple neural network, we could achieve excellent results on infrared YSO classification. However, such methods require meticulous preparation of the data and proper understanding of their generalization biases. Using such a network we aim at providing a wide catalog of Spitzer YSO candidates. Since our current limitation is the number of YSOs in our sample, we plan to use simulated data to try improving the current results. More detailed information on this research will be soon available in Cornu et al. (in prep.).

We thank PCMI (Programme National "Physique et Chimie du Milieu Interstellaire" of CNRS/INSU with INC/INP co-funded by CEA and CNES) for giving us the opportunity to present this research during their 2019 SF2A session, and for their financial support through the GALETTE project. D. Cornu acknowledge that this research is done under a PhD funding from the CNES and the "région Bourgogne Franche-Comté".

References

Allen, L. E., Calvet, N., D'Alessio, P., et al. 2004, The Astrophysical Journal Supplement Series, 154, 363

Cybenko, G. 1989, Mathematics of Control, Signals and Systems, 2, 303

Grossschedl, J. E., Alves, J., Meingast, S., et al. 2018, Astronomy & Astrophysics, 619, A106, arXiv: 1808.05952

Gutermuth, R. A., Megeath, S. T., Myers, P. C., et al. 2009, ApJS, 184, 18

Marton, G., Tóth, L. V., Paladini, R., et al. 2016, Mon Not R Astron Soc, 458, 3479

McCulloch, W. S. & Pitts, W. 1943, The bulletin of mathematical biophysics, 5, 115

Megeath, S. T., Gutermuth, R., Muzerolle, J., et al. 2012, AJ, 144, 192

Miettinen, O. 2018, Astrophysics and Space Science, 363, 197

Rapson, V. A., Pipher, J. L., Gutermuth, R. A., et al. 2014, The Astrophysical Journal, 794, 124

Rumelhart, D. E., Hinton, G. E., & Williams, R. J. 1986, in Parallel Distributed Processing: Explorations in the Microstructure of Cognition, Vol. 1, ed. D. E. Rumelhart, J. L. McClelland, & C. PDP Research Group (Cambridge, MA, USA: MIT Press), 318–362

Specht, D. F. 1990, Neural Networks, 3, 109

Werner, M. W., Roellig, T. L., Low, F. J., et al. 2004, The Astrophysical Journal Supplement Series, 154, 1

SF2A 2019
P. Di Matteo, O. Creevey, A. Crida, G. Kordopatis, J. Malzac, J.-B. Marquette, M. N'Diaye, O. Venot (eds)

METHODOLOGY FOR A PLANCK/HERSCHEL ANALYSIS OF THE INTERPLAY BETWEEN FILAMENTS AND MAGNETIC FIELDS IN STAR FORMING REGIONS

J.-S. Carrière[1], L. Montier[1], I. Ristorcelli[1] and K. Ferrière[1]

Abstract.
Interstellar matter in star forming regions appears to form filamentary structures, which were suggested to line up either parallel or perpendicular to the magnetic field. Our purpose is to investigate this possible alignment further, based on a combined analysis of Herschel and Planck data obtained towards a large variety of star forming regions. As a first step, we developed an optimized version of the original Rolling Hough Transform code, particularly well suited to extract and analyse the orientation of filamentary structures over a broad range of densities, from striations to dense filaments. In this paper, we present an overview of our new method, called the Rolling Radon Transform and we describe the preliminary results obtained for a star forming region at high galactic latitude.

Keywords: Star formation, ISM, Magnetic field, Polarization

1 Introduction

Magnetic fields are considered as one of the key physical agents, with gravitation and tubrulence, that regulate star formation, but their actual role in the formation and evolution of dense structures remains an open question. Thanks to the capability of alignment of elongated grain on magnetic fields, polarized dust emission is well-suited to probe the magnetic field structure in the cold, dense interstellar medium (ISM).

Exploring the submillimeter domain with unprecedented performances in terms of sensitivity, sky coverage and angular resolution, the complementary between the Planck and Herschel satellites has opened a new era for the study of the cold matter structures in the Galaxy. Thousands of cold cores and clumps have been detected in different Galactic environments (Planck Collaboration et al. 2016c), and the surveys have revealed a network of filamentary structures, ubiquitous over a wide range of physical conditions. Moreover, it was shown that prestellar cores and protostars form primarily within the densest filaments (André et al. 2010). Therefor, the question of the formation of prestellar cores is now closely linked to the properties of filaments, their formation, and their evolution.

The study of the relative alignment between filaments hosting cold cores and magnetic fields in star forming regions offers a unique opportunity to investigate the possible link between them. Recent studies revealed preferential relative orientations, varying from parallel in the diffuse medium (Planck Collaboration et al. 2016a) to perpendicular in denser filaments within the molecular clouds (Planck Collaboration et al. 2016b). A transition in column density between parallel and perpendicular configurations was found and shown to be consistent with simulations assuming strong magnetic fields (Planck Collaboration et al. 2016b). In a statistical analysis of a sample of filaments hosting clumps, Alina et al. (2019) found that the relative orientations (parallel, perpendicular or no preference) depended both on the environment density and on the density gradient between the filaments and their environment.

In order to gain more insight in the interplay between filaments and the magnetic field, Malinen et al. (2016) performed for the first time a combined analysis of Planck and Herschel data toward the star forming region L1642 (also called G210 here). Comparing the magnetic field traced by the dust polarized emission observed by Planck and the highly resolved matter structures observed by Herschel will give us more detailed information on the relative alignment study. Especially for the less dense filaments, called striations, that were not resolved in

[1] CNRS, IRAP, 9 Av. colonel Roche, BP 44346, 31028 Toulouse Cedex 04, France

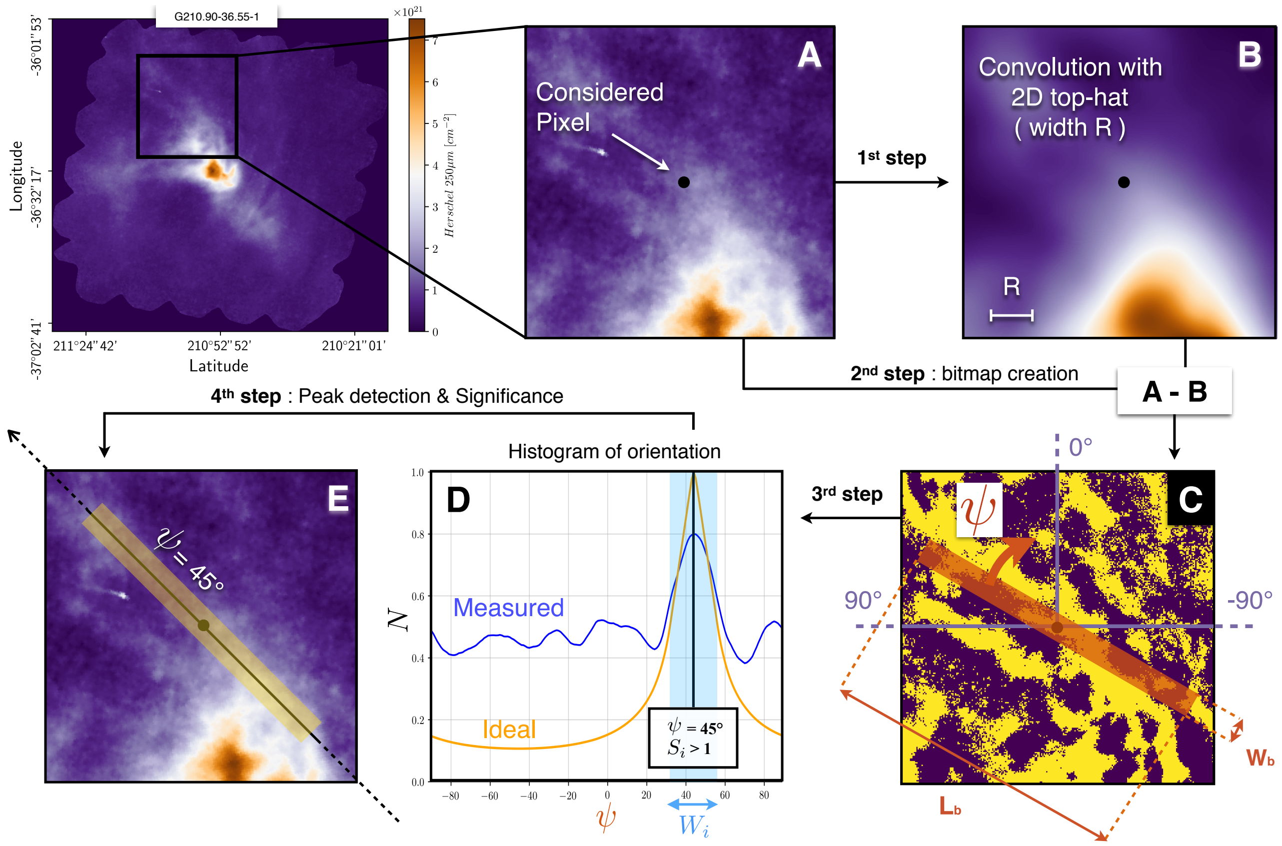

Fig. 1. Illustration of the RRT method based on the 250 μm intensity map of the G210 field observed by Herschel. **Top Left:** Entire G210 field. **Top Middle:** Region A from this field. **Top Right:** Smoothed image B from the initial image A obtained by convolving with a 2D top-hat kernel. **Bottom Right:** Binary image C in which the dark pixels have a value of 0 and the yellow pixels, which represent the sharpest structures from the initial image A, have a value of 1. **Bottom Middle:** The correlation between the nominal bar and the yellow pixels in the binary image is shown in the Histogram of orientation D. **Bottom Left:** Detected filament in the image E (with the initial image A as background) around the initial pixel considered with the orientation found in the Histogram of orientation D.

Planck data. They found a very similar transition as in Planck Collaboration et al. (2016b) in terms of column density ($N_\mathrm{H} \approx 1.7 \times 10^{21}$ cm^{-2}), and noted that diffuse filaments (called striations) are clearly parallel to the magnetic field. G210 is part of the sample of 116 selected fields from the Herschel "Galactic Cold Cores" key-program (Juvela et al. 2012), a follow-up of the Planck Galactic Cold Clumps catalogue (Planck Collaboration et al. 2016c), put together to study star formation in different Galactic environments.

Our ultimate goal is to perform a similar analysis as in Malinen et al. (2016) extended to this whole fields sample. For that purpose, we first developed an improved methodology to extract filaments, especially useful in the case of a statistical analysis (Carrière et al. in prep). Here we present the main steps of this method, called the Rolling Radon Transform (RRT), which is an optimization of the Rolling Hough Transform (RHT) method (Clark et al. 2014). We also present the preliminary results derived when applying this new method to the G210 field.

2 Rolling Radon Transform Methodology

Binary map

The new RRT method is illustrated in Fig. 1, applied to one pixel from the G210 field. As for the RHT, the first step of the RRT method is to create a smoothed image B from the initial image A, by convolving A with a 2D Top-hat function of radius R. The subtraction of A by B gives C in which the negative pixels obtain the value zero and the positive pixels, representing the sharpest structures in A, obtain the value of 1. The value of R is a free parameter in RHT and thus is not taking into account the sharp structures size from C as a function of the nominal bar's width. This can lead to misunderstanding in the final output since those sharp structures should have sizes the closest possible to the nominal bar's width. This is now optimized in the RRT and the processing method will be described in Carrière et al. in prep.

Histogram of orientation

Both RHT and RRT methods are based on the approximation that filaments can be considered as bars with lengths L_b and widths W_b. The second step of both methods is to compute the correlation between this nominal bar and the binary image for any main axis bar's orientation ψ, in the range -90° to +90°. This provides a "measured" histogram against orientation (panel D in Fig. 1). This histogram thus gives the fraction N of the bar surface that is yellow.

From this histogram of orientation, the RHT uses two important assumptions. The first one is to apply a threshold N_{ct} on N and consider the the filament's orientation as the mean value of the angles ψ in the histogram part that is higher than N_{ct}. The second assumption of the RHT is to consider that this free parameter N_{ct} is sufficient to quantify the reliability of the extracted filaments. For the first assumption, an important issue may occur when we have two different peaks at two different positions (in terms of angle) that are higher than N_{ct} in the histogram of orientation. Indeed, in that case, the mean value of the angles ψ will give a wrong filament's orientation between the two different peaks and miss the fact that both peaks eventually correspond to two different filaments with two different orientations. For the second assumption, it is clear that this free parameter N_{ct} is intrinsic to the method and can be arbitrary. Those two assumptions are removed in the RRT and the filament's orientation and its reliability computation are now optimized. We will now focus in more details on the new RRT methodology.

The first optimization is to compute the orange curve of panel D that represents an ideal histogram as would be obtained if the binary image contained a single yellow region with the exact same shape as the nominal bar. Thus, it shows a peak at a given angle, corresponding to the preferential orientation maximising the correlation between the bar and the structures in the binary image.

Significance

We will consider each peak in the measured histogram as a potential filament with its own orientation. For each peak, we consider the ideal histogram that peaks at the same position that we compare with the measured histogram over a window W_i of orientation angles related to the bar's dimension. The comparison is done by calculating the parameter Δ as follows,

$$\Delta = \sqrt{\frac{\chi^2}{\mathrm{n}}} = \sqrt{\frac{1}{\mathrm{n}} \times \sum_{\mathrm{j}}^{\mathrm{n}} \frac{(\mathrm{I_j} - \mathrm{M_j})^2}{\sigma^2}}, \tag{2.1}$$

$$\sigma = \mathrm{MAD} = \mathrm{median}\left(|\mathrm{M} - \mathrm{median}\left(\mathrm{M}\right)|\right), \tag{2.2}$$

with n the number of considered points within the comparison window W_i, M the measured histogram, I the ideal histogram and MAD the mean absolute deviation. The next step is to decide whether a detected structure is a reliable filament or not, thus we have to define a threshold Δ_{ct} on Δ. To define a non-arbitrary threshold, we perform Monte-Carlo simulation. We can see in Fig. 2 an illustration of one Monte Carlo step. The idea is to add the RRT bar inside the field binary image, with random position and orientation. The only difference between the measured and ideal histograms is that the measured includes the field background.

The following step is to repeat this process at least ten thousand times (with random positions and orientations for the bar) in order to obtain a Δ distribution. This distribution allows us to define a threshold Δ_{ct} that is directly linked to the field background and thus specific to each field. The computation of Δ_{ct} is based on a p-value of 5%. Let's assume we have a realization Δ_{ct} of a random variable Δ following the distribution D, then

$$p := \Pr\left(\Delta > \Delta_{ct} | D\right), \tag{2.3}$$

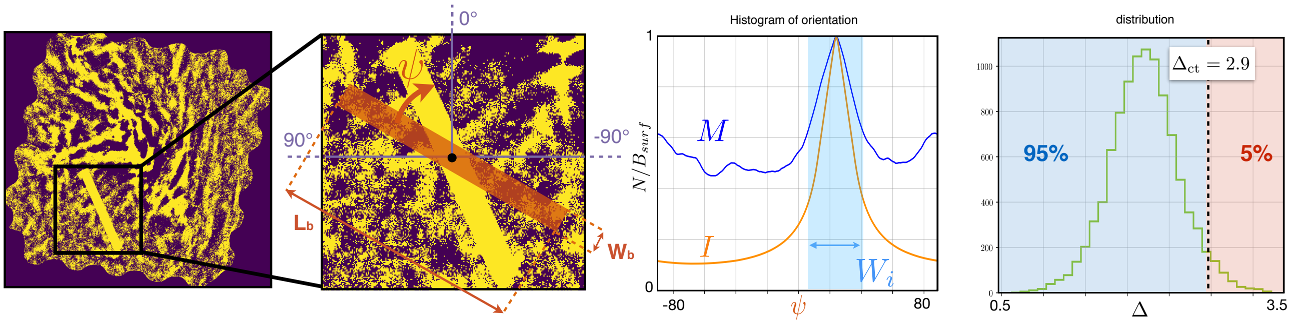

Fig. 2. Left & Middle Left: Binary image of the G210.90-36.55-1 field in which we add a bar with random position and orientation and with the exact same shape as the standard RRT bar. **Middle Right:** Resulting measured and ideal histograms of orientation. **Right:** Δ distribution (Monte-Carlo simulation) with the threshold Δ_{ct} by considering a p-value of 5%.

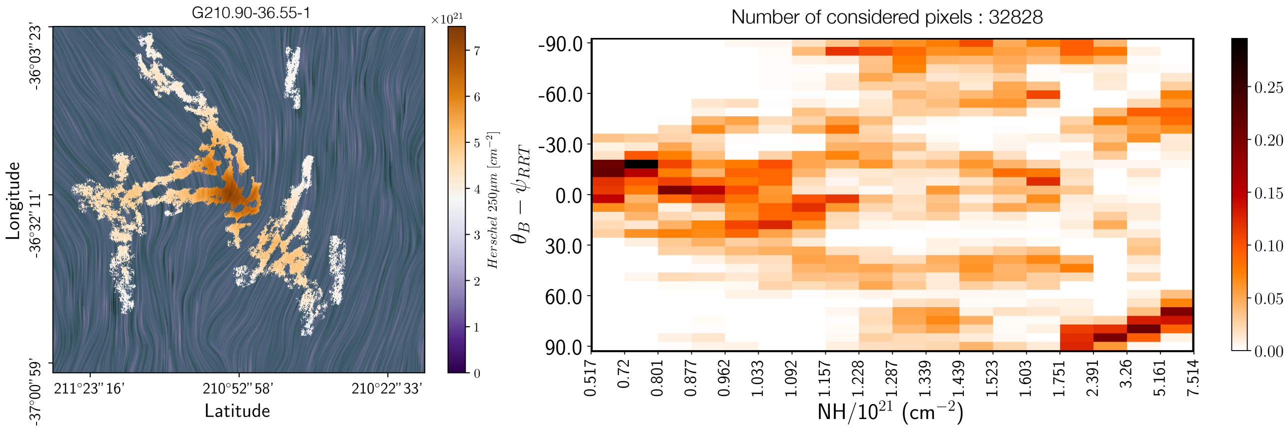

Fig. 3. Left: Filaments extracted with the RRT, with the magnetic field traced by the dust polarized emission of G210. **Right:** Histogram of Relative Orientation $\theta_B - \psi_{RRT}$ as function of column density $N_{\rm H}$.

with p the probability that Δ is larger than $\Delta_{\rm ct}$ assuming the distribution D. We can see in Fig. 2 the value of the resulting threshold $\Delta_{\rm ct}$ given a p-value of 5%. If we want to have something comparable between the different fields, we will consider a significance S_i given by $S_i = \Delta_{\rm ct}/\Delta$. This equation tells us that the significance is > 1 if Δ is lower (thus better) than the threshold $\Delta_{\rm ct}$ and vice versa. Finally, a significance > 1 means that the filament detected by the RRT is a reliable filament and its parameters, such as its orientation, will be kept for science analysis. In view of the definition of the p-value, this means we have a 5% chance of rejecting the ideal filament that we were looking for (by considering filaments as bars).

Compared to the two assumptions made by RHT, one of the main advantages of the RRT method is now the possible detection of different filamentary structures, without bias between each others, with different orientations for one pixel of the field. The second optimization is about the significance S_i that gives us a statistical, non-arbitrary and thus robust computation of the filament extraction reliability.

3 Preliminary results

Once we have extracted the orientation of filaments in a reliable way with the RRT, we can study their relative alignment with respect to the magnetic field whose orientation θ_B is based on polarization data measured by Planck. In order to illustrate these preliminary results, we use the example of the G210 field for which we apply the RRT with L_b=0.1pc and W_b=0.3pc. These width and length come from Arzoumanian et al. (2019) who found a characteristic filament width of 0.1pc by imposing an aspect ratio ≥ 3. in Fig. 3 we can see the combination of the filaments detected by the RRT with the magnetic field traced by the dust polarized emission.

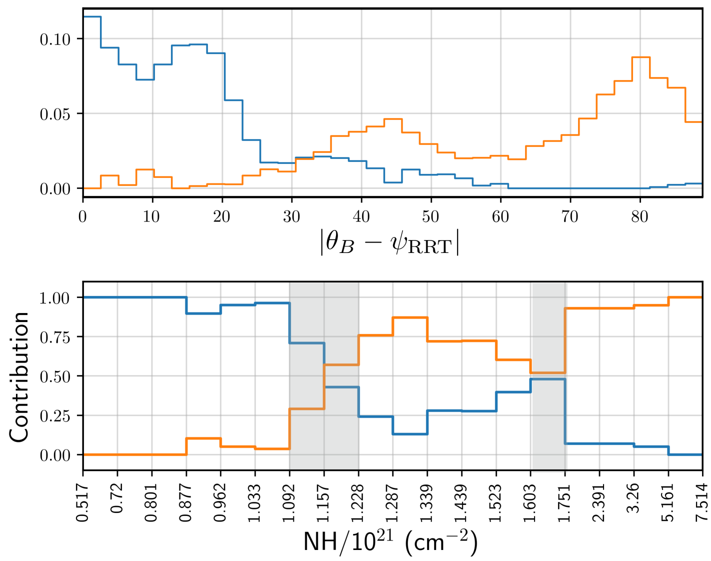

Fig. 4. Top: HROs integrated over all $N_{\rm H}$ for the two main components emerging from Resulting main components from Fig 3, Right. **Bottom:** Weights of these two components as functions of column density.

We first show (Fig. 3, Right) the Histogram of Relative Orientation (HRO) $\theta_B - \psi_{\rm RRT}$ as a function of column density $N_{\rm H}$. We can clearly see that, on the left part, at lower densities, the less dense filaments are mainly aligned parallel to the magnetic field, while they tend to be perpendicular at higher column density. This result is very consistent with the previous study of Malinen et al. (2016).

We use the Principal Component Analysis (PCA) and the Non-negative Matrix Factorization (NMF). The aim of using these two methods is to reconstruct the HRO vs $N_{\rm H}$ diagram as two different matrices representing the principal components H and their weights W as explained in Malinen et al. (2016). As we can see in Fig. 4, we obtain two main components from H that can reconstruct the HRO vs $N_{\rm H}$ diagram, thus a bimodal orientation. Here we find that the transition column density between the two modes is about 1.2×10^{21} cm^{-2}. However, we also notice a region around 1.7×10^{21} cm^{-2} without a clear distinction between the two components, where both weights are about 50%. This is close to the value found in Malinen et al. (2016) and Planck Collaboration et al. (2016b), and the reason this is not a transition in our case may come from the difference between the methods used in order to extract the filaments.

4 Conclusion

Our new RRT method provides a very robust way of extracting filaments with different sizes and in different environments, over a broad range of densities. Compared to the RHT, we improved the computation of the extracted filament significance, now based on a statistical study rather than on arbitrary parameters. It is user friendly (the only parameters to control are the bar dimensions) and relatively fast (less than 30 minutes per molecular cloud), which is a great asset for the statistical analysis that we plan to do in the future on all the 116 fields from Herschel PGCC follow-up. It is clear that combining Herschel and Planck data is quite powerful for the relative alignment study since it includes striation features, thinner structures than filaments in molecular clouds that Planck alone can't resolved. We also found a bimodal orientation between filaments and the magnetic field. This result, on G210 field, is part of a preliminary study carried on a sample of different fields studied by Alina et al. (2019) (Carrière et al. in prep).

References

Alina, D., Ristorcelli, I., Montier, L., et al. 2019, MNRAS, 485, 2825

André, P., Men'shchikov, A., Bontemps, S., et al. 2010, A&A, 518, L102

Arzoumanian, D., André, P., Könyves, V., et al. 2019, A&A, 621, A42

Clark, S. E., Peek, J. E. G., & Putman, M. E. 2014, ApJ, 789, 82

Juvela, M., Pelkonen, V. M., White, G. J., et al. 2012, A&A, 544, A14
Malinen, J., Montier, L., Montillaud, J., et al. 2016, MNRAS, 460, 1934
Planck Collaboration, Adam, R., Ade, P. A. R., et al. 2016a, A&A, 586, A135
Planck Collaboration, Ade, P. A. R., Aghanim, N., et al. 2016b, A&A, 586, A138
Planck Collaboration, Ade, P. A. R., Aghanim, N., et al. 2016c, A&A, 594, A28

PHOTODESORPTION FROM ICES CONTAINING H_2CO AND CH_3OH

G. Féraud[1], M. Bertin[1], C. Romanzin[2], R. Dupuy[1], F. Le Petit[1], E. Roueff[1], L. Philippe[1], X. Michaut[1], P. Jeseck[1] and J.-H. Fillion[1]

Abstract. The interplay between gas and ice is expected to play an important role in the observed molecular abundances in cold and dense regions of the interstellar medium (ISM). The role of non-thermal desorption from grains in the origin of the gaseous organic molecules observed in these regions is still an open question. UV photodesorption from icy grains containing formaldehyde (H_2CO) and methanol (CH_3OH) has been invoked as a possible non-thermal mechanism that participates to the observed gas phase H_2CO and CH_3OH abundance.

We studied the photon-induced desorption from H_2CO and CH_3OH-containing ices in the Far-UltraViolet (FUV) range at the SOLEIL synchrotron (DESIRS beamline, 7-13.6 eV, 910-1771 Å), and we detected the gas phase release of intact H_2CO and of intact CH_3OH, but also of photofragments as a function of the photon energy. The photodesorption of intact H_2CO from pure H_2CO ice is higher than the CH_3OH average photodesorption yield from pure CH_3OH ice. In more astrophysically-relevant H_2CO:CO ice mixtures, the photodesorption of H_2CO seems to be enhanced by the presence of CO, whereas on the contrary, the photodesorption of CH_3OH is reduced in CH_3OH:CO mixtures. This shows the ability of UV photons to desorb small organic molecules, such as H_2CO.

Keywords: gas-to-ice ratio, photodesorption, photodissociation, condensed phase, protoplanetary disks (PPD), photon dominated regions (PDR), Complex Organic Molecules (COMs)

1 Introduction

In the Interstellar Medium (ISM), icy grain mantles are mainly composed of H_2O and CO, but also of larger organic molecules such as methanol (CH_3OH), and certainly also formaldehyde (H_2CO). CH_3OH is one of the most basic Complex Organic Molecules (COMs), while H_2CO is a COM precusor. It is proposed that H_2CO and CH_3OH can both be formed on grains through the successive hydrogenation of CO. H_2CO can also be formed directly in the gas phase, but CH_3OH cannot and therefore its presence in the gas phase can only be explained by non-thermal desorption from icy grains.

Gas phase CH_3OH and H_2CO are observed in various regions, such as prestellar cores (Bacmann et al. 2003; Vastel et al. 2014), photon dominated regions (PDR) (Guzmán et al. 2011, 2013) and protoplanetary disks (PPD) (Walsh et al. 2016; Carney et al. 2019). In many cases, observations together with astrochemical modelling suggest that non-thermal desorption mechanisms must be at play to explain their gas phase abundances. Very recently, the desorption of intact CH_3OH by swift heavy ions, analogs of cosmic-rays, has been shown to be a dominant process in dense clouds (Dartois et al. 2019). UV photodesorption, where UV photons are responsible for the desorption of molecules lying in the upper layers of the icy grains, is another non-thermal mechanism, and its importance in PDR and PPD has been highlighted (eg Guzmán et al. (2011); Walsh et al. (2017)). Whereas photodesorption studies have been mostly focused on small molecules (CO, N_2, CO_2, H_2O; eg Öberg et al. (2009); Fayolle et al. (2011); Bertin et al. (2013); Fillion et al. (2014); Cruz-Diaz et al. (2018)), it is much less known for larger organic molecules. Measurements of photodesorption yields are however crucial, as their variations could increase gas phase abundances by up to several orders of magnitude in some environments, (Guzmán et al. 2011) but also induce changes in the solid-phase chemistry (Esplugues et al. 2016, 2017) and possibly in the gas phase chemistry, and even in the location of snowlines. There is thus a strong need for laboratory astrophysics

[1] Sorbonne Université, Observatoire de Paris, Université PSL, CNRS, LERMA, F-75005, Paris, France
[2] Laboratoire de Chimie Physique (LCP), CNRS UMR 8000, Univ. Paris Sud, F-91400 Orsay, France

studies to understand photodesorption mechanisms and obtain quantified data for astrophysically-relevant ices containing organic molecules. This is what is presented here, for pure H_2CO and CH_3OH ices, and for H_2CO or CH_3OH mixed with CO.

2 Experimental results

The SPICES (Surface Processes & ICES) set-up was used for these experiments. It consists in an ultrahigh vacuum (UHV) chamber within which a polycrystalline gold surface is cooled down to ∼10 K. H_2CO and CH_3OH ices of controlled thicknesses are grown on this gold surface (see Bertin et al. (2016); Féraud et al. (2019) for experimental details), either as pure ices or mixed with CO (H_2CO:CO and CH_3OH:CO). Several diagnostics are possible in this setup, both regarding gas and solid phase. In this proceeding, we focus on the detection of gas phase molecules released from the ices irradiated with photons, i.e. photodesorbing neutral molecules, with a quadrupole mass spectrometer (QMS, from Balzers).

The chamber was coupled to the undulator-based DESIRS beamline (Nahon et al. 2012) at the SOLEIL synchrotron facility, which provides monochromatic, tunable VUV light for irradiation of our ice samples. To acquire H_2CO photodesorption spectra, the narrow bandwith (∼ 25 meV) output of a grating monochromator is continuously scanned between 7 and 13.6 eV. For CH_3OH, the photodesorbing signal is close to the detection limit. Thus higher photon flux irradiation conditions, using lower resolution (0.5 eV) by sending directly the output of the undulator, are preferred in this case. The photodesorption of molecules in the gas phase following VUV irradiation of the ices monitored with the QMS is then converted into an absolute photodesorption yield, in molecule per incident photon (Dupuy et al. 2017a).

2.1 Pure H_2CO and Pure CH_3OH ices

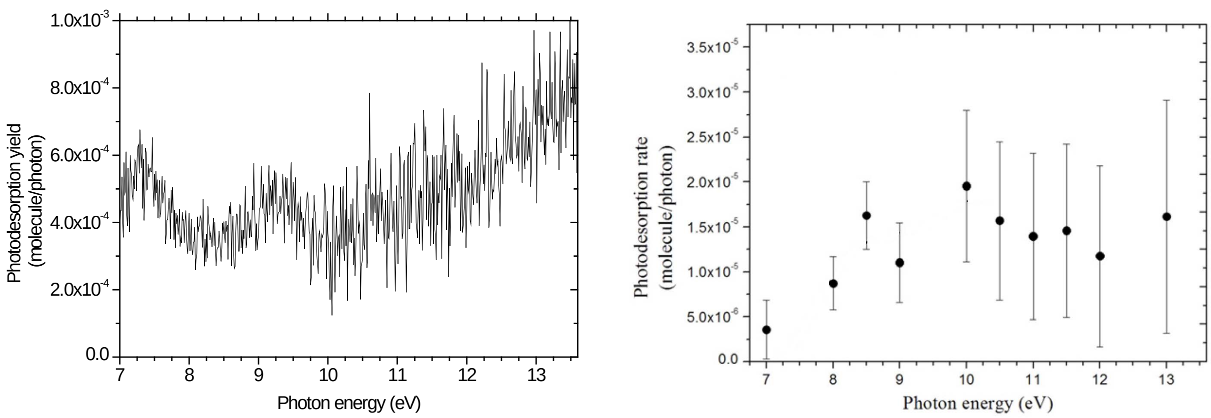

Fig. 1. Left: Absolute H_2CO photodesorption spectrum from a 15 ML thick H_2CO ice on gold at 10 K between 7 and 13.6 eV from Féraud et al. (2019). **Right:** Absolute CH_3OH photodesorption spectrum from a 20 ML thick CH_3OH ice on gold at 10 K between 7 and 13 eV from Bertin et al. (2016).

Photodesorption spectra, representing the absolute photodesorption yield, in molecule per incident photon, as a function of the photon energy, are represented in Figure 1, from Bertin et al. (2016) and Féraud et al. (2019). We notice that H_2CO photodesorption from H_2CO ice is more efficient than CH_3OH desorption from CH_3OH ice. This stengthens the fact that photodesorption yields span over orders of magnitude for different ice constituents : it is $\sim 5 \times 10^{-4}$ molecules/photon for H_2CO, $\sim 10^{-5}$ molecules/photon for CH_3OH, whereas it is $\sim 10^{-2}$ molecules/photon for CO (Fayolle et al. 2011).

Regarding the shape of the spectrum, the CH_3OH one follows the absorption spectrum from Cruz-Diaz et al. (2014) in the low energy range (cf Bertin et al. (2016)), meaning that the electronic excitation of CH_3OH is the first step prior to desorption. For H_2CO, such a comparison between absorption and photodesorption cannot be done because of the lack of VUV absorption spectrum of solid H_2CO. There are elements pointing towards the dissociative nature of the H_2CO electronic states seen at ∼ 7 eV and ∼ 9 eV (cf Féraud et al. (2019)).

Table 1. Average photodesorption yields Y_i ($\times$ 10^{-4} molecule per incident photon; i is the photodesorbed species) for pure H_2CO ice, a mixed H_2CO:CO ice (Féraud et al. 2019), Some photodesorption yields from pure CH_3OH ice and a mixed CH_3OH:CO ice are also reported (the photodesorbing species reported here are not exhaustive, see Bertin et al. (2016) for an exhaustive list), in various interstellar environments with radiation fields from 7 to 13.6 eV

Ice	Photodesorbed species i	ISRF[a]	PDR[b] A_V=1	PDR[b] A_V=5	Secondary UV [c]	Protoplanetary disk TW Hya[d]
		($\times$ 10^{-4} molecule/photon)				
Pure H_2CO[e]	H_2CO	5	4	4	4	4
	CO	45	28	22	45	40
H_2CO:CO (1:3)[e]	H_2CO	8[†]	6[†]	6[†]	6[†]	10[†]
	CO	61	40	38	42	26
Pure CH_3OH[f]	CH_3OH	0.12			0.15	
	H_2CO	0.07			0.12	
CH_3OH:CO[f]	CH_3OH	< 0.03			< 0.03	
	H_2CO	0.07			0.12	

UV fields between 7 and 13.6 eV are taken from : [a] Mathis et al. (1983); [b] PDR Meudon Code Le Petit et al. (2006); [c] Gredel et al. (1987); [d] Heays et al. (2017) (FUV observation of TW-Hydra from France et al. (2014), extrapolated to a broader spectral range); [e] Féraud et al. (2019) [f] Bertin et al. (2016)
[†] This average photodesorption yield is normalized to the fraction of the surface of the ice containing H_2CO f_s (see text for details)

Unravelling the photodesorption mechanisms is an important issue at stake for astrochemical models. For H_2CO, our experiments could not constrain much the possible mechanisms, as four mechanisms could be at play (Féraud et al. 2019) : Desorption induced by electronic transitions in H_2CO (DIET), indirect desorption induced by electronic transitions (for example if the electronic excitation of CO is transferred to H_2CO), kick-out of a H_2CO molecule by an H atom, and reactions between photoproducts HCO + H $\rightarrow$ H_2CO, or HCO + HCO $\rightarrow$ H_2CO + CO, leading to the ejection of the newly formed H_2CO. On the other hand, for CH_3OH, reactions between photoproducts were shown to be a major way of releasing CH_3OH in the gas phase (Bertin et al. 2016), through : H_3CO + H $\rightarrow$ CH_3OH or CH_2OH + H $\rightarrow$ CH_3OH. This is a good indication that a singular photodesorption mechanism could emerge for specific molecules, such as CH_3OH. Besides, for H_2CO and CH_3OH ices, we observe the photodesorption of fragments (not shown): when irradiating pure H_2CO ices, CO and H_2 fragments desorb (Féraud et al. 2019), whereas when irradiating pure CH_3OH ices, CO, CH_3, OH, H_2CO and H_3CO desorb (Bertin et al. 2016). CO fragments are more abundant when coming from H_2CO ices than from CH_3OH ices (Table 1). This enrichment of the gas phase with photoproducts is an important finding, and it could have various consequences on the gas phase chemistry of the ISM. The importance of photodissociation for organic molecules, whether for solid-to-gas exchanges, or for solid state photochemistry, has thus to be taken into account in astrochemical models.

2.2 Implications for PDR and Protoplanetary Disks

Table 1 reports photodesorption yields for different astrophysical environments, the InterStellar Radiation Field (ISRF), PDR at two different extinctions, A_V=1 and A_V=5, secondary UV generated by H_2 excited by cosmic rays, and the protoplanetary disk TW Hydra (see Dupuy et al. (2017b) for a description of the calculation of photodesorption yields). It should be noted that the experimental CH_3OH photodesorption yield of $10^{-5} - 10^{-6}$ molecule/photon (Bertin et al. 2016; Cruz-Diaz et al. 2016) is close to the detection limit of our setup, but it is nevertheless *non negligible* in an astrophysical context, as it is high enough to have an effect on the gas replenishment (Walsh et al. 2017; Ligterink et al. 2018). Photodesorption yields slightly vary from one astrophysical environment to the other (Table 1). However, they depend on the ice composition, as they change if pure or mixed ices are considered. They are slightly larger when H_2CO is mixed with CO, which is an enhancement certainly due to the CO-induced photodesorption of H_2CO. The behaviour is different for CH_3OH ices, as the CH_3OH photodesorption yield is reduced for the CH_3OH ice mixed with CO (Table 1). As a consequence, for the modelisation of an astrophysical ice, yields corresponding to the considered molecule and to the ice composition should be taken from experimental results.

In low-UV illuminated PDR, non-thermal desorption from H_2CO or CH_3OH-containing icy grains is necessary to reproduce the observed abundances,(Guzmán et al. 2011, 2013) and photodesorption was considered to be a very good candidate. The experimental finding that average photodesorption yields are approximately the same at A_V=1 and A_V=5 implies that for H_2CO, a single photodesorption yield can be used at all extinctions. Experimental photodesorption values can now be used in models, instead of arbitrary ones.

In PPD, models have proposed that photodesorption plays a key role to explain the observations (Walsh et al. 2014, 2016; Carney et al. 2017, 2019). Besides, experimental photodesorption yields of CH_3OH (Bertin et al. 2016; Cruz-Diaz et al. 2016) have triggered modelling refinements and interesting findings related to CH_3OH photodesorption have been found, such as (i) the influence of CH_3OH photodesorption on the abundance of both solid and gas phase CH_3OH by orders of magnitude, in some parts of the disk (Walsh et al. 2017; Ligterink et al. 2018) (ii) The predominance of photodesorption over chemical desorption in the majority of the disk (Ligterink et al. 2018) (iii) The specific shaping of snowlines (Ligterink et al. 2018; Agúndez et al. 2018) (iv) The effect of the desorption of CO fragments from CH_3OH ice on gas phase abundances and on the CH_3OH snowline location (Walsh et al. 2017; Ligterink et al. 2018) (v) Possible dependence of photodesorption on the star properties, that influences gas phase spatial distributions (Walsh et al. 2016; Carney et al. 2019). These conclusions on CH_3OH can directly inspire what could be done with H_2CO, with the recently available experimental photodesorption yields. In addition, detecting CH_3OH in protoplanetary disks is very difficult, so that the best tracer for cold COMs is H_2CO, up to now. However H_2CO has a complicated history, as it could be formed either in the gas phase or in the solid phase. When the release from the solid phase to the gas phase is added, the picture is even more complex. Experimental data such as those reproduced here could thus be used as inputs for models of protoplanetary disks to better constrain the observations.

3 Conclusions

Interstellar H_2CO and CH_3OH are closely intertwined and constitute molecules of wide interest, particularly for their link with COMs. We found that photodesorption from H_2CO- and CH_3OH-containing ices present differences, for example in their yields for pure or CO-mixed ices, but also similarities, as photofragments desorb. These yields and the importance of photofragments should continue to be added in astrochemical models. Based on the example of H_2CO and CH_3OH, it can be proposed that photodesorption from ices containing organic molecules, in the form of the parent molecule or of fragments, certainly plays a role in the physics and chemistry of PPD and PDR. Observational, modelling and laboratory astrophysics efforts have to continue, so that the organic molecules' case keeps clarifying.

The authors thank SOLEIL for provision of synchrotron radiation facilities under the projects 20140100 and 20150760 and also Laurent Nahon and the DESIRS beamline for their help. This work was supported by the Programme National 'Physique et Chimie du Milieu Interstellaire' (PCMI) of CNRS/INSU with INC/INP co-funded by CEA and CNES. Financial support from LabEx MiChem, part of the French state funds managed by the ANR within the investissements d'avenir programme under reference ANR-11-10EX-0004-02, and by the Ile-de-France region DIM ACAV program, is gratefully acknowledged.

References

Agúndez, M., Roueff, E., Le Petit, F., & Le Bourlot, J. 2018, Astronomy & Astrophysics, 616, A19

Bacmann, A., Lefloch, B., Ceccarelli, C., et al. 2003, The Astrophysical Journal Letters, 585, L55

Bertin, M., Fayolle, E. C., Romanzin, C., et al. 2013, The Astrophysical Journal, 779, 120

Bertin, M., Romanzin, C., Doronin, M., et al. 2016, The Astrophysical Journal, 817, L12

Carney, M. T., Hogerheijde, M. R., Guzmán, V. V., et al. 2019, 623, A124

Carney, M. T., Hogerheijde, M. R., Loomis, R. A., et al. 2017, Astronomy & Astrophysics, 605, A21

Cruz-Diaz, G. A., Martín-Doménech, R., Moreno, E., Muñoz Caro, G. M., & Chen, Y.-J. 2018, Monthly Notices of the Royal Astronomical Society, 474, 3080

Cruz-Diaz, G. A., Martín-Doménech, R., Muñoz Caro, G. M., & Chen, Y.-J. 2016, Astronomy & Astrophysics, 592, A68

Cruz-Diaz, G. A., Muñoz Caro, G. M., Chen, Y.-J., & Yih, T.-S. 2014, Astronomy & Astrophysics, 562, A119

Dartois, E., Chabot, M., Id Barkach, T., et al. 2019, Astronomy & Astrophysics, 627, A55

Dupuy, R., Bertin, M., Féraud, G., et al. 2017a, Astronomy & Astrophysics, 603, A61

Dupuy, R., Féraud, G., Bertin, M., et al. 2017b, Astronomy & Astrophysics, 606, L9

Esplugues, G. B., Cazaux, S., Meijerink, R., Spaans, M., & Caselli, P. 2016, Astronomy & Astrophysics, 591, A52

Esplugues, G. B., Cazaux, S., Meijerink, R., Spaans, M., & Caselli, P. 2017, Astronomy & Astrophysics, 598, C1

Fayolle, E. C., Bertin, M., Romanzin, C., et al. 2011, The Astrophysical Journal, 739, L36
Féraud, G., Bertin, M., Romanzin, C., et al. 2019, ACS Earth and Space Chemistry, 3, 1135
Fillion, J.-H., Fayolle, E. C., Michaut, X., et al. 2014, Faraday Discussions, 168, 533
France, K., Schindhelm, E., Bergin, E. A., Roueff, E., & Abgrall, H. 2014, The Astrophysical Journal, 784, 127
Gredel, R., Lepp, S., & Dalgarno, A. 1987, The Astrophysical Journal, 323, L137
Guzmán, V., Pety, J., Goicoechea, J. R., Gerin, M., & Roueff, E. 2011, Astronomy & Astrophysics, 534, A49
Guzmán, V. V., Goicoechea, J. R., Pety, J., et al. 2013, Astronomy & Astrophysics, 560, A73
Heays, A. N., Bosman, A. D., & van Dishoeck, E. F. 2017, Astronomy & Astrophysics, 602, A105
Le Petit, F., Nehme, C., Le Bourlot, J., & Roueff, E. 2006, The Astrophysical Journal Supplement Series, 164, 506
Ligterink, N. F. W., Walsh, C., Bhuin, R. G., et al. 2018, Astronomy & Astrophysics, 612, A88
Mathis, J. S., Mezger, P. G., & Panagia, N. 1983, Astronomy & Astrophysics, 128, 212
Nahon, L., de Oliveira, N., Garcia, G. A., et al. 2012, Journal of Synchrotron Radiation, 19, 508
Öberg, K. I., van Dishoeck, E. F., & Linnartz, H. 2009, Astronomy and Astrophysics, 496, 281
Vastel, C., Ceccarelli, C., Lefloch, B., & Bachiller, R. 2014, The Astrophysical Journal, 795, L2
Walsh, C., Loomis, R. A., Öberg, K. I., et al. 2016, The Astrophysical Journal, 823, L10
Walsh, C., Millar, T. J., Nomura, H., et al. 2014, Astronomy & Astrophysics, 563, A33
Walsh, C., Vissapragada, S., & McGee, H. 2017, IAU, 8

SF2A 2019
P. Di Matteo, O. Creevey, A. Crida, G. Kordopatis, J. Malzac, J.-B. Marquette, M. N'Diaye, O. Venot (eds)

FRAGMENTATION OF MASSIVE CORES TOWARD THE GALACTIC HII REGION RCW 120 OBSERVED WITH ALMA

M. Figueira[1], A. Zavagno[2] and L. Bronfman[3]

Abstract. Feedback from high-mass stars (stellar winds, radiation and photoionization pressure, supernova explosions) can strongly modify the surrounding cloud. As a result, the next generation of stars is affected and can present different physical properties. Using ALMA interferometric observations, we characterized the fragmentation occurring inside the massive cores previously detected with Herschel and being good candidates for high-mass star formation. Most of the fragments have a mass higher than predicted by the thermal Jeans mechanism, thus requiring external turbulence to explain it, and some of the fragments have a mass higher than 8 $M_\odot$ which make them interesting targets for further studies. One of the fragment shows different molecular emissions tracing hot core, disk and outflows and is the most promising site for the search of high-mass stars toward RCW 120.

Keywords: HII region, high-mass star, fragmentation

1 Introduction

Despite the numerous studies and surveys performed over the past years, high-mass star ($M > 8\ M_\odot$) formation remains a puzzling field of study. Regions where high-mass stars are born and in which environmental conditions they form is still debated although some points seem to stand out from different studies. High-mass stars form in massive, cold and dense cores ($\geq$70 $M_\odot$, $\sim$0.1 pc, $\sim$10−20 K) where the quantity of gas and dust is high enough. Inside these cores, two main mechanisms are proposed to explain how the future stars are gathering their mass. The first one is the model of monolithic collapse, similar to low-mass star formation, where a massive core supported by turbulence and/or magnetic pressure collapses into a massive star. The second one is the competitive accretion model which involve the growth of low-mass cores into high-mass cores thanks to the gas reservoir contained in the parental cloud. Therefore, high-mass prestellar cores do not exist in this model and high-mass stars would come from low-mass structures which would have gained mass throughout the time. High-mass stars are important due to their feedback such as winds, radiation pressure, HII regions and supernova explosions. This feedback injects momentum, energy and metallic elements into the interstellar medium which modify the properties and shape of the surrounding. During the early stages of high-mass star formation, the HII region feedback is the most powerful and easily recognizable due to the formation of an HII region surrounded by a layer of dust and gas, trapped between the ionization and the shock fronts. These so-called HII bubbles are ubiquitous in our Galaxy, with around 8000 of them (Anderson et al. 2014) and therefore important in the star formation field. The most interesting phenomenon is that more than 30% of high-mass Galactic sources are found at the edges of these bubbles, toward the layer of dust and gas (Deharveng et al. 2010; Kendrew et al. 2012, 2016; Palmeirim et al. 2017). Previous mechanisms were studied to understand how the expansion of an HII region could lead to the formation and subsequent fragmentation of this layer. Several exist such as the Collect and Collapse (C&C, Elmegreen & Lada 1977), the Radiation Driven Implosion (RDI, Kessel-Deynet & Burkert 2003), the HII region expansion in a turbulent medium (Tremblin et al. 2012) or the Cloud Cloud Collision (CCC, Torii et al. 2015). On the other hand, simulations tend to show the disruptive effect of the photoionization pressure which lower the SFR and SFE inside this layer of material (Dale et al. 2005;

[1] National Centre for Nuclear Research, ul. Pasteura 7, 02-093, Warszawa, Poland
[2] Aix Marseille Univ, CNRS, LAM, Laboratoire d'Astrophysique de Marseille, 13013, Marseille, France
[3] Departamento de Astronomía, Universidad de Chile, Casilla 36-D, Santiago, Chile

Lucas et al. 2017). Thanks to surveys done with the *Spitzer* and *Herschel* space telescopes, numerous massive cores could have been identified and their properties derived. The next step, which is currently undergone, is to observe a significant number of these cores located at the edges of these HII regions, at a sufficient spatial resolution to observe the fragmentation occurring inside (Motte et al. 1998; Bontemps et al. 2010; Palau et al. 2015; Ohashi et al. 2018; Palau et al. 2018). A statistical sample of these fragments at ∼0.01 pc resolution and higher will allow us to assess more accurately the percentage of high-mass stars toward Galactic HII bubbles as well as the fragmentation mechanism at work inside the cores (thermal Jeans, turbulent Jeans mechanism, etc.)

2 The RCW 120 region with Herschel

The Galactic HII region RCW 120 is a well studied and interesting bubble due to its close distance of 1.3 kpc, its almost perfect spherical shape and its location 0.5° above the Galactic Plane, limiting the foreground dust contamination. This HII region is powered by a single O8.5 star located in the south of the center and its expansion swept away the dust and gas initially present in the region, forming the dusty layer which can be seen on Fig. 1 (left). Toward it, several millimetric clumps can be observed and in them, several Young Stellar Objects (YSOs) are detected where the future generation of stars are currently forming. Using the *Herschel* Observations of YSOs (HOBYS), we previously extracted the cores (Fig. 1, middle) using the *getsources* algorithm (Men'shchikov et al. 2012; Men'shchikov 2013) and the recipe described in Tigé et al. (2017) to derive their envelop mass, bolometric luminosity, temperature and volume density using Spectral Energy Distribution (SED) (Figueira et al. 2017). Based on the $L_{\lambda>350\ \mu m}/L_{bol}$ criterion and the $L_{bol} - M_{env}$ diagram, the evolutionary stage of the *Herschel* cores does not seem to be correlated with the projected distance to the ionizing star but rather depends on the density of the clumps which are hosting these cores. Moreover, one of the clump clearly hosts young and massive sources, allowing the formation of high-mass stars according to the usual mass threshold of $\sim 70\ M_{\odot}$. Therefore, this clump is an interesting target to study the fragmentation mechanism inside massive cores, in order to see if fragments can give rise to high-mass stars.

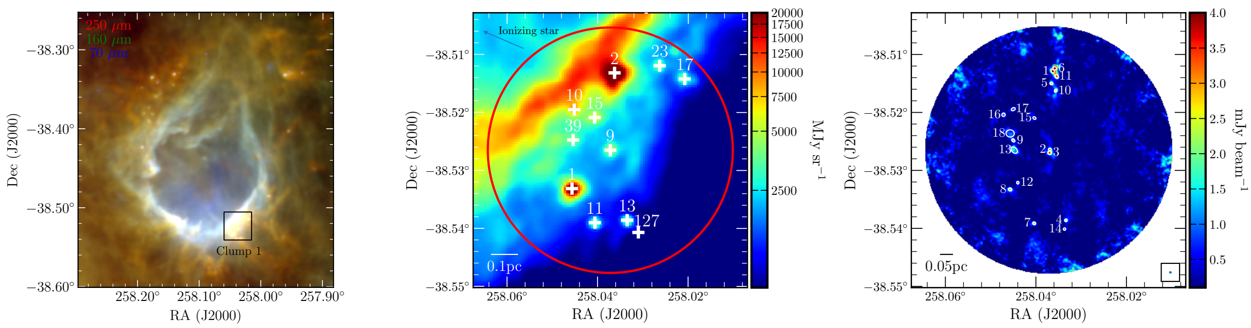

Fig. 1. Left: Composite image of RCW 120 from *Herschel* observations at 70 (blue), 160 (green) and 250 μm (red) with the clump 1 hosting massive cores enclosed by a black rectangle. **Middle:** *Herschel* 70 μm observation toward the clump 1 with the cores' label superimposed (white) and the direction to the ionizing star (grey arrow). **Right:** ALMA 3 mm observation of the clump 1 with the fragment's footprint and labels superimposed (white).

3 Massive cores of RCW 120 observed with ALMA

Observations were performed during the Cycle 4 using 38 of the 40 12 m antennas in nominal configuration C40-3 with baselines ranging from 15 to 459 m. The spectral setup consisted in four spectral windows centred on 93.17 (N_2H^+), 91.98 (CH_3CN), 104.02 (SO_2) and 102.5 GHz (2 GHz band continuum at 3 mm). Imaging was performed with the TCLEAN algorithm of the CASA software using a robust parameter of 0.5 which lead to a synthesized beam of 1.7"×1.5" and a noise level of 0.16 mJy beam^{-1} for the aggregate continuum. The cores and fragments extractions were performed using the *getimages* algorithm (Men'shchikov 2017) prior to the *getsources* extraction. Compared to the extraction in Figueira et al. (2017), the *Herschel* cores are still massive and good candidates for high-mass star formation. The number of fragments ranges from 0 to 5, the most massive *Herschel* core being the most fragmented (Fig. 1, right). Assuming optically thin emission, the mass of the fragments were computed following $M_{frag} = S_{3mm} \times R \times D^2/\kappa_{3mm} \times B_{3mm}(T_{dust}) \times \Omega_{beam}$ and ranges

Id	α	δ	T_{env}	M_{env}	L_{bol}	n_{H_2}	M_{Jeans}	N_{frag}	M_{frag}
	J2000 (°)		(K)	($M_\odot$)	($L_\odot$)	(cm^{-3})	($M_\odot$)		($M_\odot$)
1	258.04577	-38.53338	17.0 ± 0.2	85 ± 6	234 ± 28	(3.0±0.2) $\times10^5$	0.8	2	10.6 ± 0.7
2	258.03624	-38.51317	16.9 ± 0.2	376 ± 21	856 ± 93	(1.3±0.1) $\times10^6$	0.4	5	73 ± 3.6
9	258.03749	-38.52663	13.1 ± 0.2	97 ± 14	49 ± 12	(3.4±0.5) $\times10^5$	0.5	2	25.8 ± 1.6
10	258.04524	-38.51956	11.1 ± 0.4	252 ± 41	46 ± 17	(8.7±1.4) $\times10^5$	0.3	2	15.5 ± 1.4
11	258.04073	-38.53926	14.2 ± 0.4	31 ± 9	24 ± 11	(1.1±0.3) $\times10^5$	1.1	1	7.4 ± 0.5
13	258.03352	-38.53886	16.3 ± 0.8	8 ± 3	23 ± 9	(2.8±1.0) $\times10^4$	2.5	2	6.8 ± 0.8
15	258.04084	-38.52110	12.8 ± 0.5	81 ± 15	38 ± 15	(2.8±0.5) $\times10^5$	0.5	1	3.5 ± 0.6
39	258.04560	-38.52532	12.8 ± 0.3	97 ± 17	42 ± 13	(3.4±0.5) $\times10^5$	0.5	3	72.2 ± 2.7
17	258.02078	-38.51440	12.8 ± 0.2	122 ± 17	51 ± 13	(4.2±0.6) $\times10^5$	0.4	0	0
23	258.02648	-38.51204	11.9 ± 0.4	130 ± 21	37 ± 13	(4.5±0.7) $\times10^5$	0.4	0	0
127	258.03146	-38.54054	10.8 ± 0.3	80 ± 17	12 ± 5	(2.8±0.6) $\times10^5$	0.4	0	0

Table 1. Properties of the *Herschel* cores using the *getsources* (+*getimages*) algorithm. (1) Identification number, (2,3) J2000 coordinates, (4) envelope temperature, (5) envelope mass, (6) bolometric luminosity, (7) volume density, (8) Jeans mass, (9) number of fragments inside the core, and (10) total mass of the fragments.

from 2 to 32 $M_\odot$ which makes several of them massive enough for high-mass stars to form. The mechanism responsible from the appearance of these fragments is thought to be the Jeans mechanism where above a certain mass threshold, called the Jeans mass (M_{Jeans}), the core becomes gravitationally unstable. The mechanism of fragmentation in the cores is still debated: several studies show that the thermal Jeans mechanism could be at work with fragments mass in agreement with M_{Jeans} (Palau et al. 2015) while in other regions, the mass of the fragments are above this limit and addition of turbulence and/or magnetic field as a support against collapse is needed. In Tab. 1, we show the properties of the different *Herschel* cores as well as M_{Jeans} computed with the temperature derived using SED as in Figueira et al. (2017). In most of the cases, M_{Jeans} is too low to explain the mass of the fragments in the *Herschel* cores. Using the N_2H^+ molecular line transition, we computed the turbulent linewidth σ_{turb} and, assuming a Mach number of 4 in the PhotoDissociation Region (PDR), we estimated M_{Jeans} accounting from this turbulence following the model of Mac Low & Klessen (2004). For the *Herschel* cores, M_{Jeans} accounting from turbulent support can increase up to 100 $M_\odot$. This value is high enough to explain the mass of the fragments and could also explain why some of the cores have not fragmented yet.

Toward the most massive core 2, 5 fragments are observed and 3 of them have a mass higher than 15 $M_\odot$. Using the other spectral windows, one of the main fragment in this core exhibits CH_3CN and SO_2 emissions, which are tracer of hot core and outflows, respectively. In other words, this fragment shows high-mass star formation signposts which could reveal the formation of an high-mass star at the edges of RCW 120. Using a rotational diagram constructed with the *CASSIS* software, we found that the best fit was obtained with a two temperature model indicating a hot and cold component for this fragment of 210 and 40 K, respectively. Moreover, the $CH_3CN(J = 5 - 4, K = 4)$ transition is higher than expected from Local Thermodynamical Equilibrium (LTE) conditions which could mean that another molecular transition is present. Based on the CDMS database, $CH_3^{18}OH$ would be at the right frequency and furthermore, this transition line is often found where high-mass stars are forming. Using observations obtained during Cycle 5, we also detect CS emission toward this fragment, which is a tracer of high density and disk. Therefore, there is probably an accretion disk around the possible high-mass star represented by the fragment 1.

4 Conclusions

Using interferometric observations, we studied the most massive cores, potentially future sites of high-mass stars, located in the most massive millimetric clump of the Galactic HII region RCW 120. Continuum observations at 3 mm reveals that the *Herschel* cores are divided up to 5 fragments and that turbulence should be added to the common Jeans mechanism in order to explain the high-mass of these fragments. Consequently, several fragments are massive enough to host high-mass stars. Toward the most massive core of RCW 120 where 5 fragments are detected, one of them shows emission of CH_3CN, SO_2 and CS which indicates that the star forming there is in the hot core stage, with an accretion disk and outflows emission. More analysis have to be carried out in order to characterize the properties of this particular fragment such as the disk model, the accretion rate, the outflow energy and momentum released and the mass of the future high-mass star. An high-mass star forming at the edge of a bubble, such as in RCW 79, will maintain the debate on the net influence the H II region can have on the new generation of stars in the layer.

References

Anderson, L. D., Bania, T. M., Balser, D. S., et al. 2014, ApJS, 212, 1
Bontemps, S., André, P., Könyves, V., et al. 2010, A&A, 518, L85
Dale, J. E., Bonnell, I. A., Clarke, C. J., & Bate, M. R. 2005, MNRAS, 358, 291
Deharveng, L., Schuller, F., Anderson, L. D., et al. 2010, A&A, 523, A6
Elmegreen, B. G. & Lada, C. J. 1977, ApJ, 214, 725
Figueira, M., Zavagno, A., Deharveng, L., et al. 2017, A&A, 600, A93
Kendrew, S., Beuther, H., Simpson, R., et al. 2016, ApJ, 825, 142
Kendrew, S., Simpson, R., Bressert, E., et al. 2012, ApJ, 755, 71
Kessel-Deynet, O. & Burkert, A. 2003, MNRAS, 338, 545
Lucas, W. E., Bonnell, I. A., & Forgan, D. H. 2017, MNRAS, 466, 5011
Mac Low, M.-M. & Klessen, R. S. 2004, Reviews of Modern Physics, 76, 125
Men'shchikov, A. 2013, A&A, 560, A63
Men'shchikov, A. 2017, A&A, 607, A64
Men'shchikov, A., André, P., Didelon, P., et al. 2012, A&A, 542, A81
Motte, F., Andre, P., & Neri, R. 1998, A&A, 336, 150
Ohashi, S., Sanhueza, P., Sakai, N., et al. 2018, ApJ, 856, 147
Palau, A., Ballesteros-Paredes, J., Vázquez-Semadeni, E., et al. 2015, MNRAS, 453, 3785
Palau, A., Zapata, L. A., Román-Zúñiga, C. G., et al. 2018, ApJ, 855, 24
Palmeirim, P., Zavagno, A., Elia, D., et al. 2017, A&A, 605, A35
Tigé, J., Motte, F., Russeil, D., et al. 2017, A&A, 602, A77
Torii, K., Hasegawa, K., Hattori, Y., et al. 2015, ApJ, 806, 7
Tremblin, P., Audit, E., Minier, V., Schmidt, W., & Schneider, N. 2012, A&A, 546, A33

SF2A 2019
P. Di Matteo, O. Creevey, A. Crida, G. Kordopatis, J. Malzac, J.-B. Marquette, M. N'Diaye, O. Venot (eds)

AN AUTOMATED APPROACH FOR PHOTOMETER AND DUST MASS CALCULATION OF THE CRAB NEBULA

C. Nehmé[1,2], S. Kassounian[1], M. Sauvage[2] and J. Tadros[1]

Abstract. Ample evidence exists regarding supernovae being a major contributor to interstellar dust. In this work, the deepest far-infrared observations of the Crab Nebula are used to revisit the estimation of the dust mass present in this supernova remnant. Our aim in this paper is to highlight the importance of the photometric methods and spectral energy distribution construction on the accuracy of inference for astrophysical parameters. Images in filters between 70 and 500 μm taken by the PACS and SPIRE instruments on-board of the Herschel Space Observatory are used. With a novel automated approach, we constructed the spectral energy distribution of the Crab nebula to recover the dust mass. The spectral energy distribution is found to be best fitted using a single modified blackbody of temperature $T = 42.06 \pm 1.14\,\mathrm{K}$ and a dust mass of $M_d = 0.056 \pm 0.037\,\mathrm{M}_{\odot}$.

Keywords: Dust mass, Crab Nebula, Far-Infrared (FIR), Image processing, Herschel, Synchrotron

1 Introduction

The astrophysical community has been in pursuit of the dust mass budget in the universe to analyze and constrain the baryonic matter. The amount of dust produced and ejected into the interstellar medium by the Asymptotic Giant Branch (AGB) stars is not enough to compensate for the known destruction rates (Zhukovska et al. 2008). On the other hand, Supernova remnants (SNR) are important dust suppliers. They emit the brightest in the IR waveband via an excess emission upon the synchrotron continuum (Trimble 1977), (Gomez et al. 2012), (Temim & Dwek 2013), (Owen & Barlow 2015), (De Looze et al. 2017). We target our efforts in this work on the Crab nebula remnant, since it presents many advantages as an astrophysical laboratory for dust mass budget analysis. It is one of the most commonly observed celestial objects, possesses a wealth of observational data, and the mass of swept-up material is small compared to the mass in the supernova ejecta since it has a relatively young age. Finally, it provides the cleanest view along the line of sight compared to other observed SNRs with nearly no interstellar medium contamination. The dust content of the Crab nebula is still not well constrained in the literature, ranging between 0.08 to 1.4 $\mathrm{M}_{\odot}$, hence we revisit in this work the estimation of its dust content using novel photometric images and image analysis techniques, showing the importance of the photometric analysis on the dust budget calculations.

2 Observations

Images used for the calculation of the flux densities of the Crab nebula were taken by the Herschel Space Observatory (Pilbratt et al. 2010). The Crab nebula was observed between September 2009 and September 2010. The PACS (Poglitsch et al. 2010) and SPIRE (Griffin et al. 2010) instruments performed photometry at 70, 100, 160, 250, 350 and 500 μm, as part both of a calibration program for the PACS observing modes, and of a Principal Investigator observing program (Gomez et al. 2012). In the present work we have for the first time included data that was obtained on the Crab nebula during the testing and qualification of PACS observing modes. As these data were obtained in an instrumental set-up which is identical to the operational one, they can be directly combined with the already published data, thus nearly doubling the depth of the resulting maps (at 70, 100, and 160 μm).

[1] Department of Physics & Astronomy, Notre Dame University - Louaize, Lebanon
[2] AIM, CEA, CNRS, Université Paris-Saclay,Université Paris Diderot, Sorbonne Paris Cité, F-91191 Gif-sur-Yvette, France

3 Photometry and Data Analysis

In this work, the photometric analysis and flux density calculations were done via a data driven iterative approach, where the aperture selection was done based on the morphological and spatial flux density distribution of the extended object Nehmé et al. (2019b). It enabled the construction of an improved spectral energy distribution (SED) of the Crab nebula and optimized the exclusion of background pixels. The optimum apertures for each wavelength are used to impose masks on the pixels which are assumed to contain the source. The unmasked pixels are then used to model the background sky by fitting them with a surface polynomial. The previously masked regions are interpolated and subtracted from S_{ν}^{tot}. Finally, to remove the synchrotron emission contribution from the integrated global flux density values, we gathered flux densities from other observations (see Nehmé et al. 2019b). These values were fitted by a power law and were followed by an interpolation process for the Herschel wavebands and removed.

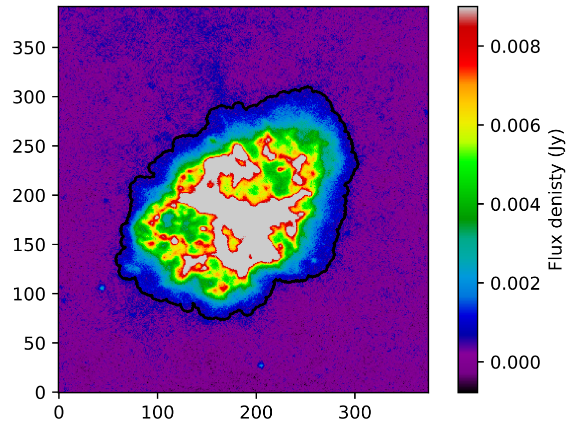

(a) Histogram of flux density values and selection of initial threshold (100 μm).

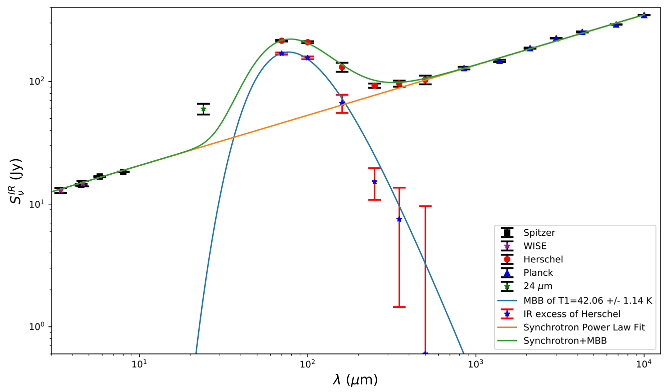

(b) log-log scale plot of the SED showing the fitting process.

4 SED construction and results

The SED of the Crab nebula (see Fig. 1b) is crucial to study the thermal emission of the dust and constrain its parameters. After removing the contribution of the synchrotron radiation and the background sky from the integrated flux densities (S_{ν}) at each wavelength, an excess S_{ν}^{IR} of IR light characterizes the dust and is fitted by a single component modified blackbody function (MBB) (Nehmé et al. 2019a). At 500 μm, the emission is mostly composed of synchrotron. The warm dust is the dominant component in the Crab nebula. The synchrotron power law was modeled using wavelengths up to 10 000 μm since a spectral break existed after that point which was indicated by the Planck observations (Gomez et al. 2012). Although the 24 μm flux is likely contributed by dust it was not included in our fit because such an emission is hardly justified to correspond to a thermal equilibrium process such as the MBB. Furthermore, this would be an emission from hotter dust which will not affect significantly the total dust mass. The best best fitted parameters of equation of the MBB for the Crab nebula are retrieved at $T = 42.06 \pm 1.14K$ and $\overline{M_{d,cal=5\%}}$ $0.056 \pm 0.037\ M_{\odot}$

5 Conclusion

We have presented an automated and improved method for calculating the flux densities using several image processing techniques. After comparing our flux densities to that of the literature (Nehmé et al. 2019b),we find that very little IR excess exist at 500 μm, leaving no place for a cold component. Thus our resulting SED is adequately modeled with a single component MBB. This produces dust parameters of mass and temperature comparable to the literature. Future works aim to better describe the mass dust budget in the Crab nebula spatially and account for the filamentary structure.

References

De Looze, I., Barlow, M. J., Swinyard, B. M., et al. 2017, MNRAS, 465, 3309

Gomez, H. L., Krause, O., Barlow, M. J., et al. 2012, The Astrophysical Journal, 760, 96

Griffin, M. J., Abergel, A., Abreu, A., et al. 2010, A&A, 518, L3

Nehmé, C., Kassounian, S., & Sauvage, M. 2019a, Experimental Astronomy, 48

Nehmé, C., Kassounian, S., & Sauvage, M. 2019b, An automated approach for photometry and dust mass calculation of the Crab nebula

Owen, P. J. & Barlow, M. J. 2015, The Astrophysical Journal, 801, 141

Pilbratt, G. L., Riedinger, J. R., Passvogel, T., et al. 2010, A&A, 518, L1

Poglitsch, A., Waelkens, C., Geis, N., et al. 2010, A&A, 518, L2

Temim, T. & Dwek, E. 2013, The Astrophysical Journal, 774, 8

Trimble, V. 1977, Astrophys. Lett., 18, 145

Zhukovska, S., Gail, H.-P., & Trieloff, M. 2008, A&A, 479, 453

SF2A 2019
P. Di Matteo, O. Creevey, A. Crida, G. Kordopatis, J. Malzac, J.-B. Marquette, M. N'Diaye, O. Venot (eds)

FORMATION OF PROTOPLANETARY DISK BY GRAVITATIONAL COLLAPSE OF A NON-ROTATING, NON-AXISYMMETRICAL CLOUD.

A. Verliat[1], P. Hennebelle[1 2], A. J. Maury[1 3] and M. Gaudel[1]

Abstract.
Protoplanetary disks are thought to be inherited from large scale rotation, through the conservation of angular momentum during the collapse of a prestellar dense core. We investigate the possibility for a protostellar disk to be formed from a motionless dense core containing non-axisymmetric density fluctuations. The rotation is thus generated locally by the asymmetry of the collapse. Our hydrodynamic simulations lead to the formation of disks of a hundred astronomical units in radius. The kinematics of our model are consistent with typically observed values of velocity gradients and specific angular momentum in protostellar cores.

Keywords: Methods: numerical , Protoplanetary disks , ISM: clouds , ISM: kinematics and dynamics , Turbulence , Stars: formation

1 Theory

Let's name $\mathcal{R}$ and O the frame and center of the simulation box, $\mathcal{R}'$ and C the frame and center of the disk, G the center of mass, m_i and M_i the mass and position of each cell i. We consider motionless initial conditions to ensure that the angular momentum computed in the simulation box frame, in relation to the center of the box — $\sigma_{\mathbf{0}}|_{\mathcal{R}}$ — is null and conserved. The angular momentum computed in the frame of the disk, in relation to the center of the disk can be expressed as:

$$\sigma_{\mathbf{C}}|_{\mathcal{R}'} \quad = \quad \sum_i m_i \mathbf{CM_i} \times \frac{\mathrm{d}\mathbf{CM_i}}{\mathrm{d}t} \quad = \quad M\mathbf{GC} \times \frac{\mathrm{d}\mathbf{GC}}{\mathrm{d}t} \tag{1.1}$$

If G and C do not coincide, and the disk have a proper motion, $\sigma_{\mathbf{C}}|_{\mathcal{R}'}$ is not null and not conserved. A rotationally supported structure naturally forms around C.

2 Numerical setup

We ran purely hydrodynamics simulations with $\mathcal{R}$AMSES. This numerical Eulerian code uses Adaptative Mesh Refinement (AMR) technique to enhance resolution locally, where it is needed, on a Cartesian mesh (Teyssier 2002).

We set a 3D cubic box with sides of 70000 AU (about 0.33 pc), in which we put a prestellar dense core of 17500 AU in diameter and 2.5 $M_{\odot}$. We use 10 levels of AMR, leading to a 0.26 AU equivalent maximum resolution. Initially we set all velocities to zero, ensuring $\sigma_{\mathbf{0}}|_{\mathcal{R}} = \mathbf{0}$. We use a barotropic equation of state. To break the axisymmetry we add random density perturbations over the flat profile of the core. These initial conditions are illustrated in Fig. 1.

We define the *perturbation level* as the ratio between the root mean square value and the mean value of the density.

[1] Laboratoire AIM, Paris-Saclay, CEA Saclay/IRFU/DAp – CNRS – Université Paris Diderot, 91191 Gif-sur-Yvette Cedex, France
[2] LERMA (UMR CNRS 8112), Ecole Normale Supérieure, 75231 Paris Cedex, France
[3] Harvard-Smithsonian Center for Astrophysics, 60 Garden street, Cambridge, MA 02138, USA

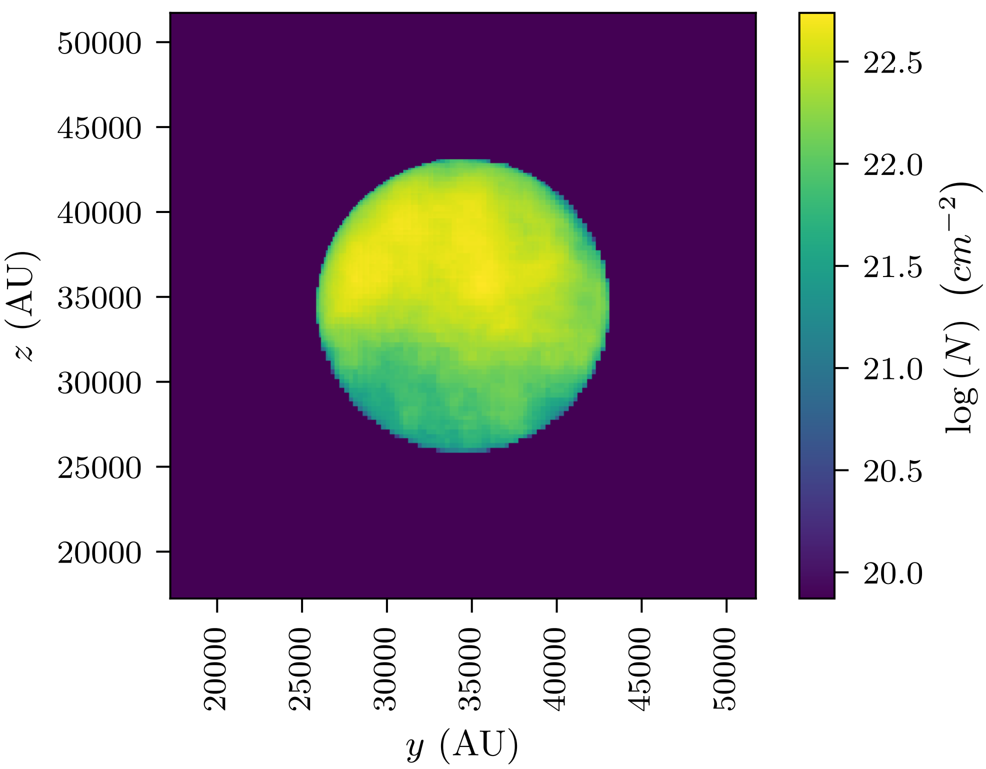

Fig. 1. Column density illustrating initial conditions for the simulation with 50% of perturbations.

3 Results

As expected from our theoretical development, we observe the formation of a disk, as illustrated in Fig. 2

4 Comparison with observations

To compare our model with observations, we analyse our simulations by computing velocity gradients as it is done observationally. To do so, we fit velocities along the line of sight with a solid-body rotation profile. The results are plotted in Fig. 3.

We observe a large dispersion of velocity gradient directions over the different scales with even reversals for the x and y projections. The specific angular momentum is roughly constant over the scales, with a mean value of $\sim 3\ 10^{-4}\ km.s^{-1}.pc$, which is consistent with the step in the observational values, showed in Fig. 4.

5 Conclusions

We showed that protostellar disks can emerge from a non-axisymmetrical gravitational collapse. The formation of these large disks in our model does no longer depend on specificities of large scales, but is due to a more generic process resulting from density perturbations of the gas. We showed that the different features of the model based on the analysis of velocity gradients are consistent with observations.

This work is the subject of a publication — Verliat et al. (submitted) — where you will find more details.

References

Belloche, A. 2013, 62, 25

Teyssier, R. 2002, A&A, 385, 337

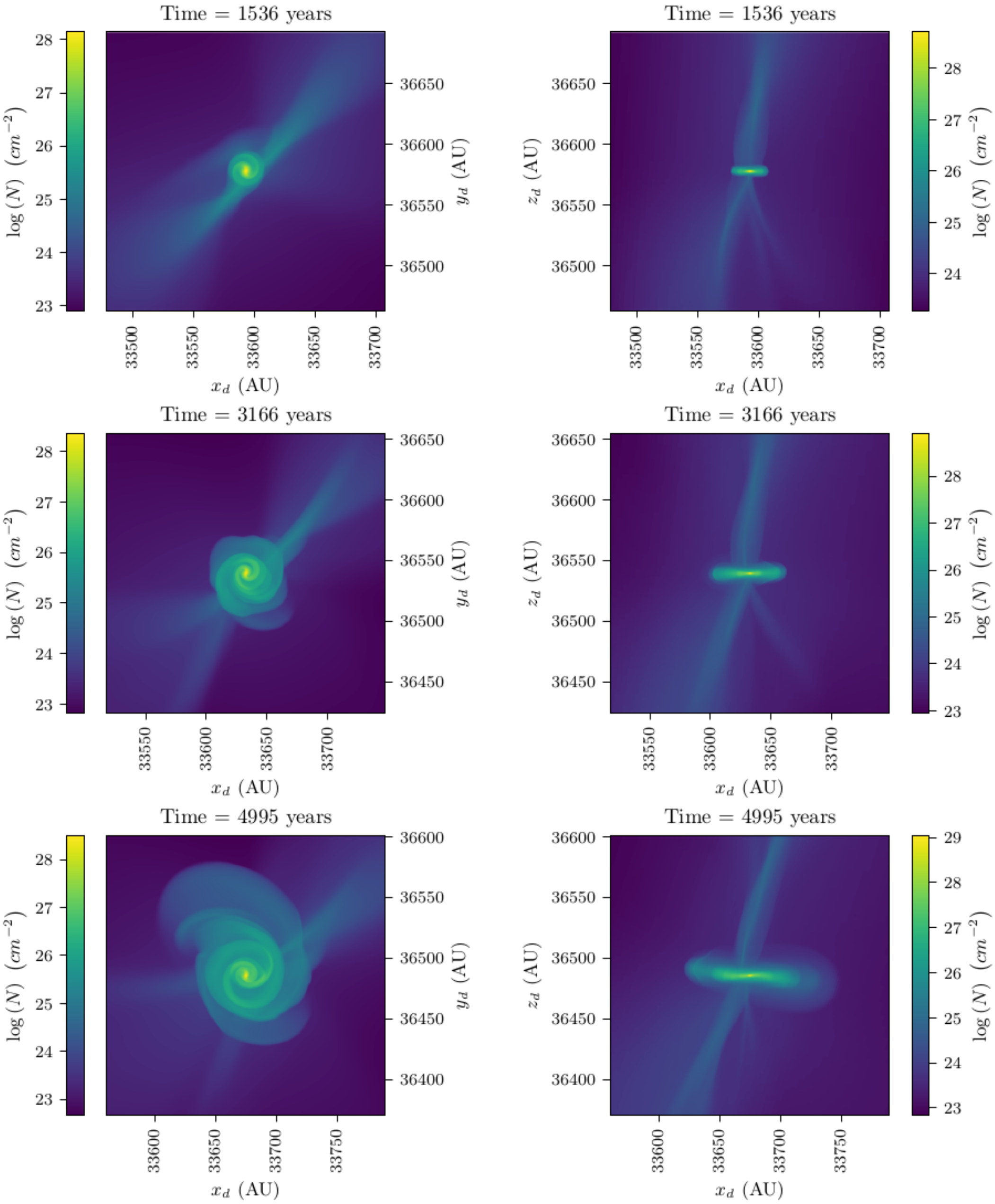

Fig. 2. Simulation with 50% of perturbations at three different times. **Left:** Face-on projection. **Right:** Edge-on projection.

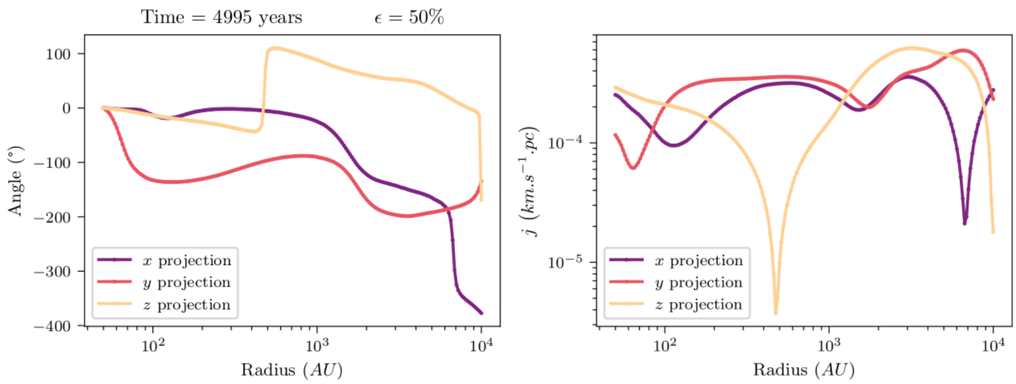

Fig. 3. Velocity gradients analysis at different scales in the simulation with 50% of perturbations. **Left**: angular direction of velocity gradients in comparison to the one of the disk scale gradient. **Right**: specific angular momentum as computed from observations.

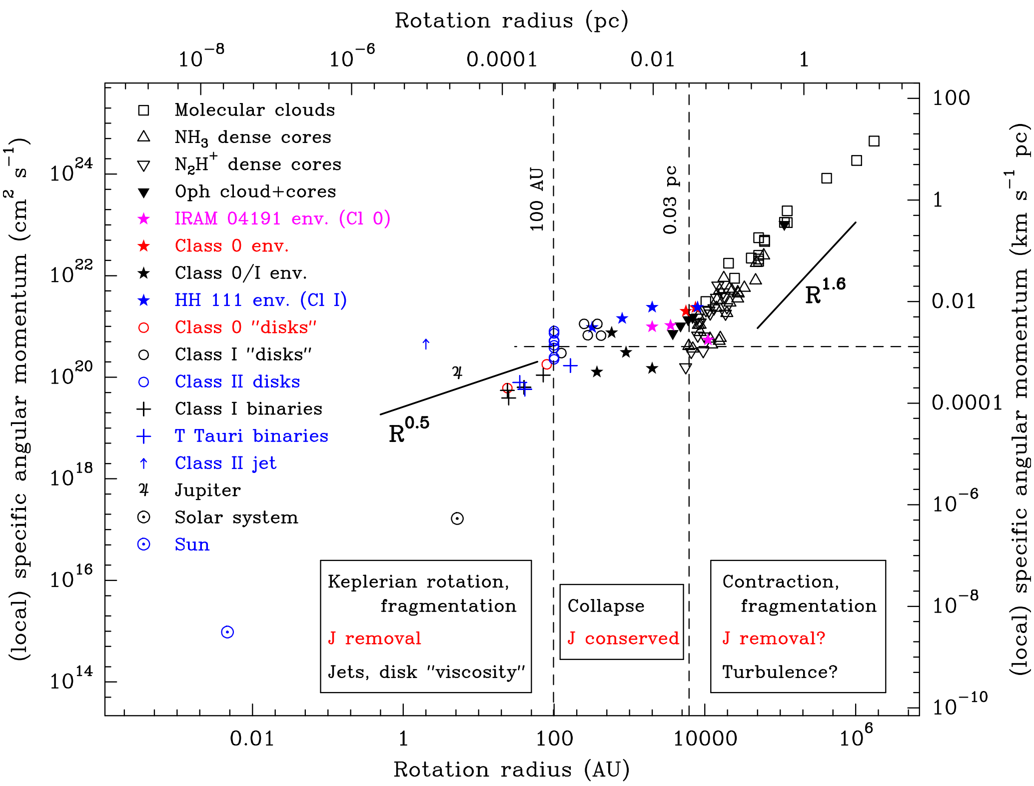

Fig. 4. Specific angular momentum in several objects, deducted from observations (Belloche 2013).

Session 02

Spectroscopic surveys: the French expertise leading to Maunakea Spectroscopic Explorer (MSE)

SF2A 2019
P. Di Matteo, O. Creevey, A. Crida, G. Kordopatis, J. Malzac, J.-B. Marquette, M. N'Diaye, O. Venot (eds)

SPECTROSCOPIC SURVEYS UNVEALING THE GALACTIC STELLAR HALO.

E. Fernández-Alvar[1]

Abstract. Large area spectroscopic surveys have greatly improved our knowledge about the formation and evolution of the Galaxy. The analysis of hundreds of thousands of stellar spectra have allowed to better characterize the stellar chemical composition of each Galactic component and reconstruct the built-up of the Milky Way. I review the main results recently obtained about the study of the stellar halo from the analysis of spectroscopic data, in particular those performed as part of my research. The later feeds on the Sloan Digital Sky Survey (SDSS) low- and high-resolution spectroscopic programs dedicated to observation of stars in the Galaxy: the Sloan Extension for Galaxy Understanding and Exploration (SEGUE) and the Apache Point Observatory Galactic Evolution Experiment (APOGEE). The recent Gaia second data release (DR2) in combination with the spectroscopic databases have provided a new insight in this area. Next generation of spectroscopic surveys, as the Maunakea Spectroscopic Explorer (MSE) are promising projects to disentangle the formation and evolution of our Galaxy and in particular its accretion history through the better characterization of the stellar halo.

Keywords: spectroscopy, Galaxy, halo

1 Introduction

Galactic archaeology aims to decipher the formation history and evolution of our Galaxy. The main tool to achieve this goal is the analysis of the chemistry as well as the kinematical and dynamical properties of the stars now belonging to the Milky Way. Consequently, the accuracy in the chemical abundances determination and the distance and velocity measurements is crucial.

The spectroscopic and astrometric surveys of the last decades (e.g., SDSS – Blanton et al. (2017), the Large Sky Area Multi-Object Fiber Spectroscopic Telescope (LAMOST) with the LAMOST Experiment for Galactic Understanding and Exploration (LEGUE) survey – Zhao et al. (2012), the GALactic Archaeology with HERMES (GALAH) survey – De Silva et al. (2015), Gaia – Gaia Collaboration et al. (2016), Gaia Collaboration et al. (2018b)) have considerably improved our knowledge of the current structure of the Milky Way. These observations have revealed the accreted origin of a large fraction of the stars, giving support to the current cosmological paradigm, the Λ-Cold Dark Matter model, which predicts that large structures in the Universe formed from the accretions of smaller subsystems. The study of the Galactic stellar halo is key in understanding the formation history of our Galaxy since it hosted old stars and accretion remnants.

Here I will explain how the improvement in quality of the spectroscopic surveys in the last decades, in combination with the unprecedent number and accuracy of the data provided by Gaia, has given a completely new perspective in this area. Finally, I will point out how the new generation of spectroscopic surveys, in particular the Maunakea Spectroscopic Explorer (MSE), will also revolutionize the halo research.

2 The Galactic stellar halo before Gaia.

The advent of large scale spectroscopic surveys which allowed the detection of numerous stellar overdensities crossing all over the Galactic halo, reliques of merger events ocurred in the past (e.g., Grillmair (2009), Bernard et al. (2016)) greatly helped to clarify our understanding of the origin of stars populating the Galactic halo, and the classical debate between the monolithic collapse (Eggen et al. (1962)) vs. the accretion of stellar systems

[1] Université Cote d'Azur, Observatoire de la Cote d'Azur, CNRS, 06300, Laboratoire Lagrange

(Searle & Zinn (1978)) models. These results were in line with the cosmological predictions of the Λ-Cold Dark Matter model. However, evidences provided by several studies pointed to different spatial, kinematical and chemical properties between the inner and the outer parts of the Galactic halo (Carollo et al. (2007), Carollo et al. (2010), de Jong et al. (2010); An et al. (2013); Allende Prieto et al. (2014)).

In particular, Fernández-Alvar et al. (2015) showed gradients of α-elements-to-iron ratios decreasing with distance across the halo, steeper for the most metal-rich stars of the sample ([Fe/H] > -1.1) and negligiable for the most metal poor ([Fe/H] < -2.5). These trends, obtained from the low-resolution SDSS/SEGUE spectroscopic database (R $\sim$ 2000), were confirmed in the APOGEE high-resolution spectra (Fernández-Alvar et al. 2017) with the analysis of chemical species with a different nucleosynthetic origin. They pointed to that the inner parts of the halo would have undergone a different chemical enrichment. However, it was not clear if these differences would be linked to the existence of a population of stars formed in-situ during the first steps of Galaxy formation, currently dominating the inner parts of the halo, or it would be the result of more massive accreted satellites contributing to the inner regions.

On the other hand, a series of works (Nissen & Schuster (1997), Nissen & Schuster (2010), Nissen & Schuster (2011), Schuster et al. (2012)) had also revealed that a hundred field halo stars in the solar neighbourhood, not currently belonging to any stellar substructure, display two different trends of [α/Fe] with metallicity: one higher and less steep (the high-α population), and the other lower and faster decreasing with [Fe/H] (the low-α population). The increase of number of stars observed at high-resolution by the spectroscopic APOGEE survey allowed the work of Hayes et al. (2018b), in which they statistically proved that these two trends were the dominating ones in metal-poor stars ([Fe/H] < -0.9). Furthermore, Fernández-Alvar et al. (2018) compared both trends with chemical evolution models and inferred differences in the IMF and SFR of the two populations: a more intense and longer SFR and a slightly top-heavier IMF for the high-α population, and a lower and shorter SFR and a IMF with a lower upper mass limit for the low-α population.

Although an in-situ and accreted origin were proposed to explain the high-α and the low-α populations respectively, the lack of evidence in the analysis prevented to go further in the conclusions.

3 The Gaia Revolution.

Gaia hugely increased the number and accuracy of distance and velocity measurements in Galactic stars. The first data release provided in combination with the Tycho-Gaia solution allowed the distance determination for around 2 million stars. A cross-match of these data with the SEGUE database led to unveal that stars in the inner halo, moderately metal-rich [Fe/H] > -1.7, would be dominated by an accreted component moving in radial orbits, which would have come from possible one of the last major merger events ocurred in the Milky Way, at the epoch of the disc formation (Belokurov et al. 2018). The authors called it the Gaia Sausage.

But it was the second Gaia data release which gave a completely new insight in the stellar halo research. Gaia Collaboration et al. (2018a) revealed that kinematically hot stars (vtot > 200 km/s – classically classified as halo stars) in the inner halo region are distributed as two overdensities in the color-magnitud diagram. Haywood et al. (2018) investigated if these two sequences correspond to the two chemically distinct populations identified by Nissen & Schuster and others, thus confirming that the inner halo would be dominated by these two stellar populations. They observed that the high- and low-α populations split over the red and blue sequences respectively at metallicities larger than -1.1, but both lay on the blue sequences at lower metallicities. They confirmed this fact with the Nissen & Schuster sample of local stars, as well as the large and more extended sample of the APOGEE database. The high-α sequence, i.e. the red sequence in the HR diagram, shares the same α/Fe trend than the thick disk, and they suggested that they would probably be thick disk stars heated by the major merger of the satellite which provided the low-α population.

At the same time, Helmi et al. (2018) discovered within the Gaia database, a large fraction of halo stars showing coherence in the proper motion space and moving in retrograde orbits, indicating an accreted origin. By performing a crossmatch with the APOGEE DR14 database they confirmed that these accreted stars correspond to the low-α sequence. They inferred that this satellite would have a mass of $\sim 6 \cdot 10^8$ solar masses and would be accreted at an epoch in agreement with that inferred for the Gaia Sausage. Other groups performed analysis comparing observations and simulations and predicted also a merger with a significantly massive satellite to explain the chemical abundance distribution in halo stars (Kruijssen et al. (2019), Mackereth et al. (2019), Fernández-Alvar et al. (2019b)).

Following works tried to shed light on the origin of the red sequence discovered in the color-magnitud diagram of Gaia stars, with disk-like chemistry but halo-like kinematics. Fernández-Alvar et al. (2019a) analysed stars located very far away from the plane, at $|z| > 5$ kpc, and revealed three groups of stars with [Fe/H] > -0.75 which chemical and dynamical properties providing evidence of accretion events. Almost half of the sample shows a high, flat trend of [α/Fe] with [Fe/H], the same displayed by thick disc stars, which decreases at [Fe/H] $\sim$ -0.4 and moving with large velocities. They suggested that these stars would have formed in the thick disc and would have been heated by a significantly massive merger event in order to be able to put them in such large z with halo-like velocities. The fact that some of the stars appear to have thin-disk like abundances gave evidence that the Galaxy was already at the time were the bulk of SNIa were exploding and contributing to the interstellar medium when this major merger occurred. They also identified a group of stars showing a decreasing trend of low α/Fe ratios that resemble those displayed by Sagitarius stars. Finally, they also detected a group of stars with α/Fe in between, which they identified, from their chemistry and dynamical properties, as components of the Triangulum/Andromeda and A13 stellar overdensities, stars heated from the thin disc, as proposed by Bergemann et al. (2018), Hayes et al. (2018a)).

Di Matteo et al. (2018) found evidence that these high-α metal-rich stars now located far from the plane would be indeed disk stars heated when the Gaia Sausage was accreted, as the increase of velocity dispersion at [Fe/H] $\sim$ -1.1 indicates. They endorsed their interpretation with the detection of metal-poor stars ([Fe/H] $\sim$ -2) moving in rotational orbits. This would mean that at the time when metal-poor stars formed, there was already a disc configuration. Finally, Gallart et al. (2019) showed that the age distribution of both populations is consistent with this picture.

4 Conclusions and future work with MSE

The increase of the number and accuracy in measurements provided by the spectroscopic surveys during the last years, and in particular the hugely improvement in astrometric data provided by Gaia, has revolutionized our view about the Galaxy structure and their formation history. The following decades will see the upcoming of the next generation of spectroscopic surveys which will increase the number, quality and coverage of observations and, with them, exciting results in the clarification of the Galaxy formation.

One of these surveys will be the Maunakea Spectroscopic Explorer (MSE). This project consists on the transformation of the CFHT 3.6 m optical telescope (located at Maunakea, Hawaii) into a 10 m multiobject spectroscopic facility, observing $\sim$ 4000 objects simultaneously with a spectral resolution spanning 3000 to 40000. It will have the capacity to observe $\sim$ 1 million objects per month.

The MSE will provide observational support to dig into the still unreachable areas of the halo. In particular, the outer halo still lacks of reliable spectroscopic observations, due to the current instrumental limitations. With the MSE it will be possible to obtain accurate chemical abundances of millions of stars in the outer regions. This will allow to characterize the spatial distribution of chemical abundances, identify distinct stellar populations and clarify the late accretion history of our Galaxy.

References

Allende Prieto, C., Fernández-Alvar, E., Schlesinger, K. J., et al. 2014, A&A, 568, A7

An, D., Beers, T. C., Johnson, J. A., et al. 2013, ApJ, 763, 65

Belokurov, V., Erkal, D., Evans, N. W., Koposov, S. E., & Deason, A. J. 2018, MNRAS, 478, 611

Bergemann, M., Sesar, B., Cohen, J. G., et al. 2018, Nature, 555, 334

Bernard, E. J., Ferguson, A. M. N., Schlafly, E. F., et al. 2016, MNRAS, 463, 1759

Blanton, M. R., Bershady, M. A., Abolfathi, B., et al. 2017, AJ, 154, 28

Carollo, D., Beers, T. C., Chiba, M., et al. 2010, ApJ, 712, 692

Carollo, D., Beers, T. C., Lee, Y. S., et al. 2007, Nature, 450, 1020

de Jong, J. T. A., Yanny, B., Rix, H.-W., et al. 2010, ApJ, 714, 663

De Silva, G. M., Freeman, K. C., Bland-Hawthorn, J., et al. 2015, MNRAS, 449, 2604

Di Matteo, P., Haywood, M., Lehnert, M. D., et al. 2018, arXiv e-prints, arXiv:1812.08232

Eggen, O. J., Lynden-Bell, D., & Sandage, A. R. 1962, ApJ, 136, 748

Fernández-Alvar, E., Allende Prieto, C., Schlesinger, K. J., et al. 2015, A&A, 577, A81

Fernández-Alvar, E., Carigi, L., Allende Prieto, C., et al. 2017, MNRAS, 465, 1586

Fernández-Alvar, E., Carigi, L., Schuster, W. J., et al. 2018, ApJ, 852, 50

Fernández-Alvar, E., Fernández-Trincado, J. G., Moreno, E., et al. 2019a, MNRAS, 487, 1462

Fernández-Alvar, E., Tissera, P. B., Carigi, L., et al. 2019b, MNRAS, 485, 1745
Gaia Collaboration, Babusiaux, C., van Leeuwen, F., et al. 2018a, A&A, 616, A10
Gaia Collaboration, Brown, A. G. A., Vallenari, A., et al. 2018b, A&A, 616, A1
Gaia Collaboration, Prusti, T., de Bruijne, J. H. J., et al. 2016, A&A, 595, A1
Gallart, C., Bernard, E. J., Brook, C. B., et al. 2019, Nature Astronomy, 407
Grillmair, C. J. 2009, ApJ, 693, 1118
Hayes, C. R., Majewski, S. R., Hasselquist, S., et al. 2018a, ApJ, 859, L8
Hayes, C. R., Majewski, S. R., Shetrone, M., et al. 2018b, ApJ, 852, 49
Haywood, M., Di Matteo, P., Lehnert, M. D., et al. 2018, ApJ, 863, 113
Helmi, A., Babusiaux, C., Koppelman, H. H., et al. 2018, Nature, 563, 85
Kruijssen, J. M. D., Pfeffer, J. L., Reina-Campos, M., Crain, R. A., & Bastian, N. 2019, MNRAS, 486, 3180
Mackereth, J. T., Schiavon, R. P., Pfeffer, J., et al. 2019, MNRAS, 482, 3426
Nissen, P. E. & Schuster, W. J. 1997, A&A, 326, 751
Nissen, P. E. & Schuster, W. J. 2010, A&A, 511, L10
Nissen, P. E. & Schuster, W. J. 2011, A&A, 530, A15
Schuster, W. J., Moreno, E., Nissen, P. E., & Pichardo, B. 2012, A&A, 538, A21
Searle, L. & Zinn, R. 1978, ApJ, 225, 357
Zhao, G., Zhao, Y.-H., Chu, Y.-Q., Jing, Y.-P., & Deng, L.-C. 2012, Research in Astronomy and Astrophysics, 12, 723

SF2A 2019
P. Di Matteo, O. Creevey, A. Crida, G. Kordopatis, J. Malzac, J.-B. Marquette, M. N'Diaye, O. Venot (eds)

REVEALING THE FAINT UNIVERSE, MILLIONS OF SPECTRA AT A TIME

N. Flagey[1]

Abstract. In this paper we present an overview of the Maunakea Spectroscopic Explorer (MSE) at the end of Conceptual Design Phase. This project aims at transforming the Canada-France-Hawaii Telescope into an large aperture wide-field multi-object fiber-fed dedicated spectroscopic facility. MSE will collect millions of spectra every few weeks, helping astronomers answer questions about the origin of elements, the nature of dark matter, the formation of large scale structures in the Universe, and the mass of neutrinos. The main subsystems for baseline architecture of MSE are described, the concept of operations is summarized, and the overall project cost, partnership, and schedule are outlined.

Keywords: Maunakea Spectroscopic Explorer, Canada-France-Hawaii telescope, spectroscopic survey, wide field, multi object spectrograph, fiber fed

1 Introduction

The Maunakea Spectroscopic Explorer (MSE, Hill et al. 2018) is a project to transform the Canada-France-Hawaii Telescope (CFHT) into an 11.25 m aperture, wide field, highly multiplexed facility dedicated to spectroscopic surveys in the visible and near-infrared. MSE will be the observatory (i.e. the summit facility and the science platform) of the next decades, which will help astronomers answer some of the most exciting questions of modern astronomy. MSE is the answer to a need expressed by the astronomy communities is Europe[*], Canada[†], Australia[‡], and the USA(Council 2015): it is the desired facility of the next decade and beyond to address some of the most pressing and exciting questions in astrophysics.

2 Science

The detailed science case (DSC) for MSE was first release in 2016 (McConnachie et al. 2016) and a second version was released in 2019 after the science team had been reopened and grew from about 100 members to about 400 members (The MSE Science Team et al. 2019). The DSC covers many topics from stars in the Milky Way to nearby galaxies, supermassive black holes, dark matter, cosmology, and time domain astronomy. Reviews on the impact that MSE will have on these topics can be found in these proceedings.

The science cases have been expanded in the form of Science Reference Observations (SROs) which describe in more details the typical observations and samples that MSE surveys will comprise. In turn, these SROs have helped define the top level science requirements for MSE. Figure 1 provides a summary of these requirements.

3 Architecture (Hill et al. 2018)

To answer the scientific requirements, the MSE Project Office (PO) was created in 2014 at the CFHT headquarters. The MSE PO initiated the Conceptual Design Phase (CoDP) of the project which lead to multiple subsystems reviews in 2017 and a system-level review at the beginning of 2018. MSE is still the only dedicated large aperture wide-field MOS facility under development in the world.

---

[1] Canada-France-Hawaii Telescope Corporation, MSE Project Office, 65-1238 Mamalahoa Hwy, Kamuela, Hawaii 96743, USA
[*] https://pdfs.semanticscholar.org/dcc0/71607435ee989f05d9396c8ecb2f372da43a.pdf
[†] https://www.casca.ca/lrp2010/11093_AstronomyLRP_V16web.pdf
[‡] https://www.science.org.au/files/userfiles/support/reports-and-plans/2015/astronomy-decadal-plan-2016-2025.pdf

Accessible sky	30000 square degrees (airmass<1.55)						
Aperture (M1 in m)	11.25m						
Field of view (square degrees)	1.5						
Etendue = FoV x π (M1 / 2)^2	149						
Modes	**Low**		**Moderate**	**High**			**IFU**
Wavelength range	0.36 - 1.8 μm		0.36 - 0.95 μm	0.36 - 0.95 μm ♯			IFU capable; anticipated second generation capability
	0.36 - 0.95 μm	J, H bands		0.36 - 0.45 μm	0.45 - 0.60 μm	0.60 - 0.95 μm	
Spectral resolutions	2500 *(3000)*	3000 *(5000)*	6000	40000	40000	20000	
Multiplexing	>3200		>3200	>1000			
Spectral windows	Full		≈Half	$\lambda_c/30$	$\lambda_c/30$	$\lambda_c/15$	
Sensitivity	m=24 *		m=23.5 *	m=20.0 ♮			
Velocity precision	20 km/s ♪		9 km/s ♪	< 100 m/s ★			
Spectrophotometic accuracy	< 3 % relative		< 3 % relative	N/A			

♯ Dichroic positions are approximate

* SNR/resolution element = 2 ♪ SNR/resolution element = 5

♮ SNR/resolution element = 10 ★ SNR/resolution element = 30

Fig. 1. Summary of the science requirements

The goal of the MSE PO was to maximize the utilization of existing designs and minimize the development of new technologies to minimize the project exposure to technical and programmatic risks while ensuring the project schedule and budget are attainable. In addition, out of environmental and cultural respect, MSE will preserve much of the external appearance of CFHT after the completion of the transformation. In particular, MSE will reuse the CFHT summit building with no additional ground disturbances and the size increase of the summit facility (building and enclosure) will be limited to 10%.

The baseline architecture of MSE at the end of CoDP is shown in Figure 2 and detailed hereafter.

3.1 Summit building (Bauman et al. 2018)

MSE will reuse the CFHT building. Both telescope and enclosure piers will be upgraded to meet more recent building regulations. The top floor of the current building will be removed to provide more room to a significantly bigger telescope. In addition, the layout of the building will be modified to adapt to new needs and lessons learned over the past decades. The piers have been shown to be able to support the new enclosure and telescope which, though they are significantly larger, are benefiting from decades of research and development.

3.2 Enclosure

During feasibility study, it was shown that a 10 m class telescope could fit in the CFHT dome though the current slit aperture is not large enough to be consistent with the primary mirror aperture. After reviewing the extensive enclosure trade study of the Thirty Meter Telescope, a calotte-style enclosure was selected for MSE. This design is structurally more efficient than conventional designs and allows for a lower mass and size. It also has a similar appearance to that of CFHT. The CoDP design was that of Dynamic Structures Ltd in Canada.

3.3 Telescope structure (Murga et al. 2018)

The telescope will use an alt-az mount similar to that of current 8 to 10 m class telescopes. Its design features a "yoke" or "rocking chair" configuration. Its high stiffen-to-mass ratio and open-truss design will promote airflow, which is critical to minimize thermal turbulence and improve the image quality, a key element for fiber-fed instruments. The CoDP design was that of IDOM in Spain. A telescope optical feedback system, a phasing and alignment system, and an acquisition and guiding camera system are located at the top-end and provide pointing and guiding feedback to the telescope structure.

3.4 Optical design (Saunders & Gillingham 2016)

The optical design of MSE is a prime focus with a segmented primary mirror and five lenses providing wide-field correction (WFC) and atmospheric dispersion compensation (ADC). The primary mirror is composed of 60 hexagonal segments of 1.44 m corner-to-corner, thus leading to an 11.25 m aperture. The WFC/ADC top-end system is optimized to provide a 1.5 square degree field of view over the 360 nm to 1800 nm spectral range that MSE will have access to. The CoDP optical design was that of the Australian Astronomical Observatory (AAO) while the segments support system has been studied by the Indian Institute of Astrophysics (IIA).

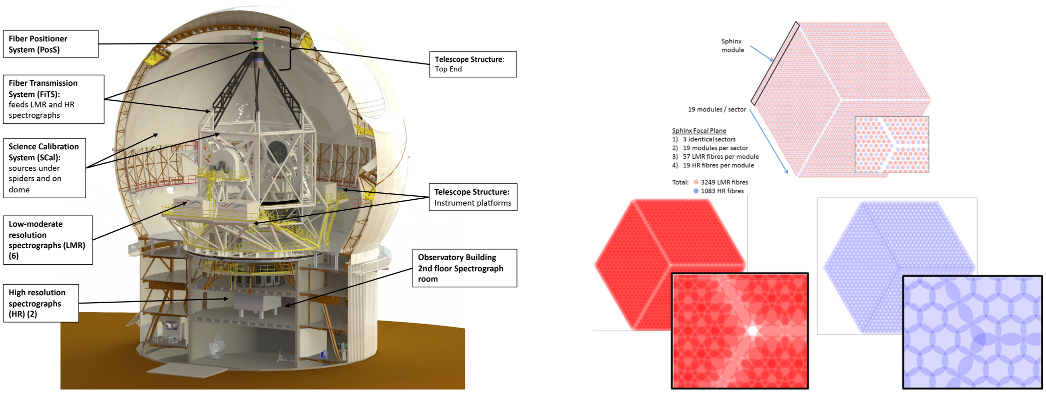

Fig. 2. Left: Schematic of the architecture of MSE with the main subsystems indicated. **Right:** Focal plane arrangement and patrol areas for the fiber positioner system.

3.5 Fiber system (Monty et al. 2018; Smedley et al. 2018)

There are 4332 positioners at the focal surface: 3249 carry a 1.0″ diameter fiber leading to low/moderate resolution (LMR) spectrographs and 1083 carry a 0.8″ diameter fiber leading to high resolution (HR) spectrographs (see Figure 2). Each positioner is a tilting spine that can reach any target within a 90″ patrol radius which means that both LMR and HR sets of positioners provide full field coverage. The CoDP design was that of AAO and competed with two other designs based on theta-phi positioners. After careful analysis of the injection efficiency (IE) and target allocation efficiency (AE) of the three designs, the AAO design was selected as its IE was only a fraction of a percent worse than that of the theta-phi designs but its AE was estimated to be about 50% better when considering the system as a whole in operations. This advantage is mainly due to the possibility offered by the AAO design to observe with both HR and LMR positioners at all time. The fibers will be bundled at the top end of the telescope structure, and run along the structure down to the LMR spectrographs located on platforms on each side of the telescope (about 35 m long) and to the HR spectrographs in the Coude room beneath the telescope (about 50 m long). The CoDP design was that of Herzberg Astronomy and Astrophysics (HAA) and Fibertech Optica in Canada.

3.6 Spectrographs (Caillier et al. 2018; Zhang et al. 2018)

The LMR spectrographs provide coverage from 360 to 1800 nm at a spectral resolution of about 2000-4000 and visible coverage at a resolution of about 4000-7000 thanks to a 4-arm design with switchable dispersive elements. The CoDP design was that of the Centre de Recherche Astrophysique de Lyon (CRAL) in France. The HR spectrographs provide three spectral windows: one about 50 nm wide in the “red” (600 to 900 nm) at a resolution of 20,000 and two about 15 nm wide in the “blue-green” (360 to 600 nm) at a resolution of 40,000. The CoDP design was that of the Nanjing institute of Astronomical optics & Technology (NIAOT) in China.

3.7 Performance

At the end of CoDP, with most of the subsystems designed, the MSE PO estimated the system-level performance and compared it with science requirements. All main science requirements are met except sensitivity at low resolution in the *H*-band (mostly because of the sky brightness) and at high resolution in the “blue” and “green” arms. The science team was then consulted via a Questionnaire to help the MSE PO refine high level requirements for the LMR and HR design ahead of the Preliminary Design Phase (PDP). More than 60 individual answers were received, covering all the science cases for MSE. The MSE PO used these answers to propose refined science requirements to the design teams along with supporting trade-off analyses to be performed before a preferred design solution is selected for PDP. For instance, the *H*-band capability was deemed critical for MSE's success but with a lower sensitivity. The desired multiplexing at those wavelengths was thus decreased and a solution was proposed for analysis to the design team: the near-IR bands (J and H) would be provided by a different spectrograph unit than that providing the visible bands.

4 Operations (Flagey et al. 2018)

MSE will be a facility 100% dedicated to spectroscopic surveys, in a way similar to the Sloan Digitial Sky Survey (SDSS). It will be remotely operated from the MSE headquarters in Waimea. Most of the operations will be automated with some human supervision to properly handle more than 4,000 spectra being observed at a given time and millions of spectra being collected every few weeks. MSE will automatically schedule observations taking into account, among others, target visibility, targets and programs priority, observing conditions (historical and in real-time), and fiber allocation completeness in a field, so that the observing sequence is optimized to provide for science outcome. MSE will also automatically extract, calibrate, and reduce data to generate a consistent set of science data products based on algorithms and recipes developed in collaboration with the science team. Finally, a science platform will be created to provide access to the data archive and visualization and analysis tools for the scientists. It is currently envisioned that about 80% of the time will be allocated to a few large legacy surveys programs (LPs) and the remaining 20% will be allocated to small strategic observing proposals (SPs). It is expected that the whole MSE partnership will have preferred access to the data with possible differences between LPs and SPs, though this is still under discussion.

5 Partnership, Cost, Schedule

The current partnership for MSE includes the historical partners of CFHT: Canada, France, and the University of Hawai'i. Australia, China, and India are new partners who have been involved in MSE since CoDP. Texas A&M University, the National Optical Astronomy Observatory (NOAO), and a consortium of United Kingdom universities have joined the project since then with the status of observers. This partnership growth is necessary to support the design, construction, and operations of a project like MSE. The estimated construction cost in 2018 US dollars is 424 millions including about 25% risk cost. The most expensive subsystems are the primary mirror (22%), the LMR spectrographs (14%), the enclosure (12%), and the HR spectrographs (8%).

After the CoDP review, the MSE PO successfully increased the partnership and the science team. More recently, the focus was on preparing MSE to enter PDP and secure funding and resources for this next phase while making sure that MSE figures at a top priority in the strategic planning of all partners (e.g. French Prospective, US Decadal Survey, Canada Long Range Plan). PDP will start in 2020 and should last about 2 years. At the end of PDP, the management board of MSE will secure and approve the plan for construction phase which will signal the beginning of the final or detailed design phase. In parallel, MSE will seek to obtain construction permit in the context of what might be a new Master Lease for the astronomy precinct on Maunakea. The MSE PO currently plans to decommission CFHT, manufacture and test subsystems, assemble, integrate, and verify the whole system in the second half of the 2020s with a goal to begin science observations (commissioning, verification, then operations) by 2030.

The MSE collaboration recognize the cultural importance of the summit of Maunakea to a broad cross section of the Native Hawaiian community.

References

Bauman, S. E., Barrick, G., Benedict, T., et al. 2018, in SPIE[§] Conference Series, Vol. 10704, Proc. SPIE, 107041E

Caillier, P., Saunders, W., Carton, P.-H., et al. 2018, in SPIE Conference Series, Vol. 10702, Proc. SPIE, 107028B

Council, N. R. 2015, Optimizing the U.S. Ground-Based Optical and Infrared Astronomy System (Washington, DC: The National Academies Press)

Flagey, N., McConnachie, A., Szeto, K., et al. 2018, in SPIE Conference Series, Vol. 10704, Proc. SPIE, 107040V

Hill, A., Flagey, N., McConnachie, A., et al. 2018, arXiv e-prints, arXiv:1810.08695

McConnachie, A., Babusiaux, C., Balogh, M., et al. 2016, arXiv e-prints, arXiv:1606.00043

Monty, S., Jahandar, F., Lee, J., et al. 2018, in SPIE Conference Series, Vol. 10702, Proc. SPIE, 107027I

Murga, G., Szeto, K., Bauman, S., et al. 2018, in SPIE Conference Series, Vol. 10700, Proc. SPIE, 107001W

Saunders, W. & Gillingham, P. R. 2016, in SPIE Conference Series, Vol. 9906, Proc. SPIE, 990638

Smedley, S., Baker, G., Brown, R., et al. 2018, in SPIE Conference Series, Vol. 10702, Proc. SPIE, 107021M

The MSE Science Team, Babusiaux, C., Bergemann, M., et al. 2019, arXiv e-prints, arXiv:1904.04907

Zhang, K., Zhou, Y., Tang, Z., et al. 2018, in SPIE Conference Series, Vol. 10702, Proc. SPIE, 107027W

[§]SPIE = Society of Photo-Optical Instrumentation Engineers

SF2A 2019
P. Di Matteo, O. Creevey, A. Crida, G. Kordopatis, J. Malzac, J.-B. Marquette, M. N'Diaye, O. Venot (eds)

EVOLUTION AND FORMATION OF GALAXIES WITH THE MAUNAKEA SPECTROSCOPIC EXPLORER FACILITY

L. Tresse[1]

Abstract. The Maunakea Spectroscopic Explorer (MSE) is a proposed major modernisation of the 3.6-m Canada-France-Hawaii Telescope into a 11.25-m aperture, 1.52 square degree field of view telescope. MSE is a fully dedicated facility to carry out multi-object spectroscopy surveys. MSE will provide a spectral resolution performance of $R \sim 2\,500 - 40\,000$ across the wavelength range of $0.36 - 1.8$ μm. The overall MSE project is presented in these SF2A2019 proceedings by N. Flagey (see also `http://www.cfht.hawaii.edu/`), here I outline the context and the challenges of MSE with respect to evolution and formation of galaxy populations.

Keywords: Astrophysics - Instrumentation and Methods for Astrophysics, Astrophysics - Astrophysics of Galaxies

1 Context

In the ΛCDM cosmological model, the baryonic content of galaxies represents less than one percent of the observable Universe, the remaining being hydrogen gas. Even though galaxies represent little of the content of the Universe, surveying them has always brought discoveries and deeper understanding towards their formation and evolution throughout cosmic epochs. Indeed they are the site of of formation of billions of stars that make them visible through several Gyrs, they are the visible blocks emerging from the dark matter halos, and they are the result of the physical processes at work of the mass-energy content of the Universe. Galaxies from baryonic gas condensed in halos, evolve in and within the dark matter halo host. The difficulty to decipher the galaxy evolution starts as soon as baryons are considered in the dark matter halo potential well, as physical processes in action are extremely complex and highly non-linear with respect to virialised properties. Under gravity, gathering and mergers of galaxies is the mean to increase their mass and design the cosmic web. The intergalactic gas connects halos, pervades structures at large scales, gives a natural reservoir of baryons to increase the stellar mass of galaxies. To reproduce today's galaxy properties one need to understand the consequences of feedback processes (stellar, AGN) on the galaxy evolution that affect the interstellar and circum-galactic media. 3D spectroscopy with the instrument MUSE/ESO-VLT (e.g., Bacon et al. 2010; Wisotzki et al. 2016) recently opened a new parameter window to study in detail the baryon circle processes in distant galaxies. These physical mechanisms predict fundamental properties of galaxies like size, angular momentum, luminosity function. To unveil and quantify the evolution of galaxy populations one need a statistical approach using wide-field facilities. Detailed studies of stellar population (ages, kinematics, chemical abundances) enable to describe a galaxy and can help to determine backward the evolution. Nevertheless it is limited by the fact that galaxies experience stochastic growth rates (merger, accretion of sub-systems, etc.) with a continuous exchange of matter end energy between in and out. Normal galaxies undergo larger star formation in the past, but if we extrapolate the mean star formation rate of our Galaxy (1 solar mass/year) for instance, we cannot explain all stars accumulated today. Thus deep surveys of galaxies is a powerful mean to trace a coherent history of galaxy population assembly; the state-of-art and difficulty is to deduce evolution over several Gyrs. At a given cosmic epoch there is a given balance between bright (exponential) and faint (power law) galaxy population volume densities versus their luminosity or stellar mass. To relate theory and observations of luminosity and stellar mass functions (see, e.g., Benson et al. 2003; Silk & Mamon 2012; Behroozi et al.

[1] Univ Lyon, Univ Lyon 1, ENS de Lyon, CNRS, CRAL UMR5574, 69000 Lyon, France

2013), one need representative samples in mass, in environment, and in type for instance, at any cosmic epoch and the precise distance of sources, i.e. spectroscopic redshifts. Nowadays massive redshift surveys sample representative volumes of the Universe to compare similar populations at different redshifts and are one of the prime tools of observational cosmology. Since the advent of multi-object spectroscopy (MOS) in the mid 90's, in particular with the nearby $z < 0.3$ 2dFGRS (Colless et al. 2001) and $z < 1.3$ CFRS (Lilly et al. 1995) surveys, spectroscopic surveys became routine using the wedding cake observational strategy with new wide-field MOS instruments, i.e., VIMOS/ESO-VLT (Le Fèvre et al. 2003), DEIMOS/Keck (Faber et al. 2003): *Wide* towards large scale structure, baryonic acoustic oscillation, and cluster studies, and cosmology probes, *Deep* towards the demographic knowledge of the sources and their environment, and *UltraDeep* towards the early Universe. Through last decades, surveys involve more and more massive data analysis on an unprecedented scale, calling for new and sophisticated approaches both for combining, analysing and archiving multi-parameter data (various wavelength ranges, spectral resolutions, point spread functions, target selections, etc.) in a meaningful and long-lasting manner (see, e.g., comments on the use of statistics (Leek et al. 2017)), and for organising large international collaborations. It represents a real challenge for future Astronomy.

2 Status and challenges in galaxy population evolution

A very robust and stable picture of the cosmic Star Formation Rate (SFR) density history is set (see, e.g., Madau & Dickinson (2014) and references therein) for a comprehensive compilation of the SFR history and mass assembly from $z = 0$ to $z \simeq 8$ using the literature spectroscopic surveys. In less than 4 Gyrs from $z = 8$ (end of reionisation epoch) down to $z \simeq 2$ (cosmic noon), the Universe reached its maximum star formation activity and half of the observed local stellar mass content is assembled. At $z > 8$ the observed accelerated evolution of the SFR density evolution (see, e.g., Oesch et al. 2018) requires further data to be confirmed. At $z > 2$ the specific SFR evolves proportionally to $(1+z)^{1.1\pm0.2}$ (Davidzon et al. 2017), illustrating a very efficient gas cooling in dark matter halos. All culminate at $z = 2$ (the cosmic noon in the so-called redshift desert): the cosmic SFR, the AGN activity, the galaxy growth mass, the massive black hole accretion history, the mass assembly, the morphological differentiation, the dust attenuation, etc. Thus, future MOS require the blue and NIR capabilities to span the redshift desert to understand this critical epoch. Galaxies above a certain mass must stop forming stars thanks to efficient quenching processes. Several scenarios are proposed that require to be corroborated with observations (i.e., e.g., Cowie et al. 1996; Faber et al. 2007; Ilbert et al. 2013). In particular, to probe the environment quenching, high spatial density sampling of targets is necessary, galaxy evolution being governed just as much on small scales as on large cosmological scales, and to prove the mass quenching (AGN, supernova, stellar feedbacks) large samples are required because of the stochasticity of the phenomena. Understanding galaxy formation is one of the most pressing issue in observational cosmology, with unsolved questions yet, like what drives the transformation from star forming to passive galaxies? at which scales environmental processes dominate galaxy properties? is there any co-evolution between massive black holes and galaxy properties, etc.

3 Multi-object spectroscopy facilities and MSE deep surveys

There are several anticipated wide-field MOS facilities brought together with imaging survey synergies. The 4-m class telescopes are dedicated MOS VIS facilities, like, e.g., WEAVE/WHT, 4MOST/ESO-VISTA, DESI/Mayall with field aperture larger than 2 deg. diameter to systematically probe large volumes at $z < 1$. The 8-m class ones are not dedicated facilities, like, e.g., MOONS/ESO-VLT and PFS/Subaru, but extend from the VIS to the NIR. The space dedicated facilities are NIR MOS, but slitless for Euclid and WFIRST-AFTA . In this context, we need further wide-field MOS facilities as described in the ESO report (Ellis et al. 2017) about the future of multi-object spectroscopy, especially for understanding the galaxy assembly and the cosmic web. That is one needs to resolve emission line doublets with sufficient signal-to-noise to measure internal stellar velocity dispersion that encode physical information, to observe enough volume at high redshift to probe the cosmic web and simultaneously encompass rare or extreme populations, to enable high spatial density to study close environment around galaxies and clustering measurements on small scales for modelling galaxy-halo properties, to optimise surveys for the physics of galaxy formation on a statistical basis and not only for cosmological studies. On the cosmological side, Colless (2019) presents key questions that will remain in 2030 that will not be refined versions of those answered by future cosmological surveys in 2020 (e.g., observation of the variation of fundamental constants, direct measure of the expansion rate, observation of non general relativity behaviour).

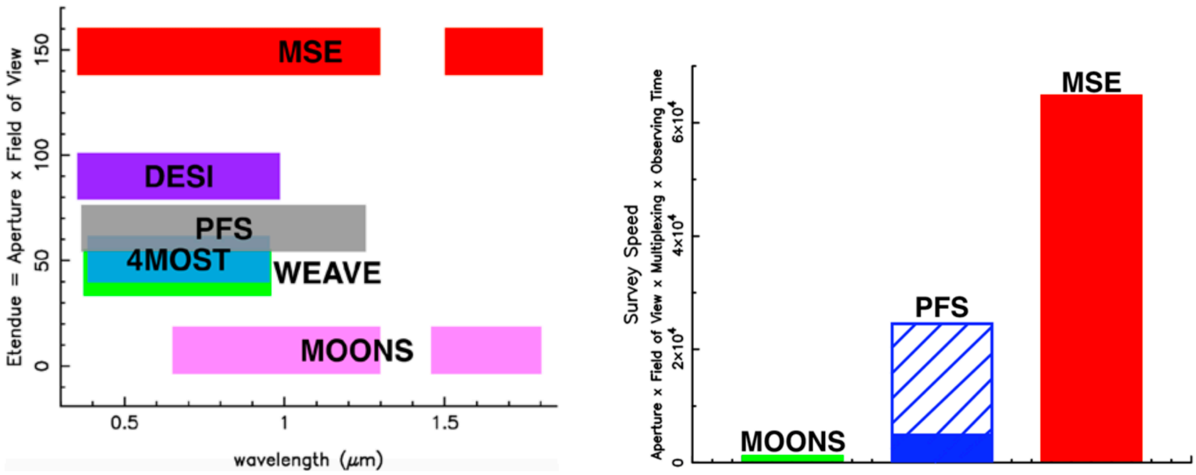

Fig. 1. Left: Etendue factor (=Aperture x Field of View) as a function of wavelength, and **Right:** Comparison of the survey speeds (Aperture x Field of View x Observing time) of the 8-10 m class anticipated wide-field MOS capabilities, published in Hill et al. (2018).

I refer also in these SF2A2019 proceedings to C. Yèche contribution, or Percival et al. (2019). MSE will enable studies which are not possible with anticipated wide-field MOS facilities, it will be the largest of these facilities and the only dedicated facility on a large aperture telescope that could be operational in 2030. MSE is designed to enable efficient massive spectroscopy surveys and to remain productive for several decades, it will surpass its original rationale as proved with most astronomical facilities. As shown in Fig. 1 its entendue (= FOV$\pi(M1/2)^2$) will be a factor 20 and 2 and its survey speed (= etendue x multiplexing x observing time) a factor 6 and 3 with respect to MOONS and PFS facilities. With its R=3000 resolution mode in VIS and NIR, MSE will enable

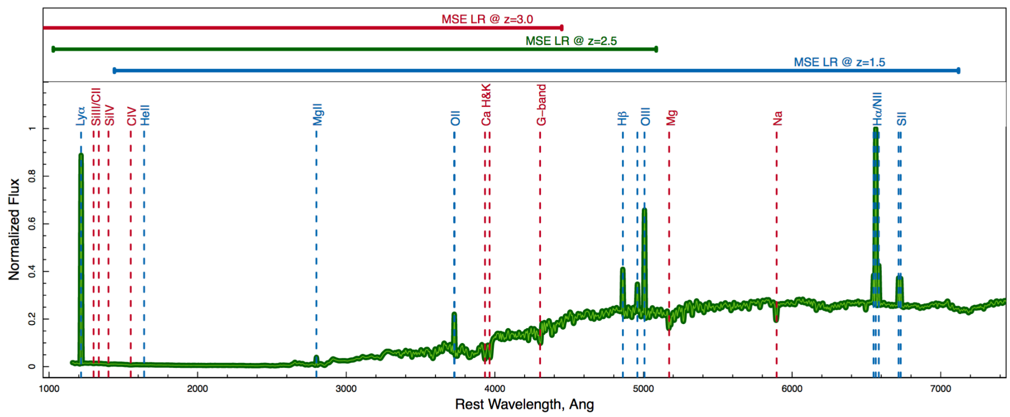

Fig. 2. A typical galaxy spectrum showing key emission and absorption lines features.The top panel displays the MSE low/mid-resolution wavelength range at $1.5 < z < 2.5$. At $z > 1.5$, MSE will observe all key optical features; at $z \approx 2.5$, it simultaneously links Lyman-and UV-absorption lines with optical emission lines; MSE retains the ability to observe [OII] and Ca H&K features to $z \approx 3$, published in The MSE Science Team et al. (2019).

the acquisition of statistical galaxy surveys at the cosmic noon epoch ($1.5 < z < 3$) in observing all key optical features at $z = 1.5$, in simultaneously linking Lyman-α and UV absorption lines with optical emission lines at $z \simeq 2.5$ and in observing [OII]$\lambda\lambda$3726,3729 and Ca H&K features to $z \simeq 3$ (see Fig. 2). MSE deep surveys over 20 - 80 sq. deg. areas will cover ranges of environment explored by local surveys with similar stellar masses, completeness and cosmological volumes. The MSE Science Team et al. (2019) present several possible surveys, for instance a 20 sq. deg. survey designed to explore galaxies and their environments at $1.5 < z < 3$ with 90% completeness at $i = 25.3$ mag using 3 million fibre hours. One major goal is to link galaxies to the large scale structure of the Universe through the peak of star formation and galaxy assembly to trace the transition from merger-dominated spheroid formation to the growth of discs, and thus to span spatial scales encompassing non-linear regime from Kpc to Mpc. Such a SDSS-like survey (`https://www.sdss.org/`) at $z \simeq 1.5$ represent a 5-7 yr programme only possible with a dedicated facility like MSE.

4 Conclusion

As a powerful, efficient and reliable survey machine, MSE will unveil fundamental quenching processes in the galaxy population on statistical basis, and will be complementary to anticipated MOS surveys or much smaller FOV instrumentation. Updates on the project are given at `http://www.cfht.hawaii.edu/`).

LT acknowledges the available contributions from the MSE science and technical teams.

References

Bacon, R., Accardo, M., Adjali, L., et al. 2010, in Society of Photo-Optical Instrumentation Engineers (SPIE) Conference Series, Vol. 7735, Proc. SPIE, 773508

Behroozi, P. S., Wechsler, R. H., & Conroy, C. 2013, ApJ, 770, 57

Benson, A. J., Bower, R. G., Frenk, C. S., et al. 2003, ApJ, 599, 38

Colless, M. 2019, in The Very Large Telescope in 2030, 3

Colless, M., Dalton, G., Maddox, S., et al. 2001, MNRAS, 328, 1039

Cowie, L. L., Songaila, A., Hu, E. M., & Cohen, J. G. 1996, AJ, 112, 839

Davidzon, I., Ilbert, O., Laigle, C., et al. 2017, A&A, 605, A70

Ellis, R. S., Bland-Hawthorn, J., Bremer, M., et al. 2017, arXiv e-prints, arXiv:1701.01976

Faber, S. M., Phillips, A. C., Kibrick, R. I., et al. 2003, in Society of Photo-Optical Instrumentation Engineers (SPIE) Conference Series, Vol. 4841, Proc. SPIE, ed. M. Iye & A. F. M. Moorwood, 1657–1669

Faber, S. M., Willmer, C. N. A., Wolf, C., et al. 2007, ApJ, 665, 265

Hill, A., Flagey, N., McConnachie, A., et al. 2018, arXiv e-prints, arXiv:1810.08695

Ilbert, O., McCracken, H. J., Le Fèvre, O., et al. 2013, A&A, 556, A55

Le Fèvre, O., Saisse, M., Mancini, D., et al. 2003, in Society of Photo-Optical Instrumentation Engineers (SPIE) Conference Series, Vol. 4841, Proc. SPIE, ed. M. Iye & A. F. M. Moorwood, 1670–1681

Leek, J., McShane, B., Gelman, A., et al. 2017, Nature, 551, 557

Lilly, S. J., Tresse, L., Hammer, F., Crampton, D., & Le Fevre, O. 1995, ApJ, 455, 108

Madau, P. & Dickinson, M. 2014, ARA&A, 52, 415

Oesch, P. A., Bouwens, R. J., Illingworth, G. D., Labbé, I., & Stefanon, M. 2018, ApJ, 855, 105

Percival, W. J., Yèche, C., Bilicki, M., et al. 2019, arXiv e-prints, arXiv:1903.03158

Silk, J. & Mamon, G. A. 2012, Research in Astronomy and Astrophysics, 12, 917

The MSE Science Team, Babusiaux, C., Bergemann, M., et al. 2019, arXiv e-prints, arXiv:1904.04907

Wisotzki, L., Bacon, R., Blaizot, J., et al. 2016, A&A, 587, A98

SF2A 2019
P. Di Matteo, O. Creevey, A. Crida, G. Kordopatis, J. Malzac, J.-B. Marquette, M. N'Diaye, O. Venot (eds)

COSMOS/GOODS-S FIELDS SPECTRO-PHOTOMETRIC ANALYSIS AND THE MOONS FUTURE PERSPECTIVES IN SED FITTING STUDIES

J. A. Villa-Vélez[1], V. Buat[1], D. Burgarella[1], M. Rodrigues[2], M. Puech[3] and H. Flores[3]

Abstract. Soon, the MOONS spectrograph will provide forefront scientific spectroscopic data enriching the current panorama of chemical composition and evolution of galaxies. Currently, multi-wavelength observations are vital to performing SED fitting analysis to understand the star-forming history of our universe and how dust attenuation affects their derivation. However, most of the analysis is carried out using only photometric data. Coupling spectroscopy and photometry gives us a more powerful tool to study the implication of dust attenuation and undergoing physics. We target objects in the COSMOS and GOODS-S fields using current spectroscopic data from the 3D-HST (i.e. H_α+[NII], H_β and [OIII] emission lines) and available photometric data to perform SED fitting using the CIGALE-code. We discuss how faithfully each emission line can be fit with CIGALE and how different dust attenuation recipes can affect the results. This work will serve as an important basis for future studies when MOONS data comes into play and we need to combine photo-spectroscopic data.

Keywords: catalogs, galaxies: high-redshift, galaxies: emission lines, ISM: dust, extinction,

1 Introduction

Deriving reliable properties of galaxies is paramount to understand the current theory of formation and evolution of galaxies. Spectral energy distribution (SED) fitting is widely used to achieve these goals. This method relies only on the analysis of photometric data using bands from the UV-to the-IR. Recently, in different SED fitting codes as CIGALE spectroscopic information as emission line fluxes or equivalent widths can be analyzed altogether with the photometric data providing a more accurate picture on the determination of stellar masses, star formation histories and the amount of dust attenuation for a given emission line.

Understanding how dust affects the emission lines allows us to determine the amount of attenuation which is vital to accurately measure the physical properties of galaxies and the possible correlations with other parameters. The SED fitting process allows us to quantify the amount of attenuation for a given emission line giving us a powerful tool for correcting the derived physical properties but also calibrating, for example, the star-formation estimates.

Traditionally the H_α line is used as a good tracer of star-formation. Even so, at high-redshift, this line is not observable and other emission lines must be implemented. In the past, [OII] has been widely studied (Kewley et al. 2004; Talia et al. 2015) and [OIII] has been recently proposed as a good tracer of SFRs in star-forming galaxies (Steidel et al. 2014; Suzuki et al. 2016; Khostovan et al. 2016). Therefore, we need to understand the correlation of [OIII] line with other physical parameters either from models or well-defined, and representative samples. Our aim, in this case, is encouraged by the previous works mentioned above to understand how current available [OIII] flux density data can be used to study its correlation with star-formation derived from SED fitting and propose a calibration for star-forming galaxies. We also aim to investigate how the different attenuation laws affect the reproducibility of [OIII]. Different authors (see: Corre et al. 2018; Buat et al. 2018; Malek et al. 2019; Buat et al. 2019) have shown how the attenuation law affects different parts of the spectrum and some modifications to current recipes have been proposed. Here a brief exercise fitting COSMOS and GOODS-S data using CIGALE and the Calzetti et al. (2000) and Charlot & Fall (2000) recipes are presented.

[1] Aix Marseille Université, CNRS, LAM (Laboratoire d'Astrophysique de Marseille) UMR 7326, 13388, Marseille, France
[2] Astrophysics, Department of Physics, Denys Wilkinson Building, Keble Road, Oxford OX1 3RH, UK
[3] GEPI, Observatoire de Paris, PSL University, CNRS, 5 Place Jules Janssen, F-92190 Meudon, France

2 Sample selection

We focus on two different fields. The COSMOS field which is centered at α(J2000) = $10^h0^m27.9^s$ and δ(J2000) = $0^h8^m50.3^s$ (Scoville et al. 2007) and the GOODS-S field centered at α(J2000) = $03^h32^m30^s$ and δ(J2000) = $-27^d48^m20^s$ (Guo et al. 2013). For COSMOS, we start with the multi-wavelength catalog of Laigle et al. (2016), COSMOS2015, which contains $UBVrizyJHK_s$ photometry from CFHT megacam and wircam, SUBARU suprime and HSC, and UKIRT WFC respectively. For the infra-red range we have Spitzer IRAC *3.6, 4.5, 5.8, and 8.0* μm data obtained from Laigle et al. (2016) and cross-matched to HELP-project Spitzer MIPS *24* μm, Herschel PACS *100, and 160* μm, and Herschel SPIRE *250, 350, 500* μm. The GALEX NUV data was obtained also from the HELP-project. Emission line density fluxes and spectroscopic redshift comes from the 3D-HST catalog of the v4.1.5 release with WFC3 G141 grism spectroscopy (Brammer et al. 2012; Momcheva et al. 2016). We kept density fluxes for H_α+[NII], H_β, and [OIII] because they are prominent lines, really well-studied and important for the determination of dust attenuation, stellar mass, metallicity among other properties.

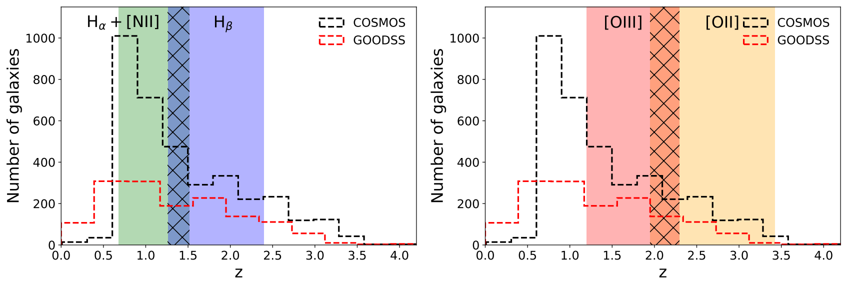

Fig. 1. Redshift distribution of COSMOS (black dashed line) and GOODS-S (red dashed line) final samples. **Left:** The H_α+[NII] and H_β expected coverage of the WFC3 G141 grism are shown in green and purple respectively. **Right:** Same as in left panel but using [OII] and [OIII] emission lines. We cover an important redshift range with several emission lines.

On the other hand for GOODS-S field we use the CANDELS GOODS-S multi-wavelength catalog (Guo et al. 2013, and references therein). The photometric data corresponds to *U-VIMOS*, and *F435W, F606W, F775W, F814W, F850LP* HST/ACS, *F098M* HST/WFC3, and *F105W, F125W, F160W* CANDELS+HUDF09, ISAAC-K_s, and Spitzer IRAC *3.6, 4.5, 5.8, and 8.0* μm. We crossmatch the PACS *70, 100, and 160* μm, and Herschel SPIRE *250, 350, 500* μm from the PEP-catalog (Lutz et al. 2011; Wang in prep.). Spectroscopic redshift and H_α+[NII], H_β, and [OIII] density fluxes are also obtained from the 3D-HST catalog. The GALEX NUV data used comes from the Great Observatories Origins Deep Survey: far-infrared imaging with Herschel" (GOODS-Herschel, Elbaz et al. (2011)) survey.

The final samples are crossmatched to X-ray CHANDRA observations for COSMOS (Civano et al. 2016; Marchesi et al. 2016) and GOODS-S Dickinson et al. (2003). Objects detected in X-ray were rejected due to potential active galactic nuclei. Besides, objects for which the GALEX NUV measurements fall below the Lyman limit (912$\AA$) are kept but the NUV information is neglected because these measurements are not reliable. For the WF3 G141 grism this corresponds to galaxies below z< 0.856. The distribution of the final sample for both fields is shown in Fig. 1 as a function of redshift along with the WFC3 G141 emission line coverage.

3 CIGALE SED fitting: H_α+[NII], H_β and [OIII]-emission lines

The final samples for COSMOS and GOODS-S are fit using CIGALE-code which allows fitting simultaneously photometry and spectroscopy. Currently, in CIGALE there are two attenuation recipes implemented (e.g. Starburst-Modified and CF00-Modified). The former uses the well-known attenuation curve of Calzetti et al. (2000) but extended between the Lyman break and 150nm as a basis and a power law as a function of the wavelength which allows the variation of the slope. A Lorentzian-like Drude profile allows adding the UV-bump in Eq. 3.1. This law is defined for the continuum and the emission lines are only dimmed by the Milky Way extinction curve. A more flexible approach allows to use an updated version of the Milky Way curve and also those of the Small and Large Magellanic Clouds Boquien et al. (2019). On the other hand, the latest is based on the Charlot & Fall (2000) recipe where young and old stellar populations are embedded in different environments thus experiencing different attenuation. The light emitted by young stars inside the birth clouds is attenuated by the birth cloud and the ISM. The old stars are only attenuated by the ISM where they are embedded in. Here, old stands for stellar age > 10Myr in Eq. 3.2.

$$A(\lambda) \quad = \quad E(B-V)_{star}\ k'(\lambda)\ \left(\frac{\lambda}{\lambda_v}\right)^{\delta} \tag{3.1}$$

$$A(\lambda) = \begin{cases} A_V^{BC}(\lambda/\lambda_v)^{n^{BC}} & \text{if stellar age} < 10\text{Myr} \\ \\ A_V^{ISM}(\lambda/\lambda_v)^{n^{ISM}} & \text{if stellar age} > 10\text{Myr} \end{cases} \tag{3.2}$$

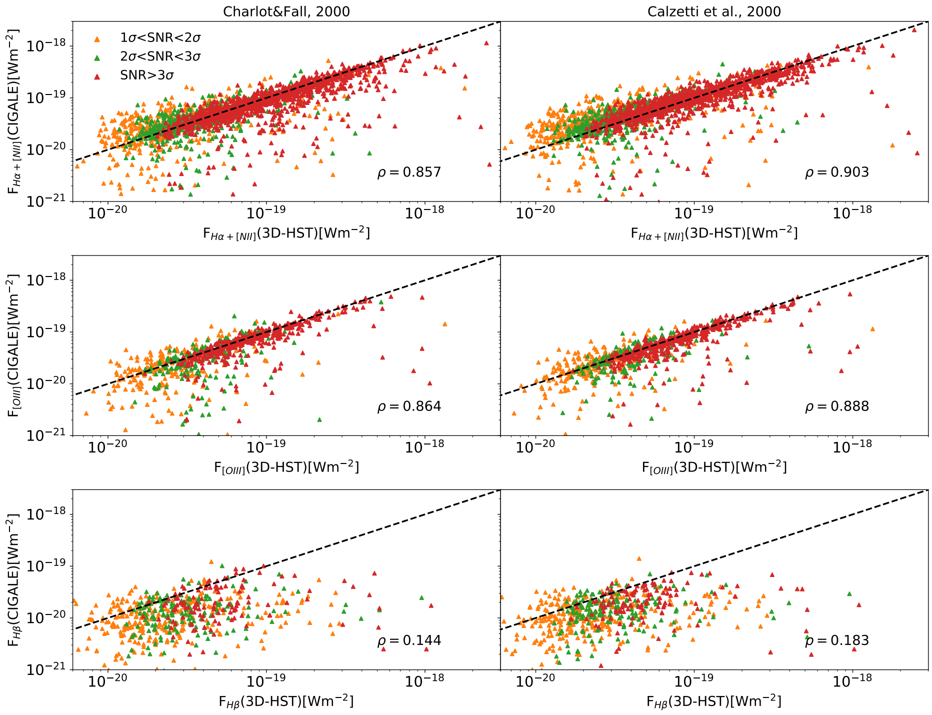

Fig. 2. H_α+[NII], H_β and [OIII] density fluxes vs CIGALE fits for COSMOS using Charlot & Fall (2000) and Calzetti et al. (2000) recipes. In all panels, the color-code stands for the signal-to-noise ratio. The black line represents the 1:1 relation and ρ corresponds to the Pearson correlation factor.

We checked and analyzed that emission line fitting works for the most simple and well-known cases we fit both the COSMOS and GOODS-S data using the traditional Calzetti et al. (2000) and Charlot & Fall (2000) (hereby: C00 and CF00 respectively) laws which can be easily retrieved from the modified laws in CIGALE. This means, that in Eq. 3.1 the reduction factor ($\mathrm{E(B\text{-}V)_{star}/E(B\text{-}V)_{lines}}$) is set to 0.44, and the slope δ of the power-law is zero. On the other hand, in Eq. 3.2, we fix the power-law slopes for the birth cloud n^{BC} and the ISM n^{ISM} to -0.7 and the ratio of the attenuation in the V band experienced by old and young stars to 0.3. In Fig. 2 the results for H_α+[NII], H_β, and [OIII] are shown for the COSMOS samples as fitted by using the C00 and CF00 attenuation laws. Same results are obtained for the GOODS-S field but only COSMOS is presented for clarity.

For the H_β line it is evident that both recipes fail to faithfully reproduce the observed density fluxes. CIGALE does not fit this line independently of the data quality which raises the question if the current attenuation laws need to be modified or any other parameters inside the physical models need to be changed to reproduce the line. However, we need to be cautious because the vast majority are below the 3σ threshold, fluxes are really small, and measuring the line is quite difficult. As can be seen in Fig. 2 the difference between the CF00 and C00 fitting is not statistically significant as shown by the Pearson correlation coefficients.

The next step consists in using the more flexible modified recipes implemented in CIGALE which allow us to vary the slopes and explore a wider range of scenarios aiming to reduce the scatter. A small test sample confirms that the scatter can be improved but no real change in the prediction of the H_β line. This also ameliorates the small offset present in the H_α fit when using CF00 as compared to C00. Both H_α+[NII] and [OIII] emission are fairly well reproduced by our fitting analysis using the two different recipes. The fact that the [OIII] line is well reproduced is very encouraging for this work because we aim to calibrate it in terms of star-formation as has been done before with the H_α line. Although the number of objects is a bit less for the [OIII] sample compared to the H_α one, we observe that the sample is less scattered. A good fit for our samples is crucial because all the physical properties derived from the SED fitting analysis as the SFR, stellar masses, metallicities, among others will strongly depend on how well we can reproduce the photometric and spectroscopic data at the same time.

4 MOONS perspectives

The Multi-Object Optical and Near-infrared Spectrograph (MOONS) will be placed on the Nasmyth platform of one of the VLT telescopes. The first light is expected around 2021. The instrument is composed of two different spectrographs both equipped with slits containing 32 slitlets, and 16 fibers. Only 1001 fibers out of 1024 are connected to the FPUs to allow for some flexibility in matching the slitlets. The instrument is planned to have a wavelength coverage between 0.8μm and 1.8μm, and to work in three different resolution modes (R$\sim$4,000-6,000 in the entire wavelength range, R$\sim$8,000 around the CaII triplet, and R$\sim$20,000 in the J-band and H-band) which makes it a valuable instrument to explore and study emission line features which are usually shifted to the IR-range and highly affected by dust attenuation Cirasuolo et al. (2012).

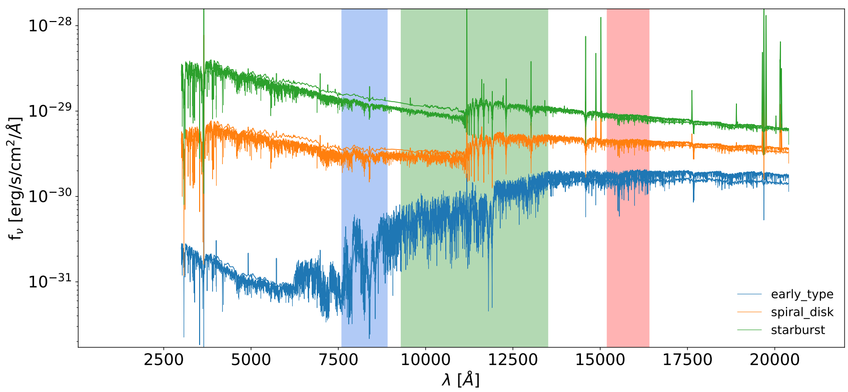

Fig. 3. High-resolution spectra for a different type of galaxies modeled using CIGALE. Each spectrum corresponds to an early-type, spiral or starburst type of galaxy. Several samples were generated varying the amount of attenuation. The vertical bands correspond to the three bands wavelength covered by MOONS.

As part of the End2End simulation for MOONS, we implemented high-resolution SSPs ELODIE-based models into CIGALE as presented by Maraston & Strömbäck (2011) (MS11). The Bruzual & Charlot (2003) (BC03) high-resolution models already implemented in CIGALE may not be sufficient to analyze the continuum as we want to degrade the spectra through the simulation. In Fig. 3 a small sample covering the three types of galaxies is presented. Each spectrum was obtained with CIGALE using the MS11-HR models for the continuum and BC03-HR models for the emission lines in a restricted wavelength range imposed by the MS11 models. Implementing emission lines along with high-resolution MS11 models will be addressed in future work. These samples represent the first attempt to test the MOONS ETC and provide some training data set for the extragalactic and redshift determination teams.

References

Boquien, M., Burgarella, D., Roehlly, Y., et al. 2019, A&A, 622, A103

Brammer, G. B., van Dokkum, P. G., Franx, M., et al. 2012, ApJS, 200, 13

Bruzual, G. & Charlot, S. 2003, MNRAS, 344, 1000

Buat, V., Corre, et al. 2019, arXiv e-prints, arXiv:1902.09435
Buat, V., Boquien, M., Małek, K., et al. 2018, A&A, 619, A135
Calzetti, D., Armus, L., Bohlin, R. C., et al. 2000, ApJ, 533, 682
Charlot, S. & Fall, S. M. 2000, ApJ, 539, 718
Cirasuolo, M., Afonso, J., Bender, R., et al. 2012, in SPIE Conference Series, Vol. 8446, Proc. SPIE, 84460S
Civano, F., Marchesi, S., Comastri, A., et al. 2016, ApJ, 819, 62
Corre, D., Buat, V., Basa, S., et al. 2018, A&A, 617, A141
Dickinson, M., Giavalisco, M., & GOODS Team. 2003, in The Mass of Galaxies at Low and High Redshift, ed. R. Bender & A. Renzini, 324
Elbaz, D., Dickinson, M., Hwang, H. S., et al. 2011, A&A, 533, A119
Guo, Y., Ferguson, H. C., Giavalisco, M., et al. 2013, ApJS, 207, 24
Kewley, L. J., Geller, M. J., & Jansen, R. A. 2004, AJ, 127, 2002
Khostovan, A. A., Sobral, D., Mobasher, B., et al. 2016, MNRAS, 463, 2363
Laigle, C., McCracken, H. J., Ilbert, O., et al. 2016, ApJS, 224, 24
Lutz, D., Poglitsch, A., Altieri, B., et al. 2011, A&A, 532, A90
Malek, K., Buat, V., Burgarella, D., et al. 2019, arXiv e-prints, arXiv:1904.12498
Maraston, C. & Strömbäck, G. 2011, MNRAS, 418, 2785
Marchesi, S., Civano, F., Elvis, M., et al. 2016, ApJ, 817, 34
Momcheva, I. G., Brammer, G. B., van Dokkum, P. G., et al. 2016, ApJS, 225, 27
Scoville, N., Aussel, H., Brusa, M., et al. 2007, ApJS, 172, 1
Steidel, C. C., Rudie, G. C., Strom, A. L., et al. 2014, ApJ, 795, 165
Suzuki, T. L., Kodama, T., Sobral, D., et al. 2016, MNRAS, 462, 181
Talia, M., Cimatti, A., Pozzetti, L., et al. 2015, A&A, 582, A80
Wang, T. in prep.

SF2A 2019
P. Di Matteo, O. Creevey, A. Crida, G. Kordopatis, J. Malzac, J.-B. Marquette, M. N'Diaye, O. Venot (eds)

STELLAR SPECTROSCOPIC SURVEYS: OVERVIEW, EXPECTATIONS AND ACHIEVEMENTS

M. Van der Swaelmen[1], L. Magrini[1], V. Hill[2] and G. Kordopatis[2]

Abstract. Multi-fibre spectrographs have made possible the run of large spectroscopic surveys targeting 10^5 to millions of Milky Way (MW) stars. The targeted stars belong to the main stellar structures of our Galaxy and mostly sample stellar evolutionary stages from the (pre-)main-sequence to the red giant branch. Their primary aim is to harvest a vast amount of data (radial velocities, stellar parameters, abundances) in order to constrain the formation and evolution of the MW. We will focus on two spectroscopic surveys France is involved in. First, we will briefly introduce the WEAVE spectroscopic survey, that will soon start to observe at the William Herschel Telescope, and show from simulations what can be expected in terms of chemical abundances. Second, we will highlight the relevance and usefulness of such large project by reminding some of the results obtained within the Gaia-ESO survey.

Keywords: Surveys, Techniques: spectroscopic, Galaxy: abundances, Instrumentation: spectrographs

1 Massive spectroscopic surveys in the recent era

1.1 A short history of spectroscopy in astronomy

Physicists and astronomers have started to use spectroscopy since 1666, the year when Newton obtained the first documented solar spectrum using a prism. However, one has to wait until the 19th century to see the birth of stellar spectroscopy. In 1802, Wollaston is the first to observe few dark lines in the solar spectrum but he failed at understanding their nature. In 1814, Fraunhofer invented the modern spectroscope and with this new instrument, he was able to detect and to label hundreds of absorption lines in the solar spectrum, some of these lines being still called the Fraunhofer lines today. He understood that those dark lines are intrinsic to the nature of the stars and by comparing the spectra of various stars, he showed that stars are different from each other: the first step towards stellar spectroscopy was made.

A technological step (ability to record a spectrum) and a scientific step (nature of the absorption lines) were still to be made in the second half of the 19th century. Stellar spectroscopy took advantage of the progress made by photographic techniques. Thus, the first successful recording of the solar spectrum was made by Becquerel in 1842 using a daguerreotype while the first record of a stellar spectrum (Vega) on a photographic plate was obtained by Draper in 1872. It was an important achievement to allow the comparison of spectra between two stars or over time. One the other hand, the understanding of Fraunhofer's lines took also several decades. Fraunhofer noticed that the solar D lines have wavelengths close to that observed in some flame spectra and Foucault understood in 1849 that a given element may produce an emission or an absorption line at the same wavelength. However, Kirchhoff is the first to identify sodium in the solar spectrum in 1859 and later, he and Bunsen identified a handful chemical species in the solar spectrum by comparing it to the flame and spark spectra of various salts. Similarly, Huggins and Miller recorded the spectra of various distant stars and identified some of the chemical elements present in their atmospheres. They demonstrated that the chemical species found on Earth are found elsewhere in the Universe and that stars do have different chemical compositions. Huggins also attempted for the first time to measure the radial velocity of a star using Doppler shifts, a field that greatly benefited from Vogel's contributions afterwards. Stellar spectroscopy was born!

[1] INAF - Osservatorio Astrofisico di Arcetri, Largo E. Fermi 5, 50125, Firenze, Italy
[2] Université Côte d'Azur, Observatoire de la Côte d'Azur, CNRS, Laboratoire Lagrange, Bd de l'Observatoire, CS 34229, 06304, Nice Cedex 4

As in other fields of science, the systematic cataloguing of objects (and their classification) is a necessary step towards the understanding of their intrinsic properties. In the early years of stellar spectroscopy, small catalogues of spectra were already being built. They allowed to highlight resemblances and differences between stars and led to the first stellar classifications (e.g, Rutherfurd, Secchi). However, the first efforts for a massive spectroscopic survey of the skies were carried out at Harvard College Observatory by Pickering and his invaluable "Harvard computers", women coworkers – among which Fleming, Maury, Cannon, Leavitt – who classified manually more than 200 000 stars and whose studies shed new lights on the nature of stars. While Pickering and Fleming started the work in 1886, 10 351 stars were already catalogued in 1890 and $\sim$ 225 000 stars were published between 1918 and 1924 in the final version of the Henry Draper Catalogue. The catalogue was extended to $\sim$ 359 000 stars in 1949. The curious reader may have a look at the excellent book by Hearnshaw (2009) for a more detailed history of stellar spectroscopy.

1.2 Spectroscopic surveys over the last two decades

The previous section recalled the reader that the idea of carrying out a spectroscopic survey is not very new in astronomy and the crucial need of a vast amount of (photometric, spectroscopic, etc) data was recalled in Freeman & Bland-Hawthorn (2002). Thus, another era of large spectroscopic surveys has started in the early 2000s and one notes an intensification since 2010. Such audacious projects have been made possible by the building of large apertures and the advent of multi-object spectrographs allowing to record simultaneously the spectra of few 100 to few 1000 stars in one single exposure. Numerous spectroscopic surveys have been designed and have been/are/will soon be carried out. They differ by their spectral resolution from low- ($R \leq\sim 5000$) to mid- ($\sim 7000 \leq R \leq\sim 15\,000$) and high-resolution ($R \geq\sim 20\,000$)*. They differ also by their spectral coverage, from the UV to mid-infrared.

The very first post-2000 spectroscopic surveys are RAVE (Steinmetz 2003) and SEGUE (Beers et al. 2004; Yanny et al. 2009) started in 2003 and 2004, respectively. RAVE ran for ten years at Anglo-Australian Telescope and recorded more than 570 000 spectra at $R = 7500$ for more than 483 000 stars belonging to the Milky Way (MW) and the Magellanic Clouds (MCs). SEGUE obtained spectra at $R = 1800$ for 240 000 targets between 2004 end 2008 and was complemented by SEGUE-2 and its 140 000 targets. Among the other notable terminated surveys, one finds: APOGEE (Apache Point Observatory; Majewski et al. 2010) and its 10^5 stars observed at $R \sim 22\,500$ in the range $[15\,100, 17\,000\,\text{Å}]$; Gaia-ESO (Very Large Telescope; Gilmore et al. 2012; Randich et al. 2013) and its 10^5 stars observed with the mid- ($R \sim 20\,000$) and high-resolution ($R = 47\,000$) FLAMES spectrographs in various wavelength ranges; LEGUE (the MW part of the LAMOST survey; Guo Shoujing Telescope; Newberg et al. 2012) and its 10^7 stars and galaxies (as of DR5) observed at $R = 1800$ in the range $[3690, 9100\,\text{Å}]$.

Many surveys are still ongoing: GALAH (Anglo-Australian Telescope; Anguiano et al. 2014) aiming at observing 10^6 stars of the MW at $R = 28\,000$ in four wavelength windows; APOGEE-2 (Apache Point Observatory + Irénéé du Pont Telescope; Majewski et al. 2016) aiming at observing 3×10^5 stars of the MW and the MCs; Gaia RVS (Gaia space probe; for the Gaia mission: Prusti 2012; for the RVS: Katz et al. 2004; Wilkinson et al. 2005) will obtain the spectra around the near-infrared Ca II triplet at $R = 11\,500$ and is expected to provide radial velocities for 150×10^6 stars and basic chemical composition for 2×10^6 stars (Recio-Blanco et al. 2016). On the other hand, DESI (Kitt Peak; DESI Collaboration et al. 2016) is designed as a high-redshift spectroscopic instrument and is mainly a tool for cosmology; however, it will observe MW stars during the bright time of the survey and is expected to provide us with low-resolution spectra for 10^7 stars.

A new generation of facilities is also being built and new spectroscopic surveys will start *tomorrow*: WEAVE (William Herschel Telescope; Dalton et al. 2012), 4MOST (VISTA Telescope; de Jong et al. 2019) and MOONS (VLT; Cirasuolo & MOONS Consortium 2016). These new surveys will take care to have numerous common targets to ease inter-survey calibrations. Tests are also carried out to upgrade LEGUE with a higher resolution of 7500 (Liu et al. 2019). In the near future ($\sim$ 2030), the community will benefit from the Maunakea Spectroscopic Explorer (McConnachie et al. 2014), a dedicated 10m-class telescope which will record about 4400 spectra at once ($\sim$ 1100 at high-resolution and $\sim$ 3300 at low-/mid-resolution) resulting in the production of millions of spectra every few weeks. France has a long-term involvement into stellar spectroscopy and has been or is contributing to the following surveys: RAVE, Gaia-ESO, Gaia RVS, DESI, WEAVE, 4MOST, MOONS and MSE.

*The boundaries between low-, mid- and high-resolution are somewhat arbitrary and may change depending on the astronomy field. Here the numbers correspond to what is often meant in the context of stellar spectroscopy.

The outputs of recent spectroscopic surveys are individual spectra (few 10^5 to few 10^7), radial velocities, atmospheric parameters and global/detailed chemical compositions. They sample the kinematics and chemistry of different populations (MW thin/thick disks, bulge, halo, clusters), different galaxies (Magellanic clouds for APOGEE-2 and 4MOST), different evolutionary phases (main-sequence and RGB, mainly). Their aims are to characterise stellar populations and Galactic structures and constrain the chemical/dynamical history of the MW (or MCs). The size of all these surveys and the number of phase space dimensions they probe are breathtaking, especially when one compares them to the $\sim 225\,000$ stars of the Henry Draper Catalogue collected over three decades.

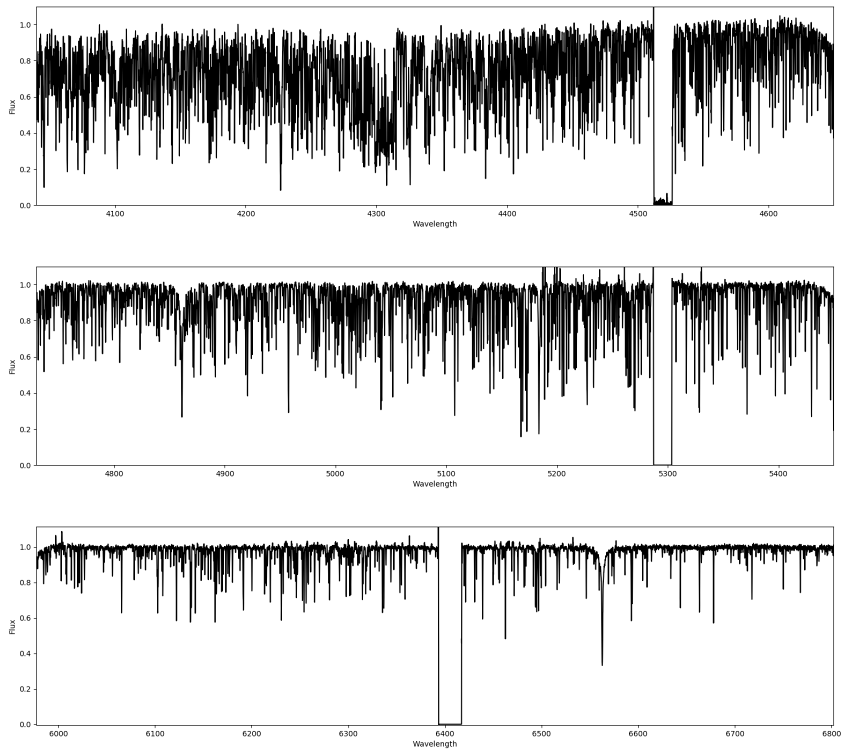

Fig. 1. From top to bottom: example of simulated WEAVE blue, green and red spectra for a mildly metal-poor giant. The signal-to-noise ratio is larger than 90.

2 The WEAVE survey

The WEAVE survey (Dalton et al. 2012) will be carried out at the William Herschel Telescope in La Palma. It will therefore give access to the Northern sky. The facility is made of 1000 fibres feeding a low- and high-resolution spectrographs. The low-resolution mode offers a resolution of 5000 and observes from the UV to the near-IR, over two wavelength windows [3660, 6060 Å] and [5790, 9590 Å]. The high-resolution mode offers a resolution of 20 000 and two configurations: the blue + red arms ([4040, 4650 Å] and [5950, 6850 Å]) or the green + red arms ([4730, 5450 Å] and [5950, 6850 Å]). It is thought to complement the Gaia phase space and in particular to provide accurate radial velocities, stellar parameters and abundances for targets fainter than $G = 12$, the faintest targets reached by WEAVE being of magnitude $G = 20$.

The Galactic archaeology component of WEAVE is divided into a low- (LR) and a high-resolution (HR) surveys. They will be the first spectroscopic surveys to use the Gaia DR2 as input catalogue. The LR survey will provide for the observed stars their atmospheric parameters, radial velocities and, at least, global abundance estimates while the HR survey will also provide detailed chemical abundances for more than ten species. The LR survey is divided into two sub-surveys: the LR-Halo survey will map the MW halo and search for stellar streams, as remnants of past accretion events; the LR-Disk survey will study the disk dynamics. The HR survey is also divided into two sub-surveys: the HR-Open-clusters will target open clusters in the disk and study, for instance, their dynamical evolution and role in stellar migration; the HR-chemo-dynamical will probe the MW thin/thick disks and halo and will constrain the chemical evolution and mass assembly of the MW. In total, LR and HR surveys will observe more than four millions of MW stars.

The choice of the configuration (blue+red arms – BR – or the green+red arms – GR) is constrained by the kind of science we are interested in and, in turn, by which chemical species are needed. Figure 1 shows the simulated WEAVE blue, green and red spectral chunks for a mildly metal-poor giant. Those spectra have been generated in the context of the operation rehearsal (OpR3). They are based on the synthetic spectral library by de Laverny et al. (2012) and simulate the resolution, signal-to-noise ratio and spectral shape of the WEAVE spectra at the end of the optical and data reduction chain.

We used a set of 3000 spectra, at various level of signal-to-noise ratio, corresponding to stars sampling the Hertzsprung-Russell diagram, over the FGK spectral types and over the dwarf and giant luminosity classes, to test which is the best configuration when it comes to study carbon, nitrogen and neutron-capture elements. We chose to study the detectability of these elements because of their importance in both stellar and galactic evolution. For instance, C and N in evolved stars trace the mixing processes and their abundance ratio can be used as a proxy for stellar ages (see, e.g. Casali et al. 2019). On the other hand, neutron-capture elements are produced by different processes and with different timescales, tracing the Galactic chemical evolution. Their ratio over alpha elements, as e.g. [Y/Mg], can be also used to measure stellar ages (e.g., Titarenko et al. 2019).

Figure 2 shows examples of fit of Ba, La and Eu atomic lines as well as molecular CH and CN bands. Our study shows that the blue spectra are indispensable to measure C and N. The blue and red spectra give access to some Ba, La and Eu lines. However, the determination of Ba and Eu abundances in the photosphere of main-sequence stars will rely on the blue lines only (the red lines are weaker and will likely lead to firm detections only in the spectra of giants). We note that the blue spectra tend to be more crowded by atomic lines and molecular bands than the green or the red spectra, which could hamper the normalisation and thus, impact the accuracy/precision of abundances determinations. On the other hand, we recall that the BR and the GR configurations perform similarly when it comes to derive Fe or α-elements abundances.

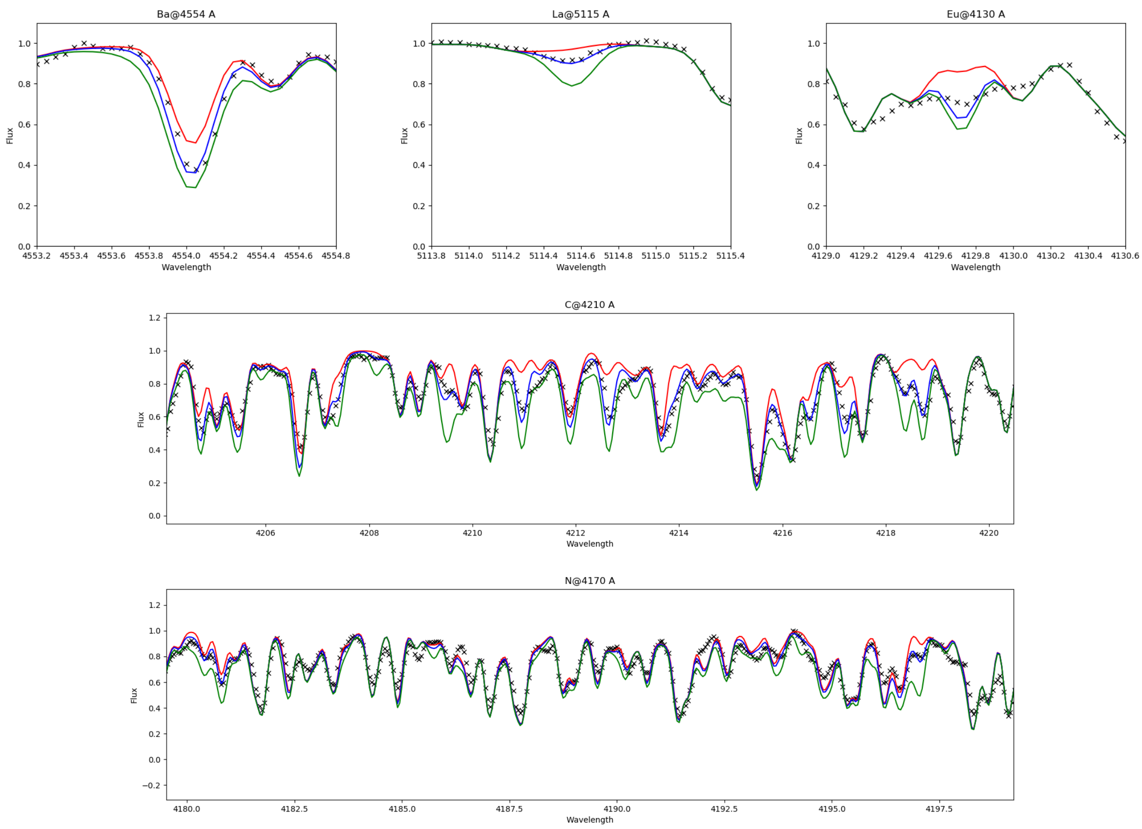

Fig. 2. From top to bottom, left to right: example of absorption line fitting for Ba, La, Eu, C (CH bands) and N (CN bands). The star shown here is the same as in Fig. 1. Black crosses stand for the simulated WEAVE spectra. The blue lines correspond to the best fit while the green and red lines correpond to syntheses obtained for [X/Fe] = ±0.3.

3 Achievements of spectroscopic surveys: example of the Gaia-ESO survey

The Gaia-ESO survey (Gilmore et al. 2012; Randich et al. 2013) is a ground-based mid- and high-resolution spectroscopic survey carried out at VLT, Chile with the multi-object spectrograph FLAMES (Pasquini et al. 2000). It aimed at recording the spectra for 10^5 stars belonging to the Galactic bulge, thin/thick disks, halo, clusters. About 90 % of the spectra have been obtained with GIRAFFE at a resolution ranging from $\sim 18\,000$ to $\sim 21\,500$ (depending on the chosen setup) and 10 % obtained with UVES at a resolution 47 000. The observing campaign is now over and the sixth (and final) data release is expected by 2020. The final release contains 700 000 individual spectra, most of the targets having two or four exposures. The survey covers the range of V magnitude from 10 to 20 with a median at 15.

The Gaia-ESO survey legacy will be significant and multiple. One should not underrate the contributions of the Gaia-ESO surveys in terms of methods and techniques. First, it was an ideal laboratory to assess good practices for future large surveys: the use of numerous calibrators, like radial velocity standards or Gaia benchmark stars, to control the results internally and externally; the use of a single source of atomic and molecular data that were checked and shared before starting any spectral analysis; etc. Its organisation in analysis nodes was also challenging since a single set of stellar parameters and abundances had to be forged out of a dozen of sets. Homogenisation procedures had to be designed and to this end, a flag dictionary had to be used in order for the nodes to report issues and comments along with the results and their errors. The flags have proven their usefulness to identify and fix problems and also to make choice during the homogenisation phase (Van der Swaelmen et al. 2018b). Numerous analysis tools and pipelines have been developed in the context of the Gaia-ESO survey and this algorithm legacy might be re-used for or adapted to future surveys, like WEAVE. The Gaia-ESO survey catalogue brings numerous primary products to the community: spectral library, radial velocities, atmospheric parameters, chemical abundances for the main nucleosynthetic families. Finally, the Gaia-ESO survey has addressed a number of fundamental topics in astronomy: stellar nucleosynthesis (e.g., Magrini et al. 2018), stellar evolution (e.g., Lagarde et al. 2019), abundance gradients (e.g., Spina et al. 2017), kinematics (e.g., Rojas-Arriagada et al. 2014), stellar migration (e.g., Hayden et al. 2018), thin/thick disk transition (Kordopatis et al. 2015), spectroscopic binaries (Merle et al. 2017), ages of clusters, interstellar medium, etc. Eighty refereed publications can be listed so far and many more are still expected.

To finish, we will recall that such surveys often bring us bonus science that was not among the primary goals. In the case of the Gaia-ESO survey, one can cite the case of spectroscopic binaries. Merle et al. (2017) and Van der Swaelmen (*in prep*, see also Van der Swaelmen et al. 2018a) designed a pipeline to compute narrow cross-correlation functions (CCFs) and analyse them to look for single-, double-, triple-lined spectroscopic binaries. Figure 3 shows the NACRE CCFs for a double-lined spectroscopic binary (SB2). Van der Swaelmen et al. (2018a) derive the mass ratio for 10 % of their SB2. The distribution, shown in Fig. 3, is biased towards 1. This is understood if one recalls that for an SB2, both components are visible in the spectra: this means that they have similar spectral types and since they are co-eval, they have similar masses.

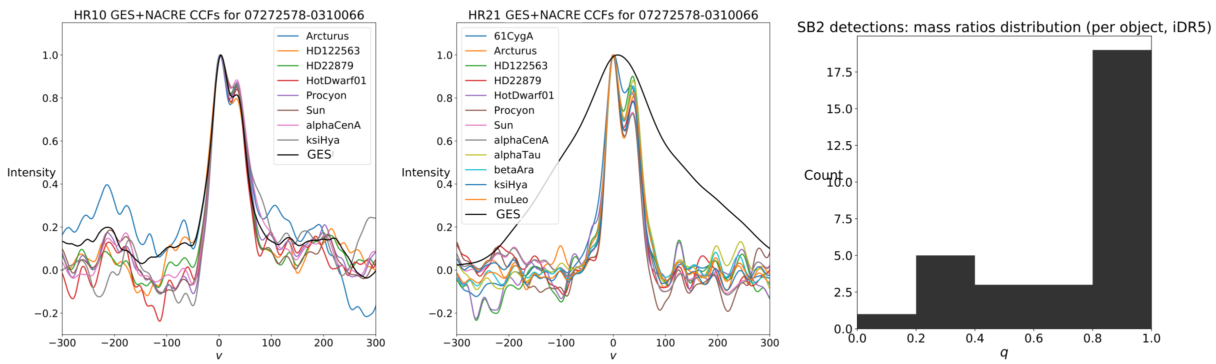

Fig. 3. Left: Example of cross-correlation functions of a Gaia-ESO SB2 observed with the GIRAFFE setup HR10. The black line is the CCF released by the Gaia-ESO while the coloured lines are the NACRE CCFs. **Middle**: Same as left but for an HR21 observation of the same object. The Gaia-ESO CCF does not display the two stellar components while our NACRE CCFs do. **Right**: Mass-ratio distribution for about 10 % of the SB2 detected in the fifth internal data release of the Gaia-ESO survey.

4 Conclusion

Astronomers live in the golden age of stellar spectroscopy. An unprecedented international effort is carried out to increase the number of observed targets and the number of known dimensions of the phase space. The aim is to constrain the chemical evolution and assembly history of the Milky Way. While a number of surveys (RAVE, APOGEE, Gaia-ESO, etc) have reached their conclusion and have shown the usefulness of a large amount of homogeneously obtained physical quantities, a new generation of survey will soon start and will allow us to increase the size of spectroscopic catalogues (and their attached products) by several orders of magnitude. Ground-based spectroscopy is fundamental to complement the Gaia exquisite dataset (proper motions, distances, etc.) and their combination is leading us to major discoveries (e.g., see the use of Gaia and APOGEE by Helmi et al. 2018 to discover Gaia-Enceladus, an ancient merger that likely contributed to the build-up of the inner halo and the thick disk).

References

Anguiano, B., Freeman, K., Bland-Hawthorn, J., et al. 2014, in IAU Symposium, Vol. 298, Setting the scene for Gaia and LAMOST, ed. S. Feltzing, G. Zhao, N. A. Walton, & P. Whitelock, 322–325

Beers, T. C., Allende Prieto, C., Wilhelm, R., Yanny, B., & Newberg, H. 2004, PASA, 21, 207

Casali, G., Magrini, L., Tognelli, E., et al. 2019, arXiv e-prints

Cirasuolo, M. & MOONS Consortium. 2016, in ASPC Series, Vol. 507, Multi-Object Spectroscopy in the Next Decade: Big Questions, Large Surveys, and Wide Fields, ed. I. Skillen, M. Balcells, & S. Trager, 109

Dalton, G., Trager, S. C., Abrams, D. C., et al. 2012, in Proc. SPIE, Vol. 8446, Ground-based and Airborne Instrumentation for Astronomy IV, 84460P

de Jong, R. S., Agertz, O., Berbel, A. A., et al. 2019, The Messenger, 175, 3

de Laverny, P., Recio-Blanco, A., Worley, C. C., & Plez, B. 2012, A&A, 544, A126

DESI Collaboration, Aghamousa, A., Aguilar, J., et al. 2016, arXiv e-prints

Freeman, K. & Bland-Hawthorn, J. 2002, ARA&A, 40, 487

Gilmore, G., Randich, S., Asplund, M., et al. 2012, The Messenger, 147, 25

Hayden, M. R., Recio-Blanco, A., de Laverny, P., et al. 2018, A&A, 609, A79

Hearnshaw, J. 2009, Astronomical Spectrographs and their History

Helmi, A., Babusiaux, C., Koppelman, H. H., et al. 2018, Nature, 563, 85

Katz, D., Munari, U., Cropper, M., et al. 2004, MNRAS, 354, 1223

Kordopatis, G., Wyse, R. F. G., Gilmore, G., et al. 2015, A&A, 582, A122

Lagarde, N., Reylé, C., Robin, A. C., et al. 2019, A&A, 621, A24

Liu, N., Fu, J.-N., Zong, W., et al. 2019, Research in Astronomy and Astrophysics, 19, 075

Magrini, L., Spina, L., Randich, S., et al. 2018, A&A, 617, A106

Majewski, S. R., APOGEE Team, & APOGEE-2 Team. 2016, Astronomische Nachrichten, 337, 863

Majewski, S. R., Wilson, J. C., Hearty, F., Schiavon, R. R., & Skrutskie, M. F. 2010, in IAUS, Vol. 265, Chemical Abundances in the Universe: Connecting First Stars to Planets, ed. K. Cunha, M. Spite, & B. Barbuy, 480–481

McConnachie, A., Murowinski, R., Salmon, D., Simons, D., & Côté, P. 2014, in Proc. SPIE, Vol. 9145, Ground-based and Airborne Telescopes V, 914519

Merle, T., Van Eck, S., Jorissen, A., et al. 2017, A&A, 608, A95

Newberg, H. J., Carlin, J. L., Chen, L., et al. 2012, in ASPC Series, Vol. 458, Galactic Archaeology: Near-Field Cosmology and the Formation of the Milky Way, ed. W. Aoki, M. Ishigaki, T. Suda, T. Tsujimoto, & N. Arimoto, 405

Pasquini, L., Avila, G., Allaert, E., et al. 2000, in Proc. SPIE, Vol. 4008, Optical and IR Telescope Instrumentation and Detectors, ed. M. Iye & A. F. Moorwood, 129–140

Prusti, T. 2012, Astronomische Nachrichten, 333, 453

Randich, S., Gilmore, G., & Gaia-ESO Consortium. 2013, The Messenger, 154, 47

Recio-Blanco, A., de Laverny, P., Allende Prieto, C., et al. 2016, A&A, 585, A93

Rojas-Arriagada, A., Recio-Blanco, A., Hill, V., et al. 2014, A&A, 569, A103

Spina, L., Randich, S., Magrini, L., et al. 2017, A&A, 601, A70

Steinmetz, M. 2003, in ASPC Series, Vol. 298, GAIA Spectroscopy: Science and Technology, ed. U. Munari, 381

Titarenko, A., Recio-Blanco, A., de Laverny, P., Hayden, M., & Guiglion, G. 2019, A&A, 622, A59

Van der Swaelmen, M., Merle, T., Van Eck, S., & Jorissen, A. 2018a, in SF2A-2018, 183–186

Van der Swaelmen, M., Van Eck, S., Gonneau, A., et al. 2018b, in SF2A-2018, 351–353

Wilkinson, M. I., Vallenari, A., Turon, C., et al. 2005, MNRAS, 359, 1306

Yanny, B., Rockosi, C., Newberg, H. J., et al. 2009, AJ, 137, 4377

Session 03

Stellar physics and Gaia

SF2A 2019
P. Di Matteo, O. Creevey, A. Crida, G. Kordopatis, J. Malzac, J.-B. Marquette, M. N'Diaye, O. Venot (eds)

GALACTIC CEPHEIDS WITH GAIA DR2 : PERIOD-LUMINOSITY RELATIONS AND IMPLICATIONS ON H_0

L. Breuval[1] and P. Kervella[1]

Abstract.
Cepheids represent a fundamental tool for measuring the distances in the Universe, thanks to the simple correlation between their pulsation periods and their instrinsic luminosity: the period-luminosity (PL) relation. In order to calibrate this relation accurately, precise distance measurements are required. However, the recent data releases of the Gaia satellite show that Cepheids parallaxes are subject to biases due to saturation and to the large amplitude of their color variation, which makes the improvement of the PL calibration impossible. In order to bypass this bias, we use the parallaxes of Cepheids detached companions as a proxy for the Cepheids parallaxes themselves, since they are stable and classical stars, to calibrate the Leavitt law. This new method also allowed us to estimate a value of 69 ± 2 km/s/Mpc for the Hubble constant, in agreement with the determination from the Planck satellite.

Keywords: Stars: variables: cepheids, Astrometry, Distance scale, Period-Luminosity relation.

1 Introduction

Through the relation between their pulsation period and absolute magnitude (Leavitt 1908), Cepheids gives us a direct access to distances and to the local value of the Hubble constant H_0. This cosmological parameter exhibits a 4.4σ tension between its two recent measurements (Planck Collaboration et al. 2018; Riess et al. 2019). However, the calibration of this law is still unsatisfactory because of the lack of precise Cepheid distances measurements. In order to determine precisely its coefficients, accurate Cepheid distance measurements are required.

The second Gaia data release (GDR2) was expected to provide the first alternative to Hubble Space Telescope distances, by publishing parallaxes of hundreds of Milky Way Cepheids of unprecedented precision. Unfortunately, several biases affect the GDR2 parallaxes of Cepheids. First, the astrometric solution is determined assuming a constant color for each star (Lindegren et al. 2018; Mowlavi et al. 2018). This ignores the color variations of pulsating stars, particularly significant in the case of Cepheids and Mira stars, which show the largest variations. Secondly, it has been shown (Riess et al. 2018b; Drimmel et al. 2019) that saturation problems affect the GDR2 astrometry of very bright stars ($G < 6$ mag). These issues make GDR2 Cepheid parallaxes unreliable for the calibration of the Leavitt law.

2 Method

Kervella et al. (2019) recently detected 28 bound resolved companion stars of Cepheids in the Milky Way. As they are photometrically stable stars, these companions are not subject to the chromaticity problem raised previously. Moreover, being a few magnitudes fainter than the Cepheids, they are not affected by saturation and belong to the best dynamical range for Gaia DR2 astrometry. For these reasons, the 28 companions from Kervella et al. (2019) represent an excellent proxy for GDR2 Cepheid parallaxes. In this work, we calibrate the Leavitt law assuming that the Cepheids and their bound companions share the same parallax.

In addition to the companions, we include in our sample two more stars with independently determined parallaxes: RS Pup, whose distance was accurately measured using the propagation of the light echoes in its

[1] LESIA (UMR 8109), Observatoire de Paris, PSL Research University, CNRS, UPMC, Univ. Paris-Diderot, 5 place Jules Janssen, 92195 Meudon, France

circumstelllar nebula (Kervella et al. 2017), and the binary Cepheid V1334 Cyg, whose distance was estimated by Gallenne et al. (2018) based on a spectroscopic and interferometric study of its orbit.

After removing the few stars with bad quality indicators, we investigated the pulsation mode of our Cepheids. We found 6 Cepheids pulsating in the first overtone mode, for which we fundamentalized the period through the relation given by Feast & Catchpole (1997), and two stars with uncertain pulsation mode that we decided to discard for safety. The final sample contains 23 companions and the two additional stars.

We adopted Astrometric Based Luminosities (ABL) as described by Arenou & Luri (1999), therefore no selection on positive parallaxes is required and the results are not subject to Lutz-Kelker bias (Lutz & Kelker 1973). We performed a weighted fit of the ABL function to determine the zero-point and the slope of the PL relation. A bootstrap technique iterated 50000 times ensures the robustness of the results and of the uncertainties.

The Gaia DR2 parallaxes are subject to a zero-point offset, a value that should be added to parallaxes and whose exact value is still under debate. Recent works estimate its value between 0.029 mas (Lindegren et al. 2018) and 0.082 mas (Stassun & Torres 2018). In our investigation, we vary this parameter and analyse its effect on the PL relation and on its dispersion.

3 Results and discussion

3.1 Cepheid versus companion parallaxes

The calibration of the Leavitt law using companion parallaxes is represented in the K_S band in Fig. 1. The same calibration obtained with Cepheid parallaxes gives a higher χ^2 value compared with companions parallaxes, even though the error bars are smaller. Moreover, GDR2 parallaxes and the two additional stars are in better agreement when the parallaxes are those of the companions. As stated previously, Cepheid parallaxes are subject to a bias due to the absence of chromaticity correction. The uncertainties on Cepheid parallaxes are therefore underestimated compared with the error bars given by GDR2. We infer that using companions as a proxy for Cepheid parallaxes is reliable.

3.2 Influence of the GDR2 parallax offset

We then vary the value of the parallax zero-point offset between 0.029 mas and 0.100 mas and we find that the dispersion of the points increases with the offset. The zero-point and the slope of the PL relation are both sensitive to the offset value. For example, for offset values of 0.029 mas and 0.070 mas, we obtain respectively $K_S = -5.893_{\pm 0.048} - 3.341_{\pm 0.161}\,(\log P - 1)$ and $K_S = -5.844_{\pm 0.057} - 3.290_{\pm 0.196}\,(\log P - 1)$. For reasonable offset values, the derived magnitudes agree within their error bars.

In the following, we fix the GDR2 zero-point offset to 0.029 mas, which gives the smallest dispersion and which is also the offset adopted by Kervella et al. (2019) in the search for the companions.

3.3 Comparison with other Leavitt law calibrations

We compare our Leavitt law calibration with different results from the literature. We considered the result of Groenewegen (2018) who uses a large sample of GDR2 Cepheid parallaxes (in the case where the parallax offset is set to 0.029 mas), and also the calibrations by Benedict et al. (2007) and Fouqué et al. (2007), based on HST/FGS parallaxes of bright Cepheids. The corresponding PL relations are represented in Fig. 1, in green, dark red and orange, respectively.

In the present range of periods, our calibration agrees well with Groenewegen (2018), even though this author finds a slightly different slope. However, the two calibrations based on HST/FGS parallaxes differ by $\sim$0.2 mag from our Leavitt law. This discrepancy may be explained by a HST/FGS zero-point offset on the order of 0.2 mas that has not yet been considered, or alternatively by a GDR2 parallax offset significantly larger than the current estimation, of at least $\sim$0.15 mas.

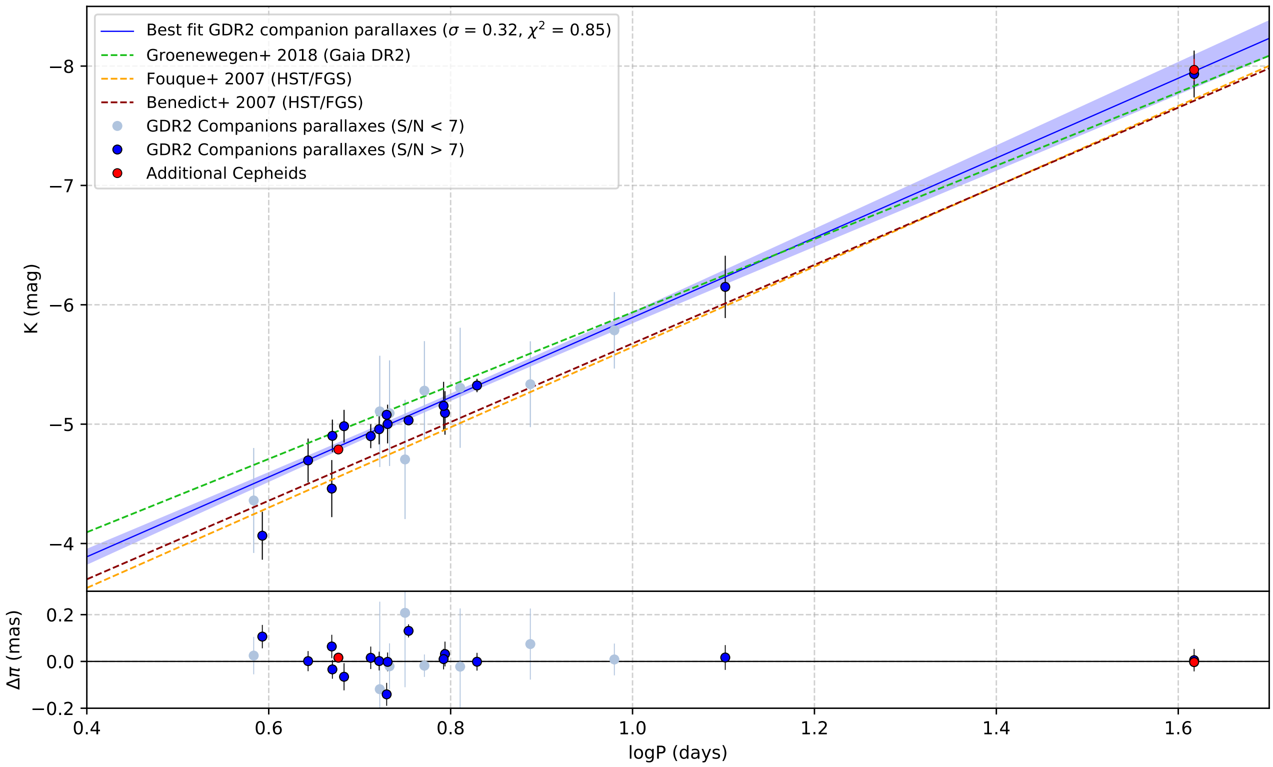

Fig. 1. PL relation in the K_S band based on GDR2 companion parallaxes, and comparison with other relations found in the literature. We adopted a GDR2 parallax offset of 0.029 mas.

4 Consequences on the local value of the Hubble constant

Following the approach presented by Riess et al. (2018a), we use our Leavitt law calibration to rescale the value of the Hubble constant from Riess et al. (2019), hereafter $H_{0,\,\mathrm{R19}}$. These authors determined $H_{0,\,\mathrm{R19}}$ based on LMC Cepheids whose distance was set to the 1% value found by Pietrzyński et al. (2019). The rescaled value $H_{0,\,\mathrm{Gaia}}$ is obtained through the relation : $H_{0,\,\mathrm{Gaia}} = \alpha\, H_{0,\,\mathrm{R19}}$ where $\alpha = \pi_{\mathrm{Gaia}}/\pi_{\mathrm{R19}}$. For each star of our sample, we estimated the parallaxes π_{Gaia} and π_{R19} respectively with our PL relation and with the corresponding Leavitt law from Riess et al. (2019), both in the Wesenheit W_H magnitude. The final estimation of $H_{0,\,\mathrm{Gaia}}$ is computed as a weighted mean of each individual value.

The result strongly depends on the GDR2 parallax offset: taking an offset of 0.029 mas leads to $H_{0,\,\mathrm{Gaia}} = 68.43 \pm 2.08\ \mathrm{km\,s^{-1}\,Mpc^{-1}}$, while an offset of 0.070 mas returns $H_{0,\,\mathrm{Gaia}} = 70.53 \pm 2.08\ \mathrm{km\,s^{-1}\,Mpc^{-1}}$. For a reasonably small offset, our Leavitt law calibration translates into a value of H_0 statistically compatible with the Planck Collaboration et al. (2018) estimate, who predicted $H_0 = 67.4 \pm 0.5\ \mathrm{km\,s^{-1}\,Mpc^{-1}}$.

5 Conclusion

The use of GDR2 companion parallaxes as a proxy for Cepheids allows to bypass the bias due to the chromaticity problem and the saturation issues. The derived PL relation exhibits a small dispersion, confirming the interest of the method. The inconsistency between the present PL calibration and results based on HST/FGS parallaxes shows that a zero-point offset may be required on the latter, or that the offset on GDR2 parallaxes is more significant than currently estimated. This discrepancy also translates into a lower value of H_0 compared with the estimation by Riess et al. (2019), in agreement with Planck Collaboration et al. (2018).

The future Gaia Data Releases are expected to provide more precise parallaxes, and possibly a better knowledge of the parallax offset. The correction of time variable chromaticity effect in the Gaia astrometry, which is not yet considered in the Gaia data reduction, is essential for a PL calibration directly based on Cepheid parallaxes.

References

Arenou, F. & Luri, X. 1999, in Astronomical Society of the Pacific Conference Series, Vol. 167, Harmonizing Cosmic Distance Scales in a Post-HIPPARCOS Era, ed. D. Egret & A. Heck, 13–32

Benedict, G. F., McArthur, B. E., Feast, M. W., et al. 2007, AJ, 133, 1810

Drimmel, R., Bucciarelli, B., & Inno, L. 2019, Research Notes of the American Astronomical Society, 3, 79

Feast, M. W. & Catchpole, R. M. 1997, MNRAS, 286, L1

Fouqué, P., Arriagada, P., Storm, J., et al. 2007, A&A, 476, 73

Gallenne, A., Kervella, P., Evans, N. R., et al. 2018, ApJ, 867, 121

Groenewegen, M. A. T. 2018, A&A, 619, A8

Kervella, P., Gallenne, A., Evans, N. R., et al. 2019, A&A, 623, A117

Kervella, P., Trahin, B., Bond, H. E., et al. 2017, A&A, 600, A127

Leavitt, H. S. 1908, Annals of Harvard College Observatory, 60, 87

Lindegren, L., Hernández, J., Bombrun, A., et al. 2018, A&A, 616, A2

Lutz, T. E. & Kelker, D. H. 1973, PASP, 85, 573

Mowlavi, N., Lecoeur-Taïbi, I., Lebzelter, T., et al. 2018, A&A, 618, A58

Pietrzyński, G., Graczyk, D., Gallenne, A., et al. 2019, Nature, 567, 200

Planck Collaboration, Aghanim, N., Akrami, Y., et al. 2018, arXiv e-prints

Riess, A. G., Casertano, S., Yuan, W., et al. 2018a, ApJ, 855, 136

Riess, A. G., Casertano, S., Yuan, W., et al. 2018b, ApJ, 861, 126

Riess, A. G., Casertano, S., Yuan, W., Macri, L. M., & Scolnic, D. 2019, ApJ, 876, 85

Stassun, K. G. & Torres, G. 2018, ApJ, 862, 61

SF2A 2019
P. Di Matteo, O. Creevey, A. Crida, G. Kordopatis, J. Malzac, J.-B. Marquette, M. N'Diaye, O. Venot (eds)

DIFFERENTIAL CHEMICAL ABUNDANCES OF BENCHMARK OPEN CLUSTERS

L. Casamiquela[1], C. Soubiran[1] and Y. Tarricq[1]

Abstract. Open Clusters (OCs) are very good laboratories to test theories of stellar evolution. They have also been widely used as tracers of the formation and evolution of the Galactic disk. Nearby OCs with different ages and metallicities are commonly used as benchmark objects for galactic and stellar studies because high precision measurements are usually achievable. We aim to perform a detailed study of ∼30 nearby (closer than 500 pc) and old (age>300 Myr) OCs. Thanks to Gaia DR2, accurate memberships, distances, motions and ages are available for a large amount of OCs, allowing us to revise their physical properties. Here we show the preliminary results of the strictly line-by-line differential abundances of three targets: the Hyades, NGC 2632 (Praesepe) and Ruprecht 147.

Keywords: (Galaxy:) open clusters and associations: individual: Hyades, NGC 2632, Ruprecht 147, Stars: abundances, Techniques: spectroscopic

1 Introduction

OCs are groups of stars which were born together and that still stay together nowadays. They have recieved much attention lately because: i) they are good targets to test theories of stellar evolution since stellar population covers a large range of spectral types, ii) they trace the history of the galactic disk, iii) nearby OCs spanning different ages and chemical compositions are used to validate and calibrate astrometric, photometric and spectroscopic surveys (e.g. Gaia, APOGEE, RAVE, WEAVE among many others).

Most of the stars are thought to be formed in clusters. However, due to internal interactions between members, encounters with giant molecular clouds, among other effects, they tend to disrupt during the first Myr of evolution. So, old OCs which have overcomed these effects are important targets to understand the formation and evolution of the Galactic disk.

We have designed a project to investigate nearby evolved OCs with a purpose of building a list of benchmark OCs. Our goal is to determine physical properties in the light of Gaia DR2 data and combined with high precision spectroscopy and photometry. We determine the shape, radii, extincion, velocity, age, chemical composition, of the most nearby OCs, allowing us to investigate a handful of things from the kinematical properties in relation with their environment, to explore their outskirts.

At small distances we can benefit of the highest accuracy of the Gaia data, obtaining very reliable memberships. Also, for these clusters we are able to obtain high quality ground spectroscopy of a large number of stars sampling different spectral types. We are computing high precision chemical abundances of highly probable member stars to investigate the chemical signature of these benchmark clusters.

In this contribution we present the results of the chemical abundance characterisation of our three first targets: the Hyades, NGC 2632 and Ruprecht 147.

2 Selection of targets

We have selected a list of evolved OCs within a radius of ∼500 pc around the Sun, with an age similar to that of the Hyades (∼300 Myr) or older.

We have used the list of clusters and their membership from Cantat-Gaudin et al. (2018), Gaia Collaboration et al. (2018) and Castro-Ginard et al. (2018). We use radial velocities in Gaia DR2 to exclude less probable

[1]

members, and perform a color cut to restrict our targets to FGK spectral types. With this we obtain a list of ∼2800 candidate stars in 43 OCs.

Several of the selected targets are very bright, so a lot of them have been observed in the literature before and we can find their spectra in public archives. We have queried the selection of stars in the available public archives for high resolution ($R > 45,000$) and high signal-to-noise (SNR> 50) spectra. We have found spectra from different instruments: UVES@VLT (Paranal Observatory), HARPS@3.6m and FEROS@2.2mMPG/ESO (La Silla Observatory), FIES@NOT and HARPS-N@TNG (El Roque de los Muchachos Observatory), ESPaDOnS@CFHT (Mauna Kea Observatory), NARVAL@TBL (Pic du Midi Observatory), ELODIE@1.93m telescope (Haute-Provence Observatory).

We have also included several spectra of stars without archive information from our own observational programs in NARVAL@TBL.

3 Method

We have analyzed more than 1200 spectra corresponding to 176 stars in 17 OCs. Several spectra correspond to the same star, in this case the spectra were coadditionated to gain SNR. Very often the same star was observed with the same instrument several times, these cases have been used for validation purposes.

We have used `iSpec` (Blanco-Cuaresma et al. 2014; Blanco-Cuaresma 2019) to derive radial velocities, atmospheric parameters ($T_{\rm eff}$, $\log g$, [M/H]) and abundances using spectral synthesis fitting. `iSpec` is a very poweful spectroscopic tool which allows to perform all types of computation to stellar spectra, including atomatic line finding and fitting from an inputed linelist, and execution of a bunch of radiative transfer codes.

The results of the atmospheric parameters of the three analyzed clusters (Fig. 1) show a clear narrow main sequence and red clump for each cluster. The locus of the main sequence turnoff and red clump for Ruprecht 147 is slightly shifted probably because of its age.

We obtain absolute and differential chemical abundances of elements belongig to different nucleosynthetic channels. We have developed a dedicated automatic pipeline (adapted from the one used in Blanco-Cuaresma & Fraix-Burnet (2018)) to perform a strictly line-by-line differential abundance method. This consists in analyzing groups of stars which have very similar spectra together, so-called twins.

Abundances are computed line-by-line and choosing one of the stars in the group as a reference, instead of the Sun. This allows to reach a very high precision in abundances because it erases the differences coming from wrong atomic parameters and other effects, which are commonly dependent on spectral type.

We have made 11 groups of stars maximizing the number of grouped stars in the HR diagram drawn by the cluster stars, see Fig. 1. We have picked as reference of each group a star in the Hyades cluster, except for the giants of Ruprecht 147, which have significantly different temperatures and gravities that the giants of the Hyades.

4 Chemical abundance results

In this section we show the abundance results of the Hyades for 14 chemical species.

We have used stars observed with different instruments to assess our uncertainties. We show in the right hand plot in Fig 1 the resulting abundances in one of the groups of the Hyades ($5700 < T_{\rm eff} < 5850$). As an example, we show Fe, Si and Ca abundances computed differentially for the different spectra (crosses) and the mean values computed per star (circles). The standard deviations obtained using the values of the different spectra are of the order of 0.01 dex, same level of the quoted uncertainties.

For all the analyzed stars in the Hyades, we have obtained overall dispersions in abundances of the order of 0.03-0.05 dex, depending of the chemical species, slightly larger than the typical uncertainties. In Fig. 2 we show an histogram of the dispersion in abundance for the Hyades divided by the mean uncertainty. All values are larger than 1, showing that indeed the dispersions are slightly significant w.r.t. the errors in all chemical species.

We have also obtained significant correlations in the differential abundances between all pairs of elements. Sometimes interpreted as a sign of chemical inhomogeity. In Fig 3 we show the dependencies of the abundances of different elements w.r.t. Fe abundances.

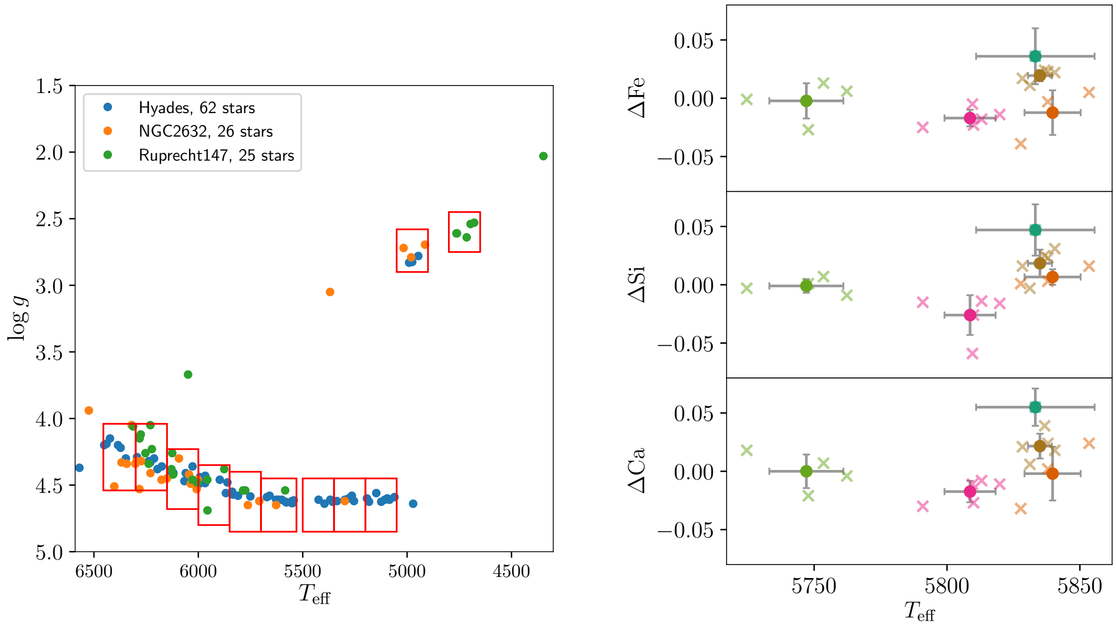

Fig. 1. Left: Resulting HR diagram of the analyzed sample of stars. Red boxes show the 11 groups made to perform the differential analysis. **Right:** Fe, Si and Ca differential abundances of one of the group of stars of the Hyades w.r.t. $T_{\rm eff}$. Crosses are the results of different instruments of the same star, circles are the mean values and standard deviations per star.

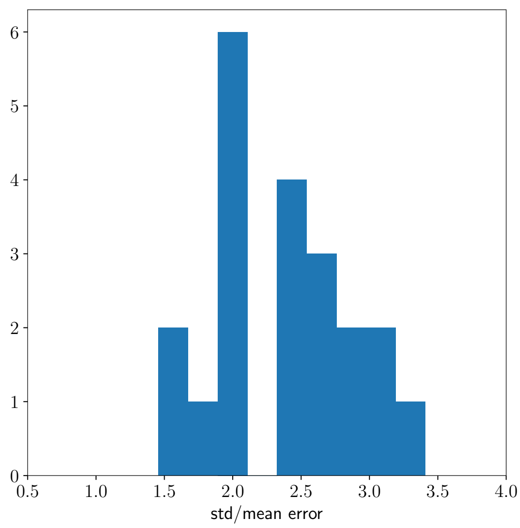

Fig. 2. Histogram of the dispersion in abundance divided by the mean uncertainties for each element analyzed.

5 Discussion

A similar analysis as the one we have done in this work was previously performed by Liu et al. (2016) using 16 solar analogs in the Hyades.

In this contribution we have extended the usage of the differential analysis technique to other spectral types, not only solar analogs. We have obtained similar results of abundance dispersions and correlations as those of

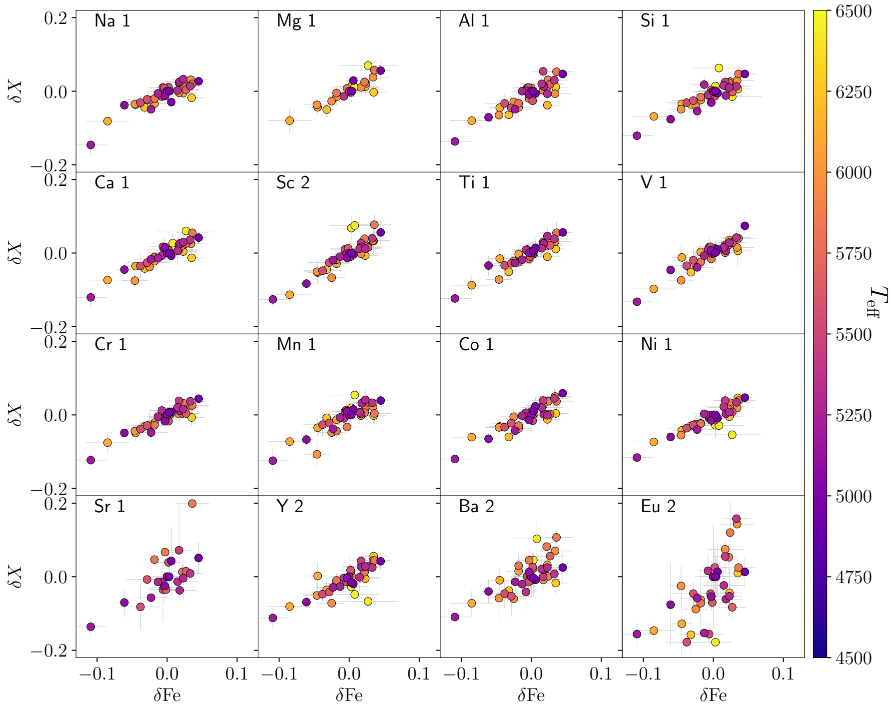

Fig. 3. Differential abundances of several elements as a function of Fe one for the stars in the Hyades cluster. The color code represents the effective temperature of each star.

Liu et al. (2016). We have shown that this is a usefull technique to investigate the abundances inside a cluster.

The results point towards the existence of some kind of inhomogeneity in the chemical abundances of the Hyades. As for future work we will analyze in detail the abundances of the other clusters.

We acknowledge support from the "programme national de physique stellaire" (PNPS) and from the "programme national cosmologie et galaxies" (PNCG) of CNRS/INSU.

References

Blanco-Cuaresma, S. 2019, MNRAS, 486, 2075

Blanco-Cuaresma, S. & Fraix-Burnet, D. 2018, A&A, 618, A65

Blanco-Cuaresma, S., Soubiran, C., Heiter, U., & Jofré, P. 2014, A&A, 569, A111

Cantat-Gaudin, T., Jordi, C., Vallenari, A., et al. 2018, A&A, 618, A93

Castro-Ginard, A., Jordi, C., Luri, X., et al. 2018, A&A, 618, A59

Gaia Collaboration, Babusiaux, C., van Leeuwen, F., et al. 2018, A&A, 616, A10

Liu, F., Yong, D., Asplund, M., Ramírez, I., & Meléndez, J. 2016, MNRAS, 457, 3934

SF2A 2019
P. Di Matteo, O. Creevey, A. Crida, G. Kordopatis, J. Malzac, J.-B. Marquette, M. N'Diaye, O. Venot (eds)

THE ATMOSPHERIC DYNAMICS OF AGB STARS REVEALED BY GAIA THROUGH NUMERICAL SIMULATIONS

A. Chiavassa[1], B. Freytag[2] and M. Schultheis[1]

Abstract.
A considerable fraction of the detected intrinsically variable stars in Gaia data are Long-Period Variables. These objects have large luminosity amplitudes and variability timescales. They have complex stellar surface dynamics that affect the measurements and amplify the uncertainties on stellar parameters.

We explore the impact of the convection-related surface structure in AGBs on the photocentric variability. We quantify these effects to characterise the observed parallax errors and estimate fundamental stellar parameters and dynamical properties.

For this purpose, we use state-of-the-art three-dimensional (3D) radiative hydrodynamics simulations of convection with CO5BOLD and the post-processing radiative transfer code OPTIM3D to compute intensity maps in the Gaia G band [325 – 1030 nm]. Then, we calculate the intensity-weighted mean of all emitting points tiling the visible stellar surface (i.e. the photocentre) and evaluate its motion as a function of time. We show that the convection-related variability accounts for a substantial part of the Gaia DR2 parallax error of our sample of semi-regular variables. We prospect the roadmap to extract quantitatively fundamental properties of AGB stars directly from Gaia errors exploiting appropriate RHD simulations.

Keywords: stars: atmospheres, stars: AGB and post-AGB, astrometry, parallaxes

1 Introduction

Gaia (Gaia Collaboration et al. 2016) is an astrometric, photometric, and spectroscopic space-borne mission. It performs a survey of a large part of the Milky Way. The second data release (Gaia DR2 Gaia Collaboration et al. 2018) brought high-precision astrometric parameters (i.e. positions, parallaxes, and proper motions) for over 1 billion sources brighter that $G \approx 20$. The time resolution of the Gaia measurements allows the classification and detailed study of an unmatched number of variable objects. A considerable fraction of the detected intrinsically variable stars are Long-Period Variables (LPVs), that have large luminosity amplitudes and variability timescales that are covered adequately by Gaia (Gaia Collaboration et al. 2019). Recently, Holl et al. (2018) found 151 761 LPV candidates that fulfil these characteristics.

LPVs are cool luminous evolved stars which reached a critical phase of their evolution and increased the mass-loss ejections. They are characterised: (i) by large-amplitude variations in radius, brightness, and temperature of the star; and (ii) by a strong mass-loss rate driven by an interplay between pulsation, dust formation in the extended atmosphere, and radiation pressure on the dust (Höfner & Olofsson 2018). LPVs eject a significant fraction of their mass by stellar winds contributing extensively to the cosmic matter cycle. They provide substantial amounts of chemically enriched gas and dust grains to the interstellar medium, and thereby to new generations of stars and planets.

The surface of the deep convection zone of those objects are characterised by large and small convective cells. The visible fluffy stellar surface is made of shock waves that are produced in the interior and are shaped by the top of the convection zone as they travel outward (Freytag et al. 2017). In addition to this, in the optical thin region and on the top of the convection-related surface structures (i.e. further up in the atmosphere with respect to the continuum-forming region) also the opacity affects the observable domain. In particular at the wavelengths in Gaia G-band (Evans et al. 2018), where TiO molecules produce strong absorptions. All these

[1] Université Côte d'Azur, Observatoire de la Côte d'Azur, CNRS, Lagrange, CS 34229, Nice, France
[2] Department of Physics and Astronomy at Uppsala University, Regementsvägen 1, Box 516, SE-75120 Uppsala, Sweden

effects alter the position of the photocentre and cause temporal fluctuations during the Gaia mission, as already pointed out for red supergiant stars in Chiavassa et al. (2011).

In this work, we explore the impact of the variability of the stellar surface granulation-related structures on Gaia parallax determination and explore the possibility to extract stellar properties, such as the fundamental stellar parameters, may be hidden behind the Gaia measurement uncertainty.

2 Observation sample

First we selected a sample of semiregular variables from different catalogues (Tabur et al. 2009; Glass & van Leeuwen 2007; Jura et al. 1993) with luminosities ($4000 < L_{\odot} < 8000$) matching the theoretical luminosities from RHD simulations introduced in next section. Then, we extracted the corresponding parallax error (σ_{ϖ}) from Gaia DR2. More details about the cross-identification with the distance catalogue of Bailer-Jones et al. (2018) are reported in Chiavassa et al. (2018). Ultimately, it has to be noted that σ_{ϖ} may still vary in the following data releases because: (i) the mean number of measurements for each source amounts to 26 (Mowlavi et al. 2018) and this number will be 70-80 in total at the end of the nominal mission; (ii) and new solutions may be applied to adjust the imperfect chromaticity correction (Arenou et al. 2018).

3 Gaia measurements decrypted with numerical simulations

3.1 Methods

We aim at obtaining intensity maps in the Gaia G photometric system (Evans et al. 2018) combining the thermodynamic structures of the outer layers of the atmosphere AGB stars with detailed radiative transfer calculation.
For this purpose, we used the radiation-hydrodynamics (RHD) simulations of AGB stars (Freytag et al. 2017) computed with the CO5BOLD code (Freytag et al. 2012). The code solves the coupled non-linear equations of compressible hydrodynamics and non-local radiative energy transfer in the presence of a fixed external spherically symmetric gravitational field in a three-dimensional (3D) cartesian grid. It is assumed that solar abundances are appropriate for M-type AGB stars. The basic stellar parameters of the RHD simulations are reported in Table 1. In the simulations, convection, waves, and shocks all contribute to the dynamical pressure and, therefore, to an increase of the stellar radius and to a levitation of material into layers where dust can form. No dust is included in any of these simulations. The regularity of the pulsations decreases with decreasing gravity as the relative size of convection cells increases. The pulsation period is extracted with a fit of the Gaussian distribution in the power spectra of the simulations. The period of the dominant mode increase with the radius of the simulation (Freytag et al. 2017).
Then, we employed the code OPTIM3D (Chiavassa et al. 2009), which takes into account the Doppler shifts caused by the convective motions, to computed intensity maps based on snapshots from the RHD simulations of Table 1. The code uses pre-tabulated extinction coefficients per unit mass (same as in Gustafsson et al. 2008) as a function of temperature, density, and wavelength for the solar composition (Asplund et al. 2009). Micro-turbulence broadening is set to zero.

Table 1. RHD simulation parameters.

Simulation	$M_\star$ $[M_\odot]$	$L_\star$ $[L_\odot]$	$R_\star$ [AU]	$T_{\rm eff}$ [K]	$\log g$ [cgs]	$t_{\rm avg}$ [yr]	$P_{\rm puls}$ [yr]	$\sigma_{\rm puls}$ [yr]	$\langle P\rangle$ [AU]	σ_P [AU]
st26gm07n002	1.0	6986	2.04	2524	-0.85	25.35	1.625	0.307	0.262	0.187
st26gm07n001	1.0	6953	1.87	2635	-0.77	27.74	1.416	0.256	0.275	0.198
st28gm06n26	1.0	6955	1.73	2737	-0.70	25.35	1.290	0.317	0.241	0.152
st29gm06n001	1.0	6948	1.62	2822	-0.65	25.35	1.150	0.314	0.266	0.174
st27gm06n001	1.0	4982	1.61	2610	-0.64	28.53	1.230	0.088	0.150	0.101
st28gm05n002	1.0	4978	1.46	2742	-0.56	25.35	1.077	0.104	0.133	0.077
st28gm05n001	1.0	4990	1.40	2798	-0.52	25.36	1.026	0.135	0.183	0.131
st29gm04n001	1.0	4982	1.37	2827	-0.50	25.35	0.927	0.100	0.152	0.078

The table shows the simulation name, the mass $M_\star$, then several time-averaged quantities: emitted luminosity $L_\star$, stellar radius $R_\star$, effective temperature $T_{\rm eff}$, surface gravity $\log g$, pulsation period $P_{\rm puls}$, the half of the distribution of the pulsation frequencies $\sigma_{\rm puls}$, and the stellar time $t_{\rm avg}$ used for the averaging. All these quantities are from Freytag et al. (2017). The last two columns are the time-averaged value of the photocentre displacement ($\langle P\rangle$) and its standard deviation (σ_P), as in Chiavassa et al. (2018).

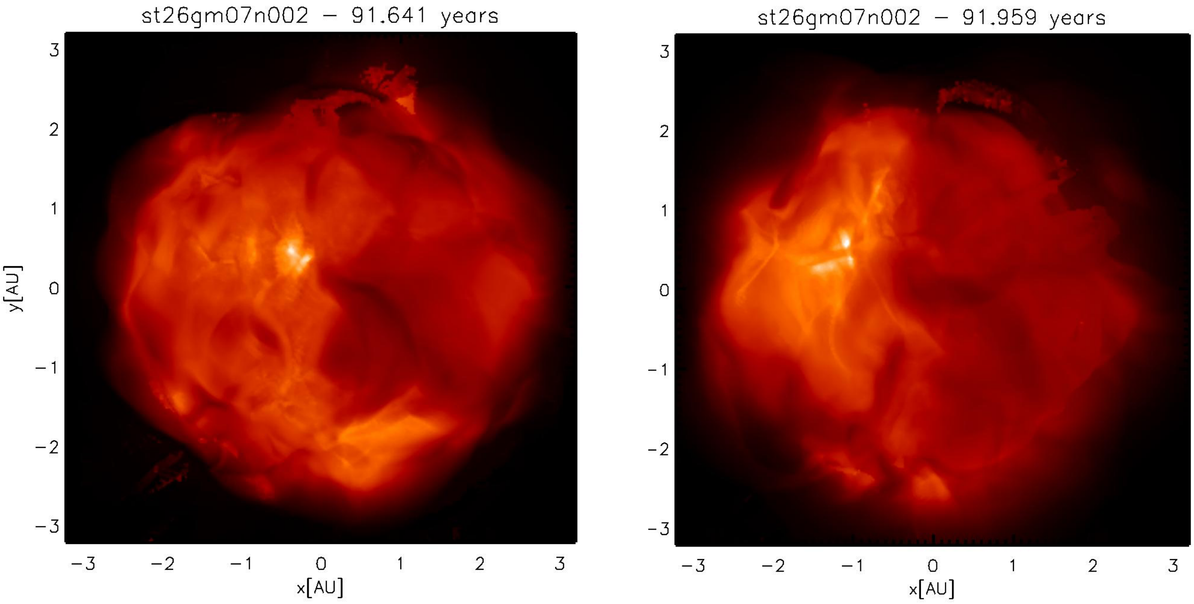

Fig. 1. Example of the squared root intensity maps (the range is $[0. - \sqrt{3000.}]$ erg/s/cm^2/Å) in the Gaia G photometric system (from 325 to 1030 nm, Evans et al. 2018) for two different snapshots of one simulation listed in Table 1. The number on the top indicates the stellar times at which the two snapshots were computed. This figure is similar to Fig. 1 of Chiavassa et al. (2018) but for another simulation.

3.2 Comparison with observations

In the Gaia G photometric system, few large surface structures with sizes of a third of the stellar radii (≈ 0.6 AU) are visible (Fig. 1). They evolve on a temporal scale of several months to a few years, as well as a few short-lived (weeks to month) convective cells at smaller scales ($< 10\%$ of the stellar radius).

We calculated the position of the photocentre for each map (i.e. as a function of time) as the intensity-weighted mean of the $x - y$ positions of all emitting points tiling the visible stellar surface according to

$$P_x = \frac{\sum_{i=1}^{N} \sum_{j=1}^{N} I(i,j) * x(i,j)}{\sum_{i=1}^{N} \sum_{j=1}^{N} I(i,j)} \tag{3.1}$$

$$P_y = \frac{\sum_{i=1}^{N} \sum_{j=1}^{N} I(i,j) * y(i,j)}{\sum_{i=1}^{N} \sum_{j=1}^{N} I(i,j)}, \tag{3.2}$$

where $I\,(i,j)$ is the emerging intensity for the grid point (i,j) with coordinates $x(i,j)$, $y(i,j)$ of the simulation, and $N = 281$ is the total number of grid points in the simulated box. In the presence of surface brightness asymmetries, the photocentre position does not coincide with the barycentre of the star and its position change as the surface pattern changes with time. The time-averaged photocentre position ($\langle P \rangle$) and its standard deviations (σ_P) are reported in Table 1 for all the RHD simulations. Depending on the simulation, σ_P varies between 0.077 and 0.198 AU ($\approx$5 to $\approx$11% of the corresponding stellar radius, Chiavassa et al. 2018). The value of σ_P is mostly fixed by the short time scales corresponding to the small atmospheric structures and it is increasing with lower surface gravity (Fig. 2).

Fig. 3 (left panel) displays Gaia parallax errors against the luminosity and compares these results to the standard deviations of the photocentre displacement in the simulations from Table 1. The latter show good agreement with the observations. This attests that convection-related variability accounts for a substantial part of the parallax error in Gaia measurements (Chiavassa et al. 2018). However, the observed and simulated luminosities do not coincide exactly and the observed error bars are still very large. One limitation of the

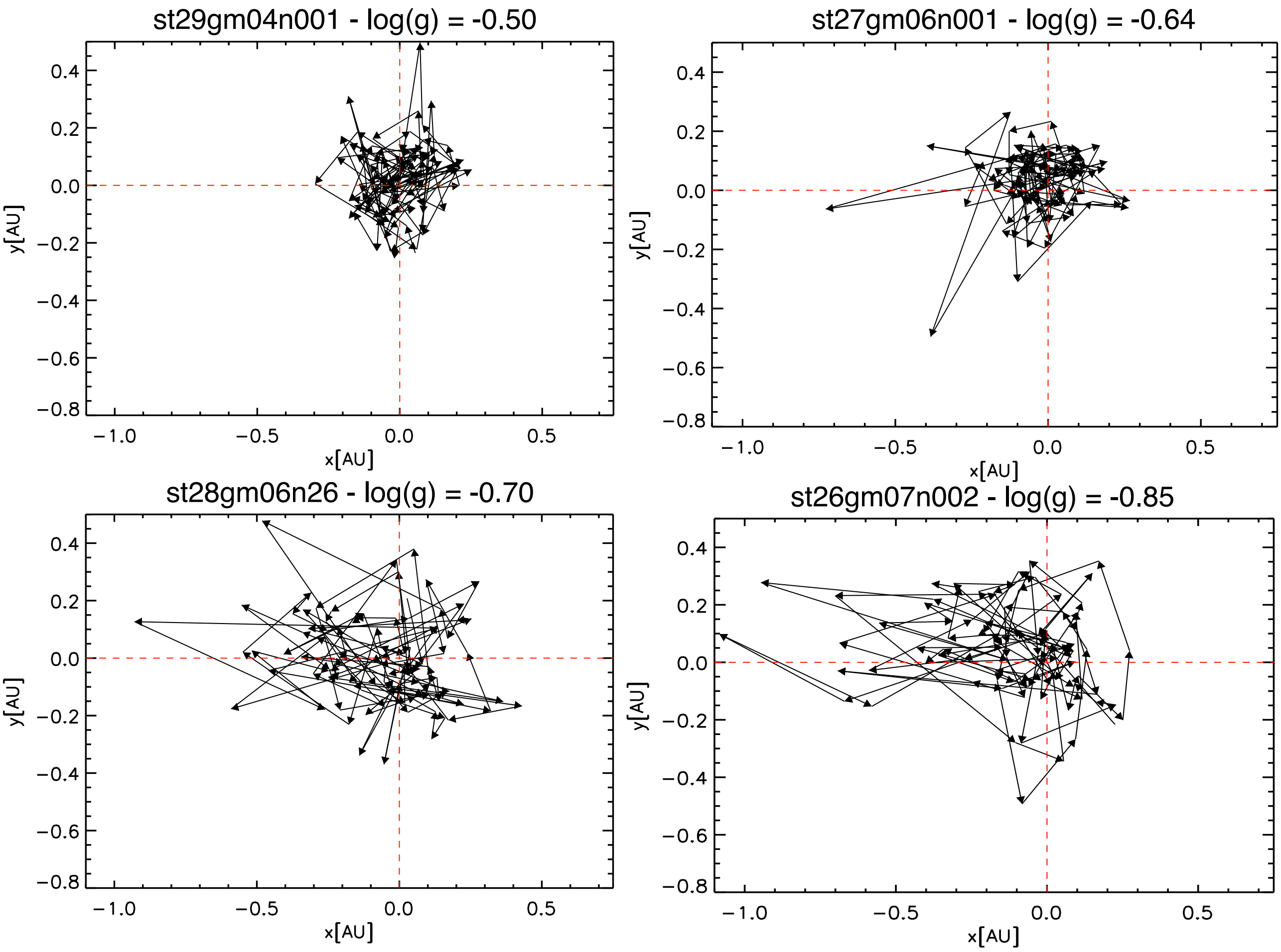

Fig. 2. Photocentre positions computed from four different RHD simulations of Table 1 in the Gaia G band filter. The different snapshots are connected by the line segments; the total time covered is reported in the Table. The dashed lines intersect at the position of the geometrical centre of the images.

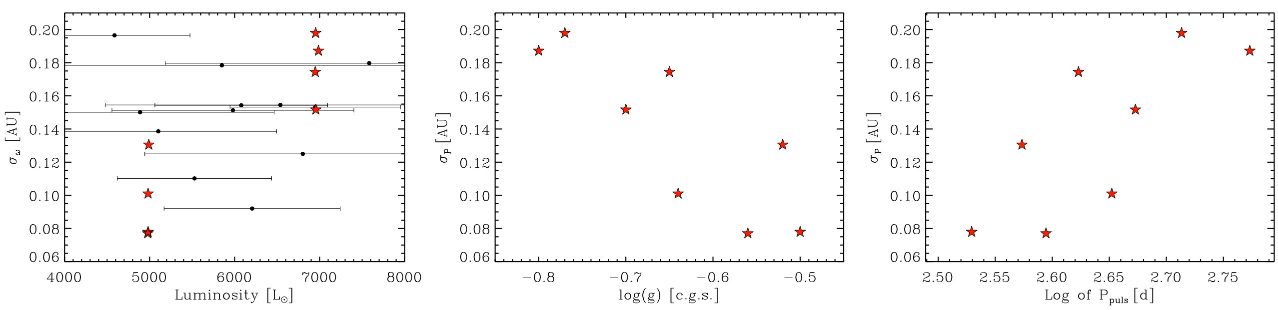

Fig. 3. *Left panel:* Luminosity against the parallax error of the observations (σ_ϖ, circle symbol in black) and the standard deviation of the photocentre displacement for the RHD simulations of Table 1 (σ_P, star symbol in red). *Central panel:* σ_P against the surface gravity for the RHD simulations. *Right panel:* σ_P against the logarithm of the period. This figure is from Chiavassa et al. (2018).

existing model grid is the restriction to 1 $M_\odot$. In the future, there will be models with other masses available.

Using the stellar parameters extracted from RHD simulations (Table 1), Chiavassa et al. (2018) denoted a correlation between the mean photocentre displacement and those quantities as plotted in Fig. 3. The central panel displays that lower surface gravity (i.e. more extended atmospheres) causes larger excursions of the photocentre. This behaviour is explained by the correlation between the stellar atmospheric pressure scale height ($H_p \approx \frac{T_{\rm eff}}{g}$) and the photocentre displacement (Freytag 2001; Ludwig 2006; Chiavassa et al. 2011). Larger values of σ_P correspond to longer pulsation periods (Fig. 3, right panel). This result is likely associated with the P-L relation found by Freytag et al. (2017), who showed that the periods in RHD simulations are consistent with observed periods of Whitelock et al. (2009).

Given the fact that σ_P explains Gaia measurement uncertainties on the parallaxes, we suggest that parallax variations from Gaia measurements could be exploited quantitatively using appropriate RHD simulations to extract, in a unique way, the fundamental properties of AGB stars such as the surface gravity and the pulsation periods. The first governs the size of granules that, in turn, controls the photometric variations. The second gives important information about stellar (mean) interior with information about global shocks induced by large-amplitude, radial, and fundamental-mode pulsations.

4 Conclusions and future perspectives within the next Gaia Dara Releases

We used the snapshots from RHD simulations of AGB stars with different stellar parameters to compute intensity maps in the Gaia G photometric system. We found that the stellar dynamics in the simulations induce an intrinsic noise to the measurement uncertainty on the parallax of a sample of AGB stars in the solar neighbourhood and cross-matched with data from the Gaia DR2. The good agreement in the comparisons suggests that convection-related variability accounts for a substantial part of the parallax error, as already pointed out in Chiavassa et al. (2018). Moreover, an important piece of information is indeed hidden in the Gaia measurement uncertainty. The fundamental properties of AGB stars could be measured directly from Gaia parallax and photometric errors exploiting quantitatively appropriate RHD simulations.

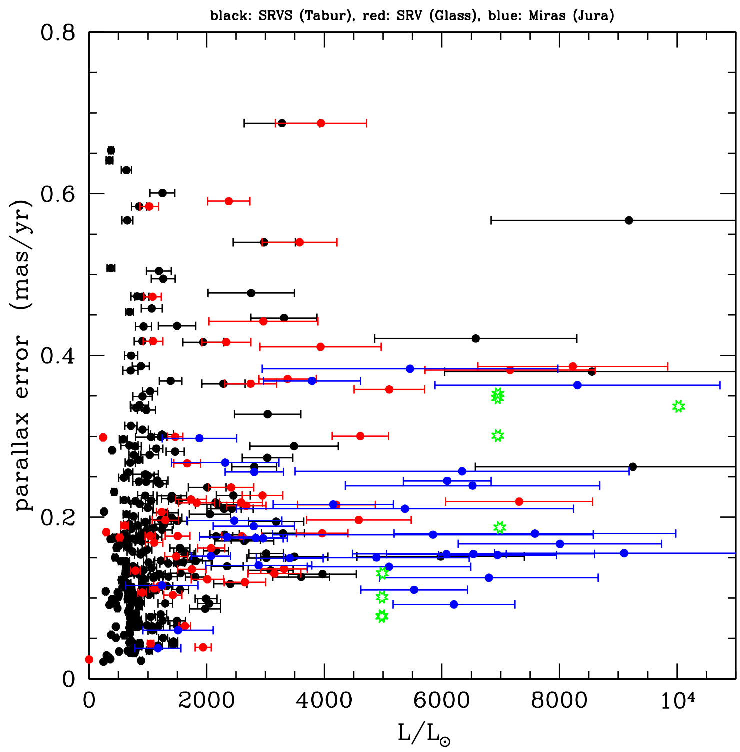

Fig. 4. Parallax error from Gaia DR2 as a function of their luminosity for a sample of semiregular variables from (Tabur et al. 2009, black), (Glass & van Leeuwen 2007, red), and (Jura et al. 1993, blue) marked with different colors. The light green stars denote the position of the RHD simulations form Table 1.

This requires a series of steps that we list here for the next years:

- Study of the photometric Radial Velocity predicted signatures from current RHD simulations grid. Chiavassa et al. (2011) showed that massive evolved red supergiant stars, with close enough stellar parameters to AGBs, have magnitude excursion up to 0.28 and 0.13 magnitudes in the blue and red Gaia photometric filters, respectively, with a strong impact on the parameter determination. We expected similar (or higher) values for AGBs.

- Significantly larger RHD simulation grid (at least 5 times more simulations with respect to the actual grid) is necessary to explore a large number of AGBs in Gaia. Fig. 4 displays a larger sample of variables from different catalogues for which Gaia DR2 data have provided measurements. Today RHD simulations (light green stars) cover only a small region of the parameter space.

- With Gaia DR2, the mean number of measurements for each source amounts to ≈ 26 (Mowlavi et al. 2018). Eventually, when Gaia DR4 will be available in 2022, the number of measurements will increase to 70-80, and possibly reducing the parallax error. In addiction to this, also the temporal variation of the photometric and astrometric measurements will be available making conceivable a direct and more precise comparison with the time-dependent RHD simulations.

In the end, combining our unique global 3D simulations with Gaia data will make it possible to systematically study the properties of convection in stars other than the sun.

This work has made use of data from the European Space Agency (ESA) mission Gaia (https://www.cosmos.esa.int/gaia), processed by the Gaia Data Processing and Analysis Consortium (DPAC, https://www.cosmos.esa.int/web/). Funding for the DPAC has been provided by national institutions, in particular the institutions participating in the Gaia Multilateral Agreement. This work has been supported by the Swedish Research Council (Vetenskapsrdet). The computations were performed on resources (rackham) provided by SNIC through Uppsala Multidisciplinary Center for Advanced Computational Science (UPPMAX) under Projects snic2017-1-41 and snic2018-3-74.

References

Arenou, F., Luri, X., Babusiaux, C., et al. 2018, A&A, 616, A17

Asplund, M., Grevesse, N., Sauval, A. J., & Scott, P. 2009, ARA&A, 47, 481

Bailer-Jones, C. A. L., Rybizki, J., Fouesneau, M., Mantelet, G., & Andrae, R. 2018, AJ, 156, 58

Chiavassa, A., Freytag, B., & Schultheis, M. 2018, A&A, 617, L1

Chiavassa, A., Pasquato, E., Jorissen, A., et al. 2011, A&A, 528, A120

Chiavassa, A., Plez, B., Josselin, E., & Freytag, B. 2009, A&A, 506, 1351

Evans, D. W., Riello, M., De Angeli, F., et al. 2018, A&A, 616, A4

Freytag, B. 2001, in Astronomical Society of the Pacific Conference Series, Vol. 223, 11th Cambridge Workshop on Cool Stars, Stellar Systems and the Sun, ed. R. J. Garcia Lopez, R. Rebolo, & M. R. Zapaterio Osorio, 785

Freytag, B., Liljegren, S., & Höfner, S. 2017, A&A, 600, A137

Freytag, B., Steffen, M., Ludwig, H. G., et al. 2012, Journal of Computational Physics, 231, 919

Gaia Collaboration, Brown, A. G. A., Vallenari, A., et al. 2018, A&A, 616, A1

Gaia Collaboration, Eyer, L., Rimoldini, L., et al. 2019, A&A, 623, A110

Gaia Collaboration, Prusti, T., de Bruijne, J. H. J., et al. 2016, A&A, 595, A1

Glass, I. S. & van Leeuwen, F. 2007, MNRAS, 378, 1543

Gustafsson, B., Edvardsson, B., Eriksson, K., et al. 2008, A&A, 486, 951

Höfner, S. & Olofsson, H. 2018, A&A Rev., 26, 1

Holl, B., Audard, M., Nienartowicz, K., et al. 2018, A&A, 618, A30

Jura, M., Yamamoto, A., & Kleinmann, S. G. 1993, ApJ, 413, 298

Ludwig, H. G. 2006, A&A, 445, 661

Mowlavi, N., Lecoeur-Taïbi, I., Lebzelter, T., et al. 2018, A&A, 618, A58

Tabur, V., Bedding, T. R., Kiss, L. L., et al. 2009, MNRAS, 400, 1945

Whitelock, P. A., Menzies, J. W., Feast, M. W., et al. 2009, MNRAS, 394, 795

SF2A 2019
P. Di Matteo, O. Creevey, A. Crida, G. Kordopatis, J. Malzac, J.-B. Marquette, M. N'Diaye, O. Venot (eds)

CEPHEID DISTANCE MEASUREMENTS OF SNIA HOST GALAXIES

B. Javanmardi[1] and P. Kervella[1]

Abstract. One of the most fundamental cosmological parameters is the current expansion rate of the Universe, i.e. the Hubble Constant (H_0). Recent studies revealed a significant tension between the local measurements of H_0 using Cepheids plus Type Ia Supernovae (SNIa) and the measurements from the cosmic microwave background (CMB) observations. This tension calls for thorough investigations and it is extremely important to understand its source which could be new physics beyond the standard model of cosmology, or systematic issues in the measurements. In this project, we aim to perform an independent accurate Cepheid distance measurement to the SNIa host galaxies in the local Universe, a crucial step for the determination of H_0.

Keywords: Stars: variables: Cepheids, Galaxies: distances and redshifts, Cosmology: distance scale

1 The Local and Cosmic Measurements of H_0 are in Tension

Before the CMB observations by the Planck satellite, the local (empirical) measurements of H_0 have been in agreement with the predictions from the CMB analyses. However, the results from Planck Collaboration et al. (2014, 2016) revealed a tension between these two sets of measurements. This tension became more significant with the reportedly precise direct measurements by Riess et al. (2016, 2018). Figure 1 shows the local and cosmic measurements of H_0 since 2001 to present.

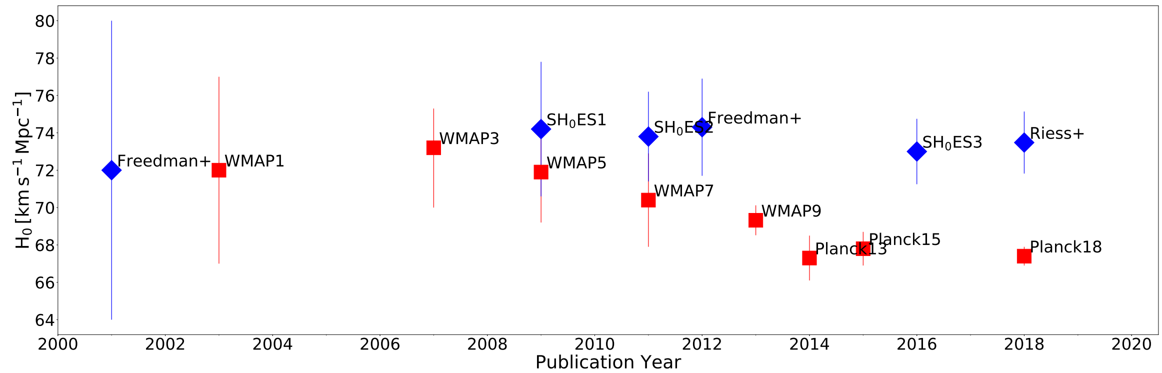

Fig. 1. Local (blue diamonds) and CMB (red squares) measurements of H_0 vs. their publication years.

2 Accurate distance measurements to SNIa hosts using Cepheids

Obtaining an accurate local value of H_0 involves a series of crucial steps each of which should be performed with utmost care. To use cepheids in distant galaxies to calibrate SNIa magnitudes, it is very important to have an accurate period-luminosity (PL) relation for Cepheids in the Milky Way (e.g. by using Gaia parallaxes, Breuval & et al. 2019) and the Large Magellanic Cloud (using independent and precise distance measurements,

[1] LESIA, Observatoire de Paris, PSL Research University, CNRS, UPMC, Univ. Paris Diderot, 5 place Jules Janssen, 92195 Meudon, France

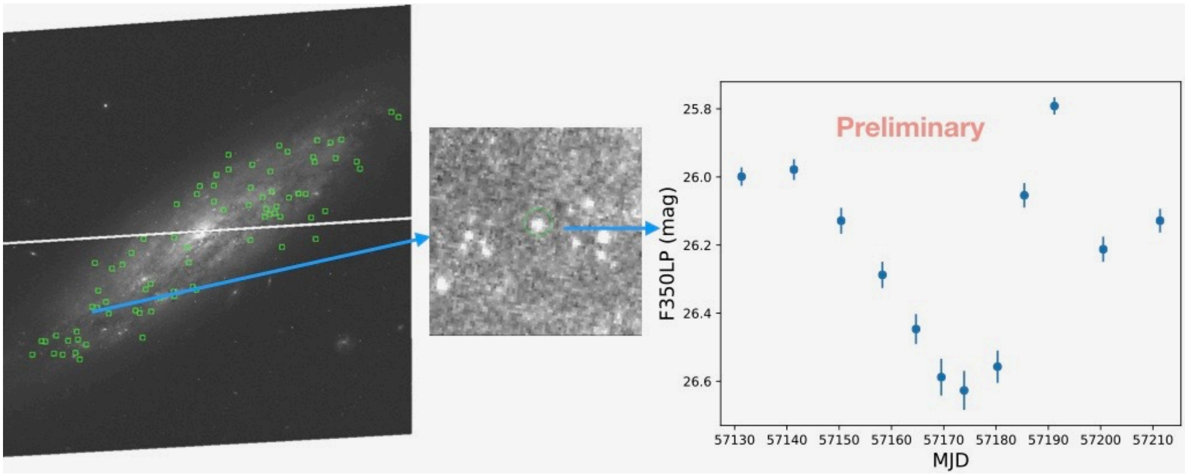

Fig. 2. Left: HST image of NGC 3972, Cepheids positions are shown with green squares. **Center**: A cutout region centered on one of the Cepheids in NGC 3972. **Right**: A preliminary photometry result of that Cepheid in F350LP band vs. Modified Julian Date (MJD).

Pietrzyński et al. 2019). In addition, to understand and control various possible systematics, it is necessary to perform detailed studies of the physics of these fascinating variable stars (see e.g. Kervella et al. 2019a,b; Borgniet et al. 2019; Hocde & et al. 2019). And last but not least, an accurate photometry of Cepheids in SNIa host galaxies by taking into account the various sources of systematic uncertainties is needed to robustly constrain the value of H_0. The latter is the main aim of this project.

Riess et al. (2016) have used the Hubble Space Telescope (HST) observations of 19 supernovae host galaxies in the local Universe. In this ongoing work, we have started with the photometry of more than 70 identified Cepheids (Hoffmann et al. 2016) in the galaxy NGC 3972 (shown in the left panel of Figure 2). This galaxy has been observed in 12 epochs in 2015 using the F350LP filter on the WFC3/UVIS camera. A representative cepheid in this galaxy and its preliminary light curve are shown in the center and the right panels of Figure 2, respectively.

3 Next Steps

We are currently working on accurate PSF photometry of the Cepheids in SNIa galaxies. The next steps involve corrections for crowding and metallicity effects, and accurate modeling of the light curves to measure periods and mean luminosities. Our independent distance measurements to these SNIa host galaxies would either reveal or rule out systematic issues as a possible source of the tensions in the H_0 measurements.

We thank Fateme Kamali for kindly providing us with the H_0 vs. publication years plot (Fig. 1). This study has made use of Astroconda, AstroDrizzle, and Matplotlib packages, and the MAST data Archive.

References

Borgniet, S., Kervella, P., Nardetto, N., et al. 2019, A&A, 631, A37
Breuval, L. & et al. 2019, A&A, submitted
Hocde, V. & et al. 2019, A&A, submitted
Hoffmann, S. L., Macri, L. M., Riess, A. G., et al. 2016, ApJ, 830, 10
Kervella, P., Gallenne, A., Evans, N. R., et al. 2019a, A&A, 623, A117
Kervella, P., Gallenne, A., Remage Evans, N., et al. 2019b, A&A, 623, A116
Pietrzyński, G., Graczyk, D., Gallenne, A., et al. 2019, Nature, 567, 200
Planck Collaboration, Adam, R., Ade, P. A. R., et al. 2016, A&A, 594, A1
Planck Collaboration, Ade, P. A. R., Aghanim, N., et al. 2014, A&A, 571, A1
Riess, A. G., Casertano, S., Yuan, W., et al. 2018, ApJ, 855, 136
Riess, A. G., Macri, L. M., Hoffmann, S. L., et al. 2016, ApJ, 826, 56

SF2A 2019
P. Di Matteo, O. Creevey, A. Crida, G. Kordopatis, J. Malzac, J.-B. Marquette, M. N'Diaye, O. Venot (eds)

NEW ULTRACOOL DWARFS IN GAIA DR2

C. Reylé[1]

Abstract. Detailed population studies of ultracool dwarfs are persistently plagued by incompleteness. While hundreds of ultracool dwarfs have been uncovered in red and infrared sky surveys, this population remains incomplete, even in the solar neighborhood, due to their faint magnitudes. The Gaia mission has provided the means to uncover nearby VLM dwarfs through astrometric, rather than purely photometric, selection. This holds the promise of a truly volume-complete sample.

In this paper, we present the content of *Gaia* DR2 at the low-mass end. We first investigate the known sample of ultracool stars and brown dwarfs retrieved in *Gaia* DR2 and compare it with the up-to-date BT-Settl atmosphere models. We next show that thousands of new candidates are revealed by *Gaia* DR2, covering the whole sky. Over 200 candidates have measured distances of less than 30 parsec, showing that even the nearby census is not complete.

Keywords: Stars: low-mass – Brown dwarfs – Solar neighbourhood – Galaxy: stellar content – Surveys: *Gaia* – Catalogs: *Gaia* DR2

1 Introduction

The *Gaia* mission (Gaia Collaboration et al. 2016b) provides full sky coverage down to the *Gaia* magnitude G = 20 (V$\simeq$20-22), at the spatial resolution of the HST, with about 70 observations per source over 5 years. Trigonometric parallaxes – with the amazing precision of 1% up to 2.5 kpc at the end of the mission– and proper motions are now measured for 1.3 billions stars.

As highlighted in the scientific demonstration paper from Gaia Collaboration et al. (2018a), *Gaia* astrometry and photometry are powerful tools for studying fine structures within the Hertzsprung-Russell (HR) diagram. It is now possible to distinguish the locus of different type of objects, as model-predicted, including at the low-mass end of the HR diagram.

Ultra-cool dwarfs have been defined by Kirkpatrick et al. (1997) as M7 and later main sequence stars. This corresponds to an effective temperature of $\lesssim$ 2700 K (Rajpurohit et al. 2013). These objects serve as a link between known stars and brown dwarfs. Indeed, they span the stellar/sub-stellar mass transition: such an effective temperature in expected in a 0.03 $M_\odot$ object of 8 Myr or in a 0.095 $M_\odot$ object of 10 Gyr (Baraffe et al. 2015), both at solar metallicity.

Smart et al. (2017) compiled an input catalogue of known L and T dwarfs, with estimated *Gaia* magnitude G<20.3, within the reach of Gaia. They identified part of them in *Gaia* DR1 (Gaia Collaboration et al. 2016a). They found 321 L and T dwarfs, with 10 >=L7, which corresponds to 45% of the brown dwarfs bright enough to be seen by *Gaia*. As they pointed out, this incompleteness is mainly due to the cuts made in the catalogue to insure the quality of the data. With eight more months of observations, *Gaia* DR2 (Gaia Collaboration et al. 2018b) should provide more complete and precise data, and help to fill that gap. Recent discoveries show that even the local census is not complete as illustrated by the discovery of a L7 at 11 pc, close to the galactic plane (Scholz & Bell 2018; Faherty et al. 2018).

In a first step, we search for known ultra-cool and brown dwarfs in *Gaia* DR2 and investigate their properties using their *Gaia* observations (section 2). In a second step, we use the properties from the known sample to show the potential of *Gaia* DR2 to reveal new candidates (section 3). The conclusions and perspectives are given in section 4.

[1] Institut UTINAM, CNRS UMR6213, Univ. Bourgogne Franche-Comté, OSU THETA Franche-Comté-Bourgogne, Observatoire de Besançon, BP 1615, 25010 Besançon Cedex, France

2 Already known ultra-cool and brown dwarfs found in Gaia DR2

We focus on the well-characterized sample of ultra-cool and brown dwarfs, having a spectroscopic spectral type. A compilation of all L, T and Y dwarfs that *Gaia*should directly observe, or indirectly constrain (e.g. in a common proper motion systems with brighter members), the so-called *Gaia*Ultracool Dwarf Sample (GUCDS), has been published in Smart et al. (2017). GUCDS is based on the on-line census compiled by J. Gagné* which contains all objects from the Dwarfarchives† database, complemented by the Dupuy & Liu (2012) and Mace (2014) catalogs. Some of these objects have an information on their age or metallicity, and are listed in the census as young candidates or subdwarfs. Smart et al. (2017) added the recent discoveries from Marocco et al. (2015); Faherty et al. (2016). This catalog has 1886 entries, with 1010 L and 58 T dwarfs having a predicted G magnitude brighter than 21.5, within the reach of *Gaia*.

To this census, we add the ultra-cool (M7-M9.5) dwarfs listed by J. Gagné‡, and the new spectroscopically confirmed objects from Rajpurohit et al. (2014); Robert et al. (2016); Faherty et al. (2018); Zhang et al. (2018). Because we want to study the location in the fine *Gaia* DR2 HR diagram of a well-characterized sample, the numerous candidates found in photometric surveys without spectroscopic confirmation are not included.

We retrieve these entries in *Gaia* DR2 and found 3671 ultra-cool ($\geq$M7), 647 L, and 16 T dwarfs. Twenty six are noted in the census as subdwarfs, and 75 as young candidates. The spectral type distribution of the input catalog (black line), the sample with an entry in *Gaia* DR2 (gray line), and the sub-sample with $\sigma_\varpi \leq 10\%$ (filled-gray) is shown in Fig. 1, left panel.

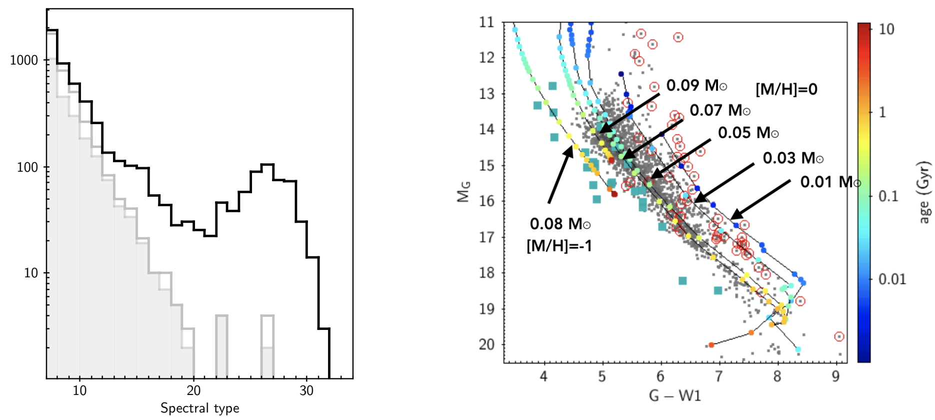

Fig. 1. Left : Spectral type distribution of the known ultracool ($\geq$M7) and brown dwarfs. 10 stands for L0 and 20 for T0, 30 for Y0 on the spectral type axis. **Right :** BT-Settl evolution tracks superimosed with the known sample. Mass and metallicity of the tracks are indicated. The color-bar gives the logarithm of the age in Gyr.

We built the HR diagram by computing the absolute *Gaia* magnitude in the G band for individual stars using $M_G = G - 5\log_{10}(1000/\varpi) + 5$, where ϖ is the parallax in milli arcsec. The simple distance determination from ϖ is valid when $\sigma_\varpi \lesssim 20\%$ (Luri et al. 2018).

Fig. 2 shows the HR diagram of the known sample. We use G-G_{RP} as the color index (upper left panel), as these faint and red objects have lower flux in the BP bandpass. In the other panels, we show the HR diagram with color indices using 2MASS and WISE bandpasses, using the cross-match of *Gaia* DR2 with 2MASS and WISE provided in the *Gaia* archive (Marrese et al. 2017).The red circles and cyan squares show the objects found to have low gravity (young objects) and low metallicity (subdwarfs) from there spectrum. Thanks to the high accuracy of these diagrams, the locus of young objects and subdwarfs can be separated from other objects, in particular when using the WISE bands, where the end of the sequence splits into two parts.

Thus this well characterized sample provides an unprecedent dataset - with distance estimate - to define absolute magnitude versus color, and versus spectral type relations (Reylé 2018; Smart et al. 2019). Furthermore the parallaxe is a strong added-value to test and refine evolution and atmosphere models. As an illustration,

*https://jgagneastro.wordpress.com/list-of-ultracool-dwarfs/
†http://dwarfarchives.org
‡https://jgagneastro.wordpress.com/list-of-m6-m9-dwarfs/

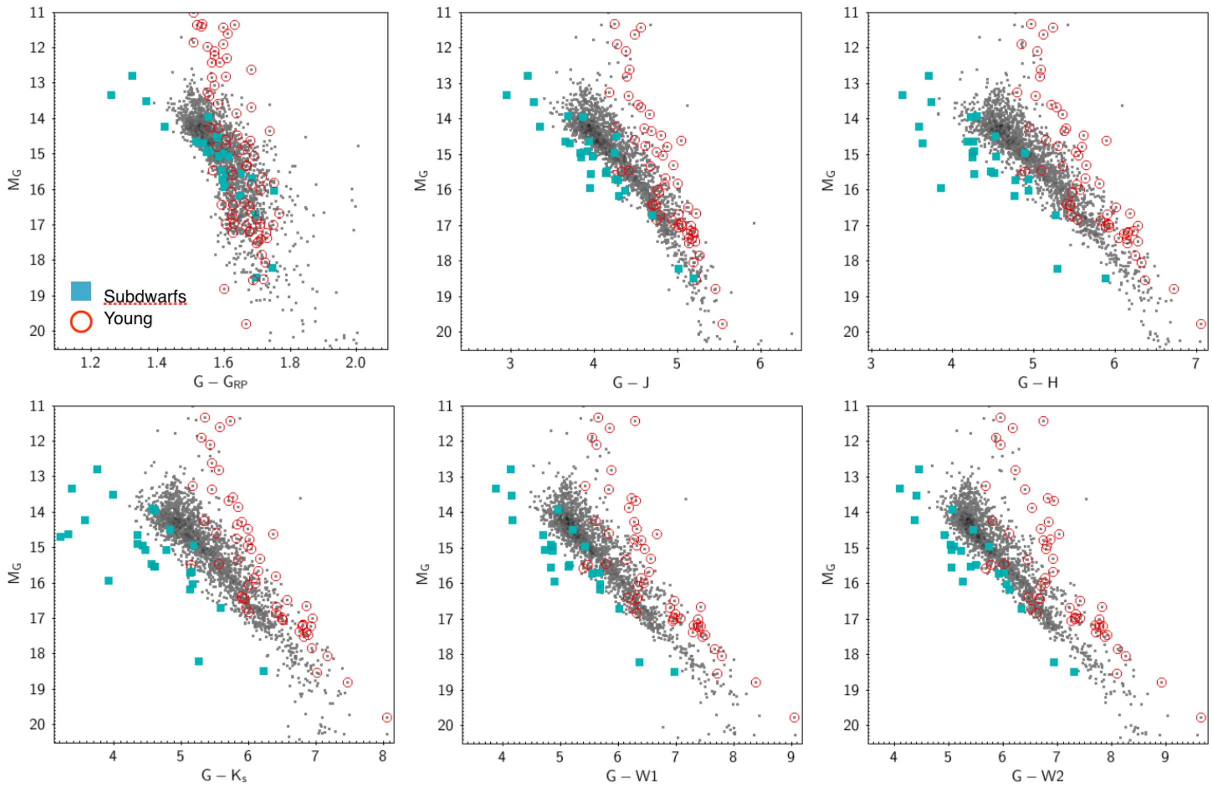

Fig. 2. HR diagram of the known ultra-cool dwarfs found in *Gaia* DR2.

Fig. 1, right panel, shows a comparison with the evolutionary models from Baraffe et al. (2015) that consistently couple interior structure calculations with the BT-Settl atmosphere models (Allard et al. 2013). The comparison tends to confirm the locus of the objects as a function of their peculiarities (age, metallicity).

3 New ultra-cool and brown dwarf candidates in Gaia DR2

Our aim is to find candidates robust candidates, so we applied trong filter on *Gaia* DR2. These filters are fully described in (Gaia Collaboration et al. 2018a, , and references therein). Here we only give a brief description of their effects. They retain objects with $\sigma_{M_G} < 0.22$ mag, $\sigma_G < 0.022$ mag, $\sigma_{G_{RP}} < 0.054$ mag, reliable five parameters solution (astrometric and photometric), and remove most artifacts. The corresponding *Gaia* archive[§] query is given in the annexe B of Gaia Collaboration et al. (2018a). Following Gaia Collaboration et al. (2018a), we also restrict the sample to low extinction regions in the Milky Way, and keep the objects with $E(B-V) < 0.015$ according to the 3D extinction map of Capitanio et al. (2017). The resulting fine HR diagram can be seen in Fig. 3 (left panel).

The HR diagram has a fuzzy appearance between the white dwarfs and the main sequence, and redward of the main sequence. This can be explained by a background contamination in the blue (BP) and red (RP) photometers. These objects with color excess can be rejected using an empirical filter, as defined by Evans et al. (2018); Arenou et al. (2018). The resulting HR diagram when applying this filter is shown in the middle panel of Fig. 3. Because ultra-cool and brown dwarfs have low flux in the BP bandpass, they are very sensitive to any background over-estimation yielding to a high color excess. As a consequence, most of these objects are rejected, as can be clearly seen at the low-mass end of the main sequence. As an illustration, applying this filter on the known sample dramatically removes 47% of the objects (68% of the L and T dwarfs) found in *Gaia* DR2.

In Reylé (2018) we define a more suitable criterion to retain these faint and red objects, which does not rest upon the BP flux, but on the 2MASS J magnitude. Note that the use of the J magnitude is rejecting ∼20% of

[§]https://gea.esac.esa.int/archive/

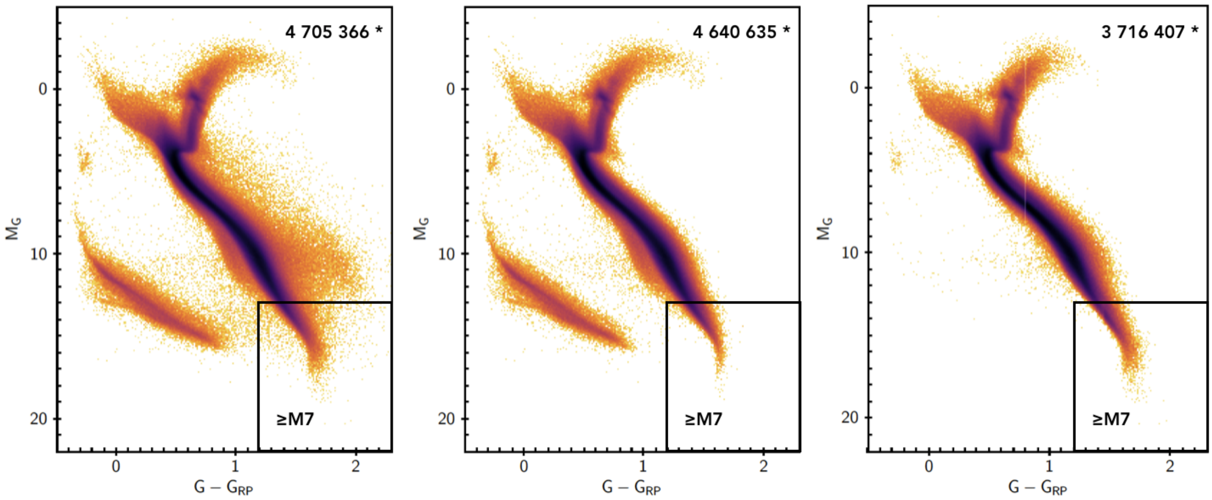

Fig. 3. The HR diagram of *Gaia* DR2. See text for the description of the different selections. The squares show the expected locus of M7 and later dwarfs.

the candidates with no 2MASS counterpart or a 2MASS photometric quality flag $Q_{fl} \neq$ AAA. The removing of objects below this limit allows to get rid of objects with spurious colors but still to retain the low-mass objects, as well as most of the already known sample. The resulting HR diagram is shown in the right panel of Fig. 3.

Fig. 4 focuses on the *Gaia* DR2 HR diagram at the low-mass end, superimposed with the sample of spectroscopically confirmed ultracool dwarfs retrieved in *Gaia* DR2.

We use the information on the spectral type to define separations in the HR diagram. They are shown by the lines on the left panel. We also use the peculiarities of the known sample to tentatively define regions where subdwarfs and young candidates are expected to be dominant (dashed lines on the right panel). These selections suggest that *Gaia* DR2 contains a large number of new candidates : 14 176 $\geq$ M7 and 488 L (all earlier than L5). Among them 233 $\geq$ M7 and 70 L are young candidates, and 466 $\geq$ M7 and 17 L are subdwarfs candidates. These are, of course, indicative numbers. They are published on a table available on-line [¶].

Fig. 5 shows the sky distribution of known (left) and new candidates (right). The new candidates are evenly distributed across the sky, filling in "missing" populations in the Southern hemisphere and Galactic plane. The imprint of the *Gaia*scanning law is visible on the plot, where no candidates are found in some Galactic regions, which are rejected as they do not fulfill our conditions. Thus new candidates are expected to be found in the forthcoming *Gaia*data releases.

Fig. 6 shows the distance distribution of known (pink) and *Gaia* DR2 new candidates (blue) L (left) and >M7 (right) dwarfs. Whereas several recent efforts (see Best et al. 2018) were made to complete the volume-limited sample of brown dwarfs up to 25 pc, *Gaia* shows that the census is not complete beyond 30 pc. The situation is even worst for >M6 dwarfs, which is not surprising since we only consider here the objects with spectroscopic confirmation. The ongoing and future spectroscopic large survey such as APOGEE (Majewski et al. 2017), LAMOST (Cui et al. 2012), WEAVE (Dalton et al. 2014), 4MOST (de Jong et al. 2016) will soon complete the census further away.

4 Conclusion

Gaia DR2 reveals numerous new ultracool candidates. The given numbers are indicative only but they also prove that the census is not complete yet, even locally. *Gaia* DR2 contains 65% of all bright enough objects estimated to be within the reach of *Gaia*. Moreover *Gaia* DR2 is an intermediate release, on which we applied strong filters. Thus further releases may provide even more candidates.

The high precision of the HR diagram allows us to give an indication of some of the characteristics of these

[¶]http://vizier.u-strasbg.fr/viz-bin/VizieR?-source=J/A+A/619/L8

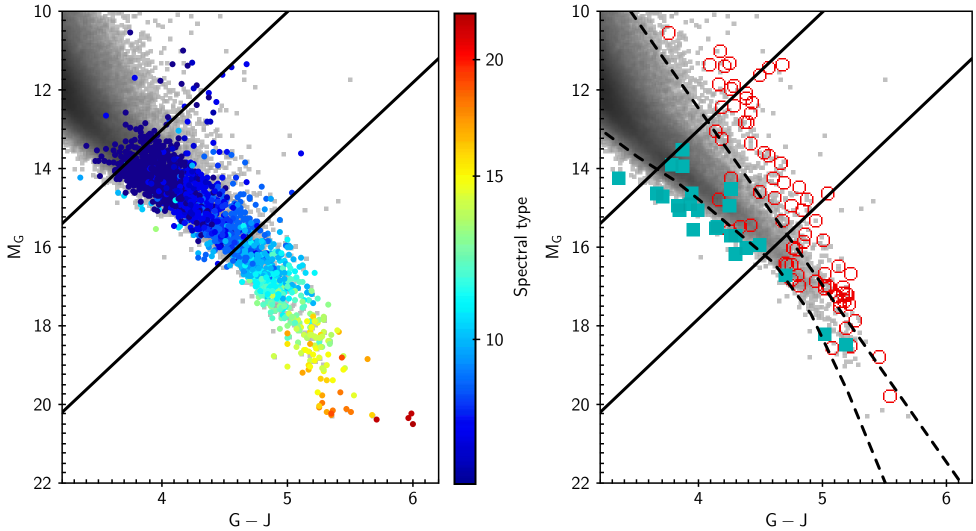

Fig. 4. HR diagram of the filtered *Gaia* DR2 at the low-mass end, superimposed with the already known, spectroscopic sample. Left: $M_G$vs G-G_{RP}. The color-code is function of spectral type and allows to define three regions, shown by the the lines: >M7, L, and T dwarfs. Right: $M_G$vs G-J. Squares are the known subdwarfs, open circles are the young candidates. The dashed lines aim to separate these different types.

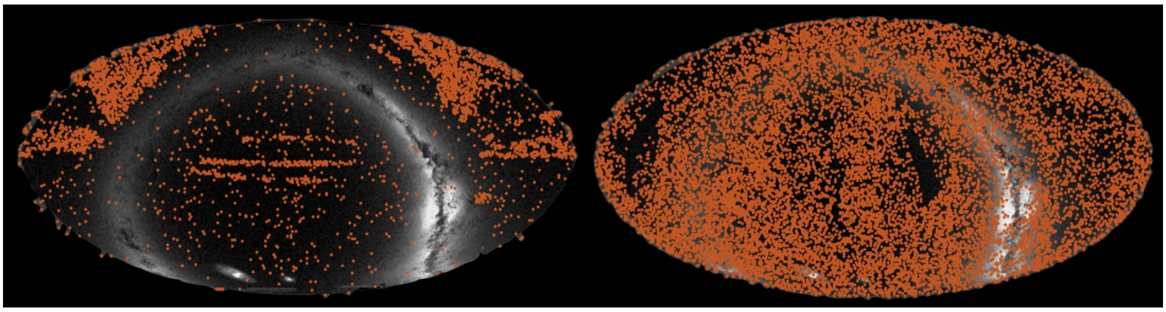

Fig. 5. Sky distribution in galactic coordinates of known ultracool dwarfs having a counterpart in *Gaia* DR2 (left), and of all candidates found in *Gaia* DR2 (right).

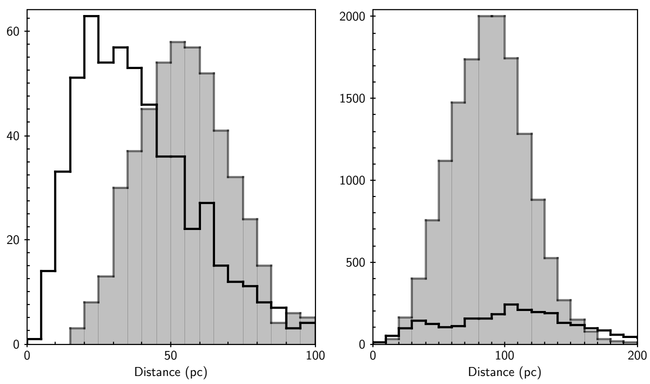

Fig. 6. Distance distribution of the L (left) and >M6 (right) dwarfs, for the already known sample (pink) and the candidates found in the filtered *Gaia* DR2 data (blue).

objects (spectral type, young, or subdwarf). This rough classification is done to guide the target selection for follow up, depending on the scientific case one may want to study. These numerous candidates are most valuable for follow-up since they benefit from the reliable *Gaia* observations, including precise parallax and proper motion.

Further exploitation of this dataset will be useful for making a complete census of late-M and at least early-type brown dwarfs, refining their luminosity function, testing stellar and substellar models, and probing the old population in the Galaxy through the subdwarf candidates.

This work has made use of data from the European Space Agency (ESA) mission *Gaia* (`https://www.cosmos.esa.int/gaia`), processed by the *Gaia* Data Processing and Analysis Consortium (DPAC, `https://www.cosmos.esa.int/web/gaia/dpac/consortium`). Funding for the DPAC has been provided by national institutions, in particular the institutions participating in the *Gaia* Multilateral Agreement. This research has made use of the VizieR catalogue access tool, CDS, Strasbourg, France. The original description of the VizieR service was published in A&AS 143, 23. This research has made use of the SIMBAD database, operated at CDS, Strasbourg, France. The author made queries at CDS using Virtual Observatory with python (Paletou & Zolotukhin 2014). All figures have been generated using the TOPCAT[‖] tool (Taylor 2005).

References

Allard, F., Homeier, D., & Freytag, B. 2013, Mem. Soc. Astron. Italiana, 84, 1053

Arenou, F., Luri, X., Babusiaux, C., et al. 2018, A&A, 616, A17

Baraffe, I., Homeier, D., Allard, F., & Chabrier, G. 2015, A&A, 577, A42

Best, W. M. J., Liu, M. C., Magnier, E., & Dupuy, T. 2018, in American Astronomical Society Meeting Abstracts, Vol. 231, American Astronomical Society Meeting Abstracts #231, 349.19

Capitanio, L., Lallement, R., Vergely, J. L., Elyajouri, M., & Monreal-Ibero, A. 2017, A&A, 606, A65

Cui, X.-Q., Zhao, Y.-H., Chu, Y.-Q., et al. 2012, Research in Astronomy and Astrophysics, 12, 1197

Dalton, G., Trager, S., Abrams, D. C., et al. 2014, in Proc. SPIE, Vol. 9147, Ground-based and Airborne Instrumentation for Astronomy V, 91470L

de Jong, R. S., Barden, S. C., Bellido-Tirado, O., et al. 2016, in Proc. SPIE, Vol. 9908, Ground-based and Airborne Instrumentation for Astronomy VI, 99081O

Dupuy, T. J. & Liu, M. C. 2012, ApJS, 201, 19

Evans, D. W., Riello, M., De Angeli, F., et al. 2018, A&A, 616, A4

Faherty, J. K., Gagné, J., Burgasser, A. J., et al. 2018, ApJ, 868, 44

Faherty, J. K., Riedel, A. R., Cruz, K. L., et al. 2016, ApJS, 225, 10

Gaia Collaboration, Babusiaux, C., van Leeuwen, F., et al. 2018a, A&A, 616, A10

Gaia Collaboration, Brown, A. G. A., Vallenari, A., et al. 2018b, A&A, 616, A1

Gaia Collaboration, Brown, A. G. A., Vallenari, A., et al. 2016a, A&A, 595, A2

Gaia Collaboration, Prusti, T., de Bruijne, J. H. J., et al. 2016b, A&A, 595, A1

Kirkpatrick, J. D., Henry, T. J., & Irwin, M. J. 1997, AJ, 113, 1421

Luri, X., Brown, A. G. A., Sarro, L. M., et al. 2018, A&A, 616, A9

Mace, G. N. 2014, PhD thesis, University of California, Los Angeles

Majewski, S. R., Schiavon, R. P., Frinchaboy, P. M., et al. 2017, AJ, 154, 94

Marocco, F., Jones, H. R. A., Day-Jones, A. C., et al. 2015, MNRAS, 449, 3651

Marrese, P. M., Marinoni, S., Fabrizio, M., & Giuffrida, G. 2017, A&A, 607, A105

Paletou, F. & Zolotukhin, I. 2014, ArXiv e-prints 1408.7026

Rajpurohit, A. S., Reylé, C., Allard, F., et al. 2013, A&A, 556, A15

Rajpurohit, A. S., Reylé, C., Allard, F., et al. 2014, A&A, 564, A90

Reylé, C. 2018, A&A, 619, L8

Robert, J., Gagné, J., Artigau, É., et al. 2016, ApJ, 830, 144

Scholz, R.-D. & Bell, C. P. M. 2018, Research Notes of the American Astronomical Society, 2, 33

Smart, R. L., Marocco, F., Caballero, J. A., et al. 2017, MNRAS, 469, 401

Smart, R. L., Marocco, F., Sarro, L. M., et al. 2019, MNRAS, 485, 4423

Taylor, M. B. 2005, in Astronomical Society of the Pacific Conference Series, Vol. 347, Astronomical Data Analysis Software and Systems XIV, ed. P. Shopbell, M. Britton, & R. Ebert, 29

Zhang, Z. H., Gálvez-Ortiz, M. C., Pinfield, D. J., et al. 2018, MNRAS

[‖]http://www.starlink.ac.uk/topcat/

PRECISE MAGNESIUM ABUNDANCES IN THE METAL-RICH DISK

P. Santos-Peral[1], A. Recio-Blanco[1], P. de Laverny[1] and E. Fernández-Alvar[1]

Abstract. The α - elements abundance provides an important fossile signature in galactic archeology to trace the chemical evolution of the different disk populations. However, a precise abundance estimation in the metal-rich disk ([M/H] ≥ 0 dex) is still complex due to the presence of blended lines and the difficulty in the continuum placement. We present a detailed Mg I abundance analysis for a sample of 2210 stars in the solar neighborhood, mostly dwarfs, observed by HARPS (ESO spectrograph ; R $\sim$ 115000) and parametrised by the AMBRE project. The abundances were derived using the the automatic spectral synthesis code GAUGUIN, analysing nine magnesium spectral lines in the optical range. Applying a better continuum treatment, we observe both the chemical distinction between thin-thick disk populations and a decreasing trend in the magnesium abundance even at supersolar metallicities. A careful continuum placement in the normalization of the observed spectra could throw some light on chemodynamical relations (e.g. [Mg/Fe] as a good age proxy for the thin disk or the contribution of radial migration in the solar neighborhood).

Keywords: Galaxy - stars: abundances , Galaxy: disk , Method: data analysis

1 Automatic magnesium abundance analysis

From the AMBRE:HARPS spectra sample (De Pascale et al. 2014), we have derived and analysed automatically the [Mg/Fe] abundances over nine Mg I spectral lines in the optical range, via the optimization method GAUGUIN (Bijaoui et al. 2012). We have observed different behaviours depending on the intensity of the line, allowing us to classify them in two categories: *weak* (4730.04, 5711.09, 6318.7, 6319.24 & 6319.49 Å) and *intense* (5167.3, 5172.7, 5183.6 & 5528.4 Å) lines. We have performed an in-depth analysis of each line separately, studying the different sources of possible uncertainties when deriving the chemical abundances.

1.1 Sensitivity to stellar rotation

The dispersion on the [Mg/Fe] abundance measurement, as a function of metallicity, is dominated by the stellar rotation, particularly in the weak lines, since the intense lines present more precise thin and thick disk sequences. We have observed this rotation effect on the intense lines at higher rotational velocities, but to a lesser degree. This results highlights the importance of a correct treating of the stellar rotation when using weak lines. Otherwise, choosing more intense lines or restricting the analysis of cooler stars (for which the rotational velocity is lower) will minimize the effects. We keep only slow-rotating stars, retaining spectra with $\mathrm{FWHM}_{CCF}{}^{*} \leq 8$ km s^{-1} for the intense lines, whereas only $\mathrm{FWHM}_{CCF} \leq 7$ km s^{-1} for the weak lines.

1.2 Normalization problems: importance of the continuum placement

In large spectroscopic stellar surveys, an automatic adjustment of the continuum is performed over the observed spectrum for every stellar type, via few iterations, searching the possible line-free or less contaminated zones, and fitting the ratio between the synthetic and the observed flux over a local interval around the line. For each line, we have applied different local normalization intervals (from short ranges, $\Delta\lambda_{norm} \sim 2$Å, to the whole window of the grid, $\Delta\lambda_{norm} \sim 70$Å), and studied the random errors caused by the change in the line χ^2 fitting due to the continuum placement.

[1] Laboratoire Lagrange (UMR7293), Université de Nice Sophia Antipolis, CNRS, Observatoire de la Côte d'Azur, Nice, France
e-mail: psantos@oca.eu

[*] radial velocity cross-correlation function; estimator provided by the AMBRE program.

We found that the normalization procedure has a direct impact on the derived abundance from every magnesium spectral line and depends on the stellar type, leading to different trends in the metal-rich regime ([M/H] $\geq$ 0 dex) and in the distinction between the thin-thick disk stellar populations. The normalization procedure needs to be optimized depending on the stellar type. Contrary to what has been done so far, the same procedure cannot be applied for every star since some abundance information might be lost.

2 Most precise Mg abundances in the Gaia era

It is shown in Fig. 1 the final stellar abundance ratios [Mg/Fe] vs [M/H], defined as the median abundance value from the multiple spectra of stars ($\geq$ 4 *repeats*), in which the abundance information from every line has been taken into account. For a given spectrum, a weighted mean (by the distance from the median abundance) was performed. For a given line and spectrum, we adopt the abundance which corresponds to the normalization interval that presents the lowest χ^2 fitting value. Fig. 1 shows a clear chemical distinction between the Galactic thin-thick disks populations (low- and high-[Mg/Fe] sequences, respectively) up to [M/H] $\sim +$ 0.1 dex.

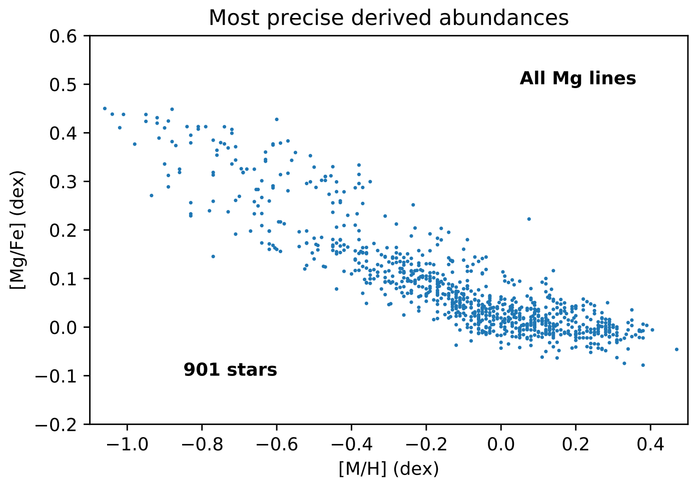

Fig. 1. Stellar abundance ratios [Mg/Fe] as a function of [M/H] following the quality criteria, taking into account the abundance information from all the studied Mg I spectral lines.

The second *Gaia* data release (*Gaia* DR2, Gaia Collaboration et al. 2018) has provided extremely precise and accurate astrometric information for millions of stars, allowing us to infer and discover the Galactic structure in unprecedented detail. For taking full advantage of these high-quality data, precise chemical abundances are strongly demanded in order to not to lose information about the different Galactic stellar populations and to improve our knowledge of the chemodynamical relations presented in the Galaxy.

3 Conclusions

The normalization procedure has a direct impact on the derived abundances and needs to be optimized depending on the stellar type, otherwise some abundance information might be lost. High-precision abundances, in combination with distances and kinematics from *Gaia*, are crucial to study the Galactic chemodynamical relations.

References

Bijaoui, A., Recio-Blanco, A., de Laverny, P., & Ordenovic, C. 2012, Statistical Methodology, 9, 55

De Pascale, M., Worley, C. C., de Laverny, P., et al. 2014, A&A, 570, A68

Gaia Collaboration, Brown, A. G. A., Vallenari, A., et al. 2018, A&A, 616, A1

SF2A 2019
P. Di Matteo, O. Creevey, A. Crida, G. Kordopatis, J. Malzac, J.-B. Marquette, M. N'Diaye, O. Venot (eds)

TRACING THE FORMATION OF THE MILKY WAY THROUGH ULTRA METAL-POOR STARS

F. Sestito[1, 2], N. Martin[1, 3] and E. Starkenburg[2]

Abstract. We use Gaia DR2 astrometric and photometric data, published radial velocities and MESA models to infer distances, orbits, surface gravities, and effective temperatures for all ultra metal-poor stars ($[Fe/H] < -4.0$ dex) available in the literature. Assuming that these stars are old (> 11 Gyr) and that they are expected to belong to the Milky Way halo, we find that these 42 stars (18 dwarf stars and 24 giants or sub-giants) are currently within ~ 20 kpc of the Sun and that they map a wide variety of orbits. A large fraction of those stars remains confined to the inner parts of the halo and was likely formed or accreted early on in the history of the Milky Way, while others have larger apocentres (> 30 kpc), hinting at later accretion from dwarf galaxies. Of particular interest, we find evidence that a significant fraction of all known UMP stars ($\sim 26\%$) are on prograde orbits confined within 3 kpc of the Milky Way plane ($J_z < 100$ km s^{-1} kpc). One intriguing interpretation is that these stars belonged to the massive building block(s) of the proto-Milky Way that formed the backbone of the Milky Way disc. Alternatively, they might have formed in the early disc and have been dynamically heated, or have been brought into the Milky Way by one or more accretion events whose orbit was dragged into the plane by dynamical friction before disruption. The combination of the exquisite Gaia DR2 data and surveys of the very metal-poor sky opens an exciting era in which we can trace the very early formation of the Milky Way

Keywords: Galaxy: formation, Galaxy: disc, Galaxy: halo, stars: distances, stars: UMP

Reminder

This proceedings has to be intended as a summary of the work from Sestito et al. (2019).

1 Introduction

Ultra metal-poor (UMP) stars, defined to have [Fe/H]* < -4 dex (Beers & Christlieb 2005), are extremely rare objects located mainly in the Milky Way (MW) halo. Because they are ultra metal-poor, also relative to their neighbourhood, it is assumed that they formed from relative pristine gas shortly after the Big Bang (e.g., Freeman & Bland-Hawthorn 2002). As such, they belong to the earliest generations of stars formed in the Universe (Karlsson et al. 2013). Because they are old, observable UMPs must be low-mass stars, however the minimum metallicity at which low-mass stars can form is still an open question (see Greif 2015, and references therein). The search for, and study of, stars with the lowest metallicities are therefore important topics to answer questions on the masses of the first generation of stars and the universality of the initial mass function (IMF), as well as on the early formation stages of galaxies and the first supernovae (e.g., Frebel & Norris 2015, and references therein). Careful studies over many decades have allowed us to build up a catalogue of 42 UMP stars throughout the Galaxy. Many of these stars were discovered in survey programs that were or are dedicated to finding metal-poor stars using some special pre-selection through prism techniques (e.g., the HK and HES surveys; Beers et al. 1985; Christlieb et al. 2002) or narrow-band photometry (such as for instance the SkyMapper and Pristine survey programmes; Wolf et al. 2018; Starkenburg et al. 2017). Others were discovered

[1] Université de Strasbourg, CNRS, Observatoire astronomique de Strasbourg, UMR 7550, F-67000 Strasbourg, France
[2] Leibniz-Institut für Astrophysik Potsdam (AIP), An der Sternwarte 16, D-14482, Potsdam, Germany
[3] Max-Planck-Institut für Astronomie, Königstuhl 17, D-69117, Heidelberg, Germany
*[Fe/H] $= \log(N_{Fe}/N_H)_\star - \log(N_{Fe}/N_H)_\odot$, with N$_X$= the number density of element X

in blind but very large spectroscopic surveys such as SDSS/SEGUE/BOSS (York et al. 2000; Yanny et al. 2009; Eisenstein et al. 2011) or LAMOST (Cui et al. 2012).

In an effort to refine the comparison with models and unveil the phase-space properties of these rare stars, we combine the exquisite Gaia DR2 astrometry and photometry (Gaia Collaboration et al. 2018) with models of UMP stars (MESA isochrones and luminosity functions; Paxton et al. 2011; Dotter 2016; Choi et al. 2016, `waps.cfa.harvard.edu/MIST`) to infer the distance, stellar properties, and orbits of all 42 known UMP stars.

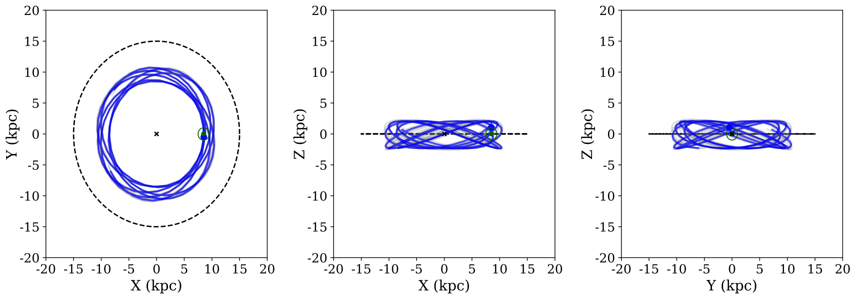

Fig. 1. Orbit of the most metal-poor star known, the Caffau star (SDSS J102915+172927). The blue line is the projected orbit of the star in the plane YX (left), ZX (center) and ZY (right). The Galactic plane within 15kpc (black line) and the Sun (green dot) are shown. Gray orbits represent randomisations around the values of position, distance, radial velocity and proper motions.

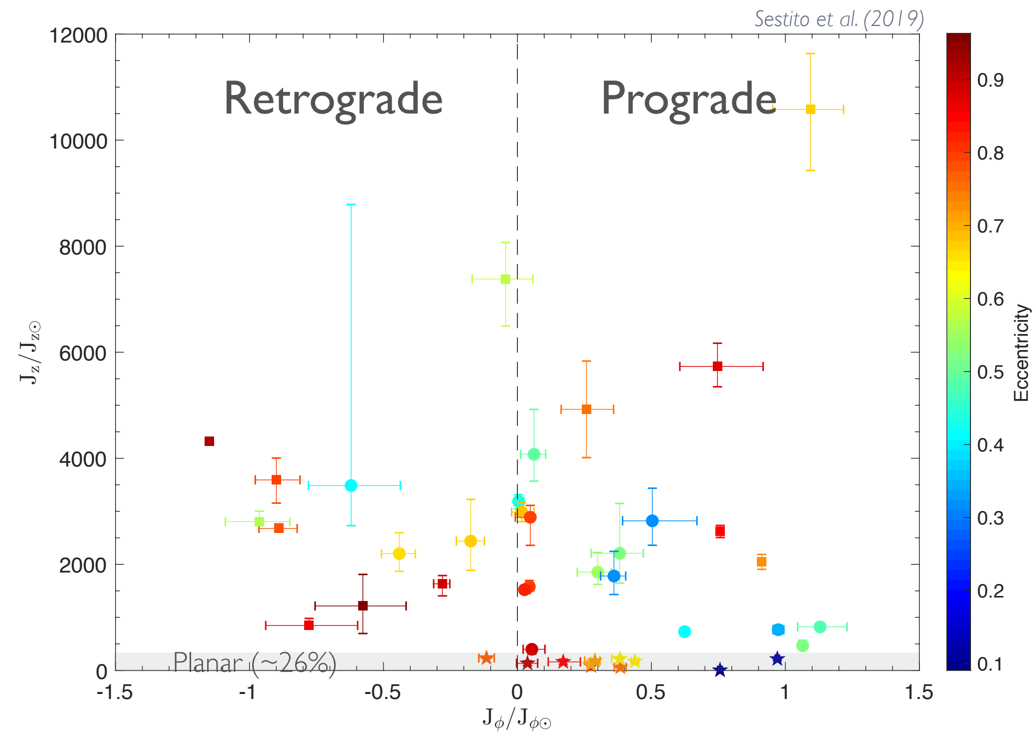

Fig. 2. Position of the sample stars in the rotational action J_ϕ $(= L_z)$ and vertical action J_z space. The rotational and vertical action are scaled by the Sun values respectively $J_{\phi\odot} = 2009.92$km s^{-1}kpc, $J_{z\odot} = 0.35$km s^{-1}kpc. Stars confined close to the MW plane are marked with a star symbols, while "inner halo" and "outer halo" stars are represented by circles and squares, respectively. The markers are colour-coded by eccentricity.

2 Conclusions

Combining the Gaia DR2 photometric and astrometric information in a statistical framework, we determine the posterior probability distribution function for the distance, the stellar parameters (temperature and surface gravity), and the orbital parameters of 42 UMPs (see Figure 2 and Sestito et al. (2019)). Given that 11 of those stars remain confined close to the MW plane, we use both a pure halo prior and a combined disc+halo prior. Folding together distance posterior and orbital analysis we find that 18 stars are on the main sequence and the other 24 stars are in a more evolved phase (subgiant or giant).

Through the orbital analysis, we surprisingly find that 11 stars are orbiting in the plane of disc, with maximum height above the disc within 3 kpc. 2 of these 11 have a quasi-circular orbit as shown in Figure 1. We hypothesise that they could have once belonged to a massive building blocks of the proto-MW that formed the backbone of the MW disc, or that they were brought into the MW via a specific, massive hierarchical accretion event. Another 31 stars are from both the "inner halo" (arbitrarily defined as having $r_{\mathrm{apo}} < 30$kpc) and were accreted early on in the history of the MW, or the "outer halo" hinting that they were accreted onto the Galaxy from now-defunct dwarf galaxies.

This research has made use of use of the SIMBAD database, operated at CDS, Strasbourg, France (Wenger et al. 2000). This work has made use of data from the European Space Agency (ESA) mission *Gaia* (`https://www.cosmos.esa.int/gaia`), processed by the *Gaia* Data Processing and Analysis Consortium (DPAC, `https://www.cosmos.esa.int/web/gaia/dpac/consortium`). Funding for the DPAC has been provided by national institutions, in particular the institutions participating in the *Gaia* Multilateral Agreement.

References

Beers, T. C. & Christlieb, N. 2005, ARA&A, 43, 531

Beers, T. C., Preston, G. W., & Shectman, S. A. 1985, AJ, 90, 2089

Choi, J., Dotter, A., Conroy, C., et al. 2016, ApJ, 823, 102

Christlieb, N., Wisotzki, L., & Graßhoff, G. 2002, A&A, 391, 397

Cui, X.-Q., Zhao, Y.-H., Chu, Y.-Q., et al. 2012, Research in Astronomy and Astrophysics, 12, 1197

Dotter, A. 2016, ApJS, 222, 8

Eisenstein, D. J., Weinberg, D. H., Agol, E., et al. 2011, AJ, 142, 72

Frebel, A. & Norris, J. E. 2015, ARA&A, 53, 631

Freeman, K. & Bland-Hawthorn, J. 2002, ARA&A, 40, 487

Gaia Collaboration, Brown, A. G. A., Vallenari, A., et al. 2018, A&A, 616, A1

Greif, T. H. 2015, Computational Astrophysics and Cosmology, 2, 3

Karlsson, T., Bromm, V., & Bland-Hawthorn, J. 2013, Reviews of Modern Physics, 85, 809

Paxton, B., Bildsten, L., Dotter, A., et al. 2011, ApJS, 192, 3

Sestito, F., Longeard, N., Martin, N. F., et al. 2019, MNRAS, 484, 2166

Starkenburg, E., Martin, N., Youakim, K., et al. 2017, MNRAS, 471, 2587

Wenger, M., Ochsenbein, F., Egret, D., et al. 2000, A&AS, 143, 9

Wolf, C., Onken, C. A., Luvaul, L. C., et al. 2018, PASA, 35, e010

Yanny, B., Rockosi, C., Newberg, H. J., et al. 2009, AJ, 137, 4377

York, D. G., Adelman, J., Anderson, Jr., J. E., et al. 2000, AJ, 120, 1579

SF2A 2019
P. Di Matteo, O. Creevey, A. Crida, G. Kordopatis, J. Malzac, J.-B. Marquette, M. N'Diaye, O. Venot (eds)

THE OPEN CLUSTER POPULATION AS SEEN BY GAIA

C. Soubiran[1]

Abstract. Thanks to Gaia DR2, the science of Open Clusters is revitalised. New memberships are now available for a large number of stars and clusters, fostering the determination of their physical properties and the study of the global properties of the population of Open Clusters in the Galaxy. A biased selection of recent resources and results is presented here.

Keywords: open clusters and associations, Galaxy: structure, Galaxy: kinematics and dynamics

1 Introduction

Positions, parallaxes, proper motions, radial velocities, together with G, B_P and R_P magnitudes delivered in Gaia DR2 (Gaia Collaboration, Brown et al. 2018) made it possible to determine new memberships for an unprecedented number of stars and clusters. Due to their large number of stars sharing the same characteristics, Open Clusters (OCs) were extensively used to validate the Gaia catalogue (Arenou et al. 2018; Katz et al. 2019). They were also used to demonstrate the exceptional potential of Gaia data to revolutionize the field of stellar physics. For instance Gaia Collaboration, Babusiaux et al. (2018) present the composite Hertzsprung-Russell diagram of 32 well known OCs, illustrating how the position of the main sequence, turn-off and giant branches changes as a function of age. Fine structures can be seen and bring new insight into stellar physics. With Gaia, ages and physical properties of OCs can be determined with an unprecedented precision.

Many groups are undertaking studies of OCs with Gaia DR2, for instance to discover new clusters, or to identify tails and evaporating stars, or to get an accurate view of their 3D distribution in the Galaxy and their kinematics. Some recent catalogues and investigations are presented below.

2 New large catalogues of OCs

Cantat-Gaudin et al. (2018) made a systematic search of members around the ∼3300 known OCs, mostly from Dias et al. (2002) and Kharchenko et al. (2013), only based on Gaia DR2 positions, parallaxes and proper motions. Membership probabilities were computed for ∼400 000 stars and the most probable distances were determined for 1229 OCs, including 60 newly discovered objects and two globular clusters previously classified as OCs. The spatial distribution of this sample confirms that young clusters follow the spiral arms while older clusters are found to be more dispersed and at higher altitudes, and are also rarer in the inner regions of the disk.

Soubiran et al. (2018) cross-matched the astrometric catalogue of Cantat-Gaudin et al. (2018) with the radial velocity survey from Gaia DR2 to provide the 6D phase-space information of 861 clusters. They showed that the RVS precision and accuracy is at the level of 0.5 km.s^{-1}. As expected, the vertical distribution of young clusters was found to be very flat, with a dispersion of vertical velocities of 5 km s^{-1}. Clusters older than 1 Gyr were found to span distances to the Galactic plane of up to 1 kpc with a vertical velocity dispersion of 14 km s^{-1}, typical of the thin disc.

Bossini et al. (2019) determined the age, distance modulus and extinction of 269 OCs with a Bayesian tool fitting stellar isochrones on Gaia magnitudes of the high probability member stars from Cantat-Gaudin et al.

[1] Laboratoire d'Astrophysique de Bordeaux, B18N allée Geoffroy Saint-Hilaire,

(2018). Other objects, like young clusters, or with high extinction or different metallicities need complementary photometry to deconvolve all the effects.

This three new catalogues form the largest data base of OC parameters derived with homogeneous and high quality data from Gaia DR2 only.

3 New methods for membership determination

A number of methodologies have been developed in the past for the detection of cluster members and sometimes require some adaptation to deal with millions of stars in Gaia DR2 and other large datasets. Cantat-Gaudin et al. (2018) adapted the code UPMASK (Unsupervised Photometric Membership Assignment in Stellar Clusters, Krone-Martins & Moitinho (2014)) to astrometric data. The only physical assumption of UPMASK is that cluster members share common properties and are more tightly distributed on the sky than a random distribution. Olivares et al. (2019) combined Gaia DR2 data and deep photometric observations to make a census of Ruprecht 147 members. They improved the method of Sarro et al. (2014) which models the multidimensional distribution of a cluster field by a Gaussian mixture. Not surprisingly the lists of members differ from one method to another depending on the kind of data considered (astrometry, photometry, radial velocities,..), and on the use or not of observational errors and correlations, and of assumptions. The Bayesian methodology of Olivares et al. (2018) seems promising since it takes into account the full covariance matrix of the observations, which can be of different types and origins, and deals with partially observed objects. However it is still too computationally expensive to deal with millions of stars.

4 New Open Clusters

While Cantat-Gaudin et al. (2018) serendipitously found 60 new OCs which were in the field of known clusters, Castro-Ginard et al. (2018) designed an automated data-mining system for the detection of OCs in Gaia. A density-based clustering algorithm, DBSCAN, finds overdensities and a supervised learning method automatically identifies real OCs. A first run led to 31 new candidates, and another run in the anticentre direction led to 53 new OCs, with about half of them being closer than 2 kpc, suggesting that the census of nearby OCs is not complete. This was also the conclusion of Cantat-Gaudin et al. (2019) who discovered 44 new OCs in the direction of Perseus, using UPMASK. Ferreira et al. (2019) reports the serendipitous discovery of three new open clusters, in the field of the intermediate-age OC NGC 5999 with Gaia DR2 data.

5 Extended structures around Open Clusters

Thanks to Gaia DR2 several groups have explored the surroundings of nearby OCs in order to find escaping members at large distance from the centre. This gives a fantastic opportunity to better understand the dissolution of clusters into the Galactic field. The Hyades being richly populated and the nearest OC in the solar neighbourhood ($\sim$47 pc), it is a benchmark object to make such studies. Röser et al. (2019) used a modified convergent-point method to search Hyades members at large distance from the centre and clearly identified a leading tail extending up to 170 pc and a trailing tail up to 70 pc. Meingast & Alves (2019) selected Hyades members in the 3D galactocentric cylindrical velocity space, thus limited to the brightest Gaia stars having a radial velocity. They identified a S-shape structure of about 200 pc in its largest extent and about 25 pc thick. Both studies are in excellent agreement with theoretical predictions for the tidal tails of the Hyades. With the same modified convergent-point method used for the Hyades, Röser & Schilbach (2019) find the Praesepe's tidal tails extending up to 165 pc from the centre of the cluster. They identify 1393 members, giving a total mass of 794 $M_{\odot}$.

The well-known star cluster Coma Berenices (Melotte 111) has also been the main subject of two studies.Tang et al. (2019) identify leading and trailing tidal tails extending $\sim$50 pc from the cluster center, seven times longer than the cluster tidal radius, $\sim$6.9 pc. This is in good agreement with the findings of Fürnkranz et al. (2019). Both studies report the discovery of a moving group at about 60pc from Coma Ber that looks younger and in an advanced dissolution process.

Ruprecht 147 is an interesting target, being the oldest OC ($\sim$2.5 Gyr) in the close solar neighbourhood ($\sim$300pc). Yeh et al. (2019) found prominent tidal features aligned with the cluster orbit suggesting that the cluster is undergoing fast dissolution into the Galactic disk.

Another old and popular OC is NGC2682 (M67), the extended halo of which was studied by Carrera et al. (2019b). They find that the cluster extends up to 50 pc, a size twice as large as previously believed.

Tarricq et al. (this volume) have undertaken a systematic analysis of the spatial extent of all the old OCs in a 550pc sphere around the Sun.

6 Chemical composition of Open Clusters

Gaia DR2 does not provide stellar metallicities. However when combining membership and OC parameters deduced from Gaia with ground-based spectroscopic surveys or high resolution studies, mean abundances of OCs can be derived (see for instance Casamiquela et al. in this volume), providing a powerful tool to study the distribution of elements across the Galactic disk. For example Carrera et al. (2019a) cross-matched the OC member lists from Cantat-Gaudin et al. (2018) with APOGEE (Majewski et al. 2017) and GALAH (De Silva et al. 2015) and were able to determine mean abundances for more than 100 OCs, for the first time for 39 of them. While a vertical gradient in metallicity could not be seen, the radial gradient has clearly two regimes, steeper around the solar radius and flatter in the outer disk.

With the final Gaia-ESO catalogue coming soon (Randich et al. 2013) and WEAVE starting observations in 2020 (Dalton et al. 2016), both having dedicated programmes focused on OCs, we will have a huge database to investigate the Galactic abundance gradients and the correlations between chemical composition and kinematics as revealed by OCs.

7 Conclusions

Thanks to Gaia DR2, unprecedented large catalogues of OCs are now available, containing lists of members or mean physical properties, and leading to exciting discoveries. This short presentation of a few examples of OC investigations intended to show how Gaia DR2 is revolutionizing the field. Many other important topics were not mentioned, such as the complex age, spatial and kinematic structure revealed in young OCs. Much more is expected in the coming years with the combination of Gaia and ground based observations, and with Gaia DR3 that will improve the memberships of distant clusters and provide metallicities, even detailed abundances for the brightest stars.

References

Arenou, F., Luri, X., Babusiaux, C., et al. 2018, A&A, 616, A17

Bossini, D., Vallenari, A., Bragaglia, A., et al. 2019, A&A, 623, A108

Cantat-Gaudin, T., Jordi, C., Vallenari, A., et al. 2018, A&A, 618, A93

Cantat-Gaudin, T., Krone-Martins, A., Sedaghat, N., et al. 2019, A&A, 624, A126

Carrera, R., Bragaglia, A., Cantat-Gaudin, T., et al. 2019a, A&A, 623, A80

Carrera, R., Pasquato, M., Vallenari, A., et al. 2019b, A&A, 627, A119

Castro-Ginard, A., Jordi, C., Luri, X., et al. 2018, A&A, 618, A59

Dalton, G., Trager, S., Abrams, D. C., et al. 2016, in Society of Photo-Optical Instrumentation Engineers (SPIE) Conference Series, Vol. 9908, Proc. SPIE, 99081G

De Silva, G. M., Freeman, K. C., Bland-Hawthorn, J., et al. 2015, MNRAS, 449, 2604

Dias, W. S., Alessi, B. S., Moitinho, A., & Lépine, J. R. D. 2002, A&A, 389, 871

Ferreira, F. A., Santos, J. F. C., Corradi, W. J. B., Maia, F. F. S., & Angelo, M. S. 2019, MNRAS, 483, 5508

Fürnkranz, V., Meingast, S., & Alves, J. 2019, A&A, 624, L11

Gaia Collaboration, Babusiaux, C., van Leeuwen, F., Barstow, M. A., et al. 2018, A&A, 616, A10

Gaia Collaboration, Brown, A. G. A., Vallenari, A., Prusti, T., et al. 2018, A&A, 616, A1

Katz, D., Sartoretti, P., Cropper, M., et al. 2019, A&A, 622, A205

Kharchenko, N. V., Piskunov, A. E., Schilbach, E., Röser, S., & Scholz, R. D. 2013, A&A, 558, A53
Krone-Martins, A. & Moitinho, A. 2014, A&A, 561, A57
Majewski, S. R., Schiavon, R. P., Frinchaboy, P. M., et al. 2017, AJ, 154, 94
Meingast, S. & Alves, J. 2019, A&A, 621, L3
Olivares, J., Bouy, H., Sarro, L. M., et al. 2019, A&A, 625, A115
Olivares, J., Sarro, L. M., Moraux, E., et al. 2018, A&A, 617, A15
Randich, S., Gilmore, G., & Gaia-ESO Consortium. 2013, The Messenger, 154, 47
Röser, S. & Schilbach, E. 2019, A&A, 627, A4
Röser, S., Schilbach, E., & Goldman, B. 2019, A&A, 621, L2
Sarro, L. M., Bouy, H., Berihuete, A., et al. 2014, A&A, 563, A45
Soubiran, C., Cantat-Gaudin, T., Romero-Gómez, M., et al. 2018, A&A, 619, A155
Tang, S.-Y., Pang, X., Yuan, Z., et al. 2019, ApJ, 877, 12
Yeh, F. C., Carraro, G., Montalto, M., & Seleznev, A. F. 2019, AJ, 157, 115

SF2A 2019
P. Di Matteo, O. Creevey, A. Crida, G. Kordopatis, J. Malzac, J.-B. Marquette, M. N'Diaye, O. Venot (eds)

NEARBY OPEN CLUSTERS SHAPE : THREE-DIMENSIONAL GAUSSIAN MIXTURE MODEL AND TWO-DIMENSIONAL DENSITY MAPS

Y. Tarricq[1], L. Casamiquela[1] and C. Soubiran[1]

Abstract. We use new memberships from Gaia DR2 to investigate the shape of the nearest open clusters. For open clusters closer than 250 pc from the Sun, we fit 3D ellipsoids on the spatial distribution of the members. At higher distances, the radial effect due to the uncertainties on the parallax measurements introduces a strong bias in the spatial distribution of members. Therefore, for more distant open clusters, we compute density maps on the sky to study their spatial properties and search for correlations with age and galactic environments of the clusters.

Keywords: Gaia, open clusters, solar neighborhood

1 Introduction

Open Clusters (OCs) are gravitationnaly bound groups of stars which formed from the same giant molecular cloud. The members of an OC share therefore the same characteristics such as their age, metallicity, proper motions or distances. These stars covering a wide range of mass and evolutionnary stages, OCs are ideal laboratories to better constrain formation and stellar evolution theories. The determination of these stars' physical properties being much more accurate than for field stars, OCs and their members are also widely used as reference objects in order to better constrain and validate large observational surveys. Finnaly, studying these objects allows us to better understand the galactic disk's history. Over their lifespan, OCs indeed dissolve themselves into the galactic disk. The study of this process, in particular by focusing on evolved OC is thus a way to know with more details the dynamical properties and stellar populations of our galaxy. In particular, the study of the shape of OCs will give us hints of the disruption process at stake in our galaxy depending on the age of the clusters, their environment,... In the first section, we describe the data we take advantage of and explain why we had to consider two ways of handling OCs, depending on their distance. In the next section, we explain the two different method we used to evaluate the shape of OCs and our results.

2 Data

We take advantage of Gaia DR2 unprecedented astrometric accuracy containing more than 1.6 billion sources with five-parameter solutions. We focused on the OCs already identified in the solar neighborhood and constructed a sample composed of 84 OCs located closer than 550pc. To investigate the shape of OCs, we have considered the members with a membership probability higher than 0.8 from Cantat-Gaudin et al. (2018), Gaia Collaboration et al. (2018) and Röser et al. (2019) for the tail of the Hyades. In Fig. 1, we have plotted the X-Y distribution of the members of our sample. A selection has been performed using the astrometric quality cuts suggested by Schönrich et al. (2019). Positions in the X-Y plane have been calculated with distances from Bailer-Jones et al. (2018). The strong radial effect seen here shows that even with bayesian distances and drastic quality cuts, there is still a strong bias in the spatial distribution of members. Therefore we limit our 3D study to the 14 OCs which lie within 250 pc from the Sun : Alessi 13, Blanco 1, the Hyades, Coma Berenices, the Pleiades, NGC 2632, NGC 2451A, IC 2391, IC 2602, Platais 3, Platais 8, Platais 9, Mamajek 1 and Alpha Persei.

[1] Laboratoire d'Astrophysique de Bordeaux, 33600 Pessac, France

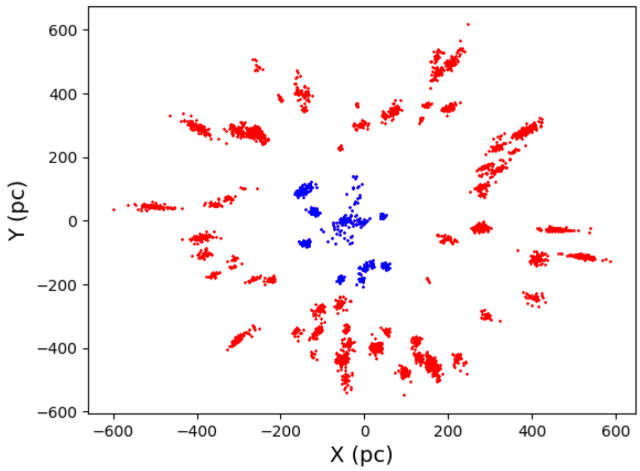

Fig. 1. Distribution of the members from our OCs sample in the X-Y plane, centered on the Sun. Blue dots indicate the closest OCs for which the 3D shape has been fitted.

3 Results

For the 14 nearest OCs, we have fitted a Gaussian Mixture Model (GMM) composed of two gaussians in order to modelize their shape. This allows us to consider the evolution of both the cores and the outer parts of the OCs by modelling them as ellipsoids. However, because of the strong radial effect seen in Fig. 1, we chose a different approach to study more distant OCs' shapes. For each OC which is not too extended on the sky, the position of its members has been projected on a tangential plane and we are computing density maps of these distributions by using a Gaussian kernel. An exemple of these two different approaches is shown on Fig. 2

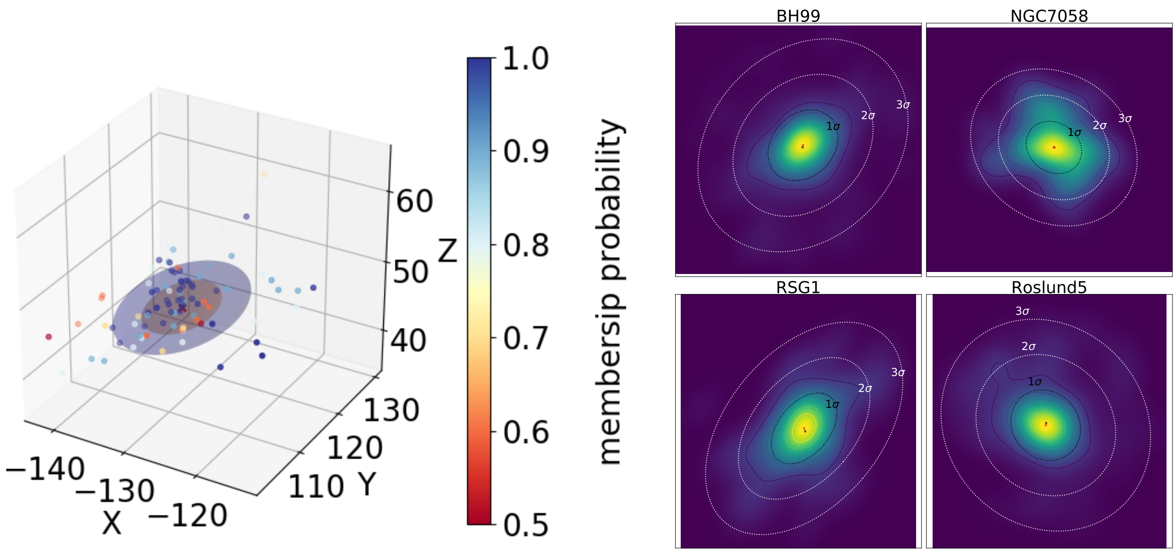

Fig. 2. Left: Example of the fit of two Gaussians on the spatial distribution of Platais 3 members. The color scale represents the membership probability of each star. **Right:** Density maps with contours computed for BH99, NGC7058, RSG1 and Roslund5. The ellipses represent the maximum extent of the 1, 2 and 3 σ contour. Red cross represent the highest density pixel and black cross represent the OC's center computed in the litterature.

As seen in the left part of Fig 3 which focus on closer OCs three dimensional shapes, the flattening (defined as $1 - \frac{c}{a}$ with c the semi minor axis and a the semi major axis) of outer OCs' parts tends to increase but we can't reach a conclusion for the inner parts due to the low amounts of points and their high dispersion. For more distant OCs, while we expect to see the flattening of the 1σ contour to increase with age, we couldn't find such a correlation but as shown in the right part of Fig 3, the flattening tends to decrease for more populated clusters.

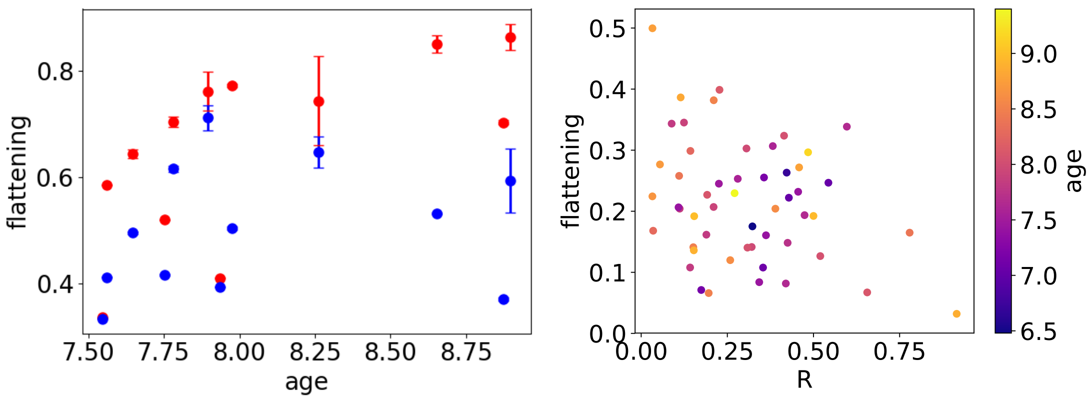

Fig. 3. Left: Evolution of the flattening of both cores (in blue) and outer parts (in red) for the nearest OCs with age. **Right:** Evolution of the flattening of the 1 σ contour ellipse of the OCs with the ratio R meaning the number of members over the number of field stars in a 10pc sphere centered on the cluster. The color scale represents OCs' ages.

4 Conclusions

We have highlighted that despite the unprecedented astrometric accuracy of Gaia DR2, the study of OCs shapes in three dimensions is still very difficult due to the increase of parallax uncertainties with distance. We focused on the closest OCs which lie closer than 250 pc from the Sun. By fitting a GMM to each of them, we noticed that their external enveloppe tends to be more and more elongated as age increases. This is consistent with what was expected : an increase of outer parts' flattening wich are disrupted by the OCs encounters. For the clusters located between 250 pc and 550pc from the Sun, we had to restrain our study to their shape in two dimensions. This still allowed us to notice that the densest clusters tend to be more spherical than others, due to their strong gravitational binding.

We acknowledge support from the "programme national de physique stellaire" (PNPS) and from the "programme national cosmologie et galaxies" (PNCG) of CNRS/INSU.

References

Bailer-Jones, C. A. L. et al. 2018, AJ, 156, 58
Cantat-Gaudin, T. et al. 2018, A&A, 618, A93
Gaia Collaboration, Babusiaux, C., et al. 2018, A&A, 616, A10
Röser, S., Schilbach, E., & Goldman, B. 2019, A&A, 621, L2
Schönrich, R., McMillan, P., & Eyer, L. 2019, MNRAS, 487, 3568

SF2A 2019
P. Di Matteo, O. Creevey, A. Crida, G. Kordopatis, J. Malzac, J.-B. Marquette, M. N'Diaye, O. Venot (eds)

SPECTROSCOPIC BINARIES WITH GAIA AND LARGE SPECTROSCOPIC SURVEYS

M. Van der Swaelmen[1], T. Merle[2], S. Van Eck[2] and A. Jorissen[2]

Abstract. Binary stars are ubiquitous in the universe and across the Hertzsprung-Russell diagram. Thanks to the Gaia mission, a big step in our understanding of stellar multiplicity will be made with the discovery of millions of (astrometric, spectroscopic, eclipsing) binaries. In parallel, large spectroscopic surveys, like the Gaia-ESO survey, can already be combined with the Gaia data releases to hunt for and characterise new spectroscopic binaries. We present our latest results about the identification and characterisation of single-lined and double-lined spectroscopic binaries (SB1, SB2) with the Gaia-ESO survey+Gaia. In particular, our results about the dependency of the SB1 fraction with metallicity and the distribution of the mass-ratio for SB2 will be discussed.

Keywords: Techniques: radial velocities, Techniques: spectroscopic, Binaries: spectroscopic, Surveys

1 Spectroscopic binaries among the Gaia-ESO survey

1.1 Introduction

The Gaia-ESO survey (Gilmore et al. 2012; Randich et al. 2013) is an ambitious spectroscopic survey carried out at Very Large Telescope, Chile. It uses the multi-object spectrographs FLAMES/GIRAFFE ($R \sim 20\,000$; Pasquini et al. 2000) and FLAMES/UVES ($R = 47\,000$) to record the spectra of 10^5 Milky Way (MW) stars belonging to the Galactic bulge, thin/thick disks, halo and stellar clusters. The science goal is to characterise the stellar populations of the MW from a kinematical and chemical point of view, in order to put constraints on the chemical evolution and formation history of our galaxy.

More than 75 % of the observations have been made with the GIRAFFE setups HR10, HR21 (mainly field stars) and HR15N (mainly stars in the vicinity of or belonging to stellar clusters). The V magnitude of the faintest objects is $V = 20$; most of the targets have two or four exposures. In this work, we focused on the analysis of HR10 and HR21 spectra of the fifth internal data release (iDR5).

Though the Gaia-ESO survey is not designed for the detection and the study of spectroscopic binaries, the fact that a large fraction of stars benefit from two or more visits allow us to address the question of binarity. Stellar multiplicity is indeed ubiquitous across the Galaxy and the Hertzsprung-Russell diagram, and thus, stellar systems are expected among the Gaia-ESO targets.

1.2 Detection of SB2

SBn ($n \geq 2$) are spectroscopic binaries which exhibit n stellar components in their spectra. It is therefore possible to detect them by inspecting their cross-correlation functions (CCFs) and look for those with two or more stellar components. Merle et al. (2017) designed the tool Doe – Detection Of Extrema – to automatise the analysis of the $\sim 200\,000$ HR10+HR21 CCFs (as of iDR5) of Gaia-ESO targets. Our tool computes the smoothed first-, second- and third-derivatives of the CCFs and uses them to detect multi-peaked CCFs, i.e. objects with two or more stellar components.

[1] INAF - Osservatorio Astrofisico di Arcetri, Largo E. Fermi 5, 50125, Firenze, Italy
[2] Institut d'Astronomie et d'Astrophysique, Université Libre de Bruxelles, Campus Plaine C.P. 226, Boulevard du Triomphe, 1050, Bruxelles, Belgium

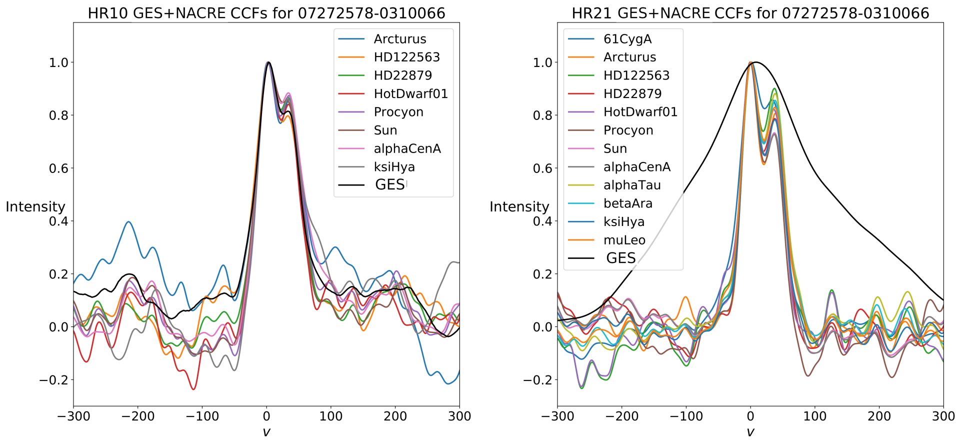

Fig. 1. Left: Example of cross-correlation functions of a Gaia-ESO SB2 observed with the GIRAFFE setup HR10. The black line is the CCF released by the Gaia-ESO while the coloured lines are the NACRE CCFs. **Right**: Same as left but for an HR21 observation of the same object. The Gaia-ESO CCF does not display the two stellar components while our NACRE CCFs do.

Van der Swaelmen et al. (*in prep.*, see also Van der Swaelmen et al. 2018) improved the detection by designing specific cross-correlating masks (called NACRE masks) which produce more narrow CCFs, and therefore allow to detect SB2 with a smaller radial velocity difference. We notice, indeed, that some objects are seen as an SB2 when looking at their HR10 CCFs but exhibit a single stellar component in their HR21 CCFs. It is for example the case of the star shown in Fig. 1. The black CCFs, released by the Gaia-ESO collaboration, is double-peaked for HR10 (left) but single-peaked for HR21 (right). Since the observations were taken within 24 h and have a good signal-to-noise ratio (≥ 15), we suspected that the binary nature was hidden in the HR21 CCFs. Our investigation showed that the HR21 wavelength range, around the near-infrared Ca II triplet, tends to host numerous strong and saturated lines (compared to the HR10 wavelength range) that broaden the CCFs. Our NACRE masks exclude these strong features to keep only weak, mildly-blended atomic lines and produce more narrow CCFs. The coloured lines in Fig. 1 show the NACRE CCFs for both HR10 and HR21 observations and for different spectral types. One sees that the binary nature is now detected in both cases. We therefore re-computed the CCFs for the $\sim 200\,000$ individual HR10 and HR21 spectra and analysed them with DOE. Some of our results are discussed in Sec. 2.1.

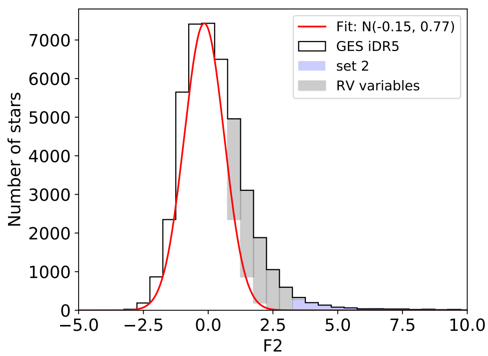

Fig. 2. F2 distribution for the Gaia-ESO iDR5 stars. The red line is the expected F2 distribution when the variation in radial velocities are explained by (Gaussian) random errors. The histogram displays the actual Gaia-ESO distribution. The departure from normality in the right tail is due to radial-velocity variables. A fraction of those variables exhibit photometric variability (grey shading) and has to be removed from the analysis to keep only the SB1 (blue shading for a selection at the 3σ confidence level).

1.3 Detection of SB1

The detection of SB1, single-lined spectroscopic binaries, is a different story. Such spectroscopic binaries do not exhibit more than one stellar component in their spectra. However, their radial velocities vary with time. Merle et al. (*submitted*) used the radial velocities (and their associated uncertainties) computed by Van der Swaelmen et al. (*in prep.*) to detect variabilities in the time series of radial velocities. To discriminate between random changes and astrophysical changes of the radial velocity, we computed the χ^2 given in Eq. 1.1. The F2 quantity given in Eq. 1.2 should then follow a normal distribution if the variations in the radial velocities are explained only by normally-distributed random errors. The departure from normality (the right heavy tail in Fig. 2) points at objects with an astrophysical change of their radial velocity. We then used the Gaia DR2 photometry to exclude photometric variables from the sample of variables. Some of our results are discussed in Sec. 2.2.

$$\chi^2_{N-1} = \sum_{i=1}^{N} \left(\frac{v_i - \bar{v}}{e_i} \right)^2 \tag{1.1}$$

$$F2(\chi^2, N) = \sqrt{\frac{9(N-1)}{2}} \left[\left(\frac{\chi^2}{N-1} \right)^{1/3} + \frac{2}{9(N-1)} - 1 \right] \tag{1.2}$$

2 Results

2.1 Mass-ratio distribution of SB2

We identify (Van der Swaelmen et al. *in prep.*) more than 300 SB2 in the Gaia-ESO iDR5. Only few of them were previously known since the Gaia-ESO survey targets fainter objects than other catalogues like RAVE (Matijevič et al. 2010) or MSC (Tokovinin 1997). When the Gaia-ESO SB2 have been observed at different epochs, we could determine their mass-ratio by computing the slope of the relation $v_{\text{secondary}}$ vs v_{primary}. Left panel of Fig. 3 shows an example of such a linear regression. We could apply this procedure to only 10 % of our SB2 and right panel of Fig. 3 shows the distribution of their mass-ratio q. We note that it is biased towards $q = 1$: it is explained by the fact that SB2 exhibit two stellar components in their spectra, which means that they have similar spectral type and therefore, similar masses (they are co-eval). The Gaia DR2 photometry allows us to go further into the characterisation of our SB2 and shows that they lie on the main-sequence.

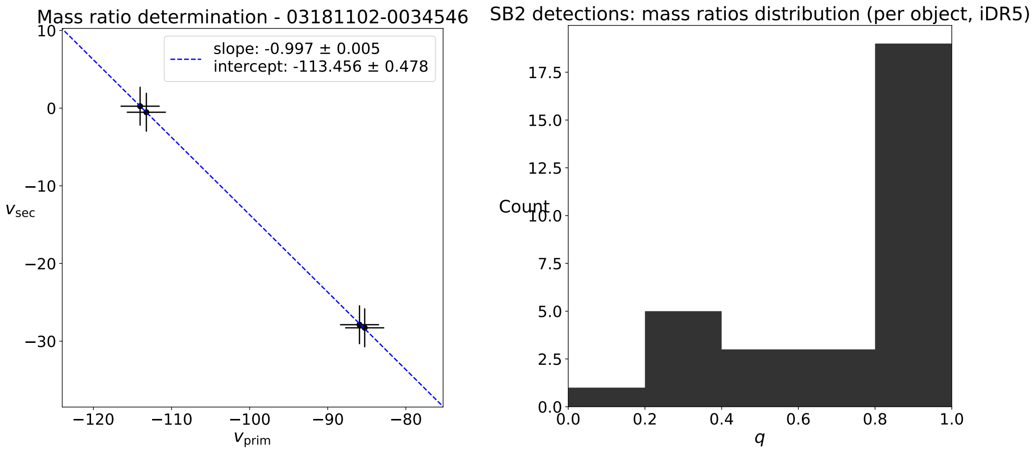

Fig. 3. Left: determination of the mass-ratio using the slope of the relation $v_{\text{secondary}}$ vs v_{primary}. **Right**: mass-ratio distribution for about 10 % of the SB2 detected in the fifth internal data release of the Gaia-ESO survey.

2.2 Metallicity-dependence of the SB1 fraction

We identify (Merle et al. *submitted*) more than 600 (resp., 800) SB1 in the Gaia-ESO iDR5 at the 5σ (resp., 3σ) confidence level. Figure 4 shows an example of SB1 for which we could determine its orbital elements. The

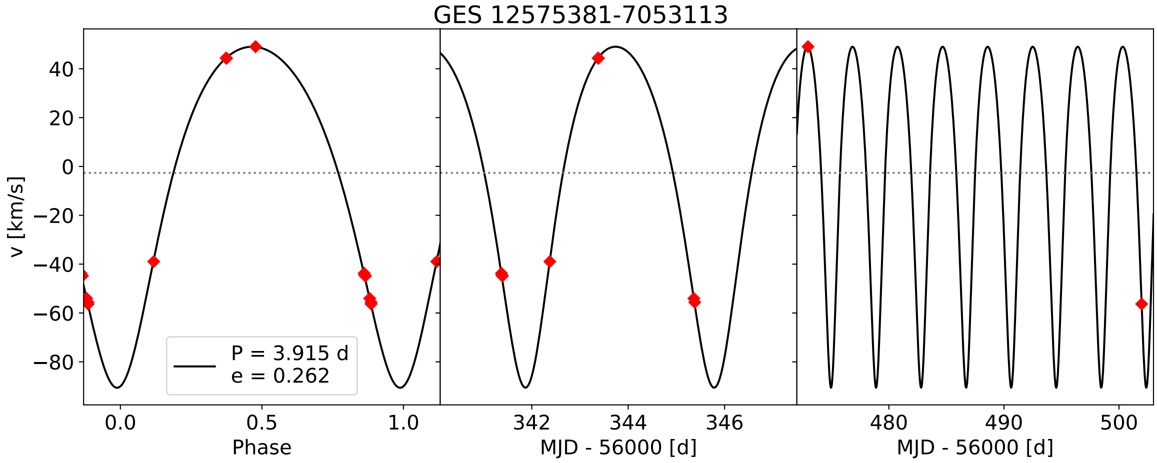

Fig. 4. One of the few SB1 for which we could fit an orbit. The period and eccentricity are indicated in the legend. Red dots stand for the measured radial velocities. The left panel shows the evolution of the radial velocity with respect to the phase while the middle and right panels show the time evolution.

period is $P \sim 4\,\mathrm{d}$ and the eccentricity is $e \sim 0.26$. Using the Gaia-ESO metallicities and after correcting for detection biases, we could estimate the evolution of the SB1 fraction as a function of the metallicity. Figure 5 shows our results as well as literature trends. We note that the SB1 fraction is anti-correlated with the metallicity and our trend is in good agreement with previous studies. Such a relation may have fundamental consequences for the formation scenarios of binary stars (e.g., Moe et al. 2019).

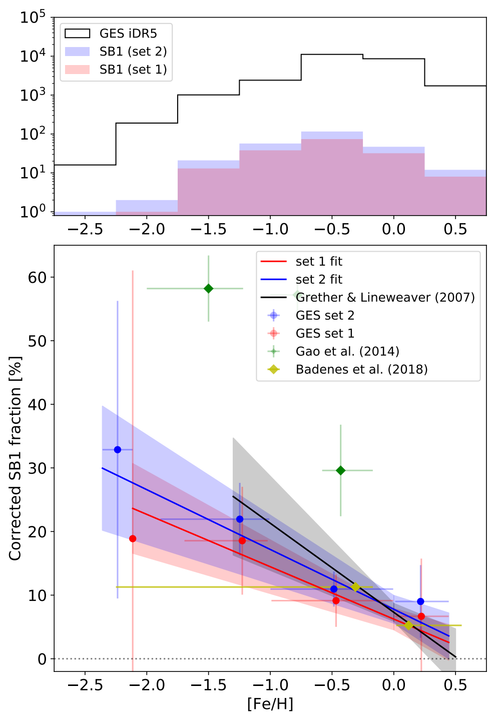

Fig. 5. Top panel: the metallicity distribution of the full Gaia-ESO sample (black line) and of the SB1 sample at the 3σ (set 2, blue) and 5σ (set 1, red) confidence levels. Notice the vertical logarithmic axis. **Bottom panel**: SB1 fraction vs. metallicity. Literature data (Grether & Lineweaver 2007; Gao et al. 2014; Badenes et al. 2018) are also shown.

3 Conclusion

Though the Gaia-ESO survey is designed for the study of the chemo-dynamical evolution of the Milky Way, it can also be successfully used to hunt for new spectroscopic binaries. We discovered few hundreds of SB1 and SB2, a handful of SB3 and one SB4. Combining the Gaia-ESO survey with the Gaia DR2 allowed us to go further into the characterisation of our spectroscopic binaries.

References

Badenes, C., Mazzola, C., Thompson, T. A., et al. 2018, ApJ, 854, 147

Gao, S., Liu, C., Zhang, X., et al. 2014, ApJ, 788, L37

Gilmore, G., Randich, S., Asplund, M., et al. 2012, The Messenger, 147, 25

Grether, D. & Lineweaver, C. H. 2007, ApJ, 669, 1220

Matijevič, G., Zwitter, T., Munari, U., et al. 2010, AJ, 140, 184

Merle, T., Van Eck, S., Jorissen, A., et al. 2017, A&A, 608, A95

Moe, M., Kratter, K. M., & Badenes, C. 2019, ApJ, 875, 61

Pasquini, L., Avila, G., Allaert, E., et al. 2000, in Proc. SPIE, Vol. 4008, Optical and IR Telescope Instrumentation and Detectors, ed. M. Iye & A. F. Moorwood, 129–140

Randich, S., Gilmore, G., & Gaia-ESO Consortium. 2013, The Messenger, 154, 47

Tokovinin, A. A. 1997, A&AS, 124, 75

Van der Swaelmen, M., Merle, T., Van Eck, S., & Jorissen, A. 2018, in SF2A-2018: Proceedings of the Annual meeting of the French Society of Astronomy and Astrophysics, 183–186

Session 04

Le nouvel outil d'observation MATISSE

SF2A 2019
P. Di Matteo, O. Creevey, A. Crida, G. Kordopatis, J. Malzac, J.-B. Marquette, M. N'Diaye, O. Venot (eds)

SYNERGIES BETWEEN VLTI/MATISSE AND ALMA: THE ATOMIUM LARGE PROGRAM

M. Montargès[1], L. Decin[1], T. Khouri[2], W. Homan[1], E. Cannon[1], E. Lagadec[3] and P. Kervella[4]

Abstract. Cool evolved stars are important contributors to the chemical enrichment of the interstellar medium. Within their important stellar winds (10^{-8} to 10^{-4} $M_{\odot}$ yr^{-1}), complex molecules and dust grains are build that represents pristine building blocks for future stellar and planetary systems. The mechanisms behind the mass loss are only partially understood, yielding to the overall mass loss process being modeled as an empirical prescription in most evolutionary models. We are engaged in a multi-wavelength approach aiming at providing a consistent view of the circumstellar environment of cool evolved stars. The accepted ALMA large program Atomium is at the center of this project. It is supported by optical observations, particularly with the new VLTI/MATISSE instrument. We present here the synergies between the radio and mid-infrared interferometric observations.

Keywords: stars: AGB and post-AGB, supergiants, stars: mass loss, circumstellar matter, techniques: high angular resolution, techniques: interferometric

1 Introduction

The winds of Asymptotic Giant Branch (AGB) and Red Supergiant (RSG) stars are key chemical laboratories in which more than 80 molecules and 15 dust species have been detected thus far (Höfner & Olofsson 2018). Through their winds, they contribute $\sim 85\%$ of gas and $\sim 35\%$ of dust to the total enrichment of the ISM (Tielens 2005), and therefore are the dominant suppliers of building blocks of interstellar material. In the wind, a large variety of chemical reactions occur, including unimolecular, 2- and 3-body reactions, cluster growth and grain formation. Hoyle & Wickramasinghe (1962) were the first to propose that the wind acceleration in AGB stars is caused by radiation pressure on newly formed dust grains. Molecules carry the analogous potential to launch a RSG wind, with grains taking over farther out in the wind (Gustafsson & Plez 1992). The prevailing streamlines in these winds are radial, although recent ALMA observations have added structural complexities to this picture (e.g. Maercker et al. 2012 or Homan et al. 2018). We will present here how simultaneous ALMA and MATISSE observations can respectively map gaseous dust precursors and dust grains to better understand the gas/dust transition.

2 The observation programs

2.1 The ATOMIUM large program

Aiming to answer this fundamental question on the gas-dust nucleation process, we have submitted for ALMA Cycle 6 a Large Program (Atomium, ALMA Tracing the Origins of Molecules forming dUst in oxygen-rich M-type stars) focusing on oxygen-rich (O-rich) stellar winds. The Atomium project was approved (113.2 hr), being as such the first ALMA Large Program in the field of stellar evolution. ALMA gives us the unique

[1] Institute of Astronomy, KU Leuven, Celestijnenlaan 200D B2401, 3001 Leuven, Belgium
[2] Department of Space, Earth and Environment, Chalmers University of Technology, Onsala Space Observatory, 43992, Onsala, Sweden
[3] Université Côte d'Azur, Observatoire de la Côte d'Azur, CNRS, Lagrange, CS 34229, Nice, France
[4] LESIA, Observatoire de Paris, Université PSL, CNRS, Sorbonne Université, Université de Paris, 5 place Jules Janssen, 92195 Meudon, France

ability to study the gaseous dust precursors in O-rich winds - the many oxides and hydroxides - something we cannot do in carbon-rich (C/O > 1) winds where the aromatic molecules and PAHs that likely grow into carbonaceous grains cannot be observed with ALMA. In addition, the abundances of the most chemically active species in M-type AGB and RSG stars are closer to the average Galactic ('cosmic') abundances. However, some crucial pieces of information are missing from the ALMA data, being the locus of the dust formation, the dust composition, the size of the dust grains, and the radial distribution of the dust species.

2.2 The optical counterpart to ATOMIUM

Unraveling the gas-dust formation pathways implies mapping the relevant molecular and dust distribution in the close vicinity of stars at a very high spatial resolution. Even more, these mappings should be done almost simultaneously (within $\sim$ 1 week) since recent VLT/SPHERE results prove that the photospheric variability of AGB and RSG stars, and by extension of their dust nucleation properties, has an impact on the dust characteristics of the order of days (Khouri et al. 2016). We obtained VLT/SPHERE (Beuzit et al. 2019) and VLTI/MATISSE (Lopez et al. 2014) Target of Opportunity time in order to observe the ATOMIUM targets with these instruments while ALMA scrutinizes them using one of its largest array configuration. This allows us to probe the same spatial scales at different wavelength domains (Fig. 1).

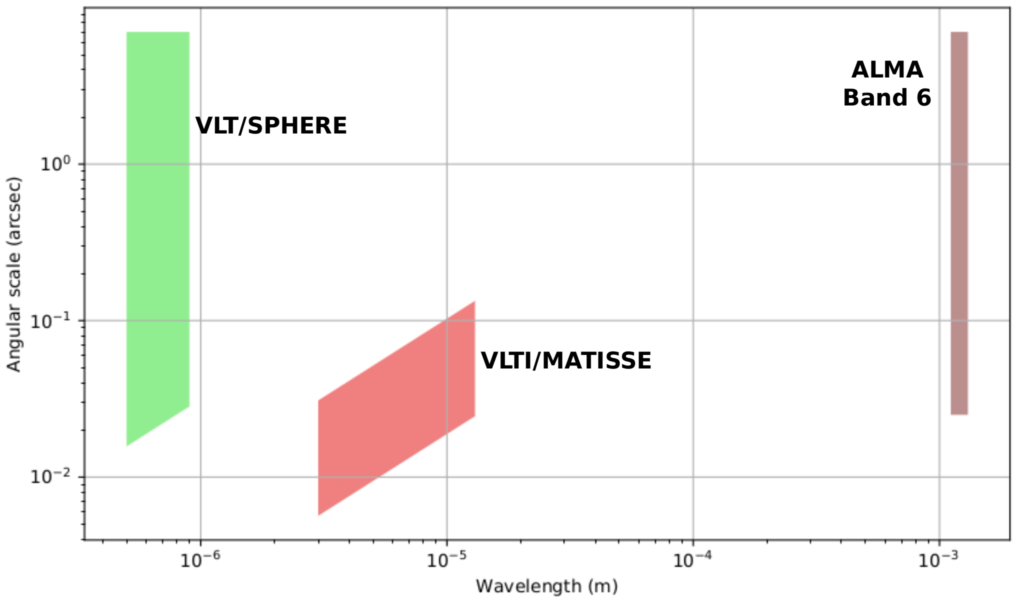

Fig. 1. Wavelength and angular resolution coverage of the ATOMIUM large program and its optical counterparts with VLT and VLTI.

The ZIMPOL visible unit of the VLT/SPHERE instrument provides detailed maps of the linear polarization degree yielding dust scattering locations and inferred dust grain sizes. The high angular resolution of VLTI/MATISSE in the mid-infrared reveals the dust composition, and the radial distribution of dust species (like e.g. Al_2O_3) and gaseous dust precursors very close to the stellar surface. Comparison between these dust density distributions and the gas density distribution retrieved from our ALMA data will pinpoint the location of the dust nucleation sites, the fraction of gaseous dust precursors that condensed into grains, the gas-to-dust mass ratio, and the dynamical behavior starting from the stellar atmosphere throughout the wind acceleration zone.

3 A simulation: the L_2 Puppis system

The acquisition of the VLT/SPHERE and VLTI/MATISSE data is scheduled from June to August 2019, when ALMA will be in its largest array configuration. Therefore, we present here how MATISSE can pinpoint the dust location using the nearby AGB star L_2 Pup as a test-case.

L_2 Pup is an O-rich AGB star located at 64 pc and surrounded by a dusty disk seen with VLT/NACO observations (Kervella et al. 2014). This circumstellar disk is caused by the mass loss of the star and its shaping by a companion first detected by Kervella et al. (2015) with VLT/SPHERE. Further observations with ALMA (Kervella et al. 2016) have refined the characterization of the system. The primary is an $0.6\,M_\odot$ AGB star, evolved from a $1\,M_\odot$ star on the main sequence. The companion is a $12\pm16\,M_{Jup}$ body. This means that it could be a planet or a brown dwarf. The authors argue that the dust clump hypothesis can be rejected due to the lifetime of the object between the VLT/SPHERE and ALMA observations. These precise mass measurements were obtained from the ALMA observations of the gas disk whose Keplerian behavior allowed to constrain the mass of L_2 Pup A, and from the difference of position between the geometrical center of the system and its photocenter for L_2 Pup B. The outer edge of the gas disk had a sub-Keplerian behavior in the area where it was cohabiting with the dust disk seen in the optical. This has been interpreted as friction on the dust grains. Indeed, the radial pressure from the primary star on the dust grains reduces the local effective gravity, which in turn reduces the orbital velocity.

We see that the geometry of the L_2 Pup system is rather well constrained. We can use it to make a simulation of the Atomium observations with the VLTI/MATISSE instrument in the mid-infrared. We used the radiative transfer code RADMC-3D (Dullemond 2012) in order to produce simulations of the dusty disk around the star. We used the same grid and disk parameters as Kervella et al. (2015). However, we used three different inner radii for the disk: 1.5, 4 and 6 au. After doing the radiative transfer, RADMC-3D uses a ray-tracing algorithm to produce cube images of the system (Fig. 2, top). This image are then used as input for the Aspro2 software to make a simulation of MATISSE observations in the N band. For the purpose of the exercise we used only 1 single point of observation at transit. The resulting squared visibilities are represented as a function of wavelength for each baseline and each inner radius on the bottom part of Fig. 2.

The dust disk appears detected by MATISSE. In particular the $10\,\mu$m silicate features is prominent on the shortest baselines where the presence of the resolved disk creates a drop in the squared visibility for each simulation. Moreover, each simulation provides a different signature in the different baselines. This means that we can pinpoint the dust location around the star. The MATISSE observation alone cannot provide enough geometrical information but by combining the ALMA high angular resolution, the SPHERE visible polarization imaging and the MATISSE velocity, we will be able to constrain the onset of dust condensation around the Atomium targets. The interpretation of the observed data will make use of the 3D radiative transfer codes RADMC-3D and McMax (Min et al. 2009). This will allow us to retrieve key parameters such as the composition and size of the dust grains as well as the density, temperature and location of the dust structures. This will prove essential in better characterizing the processes leading to dust condensation within the AGB winds.

4 Conclusions

The Atomium large program will revolutionize our understanding of the mass loss of O-rich cool evolved stars. It will unravel the phase transition from gas-phase to dust species, pinpoint the chemical pathways, map the morphological structure, and study the interplay between dynamical and chemical phenomena. VLTI/MATISSE observations will play a crucial role in this project. As demonstrated with radiative transfer simulations on the nearby AGB star L_2 Pup, they will provide us with unambiguous dust detection and will constrain the dust condensation locus.

This article is submitted on behalf of the Atomium consortium* This project has received funding from the European Union's Horizon 2020 research and innovation program under the Marie Skłodowska-Curie Grant agreement No. 665501 with the research Foundation Flanders (FWO) ([PEGASUS][2] Marie Curie fellowship 12U2717N awarded to M.M.). LD acknowledges support from the ERC consolidator grant 646758 AEROSOL. This research has made use of the Jean-Marie Mariotti Center `Aspro` service †. This research made use of Matplotlib (Hunter 2007), and Astropy‡, a community-developed core Python package for Astronomy (Astropy Collaboration et al. 2013).

*https://fys.kuleuven.be/ster/research-projects/aerosol/atomium/atomium
†Available at http://www.jmmc.fr/aspro
‡Available at http://www.astropy.org/

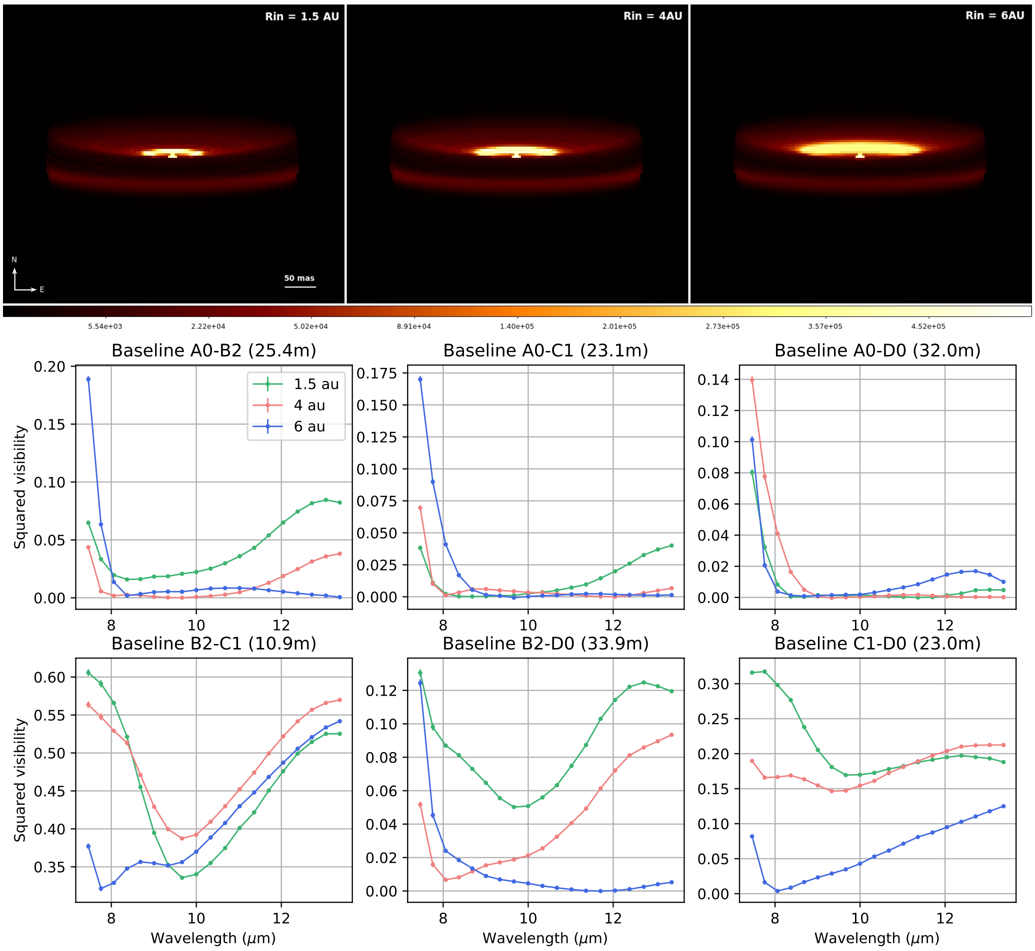

Fig. 2. Top: Simulations of the L_2 Puppis dust disk from the RADMC-3D code. Three different inner radius are used. The image is obtained at 10 μm. **Bottom:** Corresponding VLTI/MATISSE simulations using Aspro.

References

Astropy Collaboration, Robitaille, T. P., Tollerud, E. J., et al. 2013, A&A, 558, A33

Beuzit, J.-L., Vigan, A., Mouillet, D., et al. 2019, arXiv e-prints

Dullemond, C. P. 2012, RADMC-3D: A multi-purpose radiative transfer tool, astrophysics Source Code Library

Gustafsson, B. & Plez, B. 1992, in Instabilities in Evolved Super- and Hypergiants, ed. C. de Jager & H. Nieuwenhuijzen, 86

Höfner, S. & Olofsson, H. 2018, A&A Rev., 26, 1

Homan, W., Richards, A., Decin, L., de Koter, A., & Kervella, P. 2018, A&A, 616, A34

Hoyle, F. & Wickramasinghe, N. C. 1962, MNRAS, 124, 417

Hunter, J. D. 2007, Computing In Science & Engineering, 9, 90

Kervella, P., Homan, W., Richards, A. M. S., et al. 2016, A&A, 596, A92

Kervella, P., Montargès, M., Lagadec, E., et al. 2015, A&A, 578, A77

Kervella, P., Montargès, M., Ridgway, S. T., et al. 2014, A&A, 564, A88

Khouri, T., Maercker, M., Waters, L. B. F. M., et al. 2016, A&A, 591, A70

Lopez, B., Lagarde, S., Jaffe, W., et al. 2014, The Messenger, 157, 5

Maercker, M., Mohamed, S., Vlemmings, W. H. T., et al. 2012, Nature, 490, 232

Min, M., Dullemond, C. P., Dominik, C., de Koter, A., & Hovenier, J. W. 2009, Astronomy and Astrophysics, 497, 155

Tielens, A. G. G. M. 2005, The Physics and Chemistry of the Interstellar Medium

Session 05

Atelier Général PN GRAM

SF2A 2019
P. Di Matteo, O. Creevey, A. Crida, G. Kordopatis, J. Malzac, J.-B. Marquette, M. N'Diaye, O. Venot (eds)

SEARCH FOR MULTIPLY-IMAGED QUASARS IN THE GAIA DR2

C. Ducourant[1], A. Krone-Martins[2], L. Delchambre[3], O. Wertz[3,], L. Galluccio[4], R. Teixeira[5], J.-F. Le Campion[1,], S. Scarano[6], M.J. Graham[7], S.G. Djorgovski[7,], D. Stern[7,], E. Slezak[4,], C. Spindola-Duarte[5,], J. Surdej[3,], F. Mignard[4,], U. Bastian[8], J. Wambsganss[8,], J. Klüter[8,] and C. Boehm[9]

Abstract. Gaia was mainly designed for the study of stars in our Galaxy. However, by continuously scanning the entire sky, it also provides informations on all kind of objects that fall in its fields of view, including extragalactic objects. Amongst these extragalactic sources, quasars stand out to be some of the most peculiar objects that Gaia observe. Beside the fact that they play a crucial role in fixing the Gaia Celestial Reference Frame, they also have their intrinsic interest in cosmology. One of their important application occurs when a massive galaxy stands along the line of sight joining the quasar and the observer as, in this case, multiple images of this quasar may form. The time delays measurement between these lensed images then provide a reliable estimation of H0 that is independent of the commonly used cosmic distance ladder. We describe here how the precise relative positions and magnitudes, as provided by Gaia, can be used in order to probe the lensing nature of clusters of objects coming from the Gaia DR2. We present some newly discovered lenses that were spectroscopically confirmed in recent follow-up observations.

Keywords: Gravitational lensing: strong, Quasars: general, Astrometry, Methods: data analysis, Catalogues, Surveys

1 Introduction

Strong gravitational lenses probe many facets of cosmology: dark matter halos of galaxies, substructures in galaxy halos, the determination of the Hubble constant independently of the cosmic distance ladder, and properties of dark energy. However, their detection requires exceptional imaging capabilities, posing a challenge to present day all-sky surveys from the ground since these count on limited spatial resolution due to atmospheric seeing. Thus, the limited number of lensed systems has historically plagued many of the potential studies that can be performed with these objects, due to local systematics at the individual objects modelling. The data from the second release of ESA/Gaia Space Mission (Gaia Collaboration et al. 2018) is changing this situation dramatically. Gaia is at the present time conducting the largest and most accurate all-sky astrometric survey from space. Its main goal is to produce a three-dimensional dynamical map of the Milky Way based on the measurement of positions, parallaxes, proper motions and spectrophotometric parameters for more than one billion stars, but the instrument also detects millions of compact galaxies and QSOs (Krone-Martins et al. 2013; Ducourant et al. 2014; de Souza et al. 2014). Thus, a careful analysis of the GDR2 (Gaia Collaboration et al.

[1] Laboratoire d'astrophysique de Bordeaux, Univ. Bordeaux, CNRS, B18N, allée Geoffroy Saint-Hilaire, 33615 Pessac, France
[2] CENTRA, Faculdade de Ciências, Universidade de Lisboa, Ed. C8, Campo Grande, 1749-016 Lisboa, Portugal
[3] Institut d'Astrophysique et de Géophysique, Université de Liège, 19c, Allée du 6 Août, B-4000 Liège, Belgium
[4] Université Côte d'Azur, Observatoire de la Côte d'Azur, CNRS, Laboratoire Lagrange, Boulevard de l'Observatoire, CS 34229, 06304 Nice, France
[5] Instituto de Astronomia, Geofisica e Ciencias Atmosfericas - IAG/USP - Brasil
[6] Universidade Federal de Sergipe - Brasil
[7] California Institute of Technology, 1200 E. California Blvd, Pasadena, CA 91125, USA
[8] Zentrum für Astronomie der Universität Heidelberg, Astronomisches Rechen-Institut, Mönchhofstr. 12-14, 69120 Heidelberg, Germany
[9] Department of Physics - University of Sydney - Australia

2018) [5] presents a unique opportunity to perform the first magnitude-limited census of strongly lensed QSOs down to image separations of 0.18 ". Finet and Surdej Finet & Surdej (2016) estimated that from the 0.6 million QSOs to be observed by Gaia, about 2900 of them should be multiply imaged and resolved by the Gaia final data release including 250 systems formed by more than two lensed images. Gaia will lead to an increase in the number of known lensed QSOs by more than one order of magnitude with respect to what is known today, and will provide a unique dataset to study the individual lensed systems and to constitute a statistically significant sample for the study of the evolution of the population of the deflecting galaxies and to constrain cosmological parameters.

2 The Gaia GraL project

Since the Gaia DR2 (April 2018), the Gaia GraL (Gravitational Lenses) group has devoted large efforts to detect and extract from the Gaia DR2 a whole sky survey of new multiply imaged quasars. Our strategy is threefold.

First, our research focused on all known multiply imaged quasars by gravitational lensing. We first set up a database of 481 multiply imaged quasars (47 of these being quads with 4 images) and then searched counterparts of their components into the Gaia DR2. 172 lenses are detected by Gaia DR2 and 12 quads are fully detected by the satellite. A quick modelling demonstrates the improvement of fitting with the Gaia sub-mas astrometry when compared to Hubble Space Telescope measurements (Ducourant et al. 2018) and demonstrates the great potential of Gaia for a realist modelling of these complex phenomena.

In the second step, we considered all known quasars and candidates AGNs available in the litterature that we compiled in a state-of-the-art list of 3 millions objects. We then searched for the presence in the Gaia DR2 of one or more nearby (6 arcsecond) objects. The $\sim$ 20 000 resulting clusters of sources were then filtered out to exclude galactic plane and to reject clusters with discrepant parallaxes of proper motions between the components and finally a machine learning lens classifier using astrometry has been applied to the remaining clusters to test the reproducibility of the configuration by a simple model of Gravitational Lenses (NSIE) (with noise and missing images). This left us with three good candidates each with 4 images (Krone-Martins et al. 2018).

In the third and major axis of action of our strategy, we designed a method to blindly identify clusters of sources from the DR2 using the Hierarchical Triangular Mesh technique that are compatible with gravitationally lensed quasars (Delchambre et al. 2019). The list of clusters extracted with these approaches is expected to be polluted with contaminants. To discard the most obvious ones, we thus applied soft astrometric filters derived from the behaviour of known GL (Ducourant et al. 2018) as we did in the second step, to differentiate genuine candidates from fortuitous clusters of stars. Gaia also provides broad band photometric measurements in the G-band and a colour indicator for a fraction of the not too faint objects . Because the gravitational lensing phenomenon is achromatic, we also rejected clusters for which the individual colour indicators was available and significantly differ from each other. The local density of sources around the clusters have also been calculated and clusters in too dense regions were also discarded. Then we classified the remaining clusters that successfully passed the filters by assigning them a probability that reflects the match between a candidate and the learning set composed of $\sim 10^8$ simulated image configurations that we used to build Extremely Randomised Trees. From the most probable clusters thirty appeared good candidates with 4 images. From them, 15 correspond to known lenses and 15 are unknown that require spectroscopic validation.

3 Spectroscopic validation

The GraL group has applied for observing time to several large telescopes spread over both hemisphere to spectroscopically validate the candidates. Proposal were submitted to Keck/LRIS, Palomar/P200,DOT/imager, ESO-VLT/Muse, ESO-NTT/EFOSC, SOAR, Gemini south/GMOS, AAT/KOALA and LBT/MOD1-2.

The group has have been granted of one night at Keck and 2 nights at Palomar by semester for 2018 and 2019, 2h at ESO-VLT, 3 nights at ESO-NTT in 2018 and 2019, 6h at Gemini and few hours at LBT. Preliminary reduction of these observations led to the validation of 9 quadruply-imaged quasars and several doubly imaged ones (Wertz et al. 2019). We present in Figure 1 the preliminary spectroscopic validation at ESO-NTT of GRAL165105371-041724936, one of our candidates together with the Pan-STARRS image of the system with components identified.

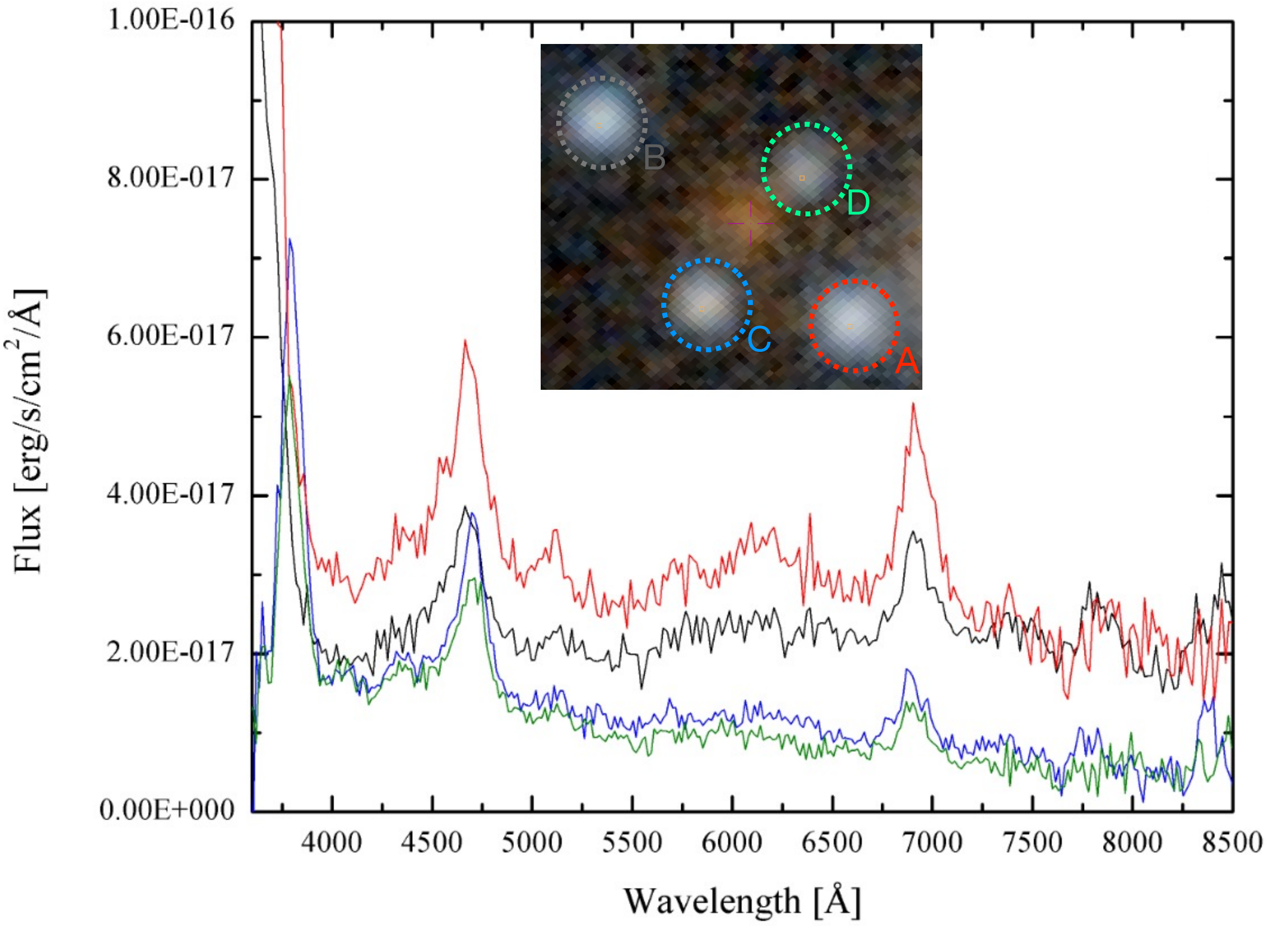

Fig. 1. GRAL165105371-041724936, a multi-imaged quasar candidate spectroscopically confirmed with NTT/EFOSC2 observations. Preliminary reduction indicates a redshift of 1.5 for the quasar. In the upper part of the spectrum is shown the Pan-StARRS image of the system with the identification of the components.

The general observational strategy of observation to reduce observing time consists in observing the candidates placing 2 components in the same slit and comparing the spectral characteristics of the components. Then another observation targets the remaining components and so forth. The spectra were processed using the IRAF package for long-slit reduction. Overscan, bias and flat were applied to all frames. No sky-flat corrections frames were available for illumination corrections. However it does not affect our results significantly, since all targets placed in the slit were very near each other (distances lower than 10 arcsec). Wavelength calibration was done using HeAr arc lamps, in slits of 1.5 and 5 arcsecs. The spectral resolution at ESO-NTT was limited by the seeing (about 1 arcsec) and the grating (smaller than 15 A), and for the observed z the velocity dispersion is lower than 1%. Flux calibration and extinction corrections were performed using spectrophotometric standards observed one night before. To recognise spectral line it was used the procedure of cross correlation of the observed spectra with an adaptation of the SDSS DR6 quasar spectral lines, with 58 emission lines. For the determination of the radial velocities of each spectra it was used the RVSAO package Kurtz & Mink (1998).

With the Keck and Palomar observations we could confirm so far the lens status of 8 quadruply-imaged quasars. With the ESO-NTT/EFOSC2 observations were able to confirm 1 new gravitational lenses with 4 images and 4 with two images., all selected from the cluster list with high ERT probability. The Gemini observations are being reduced and preliminary results indicate that probably one quad more is to be included in our list of validated lenses (Krone-Martins et al., in prep, 2019).

4 Conclusion

The Gaia GraL group has devoted large efforts, using the most advanced machine learning algorithms, to blindly extract multiply-imaged quasars from the Gaia data releases from astrometry and photometry only. Spectroscopic validation have so far shown that the method is efficient and the group is in the way to set up the first ever census of gravitational lenses (within the limitations of the Gaia instrument). The first two data releases of Gaia are known to be largely incomplete at small angular distances, where lye most multiple images of quasars. If the forthcoming Gaia EDR3 (mid 2020) is more complete to this respect we can hope to unveil a new population of these phenomena.

We acknowledge the support from 'Actions sur projet INSU-PNGRAM', from 'Actions Nationale d'Observation Gaia', from 'Service d'Observation OASU'. AKM acknowledges the support from the Portuguese Fundação para a Ciência e a Tecnologia (FCT) through grants SFRH/BPD/74697/2010, from the Portuguese Strategic Programme UID/FIS/00099/2013 for CENTRA, from the ESA contract AO/1-7836/14/NL/HB and from the Caltech Division of Physics, Mathematics and Astronomy for hosting a research leave during 2017-2018, when this paper was prepared. LD and JS acknowledge support from the ESA PRODEX Programme 'Gaia-DPAC QSOs' and from the Belgian Federal Science Policy Office. OW acknowledges support from a fellowship for Postdoctoral Researchers by the Alexander von Humboldt Foundation. RT acknowledges the support from the Brazil-France exchange programmes (FAPESP) and Coordenação de Aperfeiçoamento de Pessoal de Nível Superior (CAPES) – Comité Français d'Évaluation de la Coopération Universitaire et Scientifique avec le Brésil (COFECUB). SGD and MJG acknowledge a partial support from the NSF grants AST-1413600 and AST-1518308, and the NASA grant 16-ADAP16-0232. This work has made use of the computing facilities of the Laboratory of Astroinformatics (IAG/USP, NAT/Unicsul), whose purchase was made possible by the Brazilian agency FAPESP (grant 2009/54006-4) and the INCT-A, and we thank the entire LAi team, specially Carlos Paladini, Ulisses Manzo Castello, and Alex Carciofi for the support.This research has made use of the VizieR catalogue access tool, CDS, Strasbourg, France. The original description of the VizieR service was published in A&AS 143, 23. This research has made use of 'Aladin sky atlas' developed at CDS, Strasbourg Observatory, France. This work has made use of results from the ESA space mission *Gaia*, the data from which were processed by the *Gaia* Data Processing and Analysis Consortium (DPAC). Funding for the DPAC has been provided by national institutions, in particular the institutions participating in the *Gaia* Multilateral Agreement. The *Gaia* mission website is: http://www.cosmos.esa.int/gaia. Some of the authors are members of the *Gaia* (DPAC).

References

de Souza, R. E., Krone-Martins, A., dos Anjos, S., Ducourant, C., & Teixeira, R. 2014, A&A, 568, A124

Delchambre, L., Krone-Martins, A., Wertz, O., et al. 2019, A&A, 622, A165

Ducourant, C., Krone-Martins, A., Galluccio, L., & Teixeira, R. 2014, in SF2A-2014: Proceedings of the Annual meeting of the French Society of Astronomy and Astrophysics, ed. J. Ballet, F. Martins, F. Bournaud, R. Monier, & C. Reylé, 421–425

Ducourant, C., Wertz, O., Krone-Martins, A., et al. 2018, A&A, 618, A56

Finet, F. & Surdej, J. 2016, A&A, 590, A42

Gaia Collaboration, Brown, A. G. A., Vallenari, A., et al. 2018, A&A, 616, A1

Krone-Martins, A., Delchambre, L., Wertz, O., et al. 2018, A&A, 616, L11

Krone-Martins, A., Ducourant, C., Teixeira, R., et al. 2013, A&A, 556, A102

Kurtz, M. J. & Mink, D. J. 1998, PASP, 110, 934

Wertz, O., Stern, D., Krone-Martins, A., et al. 2019, A&A, 628, A17

SF2A 2019
P. Di Matteo, O. Creevey, A. Crida, G. Kordopatis, J. Malzac, J.-B. Marquette, M. N'Diaye, O. Venot (eds)

CHARACTERISATION OF EXTRAGALACTIC SOURCE POSITIONS THAT DEFINE THE CELESTIAL REFERENCE FRAME

C. Gattano[1] and P. Charlot[1]

Abstract. We investigated the astrometric position variations of the most observed sources in astrometric and geodetic VLBI, with the goal of characterizing such variations. In a first stage, we aimed at categorizing individually the source positions. Are they stable enough under the VLBI astrometric accuracy to materialize ultra-accurate fiducial marks on the sky. In a second stage, our goal was to determine whether there are any preferred directions in those source position variations. Our result favor source-dependent systematic variability that affect the position stability. Additionally, it was also found that the source position variations occur along particular directions that might find their origin in the intrinsic astrophysics of the sources.

Keywords: Astrometry, Reference systems, Techniques: interferometric

1 Introduction

The International Celestial Reference Frame (ICRF3, Charlot et al. in prep.) is based on 4 536 radio sources which are associated with Active Galactic Nuclei (AGN, Padovani et al. 2017). Those sources have been observed with Very Long Baseline Interferometry (VLBI) in its geodetic mode since 1979 in S/X (2GHz/8GHz) bands. In geodetic mode, the technique measures the source positions on the sky with an uncertainty which ranges from 30 μas to 1 mas or more, depending mostly on the number of times the source has been observed, from a few times to more than a thousand times. Given their cosmological distances, the detection of the proper motion of those sources is unreachable at these accuracies, and furthermore, they are compact on VLBI scales*. It is for all these reasons that these sources are well suited to realise the ICRF.

Since the first ICRF realisation in 1998 (Ma et al. 1998), it has been known however that some sources amongst the extensively observed ones show noticeable variations in their coordinates over time. Hence, the sources observed for astrometric and/or geodetic purposes are not always ideal fiducial marks on the sky, and it is necessary to select a set of primary sources, amongst the most stable ones, to define the fundamental axes of the frame at best. For the ICRF3, there are 303 such defining sources. Together, they ensure the axis stability of ICRF3 at the order of 10 μas (Charlot et al. in prep.).

Ten years ago, the number of very "unstable" sources (called special handling sources) was found to be 39, which is a small proportion† considering the 3 414 sources of the whole ICRF2 (Fey et al. 2015). Recently, we have assessed the individual source stability, in an astrometric point of view, i.e. how much the source position varies. The next section describes the methodology used to this end and reports about the results (details are reported in Gattano et al. 2018).

2 Analysis of source astrometric behaviour

We used the observations from 24-hour sessions publicly available in the data centres of the International VLBI Service for astrometry and geodesy (IVS, Nothnagel et al. 2017) until august 2018. We computed the coordinate times series of 663 sources observed in more than 20 VLBI sessions (see Fig. 1 on the left for an

---

[1] Laboratoire d'astrophysique de Bordeaux, Univ. Bordeaux, CNRS, B18N, allée Geoffroy Saint-Hilaire, 33615 Pessac, France.
*VLBI images of a number of sources used to define the ICRF are available from the Bordeaux VLBI Image Database (BVID, Collioud & Charlot 2019) → `http://bvid.astrophy.u-bordeaux.fr/database.html`.
†Mainly due to the fact that most of the sources have not been observed enough to assess their coordinate variability.

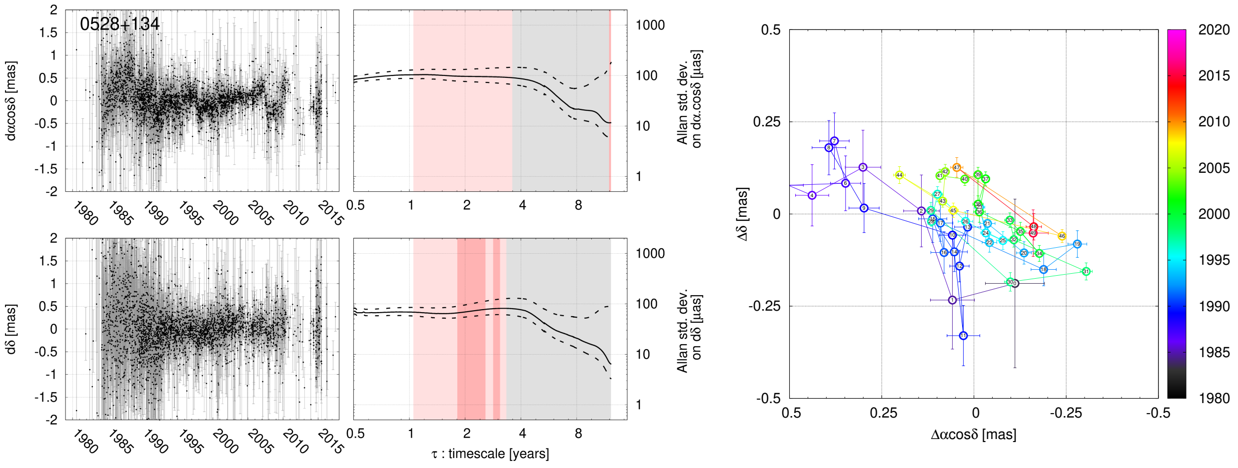

Fig. 1. Left: Coordinate time series of the source 0528+134 presented as right ascension (top) and declination (bottom) offsets with respect to the mean position of the source. Aside is the corresponding Allan standard deviation functions. They are given in a log-log scale with respect to the time scale, i.e. the length of the window used to compute the averaged positions of the source. A gray background indicates a stable position at the corresponding time scales, a red background indicates an unstable position, and a pink background indicates an intermediate phase. **Right:** Projection of the two coordinate times series (reduced to a few tens of points) trajectory on the sky plane.

example of the coordinate time series of a source observed several hundreds of times). Then, we analysed those time series using the Allan standard deviation, a statistical tool developed originally in the field of time metrology to analyse the stability of atomic clocks (Allan 1966). This tool enables (1) to estimate the standard deviation of the position at different time scales and (2) to distinguish the stability of the position (of which the measurements are considered as resulting from noise processes) at each of these time scales. The position stability is qualified from the slope of the Allan standard deviation function with respect to the time scale in a log-log representation (see Fig. 1). If the slope is negative, the position is defined as stable at the considered time scale in the sense that, if we pursue the observation of the considered source further (and access longer time scales), the position uncertainty will be improved (the time scale ranges associated with position stability are shown by a grey background in Fig. 1). An example is given by a purely white noise process, characterized with a slope equal to -0.5. If the slope is positive, the position is defined as unstable at the considered time scale with an uncertainty degrading as the time scale increases (the time scale ranges associated with instability are shown by a red background in Fig. 1). For example, in the case of a purely red noise process, also called random walk, the slope is $+0.5$. The boundary in between is given by the pink noise process, also called flicker noise, which provides a position uncertainty that remains constant as the observations of the source accumulate.

We introduced as the source *astrometric behaviour* the sequence of the time scale dependent position stability considering the time scales starting from 1 year and increasing. For example, the declination of the source in Fig. 1 is characterized by a sequence "unstable (1–3 yrs) – stable (3–10 yrs)". The astrometric behaviour is defined as stable in absence of instability in such a sequence. It is defined as unstable if instability is found on the longest time scales. Otherwise, it falls into an intermediate category. In practice, the two source coordinate time series were treated independently and we kept the worst category to decide upon the astrometric behaviour which qualify the source stability. A global indicator is also computed to quantify the source position stability based on the level of the source coordinate Allan standard deviation functions.

Figure 2 provides the results for our entire sample of 663 sources. By strictly applying the process above, the source sample counts 57 stable sources (designated AV0 sources), 160 unstable sources (designated AV2 sources) and 446 intermediate sources (designated AV1 sources). We further developed a statistical validation process based on a Monte-Carlo simulation of pure white noise signals sampled on the source observation epochs. This process enables the rehabilitation of AV2 and AV1 sources into AV1 or AV0 categories under the argument that a change of slope may originated from the irregularity of the sampling. It is based on the analysis of the spread

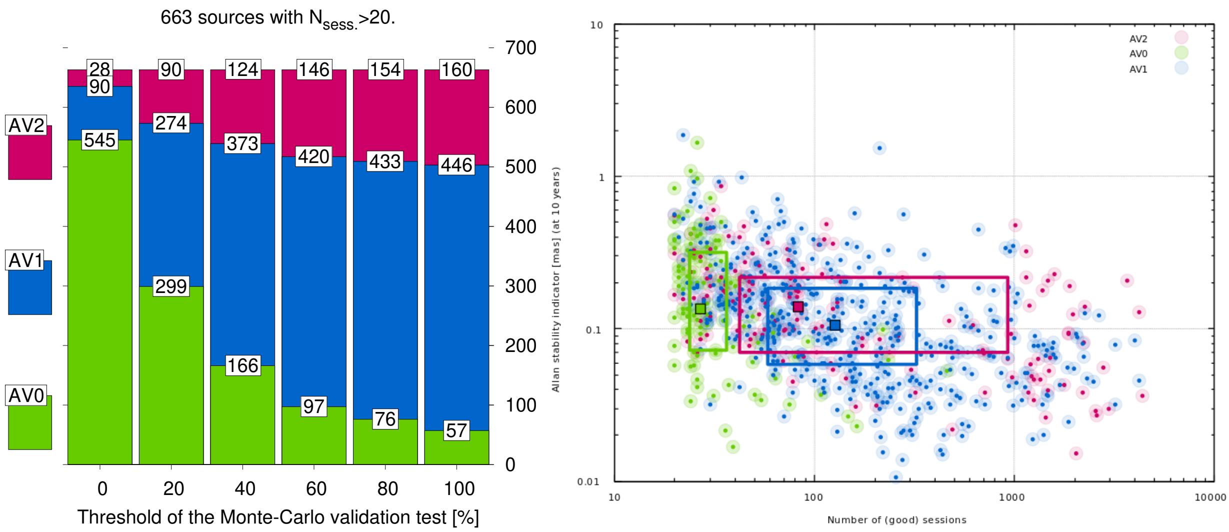

Fig. 2. Left: Source categorization depending on astrometric behaviour : stable (AV0, green), intermediate (AV1, blue), unstable (AV2, red). The percentage in abscissa indicates the threshold of a statistical validation test dealing with the trend of the computed Allan standard deviation functions. It enables rehabilitation for an increasing number of AV2 sources into AV1 or AV0 categories and AV1 sources into AV0 category when loosening the threshold (see text for details). **Right:** Distribution of the sources (categorized using a threshold at 60%, i.e. corresponding tp the third bar from the right side of the left figure) according to the number of sessions in which they are observed and their position stability indicator based on the coordinate Allan standard deviation function. Filled squares indicate the median position for each category while the larger empty rectangles indicate the associated inner quartiles boundaries.

of simulated purely white noise Allan standard deviation functions which is due to this irregularity[‡] and how the source Allan standard deviation functions compare with this spread. The different bars on the left panel of Fig. 2 indicate the evolution of the categorization as the threshold of the rehabilitation is loosened. As shown in this graph, the threshold needs to be quite loosened to get a significantly different distribution. The right part of Fig. 2 presents the distribution of the sources (as categorized with the threshold fixed at 60%) with respect to the number of sessions in which they were observed and their source stability indicator. This distribution reveals that the stable sources are in majority the less observed sources. Our interpretation is that the accuracy of the astrometric VLBI technique is now such that all sources may show position instabilities if observed long enough.

Given this astrometric variability, nearly generalised to all the sources, we investigated in a second stage if the variation arises in random or peculiar source-dependent directions. The next section presents approach used and the results of this study.

3 Preferred directions for source astrometric variations

For the 215 sources observed more than 200 times, we attempted to extract preferred directions from the observed astrometric variations. We worked with reduced coordinate times series (i.e. with coordinates averaged every 50–100 observations) as shown for example in the right part of Fig. 1. Each successive pair of points was converted into a vector that provides the direction of the position variation between the two epochs. Coordinate uncertainties were converted in the direction uncertainty. Then, each vector direction was weighted with its normalized length and all directions and their uncertainties were combined to derive a Probability Density Function (PDF) characterizing the distribution of directions. From this PDF, the preferred direction and its uncertainty are then extracted from the peak of the PDF and its width, respectively. For some sources, two (or more) peaks show up, indicating that the variation arises in multiple preferred directions.

[‡]In the case of a regular sampling, a pure white noise signal provides a slope of -0.5 for the Allan standard deviation function in a log-log scale.

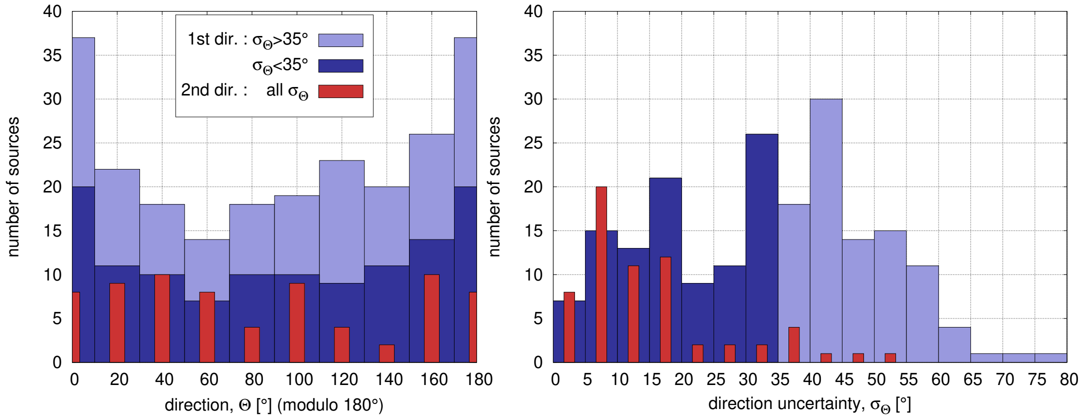

Fig. 3. Left: Distribution of the directions extracted from the source astrometric variations. In blue are presented the primary directions (successfully extracted for 90% of the sources), and in red the secondary directions (which are found for 30% of the sources). **Right:** Distribution of the direction uncertainties. Dark blue colour indicates well-constrained directions, i.e. with an uncertainty lower than 35°, while light blue colour indicates the directions that are not well-constrained, i.e. with an uncertainty larger than 35°.

Considering our sample, it is found that the astrometric variation arises in one (and only one) preferred direction for about 60% of the sources while for another 30%, it arises in two preferred directions. Figure 3 presents the distribution of those directions in the range 0°–180°. The uncertainties are up to 80°. In this regard, we consider that a direction is well constrained if its uncertainty is lower than 35°. For the primary directions, the population is divided in two similar halves with about the same number of sources that have well-constrained directions and less constrained directions. On the opposite, the secondary directions are in majority well-constrained.

We note a peculiar excess of primary directions near 0° which corresponds to the north-south direction. It is known that the VLBI antenna network suffers for a lack of baselines oriented in this particular direction. This deficiency in the network induces a generally lower declination precision and potential systematics compared to the right ascension accuracy which may explain the excess of primary direction near 0°. On the contrary, the distribution of the rest of the sample is homogeneous and hence possibly indicates in that the astrometric variations originate from source intrinsic astrophysical phenomena. Finally, we note that the distribution of the secondary directions found for 30% of the sources does not show any particular excess.

4 Discussion and conclusion

In conclusion, the sources observed with geodetic VLBI and used to define the ICRF often show variations in their coordinates that limit their potential as ultra-accurate fiducial marks on the sky. Such source-dependent variations arise preferably in a particular direction, and occasionally in two different directions.

By observing AGN with VLBI, we focus on a small part of the source jet with a relatively compact structure. Nevertheless, this structure may be variable. It can become extended, or even split into one VLBI core and separate knots potentially moving down the jet, with the direction of the extension or the direction joining the VLBI core and the knots representing the direction of the source jet projected on the sky plane. A change of the source structure induces a variation of the VLBI delays depending on the relative orientation of this structure with respect to the projected observing baselines. Without correcting for such effect, the measured astrometric position of the source may thus vary without any true changes of the coordinates of its VLBI core.

Additionally, the VLBI core position may change as well. For example, if the jet is precessing, the VLBI core may follow an elliptical trajectory as projected on the sky. It is also suspected that the VLBI core could be subjected to position instability along the jet, shifted downstream and upstream, due to occasional burst of the AGN activity. Finally, the presence of two (or more) supermassive black holes orbiting around each, each possibly having a variable VLBI core, may further complicate the picture. In this case the astrometric position measured with VLBI may be switched between the locations of the different VLBI cores depending on which one is brighter at a given time.

Observations of the ICRF3 sources continue. As time goes, these will keep bringing new information for a better understanding of the astrometric position variations, and hence of the underlying source physics. All such information will also contribute to adapting our strategies for the scheduling of the observations and further improve the realisation of the celestial reference frame.

This work has been supported by a CNES post-doctoral grant. These studies use data and products from the International VLBI Service for astrometry and geodesy.

References

Allan, D. W. 1966, IEEE Proceedings, 54, 221

Charlot, P., Jacobs, C. S., Gordon, D., et al. in prep., A&A

Collioud, A. & Charlot, P. 2019, in Proceedings of the 24$^{\text{th}}$ meeting of the European VLBI group for Geodesy and Astrometry

Fey, A. L., Gordon, D., Jacobs, C. S., et al. 2015, AJ, 150, 58

Gattano, C., Lambert, S. B., & Le Bail, K. 2018, A&A, 618, A80

Ma, C., Arias, E. F., Eubanks, T. M., et al. 1998, AJ, 116, 516

Nothnagel, A., Artz, T., Behrend, D., & Malkin, Z. 2017, Journal of Geodesy, 91, 711

Padovani, P., Alexander, D. M., Assef, R. J., et al. 2017, Astronomy and Astrophysics Review, 25, 2

THE NAROO PROGRAM

V. Robert[1], J. Desmars[2] and J.-E. Arlot[3]

Abstract. The astrometric monitoring of Solar System objects is an important step to assess their formation and evolution. However, it is necessary to have very accurate observations over a large timespan to quantify relevant effects and thus, improve dynamical models. In this framework, observations realized with "old" astro-photographic plates provide original, valuable and essential scientific data, that most recent technological means and computing tools can fully exploit. With the New Astrometric Reduction of Old Observations (NAROO) program, we intent to measure and (re-)reduce such observations, using a new generation sub-micrometric digitizer at Paris Observatory, and Gaia-DR2 star catalog for the astrometric reduction.

Keywords: Instrumentation: miscellaneous, Astrometry & Celestial Mechanics

1 History of the program and previous results

Most of the observatories and national archives have old and useful astro-photographic observations, but only a few part was already analyzed, used to support first space reconnaissance projects and dynamical studies. We estimate that less than 30% of the total amount was effectively analyzed, and mainly with manual methods that only allowed to provide relative data.

In 2006, we started thinking that digitization of such materials could be an attractive method to get original and accurate data over a large timespan, but a high accuracy in the measurement and the reduction of those plates was absolutely necessary (Robert et al. 2011). In the framework of a first partnership, we developed methods and algorithms adapted to specific plates provided by USNO (Washington D.C., USA), using the DAMIAN digitizer of ROB (Brussels, Belgium). From a set of about 550 plates of the Jovian system, taken from 1967 to 1997, and resulting in about 2600 single observations, we have been able to produce rms residuals of 35 mas for intersatellite positions (when the original reduction provided 100 mas), and of 72 mas for equatorial positions (which were not possible to get with the original reduction). We demonstrated the value of a new astrometric analysis of old photographic plates, resulting from their accurate measurement with the DAMIAN digitizer, and we were able to extract all the important information contained in the plate data, while correcting for instrumental and spherical effects during the reduction. The new reduction provided final accurate positions which were not only more accurate than those previously derived from manual measurements, but provided new information since we obtained equatorial positions for the first time with these plates.

Since we had demonstrated that a precise digitization and a new astrometric reduction of old photographic plates could provide very accurate positions, the leaders of the European Satellites Partnership for Computing Ephemerides (ESPaCE) project chose to consider such observations as a significant task. This project aimed at strengthening the collaboration and at developing new knowledge, new technology, and products for the scientific community in the domains of the development of ephemerides and reference systems for natural satellites and spacecraft (Thuillot et al. 2013). Several European research centers involved in space sciences and dynamics were associated. From 2011 to 2013, we obtained the large photographic plate archive of the Martian satellites taken at USNO from 1967 to 1997 for remeasurement and reanalysis, and the complete set of the Saturnian satellites taken from 1974 to 1998, as well. We had significant results since we demonstrated, in particular,

[1] IMCCE - Paris Observatory / IPSA, 75014 Paris, France
[2] LESIA - Paris Observatory, 75014 Paris, France
[3] IMCCE - Paris Observatory, 75014 Paris, France

that astrometric data derived from photographic plates can compete with those of old spacecraft (Robert et al. 2015, 2016). As a last demonstration, in Fig. 1, we investigated the effect of the signal-to-noise ratio (S/N) on the precision of the Saturnian observations. Comparing the decline in precision between new and former measurements, we confirmed the high value in continuing the reduction of old observations.

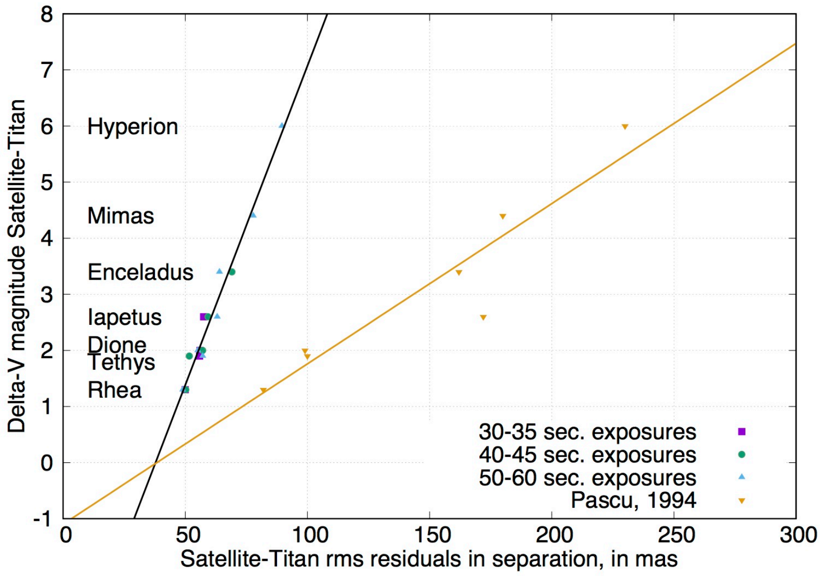

Fig. 1. rms residuals in separation from Titan as an indicator of the decline in positioning precision. Red line denotes new measurements by Robert et al. (2016). Orange line denotes former measurements made by Pascu (1994).

2 The NAROO centre

With the arrival of the Gaia-DR2 catalog (Lindegren et al. 2018), we are now allowed to analyze until the oldest photographic plates (close to 1890) without degrading the astrometric precision, due to errors on reference star positions and/or proper motions. Thus, in 2013, we have started creating a digitization centre*., at Paris Observatory, dedicated to the analysis of old astro-photographic plates for scientific purposes, and we are now almost to "open".

2.1 Hardware

Fig. 2 shows the NAROO digitizer as on 2019 April. The machine consists of a granite based Newport-Microcontrol air-bearing XY positioning table suited for mounting glass plates up to 350-mm wide. The complete set measures 1.90m x 1.29m x 1.60m, for about of 2 tons weight.

The optical unit consists of a Neo 5.5, 16 bit sCMOS Camera from Andor, mounted on a VS-TCM1-130/S telecentric 1:1 objective. This system is attached to the Z-axis above the XY table. The 2D sCMOS Camera provides images with 2560 x 2160 pixels of 6.5 μm x 6.5μm. The photographic images are illuminated from below with suitable very bright Light Emitting Diode's, controlled by a high precision DC power supply. The complete optical system was designed at Paris Observatory to avoid any distortion effects. The position of the XY table is read by Heidenhain encoders. The linearity and orthogonality of the (X, Y) axes were calibrated by Newport-Microcontrol using a laser interferometer. The local XY table positioning stability (how closely the

---
*https://bibnum.explore.univ-psl.fr/s/naroo/page/accueil

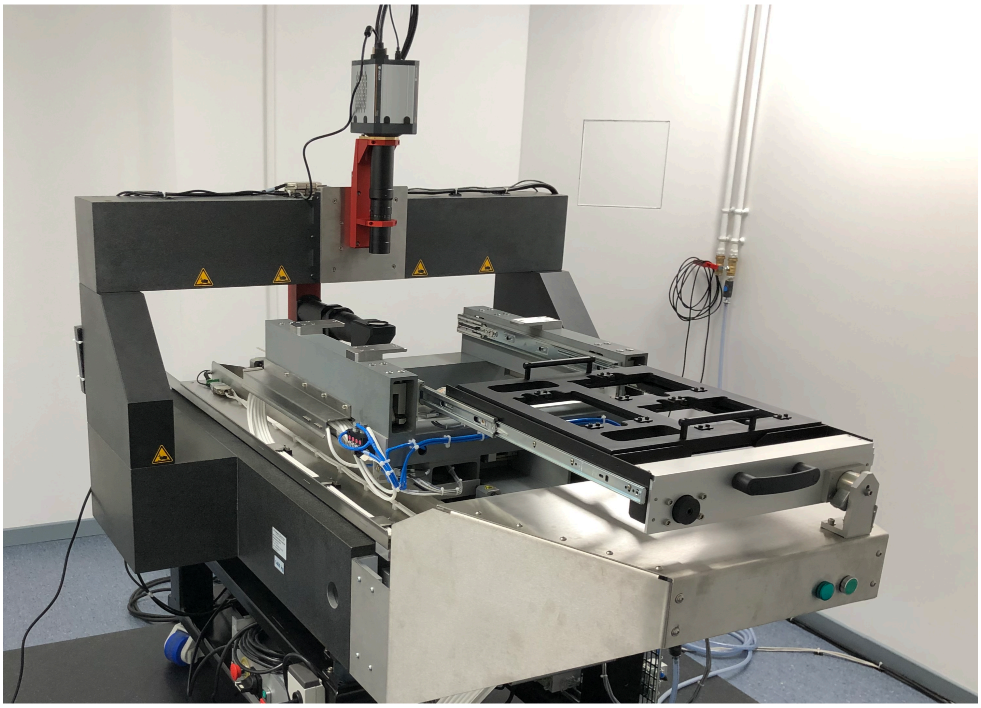

Fig. 2. The NAROO digitizer, Paris Observatory.

table can fix a position) was measured by the manufacturer at ± 0.010 μm. With real data, we measured the stability at ± 0.025 μm. In order to reach and maintain a high geometric and radiometric accuracy, the digitizer is placed in an air-conditioned clean room, at a temperature of 20 Celsius degrees ± 0.1 Celsius degrees, and a relative humidity of 50 per cent RH ± 5 per cent RH. Fig. 3 shows the "First light" of the NAROO machine: the Saturnian system on a 1975 USNO photographic plate, taken on 2019 April.

2.2 Scientific objectives

The NAROO centre is mainly dedicated for science purposes, not for archiving or saving. That's why we have started discussing with different members of the community, in order to develop a team which would be able to estimate all the capacities of the machine for their topics, and use it for their research. Since astro-photographic plates were used for different purposes, we first separated the categories with plates dedicated to Astrometry, those dedicated to Spectrometry, and those dedicated to Photometry.

With astrometric plates, we intend to: improve ephemerides of Solar System objects by the addition of numerous high-precise positions in database, estimate long-term dissipation and secular phenomena since dynamical models will be refine over large time span, make pre-discoveries of small bodies (NEOs, PHAs,n TNOs, comets) since such objects could have been observed with very old plates before their official detection, work on the Yarkovsky effect, work on General Relativity.

With spectrometric plates, we intend to digitize old spectra of variable stars, and Be stars in particular to complete the database before the 90's.

With photometric plates, we intend to: complete the database of body surfaces to create and/or refine object albedo maps, to pay particular attention to the Sun by analyzing its long-term evolution regarding to sunspots and magnetic field.

3 Conclusions

We have demonstrated the value of a new astrometric analysis of old photographic plates, resulting from their accurate measurement with new generation digitizers. The new reduction, using new astrometric catalogs, provides final accurate positions satellites that are not only more accurate than those previously derived from

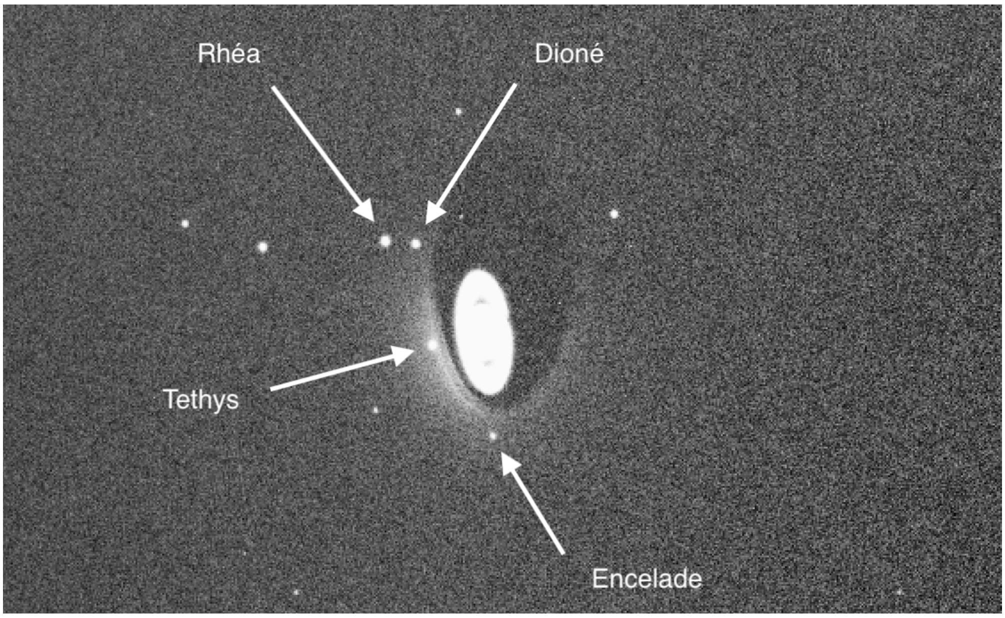

Fig. 3. NAROO First light - April 2019 - 1975 USNO plate.

manual measurements, but provides new information since we obtain equatorial positions for the first time with these plates.

With the NAROO program, we open a centre dedicated for science purposes in various fields of research. We are now realizing the last calibration tests before our new generation digitizer will be fully operational and automized. A first call for digitization time will be published by the beginning of 2020, since the centre will be open to researchers involved in astro-photographic plate analysis.

This work was supported by the Programme National GRAM of CNRS/INSU with INP and IN2P3 co-funded by CNES, by IMCCE - Paris Observatory, IPSA, DIM-ACAV, FP7 ESPaCE, and PSL Research University.

References

Lindegren, L., Hernández, J., Bombrun, A., et al. 2018, A&A, 616, A2

Pascu, D. 1994, in Galactic and Solar System Optical Astrometry, ed. L. Morrison & G. Gilmore (Cambridge University Press), 304

Robert, V., de Cuyper, J.-P., Arlot, J.-E., et al. 2011, MNRAS, 415, 701

Robert, V., Lainey, V., Pascu, D., et al. 2015, A&A, 582, A36

Robert, V., Pascu, D., Lainey, V., et al. 2016, A&A, 596, A37

Thuillot, W., Lainey, V., Arlot, J. E., et al. 2013, in European Planetary Science Congress, EPSC2013–513

Session 06

Demain l'ELT ! Quelle science avec ses 1ers instruments ?

SF2A 2019
P. Di Matteo, O. Creevey, A. Crida, G. Kordopatis, J. Malzac, J.-B. Marquette, M. N'Diaye, O. Venot (eds)

EXOPLANETARY SYSTEMS STUDY WITH MICADO

P. Baudoz[1], E. Huby[1], Y. Clénet[1] and the MICADO Team

Abstract. The observation and characterization of the exoplanets and planetary architectures are crucial to broaden and complete our vision of the formation and evolution of planetary systems but also of the physics of the atmospheres of the exoplanets. In this context, MICADO, the European Extremely Large Telescope first-light imager will be equipped with an imaging mode dedicated to exoplanets and a long slit spectroscopy mode (R = 20 000) with an unbeaten sensitivity. The 5-fold increase in the angular resolution between the current instruments like SPHERE or GPI and MICADO will allow a quantitative and qualitative jump on the study of these planetary systems. Among the promising scientific cases: the characterization of exoplanets in synergy with GAIA and radial velocity surveys (eg SPIRou), the study of disk-planet interactions, the high-resolution study of exoplanetary atmospheres.

Keywords: exoplanet, high contrast imaging, coronagraph, MICADO

1 Introduction

Instruments based on extreme adaptive optics like SPHERE on the VLT (Beuzit et al. 2019) or GPI on GEMINI (Macintosh et al. 2015) improved our understanding of the formation and evolution of planetary systems. However, questions are still pending on formation scenarii, the physics of planet atmospheres, the frequency of giant planets in long orbits (> 5-10 AU), etc. While space instruments aboard JWST (2020) will bring new insights to exoplanet science, they will be limited in contrast and angular resolution compared to an instrument that would take place on the ELT. Such an instrument that would be dedicated to direct imaging and spectroscopy of exoplanets on the ELT will only come after the first light instruments. Taking advantage of the 5-fold increase in the angular resolution between the ELT and the current ground-based telescope (or the planned space-based telescope), there is an opportunity for exoplanet science before this dedicated ELT planet finder comes online in 2030s.

2 MICADO

MICADO is the European Extremely Large Telescope first-light imager. The instrument will work in the near-infrared, from 0.8 to 2.4 microns, with a field of view of about one arcmin, delivering images at the telescope diffraction limit thanks to adaptive optics correction (Clenet 2019). MICADO will offer to the astronomers four observing modes:

1. Classical imaging with a field of view (FOV) up to 50"x50" and more than 30 broad and narrow filters.
2. Astrometric imaging with a precision of 10 to 50 μas relative to a set of reference sources in the field.
3. Long-slit spectroscopy covering simultaneously several spectral bandwith (IJ or HK) with a spectral resolution up to 20 000 for point sources that can be used to study exoplanet atmospheres.
4. High contrast imaging with a FOV of 6"x6" that can use either focal plane coronagraphic masks (classical Lyot or more complex phase mask) or pupil plane coronagraphic masks. This mode is design for the observations of exoplanetary systems.

The project kick-off took place in October 2015. The preliminary design took place in 2018 and first light is expected in 2025-2026.

[1] LESIA, Observatoire de Paris, Université PSL, CNRS, Sorbonne Université, Université de Paris, 5 place Jules Janssen, 92195 Meudon, France

3 MICADO high contrast mode

Unlike SPHERE, MICADO is not fully dedicated to exoplanet science. The optical design of MICADO is thus the results of a trade-off between all the modes of the instrument. The main components of the high contrast mode of MICADO are described below:

1. **Three Focal plane coronagraphs**
   (a) **Classical Lyot Coronagraph with the radius of 25.34 mas**
   Because of its large central obscuration and its segmented pupil, the ELT pupil is not optimized for coronagraphy. Indeed, the large central obscuration and the presence of gaps increase the number of edges in the pupil, thus the amount of stellar light diffracted by these edges. One solution to overcome this problem is to couple the focal plane mask with an apodization mask at the entrance pupil of the instrument to compensate the effect of the diffraction by the central obscuration. This solution is used on SPHERE and GPI but the final design of MICADO does not permit it. Thus, simple Classical Lyot Coronagraphs (CLC), without apodization are selected as a baseline. A CLC is an occulting mask in the focal plane and must be coupled with a Lyot stop located in a pupil plane downstream of the focal plane mask. To take full advantage of the high angular resolution of the ELT, we decided to select one CLC that allows the detection of planet at short distance from the star (coronagraph with a small Inner Working Angle, IWA).
   (b) **Classical Lyot Coronagraph with the radius of 50.68 mas**
   Correction of atmospheric dispersion can only be apply downstream of the focal plane coronagraph. This will limit the spectral bandwidth for a small inner working angle coronagraph. A second CLC is optimized with a medium IWA (4-5 λ/D) to take care of the PSF atmospheric dispersion with broadband filter and to ensure a good sensitivity of the coronagraphic mode. The selection of the size of the 2 focal plane masks is linked to the selection of the dimension of the Lyot stop. The sizes of the 3 elements are optimized at the same time and the final radius of the CLC are 25.34 mas and 50.68 mas. For more information on this optimization, see Perrot et al. (2018).
   (c) **One focal plane slot for a more complex phase mask coronagraph**
   One of the drawbacks of the CLC is the limited attenuation of the coronagraph when decreasing the size of the occulting mask. Thus, the detection of a planet located at shorter angular separation to its star is limited. To improve the sensitivity to planet close to the star, one can use a phase mask with a smaller IWA to allow detection of planets at small angular separation of the star (1-1.5 λ/D in K band : 10-15 mas). We define a slot for such a coronagraph but the exact type of coronagraph planned for this slot is still under study.

2. **Three Lyot stops** coupled with these focal plane coronagraphs. These Lyot stop are located downstream of the focal plane coronagraph and will block the stellar light diffracted by the mask. These Lyot stop have an identical shape but 3 different transmissions (60%, 6%, 0.06%) to allow calibration of the star flux even for bright stars (K=3).

3. **One or two pupil plane coronagraphs based on phase apodization**
   These coronagraphs use interferences to attenuate the diffraction wings in a limited area of the field of view (FOV) without decreasing the total transmission of the instrument. This apodization decreases the Strehl ratio though and an optimization needs to be done to maximize the Strehl ratio and the useful FOV while minimizing the diffracted light at the shortest angular separation. In MICADO, we plan to use the implementation of vector Apodizing Phase Plate (vAPP, Snik et al. 2012). The vAPP can be designed for any pupil geometry even though complex pupil structure might decrease the Strehl ratio when trying to reach short angular separation.

4. MICADO will also include **one or two Sparse Aperture Masks (SAM)**. The principle of SAM is to insert in the pupil an opaque mask with a number of holes spatially distributed so that each pair of holes will contribute to a unique spatial frequency. Thus SAM imaging mode avoids the combinations of multiple spatial frequencies which – adding incoherently – may degrade the transfer function. With a well known transfer function of the instrument, one can partly distinguish the effect of optical aberrations from astronomical information and retrieve more precisely the environment of the star at very short angular separation (Lacour et al. 2011).

5. A **series of filters** partly optimized for high contrast imaging are located inside the MICADO cryostat.

6. The field of view will be rotating during observations to allow the stabilization of the pupil on the instrument (**pupil tracking mode**). This solution already used on all the high contrast imaging techniques helps improving the stability of the data and use optimized post-processing techniques for exoplanet study, such as Angular Differential Imaging or its derivatives (Galicher et al. 2018).

7. **A fine pointing control of the PSF** will be ensured by a dedicated coronagraphic image analysis to avoid potential drift between the coronagraph and the PSF position define by the adaptive optics (AO).

4 Performance of the MICADO high contrast mode

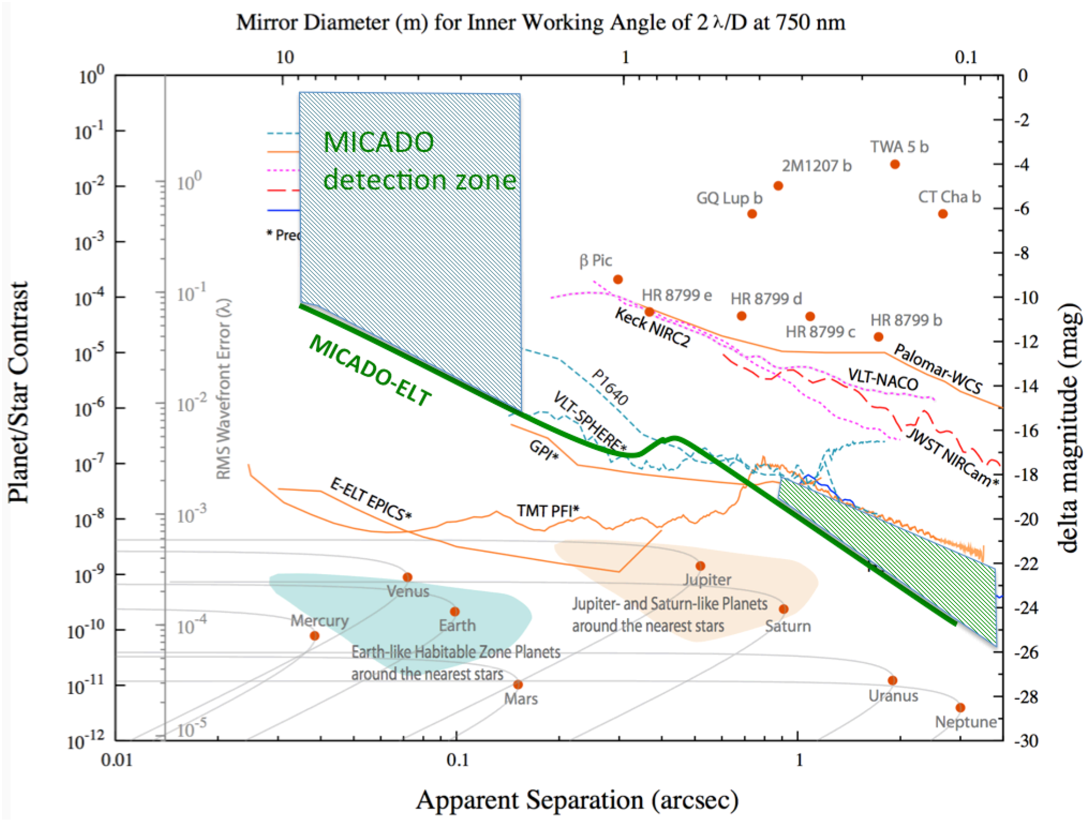

Fig. 1. Current and projected high contrast imaging capabilities in space and from the ground (adapted from Mawet et al. 2012). The left axis shows the planet/star contrast ratio. The x axis shows the angular separation in arcsec. All detectivity curves are 5σ for bright stars and scaled for a 1-hour observing time. MICADO expected performance is added to the figure. Shaded areas correspond to discovery space unreachable by actual instruments like SPHERE or GPI.

We developed a dedicated simulation tool that uses the output of MICADO single conjugated AO simulation (Vidal et al. 2018) to estimate the performance of MICADO in the context of exoplanet detection. The main inputs of this simulator are recalled below:

1. **Adaptive Optics residuals**
The residual dynamical phase aberrations are calculated using a dedicated COMPASS simulation for a conservative seeing (0.79") assuming telescope wind shake compensated by guide probe. The AO system simulated is a pyramid with a frequency of 500Hz (Vidal et al. 2018).

2. **Optical elements**
The simulation takes into account missing segments on the primary mirror, aberrations at different po-

sitions in the optical train (segments, upstream and downstream of the coronagraph). These aberrations can be either static or varying. The simulator tool includes the different CLC and vAPP coronagraphs

3. **Configurations**
Other inputs of the simulator are the declination of the star (to calculate parallactic rotation and atmospheric refraction), the total observation time (typically 1hr centered around the transit of the star), star magnitude, planet spectrum. The simulation also takes into account photon noise for a given magnitude, detector readout noise and atmospheric emission. Different astrophysical scenes can be simulated: planets, disks.

4. **Post-processing** is included in the performance analysis using classical Angular Differential Imaging.

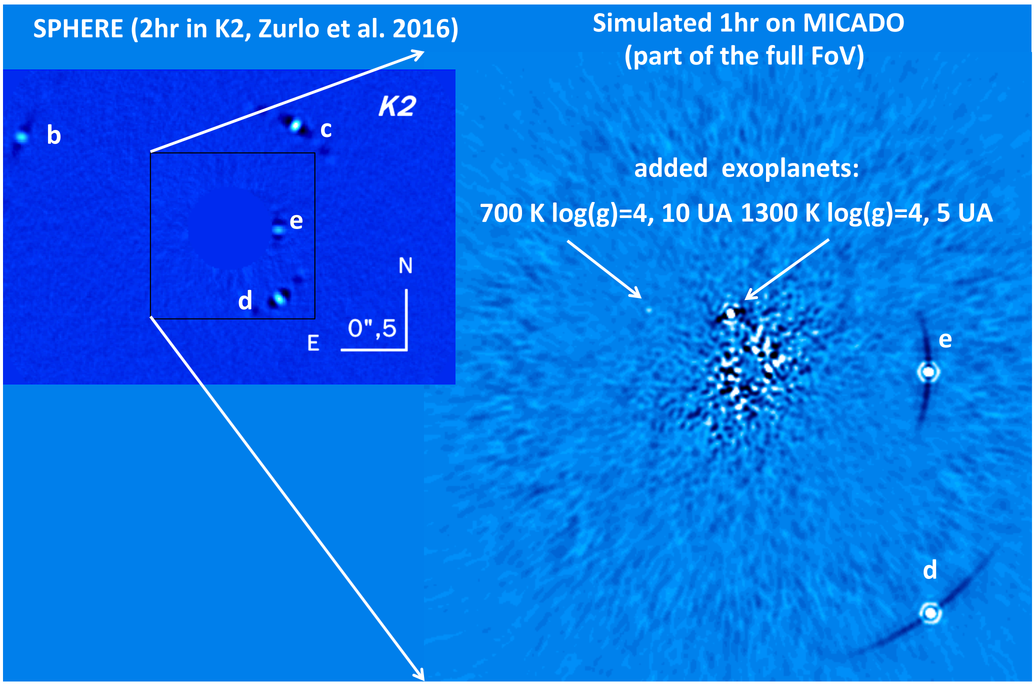

Fig. 2. Example of post ADI image showing: *on the left:* actual detection of 4 planets around HR 8799 by SPHERE (Zurlo et al. 2016) in K2 band ($\lambda = 2.255\mu m$), *on the right:* detection of simulated planets around HR 8799 using the actual measured flux for the closest planet *d* and *e* and using synthetic planet spectrum from EXOREM (Charnay et al. 2018) assuming 1 hour observation on MICADO at the same wavelength.

Simulation of MICADO performance for bright stars showed that the high contrast mode can improve the planet detection in two ways. On one hand, the ability to reach angular resolution below 200 mas is unprecedented and, on the other hand, a deep sensitivity at distance larger than one arcsecond is expected (Fig. 1).

Thus, MICADO should allow the search of new planets in already known planetary systems. These planets could be closer to their star or less massive than the one already detected. An example of such detection is shown in Fig. 2 where we simulated the observation of two additional inner planets in the HR8799 planetary systems, one of which with a temperature of only 700K. Note that the planets simulated are located at an angular distance where SPHERE is virtually blind as show on the left part of Fig. 2 where the central area is set numerically to zero.

The improvement in angular resolution will also enlarge the samples of ages of planetary systems by observing in more distant young associations (100-150 pc) and at close distance to these young stars (10 AU). Morphological and dynamical studies of planet-disk interactions will also be improved with the increase in both angular resolution and sensitivity. Finally, the simultaneous coverage of H+K of the long-slit spectroscopy at a resolution of 20 000 is also well suited to better define the composition of exoplanet atmospheres by removing systematics in the spectrum.

5 Conclusions

The high contrast imaging mode of MICADO includes focal plane and pupil plan coronagraphs, a series of Lyot stops and spectral filters, as well as a dedicated observation mode. A detailed simulation has started during the preliminary design phase and the estimated performance is very exciting by extending the search area of SPHERE for very young giant and massive planets at shorter orbital separations (a few AU) of nearby stars and around more distant star associations (100-150 pc). Gain in angular resolution and sensitivity should also allow MICADO to characterize more distant debris disks than SPHERE and gives a more detailed images of the closest ones. Performance will be refine during the final design phase with a better knowledge of detection signal to noise allowing to estimate the spectral and/or physical information we should be able to derive from the measurements.

References

Beuzit, J. L., Vigan, A., Mouillet, D., et al. 2019, arXiv e-prints, arXiv:1902.04080

Charnay, B., Bézard, B., Baudino, J. L., et al. 2018, ApJ, 854, 172

Clenet, Y. 2019, in Proceedings of the SF2A, this volume

Galicher, R., Boccaletti, A., Mesa, D., et al. 2018, A&A, 615, A92

Lacour, S., Tuthill, P., Amico, P., et al. 2011, A&A, 532, A72

Macintosh, B., Graham, J. R., Barman, T., et al. 2015, Science, 350, 64

Mawet, D., Pueyo, L., Lawson, P., et al. 2012, in Society of Photo-Optical Instrumentation Engineers (SPIE) Conference Series, Vol. 8442, Proc. SPIE, 844204

Perrot, C., Baudoz, P., Boccaletti, A., et al. 2018, in Proceedings of Adaptive Optics for Extremely Large Telescopes (AO4ELT5), 159

Snik, F., Otten, G., Kenworthy, M., et al. 2012, in Proc. SPIE, Vol. 8450, Modern Technologies in Space- and Ground-based Telescopes and Instrumentation II, 84500M

Vidal, F., Ferreira, F., Déo, V., et al. 2018, in Proceedings of Adaptive Optics for Extremely Large Telescopes (AO4ELT5), 43

Zurlo, A., Vigan, A., Galicher, R., et al. 2016, A&A, 587, A57

SF2A 2019
P. Di Matteo, O. Creevey, A. Crida, G. Kordopatis, J. Malzac, J.-B. Marquette, M. N'Diaye, O. Venot (eds)

UV DUST ATTENUATION AS A FUNCTION OF STELLAR MASS AND ITS EVOLUTION WITH REDSHIFT

J. Bogdanoska[1] and D. Burgarella[1]

Abstract. Describing the Universe in its early stages requires obtaining knowledge about the various components in distant galaxies (stars, gas, dust). This work aims to further constrain the relationship between the ultraviolet dust attenuation and stellar mass, as well as the evolution of the dust attenuation with redshift, by creating a three dimensional model for the dust attenuation, which uses these two galactic parameters (redshift and stellar mass). By combining data from different literature sources, we were able to compile a data set comprised of estimates of photometric redshift, stellar mass and dust attenuation calculated by the infrared excess (IRX) method, i.e. by converting the ratio of the infrared-to-ultraviolet luminosity of galaxies to ultraviolet dust attenuation. Using this result, we will be able to model and predict what the emission of galaxies at high redshifts is. This information will be useful to understand and interpret the data that the ELT will collect, especially the first imaging instruments MICADO and METIS.

Keywords: Galaxies: evolution – Galaxies: high-redshift – Cosmology: early Universe

1 Introduction

Cosmic dust, alongside the interstellar gas and the stars, is one of the main visible components of galaxies. Even though it takes up only a small portion of the interstellar medium (the gas-to-dust ratio is usually taken to be 100), it is nonetheless a very important constituent of the complex system that is a galaxy. Dust has several important roles within the galaxy; it plays a part in the creation of stars, it enables the creation of planets, and its presence is necessary to create molecules and thus have astrochemistry present in the interstellar medium.

The light emerging from a galaxy is heavily influenced by the presence of dust. The size of the dust grains is such that they are very efficient in absorbing the ultraviolet (UV) light. The young stars that can be found within a galaxy have strong UV radiation, which enables us to trace the formation of stars in galaxies, so, the fact that the UV part of the spectrum is attenuated by dust is very inconvenient. Due to the laws of energy balance, however, the absorbed UV light is then re-emitted by the dust as thermal energy, so we observe it as infrared (IR) radiation. If we look at the Spectral Energy Distribution (SED) of a galaxy, we can estimate the total IR luminosity $L_{\rm IR}$ of the galaxy, as well as the far-UV (FUV) luminosity emitted by the galaxy (and attenuated by dust) $L_{\rm FUV}$. The ratio of these two values is usually referred to as the Infrared Excess (IRX) (Meurer et al. 1999), can be translated to dust attenuation with the help of a conversion relation, such as the one proposed by Hao et al. (2011).

In this work, we are interested in the dust attenuation of galaxies throughout the history of the Universe, as well as the dependence of the dust attenuation on stellar mass M_*. The main goal is to model the dust attenuation as a function of both the galactic stellar mass and redshift so that it would be possible to give an estimate of the average of the properties of galaxies in the Universe knowing only these two parameters. This will be very useful in simulating how observations by different instruments would look like, which in turn would prepare us for the data and science these instruments of the future will bring.

[1] Aix-Marseille Université, CNRS, LAM (Laboratoire d'Astrophysique de Marseille) UMR 7326, 13388, France

2 Dust attenuation vs. Stellar mass

The relationship between the stellar mass of a galaxy and the dust attenuation (or in some cases, directly the relation IRX-M_*) has been studied by a few different groups (Heinis et al. 2014; Whitaker et al. 2014, 2017; Pannella et al. 2015; Álvarez-Márquez et al. 2016; Bouwens et al. 2016; McLure et al. 2018). These groups came to the conclusion that the $A_{\rm FUV} - M_*$ relationship is the same throughout cosmic time. In this work, however, we start with the assumption that this relationship does in fact evolve, and thus we arrive at some results about the evolution of the average dust attenuation in the Universe that coincide with other studies of the same problem, where a different approach is used.

Finding a relationship between the stellar mass and dust attenuation that evolves with redshift included compiling existing data from the literature in as many redshift ranges as possible. The references and the redshifts studied by the different groups are shown in Fig. 1 (right), marked with the coloured squares. Taking each redshift given in the various papers as a separate redshift bin, as well as dividing galaxies in redshift bins of width $\Delta z = 1$ for where data of individual galaxies is given (Bouwens et al. 2016; Schaerer et al. 2015), we are left with 18 redshift bins, shown in Fig. 1 (left). Some of the bins purposefully have the same redshift, in order to avoid mixing data of different types (stacked vs. individual galaxies).

Once separated by redshift, the data has been fitted with a function that has the same shape in each redshift bin, differing only by a multiplicative factor between the redshift bins. The chosen function gives the lowest reduced chi-square on average throughout the redshift bins. As the amount of data for low mass galaxies is not very significant, the low-mass end of the function has been set to have a constant constant value until $\log(M_*/M_\odot) = 10.1$. For the high-mass end there has been evidence for saturation and flattening (e.g. Whitaker et al. 2014, 2017), so, for the high-mass range we chose first an increasing function until stellar mass $\log(M_*/M_\odot) = 13$, and then a decreasing function which reaches zero dust attenuation for $\log(M_*/M_\odot) = 14$. We justify this sudden drop in dust attenuation for high stellar masses by pointing out that there is an extremely low number of galaxies with such high masses, as indicated by the mass functions suggested by, for example, Song et al. (2016). The function has the following form, where the parameter a is different for each redshift bin, and the stellar mass is expressed in units of solar masses ($M_\odot$):

$$A_{\rm FUV}(\log M_*) = a \begin{cases} 0.85, & \log M_* < 10.1 \\ \log M_* - 9.25, & 10.1 < \log M_* < 13 \\ -3.75 \log M_* + 52.5, & 13 < \log M_* < 14 \\ 0, & \log M_* > 14 \end{cases} \tag{2.1}$$

We have updated our result in the time between the SF2A meeting and the writing of the proceedings, so here the latest results are shown. For the results presented in the meeting, refer to the paper published by the same authors.

3 Dust attenuation vs. Redshift

The main purpose of this work is to quantify the evolution of the average dust attenuation in the Universe as a function of cosmic time. Thus, the work of Sect. 2 is only the beginning. As the parameter a in Eq. (2.1) is the only difference between redshift bins, we fit its dependence on the redshift $a(z)$. The function used to fit this dependence is the following, with the best fit values for the parameters being $\alpha = 1.69$, $\beta = 2.51$, $\gamma = 0.30$, and $\delta = 0.92$:

$$a(z) = \delta \ (z + \gamma) \cdot \alpha^{(\beta - (z+\gamma))} \tag{3.1}$$

We now have the *dependence* of the dust attenuation on redshift, but, if we wish to calculate the numerical values of the dust attenuation we either need to do it for all stellar masses (in three dimensions, as in Sect. 4), or select a value for $\log M_*$, and show the dust attenuation only for this mass. This is equivalent to drawing a vertical line in Fig. 1 (left) at the given $\log M_*$ and selecting the intersections with the coloured lines as the values of the dust attenuation. That is exactly what is presented in Fig. 1 (right), for $logM_* = 8$, represented by the dashed black line.

Due to the fact that the evolution of the $A_{\rm FUV} - M_*$ has been disputed in the literature, we performed an additional check to make sure of the validity of our results. We calculated the average value of the dust

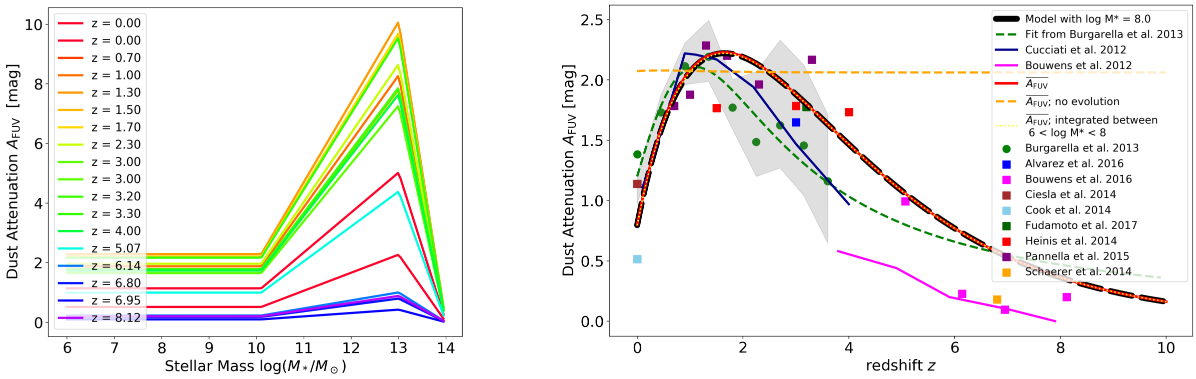

Fig. 1. Left: The dependence on the dust attenuation in the UV on stellar mass. The different lines represent the model given in Eq. (2.1) calculated in different redshift bins. **Right:** The evolution of the dust attenuation in the UV with redshift. The dashed black line gives the model of Eq. (3.1) calculated for a stellar mass $\log(M_*/M_\odot) = 8$. The full red line represents the average dust attenuation, calculated by integrating the model of Eq. (3.1), weighted by the mass function. The dashed purple line gives the same quantity as the full red line, but calculated only by integrating within different mass limits, namely $6 < \log(M_*/M_\odot) < 8$. The dashed orange represents again the mean dust attenuation calculated using a constant model for $a(z)$. The data points represented by squares are the values of the $A_{\rm FUV} - M_*$ relation of each redshift bin (Fig. 1, left) also for $\log(M_*/M_\odot) = 8$.

attenuation for each redshift bin by integrating the function of Eq. 2.1 and by weighting the integral by the mass function calculated at the given redshift. The mass function has been estimated based on work available in the literature (Tomczak et al. 2014; Grazian et al. 2015; Mortlock et al. 2015; Song et al. 2016). The result of this test is presented by the full red line. If instead of integrating Eq. (2.1) we use a constant function (corresponding to the idea that the $A_{\rm FUV} - M_*$ relationship does not evolve), we get the result represented by the dashed yellow line. This is supportive of the idea that the $A_{\rm FUV} - M_*$ relationship does not remain the same throughout cosmic time, as the red line corresponds to the results found by other authors, most notably Burgarella et al. (2013) and Cucciati et al. (2012), who use different methods to estimate the same quantity.

4 Synthesis in a 3D model

Being able to compute the dust attenuation of a large number of galaxies by assuming a realistic mass function in multiple points in cosmic time will enable us to simulate the SEDs of galaxies up to redshift $z \sim 10$. With that aim in mind, we first created a model for a set of redshift bins (Sect. 2) and then fitted the parameter $a(z)$ to be able to calculate such a model at any redshift, as opposed to only the redshifts for which we have data. This also enables us to extrapolate to higher redshifts. Combining, Eqs. (2.1) and (3.1), we obtain a 3D model for the dust attenuation $A_{\rm FUV}$ as a function of both redshift and stellar mass. This is shown in Fig. 2. The functional form of this, using the same parameters with the same numerical values as described before, is the following:

$$A_{\rm FUV} = \delta\ (z+\gamma)\cdot\alpha^{(\beta-(z+\gamma))} \times \begin{cases} 0.85, & \log M_* < 10.1 \\ \log M_* - 9.25, & 10.1 < \log M_* < 13 \\ -3.75\log M_* + 52.5, & 13 < \log M_* < 14 \\ 0, & \log M_* > 14 \end{cases} \tag{4.1}$$

Saying that we know how the dust attenuation behaves at redshifts as high as $z \sim 10$ is very ambitious and, in fact, untruthful. However, with the new generation of observing facilities, such as the *James Webb Space Telescope* (JWST) and the *Extremely Large Telescope* (ELT) we can hope to discover in more detail the truth about this behaviour (and many many others!). As the method used in this work is based on both UV and IR multiwavelength data, and we are interested in high-redshift galaxies, both of the aforementioned observatories would provide a lot of data useful for this project, especially if we combine the data from JWST with the one provided by the ELT instruments MICADO and METIS. Finally, it is interesting to note that it is possible to use the findings of this project to predict what the observations from any facility would look like by performing simulations with the code CIGALE (Noll et al. 2009), developed at LAM, which would prepare us to handle the data analysis, as well as the new science, which will be brought to the world of science by these instruments.

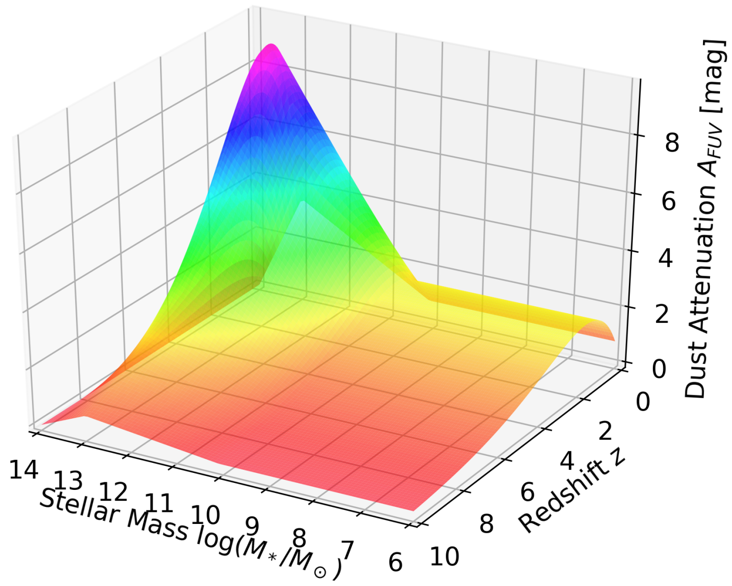

Fig. 2. Three-dimensional representation of the dust attenuation in the UV as a function of both redshift and stellar mass. The colour map used also represents the dust attenuation, and, as it does not provide any additional information, it is used only for improving the clarity of the figure.

References

Álvarez-Márquez, J., Burgarella, D., Heinis, S., et al. 2016, Astronomy and Astrophysics, 587
Bouwens, R. J., Aravena, M., Decarli, R., et al. 2016, The Astrophysical Journal, 833, 72
Burgarella, D., Buat, V., Gruppioni, C., et al. 2013, Astronomy and Astrophysics, 554, A70
Cucciati, O., Tresse, L., Ilbert, O., et al. 2012, Astronomy and Astrophysics, 539, A31
Grazian, A., Fontana, A., Santini, P., et al. 2015, Astronomy and Astrophysics, 575, A96
Hao, C.-N., Kennicutt, R. C., Johnson, B. D., et al. 2011, The Astrophysical Journal, 741, 124
Heinis, S., Buat, V., Béthermin, M., et al. 2014, Monthly Notices of the Royal Astronomical Society, 437, 1268
McLure, R. J., Dunlop, J. S., Cullen, F., et al. 2018, Monthly Notices of the Royal Astronomical Society, 476, 3991
Meurer, G. R., Heckman, T. M., & Calzetti, D. 1999, The Astrophysical Journal, 521, 64
Mortlock, A., Conselice, C. J., Hartley, W. G., et al. 2015, Monthly Notices of the Royal Astronomical Society, 447, 2
Noll, S., Burgarella, D., Giovannoli, E., et al. 2009, Astronomy and Astrophysics, 507, 1793
Pannella, M., Elbaz, D., Daddi, E., et al. 2015, The Astrophysical Journal, 807, 141
Schaerer, D., Boone, F., Zamojski, M., et al. 2015, Astronomy & Astrophysics, 574, A19
Song, M., Finkelstein, S. L., Ashby, M. L. N., et al. 2016, The Astrophysical Journal, 825, 5
Tomczak, A. R., Quadri, R. F., Tran, K.-V. H., et al. 2014, The Astrophysical Journal, 783, 85
Whitaker, K. E., Franx, M., Leja, J., et al. 2014, The Astrophysical Journal, 795, 104
Whitaker, K. E., Pope, A., Cybulski, R., et al. 2017, The Astrophysical Journal, 850, 208

SF2A 2019
P. Di Matteo, O. Creevey, A. Crida, G. Kordopatis, J. Malzac, J.-B. Marquette, M. N'Diaye, O. Venot (eds)

SPECTROIMAGING OF YOUNG PLANETS WITH ELT-HARMONI

A. Carlotti[1], A. Vigan[2], M. Bonnefoy[1], M. Houlé[2], G. Chauvin[1,3], E. Choquet[2], J. Rameau[1] and N. Thatte[4]

Abstract. HARMONI, the first-light VIS & near-IR integral field spectrograph (IFS) of the ELT, will include a high-contrast imaging mode. Thanks to the high angular resolution of the ELT, to the spectral resolution of HARMONI (R=3500-18000), and to its adaptive optics system, this mode will enable the spectral characterization of young giant planets, in particular to constrain their formation processes. By creating 10^{-6} contrast at minimum separations of 50-100mas in the H & K bands, it will make it possible to study a much larger number of planets than with the current high-contrast instruments, and thanks to the GAIA catalogue, it will help measuring their mass-luminosity relation. This contrast level assumes that classical post-processing techniques will be used, but lower contrast values could be obtained by using the high spectral resolution of HARMONI to look through the speckle noise, especially at close separation.

Keywords: exoplanets, high-contrast imaging, high spectral resolution, ELT

1 Introduction

As of mid-2019, more than 4000 planets have been detected, most of them indirectly, using the radial velocity method, or the transit method. Transmission spectroscopy can be performed during transits, but only the upper part of the atmosphere is probed (Tinetti et al. 2013), and only a small fraction of planets transit their star.

The alternative is to directly image the planets. This is difficult because of the very small separation between a star and its planets, and because of the very high flux ratio between them. Instruments like VLT-SPHERE (Beuzit et al. 2019) have been specifically designed to observe young giant planets.

The current direct imagers provide R$\sim$50 spectra in the near-IR. This is enough to roughly measure the effective temperature and the surface gravity of the planet, but determining the physics of planet formation requires to measure the relative abundances of key molecules to determine the C/O ratio, and this will require higher, R$\sim 10^4 - 10^5$, spectral resolution.

Following the suggestion of Snellen et al. (2015), the detection limit set by the speckle noise in direct imagers could be partially removed by correlating an observed spectrum observed at a sufficiently high resolution with a template spectrum (based on a single molecule, or a combination of molecules).

Recent observations highlight the high potential of IFS for direct imaging. SINFONI observations have been processed to spatially map the presence of a few molecules (H20, CH4, NH3, CO), resulting in the detection and the partial characterization of planet Beta Pictoris b in spite of a low, 20 %, Strehl (Hoeijmakers et al. 2018). MUSE observations have been processed to look for the H-α hydrogen emission line around star PDS70, resulting in the detection of planets PDS70b and c (Haffert et al. 2019). While the former has been imaged before (Keppler et al. 2018), the latter is a new detection that was not possible with photometric observations, as the planet appears to be embedded in the formation disk.

HARMONI is the first-light, AO-assisted, visible and near-IR IFS of the ELT(Thatte et al. 2016). It will provide mid to high spectral resolution datacubes in a 1" Nyquist-sampled field of view. It will address a large variety of science cases, from solar system objects to the first galaxies. This also includes the spectral characterization of exoplanets, both through transmission spectroscopy, and through direct imaging. In the latter case, a dedicated sub-system is used to perform these observations, and this paper presents it.

[1] Univ. Grenoble Alpes, CNRS, IPAG, 38000 Grenoble, France
[2] Aix Marseille Univ, CNRS, CNES, LAM, Marseille, France
[3] Unidad Mixta Internacional Franco-Chilena de Astronomia, CNRS/INSU UMI 3386 and Departamento de Astronomia, Universidad de Chile, Casilla 36-D, Santiago, Chile
[4] Department of Physics, University of Oxford, Oxford OX1 3RH, United Kingdom

2 Design of the HARMONI High Contrast Subsystem

The high-contrast (HC) imaging mode of HARMONI aims at providing the instrument with the capability to image exoplanets with a 10^{-6} contrast at 100mas from the star (goal: 70mas) from 1.45 to 2.45 μm (goal: 1.25 to 2.45 μm). As illustrated in fig 1, this would allow HARMONI to study many more young giant planets than instruments like SPHERE, and to characterize their atmosphere. The HC subsystem will rely on the single-conjugate AO subsystem (SCAO) that will provide a ∼75% Strehl ratio. Note that HARMONI also uses a laser tomographic AO subsystem (LTAO) (Neichel et al. 2016).

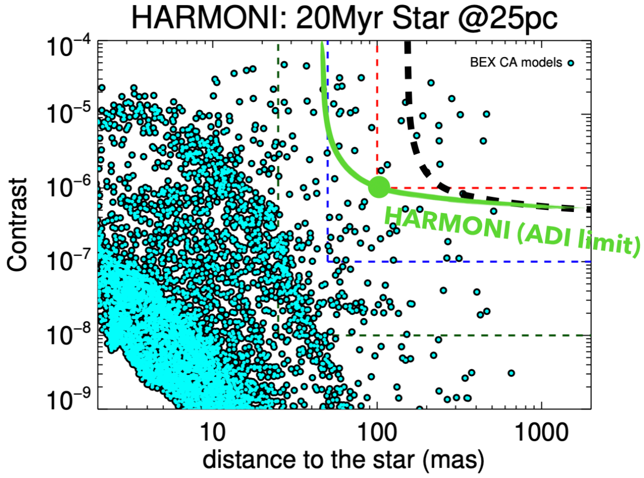

Fig. 1. Contrast separation diagram showing a simulated population of young giant planets around 25pc stars based on the Bern model (Mordasini 2014). The dashed black line represents the contrast limit of VLT-SPHERE, while the solid green line does the same for HARMONI, assuming an ADI-based post-processing of the data.

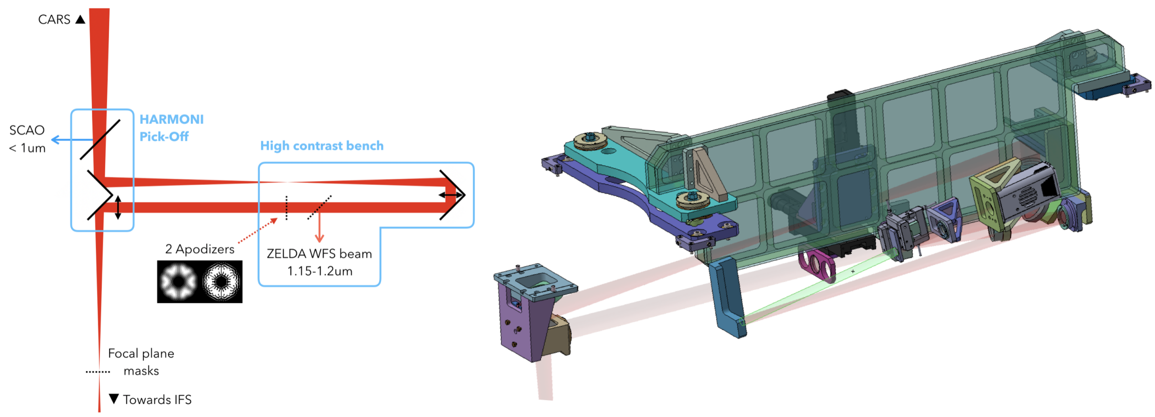

Fig. 2. Conceptual view (left) and 3D rendering (right) of the HC subsystem of HARMONI. Light is picked right after the SCAO dichroic and sent towards the HC bench where it is optically processed before being returned towards the IFS. The front facing optics are those of the Zernike wavefront sensor.

2.1 *Attenuating the diffracted intensity & Monitoring the quasi-static aberrations*

Like other direct imaging instruments, the HC subsystem must rely on a coronagraph to attenuate the intensity of the diffracted light, and to limit the dynamics of the PSF on the detector. Since HARMONI does not use an atmospheric dispersion corrector (ADC), and to keep the design of the HC subsystem as simple as possible, the coronagraph cannot use a focal plane mask to create contrast, like an APLC does in SPHERE. Instead, the coronagraph uses apodizers (Carlotti et al. 2011), and a focal plane mask to prevent saturating the detector.

Two apodizers will create a 10^{-6} contrast in complementary regions: from 4.5 to $11.5\lambda/D$, and from 7 to $39\lambda/D$. This translates into a 44-60mas minimum separation for the H and K bands, or, alternatively, into a 0.9-1.2 minimum AU distance for a 20pc star. The largest separation is chosen to match the SCAO angular cut-off frequency, as well as the FoV of HARMONI in its Nysquist sampling mode (4mas platescale).

As the SCAO analyses light at $\sim 0.8\mu m$, and because its optics introduce significant non-common path aberrations, a dedicated Zernike wavefront sensor(N'Diaye et al. 2013) is part of the HC subsystem. It picks light right before the apodizer, below $1.25\mu m$, and analyzes it in a narrow band centered at $1.175\mu m$. It will provide a 0.1-10 Hz monitoring of the quasi-static wavefront aberrations. Its cutoff wavelength makes it possible to observe the $1.27\mu m$ oxigen lines, as well as the $1.28\mu m$ Paschen-β line. It reimages the pupil, and this data will be used to monitor the pupil movement to control the apodizer position in an open loop.

2.2 Opto mechanical implementation

The HC subsystem is part of the natural guide star system (NGSS), which is located between the calibration and relay system (CARS) and the IFS. An illustration is given in fig.2. It is composed of a pick-off unit, and a vertical bench onto which the apodizer unit and the Zernike wavefront sensor are attached. The focal plane masks are located downstream, at the entrance of the cryostat. They will provide a 10^{-4} attenuation so that the star spectrophotometry and rough astrometry can be monitored during observations. Because of the absence of an HDC, the focal plane masks are asymmetric, and the minimum separation changes with the position around the star. A static ADC could be added to attenuate this effect by $\sim 60\%$ for a $z = 5 - 50$ deg zenith angle.

2.3 Error budget

The ability of the HC subsystem to achieve its goal will greatly depend on the surface quality of the optics of the instrument, and, in a lesser way, of the aberrations due to the telescope. An extensive Fourier optics simulation, based on PROPER (Krist 2007), has been used to estimate the surface quality of each of the optics so that the total quasi-static aberrations that they introduce does not exceed 10^{-5}. This contrast value has been chosen conservatively, assuming the final contrast, after post-processing, will be 10^{-6}.

3 Performance estimation

3.1 Simulations

Coronagraphic PSF have been computed while taking into account quasi-static aberrations, purely static aberrations (in particular due to missing segments and reflectivity errors of the primary mirror), and fast-changing residual atmospheric aberrations derived from the SCAO analysis (Schwartz et al. 2016). Planets are then injected in the data, using synthetic spectra, while the spectrum of the star comes from real observations. We have for instance considered the case of 51 Eri, and injected four 51 Eri b-like planets at 100, 150, 200, and 250 mas from the star, and with a 10^{-6} contrast. In addition to the photon noise, the detector RON, the sky background, and the cross-talk and the diffusion in the IFS are simulated. Various observations have been simulated, starting with low, R=3000 observations in the H+K band, to R=17000 observations in one half of the K band. We assume that observations occur over 2 to 4 hours, centered across the meridian.

3.2 Post-processing

3.2.1 ADI-based

Datacubes have first been processed with ANDROMEDA (Mugnier et al. 2009; Cantalloube et al. 2015), which is based on angular differential imaging. Results have been presented in Carlotti et al. (2018). They indicate that planets with a 10^{-6} contrast can be detected at 100mas, and the comparison between the injected and extracted spectra shows some differences which must be further investigated.

3.2.2 Molecular mapping

Molecular mapping has been applied on the data. After removing the star and the tellurics, a cross-correlation algorithm is applied using template spectra based on a BT-Settl model (Allard et al. 2012) that is adjusted

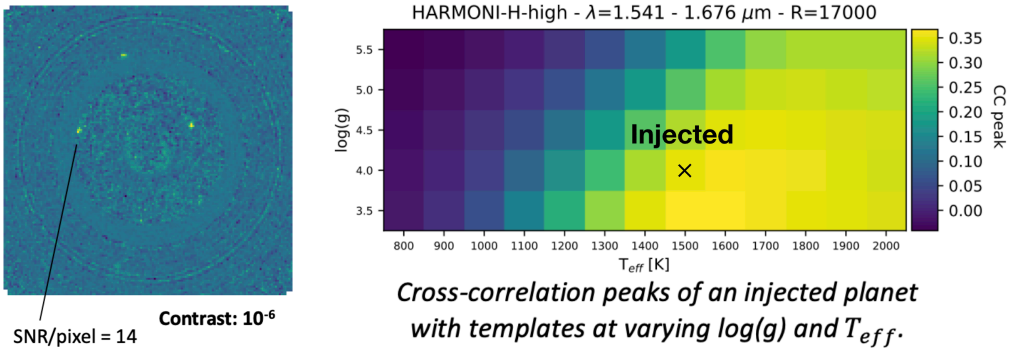

Fig. 3. Left: detection map showing planets detected at 100-250mas from the star (the 4th is in the lower part of the image). Right: Cross-correlation strength plotted as a function of the effective temperature and the $\log(g)$.

to maximize the cross-correlation peak. In the latter case, the result of this method applied to R=17000 K-band data shows that the effective temperature and the $\log(g)$ used in the injected spectra are retrieved with a precision better 200K and 0.5. A comparison to the classical ADI-based techniques will be performed in the near future, and new simulations will assess how faint a planet could be studied using this method.

4 Conclusions

The high-contrast imaging subsystem that is presented here will give HARMONI the capability to measure the relative abundances of various molecules in the atmosphere of young giant planets with a 10^{-6} contrast and located as close as 1 AU from a 20pc star. This should greatly increase the number of planets that could be studied. The high spectral resolution of HARMONI will make it possible to apply molecular mapping on coronagraphic data, which should further increase the contrast limit of the instrument.

References

Allard, F., Homeier, D., & Freytag, B. 2012, Philosophical Transactions of the Royal Society of London Series A, 370, 2765

Beuzit, J. L., Vigan, A., Mouillet, D., et al. 2019, arXiv e-prints, arXiv:1902.04080

Cantalloube, F., Mouillet, D., Mugnier, L. M., et al. 2015, A&A, 582, A89

Carlotti, A., Hénault, F., Dohlen, K., et al. 2018, in Society of Photo-Optical Instrumentation Engineers (SPIE) Conference Series, Vol. 10702, Proc. SPIE, 107029N

Carlotti, A., Vanderbei, R., & Kasdin, N. J. 2011, Optics Express, 19, 26796

Haffert, S. Y., Bohn, A. J., de Boer, J., et al. 2019, Nature Astronomy, 329

Hoeijmakers, H. J., Schwarz, H., Snellen, I. A. G., et al. 2018, A&A, 617, A144

Keppler, M., Benisty, M., Müller, A., et al. 2018, A&A, 617, A44

Krist, J. E. 2007, in Society of Photo-Optical Instrumentation Engineers (SPIE) Conference Series, Vol. 6675, Proc. SPIE, 66750P

Mordasini, C. 2014, A&A, 572, A118

Mugnier, L. M., Cornia, A., Sauvage, J.-F., et al. 2009, Journal of the Optical Society of America A, 26, 1326

N'Diaye, M., Dohlen, K., Fusco, T., & Paul, B. 2013, A&A, 555, A94

Neichel, B., Fusco, T., Sauvage, J. F., et al. 2016, in Society of Photo-Optical Instrumentation Engineers (SPIE) Conference Series, Vol. 9909, Proc. SPIE, 990909

Schwartz, N., Sauvage, J.-F., Correia, C., et al. 2016, in Society of Photo-Optical Instrumentation Engineers (SPIE) Conference Series, Vol. 9909, Proc. SPIE, 990978

Snellen, I., de Kok, R., Birkby, J. L., et al. 2015, A&A, 576, A59

Thatte, N. A., Clarke, F., Bryson, I., et al. 2016, in Society of Photo-Optical Instrumentation Engineers (SPIE) Conference Series, Vol. 9908, Proc. SPIE, 99081X

Tinetti, G., Drossart, P., Hartogh, P., et al. 2013, in European Planetary Science Congress, EPSC2013–1082

SF2A 2019
P. Di Matteo, O. Creevey, A. Crida, G. Kordopatis, J. Malzac, J.-B. Marquette, M. N'Diaye, O. Venot (eds)

MICADO, THE ELT FIRST-LIGHT IMAGER

Y. Clénet[1], P. Baudoz[1], R. Davies[2], E. Tolstoy[3], K. Leschinski[4] and the MICADO consortium

Abstract. The MICADO instrument is the first light imager of the European ELT. It will work in the near-infrared (0.8-2.4 μm), over a large field (up to 50″) and high sensitivity (similar to JWST).

MICADO will benefit from two modes of adaptive optics correction: a MCAO correction, uniform on the field of MICADO and developed by the MAORY consortium, and a classic correction of the SCAO type, with high performance in the direction of the star guide and developed under the responsibility of the MICADO consortium. In a phased approach of the integration of adaptive optics to the ELT, MICADO will first be operational in SCAO mode.

Offering four observing modes (imaging mode, astrometry, long-slit spectroscopy with R$\sim$20000 and high contrast imaging), MICADO aims to scan a wide range of scientific objectives: small bodies and planets of the solar system, exoplanets and exo-disks, stellar populations in distant galaxies, black holes and the center of our galaxy, evolution and dynamics of galaxies.

Keywords: MICADO, ELT, SCAO, MCAO, observing modes, science cases

1 MICADO: the project and its French contribution

MICADO (Multi-AO Imaging Camera for Deep Observations) is the European Extremely Large Telescope (ELT) first-light imager, working at the telescope diffraction limit in the near-infrared (Davies et al. 2018).

The consortium is lead by R. Davies, from the Max Planck Institute for Extraterrestrial Physics (MPE), and comprises, in addition to MPE, the Max Planck Institute for Astronomy (MPIA), the University Observatory Munich (USM), the Institute for Astrophysics of Göttingen, the Netherlands Research School for Astronomy (NOVA), the Institut National des Sciences de l'Univers (INSU, acting on behalf of LESIA, GEPI, IPAG, Observatoire de Besançon and the INSU Technical Division), the A* Austrian partnership and the Instituto Nazionale di Astrofisica (INAF).

The project started in October 2015, with the signature of the contract between ESO and the MPE, representing the consortium. The Preliminary Design Review occurred as planned after three years, in November 2018, and has been successful. The Final Design Review is planned in late 2020. It will be followed for 3.5 years by the Manufacturing, Assembly, Integration and Test phase, ending with the Preliminary Acceptance in Europe, mid 2024. The instrument will then be shipped to Chile, integrated and commissioned after the technical first light of the telescope, now planned in November 2025.

In the project, INSU is responsible for the development of the Single Conjugate Adaptive Optics (SCAO) mode, made of a wavefront sensor, a real-time computer, a dedicated calibration unit as well as their corresponding, either non real-time or real-time, software (see Sect. 3). INSU is also responsible for the development of the MICADO high contrast imaging mode (see Sect. 2).

[1] LESIA, Observatoire de Paris, Université PSL, CNRS, Sorbonne Université, Université de Paris, 5 place Jules Janssen, 92195 Meudon, France
[2] Max Planck Institute for extraterrestrial Physics, 85748 Garching, Germany
[3] Kapteyn Astronomical Institute, 9700 AV Groningen, The Netherlands
[4] Institute for Astrophysics, University of Vienna, Türkenschanzstrasse 17, 1180 Vienna, Austria

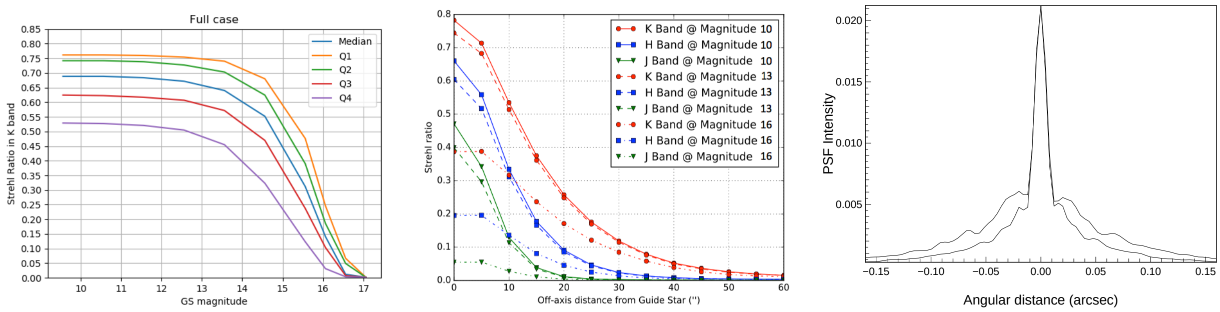

Fig. 1. Left: K-band SCAO performance vs. the guide star magnitude for the different ESO atmospheric conditions. Note that the complete SCAO performance is obtained from these end-to-end AO simulations results and additional instrumental error terms (130 nm rms left for these instrumental contributors to fulfil the SCAO performance specifications of SR=60%). Middle: Off-axis SCAO performance under Q2 seeing conditions for magnitudes R=10, 13 and 16. Right: SCAO PSF radial and transversal cuts obtained for L_0=25 m and 60 arcsec off-axis distance. The maximum intensity is equal to the K-band Strehl ratio, i.e. about 2%.

2 MICADO observing modes

MICADO is being designed to provide four observing modes: imaging, astrometric imaging, spectroscopy and high contrast imaging.

MICADO will provide images in the near-infrared, between 0.8 and 2.4 μm. More than 30 broad-band and narrow-band filters will be available to cover the numerous science cases that such an ELT first-light instrument will address. The default pixel size will be 4 mas, with a corresponding field of view of $\sim 50'' \times 50''$, allowing the instrument to work at the diffraction limit of the telescope in the H and K bands. A zoom mode, with a 1.5 mas pixel size over a field of view of $\sim 19'' \times 19''$, will be available to work at the telescope diffraction limit over the whole MICADO bandpass as well as to increase the instrument astrometric precision. Hence, MICADO will have a sensitivity similar to JWST with a six times better spatial resolution.

MICADO aims at bringing astrometry into mainstream. The instrument is being designed for that purpose: in a gravity-invariant configuration, it will make use of only fixed mirrors and specific calibration procedures will be developed. The goal is hence to reach 50 microarcsecond precision anywhere in MICADO field of view, which translates into 10 microarcseconds per year after 3-4 years of observation, i.e. 5 km/s at 100 kpc distance. From Fritz et al. (2015), the absolute proper motion measurement errors with MICADO could be reduced down to 1 km/s at a distance of 100 kpc for 5 year observation baseline.

MICADO will also come with spectroscopic capabilities. This mode will provide coverage of a wide wavelength range simultaneously (1.15-1.345 μm, 1.48-2.45 μm or 0.845-1.48 μm) at a resolution of $\sim$20000 on faint compact or unresolved sources. Three slits will be available: $3'' \times 16$ mas, $15'' \times 20$ mas (for sky subtraction along the slit), $3'' \times 48$ mas (ÒwideÓ).

The high contrast imaging mode will use the central detector and will be enabled via a classical configuration of focal plane coronagraphs and Lyot stops, as well as pupil plane vAPP coronagraphs and sparse aperture masking (Baudoz et al. 2019). Pupil tracking will be available for angular differential imaging.

3 Adaptive optics for MICADO

MICADO will benefit from two modes of adaptive optics (AO). The first one is a Multi-Conjugate AO (MCAO) correction, uniform over the field of MICADO (Strehl ratio at K of $\sim$30-40% on 50% of the sky), developed by the MAORY consortium, and for which the design of MICADO is optimized. See Ciliegi et al. (2018) and Douté et al. (2019) for additional information, in particular regarding AO performance.

MICADO will also benefit from a SCAO correction developed under MICADO's responsibility and jointly by MICADO and MAORY(Clénet et al. 2018, 2019). The AO performance is expected to reach SR(K)$\sim$60% nearby the reference source (Fig. 1, left), degrading with the distance to it (Fig. 1, middle). One has to remember that at the ELT, with a telescope diameter larger than the outer scale L_0, the coherent core in the PSF is preserved even at low Strehl ratio (Fig. 1, right, Clénet et al. 2015), making possible to address astrometry over a large field even in SCAO.

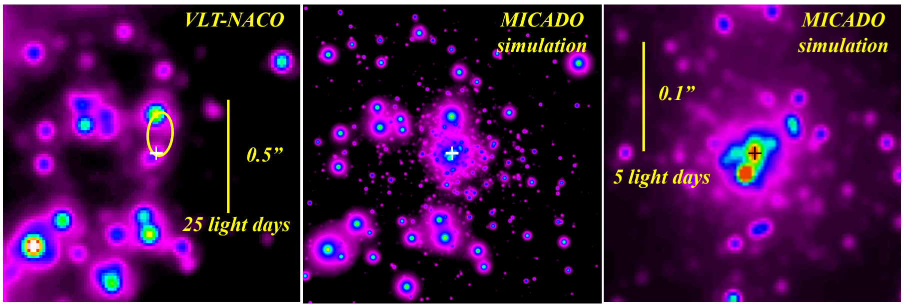

Fig. 2. Simulated MICADO image of the central cusp in the Galactic Centre (middle and zoomed on the right), compared to a current high-quality VLT/NACO K-image (left).

In a phased approach of the AO integration at the ELT, SCAO will be the first AO mode to be tested with MICADO at the telescope and will be ultimately offered as a MAORY mode.

4 MICADO science

4.1 Main science objectives

MICADO has the potential to address a large number of science topics that span the key elements of modern astrophysics. The science drivers focus on several main themes: the dynamics of dense stellar systems, black holes in galaxies and the centre of the Milky Way, the star formation history of galaxies through resolved stellar populations, the formation and evolution of galaxies in the early universe, planets and planet formation, and the solar system. To address these, MICADO will exploit its key capabilities of sensitivity and resolution, which are in turn leveraged by its observing modes of imaging, astrometry, coronagraphy, and spectroscopy. With a point-source sensitivity that is comparable to JWST and a resolution about a factor 6 better, MICADO is well suited to numerous science cases. Two examples of these, in the extragalactic field, are highlighted below. The MICADO science cases related to the exoplanet characterization and to the solar system study are described in Baudoz et al. (2019) and Merlin et al. (2019), respectively.

4.2 Galaxy evolution, structure of high-z galaxies

We now have a fairly robust outline of the cosmic evolution of global galaxy properties, and hence the first pieces of evidence about how galaxies assembled and transformed into the present day Hubble sequence. An obvious next step is to resolve the faint distant galaxies on sufficiently small scales to assess their sub-galactic components including disk structures, nascent bulges, clumps, and globular cluster progenitors.

The current view is limited by spatial resolution, which corresponds to $\sim$1 kpc in the best cases (space-based telescopes or adaptive optics on 8-m class ground-based telescopes). In particular, relatively unexplored regimes include lower mass galaxies, comprising the bulk (by number) of the galaxy population, and galaxies at early cosmic times, when they were building their first stars.

An alternative probe of galaxy evolution is via the relic populations in local galaxies, by performing photometry on individual stars to generate a color magnitude diagram (CMD). The various features of a CMD relate to stars formed at different cosmic times. In particular, detecting stars on the horizontal branch enables one to trace the star formation history of galaxies to $z>6$, to the reionization epoch. The ultimate goal for resolved stellar populations is to probe the central regions of elliptical galaxies in the Virgo Cluster. The high surface brightness, due to extreme stellar crowding, makes this very challenging. JWST will only be able to probe the outskirts of these galaxies, while the higher resolution of MICADO will enable it to reach almost to the centre where the bulk of the stars are to be found.

4.3 Black holes near & far

All reasonably massive galaxies appear to host supermassive black holes in their centres ranging in mass from several million to several billion solar masses (e.g., Kormendy & Ho 2013). Understanding why this is so and

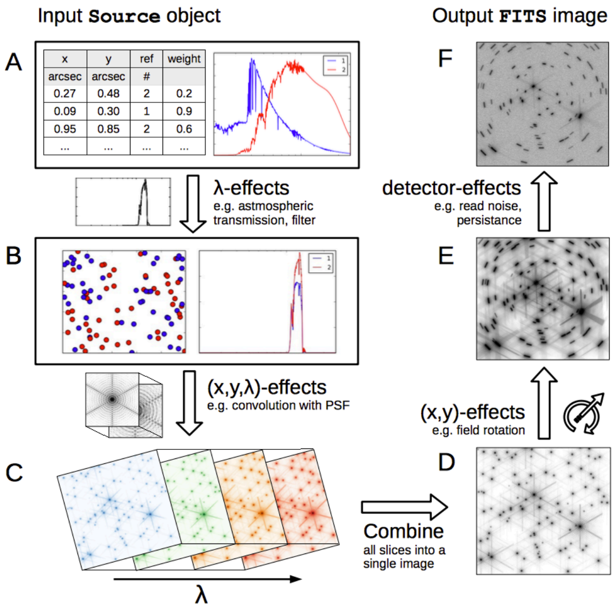

Fig. 3. SimCADO data model, representing the flow of events from the creation of the source object (here a mock open cluster) to the output FITS image. More details in Leschinski et al. (2016)

what is the link with galactic evolution processes, and how their properties depend on, or are affected by their environment are long standing and important issues.

We still need to understand the formation of galaxy cores, central star clusters and supermassive black holes, and the mechanisms of mass transport into these central regions and the influence of and on the galaxy-scale and larger environment. A suite of different mechanisms is expected to be at work, spanning nine orders of magnitude in linear scales from galaxy environment down to the sphere of influence of a central black hole.

So far, the fundamental limiting factor has been that of spatial resolution of current imaging and spectroscopic instrumentation. The highest fidelity measurements of supermassive black hole masses are obtained either through the observation of quasi-Keplerian orbits of stars around the black hole in our own Milky Way (e.g., Gillessen et al. 2017) or from the measurements of the circular motions of water masers (e.g., Kuo et al. 2011). But such measurements are only possible for a very few cases. The size of the spatial region where black holes directly influence the motions of stars and gas through their gravity – the sphere of influence – ranges from 1 pc (for $M_{BH} \sim 10^6\, M_\odot$) to 1 kpc (for the most massive $M_{BH} \sim 10^{10}\, M_\odot$ black holes). To obtain accurate measurements this sphere of influence must be at least marginally resolved.

MICADO will reach 10 mas spatial resolution, and consequently the observable volume will increase by a factor of >300 over what is possible today. With this, MICADO will be the first instrument able to probe core properties and nuclear morphologies for a large number of objects over a range of distance. MICADO will be able to determine black hole masses down to $\sim 10^6\, M_\odot$ and out to redshifts, z∼3. This will increase the number of direct stellar dynamical black hole mass measurements from the current few hundred to several tens of thousands. MICADO will also deliver superior sky subtraction compared to small IFUs, such as on HARMONI. This is crucial for the study of extended objects where the surface brightness typically lies below that of the night sky.

5 MICADO data simulation software packages: SimCADO & SpecCADO

SimCADO is a python package designed to simulate the effects of the atmosphere, ELT, and MICADO instrument on incoming light (Leschinski et al. 2016). It provides a framework for simulating raw output images based on the most recent design of the instrument. SimCADO is also highly configurable. The user is able to simulate various observational scenarios, e.g. the use of different adaptive optics (AO) systems, or set the effectiveness of different subsystems along the optical train, e.g. the performance of the derotator or atmospheric dispersion corrector (ADC). SimCADO is available on GitHub.

While SimCADO only provides functionality for imaging in the wide-field and zoom modes, a similar simulation package exists for the MICADO spectroscopic mode: SpecCADO. Soon available on GitHub, SpecCADO currently only simulates point sources (represented by the PSF) and background sources (that fill the slit homogeneously). It produces 2D spectra, accounting for various instrumental effects, and reproduces in the end the spectral layout on the MICADO's detectors.

References

Baudoz, P., et al. 2019, this conference

Ciliegi, P., Diolaiti, E., Abicca, R., et al. 2018, Proc. SPIE, 10703, 1070311

Clénet, Y., Gendron, E., Gratadour, D., Rousset, G., Vidal, F., 2015, A&A, 583, id. A102

Clénet, Y., Buey, T., Gendron, E., et al. 2018, Proc. SPIE, 10703, 1070313

Clénet, Y., Buey, T., Gendron, E., et al. 2019, Proceeding of the AO4ELT6 conference

Davies, R., Alves, J., Clénet, Y., et al. 2018, Proc. SPIE, 10702, 107021S

Douté, S., et al. 2019, this conference

Fritz, T., Kallivayalil, N., Carrasco, R., et al. 2015, Proceedings of the AO4ELT4 conference, http://dx.doi.org/10.20353/K3T4CP1131720

Gillessen, S., Plewa, P., Eisenhauer, F., et al. 2017, ApJ, 837, id. 30

Kormendy, J., & Ho, L. 2013, ARA&A, 51, 511

Kuo, C., Braatz, J., Condon, J., et al. 2011, ApJ, 727, id. 20

Leschinski, K., Czoske, O., Köhler, R., et al. 2016, Proc. SPIE, 9911, id. 991124

Merlin, F., et al. 2019, this conference

SF2A 2019
P. Di Matteo, O. Creevey, A. Crida, G. Kordopatis, J. Malzac, J.-B. Marquette, M. N'Diaye, O. Venot (eds)

POWER SPECTRUM EXTENDED: PRELIMINARY RESULTS

É. Cottalorda[1,2], É. Aristidi[1], M. Carbillet[1], M. Guinard[2] and S. Vourc'h[2]

Abstract. We propose, in the framework of short-exposure high-angular-resolution imaging (Lucky Imaging, speckle techniques), a simple improvement of the original Labeyrie's speckle interferometry technique. This new method, denoted as Power Spectrum Extended, allows to perform direct imaging of extended objects in the case of post-adaptive optics images and/or small diameter telescopes. The algorithm works in the Fourier domain. It combines informations from the average power spectrum of an ensemble of images with phase information estimated from an ad hoc shift-and-add process. It can be used together with a Lucky Imaging selection process. Preliminary results are presented, with application to images of both an astronomical object and an artificial satellite.

Keywords: high angular resolution imaging, speckle techniques, lucky imaging

1 Introduction

Atmospheric turbulence degrades the angular resolution of astronomical images. Labeyrie's speckle technique (Labeyrie 1970) was a first attempt to give a solution, but does not allow direct imaging. A lot of powerful but somewhat cumbersome techniques were developed during the 80's and the 90's (see Aime (2001) for a review).

In the case of small diameter telescopes (indeed small D/r_0) we observed that the high angular resolution information contained in images is present even in the case of long exposure times (several seconds). In particular, the phase of the Fourier transform of long-exposure images is not totally destroyed by the turbulence and can be used for imaging, providing that a tip-tilt correction is applied.

In this communication we present a new technique, denoted as Power Spectrum Extended (PSE), which is quite simple. It combines information from Labeyrie's speckle technique and from the phase of the sum of re-centered short-exposure images. We successfully applied the technique to images of a binary star in the near infrared with a 1-m telescope, as well as to images of the International Space Station in the visible with a 50-cm telescope.

2 Power Spectrum Extended

The PSE algorithm is a combination of a tip-tilt correction (shift and add) and a speckle method (well adapted to post adaptive optics short exposure images and/or small D/r_0). It takes for input a sequence of short exposure (a few milliseconds) images of an astronomical object. With these images we can reconstruct the Fourier transform of the object. The algorithm proceeds in two steps: the first for the modulus of the Fourier transform, and the second for the phase. To compute the modulus, we make use of the Labeyrie's original speckle technique: computation of the ensemble average of the square of the modulus of the Fourier transform of short-exposure frame . For the phase, we apply a shift-and-add processing (Cady & Bates 1980) to individual frames, which is equivalent to compensate from the atmospheric tip-tilt. We then take the phase of the Fourier transform of the resulting image. With the modulus and the phase, we can then reconstruct the objet by applying an inverse Fourier transform.

[1] UMR 7293 Lagrange, Université Côte d'Azur, Observatoire de la Côte d'Azur, CNRS, Parc Valrose, 06100 Nice, France
[2] Ariane Group 51/61 route de Verneuil - BP 71040, 78131 Les Mureaux Cedex, France

3 Preliminary results

We have tested PSE on the double star 16 Vul, observed with the 1-m telescope of the Plateau de Calern C2PU facility (Bendjoya et al. 2012), in H band (1.6 microns), with a very good seeing with respect to the diffraction limit (0.3 ″). This is a double star with a separation of 0.8 ″ and a magnitude difference of 0.4. The reconstruction seems definitely better than a simple shift-and-add reconstruction (see Fig. 1). These data were obtained with an exposure time of 50 ms.

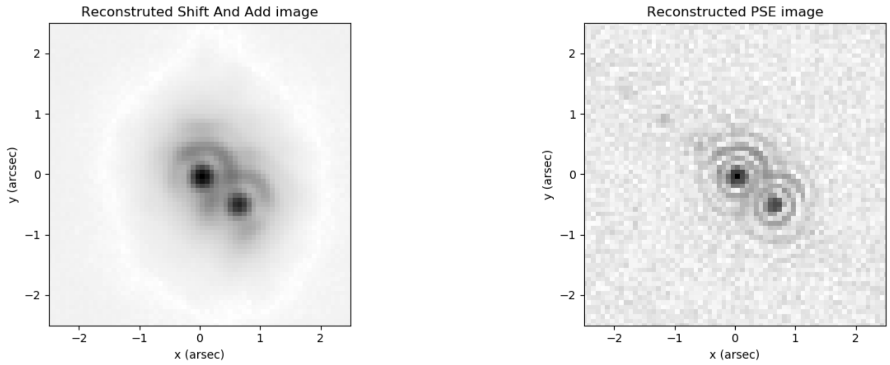

Fig. 1. Left: Shift-and-add reconstruction of 16 Vul. **Right:** PSE reconstruction of 16 Vul.

The PSE technique gives a better resolution than a simple tip-tilt correction, and it still works for an extended object. We tested it on images of the ISS (see Fig. 2), whose angular diameter of 30″ is larger than the isoplanatic angle. These images were taken with a 50-cm telescope at 650 nm (Ariane-Group facility).

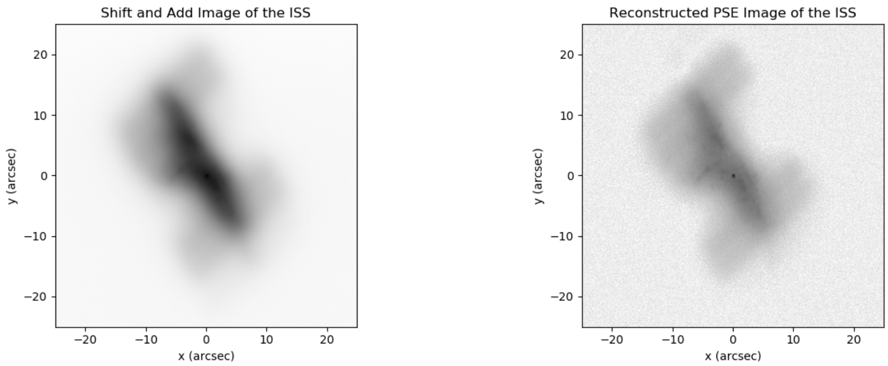

Fig. 2. Left: Shift-and-add reconstruction of the ISS. **Right:** PSE reconstruction of the ISS.

4 Conclusions

This new simple technique seems very promising. It gives better results than a mere tip-tilt compensation for weak turbulence: we tested it successfully with $D/r_0 \sim 10$. It may be combined with a Lucky Imaging process to increase image quality. Further investigations are currently performed in order to quantify the gain and limits of the method, and to compare it with other existing techniques.

References

Aime, C. 2001, European Journal of Physics, 22, 169
Bendjoya, P., Abe, L., Rivet, J. P., et al. 2012, Proceedings of the SF2A 2012, 643
Cady, F. M. & Bates, R. H. T. 1980, Optics Letters, 5, 438
Labeyrie, A. 1970, Astronomy and Astrophysics, 6, 85

SF2A 2019
P. Di Matteo, O. Creevey, A. Crida, G. Kordopatis, J. Malzac, J.-B. Marquette, M. N'Diaye, O. Venot (eds)

THE MULTI CONJUGATE ADAPTIVE OPTICS RELAY FOR MICADO

S. Douté[1], F. Feautrier[1], G. Chauvin[1, 2], E. Moraux[1] and the MAORY consortium

Abstract. MAORY (Multi-Conjugate Adaptive Optics RelaY) is the adaptive optics module that will restore the full angular resolution of a 39m telescope at the focal plane of the ELT's camera MICADO and of another instrument in a more distant future. MAORY is designed to be delivered in first light and must provide a multi-conjugate correction (MCAO) of atmospheric turbulence effects over the entire MICADO field of view (up to 50 ") with excellent uniformity. For that purpose it will use up to 8 laser guide stars (LGS) and 3 natural guide stars (NGS). MAORY will be able to operate in MCAO mode over more than 50% of the accessible sky from the ELT site instead of a few percents with a conventional Single Conjugated Adaptive Optics (SCAO). Two observational techniques will particularly take advantage of MAORY : astrometry and deep photometry in primary science cases such as small bodies and planets of the Solar System, young stellar populations, black holes and galaxies, and the evolution of the young Universe.

Keywords: European Large Telescope, Multi-Conjugate Adaptive Optics, MAORY, MICADO, science cases.

1 Adaptative Optics at the dawn of the extremely large telescope era

At present there is a zoo of AO concepts, which spans different sub-spaces in the Strehl ratio/sky coverage/Field-of-View (FoV): SCAO, LGSAO, GLAO, LTAO, MCAO, MOAO, and ExAO (Davies & Kasper 2012).The Strehl ratio S is a useful figure of merit to characterise the performance of an adaptive optics system which is defined as the ratio of the central intensity of the actual Point Spread Function (PSF) to the central intensity of an ideal diffraction-limited PSF. Equivalently S determines the relative flux in two components of the PSF: the diffraction-limited core and the seeing halo. The sky coverage is the fraction of the sky over which a suitable AO correction can be achieved. The Single Conjugated AO (SCAO) provides wavefront correction at an angular distance no larger than 30 to 40 arcsec from a bright (e.g., $R < 16$) natural guide star with a fast decrease of the Strehl ratio. This leads to a very limited sky coverage of approximately 1%. Laser Guide Star AO (LGSAO) somewhat relaxes this hard constraint by shooting a laser beam at the sodium layer, $\approx$ 90 km high in the Earth atmosphere, creating an artificial guide star by resonant excitation. The sky coverage increases to nearly 30% but at the expense of the Strehl ratio (30% instead of 60% with SCAO). Indeed the correction suffers from the fact that the light is coming from a single LGS that is not point like and not at infinity. The artificial light thus does not probe the entire cylindrical volume of turbulence in the telescope line of sight (cone effect). In addition a NGS is still needed for tip-tilt (TT) compensation. Laser tomography AO (LTAO) mitigates, or entirely solves, the cone effect limitation with several LGSs to probe the cylindrical volume of turbulence. However the so-called tomographic information extracted from the different Wave Front Sensor (WFS) measurements is not fully exploited because the correction of the wavefront is only achieved with one Deformable Mirror (DM). Performances close to SCAO are achieved also over a very limited field of view (anisoplanatic limitation) but around the sky direction of interest that is not tied to a NGS. Sky coverage is similar to LGSAO. With the Multiple Conjugated AO (MCAO) concept (Rigaut & Neichel 2018), the idea is to operate several DMs that are optically focused to different levels of the whole turbulent volume. A DM optically conjugated to some layer will be able to exactly compensate for phase aberrations occurring in this layer. This requires multiple guide stars (NGS or LGS) and a real-time tomographic processor. As a result MCAO reaches a good

[1] IPAG, Université Grenoble Alpes, 38058 Grenoble Cedex 9
[2] International Franco-Chilean Laboratory of Astronomy, CNRS/INSU UMI3386, Department of Astronomy, University of Chile, Casilla 36-D, Santiago, Chile

compromise between the Strehl ratio (up to 40%), the field of view over which the uniformity of the PSF is achieved (up to several arcmin) and the sky coverage (50% and more). Note that probing NGS wavefronts is still mandatory to disentangle between sodium altitude fluctuations and atmospheric focus changes in addition to TT compensation. MCAO has been demonstrated for correction in the NIR on 8-m telescopes on NGS only (Multiconjugate Adaptive Optics Demonstrator at the VLT) and LGS (Gemini MCAO System) with excellent performances (Fig. 1). MCAO is particularly adapted for extremely large telescopes because most WFSs become more sensitive. Besides the overlap of the beams coming from the stars of a given asterism becomes larger for larger apertures, making the tomography easier and more stable. Out of the three extremely large telescope projects, two have MCAO as part of their first generation instruments: NFIRAOS at TMT (Herriot & 19 co-authors 2014) and MAORY at ELT (Ciliegi et al. 2018).

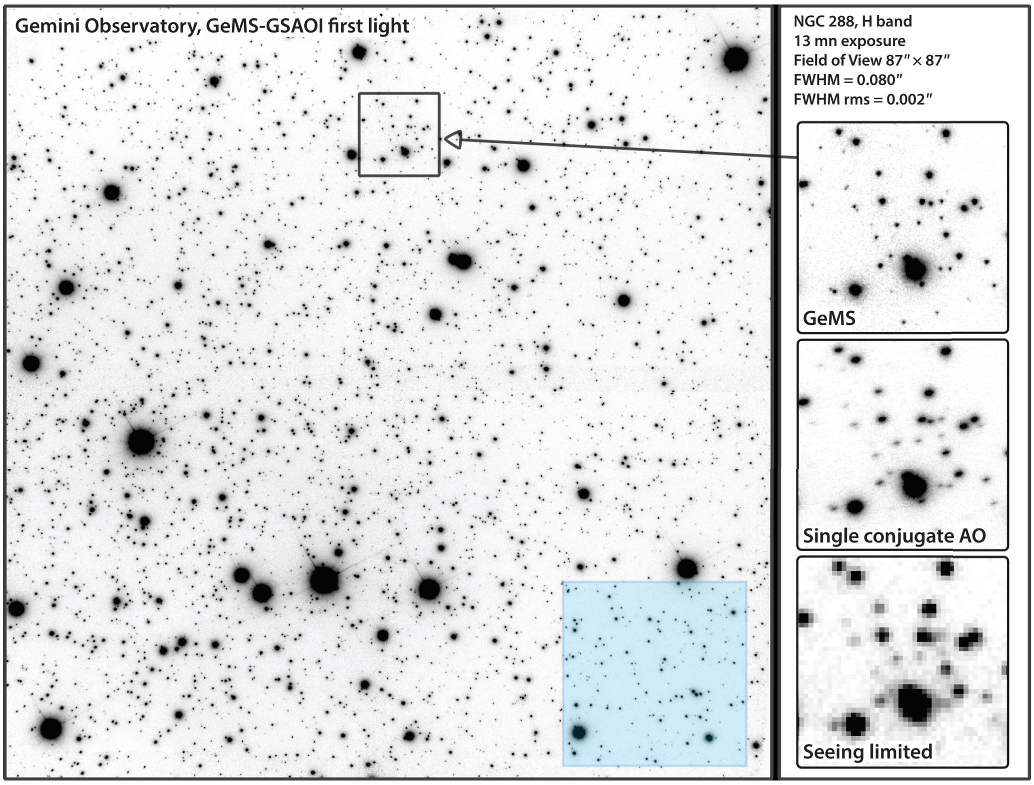

Fig. 1. Figure illustrating the gain in FoV brought by MCAO with NGC 288 observed by GeMS in the H band. Figure extracted from Rigaut & Neichel (2018).

2 MAORY: the project and its French contribution

MAORY is the Multi-Conjugate Adaptive Optics RelaY for the ELT; PI, Paolo Ciliegi, INAF-Bologna. The agreement for the MAORY instrument was signed on December 10th 2015 between ESO and a consortium of European institutes composed of the Istituto Nazionale di Astrofisica (Italy) and the INstitut des Sciences de l'Univers of Centre National de la Recherche Scientifique (France). The MAORY kick-off meeting was held in Bologna, Italy on February 2, 2016. MAORY will support the MICADO near-infrared camera by offering two adaptive optics modes: MCAO and SCAO. Currently the former mode of MAORY is developed in collaboration with 3 Italian institutes (OAS Bologna, OA Padova, OA Arcetri Firenze) and one french IPAG (co-I P. Feautrier), the latter being responsible for the wavefront sensors of the LGSs (Schreiber et al. 2018). The SCAO mode (Clénet & 39 co-authors (2018), and Clénet et al. 2019, these proceedings) is being developed under the responsibility of MICADO by INSU (LESIA, GEPI, Observatoire de Besançon, DT INSU, IPAG) in collaboration with OA Arcetri, first as a stand-alone module that will serve directly MICADO then, integrated within the main MAORY system upon completion and commissioning (2027). The Preliminary Design Review

(PDR) of MAORY is planned for mid 2020 and the Final Design Review (FDR) less than two years latter. A scientific team has been gathered within the MAORY project with 15 members including 3 from IPAG. The leader of the team is Carmelo Arcidiacono researcher at Instituto Nazionale di Astrofisica (INAF), Padova.

3 Characteristics and performances of MAORY

MAORY is a post-focal adaptive optics module which functional diagram appears in Fig. 2. In the MCAO mode, wavefront sensing is performed by a system based on six to eight Laser Guide Stars (LGS) for high-order wavefront sensing and three Natural Guide Stars (NGS) for low-order wavefront sensing. The six LGS are produced by excitation of the atmospheric sodium layer with six laser beacons (with $\lambda = 589.2$ nm) propagated from E-ELT. Wavefront compensation is achieved by up to two deformable mirrors in MAORY, which work together with the telescope adaptive and tip-tilt mirrors M4 and M5 respectively. In the present baseline, the AO correction will be performed over the whole D = 160" technical FoV that contains MICADO 53 × 53" FoV. The approximate faint magnitude limit for a star to be eligible as a NGS is $Hlim \sim 18.0 - 19.0$ mag; the bright magnitude limit should be $H \sim 6.0$. Note that the NGS will be analyzed by two independent set of wavefront sensors (three optical NGS WFS and three infrared NGS WFS, respectively). From simulations (Arcidiacono et al. 2018) the expected performances of MAORY are the following. The average Strehl ratio in the K band will be ≈ 35% (22% in H, 6% in J) throughout MICADO wide field of view (51") on 50% of the sky. With excellent seeing conditions the Strehl ratio could reach 50-55% for the same sky coverage. With a NGS asterism closer to the central part, the average Strehl ratio could reach 40-45% throughout MICADO medium field of view of (20") on 50% of the sky. PSF uniformity across the corrected field of view is very important and, from past experiences, variation of the FWHM across the images should be less than 10% over MICADO wide field of View. One should emphasise the fact that astrometry is one of the main science drivers for building the next generation MCAO systems like MAORY for future extremely large telescopes. The goal is to reduce the amount of distortion, provide a large number of uniformly high-quality astrometric reference sources, deliver uniformity of the corrected point spread function (PSF) thus improving the accuracy of the image analysis. Through calibration, observation, and data reduction processes dedicated to astrometry, the MICADO/MAORY system will offer a 10-50 μas precision relative to a reference source anywhere in the field.

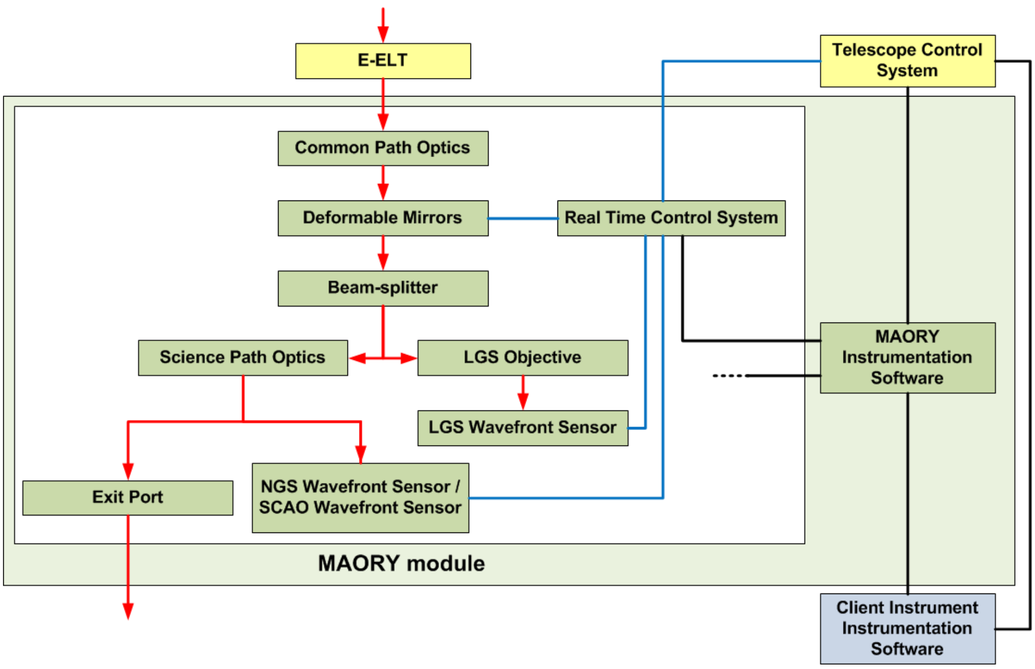

Fig. 2. MAORY functional diagram of the instrument.

4 Contribution of MAORY to MICADO Science

There is an ongoing work by the scientific team of MAORY to define priority cases that will be adressed by MICADO with the added value of MAORY in various themes: cluster of stars in formation, stellar cluster of galactic centers, evolution and dynamics of galaxies, gamma-ray bursts, protoplanetary disks, exoplanets and objects of the System Solar. A white book was published (Fiorentino et al. 2017) from which we summarize the main objectives.

4.1 Solar System

MICADO-MAORY will address two main themes, the formation and evolution of the minor bodies in the Solar System and the study of the composition of Giant planets and their satellites. For the first theme, imaging and spectroscopy will be put to work to determine the size, shape, colors, and chemical composition of the main asteroids, Centaurs, and trans-Neptunian objects. High-resolution astrometry will allow to determine their orbital and internal properties when these objects are in multiple systems. For the second theme, temporal variation of the atmospheres of Giant Planets will be monitored and spectroscopy will be used to measure the abundance of CH_4, N_2, and hydrocarbons in the atmosphere of Titan. In both themes a MCAO mode is required to resolve faint asteroids and KBO (mag. <15 in H band) and to get the maximal spatial resolution for objects with an apparent diameter $>$ 300 to 400 mas.

4.2 Stellar Systems

The formation and evolution of stellar systems notably globular clusters (GCs), young massive clusters, and star-forming regions is an objective of paramount importance for MICADO-MAORY. Indeed MCAO shines for such fields with a high density of stars because it provides the advantage of a large field of view with a more uniform PSF. The result is a sensitivity gain for point sources, a minimization of the confusion of the stellar population, a more complete and stable photometry as well as the possibility to measure the proper motion of many individual stars at once increasing statistics. As a consequence the following objectives become accessible: (i) a better determination of the initial mass function (IMF) accessing the high mass, the low mass, and the substellar part of the stellar IMF, (ii) the IMF study in far away very massive young clusters such as the Arches, Westerlund 1, or NGC3603 in our galaxy as well as young clusters in the SMC/LMC (e.g. 30 Doradus), (iii) spatial properties and internal kinematics of multiple stellar populations in (young) globular clusters (an accuracy of 0.05 mas over at least 1 year corresponds to a few km/s at 10 Kpc), and (iv) accretion and disk fraction of young stellar objects in low-metallicity environments. It is worth noting that NIR MCAO astrometry studies such as the one conducted with MAORY are fully relevant even in the Gaia era as they provide complementary information for very embedded regions (like the Galactic Center) and/or very crowded regions (like GCs) in which Gaia is blind.

4.3 Disks & Exoplanets

MICADO will be the instrument of choice to understand the formation, the physics of Giant Planets, and planetary architectures in general thanks to its high contrast mode mixing SCAO correction, coronography, and angular differential imaging (see P. Baudoz et al. 2019, these proceedings). The MAORY science team is there closely collaborating with the MICADO consortium for this key science case. The use of MAORY in MCAO mode might be an option for the direct imaging or astrometric monitoring of fainter targets/lower mass stars and younger and more embedded objects, for the search and characterization of brown dwarf to planetary mass companions.

4.4 Extragalactic

Extragalactic studies are main scientific drivers for MICADO and most investigations will benefit greatly from the MCAO correction provided by MAORY because of sky coverage issue, the PSF uniformity over large field, and the target magnitude constraint. Compared to seeing-limited observations, the expected signal-to-noise ratio gain provided by MCAO for extended objects will be of the order of 2 to 3. Considering average Strehl ratio provided by MAORY, typical sensitivity obtained in 5hr acquisitions is 29.5mag in Kband, 30.4mag in H band, and 29.7mag in J band. Under the best conditions an additional gain of 0.3 mag can be expected. Such performance is the way to a much more detailed view of the local Universe and a new window on the High redshift Universe.

4.4.1 Local Universe

MICADO-MAORY will address three main themes: co-evolution between Black Holes (BHs) and their host galaxies, galaxy formation, growth, and assembling through composition studies, and finally measuring the local universe with greater precision (Cepheids, TRGB, and Surface brightness fluctuations). Different objectives can be cited for each theme like revealing the intermediate-mass BHs in dwarf galaxies by modelling the kinematic of the gas around the BH with high resolution spectroscopic observations, studying the stellar population in a variety of galaxies, in their nuclear star clusters, and in their massive GCs within ≈5-18 Mpc, and constraining formation scenarii of early-type galaxies (e.g. NGC 3379) by identifying individual planetary nebulae and deriving their abundance. A benefit of a high angular resolution combined to confusion reduction is the possibility of detecting and characterizing (distance, stellar content) for the first time nearby galaxies in the Zone of Avoidance.

4.4.2 High redshift Universe

MICADO-MAORY should contribute greatly to the understanding of the star formation history in early galaxies because it will be able alone to resolve galactic structures and kinematics as well as characterizing the young stellar population in the distant Universe (at redshift 2-4). Other possible contributions in studying galactic evolution is probing the assembly of high redshift early-type galaxies and confirming the primordial nature of $z>10$ galaxy candidates. The co-evolution theme between BHs and their host galaxies can be extended to the high redshift universe. Super Massive Black Holes will be probed in several AGN ($d<100$ Mpc) with high resolution observations of stellar kinematics. The accretion processes around the nuclei of AGN will be studied by imaging the warm dust in the near-IR on parsec scales. The mass of the central BH and the properties of its host will be measured for a suitable sample of galaxies (quasars) at different redshift.

5 Conclusions

After a slow start, perhaps due to the disbelief of the community that such a complex technique could be put to work, the interest of the community in MCAO is growing. MAD at ESO, GeMS at Gemini and Clear at the Big Bear Solar Observatory have demonstrated that MCAO works and provides uniform, almost diffraction-limited images over fields of 1 arcmin^2 or more. MCAO is still the subject of active research and development but it is mature enough to be developed for a commissioning at the ELT at the horizon 2027. This is of paramount importance so that the imager MICADO (and, latter, a second instrument) reaches its optimal performance in terms of angular resolution and sensitivity over a large portion of the accessible southern sky. This is also a requirement to be fully competitive against concurrent future telescopes such as the JWST and the TMT.

The authors thank the teams of instrument scientists and engineers belonging to the MAORY consortium for their hard work in designing the instrument and fulfilling the specifications that will allow great science to be accomplished.

References

Arcidiacono, C., Schreiber, L., Bregoli, G., et al. 2018, in Society of Photo-Optical Instrumentation Engineers (SPIE) Conference Series, Vol. 10703, Proc. SPIE, 107034I

Ciliegi, P., Diolaiti, E., Abicca, R., et al. 2018, in Society of Photo-Optical Instrumentation Engineers (SPIE) Conference Series, Vol. 10703, Proc. SPIE, 1070311

Clénet, Y. & 39 co-authors. 2018, The MICADO first-light imager for the ELT: towards the preliminary design review of the MICADO-MAORY SCAO

Davies, R. & Kasper, M. 2012, Annual Review of Astronomy and Astrophysics, 50, 305

Fiorentino, G., Bellazzini, M., Ciliegi, P., et al. 2017, arXiv e-prints, arXiv:1712.04222

Herriot, G. & 19 co-authors. 2014, NFIRAOS: first facility AO system for the Thirty Meter Telescope

Rigaut, F. & Neichel, B. 2018, Annual Review of Astronomy and Astrophysics, 56, 277

Schreiber, L., Feautrier, P., Stadler, E., et al. 2018, in Society of Photo-Optical Instrumentation Engineers (SPIE) Conference Series, Vol. 10703, Proc. SPIE, 107031Y

SF2A 2019
P. Di Matteo, O. Creevey, A. Crida, G. Kordopatis, J. Malzac, J.-B. Marquette, M. N'Diaye, O. Venot (eds)

DARK MATTER DISTRIBUTION IN DISTANT GALAXIES WITH HARMONI

B. Epinat[1], P. Adamczyk[1], S. Bounissou[1,2], P. Amram[1] and B. Neichel[1]

Abstract.
The study of the distribution of dark matter (DM) in local galaxies has revealed the cusp-core problem. Looking back in time will enable us to understand whether DM halos were already cuspy in the past and evolved with time or if the situation was already similar. We have undertaken HARMONI simulations of galaxies at high redshift from high resolution observations of galaxies in the local Universe to study the potential of HARMONI observations. These simulations show that HARMONI will be able to provide meaningful constraints on DM distribution down to galaxies with stellar masses as low as 10^9 M$_\odot$ at $z = 1.4$ and that the gain in sensitivity of the 30×60 mas pixel scale is balanced by the better spatial resolution of the 20×20 mas pixel scale to recover the shape of rotation curves.

Keywords: Galaxies: kinematics and dynamics, halos, high-redshift, evolution, dark matter

1 Introduction

The core-cusp discrepancy of dark halo central density distribution between observations and simulations (e.g. Navarro et al. 1997, 2010) remains a challenge for the standard cosmological model. Dynamical processes might be at work to transform cuspy halos into core during galaxy evolution (e.g. Navarro et al. 1996; Teyssier et al. 2013; Ogiya et al. 2014). The dependence of halo concentration with galaxy merger history has been intensively studied from numerical cosmological simulations (e.g. Zhao et al. 2003, 2009). Lambda-CDM numerical simulations like Millennium I-II (Springel et al. 2005; Boylan-Kolchin et al. 2009) indicate that dark halo concentration declines with increasing mass and redshifts (e.g. Bullock et al. 2001). The study of rotation curves enables to constrain dark matter (DM) halo distribution. For this, high resolution kinematics in the inner parts (and ideally neutral gas kinematics beyond the optical disk) are necessary as well as imaging to constrain baryonic mass distribution. Using these techniques Spano et al. (2008) were able to constrain DM distribution for some low mass systems in the local Universe, and suggested that galaxies hosted cored halos. This result was extended to higher masses by Korsaga et al. (2018, 2019). At higher redshift, rotation curves are not yet resolved enough to tackle the cusp-core problem. However, recently, using SINFONI and KMOS data, Genzel et al. (2017) and Lang et al. (2017), tried to constrain the DM fraction in the inner regions of galaxies using both seeing limited and observations assisted with adaptive optics (AO) as well as stacking techniques. Their results points towards a low DM fraction which is supported by the observation of decreasing rotation curves. However, these results remains controversial because the spatial resolution is rather low, the extent of rotation curves is limited and because the seeing may not be properly taken into account. HARMONI on the ELT will be the first instrument able to reach the spatial resolution needed to disentangle the baryonic from the DM distribution for high redshift galaxies. Models of mass distribution will provide constraints on DM halo central density and core radius for galaxies in a redshift range that will remain unreachable with nowadays 8-10 meter class telescopes.

2 Simulations of HARMONI observations: sample selection and description

We have performed a series of simulations to understand the trade off between sensitivity and spatial resolution of kinematics needed to study the DM halo density profiles in distant galaxies. We projected real high resolution

[1] Aix Marseille Univ, CNRS, CNES, LAM, Marseille, France
[2] CEA Saclay, Service d'Astrophysique, L'Orme des Merisiers, Bat 709, BP 2, 91191 Gif-sur-Yvette Cedex, France

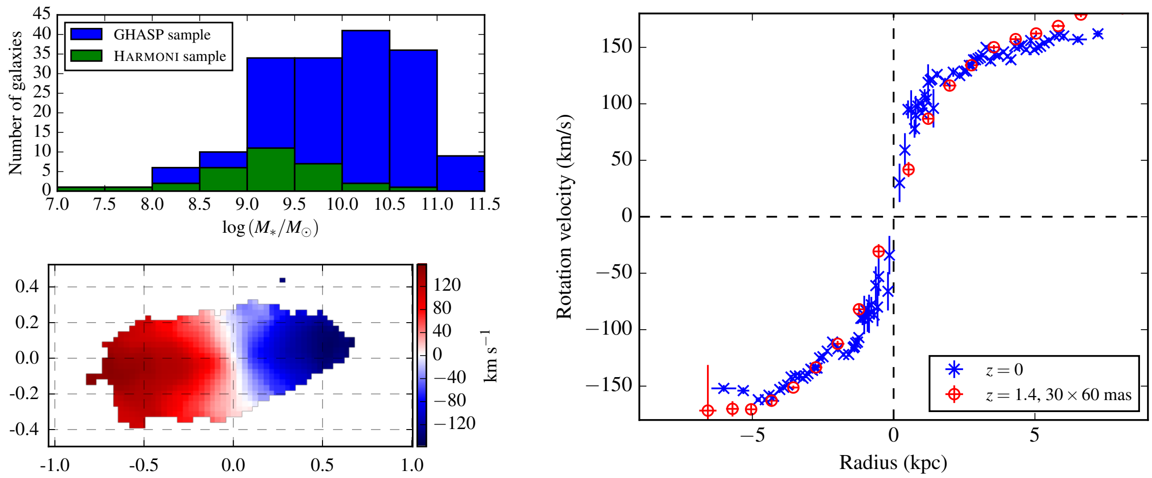

Fig. 1. Top-Left: Stellar mass histogram of both GHASP parent sample (blue) and the HARMONI sub-sample (green). Bottom-left: Velocity field of UGC 7045 with the 30 × 60 pixel scale. Positions (in arc-seconds) and velocities (km/s) are provided with respect to the adopted centre and systemic velocity of the galaxy respectively. Right: Rotation curve extracted from the velocity field (red). Blue points correspond to the rotation curve obtained at $z = 0$.

Fabry-Perot observations of local galaxies of the GHASP sample (Epinat et al. 2008) at $z = 1.4$, where the angular size is close to the maximal angular distance and where galaxy brightness might be favourable. The GHASP sample consists of 203 spiral galaxies in the local Universe over a large mass range observed using Fabry Perot techniques around the Hα line ($\sim$ 20 Å wide) with a spectral resolution $R \sim 9000$, a spectral sampling of 0.35 Å and with a spatial resolution of around 3" over a field of view of either 4 or 6 arcmin^2. To ensure that input data cubes have a sufficient spatial resolution to simulate high redshift galaxies, we imposed that the actual physical resolution (FWHM) is larger than the scale corresponding to 20 mas at redshift 1.4, leading to a sub sample of 31 local galaxies. We removed galaxies (i) with ill-defined rotation curves at $z = 0$, (ii) with an inclination larger than 75°, and (iii) with no available stellar mass estimate (from WISE infra-red photometry, Cluver et al. 2014). The HARMONI sub-sample is mainly composed by the low mass galaxies of GHASP (see Fig. 1, top-left). This is due to the fact that high mass galaxies were selected at larger distance to fit within the GHASP field of view and therefore have a lower physical spatial resolutions. Since local galaxies have intrinsic line fluxes much fainter than high redshift ones due to a lower star formation rate (SFR), we have normalised the Hα flux of GHASP galaxies projected at $z = 1.4$ so that all galaxies lie on the Main Sequence of star forming galaxies at $z = 1.4$ using the prescriptions of Whitaker et al. (2014) to convert stellar masses into SFR. The total Hα flux was derived using the Kennicutt (1998) relation using the luminous distance at $z = 1.4$. Assumed SFR range between 10^{-2} and 10^2 M$_\odot$ yr^{-1} and Hα fluxes between 10^{-19} and 5×10^{-16} erg s^{-1} cm^{-2}.

We used these datacubes as input for the HARMONI Simulator (HSIM v1, Zieleniewski et al. 2015). We have generated two sets of pseudo-observations both with a on-source exposure of 2 hours (8×900 s): one with the 20×20 mas pixel scale and another with the 30×60 mas pixel scale to investigate the trade off between sensitivity (larger with a large pixel), and spatial resolution (better with a small pixel). We used the H-band grism with $R = 7500$ to observe the Hα line at 1.575 μm ($z = 1.4$) and a LTAO PSF using 6 laser guide stars under good seeing conditions (FWHM = 0.64").

3 Simulation analysis

We used CAMEL* (Epinat et al. 2012) on the datacubes produced by HSIM to extract kinematics maps by fitting the spectrum in each spaxel by a Gaussian. For the cubes with the 30× 60 mas pixel scale, the data was replicated along the y axis to have a square 30×30 mas final sampling. Priori to kinematics extraction, a 2×2 pixel-wide Gaussian smoothing was applied to increase the signal to noise ratio (SNR). The velocity field was cleaned by removing all spaxels with a SNR below 5 (Fig. 1, bottom-left). The rotation curve (Fig. 1, left) was

*https://gitlab.lam.fr/bepinat/CAMEL

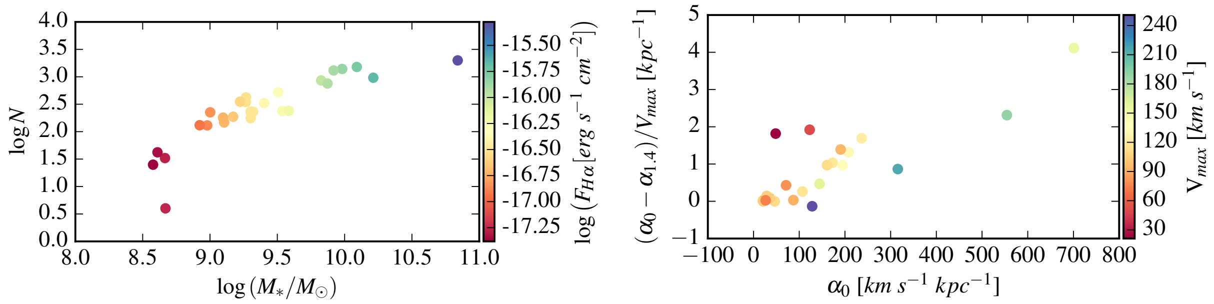

Fig. 2. Left: Number of pixels with a SNR above a threshold of 5 for the 30 × 60 mas simulations with respect to stellar mass. Hα fluxes are indicated using colours. Right: Difference between the slope obtained from high resolution kinematics and HARMONI kinematics using the 30 × 60 mas simulations, normalised by the maximum rotation velocity as a function of the inner slope from high resolution kinematics. Maximum rotation velocity (from high resolution) is indicated using colours.

then computed using the projection parameters (centre, major axis and inclination) derived from actual data at $z = 0$ by deprojecting off-axis spaxels, as done for local galaxies (e.g. Epinat et al. 2008), within a sector of 30° in the galaxy plane. The point spread function (PSF) was not taken into account. This work therefore represents a lower limit on the capability of HARMONI.

3.1 Signal to noise ratio analysis

Among the 31 galaxies that were simulated, 8 galaxies have less than 100 spaxels with a SNR greater than 5 with both the 20 × 20 mas and the 30 × 60 mas pixels scale. These galaxies are those with stellar masses lower than $10^{8.8}$ $M_\odot$ and have integrated fluxes lower than 10^{-17} erg s^{-1} cm^{-2}. In Fig. 2 (left), we show the correlation between the number of points have a SNR above 5 and the stellar mass and integrated line flux. From this figure, it is obvious that the most massive galaxies, i.e. those that were not included in the final sub-sample (cf. Fig. 1, top-left) would have a large number of pixels, as expected. Therefore the relatively low number of galaxies with masses above 10^{10} $M_\odot$ is not a problem in the present analysis. The observed trend is due to the correlation of size and flux with stellar mass: more massive galaxies have larger number of pixels with good SNR. The 100 pixels threshold corresponds to different area in the galaxies frame depending on the pixel scale. For the 20 × 20 (30 × 60) mas pixel scale, this roughly corresponds to 0.04 (0.09) arcsec^2. The difference observed between the two pixel scales is not very significant and this may be due to the fact that sensitivity gain with the coarser pixel enables to go a bit further. However, it is noticeable that galaxies above the same thresholds in mass and flux are observable under good conditions within the same exposure time with both pixel scales even if surface is slightly larger with the largest pixel. In some cases, the 20 × 20 mas pixel scale even provides a better detection because emission is clumpy, hence the SNR is better because clumps are not resolved. For the lowest mass galaxies, except in specific cases, the gain in sensitivity using the coarser pixel is not sufficient to compensate the intrinsically small size of galaxies. It is remarkable that in 2 observing hours we are able to spatially resolve galaxies down to masses of 10^9 $M_\odot$ at $z = 1.4$, which is very challenging with actual telescopes in tens of hours (e.g. Contini et al. 2016; Newman et al. 2012).

3.2 Rotation curve analysis

With actual telescopes without AO, the maximum rotation velocity can already be quite efficiently recovered. However, it is almost impossible to constrain the inner slope which contains information about a cuspy or core DM halo. The visual inspection of rotation curves for our sub-sample is promising (cf. Fig. 1, right). For all galaxies that passed the selection threshold on SNR, the derived rotation curves have a fairly good overall agreement for both the 30 × 60 and 20 × 20 pixel scales. There are two exceptions, the two faintest galaxies, where the rotation curve obtained with the 30 × 60 mas scale looks better. The 20 × 20 mas rotation curve shows more resolved details than the 30 × 60 mas one. In addition, the inner slope seems better resolved. The inner velocity gradient is usually well recovered, even if it seems slightly underestimated.

We further quantified the recovery of the inner velocity gradient from the rotation curve. We have estimated the inner gradient within the inner 500 pc of each galaxy on both the 20 × 20 mas and 30 × 60 mas pixel scales. We compared these values to inner slopes that were estimated from the high resolution data in Epinat et al. (2010). Fig. 2 (right) shows the inner slope difference between $z = 0$ data and projected data, normalised by the maximum velocity inferred at $z = 0$ as a function of the $z = 0$ inner slope. We observe a trend that the normalised slope difference is larger when the inner gradient is large. For a given inner slope, the normalised difference is lower for the fastest rotators. The inner slopes are also better recovered with the smallest pixel scale, even if the difference is not strong. For the slow rotators, the difference is larger with the small pixel scale, probably because these galaxies are the lowest mass galaxies, and hence have a lower SNR, preventing accurate velocity measurements.

4 Conclusions

We have performed analysis of advanced HSIM simulations of local galaxies projected at redshift z=1.4 and have found that: (i) HARMONI will be able to study spatially resolved kinematics with sufficient details and signal to noise ratio to perform mass models and recover the shape of DM halos down to stellar masses of 10^9 $M_\odot$ at $z = 1.4$ and $10^{9.5}$ $M_\odot$ at $z = 2.7$ using the Hα line in 2 hours of exposure. This translates into a line flux limit of 10^{-17} erg s^{-1} cm^{-2} and can be at first approximation applied for any other emission line. (ii) The gain in sensitivity of the coarser pixel scale (30 × 60 mas) enables to go slightly deeper than the 20 × 20 mas pixel scale. (iii) This gain in sensitivity is balanced by the lower spatial resolution of the 30 × 60 mas pixel scale. The 20 × 20 mas pixel scale enables to better recover the details and shape of the rotation curve.

Mass models will need methods taking into account beam smearing. In addition, in this study, we did not recover projection parameters (PA, inclination and centre) from the data. These parameters might be either recovered from kinematics, using 2D or 3D modelling techniques or using continuum emission. In order to perform mass model analyses one also needs to know stellar and gas distributions. We will investigate whether HARMONI data will enable to perform photometry and morphology analyses or if ancillary data are necessary.

Studying the capabilities of ELT-MOS on this topic is of major importance to assemble a statistical sample.

This is work is supported by CNRS/INSU, with funding from CSAA, ASHRA, PNCG.

References

Boylan-Kolchin, M., Springel, V., White, S. D. M., Jenkins, A., & Lemson, G. 2009, MNRAS, 398, 1150
Bullock, J. S., Kolatt, T. S., Sigad, Y., et al. 2001, MNRAS, 321, 559
Cluver, M. E., Jarrett, T. H., Hopkins, A. M., et al. 2014, ApJ, 782, 90
Contini, T., Epinat, B., Bouché, N., et al. 2016, A&A, 591, A49
Epinat, B., Amram, P., Balkowski, C., & Marcelin, M. 2010, MNRAS, 401, 2113
Epinat, B., Amram, P., Marcelin, M., et al. 2008, MNRAS, 388, 500
Epinat, B., Tasca, L., Amram, P., et al. 2012, A&A, 539, A92
Genzel, R., Schreiber, N. M. F., Übler, H., et al. 2017, Nature, 543, 397
Kennicutt, Robert C., J. 1998, ApJ, 498, 541
Korsaga, M., Amram, P., Carignan, C., & Epinat, B. 2019, MNRAS, 482, 154
Korsaga, M., Carignan, C., Amram, P., Epinat, B., & Jarrett, T. H. 2018, MNRAS, 478, 50
Lang, P., Förster Schreiber, N. M., Genzel, R., et al. 2017, ApJ, 840, 92
Navarro, J. F., Frenk, C. S., & White, S. D. M. 1996, ApJ, 462, 563
Navarro, J. F., Frenk, C. S., & White, S. D. M. 1997, ApJ, 490, 493
Navarro, J. F., Ludlow, A., Springel, V., et al. 2010, MNRAS, 402, 21
Newman, S. F., Genzel, R., Förster-Schreiber, N. M., et al. 2012, ApJ, 761, 43
Ogiya, G., Mori, M., Ishiyama, T., & Burkert, A. 2014, MNRAS, 440, L71
Spano, M., Marcelin, M., Amram, P., et al. 2008, MNRAS, 383, 297
Springel, V., White, S. D. M., Jenkins, A., et al. 2005, Nature, 435, 629
Teyssier, R., Pontzen, A., Dubois, Y., & Read, J. I. 2013, MNRAS, 429, 3068
Whitaker, K. E., Franx, M., Leja, J., et al. 2014, ApJ, 795, 104
Zhao, D. H., Jing, Y. P., Mo, H. J., & Börner, G. 2009, ApJ, 707, 354
Zhao, D. H., Mo, H. J., Jing, Y. P., & Börner, G. 2003, MNRAS, 339, 12
Zieleniewski, S., Thatte, N., Kendrew, S., et al. 2015, MNRAS, 453, 3754

SF2A 2019
P. Di Matteo, O. Creevey, A. Crida, G. Kordopatis, J. Malzac, J.-B. Marquette, M. N'Diaye, O. Venot (eds)

MOSAIC FOR THE ESO ELT: THE FRENCH PERSPECTIVE

F. Hammer[1], O. Le Fèvre[2], J. G. Cuby[2], T. Contini[3], G. Rousset[4], S. Charlot[5], J. M. Conan[6], M. Puech[1], P. Jagourel[1], D. Le Mignant[2], F. De Frondat[1], K. Dohlen[2], K. El Hadi[2], M. Frotin[1], E. Gendron[4], M. Larrieu[3], L. Tasca[2], Y. B. Yang[1], S. Zanchetta[1] and
The International MOSAIC Team

Abstract. MOSAIC at the ELT will be the most powerful facility to observe a large number of faint sources that are unreachable by other optical facilities, and its exploitation will lead to a gigantic step into the deep Universe. It will also become the largest ground-based instrument and Consortium ever implemented in the astronomy and astrophysics domain. The French community is leading the MOSAIC effort, which will be rewarded by a strong leadership in many astrophysical fields, including by operating surveys for an equivalent amount of more than 50 nights on the largest world class telescope of the 2020s.

Keywords: Multi-object spectrograph, ELT, cosmology, galaxies, dark and baryonic matter, Local Universe, Local Group, the Galaxy, stars

1 Introduction

The ELT will be the world largest visible/NIR telescope in the 2020s, with a collecting area similar to the total of the 16 currently existing 8-10 meter class telescopes. When combined with the huge collecting area of the ELT, MOSAIC ($http://www.mosaic-elt.eu/$) will be the most effective and flexible Multi-Object Spectrograph (MOS) facility in the world, having both a high multiplex and a multi-Integral Field Unit (Multi-IFU) capability. It will be the fastest way to spectroscopically follow-up the faintest sources, probing the reionisation epoch, as well as evaluating the evolution of the dwarf mass function over most of the age of the Universe (Evans et al. 2016; Hammer et al. 2016; Morris et al. 2018a). MOSAIC will be world-leading in generating an inventory of both the dark matter (from realistic rotation curves with adaptive optics fed NIR IFUs) and the cool to warm-hot gas phases in z=3.5 galactic haloes. Galactic archaeology and the first massive black holes are additional targets for which MOSAIC will also be revolutionary. MOAO (Morris et al. 2018b) and accurate sky subtraction with fibres (Yang et al. 2013) have now been demonstrated on sky, removing all low Technical Readiness Level (TRL) items from the instrument. A prompt implementation of MOSAIC is feasible, and indeed could increase the robustness and reduce risk on the ELT, since it does not require diffraction limited adaptive optics performance.

Science programmes and survey strategies are currently being investigated by the Consortium together with ESO. Given the paradigm proposed by ESO for financing the hardware cost of the instrument, we are hoping to welcome a few new partners in the next few years, in particular those interested in financially supporting the project in exchange of Guaranteed Observing Time. The Phase A Consortium includes countries in the core of the project (Partners: France, United Kingdom, The Netherlands, Brazil, Germany) as well as other participating countries (Associate Partners: Austria, Finland, Italy, Portugal, Spain, Sweden). Since that time, the University of Michigan has joined the project, and discussions are in course with other partners (e.g., STSci).

[1] GEPI, Observatoire de Paris, Université PSL, CNRS, Place Jules Janssen 92195, Meudon, France
[2] Aix Marseille University, CNRS, LAM UMR 7326, 13388, Marseille, France
[3] IRAP, Université de Toulouse III-CNRS, 9, avenue du Colonel Roche, BP 44346 - 31028 Toulouse Cedex 4
[4] LESIA, Observatoire de Paris, Université PSL, CNRS, Place Jules Janssen 92195, Meudon, France
[5] Sorbonne Universités, UPMC-CNRS, UMR7095, Institut d'Astrophysique de Paris, F-75014 Paris, France
[6] ONERA, France

We are actively preparing the final top level requirements for the instrument as well as the management of the Consortium, which is expected to gather about 15 Countries or main Institutes, and up to 40 laboratories. In particular the Project Office is implemented in France under the Principal Investigator responsibility, and it will supply for many activities on behalf of the Lead Technical Institute hosted at CNRS.

2 Science

During the Phase A study, the MOSAIC Consortium gathered with the science community at large in four key international meetings (Cefalu, September 2015; Paris, March 2016; Toledo, October 2017, Heidelberg, March 2019), and prioritized the numerous science cases developed over the years for MOSAIC, and which are expected to open many new astronomical avenues in the coming decade. These discussions identified four key science cases which have been used to help with instrument tradeoffs (HDM: High Definition Mode; HMM: High Multiplex Mode):

1. First-light galaxies: only a MOS at the ELT is able to catch the population at z=6 to 15, which is very rare and need a significant multiplex (HMM-NIR) for disentangling them from the huge population of foreground objects. With the HDM that allows an accurate sky-subtraction, MOSAIC will be unique for catching the faintest galaxies (e.g., the most distant) and to identify the origin of the ionizing photons possibly responsible for the reionisation of the universe up to one or two magnitudes deeper than what JWST will provide (Vanzella et al. 2014).

2. Evolution of dwarf galaxies that is the largest galaxy population in number, which is also candidate for being responsible of the reionisation. MOSAIC will provide comprehensive studies of their chemistry, stellar population and also of their kinematics up to depth, distances, and spectral resolution unreachable by any other means including JWST (main modes: HDM & HMM-NIR)

3. Inventory of baryonic and dark matter in the distant Universe, up to z=4. The numerous rest-frame UV lines are probing the cold to warm and warm-hot gas in galactic haloes allowing to estimate their baryonic content (Werk et al. 2014). MOSAIC will be able to observe in the visible range (HMM-VIS) their redshifted counterparts (Japelj et al. 2019) at z=3-4 thanks to the gigantic ELT aperture. Using multi-IFUs in the near-IR (HDM) will allow to study the rotation curves of many high-z galaxies allowing to sample the dark matter in the distant Universe.

4. Extragalactic stellar populations: only MOSAIC will be able to study very distant red super-giant stars up to 30 Mpc allowing to directly study the chemistry of all types of galaxies, as well as to distinguish the main sequence star population in the Local Group to determine the distance of galaxies even those containing less than a thousand stars (main modes: HDM & HMM-NIR).

Many of the above science cases have ben simulated (Puech et al. 2018). It results that the main goals of MOSAIC are unreachable by any other means, and that it is very complementary with, e.g., JWST and HARMONI.

3 Top level requirements and design

The top level requirements have been refined since the end of the Phase A in March 2018, also in order to reduce the number of modes and then the instrument complexity and cost, as well as keeping sufficiently large multiplex. In particular it has led us to keep the HMM in both visible and Near-IR with a multiplex ranging from 100 to 200. The HDM multi-IFUs are kept only in the Near-IR and are intended to provide the best sky-subtraction for detecting ultra faint sources, and also to derive distant galaxy kinematics. The instrument concept is summarized in Fig. 1 and will include not less that 4 spectrographs in Near-IR and 2 spectrographs for addressing the visible range, with the interesting feature that observations can be operated in parallel in the two wavelength ranges.

4 MOSAIC status at ESO

MOSAIC is currently in pre-Phase B under Consortium responsibility. Besides finalizing the instrument design for the construction phase, we are working at preparing the Consortium and its overall management. This

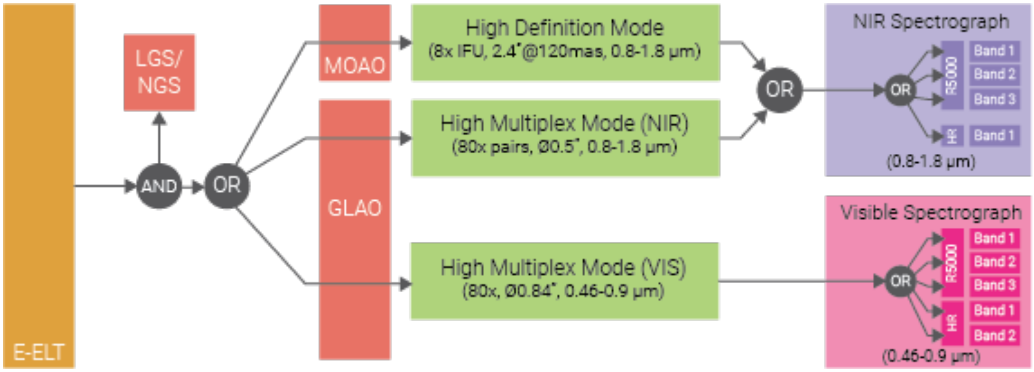

Fig. 1. The MOSAIC instrument concept. Notice that the multiplex number as well as apertures are still in discussion and are expected to be consolidated this Autumn 2019.

includes the Memorandum of Understanding between partners, which will determine their contribution in the making of the instrument as well as how they will be retributed in guaranteed time observations (GTO), which amounts to a total of not less than 125 nights. For the later, the partners gathered into the Steering Committee have already agreed for a share of common surveys, which renders more ambitious the GTO exploitation and simplifies the scientific coordination of the project.

MOSAIC (as well as HIRES) is a second generation instrument that will be on sky after the first light instruments. This situation has generated significant delays for its implementation related to the management of the telescope and of other instruments. We are grateful to ESO for the recent increase of the managerial support for preparing Phase B and its associated documentation.

5 Conclusions

MOSAIC is supported by a very large community in astronomy, and has been part of the ELT instrumentation plan for over a decade. When implemented on the largest telescope in a foreseeable future, it will be the most efficient facility to study the early Universe and its composition (baryons and dark matter) as well as many programs requiring statistics (stars or galaxies), source identifications, and environmental studies. MOSAIC is unique in studying all sources not reachable by spectrographs not implemented on the 10 meter class telescopes. For example, it will increase by a factor 125 the volume within which individual stars can be observed and analysed, and allow proper analyses of the first galaxies up to 27 (29) AB magnitudes for quiescent (emission line) galaxies, respectively (see Fig. 2).

MOSAIC is also the largest ground-based instrument ever undertaken in astronomy, both from an instrumental and a managerial viewpoints. Its weight allocation on the ELT Nasmyth Platform 2 is up to 40 tons, and its total cost could reach 80 million euros. It is the only ELT instrument with a French leadership, which implies the need for a substantial support in the community and from the French Institutes. In exchange, the French community may have a privileged access to more than a third of the scientific exploitation of the instrument, through the scientific management (preparation, implementation, observations & data analyses) of a significant part of the surveys (Evans et al. 2018) that will be accomplished during the GTO time. Since the next year should be the time for starting the Construction Phase, and because the project is expected to be on sky in the late 2020s, contributions of scientists and engineers from all French laboratories are highly welcomed. In particular, we hope that young scientists will join or will be hired by the Consortium for performing simulations in order to consolidate the instrument design, its operability, and the surveys that will lead to significant breakthroughs in most astrophysical domains. With MOSAIC the French scientific community will access to the leadership for studying the most distant objects (galaxies or stars) ever observed in the Universe.

We are very grateful and indebted to the international MOSAIC team without which making MOSAIC a reality would not be possible. We warmly thank the support of the CNRS-INSU, the Paris Observatory and the LAM, GEPI, LESIA, and IRAP laboratories for their active roles during the early phases of the MOS for the ELT.

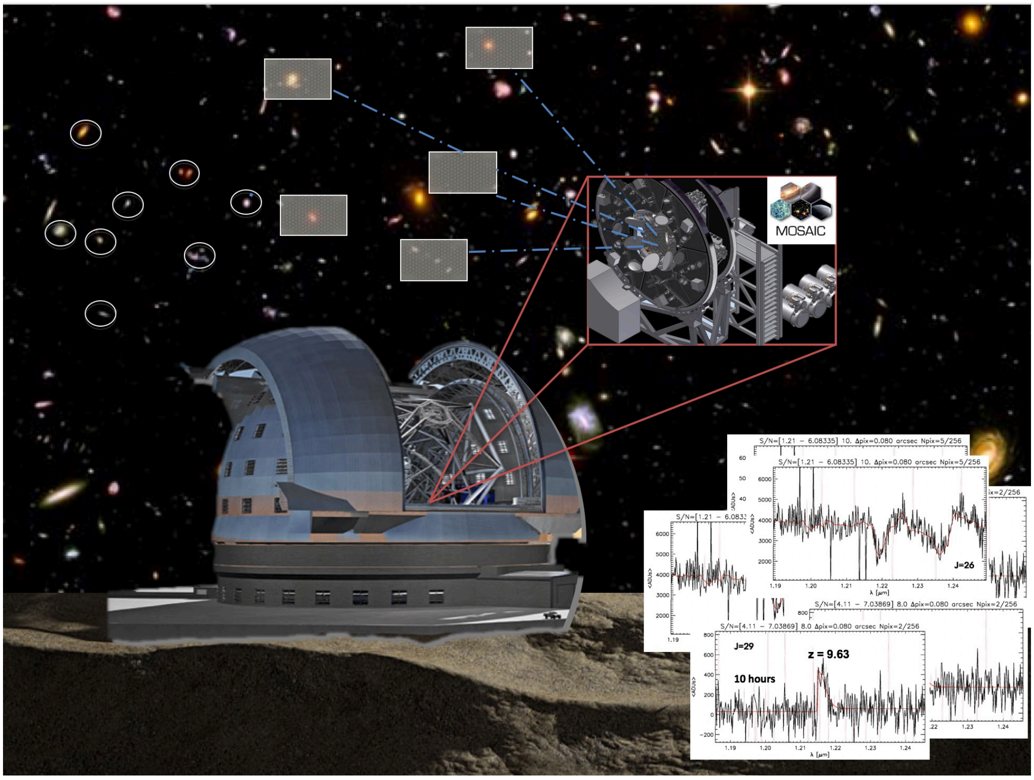

Fig. 2. A montage to illustrate how MOSAIC, when implemented on the E-ELT, will take hundreds of spectra exploiting its HDM-IFUs (rectangles) and HMM-fibres (circles), allowing the discovery and the quantitative study of the faintest and most-distant galaxies in the Universe. Spectra of AB=29 (AB=26) emission (absorption) line galaxies at very large redshifts are from simulations made by Disseau et al. 2014

References

Disseau, K., Puech, M., Flores, H., et al. 2014, Ground-based and Airborne Instrumentation for Astronomy V, 914791

Evans, C. J., Puech, M., Rodrigues, M., et al. 2016, Ground-based and Airborne Instrumentation for Astronomy VI, 99089J

Evans, C., Puech, M., Hammer, F., et al. 2018, The Messenger, 171, 47

Hammer, F., Morris, S., Kaper, L., et al. 2016, Ground-based and Airborne Instrumentation for Astronomy VI, 990824

Japelj, J., Laigle, C., Puech, et al. 2019, A&A, submitted

Morris, S., Hammer, F., Jagourel, P., et al. 2018a, Ground-based and Airborne Instrumentation for Astronomy VII, 107021W

Morris, T., Basden, A., Calcines-Rosario, A., et al. 2018b, Adaptive Optics Systems VI, 1070316

Puech, M., Evans, C. J., Disseau, K., et al. 2018, Ground-based and Airborne Instrumentation for Astronomy VII, 107028R

Vanzella, E., Fontana, A., Pentericci, L., et al. 2014, The Messenger, 157, 46

Werk, J. K., Prochaska, J. X., Tumlinson, J., et al. 2014, The Astrophysical Journal, 792, 8

Yang, Y., Rodrigues, M., Puech, M., et al. 2013, The Messenger, 151, 10

RECONCILING CORONAGRAPHY AND KERNEL-PHASE FOR DIRECT DETECTION OF EXOPLANETS

R. Laugier[1] and F. Martinache[1]

Abstract. The kernel-phase and coronagraphy are considered profoundly incompatible. We present three approaches aimed at combining the two methods despite their incompatibility:

*We applied kernel-phase in a more benign case of transfer function destruction: saturated images. Using an advanced interpolation technique, we mended archival images and were able to apply kernel-phase analysis and detect a stellar companion around Gl 494 well beyond the reach of classical methods.

*One technique used with coronagraphy, Angular Differential Imaging, is used to self-calibrate observations using the field rotation. We have designed a kernel-phase version of this algorithm and are currently evaluating its on-sky performance.

*The "shaped pupil" apodizing masks, only change the shape of the telescope's aperture in order to obtain a more favorable PSF and do not destroy the Transfer Function. We designed one specifically to work with kernel at the SCExAO instrument, and to evaluate the performance boost.

Keywords: High angular resolution, high contrast, image processing, kernel-phase

1 Introduction

Even for the most nearby systems, the direct detection of exoplanets at Solar-system scales requires very high contrast sensitivity ($c \leq 10^{-6}$) at small angular separations ($\rho \leq 1$ arcsec).

Suppressing the diffraction of the central bright star, coronagraphs theoretically address the contrast problem. They are however highly vulnerable to the unavoidable residual wavefront errors left by adaptive optics. Alternatively, the kernel-phase approach that generalizes the idea of closure-phase, is built around robustness to small wavefront errors (Martinache 2010): its high-contrast detection is limited by the photon noise.

Unfortunately, this approach cannot be applied to the processing of coronagraphic observations because coronagraphs destroy the transfer function usually provided by imaging instruments. This work explores synergies that can be developed despite this limitation between kernel-phase and coronagraphy through the use of apodization masks, extended image dynamic range enabled by partial saturation, and borrowed post-processing techniques like ADI.

2 Blind saturation recovery

In coronagraphy, the transfer function of the instrument is destroyed, making Fourier domain techniques irrelevant. We experimented with a less dramatic case of transfer function invalidation: the case of saturated images.

In conditions where the Point Spread Function was sufficiently stable (Hubble Space Telescope), we were able to reconstruct saturated images to detect (Fig.1) and characterize a companion to Gl494 (Laugier et al. 2019) on archival images dating from 1997, years before its first direct measurement in 2000 by Beuzit et al. (2004). This new measurement at older epoch improves the constraints on orbital and physical properties of these red dwarf stars.

3 Angular Differential Kernel (ADK)

[1] Université Côte d'Azur, Observatoire de la Côte d'Azur, CNRS, Laboratoire Lagrange, France

Angular Differential Imaging (Marois et al. 2006) and its variants are used extensively in coronagraphy. We are currently experimenting with an algebraic projection based on the same principles of field rotation to calibrate the static instrumental biases on the scientific target itself, while retaining the statistical properties of the analysis. SCExAO observations of the binary star 3 Ser show good performance despite the poor observing conditions (Low Wind Effect) mitigated here by frame selection.

The resulting maps shown in Fig.2 show a calibration performance on par with the classical method, without the need to find and oserve a calibrator.

4 Apodization mask for improved contrast

Binary (shaped pupil) masks (Carlotti et al. 2011) simply modify the transfer functions and are therefore compatible with kernel-phase analysis. We designed a mask with a geometry suited to the kernel-phase analysis and installed it as part of the SCExAO instrument at the Subaru telescope (Fig.3). The mask provides somewhat uniform 10^{-4} contrast in the the PSF over an annular region contained between 3 and 7 λ/D. The relative simplicity of the geometry of the mask makes it easy to build the discrete representation for the extraction of kernel-phase. A prototype was laser-cut and installed in the pupil mask wheel of SCExAO for on-sky experimentation. Preliminary tests suggest that the detection limits of kernel-phase are indeed boosted by the apodizer.

References

Beuzit, J.-L., Ségransan, D., Forveille, T., et al. 2004, Astronomy & Astrophysics, 425, 997

Carlotti, A., Vanderbei, R., & Kasdin, N. J. 2011, Optics Express, 19, 26796

Laugier, R., Martinache, F., Ceau, A., et al. 2019, Astronomy & Astrophysics, 164, 1

Marois, C., Lafreniere, D., Doyon, R., Macintosh, B., & Nadeau, D. 2006, The Astrophysical Journal, 641, 556

Martinache, F. 2010, The Astrophysical Journal, 724, 464

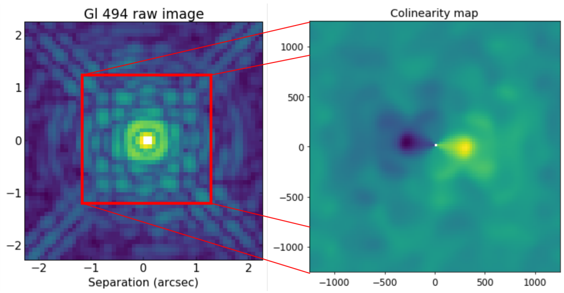

Fig. 1. Image of Gl 494 with saturation in 4 pixels shown in white (left), and a matched filter map revealing the companion at $\approx 55\times$ and separation of $\approx 1.3\lambda/D$.

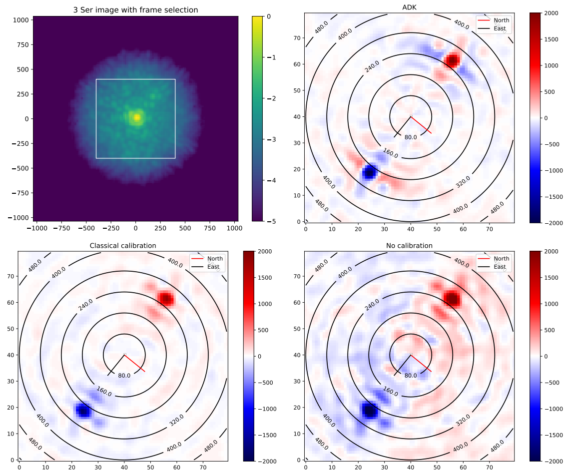

Fig. 2. On-sky image of 3 Ser with the Region of Interest (upper left), kernel colinearity maps of the ADK signal (upper right), classical calibration (lower left) and raw signal (lower right) showing the x62 contrast companion as a red spot.

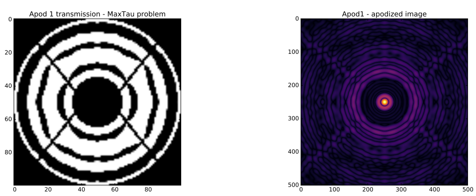

Fig. 3. The binary pupil mask designed with M. N'Diaye's implementation of the Carlotti's algorithm for the Subaru SCExAO pupil (left), the apodized PSF (right). The mask was optimized for a moderate contrast boost and simple shapes.

SF2A 2019
P. Di Matteo, O. Creevey, A. Crida, G. Kordopatis, J. Malzac, J.-B. Marquette, M. N'Diaye, O. Venot (eds)

OPTICAL TURBULENCE PREDICTION USING WRF MODEL

A. Rafalimanana[1], C. Giordano[1], A. Ziad[1] and E. Aristidi[1]

Abstract. The optical turbulence forecasting has become a necessary information for an optimal programmation of the astronomical observations, called "flexible scheduling". We propose the prediction of the optical turbulence by means of the Weather Research and Forecasting (WRF) model combined with an optical turbulence model. We performed a set of simulations to obtain a 24-hours period forecast for optical turbulence parameters above the Calern observatory. We present the results of our forecasting and comparisons with the CATS (Calern Atmospheric Turbulence Station) measurements.

Keywords: Atmospheric turbulence, turbulence prediction, flexible scheduling, astronomical observations

1 Introduction

In order to optimize the exploitation of the next generation of extremely large telescope (ELT), the prediction of atmospheric turbulence becomes necessary to schedule the observations and to choose the appropriate observing method with the appropriate instruments to be used at a specific time of the night. Thus, to have all the necessary informations about the optical turbulence several hours before the observation, we use a numerical weather prediction model to forecast the useful meteorological parameters relevant to the physics of the optical turbulence. In this study, we propose the use of WRF (Skamarock et al. 2019) model coupled with a turbulence model (Trinquet & Vernin 2006; Giordano 2014) above the Calern observatory. This site hosts a new generation station of atmospheric turbulence measurement (CATS) (Ziad et al. 2018) equipped with turbulence monitors. The PML (Profiler of Moon Limb) measures the vertical distribution of turbulence (profile of refractive index structure constant C_n^2) with high spatial and temporal resolution, 100 meters and 3minutes respectively. The G-DIMM (Generalized Differential Image Motion Monitor) measures the integrated parameters (seeing, outer scale, coherence time and isoplanatic angle) (see also `https://cats.oca.eu`). In this paper, we present our prediction method, the results of our forecasting and comparisons between the predictions and the CATS measurements.

2 Principle of the prediction

We use WRF to predict meteorological parameters (pressure, temperature, wind speed and direction, and relative humidity). WRF is a mesoscale numerical weather prediction system developped by a collaborative partnership (the National Center for Atmospheric Research (NCAR), the National Centers for Environmental Prediction (NCEP), and others institutes). The meteorological parameters predicted by WRF are injected into an optical turbulence model. Trinquet & Vernin (2006) have established a model to retrieve the temperature structure constant C_T^2 as a product of 3 quantities:

$$C_T^2 = \phi(z) \cdot \chi(z) \cdot S(z)^{1/2} \tag{2.1}$$

with $\chi(z)$ is the vertical gradient of the potential temperature, $S(z)$ is the wind shear and $\phi(z)$ is a vertical profil parameter deduced from a statistical analysis of radiosoundings balloons that we extended to CATS data. Then, C_T^2 is used to deduce the vertical distribution of optical turbulence described by the refractive index structure constant C_n^2 which is computed using the Gladestone's law:

$$C_n^2 = \left(\frac{80 \cdot 10^{-6} P}{T^2}\right)^2 \cdot C_T^2 \tag{2.2}$$

[1] Université Côte d'Azur, Observatoire de la Côte d'Azur, CNRS, Laboratoire Lagrange, Parc Valrose 06108 Nice Cedex 2, France

where P is the atmospheric pressure in hPa and T is the air temperature in Kelvin.
Our approach is now to use local CATS statistics to constrain the function $\phi(z)$ of the equation (2.1) to better take into account the specificities of the Calern site.

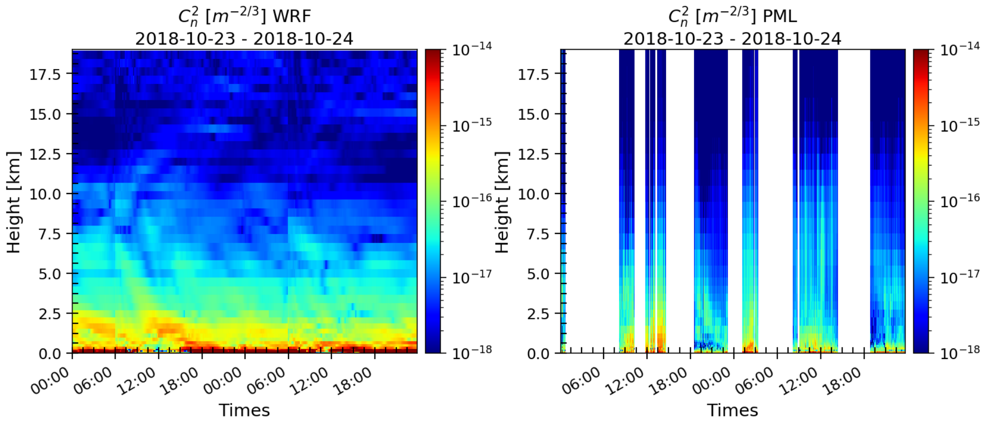

Fig. 1. Left: times series forecasting of C_n^2 by WRF. **Right:** times series of C_n^2 observed by PML.

3 Results

Fig. 1 (left) panel shows results of WRF forecast of C_n^2 profile for a 48h period. CATS measurements are shown on the right panel. We can notice that WRF provides a continuous temporal resolution and may complete missing data from turbulence monitors. One can see also that the turbulence is more intense in the planetary boundary layer. This is due to its direct interaction with the earth's surface. Fig. 2 shows a good agreement between 24h median profiles predicted by WRF and measured by the PML in the free atmosphere while differences remain in the boundary layer. This difference between the free atmosphere and the atmospheric boundary layer occurs because the meteorological parameters behave differently. For example, the near-surface temperature is characterized by diurnal variations, with maximum at local afternoon and minimum at local midnight. However, in the free atmosphere, the temperature shows a small diurnal variation.

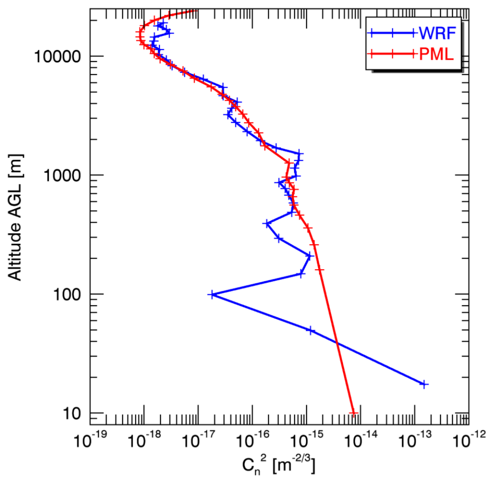

Fig. 2. Median profiles of C_n^2 on 2018/08/27

4 Conclusions

We have shown for a 24h forecasting, the capability of WRF model combined with an optical turbulence model to predict the vertical distribution of the optical turbulence above the Calern observatory. The predictions agree well with the PML measurements in the upper part of the planetary boundary layer and also in the free atmosphere. By contrast, there is a significant difference between WRF and PML results in the lower part of the boundary layer. As a perspective, a thorough study is required to find an optimal configuration of WRF by concentrating especially on the physical parameterization schemes and the use of a fine grid resolution to take into account the ground effects (topography, land use, surface heat flux, etc.) and properly represent the near-surface atmospheric processes that generate the optical turbulence.

References

Giordano, C. 2014, PhD thesis, Université de Nice-Sophia Antipolis - UFR Sciences

Skamarock, W. C., Klemp, J. B., Dudhia, J., et al. 2019, NCAR Tech. Note NCAR/TN-556+STR, 145pp.

Trinquet, H. & Vernin, J. 2006, Publ., Astron. Soc. Pac., 118, 756

Ziad, A., Chabé, J., Fantei-Caujolle, Y., et al. 2018, in Society of Photo-Optical Instrumentation Engineers (SPIE) Conference Series, Vol. 10703, Adaptive Optics Systems VI, 107036L

Session 07

The low surface brightness universe

SF2A 2019
P. Di Matteo, O. Creevey, A. Crida, G. Kordopatis, J. Malzac, J.-B. Marquette, M. N'Diaye, O. Venot (eds)

STUDYING ULTRA DIFFUSE GALAXIES IN VIRGO WITH CFHT-NGVS, GALEX-GUVICS AND CFHT-VESTIGE

S. Boissier[1] and Junais[1]

Abstract. In the recent years, Ultra Diffuse Galaxies (UDGs) have been found in large numbers first in clusters (e.g. Koda et al. 2015), and then also in the field, with a very wide range of properties. The Virgo cluster being both nearby, and deeply observed at all wavelength, it is a prime target to search and study such galaxies in the cluster environment. It was not necessary the easier place to do so because of the large spatial extent of the galaxies due to its proximity. Recently, however, the Next Generation Virgo Survey (NGVS) (Ferrarese et al. 2012) has allowed us to characterize thousands of galaxies in Virgo, and to find more than 100 UDGs or LSB galaxies.

After discussing some of the vague definitions of low/diffuse galaxies, this contribution presents some on-going work concerning the study of such galaxies in Virgo, on the basis on the NGVS survey. We focus especially on the contribution of GALEX data in the UV and of the VESTIGE survey for the Hα emission.

Finally, we show that simple models of galaxy evolution can allow us to test what can be the effect of ram-pressure stripping (by purely modifying the star formation history of galaxies that would be usual star forming galaxies if it was not the case). UDGs may be affected by a combination of effects but simple models allow us to study an effect that SHOULD be present in the cluster environment.

Keywords: galaxies, low surface brightness

1 About the notions of Diffuse, Ultra-Diffuse, Low Surface Brightness and outlier galaxies

Low Surface Brightness galaxies (LSBs) have often been loosely defined as galaxies with "central surface brightness well below" the Freeman (1970) value (of 21.65 mag arcsec^{-2}), without any precision on the photometric band, or on the definition of the central surface brightness. Historically, it was usually the surface brightness extrapolated at R=0 for the disk component in a bulge/disk decomposition (Impey & Bothun 1997).

Early-on, it was obvious that this was not very satisfactory as dwarf galaxies are usually LSB by this definition, but are incomparable to giant LSBs such as the massive Malin 1 galaxy (see Junais & Boissier contribution in this volume). Sprayberry et al. (1995) proposed a definition based on the "diffuseness" of galaxies defined as $\mu_g(0) + 5log(R_s)$ (R_s being the scale-length), allowing them to take into account this difference.

Recently, van Dokkum et al. (2015) coined the term "ultra-diffuse galaxies" (UDGs) that became very fashionable (a good communication move), corresponding to another selection, more extreme in surface brightness, but excluding very small galaxies that were known before-hand. UDGs are very numerous, at least in clusters (Koda et al. 2015). However, as before, the definition is somewhat arbitrary (different photometric bands and different size thresholds are used by different authors). Considering the overlap with previous definitions, a few of these UDGs were known, but were not identified as such before the few recent years. Moreover, there is a form of continuity between all these diffuse galaxies, as well as with the more usual ones (Danieli & van Dokkum 2019).

In the Virgo Cluster, Lim et al. (in preparation) have used the NGVS survey (Ferrarese et al. 2012) to find outliers in scaling relationship for Virgo Galaxies. The outliers to these relationships is another way to select galaxies that are (by definition) different from the "usual" ones. Some LSBs, UDGs or diffuse galaxies are indeed found among those, as can be seen in Fig. 1, where are shown the Virgo galaxies in the NGVS survey, the outliers, and an illustration of the definitions given above.

[1] Aix Marseille Univ, CNRS, CNES, LAM, Marseille, France

From Fig. 1, it can be seen that all outliers are not necessarily of low surface brightness, that the "UDG" box may select galaxies that are within the dispersion of the scaling relation (in fact, regular galaxies), that the LSB, UDG, or diffuse selections have of course some overlap, although they are not similar despite the obvious continuity between all these types of galaxies.

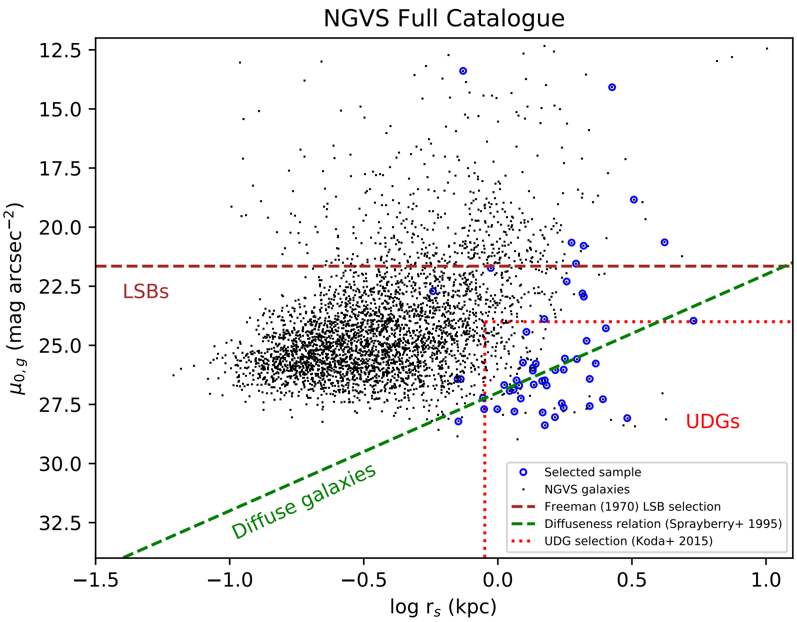

Fig. 1. Central surface brightness as a function of scale-length. The lines illustrate different definitions of low surface brightness galaxies: classical threshold in red, diffuseness of Sprayberry et al. (1995) in green, ultra-diffuse galaxies in orange. The points are a sample of galaxies in the Virgo Cluster, found in the NGVS survey (Ferrarese et al. 2012). Blue circles indicates galaxies that are outliers in the scaling relationships described by these galaxies.

2 Diffuse galaxies in the Virgo cluster

Figure 1 shows the distribution in the central surface brightness vs scale-length plane of the 3688 galaxies found in the Virgo Cluster, based on the NGVS data. In this plot, we show on the x-axis a scale-length for comparison with the definition of Sprayberry et al. (1995), but we actually use the effective radius measured in the NGVS, that we transform into a scale-length assuming a disk geometry (i.e., dividing by 1.678).

Among these galaxies, Lim et al. (in preparation) defined a sample of 52 outliers, based on the scaling relationship of the sample. As demonstrated by Singh et al. (2019) in the COMA cluster, UV data can bring more information on UDGs (how many among them are star-forming, or could be star-forming). In the Virgo cluster, we have access to the GUViCS survey (Boselli et al. 2011). In the coming year, we will proceed to study the UV properties of our samples (the outliers, but also "diffuse" galaxies of interest). Moreover, we will have also access to Hα data owing to the VESTIGE (Boselli et al. 2018) project. We will thus be able to pinpoint the quenching time as optical, UV, and the Hα emission line probe different typical timescales from 10 to several 100 Myrs (Boissier 2013). We should determine how much residual star formation is present in our samples. Preliminary image inspection suggests that we may find nuclei activity in some cases. Any detection in the narrow-band filter of VESTIGE will moreover confirm the membership to Virgo, that is not fully established for all the galaxies.

3 One context to model them all

One of the main issue concerning Ultra Diffuse Galaxies is the question of their formation (which processes are responsible for the low surface brightness, and for the quenching of star formation when they are red). It is difficult to address this question in isolation to the formation and evolution of other galaxies since a continuity exists as discussed in the first section.

Answers to the question may come from global simulations of large volume implementing all the needed physics (e.g. Di Cintio et al. 2017), however these models are very complex and implement a lot of sub-grid physics. It is sometimes hard in this context, however, to understand what is the result of which assumptions. Another approach is to take galaxies such as those observed today, and add some processes that may "transform" them into ultra-diffuse galaxies (Román & Trujillo 2017).

Finally, we propose here to study samples of diffuse, LSB, or UDG galaxies with a grid of models that was initially built for nearby spiral galaxies (Boissier & Prantzos 2000; Muñoz-Mateos et al. 2011). In this grid, the evolution of any galaxy is basically fixed once is chosen its circular velocity (or its total final mass, in the absence of interactions with the environment), and its specific angular momentum (spin). The grid is build for the baryonic matter, and the velocity and spin are transformed into baryon's properties through simple scaling relationships. The physical ingredients (accretion time-scale, star formation law) are fixed and universal for all the galaxies. The same family of models was used to study samples of giant LSBs under the classical definition (Boissier et al. 2003), and to study the effect of ram-pressure stripping in Virgo (Boselli et al. 2006, 2008). Finally, in Boissier et al. (2016), it was found that when adopting a very large spin parameter, the model is consistent with the properties of the giant LSB disk of Malin 1.

However, so far, all of these models had not been computed in an homogeneous way, and were not covering the full expanse of parameter space. For instance the ram-pressure stripping effect was only applied to average spin-parameters, and models with spin parameter intermediate between regular LSBs and the Malin 1 disk had not been computed. This is now corrected, as we present in Fig.2 a grid of models covering in a homogeneous way the full range of velocity and spin parameters (in the left). We show how this full grid is affected by a ram-pressure stripping event (for different peak-epochs of the stripping) in the right. This illustration shows that the sample of UDGs of Koda et al. (2015) is consistent with galaxies of intermediate spins, relatively low velocities. However, in the absence of ram-pressure stripping, these galaxies would have blue colour today. A ram-pressure even around 1.5 Gyr ago make them consistent with the observed colours.

In conclusion, such simple models allow the existence of blue or red UDGs depending on the advent (or not) of ram-pressure stripping during their history. While this comparison does not exclude other processes, it allows us to test in a very simple way what can be the destiny of diffuse galaxies within and outside clusters. We plan to use them to interpret the observations of diffuse, LSB, or UDG samples such as the ones discussed in the previous section.

We express our thanks to the organisers and SOC of the SF2A meeting, and to the inspiring band "The WatHermelons". The mission to SF2A was supported by the Programme National Cosmology et Galaxies (PNCG) of CNRS/INSU with INP and IN2P3, co-funded by CEA and CNES. We also thanks the many collaborators involved in the studies mentioned in this proceedings, and especially A. Boselli, G. Gavazzi, A. Gil de Paz, J. Koda, B. Madore, J.C. Munos Mateos, N. Prantzos.

References

Boissier, S. 2013, Star Formation in Galaxies, Vol. 6, 141

Boissier, S., Boselli, A., Ferrarese, L., et al. 2016, A&A, 593, A126

Boissier, S., Monnier Ragaigne, D., Prantzos, N., et al. 2003, MNRAS, 343, 653

Boissier, S. & Prantzos, N. 2000, MNRAS, 312, 398

Boselli, A., Boissier, S., Cortese, L., & Gavazzi, G. 2008, ApJ, 674, 742

Boselli, A., Boissier, S., Cortese, L., et al. 2006, ApJ, 651, 811

Boselli, A., Boissier, S., Heinis, S., et al. 2011, A&A, 528, A107

Boselli, A., Fossati, M., Ferrarese, L., et al. 2018, A&A, 614, A56

Danieli, S. & van Dokkum, P. 2019, ApJ, 875, 155

Di Cintio, A., Brook, C. B., Dutton, A. A., et al. 2017, MNRAS, 466, L1

Ferrarese, L., Côté, P., Cuillandre, J.-C., et al. 2012, ApJS, 200, 4

Freeman, K. C. 1970, ApJ, 160, 811

Impey, C. & Bothun, G. 1997, ARA&A, 35, 267

Koda, J., Yagi, M., Yamanoi, H., & Komiyama, Y. 2015, ApJ, 807, L2

Muñoz-Mateos, J. C., Boissier, S., Gil de Paz, A., et al. 2011, ApJ, 731, 10

Román, J. & Trujillo, I. 2017, MNRAS, 468, 4039

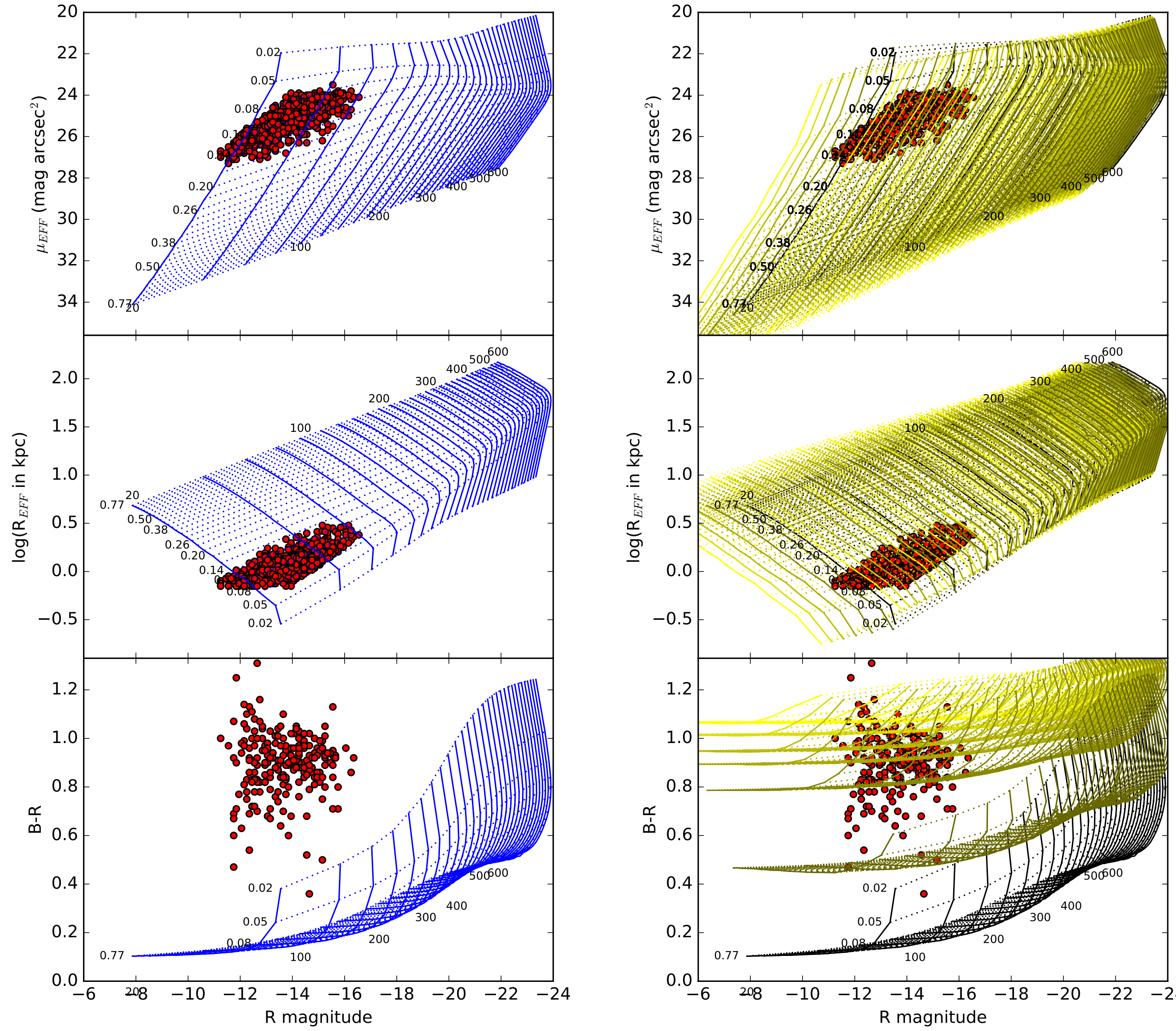

Fig. 2. Left: Grid of models for a very large range of angular momentum and mass. **Right:** The same grid is shown in black, while the different colored grids show the properties of the same galaxies, if they entered a cluster and undergone ram-pressure event at different epochs (from the bluer to the redder grids with a peak of ram-pressure now, 1, 2, 3, 4 or 5 Gyr ago).

Singh, P. R., Zaritsky, D., Donnerstein, R., & Spekkens, K. 2019, AJ, 157, 212
Sprayberry, D., Bernstein, G. M., Impey, C. D., & Bothun, G. D. 1995, ApJ, 438, 72
van Dokkum, P. G., Romanowsky, A. J., Abraham, R., et al. 2015, ApJ, 804, L26

SF2A 2019
P. Di Matteo, O. Creevey, A. Crida, G. Kordopatis, J. Malzac, J.-B. Marquette, M. N'Diaye, O. Venot (eds)

STAR FORMATION EFFICIENCY IN LOW SURFACE BRIGHTNESS REGIONS

F. Combes[1]

Abstract. Low surface brightness regions are found not only in dwarf and ultra-diffuse galaxies, but also on the outer parts of giant spirals, or in galaxy extensions (tidal or ram-pressure tails, outflows or jets). Sometimes molecular gas is detected in sufficient quantities to allow star formation, but the efficiency is much lower than in disk galaxies. This presentation reviews different environments showing low-surface brightness, their gas content and surface densities, and their star formation efficiency. Some interpretations are proposed to account for this low efficiency.

Keywords: Galaxies, Star formation, Molecular clouds, Ram-pressure, Cooling flow cluster

1 XUV disks

The extended ultraviolet disks (XUV disks) have been discovered by the GALEX satellite, and are characterized by UV emission well beyond the optical disk, traced by an Hα emission drop. A prototypical example of XUV disks is the galaxy M83 (Thilker et al. 2005). To explore the star formation efficiency in the outer parts of the galaxy, we conducted ALMA observation in CO(2-1) of the M83 XUV disk, with a spatial resolution of 17pc x 13pc, well adapted to detect Giant Molecular Clouds (GMC). Although a significant region was observed (about 2 x 4 kpc) with a 121 point mosaic (see Figure 1), and although the region includes several HII regions and is rich in HI-gas, no CO emission was detected (Bicalho et al. 2019). This result is surprising, especially since we detected CO emission in another XUV disk with the IRAM-30m, e.g. in M63 (Dessauges-Zavadsky et al. 2014).

A compilation of all results from the literature is plotted in the Kennicutt-Schmidt diagram of Figure 2, in comparison with normal galaxies. This diagram is focussed on the H_2 gas, and shows the depletion time of the local main sequence galaxies of 2x 10^9 yrs (Bigiel et al. 2008). The outer disks of M63, NGC 6946 and NGC 4625 have a much larger depletion time, or equivalently a much lower star formation efficiency (SFE), by several orders of magnitude. As for M83, globally the large region observed will also have a low SFE; however, if we consider the two main HII regions, of size $\sim$ 200pc, and compute the upper limits of CO emission, the non detection is an exception (cf Figure 2). This absence of CO cannot be attributed solely to a low metallicity, since the gas abundance in this region is half solar (Bresolin et al. 2009). It is possible that in these outer regions, molecular clouds are not enough shielded from the UV field, and the CO molecules are photo-dissociated, while the H_2 is still there. Clouds could be smaller, and the carbon mostly in C and C^+.

2 Cooling filaments

Another situation where the SFE is low involves gas flows in cool core clusters. The prototype is the Perseus cluster, where Hα filaments are known since a long time, most of them excited by shocks, but in some places by star formation (Canning et al. 2014). The hot X-ray gas reveals large cavities, sculpted by the central AGN with its radio jets (Fabian et al. 2011). It is now well established that the AGN feedback moderates the gas cooling, and cold molecular gas is detected around the cavities (Salomé et al. 2006). The gas is still raining down around the cavities towards the AGN to fuel it. CO and Hα emissions are well correlated in cool core clusters (Salomé & Combes 2003). There is a relation between the star formation rate (SFR) and the gas cooling rate with a slope larger than unity for strong cooling rates (McDonald et al. 2018). For low cooling rate, however (lower than 30 $M_\odot$/yr) SFR and cooling rate are not correlated, pointing to SFR fuelled by recycled gas then. The star formation efficiency may then be low; globally, for the Perseus cluster, it is not far from the mean, as seen in Figure 3.

[1] Observatoire de Paris, LERMA, Collège de France, CNRS, PSL Univ., Sorbonne Univ., Paris

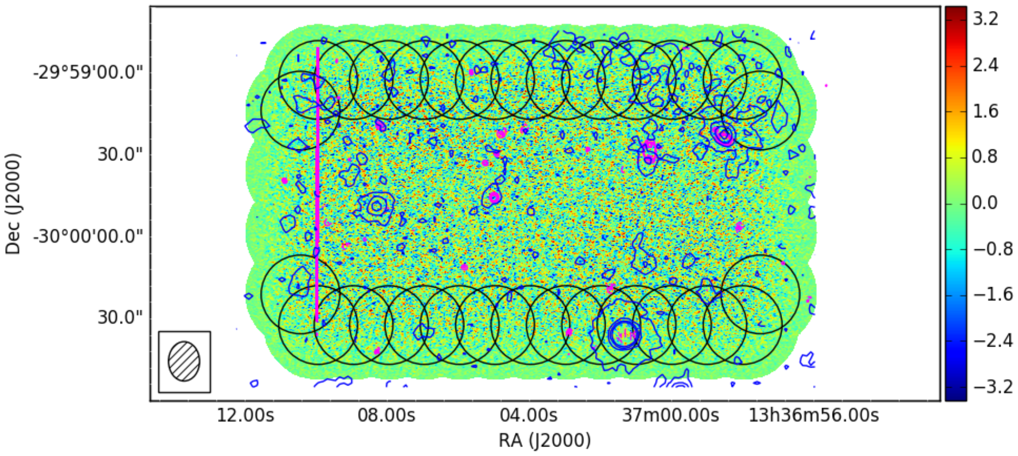

Fig. 1. Schematic representation of the 121-point mosaic of the ALMA observations, in the XUV disk of M83.The black circles indicate some of the 27"-diameter primary beams of the CO(2-1) emission. In the background, the color map is the moment zero of the CO(2-1) data cube. The magenta contours are Hα and the black contours are FIR 24μm emission. From Bicalho et al. (2019).

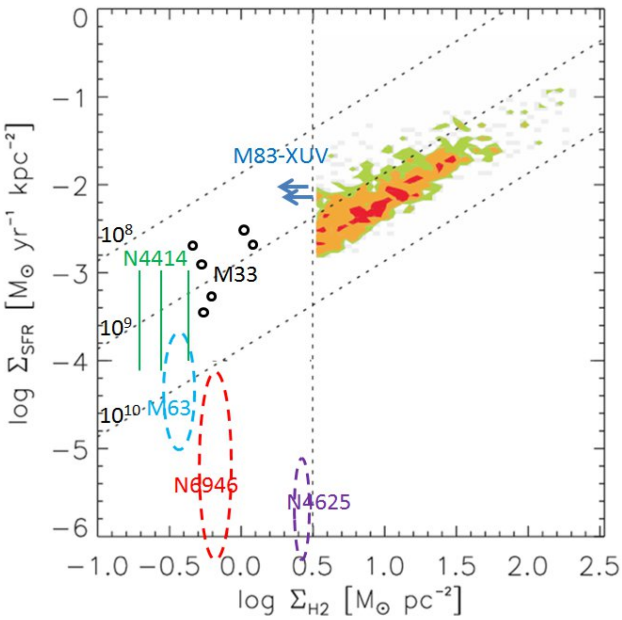

Fig. 2. Resolved Kennicutt-Schmidt diagram, in several galaxies and low surface brightness regions, adapted from Bigiel et al. (2008) and Verdugo et al. (2015). Dashed ovals indicate the location of XUV disk galaxies. The vertical dash line, at 3 $M_\odot/pc^2$ corresponds to the sensitivity limit of the CO data in Bigiel et al. (2008). Depletion times of 10^8, 10^9 and 10^{10} years are represented by 3 inclined dashed lines. When considering two of the main Hα regions, of $\sim$ 200pc size, and the upper limits on their molecular gas surface density, we obtain the blue horizontal arrows in M83. From Bicalho et al. (2019).

3 Ram-pressure stripped tails

In galaxy clusters, galaxies suffer tidal and ram-pressure stripping from the Intra-Cluster-Medium (ICM), and lose their gas which constitutes a diffuse circum-galactic medium. This loss of gas leads to what is called environmental quenching of star formation. The importance of this quenching depends on the richness of the cluster. Ram pressure is relative mild in the Virgo cluster, where many spirals are HI deficient, but not perturbed

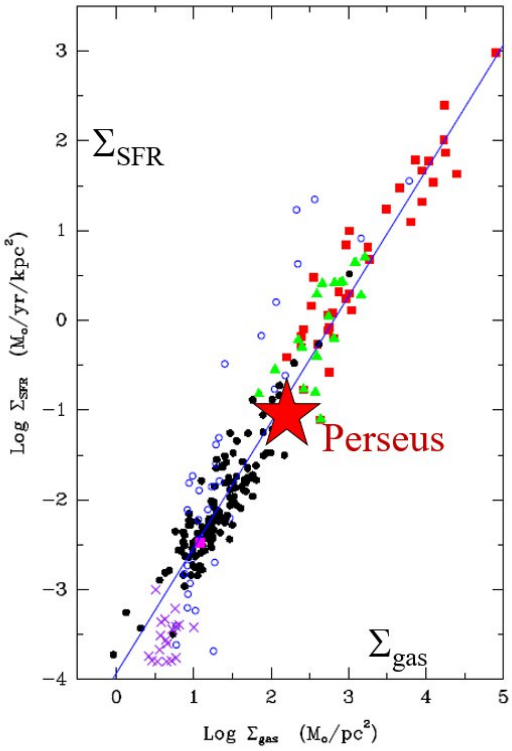

Fig. 3. The position of Perseus cluster in the global Kennicutt-Schmidt diagram is indicated as a large red star, and compared to local main sequence galaxies and starbursts (Kennicutt & Evans 2012).

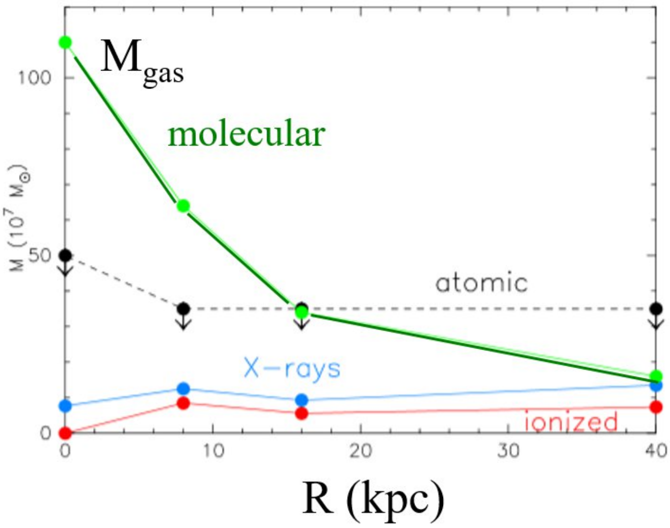

Fig. 4. Radial distribution of the various gas phases in ESO137-001: the molecular gas in green, the atomic HI gas in black (upper limits), the X-ray gas in blue, and the Hα gas in red. From Jáchym et al. (2014).

in their molecular gas (Kenney & Young 1989).

There is however a giant Hα tail in the center of Virgo linking the NGC 4438 galaxy to M86, over scales $\sim$ 100 kpc (Kenney et al. 2008). Although M86 is a lenticular galaxy devoid of gas, there is CO emission detected at 10kpc south of this galaxy, in prolongation of the long tail from NGC 4438. Apparently, this gas comes from the latter spiral. It is suprising to find 2 10^7 $M_\odot$ of H_2 gas in such an hostile environment, embedded in hot 10^7K ICM gas. Either the H_2 molecules have survived during the 100 Myr path, or they were re-formed in situ (Dasyra et al. 2012).

One of the Hα tail, linking NGC 4388 and M86 is rich in HI gas. Verdugo et al. (2015) have detected CO emission in some of the clumps along the tail. When plotted on the Kennicutt-Schmidt diagram, as in Fig. 2, the star formation efficiency is much lower there than in galaxy disks, similar to XUV disks (Verdugo et al. 2015). It is possible that the gas in the tail is more 3D distributed than in 2D-like disks, and also they are lacking the pressure from the gravity of disk stars.

In richer galaxy clusters, such as the Norma or Coma clusters, ram-pressure can strip the gas from galaxies much faster: this is the case of ESO137-001 (Jáchym et al. 2014). The tail of 80kpc is spectacular and double in X-ray emission, and in Hα. CO emission has been detected easily all along the double-tail, and the molecular gas dominates the gas content, as shown in Figure 4. The total molecular content of the tail, a few 10^9 $M_\odot$ is larger than the molecular content of the galaxy disk itself. ALMA has shown that the tail emission is very clumpy, and that the molecular gas is reforming in situ (Jachym et al. 2019). The galaxy D100 in Coma has a similar ram-pressure tail, remarkably straight, and consisting of only one thin component starting from the galaxy center, as shown by MUSE (Fumagalli et al. 2014). This is expected from a later stage of stripping. Again the molecular gas dominates in mass the gaseous tail (Jáchym et al. 2017), but the SFE is much lower than in normal galaxy disks.

4 Importance of pressure

In all these low surface density environments, the SFE is found much lower than in normal disks. This suggests that the surface density of stars is very important for the star formation efficiency. Already Shi et al. (2011) have shown that the SFE in all kinds of environments is strongly correlated to the stellar surface density, and much less on the gas surface density. The HI to H_2 transition is favored by external pressure (Blitz & Rosolowsky 2006).

An example of radio jet-induced star formation in Centaurus A have indeed demonstrated that the HI gas is preferentially transformed in molecular gas on the jet passage (Salomé et al. 2016). Here again the SFE is much lower than normal, the depletion time in the induced star forming region is between 7 and 16 Gyr.

5 Conclusions

There are several environments showing low surface brightness in stars: not only dwarf and ultra-diffuse galaxies, but also the outer parts of galaxies, or stars belonging to circum-galactic regions, either from a cooling flow, or in tidal and ram-pressure stripped tails. In all these environments, XUV disks, cooling filaments in cool-core clusters, or ram-pressure tails, the disk pressure due to the gravity of stars is deficient or non-existing. First, the gas is not confined in a thin disk, and the star formation might be not only proportional to the gas surface density, but to the volumic gas density, which is then lower. But also the stellar pressure is missing to trigger the transformation of diffuse atomic gas to dense molecular gas, which reduces the efficiency of star formation. Even in hostile environments like the hot ICM medium, the molecular gas is resilient and can form in situ, in cooling filaments, in ram-pressure stripped tails. Star formation is observed, but with a low efficiency.

I thank Samuel Boissier for having organised such an interesting workshop.

References

Bicalho, I. C., Combes, F., Rubio, M., Verdugo, C., & Salome, P. 2019, A&A, 623, A66
Bigiel, F., Leroy, A., Walter, F., et al. 2008, AJ, 136, 2846
Blitz, L. & Rosolowsky, E. 2006, ApJ, 650, 933
Bresolin, F., Ryan-Weber, E., Kennicutt, R. C., & Goddard, Q. 2009, ApJ, 695, 580
Canning, R. E. A., Ryon, J. E., Gallagher, J. S., et al. 2014, MNRAS, 444, 336
Dasyra, K. M., Combes, F., Salomé, P., & Braine, J. 2012, A&A, 540, A112
Dessauges-Zavadsky, M., Verdugo, C., Combes, F., & Pfenniger, D. 2014, A&A, 566, A147
Fabian, A. C., Sanders, J. S., Allen, S. W., et al. 2011, MNRAS, 418, 2154
Fumagalli, M., Fossati, M., Hau, G. K. T., et al. 2014, MNRAS, 445, 4335
Jáchym, P., Combes, F., Cortese, L., Sun, M., & Kenney, J. D. P. 2014, ApJ, 792, 11
Jachym, P., Kenney, J. D. P., Sun, M., et al. 2019, arXiv e-prints, arXiv:1905.13249
Jáchym, P., Sun, M., Kenney, J. D. P., et al. 2017, ApJ, 839, 114
Kenney, J. D. P., Tal, T., Crowl, H. H., Feldmeier, J., & Jacoby, G. H. 2008, ApJ, 687, L69
Kenney, J. D. P. & Young, J. S. 1989, ApJ, 344, 171
Kennicutt, R. C. & Evans, N. J. 2012, ARA&A, 50, 531
McDonald, M., Gaspari, M., McNamara, B. R., & Tremblay, G. R. 2018, ApJ, 858, 45
Salomé, P. & Combes, F. 2003, A&A, 412, 657
Salomé, P., Combes, F., Edge, A. C., et al. 2006, A&A, 454, 437
Salomé, Q., Salomé, P., Combes, F., & Hamer, S. 2016, A&A, 595, A65
Shi, Y., Helou, G., Yan, L., et al. 2011, ApJ, 733, 87
Thilker, D. A., Bianchi, L., Boissier, S., et al. 2005, ApJ, 619, L79
Verdugo, C., Combes, F., Dasyra, K., Salomé, P., & Braine, J. 2015, A&A, 582, A6

SF2A 2019
P. Di Matteo, O. Creevey, A. Crida, G. Kordopatis, J. Malzac, J.-B. Marquette, M. N'Diaye, O. Venot (eds)

A SIMULATION VIEW ON THE FORMATION OF ULTRA-DIFFUSE GALAXIES IN THE FIELD AND IN GALAXY GROUPS

F. Jiang[1], A. Dekel[1, 2] and J. Freundlich[1]

Abstract. Ultra-diffuse galaxies (UDGs) with dwarf stellar masses and Milky Way sizes appear to be ubiquitous in groups and clusters and are also observed in the field. We study such galaxies in cosmological zoom-in simulations, aiming at understanding their formation both in groups and in the field. We find that while field UDGs arise from dwarfs in a specific mass range from successive episodes of supernova feedback, group UDGs can also form by tidal puffing up and become quiescent by ram-pressure stripping. The host haloes of both field and group UDGs have typical spin but significant cores. Field UDGs tend to be dark-matter dominated towards their center and to be more prolate than dwarf galaxies of similar mass. In groups, satellite dwarfs can become UDGs after pericenter passage by tidal heating and simultaneously lose most of their gas by ram-pressure stripping, suppressing star formation and inducing a color gradient in agreement with observations.

Keywords: galaxies:evolution, galaxies:formation, galaxies:haloes

1 Introduction

Ultra-diffuse galaxies (UDGs) are low-surface brightness systems ($\mu_{0,\mathrm{g-band}} > 24$ mag arcsec^{-2}) with surprisingly large effective radii ($r_{1/2} > 1.5$kpc) (van Dokkum et al. 2015). They have stellar masses similar to those of dwarf galaxies and their surface density profiles show similar Sérsic indices to those of disk galaxies (e.g., Mowla et al. 2017). UDGs are ubiquitous in clusters and groups (e.g., Koda et al. 2015), where they exhibit intermediate-to-old stellar populations (e.g., Ferré-Mateu et al. 2018). UDGs are also common in the field (e.g., Martínez-Delgado et al. 2016; Román & Trujillo 2017; Leisman et al. 2017), where they are modestly rich in cold gas and forming stars. A leading scenario is that they form in the field as blue UDGs, and, when accreted by a group/cluster, get environmentally processed to become quiescent red UDGs. Our work explores UDG formation in the field and in a galaxy group using cosmological simulations (Wang et al. 2015; Dutton et al. 2015) and simple analytical modeling. We pay special attention to whether UDGs are special compared to the other dwarfs and also to Milky-Way-mass galaxies.

2 UDGs in the field – Are they special?

Fig. 1 contrasts the UDGs with the control samples regarding the distribution function of a collection of properties. We can see that the host haloes of UDGs lie in a narrow mass range of $M_{\mathrm{vir}} = 10^{10-11.2}M_\odot$, clearly lower than the $L^\star$ regime. The UDGs do not particularly occupy the high halo-spin tail – in fact, the spin parameters (Bullock et al. 2001) are distributed similarly to the other galaxies, with a median of $\langle\lambda_{\mathrm{halo}}\rangle = 0.043$. While the spin-parameter distribution of the UDGs is not special, the NFW concentrations (Navarro et al. 1997) are on average lower than those of both the low-mass sample and the $L^\star$ galaxies. With a median of $\langle c_{\mathrm{NFW}}\rangle = 7.3$, the concentration of UDG haloes is significantly lower than what is expected for haloes of the same mass ($M_{\mathrm{vir}} = 10^{10-11.2}M_\odot$) in N-body simulations, which have $\langle c_{\mathrm{NFW}}\rangle \simeq 10.5 - 13.3$ according to the concentration-mass relation of Dutton & Macciò (2014). Related, the Einasto (1965) shape parameters, α_{Ein}, of the UDGs are on the higher end, with a median of $\langle\alpha_{\mathrm{Ein}}\rangle = 0.32$. The shape parameter describes

[1] Centre for Astrophysics and Planetary Science, Racah Institute of Physics, The Hebrew University, Jerusalem 91904, Israel
[2] Santa Cruz Institute for Particle Physics, University of California, Santa Cruz, CA 95064, USA

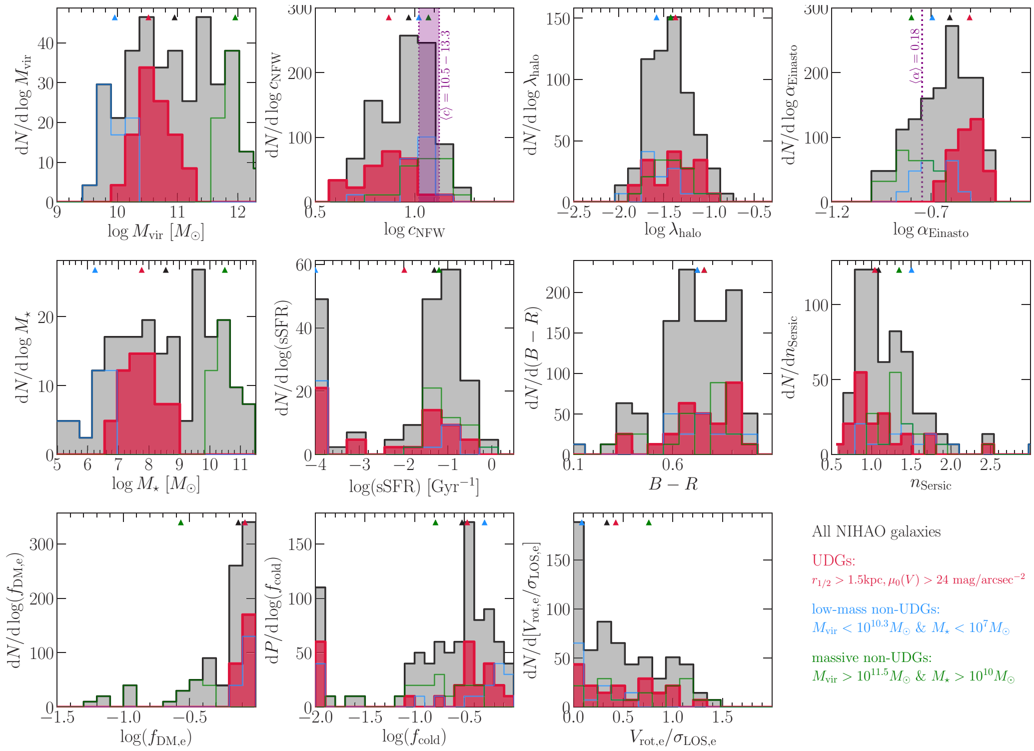

Fig. 1. Properties of field UDGs in the NIHAO simulations.

the curvature of the logarithmic density profile, with haloes that obey NFW profiles having $\alpha_{\rm Ein} \simeq 0.18$. A higher $\alpha_{\rm Ein}$ manifests a sharper transition between the inner and outer logarithmic density slopes than that of a NFW profile (e.g., Ludlow et al. 2013). The peculiarity of $c_{\rm NFW}$ and $\alpha_{\rm Ein}$ of the UDGs implies that their host haloes have responded dramatically to baryonic processes, and have dark-matter density profiles significantly different from the NFW form. Di Cintio et al. (2017) showed that the formation of the field UDGs are associated with bursty star formation histories, which result in episodic SNe outflows. The SNe outflows are believed to be responsible for the cusp-to-core transformation of dark-matter profiles (e.g., Pontzen & Governato 2012). Indeed we found that UDGs exhibit a prominent dark matter core, with logarithmic density slope $\alpha = -{\rm d}\log\rho/{\rm d}\log r$ evaluated at $r = 0.01R_{\rm v}$, $\alpha_{0.01}$, in a narrow range of $0 - 0.5$. Despite having dark-matter cores, the UDGs are among the most dark matter dominated systems: their dark-matter mass fractions within the effective radius ($f_{\rm dm,e}$) are typically over 80 per cent.

The UDGs have a median Sérsic index of $\simeq 1$, showing a mode of the $n_{\rm Sersic}$ distribution at $\simeq 0.8$, lower than that of the non-UDGs. The low Sérsic indices do not mean that UDGs are flattened, rotation-supported systems. In fact, the UDGs are not fast rotators, with the ratios of rotation speed to the radial velocity dispersion (v/σ) at $r_{1/2}$ similar to those of the full sample. We find that UDGs are mostly *not* oblate in shape. Instead, the UDGs are significantly more prolate than the $L^\star$ galaxies, and marginally more prolate than dwarf galaxies of similar and smaller masses.

The UDGs show a wide range of sSFR and colour. While the $L^\star$ analogues are mostly star-forming, with sSFR> 0.01Gyr^{-1}, the UDGs seem to show a bimodality in sSFR, and are overall slightly redder. About 30 per cent of the field UDGs are not forming stars instantaneously at $z = 0$. The star-forming UDGs have modestly high cold gas fractions, with $f_{\rm cold} \equiv M_{\rm cold}/(M_\star + M_{\rm cold}) >\approx 0.4$, which is consistent with those of a few observed field UDGs (Papastergis et al. 2017).

3 Satellite UDGs – tidally puffed up or relics of field UDGs?

Since UDGs are observed both in the field and in clusters and groups, an intuitive scenario for the formation of satellite UDGs is that they were already puffed up when in the field and became quenched after falling into a dense environment, as implied by several studies (e.g., Román & Trujillo 2017, Alabi et al. 2018, Ferré-Mateu

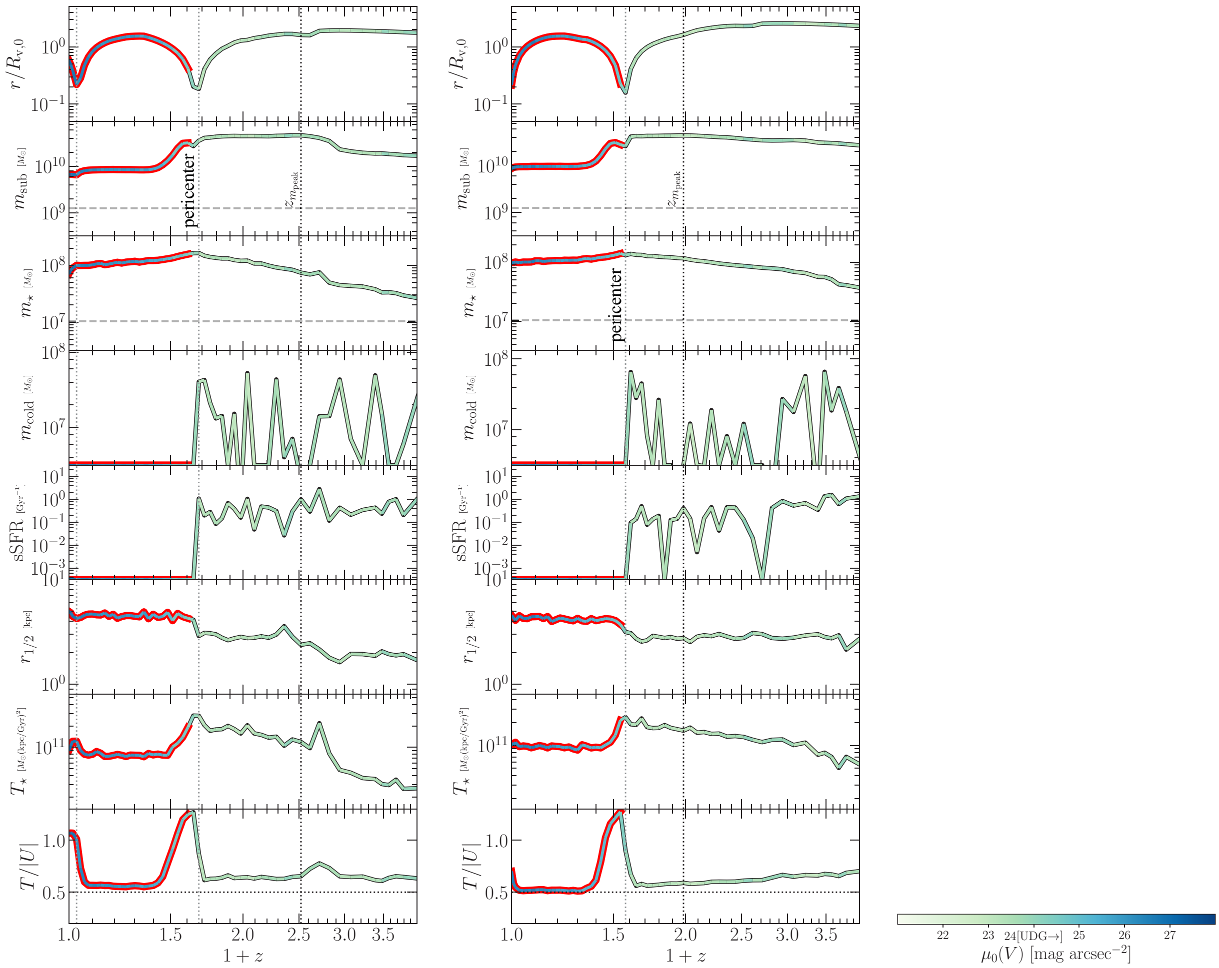

Fig. 2. Evolution of satellite galaxies that become UDGs at orbital pericentre. Two examples are presented here, showing the following quantities as functions of redshift – from the top to the bottom – group-centric distance r in units of the present-day virial radius of the host; subhalo mass (with the dashed line marking the resolution mass of $m_{\rm res} = 10^{9.1} M_\odot$, which corresponds to 250 dark-matter particles); stellar mass (with the dashed line marking the resolution mass of $m_{\rm res} = 10^7 M_\odot$, which corresponds to ~ 100 star particles); the mass of cold gas ($< 1.5 \times 10^4 K$); the specific star-formation rate (sSFR); the half stellar-mass radius $r_{1/2}$; the kinetic energy in stars $T_\star$; the ratio of the total kinetic energy to the binding energy $T/|U|$ (with the horizontal dotted line marking the virial-equilibrium value of 0.5). The facecolour of the lines reflects the V-band central surface brightness, as indicated by the colour bar. The UDG-phases are highlighted with red edges. The thicker vertical line marks the infall redshift, $z_{\rm peak}$, when $m_{\rm sub}$ reaches the maximum. The thin vertical lines indicate the orbital pericentres.

et al. 2018, and Chan et al. 2018). Recent observations seem to show evidence of the aforementioned scenario (Román & Trujillo 2017; Alabi et al. 2018). In this picture, what causes UDGs to lose their gas reservoir in the host system is either tidal stripping or ram pressure stripping.

We find a population of satellite galaxies that were not UDGs at infall but become UDGs inside the group. This amounts to 50 per cent of the surviving satellite-UDG population. Fig. 2 presents two examples, showing the evolution of a collection of quantities. The two satellites are both puffed up right after the first pericentre passage, becoming UDGs. The expansion at the pericentre is accompanied by a few other changes, including significant dark matter mass loss and a complete removal of cold gas. The change in stellar mass is small, implying that tidal stripping is marginal inside the baryonic range of the galaxy where stars and cold gas reside. Given that the cold gas is completely lost at the pericentre, ram pressure seems to be the main cause of the quenching of their star formation.

The increase in size also coincides with a spike in the kinetic energy of stars, and a deviation from virial equilibrium of the whole system, as can be seen from the ratio of kinetic energy and potential energy, $T/|U|$.

These phenomena together are indicative of *impulsive tidal heating* – a process describing what happens when the duration of the encounter of the system of interest (i.e., the satellite) and the perturber (i.e., the centre of the host system) is shorter than the crossing time of the constituent particles within the system of interest. During an impulsive encounter, the particles will be given a kinetic energy ΔT while retaining their potential energy instantaneously; after the satellite relaxes to a new equilibrium state (i.e., when $T/|U|$ drops back to ~ 0.5), the kinetic energy of the particles will decrease by the amount of $2\Delta T$ (if they are not stripped away); and finally, conserving the total energy, the potential energy of the affected particles increases, resulting in a size growth. This picture is manifested exemplarily in Fig. 2 – over the period of time between the initial and the new equilibrium states, the kinetic energy of the stars first rises, and then drops to a value that is lower than that before the pericentre encounter, accompanied by the increase in $r_{1/2}$. Therefore, new UDGs can be created out of normal dwarf satellites through tidal heating in a dense environment.

There are also satellite galaxies that were already UDGs at infall. Some of them survive the group environment and continue to exist at $z = 0$; others have been disrupted or merged into the central galaxy. We find in our group simulation that among the galaxies that entered the host halo as UDGs, about 20 per cent survive (as UDGs) till $z = 0$. About 20 per cent manage to coalesce with the central galaxy, while about 60 percent are disrupted before they penetrate to the inner $0.15R_\mathrm{v}$ radius. Along the way to their current positions, the surviving UDGs are somewhat puffed up further by tides and become quiescent due to ram-pressure stripping.

4 Conclusions

We have shown that the field UDGs that lie in a characteristic narrow halo mass range, $M_\mathrm{vir} = 10^{10.5\pm0.6} M_\odot$, tend to be triaxial and prolate, far from rotating, exponential discs, but their Sérsic indices are near unity. Their dark-matter density profile exhibits a flat density core dominating the regime within the stellar effective radius. We find a colour/sSFR gradient of group UDGs with distance from the host-halo centre, as observed. Given the mild stellar mass evolution and the significant loss of gas mass at pericentres, we infer that it is ram pressure, rather than tides, that removes the gas from group UDGs when they are near orbital pericentres and quenches star formation. We have identified two equally important origins of group UDGs. Satellite galaxies that were already UDGs at infall can survive the dense environment. In addition, more compact field galaxies can get puffed up and become UDGs near orbital pericentres. The size expansion is accompanied by energetics indicative of impulsive tidal heating. We present analytic understanding of the aforementioned formation mechanisms in Jiang et al. (2019) and Freundlich et al. (2019).

References

Alabi, A., Ferré-Mateu, Anna, Romanowsky, Aaron J, et al. 2018, MNRAS, 479, 3308
Bullock, J. S., Dekel, A., Kolatt, T. S., et al. 2001, ApJ, 555, 240
Chan, T. K., Kereš, D., Wetzel, A., et al. 2018, MNRAS, 478, 906
Di Cintio, A., Brook, C. B., Dutton, A. A., et al. 2017, MNRAS: Letters, 466, L1
Dutton, A. A. & Macciò, A. V. 2014, MNRAS, 441, 3359
Dutton, A. A., Macciò, A. V., Stinson, G. S., et al. 2015, MNRAS, 453, 2447
Einasto, J. 1965, Trudy Astrofizicheskogo Instituta Alma-Ata, 5, 87
Ferré-Mateu, A., Alabi, A., Forbes, D. A., et al. 2018, MNRAS, 479, 4891
Freundlich, J., Dekel, A., Jiang, F., et al. 2019, arXiv:1907.11726
Jiang, F., Dekel, A., Freundlich, J., et al. 2019, MNRAS, 487, 5272
Koda, J., Yagi, M., Yamanoi, H., & Komiyama, Y. 2015, ApJ, 807, L2
Leisman, L., Haynes, M. P., Janowiecki, S., et al. 2017, ApJ, 842, 133
Ludlow, A. D., Navarro, J. F., Boylan-Kolchin, M., et al. 2013, MNRAS, 432, 1103
Martínez-Delgado, D., Läsker, R., Sharina, M., et al. 2016, ApJ, 151, 96
Mowla, L., van Dokkum, P., Merritt, A., et al. 2017, ApJ, 851, 27
Navarro, J. F., Frenk, C. S., & White, S. D. M. 1997, ApJ, 490, 493
Papastergis, E., Adams, E. A. K., & Romanowsky, A. J. 2017, A&A, 601, L10
Pontzen, A. & Governato, F. 2012, MNRAS, 421, 3464
Román, J. & Trujillo, I. 2017, MNRAS, 468, 4039
van Dokkum, P. G., Abraham, R., Merritt, A., et al. 2015, ApJ, 798, L45
Wang, L., Dutton, Aaron A, Stinson, Gregory S, et al. 2015, MNRAS, 454, 83

A SPECTROSCOPIC STUDY OF THE GIANT LOW SURFACE BRIGHTNESS GALAXY MALIN 1

Junais[1] and S. Boissier[1]

Abstract. Low Surface Brightness galaxies (LSBs) represent a significant fraction of galaxies in the nearby universe. However, despite their large fraction, the structure and origin of this class of galaxies is still poorly understood, especially due to the lack of high-resolution kinematics and spectroscopy.

Malin 1 is the largest known low surface brightness galaxy to date, the archetype of so-called giant LSBs. We present new results based on spectroscopic observations of Malin 1, using the Hα and [OII]$_{3727}$ emission lines in order to bring new constraints on the internal dynamics of this galaxy. We have extracted a total of 16 spectra from different regions of Malin 1 and calculated the inner rotational velocities using the observed shift in the emission line wavelengths.

We show for the first time a steep rise in the rotation curve of Malin 1 up to ∼400 km s^{-1} (within r < 10 kpc), which had not been observed in any of the previous works on this galaxy. We will discuss the implications of this result in comparison with existing works on Malin 1 and also the possibility for making a new mass model for this galaxy.

Keywords: Low surface brightness galaxy, Rotation curve, Dynamics

1 Introduction

Low Surface Brightness galaxies (LSBs) can be historically defined as the galaxies with a central disk surface brightness (μ_0) fainter than the typical Freeman (1970) value for disk galaxies ($\mu_{0,B}$ = 21.65 mag arcsec^{-2}). LSBs may account up to a total of 50% of all galaxies in the universe according to O'Neil & Bothun 2000; 40% for Galaz et al. 2011. So it is really important to study this large population of galaxies in order to have an unbiased view of galaxy formation and evolution scenarios.

Malin 1 is an extreme example of an LSB galaxy with a disk central surface brightness $\mu_{0,V} \approx 25.5$ mag arcsec^{-2} (Impey & Bothun 1997) and a diameter of ∼240 kpc (Moore & Parker 2006). Therefore Malin 1 can be clearly considered as a prototype for the study of LSBs and giant LSBs (GLSBs) in general.

In the recent years with the advancement in our technology and the advent of powerful imaging instruments, there has been a new interest in Malin 1 and other similar GLSBs (e.g. Galaz et al. 2015; Boissier et al. 2016; Hagen et al. 2016; Mishra et al. 2017; Zhu et al. 2018; Saburova et al. 2018). However the origin and evolution of this class of galaxies is still poorly understood, mainly due to the lack of good quality spectroscopic data. So we present here an on-going work on a new spectroscopic study of Malin 1 from Junais et al. (in preparation).

2 Data and reduction

We obtained some long-slit spectroscopic data for Malin 1 using the IMACS-Magellan spectrograph of the 6.5m Magellan Baade telescope in the Las Campanas Observatory, Chile. We initially used observations made in 2016 of 4 slit positions each of slit-width 2.5″, out of which we extracted spectra from 12 different regions within 3 slits where it was possible to obtain a clear signal. This includes a region at ∼26 kpc which is relatively far from the center of Malin 1. In 2019 we obtained new data for Malin 1 using the same instrument and a relatively smaller slit-width of 1.2″, from which we extracted a total of 4 spectra (see Fig.1). The orientation of the wider slits (2.5″ slits) was chosen on the basis of UV images from Boissier et al. (2008) and the smaller slit (1.2″ slit)

[1] Aix Marseille Univ, CNRS, CNES, LAM, Marseille, France

was placed passing through the major axis of the galaxy. All the data reduction processes to extract the spectra were done using standard IRAF procedures.

Within the extracted spectra, we focused on the Hα and $[OII]_{3727}$ emission lines (Hα was observed in the wider slits and $[OII]_{3727}$ observed in the narrower slit) which was the strongest of all. The emission line fitting was done using Python routines implementing a Markov Chain Monte Carlo (MCMC) method in order to obtain the peak wavelengths and the associated errorbars of each emission line. Various constraints were also applied on the emission lines during the fitting procedure, including a fixed line ratio for the [NII] and [OII] doublets (Ludwig et al. (2012); Comparat et al. (2013)) and a fixed line separation using the laboratory wavelengths. The results of this fitting procedure will be used for our further analysis.

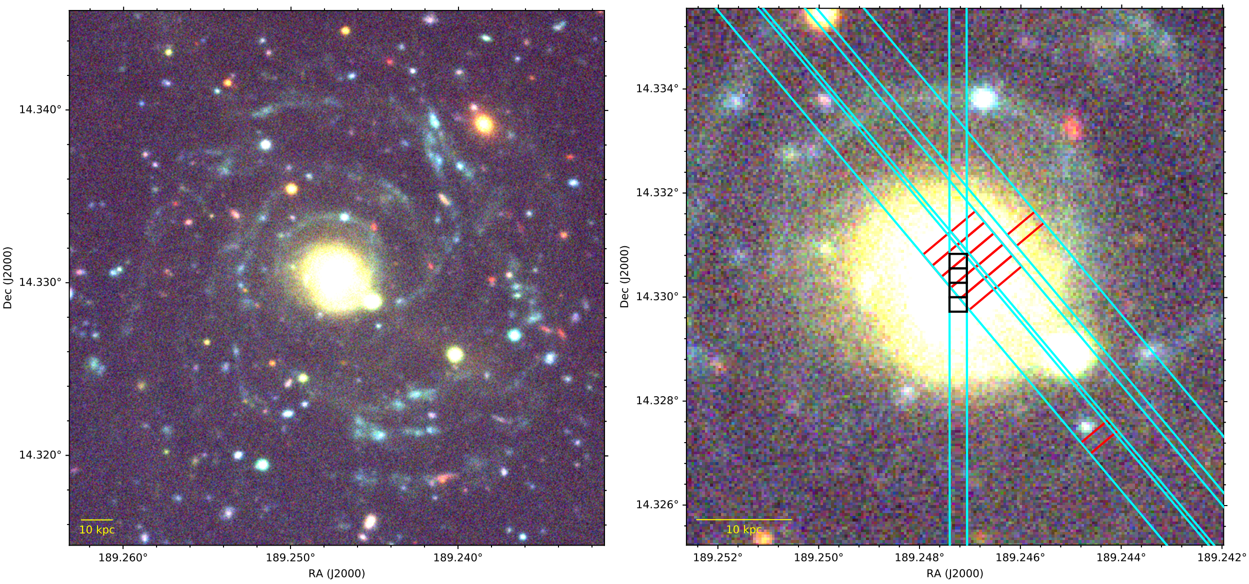

Fig. 1. Left: Colour composite image of Malin 1 from the CFHT-Megacam Next Generation Virgo cluster Survey (NGVS, Ferrarese et al. 2012) u, g and i band images. **Right:** The slit positions of our observations are shown (in blue) along with the 16 apertures (in red and black for the Hα and $[OII]_{3727}$ data respectively) in which we could extract a spectrum.

3 A new Rotation Curve for Malin 1

The observed wavelength shift with respect to their laboratory wavelengths of the Hα and $[OII]_{3727}$ emission lines in our extracted spectra was used to calculate the circular velocities on Malin 1 galaxy plane as a function of radius. We also applied a correction for the galaxy inclination angle, PA and systemic velocity (V_{sys}) using the values adopted from the HI study of Lelli et al. 2010. A few data points which are too close to the minor axis of the galaxy with a large correction for the intrinsic rotational velocity values (points with the azimuth in the galaxy plane $> 70°$) were eliminated considering to be unrealistic for the rotation curve. Moreover we have also done a 3 pixel re-binning of the two outermost data points (the ones at 10 kpc and 26 kpc) in order to obtain a better signal-to-noise in these regions.

Fig.2 shows the extracted rotation curve for Malin 1 along with the data points from Lelli et al. 2010 using low resolution HI data. We observe for the first time a steep rise in the rotational velocity for the inner regions of Malin 1 (inside $\sim$10 kpc) up to $\sim$ 400 km s^{-1}, and a subsequent decline to reach the plateau observed on large scales with HI. The implications of this new result and its future prospects are discussed in Section 4.

4 Discussions

A steep rise in the rotation curve is not typical for an LSB galaxy. Therefore the observed steep rise in the newly extracted rotation curve for Malin 1 could imply that in its central regions Malin 1 shows a behaviour different from an LSB galaxy, despite the presence of its huge LSB disk. This is also in accordance with the observation

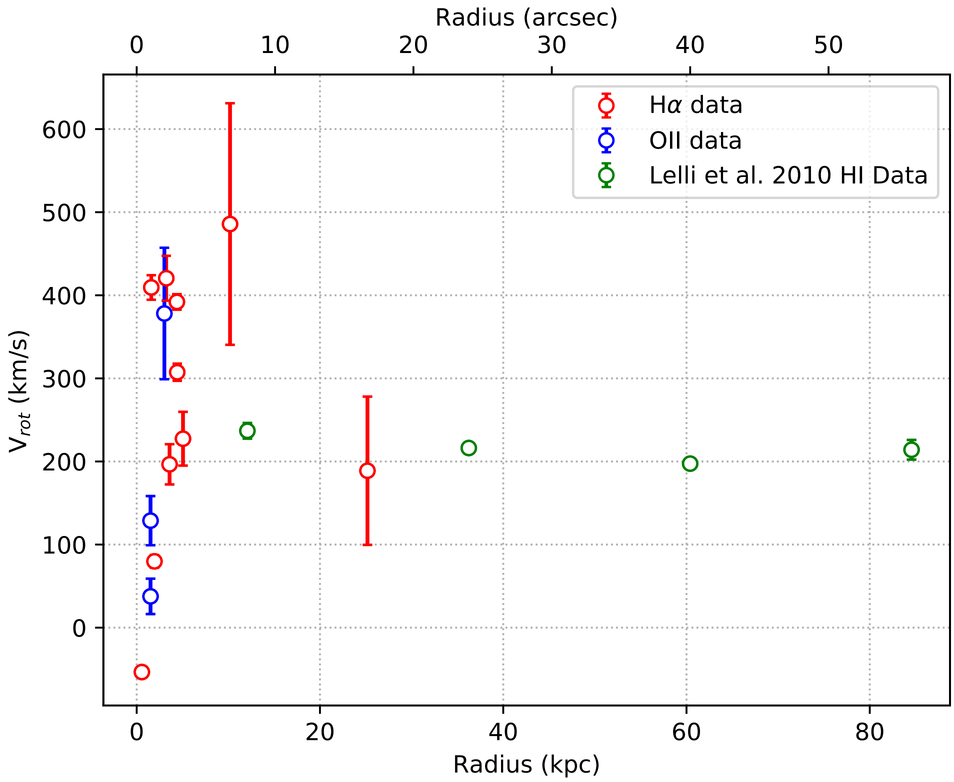

Fig. 2. Rotation curve for Malin 1. The red and black points indicate the Hα and $[OII]_{3727}$ data respectively from this work along with the Lelli et al. (2010) HI data points (green).

from Barth (2007) that described Malin 1 as an early type SB0/a galaxy with a central bulge, surrounded by a huge LSB disk.

Lelli et al. (2010) provides a rotation curve and mass model for Malin 1 using HI data, and observes that Malin 1 has a steep rising rotation curve in contrast with the slowly rising rotation curve from Pickering et al. (1997). He also indicates that from the observation of surface photometry and gas dynamics of Malin 1, it tends to have a double HSB-LSB structure. However the poor resolution of HI data used in the analysis of Lelli et al. (2010) (a resolution of ∼21′′ corresponding to ∼32 kpc) makes it hard to bring strong constraints on the internal dynamics of the galaxy (r < 10 kpc).

Therefore this work, with a better resolution than any of the previous works on Malin 1, could be crucial in bringing new constraints on the dynamics and mass distribution in the inner regions of Malin 1. We are currently in the final stages of preparation of a mass model for Malin 1 using the constraints from our new rotation curve in combination with the HI measurements from Lelli et al. (2010) and Hubble Space Telescope (HST) I-band photometry from Barth (2007). With a new mass model we expect to have a better understanding of the overall matter distribution within Malin 1, especially the dark matter distribution which is often debated for LSB galaxies (de Blok & McGaugh 1997).

Reshetnikov et al. (2010) also provides yet another spectroscopic study of the internal dynamics of Malin 1 using stellar absorption lines. However they only provide a single slit of observation with a position angle of 55° and relatively poor sampling. The rotational velocities from their data, when converted to the rotational velocity in the galaxy plane using the same geometrical approximations we did in this work, are in good agreement with our data (within r ∼10 kpc) considering their huge errorbars. This suggest that the stellar and gas kinematics are coherent in the central regions of Malin 1.

A recent IllustrisTNG simulation result from Zhu et al. (2018) also produces some interesting results similar to our observations in this work. They were able to produce a Malin-like galaxy in their simulations with similar observed features of Malin 1 and a rotation curve with a maximum rotational velocity of ∼430 km s^{-1}, close to the value we observed for Malin 1 in this analysis. However they do not observe a rotation curve with a steep rise followed by a decline to $\sim$200 km s^{-1}, contrary to what we observe in this work. This comparison of our observational data with that of a simulation indicates that our work can offer more constraints for future simulations like this regarding Malin 1 like galaxies or GLSBs in general.

It will be important in the future, however, to obtain better quality data for the proper understanding of the formation and evolution of Malin 1 like galaxies. Recently we have obtained a LAM grant for the purchase of a new Hα filter at the redshift of Malin 1, which will provide us with the possibility to obtain an Hα emission map of the galaxy, crucial for the study of the dynamics and star formation within Malin 1.

References

Barth, A. J. 2007, The Astronomical Journal, 133, 1085

Boissier, S., Boselli, A., Ferrarese, L., et al. 2016, Astronomy & Astrophysics, 593, A126

Boissier, S., Gil de Paz, A., Boselli, A., et al. 2008, ApJ, 681, 244

Comparat, J., Kneib, J.-P., Bacon, R., et al. 2013, A&A, 559, A18

de Blok, W. J. G. & McGaugh, S. S. 1997, Monthly Notices of the Royal Astronomical Society, 290, 533

Ferrarese, L., Côté, P., Cuillandre, J.-C., et al. 2012, ApJS, 200, 4

Freeman, K. C. 1970, The Astrophysical Journal, 160, 811

Galaz, G., Herrera-Camus, R., Garcia-Lambas, D., & Padilla, N. 2011, The Astrophysical Journal, 728, 74

Galaz, G., Milovic, C., Suc, V., et al. 2015, The Astrophysical Journal, 815, L29

Hagen, L. M. Z., Seibert, M., Hagen, A., et al. 2016, ApJ, 826, 210

Impey, C. & Bothun, G. 1997, Annual Review of Astronomy and Astrophysics, 35, 267

Lelli, F., Fraternali, F., & Sancisi, R. 2010, Astronomy and Astrophysics, 516, A11

Ludwig, R. R., Greene, J. E., Barth, A. J., & Ho, L. C. 2012, ApJ, 756, 51

Mishra, A., Kantharia, N. G., Das, M., Omar, A., & Srivastava, D. C. 2017, MNRAS, 464, 2741

Moore, L. & Parker, Q. A. 2006, PASA, 23, 165

O'Neil, K. & Bothun, G. 2000, The Astrophysical Journal, 529, 811

Pickering, T. E., Impey, C. D., van Gorkom, J. H., & Bothun, G. D. 1997, AJ, 114, 1858

Reshetnikov, V. P., Moiseev, A. V., & Sotnikova, N. Y. 2010, Monthly Notices of the Royal Astronomical Society: Letters, 406, L90

Saburova, A. S., Chilingarian, I. V., Katkov, I. Y., et al. 2018, MNRAS, 481, 3534

Zhu, Q., Xu, D., Gaspari, M., et al. 2018, MNRAS, 480, L18

SF2A 2019
P. Di Matteo, O. Creevey, A. Crida, G. Kordopatis, J. Malzac, J.-B. Marquette, M. N'Diaye, O. Venot (eds)

CURVED FOCAL PLANE TELESCOPE FOR OBSERVATION OF ULTRA-LOW SURFACE BRIGHTNESS OBJECTS

S. Lombardo[1], E. Muslimov[1], G. Lemaître[1] and E. Hugot[1]

Abstract. In spite of major advances in both ground- and space-based instrumentation, the ultra-low-surface universe (ULSB) still remains a largely unexplored volume in observational parameter space. These ultra-low levels (>28-29 mag/arcsec^2) are achieved by minimising internal scattering to produce a point spread function (PSF) as compact as possible while achieving a wide field of view within a fast optical design. We present here the results of full-system photon Monte Carlo simulations of a ground-based telescope with a curved focal plane design, that aims at testing the breakthrough technologies of curved sensors and carrying out ULSB observations. While the telescope has only one inevitable single refractive surface, it delivers a PSF with ultra-compact wings, which allows the detection of ULSB features.

Keywords: telescopes, detectors, ultra-low surface brightness, technology

1 Introduction

In spite of major advances in both ground- and space-based instrumentation, the ultra-low surface brightness universe (ULSB) still remains a largely unexplored part in observational parameter space. Yet, ULSB observations would critically improve our understanding of the evolution of the universe by detecting and characterizing ultra-faint galaxies and features, currently predicted to be abundant but missed by current surveys due to their lack of sensitivity to these extended objects (Bullock & Boylan-Kolchin 2017; Kazantzidis et al. 2008; Cooper et al. 2010, 2013; Barton & Thompson 1997; Fry et al. 1999; Atkinson et al. 2013). We present here the telescope demonstrator aimed at testing the breakthrough technologies of curved detectors and carrying out ULSB observations (Muslimov et al. 2017; Lombardo et al. 2019). This telescope has one inevitable refractive surface, the window for the cryostat, but it still delivers a Point Spread Function (PSF) with extremely compact wings, a key factor for the detection of ULSB features in the sky. As its focal surface is curved, the use of a curved CCD enhances the performances in terms of transmission and PSF shape. We also present here the design and the first results obtained through full-system photon Monte Carlo simulations. The great potential of our optical design is enhanced by the introduction of curved CCDs. This new technology hugely simplifies the overall system and also eliminates the need for field-flattening lenses, while preserving the wide field of view.

The impact of the curving process on the characteristics of the detectors has not been fully determined yet, while some manufacturer tested few prototypes and found increased values for the dark current (Gregory et al. 2015), others found no clear performance degradation with respect to the flat sensor case (Lombardo et al. 2019).

2 Telescope design & its End2End simulation software

The telescope is a fully reflective Schmidt design with an anamorphic primary, flat secondary and spherical tertiary mirror, and features a curved focal surface (Figure 1). In Table 1 its main characteristics are described. In spite of a small primary mirror (35.6 cm), it allows observations over a wide field of view of 1.6° × 2.6°.

It has one refractive element: the window of the dewar, which is necessary to cool down the CCD. In order to reduce as much as possible the number of refractive elements, we combined the window with the bandpass filter. It is also possible to design a solution in which we have two different filters, side by side, on the window

[1] Aix Marseille Univ, CNRS, CNES, LAM, Marseille, France

Table 1. Parameters of telescope design.

Quantity	Value
Field of view	$1.6^\circ \times 2.6^\circ$
F/#	2.5
Diameter	356 mm
Detector shape/radius of curvature	Convex/$\sim$800 mm

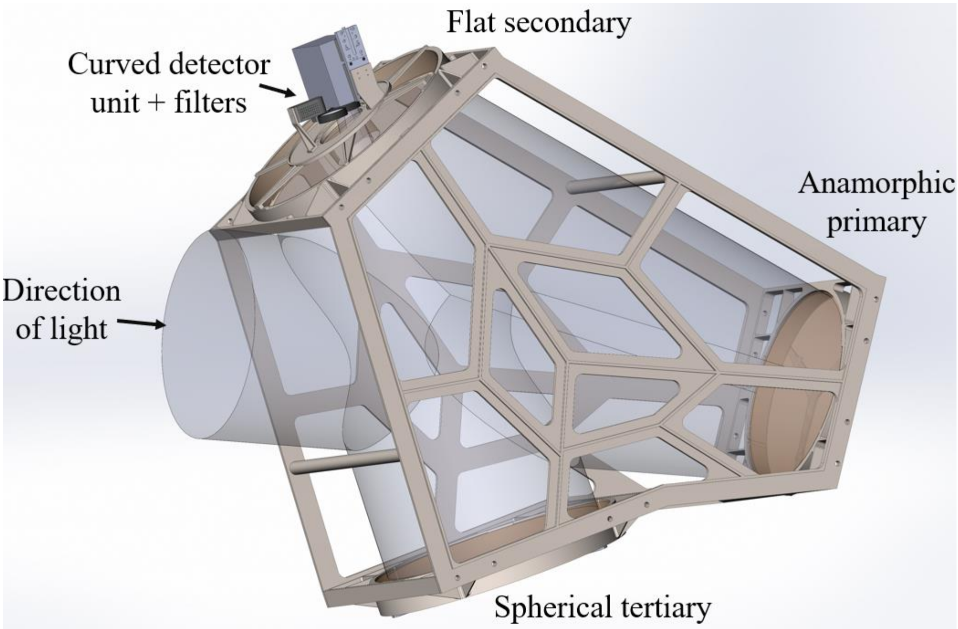

Fig. 1. Opto-mechanical design of the pathfinder: light reaches an anamorphic primary, is reflected by a flat secondary and a spherical tertiary yields a simple spherically-curved focal surface where a curved detector is placed.

so that we are able to observe in two wavelength bands. For simplicity, in the rest of the paper, we only consider one filter band that is a g LSST-like filter.

The location considered for the simulations is within the Observatorio del Roque de los Muchachos in La Palma. We use an end-to-end photon Monte Carlo simulation software `PhoSim` (Peterson et al. 2015) to verify the performances of the full telescope and characterise the PSF at very large distances from the center of the field of view.

The software simulates the full light path from the astrophysical source, passing through the Earth atmosphere, the telescope and can model also the CCD effects such as dark current, read out noise, CTE, etc. We also account for the altitude, typical seeing and wind speed/direction values for La Palma, to make the simulation as realistic as possible.

3 Results

The quality of the PSF of the telescope is a key aspect to consider in ultra-low surface brightness objects observations, as already discussed in previous publications (Abraham & van Dokkum 2014; Mihos et al. 2017). The telescope must provide PSF whose wings are as low as possible, such that the faint emission of these objects is not dominated by the PSF residuals of brighter stars or galaxies in the same observed field.

The PSF of the telescope is shown in Figure 2 as function of the radial distance in arcmin. This PSF is obtained from a simulation of a 9 mag star in the centre of the field of view and it includes all the effects of

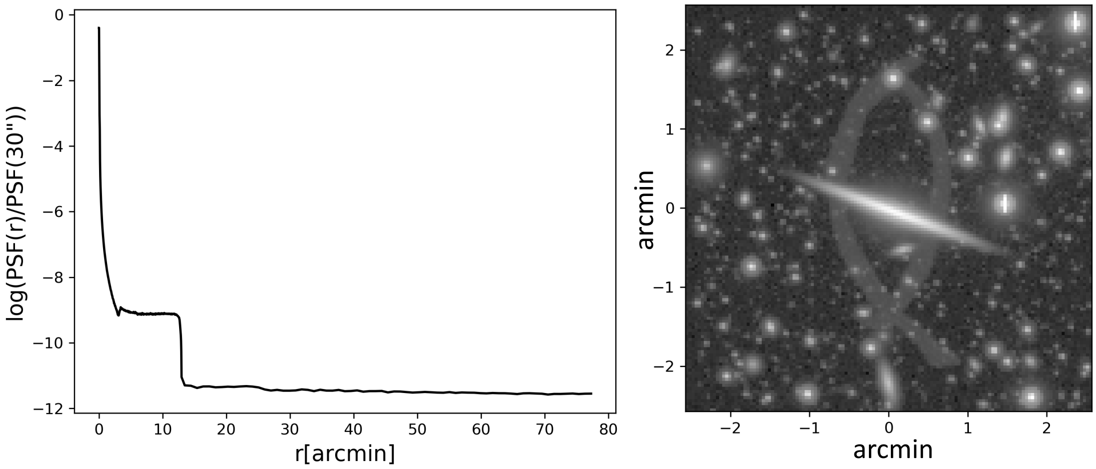

Fig. 2. Left: PSF of the telescope presented in this paper from photo Monte Carlo simulations. The PSF is normalized with its value within 30". Right: Simulation of a 5'×5' field observed by the ground-based pathfinder after an exposure time of 30 h.

optical design perturbations, atmosphere and seeing. The PSF is computed from an image composed of 140 different observations where the CCD was exposed for 40.5 s each time. The PSF of the pathfinder features very compact wings even at large distances from the center of the field of view, reaching averaged values of 10^{-9} around 3.0'. At this distance it plateaus until 13', due to the reflection off the CCD and by the scattering of the dewar window. Then it decreases again reaching averaged values of $10^{-11.5}$. This ghost, hence, does not degrade the PSF as it is suppressed by 8 orders of magnitudes with respect to the centre. These results show the importance of producing full-scale realistic simulations during the design stage, in order to test all the performances of the system and improve its possible weak points before the construction phase.

We can perform more tests and ascertain the capacity of the telescope to observe the ULSB realm, by simulating a field observed in the sky and injecting an ULSB feature of known surface brightness. The field is large 5'×5' and it is composed of stars and galaxies drawn from the Millennium Simulation and generated using `CatSim`*. In addition to this, a large elliptical galaxy (of 2.5' observed angular diameter) and an arch-like structure have been added to the simulation at the centre of the field. The galaxy has an integrated brightness of 13.5 mag and the arches have surface brightness of 29 mag/arcsec^2 which makes the full image similar to NGC5907 (Martínez-Delgado et al. 2010).

The results of the simulations of the 5'×5' field observed at the centre of the field of view of the pathfinder are shown in Figure 2. This image is integrated over 30 hours of exposures and it is composed by adding 288 images of 382 s each.

We can clearly observe the injected ULSB feature. Its presence in the image implies the capability of the pathfinder of observing such extremely faint and extended objects and of reaching a good S/N, even after just one week of nightly integration time.

4 Conclusions

The ultra-low surface brightness universe still remains a niche for observations, as a full-sky survey is missing. As observations of this kind demand a telescope with a highly optimized design, we propose here an alternative concept that uses a curved detector. The proposed telescope is a fully reflective, off-axis Schmidt design, with an anamorphic primary mirror of 35.6 cm diameter, a flat secondary mirror and a spherical tertiary mirror that focuses the light onto a convex spherically-curved CCD. In this paper we tested the full system through full scale photon Monte Carlo simulations, with the software `PhoSim`.

The results from the simulation of a star at the centre of the field of view have shown firstly that the wings

*`https://www.lsst.org/scientists/simulations/catsim`

of the PSF reach unprecedentedly low level. The normalised PSF decreases down to $10^{-11.5}$ at a radial distance from its centre of ∼13'. Before reaching these values, the PSF shows a plateau of $\sim 10^{-9}$ due to the ghost image of the star itself.

This unfocused image of the star creates a halo of photons that extends from ∼3' to ∼13' from the centre of the PSF. The PSF quality is not degraded by the presence of such ghost, as it is suppressed by 8 orders of magnitude with respect to the PSF central value.

Finally we simulated a field of galaxies and stars of 5'×5' observed at the centre of the field of view for a total exposure time of 30 hours. The final image clearly shows the presence of the extended structure injected in the simulation and that is faintly emitting at 29 mag/arcsec^2, typical brightness for the ultra-low surface brightness objects. These results illustrate the full potentiality of the pathfinder, that will not only be used to test the groundbreaking technology of the curved sensors, but also provide important science outcome.

The authors acknowledge the support of the European Research council through the H2020 - ERC-STG-2015 – 678777 ICARUS program, the MERAC foundation and the European Astronomical Society who are both funding the project. This activity was partially funded by the French Research Agency (ANR) through the LabEx FOCUS ANR-11-LABX-0013.

References

Abraham, R. G. & van Dokkum, P. G. 2014, PASP, 126, 55
Atkinson, A. M., Abraham, R. G., & Ferguson, A. M. N. 2013, ApJ, 765, 28
Barton, I. J. & Thompson, L. A. 1997, AJ, 114, 655
Bullock, J. S. & Boylan-Kolchin, M. 2017, ARA&A, 55, 343
Cooper, A. P., Cole, S., Frenk, C. S., et al. 2010, MNRAS, 406, 744
Cooper, A. P., D'Souza, R., Kauffmann, G., et al. 2013, MNRAS, 434, 3348
Fry, A. M., Morrison, H. L., Harding, P., & Boroson, T. A. 1999, AJ, 118, 1209
Gregory, J. A., Smith, A. M., Pearce, E. C., et al. 2015, Applied Optics, 54, 3072
Kazantzidis, S., Bullock, J. S., Zentner, A. R., Kravtsov, A. V., & Moustakas, L. A. 2008, ApJ, 688, 254
Lombardo, S., Behaghel, T., Chambion, B., et al. 2019, Appl. Opt., 58, 2174
Lombardo, S., Muslimov, E., Lemaître, G., & Hugot, E. 2019, MNRAS, 488, 5057
Martínez-Delgado, D., Gabany, R. J., Crawford, K., et al. 2010, AJ, 140, 962
Mihos, J. C., Harding, P., Feldmeier, J. J., et al. 2017, ApJ, 834, 16
Muslimov, E., Valls-Gabaud, D., Lemaître, G., et al. 2017, Appl. Opt., 56, 8639
Peterson, J. R., Jernigan, J. G., Kahn, S. M., et al. 2015, ApJS, 218, 14

SF2A 2019
P. Di Matteo, O. Creevey, A. Crida, G. Kordopatis, J. Malzac, J.-B. Marquette, M. N'Diaye, O. Venot (eds)

PROBING THE Hα, HI AND FIR EMISSION IN LOW SURFACE BRIGHTNESS TAILS OF VIRGO GALAXIES AND THEIR CONNECTION WITH THE VIRGO INTRA-CLUSTER COMPONENT

A. Longobardi[1]

Abstract. Understanding the formation and evolution of structures remains a primary goal of modern astrophysics. Both observations and simulations point to a scenario in which structure formation follows hierarchical laws where galaxies and clusters grow by mergers and accretion of smaller subsystems. No model for structure evolution, however, can be complete without a detailed understanding of the physical mechanisms that take place. Hence, it is only through the detailed study of the local volume that we can hope to understand the role of the interactions in the hierarchical assembly of baryonic substructures. In this work we carry out a multi-wavelength mapping of the intra-cluster component, a direct product of the interactions within a cluster. The focus of this project is on the nearby Virgo cluster, for which we have unique multi-frequency data in terms of extension, sensitivity and resolution, allowing us to study galaxies that show low surface brightness tails of stripped material with ionised gas emission (Hα) that also present HI (neutral) and FIR (dust -HeViCS data-) emission.

Keywords: galaxies: clusters: individual (Virgo cluster) - galaxies: cluster: intracluster medium - galaxies: evolution

1 Introduction

In galaxy clusters a fraction of the baryonic content is represented by the intra-cluster component (ICC), i.e. a fraction of matter that is gravitationally bound to the cluster potential. Galaxy interactions, as well as tidal interactions between galaxies and the cluster potential, are believed to play an important role in the production of the ICC (Willman et al. 2004; C. S. Rudick et al. 2006), even though a portion of it may come from in-situ star formation (Puchwein et al. 2010), wherein stars form in cold gas clouds stripped from infalling substructures. In a complex environment, such as galaxy clusters, it is plausible that all these processes are involved in the building up of the ICC and that different paths of formation are followed depending upon the dynamical evolution of the system. While the ICC is an important component to study and its existence is well established, historically it has proved difficult to analyse, due to its low surface brightness. A clear census on the fraction of matter that form the ICC has not been reached yet, and no uniform information as yet been gathered on its properties across the electromagnetic spectrum. IC stars are studied through their optical properties (e.g., Mihos et al. 2017), and near infra-red (NIR) analyses of optically identified IC features show that these have NIR emission (Krick et al. 2011). Finally, the hot IC plasma, or ICM, is studied through X-ray data (e.g., Nulsen & Bohringer 1995; Simionescu et al. 2017). However, little is known about its properties in the form of gas, and the diffuse IC dust has long been tried to be detected (e.g., Muller et al. 2008), but the results are still controversial and inconclusive. In this work we look for the on-going build up of the Virgo cluster ICC studying the tails of stripped gas and dust through state-of-art observations.

2 The Virgo cluster: a unique laboratory for astrophysics

At a distance of 16.5 Mpc (Mei et al. 2007), the Virgo cluster is the dominant mass concentration in the local universe and the largest concentration of galaxies within ∼35 Mpc. Characterised by both spatial and kinematic

[1] Aix Marseille Univ, CNRS, CNES, LAM, 13388 Marseille, France

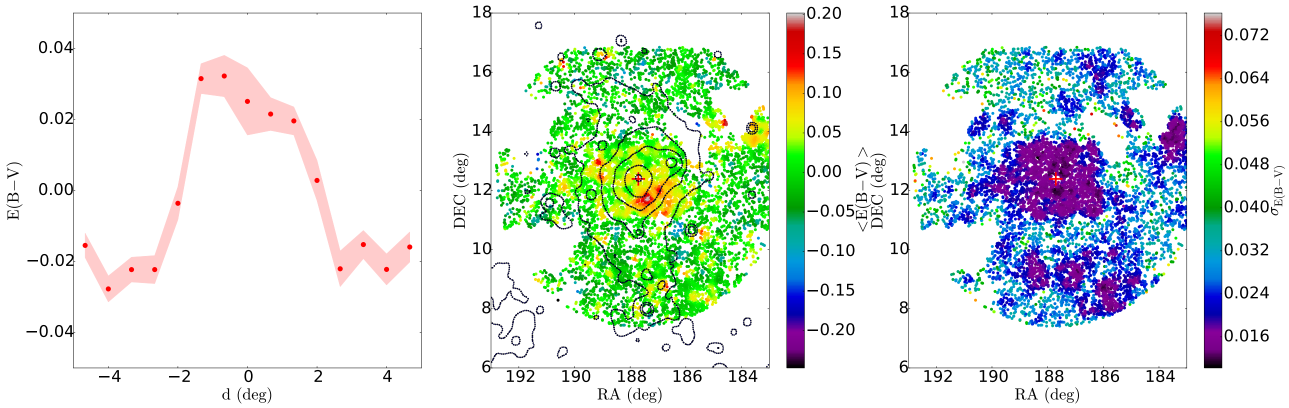

Fig. 1. Left Panel: Radial profile of the E(B-V) extinction of the Virgo IC dust component (filled dots) and its uncertainty (shaded area) from the centre of the cluster out to 5 degrees (1440 kpc); Positive and negative distances trace the northern and southern halves with respect to the cluster's centre. The radial distribution shows a centrally concentrated profiles on both sides of the galaxy. **Central Panel:** Spatial distribution of the SDSS background galaxies colour-coded according to the smoothed means of the E(B-V) values. Black contours trace the cluster X-ray emission as traced by the ROSAT All-Sky survey in the hard band. **Right Panel:** Errors on the smooth extinction map computed by means of Monte Carlo simulations. Closer to the centre of the cluster E(B-V) values are statistically significant, and higher than what is measured going outwards. The peak measured south-west of M87 traces the presence of a background clustered galaxies characterised by redder colours.

substructures, with different subgroups possessing different morphological mixes of galaxies (Binggeli et al. 1987), Virgo has historically played a key role in studies of how galaxies form and evolve in dense environments. The physical properties of late-type galaxies vary dramatically from the periphery (where galaxies are unperturbed in terms of gas content and star formation activity) to the cluster core (dominated by systems deprived of their gas reservoir and with a significantly reduced star formation activity (Boselli et al. 2014)), and a wealth of observational evidence consistently indicates that Virgo is a young cluster still in formation (e.g., Mihos et al. 2005; Conselice et al. 2001). Virgo can thus be considered a local analogue of the over-dense regions in the high-redshift universe, and an ideal laboratory for studying the perturbing mechanisms that shaped galaxy evolution. The information astronomers have gathered on the Virgo system is unique, with an extended collection of multi-frequency data that survey this system at good/optimal resolution and sensitivity. Dedicated surveys made it possible to gather X-ray (ROSAT; Nulsen & Bohringer 1995), UV (the GALEX Ultraviolet Virgo Cluster Survey, GUViCS; Boselli et al. 2011), and deep broad-band optical (NGVS; Ferrarese et al. 2012, BSDVCS; Mihos et al. (2017)) and narrow-band Hα (VESTIGE; Boselli et al. 2018) data. In addition to this, NIR (SPITZER; Werner et al. 2004), FIR (Herschel Virgo Cluster Survey, HeViCS; Davies et al. 2010, ; Planck, http://www.esa.int/Planck), and radio HI (VIVA; Chung et al. 2009) surveys allowed astronomers to complete the mapping of the different constituents of the cluster.

3 The Virgo intra-cluster component formation: study of the tails of stripped galaxies

On a theoretical side the presence of an ICC in clusters is a natural result of the fact that young concentrations of mass are still in the process of forming. However, observationally its detection across the entire spectrum has been elusive, mainly due to its very low surface brightness. Here we aim in identifying the ICC in the form of gas and dust in the dynamically young Virgo cluster by looking at the stripped material from processed galaxies in the system. This study is motivated by the wealth of information we have on the Virgo ICC. Optical studies, that used Planetary Nebulas (PNS) and Globular Clusters (GCs) to trace the Virgo IC light (ICL) have shown that at the centre of Virgo the ICL is superposed to, however dynamically separated from, the stellar halo of the cluster's central, M87. They both grow through accretion events, however they have different velocity, and density distribution and parent stars, consistent with the M87 halo being redder and more metal rich than the ICL. Moreover the Virgo ICL is found to have a total dynamical mass of $M_{ICC} = 10.8 \pm 0.1 \times 10^{11}\,M_{\odot}$ within 1 deg radius from the cluster's centre (Longobardi et al. 2018a), and it is the accreted component from low and intermediate mass star-forming and dwarf-ellipticals galaxies (Longobardi et al. 2013, 2015a, 2018a,b). In

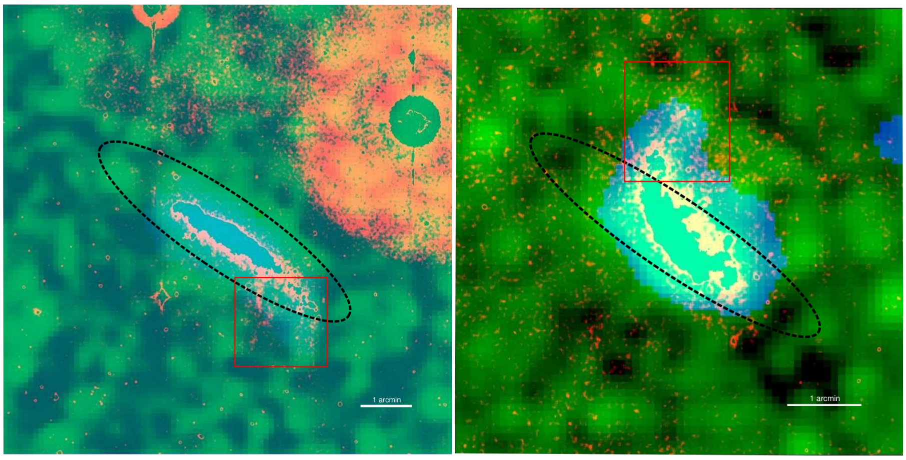

Fig. 2. From left to right, RGB colour composite images of NGC 4330 and NGC 4522, sub-sample of the galaxies studied in this work. Red, green and blue colours trace the Hα (VESTIGE), FIR (HeViCS), and HI (VIVA) emissions, respectively. The red boxes identify the regions we will propose to follow-up with ALMA, all enclosing the low surface-brightness tails of gas and dust extending outside the optical disk (black dotted ellipses). 1 arcmin scale bars are in white. North is up, East to the left.

parallel, studies of the gas/dust content in cluster members has shown that systems approaching regions of high density are found to be redder and gas/dust deficient with respect to the population of galaxies in the field (Boselli et al. 2006; Gavazzi et al. 2010; Cortese et al. 2012), scenario even more dramatic for low-mass galaxies (Davies et al. 2010; Boselli et al. 2014). If then the Virgo ICL is built up predominantly by tidal stripping of low mass star-forming and dwarf-elliptical galaxies, we do expect the presence of gas and dust in the IC space. They, in fact, could be removed from the cluster galaxies and transported to the IC component by the same environmental processes which remove their stellar content and/or by additional ram pressure phenomena (Cortese et al. 2010, 2012). In agreement with this scenario is a recent finding (Longobardi et al. 2019, in prep.) showing that it exists a diffuse dust component in the Virgo intra-cluster space (Fig.1), and characterised by a centrally concentrated profile, hence in agreement with what has been measured for its optical counterpart (Mihos et al. 2005; Longobardi et al. 2015b, 2018a,b). Thus, we have a unique opportunity to hunt for the ICC in the process of forming. Thanks to the complete and unique set of multifrequency data available for Virgo, the study is based on galaxies with clear HI (VIVA survey) and Hα (VESTIGE survey) asymmetric morphologies, that show similar distribution in their Herschel FIR emission. NGC4302, NGC4330, NGC4396, NGC4522, are four Virgo late-type galaxies with long tails of neutral and ionised gas, and dust. They are systems with stellar masses of the order of $M_* \sim 10^9\ M_\odot$, sitting at different distances from the cluster's centre, however all within 4 degrees from the cluster's core where the IC diffuse dust emission peaks (Longobardi et al., 2019, in prep.). Moreover, their low surface brightness tails of stripped material present patchy morphologies in their ionised gas distribution, that may trace recent star formation events, and lie outside the galaxies' optical disks (see Fig.2). Thus, they are likely going to be removed from the cluster spirals and to contribute to the ICC. The regions of interest for this study reach levels of Hα surface brightness $\Sigma_\alpha \sim 0.5 \times 10^{-17}\,\mathrm{erg\,s^{-1}\,cm^{-2}}$, HI column densities of the order of $2 \times 10^{19}\,\mathrm{cm^{-2}}$, hence dust flux densities $I_D \sim 0.1\,\mathrm{MJy\,sr^{-1}}$[*].

4 Summary and Conclusions

The ICC production in a cluster is an inevitable consequence of the hierarchical structure formation. It can reveal a great deal of information about the cluster's accretion history and its evolutionary state being tightley connect with the transformation and evolution of the galaxies in the cluster. The Virgo cluster is a dynamically young cluster where its IC stars are the accreted component from low and intermediate mass star-forming and dwarf-ellipticals galaxies. Based on this result, we are carrying out a multi-wavelength analysis of Virgo

[*]The dust flux densities have been obtained from the measured HI column densities via the relations described in Planck Collaboration et al. (2014), adopting $T = 20\,\mathrm{K}$ and a dust emissivity index, $\beta = 2$. Consistent values have been obtained when dust flux densities are estimated directly from the HeViCS FIR images

galaxies subject to environmental processing with the aim of tracing the undergoing formation of the ICC in the form of neutral and ionised gas, and dust. NGC4302, NGC4330, NGC4396, NGC4522, are our sample of Virgo late-type galaxies with clear HI (VIVA survey) and Hα (VESTIGE survey) asymmetric morphologies, that show similar distribution in their Herschel FIR emission. This study is tracing the relative fraction of the different components that constitute the IC content, also allowing us to answer the open question as to whether dust-to-gas ratios as measured in the main body of the galaxies also apply to the tails of the stripped material. Future follow-up observations with ALMA (Fig.2) will be able to resolve the FIR emission within compact regions of star formation providing the missing observational evidence of the in-situ origin of the ICC. Moreover, the VESTIGE survey is revealing for the first time long tails of ionised gas in several Virgo cluster galaxies also observed to have long HI tails. Similar studies will be then proposed to pursue a similar analysis on a larger sample of targets, with different physical properties (mass, environment, etc.), providing strong constraints for hydrodynamic simulations of structure formation.

This study is supported by the French Centre National d'Etudes Spatiales (CNES).

References

Binggeli, B., Tammann, G. A., Sandage, A., & Sandage, A.and Sandage, A. 1987, AJ, 94, 251
Boselli, A., Boissier, S., Cortese, L., et al. 2006, ApJ, 651, 811
Boselli, A., Boissier, S., Heinis, S., et al. 2011, A&A, 528, A107
Boselli, A., Fossati, M., Ferrarese, L., et al. 2018, A&A, 614, A56
Boselli, A., Voyer, E., Boissier, S., et al. 2014, A&A, 570, A69
C. S. Rudick et al. 2006, ApJ, 648, 936
Chung, A., van Gorkom, J. H., Kenney, J. D. P., Crowl, H., & Vollmer, B. 2009, AJ, 138, 1741
Conselice, C. J., Gallagher, III, J. S., & Wyse, R. F. G. 2001, ApJ, 559, 791
Cortese, L., Bendo, G. J., Isaak, K. G., Davies, J. I., & Kent, B. R. 2010, MNRAS, 403, L26
Cortese, L., Ciesla, L., Boselli, A., et al. 2012, A&A, 540, A52
Davies, J. I., Baes, M., Bendo, G. J., et al. 2010, A&A, 518, L48
Ferrarese, L., Côté, P., Cuillandre, J.-C., et al. 2012, ApJS, 200, 4
Gavazzi, G., Fumagalli, M., Cucciati, O., & Boselli, A. 2010, A&A, 517, A73
Krick, J. E., Bridge, C., Desai, V., et al. 2011, ApJ, 735, 76
Longobardi, A., Arnaboldi, M., Gerhard, O., et al. 2013, A&A, 558, A42
Longobardi, A., Arnaboldi, M., Gerhard, O., & Hanuschik, R. 2015a, A&A, 579, A135
Longobardi, A., Arnaboldi, M., Gerhard, O., & Mihos, J. C. 2015b, A&A, 579, L3
Longobardi, A., Arnaboldi, M., Gerhard, O., Pulsoni, C., & Söldner-Rembold, I. 2018a, A&A, 620, A111
Longobardi, A., Peng, E. W., Côté, P., et al. 2018b, ApJ, 864, 36
Mei, S., Blakeslee, J. P., Côté, P., et al. 2007, ApJ, 655, 144
Mihos, J. C., Harding, P., Feldmeier, J., & Morrison, H. 2005, ApJ, 631, L41
Mihos, J. C., Harding, P., Feldmeier, J. J., et al. 2017, ApJ, 834, 16
Muller, S., Wu, S. Y., Hsieh, B. C., et al. 2008, ApJ, 680, 975
Nulsen, P. E. J. & Bohringer, H. 1995, MNRAS, 274, 1093
Planck Collaboration, Abergel, A., Ade, P. A. R., et al. 2014, A&A, 571, A11
Puchwein, E., Springel, V., Sijacki, D., & Dolag, K. 2010, MNRAS, 406, 936
Simionescu, A., Werner, N., Mantz, A., Allen, S. W., & Urban, O. 2017, MNRAS, 469, 1476
Werner, M. W., Roellig, T. L., Low, F. J., et al. 2004, ApJS, 154, 1
Willman, B., Governato, F., Wadsley, J., & Quinn, T. 2004, MNRAS, 355, 159

SF2A 2019
P. Di Matteo, O. Creevey, A. Crida, G. Kordopatis, J. Malzac, J.-B. Marquette, M. N'Diaye, O. Venot (eds)

DETECTION OF INTRA-CLUSTER DIFFUSE LIGHT: PRESENTING DAWIS

A. Ellien[1], F. Durret[1] and C. Adami[2]

Abstract. We present our new wavelet package, `DAWIS`, developped to detect intra-cluster light (ICL), the optical diffuse component of galaxy clusters. We use it to investigate the properties of a massive galaxy cluster at $z \sim 0.5$, MACS J0717.5+3745, and of its extended filament. Using *Hubble* Frontier Fields* (HFF) data in the F105W, F814W, F606W, and F435W filters, we compute the ICL fractions in the core of MACS J0717.5+3745, and find large contributions of ICL, a result that is consistent with other studies.

Keywords: Image processing, Galaxies, Galaxy clusters, Photometry

1 Introduction

Since the first mention by Zwicky (1951) of a very diffuse and extended halo of light around the central galaxy of the Coma cluster, the so-called ICL has been a growing field of research in astronomy. We now believe that it is composed of stars which are not gravitationally bound to any galaxy in particular, but are rather bound to the global gravitational potential of a galaxy cluster. While the presence of ICL in galaxy clusters is no longer questioned, its formation mechanisms are still a matter of debate, whether it is due to violent galaxy-galaxy interactions (Mihos 2004), to tidal stripping (Byrd & Valtonen 1990) or to star formation (Sommer-Larsen 2006).
The ICL is a very low-surface-brightness source, and its detection is a tricky task, due to the various instrumental effects (point spread function, scattered light, flat-fielding error...), the need for deep photometric data, and contamination by other astronomical features (bright foreground stars, galaxtic cirrus). Various methods have been used to perform this analysis, such as galaxy light profile fitting (Jiménez-Teja & Dupke 2016)), raw masking of sources (Montes & Trujillo 2018) or wavelet analysis (Da Rocha et al. 2008). Here we chose a wavelet analysis approach and created `DAWIS`, a Detection Algorithm with Wavelets for Intra-cluster light Surveys which is parallelized and optimized to run on large images.

2 `DAWIS` in a nutshell

`DAWIS` is based on Mallat's *à trous* wavelet algorithm (Shensa 1992), which is particularly suited for astronomical images. It is a fast, discrete, redundant wavelet transform that respects flux conservation. By applying this algorithm, an image is convolved in N_{lvl} wavelet planes, following a multi-scale vision as described in Bijaoui & Rué (1995). The process is done by iteratively smoothing the original image $N_{\mathrm{lvl}} + 1$ times with a varying B-spline kernel, the difference between two successive smoothed images giving a wavelet plane. Each wavelet plane contains features with a characteristic size of 2^n pixels, n being the index of the plane ($n = 0, 1, 2, 3, ..., N_{\mathrm{lvl}}$). Small values of n correspond to bright and compact luminous features, while greater values correspond to large and low-intensity ones, with $n = N_{\mathrm{lvl}}$ corresponding to the large sky background variations.
After the wavelet convolution, astronomical objects are decomposed into several features through the different wavelet planes. In each plane, we apply a thresholding to determine the statistically significant pixels composing these features. The detection threshold is estimated in each wavelet plane separately: a standard deviation of the intensity, σ_n, is computed using a 3σ clipping algorithm, and the significant pixels are set to have intensity

[1] Sorbonne Université, CNRS, UMR 7095, Institut d'Astrophysique de Paris, 98bis Bd Arago, F-75014 Paris
[2] Aix-Marseille Univ., CNRS, CNES, LAM, Marseille, France
*`https://archive.stsci.edu/pub/hlsp/frontier/`

Table 1. Detection thresholds and ICL fractions computed for each of the four filters of the HFF. The thresholds are used to create the ICL maps from the residual images (see Fig. 2). The fractions are computed from the ICL maps and the reconstructed images in the four filters within the radius that is indicated for each filter. Error bars correspond to the 95% confidence intervals. The radii are the same as in Jiménez-Teja et al. (2019) for comparison purposes.

HFF	F435W	F606W	F814W	F105W
$3\sigma_{\rm bkg}$ (mag.arcsec^{-2})	29.89	29.96	30.03	29.97
$5\sigma_{\rm bkg}$ (mag.arcsec^{-2})	29.34	29.41	29.50	29.41
Radius (kpc)	275.3	562.5	421.5	FoV
$f_{\rm ICL}(\%)$	$2.48^{+0.19}_{-0.20}$	$24.43^{+3.37}_{-1.71}$	$16.10^{+1.03}_{-1.03}$	$13.22^{+1.76}_{-1.49}$

values higher than $k\sigma_n$. This threshold is different for each wavelet plane, but the same value k is applied everywhere.
After thresholding, the significant pixels are grouped in regions using scale-by-scale segmentation. We then create inter-scale trees by linking together significant regions from different planes by looking at their spatial distribution. Trees with connected regions from at least three different planes are recognized as valid representations of astronomical objects in the wavelet space. The objects are then reconstructed using a conjugate gradient algorithm (Starck et al. 1998).

3 ICL in MACS J0717.5+3745

After pre-processing (binning, point spread function deconvolution, masking of foreground sources, see Ellien et al. (2019) for more details), we apply `DAWIS` to images from the HFF in four bands: F105W, F814W, F606W, and F435W. For each image we detect and reconstruct all the galaxies (see Figure 1), and then create residual images by subtracting all those features from the original one (see Figure 2). We then detect ICL in the residual images by computing a detection threshold $\sigma_{\rm bkg}$ from the sky background (see Table 1). The ICL fractions are computed using the following formula

$$f_{\rm ICL} = \frac{F_{\rm ICL}}{F_{\rm gal} + F_{\rm ICL}}, \tag{3.1}$$

where $F_{\rm ICL}$ is the integrated flux of ICL and $F_{\rm gal}$ is the integrated flux of MACS J0717.5+3745's galaxies. $F_{\rm ICL}$ is obtained by summing the pixel values with values greater than $3\sigma_{\rm bkg}$ in the ICL maps, and $F_{\rm gal}$ is obtained by summing the pixel values of the cluster's galaxy profiles in the reconstructed images. The errors on the ICL fraction are computed with a bootstrap on the values of the pixels of the galaxies and of the pixels of the ICL. For each filter, we create a sample with all the pixels belonging to Red Sequence galaxies of the reconstructed image, and a sample with all the ICL pixels of the residual image. We draw $N = 10000$ sub-samples randomly from each sample, allowing the same pixel value to be drawn multiple times. We then compute the given ICL fraction for each sub-sample which gives N values of ICL fractions for each filter. The errors on the true ICL fraction value are then estimated by computing a 95% confidence interval on the sub-sample values.

4 Conclusions

Our resulting ICL fractions (see Table 1) are coherent with previous studies such as Jiménez-Teja et al. (2019) where they find ICL fractions (in %) of 7.22 ± 0.81 in the F435W, 22.27 ± 3.68 in the F606W and 13.63 ± 3.60 in the F814W. This showcases `DAWIS` ability to detect and reconstruct galaxies in an image up to high precision. We find that there is almost no ICL in the F435W filter (UV rest frame), indicating that there is little star formation in the ICL. The ICL fraction seems to peak in the F606W before slowly decreasing as it gets redder. In parallel, we tried to detect intra-filament light (IFL) in the extended cosmic filament associated to MACS J0717.5+3745 using the same analysis method but in a different *Hubble* Space Telescope mosaic, without success. More informations about the core of MACSJ 0717.5+3745 and a study of its extended filament can be found in Ellien et al. (2019).

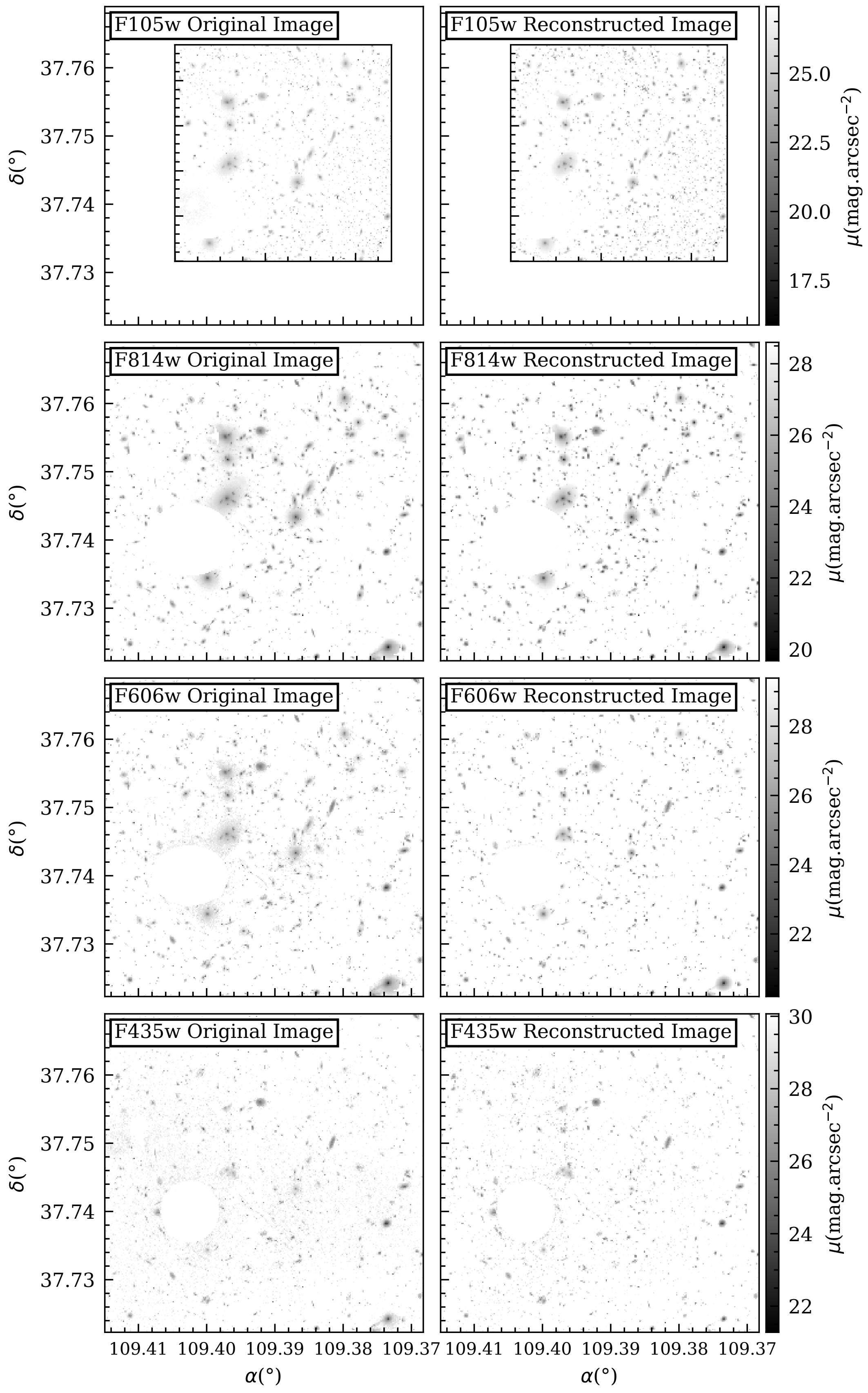

Fig. 1. Left column: original HFF images in the four filters after PSF deconvolution and masking of star residuals and of the large foreground galaxy. Right column: stacked images of objects detected and reconstructed by three runs of `DAWIS`.

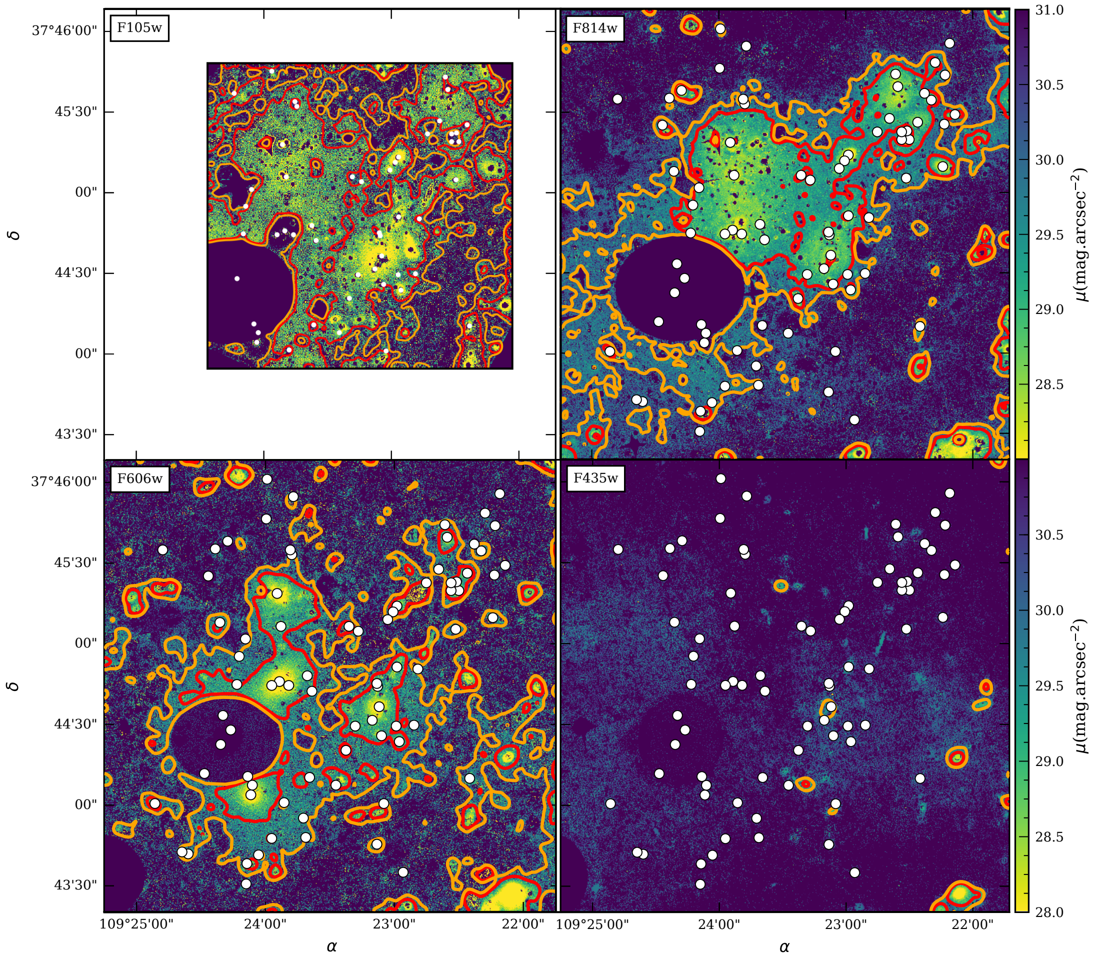

Fig. 2. Surface brightness maps of the residuals after wavelet processing by `DAWIS` in each band. The orange contours show $3\sigma_{\rm bkg}$ detection and the red ones $5\sigma_{\rm bkg}$. The white dots show the galaxies in the cluster redshift range ($0.53 < z < 0.56$). From top to bottom and left to right: F435W, F606W, F814W, and F105W. The contours are smoothed with a Gaussian kernel of $\sigma = 5$ for the map to be readable.

References

Bijaoui, A. & Rué, F. 1995, Signal Processing, 46, 345

Byrd, G. & Valtonen, M. 1990, ApJ, 350, 89

Da Rocha, C., Ziegler, B. L., & Mendes de Oliveira, C. 2008, MNRAS, 388, 1433

Ellien, A., Durret, F., Adami, C., et al. 2019, A&A, 628, A34

Jiménez-Teja, Y. & Dupke, R. 2016, ApJ, 820, 49

Jiménez-Teja, Y., Dupke, R. A., Lopes de Oliveira, R., et al. 2019, A&A, 622, A183

Mihos, J. C. 2004, in IAU Symposium, Vol. 217, Recycling Intergalactic and Interstellar Matter, ed. P.-A. Duc, J. Braine, & E. Brinks, 390

Montes, M. & Trujillo, I. 2018, MNRAS, 474, 917

Shensa, M. J. 1992, IEEE Trans. Signal Processing, 40, 2464

Sommer-Larsen, J. 2006, MNRAS, 369, 958

Starck, J.-L., Murtagh, F. D., & Bijaoui, A. 1998, Image Processing and Data Analysis, 297

Zwicky, F. 1951, PASP, 63, 61

Session 08

Particle acceleration in astrophysical and space plasmas

ELECTRON ACCELERATION IN THE CRAB NEBULA

G. Giacinti[1] and J. G. Kirk[1]

Abstract. We study electron and positron acceleration at the termination shock of a striped pulsar wind. Drift motion along the shock surface keeps either electrons or positrons —but not both, close to the equatorial plane of the pulsar, where they are accelerated by the first-order Fermi process. Their energy spectrum is a power law, and both the X-ray flux and photon index of the Crab Nebula, as measured by NuSTAR, can be reproduced for sufficiently large downstream turbulence levels. The fact that one sign of charge is preferentially accelerated could have important implications for the interpretation of the positron fraction in cosmic-rays.

Keywords: acceleration of particles, plasmas, pulsars: general, shock waves, X-rays: individual (Crab)

1 Introduction

The Crab Nebula is thought to accelerate electrons and/or positrons up to at least a PeV (e.g., Bühler & Blandford 2014). However, the mechanisms and sites of particle acceleration still remain uncertain. The photon index of the Nebula in X-rays (Madsen et al. 2015) is very close to expectations for electrons accelerated by the first order Fermi mechanism at an ultra-relativistic shock with isotropic particle scattering (Bednarz & Ostrowski 1998; Kirk et al. 2000). However, the magnetic field is expected to be toroidal close to the pulsar wind termination shock (TS), i.e., the TS is perpendicular. On the one hand, diffusive shock acceleration is known to be inoperative at perpendicular shocks (Begelman & Kirk 1990; Sironi & Spitkovsky 2009). On the other hand, the toroidal field in the downstream region of the TS is expected to change sign across the equatorial plane of the pulsar (e.g., Porth et al. 2016): in this region, turbulence levels may be higher, and diffusive shock acceleration might still operate. We study here electron and positron acceleration in this region of the TS, by propagating individual particles in a model of the magnetic field and flow pattern (Giacinti & Kirk 2018).

2 Model

We show in Fig. 1 a sketch of the Crab Nebula with the location of the region of interest. In the left panel, the extents of the X-ray and optical nebulae are drawn as they appear on the sky, together with an estimate of the position of the TS. The centre panel is an enlargement of the equatorial region of the Crab pulsar wind (labelled "wind"). The TS is plotted with the solid red line. Its radius is $r_{\rm TS} \simeq 4.3 \times 10^{17}$ cm. The rotation axis of the pulsar (blue arrow) is contained in the plane of the figure, and the magnetic axis (green arrow) is drawn at a phase at which it lies in this plane too. The horizontal dashed blue line corresponds to the equatorial plane. Magnetic field oscillations, or stripes, are present upstream of the TS between the latitudes $-\Theta$ and $+\Theta$, where Θ denotes the angle between the magnetic and rotation axes. The magnetic field is toroidal and points in opposite directions above and below the current sheet (thin green line). The stripes are destroyed at the TS, and the field in the downstream ("nebula") is expected to be toroidal too. It reverses sign across the equatorial plane, and its amplitude grows with distance to this plane (e.g., Porth et al. 2016). The black rectangle in the centre panel, and its enlargement in the right panel correspond to the region we model hereafter. It is typically a few percent of the shock area, and we therefore assume that the TS is a plane and that the flow is planar. In the cartesian coordinate system defined in Fig. 1, the fluid flows along $+\hat{\mathbf{x}}$. In the simulations, we set the Lorentz factor of the fluid in the upstream ($x < 0$) to $\Gamma_{\rm s} = 100$, but results do not depend on $\Gamma_{\rm s}$ as long as it is $\gg 10$. In

[1] Max-Planck-Institut für Kernphysik, Postfach 103980, 69029 Heidelberg, Germany

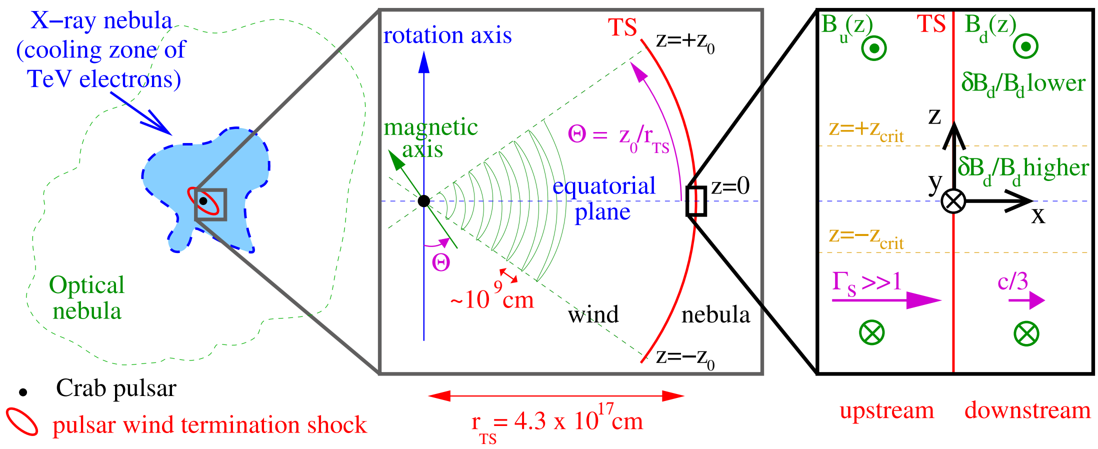

Fig. 1. Sketch of the Crab Nebula (left panel), with the location and characteristics of the region studied in this work (right panel). A description of this Figure is provided in the text in §2.

the downstream, the fluid velocity is assumed to be $c/3$. For the toroidal magnetic field in the downstream, we take $\mathbf{B}_{\rm d}(z) = -B_{\rm d,0}(z/z_0)\hat{\mathbf{y}}$ —defined in the downstream rest frame (RF), with $z_0 = \Theta r_{\rm TS}$ and $B_{\rm d,0} = +1$mG. $B_{\rm d,0} > 0$ sets the polarity of the pulsar. In the upstream, the wavelength of the stripes ($\approx 10^9$ cm) is significantly smaller than the gyroradii of the particles considered here, which effectively probe the phase-averaged field. For the upstream magnetic field, we then take $\mathbf{B}'_{\rm u}(z) = (-B_{\rm d,0}/(2\sqrt{2}\beta_{\rm s})) \times (z/z_0)\hat{\mathbf{y}}$ —defined in the shock RF, where $\beta_{\rm s}$ is the velocity of the upstream fluid in the shock RF. We also add a 3D homogeneous turbulent field in the downstream, with root-mean-square strength $\delta B_{\rm d}$ —defined in the downstream RF. Consequently, turbulence levels $\eta = \delta B_{\rm d}/|\mathbf{B}_{\rm d}|$ are larger close to the equatorial plane, which is in line with results from MHD simulations of the Nebula (e.g., Porth et al. 2016). The turbulent field is defined on a 3D grid with 256 vertices per side, repeated periodically in space, using the method of Giacinti et al. (2012). We use isotropic turbulence with a Bohm spectrum, but our results do not noticeably depend on the spectrum. For technical reasons (Giacinti & Kirk 2018), we add weak turbulence in the upstream, but our results are not influenced by it. We inject electrons and positrons at the TS with their momenta directed along $+\hat{\mathbf{x}}$, and with an energy $E_{\rm inj,d} = 1\,$TeV which is in the relevant range for the Crab Nebula. We integrate the particle trajectories in the downstream and upstream RFs where the electric fields vanish, and do a Lorentz transformation at each shock crossing. Defining $z_{\rm crit}$ as the height at which the gyroradius in $\mathbf{B}_{\rm d}(z_{\rm crit})$ of an injected particle is equal to $z_{\rm crit}$, one has $z_{\rm crit} = \sqrt{z_0 E_{\rm inj,d}/eB_{\rm d,0}} \simeq 5.8 \times 10^{14}\,{\rm cm}\sqrt{z_0/10^{17}\,{\rm cm}}$. The region where injected particles are efficiently accelerated is typically $|z| \lesssim$ several $z_{\rm crit}$.

3 Results

We show in Fig. 2 the trajectories of 4 electrons (left panel) and 4 positrons (right) injected at the TS ($x = 0$, solid black lines) at $|z| < 1.5 \times 10^{15}$ cm, and accelerated via the first-order Fermi process, in a simulation where $z_0 = 10^{17}$ cm and $\delta B_{\rm d} = 30\,\mu$G. The trajectories are plotted in the shock RF and projected onto the (x,z) plane. The dashed orange lines represent $z = \pm z_{\rm crit}$. In the simulations, about 90 to 95% of injected particles are advected in the downstream without gaining energy. By comparing the two panels, one can see that the two signs of charge behave differently. For this pulsar polarity ($B_{\rm d,0} > 0$), electrons are focused towards the equatorial plane (black dotted line), whereas positrons tend to be pushed away from it. This is due to drift motion on the shock surface: electrons entering the upstream at an altitude z_1 tend to come back in the downstream at z_2 such that $|z_2| < |z_1|$, whereas positrons tend to re-enter the downstream at $|z_2| > |z_1|$. Since the turbulence levels are larger at small $|z|$, electrons remain confined in the region which is the most favourable for diffusive shock acceleration. A number of them stay on "Speiser" orbits (e.g., the magenta trajectory in the left panel), and cross and re-cross the TS many times. In contrast, positrons are pushed away from this favourable region, and their acceleration quickly stops. Therefore, only electrons are accelerated to very high energies. For the opposite pulsar polarity ($B_{\rm d,0} < 0$), the situation would be the opposite. The energy spectrum of the particles that are efficiently accelerated is a power-law $dN/dE \propto E^{\alpha_{\rm e}}$, where $\alpha_{\rm e}$ depends on the downstream turbulence level and lies in the range $\simeq -1.8$ to -2.4. We plot in Fig. 3 (left panel) the values of $\alpha_{\rm e}$ obtained in our simulations,

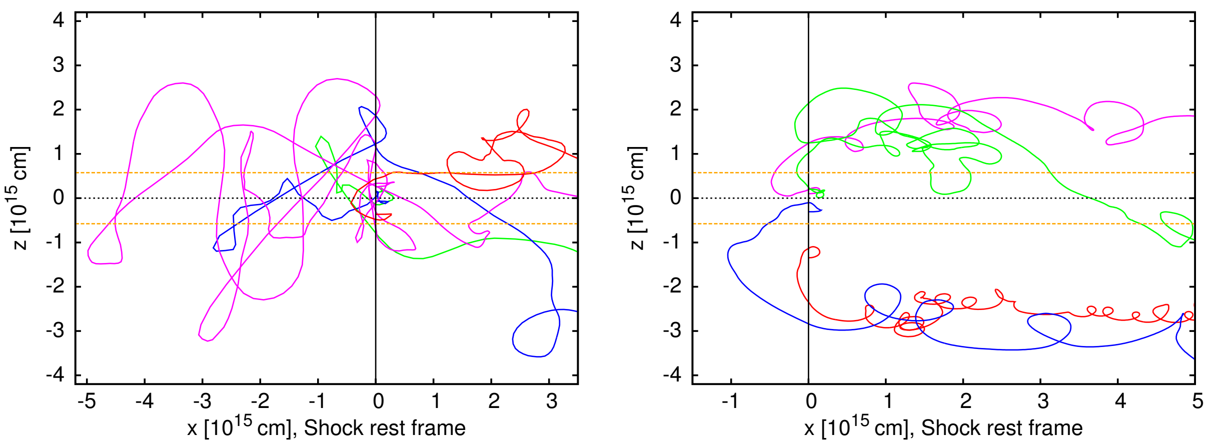

Fig. 2. Left: Trajectories of electrons injected in the equatorial region of the TS. The upstream is on the left hand side of the shock ($x = 0$, solid black line). **Right:** Trajectories of positrons for the same parameters. See §3 for more details.

versus $\eta_{\rm crit} \equiv \delta B_{\rm d}/|\mathbf{B}_{\rm d}|\,|_{z=z_{\rm crit}}$, for $z_0 = 10^{17}$ cm (solid red line) and $z_0 = 6 \times 10^{17}$ cm (black circles). We find that $\alpha_{\rm e}$ is a function of $\eta_{\rm crit}$ and does not depend on z_0. For low levels of turbulence $\eta_{\rm crit} \approx 1 - 30$, the spectrum is harder than E^{-2}. It softens to $E^{-2.2}$ for larger turbulence levels, which corresponds to the slope that is required to explain the X-ray photon index of the Crab Nebula as measured by NuSTAR. At $\eta_{\rm crit} < 1$, the spectrum also softens, but too few electrons are accelerated to explain the X-ray flux from the Nebula.

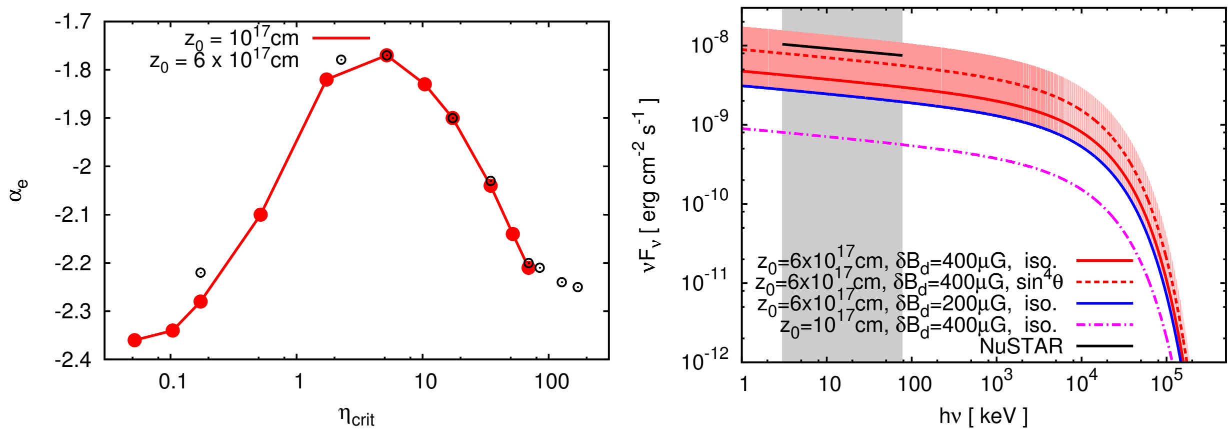

Fig. 3. Left: Spectral index of the accelerated electrons, $\alpha_{\rm e}$, as a function of $\eta_{\rm crit}$. **Right:** Predicted synchrotron spectra for the Crab Nebula versus NuSTAR measurements. See the text in §3 for explanations.

Electrons accelerated at the TS are advected in the Nebula where they cool. Assuming that the maximum electron energy at the TS is equal to 1 PeV —as would be expected if it is limited by synchrotron losses in a typical magnetic field strength of ~ 0.5 mG, we calculate the synchrotron spectrum from the cooled electrons and plot the results in Fig. 3 (right panel), for four sets of parameter values. See the key for the values of z_0 and $\delta B_{\rm d}$, and for the isotropy ("iso.") or anisotropy of the pulsar wind. We consider both isotropic and $\propto \sin^4\theta$ winds, where θ denotes the colatitude. We use 2.0 kpc for the distance to the Crab pulsar. The effect of the uncertainty on this distance (± 0.5 kpc) for the two red lines is shown with the area shaded in red. The solid black line corresponds to the measurements from NuSTAR in the $3 - 78$ keV band (Madsen et al. 2015). Our model can reproduce them for sufficiently large values of $\delta B_{\rm d}$ ($\geq 200\,\mu$G) and z_0. The magenta dashed-dotted line for $z_0 = 10^{17}$ cm (i.e., $\Theta \simeq 13°$) and $\delta B_{\rm d} = 400\,\mu$G is about an order magnitude below the measurements, but we obtain a larger X-ray flux for $z_0 = 6 \times 10^{17}$ cm (i.e., $\Theta \simeq 80°$): the blue and red solid lines correspond to $\delta B_{\rm d} = 200\,\mu$G and $\delta B_{\rm d} = 400\,\mu$G for an isotropic wind. The red dashed line is for a $\propto \sin^4\theta$ wind and $\delta B_{\rm d} = 400\,\mu$G. We can reproduce the data with these parameters. $|\mathbf{B}_{\rm d}|(z) \propto |z|$ here, and the measurements would be reproduced with smaller values of Θ and δB_{d}, if one adopts a shallower dependence of $|\mathbf{B}_{\mathrm{d}}|$ on z.

4 Discussion

We find that the acceleration of X-ray emitting electrons occurs preferentially in the equatorial region of the TS. Interestingly, modeling of the high-energy emission from the Crab Nebula is compatible with these electrons being accelerated in, or close to, this region (Olmi et al. 2016). Shock-drift plays an important role, and ensures that the accelerated electrons remain in the equatorial region of the TS. For sufficiently large turbulence levels, the electron spectral index tends towards -2.2, which is compatible with theoretical expectations (e.g., Bednarz & Ostrowski 1998). For lower turbulence levels, the spectral index increases up to -1.8. This may explain the hard photon index measured in the central regions of the Nebula by the Chandra X-ray Observatory (Mori et al. 2004), as turbulence levels may vary with time and position at the TS. We note that other effects, such as shock corrugation (Lemoine 2016), may also play a role in the acceleration of X-ray emitting electrons, and that another acceleration mechanism may operate upon the electrons responsible for the radio to optical emission of the Nebula (Olmi et al. 2016; Lyutikov et al. 2019). The gamma-ray flares detected by AGILE and Fermi-LAT from the Crab Nebula require another acceleration mechanism too, such as inductive acceleration in the striped wind (Kirk & Giacinti 2017, 2019). Finally, the fact that each pulsar may accelerate preferentially either electrons or positrons to high energy, but not both, could have important implications for the interpretation of the positron fraction in cosmic-rays. Studies usually assume that pulsars accelerate electrons and positrons in equal numbers. Under this assumption, the fact that the AMS-02 positron fraction saturates well below 0.5 seems to rule out nearby pulsars as the main source of the high-energy electrons and positrons detected at Earth (Recchia et al. 2019). However, our above findings show that pulsars do remain viable candidates, as long as the local pulsar(s) responsible for these fluxes favour electrons over positrons.

5 Conclusions

We study particle acceleration at the TS of a striped pulsar wind. We find that either electrons or positrons are accelerated to very high energy, depending on the relative orientations of the magnetic and rotation axes of the pulsar. Drift motion on the shock surface keeps the accelerated particles close to the equatorial plane of the pulsar, allowing them to be accelerated by the first order Fermi process at the TS. Their energy spectrum is a power law, with index in the range -1.8 to -2.4. Both the X-ray flux and photon index of the Crab Nebula, as measured by NuSTAR, can be reproduced for sufficiently large turbulence levels downstream of the shock. Our results strongly question the assumption often used in studies of the positron fraction that pulsars accelerate electrons and positrons to high energy in equal numbers.

This research was supported by a Grant from the GIF, the German-Israeli Foundation for Scientific Research and Development.

References

Bednarz, J. & Ostrowski, M. 1998, Physical Review Letters, 80, 3911
Begelman, M. C. & Kirk, J. G. 1990, ApJ, 353, 66
Bühler, R. & Blandford, R. 2014, Reports on Progress in Physics, 77, 066901
Giacinti, G., Kachelrieß, M., Semikoz, D. V., & Sigl, G. 2012, JCAP, 7, 031
Giacinti, G. & Kirk, J. G. 2018, ApJ, 863, 18
Kirk, J. G. & Giacinti, G. 2017, Physical Review Letters, 119, 211101
Kirk, J. G. & Giacinti, G. 2019, arXiv e-prints, arXiv:1908.06507
Kirk, J. G., Guthmann, A. W., Gallant, Y. A., & Achterberg, A. 2000, ApJ, 542, 235
Lemoine, M. 2016, Journal of Plasma Physics, 82, 635820401
Lyutikov, M., Temim, T., Komissarov, S., et al. 2019, Monthly Notices of the Royal Astronomical Society, 2051
Madsen, K. K., Reynolds, S., Harrison, F., et al. 2015, ApJ, 801, 66
Mori, K., Burrows, D. N., Hester, J. J., et al. 2004, ApJ, 609, 186
Olmi, B., Del Zanna, L., Amato, E., Bucciantini, N., & Mignone, A. 2016, Journal of Plasma Physics, 82, 635820601
Porth, O., Vorster, M. J., Lyutikov, M., & Engelbrecht, N. E. 2016, MNRAS, 460, 4135
Recchia, S., Gabici, S., Aharonian, F. A., & Vink, J. 2019, Physical Review D, 99, 103022
Sironi, L. & Spitkovsky, A. 2009, ApJ, 698, 1523

SF2A 2019
P. Di Matteo, O. Creevey, A. Crida, G. Kordopatis, J. Malzac, J.-B. Marquette, M. N'Diaye, O. Venot (eds)

OBSERVATION OF PARTICLE ACCELERATION IN THE SOLAR CORONA WITH NEUTRON MONITORS AND RADIO INSTRUMENTS

K.-L. Klein[1]

Abstract. In the attempt to identify regions and mechanisms of relativistic proton acceleration at the Sun, we compare the arrival of the first particles at Earth, measured by neutron monitors, with radio signatures of electron acceleration in the corona. The first proton arrival is often, but not always, delayed with respect to the early radio signatures at the Sun. But the release at the Sun always occurs at times when the radio emission is ongoing. This is in line with earlier studies of individual events, which made us conclude that relativistic protons are accelerated in flare-like processes related to magnetic reconnection or turbulence in the wake of a coronal mass ejection, rather than at the shocks driven by the ejected magnetic stuctures.

Keywords: Sun: particle emission, Sun: radio radiation, Sun: flares, Sun: coronal mass ejections (CMEs)

1 Introduction

The solar corona, structured by magnetic fields that emanate from the convection zone, accelerates episodically particles from suprathermal to sometimes relativistic energies. Energetic electrons can be probed in the solar atmosphere through their hard X-ray and radio emission, and ions through gamma-rays (see review by Vilmer and Musset, these proceedings). Due to its proximity, the Sun has the unique advantage that one can also probe directly energetic particle populations, provided they escape into the interplanetary space.

Spacecraft usually measure electrons up to MeV energies, and protons and ions up to about 100 MeV. Ground-based measurements of secondary particles generated by solar protons and ions in the Earth's atmosphere demonstrate that on occasion the Sun accelerates nuclei to GeV energies. The rarity of the events (one/year on average seen since 1942, but only three between 2006 and 2019) and the downward-curved shape of the energy spectra (Tylka & Dietrich 2009) show that the highest energies are in the GeV to a few tens-of-GeV range. While three such events were also detected in space by the PAMELA mission (Bruno et al. 2018), 72 have been seen by ground-based detectors, mostly detectors of secondary neutrons. These detectors are called neutron monitors. Particle events detected on the Earth are called ground-level events (GLEs).

Theory and modelling show that relativistic particles can in principle be accelerated in two different environments in the solar corona: in reconnecting current sheets (e.g., Heerikhuisen et al. 2002) and at large-scale shock waves (e.g., Afanasiev et al. 2018) driven by coronal mass ejections (CMEs). Since both processes occur in the eruptive events at the Sun that accompany GLEs, observational criteria are needed to identify which is most plausible. A key observable is the start time of a GLE, i.e. the time of detection of the first relativistic protons at the Earth, with respect to the timing of the particle acceleration in the solar corona. In the present report we compare the start time of relatively strong GLEs with the time evolution of electron acceleration in the corona, as traced by the radio emission.

2 Onset timing of relativistic solar particle events

Gopalswamy et al. (2012) measured the onset of 16 GLEs between 1997 and 2006, and concluded that it is later than expected if the first relativistic protons were accelerated together with the electrons in the associated flare traced by the rise of the soft X-ray emission. They ascribed the delay to the time needed by a CME to form a shock wave in the corona, and concluded that the accelerator of the relativistic protons was the shock,

[1] LESIA, Observatoire de Paris, Université PSL, CNRS, Sorbonne Université, Université Paris, 92190 Meudon, France

Table 1. Onset times and onset-time delays of GLEs.

Date	Duration cm-λ	m-λ	GLE start	Delay [min] (GLE-m-λ)	GLE start (Gopalswamy et al.)
1997 Nov 06 OULU	11:52-12:10	11:52-14:00	12:08 (11:46,12:28)	16 (-6, 36)	12:10
2000 Jul 14 SOPO	10:10 (HXR)	10:16-10:40	10:34 (10:34,10:35)	18 (18, 19)	10:30
2001 Apr 15 SOPO	13:45-15:20	13:47-14:50	13:58 (13:58, 13:58)	11 (11, 11)	14:00
2003 Oct 28 MCMU	11:01-12:15	11:03-12:05	11:13 (11:10, 11:16)	10 (7, 13)	11:20
2003 Oct 29 SOPO	20:38-21:30	20:38-$>22:00$	21:01 (21:00, 21:02)	23 (22, 24)	21:05
2005 Jan 20 TERA	06:38-08:00	06:44-07:50	06:49 (06:49, 06:49)	5 (5, 5)	06:50
2006 Dec 13 OULU	02:22-04:45	02:24-04:45	02:50 (02:49, 02:51)	26 (25, 27)	02:45
2017 Sep 10 FSMT	15:52-16:50	15:50-16:40	16:02 (15:57-16:06)	12 (7, 16)	-

rather than the reconnection processes in the lower corona. This conclusion was contradicted by the timing of the strongest GLE observed during the space age, on 2005 Jan 20 (Masson et al. 2009; Klein et al. 2014, and references therein). Those studies found that the onset of the GLE, which was particularly well-identified due to its fast rise, was consistent with acceleration since the early signatures of the associated flare at radio and hard X-ray wavelengths, as well as gamma-rays from pion-decay photons, which are due to protons or ions with energies comparable to those detected by neutron monitors. So there seems to be a contradiction between conclusions drawn from a sample of GLEs, and conclusions based on a detailed timing analysis of the best-observed event.

2.1 Determination of GLE onset

To explore this apparent contradiction, we conduct a new timing analysis of GLEs observed since 1997, with the exception of very weak events detected only marginally by neutron monitors. Neutron monitor data were provided by the neutron monitor data base NMDB (`www.nmdb.eu`) hosted at the University of Kiel. The start times were determined for the first responding neutron monitor, which detects particles that propagate along the heliospheric magnetic field. The usual estimate of the start time is the instant when the count rate exceeds the pre-event level. This is overestimated, since the previously existing signal is buried in the detector noise. In the present study start times were determined through a linear fit to the early rise of the logarithm of the count rate (i.e. it is supposed that the early rise is exponential). The start time given in col. 4 of Table 1 is the time when the straight line fit intersects the pre-event background. The values within parentheses give the times when the line intersects the pre-event background plus and minus three times the standard deviation. Column 5 is the delay with respect to the start of the m-λ emission. Column 6 gives the start times of Gopalswamy et al. (2012). These authors considered the onset as the time when the signal exceeded the background by at least 2%. The two determinations of the onset are consistent to within a few minutes. The start time determination is therefore not the reason for the conflicting conclusions.

2.2 Comparison with the timing of radio emission

Columns 2 and 3 of Table 1 give the onset and approximate end of the radio emission at centimetre and metre-wavelengths, inferred from whole Sun flux densities observed by the RSTN network of the US Air Force*. Delays of a few minutes are observed, with the m-λ emission lagging behind the cm-λ burst. Since higher frequencies correspond to lower coronal heights, this may show a confinement of the first accelerated electrons in the lower corona. The delays of the GLE start with respect to the start of the m-λ emission are listed in col. 5. A few GLEs start within a few minutes of the coronal signatures of electron acceleration. Since the travel time of protons of 450 MeV, which is the lower limit of the energy spectrum detectable by neutron monitors, and which travel at a speed of $0.75c$, is about 13 min (i.e. light travel time + 5 min), these delays may be consistent with acceleration of the first protons of the GLE in the very early phase of energy release in the corona, which points to the parent flare and the associated magnetic reconnection and turbulence. Among them is the 2005 Jan 20 GLE, for which Masson et al. (2009) demonstrated the relationship in detail. The 1997 Nov 06 GLE has a very uncertain start, due to a long shallow rise. Three GLEs have more substantial delays (18-26 min).

*Data provided by the National Centers for Environmental Information (NOAA) `https://www.ngdc.noaa.gov/stp/space-weather/solar-data/solar-features/solar-radio/rstn-1-second/`

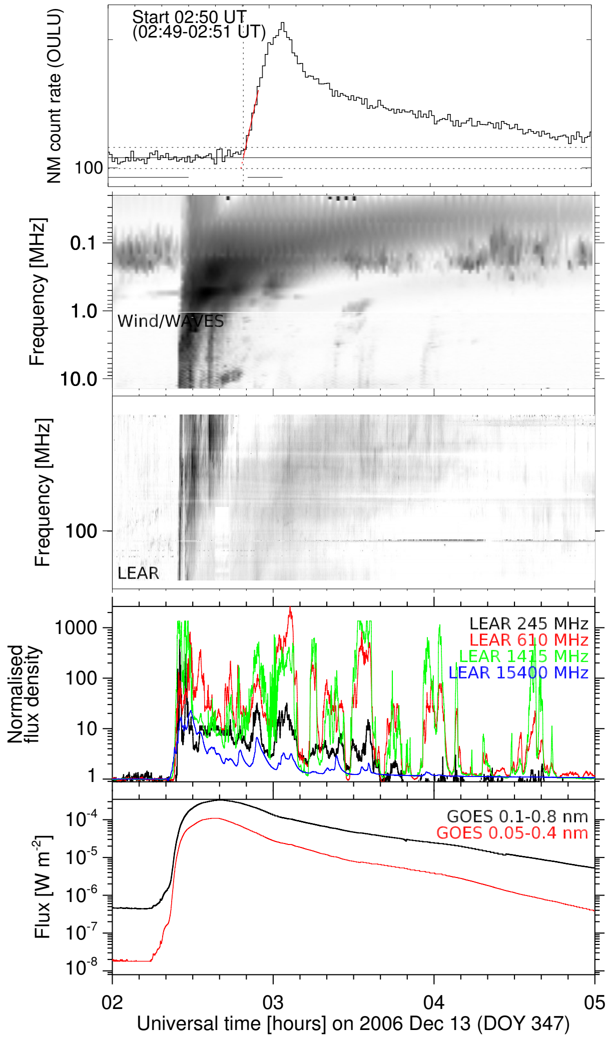

Fig. 1. Time history of soft X-ray and radio emission associated with the relativistic solar proton event on 2006 Dec 13. From bottom to top: thermal soft X-ray emission, cm-m-λ emission at fixed frequencies, dynamic spectra at long metre waves (180-30 MHz; dark shading shows bright emission) and decametre-to-kilometre waves (14 MHz-20 kHz). The ordering of the radio waves from high to low frequencies roughly corresponds to progression from the chromosphere (15400 MHz) through the high corona (10 solar radii at 1 MHz) to 1 AU. The top panel shows the count rate time history of the Oulu neutron monitor and the fit (red line) used to derive the onset time.

2.3 *An illustration: the GLE on 2006 Dec 13*

While the GLEs may start up to 20-30 minutes after the accompanying radio emission, all radio bursts have an extended duration. The long duration indicates the time-extended acceleration of electrons in the corona. Figure 1 displays the soft X-ray (bottom) and radio emission during the event with the longest onset delay. The second panel from the bottom shows the whole-Sun emission at selected frequencies. Microwave emission (15400 MHz) is gyro-synchrotron radiation of near-relativistic electrons (hundreds of keV to some MeV), while m-λ emission is generally ascribed to plasma instabilities. In this case the radio emission in the cm-m-band shows correlated strong variablity, independent of the emission process. This suggests that electrons are accelerated in a 2-3 hours-lasting series of impulsive events. The third panel from bottom shows the dynamic spectrum at long metre waves. The initial bright bursts ("type III" bursts) are produced by electron beams that travel outward through the corona. Their spectrum extends into the decametre-to-kilometre waveband as shown in the Wind/WAVES (Bougeret et al. 1995) observations in the second panel from top. The m-λ type III bursts are followed by a fainter broadband continuum ("type IV" burst) from a confined electron population. The acceleration is related to a different process, probably occurring in a current sheet behind the rising CME. The downward drift of the high-frequency border shows that the radio source takes part in the rise. The start of the continuum and of the GLE (near 02:50 UT) are close in time. At the time of the continuum the WAVES spectrum shows faint traces of short bursts similar to the type III bursts. The time coincidence suggests they are tracers of electrons escaping from the type IV radio source in the middle corona to interplanetary space.

Another feature of the WAVES spectrum are two bright packets of narrow-band bursts (near 02:40 around 10 MHz, near 03:30 at a few hundreds of kHz). They are part of a burst ascribed to electrons accelerated at the shock wave driven by the corona. The gradual outward progression of the shock explains the gradual shift of the emission to lower frequencies ("type II" burst). The emission demonstrates that at the time of the long-lasting electron acceleration shown at cm-m-λ a shock wave has been formed by the outward-travelling CME.

3 Discussion

The arrival of relativistic protons and ions accelerated in solar eruptive events is often, but not always, delayed with respect to the earliest signatures of particle acceleration at the Sun, especially of electron acceleration as traced by hard X-ray and radio emissions. This delay, which is well known in the literature, has been often interpreted as the time that a CME needs to form a shock wave, which subsequently accelerates the particles detected in space. The present study demonstrates, however, that this is not the only possible interpretation. For at the time when the particles are released near the Sun electron acceleration is ongoing in the corona. The extended emission from microwaves to metre waves shows indeed that the acceleration occurs within one solar radius above the photosphere. The observed GLE start could therefore be consistent with particle acceleration in the low corona, sometimes starting with the first flare signatures (as on 2005 Jan 20, Masson et al. 2009), more often during later phases of the eruptive event, after the liftoff of the CME. The late radio emission, and hence by inference the relativistic proton acceleration, would occur in the wake of the CME where the stressed coronal magnetic field relaxes. It does so through magnetic reconnection in current sheets below the magnetic flux rope that forms the core of the CME, or in the turbulence generated during the CME liftoff. The accelerated particles could escape to the interplanetary space via reconnection of the magnetic field in the CME with ambient open field lines, which likely proceeds as the CME travels outwards (Masson et al. 2013).

The radio emission in Figure 1 shows also that a CME-driven shock wave exists at the time of the late relativistic proton acceleration. This makes the interpretation of a single event ambiguous. In the present author's view the fact that in detailed event studies the onset - and in the 2005 Jan 20 event also a second late release - occurs with distinct episodes of electron acceleration in the solar corona (Klein et al. 1999; Masson et al. 2009; Klein et al. 2014) rather supports the view that the particles are accelerated behind the CME, not at its shock wave.

The *Parker Solar Probe* (NASA) and *Solar Orbiter* (ESA/NASA) space missions will provide energetic particle measurements much closer to the Sun than 1 AU. The particle signatures will then be much less distorted by the turbulent heliospheric magnetic field than in traditional measurements. This should allow better-documented conclusions on the acceleration region. The response may depend on the particle energy. Since in situ measurements are limited to about 100 MeV, neutron monitors on Earth will remain state-of-the art to investigate acceleration to the highest energies that the Sun may produce.

References

Afanasiev, A., Vainio, R., Rouillard, A. P., et al. 2018, A&A, 614, A4

Bougeret, J.-L., Kaiser, M. L., Kellogg, P. J., et al. 1995, Space Sci. Rev., 71, 231

Bruno, A., Bazilevskaya, G. A., Boezio, M., et al. 2018, ApJ, 862, 97

Gopalswamy, N., Xie, H., Yashiro, S., et al. 2012, Space Sci. Rev., 171, 23

Heerikhuisen, J., Litvinenko, Y. E., & Craig, I. J. D. 2002, ApJ, 566, 512

Klein, K.-L., Chupp, E. L., Trottet, G., et al. 1999, A&A, 348, 271

Klein, K.-L., Masson, S., Bouratzis, C., et al. 2014, A&A, 572, A4

Masson, S., Antiochos, S. K., & DeVore, C. R. 2013, ApJ, 771, 82

Masson, S., Klein, K.-L., Bütikofer, R., et al. 2009, Sol. Phys., 257, 305

Tylka, A. & Dietrich, W. 2009, in 31st International Cosmic Ray Conference, ed. M. Giller & et al. (http://icrc2009.uni.lodz.pl/proc/pdf/icrc0273.pdf)

SF2A 2019
P. Di Matteo, O. Creevey, A. Crida, G. Kordopatis, J. Malzac, J.-B. Marquette, M. N'Diaye, O. Venot (eds)

YOUNG STARS AS SOURCES OF ENERGETIC PARTICLES

A. Marcowith[1]

Abstract. This short review discusses the possible role of energetic particles (EP) in the physics and the evolution of young stellar objects (YSO). It also shortly addresses the interest of EP production in M-dwarf stars and their impact over their planetary system. It is advocated here that the role EPs in such systems needs to be properly evaluated in the light of a series of new observations which support the possibility of an in-situ production of high fluxes of EP.

Keywords: Young Stellar Objects - Energetic particles - Acceleration mechanisms - Cosmic Rays.

1 Introduction

Young stellar objects (YSO) share some similarities with compact objects: both have an accretion disk dragging external matter towards the central object under the effect of gravitation and magnetic fields, both show ejection in the form of outflows or jets that originate either from the central object itself or from the disk. YSOs are very active objects (Feigelson & Montmerle 1999); they show a strong X-ray activity which likely originates from the interaction between the stellar magnetosphere and the accretion disk (but not only). YSO are important objects for different active scientific contexts. First, YSO contribute to the feed-back process in the star formation cycle as a strong source of radiation and kinetic energy via their jets which impact the surrounding interstellar medium (Nakamura & Li 2007; Offner & Chaban 2017). Secondly, YSO at the end of their formation stage are the birth place of planets through the formation of proto-planetary disks (Armitage 2011). In at least these two contexts the possible impact of energetic particles (EP), ie particles with kinetic energies above the typical temperature of the medium, hence which can be renamed as non-thermal, have been largely overlooked until recently.
Besides these considerations, we are now entering in an unprecedented precision era in the study of the solar corona activities as we expect soon the first data from the Solar Parker probe [*]. We know that the Sun is a source energetic particles (Klein & Dalla 2017), and was also more active in the past (Feigelson & Montmerle 1999). It is highly tempting then to see YSO as test-bed objects at the intersection of solar and space plasma physics and high-energy Astrophysics communities interests. Theoretical models of particle acceleration developed in these fields may be used to investigate the loosely known effect of EP over their dynamics. This is the main motivation of this short review. On the specific aspect of the study of particle acceleration, YSO are also interesting objects because –as we will see below– the maximum energies reached by in-situ accelerated EPs are more modest (but still relativistic) with respect to typical usual Cosmic Ray (CR) sources (Supernova remnants, pulsar wind nebula), hence the study of particle acceleration in these objects necessitates less dynamics in space, time (and energy) and are more accessible to modern numerical tools specifically developed for this subject. This aspect should motivate theorists to consider YSO as promising test beds for particle acceleration studies in the view to evaluate the potential impact of EPs on star and planet formation.
The outlines of the article are as follows. After this short introduction, section 2 presents some recent evidences of the presence of energetic particles in YSO, we will then argue with simple energetic arguments that these EP are in-situ produced and not background CRs; these are unable to propagate close to the star. In section 3 we give an overview of the different acceleration mechanisms and EP production sites in YSO. This section also shortly discusses the case of EP in active M-dwarfs. In section 4 we focus on some recent work done in solar-mass and high-mass YSO on the possibility to accelerate particle by first order Fermi acceleration at shocks. Section 5 lists different issues associated with particle acceleration models and suggests some research directions before our final conclusion in section 6.

---

[1] Laboratoire Univers et Particules de Montpellier, UMR 5299 du CNRS, Université de Montpellier, place E. Bataillon, cc072, 34095 Montpellier, France
[*]http://parkersolarprobe.jhuapl.edu/

2 Observational evidences of non-thermal particles in young stellar objects

2.1 Schematic view of YSO

YSO are multi-scale physics objects. At scales of 0.1-1 pc they show outflows and jets harboring complex substructures composed of knots and hot spots (Bally 2016). At scales of 0.1-100 AU a central magnetized star in rotation accretes matter from an outer enveloppe of gas. The bipolar outflows and jets are launched from the disk or from the star magnetosphere (or from the interaction zone between the two). Low and intermediate mass (with masses between 0.2-2 $M_\odot$) YSOs belong to class 0, I, II, III depending on their evolution stage before entering in the main sequence phase (Feigelson & Montmerle 1999). The T Tauri phase which covers classes II and III typically lasts for 1-10 Myrs.

2.2 Magnetic activity in M-dwarfs

M-dwarfs are low mass stars with masses 0.1-0.5 $M_\odot$, with low surface temperatures and luminosities $\sim 0.01 L_\odot$. They have surface magnetic fields reconstructed by Zeeman Doppler imaging techniques in the range of 100-1000 Gauss (Vidotto et al. 2013). As for these stars the so-called habitable zone is typically of the order of 0.1 AU, their strong magnetic activity can then have a direct impact over the orbiting planets in this zone (Lammer et al. 2007).

2.3 Energetic particles in YSO: observations

EP can back-react over the structures in YSO through different mechanisms. MeV protons and keV electrons can ionize and produce a heating of the surrounding matter at high density columns where either U.V. or X-ray radiation can not penetrate (Padovani et al. 2018b). These EP can also trigger molecular Hydrogen dissociation (Padovani et al. 2018a). Particles produced by radioactive decay can also contribute to a minimum ionization rate (Cleeves et al. 2013). MeV-GeV hadrons can interact with the local matter and induce spallative nucleosynthesis (Padovani et al. 2016). Relativistic electrons can produce radio synchrotron emission and then trace the local magnetic field amplitude and topology (the synchrotron radiation is polarized), see eg Rodríguez-Kamenetzky et al. (2016). Finally, high energy protons/electrons can also produce gamma-rays via different processes: Bremsstrahlung and Inverse Compton (for electrons) and pion decay (for protons), see eg Bosch-Ramon et al. (2010). Gamma-ray emission if detected can put constraints on the magnetic field amplitude, or/and background photon and matter densities. Gamma-ray emission through the kinetic energy imparted into EP can also help to constrain source energetics.
Let us now discuss some recent observations which probe the presence of EP in YSO. We will then argue that these EP are necessarily in-situ produced.

Ionization rates Ceccarelli et al. (2014) present Herschel-HIFI observations of the young protostar, OMC-2 FIR 4 with enhanced abundances of two molecular ion species HCO^+ and N_2H^+ in the envelope of the object. These abundances are compatible with ionization rates up to 3-5 orders of magnitude above the standard Sptizer value of $\xi = 3\ 10^{-17}\mathrm{s}^{-1}$. The flux of EP extrapolated at a distance of 1 AU from the emitting source can easily account for the irradiation required by meteoritic observations (see below). Since then, several observations have confirmed these results and also show the presence of non-thermal radio emission (Favre et al. 2017; Fontani et al. 2017). Still using Herschel observations Podio et al. (2014) obtained enhanced ionization rates in the hotspot region of the low mass YSO LH1157-B1.
These ionization rates are difficult to explain only invoking the effect of background (ISM) CR. Indeed, the gravitational luminosity of accretion shocks impinging the stellar surface at a radius $R_{\rm sh} = 0.02$ AU is $L_{\rm grav} = GM\dot{M}/R_{\rm sh} \sim 3\ 10^{34}$ erg/s for a class 0 YSO with 0 protostar with $M = 0.1 M_\odot$, $\dot{M} = 10^{-5} M_\odot$yr. The background (ISM) CR luminosity impinging the core of a molecular cloud of radius $R_{\rm core} = 0.1$ pc is $L_{\rm CR} \simeq R_{\rm core} V_{\rm a} e_{\rm CR} \sim 10^{29}$ erg/s, for a typical Alfvén speed $V_{\rm a} = 1$ km/s and a CR energy density $e_{\rm CR} \simeq 1$ ev/cm^3 (Padovani et al. 2016). Now the CR luminosity close to the star is strongly reduced due to strong ionization losses and/or modulation, hence a small fraction of $L_{\rm grav}$ injected into in-situ accelerated EP can easily dominates $L_{\rm CR}$. A conclusion also true in high mass YSO since $\dot{M}$ can be higher.

Meteoritic measurements Carbonaceous chondrules are conglomerates of melted rock (chondrules), rare melted Ca-Al rich inclusions (CAIs) and presolar (interstellar) carbonaceous grains. They have been flash-melted to temperatures ∼2000 K. Polarization analysis show they have been formed in the presence of Gauss-level magnetic fields 4.55 Gyr ago (Feigelson & Montmerle 1999). Radioactive nuclei (for instance ^{10}Be, with a half-time live of $t_{1/2} \sim 1.4$ Myr) have been detected in CAIs is such abundance that they require the young solar system to have been plunged in an intense flux of EP (Jacquet 2019). The origin of this flux is still debated: it is either associated with the activity of massive stars in the environment of the young Sun (Tatischeff et al. 2014) or due to solar flare particles (Gounelle et al. 2013).

Flaring activity YSO show intense X-ray activity in form of flares with keV luminosities $L_{\rm X} \sim 10^{33-35}$ erg/s (Feigelson et al. 2002) consistent with magnetic power released during intense reconnection events (see below). In fact the energy released in X-ray domain is a small fraction of the total flare energy (Emslie et al. 2012). The typical flare duration last from 0.5 to 12 hr, the flares are $10^{2.5}$ more frequent with respect to Solar flares and $10^{1.5}$ more luminous. This supports an expected EP fluence 5 orders of magnitude larger than the one produced by the present Sun (Feigelson et al. 2002). Longer term observations (over 13 days) by Chandra allow the analysis of the flare decay profile. The profile and the duration of the flares point toward a spatial extension of the stellar corona- inner disk region $L/R_\star$ larger than 5-10 (Favata et al. 2005). Getman et al. (2008) scan X-ray flares from a sample of disk-free and accreting stars, the authors find flaring regions which are large and in corotation. Class II & III YSO also show non-thermal variable radio emission (Andre 1996).

Synchrotron emission from jets Several recent observations have reported negative (lower than -0.3) index non-thermal radio emission at cm wavelengths in several YSO (Anglada et al. 2018; Purser et al. 2016; Rodríguez-Kamenetzky et al. 2016). In particular (Rodríguez-Kamenetzky et al. 2017) propose unprecedented precise observations of HH80 and HH81 using the JVLA facility. These observations show a modulation of the cm radio index with the jet geometry: positive indexes correspond to the regions where the jet gets narrow while negative indexes correlate with a widening. This may be interpreted as a result of recollimation shocks in the jet pattern.

3 Acceleration sites and acceleration mechanisms

3.1 Acceleration sites

Jets YSO produce complex jet structures composed of outflows with speed of a few tens km/s and internal spines moving at higher speed from a few hundred km/s in low mass YSO up to 1000 km/s or more in high mass YSO. In these jets transitory structures appear as knots or spots that may be due to recollimation shock waves or may be associated with an unstable ejection mechanism (Raga et al. 2002). The fast jet are expected to end as a hot spot composed of an external bow shock and an internal shock (Bosch-Ramon et al. 2010). One of major limiting factor for particle acceleration at fast shock in jets is the level of ionization of the upstream medium (Padovani et al. 2016). Neutrals indeed through their collisions with ions produce some damping of ion motions and thus of waves supporting the scattering of EPs. Another unknown is the magnetic field strength in the jet which controls the confinement of particles around the shock. Finally, probably the most important unknown is the fraction of shock kinetic energy imparted into EP (see section 4 for some estimates).

Accretion disk corona Accretion disks around YSO are composed of multi-layered materials. The outer part of the accretion disk have smaller density column and are more prone to be ionized. Another aspect, is that the magnetic field carried with the accreted material can have some turbulent component or be subject to some instability (buoyancy, magneto-rotational instability, ...) which can eventually reconnect during the rotation motion around the central object. Also here the main unknown is the fraction of magnetic energy which can be transferred to EPs. The magnetic energy is also transfer into heat that participes to the production of some transitory coronas, there the magnetic energy can also be dissipated into some turbulence which can produce stochastic Fermi acceleration (see below) as it has been argued in the context of compact objects (Dermer et al. 1996).

Magnetosphere-disk interaction zone As stated above, the zone of interaction between the stellar magnetosphere and the accretion is known to be active, an activity also likely connected with magnetic reconnection. These events can lead to particle acceleration (de Gouveia Dal Pino et al. 2010; del Valle et al. 2011). Some non-thermal radio emission has been detected during intense X-ray activity which can marks such an acceleration process (see above). The stellar magnetic field can also channel accreted matter towards the stellar surface which end as accretion shocks (Feigelson & Montmerle 1999).

Stellar energetic particles Of course, as young stars are active stars they can be sources of stellar energetic particles accelerated during magnetic reconnection in the stellar corona or produced at shocks associated with coronal mass ejections events as it is the case for our Sun. This process is of particular relevance in M-dwarfs (Tabataba-Vakili et al. 2016).

3.2 *Acceleration mechanisms*

These mechanisms are (rather) well known. My intent here is to discuss some specific aspects of these processes in the environment of YSOs.

First order Fermi acceleration at shocks Fermi regular or first order acceleration is produced because shock waves carry the scattering waves and then impose a bulk motion. At each shock crossing then particles start to interact via head-on collisions and then have a systematic gain in energy. On average (over a Fermi cycle, eg up-down-up stream) EP gain $\langle \Delta E/E \rangle \propto (v/U)$. This process is of particular interest because beside being more efficient it also produces solutions in form of power-laws which only depend on one parameter, ie the shock compression ratio (at least in the linear stage).
The typical energy density available for EPs in these environment can be scaled as $E_{\rm kin} \simeq 10^3\ \mu n_{\rm H,5} V_{\rm sh,1}^2\ {\rm eV/cm^3}$, where μ is the mean gas mass, $n_{\rm H,5}$ is the hydrogen density in units of $10^5\ {\rm cm^{-3}}$, and $V_{\rm sh,1}$ is the shock speed in units of km/s. Unless a fraction less than $10^{-3}\%$ of this energy is converted into EP, the energy density imparted in these particles is higher than the background CR local energy density. The total power released into EP can be evaluated by estimating a ratio of the volume V over which particles are injected divided by a typical time T which can be at most the dynamical time of the shock, then $E_{\rm kin} \sim 7\ 10^{23}\ \mu n_{\rm H,5} V_{\rm sh,1}^2 V_{\rm AU}/T_{\rm yr}$ erg/s, where we have estimated the volume $V_{\rm AU}$ in units of AU^3 and the time in year units. Using the above example of a class 0 object we find $E_{\rm kin} \sim 2\ 10^{26}\ \mu n_{\rm H,12} V_{\rm sh,250}^2$ erg/s, the shock speed is now in units of 250 km/s and the Hydrogen density in units of $10^{12}\ {\rm cm^{-3}}$, hence a typical power of 10^{24} erg/s can be imparted into EPs (Padovani et al. 2016), still much higher than the power in background CR propagated into high density columns (more than $10^{25}\ {\rm cm^{-2}}$). For jets, one may expect roughly $E_{\rm kin} \sim 10^{33}\ \mu n_{\rm H,5} V_{\rm sh,100}\ R_{\rm perp,100}^2$erg/s, so about 10^{31} erg/s in EPs, making shock acceleration a probable acceleration mechanism (see section 4). Here we use as jet cylindical radius $R_\perp = 100$ AU.

Magnetic reconnection There is not a unique way to accelerate particles in magnetic reconnection (REC), ie the process by which the topology of magnetic field lines get rearranged and are converted into magnetic energy, heat, plasma bulk motion and EPs. Actually, there are at least 7 ways particles can gain kinetic energy is such events: in thermal exhausts, in contracting plasmoid, in colliding plasmoid, by the reconnecting electric field, by Fermi first order acceleration in converging reconnection flows, by magnetic drifts, by turbulence generated by for instance the tearing instability appearing during the reconnection process.
Here the available energy density is stored in the magnetic field. Typical values in the disk are $E_{\rm B} \sim 2.5\ 10^{10}\ B_{\rm G}^2 {\rm eV/cm^3}$, where the magnetic field strength is in Gauss units. It is easy to understand why, at least locally, especially close to the star where kG field strengths are found, REC can be an important source of EP. In solar reconnection events gamma-ray observations show that a significant fraction (up to 50%) of the magnetic energy released in the events can be converted into EP (Krucker et al. 2010). A rough estimate by del Valle et al. (2011) for conditions that prevail in the magnetosphere of a T Tauri star gives about a power of 10^{32} erg/s injected into EP per event. Compared to the above estimate this process may dominate over Fermi first order acceleration in the stellar magnetosphere but less likely in jets as the magnetic field strength is expected to drop along the jet (however a clear answer necessitates to evaluate the reconnection area, and the variation of the Alfvén speed).

Stochastic Fermi acceleration Stochastic Fermi acceleration (SFA) occurs because, on average EPs at a speed v interact with scattering centers moving at a speed U more often through head-on collisions than through rear-on collisions because $v \gg U$. At each head-on interaction EPs have a relative energy boost while they are decelerate in rear-on collisions. The averaged relative energy gain is $\langle \Delta E/E \rangle \propto (v/U)^2$. Usually in Astrophysics

U is close to the local Alfvén speed which is the typical speed of MHD waves (unless the plasma parameter is much larger than one). SFA is especially interesting if the magnetic field amplitude is high and the plasma density is low enough for U to be close to the speed of light and/or for moderately relativistic particles.
Here the value of available energy density is rather uncertain because it requires to know what fraction of primary source of energy (gravitation, kinetic or magnetic) goes into turbulent motions and what fraction of it goes into magnetic turbulent fluctuations. Actually there are no consensus on the main instability at the origin of turbulent motions in either accretion disks or jets, so any derivation of the turbulent energy density seems premature (see however some estimates in the context of black hole accretion flows in Dermer et al. (1996)).

4 Shock acceleration in YSO

We now focus a bit more on one mechanism in particular: the Fermi first order shock acceleration in YSO jets.

4.1 Modeling low-mass YSO

Ionization rates obtained in section 2.3 are difficult to explain unless invoking an in-situ source of EP. Padovani et al. (2016) consider the possibility to accelerate EP at shocks propagating in the jet of low mass YSO. The main parameters of the model necessary for the calculation of the acceleration time are: the shock speed $V_{\rm sh}$ in the range 40-300 km/s, the upstream (jet) temperature $T_{\rm u}$ in the range $10^4 - 10^5$ K, the jet Hydrogen density $n_{\rm H}$ in the range $10^3 - 10^7$ cm^{-3}, the jet magnetic field strength $B_{\rm u}$ in the range $0.05 - 1$ mG and an ionization fraction X in the range 0.01-0.9.
To derive the flux of in-situ accelerated CR one need a last parameter which is the fraction ξ of the shock ram pressure $n_{\rm H} m_{\rm p} V_{\rm sh}^2$ imparted into EP: $m_{\rm p}$ is the proton mass. This parameter is one of the main unknown in shock acceleration theories and is usually adjusted using observations. In this work Padovani et al. (2016) consider ξ of the order of a few %. Maximum EP energies are obtained by comparing the acceleration timescale $t_{\rm acc} \propto \kappa_{\rm u}/V_{\rm sh}^2$ to a series of loss times. In a jet different loss effects can occur: transversal diffusive escape, escape by advection downstream, escape by diffusion upstream, radiative losses (ionization losses at low energies), escape due to wave damping by ion-neutral collision. A last modeling effort is needed to characterize $\kappa_{\rm u}$ the diffusion coefficient of EPs in the upstream medium. This one is parametrized with respect to its Bohm value; ie $\kappa_{\rm u} = k_{\rm u} r_{\rm L} v/3$, where $r_{\rm L}$ and v are the EP gyroradius and speed respectively and $k_{\rm u}$ is a constant.
Padovani et al. (2016) find that shock in jets of low mass YSO under these conditions are able to accelerate EP up to energies of a few tens of GeV. Particle distribution follow power-laws with an energy index close (but larger) to 2. Fluxes are able to explain, accounting for the uncertainty in the propagation of the particles between the shock and the interaction zone, the high ionization rates observed in OMC-FIR4 [†]and LH1157-B1 and also to explain the radio emission of one hot spot of DG Tau (Ainsworth et al. 2014).

4.2 Modeling high-mass YSO

In high mass YSO, shock speeds are expected to reach 1000 km/s or a bit beyond. This results in a reduction of the acceleration time by one to two orders of magnitude. As the other main parameters do not change as much the maximum particle energies get boosted by the same amount and may reach TeV energies for both electrons and protons (see also Bosch-Ramon et al. (2010)). The main interest to have faster shocks moving in dense media is that EP can produce magnetic fluctuations and in fine generate some magnetic field. The magnetic field strength thus produced can be compared with constraints obtained from observations of non-thermal radio emission in a sample of jets (Purser et al. 2016). It can be found that the magnetic field produced by EP accelerated at the termination shock of high mass YSO can partly explain the strength of the equipartition magnetic field deduced from centimetric radio emission of the objects (Araudo et al, in prep).

5 Perspectives

Although the above results are appealing, a lot still remains to be done to properly evaluate the impact of EP on the dynamics of these objects. I see three main issues.

[†]for this object see also Gaches & Offner (2018) for a similar approach although with different assumptions concerning the main EP sources.

5.1 The issue with particle acceleration

As noticed in the above discussions, there are still large uncertainties about which acceleration mechanism dominates in YSO. Also, the power imparted into EP is loosely constrained and need more observational work oriented towards the determination of the key parameters of these acceleration models.

5.2 The issue with particle transport

One major issue is the control of particle propagation from their acceleration sites to their interaction sites. This is a complex modeling. It involves to account for the correct calculation of ionization losses by a correct evaluation of the column density N crossed by the particles (Padovani et al. 2018b; Rab et al. 2017; Padovani et al. 2013). N can vary considerably depending on the magnetic field geometry, hence refined MHD simulations are required to gain knowledge about this parameter. Such an approach has been for instance adopted by Fraschetti et al. (2019) who use a MHD model of M-dwarf magnetosphere to model EP propagation up to planets in the habitable zone. This work also adopted an ad-hoc model for the turbulent component of the magnetic field simply added to the MHD solution. As it may be expected, the EP fluxes at planets sensitively depend on the amplitude of the turbulent component which controls the diffusion coefficient of the particles. Similar ad-hoc models of diffusion coefficients in the context of YSO show a strong impact of propagation effects over the EP flux expected in the accretion disk and hence over the ionization fraction of the different disk layers (Rodgers-Lee et al. 2017).

5.3 Dynamical effects ?

A better knowledge of these two previous issues is not enough. One of the main characteristic of YSO is that these systems are highly transitory, time dependence ultimately connected to the accretion process and hence to the way angular momentum is transferred outwardly. EP acceleration does not escape to this rule and is likely a time-dependent phenomenon which has to find its place in the global dynamics of these objects. A proper account of acceleration processes duty cycles are also necessary to a proper account of feedback on star formation to evaluate the total amount of energy released by YSO in the ISM. In M-dwarfs links with Solar studies are may be more direct because of the absence of any disk but still there time-dependent effects are important to consider if we want to address the impact of EP over planet atmo/magneto-spheres (Fraschetti et al. 2019; Tabataba-Vakili et al. 2016).

5.4 Numerical modelling

If we consider the complexity of the environments considered in young stars, the numerical tools developed over the recent years to investigate multi-scale particle acceleration and transport in space plasma and high-energy Astrophysics communities (Marcowith et al. 2016) can only bring some progress in this field of research.

6 Conclusions

In conclusion we see from this short review that the role of EP in YSO and in more evolved stars needs to be clarified for several purposes. 1) Explain some observables (high ionization rates, synchrotron radiation from jets, non-thermal radio emission associated with magnetospheric activity, meteoritic element abundances). It appears that, unless for some very particular environment, galactic CR can not explain these observables completely. 2) Explore their role in the dynamics of these objects, in particular in the accretion process and the jet ejection. 3) Evaluate their potential impact over planet formation and planet atmospheres (thus on the appearance of life). Three main issues which still preclude any strong progress in the field have been listed: particle acceleration, particle transport, time-dependent effects. These uncertain aspects need some specific observations to constrain the main model parameters. The advent of powerful numerical tools, especially in the space plasma community, to investigate particle acceleration and transport could be applied to these systems.

I thank my collaborators on the subject A. Araudo, P. Hennebelle, K. Ferrière, M. Padovani. I thank V. Guillet, C. Sauty for many fruitful discussions and a reading of the manuscript. Some of the material used to write this review is extracted from the training work of two master students: S. Le Stum and H. Plombat.

References

Ainsworth, R. E., Scaife, A. M. M., Ray, T. P., et al. 2014, The Astrophysical Journal, 792, L18

Andre, P. 1996, in Astronomical Society of the Pacific Conference Series, Vol. 93, Radio Emission from the Stars and the Sun, ed. A. R. Taylor & J. M. Paredes, 273–284

Anglada, G., Rodríguez, L. F., & Carrasco-González, C. 2018, A&A Rev., 26, 3

Armitage, P. J. 2011, Annual Review of Astronomy and Astrophysics, 49, 195

Bally, J. 2016, Annual Review of Astronomy and Astrophysics, 54, 491

Bosch-Ramon, V., Romero, G. E., Araudo, A. T., & Paredes, J. M. 2010, A&A, 511, A8

Ceccarelli, C., Dominik, C., López-Sepulcre, A., et al. 2014, ApJ, 790, L1

Cleeves, L. I., Adams, F. C., Bergin, E. A., & Visser, R. 2013, ApJ, 777, 28

de Gouveia Dal Pino, E. M., Piovezan, P. P., & Kadowaki, L. H. S. 2010, Astronomy and Astrophysics, 518, A5

del Valle, M. V., Romero, G. E., Luque-Escamilla, P. L., Martí, J., & Ramón Sánchez-Sutil, J. 2011, The Astrophysical Journal, 738, 115

Dermer, C. D., Miller, J. A., & Li, H. 1996, The Astrophysical Journal, 456, 106

Emslie, A. G., Dennis, B. R., Shih, A. Y., et al. 2012, ApJ, 759, 71

Favata, F., Flaccomio, E., Reale, F., et al. 2005, The Astrophysical Journal Supplement Series, 160, 469

Favre, C., López-Sepulcre, A., Ceccarelli, C., et al. 2017, A&A, 608, A82

Feigelson, E. D., Broos, P., Gaffney, James A., I., et al. 2002, The Astrophysical Journal, 574, 258

Feigelson, E. D. & Montmerle, T. 1999, Annual Review of Astronomy and Astrophysics, 37, 363

Fontani, F., Ceccarelli, C., Favre, C., et al. 2017, A&A, 605, A57

Fraschetti, F., Drake, J. J., Alvarado-Gómez, J. D., et al. 2019, The Astrophysical Journal, 874, 21

Gaches, B. A. L. & Offner, S. S. R. 2018, The Astrophysical Journal, 861, 87

Getman, K. V., Feigelson, E. D., Micela, G., et al. 2008, The Astrophysical Journal, 688, 437

Gounelle, M., Chaussidon, M., & Rollion-Bard, C. 2013, ApJ, 763, L33

Jacquet, E. 2019, A&A, 624, A131

Klein, K.-L. & Dalla, S. 2017, Space Science Reviews, 212, 1107

Krucker, S., Hudson, H. S., Glesener, L., et al. 2010, The Astrophysical Journal, 714, 1108

Lammer, H., Lichtenegger, H. I. M., Kulikov, Y. N., et al. 2007, Astrobiology, 7, 185

Marcowith, A., Bret, A., Bykov, A., et al. 2016, Reports on Progress in Physics, 79, 046901

Nakamura, F. & Li, Z.-Y. 2007, The Astrophysical Journal, 662, 395

Offner, S. S. R. & Chaban, J. 2017, The Astrophysical Journal, 847, 104

Padovani, M., Galli, D., Ivlev, A. V., Caselli, P., & Ferrara, A. 2018a, A&A, 619, A144

Padovani, M., Hennebelle, P., & Galli, D. 2013, Astronomy and Astrophysics, 560, A114

Padovani, M., Ivlev, A. V., Galli, D., & Caselli, P. 2018b, A&A, 614, A111

Padovani, M., Marcowith, A., Hennebelle, P., & Ferrière, K. 2016, A&A, 590, A8

Podio, L., Lefloch, B., Ceccarelli, C., Codella, C., & Bachiller, R. 2014, A&A, 565, A64

Purser, S. J. D., Lumsden, S. L., Hoare, M. G., et al. 2016, MNRAS, 460, 1039

Rab, C., Güdel, M., Padovani, M., et al. 2017, Astronomy and Astrophysics, 603, A96

Raga, A. C., Velázquez, P. F., Cantó, J., & Masciadri, E. 2002, Astronomy and Astrophysics, 395, 647

Rodgers-Lee, D., Taylor, A. M., Ray, T. P., & Downes, T. P. 2017, Monthly Notices of the Royal Astronomical Society, 472, 26

Rodríguez-Kamenetzky, A., Carrasco-González, C., Araudo, A., et al. 2017, ApJ, 851, 16

Rodríguez-Kamenetzky, A., Carrasco-González, C., Araudo, A., et al. 2016, ApJ, 818, 27

Tabataba-Vakili, F., Grenfell, J. L., Grießmeier, J. M., & Rauer, H. 2016, Astronomy and Astrophysics, 585, A96

Tatischeff, V., Duprat, J., & de Séréville, N. 2014, ApJ, 796, 124

Vidotto, A. A., Jardine, M., Morin, J., et al. 2013, Astronomy and Astrophysics, 557, A67

SF2A 2019
P. Di Matteo, O. Creevey, A. Crida, G. Kordopatis, J. Malzac, J.-B. Marquette, M. N'Diaye, O. Venot (eds)

ENERGETIC PARTICLES IN THE SOLAR ATMOSPHERE

N. Vilmer[1] and S. Musset[2]

Abstract. The Sun is an efficient particle accelerator. These particles play a major role in the active Sun because they contain a large amount of the magnetic energy released during flares. Energetic electrons and ions interact with the solar atmosphere and produce high-energy X-rays and γ-rays. Energetic particles can also escape to the corona and interplanetary medium and may eventually reach the Earth's orbit. It is currently admitted that solar flares are powered by magnetic energy previously stored in the coronal magnetic field and that magnetic energy release is likely to occur on coronal current sheets along regions of strong gradient of magnetic connectivity. Particle transport from the acceleration region to the emission sites must also be considered to infer properties of the accelerated particles (and thus of the acceleration processes) from the observations of their radiation. In this paper, we will present the results of some recent studies using RHESSI observations: relationship found in some flares between ribbons of electric currents observed at the photospheric level and the flare energetic electrons traced by their X-ray emissions. We will also present some results on electron transport in solar flares and comment on the role of scattering in this process. We will finally describe some recent results from FERMI/LAT observations on the production of GeV protons in connection with solar flares and/or coronal mass ejections.

Keywords: Sun, Solar Flares, Energetic Particles, X-ray, γ- ray, RHESSI, FERMI/LAT

1 Introduction

The Sun is a powerful particle accelerator.This has been known since the first detection of solar energetic protons by ground-based neutron monitors in 1942, the first detection of solar flares in radio and X-rays, in the 1970s and the first observations of γ-ray lines in 1972. Since then, many observations of solar X-ray flares have been observed with several solar-dedicated missions. The last of this mission is the RHESSI (Reuven Ramaty High Energy Solar Spectroscopic) mission (Lin et al. 2002) which observed more than 120000 X-ray flares above 6 keV between 2002 and 2018. If this large amount of HXR observations has provided a substantial knowledge of electron acceleration in solar flares, our knowledge on ion acceleration in flares is still limited given the total number of γ-ray line flares (< 30) which has been observed both by solar-dedicated and general γ-ray missions. Recent FERMI/LAT γ-ray observations have however shown that the production of relativistic ($>$ GeV) protons in flares and eruptions is more common than previously expected and may last for several hours after the main flaring episode at the Sun. The most direct quantitative diagnostics of energetic particles interacting at the Sun come from HXR/ γ-ray observations. They carry information on electron and ion energy spectra, numbers, energy contents and abundances of accelerated ions. While bremsstrahlung X-ray continuum emission observed from 1 keV to 100 MeV provides diagnostic information about energetic electrons, γ-ray lines from 0.5 to 8 MeV tell us about ions above a few MeV/nuc in energy, and the continuum above 100 MeV (pion decay radiation) yields information about ions > 0.2 GeV/nuc (e.g. Share & Murphy 2006, Vilmer et al. 2011, Vilmer 2012 for reviews). This paper is focussed on the X-ray part of the RHESSI observations(dealing mostly with energetic electrons) and on the input ot the recent FERMI/LAT observations (dealing with the highest energetic protons).

2 Energetic electron acceleration and transport in solar flares

Figure 1 shows a typical X-ray flare spectrum observed with RHESSI between 3 and 100 keV. At energies up to 10-20 keV (depending on the event) the emision is dominated by emission from the hot plasma ($\simeq 30$

[1] LESIA, Observatoire de Paris, Université PSL, CNRS, Sorbonne Université, Université de Paris, 5 place Jules Janssen, 92195 Meudon, France
[2] School of Physics and Astronomy, University of Minnesota, 116 Church St SE, Minneapolis, MN 55455, USA

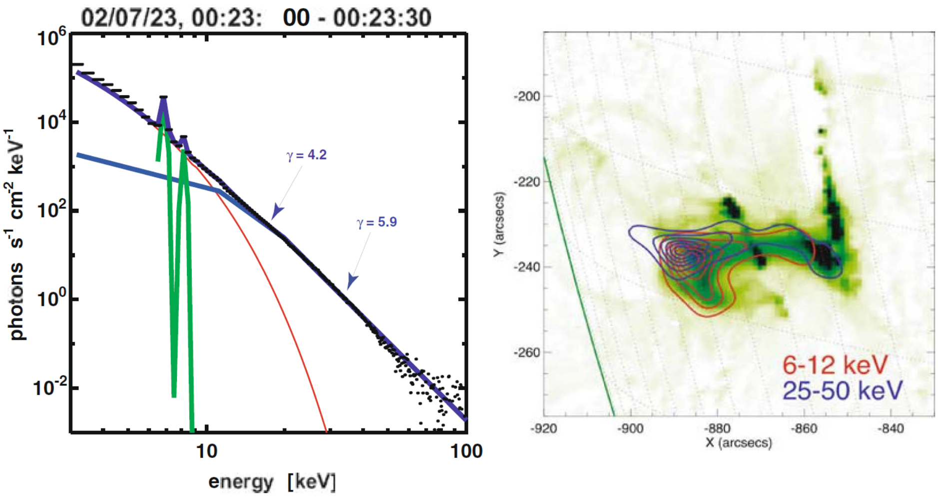

Fig. 1. Left: photon spectrum showing thermal emission (red) including the Fe and Fe/Ni line complexes in green (Phillips 2004), and the non-thermal emission in blue. **Right:** RHESSI contours in the thermal range (red) and at higher energies in the non-thermal range. The image shown is a TRACE 195 Å image taken at 00:26:00 UTC (from Krucker et al. 2008)

MK) (thermal free-free and free-bound continua as well as two line features at $\simeq$ 6.7 and 8 keV coming from Fe and Fe/Ni line complexes). Bremsstrahlung emission from non-thermal electrons (typically above $\simeq$ 10 keV) produces the non-thermal part of the HXR spectrum. RHESSI images usually show that the thermal emission comes from magnetic loops filled with hot plasma above the flare brightening (ribbons) seen here in EUV. The emission from non-thermal electrons usually comes from footpoints (which reveal the interaction sites of the energetic electrons with the dense chromosphere). In addition with the HXR footpoint sources, strong HXR sources are sometimes observed in the corona (Figure 2).This indicates the presence of high energy particles confined in the corona which can either trace the acceleration or trapping sites. In the context of solar flares, the source of the energy going to energetic particles is the magnetic energy stored in non-potential magnetic fields which can be released due to magnetic reconnection. From observations and models of the emissions, the general questions are related to the link between plasma heating and particle acceleration, the nature of the acceleration mechanisms and the conditions under which acceleration mechanisms operate, the location of the acceleration sites and the transport of particles from acceleration sites to X-ray emitting sites mostly present in dense regions of the solar atmosphere. As in all astrophysical plasmas, several acceleration mechanisms are possible: acceleration by shocks linked to the reconnection processes, stochastic acceleration by e.g. wave-particle interaction or direct electric field acceleration in connection e.g. reconnecting current sheets.

2.1 High energy electrons and Electric Currents in Solar Flares

It is commonly accepted that solar flares are the result of the sudden release of magnetic energy stored in non-potential magnetic fields associated with electric currents in the corona. Electric currents can be derived from vector magnetic field measurements which are mostly achieved at the photospheric level. Therefore, only measurements of photospheric electric currents can be deduced from the observations. Polarimetric measurements obtained continuously with high temporal and spatial resolution with the Helioseismic and Magnetic Imager (HMI) aboard Solar Dynamic Observatory (SDO) allow to derive maps of photospheric vertical electric currents for flaring active regions at a time cadence of 12min (or less) which allows to study the evolution of currents on a flare timescale (Petrie 2012; Janvier et al. 2014; Musset et al. 2015; Sharykin et al. 2019). The combination of these polarimetric measurements with RHESSI HXR images allows the comparison of electric current maps and electron interaction/acceleration sites during flares.

Figure 3 shows the first published comparison of the evolution with time of hard X-ray sources and of the current density maps at the photospheric level. The observations reveal a good spatial correlation between

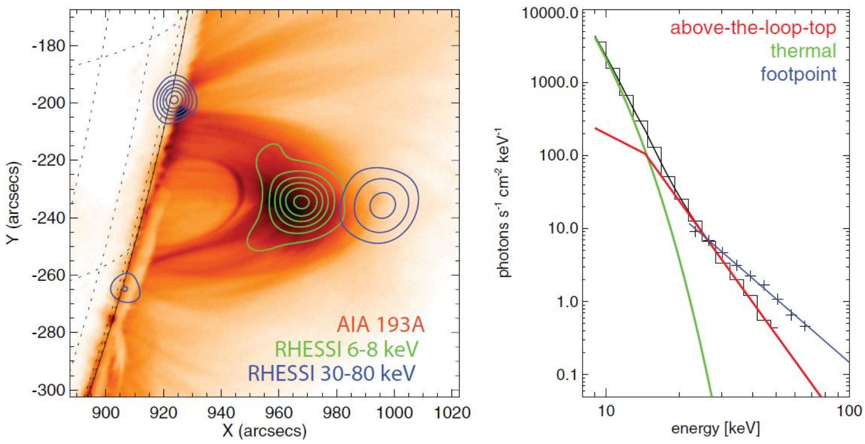

Fig. 2. Left: The thermal emissions (green contours) in the 6-8 keV range show the location of the main flare loops also seen in the 193 Å AIA image. The non-thermal HXR emissions come from the footpoints of the thermal flare loops, but also from above the main flare loop as outlined by the 30-80 keV (blue) contours. **Right:** imaging spectroscopy results: the black histogram gives the imaging spectroscopy results for the combined coronal sources; the observed footpoint spectrum is given by crosses. The green and red curves are the thermal and non-thermal fit to the combined coronal sources, while the power-law fit to the footpoints is given in blue. (Krucker & Battaglia 2014)

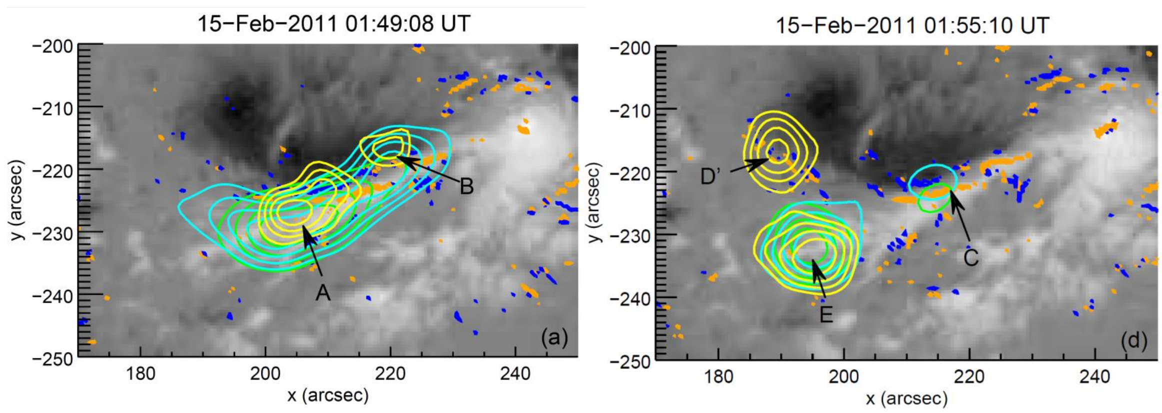

Fig. 3. Left: Magnetic field map (in grey scale) from SDO/HMI on February 15, 2011, at 01:48:00 UT (left) overlaid with positive and negative vertical electric current densities, respectively, with amplitude>100 mA/m^2 and RHESSI contours at 12 - 25 keV, 25 - 50 keV, and 50 - 100 keV (green, cyan, yellow) integrated between 01:49:00 and 01:49:16 UT **Right:** Same for magnetic field map and electric currents at 02:00:00 UT and RHESSI contours integrated between 01:55:02 and 01:55:18 (from Musset et al. 2015)

photospheric current ribbons (interpreted as footprints of coronal electric currents (Janvier et al. 2014) and the coronal elongated X-ray sources observed between 12 and 50 keV (figure 3 left) indicative of the acceleration region. A coincident appearance of a new X-ray source at 50-100 keV (D') and of new vertical electric currents in the same region (Musset et al. 2015) is also observed (figure 3 right). These observational results can be interpreted in the context of magnetic reconnection and subsequent electron acceleration preferentially occurring at current-carrying (reconnecting) sheets in the corona.

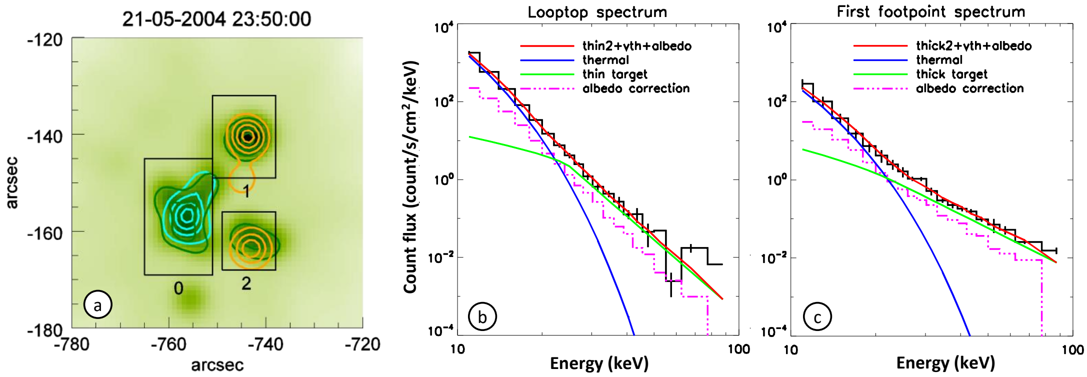

Fig. 4. (a) X-ray image between 23:49:30 and 23:50:30 UT at 25-50 keV overlaid with contours at 10-25 keV (blue), 25-50 keV (green), and 50-100 keV (orange). Boxes 0, 1, 2 are used for imaging spectroscopy of the looptop source, the first footpoint, and the second footpoint, respectively. Count flux spectra (data and fit) with residuals for looptop source (b), first footpoint (c), as defined by the black boxes in (a). The spectra derived from the data are shown in black. The blue curve represents the thermal component of the fit and the green curve represents the non-thermal component. The red curve indicates the total fitted spectrum.The thermal emissions in the 6-8 keV range show the location of the main flare loops also seen in the 193 Å AIA image. (Musset et al. 2018)

2.2 Transport of energetic electrons in the solar corona

As mentioned above, energetic electrons are believed to be accelerated in the low corona and to produce X-ray emissions dominantly in the chromosphere. Therefore, particle transport must be studied and evaluated since it can modify the spatial and spectral characteristics of the energetic particles produced in the acceleration region. Imaging spectroscopy capabilities provided by RHESSI has allowed to study transport effects in an unprecedented manner by measuring X-ray producing electron spectra in the coronal source (close to the presumed acceleration region) and in the footpoints (e.g. Battaglia & Benz 2006, Simões & Kontar 2013, Musset et al. 2018). Figure 4 shows one the event for which imaging spectroscopy has been performed. The results of the analysis show that the energetic electron spectra derived from the X-ray analysis in the corona and in the footpoints are different and that the non-thermal electron rate in the coronal source is larger by a ratio of 2.2 than the footpoint rate. This shows that in these events the transport of electrons from the acceleration site to the dense emitting footpoint does not agree with the standard transport model (e.g. Syrovatskii & Shmeleva 1972) in which energetic electrons accelerated in the corona propagate freely along the magnetic field lines of coronal loops losing only a small amount of energy through collisions with the ambiant plasma until they real the dense footpoints. Both the hardening of the electron spectrum during the transport from the corona to the footpoints and the larger electron rate in the coronal source can be explained by trapping of electrons in the coronal part of the loop (Musset et al. 2018). Such a confinement at the top of a loop can be due to magnetic mirroring (e.g. Kennel & Petschek 1966; Melrose & Brown 1976; Vilmer et al. 1986) or to confinement by strong turbulent pitch-angle scattering due to small scale magnetic field fluctuations leading to diffusive parallel transport (e.g. Bian et al. 2011; Kontar et al. 2014). In the last case, the comparison of observations with the results of a diffusive transport model allows to deduce the scattering mean free path of electrons. For the event shown in Figure 4, the mean free path for electron energies between 25 and 100 keV is around 1.4×10^8 cm. Radio observations of the same event achieved with the Nobeyama Radioheliograph also show evidence of the confinement of radio emitting electrons (energies around 400 keV) in the corona. The confinement is however stronger for these higher energy electrons (10^7 cm) showing a decrease with energy of the scattering mean free path of energetic electrons in the corona. This is the first report of such an effect in the low corona. Similar dependence of the scattering mean free path over electron energies has been also found in the case of interplanetary electron transport (e.g. Agueda et al. 2014) and must related to the properties of the scattering agents.

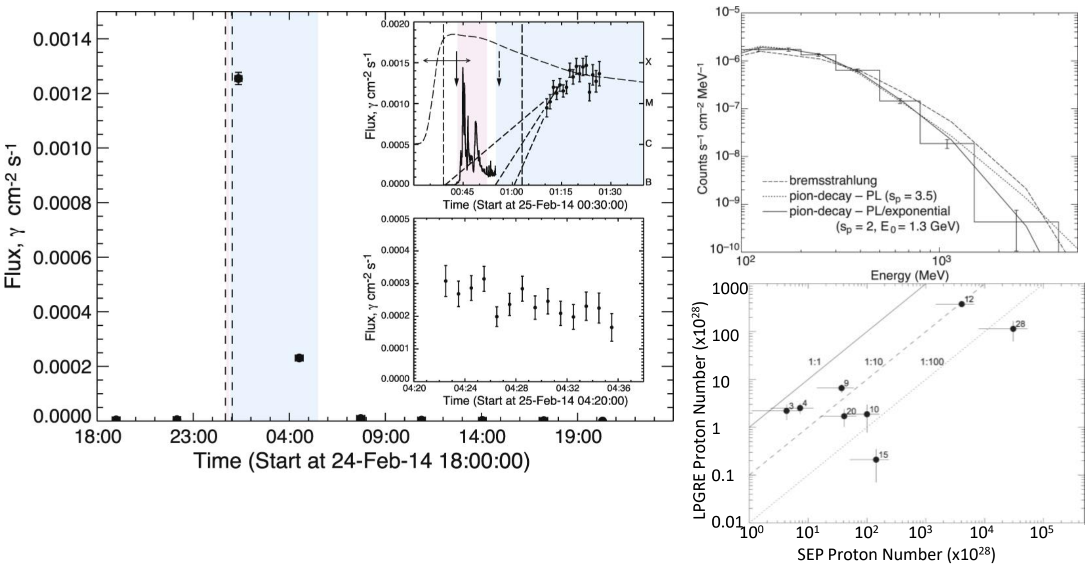

Fig. 5. Left: Time profile of the 2014 February 25 long duration event observed by FERMI/LAT above 100 MeV. *The top inset* shows RHESSI 100-300 keV rates (thick line in pink shaded region) plotted on the same scale as > 100 MeV γ-ray fluxes (points). The pink and blue shaded regions indicate the time intervals for the impulsive γ-ray emission and the late phase γ-ray emission respectively. The dashed curve shows the GOES time history. *The bottom inset* is a blowup of the time profile after 04:24 UT second showing a declining γ-ray flux. **Top right:** Background-subtracted LAT count spectrum with $\pm$ 1 σ statistical uncertainties measured with LAT between 01:13:30 and 01:17:30 UT. Best fits to the observed count spectrum are shown: (1) a pion-decay spectrum produced by a power-law spectrum of protons with spectral index $s_p = 3.5$ (dotted curve); (2) a pion-decay spectrum produced by a power-law spectrum of protons with spectral index $s_p = 2$ and 1.3 GeV exponential cutoff energy (solid curve); and (3) a bremsstrahlung spectrum produced at a density of 10^{16} cm^{-3} from a power-law spectrum of primary electrons with index $s = 1$ and 1 GeV exponential cutoff energy, in a 10^3 G magnetic field (dashed curve). **Bottom right:** Number of > 500 MeV protons producing the late > 100 MeV γ-ray event vs. the estimated number in the associated SEP event. The lines represent ratios of 1:1, 1:10, and 1:100 (from Share et al. 2018)

3 FERMI/LAT observations of long duration γ-ray events

Previous to the arrival of new data from FERMI/LAT, around 20 solar events had been observed with significant emission above 60 MeV from pion decay radiation (see Chupp & Ryan 2009; Vilmer et al. 2011 for reviews and Forrest et al. 1985 and Murphy et al. 1987 for the first observations and interpretations with Solar Maximum Mission). For some of the events, pion decay radiation is observed during the impulsive phase of the event as defined by the production of hard X-rays above 100 keV, but some events show extended pion decay radiation lasting for several hours (Kanbach et al. 1993; Ryan 2000;Rank et al. 2001). Several interpretations were proposed to explain these long duration emissions, either continuous acceleration of protons above 300 MeV (see e.g. Ryan & Lee 1991) or trapping of protons on very long time-scales. In particular, Mandzhavidze & Ramaty 1992 showed that the long duration phase could be explained by the injection of energetic protons in the impulsive phase and subsequent trapping. An efficient trapping on such long timescales required a strong mirror ratio in the trapping region (>10) as well as a coronal density less than 5×10^{11} cm^{-3}.

FERMI/LAT more sensitive observations provided new surprising results. High energy emission above 100 MeV was first detected for a "weak" impulsive GOES M2 class flare (Ackermann et al. 2012) and around $\simeq$ 30 solar events were reported above 100 MeV (Ackermann et al. 2014). FERMI/LAT observations also allows to deduce the location of the centroid of the γ-ray source above 1 GeV and to show that these locations are consistent with the location of solar flaring active regions even in the case of sustained emissions (see e.g. Klein et al. 2018 for a review).

In a recent study, Share et al. (2018) analyzed 30 events with late phase > 100 MeV γ-ray emissions (see figure 5 left). For most of the events (27 events) the spectral analysis shows that spectra are consistent with pion decay radiation produced by > 300 MeV protons and are not consistent with relativistic electron bremsstrahlung emissions (see e.g. figure 5 top right). This confirms that the Sun is able to produce a significant number of high energy protons (> 300 MeV) for several hours after the impulsive flare. The number of accelerated protons above 500 MeV interacting at the Sun can be then deduced from the derived pion decay spectrum using the models developed in Murphy et al. (1987). The number of protons above 500 MeV is in the range 10^{27} - 10^{30} and is at least a factor of 10 larger than the number of protons above 500 MeV which is responsible for the production of the impulsive > 100 Mev γ-ray emission when observed (see Share et al. 2018). Figure 5 bottom right panel shows the comparison for 8 events of the number of > 500 Mev protons producing the late $> \gamma$-ray emissions and of the number of > 500 MeV protons emitted at the vicinity of the Sun and propagating in the interplanetary medium (see Share et al. 2018). It is found that the number of > 500 Mev protons needed to produce the late high energy γ- rays is 0.1 to 50 % of the number of protons of the associated interplanetary event.

The recent FERMI/LAT results initiated new discussions on the origin of the long duration high energy radiation which is most of the time not accompanied by any other radiative signature apart from a type II radio emission indicative of the production of a shock wave propagating from the corona to the interplanetary medium and usually associated with a coronal mass ejection (see e.g. Klein et al. 2018). Several papers have recently addressed the origin of this long lasting radiation, attributing their production to energetic protons escaping the turbulent downstream region of the CME shock back to the Sun along converging field lines (e.g. Jin et al. 2018) or accelerated by the CME shock and going back to the solar surface (e.g. Plotnikov et al. 2017).

4 Conclusions

High energy emission during solar flares is a powerful diagnostics of the fundamental processes of magnetic energy release, particle acceleration and transport in the solar corona. X-ray and γ-ray observations provide information on solar energetic particles at their source. RHESSI and Fermi/LAT provide novel observations of energetic particle during solar flares, but also raise new questions and challenge our understanding of particle acceleration and transport during these events. Among the next observational challenges lie the observation of faint X-ray emission in the corona, supposedly close or in the acceleration region, and imaging of the pion-decay radiation during solar flares. The next solar-dedicated X-ray spectro-imager, STIX, on Solar Orbiter, will provide observations at high sensitivity and high temporal cadence. Focusing optics for solar X-ray observation, as demonstrated by the FOXSI sounding rocket, is under consideration to provide X-ray imaging spectroscopy with a high sensitivity and high dynamic range. A white paper on Solar Particle Acceleration, Radiation and Kinetics (SPARK) has been proposed by Matthews and collaborators to the ESA Voyager 2050 call promoting a future solar γ-ray mission. The combination of these diagnostics of the sources of energetic particles that can escape and propagate through the heliosphere with the in-situ measurements of particles close to the Sun in the heliosphere that are possible with Solar Orbiter and Parker Solar Probe, will greatly improve our understanding of particle acceleration and transport in our heliosphere.

References

Ackermann, M., Ajello, M., Albert, A., et al. 2014, ApJ, 787, 15

Ackermann, M., Ajello, M., Allafort, A., et al. 2012, ApJ, 745, 144

Agueda, N., Klein, K. L., Vilmer, N., et al. 2014, A&A, 570, A5

Battaglia, M. & Benz, A. O. 2006, A&A, 456, 751

Bian, N. H., Kontar, E. P., & MacKinnon, A. L. 2011, A&A, 535, A18

Chupp, E. L. & Ryan, J. M. 2009, Research in Astronomy and Astrophysics, 9, 11

Forrest, D. J., Vestrand, W. T., Chupp, E. L., et al. 1985, in International Cosmic Ray Conference, Vol. 4, 19th International Cosmic Ray Conference (ICRC19), Volume 4, 146

Janvier, M., Aulanier, G., Bommier, V., et al. 2014, ApJ, 788, 60

Jin, M., Petrosian, V., Liu, W., et al. 2018, ApJ, 867, 122

Kanbach, G., Bertsch, D. L., Fichtel, C. E., et al. 1993, A&AS, 97, 349

Kennel, C. F. & Petschek, H. E. 1966, J. Geophys. Res., 71, 1

Klein, K.-L., Tziotziou, K., Zucca, P., et al. 2018, in Solar Particle Radiation Storms Forecasting and Analysis, ed. O. E. Malandraki & N. B. Crosby, Vol. 444, 133–155

Kontar, E. P., Bian, N. H., Emslie, A. G., & Vilmer, N. 2014, ApJ, 780, 176

Krucker, S. & Battaglia, M. 2014, ApJ, 780, 107
Krucker, S., Battaglia, M., Cargill, P. J., et al. 2008, A&A Rev., 16, 155
Lin, R. P., Dennis, B. R., Hurford, G. J., et al. 2002, Sol. Phys., 210, 3
Mandzhavidze, N. & Ramaty, R. 1992, ApJ, 396, L111
Melrose, D. B. & Brown, J. C. 1976, MNRAS, 176, 15
Murphy, R. J., Dermer, C. D., & Ramaty, R. 1987, ApJS, 63, 721
Musset, S., Kontar, E. P., & Vilmer, N. 2018, A&A, 610, A6
Musset, S., Vilmer, N., & Bommier, V. 2015, A&A, 580, A106
Petrie, G. J. D. 2012, Sol. Phys., 281, 577
Phillips, K. J. H. 2004, ApJ, 605, 921
Plotnikov, I., Rouillard, A. P., & Share, G. H. 2017, A&A, 608, A43
Rank, G., Ryan, J., Debrunner, H., McConnell, M., & Schönfelder, V. 2001, A&A, 378, 1046
Ryan, J. M. 2000, Space Sci. Rev., 93, 581
Ryan, J. M. & Lee, M. A. 1991, ApJ, 368, 316
Share, G. H. & Murphy, R. J. 2006, Washington DC American Geophysical Union Geophysical Monograph Series, 165, 177
Share, G. H., Murphy, R. J., White, S. M., et al. 2018, ApJ, 869, 182
Sharykin, I. N., Zimovets, I. V., & Myshyakov, I. I. 2019, arXiv e-prints, arXiv:1905.03352
Simões, P. J. A. & Kontar, E. P. 2013, A&A, 551, A135
Syrovatskii, S. I. & Shmeleva, O. P. 1972, Soviet Ast., 16, 273
Vilmer, N. 2012, Philosophical Transactions of the Royal Society of London Series A, 370, 3241
Vilmer, N., MacKinnon, A. L., & Hurford, G. J. 2011, Space Sci. Rev., 159, 167
Vilmer, N., Trottet, G., & MacKinnon, A. L. 1986, A&A, 156, 64

Session 09

Interaction étoile-disque

SF2A 2019
P. Di Matteo, O. Creevey, A. Crida, G. Kordopatis, J. Malzac, J.-B. Marquette, M. N'Diaye, O. Venot (eds)

PAMPERO: A NEW PHYSICAL APPROACH OF MOLECULAR PHOTOSPHERIC EJECTION AT HIGH ANGULAR RESOLUTION FOR EVOLVED STARS

M. Hadjara[1] and P. Cruzalèbes[2]

Abstract. PAMPERO is a numerical code for studying spectra-interferometric data for evolved stars. By using MARCS stellar atmospheric models for the simulation of a photosphere surrounded by a continuous and multi-layer molecular circumstellar disk, which is characterized according to the observed wavelength band. The model presented deduces the distributions of temperature and molecular density of the "MOLsphere" along the stellar radius. We aim to better understand the different mechanisms generating the important mass-loss which characterizes the large and rich family of evolved stars.

Keywords: methods: numerical – methods: observational – techniques: high angular resolution – techniques: interferometric – Infrared: stars – Stars: AGB and post-AGB, atmospheres – Stars: atmospheres – stars: fundamental parameters – stars: late-type

1 Introduction

In this work, we present simulations of two different prototypes of evolved stars (an Asymptotic Giant Branch -AGB- and a Red Giant Branch -RGB-), hypothetically observed by VLTI-AMBER (Petrov et al. 2007) at high spectral resolution in the K-band. We use the numerical model PAMPERO (for Physical Approach of Molecular Photospheric Ejection at high-angular-Resolution for evOlved-stars) in order to play with the physical proprieties of CO outer layers, namely : the distributions of the CO column density N_{CO} and the temperature T_{mol} along the stellar radius, to reproduce the observed flux and visibilities (further details in Hadjara et al. 2019b). In Sec. 2, we briefly describe the model and its results.

2 The model

PAMPERO is a multilayer MOLsphere model (inspired by Ohnaka 2013; Montargès et al. 2014), which surrounds the stellar Center-to-Limb intensity Variations (CLVs) obtained by preselected MARCS models (Gustafsson et al. 2008), by using Turbospectrum (Alvarez & Plez 1998; Plez 2012)* over the observed wavelength range thanks to the listed CO lines of Goorvitch (1994). PAMPERO is written in `Matlab` (for MATrix LABoratory). The description of our model is summarized on the synoptic diagram (Fig. 1-top-), while a sample of spectro-interferometric results are shown in Fig. 1-bottom-.

3 Conclusions

In the current paper, we show an application of PAMPERO for the molecule of CO on K-band. This is a small part of an important wok of a sample of eight different evolved stars observed with VLTI/AMBER (Hadjara et al. 2019a). We can also use PAMPERO for CHARA/VEGA (Mourard et al. 2011) data to study the Titanium monoxide (TiO) for Yellow Hyper-Giants (YHG) as an example, as well as characterize the temperature-density distribution of dust around evolved stars with the new instrument VLTI/MATISSE (Lopez et al. 2014).

[1] Astrophotonics group laboratory. University of Chile, Av. Tupper 2007, Santiago, Chile
[2] Université de la Côte d'Azur (UCA), Centre National de la Recherche Scientifique (CNRS), Observatoire de la Côte d'Azur (OCA), Laboratoire J. L. Lagrange, UMR 7293,Campus Valrose, 06108 Nice Cedex 2, France
*To correct the spectral splitting caused by earth atmospheric air, we use Edlén's formula (Edlén 1966).

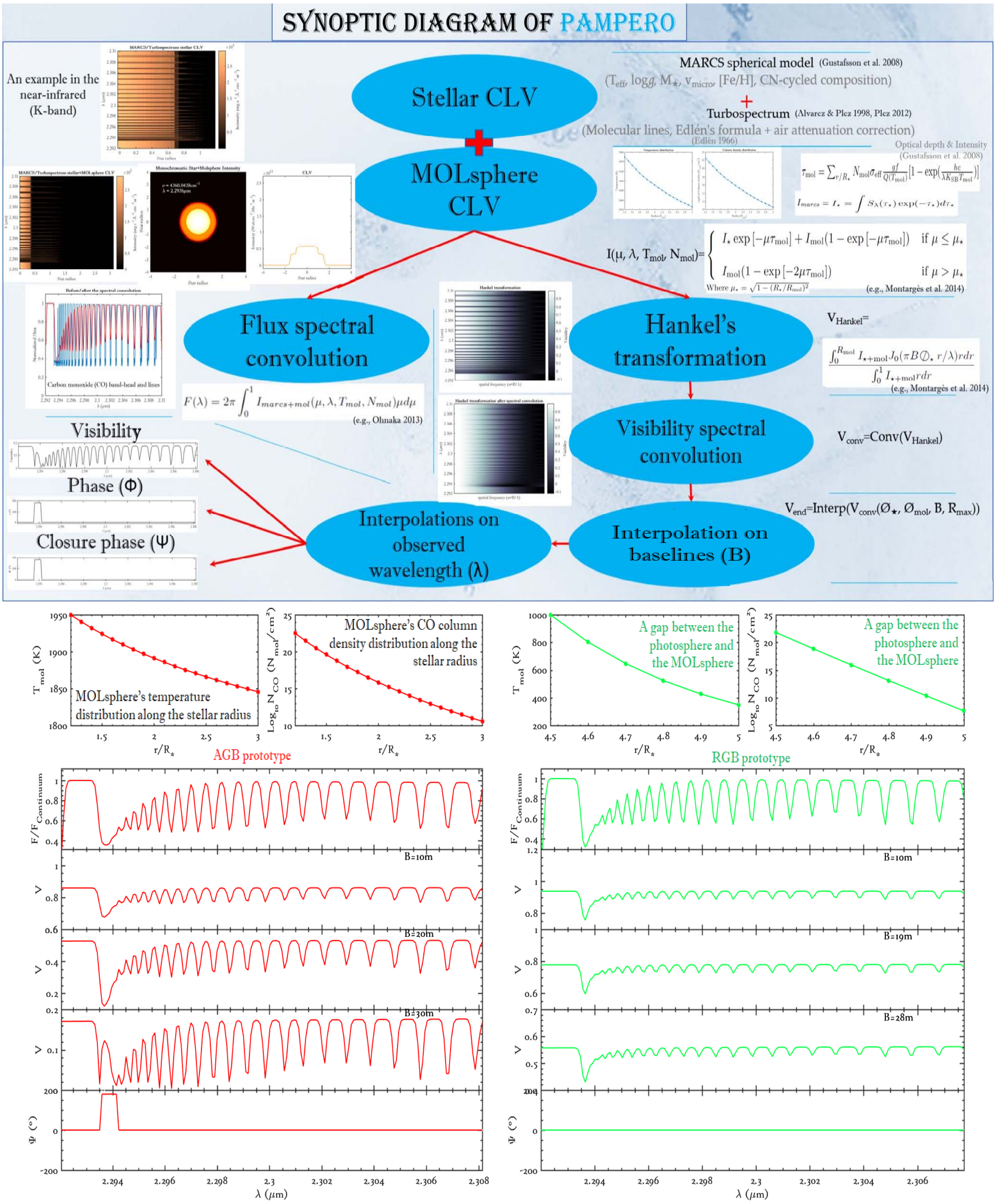

Fig. 1. Top: Synoptic diagram of PAMPERO. **Bottom:** Results for an AGB (in red lines) and a RGB prototypes (in green lines). ***Top panels:*** Temperature-density distribution along the stellar radius. ***Bottom panels:*** Spectro-interferometric data, namely : The normalized flux, visibilities (for a triplet of baselines B) and closure phase (Ψ).

References

Alvarez, R. & Plez, B. 1998, A&A, 330, 1109

Edlén, B. 1966, Metrologia, 2, 71
Goorvitch, D. 1994, ApJS, 95, 535
Gustafsson, B., Edvardsson, B., Eriksson, K., et al. 2008, A&A, 486, 951
Hadjara, M., Cruzalèbes, P., Nitschelm, C., et al. 2019a, MNRAS, (in press)
Hadjara, M., Cruzalèbes, P., Nitschelm, C., et al. 2019b, MNRAS, 489, 2595
Lopez, B., Lagarde, S., Jaffe, W., et al. 2014, The Messenger, 157, 5
Montargès, M., Kervella, P., Perrin, G., et al. 2014, A&A, 572, A17
Mourard, D., Bério, P., Perraut, K., et al. 2011, A&A, 531, A110
Ohnaka, K. 2013, A&A, 553, A3
Petrov, R. G., Malbet, F., Weigelt, G., et al. 2007, A&A, 464, 1
Plez, B. 2012, Turbospectrum: Code for spectral synthesis, Astrophysics Source Code Library

SF2A 2019
P. Di Matteo, O. Creevey, A. Crida, G. Kordopatis, J. Malzac, J.-B. Marquette, M. N'Diaye, O. Venot (eds)

CAVITY SIZE IN CIRCUMBINARY DISCS

K. Hirsh[1, 2], D. J. Price[2] and J.-F. Gonzalez[1]

Abstract. What sets the cavity size in circumbinary discs? We investigate this by simulating circumbinary discs using smoothed particle hydrodynamics (SPH). In agreement with previous findings, we find that the cavity is largest when the binary is highly eccentric or the disc has low viscosity. We also find that discs with a low initial inclination with respect to the binary orbital plane tend towards a coplanar orbit, either through warping or tearing, leading to a cavity that is the same size as an initially coplanar disc.

Keywords: accretion, accretion discs - binaries - hydrodynamics - methods: numerical

1 Introduction

Recent highly resolved observations of the cavities in circumbinary discs, such as the one found in HD 142527 (Casassus et al. 2013; Avenhaus et al. 2017), and later attempts to model them (Price et al. 2018a) show that binaries can be responsible for cavities many times larger than their projected separation.

The formation of these cavities is thought to be a competition between Lindblad torques, which act to open the cavity, and viscous torques, which act to close it. Artymowicz & Lubow (1994) predicted that this competition results in a cavity that is largest both for the most eccentric binaries and the least viscous discs, with computational studies confirming this basic picture (Artymowicz & Lubow 1994; Pierens & Nelson 2013).

Miranda & Lai (2015) generalised this model to include discs that are misaligned to the binary orbital plane, but few computational studies have been performed to investigate the effects of inclination, focusing mainly on polar discs (Martin & Lubow 2017).

To this end we perform a series of three dimensional smoothed particles hydrodynamics (SPH) simulations to understand the effects of disc inclination, disc scale height, and binary eccentricity on the cavity size.

2 Methods

Using the SPH code `PHANTOM` (Price et al. 2018b) we set up a disc of one million particles with $R_{\rm in} = 1.4$ AU and $R_{\rm out} = 14.5$ AU around a binary with semi-major axis $a = 1$ AU. We take a binary with mass ratio $q = 0.1$, where $q = M_2/(M_1 + M_2)$ and $M_1 = 1$ M$_\odot$ is the mass of the primary. We take a disc mass of $M_{\rm disc} = 0.0001$ M$_\odot$ with surface density varying as $\Sigma \propto R^{-1}$. We prescribe a vertically isothermal equation of state, that is $P = c_s^2(R)\rho$, with sound speed varying as $c_s \propto R^{-0.25}$. This gives a temperature profile $T \propto R^{-0.5}$ and a disc aspect ratio varying as $H/R \propto R^{0.25}$. This allows us to set the sound speed, temperature and aspect ratio by specifying the aspect ratio at $R_{\rm in}$. We simulate discs with $H/R_{\rm in} = 0.01, 0.02, 0.04, 0.05, 0.06, 0.08, 0.10$ and 0.12.

We prescribe an α disc, i.e. $\nu = \alpha c_s H$, where ν is the disc viscosity, α is the Shakura & Sunyaev (1973) viscosity parameter, c_s is the sound speed in the disc, and H is the scale height of the disc. We model the disc viscosity with an artificial viscosity parameter, α^{av} such that $\alpha = (\alpha^{av}/10)(\langle h\rangle/H)$, where $\langle h\rangle$ is the mean smoothing length. Since $H \equiv c_s/\Omega$, where Ω is the Keplerian frequency, we have $\nu = (\alpha^{av}/10)\langle h\rangle H\Omega$. This allows us to vary the viscosity by varying the scale height, with an increasing scale height leading to a stronger viscosity.

[1] Univ Lyon, Univ Claude Bernard Lyon 1, ENS de Lyon, CNRS, Centre de Recherche Astrophysique de Lyon UMR5574, F-69230, Saint-Genis-Laval, France
[2] Monash Centre for Astrophysics (MoCA) and School of Physics and Astronomy, Monash University, Vic. 3800, Australia

3 Results

3.1 Time Evolution and Binary Eccentricity

Fig. 1 shows snapshots of the cavity opening process. We see that a cavity is quickly opened within $10 - 100$ binary orbits, but only reaches an equilibrium at late stages of evolution.

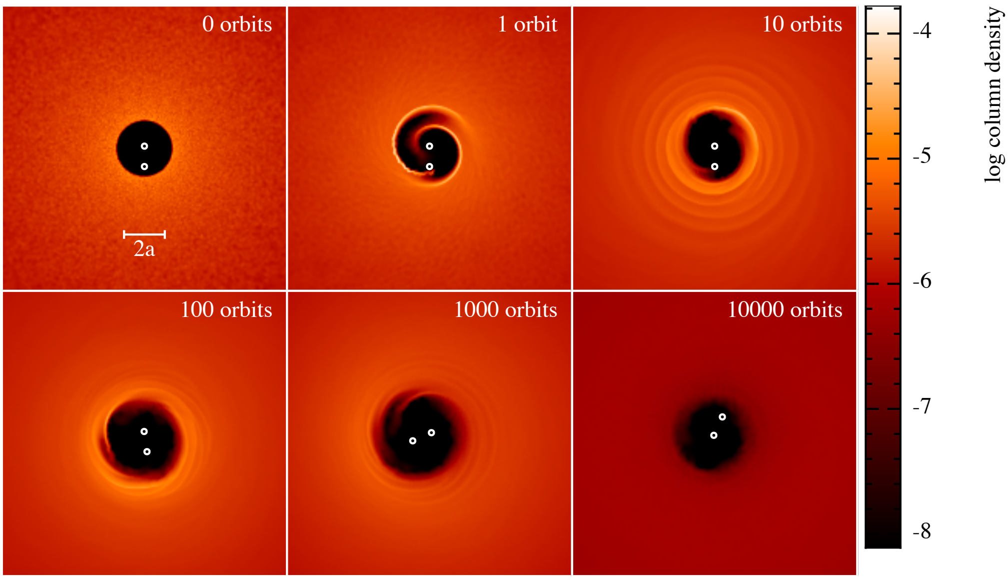

Fig. 1. Surface density rendered face-on views of the time evolution of a coplanar disc with aspect ratio $H/R = 0.05$ at R_{in}.

Fig. 2 shows the evolution of the cavity size as a function of time for the disc in Fig. 1, and compares it to discs with differing binary eccentricities. The panel on the left shows the first 100 binary orbits. We see that, as in Fig. 1, a cavity is quickly opened on this short time, and the size appears to be steady at $2 - 3$ times the binary semi-major axis. The panel on the right, however, shows the importance of evolving the viscous time ($\sim 10,000$ binary orbits). On this longer timescale we see that, for eccentric binaries, the cavity continues to grow after thousands of binary orbits, eventually settling at $2.5 - 3.5$ times the binary semi-major axis. Circular binaries are unique in that they reach their maximum cavity size after only hundreds of binary orbits.

Examining the right panel of Fig. 2 also allows us to see the late stage effects that binary eccentricity has on the cavity size. Consistent with the previous works of Artymowicz & Lubow (1994) and Miranda & Lai (2015) we find that the cavity size increases with binary eccentricity, with the sharpest increase occurring at the lowest eccentricities.

3.2 Disc Scale Height

The left panel of Fig 3 shows the cavity size as a function of disc aspect ratio after 100 binary orbits. We see that at this time the cavity size does not depend on the aspect ratio. This is because the viscous time is on the order of 10,000 binary orbits, so changing the scale height, and thus the viscosity, does not affect the cavity size at this early evolutionary stage.

The right panel of Fig. 3 shows the dependence of cavity size on disc aspect ratio after 1,000 binary orbits. While this is an order of magnitude less than the viscous time some dependence is already seen. For thin discs ($H/R \leq 0.06$) an increasing scale height leads to a decreasing cavity size. Thicker discs, however, have a cavity size that is independent of the scale height, though this may no longer be the case after the viscous time is fully resolved.

3.3 Inclination

Fig. 4 shows snapshots of the time evolution of discs initially inclined to the binary orbital plane. Both discs have a scale height $H/R = 0.05$ at $R_{\rm in}$ and orbit a binary with mass ratio $q = 0.5$. The left panel has an initial

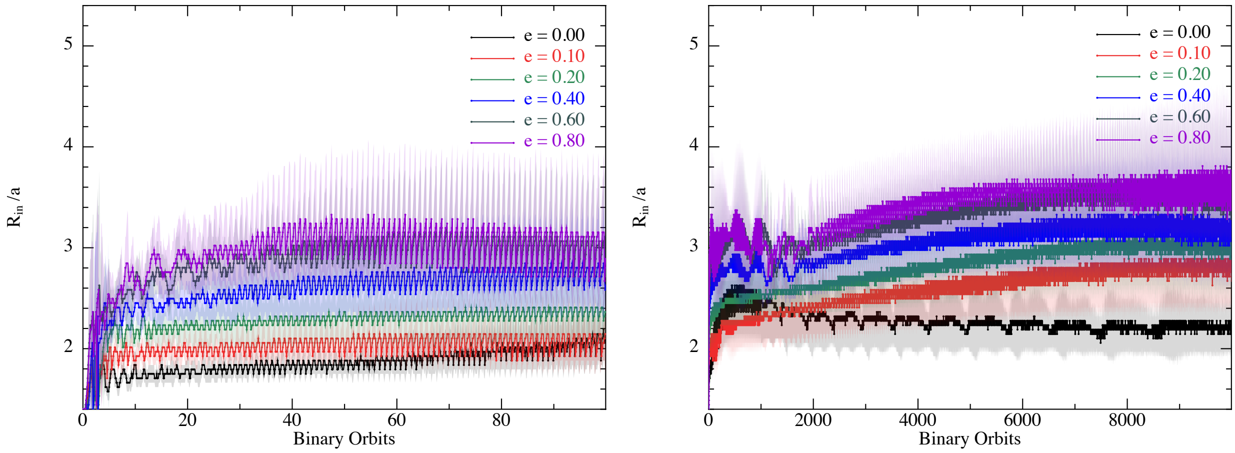

Fig. 2. Cavity size (in units of binary semi-major axis) as a function of time for coplanar discs with aspect ratio $H/R = 0.05$ at R_{in}, surrounding a binary with mass ratio $q = 0.1$ and various eccentricities. The shaded regions represents the error bars. **Left:** First 100 binary orbits. **Right:** Up to 10,000 binary orbits.

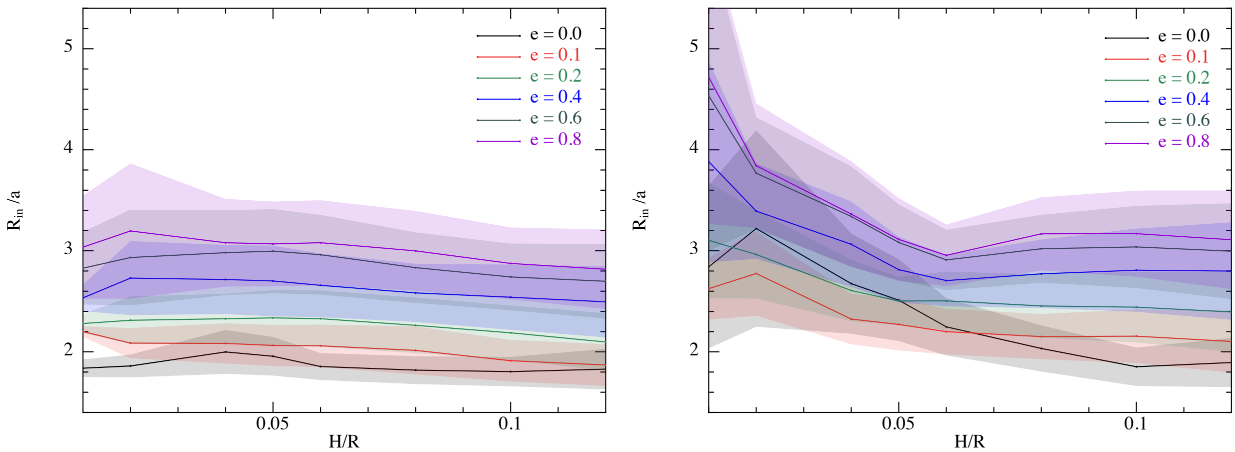

Fig. 3. Cavity size (in units of binary semi-major axis) as a function of disc aspect ratio for coplanar discs surrounding a binary with mass ratio $q = 0.1$. The shaded regions represents the error bars. **Left:** After 100 binary orbits. **Right:** After 1,000 binary orbits.

inclination of $i = 22.5°$ and the right panel has an initial inclination of $i = 45°$. In both cases the inner disc tends to align with the binary orbit. At 22.5° this alignment is driven by a warp in the disc, while at 45° the inner disc tears away, leaving an aligned inner disc and a misaligned outer disc.

The alignment of the inner disc with the binary orbital plane leads to a cavity size which is independent of the initial disc inclination, as shown in Fig. 5. This means that the cavity size gives no knowledge of the initial angle between the binary and the disc, however evidence of warps or tears within the disc may indicate some previous misalignment.

It is important to note that we only consider discs with a low initial inclination that evolve to a coplanar orbit. Highly inclined discs can evolve to a polar orbit (e.g. Martin & Lubow 2017), which may lead to a different cavity size.

4 Conclusions

We have performed a suite of 3D SPH simulations to examine the opening of a cavity in a circumbinary accretion disc, revisiting the original numerical and analytic study by Artymowicz & Lubow (1994) and comparing our results to those of Miranda & Lai (2015) for inclined discs. We considered the effects of binary eccentricity,

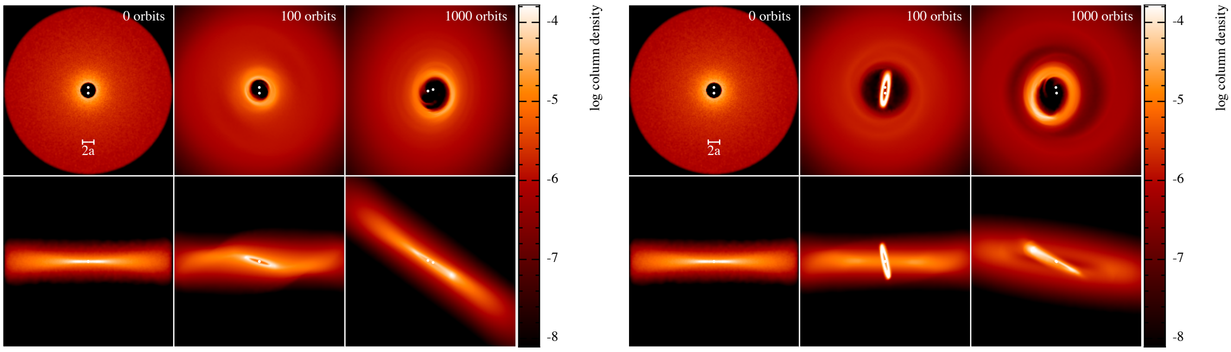

Fig. 4. Surface density rendered face-on (top row) and side-on (bottom row) views of initially inclined discs with aspect ratio $H/R = 0.05$ at R_{in} around binaries with mass ratio $q = 0.5$. **Left:** Initial inclination of $i = 22.5°$. **Right:** Initial inclination of $i = 45°$.

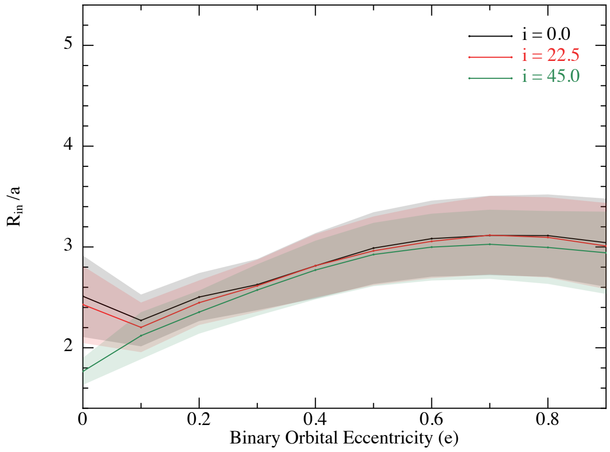

Fig. 5. Cavity size (in units of binary semi-major axis) as a function of of binary eccentricity discs with aspect ratio $H/R = 0.05$ at R_{in}, surrounding a binary with mass ratio $q = 0.1$ and various initial inclinations, after 1,000 binary orbits. The shaded regions represents the error bars.

disc viscosity, and disc inclination. Consistent with previous works, we found that the cavity size increases with binary orbital eccentricity. The effects of disc viscosity depend on the timescale considered. On a dynamical timescale the cavity size is independent of disc viscosity, while on a viscous timescale the cavity size is largest for the discs with weakest viscosity. Finally, we found that the inner regions of discs with a low initial inclination ($\leq 45°$) tend towards a coplanar orbit, either by warping or tearing, leading to a cavity size that is independent of initial inclination.

References

Artymowicz, P. & Lubow, S. H. 1994, ApJ, 421, 651
Avenhaus, H., Quanz, S. P., Schmid, H. M., et al. 2017, AJ, 154, 33
Casassus, S., van der Plas, G., M, S. P., et al. 2013, Nature, 493, 191
Martin, R. G. & Lubow, S. H. 2017, ApJ, 835, L28
Miranda, R. & Lai, D. 2015, MNRAS, 452, 2396
Pierens, A. & Nelson, R. P. 2013, A&A, 556, A134
Price, D. J., Cuello, N., Pinte, C., et al. 2018a, MNRAS, 477, 1270
Price, D. J., Wurster, J., Tricco, T. S., et al. 2018b, PASA, 35, e031
Shakura, N. I. & Sunyaev, R. A. 1973, A&A, 24, 337

SF2A 2019
P. Di Matteo, O. Creevey, A. Crida, G. Kordopatis, J. Malzac, J.-B. Marquette, M. N'Diaye, O. Venot (eds)

HIGH-ANGULAR RESOLUTION OBSERVATIONS OF HD179218: EARLY STAGES OF DISK DISSIPATION?

J. Kluska[1], S. Kraus[2], C. L. Davies[2], T. Harries[2], M. Willson[2], J.D. Monnier[3], A. Aarnio[4], F. Baron[5], R. Millan-Gabet[6], T. ten Brummelaar[7], X. Che[3], S. Hinkley[2], T. Preibisch[8], J. Sturmann[7], L. Sturmann[7] and Y. Touhami[5]

Abstract. Star/disk interactions have an important effect on disk evolution (e.g. photoevaporation). We present an extensive multi wavelength (visible, near- and mid-infrared) high-angular resolution observational campaign involving seven instruments (direct imaging and interferometry), on HD179218, a Herbig star surrounded by a (pre-)transitional disk. Its near-infrared circumstellar emission is 50 times larger than its theoretical dust sublimation radius making it very special amongst other Herbig stars observed by infrared interferometry. This emission has an unexpectedly high temperature ($\sim$1500 K) that we postulate to explain by small carbon particles super-heated by high energy photons from the central star. This points toward a scenario where the inner disk parts were accreted onto the star and the rest of the disk is being photo-evaporated by high energy stellar photons. It makes this target unique as it would be the first one to be caught in very early stages of disk dissipation.

Keywords: young stars, protoplanetary disks, transition disk, high angular resolution, interferometry, direct imaging.

1 Introduction

To understand the mechanisms of planet formation it is necessary to observe and study the place where planets form, namely the protoplanetary disks. Recent observations with direct imaging or radio interferometry revealed various structures of protoplanetary disks such as warps, spirals or gaps (e.g. Stolker et al. 2017; Andrews et al. 2018; Avenhaus et al. 2018) that are signs of disk evolution. After few million years the disks likely dissipate via photo-evaporation from inside out (e.g. Alexander et al. 2014, and references therein). The disk dissipation has a strong impact on planet formation. To constrain the disk evolution and dissipation processes it is needed to study the inner regions in detail. It was first done by studying the infrared excess in the spectral energy distributions (SED) of young stars as the near infrared emission was interpreted as coming from the dust located within the first astronomical units from the star. The intermediate-mass young stars, called the Herbig stars (Herbig 1960), were classified into two groups based on the shape of the infrared excess(Meeus et al. 2001). Group I sources have a black-body-like excess around 10μm whereas the infrared excess of group II targets can be reproduced with a power-law. It was first interpreted that group I objects are flared disks whereas group II are flat disks and that the evolution sequence goes from group I to group II objects. Nevertheless, resolved observations have shown that group I disks are rather transition disks with gaps or holes and that the evolution sequence goes the other way around (Maaskant et al. 2013; Menu et al. 2015).

[1] Instituut voor Sterrenkunde (IvS), KU Leuven, Celestijnenlaan 200D, 3001, Leuven, Belgium.
[2] Astrophysics Group, School of Physics and Astronomy, University of Exeter, Exeter EX4 4QL, UK
[3] Department of Astronomy, University of Michigan, Ann Arbor, MI 48109, USA
[4] University of Colorado Boulder, Boulder, CO 80303, USA
[5] Department of Physics and Astronomy, Georgia State University, Atlanta, GA, USA
[6] Infrared Processing and Analysis Center, California Institute of Technology, Pasadena, CA, 91125, USA
[7] Mount Wilson Observatory, The CHARA Array of Georgia State University, Mount Wilson, CA 91023, USA
[8] Universitäts-Sternwarte München, Ludwig-Maximilians-Universität, Scheinerstr. 1, D-81679, München, Germany

The aforementioned observational techniques (direct imaging and radio interferometry) can not easily probe the very inner disk regions (<5 au from the host star) where most of the detected exoplanets are located. Infrared interferometry, however, is able to reach an angular resolution of ∼1 mas and therefore to probe the first astronomical unit around a young star at a distance of few hundreds parsecs.

We here present a high angular resolution observational campaign on the transition disk surrounding HD179218. This campaign involving seven different instruments consists in polarimetric direct imaging in the visible, aperture masking observations in the near-infrared and long-baseline interferometric observations in the near and mid-infrared. The target is a group I disk located at a distance of 293 pc (Bailer-Jones et al. 2018). It has a high ionisation fraction of the PAH features (Seok & Li 2017) and the disk cavity was deduced from ^{12}CO and ^{13}CO ro-vibrational emission. Previous long-baseline interferometric observations in the mid-infrared suggested the presence of a gap (Fedele et al. 2008). Finally, it is the most extended object in the near-infrared long-baseline interferometric survey made with PIONIER at the VLTI (Lazareff et al. 2017). We will therefore first describe the observational campaign, then present the results of each individual observation and, finally, conclude with a global interpretation of the whole dataset.

2 The observations

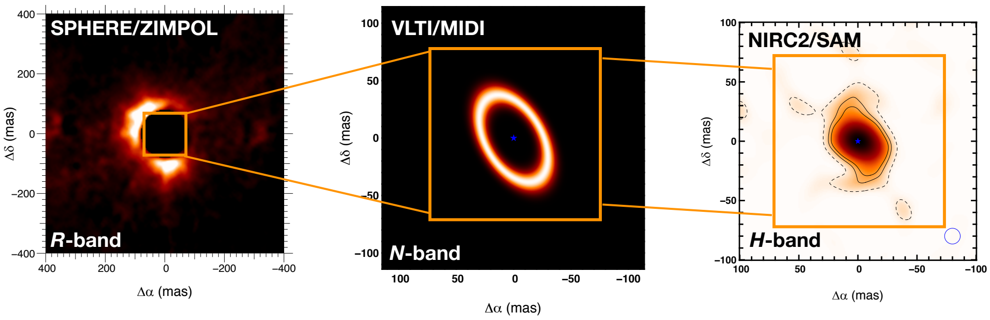

Fig. 1. Images of the circumstellar environment of HD179218 from the observing campaign. **Left:** Polarised intensity image with coronagraph in R-band from SPHERE/ZIMPOL. **Center:** image of the best-fit model to the archival visibility data from VLTI/MIDI (between 8 and 12μm). **Right:** Image reconstruction from aperture masking dataset from KECK/NIRC2 in the near infrared (at 1.65μm).

2.1 SPHERE/ZIMPOL

We obtained SPHERE/ZIMPOL observations with the P2 mode with a coronagraph of 155 mas in diameter. Those observations are mainly tracing stellar light scattered onto the surface of the disk. There is an extended emission that can be reproduced by an off-centred Gaussian that has a full-width half-maximum (FWHM) of 252±1 mas that translates into a size of ∼75 au (Fig. 1). We do not see an inner cavity as this area is masked by the coronagraph. We can retrieve the disk orientation with an inclination (i) of $47.4° \pm 0.3°$ and a position angle (PA) of $24.8° \pm 0.4°$.

2.2 VLTI/MIDI

We have also used archival data from the MIDI instrument (Menu et al. 2015) which is a two-telescope mid-infrared interferometer at the VLTI observing in the N-band (8-12μm). The visibility curve is looking like a Bessel function which is characteristic of a ring brightness distribution. We have fitted an inclined Gaussian ring to the data and found a ring radius of 42±1 mas which translates into a physical radius of 12 au (Fig. 1). The inclination was found to be $i = 53° \pm 6°$ with a PA of $26° \pm 6°$ which is similar to what we found for the SPHERE/ZIMPOL observations.

2.3 KECK/NIRC2/SAM

The KECK/NIRC2 observations were obtained in the self aperture masking (SAM) mode in the H-band (at 1.65μm). There is a clear squared visibility drop and a non-zero closure phase signal. We have first performed an image reconstruction using MiRA (Thiébaut 2008) together with the SPARCO approach (Kluska et al. 2014) that enables to subtract the star from the image and reconstruct its environment only. The image reveals an extended emission from the star to about 40 mas in major-axis and 25 mas in the minor-axis (Fig. 1).

2.4 VLTI/PIONIER&AMBER

The VLTI observations were taken with PIONIER, a 4-beam interferometric instrument observing in H-band, and with AMBER in K-band (2.2μm). The closure phase signal is consistent with 0° (i.e. with a centrally symmetric brightness distribution). The squared visibility have the same level across the baselines (V^2 around 0.35 for PIONIER and 0.15 for AMBER). However, both instruments have several channels across their observing band (3 for PIONIER and 8 for AMBER) and there is a consistent slope of the V^2 with wavelength which is the so-called chromatic effect(Kluska et al. 2014). This effect is due to the difference of spectral index between the unresolved component (here, the star) and the extended component (the disk). This can be interpreted as a difference of a temperature between the hot star and the cold environment.

2.5 CHARA/CLIMB&CLASSIC

Finally, the CHARA long-baseline observatory allows to reach a baseline of 330 m in the near-infrared. We have obtained observations with CLIMB (3-beam interferometer) and CLASSIC (2-beam combiner) in the K-band. The squared visibility curve stays flat with the baseline length at a level of 0.15.

2.6 A geometric model reproducing the near-infrared interferometric data

Given the full interferometric dataset in the near-infrared we have fitted to it a Gaussian model with a star. The Gaussian FWHM is of 51±2 mas which translates to about 10 au, which is smaller that the ring radius in the mid-infrared. The Gaussian has an inclination of 55°±3° and a PA of 26°±3°. Those orientation are in accordance with mid-infrared and visible observations. The temperature of the near-infrared circumstellar emission is $T = 1440 \pm 30\,$K.

3 The big picture

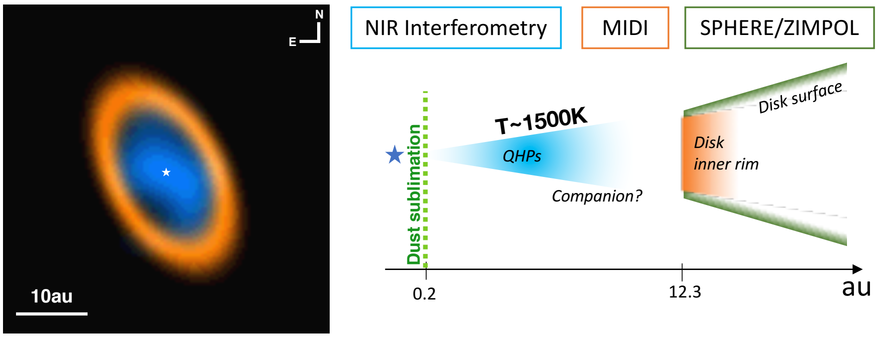

Fig. 2. A global view synthesising all our observations. **Left:** Composite image with mid-infrared emission in orange and near-infrared emission in blue. **Right:** Sketch of the emission seen by different instruments. The near-infrared emission is located inside the disk rim seen in mid-infrared, but is far more extended than the theoretical dust sublimation radius.

Finally, we can put all these high angular resolution observations to build one global picture. First, we have notified that the orientation (inclination and PA) of the extended emission is similar for all the observations, confirming that the same entity is observed, namely a disk with an inclination of ~50° and a PA of ~ 25°.

The scattered light traces the disk surface behind the disk inner rim whereas the thermal infrared emission traces the disk inner rim which is at ~12 au. However, the near-infrared emission is located inside this inner rim as it has a FWHM of ~10 au. The temperature of this near-infrared emission is about 1500 K which is close to the dust sublimation temperature. This is not surprising as around young stars, the near-infrared emission is known to trace the dust sublimation radius (Monnier & Millan-Gabet 2002; Monnier et al. 2005; Lazareff et al.

2017). Nevertheless, the theoretical radius of dust sublimation is located at ∼0.2 au, which is 50 times smaller that the observed size (Fig. 2). This points towards a special emission mechanism in this object.

Given the strong presence of PAHs, it is likely that this emission comes from quantum heated particles present inside the dust rim, as suggested by Klarmann et al. (2017). Those particles could be PAHs that are super heated by high energy photons from the central star. The last question is the origin of the disk inner rim that is not at the theoretical dust sublimation radius. It could be due to a yet unseen companion (our observations set an upper limit of $0.34\,M_\odot$) or to the evolutionary state of the disk itself that could have accreted its inner rim, revealing the dust in the gap to high energy photons, and in the very early process of dissipating the rest of the disk.

4 Conclusions

The high angular resolution campaign with different instruments operating at different spatial scales and wavelengths enabled us to work out a global picture of the disk structure that would not have been possible with observations of one or two instruments alone. The disk structure of HD179218 is special not showing signs for an inner rim at the dust sublimation temperature but, instead, emission from quantum heated dust particles inside the disk hole. The disk it self seems to start at 12 au. This gap is either caused by a yet undetected planet or by photoevaporation where the inner disk was accreted onto the central stars and the rest of the disk (and particles in the disk hole) are exposed to stellar high-energy photons.

It would be interesting to follow-up this target with additional observations within the disk hole in the search for a companion and model the whole system with radiative transfer model including quantum heated particles.

We would like to thank the organisers of the S09 session and the LOC for organising this very nice SF2A meeting in Nice. The authors acknowledge support from a Marie Sklodowska- Curie CIG grant (Grant No. 618910), Philip Leverhulme Prize (PLP-2013-110), STFC Rutherford Fellowship (ST/J004030/1), and ERC Starting Grant (Grant Agreement No. 639889). A.A. and J.D.M. acknowledge support from NSF AAG 1311698. The authors wish to recognize and acknowledge the very significant cultural role and reverence that the summit of MaunaKea has always had within the indigenous Hawaiian community. We are most fortunate to have the opportunity to conduct observations from this mountain. This work was supported by a NASA Keck PI Data Award, administered by the NASA Exoplanet Science Institute (PID 69/2013B_N104N2). Data presented herein were obtained at the W. M. Keck Observatory from telescope time allocated to NASA through the agency's scientific partnership with the California Institute of Technology and the University of California. The Observatory was made possible by the generous financial support of the W. M. Keck Foundation. This work is based in part upon observations obtained with the Georgia State University (GSU) Center for High Angular Resolution Astronomy Array at Mount Wilson Observatory. The CHARA Array is supported by the NSF under Grant No. AST-1211929. Institutional support has been provided from the GSU College of Arts and Sciences and the GSU Office of the Vice President for Research and Economic Development. This research has made use of the SIMBAD database and the VizieR catalog access tool, operated at CDS, Strasbourg, France.

References

Alexander, R., Pascucci, I., Andrews, S., Armitage, P., & Cieza, L. 2014, in Protostars and Planets VI, ed. H. Beuther, R. S. Klessen, C. P. Dullemond, & T. Henning, 475

Andrews, S. M., Huang, J., Pérez, L. M., et al. 2018, The Astrophysical Journal, 869, L41

Avenhaus, H., Quanz, S. P., Garufi, A., et al. 2018, The Astrophysical Journal, 863, 44

Bailer-Jones, C. A. L., Rybizki, J., Fouesneau, M., Mantelet, G., & Andrae, R. 2018, The Astronomical Journal, 156, 58

Fedele, D., van den Ancker, M. E., Acke, B., et al. 2008, A&A, 491, 809

Herbig, G. H. 1960, The Astrophysical Journal Supplement Series, 4, 337

Klarmann, L., Benisty, M., Min, M., et al. 2017, A&A, 599, A80

Kluska, J., Malbet, F., Berger, J.-P., et al. 2014, A&A, 564, A80

Lazareff, B., Berger, J. P., Kluska, J., et al. 2017, Astronomy and Astrophysics, 599, A85

Maaskant, K. M., Honda, M., Waters, L. B. F. M., et al. 2013, A&A, 555, A64

Meeus, G., Waters, L. B. F. M., Bouwman, J., et al. 2001, A&A, 365, 476

Menu, J., van Boekel, R., Henning, T., et al. 2015, A&A, 581, A107

Monnier, J. D. & Millan-Gabet, R. 2002, ApJ, 579, 694

Monnier, J. D., Millan-Gabet, R., Billmeier, R., et al. 2005, ApJ, 624, 832

Seok, J. Y. & Li, A. 2017, ApJ, 835, 291

Stolker, T., Sitko, M., Lazareff, B., et al. 2017, The Astrophysical Journal, 849, 143

Thiébaut, E. 2008, in Society of Photo-Optical Instrumentation Engineers (SPIE) Conference Series, Vol. 7013, Society of Photo-Optical Instrumentation Engineers (SPIE) Conference Series, 1

SF2A 2019
P. Di Matteo, O. Creevey, A. Crida, G. Kordopatis, J. Malzac, J.-B. Marquette, M. N'Diaye, O. Venot (eds)

THE HH30 T-TAURI STAR

F. Louvet[1], C. Dougados[2], S. Cabrit[3], N. Cuello[4], R. Nealon[5], D. Mardones[1], F. Menard[2], B. Tabone[6], C. Pinte[7] and W. R. F. Dent[8]

Abstract. A prerequisite to understanding the formation of stars is the comprehension of the processes linking the collapsing molecular core, the setting of the circumstellar disk, and the accretion from this disk to the protostar. Together, these processes regulate the mass that the star will acquire. The critical point of these stages is the extraction of the angular momentum, that allows the matter to be accreted from the large scale down to the protostar. It has been proposed that the extraction of angular momentum in the disk could be through the jets and outflows, that are observed in proto-stellar objects of all mass. In this proceeding, we present the recent results we obtained with ALMA observations toward the HH30 T-Tauri star. By studying the gas dynamics we could show that the outflow is transporting angular momentum away from the system disk-protostar.

Keywords: ISM, Star formation, Protostar, Accretion, Ejection, Outflow, Jets, Precession

1 Introduction

A necessary prerequisite to understand the formation of stars is the comprehension of the complex processes that permit to a particle in the molecular cloud to end up in the protostar. The major issue in the aspect is the law of the conservation of the angular momentum: $r \times v_\phi = constant$. A particle collapsing toward the potential well (r decreases) will spin faster and faster (v_ϕ increases) and reach equilibrium when v_ϕ equals the Keplerian velocity at the distance r from the proto-star. It is believed that the magnetic field permit to extract a fraction of the angular momentum from the collapsing gas before it reaches the accretion disk. With such processes, the latest numerical simulations manage to form circumstellar disk in line with the observations (e.g. Tsukamoto et al. 2018; Hennebelle & Ciardi 2009). For long, the community thought that the extraction of the angular momentum in the disk itself was due to the *magneto-rotational-instability* (MRI, Balbus & Hawley 1991). This instability produces vigorous turbulence and efficiently transports angular momentum outwards in discs with effective viscosity $\alpha > 10^{-3}$ (Hawley et al. 1995). Nevertheless, it was shown recently that when non-ideal magneto-hydro-dynamical effects are taken into account, namely the Hall effect, the ambipolar diffusion, and the Ohmic dissipation, the MRI gets inefficient (e.g. Lesur et al. 2014). Another possibility to extract angular momentum from the disk could be trough the jets and outflows, hypothesis first stated by Pudritz & Norman (1983).

Outflows and jets seem to be ubiquitous in star-forming systems of all masses, that from the formation of brown-dwarves (Whelan et al. 2018) and up to massive star formation (Duarte-Cabral et al. 2014). Outflows are also witnessed at all stages of star formation, from the Class 0 stage (Bachiller & Pérez Gutiérrez 1997) and up to the T-Tauri stage (Burrows et al. 1996). Jets are also observed toward more extreme objects such as AGNs

[1] Universidad de Chile, 1515 camino el Observatorio, Las Condes, Santiago, Chile
[2] Univ. Grenoble Alpes, CNRS, IPAG, 38000 Grenoble, France
[3] Sorbonne Université, PSL Research University, CNRS, Observatoire de Paris, LERMA, 75014 Paris, France
[4] Instituto de Astrofísica, Pontificia Universidad Católica de Chile, Santiago, Chile
[5] School of Physics and Astronomy, University of Leicester, Leicester, LE1 7RH, United Kingdom
[6] LERMA, Observatoire de Paris, PSL Research University, CNRS, Sorbonne Universités, UPMC Univ. Paris 06, 75014 Paris, France
[7] Monash Centre for Astrophysics(MoCA)and School of Physics and Astronomy, Monash University, Clayton Vic 3800, Australia
[8] ALMA/ESO, Alonso de Cordova 3107, Santiago, Chile

and X-binaries, where a compact object accrete material through an accretion disk. Therefore, it is possible that the physical process creating the outflows and jets is universal. Hence, studying the outflows arising from proto-stars could be a key path for understanding accretion in a broader context.

2 About the accretion-ejection processes

Using the interferometer ALMA, we observed the disk and the outflow of the HH30 T-Tauri star (Louvet et al. 2018). HH30 is a very well characterized proto-star of the Taurus molecular cloud, located at ∼140 pc. The left panel of the Fig. 1 summarizes our observations of the gas around HH30. The disk appears perpendicular to the plan of the sky and display a clear Keplerian rotation when traced in ^{13}CO (color scale in Fig. 1-left). The outflow of HH30 is well traced in ^{12}CO and extends in the plan of the sky up to several hundreds of au above the disk plane (grey scale in Fig. 1-left). Since the outflow develops in the plane of the sky, each cut above the mid-plane (e.g. such as the green arrow in Fig. 1) is at the same altitude, whereas in an inclined system different altitudes get mixed in a given line of sight. The middle panel of the Fig. 1 shows the position-velocity diagram (pvd) at the altitude where the green arrow is overlaid on the left panel. A pvd is basically a collection of spectra stuck one next to each over and where the flux in a given channel is levels of grey. In Fig. 1-middle one can see that at each position, two peaks are present in the spectrum. These two peaks show the red-shifted and blue-shifted faces of the outflow. Since the intermediate velocities have a very low flux (the pvd is 'empty') the best representation of the outflow is an empty cone with the gas flowing along the edges of the cone. In a more quantitative way, it is possible to derive the dynamical parameters of the gas at a given altitude (see Fig. 2-right) by fitting an ellipse to its pvd – the parameters of the ellipse being correlated to the dynamical parameters by:

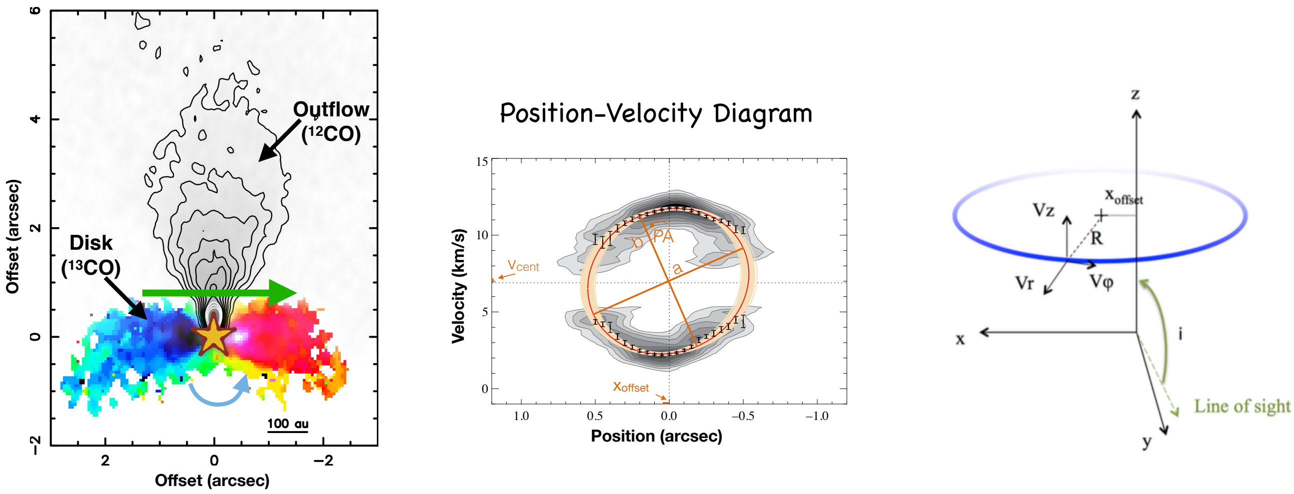

Fig. 1. Left: The figure displays in greyscale the integrated ^{12}CO(2-1) emission that traces the outflow, the colors display the moment 1 map of the ^{13}CO(2-1) emission showing the extent of the disk and its sense of rotation. **Middle:** Position-velocity diagram of the ^{12}CO(2-1) emission at the altitude $z = 0.7''$ (or 100 au at the distance of HH30), highlighted by the green arrow in the left panel. PA, a, and b design the parameters of the ellipse that best fit the CO emission. $v_{\rm cent}$ and $r_{\rm cent}$ are the offsets with respect to the $v_{\rm lsr}$ and to the center of disk as seen in continuum, respectively. **Right:** The sketch illustrates the different dynamical parameter of a cut at a given altitude above the mid-plane. For $i = 90^\circ$, V_r is the radial velocity toward the observer, V_z is the velocity along in the plane of the sky, V_ϕ is the rotation velocity, $x_{\rm offset}$ is the offset of the cut with respect to the central position of the disk, and R is the radius of the cone at this altitude. All these parameters can be derived from the fit of an ellipse on the position-velocity diagram at the corresponding altitude z (see the central panel) through the equations (2.1)-(2.5).

$$x_{\rm offset} = r_{cent} \tag{2.1}$$

$$V_{\rm z} = -(V_{cent} - V_0)/\cos i \tag{2.2}$$

$$(V_{\rm r} \sin i)^2 = \left((\cos PA)^2/a^2 + (\sin PA)^2/b^2\right)^{-1} \tag{2.3}$$

$$(V_\phi \sin i)/R = 0.5 \times (V_\mathrm{r} \sin i)^2 \times \sin 2PA \times (1/b^2 - 1/a^2) \quad (2.4)$$
$$1/R^2 = \left((\cos PA)^2/b^2 + (\sin PA)^2/a^2\right) - (V_\phi/R)^2/V_\mathrm{r}^2. \quad (2.5)$$

In Louvet et al. (2018) we derived these parameters all along the extent of the outflow. From this analysis, two major results were obtained:

- The outflow rotates. We found that v_ϕ reaches values of $\sim$0.75 km s^{-1} at 50 au above the disk plane and decreases with the altitude.
- The specific angular moment, defined as the product $R \times v_\phi$ is conserved all along the outflow with a value of $\sim$40 au km s^{-1}.

If we further assume that the specific angular momentum is conserved down to the disk-plane, we can infer a launching radius for the outflow between 1 and 7 au. The association of such ejection radius with the mass ejection rate of $\sim 9\times10^{-8}$ M$_\odot$ yr^{-1} that was infer by Louvet et al. (2018) best favour the magneto-centrifugal disk-winds to explain the outflow of HH30. Interestingly, among all the models that explain for the ejection of material through jets and outflows, the magneto-centrifugal disk-winds are the only ones that extract angular momentum from the disk – and could consequently explain for the accretion in circumstellar disks.

3 About the precession of jets and outflows

Numerous jets arising from proto-stellar systems are observed to wiggle. This is the case for the jet of HH30 (Anglada et al. 2007), but also for instance in V1331 Cyg located at 550 pc from the Sun (Mundt & Eislöffel 1998), or in RNO 15-FIR located at 350 pc from the Sun (Davis et al. 1997). It is largely believed that the wiggling of jets is caused either by orbital motions in coplanar binary system or by tidal interactions in non-coplanar binary system (e.g., Terquem et al. 1999). These two configurations are illustrated in Fig. 2. Anglada et al. (2007) computed the two solutions that reproduce the wiggling of the jet of HH30. They showed that if orbital motions is causing the wiggling of the jet of HH30 the separation of the binary shall be of $\sim$18 au, which should truncate the disk at an inner radius of $\sim$40 au. If the wiggling is due to precession of the jet, they showed that the separation of the binary would be very small, of $\sim$1 au. Later, Guilloteau et al. (2008) observed the disk of HH30 in continuum with the PdBI interferometer. They reported a possible truncation of the disk at 37$\pm$4 au, giving credit to the orbital motion scenario. Nevertheless, we could not find a sign for disk truncation in HH30 when we re-observed the system with ALMA at an angular resolution two times better than that of Guilloteau et al. (2008). The image of the continuum emission as seen with ALMA is shown on the left panel of Fig. 3. That result casts doubt on the existence of a wide binary explaining for the wiggling of HH30. Also, by studying the dynamical parameters of the outflow (see Sect. 2) we could constrain the amplitude of the wiggling of the outflow, as shown on the right panel of Fig. 3. We adapted the two solutions found by Anglada et al. (2007) so they would correspond to the dynamics of the outflow*. These solutions, over-plotted on the right panel of Fig. 3 clearly show that the orbital-motion solution predicts displacement of the outflow order of magnitudes bigger than the observed one, while the precession solution is much more in line with the observations.

4 Conclusions

In the one hand, Louvet et al. (2018) showed that the outflow of HH30 is rotating, and that the angular momentum is conserved as the outflow extends. Assuming that the angular momentum is also conserved all the way down to the disk (i.e. below our angular resolution) we could infer launching radius in between 1 and 7 au. These launching radii together with the mass ejection rate of $\sim 10^{-7}$ M$_\odot$ best favour the MDH disk wind models. In the other hand the study of the continuum, that shows no gap in the inner part, together with the very small wiggling of the outflow best favour precession to explain for the wiggling of the jet and outflow in HH30.

*The solutions of Anglada et al. (2007) depend on the jet velocity along the z-scale. We simply replaced that velocity by that of the outflow that is $\sim$10 times slower.

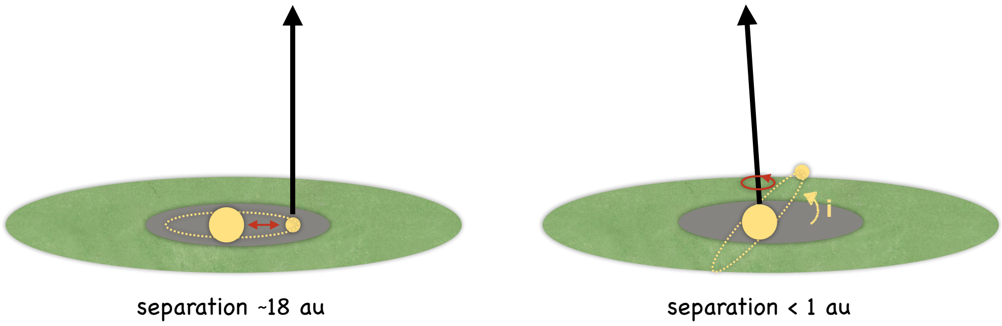

Fig. 2. Left: Sketch of the *orbital motion* scenario. In this scenario, the outflow arises from the circumstellar disk of the secondary. **Right:** Sketch of the *precession scenario*. With this hypothesis the secondary orbits out of the plane of the primary's disk. This provokes the disk of the primary to precess, a precession that gets imprinted onto the outflow. The angle i is exaggerated to ease the illustration – a few degrees are sufficient to induce precession.

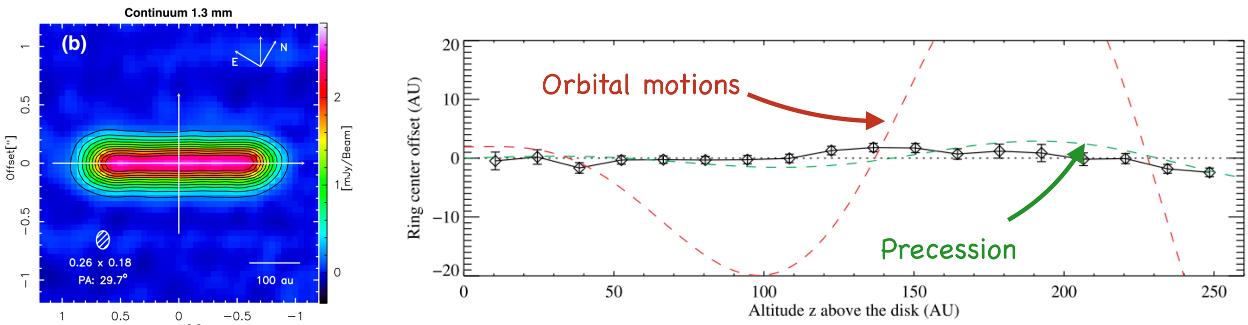

Fig. 3. Left: Continuum emission at 1.33 mm of HH30. Contrary to Guilloteau et al. (2008) no gap is seen in the continuum, casting doubts on the presence of a wide-binary as necessary in the *orbital motion* scenario (see Fig. 2-left). **Right:** The plot displays the radial offset position (see Fig. 1) of the gas as a function of altitude above the disk (hence along the outflow) with respect to the central position of the disk as seen in continuum. The red curve presents the predicted offset if the displacement in the outflow were due to orbital motion. The green curve presents the predicted offset of the outflow if due to precession. The figures were extracted from Louvet et al. (2018).

References

Anglada, G., López, R., Estalella, R., et al. 2007, AJ, 133, 2799
Bachiller, R. & Pérez Gutiérrez, M. 1997, ApJ, 487, L93
Balbus, S. A. & Hawley, J. F. 1991, ApJ, 376, 214
Burrows, C. J., Stapelfeldt, K. R., Watson, A. M., et al. 1996, ApJ, 473, 437
Davis, C. J., Eisloeffel, J., Ray, T. P., & Jenness, T. 1997, A&A, 324, 1013
Duarte-Cabral, A., Bontemps, S., Motte, F., et al. 2014, A&A, 570, A1
Guilloteau, S., Dutrey, A., Pety, J., & Gueth, F. 2008, A&A, 478, L31
Hawley, J. F., Gammie, C. F., & Balbus, S. A. 1995, ApJ, 440, 742
Hennebelle, P. & Ciardi, A. 2009, A&A, 506, L29
Lesur, G., Kunz, M. W., & Fromang, S. 2014, A&A, 566, A56
Louvet, F., Dougados, C., Cabrit, S., et al. 2018, A&A, 618, A120
Mundt, R. & Eislöffel, J. 1998, AJ, 116, 860
Pudritz, R. E. & Norman, C. A. 1983, ApJ, 274, 677
Terquem, C., Eislöffel, J., Papaloizou, J. C. B., & Nelson, R. P. 1999, ApJ, 512, L131
Tsukamoto, Y., Okuzumi, S., Iwasaki, K., Machida, M. N., & Inutsuka, S. 2018, ApJ, 868, 22
Whelan, E. T., Riaz, B., & Rouzé, B. 2018, A&A, 610, L19

SF2A 2019
P. Di Matteo, O. Creevey, A. Crida, G. Kordopatis, J. Malzac, J.-B. Marquette, M. N'Diaye, O. Venot (eds)

MAGNETOSPHERIC ACCRETION IN THE INTERMEDIATE-MASS T TAURI STAR HQ TAU

K. Pouilly[1], J. Bouvier[1], E. Alecian[1], A.-M. Cody[2], J.-F. Donati[3], S.H.P. Alencar[4], K. Grankin[5], L. Rebull[6] and C. Folsom[3]

Abstract. Magnetospheric accretion is a main interaction process between Classical T Tauri stars (CTTSs) and their inner disk. Understanding this process is therefore crucial to characterize star-disk interactions. We investigate the photometric and spectroscopic variability of HQ Tau, a CTTS of 1.8 $M_\odot$ and 2.7 $R_\odot$, from Kepler K2 light curve and a series of ESPaDOnS spectra obtained at the Canada-France-Hawaii Telescope. Balmer line profiles exhibit periodic variability, at the stellar rotation period, with high velocity redshifted absorptions appearing (Inverse P Cygni Profile - IPC). The radial velocity shows a modulation at the stellar rotation period too, but is not consistent with the time of appearance of the IPC. We therefore ascribed the radial velocity modulation to a cold spot and the IPC to the accretion column. From the spectropolarimetric analysis of the ESPaDOnS spectra , we also measure a mean longitudinal magnetic field with a maximum intensity of 430 G, which is modulated by stellar rotation. The maximum is consistent with the IPC, we deduce that the mean longitudinal magnetic field is modulated by the hot spot thus corresponds to the footprint of the magnetic pole at the stellar surface. Preliminary results of this study appear to be consistent with what is expected from magnetospheric accretion onto a global dipolar magnetic field in the intermediate-mass T Tauri star HQ Tau.

Keywords: Classical T Tauri Star, IMTTS, HQ Tau, magnetospheric accretion, hot spot, cold spot

1 Introduction

Classical T Tauri Stars (CTTSs) are low or intermediate mass young stars. There are defined by their accretion disk and their magnetic field strong enough to truncate the disk near to the corotation radius and accrete material. The material follows the magnetic field lines to fall onto the star, forming the so called accretion columns. This complete process is the magnetospheric accretion process (Bouvier et al. 2007), and it is the key of evolution of young stellar objects. We present here the study of HQ Tau, an intermediate-mass CTTS, with the aim to characterize its magnetosphere and the interactions between the star and its disk. We use 2 data sets to lead this study: first the spectropolarimetry obtained from the ESPaDOnS spectrometer (Donati 2003) mounted at Canada-France-Hawaii Telescope (CFHT) between October 28^{th} and November 9^{th} 2017. This data set is composed of 14 spectra in the visible range at a resolution or 68 000 and a SNR of 150 at 730 nm. Then, the photometric study is performed thanks to the Kepler-K2 mission (`https://archive.stsci.edu/k2/`), which observed HQ Tau during the 13^{th} campaign. Section 2 presents the stellar parameters determination and modulation from both data sets. The spectroscopic study is detailed in Section 3 trough Hα and Hβ variability and we conclude this study by the spectropolarimetric analysis in Section 4.

[1] Univ. Grenoble Alpes, CNRS, IPAG, 38000 Grenoble, France
[2] Bay Area Environmental Research Institute, 625 2nd St Ste. 209, Petaluma, CA 94952
[3] Univ. de Toulouse, CNRS, IRAP, 14 avenue Belin, 31400 Toulouse, France
[4] Departamento de Fisica – ICEx – UFMG, Av. Antônio Carlos 6627, 30270-901 Belo Horizonte, MG, Brazil
[5] Crimean Astrophysical Observatory, Nauchny, Crimea 298409
[6] Infrared Science Archive (IRSA), IPAC, California Institute of Technology, 1200 E. California Blvd, MS 100-22, Pasadena, CA 91125 USA

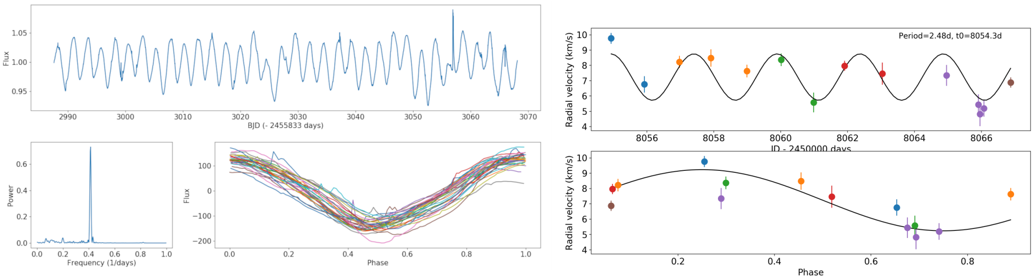

(a) **Top:** HQ Tau's Kepler K2 light curve. **Bottom left:** Lomb-Scargle periodogram with highest peak at 2.42 d. **Bottom right:** Light curve folded in phase.

(b) **Top:** Radial velocity curve, each color correspond to a rotational cycle. **Bottom:** Curve folded in phase

Fig. 1

2 Stellar parameters

We take advantage of the high resolution spectra produced by ESPaDOnS to derive the stellar parameters of HQ Tau. First we fit a synthetic spectrum produced by the ZEEMAN code (Landstreet 1988; Wade et al. 2001; Folsom et al. 2012) on 11 wavelength windows of the mean spectrum to derive HQ Tau's T_{eff} = 4950 K and vsini = 53.7 km s^{-1}. Then we couple the effective temperature with the J and V magnitudes (Cutri et al. 2003; Norton et al. 2007), the Gaia parallax (Gaia Collaboration 2018), visual extinction (Herczeg & Hillenbrand 2014) and bolometric correction (Pecaut & Mamajek 2013) to derive the bolometric luminosity of the star. We fit its position in a Hertzprung-Russel Diagram with a CESTAM (Morel & Lebreton 2008; Marques et al. 2013) evolutionary model to derive the HQ Tau's mass M = 1.8 $M_\odot$ and radius R = 2.74 $R_\odot$. Finally, we derive a mean radial velocity v_{rad} = 7.14 km s^{-1}, by cross correlation on those wavelength windows with a photospheric template, Melotte 25 151, a K2 spectral type Main Sequence (MS) dwarf (Folsom et al. 2018).

As shown in Figure 1a, HQ Tau's light curve exhibits a clear and stable modulation. The periodogram analysis (Scargle 1982; Press et al. 1992) results clearly on a 2.42 d modulation, ascribed to the stellar rotational period as expected from a spotted surface (Herbst et al. 1994). A spot also induces a modulation of photospheric line profiles which produce an apparent modulation of the radial velocity (Vogt & Penrod 1983). We compute the radial velocity for each spectrum and plot the radial velocity curve shown in Figure 1b. A sinusoidal fit yields a period of 2.48 d, consistent with the photometric period. The curve folded in phase shows the behavior expected from a spot modulation. We set the phase at 0.5 at the moment when the spot is aligned with the line of sight.

3 Hα and Hβ profile

The most significant emission lines in HQ Tau's spectrum are Hα and Hβ. As there are in part formed in the accretion column, we can study them to get insight into the magnetospheric accretion process.

Figure 2 top panels shows the 14 profiles of those lines. We notice that there are very variable, especially in the red wings. Furthermore, using 2D periodograms presented in the bottom panels of Figure 2, Hα and Hβ exhibit a periodic modulation of this red wing, on the stellar rotational period. Those absorptions are Inverse P Cygni (IPC) profiles, produced by the accretion funnel flow, and are the direct signature of this phenomenon.

The 14 profiles are presented independently in Figure 3 sorted by days and by phase. This figure shows that the maximum of IPC profile is reach at phase 0.7, corresponding to the moment when the accretion funnel flow is aligned with the line of sight. This is not consistent with the radial velocity because the spot which modulates it is on the line of sight at phase 0.5. The two parameters are therefore modulated by two different phenomena, a cold spot for the radial velocity, and the funnel flow for the line profile.

We study the different components of those lines using the correlation matrices (Johns & Basri 1995; Oliveira et al. 2000; Alencar & Batalha 2002; Kurosawa et al. 2005) presented in Figure 4. Both Hα and Hβ line show a strong correlation within the red wing on there respective autocorrelation matrices and on the cross correlation matrix Hα vs. Hβ. On Hα autocorrelation matrix we notice also a correlation within the blue wing. Those correlations suggest that different physical processes dominate the variation of the blue and the red part of the

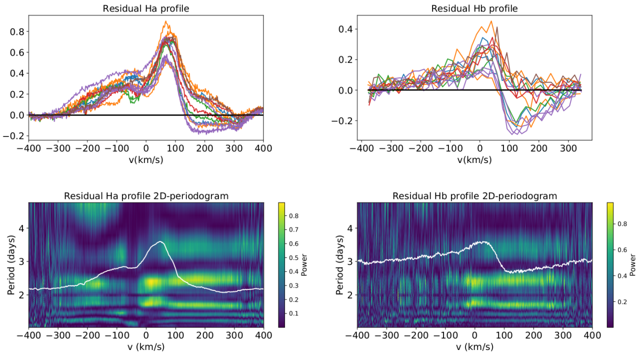

Fig. 2: **Top left:** 14 residual Hα profiles. **Bottom left:** 2D periodogram of Hα profile. **Right:** Same as left, but for Hβ profiles.

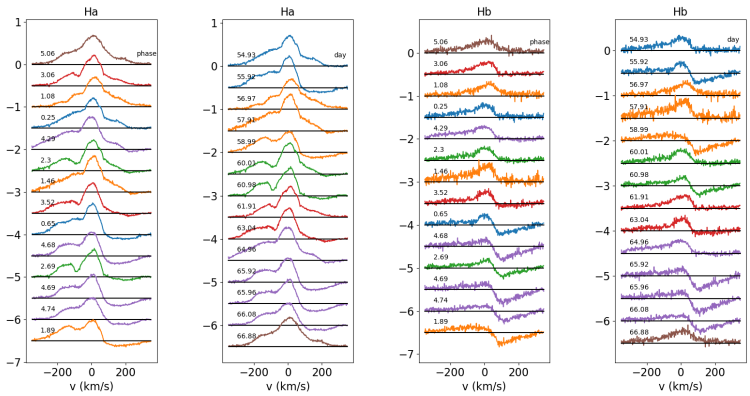

Fig. 3: **From left to right:** Successive Hα profiles sorted by phase, day, and the same for Hβ.

lines: accretion (IPC profile) for the red wing, and a wind for the blue wing of Hα. Finally, an anti correlation is highlighted on Hα (dark purple) between red and blue wing. This shows the possible accretion-ejection connection which will be detailed in a forthcoming paper (Pouilly et al., submitted).

4 Spectropolarimetry

Using the spectropolarimetric mode of ESPaDOnS, we get the unpolarized (Stokes I) and circularly polarized (Stokes V) spectra. We compute the Stokes I and V profiles by the Least Square Deconvolution (LSD - Donati et al. (1997)) method and study their variability. The Stokes I LSD profiles show a modulation which turns out to be periodic on the stellar rotational period. Unfortunately, only one third of the data set show a clear Stokes V signature, we are not able the derive any modulation from it. Nevertheless, we compute the surface average longitudinal magnetic field following the expression from Wade et al. (2001). The curve is shown in Figure 5. A sinusoidal fit yields to a period consistent with the photometric period. However the fit quality is low so the modulation is still unclear. The only correlation we can get from it is the consistency between the

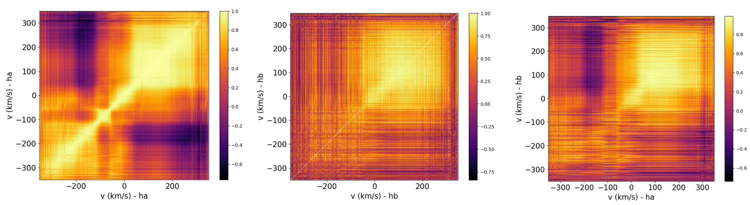

Fig. 4: **Left:** Hα autocorrelation matrix. **Middle:** Hβ autocorrelation matrix. **Right:** Hα vs. Hβ correlation matrix.

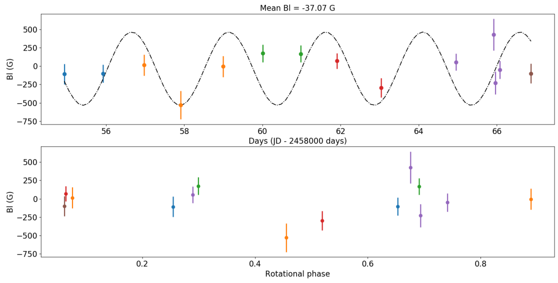

Fig. 5: **Top:** Surface averaged longitudinal magnetic field B_l curve. **Bottom:** B_l curve folded in phase.

strong minimum measured at phase 0.5, and the radial velocity curve, which indicates that the cold spot is on the line of sight at this phase.

5 Conclusions

The magnetospheric accretion process on HQ Tau is consistent with a strong magnetic field truncating the disk and the material being accreted along magnetic field lines. The accretion funnel flows are observed trough IPC profiles which modulate the Hα and Hβ lines while the radial velocity curve is modulated by a spot. From the estimated mass accretion rate, providing an estimate of the truncation radius, we conclude that the magnetospheric accretion process at work in low-mass T Tauri stars appears to extend to intermediate-mass ones.

This project has received funding from the European Research Council (ERC) under the European Union's Horizon 2020 research and innovation program (grant agreement No 742095 ; SPIDI : Star-Planets-Inner Disk- Interactions `spidi-eu.org`). This paper includes data collected by the Kepler mission. Funding for the Kepler mission is provided by the NASA Science Mission directorate. This work has made use of the VALD database, operated at Uppsala University, the Institute of Astronomy RAS in Moscow, and the University of Vienna. This project was funded in part by INSU/CNRS Programme National de Physique Stellaire and Observatoire de Grenoble Labex OSUG2020. Based on observations obtained at the Canada-France-Hawaii Telescope (CFHT) which is operated by the National Research Council of Canada, the Institut National des Sciences de l'Univers of the Centre National de la Recherche Scientifique of France, and the University of Hawaii.

References

Alencar, S. H. P. & Batalha, C. 2002, ApJ, 571, 378

Bouvier, J., Alencar, S. H. P., Harries, T. J., Johns-Krull, C. M., & Romanova, M. M. 2007, Protostars and Planets V, 479

Cutri, R. M., Skrutskie, M. F., van Dyk, S., et al. 2003, VizieR Online Data Catalog, 2246

Donati, J.-F. 2003, in Astronomical Society of the Pacific Conference Series, Vol. 307, Solar Polarization, ed. J. Trujillo-Bueno & J. Sanchez Almeida, 41

Donati, J.-F., Semel, M., Carter, B. D., Rees, D. E., & Collier Cameron, A. 1997, MNRAS, 291, 658

Folsom, C. P., Bagnulo, S., Wade, G. A., et al. 2012, MNRAS, 422, 2072

Folsom, C. P., Bouvier, J., Petit, P., et al. 2018, MNRAS, 474, 4956

Gaia Collaboration. 2018, VizieR Online Data Catalog, 1345

Herbst, W., Herbst, D. K., Grossman, E. J., & Weinstein, D. 1994, AJ, 108, 1906

Herczeg, G. J. & Hillenbrand, L. A. 2014, ApJ, 786, 97

Johns, C. M. & Basri, G. 1995, ApJ, 449, 341

Kurosawa, R., Harries, T. J., & Symington, N. H. 2005, MNRAS, 358, 671

Landstreet, J. D. 1988, The Astrophysical Journal, 326, 967

Marques, J. P., Goupil, M. J., Lebreton, Y., et al. 2013, A&A, 549, A74

Morel, P. & Lebreton, Y. 2008, Ap&SS, 316, 61

Norton, A. J., Wheatley, P. J., West, R. G., et al. 2007, A&A, 467, 785

Oliveira, J. M., Foing, B. H., van Loon, J. T., & Unruh, Y. C. 2000, A&A, 362, 615

Pecaut, M. J. & Mamajek, E. E. 2013, ApJS, 208, 9

Press, W. H., Teukolsky, S. A., Vetterling, W. T., & Flannery, B. P. 1992, Numerical recipes in FORTRAN. The art of scientific computing

Scargle, J. D. 1982, ApJ, 263, 835

Vogt, S. S. & Penrod, G. D. 1983, PASP, 95, 565

Wade, G. A., Bagnulo, S., Kochukhov, O., et al. 2001, A&A, 374, 265

SF2A 2019
P. Di Matteo, O. Creevey, A. Crida, G. Kordopatis, J. Malzac, J.-B. Marquette, M. N'Diaye, O. Venot (eds)

WAVELET ANALYSIS OF TAURUS K2 DIPPER LIGHT CURVES

N. Roggero[1], J. Bouvier[1], A.M. Cody[2] and L. Rebull[3]

Abstract. During the evolution of T Tauri stars and the formation of their planetary systems, accretion processes play a key role. However, the more complex interaction at the rim of the inner region of the disk is still not fully understood. The SPIDI (Star-Planet-Inner Disk-Interactions) project aims to further investigate this phenomenon and its influence on forming planets in the inner disk.

The magnetic field of a young star truncates the disk where the magnetic field pressure is equal to the ram pressure of the accreting material. Thus, the dust and the gas present in the disk are lifted above the plane along the magnetic field lines. If the temperature is low enough for dust to survive, this accretion warp obscures the star and causes eclipses observable with photometry, i.e. the dipper phenomenon. The periodicity of a dipper star depends on the stability of the dusty warp.

In this work, wavelet analysis of the K2 light curves from the Taurus region allows us to study the time-resolved periodicity of the dippers and other signals present in the light curves. This information, together with further fitting with an occultation model, dust survival models, and radiative transfer modelling, will allow us to isolate a possible planetary signal embedded in accretion-driven photometric variability.

Keywords: stars: variables: T Tauri, protoplanetary disks, techniques: photometric

1 Introduction

Classical T Tauri stars (CTTSs) are low-mass, pre-main sequence stars which are still accreting from their circumstellar disks. They are Class II protostars, which means that the main contribution to the SED is given by stellar radiation, while a significant infrared excess from the disk is present.
The disk itself might extend up to hundreds AU. We will focus on the very inner part of the disk –at a scale of a few stellar radii, i.e. $\sim 0.02\,\mathrm{AU}$–, where dust evaporates and the accretion takes place onto the star. This region is very challenging to observe, as it is at the limit of the resolution of interferometry. Light curves allow an indirect observation of the phenomena occurring at the inner disk rim.
In recent years, it was noticed that a significant percentage of T Tauri stars –around 30% of the disk-bearing stars– display eclipses in their light curves that cannot be traced back to binarity. It was supposed that these "dipper" light curves are caused by dusty material from the disk, that occults the star during its rotation (e.g. , Cody et al. (2014), Alencar et al. (2010)).
The occurrence of dippers might be explained by the magnetospheric accretion model (Bouvier et al. 1999). The inner disk is truncated when it reaches the magnetosphere of the star, as its material is accreted onto the star following the magnetic field lines. If the temperature in this region is cool enough for dust to survive, dust might be lifted above the disk plane in form of an accretion stream or warp. An observer at a high inclination angle will thus be able to observe a dipper light curve (Bodman et al. 2017).
Photometric observations can thus deliver information about the position and the temperature at the truncation radius, which is of vital importance for understanding the interaction between the star and the inner disk.

[1] Univ. Grenoble Alpes, CNRS, IPAG, 38000 Grenoble, France
[2] NASA Ames Research Center, Moffett Field, CA 94035, USA ; Bay Area Environmental Research Institute, 625 2nd St., Suite 209, Petaluma, CA 94952, USA
[3] Caltech-IPAC/IRSA, Pasadena, CA, United States

2 Observations and Data Reduction

The Taurus region was observed nearly continuously with the *Kepler* satellite within the framework of the K2 mission, with a cadence of 29.4 min and a duration of 80 days. The observation campaigns C13 (Mar - May 2017) and C4 (Feb - Apr 2015) delivered light curves for about 900 potential members.
K2 data are challenging to reduce and several pipelines are available for this purpose. If the light curve does not present particular issues, we used the version with moving aperture as in Cody & Hillenbrand (2018) as default and performed a more careful inspection on dipper candidates.
The process to assess the membership of each star to the cluster is explained by Rebull et al. (in prep.). We attribute higher confidence membership to candidates which already appear as members in Luhman (2018). Finally, we produce a sample of 225 Taurus members with K2 light curves and use it as basis to search for dippers.

3 Wavelet analysis of dippers

Detailed information on the periodicity of dippers is necessary to derive a number of parameters, among them the location of the dusty warp that obscures the star.
The exact configuration of the inner disk changes from cycle to cycle; dippers are thus either aperiodic or quasi-periodic phenomena. This distinction is important, as aperiodic dippers seem to be generated by different mechanisms than quasi-periodic ones (Ansdell et al. 2016; Stauffer et al. 2015). In some cases, the occultations are transient, making it difficult for classic period-finding algorithms to determine the correct period. It is also interesting to find out if the period evolves over time.
The wavelet transform is an efficient tool to analyze the frequency spectrum of a signal and to gain time resolution (see Torrence & Compo (1998)). Lately, the tool has found application in light curve analysis (e.g., Hedges et al. (2018), Bravo et al. (2014) and García et al. (2014) for *Kepler* light curves).
It can be viewed as a time-resolved Windowed Fourier Transform (WFT) with variable window width, that reveals both high and low frequency features. The wavelet, which is a finite wave in the time domain –instead of an infinite sinusoid as in the Fourier transform– is convolved with the signal at each position with a given time step. To gain time resolution, the wavelet is scaled in the time domain (i.e. stretched or compressed) and again convolved and shifted along the signal. A high correlation between the wavelet and the time series results in high power in the Wavelet Power Spectrum (WPS).
In this work, the complex Morlet wavelet is used, as it is a good compromise between time and frequency resolution and allows for adjustment of these two parameters according to one's needs.

4 Results

The dippers are identified among the Taurus members from a visual inspection of the light curve. We classified by eye 35 young stars as either dippers or variable stars that show dips in their light curves as secondary variability. Among the 23 stars classified as dippers, 12 are periodic and the rest are either aperiodic or show complex periodicities. The period range varies between 2 and 11 days and most of the stars have a period shorter than 5 d.
An example of a periodic dipper (JH 223) is shown in Fig. 1. The star displays a constant brightness and periodic dips, which vary in shape and depth. The Wavelet Power Spectrum (WPS) shows the power at different periods (y-axis) at different positions in time (x-axis). The comparison with the CLEAN periodogram (Roberts et al. 1987) illustrates the loss of frequency resolution in the wavelet transform. The exact values of the period are, where possible, retrieved from the periodogram.

GH Tau is a good example where wavelet analysis is beneficial to interpret a complex periodogram (Fig. 2, left panel). By looking at the WPS, it becomes clear that most of the peaks seen on the periodogram are local periodicities, while only the two highest peaks might be real periods. At the same time, the double peak illustrates well the uncertainty principle of time and frequency resolution, since it is not resolved on the WPS.

JH 112 is a transient, periodic dipper. The mostly constant brightness makes it difficult for the periodogram analysis to reach a high detection significance (Fig. 2, right panel). The WPS shows how the local periodicity

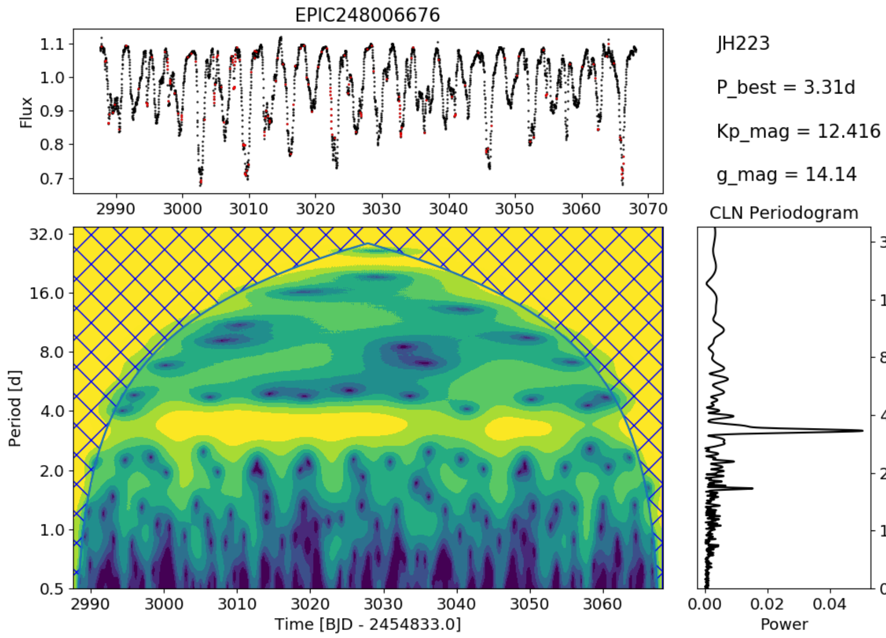

Fig. 1. In order to perform the wavelet transform, the K2 light curve (top) is linearly interpolated at the missing values (red dots). The Wavelet Power Spectrum shows the time-resolved frequency spectrum (bottom). The contours indicate the power of a certain period at a certain point in time; yellow contours have the highest power, blue ones the lowest. In order to obtain a better contrast, the contours are saturated at the 3 and 99 percentile. The Cone of Influence (crosses) delimits the area where the WPS is affected by edge effects; a high power in this region is not significant. The WPS is compared to a CLEAN periodogram (right).

corresponds to the visually detectable dipping.

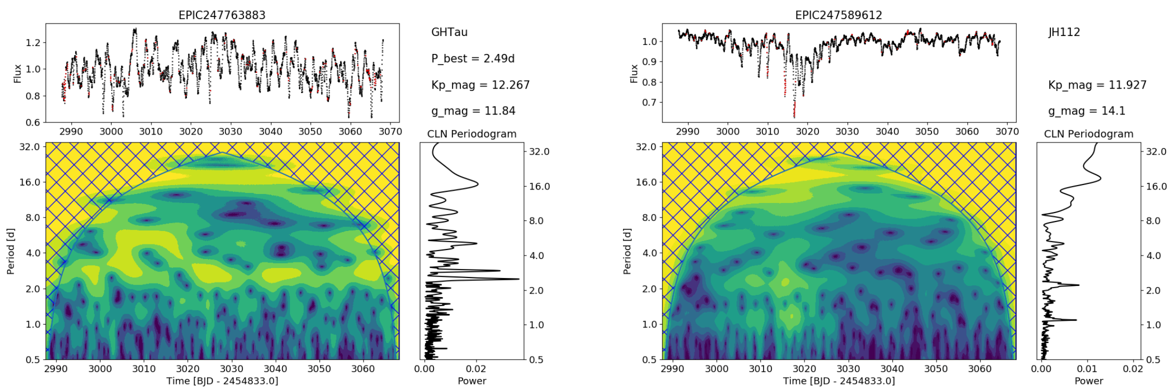

Fig. 2. Left: Light curve, periodogram and WPS of GH Tau. **Right:** Light curve, periodogram and WPS of JH 112.

5 Conclusions and Outlook

The application of wavelet analysis to dipper light curves allows us to more thoroughly study their periodicity. Among the 225 Taurus members, 35 show dipping events in their light curves. Of the 23 dippers with no other evident variability, about 50% are periodic with periods between 2 and 11 d. This information allows us to compute the location of the dusty warp. Furthermore, a simple occultation model makes it possible to derive the geometry of the system, i.e. the inclination, the warp's maximum height and its azimuthal extension. In upcoming work, a full modeling will be attempted using the MCFOST radiative transfer code (Pinte et al. 2006), to hopefully reach beyond the simple detection of the main periodicity.

This project has received funding from the European Research Council (ERC) under the European Union's Horizon 2020 research and innovation programme (grant agreement No 742095; *SPIDI*: Star-Planets-Inner Disk-Interactions). `http://spidi-eu.org/`
This paper includes data collected by the K2 mission. Funding for the K2 mission is provided by the NASA Science Mission directorate.

References

Alencar, S. H. P., Teixeira, P. S., Guimarães, M. M., et al. 2010, A&A, 519, A88

Ansdell, M., Gaidos, E., Rappaport, S. A., et al. 2016, ApJ, 816, 69

Bodman, E. H. L., Quillen, A. C., Ansdell, M., et al. 2017, MNRAS, 470, 202

Bouvier, J., Chelli, A., Allain, S., et al. 1999, A&A, 349, 619

Bravo, J. P., Roque, S., Estrela, R., Leão, I. C., & De Medeiros, J. R. 2014, A&A, 568, A34

Cody, A. M. & Hillenbrand, L. A. 2018, AJ, 156, 71

Cody, A. M., Stauffer, J., Baglin, A., et al. 2014, AJ, 147, 82

García, R. A., Ceillier, T., Salabert, D., et al. 2014, A&A, 572, A34

Hedges, C., Hodgkin, S., & Kennedy, G. 2018, MNRAS, 476, 2968

Luhman, K. L. 2018, AJ, 156, 271

Pinte, C., Ménard, F., Duchêne, G., & Bastien, P. 2006, Astronomy and Astrophysics, 459, 797

Rebull, L. R., Stauffer, J. R., Cody, A. M., & Bouvier, J. in prep.

Roberts, D. H., Lehar, J., & Dreher, J. W. 1987, AJ, 93, 968

Stauffer, J., Cody, A. M., McGinnis, P., et al. 2015, AJ, 149, 130

Torrence, C. & Compo, G. P. 1998, Bulletin of the American Meteorological Society, 79, 61

SF2A 2019
P. Di Matteo, O. Creevey, A. Crida, G. Kordopatis, J. Malzac, J.-B. Marquette, M. N'Diaye, O. Venot (eds)

SELF-INDUCED DUST TRAPS AROUND SNOWLINES IN PROTOPLANETARY DISCS

A. Vericel[1] and J.-F. Gonzalez[1]

Abstract. In the core accretion paradigm of planet formation, dust particles need to grow efficiently from micrometer sizes to thousands of kilometers. While the first stages are well understood, the growth through intermediate (mm to km) sizes is hindered by a number of barriers. While many solutions have been proposed, the recent discovery of self-induced dust traps has provided a natural and independent solution to overcome those barriers, opening the way to further investigations towards planetesimal formation. Another natural mechanism present in discs, is the condensation and sublimation of volatile species at certain locations, called snowlines. They separate regions with different grain sticking properties, because of the presence, or absence, of an ice mantle. The Carbon Monoxyde (CO) snowline has been detected in different protoplanetary discs, which raises the question: how do they affect the promising self-induced dust trap formation mechanism ? In this paper, we address this question and present the effect of snow lines on self-induced dust trap formation in a parameter study. We find that for a large number of configurations, a dust trap forms at the snow line location where the dust piles up and slowly grows. We also suggest that planetesimal formation can start at or from the CO snowline. This could provide a link between dust structures and snow lines locations in future disc observations.

Keywords: Protoplanetary discs - Hydrodynamics - Planets and satellites: formation - Methods: numerical

1 Introduction

Currently, one of the main scenarios for planet formation is the core accretion model, i.e. planets are the results of the dust slowly growing to larger sizes through coagulation (Hartmann et al. 1998). Unfortunately, it struggles explaining how mm to m dust grains are able to survive in the disc for two reasons.
1. Since the gas is sensitive to its own pressure gradient, it orbits the star slightly slower than the dust. As a result, the dust feels a headwind and lose angular momentum, which makes it drift towards the star. Intermediate (mm to m) size grains are the ones that are the most affected and drift the fastest (Weidenschilling 1977). This results in their accretion and is called the radial drift barrier (Laibe et al. 2012).
2. When grains drift to the inner part of the disc, their relative velocity increases due to the increase in temperature. This means that at a certain point, the grains shatter rather than grow, which prevents them from slowing down their drift and reaching larger sizes. This is called the fragmentation barrier (Blum & Wurm 2008).
To solve these problems, one can trap dust into pressure maxima, thus stopping its drift (Haghighipour 2005). A few mechanisms have been proposed to create such maxima. While the majority depends on specific conditions, Gonzalez et al. (2017) showed that the back-reaction of the dust onto the gas naturally leads to the formation of a pressure maximum created by the dust evolution. They called it self-induced dust trap. In this study, we focused on those self-induced dust traps and particularly on snow lines, because they also do not require *ad hoc* conditions and are naturally present in discs. Snow lines are the condensation (or sublimation) fronts of volatile species and have been observed (mainly for Carbon Monoxyde (CO)) recently (Qi et al. 2015; Macías et al. 2017). When some volatile species is freezing out at the surface of grains, it changes their sticking properties, thus affecting the way they grow, fragment and by extension drift. This should modify the self-induced dust trap formation scenario and this the investigation we conducted in this study.

[1] Univ Lyon, Univ Lyon 1, ENS de Lyon, CNRS, Centre de Recherche Astrophysique de Lyon UMR5574, F-69230, Saint-Genis-Laval, France

2 Methods

2.1 Numerical simulations

To simulate protoplanetary disc evolution, we use our 3D, two-phase (gas+dust), Smoothed Particles Hydrodynamics (SPH) code (Barrière-Fouchet et al. 2005). Gas-dust aerodynamic coupling is incorporated taking into account the back-reaction of the dust onto the gas. We simulate a typical disc, called "Steep" model that represents an "averaged" observed disc. The disc and our numerical setup are identical to the ones in Gonzalez et al. (2017) and we refer the reader to it for further information.

2.2 Growth and Fragmentation models

The implementation of grain growth is that of Laibe et al. (2008) meanwhile fragmentation is that of Gonzalez et al. (2015). The turbulent relative motion between grains allows them to grow (Stepinski & Valageas 1997) if their relative velocity is lower than a fragmentation threshold, noted $V_{\rm frag}$. The dust growth rate is either positive (i.e. if $V_{\rm rel} < V_{\rm frag}$) or negative (i.e. if $V_{\rm rel} > V_{\rm frag}$) and follows the prescription:

$$\frac{\mathrm{d}s}{\mathrm{d}t} = \pm \frac{\rho_{\rm d}}{\rho_{\rm s}} V_{\rm rel}, \tag{2.1}$$

where $V_{\rm rel}$ is the relative velocity between dust particles while $\rho_{\rm d}$ and $\rho_{\rm s}$ are the volume density of the dust phase and the intrinsic density of the dust material, respectively.

2.3 Snow lines as discontinuities in fragmentation threshold

We incorporate in our simulations a snow line. To represent its effect we adopt different values of the fragmentation velocity such that $V_{\rm fragin}$ corresponds to the inner fragmentation threshold and $V_{\rm fragout}$ to the outer one. This change in $V_{\rm frag}$ mimics the change in grain surface composition, meaning that the smaller the fragmentation threshold is, the weaker the corresponding grain will be regarding fragmentation. We define the position of the snow line $r_{\rm snow}$ either as the location where the temperature is equal to the sublimation temperature $T_{\rm subl}$ or arbitrarily. By sweeping-up the parameter space ($V_{\rm fragin}$, $V_{\rm fragout}$ and $r_{\rm snow}$), we investigate the role snow lines play in the formation of self-induced dust traps.

3 Results

3.1 The snow line position

First, we fix the fragmentation threshold to 15 $\mathrm{m\,s^{-1}}$ in the outer disc and 5 $\mathrm{m\,s^{-1}}$ in the inner disc, thus representing a significant decrease in the ability to stick for the grains inside of the snow line. In Fig. 1 we show the final snapshot of 3 simulations hosting snow lines at 50, 100 and 150 AU, representing relatively close, intermediate and far cases. The right panel shows dust grains remaining at small sizes, due to the fact that dust growth is hindered very early in its history because grains reach a zone where the fragmentation velocity is very low far from the star. As a result, grains cannot grow and drift efficiently and fail to gather enough material to decouple from the gas. Meanwhile, the left and middle panels show remarquable correlation between their dust pile up and the snow lines locations. We see that the dust is more concentrated for the closest snow line (50 AU) than for the intermediate distance one (100 AU). This is because the dust pile-up tends to happen between 80 and 90 AU, where the grains would naturally cross St $\sim$ 1 and therefore slow down their drift.
The left panel of figure 1 is really interesting because it gives a link between the dust distribution and the snow line position. This is why we decided to investigate more closely for snow lines a bit closer to the star. In Fig. 2 is presented this investigation with snow lines at 30 (top), 40 (middle) and 50 (bottom) AU. We also show the gas pressure profile for those simulations, and we cannot help but see a very clear dust pile-up located at the snow line, everytime. The more close in the snow line is, the denser the trap has become which translates into higher gas pressure bumps and bigger grains.

3.2 The Carbon Monoxyde (CO) snowline

The position of the snow line being a key parameter to understand how it affects the dust dynamics, the discontinuity also plays a major role in the evolution of self-induced dust traps at the proximity of snow lines. To

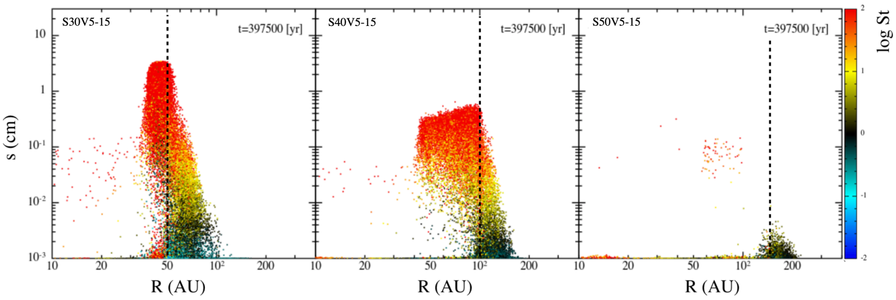

Fig. 1. Dust size as a function of their radial distance to the star for 3 simulations hosting a snow line at 50 (left), 100 (middle) and 150 (right) AU after 400,000 yr. For these simulations, the fragmentation thresholds are set to 5 ($V_{\rm fragin}$) and 15 ($V_{\rm fragout}$) m.s^{-1}. The grains are coloured with the Stokes number. The snow line is highlighted with a black dashed line on every panel.

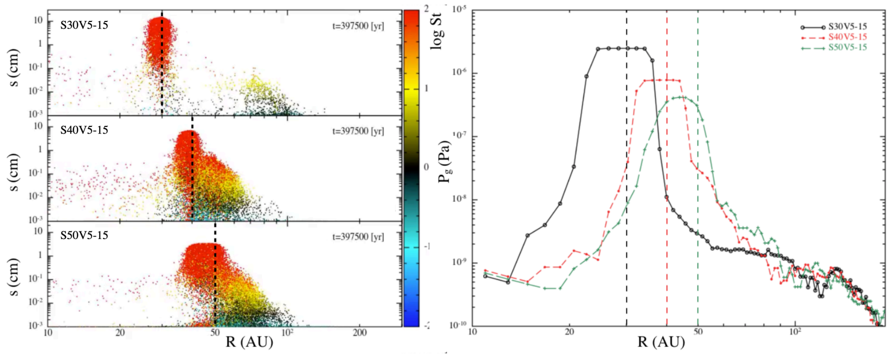

Fig. 2. Left: Dust size as a function of their radial distance to the star for 3 simulations hosting a snow line at 30 (top), 40 (middle) and 50 (bottom) AU after 400,000 yr. For these simulations, the fragmentation thresholds are set to 5 ($V_{\rm fragin}$) and 15 ($V_{\rm fragout}$) m.s^{-1}. The grains are coloured with the Stokes number. The snow line is highlighted with a black dashed line on every panel. **Right:** Gas pressure profiles for the same simulations.

understand it, we focus in this section on the physical CO snow line, which has been observed several times in recent papers (see references in Section 1).
The behaviour of CO ice is uncertain due to a lack of experimental data. While Pinilla et al. (2017) consider CO being weak with respect to fragmentation by adopting a fragmentation threshold similar to that of bare silicate grains (1 m.s^{-1}), we chose to consider multiples options. These are shown in Fig. 3. For our disc, the snow line position was evaluated by equating the CO sublimation temperature (20 K) to the disc temperature, which gives $\sim$ 100 AU. The first four panels model a stronger CO ice mantle with respect to fragmentation meanwhile the last two try the opposite.
The first 3 panels show, as we have seen in Section 3.1, a dust pile-up at the snow line location. The ability for the snow line to stop the dust drift is more and more challenged as the discontinuity (i.e. the ratio between the fragmentation thresholds) comes close to 1. As a result, the fourth panel shows that the dust traps forms inside of the snow line, even though its width seems to extend up to $r_{\rm snow}$. For the last two panels, we do not see any correlation whatsoever between the dust and the CO snow line, even though at earlier stages we see the dust starting its growth from $r_{\rm snow}$.

To translate these cases into images, we used the radiative transfer code MCFOST (Pinte et al. 2006) to produce face-on synthetic views (Fig. 4. The 1-15, 3-15, 5-15 and 10-15 cases have very different signatures (e.g the width of the dust ring) while the last two are somewhat similar at that stage, but again not at earlier stages. While this is preliminary, we could use synthetic images to constraint the CO's effect on grains and its implication for planet formation and Carbon/Oxygen rich grains delivery to the inner part of the disc.

4 Conclusions

Taking into account the effects of snow lines on dust growth is a step towards a better understanding of planet formation. We showed that snow lines affect the dust dynamics through their growth and fragmentation and that it can lead to an efficient self-induced dust trapping at a remarkable location. The increasing number of CO snow line observations in the last few years paves the way to understanding its role in planet formation. Our

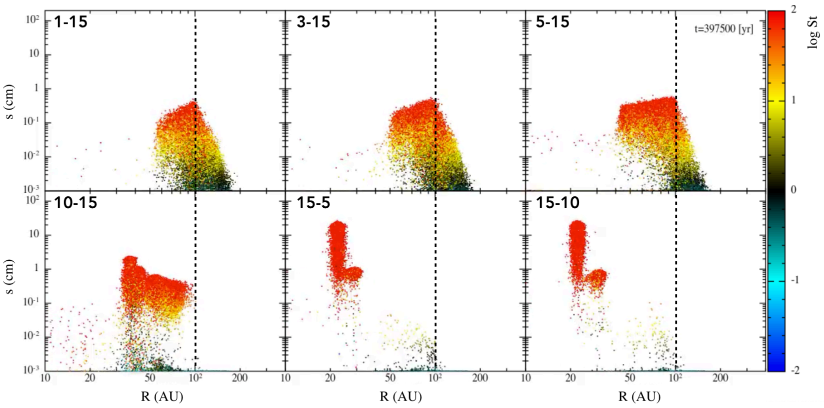

Fig. 3. Dust size as a function of their radial distance to the star after 400,000 yr for 6 simulations hosting a snow line at 100 AU representing the CO snow line. The grains are coloured with the Stokes number and the snow line is highlighted with a black dashed line on every panel.

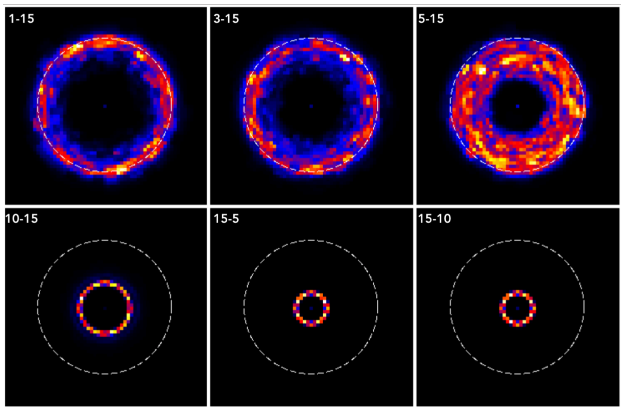

Fig. 4. Face on synthetic images at the end of the simulations shown in Fig. 3 with the nomenclature for the fragmentation thresholds on the top left of each panels. The snow line is represented by the white dashed circle on every panel.

simulations clearly show two possibilities: either dust growth happens at the snow line, or from its surroundings. To better compare these results to observations, we will use in a forthcoming paper the Atacama Large Millimetre Array (ALMA) utility CASA to give observers constraints on what to expect from the CO snow line and the dust structures.

This research was supported by the École Doctorale PHAST (ED 52) of the Université de Lyon. The authors acknowledge funding from ANR (Agence Nationale de la Recherche) of France under contract number ANR-16-CE31-0013 (Planet-Forming-Disks) and thank the LABEX Lyon Institute of Origins (ANR-10-LABX-0066) of the Université de Lyon for its financial support within the programme 'Investissements d'Avenir' (ANR-11-IDEX-0007) of the French government operated by the ANR. SPH simulations were run at the Common Computing Facility (CCF) of LABEX LIO. Figs 1, 2 and 3 were made with SPLASH (Price 2007)

References

Barrière-Fouchet, L., Gonzalez, J.-F., Murray, J. R., Humble, R. J., & Maddison, S. T. 2005, A&A, 443, 185
Blum, J. & Wurm, G. 2008, ARA&A, 46, 21
Gonzalez, J.-F., Laibe, G., & Maddison, S. T. 2017, MNRAS, 467, 1984
Gonzalez, J.-F., Laibe, G., Maddison, S. T., Pinte, C., & Ménard, F. 2015, Planet. Space Sci., 116, 48
Haghighipour, N. 2005, MNRAS, 362, 1015
Hartmann, L., Calvet, N., Gullbring, E., & D'Alessio, P. 1998, ApJ, 495, 385
Laibe, G., Gonzalez, J.-F., Fouchet, L., & Maddison, S. T. 2008, A&A, 487, 265
Laibe, G., Gonzalez, J.-F., & Maddison, S. T. 2012, A&A, 537, A61
Macías, E., Anglada, G., Osorio, M., et al. 2017, ApJ, 838, 97
Pinilla, P., Pohl, A., Stammler, S. M., & Birnstiel, T. 2017, ApJ, 845, 68
Pinte, C., Ménard, F., Duchêne, G., & Bastien, P. 2006, A&A, 459, 797
Price, D. J. 2007, PASA, 24, 159
Qi, C., Öberg, K. I., Andrews, S. M., et al. 2015, ApJ, 813, 128
Stepinski, T. F. & Valageas, P. 1997, A&A, 319, 1007
Weidenschilling, S. J. 1977, MNRAS, 180, 57

Session 10

Spécificité et généricité de notre Système Solaire dans un contexte astrobiologique (SFE)

THE INFLUENCE OF ROCKLINES ON THE MINERAL COMPOSITIONS AND FE/NI RATIOS OF SOLIDS IN THE PROTOSOLAR NEBULA

A. Aguichine[1], O. Mousis[1], B. Devouard[2] and T. Ronnet[3]

Abstract. In our solar system, meteorites and terrestrial planets show varying proportions of silicates and metallic iron, with Fe being distributed between Fe alloys and silicates. An open question remains the nature of the processes at play in the control of the redox state of these mineral assemblages, and thus the compositions of the different phases and relative proportions of metal vs. silicates. Here, we explore the roles held by the rock lines (the concept of snowlines extended to more refractory solids) of the most abundant solids in the shaping of the Fe/Mg and Fe/Ni abundance profiles in the protosolar nebula. The radial transport of solid grains through the different snowlines, coupled to the diffusion of vapours, lead to local enrichments or depletions in minerals, and imply variations of the Fe/Mg (in silicates) and Fe/Ni (in metal) ratios in the inner zone of the protosolar nebula. We discuss our results in light of the relative abundances and compositions of minerals observed in meteorites.

Keywords: planets and satellites: composition, planets and satellites: formation, protoplanetary disks, snowline

1 Model

Following the work of Mousis et al. (2019), we modelize the evolution of the protosolar nebula (PSN) as a disc of α-viscous H_2-He gas, in which trace species are advecting and diffusing. The evolution of the gas surface density Σ_g and that of a trace specie Σ_i are given by equations Mousis et al. (2019); Desch et al. (2017) :

$$\frac{\partial \Sigma_g}{\partial t} = \frac{3}{r}\frac{\partial}{\partial r}\left[r^{1/2}\frac{\partial}{\partial r}\left(r^{1/2}\Sigma_g \nu\right)\right], \tag{1.1}$$

$$\frac{\partial \Sigma_i}{\partial t} + \frac{1}{r}\frac{\partial}{\partial r}\left[r\left(\Sigma_i v_i - D_i \Sigma_g \frac{\partial}{\partial r}\left(\frac{\Sigma_i}{\Sigma_g}\right)\right)\right] + \dot{Q}_i = 0, \tag{1.2}$$

where ν is the gas kinematic viscosity. The trace species diffusivities D_i and radial velocities v_i are calculated using the two-population algorithm from Birnstiel et al. (2012). The source term $\dot{Q}_i$ accounts for sublimation and condensation, and is computed according to Drążkowska & Alibert (2017). All species evolve independently and no feedback on the gas is taken into account.

2 Trace species

For each present molecule, the initial mass fraction is derived from protosolar abundances given by Lodders et al. (2009). Table 1 summarizes all considered species, assuming all protosolar Fe, Ni, Mg, Si and S have been distributed among them. We limit our study to a case without chemical reactions.

[1] Laboratoire d'Astrophysique de Marseille, 13010 Marseille, France
[2] CEREGE, Aix Marseille Université, 13545 Aix-en-Provence, France
[3] Lund Observatory, Lund University, 22224 Lund, Sweden

Table 1. wt.% and density of considered trace species.

Formula	wt.%	density ($kg.m^{-3}$)
$FeSiO_3$	1.297×10^{-3}	3.95
$MgSiO_3$ 2	4.946×10^{-3}	3.20
Fe_2SiO_4 3	5.898×10^{-4}	4.39
Mg_2SiO_4	2.041×10^{-3}	3.22
FeS	2.870×10^{-3}	4.75
$Fe_{0.9}Ni_{0.1}$	2.103×10^{-3}	7.90
Ni	1.101×10^{-4}	8.90

3 Results

Figure 1 shows the Fe/Ni ratio profile in metal dust at different times, starting at the protosolar value of 13.21. At early ages of $0 - 50$ kyr, rocklines of FeS and $Fe_{0.9}Ni_{0.1}$ at ~ 0.5 au lead to a Fe/Ni ratio two times greater than in the outer region of the disc. Below that peak, Fe is fully vaporised, leading to a Fe/Ni ratio of 0.

As shown in figure 2, the local increase of the Fe/Mg ratio at rocklines of $FeSiO_3$ and Fe_2SiO_4 is more moderate, but remains visible until the end of the computation.

Beyond all rocklines, the atomic ratios are shaped by the drift velocity of solid particles. The denser grains are, the lesser they drift because of inertia. For this reason, Ni rich species stay longer in outermost regions of the disc, resulting in a decrease of the Fe/Ni ratio. On the other hand, Fe being slightly denser than Mg, the Fe/Mg ratio tend to increase in the disc.

The position of rocklines is shown in figure 3. As the disc cools down, all trace species condensate and the effect of rocklines is dissipated.

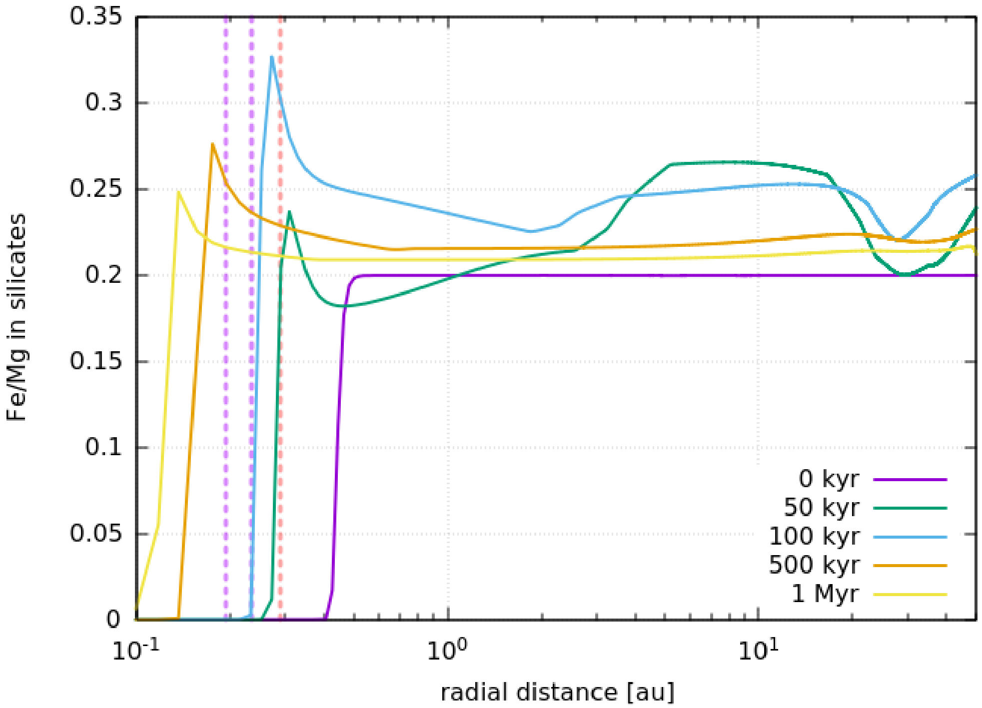

Fig. 1. Fe/Ni ratio profiles in condensed metal. Vertical red and blue dashed lines correspond to rocklines of Fe and Ni rich species, respectively, at $t = 50$ kyr.

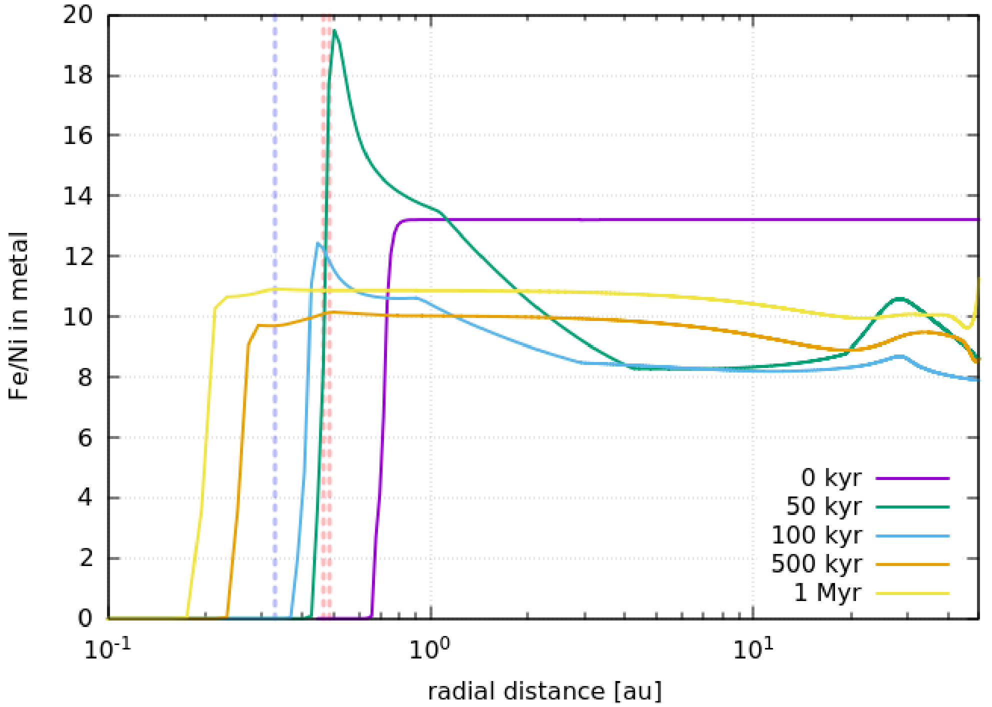

Fig. 2. Fe/Mg ratio profiles in condensed silicates. Vertical red and purple dashed lines correspond to rocklines of Fe and Mg rich species, respectively, at $t = 50$ kyr.

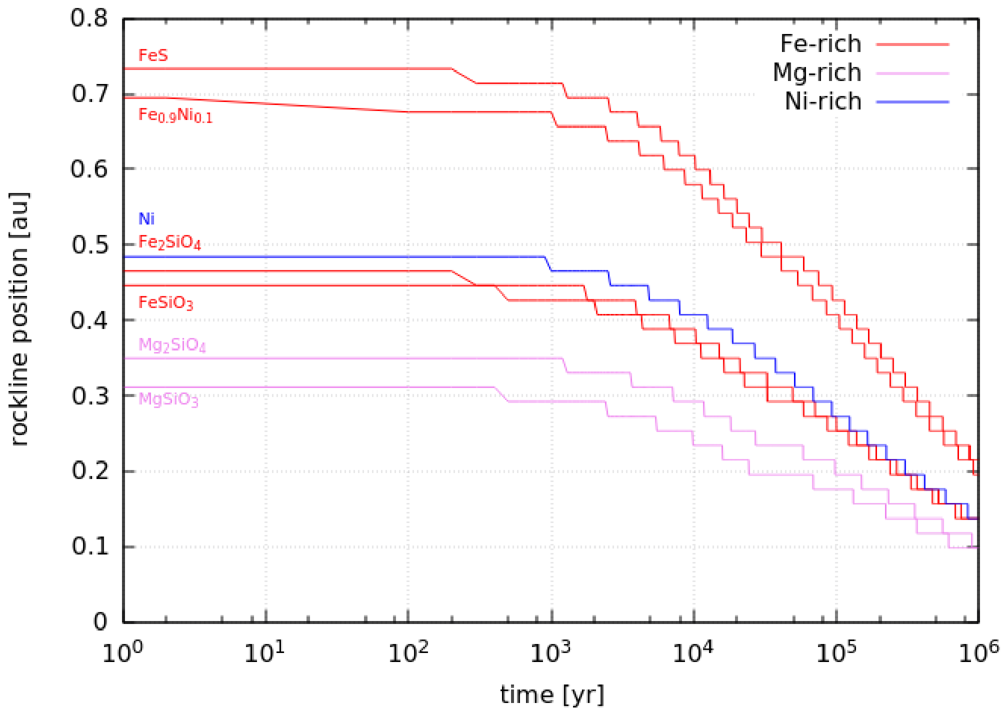

Fig. 3. Evolution of positions of rocklines in time.

4 Conclusions

Throughout the PSN evolution, local variations of atomic ratios are due to i) difference in rocklines position and ii) difference in matter density. Simple cases with one or two species can be easily interpreted, but with more components torough computations is required to extract the atomic ratios.

Because atomic ratio profiles strongly vary at early epochs of the PSN evolution, our results may explain some differences in compositional features observed among meteorites.

References

Birnstiel, T., Klahr, H., & Ercolano, B. 2012, A&A, 539, A148

Desch, S. J., Estrada, P. R., Kalyaan, A., & Cuzzi, J. N. 2017, ApJ, 840, 86

Drążkowska, J. & Alibert, Y. 2017, A&A, 608, A92

Lodders, K., Palme, H., & Gail, H.-P. 2009, Landolt Börnstein, 712

Mousis, O., Ronnet, T., & Lunine, J. I. 2019, ApJ, 875, 9

THE ROLE OF ICE LINES IN THE COMPOSITION OF SATURN'S MOONS

S. E. Anderson[1], O. Mousis[2] and T. Ronnet[3]

Abstract. The presence of ice lines induces the creation of peaks of abundances of volatile elements in both protosolar- and circumplanetary- disks. The evolution of the abundance of volatile species in the protosolar nebula as a function of the migration of ice grains, their growth, and their evaporation have been modeled in order to understand the formation of the planets. These models have been taken to the protosolar nebula level to reproduce the enrichments measured in Jupiter's atmosphere. Yet as of today, no model has attempted to evaluate the ice lines of Saturn's circumplanetary disk to see how the known compositions of its moons could be reproduced. Here, we attempt to create a simplified description of Saturn's circumplanetary disk so as to try to bring a coherent vision of the formation of Titan and Enceladus with that of Saturn.

Keywords: snowline, ice line, Saturn, Enceladus, Titan, moon formation.

1 Introduction

The Ice Line, or Snow Line, is defined as the radius where the disk temperature is equal to the sublimation/condensation temperature of water-ice (or any species of interest) in the protosolar- and circumplanetary-disk. Our goal is to determine these ice lines for separate species in the Saturnian sub nebula and evaluate their enrichments over time in order to estimate how the moons of Saturn formed. This type of research has been done on the Jupiter system, but as of this moment there has been no study of this type attempted on the Saturnian system.

2 Circumplanetary Disk Model

We adopt the model of an actively supplied accretion disk by Canup & Ward (2002). The CPD is fed through its upper layers from its inner edge up to the centrifugal radius r_c by gas and gas-coupled solids inflowing from the protosolar nebula. This is set to $r_c = 30R_{Sat}$ and is limited by the outer radius $R_d = 150R_{Sat}$.

In this study we consider a disk based on the model by Sasaki et al. (2010). The total rate of mass inflow is $F_p = \pi F_{\rm in} r_c^2$. The infall rate decays exponentially with timescale $\tau_{Dep} = 3.10^6 - 5.10^6$ yr in the final state of the Saturnian case.

$$\Sigma_g \simeq \frac{F_p}{15\pi\nu}\begin{cases}\frac{5}{4} - \sqrt{\frac{r_c}{r_d}} - \frac{1}{4}\left(\frac{r}{r_c}\right)^2 & [r < r_c]\\ \sqrt{\frac{r_c}{r}} - \sqrt{\frac{r_c}{r_d}} & [r > r_c]\end{cases}$$

$$T_d \simeq 60\Big(\frac{M_{\rm sat}}{M_J}\Big)^2\Big(\frac{r}{20R_J}\Big)^{-3/4}\exp\Big(\frac{-t}{4\tau_{dep}}\Big)$$

We consider the gas in a hydrostatic equilibrium in the vertical direction and the vertical velocity, therefore zero and allowing us to focus on a 1D model. This allows us to add a prescription to compute the velocity of the CPD's gas and describe the interaction between the solids and the gas in the radial direction. For each species of interest, we explore the sublimation temperature as a function of disk pressure. We solve the advection-diffusion equation at each radial distance in order to determine the abundance of species at the locations at which the Saturnian moons were formed.

[1] Aix Marseille University, Marseille, France
[2] Laboratoire D'astrophysique de Marseille, Marseille, France
[3] Lund Observatory, Lund, Sweden

3 Results

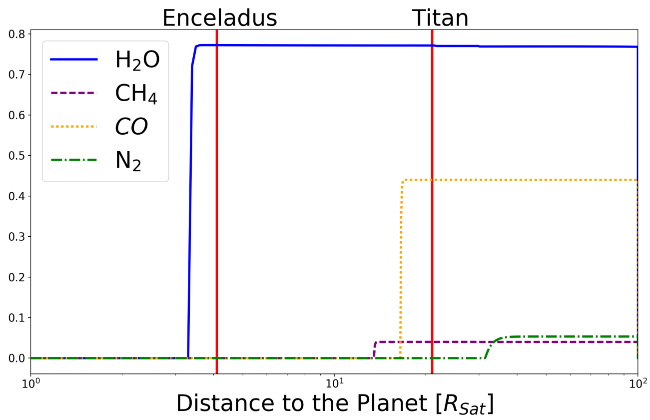

Fig. 1. Initial concentration of Water, Methane, Carbon Monoxide, and Nitrogen Ices, scaled to the protosolar abundances.

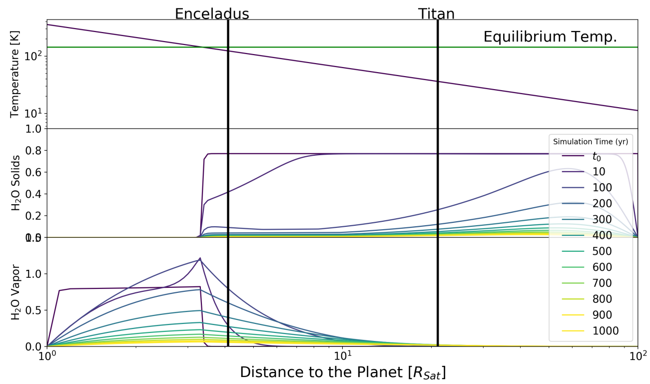

Fig. 2. Evolution of water vapor and dust in the Saturnian system over a 1000 yr as a function of radius, scaled to the protosolar abundance. The intersection of the 143 Kelvin line with the disk temperature slope indicates the position of the ice line. The dust and the vapor are normalized to protosolar quantities in the PSN. After a thousand years, almost no dust or vapor remain.

4 Conclusions

Enceladus would have formed in a location with water solids, which is supported by what we know of Enceladus's interior and composition, known to be over %90 water vapor. Titan would have formed with large quantities of solid carbon oxide and methane, however, the ice line of Nitrogen, of which Titan's atmosphere is comprised of %98, is out of reach for Titan's formation.

The disk is depleted in a few hundred years which means moon formation would be unlikely. A constant source of solids would need to be injected into the disk for it to be sustainable.

References

Canup, R. M. & Ward, W. R. 2002, AJ, 124, 3404

Sasaki, T., Stewart, G. R., & Ida, S. 2010, ApJ, 714, 1052

THE ROLE OF CLATHRATE TRAPPING IN THE COMPOSITION OF EUROPA'S OCEAN

A. Bouquet[1], O. Mousis[1], C.R. Glein[2], G. Danger[3] and J.H. Waite[2]

Abstract. We use a thermodynamic statistical model to evaluate how the composition of Europa's internal ocean may have been affected by clathrate hydrate formation. Assuming an input of the observed O_2 and CO_2 from the surface and considering the possibility of contributions by reduced (with CH_4 and H_2S) or oxidized (CO_2-bearing) hydrothermal fluids, we calculate the fractional occupancies in clathrate and deduce the effect on the ocean's composition. The structure of the clathrate formed, and therefore its density and composition, is influenced by the amount of O_2 compared to the other compounds present. In turn, the ratios of noble gases is influenced by the clathrate structure formed.

Keywords: astrobiology, Europa, clathrate hydrates

1 Introduction

The internal ocean of Jupiter's icy moon Europa is likely the host of a complex chemistry enabled by inputs from the radiation-processed icy surface (Hand et al. 2006; Paranicas et al. 2009; Greenberg 2010) and the interaction with the rocky interior (Kargel et al. 2000; McKinnon & Zolensky 2003; Vance et al. 2007). High pressure, low temperature and availability of water are favorable to the formation of clathrate hydrate (hereafter clathrate) that can preferentially trap some volatiles and affect the evolution of the ocean's composition. We apply here a thermodynamic statistical model to Europa's internal ocean. Considering an input of volatiles into the ocean, the model predicts the occupancy fraction of each chemical species in the clathrate phase and from there the evolution of these species' abundance in the ocean.

2 Model and assumptions

The thermodynamic statistical model is based on the original work of Van der Waals (1959), following the method described by Lunine & Stevenson (1985) and Thomas et al. (2007). It determines the occupancy fractions in the clathrate by describing trapping of guest molecules as a three-dimensional adsorption (see Mousis et al. (2013) for a detailed description). We considered the amount of gas coming into the ocean from the icy crust based on the estimates of Hand et al. (2006) and Greenberg (2010) for O_2 and CO_2. We add a volatile input due to hydrothermal fluids, either reduced (H_2S and CH_4) or oxidized (CO_2), in quantities within published estimates (Hand et al. 2007). We also consider the presence of noble gases argon, krypton and xenon to evaluate the evolution of their ratios in the ocean caused by clathrate formation. When considering a reduced hydrothermal input, we consider the fast oxidation of H_2S by O_2 (Millero et al. 1987) to eliminate the limiting reactant.

We calculated the amount of dissolved volatiles necessary to reach a fugacity to start clathrate formation (Mousis et al. 2013)and found that with the input we consider the ocean starts producing clathrate in less than a billion year. In every case we consider the two usual clathrate structures (sI and sII).

3 Results

The results are shown in Figures 1 and 2 for two cases: an input dominated by O_2 and CO_2 from the surface, and one dominated by CH_4 and H_2S from hydrothermal fluid.

[1] Aix Marseille Univ, CNRS, CNES, LAM, Marseille, France
[2] Space Science and Engineering Division, Southwest Research Institute, 6220 Culebra Rd., San Antonio, TX 78228, USA
[3] Aix-Marseille Université, PIIM UMR-CNRS 7345, F-13397 Marseille, France

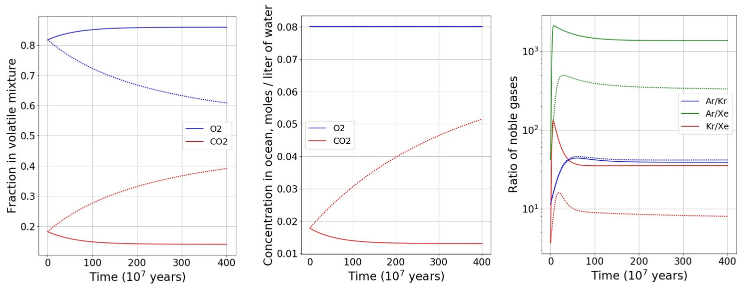

Fig. 1. Evolution of O_2 and CO_2 mole fraction (left) and concentration (center) in the ocean, and noble gases ratios (right), in the case of a O_2-CO_2 input mostly from the icy crust. Full lines represent the formation of sI clathrate, dotted lines the formation of sII (more likely due to the prevalence of O_2).

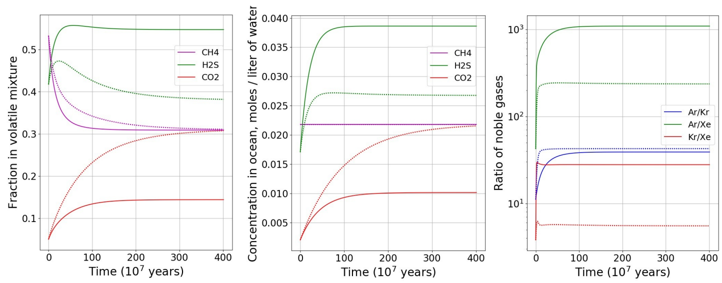

Fig. 2. Same as Figure 1 but with a large reduced input of CH_4 and H_2S. The reduction of O_2 by H_2S is sufficient to eliminate O_2. Due to the large input of CH_4, formation of sI (full lines) is the most likely outcome.

4 Conclusions

Clathrate formation may influence the abundance of several species in Europa's ocean, in particular the noble gas ratios evolution depends on what clathrate structure (sI or sII) is formed. When CH_4 and H_2S are present, their abundance in the ocean become less representative of the hydrothermal input due to preferential trapping of CH_4 over H_2S. We find the clathrate density to be lower than that of seawater, indicating it would be incorporated into the icy crust and its volatile content possibly measurable by future missions such as Europa Clipper and JUICE.

A.B. and O.M acknowledge support by CNES. C.R.G. and J.H.W. were supported by the Europa Clipper MASPEX investigation.

References

Greenberg, R. 2010, Astrobiology, 10, 275

Hand, K. P., Carlson, R. W., & Chyba, C. F. 2007, Astrobiology, 7, 1006

Hand, K. P., Chyba, C. F., Carlson, R. W., & Cooper, J. F. 2006, Astrobiology, 6, 463

Kargel, J. S., Kaye, J. Z., Head III, J. W., et al. 2000, Icarus, 148, 226

Lunine, J. I. & Stevenson, D. J. 1985, The Astrophysical Journal Supplement Series, 58, 493

McKinnon, W. B. & Zolensky, M. E. 2003, Astrobiology, 3, 879

Millero, F. J., Hubinger, S., Fernandez, M., & Garnett, S. 1987, Environmental science & technology, 21, 439

Mousis, O., Lakhlifi, A., Picaud, S., Pasek, M., & Chassefiere, E. 2013, Astrobiology, 13, 380

Paranicas, C., Cooper, J., Garrett, H., Johnson, R., & Sturner, S. 2009, Europa. University of Arizona Press, Tucson, 529

Thomas, C., Mousis, O., Ballenegger, V., & Picaud, S. 2007, Astronomy & Astrophysics, 474, L17

Van der Waals, J. 1959, Adv. Chem. Phys., 2, 1

Vance, S., Harnmeijer, J., Kimura, J., et al. 2007, Astrobiology, 7, 987

SF2A 2019
P. Di Matteo, O. Creevey, A. Crida, G. Kordopatis, J. Malzac, J.-B. Marquette, M. N'Diaye, O. Venot (eds)

FROM THE SOLAR SYSTEM TO EXO-PLANETARY SYSTEMS HISTORICAL AND EPISTEMOLOGICAL CONSIDERATIONS

D. Briot[1]

Abstract. We relate the path of the knowledge, from the world centered on the Earth, and the stars located in the sphere of fixed, to the progressive discovery that stars are suns with multiple planet systems.

Keywords: History, Solar system, Extrasolar planets

1 Introduction

How did the Solar System come out as a physical entity, an object? How and when did we understand that many such systems actually exist? As a preamble, let us note that, whereas we use to refer to the system made of our Sun and its cortege of planets as the Solar System, on the contrary, systems made of any other star accompanied by planets are referred to as planetary systems rather than stellar systems, the later designation being reserved to multiple stars. Before the name solar system came in use, men knew it as the world system.

2 Antiquity

For centuries, the mathematical model established by Claudius Ptolemeus (c.90 A.D.-c.168A.D.), combining his own observations with those of many predecessors including Hipparchus (190-120 B.C.), had been the reference for predicting the positions and motions of stars and planets. Based on this model, motions of celestial objects would be calculated by combining the motions of a series of nested spheres. In the Ptolemaic representation, the Earth is the center of the world. A series of mobile spheres correspond to the motions of the Moon and the planets known at that time. The last sphere is the sphere of fixed stars which rotates as a solid body. So our world was spherical, limited by the "sphere of the fixed".

The question was raised very early in the Antiquity by Greek philosophers: Can other worlds possibly exist outside the sphere of the fixed stars, similar or not to our own? This question is known as "the debate on the multiplicity of worlds". Obviously, at that time, those words did not assume the same meaning as they do nowadays. Indeed, in the context of our knowledge and our understanding today, the locution "multiplicity of worlds" suggests the existence of planets orbiting remote stars unrelated to the Sun. In the past, stars glued on the sphere of the fixed were far from being considered as other suns. Multiple worlds were conceived as outside the closed world centered on the Earth and containing any visible celestial body inside the volume delimitated by the sphere of the fixed. The existence of other worlds, similar or not to our own, may be in infinite number, was considered a possibility, out of reach of our observations. It was conceptually acceptable to imagine such hypothetic and inaccessible worlds centered on a planet which could shelter living creatures. The oldest known references about such other worlds come from the Greek philosophers, in particular Democritus (470-365 BC) and Epicure (342-270 BC). *"There is an infinite number of worlds of different sizes: some are larger than ours, some have no sun or moon, others have suns or moons that are bigger than ours. Some have many suns and moons. Worlds are spaced at differing distances from each other; in some parts of the universe there are more worlds, in other parts fewer. In some areas they are growing, in other parts, decreasing... There are some worlds with no living creatures, plants, or moisture."* Democritus. *"There is an infinity of worlds both like and unlike our world. For the atoms being infinite in number, as was already proved, are borne on far out into*

[1] Observatoire de Paris, 61 avenue de l'Observatoire, 75014 Paris, France

space. For those atoms which are of such nature that a world could be created by them or made by them, have not been used up either on one world or a limited number of worlds, nor again on worlds which are alike, or on those which are different from these. So that there nowhere exists an obstacle to the infinite number of worlds". Epicure, disciple of Democritus, *"Letter to Herodotus"*. Plato (427-348 BC) and Aristotle (384 -322 BC) were of the opposite opinion : *"...it follows from the same evidence and by the same compulsion, that the world must be unique. There cannot be several worlds."* Aristotle.

3 Middle Age

In the course of the Middle Age, another parameter came into the picture: the scientific theory had to comply with the religious doctrine. Concerning the multiplicity of worlds, there were however two competing theological interpretations. The first one stated that, according to the Biblical account of the creation, God creates one and only one world, thus leaving no room to other worlds. The other interpretation, on the contrary, stressed that since the Bible does not specify that God did not create several worlds, the omnipotence of God implies that He could create other worlds. The question of other worlds gave birth to a violent controversy. In 1277, Etienne Tempier, the bishop of Paris, condemned 219 beliefs which he considered heretical since they contravened the power of God. One of these beliefs was that *"the First Cause cannot make many worlds"*.

The system of the world according to Hipparchus and also to Ptolemy implied that the whole world beyond the Moon was perfect. The perfect geometrical figures being the circle and the sphere, celestial bodies had to assume perfect motions (i.e. circular motions). The sky was immutable. However, it had been known for long that astronomical observations of planetary motions did not correspond to the perfect figure. Planets did not follow plain circular trajectories. Observed motions, particularly the apparent retrograde motions of some planets, were then explained by circles moving on other circles, that is epicycloids or epicycles. As astronomical observations grew in precision epicycles were added to epicycles, until the system reached deterrent complexity.

4 Sixteenth century - Heliocentrism

In 1543, Nicolaus Copernicus (1473-1543), in his book *De Revolutionibus*, had the brilliant idea to establish the Sun at the center of the world. Doing so, he drastically simplified the system of epicycles. The heliocentric system had taken the place of the geocentric system. The modern description of the solar system is still basically unchanged. But, how about the sphere of the fixed ? One of the first observational evidence against the immutability of the sky was the surge of a "New Star" in 1572. This star has been accurately observed by Tycho Brahe (1546-1601). It is described in his book *De Nova Stella, (About a New Star)*. The modern astronomical word *Nova* has its origin in this book. However, we know now that the stellar phenomenon observed by Tycho Brahe was what we nowadays call a *Supernova*. When this star appeared, it was very bright, then its luminosity decreased. Tycho Brahe could not determine its parallax, and after several months of observations, established that its position did not vary with respect to the fixed stars. So there was a new star attached to the sphere of the fixed. This implied that contrary to the many century belief, the sky is not immutable.

By the end of the sixteenth century, Giordano Bruno (1548-1600) defended the idea of multiple worlds, inhabited by a multiplicity of living beings. His argument was theological. The power of God being infinite by nature, His creation could not be limited to only one finite world. Yet, Bruno's multiple worlds were not unobservable abstractions, he adopted the Copernican system, and he considered that stars are Suns, with planets. *"That is how the excellence of God is magnified and the greatness of His empire is demonstrated. He is not glorified in only one Sun, but in countless suns, not in only one Earth and one world, but in thousands of thousands, no, an infinity [of worlds]." "Innumerable suns exist; innumerable earths revolve around these suns in a manner similar to the way the seven planets revolve around our sun"*. Giordano Bruno was sentenced to death and burnt in Roma by order of the Inquisition. Since the nineteenth century, he is sometimes considered as a martyr for science. Actually, his religious beliefs against the dogma, estimated as heretical, were probably more important for the sentence.

5 Seventeenth century - Plurality of Worlds

In 1609, Galileo Galilei (1564-1642) pointed an optical instrument, his refracting telescope towards a number of celestial objects. The tremendous harvest of results that followed was reported in *Sidereus Nuncius, (The*

Sidereal Messenger) a book published quite rapidly. In particular, he discovered satellites, i.e. moons, orbiting around planet Jupiter. This result demonstrated that celestial objects may be orbiting around something else than the Earth. So the Earth was not anymore the centre of the world. Browsing the Milky Way with his telescope Galileo discovered that the milk is made of a multitude of stars. So the number of stars in the sphere of the fixed increased dramatically. Galileo considered every star as a Sun.

As for Bruno and Galileo, René Descartes (1596-1650) in his book *Le Monde ou le Traité de la lumière (The World or Treatise on Light)*, takes it for granted that the number of stars is infinite and each star is a Sun. His book was written in 1632 and 1633, at the time of the trial of Galileo, but for fear of the Inquisition, this book was published only in 1664, after the death of Descartes.

Christiaan Huygens (1629-1695) evaluated the distance to Sirius by comparing its luminosity with the Sun luminosity. His evaluation was based on the assumption that the Sun and the stars are similar objects.

In 1686, Bernard le Bouyer de Fontenelle (1657-1757) published *Entretiens sur la Pluralité des Mondes*, translated in English as *A Discovery of New Worlds* or *Conversation on the Plurality of Worlds.* It was a real "best-seller" , in the modern acception. The book was quite often re-edited and translated in many languages. Its influence was great throughout Europe. *"Les étoiles sont autant de soleils dont chacun éclaire un monde." (Every fixed star is a sun illuminating its surrounding worlds)* Fontenelle assumed that the Moon and all planets might be inhabited. He considered that the inhabitants might be different from humans. He also envisaged a broad diversity of forms of life on earth even under extreme conditions. Fontenelle wrote his book 76 ans after the decisive observations of Galileo, giving a measure of the progresses of astronomy in between. During the 18th century, the possibility of life on planets orbiting stars other than our sun was commonly accepted.

"Les cieux sont peuplés de corps lumineux qui, semblables à notre soleil, font vraisemblablement rouler des planètes dans différentes orbites". (Skies are crowded with luminous bodies, which, similar to our sun, most likely drive planets on various orbits) Condillac, Cours d'étude pour l'Instruction du prince de Parme (1775) Condillac again : *"et l'univers est un espace immense, où il n'y a point de désert. Notre imagination est aussi embarrassée à lui donner des bornes qu'à ne lui en pas donner" (Universe is an immensity where there are no deserts. Assigning or not assigning limits to its immensity is an equal challenge to our imagination).*

6 How did planets form: nebula or catastrophe ?

Earliest models for the formation of planetary systems adopt the evolutionist scheme, assuming that planet birth is a natural part of the star formation process. According to the ideas formulated by Descartes (1633), the early universe is crowded with whirlpools. Heaviest elements tend to concentrate at the center of each vortex, giving birth to central stars, while the lightest ones stay at the periphery and form planets. One century later, Emmanuel Kant (1724-1804) in 1755, proposed a scenario where star formation occurs by collapse of a swinging material cloud, a swinging nebula. Then Pierre-Simon de Laplace (1749-1827) in 1796 developed the mathematical principles necessary to control the model. During the collapse, the angular momentum must be preserved; hence the centrifugal force creates a disc in the plane perpendicular to the main rotation axis. Then the disc splits into concentric rings out of which planets will form. Catastrophic models, on the contrary, assume that planets result from isolated, violent cataclysmic events. According to Buffon (1707-1788) in 1741, a comet colliding the Sun would snatch a cloud of debris which would later condense into a planet. By the beginning of the XXth century, the collisional scenario was generally favoured. The swinging nebula scenario suffered from arguments in relation with sharing angular momentum between the Sun and planets. At that time the Solar system was the only known system, there was no indication concerning the frequency of the phenomenon. Obviously, depending on the adopted scenario, the probability for a star to be escorted by a swarm of planets changes drastically. In the catastrophic scenario, planets are formed under accidental circumstances and this is not expected to occur frequently. On the contrary, in the swinging nebula picture, planets form naturally under common circumstances. In the recent decades, the situation changed drastically and the catastrophic scenario lost its precedence. During year 1995, the astronomical community experienced a strong excitement : for the first time evidence was given for the existence of a planet orbiting a star which was not the Sun. The star is known as 51 Pegasi. The planet was betrayed by small variations of the central star's radial velocity. The discoverers, Michel Mayor and Didier Queloz, two Swiss astronomers operating at Observatoire de Haute Provence, used a new camera they had developed to monitor small radial velocity variations in a selection of nearby stars. They were actually in search of the slightest sign of an extrasolar planet, but what they got was surprisingly different from what they expected. The planet orbited around 51Peg with a period of 4.23 days. According to the laws of celestial mechanics, such rapid radial velocity variations imply a planet much closer to the central star than Mercury to the Sun, but the amplitude of the observed variations signed a mass equivalent to Jupiter. Planetology at that time admitted that giant planets like Jupiter or Saturn would necessarily be icy, requiring orbits that keep them away from the heat of the central star, that is long period orbits. Jupiter's period is 12 years. So the first extrasolar planet ever found imposes immediately a new category, it is a "hot Jupiter". Had the new thing been more conformist, the discoverers would have needed years of efforts before getting the result. Yet it is their merit to have identified in quasi real time the anomaly and to give it the right interpretation against their own prejudices. A quarter of a century later in 2019, there are more than 4000 planets identified in 3039 systems, out of which 658 are multiple. Every day brings its lot of new discoveries. The sample survey achieved by the dedicated space telescope Kepler establishes that there are more planets than stars in the Milky Way, that is hundreds of billions. Based on this flood of new facts, scenarios of planetary formation had to be completely re-considered. Recent models almost universally accepted, keep the idea of star and planets born from a nebula in a unique process, but they give a major importance to mechanisms of migration. Planets were born very far from the central star and do migrate on the long range towards the center. So planetary systems around stars are common and it is tempting to admit that a large fraction of them are more or less similar to our good old Solar System. Implying, in the back of minds that circumstances permitting the surge and evolution of life could be rather common. However...

7 Inhabited ?

However, a result published in 1993 shows that the development of life on earth might result from a highly improbable random event. This event is not the product of an imaginative fiction; it came as a result of extremely rigorous investigations in celestial mechanics. Laskar, Joutel and Robutel (*Nature*, vol. 361, 1993) demonstrated that on the very long range, the Earth axis would not be kept at almost stable inclination with respect to the plane of the ecliptic unless it is constrained to do so by a specific stabilising mechanism. And this specific mechanism is the Moon. Without the Moon, the so-called inclination which controls seasons and climate would be subject to large amplitude chaotic variations making the development of evolved and complex forms of life impossible. However, there is a general agreement that the Moon itself is the result of a random cataclysmic collision. The catastrophic theory is back. Is the solar system sheltering a very developed life on a planet with stable climate a unique or very rare in the Galaxy ? Future will give the answer may be, or certainly.

Many thanks are due to Frédéric Arenou, Jean-Patrice Boudet, Michel Crézé, Louis Le Sergeant d'Hendecourt, Florence Raulin-Cerceau and Monique Spite for many fruitful discussions, interesting suggestions and efficient help.

DERIVATION OF ENCELADUS' OCEAN COMPOSITION FROM THE LAST CASSINI MEASUREMENTS

S. Delcamp[1], A. Bouquet[2] and O. Mousis[2]

Abstract. The last Cassini measurements over Enceladus' south pole have redefined our understanding of its plumes' composition. These measurements provide important information about the internal ocean's composition since the source of the geysers is likely connected to it. Here, we applied a thermodynamic statistical model allowing the quantification of the effect of volatiles trapping into clathrates on the resulting internal ocean's composition, to reproduce the observed plumes measurements. Two end-members were considered for the plumes composition. In both cases, a gas input made predominantly of 80–90% CO_2 is required to enable the convergence of the CO_2/CH_4 ratio in the ocean towards the plumes' measured value.

Keywords: Enceladus, ocean's composition, clathrate, astrobiology, Cassini

1 Introduction

The Cassini spacecraft has greatly improved our knowledge of the Saturnian system, especially in the case of Enceladus, one of the most intriguing moons orbiting the ringed planet. Enceladus is expected to harbor an internal ocean (Iess et al. 2014; Soucek et al. 2017). One of the major discoveries of the Cassini spacecraft is the gas and ice emission creating plumes over the south pole of Enceladus. Thanks to the presence of the Ion and Neutral Mass Spectrometer (INMS) aboard Cassini, the chemical composition of these plumes has been measured. The goal of our work is to quantify the chemical evolution of the Enceladus' ocean, considering a gas input into the ocean and clathrate production. At the end of our calculations, we aim at obtaining the same chemical abundance ratios in the ocean as those detected in the plumes, assuming the plumes composition is representative of the ocean's.

2 Model

Our thermodynamic statistical model gives the abundances of species dissolved in the ocean, and the proportion of guests trapped in clathrate, produced at each time step (Mousis et al. 2013; Bouquet et al. 2015). We assume that Enceladus' ocean is in a steady state, implying a gas input to balance the expulsion of volatiles with the plumes. Clathrate formation is triggered when a significant amount of a chemical species is reached in the ocean and exceeds the solubility limit. As different species are more or less prone to be trapped into clathrates, this process leads to a chemical evolution of the ocean. The ocean reaches an equilibrium when the clathrate formed contains the same gas mixture as the one provided to the ocean. Table 1 shows the abundances of the main volatiles detected in the plumes. H_2 does not form clathrate at the considered pressure conditions, and NH_3 forms a stoichiometric hydrate. We finally obtain two end-members ratios for the plumes composition, i.e. $CO_2/CH_4 = 8$ and 1. Different ice shell thicknesses have been considered, with densities of 940 kg/m^3 for the ice and 1040 kg/m^3 for the ocean (Soucek et al. 2017). Gravity is set to 0.113 m/s^2 (Olgin et al. 2011; Iess et al. 2014). This conducts to pressures of $\sim$80 bar and 108 bar for 3 km and 40 km ice thicknesses, respectively.

[1] University of Bordeaux, Department of Physics, Bordeaux, France
[2] Aix Marseille Université, CNRS, CNES, LAM, Marseille, France

Table 1. Cassini measurements in Enceladus' plumes (Waite et al. 2017).

Chemical species	H_2O	CO_2	CH_4	NH_3	H_2
Ratio (%)	96–99	0.3–0.8	0.1–0.3	0.4–1.3	0.4–1.4

3 Results

Figure 1 showss the time evolution of Enceladus ocean's composition. The amount of gas injected into the ocean is modeled after estimates Cassini measurements, leading to a value of (1-5)$\times 10^9$ mol/yr (Waite et al. 2017). Left panel shows that steady state is reached after $\sim$200 millions years of evolution for enabling the convergence of the CO_2/CH_4 ratio to 1 and requires the adding of 3.1 times more CO_2 than CH_4 to the ocean at each time step. Right panel shows that steady state is reached after 3 billion years of evolution for enabling the convergence of the CO_2/CH_4 ratio to 8. Here, 34 times more CO_2 than CH_4 must added to the ocean at each time step.

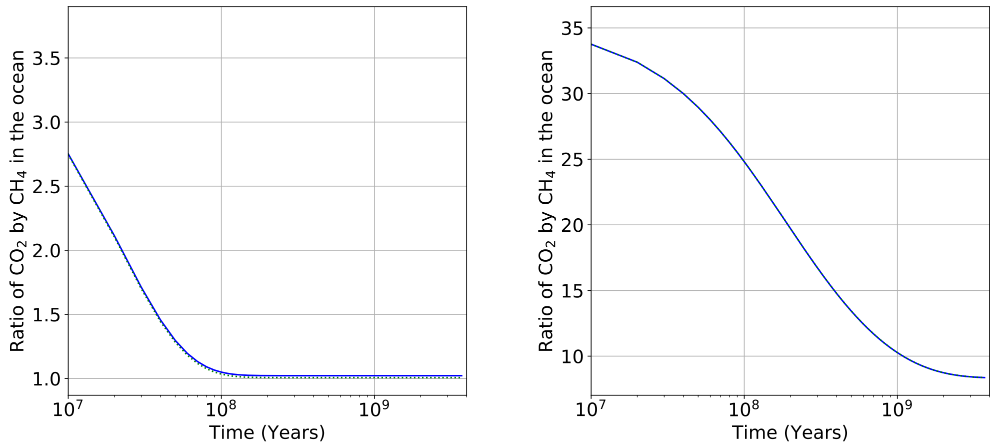

Fig. 1. Composition of Enceladus' ocean over time, assuming convergence of its CO_2/CH_4 ratio toward 1 (left panel) and 8 (right panel).

4 Conclusions and perspectives

Our calculations indicate that Enceladus' ocean could need a time of evolution as long as the Solar System lifetime to reach equilibrium. Further investigation is needed to support this preliminary conclusion. Future studies will be also devoted to the consideration of the ocean's pH. In Enceladus' alkaline ocean, the speciation of CO_2 is expected to be shifted towards HCO_3^- ions (Glein et al. 2015), reducing the amount of CO_2 available to form clathrates. Moreover, we will consider a possible variation over time of the flux of volatiles into the ocean, to account for possibly more intense initial hydrothermal activity.

References

Bouquet, A., Mousis, O., Waite, J. H., & Picaud, S. 2015, European Planetary Science Congress, EPSC2015

Glein, C. R., Baross, J. A., & Waite, J. H. 2015, Geochim. Cosmochim. Acta, 162, 202

Iess, L., Stevenson, D. J., & Parisi, M. e. a. 2014, Science, 344, 78

Mousis, O., Lakhlifi, A., & Picaud, S. e. a. 2013, Astrobiology, 13, 380

Olgin, J. G., Smith-Konter, B. R., & Pappalardo, R. T. 2011, Geophysical Research Letters, 38

Soucek, O., Behounkova, M., & Cadek, O. e. a. 2017, EGU General Assembly Conference Abstracts, 19, 16357

Waite, J. H., Glein, C. R., & Perryman, R. S. e. a. 2017, Science, 356, 155

SF2A 2019
P. Di Matteo, O. Creevey, A. Crida, G. Kordopatis, J. Malzac, J.-B. Marquette, M. N'Diaye, O. Venot (eds)

IMPLEMENTATION OF HIGH-PRESSURE PHASES OF WATER ICE IN THE MARSEILLE SUPER-EARTH INTERIOR MODEL

M. Levesque[1], O. Mousis[1] and M. Deleuil[1]

Abstract. Measurements of the mass and radius of an exoplanet allow the body's mean density to be derived. This quantity gives a rough estimate of the planet's bulk composition, which ranges between those of the terrestrial planets and Jupiter. To better constrain the composition of exoplanets, interior models have been developed, based on our knowledge of the properties of the Earth and other Solar System bodies. We present an evolution of the Marseille super-Earth Interior model developed to assess the composition of solid planets. The Marseille super-Earth Interior model now includes a precise description of the various high-pressure phases of water ice, allowing one to precisely describe the interiors of solid icy planets with densities lower than that of the Earth and located far enough from the host star to harbor significant icy materials in their interiors. We illustrate the results achieved on one exoplanet example.

Keywords: planets and satellites: composition, planets and satellites: interiors

1 Interior model

The Marseille super-Earth interior (MSEI) model consists in a one-dimensional description of a planet made of fully differentiated concentric layers: core, silicate mantle, and hydrosphere. Their respective proportions are controlled by the Core Mass Fraction (CMF) and the Water Mass Fraction (WMF). The model iteratively solves the differential equations for gravitational acceleration, pressure, temperature and density inside the planet (Brugger et al. 2016, 2017). When the surface temperature of an exoplanet is below 250K, different phases of water ice could exist inside those planets, due to the augmentation of pressure and temperature. However, previously in the model, the treatment of the high-pressure ice was restricted to the use of the equation of state (EoS) of ice VII. Here, we implemented the EoS of additional phases of high-pressure water ice to provide a better description of the interiors of low-density Earth-like planets.

2 High-pressure ice phases

There exists a multitude of high-pressure phases of water ice. This is due to the change of crystal structure of the water ice when this one is progressively crushed under high-pressure. The objective is to incorporate four high-pressure ices into our model: ice II, ice III, ice V, and ice VI. They are likely to be present in the interior of planets due to their locations in the water-phase diagram. To implement those ices into the model, it is necessary to find their equation of state (EoS), their thermal parameters and the interfaces between them, which corresponds to their validity range in pressure and temperature. The different EoS forms are displayed in Tab. 1. The thermal parameters and the expressions of the interfaces were found in the literature (Choukroun & Grasset 2010; Dunaeva et al. 2010).

3 Case of Kepler-441b

Kepler-441b is a Super-Earth with a mass and radius of 3.88 ± 0.83 $M_\oplus$ and 1.60 ± 0.23 $R_\oplus$, respectively (Torres et al. 2015). Its equilibrium temperature is $\sim 206 \pm 20$ K and its low bulk density suggest the presence of high-pressure phases of water ice in its interior. The fractions of the various layers calculated in our model

[1] Aix Marseille Univ, CNRS, CNES, LAM, Marseille, France

	Reference density kg.m^{-3}	Form of the EoS	Reference
Ice II	1169.8	V(P, T)	Leon et al. (2002)
Ice III	1139	V(P, T)	Tchijov et al. (2004)
Ice V	1235	V(P, T)	Tchijov et al. (2004)
Ice VI	1270	Second-order Birch-Murnaghan	Bezacier et al. (2014)

Table 1. Reference density, temperature and the form of equation of state used for each phase of water ice.

come from the Core Mass Fraction (CMF) and the Water Mass Fraction (WMF) determined as inputs. The different solutions of the parameters space are represented in a ternary diagram represented in the left panel of Fig. 1. The CMF and WMF are found to be 10.02 % and 9.87 % to derive a radius of 1.60 $R_\oplus$, respectively. These values also allow the model to determine the proportion of each layer in the interior of Kepler-441b (see right panel of Fig. 1).

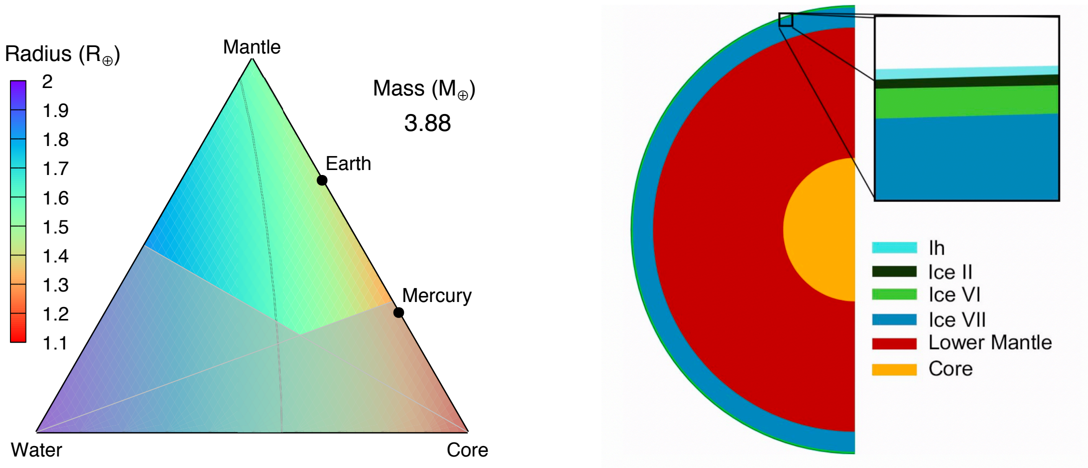

Fig. 1. Left: Ternary diagram displaying the investigated compositional parameter space for a mass $M_p = 3.88 M_\oplus$. The compositions of the Earth and Mercury are indicated for the sake of information. The shaded area corresponds to planet compositions that do not exist in our solar system. **Right:** Interior of Kepler-441b.

4 Conclusions

The implementation of the high-pressure phases of water ice to the MSEI model allows us to provide a better description of the interiors of icy worlds (exoplanets or exomoons) located far from their host stars. This update of the MSEI model will allow to derive the composition of exoplanets at large orbital distance from their host stars, as the upcoming PLATO mission will detect.

References

Bezacier, L., Journaux, B., Perrillat, J.-P., et al. 2014, The Journal of chemical physics, 141, 104505

Brugger, B., Mousis, O., Deleuil, M., & Deschamps, F. 2017, The Astrophysical Journal, 850, 93

Brugger, B., Mousis, O., Deleuil, M., & Lunine, J. I. 2016, The Astrophysical Journal, 831, L16

Choukroun, M. & Grasset, O. 2010, The Journal of Chemical Physics, 133, 144502

Dunaeva, A. N., Antsyshkin, D. V., & Kuskov, O. L. 2010, Solar System Research, 44, 202

Leon, G. C., Rodrguez Romo, S., & Tchijov, V. 2002, Journal of Physics and Chemistry of Solids, 63, 843

Tchijov, V., Ayala, R., Leon, G., & Nagornov, O. 2004, Journal of Physics and Chemistry of Solids, 65, 1277

Torres, G., Kipping, D. M., Fressin, F., et al. 2015, ApJ, 800, 99

SF2A 2019
P. Di Matteo, O. Creevey, A. Crida, G. Kordopatis, J. Malzac, J.-B. Marquette, M. N'Diaye, O. Venot (eds)

TWO EXAMPLES OF HOW TO USE OBSERVATIONS OF TERRESTRIAL PLANETS ORBITING IN TEMPERATE ORBITS AROUND LOW MASS STARS TO TEST KEY CONCEPTS OF PLANETARY HABITABILITY

M. Turbet[1]

Abstract. Terrestrial planets in temperate orbit around very low mass stars are likely to have evolved in a very different way than Solar System planets, and in particular Earth. However, because these are the first planets that are and will be accessible for in-depth atmosphere, clouds and surface characterizations with existing and forthcoming telescopes, we need to develop the best possible observational strategies to maximize the scientific return from these characterizations. Here I discuss and expand on the recent works of Bean et al. (2017) and Turbet et al. (2019) to show that terrestrial planets orbiting in temperate orbits around very low mass stars are potentially an excellent sample of planets to test how universal the processes thought to control the habitability of Solar System planets and in particular Earth are. Precise measurements of density or amospheric CO_2 concentration for planets located both inside and outside the Habitable Zone could be used to statistically test habitability concepts such as the silicate-weathering feedback, CO_2 condensation, or runaway greenhouse, which have been identified as key processes controlling the present and past habitability of Venus, Mars and Earth.

Keywords: exoplanet, habitability, statistical tests, carbonate-silicate cycle, runaway greenhouse

1 Introduction

As of August 2019, astronomers have already detected about forty exoplanets in temperate orbit (Pepe et al. 2011; Tuomi et al. 2013; Borucki et al. 2013; Anglada-Escudé et al. 2013; Quintana et al. 2014; Lissauer et al. 2014; Anglada-Escudé et al. 2014; Torres et al. 2015; Crossfield et al. 2015; Wright et al. 2016; Gillon et al. 2016; Morton et al. 2016; Anglada-Escudé et al. 2016; Crossfield et al. 2016; Gillon et al. 2017; Luger et al. 2017; Astudillo-Defru et al. 2017; Bonfils et al. 2018; Díaz et al. 2019; Tuomi et al. 2019; Zechmeister et al. 2019), with masses or radii or sometimes even both that are similar to the Earth. Most of these recently detected exoplanets are orbiting around nearby, very low mass stars. This specificity make them not only easier to detect, but also easier to characterize with respect to planets orbiting more massive, e.g. solar-type stars. In-depth characterization of these exoplanets could be achieved through:

1. combined mass and radius precise measurements. This allows to estimate the planet density, and thus to gain information on its bulk interior and possibly atmospheric composition.
2. atmospheric, clouds and/or surface measurements, through a variety of techniques such as transit spectroscopy, direct imaging, secondary eclipse or thermal phase curves.

However, planets orbiting around very low mass stars have at least two characteristics that are likely to make them evolve very differently from Solar System planets, and in particular Earth. These two characteristics are:

1. **A hot history.** Very low mass stars can stay for hundreds of millions of years in the Pre Main Sequence (PMS) phase, a phase during which their luminosity can decrease possibly by several orders of magnitude (Chabrier & Baraffe 1997; Baraffe et al. 1998, 2015). During this PMS phase, planets are exposed to strong irradiation, which make them really sensitive to atmospheric processes such as runaway greenhouse (Ramirez & Kaltenegger 2014), indicating that all the so-called volatile species (e.g. H_2O, CO_2, CH_4, NH_3) and most of their byproducts must be in gaseous form in the atmosphere. Note that the runaway greenhouse atmospheric process is discussed in more details below.

[1] Observatoire astronomique de l'Université de Genève, 51 chemin des Maillettes, 1290 Sauverny, Switzerland

2. **An exposition to strong atmospheric escape.** Very low mass stars emit much more high energy X/EUV photons than solar-type stars, in proportion to their total bolometric emission (Ribas et al. 2017), exposing therefore the atmosphere of close-in planets to strong atmospheric erosion mechanisms such as hydrodynamic escape (Lammer et al. 2009; Zahnle & Catling 2017; Bolmont et al. 2017).

Combining these two previous constraints lead Tian & Ida (2015) to infer that terrestrial planets in temperate orbit around very low mass stars are likely to end up in two very different states: (i) If the initial amount of volatile species present at the time of the planet's formation exceeds what can be lost through atmospheric erosion processes, then the planet should remain volatile-rich, and likely water-rich since water is the most abundant volatile species, and also the most likely to condense on the surface among all common volatile species. (ii) Otherwise, the planet would have to be completely dry by the end of the PMS phase, but could later have been replenished with some volcanic and/or volatile gases delivered by impacts. In summary, these planets are likely to be either (i) **extremely water-rich** or (ii) **water-poor***, i.e. planets that have low enough water to have continents present.

Despite exotic characteristics, here I arguee that planets orbiting very low mass stars are still potentially an excellent sample of planets to test processes thought to control the past and present habitability of Solar System planets, and therefore an excellent way to test how universal these processes are. In particular, I discuss and expand on two processes that are thought to be key of the Earth's habitability, and which have led to proposals of observational tests (Bean et al. 2017; Turbet et al. 2019) in extrasolar planet populations, namely (i) **the carbonate-silicate cycle**, that could be tested for the **water-poor** category of planets, and (ii) **the runaway greenhouse**, that could be tested for the **extremely water-rich** category of planets.

2 First example: Testing the carbonate-silicate cycle and more broadly the CO_2 cycle

The CO_2 cycle is thought to be a key element for the stabilization of Earth's climate on geologically long timescale, through the carbonate-silicate cycle (Walker et al. 1981) which acts as a geophysical thermostat. This stabilizing cycle is thought to regulate the atmospheric CO_2 level in order to maintain surface temperatures that allow surface liquid water, based on two distinct processes: CO_2 degassing by volcanoes and silicate weathering, which strongly depends on temperature. If a planet – on which the carbonate-silicate feedback operates – gets too warm, then the silicate weathering rate increases, which decreases the amount of CO_2 in the atmosphere, which further decreases the surface temperature of the planet. If a planet gets too cold, the silicate weathering rate decreases, and CO_2 accumulates through volcanic outgassing, which leads to surface warming through CO_2 greenhouse effect.

Assuming the carbonate-silicate cycle is a universal geochemical process, Bean et al. (2017) proposed that it could be detected if we observe – with statistical significance – that Habitable Zone planets have a CO_2 content (or mixing ratio, for the observational point of view) that decreases with incident irradiation, as illustrated in Figure 1 (solid blue line). This is in fact what would be expected for planets that are sufficiently water-poor (first category) that they have both liquid water oceans or lakes, and continents. For planets very rich in water (second category), the CO_2 mixing ratio versus irradiation might look very different, because the CO_2 content is governed by other processes such as seafloor weathering or CO_2 oceanic dissolution (Kitzmann et al. 2015; Nakayama et al. 2019). We encourage future studies to better estimate how the CO_2 versus irradiation curve is expected to look like in the population of water-rich terrestrial planets.

In the water-poor limit planet population (i.e. planets that have oceans or lakes, and continents), I expand here the work of Bean et al. (2017) on how the CO_2 content should vary as a function of irradiation for planets located outside the limits of the Habitable Zone:

1. For planets receiving more irradiation than the inner edge of the Habitable Zone, water is expected to have completely evaporated into the atmosphere and thus to be exposed to photodissociation and subsequent atmospheric escape processes. This is likely what happened to Venus (see the introduction section of Way et al. 2016 for a recent review). Not only could the O_2 remaining in the atmosphere have oxidized the surface, thus producing CO_2; but also the absence of a hydrological cycle should have shut-down the silicate-weathering feedback, thus leading to the accumulation of CO_2 by volcanic degassing. Therefore,

*The Earth and other Solar System terrestrial planets fit in this second category.

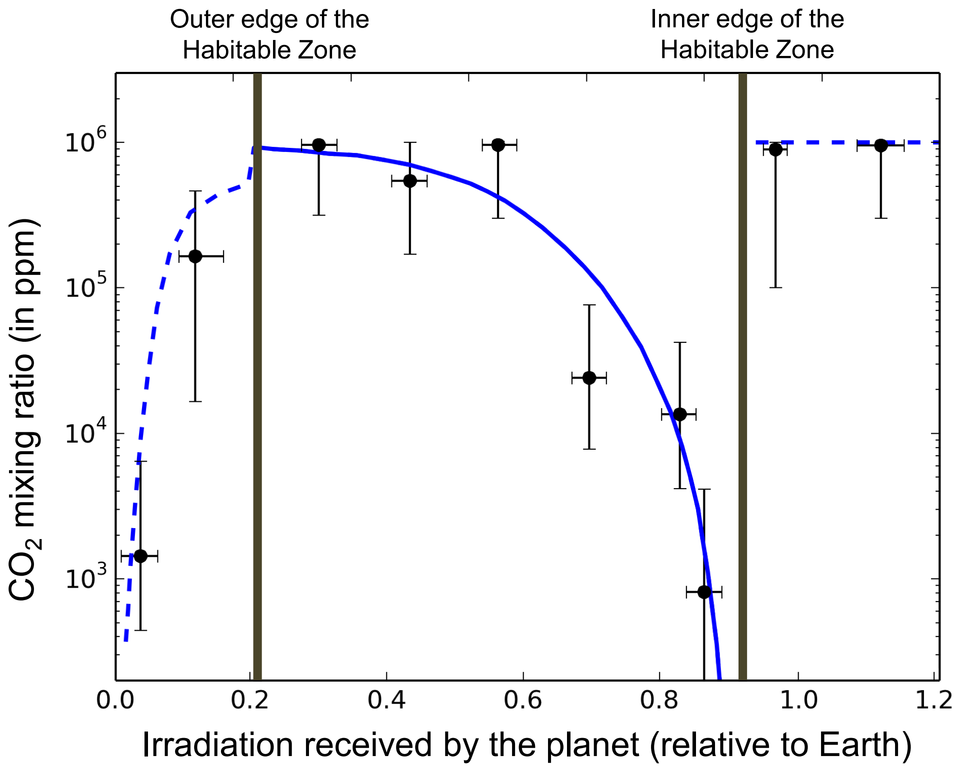

Fig. 1. This plot shows how measurements of CO_2 atmospheric mixing ratio for a sample of terrestrial-size planets spanning a wide range of irradiations could be used to statistically infer the existence of a CO_2 cycle, and even possibly the existence of a carbonate-silicate cycle. Between the inner and outer edges of the Habitable Zone (Kopparapu et al. 2013), the blue solid curve (adapted from Bean et al. 2017) shows the predicted CO_2 needed to maintain a surface temperature of 290 K. While planets located beyond the inner edge of the Habitable Zone are expected to accumulate large amount of CO_2, planets located below the outer edge of the Habitable Zone are expected to be depleted in CO_2 because of CO_2 condensation. The black points are binned data for hypothetical planets.

the CO_2 mixing ratio could reach unity for planets beyond the inner edge of the Habitable Zone (see dotted blue line in Figure 1, right of the Inner edge of the Habitable Zone).

2. For planets receiving less irradiation than the outer edge of the Habitable Zone, CO_2 is limited by surface condensation (Turbet et al. 2017, 2018), which should be more and more severe as the planet is further out of the host star. Therefore, it is expected that for planets receiving less irradiation than the outer edge of the Habitable Zone, the CO_2 atmospheric mixing ratio should decrease with decreasing irradiation, with possibly a gap at the exact position of the outer edge of the Habitable Zone, due to the ice albedo feedback (see dotted blue line in Figure 1, left of the Outer edge of the Habitable Zone). However, this gap is likely to be small for planets orbiting very low mass stars because the ice albedo feedback should not be very effective, due to (i) the spectral properties of water ice and snow(Joshi & Haberle 2012; Shields et al. 2013) and (ii) the fact that these planets are likely in synchronous rotation, with all ice trapped on the nightside (Menou 2013; Leconte et al. 2013b; Turbet et al. 2016).

CO_2 measurements could be attempted first through the transmission spectroscopy technique as soon as the James Webb Space Telescope (JWST) is operational, possibly through the 4.3 microns CO_2 ν_3 absorption band, which has been shown to be one of the most accessible molecular absorption band in terrestrial-type atmospheres (Morley et al. 2017; Lincowski et al. 2018; Fauchez et al. 2019; Wunderlich et al. 2019; Lustig-Yaeger et al. 2019). Not only this feature is present for a wide range of CO_2 mixing ratio, but it is also weakly affected by the presence of clouds and photochemical hazes (Fauchez et al., submitted to the Astrophysical Journal).

3 Second example: Testing the runaway-greenhouse

Planets similar to Earth but slightly more irradiated are expected to experience a runaway greenhouse transition, a state in which a net positive feedback between surface temperature, evaporation, and atmospheric opacity causes a runaway warming (Ingersoll 1969; Goldblatt & Watson 2012). This runaway greenhouse positive feedback ceases only when oceans have completely boiled away, forming an optically thick H_2O-dominated atmosphere. Venus may have experienced a runaway greenhouse transition in the past (Rasool & de Bergh 1970; Kasting et al. 1984), and we expect that Earth will in ~ 600 million years as solar luminosity increases by $\sim 6\%$ compared to its present-day value (Gough 1981). However, the exact limit at which this extreme, rapid climate transition from a temperate climate (with most water condensed on the surface) to a post-runaway greenhouse climate (with all water in the atmosphere) would occur, and whether or not a CO_2 atmospheric level increase would affect that limit, is still a highly debated topic (Leconte et al. 2013a; Goldblatt et al. 2013; Ramirez et al. 2014; Popp et al. 2016). This runaway greenhouse limit is traditionally used to define the inner edge of the habitable zone (Kasting et al. 1993; Kopparapu et al. 2013).

Assuming the runaway greenhouse feedback is a universal atmospheric physics process, Turbet et al. (2019) recently proposed that the runaway greenhouse could be identified through a radius gap at the position of the runaway greenhouse irradiation. Turbet et al. (2019) actually showed two same planets – but one being located just below and the other just above the runaway greenhouse irradiation threshold – should have a different transit radius and which should be all the more different as the planet water content get higher. This radius difference or gap is a consequence of the runaway greenhouse radius inflation effect introduced in Turbet et al. (2019), resulting from the fact that for a fixed water-to-rock mass ratio, a planet endowed with a steam H_2O-dominated atmosphere has a much larger physical size than if all the water is in condensed form (liquid or solid). For Earth, the net radius increase should be around ~ 500 km, but is expected to be significantly larger (up to thousands of km) for planets with much larger total water content (Turbet et al. 2019).

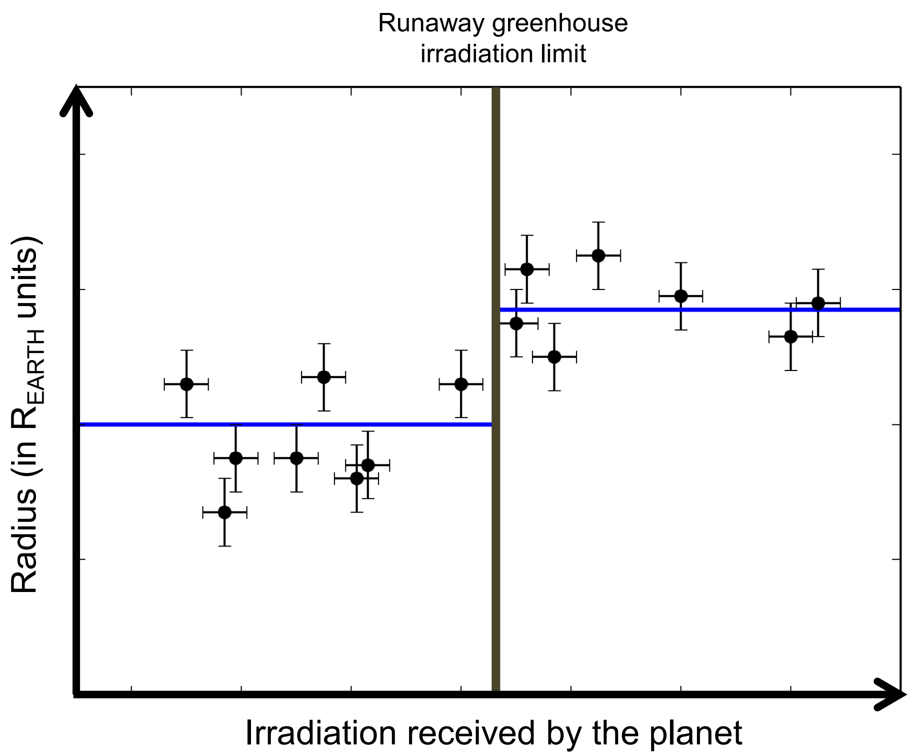

Fig. 2. This plot shows how combined measurements of masses and radii for a sample of terrestrial-size planets spanning irradiation on both sides of the runaway greenhouse irradiation limit could be used to validate the concept of runaway greenhouse. The blue solid curve (adapted from Turbet et al. 2019) shows the predicted radius gap arising from the runaway greenhouse radius inflation effect. The black points are binned data for hypothetical planets which are in a fixed terrestrial mass range.

As a result, for a sample of water-rich planets[†], the runaway greenhouse irradiation could be determined if we observe – with statistical significance – that planets located beyond the inner edge of the Habitable Zone have – for a fixed terrestrial mass range – a larger radius than planets located inside the Habitable Zone or colder, as illustrated in Figure 2 (solid blue line).

Precise density measurements for terrestrial-size planets could be attempted by combining precise transit photometry with ongoing and upcoming space missions such as HST, TESS, CHEOPS and PLATO, with precise radial velocity mass measurements with ground-based spectrographs such as ESPRESSO, CARMENES or SPIRou.

4 Conclusions

In this proceeding, I discussed and expanded on two possible observational strategies recently introduced in Bean et al. (2017) and Turbet et al. (2019) to constrain two key processes that are believed to be crucial to sustain habitability of Solar System planets: the CO_2 cycle and the runaway greenhouse. While the former could be first attempted as soon as JWST will be operational, the later could be tested with ongoing and future precise combined mass and radius measurements of terrestrial exoplanets.

Although these strategies require more work (Checlair et al. 2019) to better constrain how to carry them out (how to make these observations? with which instruments? to what precision? what is the minimum number of planets needed? what are the best planets to be selected? how to deal with confounding factors? etc.), they demonstrate at least in theory how we could use observations and characterizations of exotic planets orbiting very low mass stars to test the universality of the processes that shape the habitability of planets in the Solar System and possibly in many other exoplanetary systems.

This project has received funding from the European Union's Horizon 2020 research and innovation program under the Marie Sklodowska-Curie Grant Agreement No. 832738/ESCAPE. M.T. would like to thank the Gruber Foundation for its generous support to this research.

References

Anglada-Escudé, G., Amado, P. J., Barnes, J., et al. 2016, Nature, 536, 437

Anglada-Escudé, G., Arriagada, P., Tuomi, M., et al. 2014, Monthly Notices of the Royal Astronomical Society: Letters, 443, L89

Anglada-Escudé, G., Tuomi, M., Gerlach, E., et al. 2013, Astronomy & Astrophysics, 556, A126

Astudillo-Defru, N., Forveille, T., Bonfils, X., et al. 2017, Astronomy & Astrophysics, 602, A88

Baraffe, I., Chabrier, G., Allard, F., & Hauschildt, P. H. 1998, Astronomy & Astrophysics, 337, 403

Baraffe, I., Homeier, D., Allard, F., & Chabrier, G. 2015, Astronomy & Astrophysics, 577, A42

Bean, J. L., Abbot, D. S., & Kempton, E. M.-R. 2017, The Astrophysical Journal Letters, 841, L24

Bolmont, E., Selsis, F., Owen, J. E., et al. 2017, Monthly Notices of the Royal Astronomical Society, 464, 3728

Bonfils, X., Astudillo-Defru, N., Díaz, R., et al. 2018, Astronomy & Astrophysics, 613, A25

Borucki, W. J., Agol, E., Fressin, F., et al. 2013, Science, 340, 587

Chabrier, G. & Baraffe, I. 1997, Astronomy & Astrophysics, 327, 1039

Checlair, J., Abbot, D. S., Webber, R. J., et al. 2019, in Bulletin of the American Astronomical Society, Vol. 51, Bulletin of the American Astronomical Society, 404

Crossfield, I. J. M., Ciardi, D. R., Petigura, E. A., et al. 2016, The Astrophysical Journal Supplement Series, 226, 7

Crossfield, I. J. M., Petigura, E., Schlieder, J. E., et al. 2015, The Astrophysical Journal, 804, 10

Díaz, R. F., Delfosse, X., Hobson, M. J., et al. 2019, Astronomy & Astrophysics, 625, A17

Fauchez, T., Turbet, M., Villanueva, G. L., et al. 2019, submitted to the Astrophysical Journal

Gillon, M., Jehin, E., Lederer, S. M., et al. 2016, Nature, 533, 221

Gillon, M., Triaud, A. H. M. J., Demory, B.-O., et al. 2017, Nature, 542, 456

Goldblatt, C., Robinson, T. D., Zahnle, K. J., & Crisp, D. 2013, Nature Geoscience, 6, 661

Goldblatt, C. & Watson, A. J. 2012, Philosophical Transactions of the Royal Society of London Series A, 370, 4197

[†]This runaway greenhouse radius inflation effect is expected to be absent from the population of water-poor planets orbiting low mass stars.

Gough, D. O. 1981, Solar Phys., 74, 21

Ingersoll, A. P. 1969, Journal of Atmospheric Sciences, 26, 1191

Joshi, M. M. & Haberle, R. M. 2012, Astrobiology, 12, 3

Kasting, J. F., Pollack, J. B., & Ackerman, T. P. 1984, Icarus, 57, 335

Kasting, J. F., Whitmire, D. P., & Reynolds, R. T. 1993, Icarus, 101, 108

Kitzmann, D., Alibert, Y., Godolt, M., et al. 2015, Monthly Notices of the Royal Astronomical Society, 452, 3752

Kopparapu, R. K., Ramirez, R., Kasting, J. F., et al. 2013, The Astrophysical Journal, 765, 131

Lammer, H., Bredehöft, J. H., Coustenis, A., et al. 2009, The Astronomy & Astrophysics Review, 17, 181

Leconte, J., Forget, F., Charnay, B., Wordsworth, R., & Pottier, A. 2013a, Nature, 504, 268

Leconte, J., Forget, F., Charnay, B., et al. 2013b, Astronomy & Astrophysics, 554, A69

Lincowski, A. P., Meadows, V. S., Crisp, D., et al. 2018, The Astrophysical Journal, 867, 76

Lissauer, J. J., Marcy, G. W., Bryson, S. T., et al. 2014, The Astrophysical Journal, 784, 44

Luger, R., Sestovic, M., Kruse, E., et al. 2017, Nature Astronomy, 1, 0129

Lustig-Yaeger, J., Meadows, V. S., & Lincowski, A. P. 2019, The Astronomical Journal, 158, 27

Menou, K. 2013, The Astrophysical Journal, 774

Morley, C. V., Kreidberg, L., Rustamkulov, Z., Robinson, T., & Fortney, J. J. 2017, The Astrophysical Journal, 850, 121

Morton, T. D., Bryson, S. T., Coughlin, J. L., et al. 2016, The Astrophysical Journal, 822, 86

Nakayama, A., Kodama, T., Ikoma, M., & Abe, Y. 2019, Monthly Notices of the Royal Astronomical Society, 488, 1580

Pepe, F., Lovis, C., Ségransan, D., et al. 2011, Astronomy & Astrophysics, 534, A58

Popp, M., Schmidt, H., & Marotzke, J. 2016, Nature Communications, 7, 10627

Quintana, E. V., Barclay, T., Raymond, S. N., et al. 2014, Science, 344, 277

Ramirez, R. M. & Kaltenegger, L. 2014, The Astrophysical Journal Letters, 797, L25

Ramirez, R. M., Kopparapu, R. K., Lindner, V., & Kasting, J. F. 2014, Astrobiology, 14, 714

Rasool, S. I. & de Bergh, C. 1970, Nature, 226, 1037

Ribas, I., Gregg, M. D., Boyajian, T. S., & Bolmont, E. 2017, Astronomy & Astrophysics, 603, A58

Shields, A. L., Meadows, V. S., Bitz, C. M., et al. 2013, Astrobiology, 13, 715

Tian, F. & Ida, S. 2015, Nature Geoscience, 8, 177

Torres, G., Kipping, D. M., Fressin, F., et al. 2015, The Astrophysical Journal, 800, 99

Tuomi, M., Jones, H. R. A., Butler, R. P., et al. 2019, arXiv e-prints

Tuomi, M., Jones, H. R. A., Jenkins, J. S., et al. 2013, Astronomy & Astrophysics, 551, A79

Turbet, M., Bolmont, E., Leconte, J., et al. 2018, Astronomy & Astrophysics, 612, A86

Turbet, M., Ehrenreich, D., Lovis, C., Bolmont, E., & Fauchez, T. 2019, A&A, 628, A12

Turbet, M., Forget, F., Leconte, J., Charnay, B., & Tobie, G. 2017, Earth and Planetary Science Letters, 476, 11

Turbet, M., Leconte, J., Selsis, F., et al. 2016, Astronomy & Astrophysics, 596, A112

Walker, J. C. G., Hays, P. B., & Kasting, J. F. 1981, Journal of Geophysical Research, 86, 9776

Way, M. J., Del Genio, A. D., Kiang, N. Y., et al. 2016, Geophysical Research Letters, 43, 8376

Wright, D. J., Wittenmyer, R. A., Tinney, C. G., Bentley, J. S., & Zhao, J. 2016, The Astrophysical Journal Letters, 817, L20

Wunderlich, F., Godolt, M., Grenfell, J. L., et al. 2019, Astronomy & Astrophysics, 624, A49

Zahnle, K. J. & Catling, D. C. 2017, The Astrophysical Journal, 843, 122

Zechmeister, M., Dreizler, S., Ribas, I., et al. 2019, Astronomy & Astrophysics, 627, A49

Session 11

Faire de l'astrophysique avec les ondes gravitationnelles

SF2A 2019
P. Di Matteo, O. Creevey, A. Crida, G. Kordopatis, J. Malzac, J.-B. Marquette, M. N'Diaye, O. Venot (eds)

MULTI-MESSENGER ASTRONOMY WITH SVOM

J.-L. Atteia[1] and the SVOM collaboration.

Abstract. The Sino-French space mission *SVOM* (Space-based multi-band astronomical Variable Objects Monitor) is mainly designed to detect, localize and follow-up Gamma-Ray Bursts. The satellite, to be launched late 2021, embarks two wide-field gamma-ray instruments and two narrow-field telescopes for X-ray and optical imaging. It is complemented by a dedicated ground segment encompassing a set of wide-field optical cameras and two 1-meter class follow-up telescopes.

With the advent of multi-messenger astronomy, which detects and exploits the information transported by gravitational waves and particles in addition to photons, there is a renewed interest for cosmic explosions and compact objects, which are the main targets of *SVOM*. We describe here the main characteristics of the mission and its expected contribution to multi-messenger astronomy.

Keywords: gamma-ray bursts, gravitational waves, space instrumentation.

1 The SVOM mission

The *SVOM* mission* is the result of a bilateral collaboration between France (CNES) and China (CAS, CNSA), involving many research institutes from these two countries and contributions from the University of Leicester, the Max Planck Institut für Extraterrestische Physik and the Universidad Nacional Autónoma de México. *SVOM* is lead by J.Y. Wei in China and B. Cordier in France. The mission encompasses a space segment, with four instruments embarked on-board a low earth orbit satellite, and a ground segment with two sets of wide-field optical cameras, two 1-meter class ground follow-up telescopes, and a network of $\sim$ 45 VHF receiving stations distributed along the footprint of the orbit (Fig. 1). The launch of *SVOM* is scheduled late 2021 with three years of nominal operations and a possible extension of two years.

The main science driver of *SVOM* is gamma-ray burst (GRB) physics. This is the core program, which includes the GRB-Supernova connection, the nature of the central engine, the identification of the progenitors of short GRBs and the physics of GRB jets. Between GRBs, *SVOM* will carry out other programs driven by the narrow-field instruments: a general program and a target of opportunity program mostly focused on non-GRB science. A detailed description of *SVOM* science objectives can be found in Wei et al. (2016).

2 SVOM instrumentation and system

SVOM is designed as a multi-wavelength observatory. The satellite embarks four instruments whose main characteristics are presented in Fig. 4. They work in synergy: while the two narrow-field telescopes, the Micropore X-ray Telescope (MXT – Götz et al. (2014); Mercier et al. (2018)) and the Visible Telescope (VT – Wu et al. (2012)) observe pre-planned sources, ECLAIRs† (Godet et al. 2014; Schanne et al. 2014) and the Gamma-Ray Monitor (GRM – Dong et al. (2010)) monitor the hard X-ray sky to detect and characterize high-energy transients over a broad energy range (4 keV – 5 MeV). When a transient is detected, its position is immediately sent to the ground and to the satellite, which may repoint its narrow field telescopes in minutes. The soft response of the ECLAIRs wide-field camera and a fast link to ground-based infrared telescopes should facilitate the identification of high redshift events.

[1] IRAP, Université de Toulouse, CNRS, CNES, UPS, Toulouse, France
* `http://www.svom.fr/`
† ECLAIRs means "lightning flash" in French

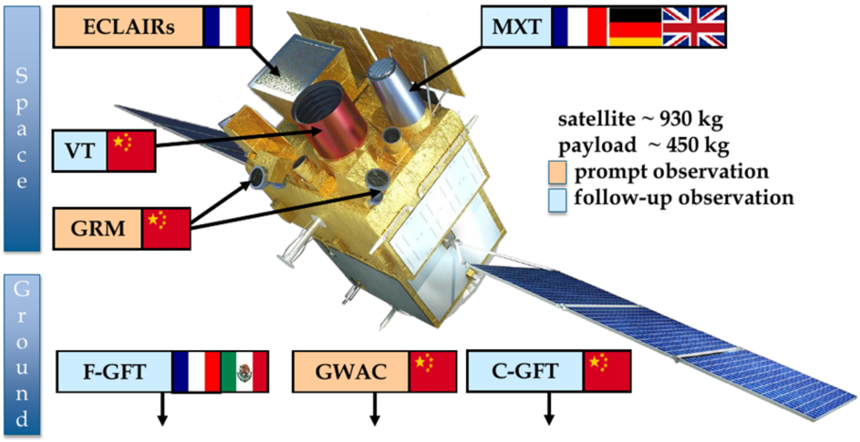

Fig. 1. Schematic view of the "*SVOM* system", including the satellite and its four instruments (GRM, ECLAIRs, MXT and VT), and the ground segment with two sets of wide-field optical cameras and two robotic follow-up telescopes.

In addition to the space instruments, *SVOM* encompasses a ground segment with two sets of Ground Wide Angle Cameras, located in China and Chile, which observe several thousands square degrees down to $M_V = 16 - 17$ (GWACs – Fu et al. (2017)), and two 1-meter class Ground Follow-up Telescopes located in China and Mexico (with a NIR imaging camera for the second one) (GFTs – see e.g. Floriot et al. 2018; Corre et al. 2018). Fig. 3 shows a set of GWACs at the Xinglong Observatory (China) and the Colibrí telescope under construction. Several GWACs are already operational and used to follow-up GW alerts from LIGO and Virgo (Turpin et al. 2019). Overall, *SVOM* is similar to the very successful Neil Gehrels Swift Observatory with some important differences: a smaller satellite with smaller instruments (at the notable exception of VT), the addition of gamma-ray spectrometers comparable to the NaI modules of *Fermi*/GBM, and a set of unique ground-based instruments dedicated to the photometric follow-up of HE transients detected by the satellite.

In order to promote the follow-up and spectroscopy of *SVOM* GRBs with large facilities on Earth, the space borne instruments are pointed close to the anti-solar direction ("à la HETE"). One consequence of this choice is that the instruments will see the Earth crossing their field of view every orbit. In normal operations, the narrow-field instruments look at pre-planned targets (this is the General Program, GP) and wide-field instruments stare the sky for high-energy transient sources (this is the Core Program, CP). When a new transient source is detected, its position is sent to the ground and a pointing request is sent to the satellite, which will execute it, depending on its feasibility. *SVOM* can also perform target of opportunity (ToO) observations within minutes of request with one GFT and within hours of request with MXT and VT. The time sharing between the three observing programs CP, GP, ToO is shown in (Fig. 2).

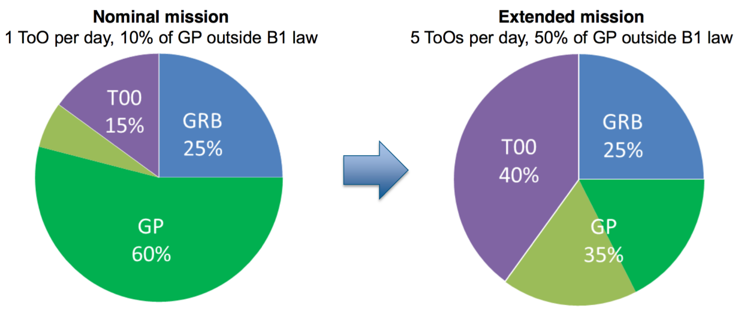

Fig. 2. Time sharing between the three observing programs of SVOM. The light green zone shows the GP time spent outside the nominal pointing law, called the "B1 law" (a nearly anti-solar pointing law, which avoids the galactic plane). The GRB time is an estimate based on a predicted trigger rate of ~ 65 GRB/yr.

3 SVOM in the multi-messenger era

The recent discovery of multi-wavelength electromagnetic radiation (GRB + afterglow + kilonova) associated with the merger of two neutron stars that produced a burst of gravitational waves (Abbott et al. 2017a,b, and ref. therein) opened the window of multi-messenger astronomy, which is the joint observation of photonic and non-photonic signals from astronomical sources.

Considering the science goals of the *SVOM* mission, the great diversity of its instruments, and the possibility to organize multi-wavelength observing campaigns quickly, we expect a strong involvement in multi-messenger astronomy. First, it will be possible to search for non-photonic signals (neutrino or GW) coincident in space and time with *SVOM* HE transients. *SVOM* presents two interesting features for this task: the low energy threshold of ECLAIRs, which permits the detection of faint and soft X-Ray Flashes (XRFs) and the wide-field of view of GRM with a good sensitivity to short GRBs (sGRBs). Since XRFs and sGRBs are fainter and more numerous than classical GRBs, they can be detected at smaller distances. The increased sensitivity of GW interferometers and neutrino detectors at the beginning of the next decade will offer a unique opportunity to find the non-photonic counterparts of nearby XRFs or sGRBs detected by *SVOM*, if they exist. Second, *SVOM* will participate to the searches for multi-wavelength afterglows of GW or neutrinos events: the wide field of view of the MXT and the possibility to schedule tiled observations with MXT, VT and the GFTs, will allow to quickly explore regions of several square degrees in X-rays, visible and NIR with a good sensitivity, in order to detect and characterize the photonic counterparts of GW or neutrino bursts. We are working hard to ensure that *SVOM* will fully contribute to the development of multi-messenger astronomy in the next decade.

References

Abbott, B. P., Abbott, R., Abbott, T. D., et al. 2017a, ApJ, 848, L13

Abbott, B. P., Abbott, R., Abbott, T. D., et al. 2017b, ApJ, 848, L12

Corre, D., Basa, S., Klotz, A., et al. 2018, in Society of Photo-Optical Instrumentation Engineers (SPIE) Conference Series, Vol. 10705, Proc. SPIE, 107051R

Dong, Y., Wu, B., Li, Y., Zhang, Y., & Zhang, S. 2010, Science China Physics, Mechanics, and Astronomy, 53, 40

Floriot, J., Marcos, M., Fuentes-Fernandez, J., et al. 2018, in Society of Photo-Optical Instrumentation Engineers (SPIE) Conference Series, Vol. 10706, Proc. SPIE, 107060M

Fu, X.-n., Huang, L., & Wei, J.-y. 2017, Chinese Astron. Astrophys., 41, 577

Godet, O., Nasser, G., Atteia, J. ., et al. 2014, in Society of Photo-Optical Instrumentation Engineers (SPIE) Conference Series, Vol. 9144, Proc. SPIE, 914424

Götz, D., Osborne, J., Cordier, B., et al. 2014, in Society of Photo-Optical Instrumentation Engineers (SPIE) Conference Series, Vol. 9144, Proc. SPIE, 914423

Mercier, K., Gonzalez, F., Götz, D., et al. 2018, in Society of Photo-Optical Instrumentation Engineers (SPIE) Conference Series, Vol. 10699, Proc. SPIE, 1069921

Schanne, S., Le Provost, H., Kestener, P., et al. 2014, arXiv e-prints, arXiv:1411.7810

Turpin, D., Wu, C., Han, X. H., et al. 2019, arXiv e-prints, arXiv:1902.08476

Wei, J., Cordier, B., Antier, S., et al. 2016, arXiv e-prints, arXiv:1610.06892

Wu, C., Qiu, Y. L., & Cai, H. B. 2012, in Death of Massive Stars: Supernovae and Gamma-Ray Bursts, ed. P. Roming, N. Kawai, & E. Pian, Vol. 279, 421–422

Fig. 3. Left: A set of GWAC, at the Xinglong Observatory in China. **Right:** The Colibrí GFT at the 'Observatoire de Haute-Provence' (France) before its installation at the 'Observatorio Astrónomico Nacional' (Baja California, México).

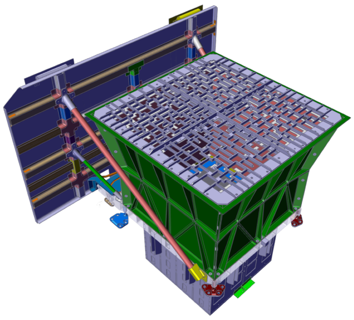

ECLAIRs (CNES, IRAP, CEA, APC)

- 40% open fraction
- Detection area: **1000 cm²**
- **6400 CdTe pixels** (4x4x1 mm^3)
- **FoV: 2 sr** (zero sensitivity)
- Energy range: **4** - 150 keV
- **Localization** accuracy **<12 arcmin** for 90% of sources at detection limit
- Onboard trigger and localization: **~65 GRBs/year**

Well adapted for the detection of long GRBs with low E_{PEAK}

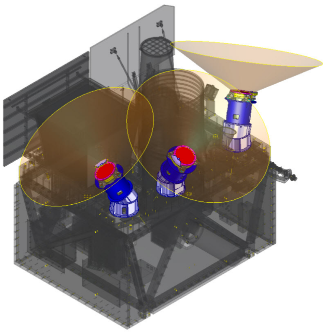

GRM Gamma-Ray Monitor (IHEP)

- **3 Gamma-Ray Detectors** (GRDs)
- **NaI(Tl)** (16 cm Ø, 1.5 cm thick)
- Plastic scintillator (6 mm) to monitor particle flux and reject particle events
- **FoV:2.6 sr per GRD**
- **Energy range: 15-5000 keV**
- Aeff = 190 cm² at peak
- Rough localization accuracy
- Expected rate: **~90 GRBs / year**

Will provide E_{PEAK} measurements for most ECLAIRs GRBs
Will detect GRBs and transients out of the ECLAIRs FOV (with poor localization)

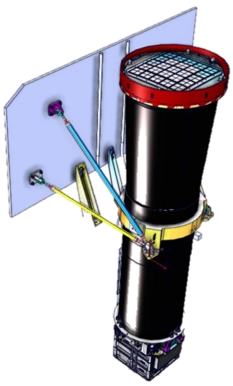

MXT Micro-channel X-ray Telescope (CNES, CEA, UL, MPE)

- **Micro-pores optics** (Photonis), with **square 40 μm pores** in a "Lobster Eye" conf. (UL design)
- pnCCD (MPE) based camera (CEA)
- **FoV: 64x64 arcmin²**
- Focal length: 1 m
- **Energy range: 0.2 - 10 keV**
- Aeff = 27 cm² @ 1 keV (central spot)
- Energy resolution: ~80 eV @ 1.5 keV
- **Localization accuracy <13 arcsec** within 5 min from trigger for 50% of GRBs (statistical error)

Innovative focusing X-ray optics based on « Lobster-Eye » design
Will be able to promptly observe the X-ray afterglow

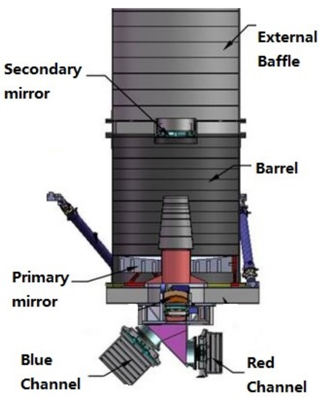

VT Visible Telescope (XIOMP, NAOC)

- Ritchey-Chretien telescope, 40 cm Ø, f=9
- **FoV: 26x26 arcmin²**, covering ECLAIRs error box in most cases
- **2 channels: blue (400-650 nm) and red (650-1000 nm)**, with 2k * 2k CCD detector each
- **Sensitivity M_V=23 in 300 s**
- Will detect ~80% of ECLAIRs GRBs
- **Localization accuracy <1 arcsec**

Able to detect high-redshift GRBs up to z~6.5
Can provide redshift indicators due to the presence of two channels

Fig. 4. The four space borne instruments of SVOM. **Left:** schematic drawings. **Right:** main characteristics.

SF2A 2019
P. Di Matteo, O. Creevey, A. Crida, G. Kordopatis, J. Malzac, J.-B. Marquette, M. N'Diaye, O. Venot (eds)

EVOLUTION OF MASSIVE STARS AND BINARY SYSTEMS AS PROGENITORS OF GRAVITATIONAL WAVES EMITTERS

F. Martins[1] and J.-C. Bouret[2]

Abstract. In this contribution we give a brief overview of the effects of rotation, stellar winds, metallicity and binarity on the evolution of massive stars. We focus on the role of these parameters in shaping the end states of stellar evolution. Special attention is given to the mass of the stellar remnants that has been questionned by the detection of heavy black holes in merger events leading to gravitational waves emission.

Keywords: Stars: massive, Stars: rotation, Stars: mass loss, Stars: binary, Gravitational waves

1 Introduction

The detection of gravitational waves from binary black hole mergers by the LIGO-VIRGO collaborations has revealed surprisingly high masses for the black holes involved (Abbott et al. 2016, 2017a,b). With masses in excess of 15 $M_\odot$ and reaching about 40 $M_\odot$, such black holes are more massive than those detected so far in X-ray binaries and for which masses do not exceed 15 $M_\odot$(Khargharia et al. 2010; Orosz et al. 2011), with values typically around 5 to 10 $M_\odot$. This raises the question of the conditions required to form such black holes in the framework of massive stars evolution.

The evolution of massive stars, and thus the end states and the properties of the compact objects, depend crucially on rotation, mass loss, metallicity, the presence of a companion. In the following we will summarize the main effects caused by these processes. We will focus on the properties of the stellar core prior to supernova explosion, as well as on the remnant masses. Exhaustive reviews on the evolution of massive stars are found in Maeder & Meynet (2000); Langer (2012). We refer the reader to e.g. Keszthelyi et al. (2019) for a summary of the effects of magnetic fields, which are expected to be important for about 5-10% of massive stars (Grunhut et al. 2017).

2 Stellar rotation

Rotation affects the evolution of massive stars in various ways. First, due to the geometrical deformation, the equatorial radius is larger than the polar radius. Given the definition of effective temperature, this means that it is not uniform over the surface. Quantities depending directly on $T_{\rm eff}$ (and $logg$, such as the flux of ionizing photons) are thus also varying with latitude. Departure from sphericity triggers large scale motion (the Eddington-Swift circulation) that efficiently transports angular momentum from the core to the surface. Differential rotation between layers located at different radii triggers additional mixing processes (e.g. shear turbulence) that convey both anguar momentum and chemical species from the inner to the outter regions of the star.

These general effects impact the star's properties and evolution. Except on the zero-age main sequence, the luminosity of a rotating star is increased compared to a non-rotating star. Mixing processes extend the size of the convective core which increases the lifetime of the successive burning sequences (H, He, C...). A natural consequence is the increase of the mass of the CO core, and thus of the remnant. Limongi & Chieffi (2018) estimate that at low metallicity and below about 60 $M_\odot$ the CO core mass can be multiplied by a factor $\sim$1.5 due to rotation (see their Fig. 18). The conversion of the CO core mass to the remnant mass depends on the

[1] LUPM, Université de Montpellier, CNRS, Place Eugène Bataillon, F-34095 Montpellier, France
[2] Aix Marseille Université, CNRS, CNES, LAM, Marseille, France

assumptions used for the explosion: either a fixed amount of ^{56}Ni (usually 0.1M$_\odot$) is assumed to be produced, or direct collapse to a black hole is considered. The range of remnant mass is thus very wide, from about 1 to $\sim$80 M$_\odot$ according to Limongi & Chieffi (2018). Uncertainties on the CO core-remnant mass transformation dominate the error budget on the final compact object mass.

3 Mass loss

Massive stars experience strong mass loss of different nature. For O and B stars, the winds are radiatively driven by acceleration through numerous metallic lines (Castor et al. 1975). The same mechanism is probably at work in Wolf-Rayet stars. For cool red supergiants, no theory exists so far to explain the large mass loss whose measurements are highly uncertain (e.g. Mauron & Josselin 2011). Episodic huge mass ejections of debated nature happen in luminous blue variables. Mass loss is one of the main drivers of massive stars evolution (Chiosi & Maeder 1986). It affects the internal structure, lifetimes, remnant masses, among others. For instance, Georgy (2012) showed that changing the mass loss rates of red supergiants within the range of measured values leads to different progenitors of type II supernovae (i.e. blue, yellow or red supergiant progenitors).

This highlights the importance of quantifying accurately mass loss rates in different phases of evolution. Various prescriptions exist, based either on observational results or theoretical predictions. Renzo et al. (2017) performed a systematic study of the effect of varying these prescriptions in stellar evolution models. They showed that the final masses could change by 15 to 30%. If in addition a scaling is applied to take into account "clumping" (i.e. the fact that stellar winds are not homogeneous), variations up to more than 50% can be expected on final masses (see their Fig. 1).

4 Metallicity

The metal content of massive stars affects their evolution in the following two main ways. First, due to reduced opacities, low metallicity stars are more compact and hotter. The reduced size implies stronger gradients, which increases the efficiency of mixing processes due to rotation. Second, radiatively-driven winds are by nature metallicity dependent. Mass loss rates depend on Z^α, whith α between 0.7 and 0.8 (Mokiem et al. 2007; Vink et al. 2001). Consequently, lower metallicity stars lose less mass and produce more massive compact objects.

Groh et al. (2019) computed evolutionary models at $1/30^{th}$ solar metallicity and obtained CO core masses up to 70 M$_\odot$ (for initial masses of 120 M$_\odot$). The corresponding remnant masses are as high as 20 M$_\odot$. Limongi & Chieffi (2018) find similar CO core masses. From these calculations, it is clear that the heavy black holes detected by the LIGO-VIRGO detections should have been formed at low metallicity. At solar metallicity, Groh et al. (2019) do not produce remnants with masses higher than 10 M$_\odot$.

5 Chemically homogeneous evolution

From the effects described in the two previous sections, a favorable situation to form high mass remnants is when fast rotation is combined with low metallicity. Both cases increase the core size and the remnant mass. In these conditions, a peculiar evolutionary channel may occur: quasi-chemically homogeneous evolution (Maeder 1987; Langer 1992; Yoon et al. 2006). Actually, it should occur with the single condition that the star rotates fast enough, but this is favoured at low metallicity due to reduced mass and angular momentum loss. If rotation is fast enough, the timescale for mixing processes may become shorter than the nuclear timescale, implying that material synthetized in the core is immediately transported to the surface. The chemical composition is thus quasi homogeneous. This implies a reduction of the surface opacity, and consequently a higher effective temperature. At the same time the mean molecular weight increases and so does the luminosity. As a consequence the star evolves to the blue side of the Hertzsprung-Russell diagram, and remains compact, contrary to normal evolution in which the surface cools down and the star expands (e.g. Brott et al. 2011; Szécsi et al. 2015).

This type of evolution may lead to rapidly rotating CO core, prior to supernova explosion. It is thus a good candidate to form progenitors of long-soft gamma-ray bursts (Yoon et al. 2006). The properties of some Wolf-Rayet stars in the Galaxy and the Magellanic Clouds may be compatible with quasi-homogeneous evolution (Martins et al. 2009; Bestenlehner et al. 2011; Martins et al. 2013). The preference for low metallicity of LGRB hosts (e.g. Palmerio et al. 2019) also argues in favour of this type of evolution.

The formation of binary black holes may require quasi-chemical evolution as claimed by Mandel & de Mink (2016). In the following we describe the effects of binarity on stellar evolution and come back to this scenario.

6 Binarity

The presence of a companion can affect significantly the evolution of a massive star, provided the companion is close enough. There are two main categories of effects at play: tides and mass transfer. The former trigger energy exchange and modification of the internal structure (Zahn 1989; Mathis & Remus 2013). This can lead to spin-up or spin-down of the stars, and ultimately to synchronization of the stellar and orbital periods (Zahn & Bouchet 1989). The transport of angular momentum and chemical species due to rotation is thus affected. Mass transfer has the same effects as mass loss through winds, but can be more efficient. It does not depend (in principle) on metallicity and is accompanied by transfer of chemicals and angular momentum. Parameters governing mass transfer (efficiency, geometry) are poorly known, leading to uncertainties on its effects. Both tidal and mass transfer effects depend on the orbital parameters (stellar mass ratio, separation, eccentricity). The evolution of binary systems is thus even more complex than that of single stars.

de Mink & Belczynski (2015) performed a systematic study of the effects of various binary parameters on the merger rate of black hole-black hole systems. Their conclusion is that this rate is actually dominated by uncertainties on the mass function, rather than on specific binary parameters.

The formation of compact objects binary systems like those leading to mergers detected by the LIGO-VIRGO collaborations is classicaly explained by a phase of common-envelope evolution (Postnov & Yungelson 2014). This is briefly summarized on the left side of Fig. 1. After the primary has exploded as supernova the secondary expands, fills its Roche lobe and engulfs the compact object formed from the primary. During the common envelope phase, the envelope is ejected, leading to a system in which the secondary core subsequently explode as supernova. A double compact object system is formed. This channel assumes that the successive supernova events do not disrupt the system, and that during the common-envelope phase the compact object does not merge with the secondary's core. The common-envelope phase is required to shrink the orbit by dynamical friction.

To overcome the latter possibility, Mandel & de Mink (2016) have considered the possibility that chemically homogeneous evolution is followed by the binary's components (see also Song et al. 2016). The rationale for this scenario is that tidal interaction may spin-up stars sufficiently to encounter the conditions for homogeneous evolution, even if the initial rotational velocity of the individual components was not sufficient. The stars thus remain compact and avoid the common envelope phase, leading to a higher probability to remain bound until the double compact object phase. This is illustrated on the right side of Fig. 1. Another advantage of this channel is that much less mass is lost from the system (since there is no mass transfer). Consequently, remnants of higher masses are expected. The major uncertainty of this model lies in the conditions required to produce chemically homogeneous evolution. The internal rotation profile and its modificationby transport mechanisms during stellar evolution seem to be a key parameter (Brott et al. 2011; Song et al. 2016; Cui et al. 2018; Song et al. 2018). Song et al. (2016) predict that chemically homogeneous evolution in binary systems is favoured at high metallicity, when stars are less compact than at lower metallicity and thus more prone to experience tidal effects.

According to Mandel & de Mink (2016) the binary scenario involving chemically homogeneous evolution predicts a maximum merger rate at a redshift of about 0.5 but basically no event at high redshift. Equal-mass systems are also favoured, contrary to the common-envelope scenario.

7 Conclusions

The evolution of single and binary massive stars is rather complex and depends on many parameters: rotation, mass loss, metallicity, binary parameters, mass transfer properties, not to mention magnetic field. In the case of single stars, lower metallicity favours higher masses for the stellar remnants. The range of masses constrained by the gravitational wave merger events is accounted for only by low metallicity single star evolutionary models. In the binary scenario involving chemically homogeneous evolution, higher metallicity seems to be favoured. In that respect, the identification of the host environments of gravitational wave events will likely bring constraints to the evolution of massive stars. The redshift distribution of compact objects mergers will also shed light on the evolution of massive binary systems.

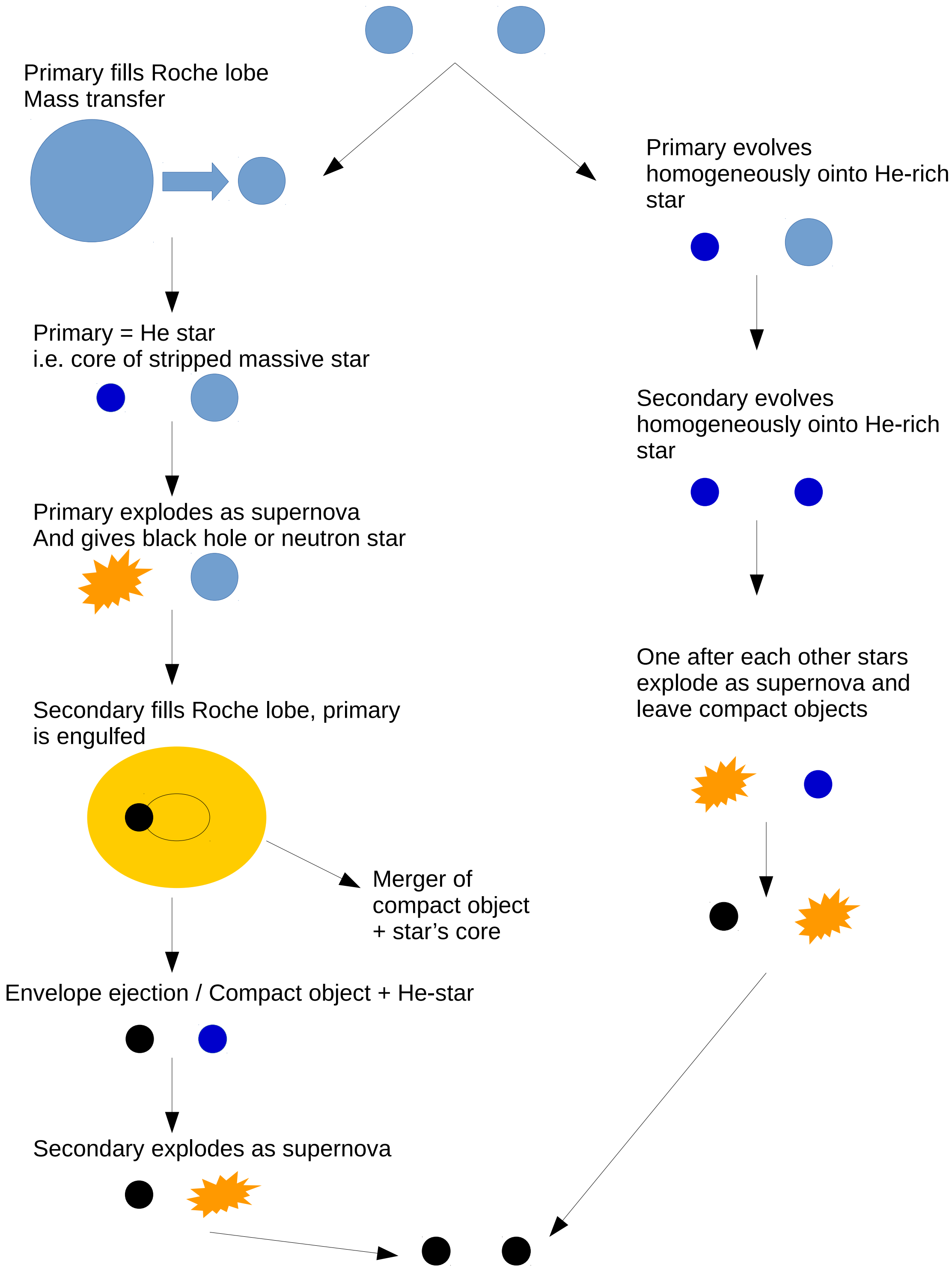

Fig. 1. Sketch of the two channels expected to form compact objects binaries. The left side is the "classical" channel involving a phase of common envelope evolution. The right side is the channel involving chemically homogeneous evolution. Adapted from Postnov & Yungelson (2014) and Mandel & de Mink (2016).

We thank the organizers for the invitation.

References

Abbott, B. P., Abbott, R., Abbott, T. D., et al. 2016, Phys. Rev. Lett., 116, 061102
Abbott, B. P., Abbott, R., Abbott, T. D., et al. 2017a, Phys. Rev. Lett., 118, 221101
Abbott, B. P., Abbott, R., Abbott, T. D., et al. 2017b, Phys. Rev. Lett., 119, 141101
Bestenlehner, J. M., Vink, J. S., Gräfener, G., et al. 2011, A&A, 530, L14
Brott, I., de Mink, S. E., Cantiello, M., et al. 2011, A&A, 530, A115
Castor, J. I., Abbott, D. C., & Klein, R. I. 1975, ApJ, 195, 157
Chiosi, C. & Maeder, A. 1986, ARA&A, 24, 329
Cui, Z., Wang, Z., Zhu, C., et al. 2018, PASP, 130, 084202
de Mink, S. E. & Belczynski, K. 2015, ApJ, 814, 58
Georgy, C. 2012, A&A, 538, L8
Groh, J. H., Ekström, S., Georgy, C., et al. 2019, A&A, 627, A24
Grunhut, J. H., Wade, G. A., Neiner, C., et al. 2017, MNRAS, 465, 2432
Keszthelyi, Z., Meynet, G., Georgy, C., et al. 2019, MNRAS, 485, 5843
Khargharia, J., Froning, C. S., & Robinson, E. L. 2010, ApJ, 716, 1105
Langer, N. 1992, A&A, 265, L17
Langer, N. 2012, ARA&A, 50, 107
Limongi, M. & Chieffi, A. 2018, ApJS, 237, 13
Maeder, A. 1987, A&A, 178, 159
Maeder, A. & Meynet, G. 2000, ARA&A, 38, 143
Mandel, I. & de Mink, S. E. 2016, MNRAS, 458, 2634
Martins, F., Depagne, E., Russeil, D., & Mahy, L. 2013, A&A, 554, A23
Martins, F., Hillier, D. J., Bouret, J. C., et al. 2009, A&A, 495, 257
Mathis, S. & Remus, F. 2013, in Lecture Notes in Physics, Berlin Springer Verlag, Vol. 857, Lecture Notes in Physics, Berlin Springer Verlag, ed. J.-P. Rozelot & C. . Neiner, 111–147
Mauron, N. & Josselin, E. 2011, A&A, 526, A156
Mokiem, M. R., de Koter, A., Vink, J. S., et al. 2007, A&A, 473, 603
Orosz, J. A., McClintock, J. E., Aufdenberg, J. P., et al. 2011, ApJ, 742, 84
Palmerio, J. T., Vergani, S. D., Salvaterra, R., et al. 2019, A&A, 623, A26
Postnov, K. A. & Yungelson, L. R. 2014, Living Reviews in Relativity, 17, 3
Renzo, M., Ott, C. D., Shore, S. N., & de Mink, S. E. 2017, A&A, 603, A118
Song, H. F., Meynet, G., Maeder, A., Ekström, S., & Eggenberger, P. 2016, A&A, 585, A120
Song, H. F., Meynet, G., Maeder, A., et al. 2018, A&A, 609, A3
Szécsi, D., Langer, N., Yoon, S.-C., et al. 2015, A&A, 581, A15
Vink, J. S., de Koter, A., & Lamers, H. J. G. L. M. 2001, A&A, 369, 574
Yoon, S.-C., Langer, N., & Norman, C. 2006, A&A, 460, 199
Zahn, J.-P. 1989, A&A, 220, 112
Zahn, J.-P. & Bouchet, L. 1989, A&A, 223, 112

Session 13

Gaia: astrométrie, photométrie et alertes pour l'étude du système solaire

SF2A 2019
P. Di Matteo, O. Creevey, A. Crida, G. Kordopatis, J. Malzac, J.-B. Marquette, M. N'Diaye, O. Venot (eds)

ECLIPSE 2017: NEW RESULTS ON THE DYNAMICAL INNER-CORONA

S. Koutchmy[1], B. Filippov[2], J-M. Lecleire[1], N. Lefaudeux[1], J. Mouette[1], F. Sèvre[1], E. Tavabi[3], Ch. Viladrich[1] and Sh. Abdi[1,4,5]

Abstract.

The total solar eclipse of 21 Aug. 2017 was observed by our teams in excellent conditions for almost 1 hour (from Oregon at 17h12, Idaho 17h27, see Fig. 1, Wyoming 17h36 and Missouri, 18h12 U.T.). Excellent images were recorded in white-light (W-L), including a very high spatial-temporal resolution (HR) sequence covering faint dynamical phenomena related to an exceptionally slow CME that evolved over the E-limb. In addition:

i) The overall polarized K-corona, from linearly polarized images taken in 12 positions with a green filter, was analyzed, to be compared to the latest quantitative magnetic dynamical coronal modeling of the Mikic team (Mikić et al. 2018). The complex fine scale structure reflecting the magnetic field topology is analyzed using specially designed algorithms with suggestion of a more turbulent field in the outer corona above r= 2Rs.

ii) The more simple Polar- cap Regions are considered to compare the impressive fine- scale more linear W-L plumes with the EUV plumes simultaneously observed in the lower corona with the AIA filtergrams of the SDO mission; we integrate 60 successive AIA images taken with the 171, 193, 211 Å filters to improve the S/N ratio of EUV frames. The new view of dynamical polar plumes is illustrated at different temperature regimes, including a high temperature regime. Some evidence of fast propagating transverse waves is obtained by comparing deep spatially Fourier- filtered W-L images of plumes and jets separated by typically 1 min of time; amplitudes are larger for larger radial distances, suggesting that they reflect the propagation of alfvenic disturbances and possibly their dissipation.

iii) The most notable dynamic phenomenon is analyzed at the E- limb: it is a slow CME that shows a constant 250 km/s velocity from the LASCO (SoHO) observations. It is analyzed here in W-L with HR eclipse images and with images from the SECCHI EUV filtergrams of the STEREO mission and from the AIA of the SDO mission. Very small scale and faint moving and curved W-L features at r= 1.7 Rs, possibly owning to high disrupted loops, are analyzed for the 1st time with a 20 sec temporal resolution movie; falling back remnants of the erupted high latitude polar crown filament- prominence found at the feet of the CME are detected in W-L, well after the eruption. It is suggested that such processes are a component of the slow wind that is more easily demonstrated at time of this minimum corona using eclipse images in the r = 1.5 to 2 Rs region where instabilities grow and outwardly propagate.(Boulade et al. (1997) Tavabi et al. (2018))

Keywords: Total Solar Eclipse, Solar Corona, CME

References

Boulade, S., Delanné, C., Koutchmy, S., et al. 1997, in ESA Special Publication, Vol. 404, Fifth SOHO Workshop: The Corona and Solar Wind Near Minimum Activity, ed. A. Wilson, 217

Mikić, Z., Downs, C., Linker, J. A., et al. 2018, Nature Astronomy, 2, 913

Tavabi, E., Koutchmy, S., & Golub, L. 2018, ApJ, 866, 35

[1] Institut d'Astrophysique de Paris, CNRS/Sorbonne Université, Paris, France
[2] Pushkov Institute (IZMIRAN) of Russian Acad. Sc. Troitsk
[3] Physics Departement Payame Noor Univ. Tehran, I.R. of Iran
[4] Observatoire de Paris, Université PSL, Meudon, France
[5] Institut d'Astrophysique Spatiale, CNRS/Université Paris-Sud, Orsay, France

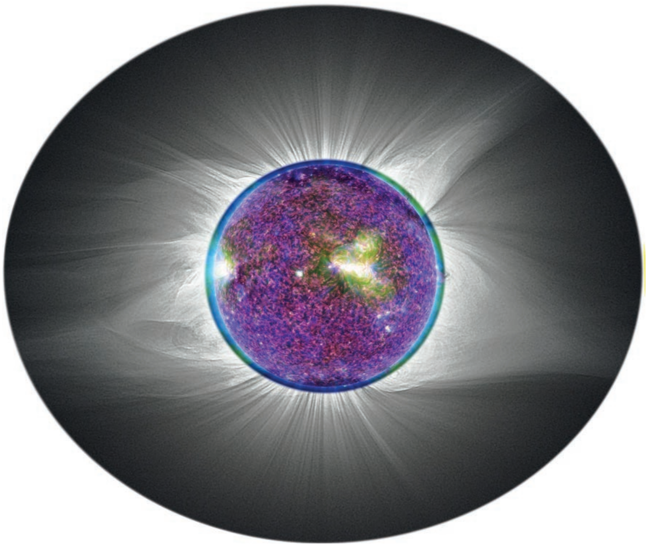

Fig. 1. Reconstructed image (J. Mouette) of the W-L corona observed in Idaho (17h 27 UT) using a sequence made for producing a full movie of the totality, with the AIA (SDO) composite coronal image put instead of the Moon image to show the correlated coronal line emissions just above the solar limb. Note the bright "point" at the South pole seen right above the limb and the strong long polar plume rising above in W-L, with several quasi- radial components.

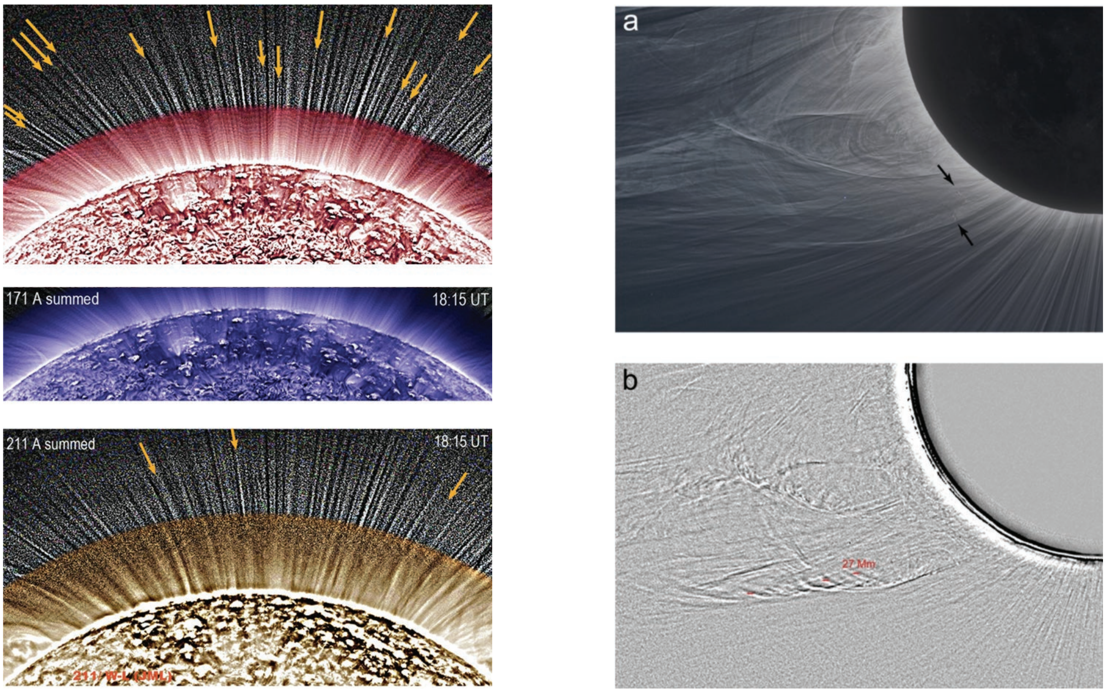

Fig. 2. Left: Analysis of the N- pole region with polar plumes and jets: search for correlations in position and intensities using the highly processed W-L image of J-M. Lecleire (18:12 UT) reflecting i) small- scale density variations (shown in the outer B&W parts of the composites); ii) temperature variations (indeed Emission Measures) as visualized using processed and integrated over 10 min filtergrams from AIA (SDO). Top parts are for 171 Å emissions at T° $< 1\,$MK and the bottom part, for 211 emissions with T° $> 2.5\,$MK. Arrows show AIA plumes and jets with obvious correlation with the W-L density structures. The analysis suggests a dominance of plumes of low coronal T° and also, of linear jets/plumes of high T° (best ex. is the central linear jet not existing in 171). For the most inner corona W-L parts see the image at left. **Right:** Analysis of the E- limb slow CME: a- the W-L K-corona image at 17:24 UT (Observation and processing by N. Lefaudeux) to show fine coronal structures everywhere; b- difference image of the corona with a time lapse of 2 min. Black arrows in a) point to eruptive prominence remnants observed as reddish features owing to $H\alpha$ and D3 emissions. Red arrows in b) indicate the displacement in 2 min of coronal structures giving 200 km/s in proper motion, in agreement with the values deduced after from the LASCO space- born (SoHO) movie analysis. (Nicolas Lefaudeux : https://hdr-astrophotography.com/high-resolution-2017-total-solar-eclipse/)

SF2A 2019
P. Di Matteo, O. Creevey, A. Crida, G. Kordopatis, J. Malzac, J.-B. Marquette, M. N'Diaye, O. Venot (eds)

TOTAL SOLAR ECLIPSE 2017 IN USA: DEEP CORONAL SPECTRA

S. Koutchmy [1], F. Baudin [2], Sh. Abdi [1,2,3], L. Golub [4] and F. Sèvre [1]

Abstract.
Total eclipses permit a deep analysis of both the inner and the outer parts of the solar corona using the Thomson scattered (inverse Compton effect on free electrons at millions degrees T°) continuum White-Light (W-L) radiations and the spectrum of forbidden emission lines from hot highly ionized ions of iron, nickel, argon, etc. Spectra are largely affected by the superposition of the solar light scattered and diffracted by the interplanetary dust particles orbiting the Sun at large distances but intercepted along the line of sight (los)(Koutchmy & Magnant 1973). Sometimes the parasitic light due to multiple scattering from the ground and from the Earth atmosphere should be removed using the light observed on the Moon image background. After sufficiently dispersing the W-L corona, the Fraunhofer (F) spectrum of the dust corona appears with its absorption (dark) lines of known equivalent widths and the continuum Thomson radiation can be extracted. The identified emission (bright) lines of ions with different degrees of ionization are studied to permit an evaluation of i/ relative abundances (compared to photospheric abundances), ii/ temperatures, iii/ non-thermal velocities and the resulting from the analysis of the departures from a Gaussian profile of net Doppler shifts after integration along the los.

60 spectra were obtained during the totality using a specially designed slit spectroscopic experiment for providing an accurate analysis of the most typical "broadly averaged" parts of the quasi-minimum of activity type corona. With the scanning +/- 3 solar radii long slit a .072 nm FWHM effective resolution was obtained in the range of 510 to 590 nm. The background sky was exceptionally clear during this US total eclipse of Aug. 21, 2017 as observed from our site in Idaho; spectra are without significant parasitic light on the Moon disk. The K+F continuum corona is well exposed up to at least 1 solar radius (Rs) from the limb and further out with a lower S/N ratio, showing several forbidden coronal emission lines. The F-corona can be measured even at the solar limb where its intensity reached near 6% of the K-corona intensity.

Streamers, active region enhancements and polar coronal holes (CHs) are well measured on each 1 sec exposure time coronal spectra see Fig. 1; the 2^{nd} contact showing the chromospheric and the most inner layers emission lines was observed with a fast sequence and exposure time 10 times shorter. New weak emission lines were also discovered and/or confirmed see Fig. 2 ; their identifications are proposed. The rarely observed high FIP ArX (Del Zanna & DeLuca 2018) line is recorded almost everywhere and a new nearby FeX line is well identified; the classical low FIP FeXIV and NiXIII lines are well recorded everywhere without over-exposure. For the 1st time hot lines are also measured at low levels inside the CH regions, at both poles. The radial variations of the corrected non-thermal turbulent velocities of the lines do not show a great departure from the average values. No significantly large Doppler shifts are seen nowhere in the inner and the middle corona although the whole corona is almost covered.(Contesse et al. 2004)

The corona is confirmed to be made of a mixing of hot and less hot components everywhere around the Sun, due to the yet unidentified magnetic origin heating processes reflected in our spectra and in the line profiles. Coronal density variations are well reflected by the K-corona continuum intensity variations the azimuthal and radial direction variations will permit the interpretation of the emission measures to be compared with the simultaneously obtained AIA images from the SDO space mission. The W-L images taken simultaneously shows a much better spatial resolution with images of bright background well known stars that permit to deduce an excellent absolute calibration needed to deduce the electron densities and to check our F-corona model, see 3.

Keywords: Total Solar Eclipse, Solar Corona, Forbidden coronal emission lines

[1] Institut d'Astrophysique de Paris, CNRS/Sorbonne Université, Paris, France
[2] Institut d'Astrophysique Spatiale, CNRS/Université Paris-Sud, Orsay, France
[3] Observatoire de Paris, Université PSL, Meudon, France
[4] Smithsonian Astrophysical Observatory, Cambridge MA, USA

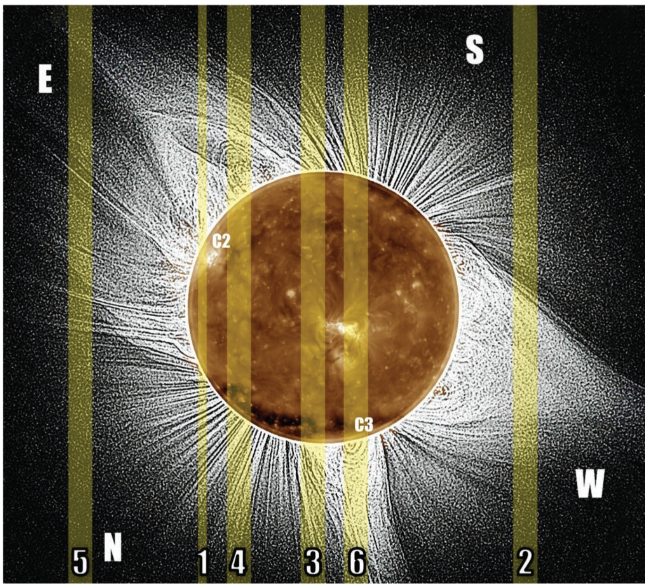

Fig. 1. W-L coronal structures obtained from a highly processed image by J. Mouette, combined with an AIA/SDO 19.4 nm simultaneous image inserted with a correct scaling. Yellow vertical bands show the region covered by the different positions of the entrance slit during the totality, including the scanning transverse to the slit due to the diurnal motion during the burst of 10 spectra taken at each successive position 2, 3, 4, 5 and 6. Position 1 was used to obtain fast spectra (0.1 s exposure time) in the region of the C2 contact. The orientations correspond to a reversed image of the corona seen in the sky on the entrance slit.

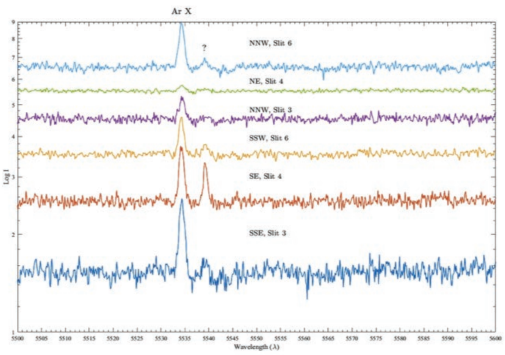

Fig. 2. Summed spectra showing the new line discovered near the predicted and confirmed line of the Ar X at 5534 Å. This line (5540 Å) would be attributed to Fe X or Fe XI (Mason & Nussbaumer 1977). Note the log scale of the intensities and the different positions (see Fig. 1) in the corona giving different intensities depending on the position. Spectra are corrected of the F-corona component.

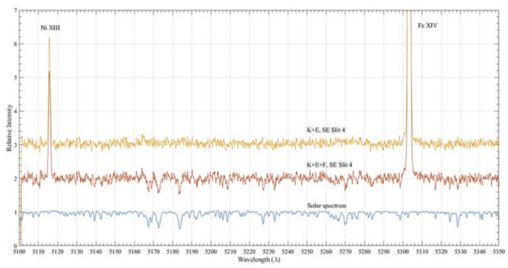

Fig. 3. Extracted deep spectra of the inner corona (slot position "4" see Fig. 1) showing the influence of the F component (contribution about 6 to 7% of the solar spectrum). Note the extended wings of the green line of Fe XIV (Non-Gaussianity).

References

Contesse, L., Koutchmy, S., & Viladrich, C. 2004, Annales Geophysicae, 22, 3055
Del Zanna, G. & DeLuca, E. E. 2018, ApJ, 852, 52
Koutchmy, S. & Magnant, F. 1973, ApJ, 186, 671
Mason, H. E. & Nussbaumer, H. 1977, A&A, 54, 547

SF2A 2019
P. Di Matteo, O. Creevey, A. Crida, G. Kordopatis, J. Malzac, J.-B. Marquette, M. N'Diaye, O. Venot (eds)

SOLAR WIND HEATING BY ALFVÉN WAVES: COMPRESSIBLE EFFECTS

V. Réville[1], M. Velli[1], A. Tenerani[1,2] and C. Shi[1]

Abstract. We study the heating produced by a compressible cascade in unidimensional solutions of the solar wind using the numerical setup described in Réville et al. (2018). Alfvén waves are injected from the photosphere and may be, depending on their frequency and amplitude, unstable to parametric decay, in which case they create a compressible cascade of forward and inward Elsässer variables. Dissipation at small scales then create an extended heat deposition in the corona, which accelerates the wind in addition to the wave pressure. This process can provide enough heating to fully sustain a solar wind solution.

Keywords: Solar wind, Alfvén Waves, Turbulence

1 Introduction

Alfvén wave turbulence is believed to be a fundamental part of the acceleration and heating of the solar wind. Particularly in the fast solar wind, spherically polarized Alfvénic perturbations are observed, $i.e$ where the total magnetic field remains constant and density perturbations are weak (Belcher 1971; Tu & Marsch 1995). These perturbations nonetheless form a well developed spectrum with frequencies ranging to $10^{-6} - 10^{-1}$Hz (Bruno & Carbone 2013). If created throughout the solar wind expansion, the observed Kolmogorov-like spectrum at inertial scales must involve non-linear interactions of counter-propagating waves (Velli et al. 1989). The usual picture for incompressible turbulence goes as follows: outward going waves launched from the Sun reflects on large scale gradients of the wind velocity and Alfvén speed to create a inward component. A cascade from large scales to smaller and smaller scales occurs creating a self-similar distribution of energy and eventually leading to dissipation at kinetic scales (through for instance wave-particle interactions).

However, recent studies have shown that the fully incompressible picture may fail in the details as the heating rate obtained is not enough to fully power the solar wind. Very high resolution simulations and spectral approaches show that the incompressible perpendicular cascade heating rate is less than what phenomenological models (see e.g. Dmitruk et al. 2002) have predicted (van Ballegooijen & Asgari-Targhi 2016; Shoda et al. 2018a; Verdini et al. 2019). Moreover, Alfvén waves are known to be unstable to the parametric decay instability (PDI), when $\beta < 1$, for typical chromospheric frequencies, even considering the solar wind expansion (Tenerani & Velli 2017; Shoda et al. 2018b; Réville et al. 2018). The PDI is able to create an inward wave component through a coupling with a compressible forward sound wave and a turbulence spectrum much faster than the incompressible reflection on large scale gradients (Réville et al. 2018). Hence, this process could play an important in coronal heating as a trigger for the creation of a large scale inward component.

In this work, we look at the heating produced in simulations akin the one presented in Réville et al. (2018), where Alfvén waves are launched from the photosphere into a fully compressible MHD simulations of a flux tube. When the system is unstable to PDI, counter-propagating Alfvén and acoustic wave interact to create a turbulent cascade and heat the solution through dissipation at small scales. With enough energy flux at the photosphere, a solar wind solution can be powered only by compressible wave heating.

2 Onset of the parametric decay instability

Parametric decay is a low beta instability, where a forward Alfvén decays into a forward sound wave and an inward Alfvén wave (Galeev & Oraevskii 1963; Derby 1978; Goldstein 1978). In Réville et al. (2018), we used

[1] UCLA Earth, Planetary and Space Sciences Department, Los Angeles, CA, USA
[2] Department of Physics, University of Texas, Austin, TX, USA

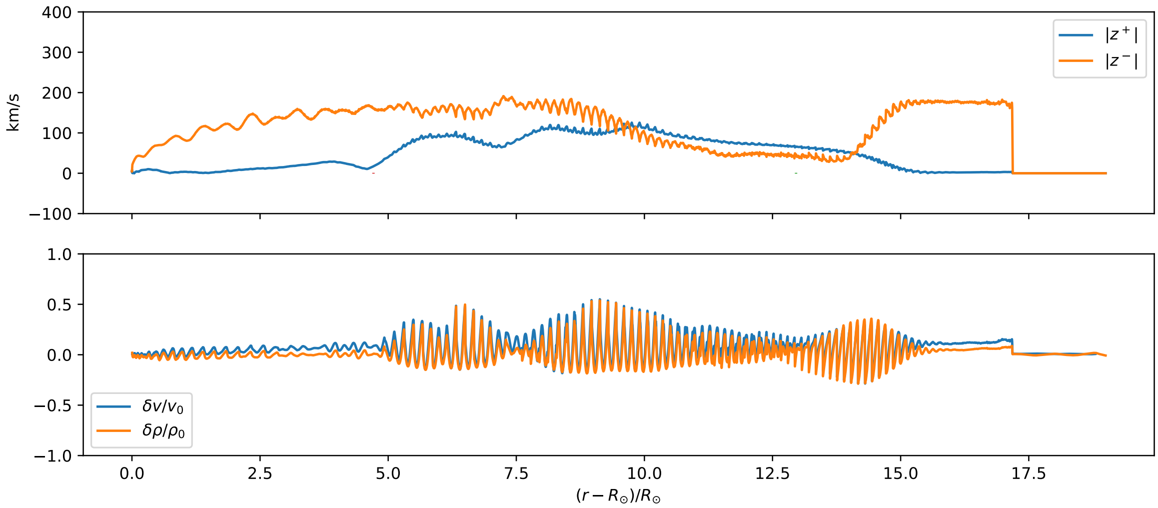

Fig. 1. Profiles of the Alfvénic perturbations ($z^{\pm}$) in module and of the density and velocity perturbation associated with the forward sound wave and the parametric decay. The wave front has not yet crossed the whole domain and is located at $17R_\odot$, while the instability has been triggered below $15R_\odot$.

ideal MHD simulations of a single flux tube, starting at the photosphere to show that the parametric decay instability is triggered for Alfvén waves with typical chromospheric periods (between 50 and 1000 seconds) and amplitudes of a few km/s. In Figure 1, we show the onset phase of the instability where the forward Alfvén wave (here z^-) is propagating and suddenly decays, creating a inward wave (z^+) and a forward sound wave here displayed with correlated density and velocity perturbations. We recall the definition of the Elsässer variables used here:

$$\mathbf{z}^{\pm} = \delta\mathbf{v}_\perp \pm \delta\mathbf{b}_\perp/\sqrt{4\pi\rho}. \tag{2.1}$$

The perturbations $\delta\rho = \rho - \rho_0$ and $\delta v = v - v_\rho$ are built with respect to the initial equilibrium profile without transverse wave (see Réville et al. 2018, for more details). We force the forward Alfvén wave from the lower boundary as:

$$\mathbf{z}^- = 2|\delta v|(\cos(\omega_0 t)\mathbf{e}_\theta + \sin(\omega_0 t)\mathbf{e}_\varphi), \tag{2.2}$$

where $\omega_0 = 2\pi f_0$ is the input pulsation.

Among the main results of Réville et al. (2018) is the demonstration that PDI is a fast process to create a well developed turbulent spectrum of both z^+ and z^- from monochromatic and non-monochromatic inputs. In Figure 2, we show the magnetic perturbations spectra computed at $10R_\odot$ for a stable and an unstable case. In these two cases a monochromatic wave is launched from the photosphere with an amplitude of $\delta v = z^-_\odot/2 = 2$ km/s. In the left panel the wave has a frequency of 10^{-3} Hz, in the right panel the input frequency is 5×10^{-3} Hz. Hence for this amplitude, the threshold for the onset of the parametric decay instability is located between these two input frequencies. For the stable case (left panel), the forward stays mostly monochromatic, while a small inward component is created through reflection on the large scale gradients. Velli et al. (1991) have indeed shown that reflection is only efficient for waves with periods larger than a few hours. In the unstable case, a significant inward wave is developed through the instability (which acts as a trigger), and a well developed spectrum is created for both component, with a clear inverse cascade exciting lower frequencies.

When the wave is unstable, the power spectra show decays roughly proportional to f^{-2}. This is related to the compressible nature of the processes occurring. Shocks are created and provide a way to dissipate energy and heat the solar wind.

3 Compressible cascade and heating of the solar wind

The pioneering work of Suzuki & Inutsuka (2005, 2006) has shown that in a similar configuration, a unidimensional solar wind solution could be self-sustained injecting Alfvén waves at the photosphere. Inside such a compressible flux tube configurations, the cascade is by definition only parallel to the magnetic field and as such omits everything happening into the perpendicular plane. Yet the numerical dissipation, associated with

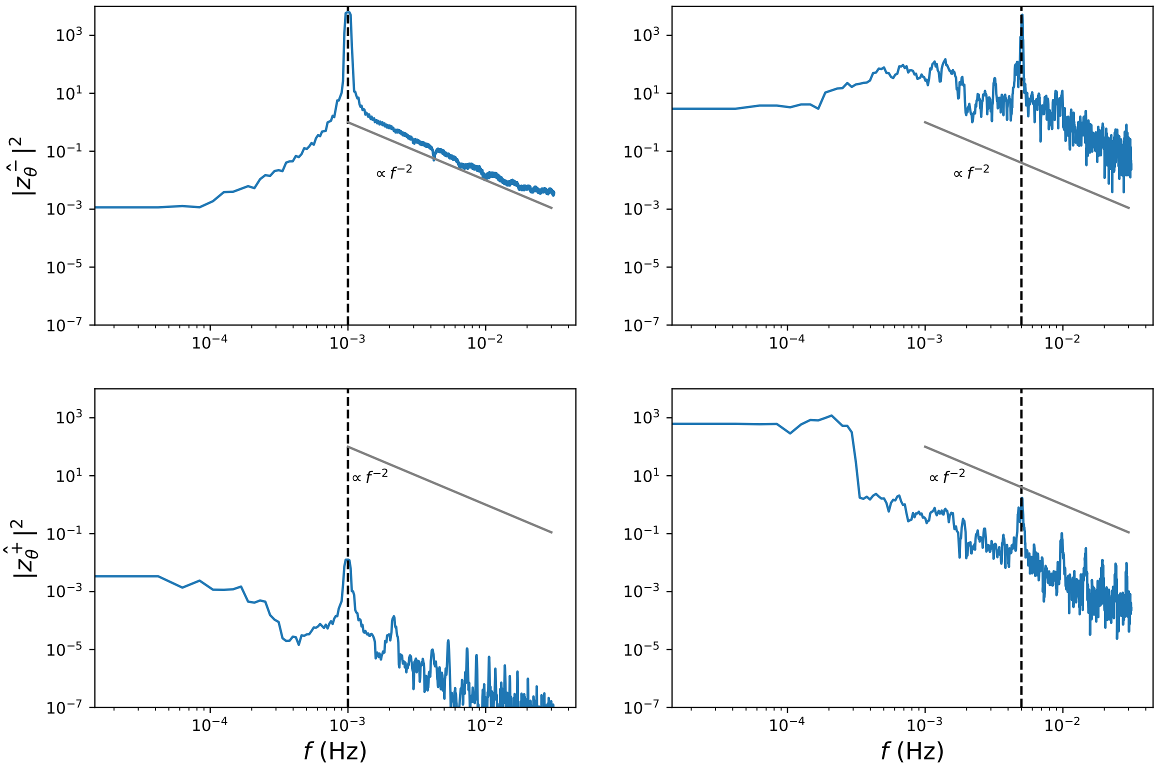

Fig. 2. Power spectra of the forward (z^+) and inward (z^-) Elsässer variable at $10R_\odot$ after three Alfvén crossing time. In the left panel the wave is launched at a frequency of 10^{-3} Hz and is therefore stable. In the right panel, the input frequency is 5×10^{-3} Hz and the instability grows, creating a inward wave of the order of the forward wave. Both component show sign of a forward and inverse cascade with slopes close to f^{-2}.

compressible effects at small scales (shocks or rotational discontinuities) in 1D, was proven to be roughly equivalent to later multi-D turbulent studies (Matsumoto & Suzuki 2012). In a recent study, Shoda et al. (2018b) compared the heating provided by shocks and compressible effects and the heating provided by a phenomenological turbulent dissipation. The study finds that depending on the correlation length scale of the turbulence the contribution of both effects vary. Compressible effects are however always very important for generating a large scale inward component and the (inverse) cascade.

In Figure 3, we compare several simulations of a solar wind flux tube with different wave inputs. In order to compare our results consistently, we fix the energy input at the photosphere. The energy flux is the combination of an ad-hoc flux that decays exponentially (over a scaleheight of $1R_\odot$, see Réville et al. 2018) and of the Alfvén wave flux. We set the total photospheric flux

$$F_{\rm tot} = F_{h,\odot} + F_{A,\odot} = F_{h,\odot} + \rho_\odot v_{A,\odot}\delta v^2 = 1.5 \times 10^5 {\rm erg.s^{-1}cm^{-2}}. \tag{3.1}$$

The four cases are then split as follows: the first case (plain black curve) is the simulation without waves, the heating being only provided through the ad-hoc function. Then, two mixed cases are presented, with the energy flux split half and half between the ad-hoc function and the Alfvén wave flux (blue and orange curves). This requires $\delta v = 3.75$ km/s with the base Alfvén speed $v_{A\odot} = 3.27$ km/s and $\rho_\odot = 1.67 \times 10^{-12}$ g/cm^3. We use two different input frequencies, on both side of the parametric decay instability threshold for this amplitude. Finally the last case (red curve) is only powered through waves with $\delta v = 5.25$ km/s, and a frequency of 10^{-3} Hz, allowing a rapid onset of the PDI. In dashed black, we also show the result of the simulation without wave and with half the ad-hoc heating $F_h, \odot = 7.5 \times 10^4 {\rm erg.s^{-1}cm^{-2}}$.

To compute the heating rate Q_h, we have assumed a quasi steady-state on the energy equation and wrote

$$\langle Q_h \rangle = \langle v_r \frac{\partial \rho e}{\partial r} + (\rho e + p)\nabla \cdot v_r - Q_r - Q_c \rangle, \tag{3.2}$$

where $\rho e = p/(\gamma - 1)$ and Q_r and Q_c are the radiative and the thermal conduction losses respectively.

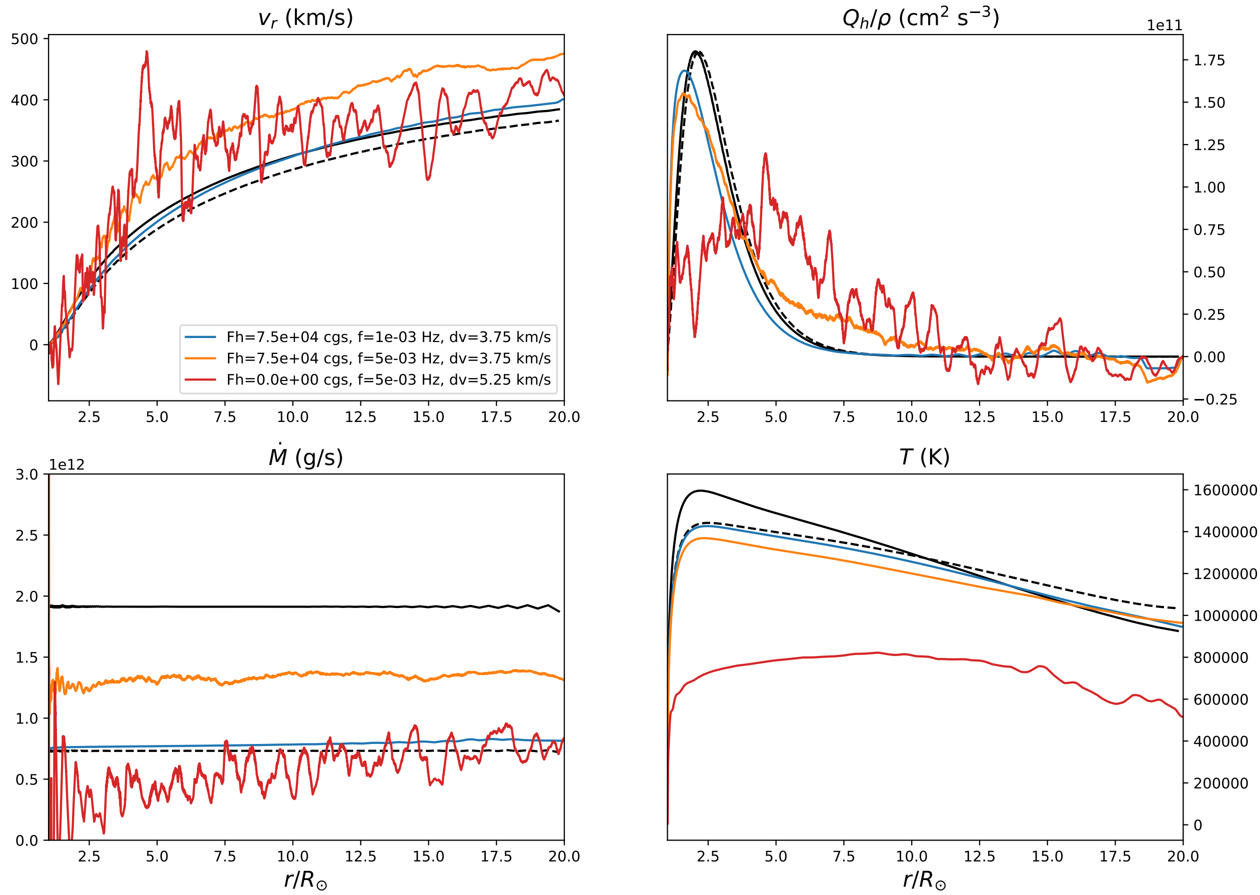

Fig. 3. Averaged speeds, heating per unit mass, mass loss and temperature for different cases in quasi steady states. The plain black curve correspond to the reference case without wave injection and $F_h = 1.5 \times 10^5$erg.s^{-1}cm^{-2}. The blue curve is a mixed case with a Alfvén wave input at stable frequencies. It notably shows the influence of wave pressure on the wind acceleration. Finally, the orange and red curve are cases where PDI develops and creates a cascade leading to heat deposition. In the red case, the heating of the corona is only maintained by the wave energy dissipation.

In Figure 3, we first notice that all our simulations are able to produce a supersonic wind. All speeds are comparable, between 300 km/s and 500 km/s at $20R_\odot$. The mass losses however are quite different. For the black curve, the heating is provided with the ad-hoc function only, and with the largest amplitude, which yields the highest mass loss. The blue curve, for which the wave is stable, yields about half the mass loss. This seems to mean that without wave heating, or for a given heat deposition profile, the mass loss is a roughly linear function of the input heat flux. Moreover, for the same amplitude of the wave but a higher frequency, the PDI is triggered and additional heating is deposited between 2 and 5 solar radii in comparison with the stable case (see the blue and orange curve in Figure 3). Because part of the energy is deposited below the sonic point, it helps lift material and indeed yields a higher mass loss. This additional heat also provide an additional acceleration of the wind. Note that the temperature of the unstable case is slightly lower as the energy is advected by the faster wind.

In the last, red, case, the heat is only provided by the compressible cascade triggered by PDI. The heating peak is more extended in the corona than in the other cases, and leads to a lower mass loss. The mass loss is approximately half the one of the no wave case, and hence is equivalent to the two other mixed cases. The temperature is however much lower, around 7.5×10^5 K at the maximum and is as such not a good proxy to determine the energy output of the wind.

4 Conclusion

In this proceeding, we have computed the heating generated by the non-linear interaction of counter-propagating Alfvén waves in a compressible simulation of a solar wind flux tube. As shown in Réville et al. (2018), the parametric decay is a very efficient way to produce inward Alfvén waves and to trigger a cascade that eventually provides heating in the solar wind solution. Although a full MHD turbulence cannot be developed in such unidimensional simulations, we can power a solar wind solution with waves only, provided that they are unstable to the parametric decay instability. Wave heating is in general more extended than the ad-hoc function, at least assuming a heating scale height of $1R_\odot$, and as such produce a faster, more tenuous wind for a given photospheric energy flux. Future works will investigate how this heating profile compares with other models of MHD turbulence including a full perpendicular cascade.

References

Belcher, J. W. 1971, ApJ, 168, 509

Bruno, R. & Carbone, V. 2013, Living Reviews in Solar Physics, 10, 2

Derby, Jr., N. F. 1978, ApJ, 224, 1013

Dmitruk, P., Matthaeus, W. H., Milano, L. J., et al. 2002, ApJ, 575, 571

Galeev, A. A. & Oraevskii, V. N. 1963, Soviet Physics Doklady, 7, 988

Goldstein, M. L. 1978, ApJ, 219, 700

Matsumoto, T. & Suzuki, T. K. 2012, ApJ, 749, 8

Réville, V., Tenerani, A., & Velli, M. 2018, ApJ, 866, 38

Shoda, M., Yokoyama, T., & Suzuki, T. K. 2018a, ApJ, 853, 190

Shoda, M., Yokoyama, T., & Suzuki, T. K. 2018b, ArXiv e-prints

Suzuki, T. K. & Inutsuka, S.-i. 2005, ApJ, 632, L49

Suzuki, T. K. & Inutsuka, S.-I. 2006, Journal of Geophysical Research (Space Physics), 111, 6101

Tenerani, A. & Velli, M. 2017, ApJ, 843, 26

Tu, C.-Y. & Marsch, E. 1995, Space Sci. Rev., 73, 1

van Ballegooijen, A. A. & Asgari-Targhi, M. 2016, ApJ, 821, 106

Velli, M., Grappin, R., & Mangeney, A. 1989, Physical Review Letters, 63, 1807

Velli, M., Grappin, R., & Mangeney, A. 1991, Geophysical and Astrophysical Fluid Dynamics, 62, 101

Verdini, A., Grappin, R., & Montagud-Camps, V. 2019, Sol. Phys., 294, 65

SF2A 2019
P. Di Matteo, O. Creevey, A. Crida, G. Kordopatis, J. Malzac, J.-B. Marquette, M. N'Diaye, O. Venot (eds)

MARS IONOSPHERE VARIABILITY

B. Sánchez-Cano[1], M. Lester[1], P.-L. Blelly[2], O. Witasse[3] and H. Opgenoorth[1,4]

Abstract. The ionosphere of Mars is an integral part of the atmosphere that links the lower atmosphere with the solar wind. Understanding the ionospheric response to internal and external forcing is essential to determining the whole atmosphere variability, as the ionospheric and atmospheric systems are strongly coupled. This proceeding focus on two main aspects of this variability, one from inside the planet and another one from outside. Starting from internal sources, it focuses on how lower atmosphere cycles, such as the seasonal carbon dioxide cycle, have a seasonal influence on the upper atmosphere, especially notable at Northern hemisphere spring when the Northern polar cap sublimates. Then, moving to external sources, it focuses on the effect of electron precipitation from a large space weather event in the Martian atmosphere. This event is important because it created lower-ionosphere absorption layers at ∼60-80 km on both the day and night-sides that strongly affect instrument performances for several days. This work is based on observations from Mars Express, Mars Reconnaissance Orbiter, and Mars Atmosphere and Volatile EvolutioN (MAVEN) missions, as well as on numerical ionospheric modelling.

Keywords: Mars, ionosphere, variability, space weather, atmospheric cycles

1 Introduction

The ionosphere of Mars is an integral part of the atmosphere that links the lower atmosphere with the solar wind. The different regions of the Martian atmosphere are fundamentally interconnected, behaving as a unique and coherent system (e.g. Sánchez-Cano et al. 2019b, and references there). This means that the whole atmospheric structure reacts together to external and internal sources of variability, and therefore, plays an important role in the volatile escape processes that have dehydrated Mars over the Solar System's history, holding clues to the evolution of Mars' climate. Understanding the ionospheric response to internal and external forcing is essential to determining the whole atmospheric variability.

The dayside ionosphere of Mars consists of two layers, formed mainly by solar photoionization, and located on average at ∼135 km and ∼110 km altitude, respectively, with typical electron densities of $10^{11}m^{-3}$ and $10^{10}m^{-3}$, respectively. Sometimes other layers above and below the two main ones occur. The phenomena that produce these extra layers are diverse, such as for example, topside extra layers can be associated with local current sheets in the upper Martian ionosphere (related in turn to Kelvin-Helmholtz instabilities) (e.g. Kopf et al. 2017), and bottomside extra layers can be associated with particle precipitation such as meteor or solar energetic particles showers (e.g. Sánchez-Cano et al. 2019a). Since the Sun is the main source of ionization, any variations in the solar radiation produce large variability in the electron density, both in time and in space. In this sense, the solar cycle is the factor that plays the most important long-term role and dominates the ionospheric variability at Mars (e.g. Sánchez-Cano et al. 2015, 2016). However, additional ionospheric variability can be caused by many other factors. External factors such as solar flares, coronal mass ejections (CMEs) or corotating interaction regions (CIR), among others contribute significantly to that. In addition, internal factors such as seasons, gravity waves, atmospheric tides, dust storms, or crustal magnetic fields are also major driving sources that modulate the behaviour of the ionosphere.

[1] University of Leicester, Physics and Astronomy Department, Leicester, UK
[2] Institut de Recherche en Astrophysique et Planétologie, Toulouse, France
[3] European Space Agency, ESTEC, Noordwijk, The Netherlands
[4] Department of Physics, Umeå University, Umea, Sweden

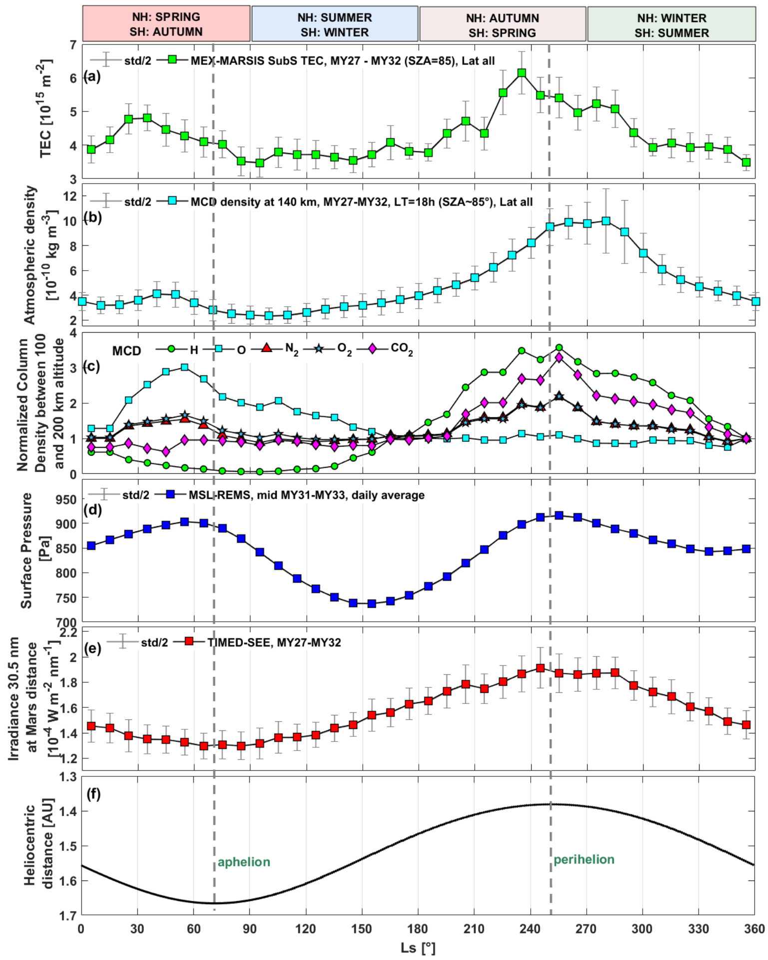

Fig. 1. Annual Martian ionospheric observations. Figure from Sánchez-Cano et al. (2018). (a) MEX MARSIS-TEC of MY 27-32 averaged over all latitudes and for SZA = 85°. (b) Averaged atmospheric density obtained at 140 km for MY27-32 and all latitudes. (c) Temporal variability of the averaged column density between 100 and 200 km and latitude for the major neutral species and normalized to their relevant value at Ls = 355°. (d) MSL-REMS surface pressure average of mid MY 31-33. (e) TIMED-SEE solar irradiance for the 30.5-nm wavelength extrapolated to Mars' distance from MY 27 to 32. (f) Mars' heliocentric distance.

This proceeding focuses on two main aspects of this Martian ionospheric variability that have been recently discovered. First, we focus on the annual role of lower atmosphere cycles, such as the seasonal carbon dioxide cycle, on the upper atmosphere. Then, we focus on the strong and sudden effects of electron precipitation from a large space weather event in the Martian atmosphere. The objective is to give a coherent view of the reaction of the Martian upper atmosphere under two major drivers of variability.

2 Internal Sources of Variability

Mars lower atmospheric variability is known to affect the upper atmosphere through different aspects, such as planetary and tidal waves that move from the low atmosphere to the thermosphere, gravity waves, northern polar warming of the lower thermosphere near the perihelion/winter solstice, seasonal thermal expansion/contraction of the Mars lower atmosphere or the expansion of the entire atmosphere during dust storms (e.g. Sánchez-Cano et al. 2018, and references there). There are other processes that occur in the lower-middle atmosphere, such as atmospheric cycles of different species, which can propagate upward to the upper atmosphere, e.g. the carbon dioxide, water vapour and ozone cycles. These cycles are a direct consequence of the carbon dioxide condensation that every winter occurs at high latitudes and the subsequent sublimation during the spring and summer seasons. The carbon dioxide cycle induces a large semiannual variation in the daily averaged surface pressure all over the planet (e.g. Forget et al. 2007).

The European Mars Express mission, in orbit about Mars since December 2004, has the capability of routinely measure the total electron content (TEC) of the Martian atmosphere with its Mars Advanced Radar for Subsurface and Ionosphere Sounding (MARSIS). The TEC is an important parameter for monitoring the state of the ionosphere, and it is defined as the number of free electrons that are contained in an atmospheric column. Sánchez-Cano et al. (2018) recently showed that, in fact, the TEC is not only a good tracer of the state of the thermosphere but seems to be a reliable indicator of the state of the lower-upper atmospheric coupling.

Figure 1 shows different ionospheric-atmospheric observations from several Martian Years (MY) that have been averaged together and plotted with respect to the solar longitude (Ls), which can be used as a proxy for the MY. For more details of the data processing analysis, please refer to Sánchez-Cano et al. (2018).The entire TEC data set from MEX and for a narrow solar zenith angle interval (SZA=85°) and local time 18h is shown in panel a). In addition, other atmospheric parameters are including, such as the averaged atmospheric density at 140 km obtained from the Mars Climate Database (MCD, version 5.3) in panel b), and the global averaged thermospheric column density profile between 100 and 200 km altitude for each of the major species in Mars' thermosphere in panel c). To complete the figure, the daily averaged surface pressure (as a proxy for the atmospheric mass column variation) measured by the Mars Science Laboratory (MSL) mission for MY mid-31 to -33 is included in panel d), the solar irradiance measured in Earth's orbit and extrapolated to Mars in panel e), and the Mars' heliocentric distance in panel f). In general, the TEC observations follow pretty well the irradiance profile, which in turn is directly proportional to the heliocentric distance. This is somehow expected because the solar flux is the dominant ionization source in Mars' atmosphere. Therefore, both the TEC and the irradiance are maxima near Mars' perihelion and minima near aphelion. However, the TEC profile shows a secondary maximum between Ls = 25° and 75°, which is not related to the annual irradiance variation. This secondary peak occurs during the northern spring season and before aphelion, and nearly coincides with an increasing trend in both the thermospheric density and the surface pressure. This indicates that the neutral atmosphere is the dominant force for this TEC rise. The main TEC peak (Ls = 220°-290°) is also formed while there is an increase in the thermospheric density and surface pressure (during spring in the southern hemisphere), which is related to a larger abundance of CO_2, H, O_2, and N_2 with respect to their annual trends. However, it is difficult to evaluate whether there is an effect of the neutral atmosphere because the irradiance flux is clearly the dominant ionization factor and masks any other secondary ionospheric variability sources.

Focusing on the chemistry of the first peak (Ls = 25°-75°), oxygen and nitrogen (O, O_2 and N_2) species have their largest abundances in the annual profile at this time of the year, indicating that these three components may have a more prominent role during this period. The increase of these neutral species results in more N_2^+, O_2^+, O^+, and NO^+ ions during this time of the year, and therefore, in a significant TEC increase. This thermospheric variability is likely linked to atmospheric variability produced by cycles at lower atmospheric levels. Our results seem to be supported by the MEX-SPICAM observations of the lower atmosphere as thermospheric O_2 column densities have similar increases both in latitude and Ls with respect to O_2 column density observations of the low-middle atmosphere (Montmessin et al. 2017), being maximum in the early northern and southern springs in both hemispheres. As a consequence, the double peak in the TEC as a function of a MY seems consistent with a larger increase in the column density of oxygen species, caused by the semiannual atmospheric cycles produced by the sublimation of the polar caps.

3 External Sources of Variability

In addition to internal sources, external drivers like space weather are other important sources of very intense and short variability that affect the entire Martian system. Its study is very important because they enhance atmospheric escape, currently a major topic in the research at Mars. In counterpoint with Earth, the solar wind directly interacts with the Martian upper atmosphere because of the absence of a global inner magnetic field, creating many different effects on the structure of the ionosphere (e.g. Ramírez-Nicolás et al. 2016; Andrews et al. 2016; Sánchez-Cano et al. 2017). This interaction is also dependent on the solar cycle as the ionosphere becomes more magnetized during periods of low solar activity because less ionization is produced (Sánchez-Cano et al. 2017).

Despite the numerous effects that space weather events produce on Mars' ionosphere, very little is known about the ionization processes that occur at low altitude from solar energetic particles (SEP) that precipitate into the atmosphere during these events. The recent study of Sánchez-Cano et al. (2019a) has shown that in fact particle precipitation greatly enhances the low ionosphere (at ∼90 km, below the main peak) at all local times, and locations over the planet (and not only over crustal magnetic fields). In turn, these low ionospheric layers are able to absorb radar signals because they are formed in regions where the atmosphere is denser and collisions between electrons and neutral species (mainly CO_2 at Mars) are not negligible. As consequence, instruments that operate in high frequency (HF) do not work for many days (as long as particle precipitation persists), which has fatal consequences for both science and exploration purposes. However, we do not know the exact nature and formation of these layers as no mission has been able to measure them.

Thanks to the co-joined study of radar measurements from Mars Express (MARSIS radar) and Mars Reconnaissance Orbiter (SHARAD radar), together with analysis of the high energetic particles recorded by the Mars Atmosphere and Volatile EvolutioN (MAVEN) mission, Sánchez-Cano et al. (2019a) has shown for the first time that high energetic electrons are mainly the responsible for these blackouts, contrary to the proton events that occur at Earth. Figure 2 shows this proof based on a large space weather event that hit Mars in September 2017, where X-rays (0.1-7 nm) and differential flux spectra from solar energetic particles (electrons and ions) from MAVEN are plotted in the three first panels, together with the timing when both MARSIS and SHARAD radars were blackout (i.e., the radars were transmitting but not receiving signals). For this event,

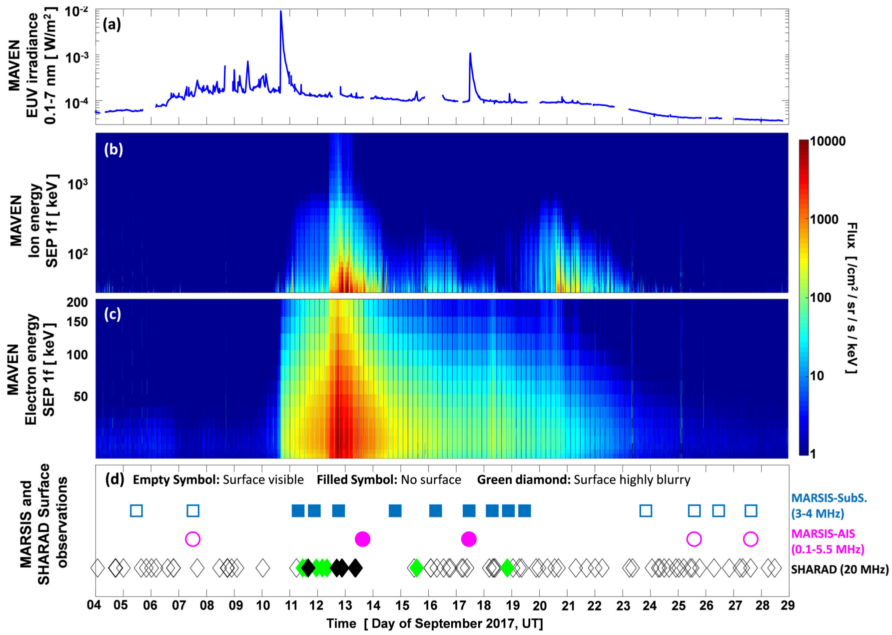

Fig. 2. Mars radio blackouts caused by a large space weather event. Figure from Sánchez-Cano et al. (2019a) a) MAVEN-EUV irradiance observations of wavelength 0.1-7 nm. (b) MAVEN-SEP ion differential flux spectra.(c) MAVEN-SEP electron differential flux spectra. (d) Radio blackouts. Each symbol denotes when MARSIS and SHARAD were in operation. Empty symbols designate the cases when the surface was observed, and filled symbols when was not observed. The exceptions are green diamonds that indicate the times when SHARAD observed a highly blurry surface.

the Active Region (AR) 12673 at the western limb of the solar disk emitted a X8.2-class flare on 10 September 2017 and also released a powerful coronal mass ejection (CME). The SEP electrons (20-200 keV) started to arrive at Mars ~3 hr later, and the ions (20 keV-6 MeV) ~6 hr later. Both SEP electrons and ions show a sharp flux increase on 12 September 2017 (reddish colors) when the CME shock passed over Mars. After that, SEP electrons gradually decreased over 13 days until 23 September, but with a small enhancement on 18 September caused by another solar flare. In contrast, SEP ions sharply decreased on 14 September when the CME completed its passage past Mars. After that, the ion flux was very low until 20 September.

As can be seen in Figure 2, the blackout lasted at least ~10 days for the MARSIS radar, but the blackout lasted only ~3 days for SHARAD because radio absorption processes are frequency-dependent and SHARAD carrier frequency is much larger than the MARSIS one (20 and 1.8-5 MHz, respectively). Since MARSIS blackouts occurred also while the ion SEP flux was very low but the electron SEP flux was still enhanced, we can conclude that precipitating electrons, rather than ions, were responsible for the creation of a lower ionospheric layer all over the planet that absorbed the radar signals.

Based on Figure 2, Sánchez-Cano et al. (2019a) performed a numerical simulation with the Mars version of the numerical/physical Institut de Recherche en Astrophysique et Planétologie (IRAP) plasmasphere-ionosphere model (IPIM) (Marchaudon & Blelly 2015). The simulation was performed for the conditions of the MARSIS observations and with a flux of downward precipitating electrons at 500 km as input. Results from the Sánchez-Cano et al. (2019a) simulation shows that indeed a layer of density of $\sim 10^{10}$ m^{-3} peaking at 90 km was formed, mainly composed of O_2^+ with a lesser contribution of NO^+. Such a layer had its peak absorption at 70 km and was the responsible for the blackout observed in September 2017 at Mars.

4 Conclusions

The Martian space environment is a complex system with simultaneous downward and upward couplings, which still need much work to be understood. The ionosphere is in the end the mediating layer between the lower and middle atmosphere and the solar wind, where most of the atmospheric coupling processes occur. Therefore, driven variability from outside and inside the planet need to be totally understood in order to have a broader control of the system dynamics as a whole. This proceeding has focused on two of these drivers, that have been recently discovered and have important roles in the Martian plasma and atmospheric systems, such as the seasonal effect of lower-middle atmospheric cycle on the upper atmosphere, and the effect of electron precipitation from space weather events on the lower atmosphere of Mars. In both cases, a good characterization of the ionosphere is clearly necessary.

B.S.-C., and M.L. acknowledge support through STFC grant ST/S000429/1. B.S.-C also acknowledges support from the ESA-ESTEC Faculty, and from the Société Francaise d'Astronomie et d'Astrophysique (SF2A) to attend the annual meeting. All data can be downloaded from the ESA PSA archive.

References

Andrews, D. J., Barabash, S., Edberg, N. J. T., et al. 2016, Journal of Geophysical Research: Space Physics, 121, 3139

Forget, F., Spiga, A., Dolla, B., et al. 2007, Journal of Geophysical Research: Planets, 112

Kopf, A. J., Gurnett, D. A., DiBraccio, G. A., Morgan, D. D., & Halekas, J. S. 2017, Journal of Geophysical Research: Space Physics, 122, 5579

Marchaudon, A. & Blelly, P.-L. 2015, Journal of Geophysical Research: Space Physics, 120, 5728

Montmessin, F., Korablev, O., Lefèvre, F., et al. 2017, Icarus, 297, 195

Ramírez-Nicolás, M., Sánchez-Cano, B., Witasse, O., et al. 2016, Planetary and Space Science, 126, 49

Sánchez-Cano, B., Blelly, P.-L., Lester, M., et al. 2019a, Journal of Geophysical Research: Space Physics, 124, 4556

Sánchez-Cano, B., Hall, B. E. S., Lester, M., et al. 2017, Journal of Geophysical Research: Space Physics, 122, 6611

Sánchez-Cano, B., Lester, M., Andrews, D. J., et al. 2019b, arXiv e-prints, arXiv:1908.05497

Sánchez-Cano, B., Lester, M., Witasse, O., et al. 2018, Journal of Geophysical Research: Planets, 123, 1746

Sánchez-Cano, B., Lester, M., Witasse, O., et al. 2015, Journal of Geophysical Research: Space Physics, 120, 10,913

Sánchez-Cano, B., Lester, M., Witasse, O., et al. 2016, Journal of Geophysical Research: Space Physics, 121, 2547

SF2A 2019
P. Di Matteo, O. Creevey, A. Crida, G. Kordopatis, J. Malzac, J.-B. Marquette, M. N'Diaye, O. Venot (eds)

MAGNETIC HIDE & SEEK IN THE KEPLER-78 SYSTEM: WIND MODELLING AND STAR-PLANET MAGNETIC INTERACTIONS

A. Strugarek[1], J. Ahuir[1], A. S. Brun[1], J.F. Donati[2], C. Moutou[2] and V. Réville[2]

Abstract. Observational evidences for star-planet magnetic interactions (SPMIs) in compact exosystems have been looked for in the past decades. Their theoretical description has significantly progressed in the past years. Nevertheless, their complete description requires a detailed knowledge of the host star, and in particular its coronal magnetic and plasma characteristics. We explore here the robustness of SPMIs models with respect to the basic coronal properties commonly assumed for cool stars, in the particular context of the Kepler-78 system. We show that the amplitude of SPMIs is constrained only within one to two orders of magnitude as of today. However, the temporal signature of SPMIs can be robustly predicted from models, paving the road toward their future detection in compact exosystems through dedicated observational strategies.

Keywords: planet-star interactions – stars: wind, outflows – magnetohydrodynamics (MHD)

1 Introduction

Planets on short-period orbit around cool stars interact strongly with their host in a variety of physical processes: gravitational (tidal) interaction (Mathis 2017), stellar irradiation (e.g. Daley-Yates & Stevens 2019), and star-planet magnetic interaction (SPMI, Strugarek 2018). The latter occurs when the planet orbital path is within the Alfvén surface of the star, which is the characteristic surface at which the accelerating wind of the star reaches the local Alfvén speed and becomes super-Alfvénic.

Recently, Cauley et al. (2019) showed evidences of tracers of SPMIs in the CaII K line for four observed compact exosystems. Among the compact exosystems, ultra-short period planets (Winn et al. 2018) such as Kepler-78b are particularly favorable candidates to exhibit traces of SPMIs. Nevertheless, the unambiguous detection of SPMIs requires *a priori* a detailed knowledge of the star and the planet. Indeed, the temporal traces of SPMIs are primarily controlled by the magnetic field amplitude and topology of the hosting star (Strugarek et al. 2015). Their amplitude is in turn controlled by both the magnetic properties of the star and the magnetic (or lack of thereof) properties of the orbiting planet (Saur et al. 2013; Strugarek 2016).

The ultra-short period system Kepler-78 was recently modelled in 3D by Strugarek et al. (2019). The corona and wind of Kepler-78 was modelled under the magnetohydrodynamic (MHD) framework to assess the properties of SPMIs in this system. Their modelling made use of an observed magnetic map of Kepler-78 for this period (Moutou et al. 2016). It allows detailed estimates of the SPMI properties along the planetary orbit. They found that SPMIs could carry a sufficient amount of energy to be detectable with present telescope capabilities. This study shed the light on the importance of considering the 3D magnetic topology of the star to accurately predict and identify the complex temporal signture of SPMIs in compact exosystems.

In this proceeding we explore the robustness of the results of Strugarek et al. (2019) with respect to their wind modelling assumptions. In particular, the detection of stellar wind and the associated mass loss rate is extremely challenging (e.g. Wood et al. 2005). As a result, modelling the wind of a given star requires today some assumption on, *e.g.* the density and temperature at the base of their corona. Even though some aspects of these plasma characteristics can be constrained through observations (for in-depth discussions, see Ahuir et al. 2019), we still have today quite some liberty in setting these parameters. We henceforth discuss these modelling choices for Kepler-78 in Section 2, and their implication for our estimates of SPMIs in Section 3. We finally conclude our study in Section 4.

[1] AIM, CEA, CNRS, Université Paris-Saclay, Université Paris Diderot, Sorbonne Paris Cité, F-91191 Gif-sur-Yvette, France
[2] Université de Toulouse / CNRS-INSU, IRAP / UMR 5277, F-31400 Toulouse, France

2 Modelling the environment of Kepler-78

2.1 A 1D+3D stellar wind model

We model the corona and wind of Kepler-78 following a 1D+3D approach developed in Strugarek et al. (2019). The model is based on a 1D polytropic Parker-like solution stellar wind. It assumes a given density and temperature at the base of the corona (the chosen values are discussed in Section 2.2) to compute a spherically-symmetric wind solution for Kepler-78.

A purely spherically-symmetric solution is nevertheless not precise enough to properly model SPMIs (Strugarek et al. 2015). We consequently leverage our knowledge of the global magnetic topology of Kepler-78 deduced from Zeeman-Doppler Imaging by Moutou et al. (2016). We then extrapolate the coronal magnetic field with a potential field source-surface technique (e.g. see Schrijver & DeRosa 2003). Réville et al. (2015) developed an estimate of the optimal source-surface radius $R_{\rm ss}^{\rm opt}$ that allows to reproduce as close a possible the coronal topology obtained from a fully 3D MHD modelling. In the case of Kepler-78 we find $R_{\rm ss}^{\rm opt} \in [4.8R_\star, 7.R\star]$ in the parameter space we explored (see Section 2.2).

Combined with the spherically-symmetric wind solution, this coupled 1D-3D approach was shown to reproduce satisfyingly the low corona of fully 3D MHD models for Kepler-78 (Strugarek et al. 2019). We note here that this technique breaks close to the source-surface and beyond. Henceforth, we use it here to model Kepler-78 low corona at the planetary orbit ($R_{\rm orb} < R_{\rm ss}$), but it cannot *a priori* be generically used for any close-in planet.

2.2 Coronal parameters for Kepler-78

Star Kepler-78	
$T_{\rm eff}$ $[K]$	5089 ± 50
$M_\star$ $[M_\odot]$	0.81 ± 0.08
$R_\star$ $[R_\odot]$	0.74 +0.1,-0.08
$P_{\rm rot}$ [days]	12.5
Planet Kepler-78b	
R_p $[R_\oplus]$	1.16 +0.19,-0.14
M_p $[M_\oplus]$	1.86 ± 0.25
$P_{\rm orb}$ [days]	0.36
Semi-major axis $[R_\star]$	2.66

Table 1. Global properties of the Kepler-78 system. Values were taken from Sanchis-Ojeda et al. (2013); Pepe et al. (2013); Howard et al. (2013).

The basic stellar and planetary parameters of the Kepler-78 system are given in Table 1. Modelling the wind and corona of a distant star generally further requires to estimate the density and temperature at the base of the corona. These two quantities are not easily constrained through observations (*e.g.* Johnstone & Güdel 2015), and a choice has generally to be made. Holzwarth & Jardine (2007) proposed that the coronal proton density and temperature should scale with the stellar rotation rate $\Omega_\star$ of the star such that

$$n_c \simeq n_\odot \left(\frac{\Omega_\star}{\Omega_\odot}\right)^{0.6} \quad \text{and} \quad T_c \simeq T_\odot \left(\frac{\Omega_\star}{\Omega_\odot}\right)^{0.1}, \tag{2.1}$$

which leads to $n_c = 1.6 \times 10^8$ cm^{-3} and $T_c = 1.63$ MK for Kepler-78.

This approach was followed in Strugarek et al. (2019) to model the corona of Kepler-78. Nevertheless, assuming a given mass-loss rate for Kepler-78, this choice of coronal density is not unique. For instance, Johnstone & Güdel (2015) derived a scaling law for the closed loop coronal temperature based on the X-ray luminosity of the star that can be written as

$$T_{\rm cor} = T_{\rm cor}^\odot \left(\frac{M_\star}{M_\odot}\right)^{-0.42} \left(\frac{\Omega_\star}{\Omega_\odot}\right)^{0.52}, \tag{2.2}$$

where in their notation $T_{\rm cor}^{\odot} = 0.94$ MK. This relationship gives $T_{\rm cor} = 1.56$ MK for Kepler-78. If one assumes that the closed coronal loop temperature gives a satisfying proxy for the open field lines regions, this estimate gives a slightly cooler corona than the Holzwarth & Jardine (2007) prescription 2.1. Nevertheless, with this approach the coronal density still needs to be prescribed.

In this proceeding we aim to assess the impact of our wind modelling on our ability to estimate and predict the characteristics of star-planet magnetic interactions. As a result, we explore a somewhat broad range of coronal temperatures $T_c \in [1.15, 5]$ MK for Kepler-78. We then follow two strategies:

- We maintain the density constant to the canonical value $n_c = 1.6 \times 10^8$ cm^{-3} chosen in Strugarek et al. (2019).

- We maintain the mass loss rate to the canonical value of 2.88×10^{-14} $M_\odot$/yr chosen in Strugarek et al. (2019). The coronal density n_c is chosen to maintain a constant mass loss rate with the approximate mass-loss equation (Lamers & Cassinelli 1999)

$$\dot{M} \propto M_\star^2 n_c T_c^{-3/2} \left[1 - \frac{T_{\rm min,\odot}}{T_c} \frac{M_\star}{M_\odot} \frac{R_\odot}{R_\star}\right]^{\frac{5-3\gamma}{2(\gamma-1)}} , \tag{2.3}$$

  where γ the polytropic index of the modelled wind, and $T_{\rm min,\odot} \simeq 11(1 - 1/\gamma)$ (for more details, see Ahuir et al. 2019).

We illustrate the resulting wind speed profiles in Fig. 1 for three representative cases in each approach. On the left panel we show the profiles for a constant mass-loss rate. As the coronal density varies by 2 orders of magnitude, the wind speed at the average Alfvén radius r_A (dots in Fig. 1) varies by about a factor of 3. The average Alfvén radius itself does not change significantly because we fixed the mass loss rate to a constant value here.

In the right panel of Fig. 1, the base coronal density n_c is held constant. Similarly, the wind speed at the average Alfvén radius varies by factor 2 to 3 while the mass-loss rate varies by 2 orders of magnitude. In this case the average Alfvén radius changes significantly from $6R_\star$ to $11.6R_\star$ when the mass loss is multiplied by 100.

It is worth to note that the planet is found to orbit within the sub-Alfvénic region of the wind (*i.e.* below r_A) in all cases. This does not necessarily imply that the interaction between the planet and the stellar wind is sub-Alfvénic, because the orbital motion of the planet can be super-Alfvénic itself (this will be made clear in Section 3, the interested reader will find more in depth-discussion on this aspect in Vidotto et al. 2010; Strugarek 2018).

For all the scenarii, the plasma characteristics change in the corona and hence change as well at the planetary orbit. We can thus expect that these different choices of modelling will have an impact on our estimates of star-planet magnetic interactions. We now quantify this impact in Section 3.

3 Impact of the stellar wind modelling on star-planet magnetic interaction properties

SPMIs are first determined by the *relative* Alfvénic Mach number which is defined as

$$M_a = \frac{|\mathbf{v}_w - \mathbf{v}_{\rm kep}|}{v_a} , \tag{3.1}$$

where $\mathbf{v}_w$ is the stellar wind speed, $\mathbf{v}_{\rm kep}$ is the keplerian speed of the orbiting planet, and v_a is the Alfvén speed in the stellar wind. M_a is shown as a function of the orbital phase $\phi_{\rm orb}$ and the coronal parameters in the top left panel of Fig. 2. The left axis labels the coronal density n_c, and the right axis the coronal temperature T_c. We show here the results for the constant-$\dot{M}_\star$ parameter-space exploration. We see that M_a varies by a factor 5 as the coronal density is increased by an order of magnitude. Interestingly, for high densities M_a becomes larger than 1 around $\phi_{\rm orb} \simeq 0.25$ while the average Alfvén radius remains around 8 $R_\star$ (see left panel in Fig. 1). This means that the relative keplerian motion becomes super-Alfvénic, because the local alfvén speed of the wind decreases significantly as the coronal density increases.

The energy available for SPMIs then depends on the stellar wind Poynting flux density

$$S_w = |\mathbf{v}_w - \mathbf{v}_{\rm kep}| \frac{B_w^2}{\mu_0} \sin(\Theta_0) \tag{3.2}$$

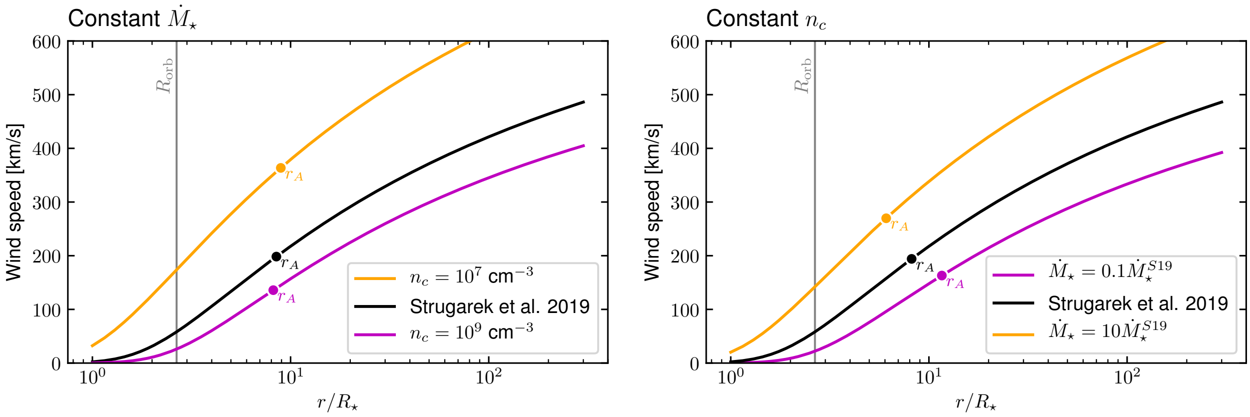

Fig. 1. Radial velocity profile of a polytropic Parker-like wind. On the left, the density and temperature at the base of the corona are changed while the mass loss-rate is held constant. On the right, the density at the base of the corona is held fixed, while the coronal temperature is altered (and thus the wind mass loss rate changes). The average Alfvén radius is labelled by the coloured dot on each curve. The black lines represent the modelling choices made in Strugarek et al. (2019). Two other modelling choices are illustrated in orange and magenta on each panel.

intercepted by the planet, where B_w is the local magnetic field amplitude and Θ_0 is the inclination of the wind magnetic field with respect to the orbital motion. The Poynting flux density is shown on the top right panel of Fig. 2. The available Poynting flux density shows no dependancy on the chosen coronal density. This is due to the fact that we chose to explore the parameter-space with a fixed mass-loss, which leads to a fixed open-flux and hence a fixed magnetic structure in the corona as the plasma parameters are varied (see Réville et al. 2015).

Thanks to our SPMI modelling we can estimate the minimal magnetic dipole $B_{\rm min}$ Kepler-78b needs to sustain a magnetosphere (bottom left panel in Fig. 2), as well as the Poynting flux $\mathcal{P}$ channeled by the interaction from the planetary orbit towards Kepler-78 (bottom right panel, for the full formulation of $\mathcal{P}$ see Strugarek 2017). We see that both quantities vary by one to two orders of magnitude as the coronal density increases by three orders of magnitude.

The wind modelling choices –namely the prescribed density and temperature at the base of the corona of Kepler-78– heavily influences the estimated *amplitude* of SPMI. Nonetheless, the relative variations of $B_{\rm min}$ and $\mathcal{P}$ along the planetary orbit remain remarkably similar as the parameter space is explored (albeit their absolute value differ). These two aspects were also found in the second parameter-space exploration (constant n_c), we did not illustrate them here for the sake of brevity.

4 Conclusions

In this proceeding we have studied the influence of wind-modelling parameters on estimates of star-planet magnetic interactions. In particular, we have focused our discussion on the choice of plasma density and temperature at the base of the corona. We have illustrated here this dependancy in the context of Kepler-78. This system has been modeled in details in Strugarek et al. (2019) with one possible choice of plasma parameters at the base of the stellar corona. We have explored a large parameter-space following two strategies: keeping a constant density at the base of the corona (and thus exploring five orders of magnitude in mass-loss rate), and keeping a constant wind mass-loss rate (and thus exploring four orders of magnitude in coronal density).

On one hand, we found that the important plasma parameters for SPMIs are very sensitive to the wind modelling choice. This leads to a typical uncertainty of one to two orders of magnitude in the power channeled by the SPMI in systems such as Kepler-78. On the other hand, the temporal variability of the signal is much less sensitive to the wind modelling choices as long as the overall coronal magnetic topology is known. This was already hinted in Strugarek et al. (2019) and opens up promising research avenues to properly characterize observable signatures of SPMIs in compact systems (see Cauley et al. 2019, for a recent attempt in this direction).

A.S. and A.S.B. acknowledge funding from CNES-PLATO and CNES-Space Weather grants. A.S. and A.S.B. acknowledge funding from the Programme National Soleil-Terre (PNST). A.S. acknowledges funding from the Programme National de Planétologie

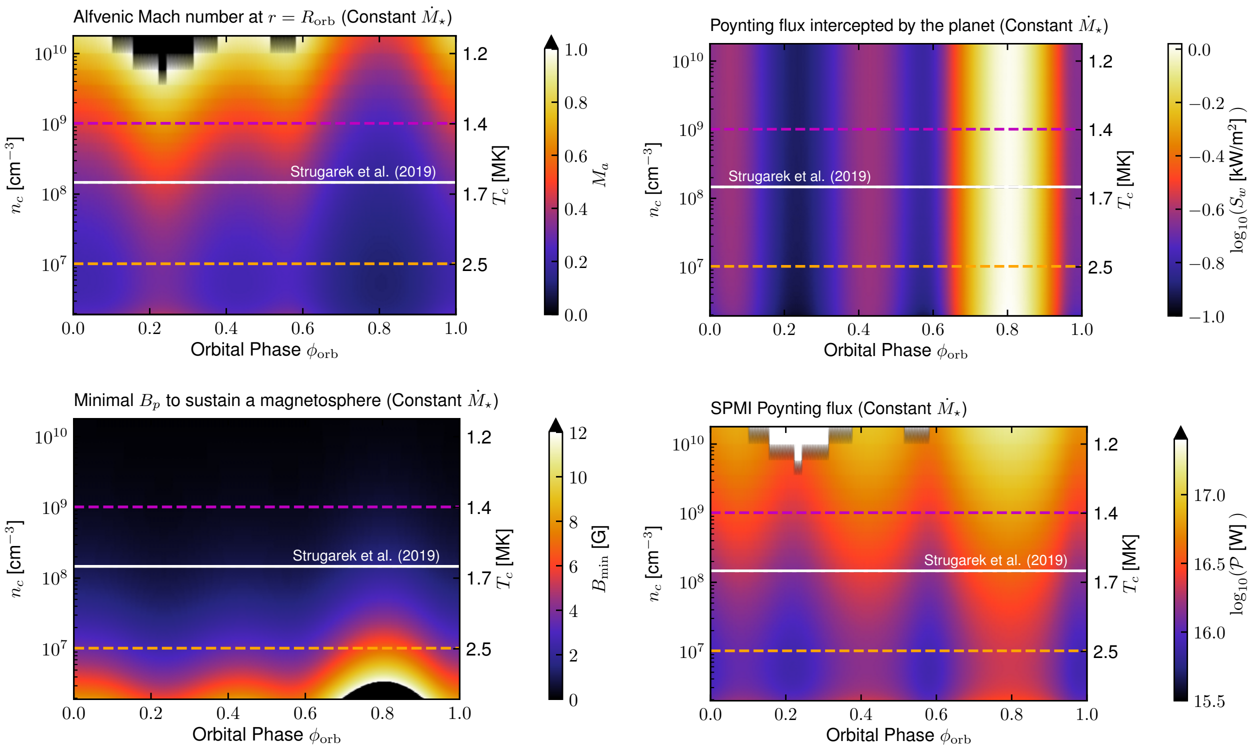

Fig. 2. SPMI characteristics for varying density and temperature at the base of the corona of Kepler-78, at constant $\dot{M}_\star$. From top left to bottom right, we show the relative Alfvénic Mach number M_a, the Poynting flux density intercepted by the Kepler-78b, the minimal dipolar field $B_{\rm min}$ of Kepler-78b required to sustain a magnetosphere, and the Poynting flux $\mathcal{P}$ channeled by the SPMI toward Kepler-78. Each panel follows the same layout: the x-axis represents the orbital phase $\phi_{\rm orb}$ of Kepler-78b, the left y-axis the assumed coronal density, and the right y-axis the assumed coronal temperature. The horizontal white line correspond to the wind model of Strugarek et al. (2019). The dashed orange and magneta lines correspond to the orange and magenta lines in Fig. 1 ($n_c = 10^7$ cm^{-3} and 10^9 cm^{-3}, respectively).

(PNP). J.F.D. acknowledges funding from the European Research Council (ERC) under the H2020 research & innovation program (grant agreement #740651 NewWorlds).

References

Ahuir, J., Brun, A. S., & Strugarek, A. 2019, Submitt. to A&A

Cauley, P. W., Shkolnik, E. L., Llama, J., & Lanza, A. F. 2019, Nat. Astron., 1

Daley-Yates, S. & Stevens, I. R. 2019, MNRAS, 483, 2600

Holzwarth, V. & Jardine, M. 2007, Astron. Astrophys., 463, 11

Howard, A. W., Sanchis-Ojeda, R., Marcy, G. W., et al. 2013, Nature, 503, 381

Johnstone, C. P. & Güdel, M. 2015, Astron. Astrophys., 578, A129

Lamers, H. J. G. L. M. & Cassinelli, J. P. 1999, Introduction to Stellar Winds

Mathis, S. 2017, in Handb. Exopl. (Springer International Publishing), 1–30

Moutou, C., Donati, J.-F., Lin, D., Laine, R. O., & Hatzes, A. 2016, Mon. Not. R. Astron. Soc., 459, 1993

Pepe, F., Cameron, A. C., Latham, D. W., et al. 2013, Nature, 503, 377

Réville, V., Brun, A. S., Strugarek, A., et al. 2015, Astrophys. J., 814, 99

Sanchis-Ojeda, R., Rappaport, S., Winn, J. N., et al. 2013, Astrophys. J., 774, 54

Saur, J., Grambusch, T., Duling, S., Neubauer, F. M., & Simon, S. 2013, Astron. Astrophys., 552, A119

Schrijver, C. J. & DeRosa, M. L. 2003, Sol. Phys., 212, 165

Strugarek, A. 2016, Astrophys. J., 833, 140

Strugarek, A. 2017, EWASS Spec. Sess. 4 Star-planet Interact.

Strugarek, A. 2018, in Handb. Exopl. (Cham: Springer International Publishing), 1833–1855
Strugarek, A., Brun, A. S., Donati, J.-F., Moutou, C., & Réville, V. 2019, Astrophys. J., 881, 136
Strugarek, A., Brun, A. S., Matt, S. P., & Réville, V. 2015, Astrophys. J., 815, 111
Vidotto, A. A., Jardine, M., & Helling, C. 2010, Astrophys. J. Lett., 722, L168
Winn, J. N., Sanchis-Ojeda, R., & Rappaport, S. 2018, New Astron. Rev., 83, 37
Wood, B. E., Müller, H.-R., Zank, G. P., Linsky, J. L., & Redfield, S. 2005, Astrophys. J., 628, L143

SF2A 2019
P. Di Matteo, O. Creevey, A. Crida, G. Kordopatis, J. Malzac, J.-B. Marquette, M. N'Diaye, O. Venot (eds)

MEASURING RELATIVE ABUNDANCES IN THE SOLAR CORONA WITH OPTIMIZED LINEAR COMBINATIONS OF SPECTRAL LINES

N. Zambrana Prado[1] and E. Buchlin[1]

Abstract. Elemental abundances in some coronal structures differ significantly from photospheric abundances, with a dependence on the First Ionization Potential (FIP) of the element. Measuring these FIP-dependent abundance biases is important for coronal and heliospheric physics. We aim at building a method for optimal determination of FIP biases in the corona from spectroscopic observations, in a way that is in practice independent from Differential Emission Measure (DEM) inversions. We optimize linear combinations of spectroscopic lines of low-FIP and high-FIP elements so that the ratio of the corresponding radiances yields the relative FIP bias with a good accuracy, for any DEM in a small set of typical DEMs. These optimized linear combinations of lines allow to retrieve a test FIP bias map with a good accuracy, for all DEMs in the map. The method provides a convenient, fast, and accurate way of computing relative FIP bias maps. It could be used to optimize the use of existing observations and the design of new observations and instruments.

Keywords: techniques: spectroscopic – Sun: abundances – Sun: corona – Sun: UV radiation

1 Introduction

Accurate plasma diagnostics of the Solar Wind (SW) and corona as well as precise modeling of the solar magnetic field and plasma flows in the interplanetary medium are crucial when trying to determine the source regions of the SW (Peleikis et al. 2017). Indeed, the chemical composition of coronal plasma (the abundances of the different elements) may vary from structure to structure (Baker et al. 2013; Guennou et al. 2015; Saba 1995) and in time (Feldman & Widing 2003), but it becomes fixed at low heights in the corona. Determining the composition of the different structures would then allow us to pinpoint the source of the SW by comparing and linking remote sensing abundance measurements to in situ analysis. These variations are linked to the FIP or First Ionization Potential (Saba 1995) of the different elements. Coronal abundances, which are derived from UV spectroscopy, are difficult to measure accurately (Schmelz et al. 2012). FIP biases (the ratio of the coronal vs the photospheric abundance of a given element) are usually calculated either from the line ratio of two spectral lines (hereafter 2LR method) or following Differential Emission Measure (DEM) analysis; both these methods can yield different results when used on the same data. Using DEM inversions yields the most accurate results, but DEMs are difficult to estimate accurately (Craig & Brown 1976; Judge et al. 1997; Landi et al. 2012; Testa et al. 2012; Guennou et al. 2012), especially when trying to design an automated method.

We present a method that aims at providing an optimal determination of the abundance biases in the corona from a spectroscopic observation, even when the DEM cannot be precisely determined.

2 The Linear Combination Ratio (LCR) method for FIP bias determination

To determine the FIP bias, let us consider two spectroscopic lines, emitted by ions of two different elements, X_{LF} that has a low FIP ($< 10\,\mathrm{eV}$) and X_{HF} that has a high FIP. We will denote the radiance of the low FIP element's considered spectral line I_{LF} and I_{HF} that of the high FIP element line. Assuming that abundances

[1] Institut d'Astrophysique Spatiale, CNRS/Université Paris-Sud, Université Paris-Saclay, batiment 121, Université Paris-Sud, 91405 Orsay cedex, France

are uniform along the relevant part of the line-of-sight, in the corona, we can write the radiances for both lines as

$$I_{\rm LF} = A^{\rm P}_{X_{\rm LF}} f_{X_{\rm LF}} \langle C_{\rm LF}, {\rm DEM}\rangle \quad \& \quad I_{\rm HF} = A^{\rm P}_{X_{\rm HF}} f_{X_{\rm HF}} \langle C_{\rm HF}, {\rm DEM}\rangle \tag{2.1}$$

where we define the FIP bias $f_X \equiv A^{\rm C}_X / A^{\rm P}_X$ for element X in which $A^{\rm C}_X$ and $A^{\rm P}_X$ are the coronal and photospheric abundances for that element, $C_{\rm LF}$ and $C_{\rm HF}$ are the contribution functions for the lines of the low-FIP and high-FIP elements, and $\langle a, b\rangle \equiv \int a(T)\, b(T)\; dT$ is a scalar product. The contribution functions contain all the atomic physics necessary for line formation, while the DEM reflects the plasma conditions along the line-of-sight. The ratio of the FIP biases (the relative abundance between element $X_{\rm LF}$ and $X_{\rm HF}$) is

$$\frac{f_{X_{\rm LF}}}{f_{X_{\rm HF}}} = \frac{I_{\rm LF}}{I_{\rm HF}} \left(\frac{A^{\rm P}_{X_{\rm LF}}}{A^{\rm P}_{X_{\rm HF}}} \frac{\langle C_{\rm LF}, {\rm DEM}\rangle}{\langle C_{\rm HF}, {\rm DEM}\rangle} \right)^{-1} \tag{2.2}$$

One then needs to either determine the DEM in order to compute this ratio or use the 2LR method which requires finding two lines with contribution functions similar enough that the ratio $\langle C_{\rm LF}, {\rm DEM}\rangle / \langle C_{\rm HF}, {\rm DEM}\rangle$ is constant for any DEM.

The idea of the LCR method is to use two sets of lines instead of only two lines. We ought to use linear combinations of lines, so that the corresponding contribution functions for low FIP (LF) and high FIP (HF) elements match better. We start by defining two radiance-like quantities, that would be the analogs of the radiances of Eqs. 2.1, as linear combinations of radiances from individual lines of low-FIP and high-FIP elements:

$$I_{\rm LF} \equiv \sum_{i \in ({\rm LF})} \alpha_i \, \frac{I_i}{A^{\rm P}_i} \quad \& \quad I_{\rm HF} \equiv \sum_{i \in ({\rm HF})} \beta_i \, \frac{I_i}{A^{\rm P}_i} \tag{2.3}$$

If the FIP biases of all used low-FIP elements are the same (and equal to $f_{\rm LF}$), and the FIP biases of all used high-FIP elements are the same (and equal to $f_{\rm HF}$), the ratio of the FIP biases is

$$\frac{f_{\rm LF}}{f_{\rm HF}} = \frac{I_{\rm LF}}{I_{\rm HF}} \left(\frac{\langle C_{\rm LF}, {\rm DEM}\rangle}{\langle C_{\rm HF},\ {\rm DEM}\rangle} \right)^{-1}, \tag{2.4}$$

where the low FIP and high FIP contribution functions have been defined by

$$C_{\rm LF}(T) \equiv \sum_{i \in ({\rm LF})} \alpha_i \; C_i(T) \quad \& \quad C_{\rm HF}(T) \equiv \sum_{i \in ({\rm HF})} \beta_i \; C_i(T) \tag{2.5}$$

We have developed a Python module (`https://git.ias.u-psud.fr/nzambran/fiplcr`) to compute the optimal coefficients α_i and β_i so that the linear combinations of spectral lines can be used to obtain accurate relative FIP bias maps from observations.

3 Testing the LCR method with synthetic radiances

We test the LCR method by applying it to maps of synthetic radiances. We also test the 2LR method with the same criteria for comparison. The test case consists in a uniform abundance map for any given element, combined with a data cube of DEMs, as detailed below. Using both these inputs and atomic physics, we can build "synthetic" radiances, from which we compute FIP biases with both methods. The test is considered successful for a given FIP bias determination method if the output relative FIP bias map is consistent with the input elemental abundance maps, both in uniformity and in value.

The test has four main steps, detailed below:

1. We derive a DEM cube from an observation (active region shown in the left hand side of Fig. 1) obtained with the AIA (AIA; Lemen et al. 2012) instrument aboard the Solar Dynamics Observatory (SDO; Pesnell et al. 2012) using the Cheung et al. (2015) code.

2. We choose the sets of lines to use for the test (listed in Table 1). Then, using the CHIANTI atomic database (Dere et al. 1997, Del Zanna et al. 2015) for the contribution functions, and the DEMs derived just earlier, we calculate the synthetic radiances. We assume different uniform abundances for different elements.

Ion	Wavelength (Å)	$\log T_{\max}$ (K)	LCR coeff	2LR coeff (10^{20})	FIP (eV)	f_X/f_S
Fe XII	195.119	6.2	0.0845		7.90	2.05
Fe XIII	201.126	6.2	-0.0738		7.90	2.05
Fe XIII	202.044	6.2	0.0294		7.90	2.05
Si X	**258.374**	6.1	1.36	4.26	8.15	1.82
Si X	261.056	6.1	1.46		8.15	1.82
S X	**264.231**	6.2	2.16	3.34	10.36	1.00
Fe XIV	264.789	6.3	0.503		7.90	2.05
Fe XIV	274.204	6.3	0.0404		7.90	2.05

Table 1. Spectral lines used to perform the calculations for both methods (coefficients computed for a density of $\log n = 8.3$). The lines in bold correspond to those used for the 2LR method. We also include the FIP of the elements used for the tests, and their abundance bias relative to sulfur (Schmelz et al. 2012; Grevesse et al. 2007).

3. We determine the optimal linear combination coefficents for the LCR method, and the coefficients for the 2LR method.
4. We use these coefficients to retrieve the FIP bias (see right panel of Fig. 1) in each pixel assuming $\langle C_{\mathrm{LF}}, \mathrm{DEM}\rangle / \langle C_{\mathrm{HF}}, \mathrm{DEM}\rangle \approx 1$ is verified for any DEM. If this is the case, the retrieved FIP bias map should be uniform.

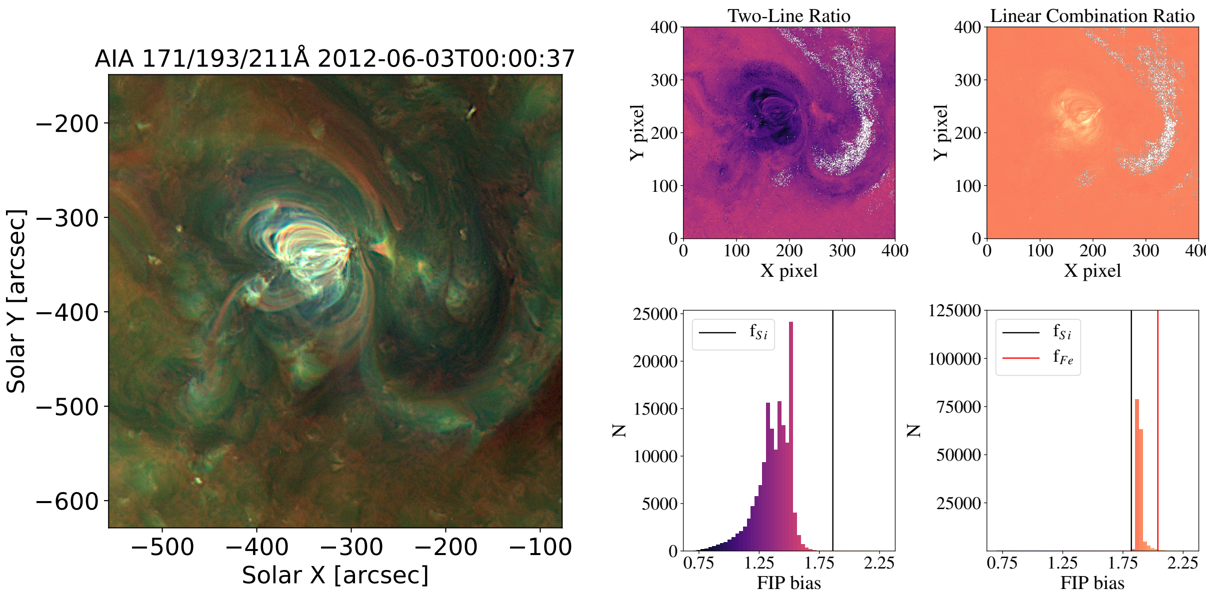

Fig. 1. Left: Composite map of an AR observed on June 3rd 2012, in the 171 Å (red), 193 Å (green), and 211 Å (blue) channels of the AIA instrument aboard SDO. **Right:** Results of FIP bias determination using the 2LR (left) and LCR (right) methods on the synthetic radiances in the AR: relative FIP map (top) and its corresponding histogram (bottom), with matching color scales. The vertical lines in the histograms correspond to the imposed uniform values of the relative FIP bias (for each of the low-FIP elements, see Table 1), that should ideally be retrieved.

We obtain relative FIP bias maps for both methods. We present the results in the right hand side of Fig. 1. The top left panel clearly shows that we do not retrieve a uniform relative FIP bias using the 2LR method, as confirmed by the width of the corresponding histogram (bottom left). Its standard deviation is of 0.15. Furthermore, the histogram peak at about 1.51 is far from the imposed value for the relative FIP bias between the two elements used, silicon and sulfur (1.82). The LCR method gives a much more uniform map (top right panel), as confirmed by the corresponding histogram (bottom right) that has a standard deviation of 0.03. This histogram peaks at 1.87, and almost all obtained values are between the relative FIP biases for Fe and Si. These results show the accuracy of the linear combination ratio method.

4 Conclusions

We have presented the Linear Combination Ratio (LCR) method, which aims at providing an optimal determination of the relative FIP biases in the corona from spectroscopic observations without the need to previously determine the DEM. This technique relies on linear combinations of spectral lines, optimized for FIP bias determination. We have developed a Python module implementing the method and that can be found at `https://git.ias.u-psud.fr/nzambran/fiplcr`.

Using two linear combinations of spectral lines, one with low FIP elements and one with high FIP elements, we tested the accuracy of the method performed on synthetic observations: these tests show that the method does indeed perform well, without prior DEM inversions.

Once the optimized linear combination coefficients have been determined for a given set of lines, the LCR method directly gives the corresponding FIP bias maps. This makes the method simple to apply on observations containing a pre-defined set of lines, with a potential for automation.

Hopefully, producing such FIP bias maps semi-automatically would allow for direct comparison with in-situ data of the Solar Wind. This method could also allow better exploitation of observations not specifically designed for composition studies, and an optimal design of future observations. We plan to apply the method to the future Solar Orbiter/SPICE spectra, to prepare the observations and analysis of the SPICE data.

NZP is grateful for the opportunity of giving a talk about this work at the 2019 SF2A meeting. The authors thank Mark Cheung for the SDO/AIA DEM inversion code, and Giulio Del Zanna, Susanna Parenti, and Karine Bocchialini for their comments. The idea for this work came following a presentation by Hardi Peter at the Solar Orbiter joint SPICE-EPD-SWA meeting in Orsay in November 2015. AIA is an instrument on board SDO, a mission for NASA's Living With a Star program. NZP thanks ISSI for support and participants to the ISSI team "Linking the Sun to the Heliosphere using Composition Data and Modelling" led by Susanna Parenti. CHIANTI is a collaborative project involving George Mason University, the University of Michigan (USA) and the University of Cambridge (UK). This work used data provided by the MEDOC data and operations centre (CNES / CNRS / Univ. Paris-Sud), `http://medoc.ias.u-psud.fr/`.

References

Baker, D., Brooks, D. H., Démoulin, P., et al. 2013, ApJ, 778, 69

Cheung, M. C. M., Boerner, P., Schrijver, C. J., et al. 2015, ApJ, 807, 143

Craig, I. J. D. & Brown, J. C. 1976, A&A, 49, 239

Del Zanna, G., Dere, K. P., Young, P. R., Landi, E., & Mason, H. E. 2015, A&A, 582, A56

Dere, K. P., Landi, E., Mason, H. E., Monsignori Fossi, B. C., & Young, P. R. 1997, A&AS, 125

Feldman, U. & Widing, K. G. 2003, Space Sci. Rev., 107, 665

Grevesse, N., Asplund, M., & Sauval, A. J. 2007, Space Science Reviews, 130, 105

Guennou, C., Auchère, F., Soubrié, E., et al. 2012, The Astrophysical Journal Supplement Series, 203

Guennou, C., Hahn, M., & Savin, D. W. 2015, The Astrophysical Journal, 807, 145

Judge, P. G., Hubeny, V., & Brown, J. C. 1997, ApJ, 475, 275

Landi, E., Reale, F., & Testa, P. 2012, A&A, 538

Lemen, J., Title, A., Akin, D., et al. 2012, Sol. Phys., 275, 17

Peleikis, T., Kruse, M., Berger, L., & Wimmer-Schweingruber, R. 2017, Astronomy & Astrophysics, 602, A24

Pesnell, W., Thompson, B., & Chamberlin, P. 2012, Sol. Phys., 275, 3

Saba, J. L. R. 1995, Advances in Space Research, 15

Schmelz, J. T., Reames, D. V., von Steiger, R., & Basu, S. 2012, ApJ, 755, 33

Testa, P., De Pontieu, B., Martínez-Sykora, J., Hansteen, V., & Carlsson, M. 2012, ApJ, 758

Session 13

Gaia: astrométrie, photométrie et alertes pour l'étude du systeme solaire (S13)

SF2A 2019
P. Di Matteo, O. Creevey, A. Crida, G. Kordopatis, J. Malzac, J.-B. Marquette, M. N'Diaye, O. Venot (eds)

PREDICTION OF STELLAR OCCULTATIONS BY DISTANT SOLAR SYSTEM OBJECTS WITH GAIA

J. Desmars[1], B. Sicardy[1], F. Braga-Ribas[1,3,2], G. Benedetti-Rossi[1,3], J. Marques Oliveira[1], P. Santos-Sanz[4], J.L. Ortiz[4], J. Camargo[3], R. Vieira Martins[3], F.L. Rommel[3], M. Assafin[5] and A.R. Gomes-Júnior[5,6]

Abstract. Predictions of stellar occultations by outer Solar System objects require accurate positions of stars and accurate orbits. In the recent years, Gaia catalogues allow a huge improvement thanks to stellar positions accurate to less than 1 milliarcsec (mas). On the contrary, the orbits of outer Solar System objects are not so precise because these objects are distant and were observed only during a short period of their orbit. In this document, we present several techniques to improve the orbits of distant Solar System objects for the occultation purpose, in particular thanks to : 1) the astrometry deduced from previous occultations, 2) a new reduction of astrometric position using Gaia catalogues and 3) the direct observations of the objects by Gaia.

Keywords: astrometry, celestial mechanics, ephemerides, occultations, Kuiper belt objects

1 Introduction

Stellar occultation is the only technique to obtain, from ground-based observations, an accurate estimation of physical parameters of distant objects or to probe their atmosphere and surroundings. For example, size and shape can be determined to kilometric precision, atmospheric pressure can be measured down to nanobar levels, and ring system around the body can be characterised (Braga-Ribas et al. 2014; Ortiz et al. 2017; Meza et al. 2019, for instance).

The first step of these works is the prediction of stellar occultations to know where and when the event could be observed. Predictions require an accurate position of the star and an accurate ephemeris of the object. Thanks to Gaia catalogues (Gaia Collaboration et al. 2016, 2018a), the position of the stars is now known at the tenth of mas level accuracy. Ephemerides of these objects are less precise since they depend on the quality of the astrometry used to determine their orbit. For distant Solar System objects (DSSO), the precision is usually around several dozens of mas. Due to their distance, a small angular error corresponds to large error on the path at the surface of the Earth, making the occultation quite uncertain to observe. For example, 10 mas corresponds to 35 km at the Jupiter distance (5.2 AU), 100 km at Chariklo distance (15 AU), 200 km at Neptune distance (30 AU) and 700 km at Eris distance (97 AU).

Desmars et al. (2015) propose the NIMA method in order to refine predictions thanks to a better orbit determination. This method uses all the astrometric positions available on Minor Planet Center and additional observations from Observatório Pico dos Dias and Granada (from our astrometric survey). This method also allows to use astrometry of previous occultations.

In this document, we present how Gaia is also helping to improve the ephemerides of DSSO, in particular thanks to 1) the astrometry deduced from previous occultations, 2) a new reduction of astrometric position using Gaia catalogues, and 3) the direct observations of the objects by Gaia.

[1] LESIA/Observatoire de Paris, univ. PSL, CNRS, Paris, France
[2] Federal University of Technology of Paraná (UTFPR-Curitiba), Brazil
[3] Observatório Nacional, Rio de Janeiro, Brazil
[4] Intituto de Astrofisica de Andalucia, Granada, Spain
[5] Observatório do Valongo, UFRJ, Rio de Janeiro, Brazil
[6] UNESP-São Paulo State University, Guaratinguetá, Brazil

2 Predictions with previous occultations

As of August 2019, about 168 occultations have been successfully observed for 63 differents DSSO*. These occultations not only help to determine the body shape, size, etc, they also provide an accurate astrometric position of the body's center at the time of the occultation. The full technique is detailed in Desmars et al. (2019).

This position only depends on the position of the occulted star (about 0.1 mas) and the global analysis of the occultation (about few km representing few mas). Finally, the precision of the deduced position from the occultation generally reach 2 mas for multi-chord occultations to 10-20 mas for single-chord occultations. For comparison, astrometric positions deduced from CCD have a precision from 50 mas (in the best case) to 300 mas in the general case. These positions are then used in the orbit determination process (for example NIMA) in order to refine the orbit and the future predictions of occultations.

This method was, for instance, used with Pluto thanks to 19 occultations observed between 1988 and 2016 allowing an orbit with a precision of few mas instead of hundred mas with other ephemerides (Desmars et al. 2019). Predictions of Pluto's occultations in the near future now reach a precision of 60-80km on the path of the shadow, allowing to observe the central flash in an area around 50 km along the centrality (Meza et al. 2019). The same method was used for Chariklo for which we observed 15 occultations from 2013 to 2017 (Bérard et al. 2017; Leiva et al. 2017; Desmars et al. 2018) and is applied to refine the orbits as soon as positive occultations are detected.

3 Predictions with astrometry reduced with Gaia catalogues

Occultations remain usually rare events and hard to observed for DSSO. Most of the DSSO were not observed yet by occultations and the previous method can not be used to refine orbit and future predictions. In such case, the only option is to use the classic astrometry using the Gaia catalogues.

Before Gaia catalogues, the most precise stellar catalogues reach an astrometric precision of 50 to 70 mas, as for example UCAC4 (Zacharias et al. 2013) with additional zonal errors. The first release of Gaia catalogue (Gaia Collaboration et al. 2016) provides stellar positions with a precision of 1-20 mas but no proper motions of the stars. The second release of Gaia catalogue (Gaia Collaboration et al. 2018a) provides stellar positions, proper motions and parallaxes. The global precision of the star now reaches 0.1-0.2 mas. Moreover, there is no more zonal errors in Gaia catalogues as it was the case with former catalogues. Classical astrometry can be improved by using Gaia catalogues for the astrometric reduction.

In order to study the benefit of the use of Gaia catalogues, we took the example of an occultation by Triton on 5^{th} October 2017. For this occultation, we specifically observed Triton during 8 nights before the occultation in order to refine its position. For these observations, we first made an astrometric reduction with Gaia DR1 and obtained a mean offset for the 8 nights: $\Delta\alpha \times \cos\delta = -5.3 \pm 8.0$mas and $\Delta\delta = -4.8 \pm 5.7$ mas. Then we used Gaia DR2 for astrometric reduction leading to a mean offset of : $\Delta\alpha \times \cos\delta = +7.8 \pm 5.4$ mas and $\Delta\delta = -17.6 \pm 2.6$ mas. The residuals in right ascension and declination per night are represented on Fig.1. The residuals are better and more precise with the reduction with Gaia DR2. They are also constant over the nights, which is less the case with the Gaia DR1 reduction. At the end, the offset deduced from the Gaia DR2 reduction was used for the prediction.

Finally, the occultation was successfully observed over Europe and preliminary results show that the offset between prediction and the occultation was around 2 mas in declination which represents a shift of only 40 km on the path (Marques Oliveira et al. 2018). Astrometric reduction with Gaia catalogues provide more accurate astrometric reduction and particularly less affected by zonal errors coming, for example, from unknown proper motions.

4 Predictions with Gaia DR2 astrometry

Gaia DR2 catalogue provide astrometric positions for more than 14000 Solar System objects (Gaia Collaboration et al. 2018b). Unfortunately, only 2 DSSO are included in the catalogue. To analyse the improvement of Gaia DR2 positions for occultations, we deal with Trojans objects as the biggest are included in Gaia DR2.

---

*`http://occultations.ct.utfpr.edu.br/results/`

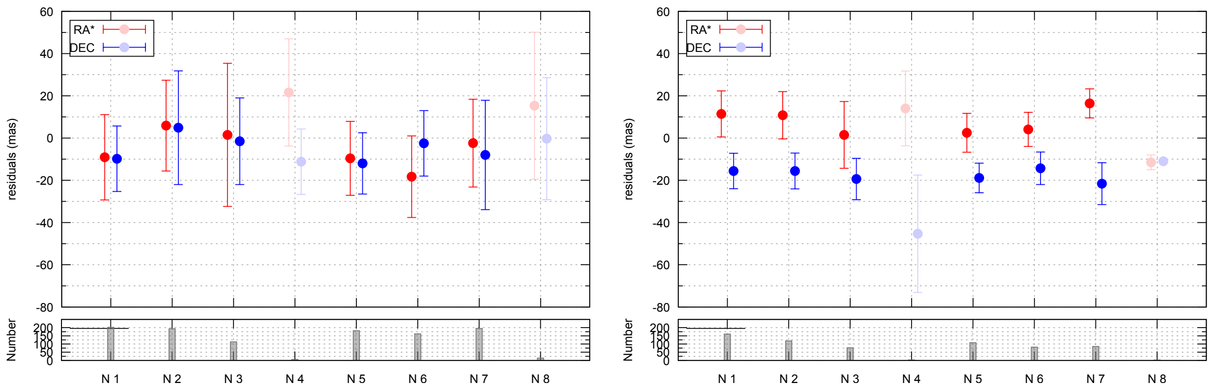

Fig. 1. Astrometric residuals in right ascension and declination for 8 nights of Triton observations using Gaia DR1 (**Left**) and Gaia DR2 (**Right**) catalogues for the reduction. Histograms also give the number of observations per night. Data in light colors were not used in the mean offset determination.

Due to the scanning process of the Gaia spacecraft, the astrometric positions in right ascension and in declination are highly correlated with a precision of about few mas in the along-scan direction whereas it is hundreds of mas (like classical CCD astrometry) in the across-scan direction (Gaia Collaboration et al. 2018b). Correlations have to be taken into account in the orbit determination process.

Gaia DR2 astrometric positions were used to predict an occultation by Deikoon on 23 February 2019. Figure 2 shows the predictions of this occultation with two different ephemerides : NIMAv2 by using only astrometric positions from Minor Planet Center (between 1988 and 2019) and NIMAv3 using in addition the Gaia DR2 positions (between 2014 and 2016). The uncertainty of the path is also represented with red dotted lines showing that the prediction with NIMAv3 is more precise.

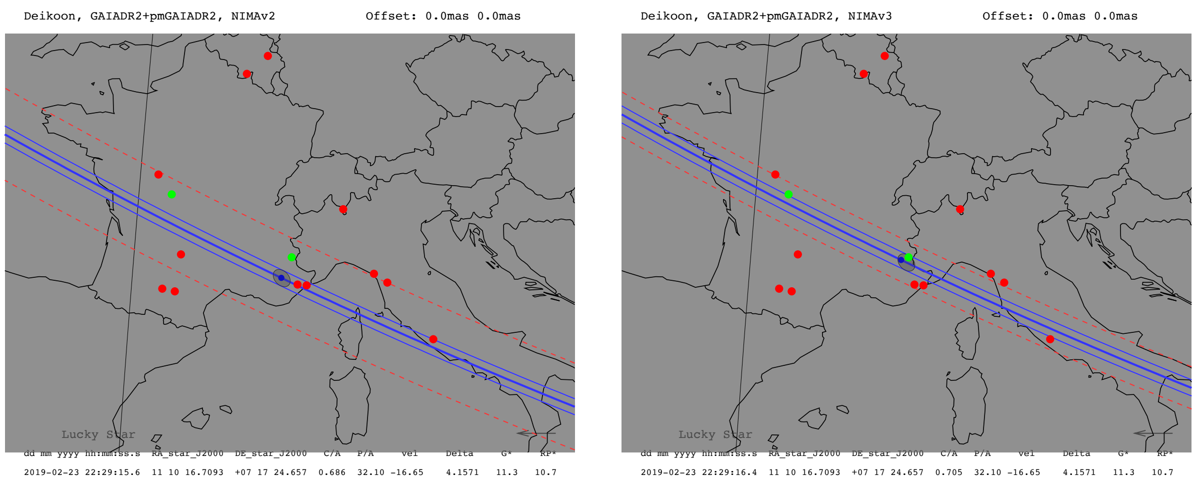

Fig. 2. Prediction of the occultation by Deikoon on 23 February 2019 using NIMAV2 with only the MPC astrometry (**Left**) and NIMAv3 using the MPC + Gaia DR2 astrometry (**Right**). Red dotted lines give the 1-σ uncertainty on the body limits. Green dots indicate stations that report a positive occultation, red dots are for stations reporting a negative observation. The dark disc represent the shadow of Deikoon at the mid-time reported by the eastern green station.

Finally, the occultation was detected in two stations in France. The shadow of Deikoon at the mid-time of the occultation reported by the Eastern station (in green) is also represented on the figures. Other stations (in red) also reported a negative observation still useful to provide constraints on the size of the object. The preliminary analysis of the light curve and timing show that the prediction using the Gaia DR2 positions was very accurate both for the path (impact parameter *i.e.* the closest distant between the center of the shadow and the station on the fundamental plane) and the timing (Table. 1).

ephem	Δt		$\Delta\rho$
	s	mas	mas
NIMAv2	1.0	5.5	21
NIMAv3	0.2	1.1	2

Table 1. Residuals in timing and impact parameter for Deikoon occultation in on 23 February 2019 using NIMAv2 (with only MPC positions) and NIMAv3 (with MPC and GaiaDR2 positions).

In 2019, we have also detected positive occultations for other Trojans with less promising results, *i.e.*the prediction was not necessarily better by using Gaia DR2 astrometry. As these occultations were single chord occultation (observed by only one station), systematic errors such as timing issue are possible and careful analysis will be done in the future. The Trojans are a good test as future Gaia releases will provide astrometric positions of most of the Solar System objects during the mission period.

5 Conclusions

Predictions of stellar occultations by distant Solar System objects were greatly improved thanks to Gaia. The star positions now reach less than 1 mas whereas orbits of DSSO can also be improved with the help of Gaia: with astrometric position deduced from previous occultations, with astrometry of CCD reduced with Gaia catalogues or with direct astrometric positions from Gaia itself. For some specific objects (Pluto, Chariklo, etc), the prediction of stellar occultations now reaches the mas level accuracy representing only few tens of km, which ten to hundred times better than what we had only five years ago.

Future Gaia releases as well as the Large Synoptic Survey Telescope (Hsieh et al. 2019) will provide astrometric positions for most of the Solar System objects allowing to greatly improve the orbits and the future predictions of stellar occultations. Accurate predictions allow to gather and place precisely observing stations on the Earth surface to observe for example a grazing occultation to study the structure of a ring system or the topographic features at the surface of the object, or to observe a central flash in order to probe the atmosphere of some objects (Pluto, Triton).

This work received funding from the European Research Council under the European Community's H2020 (2014-2020/ERC Grant Agreement No. 669416 "LUCKY STAR"). This work has made use of data from the European Space Agency (ESA) mission *Gaia* (`https://www.cosmos.esa.int/gaia`), processed by the *Gaia* Data Processing and Analysis Consortium (DPAC, `https://www.cosmos.esa.int/web/gaia/dpac/consortium`). Funding for the DPAC has been provided by national institutions, in particular the institutions participating in the *Gaia* Multilateral Agreement. P.S-S. acknowledges financial support by the Spanish grant AYA-RTI2018-098657-J-I00. P.S-S. and J.L.O. acknowledge financial support from the State Agency for Research of the Spanish MCIU through the Center of Excellence Severo Ochoa3 award for the Instituto de Astrofísica de Andalucía (SEV-2017-0709), they also acknowledge the financial support by the Spanish grant AYA-2017-84637-R.

We thank the observers of the Deikoon occultation on 23 February 2019 : W. Beisker, P. Le Cam, M. Boutet, L. Rousselot, P. André, E. Frappa, R. Boninsegna, O. Schreurs, A. Figer, A. Klotz, M. Conjat, A. Ossola, P. Baruffetti, M. Bachini, M. Masucci, E. Dal Canto and C. Costa. We also thank P. Tanga, F. Spoto, and J. Ferreira to alert us about the Gaia astrometry for Deikoon.

References

Bérard, D., Sicardy, B., Camargo, J. I. B., et al. 2017, AJ, 154, 144

Braga-Ribas, F., Sicardy, B., Ortiz, J. L., et al. 2014, Nature, 508, 72

Desmars, J., Bérard, D., Sicardy, B., et al. 2018, in European Planetary Science Congress, EPSC2018–821

Desmars, J., Camargo, J. I. B., Braga-Ribas, F., et al. 2015, A&A, 584, A96

Desmars, J., Meza, E., Sicardy, B., et al. 2019, A&A, 625, A43

Gaia Collaboration, Brown, A. G. A., Vallenari, A., et al. 2018a, A&A, 616, A1

Gaia Collaboration, Brown, A. G. A., Vallenari, A., et al. 2016, A&A, 595, A2

Gaia Collaboration, Spoto, F., Tanga, P., et al. 2018b, A&A, 616, A13

Hsieh, H. H., Bannister, M. T., Bolin, B. T., et al. 2019, arXiv e-prints, arXiv:1906.11346

Leiva, R., Sicardy, B., Camargo, J. I. B., et al. 2017, AJ, 154, 159

Marques Oliveira, J., Sicardy, B., Meza, E., et al. 2018, in European Planetary Science Congress, EPSC2018–172

Meza, E., Sicardy, B., Assafin, M., et al. 2019, A&A, 625, A42

Ortiz, J. L., Santos-Sanz, P., Sicardy, B., et al. 2017, Nature, 550, 219

Zacharias, N., Finch, C. T., Girard, T. M., et al. 2013, AJ, 145, 44

SF2A 2019
P. Di Matteo, O. Creevey, A. Crida, G. Kordopatis, J. Malzac, J.-B. Marquette, M. N'Diaye, O. Venot (eds)
*
†

DETECTION OF NEW ASTEROIDS BY GAIA

W. Thuillot[1], B. Carry[2], F. Spoto[2], P. Tanga[2], P. David[1], J. Berthier[1], Gaia-FUN-SSO team* and CU4-SSO members †

Abstract. We present our results about the detection of new asteroids by Gaia. Since the end of 2016, an alerting system is operating and it reacts when unknown and moving objects are detected by the probe. In spite of the short length of the orbital arcs observed by transits in the Gaia focal plane, it is possible to calculate preliminary orbital beams and to determine search areas for a ground-based observatory. On the basis of these data, the Gaia-FUN-SSO network of observatories, set up for this task, is able to validate the detections and to consolidate the asteroid orbits.

Keywords: Gaia, Solar System Objects, asteroids, alerts, follow-up, astrometry

1 Introduction

The Gaia satellite, during its rotating sky scans, performs measures of all light sources of magnitude brighter than 20.7 and, among these sources, it can detect moving objects compared to stars. These Solar System Objects (SSO) are essentially asteroids. A specific task has been dedicated to the triggering of alerts in the short term data processing in order to deal with these detection, to broadcast public alerts and to validate the detection thanks to ground-based observatories (Tanga et al. 2016). Thus, in addition to the data on asteroids published during the DR2 in April 2018 (Gaia Collaboration et al. 2018), there is therefore a continuous publication of Gaia detections of asteroids not yet known and cataloged. These alerts are regularly accessible to the network of Gaia-FUN-SSO observatories via a website to encourage a follow-up of these new objects (Thuillot & Dennefeld 2018) .

2 The process

In case of detection of a new Solar System Object by Gaia and validation from the ground, all the astrometry measurements are sent to the Minor Planet Center to feed its database and are subsequently used to update the Gaia reference catalog of asteroids. The Gaia observations are performed for short arcs of the asteroid orbits which, despite a high precision, make impossible the determination of a reliable and unique orbit. Therefore a statistical approach is used and a bundle of possible orbits is computed (Muinonen et al. 2016) which leads to projected positions of the new asteroid on the sky. As shown in Fig. 1 our web site provide this information under the format of a skymap on a daily basis at the address: `https://gaiafunsso.imcce.fr`.

*Gaia-FUN-SSO: L. Abe[2], K. Baillié[1],P. Bendjoya[2], S. Bouquillon (SYRTE, Paris Obs. France), M. Delbo[2], M. Dennefeld (IAP, Paris, France), V. Godunova (ICAMER Observatory Kiev, Ukraine), D. Hestroffer[1], Y. N. Krugly (Kharkiv National Univ. Ukraine), R. Mendez (Univ. de Chile, Santiago), J.P. Rivet[2], V. Robert[1], D. Souami (SYRTE, Paris Obs. France), F. Taris, (SYRTE, Paris Obs. France), V. Troianskyi (Astron. Obs. of Odessa, Ukraine), D. Vernet[2]

†DPAC-CU4-SSO members: A. Cellino (Astron. Inst. Torino), A. Dell'Oro (AstroN. Obs. Firenze), G. Fedorets (Helsinki Univ.), D. Hestroffer (Paris Obs.), K. Muinonen (Helsinki Univ.), J.-M. Petit (Besancon Obs.), Th. Pauwels (Roy. Obs. Belgium)

[1] IMCCE, Observatoire de Paris, PSL University, CNRS, Sorbonne Université, Université de Lille, 77 Avenue Denfert Rochereau, 75014 Paris, France

[2] Université de la Côte d'Azur, Observatoire de la Côte d'Azur, CNRS, Laboratoire Lagrange, France

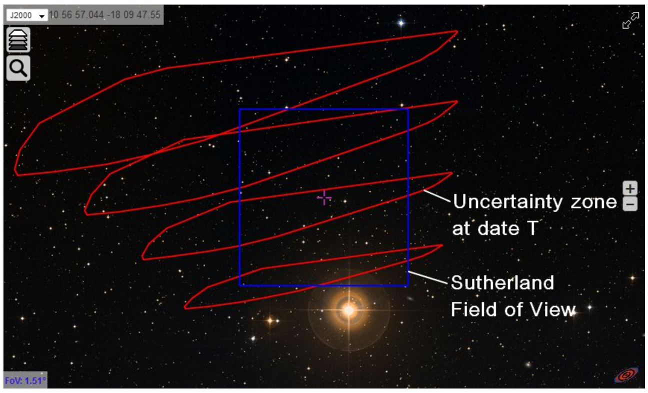

Fig. 1. Gaia-FUN-SSO website: Skymap providing at different dates the zone to search from the ground for the new asteroids detected by Gaia

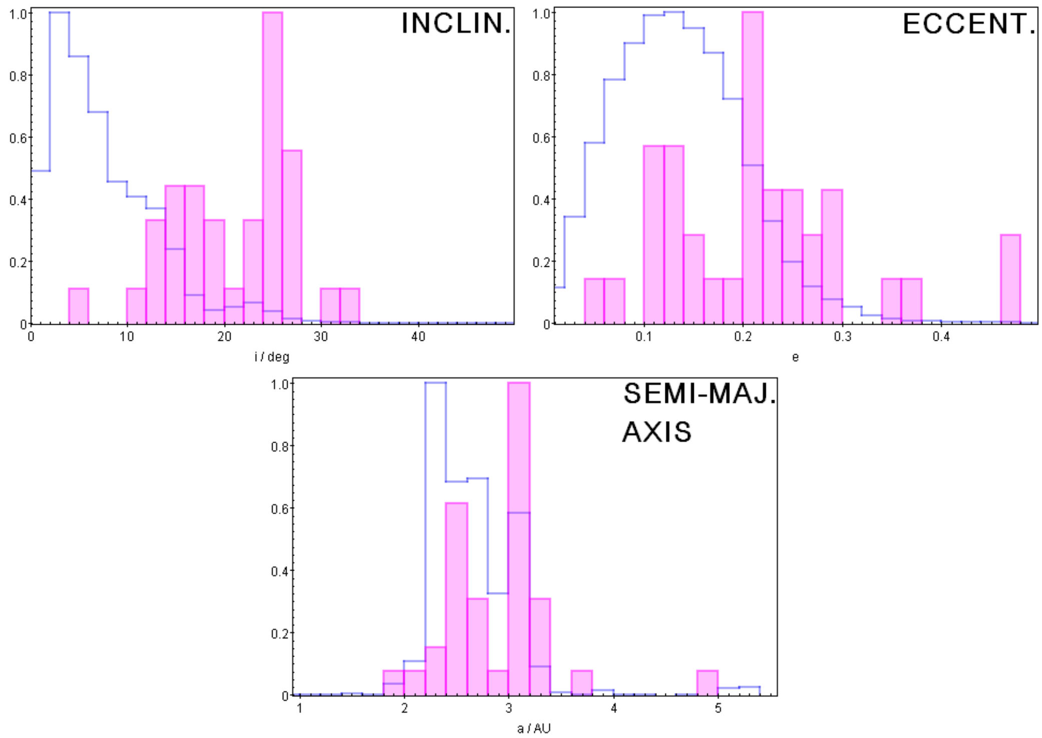

Fig. 2. Normalized histogram of the detected asteroids inclinations to ecliptic, histogram of the excentricities and histogram of the semi-major axis compared to the ones of all the population (line)

3 Results obtained

The task is rather challenging. Since the end of 2016, more than 4500 alerts have been triggered but only 150 new asteroids have been detected from the ground and 55 are validated: i.e. we got ground-based measurements dynamically compliant with the Gaia ones. These are essentially objects of the main belt, located between Mars and Jupiter. Most part of the detections were performed by the following observatories:

- Haute-Provence Observatory with the 1.2m telescope, Saint-Michel, France;
- Las Cumbres Observatory Global Telescope Network, Cal. USA, which provides a network of 1m telescopes located at Cerro Tololo in Chile, at Siding Spring in Australia, and at SAAO Sutherland in South Africa;
- Kiev Comet Station, with a 0.7m telescope, Ukraine;

- Odessa Mayaki Observatory, with a 0.8m telescope, Ukraine;
- Terskol Observatory with the 2m telescope, Kabardino-Balkarie, Russie;
- C2PU, a 1m telescope at Calern, Caussol plateau, Côte d'Azur Observatory, France.

Starting from Nov. 2018, we considered well stabilized the alert system for SSOs and we have systematically provided every Gaia data and ground based astrometry of the new detected and validated asteroids to the Minor Planet Center. Once this center is able to check the orbit, these new asteroids receive a standard provisional designation. Recently, four objects (2018 YK4, 2018 YL4, 2018 YM4, 2019 CZ10) have received designations and, unlike many other detections, Gaia was the first to observe them. These detections were validated from the ground by observations performed by the Gaia-FUN-SSO network. The European Space Agency (ESA) published on 29 April 2019 a newsletter on this subject at the address: `http://www.esa.int/spaceinimages/Images/2019/04/`

From the study of our sample of new asteroids detected by Gaia, as shown in Fig. 2 we see that they are statistically more on highly inclined orbits. We probably can account that this is partly due to the higher observation density of high ecliptic latitude zones explored through the scanning law. But this means also that this kind of asteroids are still missing in the databases. Gaia will complete our knowledge of the asteroid population even for MBAs brighter than 20.7 mag.

4 Conclusion

Many new Solar System Objects are detected by Gaia on a quasi daily basis. They require ground based validation and follow up. Observers are welcome to participate to the Gaia-FUN-SSO network for this goal. On date almost 150 new objects have been confirmed. Our first analysis shows that Gaia detects mostly high inclination and high eccentricity objects which helps for a better knowledge of the asteroid population.

The authors are grateful to the CNES team of engineers who have set up and are dealing with the short term Gaia data processing for triggering alerts. This work has made use of data from the European Space Agency (ESA) mission Gaia (https:/www.cosmos.esa.int/gaia), processed by the Gaia Data Processing and Analysis Consortium (DPAC, https:/www.cosmos.esa.int/web/gaia/dpac/consortium). Funding for the DPAC has been provided by national institutions, in particular the institutions participating in the Gaia Multilateral Agreement.

References

Gaia Collaboration, Tanga, P. et al. 2018, A&A, 616, A 13

Muinonen, K. et al. 2016, Planet. Space Sc., 123, 95

Tanga, P. et al. 2016, Planet. Space Sc., 123, 87

Thuillot, W. & Dennefeld, M. 2018, in SF2A-2018: Proceedings of the Annual meeting of the SF2A, ed. P. Di Matteo, F. Billebaud, F. Herpin, N. Lagarde, J. Marquette, A. Robin, & O. Venot, 463–465

Session 14

La médiation scientifique de l'astronomie

SF2A 2019
P. Di Matteo, O. Creevey, A. Crida, G. Kordopatis, J. Malzac, J.-B. Marquette, M. N'Diaye, O. Venot (eds)

EDUCATIONAL TOOLS AND ACTIVITIES IN ASTRONOMY ON-LINE

Q. Branchereau[1], A. Marcotto[1], A. Bacalhau[1] and O. Suarez[1]

Abstract. For several years, the outreach team of the educational office of the Observatoire de la Côte d'Azur has developed several tools and activities to disseminate knowledge in astronomy. Our pedagogical contents and activities are initially conceived for a school use, to be led in the classroom by scientists and members of our team. However, we have made them available on-line, for a larger use. With this aim, we have developed several sheets defined by the target audience (age and school level) that are available on our Observatory website. Thanks to them, it is now possible for everyone (other outreach professionals, scientists, teachers, parents and so on) to download our contents and carry out our activities in total autonomy. Activity-explanation and communication videos will be soon available.

Keywords: outreach, education, teaching skills, astronomy activities

1 Introduction

Outreach is one of the four missions of the Observatoire de la Côte d'Azur (OCA) and is the core of the work done by the educational office team. Each year, we develop projects with several schools and we provide many astronomy sessions in the classes. We also host stands during public science events. The projects developed with the teachers, offer a progression in astronomy knowledge. Some of them conclude by the participation in a real research project, with an observation with a professional telescope that provides data to professional astronomers (Suarez et al. 2019).

This work has allowed us to develop and improve many activities to deal with different topics in astronomy and especially those related to the research work at the OCA. To make public profit from these educational contents, we decided to make them available on-line. Thus, our outreach team adapted the activities to be used independently and developed a series of educational sheets intended for a large audience.

2 Description of the activities

Each activity contains a sheet for teachers or any kind of tutors, and a sheet for pupils or any kind of learners. A corrected sheet and annexes can also be found.

For all activities, teacher's sheets follow the same pattern:

- A first page (Fig. 1) indicating the activity title, the objectives, the target audience, the duration of the activity, the material, links with school programs and connected activities. A colour-code, following a gradient of " star-temperature colours ", is used to define the level of the activityÂ (red for 6-10-year-olds, orange for 8-13-year-olds, yellow for 12-16-year-olds, blue for 14-17-year-olds and purple for 16-18-year-olds).
- Contents combining objectives, timing and background information for each exercise or construction.

The student's sheet contains the title, objectives, exercises and construction statements.

[1] Observatoire de la Côte d'Azur, 06304 Nice, France

3 List of activities

For the time being, eight/nine activities have been completed and are available on our website:
`http://www.oca.eu/materiel-pedagogique`

- **White light and coloured light.** (*Construction activity for 6-10-year-olds − 1 sheet and 1 annex*): The white light is a combination of several coloured lights, from purple to red (rainbow colours). How is it possible to decompose white light and observe each colour radiation? Furthermore, how could we recombine colours to make white?
- **Construction of a spectroscope with a CD.** (*Construction activity for 8-13-year-olds 2 file and 1 annex*). This device enables users to disperse light and observe the spectrum of a luminous source.
- **Invisible light.** (*Exercise for 12-16-year-olds − 2 sheets and 1 correction*). Is visible light the only type of radiation used in astronomy? Is it possible to become invisible?
- **Discover the sky with Stellarium.** (*Exercise for 14-17-year-olds − 2 sheets and 1 correction*). An activity with Stellarium software that makes everyone understand the sky and want to observe it night and day.
- **Constellation machine.** (*Construction activity for 14-17-year-olds − 2 sheets and 2 annexes*). A construction activity to understand that constellations are human-mind compositions and to see the 3D positions of stars in three very-known constellations: Orion, Cassiopeia and the Lion.
- **Sky chart.** (*Exercise activity for 14-17-year-olds − 2 sheets and 1 correction*). The most useful device to get your bearings in the night sky!
- **From bulbs to stars.** (*Exercise activity for 14-17-year-olds − 2 sheets and 1 correction*): What information can we get from the light provided by stars and nebulae? A parallel with different light bulbs might be helpful to understand it!
- **Solar spectrum.** (*Exercise activity for 16-18-year-olds − 2 sheets and 1 correction*). The solar spectrum gives us information to determine the chemical components of our star.
- **Importance of precision.** (*In development, exercise activity for 16-18-year-olds − 2 sheets and 1 correction*). How critical is precision in astronomy?

4 Hyperlinks

To download our activities, get information about all our actions and contact us:
`https://www.oca.eu`

To discover on the web other contents and activities developed by our team:
`http://medites.fr/parcours-pedagogiques/observation-univers`

5 Conclusions

We have made available on-line several educational activities about astronomy. They will help us to fulfil our main goal: the dissemination of astronomy knowledge to a large audience. We have also made short videos to promote our activities and to help with their understanding.

The development of new contents is on-going, and for this reason we will be grateful to anyone who shares experiences and gives us a return about our activities led in classroom or anykind of event. (For any return, please contact eduoca@oca.eu).

References

Suarez, O., Branchereau, Q., Abe, L., et al. 2019, in Proceedings of the Société Francaise d'Astronomie et d'Astrophysique (SF2A) 2019, ed. P. Di Matteo, O. Creevey, A. Crida, G. Kordopatis, J. Malzac, J.-B. Marquette, M. N'Diaye, & V. O. (SF2A)

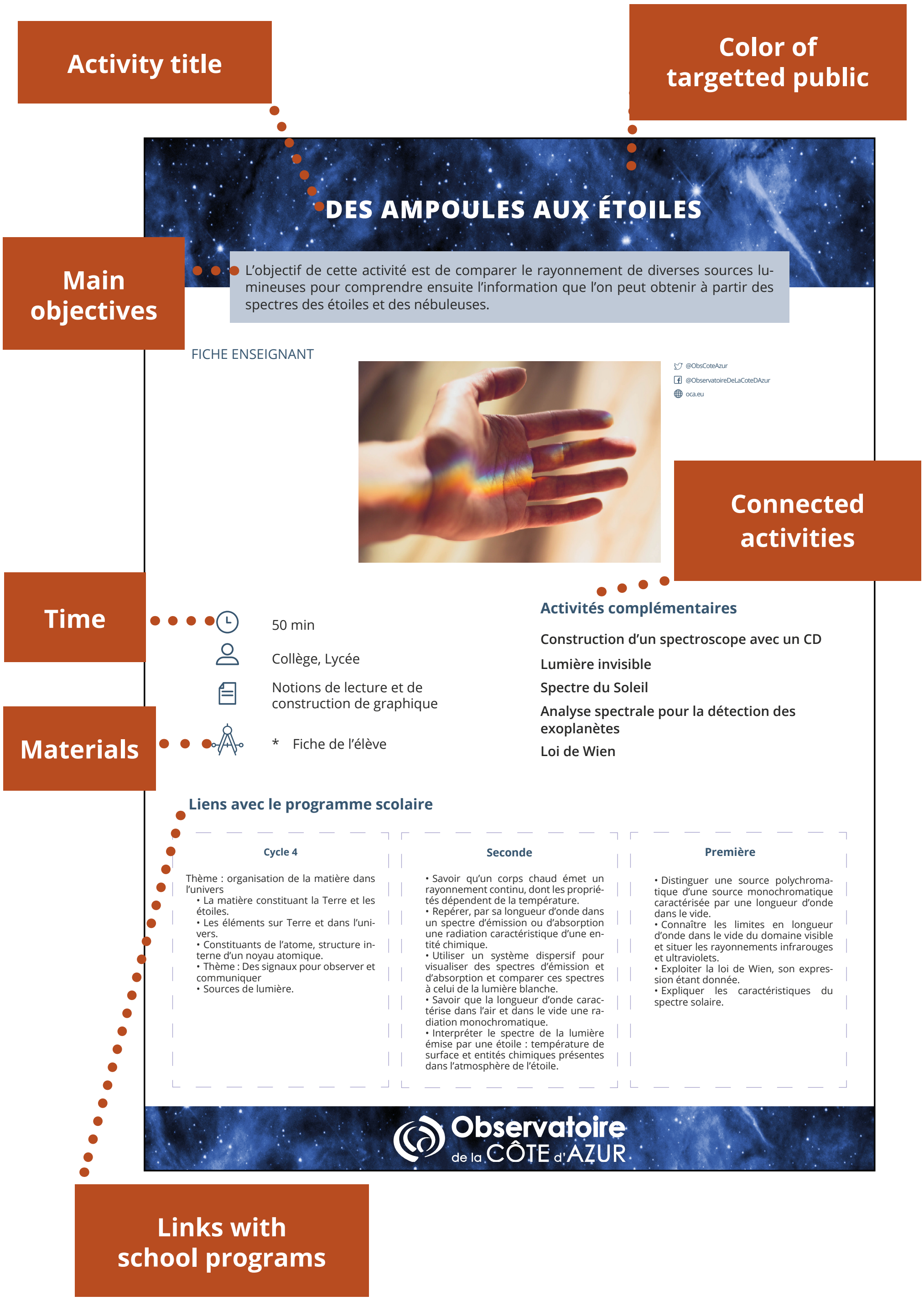

Fig. 1. Pattern for the first page of a teacher's sheet

SF2A 2019
P. Di Matteo, O. Creevey, A. Crida, G. Kordopatis, J. Malzac, J.-B. Marquette, M. N'Diaye, O. Venot (eds)

THE UNIVERSE BEHIND BARS - ASTRONOMY IN PRISONS

D. Briot[1]

Abstract. For more than two decades, we go in prisons in France and overseas territories for astronomy talks i.e. courses, lectures and discussions with prisoners. Paradoxically, these talks are very successful. It is very important for both prisoners and society that the time spent in prison would not totaly lost time, but could be used to improve knowledge and culture of prisoners. We explain some aspects of these talks, we note some specificities, and we detail some organizational points

Keywords: teaching, popularization, society

1 Introduction

For more than twenty years, Régis Courtin and I, astronomers at the Paris-Meudon Observatory, are going in some prisons for astronomy talks to the prisoners.Whereas the prisoners are really interested, as proved by their requests for additional talks, this activity is a very interesting experience for the lecturer. A part of this study was already published (Briot 2011) and we briefly recall it. It could appear rather strange that people with and a complicated past, a very hard present way of life and an agonising future could be interested by astronomy, that is a science without direct utility for locked up people. Moreover, the aim of astronomy is to discover and open the whole Universe in all its infinite totality, whereas, in prisons, the audience is locked and confined as much as possible. This apparent contradiction is specially striking during the talks at the Prison de la Santé which is located in the block next to the Paris observatory. However as we shall see below, the audience listens carefully and is really interested.

2 Some reasons to come and talk about astronomy in prisons

We already expound this argumentation (Briot 2011), however, because it is a very important point, we recall it now. So many reasons justify to go and speak about astronomy in prisons.

1) First of all, that is a significant point for prisoners who are cut off from society, and who can sometimes have a feeling that they are forgotten from everybody and from everything, to see that professional scientists come for them, as for any other audience.

2) It is important to use a special moment in the life of these people to organise some meetings with scientists. Actually, most of imprisoned people have had very rarely the opportunity to meet and to discuss with scientists when they were outside.

3) It is also important to take advantage of this special moment to give them an opportunity to increase their knowledge. In some cases, the point is to increase a field of already acquired knowledge, whereas in other cases, it is to initiate in a new domain of knowledge, to open a door onto a new world.

4) Life in prison can be very hard and distressing, physically as well as mentally. Accession to pure and disinterested knowledge, uniquely connected to the pleasure of discovering a new field of knowledge or increasing it, can allow to escape ever so slightly of the awful daily life, and to keep one's mind occupied with other things. Our aim is to use constructively the prison time and to reduce its harmful effects.

5) Of course, reasons which hold for any popularising astronomy lecture in front of any audience, are still valid. Namely, astronomers being civil servants and it is quite natural to explain to the society the use of taxes.

[1] Observatoire de Paris, 61 avenue de l'Observatoire, 75014 Paris, France

6) The last, but not the least, let us not neglect the pleasure to speak about a subject of which we are very fond, with some people who are very interested. Giving to prisoners any opportunity to think and learn can surely help them to be re-integrated in the society after they come out of the prison, besides of the interest of the prisoners for science and the entertainment brought by any distraction which breaks the routine of the prisoner life. More we give elements to think, more people become clever and cultivated, afterwards more tools will be at their disposal to choose their way on their discharge from prison, more they will have chance to become reintegrated in society.

3 Some information and technical details

Nowadays, the number of prisoners in France reached a new peak : 71828 prisoners (1st of April 2019), what is more that the population of cities like Drancy or Colmar. Among those prisoners, 3.5% are women. The rate of overpopulation which is particularly high in pretrial detention causes additional work for warders. So activities involving some people coming from outside and transfers of prisoners outside their cells are not encouraged.

4 Some ways to enter in prisons

A way for an astronomer who wish to go and talk about astronomy in prisons is to get in touch with the teaching team, or the cultural service of the prison, which may be dependent of the Service Pénitentiaire d'Insertion et de Probation (SPIP). This activity can be also organised by associations as those which manage the libraries of Fleury-Mérogis, that is the largest prison in Europe, or some organism as La Ligue de l'Enseignement. In order to improve efficiency, we talk about our activity all around when possible, so when any request arrives to the Paris-Meudon Observatory or in a astronomical association, for astronomy talks in prison, this request is not rejected but is transmitted to us.

5 What is allowed and what is forbidden

Rules are different according the various prisons and may vary substantially over time. It is the same for the available teaching in the various prisons. And there is a widely shared opinion that safety measures and the rules in prisons can vary according to politics and circumstances, like a pendular movement. A basic principle is an authorisation renewed for years can be supressed or on contrary some ban can be lifted. Some examples of things allowed or prohibited, according places or times : - to give some posters, calendars, ring notebooks, bookmarks, any object with cardboard... - to bring a laptop, a Macintosh, USB keys.. Sometimes the use of a laptop is possible, other times the talk is to be registered on a CD, or a USB key.

6 Some of our activities

Since 1998 we have made talks, courses, or other activity in numerous prisons. That is, in Paris and the surroudings : La Santé, Fresnes (men) and Fresnes (women), Fleury-Mérogis, Nanterre, Porcheville (juvenile prison), Poissy (for long prison sentences), Bois d'Arcy ; other parts in France : Melun, Liancourt (juvenile prison), Laval, Angers ; overseas territories : Domenjod in the Réunion island. That list is non-exhaustive. Most of the time, we give some courses or talks, adapted for the audience, juvenile as an example, and to the subject treated. The subject is sometimes chosen by us, sometimes by the teacher and some other times by the prisoner audience. In two circumstances, we organised observations for a partial solar eclipse in France, one time in the prison of Fresnes and another time in the juvenile prison of Liancourt. The sky was cloudy both times, that was actually better, because no special sunglasses for solar eclipses were provided for prisoners, but our audience. We invigilated an astronomy examination for a prisoner in the prison of Poissy. A few years ago, we set a continued astronomical program up, at the request of the SPIP of the prison La Santé. This program comprised three parts. First we gave five astronomical talks in the prison. Second we organised an outing from the prison to the Paris-Meudon Observatory, with a visit of the observatory during the day and some astronomical observations after the sunset. Third we exhibited astronomical documents and pictures in the library of the prison. It was rather complicated to finalise this exhibition because the library was closed during several weeks, no warder accepting this post. This program was extended by two additional talks, and a “meridian outing”. This outing comprised an other visit of the Paris-Meudon observatory, a visit of the meridian sundial of the Saint-Sulpice church, and an organ concert in this church by the titular organist that we thank very much. Let us note that the organ of the church Saint-Sulpice in Paris is often considered as the best organ in the world.

7 Some features of these talks

As for any talks in front of an non-specialized audience, its knowledge is very inhomogeneous. It depends also of the organisation of this lecture. As an example, if the lecture is organized by the library of the prison, the mean level of the audience is higher that in the case of a class for illiterate people. Whereas the audience of a public astronomy talk is generally composed of people who are interested by astronomy, an astronomy talk in prison is the first introduction to astronomy for the major part of the audience. However the questions can be of a rather good standard. The references to religion, particularly to the Coran, are frequent, and actually more and more frequent. How could those questions and comments be answered?:
"Yes, I believe in planets, because this is in the Coran."
"The Coran speaks about the expanding universe. What do you say about that?"
"Anyway, it is God who created the world."
"What about the seven skies?"
"Earth is flat, the proof is that all the planes fly over Europe."
"Anyway, astronomers are not religious."
Simple answers do not exist. In this case, I suggest that there are several independent ways to search the truth: science, religion, and also art, philosophy... For example, I explain that the seven skies do not correspond to the Universe studied by astronomers, that it is a symbol, an allegorical figure.

Some (personal) rules :

- as much as possible, answer to the questions. Do not forget that the audience has no access to internet and has only few books at disposal.

- be careful to avoid to humiliate somebody who asks a question, whatever the question.

- stay neutral, do not expose personal beliefs, do not give private information, never give an opinion about any religion.

It is very likely that many middle and high school teachers have similar problems They have to answer to the same questions, as well as some astronomers who go in schools for astronomical talks. It would be very useful that special sessions would be organized to help astronomers in front of this kind of problems to find some answers.

8 Our present activities

We expose as an example our activities during the recent time. The last year, we were asked by a mathematics teacher in the prison in Fresnes who organised a series of multidisciplinary lectures about "Black". During our cycle of six talks about "Black in Astronomy", we untiringly answered to countless questions about near and far the Muslim religion. Questions about astronomy happen only about during the third talk. However, to our satisfaction, when the cycle of planned talks was over, we were earnestly requested by prisoners to come again for an additional series of six astronomy talks. The subjects were chosen by prisoners by a democratic vote on our proposals. A few weeks ago, with the same mathematics teacher, we made again two talks about astronomy, and then at the end of the session, the audience asked insistently that we come again. The subjects were chosen among the questions of the participants. We gave also some talks in the prisons of Fleury-Mérogis and Poissy.

9 Conclusions

Any opportunity to increase the knowledge, the culture, and the though of prisoners is very important. This can help them to take relevant decisions after coming out of prison. When a former prisoner recognises me in the Paris metro, what happened several times, and discusses with me for a long time, I think that I did not waste my time when coming in prison About lectures organised by the philosopher François Chouquet at the Prison de la Santé some years ago, lectures to which I participated many times, a prisoner has written: "After years in isolation quarters, I took tremendous comfort from this cultural activity, which is a real opening on the world of lights, because I had the impression to rediscover the beauties of civilisation."

I wish to express my grateful thanks to :

Régis Courtin, astronomer at the Paris-Meudon observatory, my collaborator for more than thirteen years, with the hope that our collaboration will last a long time.

François Chouquet, philosopher, former in charge of the teaching for prisoners of the Parisian university Denis Diderot, who understood at once that prisoners could be interested by knowing the the largest part of atoms of our bodies are made in the cores of stars, and who asked to me for explaining this point to prisoners, and then many other astronomical subjects.

Eliane Lagrée, former teacher for illiterate prisoners at Fresnes, with whom I collaborated during many years.

References

Briot, D. 2011, in IAU Symposium, Vol. 260, The Role of Astronomy in Society and Culture, ed. D. Valls-Gabaud & A. Boksenberg, 475–480

SF2A 2019
P. Di Matteo, O. Creevey, A. Crida, G. Kordopatis, J. Malzac, J.-B. Marquette, M. N'Diaye, O. Venot (eds)

SSOCA (SYSTÈME SOLAIRE DE LA CÔTE D'AZUR) : THE FRENCH RIVIERA SOLAR SYSTEM

A. Crida[1], C. Durst[1] and M. Fulconis[1]

Abstract. We present SSOCA, the project of a representation of the Solar System to scale unique in its kind. The scale will be the same for the distances and the sizes of the bodies: 1:60 000 000. The Sun will be represented by the great dome of Nice Observatory (23m diameter) and the planets will be spread in the city of Nice and the French Riviera, at locations visible from the Observatory (and reciprocally). This will make SSOCA the world largest scale model of the Solar System that can be seen as a whole in one glance.

Keywords: Solar System, miniature model, outreach, scientific tourism

1 Introduction

Many miniature Solar System models exist. Most of them use a different scale for the sizes of the planets and for the distances, because of the hard constraint of the Earth's size compared to the astronomical unit (10^4 times smaller), so that the Earth is only a millimeter large if the astronomical unit is 10 meters long (which does not fit in most rooms) and the Sun-Neptune distance is 300 meters (which does not fit in many courtyards). But exaggerating the sizes compared to the distances gives people the wrong impression that the distances are not that long, and the Solar System not that empty.

There exists also a lot of models which respect the same scale for the sizes and the distances. All of them suffer either one of the two following issues, though: (i) the planets are too small to see details on their surfaces[*], or (ii) the miniature is so expanded that one can not see any celestial body from an other one, making the distances hard to perceive[†].

The Système SOlaire de la Côte d'Azur (SSOCA) will be the first to circumvent both disadvantages, while being the third largest Solar System scale model in the world. This facility will be accessible in public space and offer a lot of outreach possibilities, from scientific tourism to guided tours for classes or general public.

2 What is SSOCA ?

The headquarters and many researchers of the Observatoire de la Côte d'Azur are located on the gorgeous site of the Observatoire de Nice. This observatory was built thanks to sponsor Raphaël Bischoffsheim at the end of the XIX$^{\text{th}}$ century on a small mountain on the east side of the city. The site still harbours the fifth largest refracting telescope ever built. To host this huge instrument, with 17.89 m focal length, a huge dome was necessary. It has been designed by the famous engineer Gustave Eiffel, on top of a majestic building designed by the non less famous architect Charles Garnier. The resulting dome is 23 m in diameter (see Fig. 1). Implanted on the crest of the Mont Gros, at 380 m altitude, it is visible from all the city of Nice which lies at its feet, and from large distances along the French riviera.

We can use this dome as the Sun, defining a scale of 1:60 000 000. At this scale, an au is about 2.5 km so that the planets will not fit on the site of the Nice observatory, and our model should extend to 75 km. Fortunately, the Mont Gros site had been described by Garnier himself as "*the most beautiful balcony over the Côte d'Azur*". The view from here dominates the city of Nice, and provides a great overview of all the coast all the way to

[1] Observatoire de la Côte d'Azur, Boulevard de l'Observatoire, CS34229, 06304 Nice cedex 4, France – ssoca@oca.eu.
[*]E.g.: Sagan planet walk in Ithaca (USA) (scale: 1 to 5 billions) is 1.2 km long with a 3 mm Jupiter.
[†]E.g.: the largest of all, the Sweden Solar System (scale: 1 to 20 millions). See http://www.swedensolarsystem.se/en/.

Fig. 1. Left : Great dome of the Nice observatory, SSOCA's Sun. **Right:** Large refracting telescope inside the dome.

beyond Saint-Tropez when the sky is clear, through the Cap d'Antibes and the bay of Cannes. This offers the possibility to place the model planets in strategic locations from which the observatory can be seen, and that can be recognised from the observatory. Fig. 2 shows the places we foresee at the moment. The four terrestrial planets will be in Nice, and the four giant planets outside the city, at mountain tops or by the sea, all in spots accessible after a nice and easy hike.

In this way, visitors of the Observatory of Nice will be able to see at the same time the great dome and the places where the planets are displayed. The planets themselves, which will be between 10 cm and 2.2 m won't be visible with the naked eye, just like the real planets. Nonetheless, their position will be clearly identifiable, providing people with a great sense of the real immensity of the Solar System.

Reciprocally, hikers or pedestrians who stand by the representation of a planet will be able to appreciate how large the real Sun would appear from this planet by looking at the great dome of the Nice Observatory.

3 Models of the terrestrial planets

The four terrestrial planets should have diameters of 8.1, 20.2, 21.3 and 11.3 cm for Mercury, Venus, the Earth and Mars, respectively. These are sizeable, but not huge. Hence, their insertion in the urban landscape needs to be thought through. The sustainable design company *Le Collectif* (`http://www.lecollectif-sd.com`) proposes that each planet lays on a circular orientation table, on which the positions and distances of the other planets will be shown, thanks to a simplified fish-eye map of the surroundings and the region. In addition, we hope to have a two to three meters post with a recognisable sign on top to ease finding the planet from the distance. Each planet will be accompanied by two metallic plates engraved with information, one on the global SSOCA project and the Observatoire de la Côte d'Azur, and one on the planet itself, with scientific data and fun facts.

On top of that, each planet should have a unique animation. We have thought of the following.

Mercury The smallest planet will be located at Pont-Michel, a very animated crossroad next to a tram stop, in a popular neighbourhood. The tramway here drives at about 18 km/h, which turns out to be the speed of light at our scale: $\frac{3{\cdot}10^8 \text{ m/s}}{60\,000\,000} = 5$ m/s $= 18$ km/h. Looking at the tramway will therefore give people an idea of how long it takes for light to travel in the Solar System.

We plan to challenge visitors to run at the speed of light, by passing a few 5 m spaced lines on the walkway every second.

Venus For this planet, our preferred site is the garden of the Cimiez monastery, a peaceful place on a hill opposite the observatory. From here, one sees clearly the great dome just in front, but also the locations of Mercury and the Earth. Hence, we would like to have 3 fixed small spotting scopes pointed at these places.

Earth and Moon A perfect location for the Earth is the Nice-Riquier train station, which is the second busiest one in the Alpes-Maritimes département, and also the starting point of the bus line that goes to the Nice Observatory. Here, the plan is to recreate the conditions of a Sun eclipse, by putting the Moon between

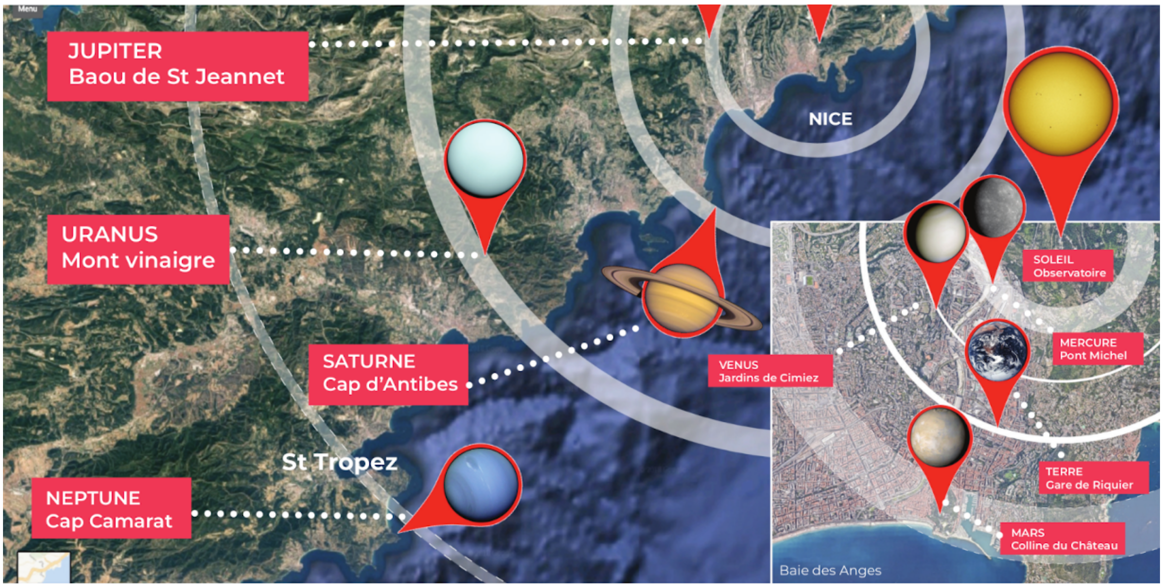

Fig. 2. Possible localisations of the planets in Nice and along the French Riviera. Grey circles represent the orbits.

the Earth and the Observatory, so that visitors sitting in a dedicated chair next to the Earth will see the Moon just in front of the great dome, with exactly the same angular diameter (as the scale will be respected).

Mars The castle hill in Nice, which is a nice and popular park between the harbour and the old town offers on its top a great spot to put Mars model, with view over the observatory and the Baie des Anges. We would like to use this space to put a seesaw in which the two arms would be of uneven length to recreate the gravity difference between Mars and the Earth. The necessary pedagogical explanation about the difference between the mass and the weight will be carefully displayed.

Main Asteroid Belt Many asteroids of the Main Belt have an orbit that, at the scale of SSOCA, runs through the western part of Nice, including the world famous Promenade des Anglais. In many points on the western hills or on the sea front, we would like to insert on the ground a metal plate on which the name of the asteroid would be engraved, together with its orbit and main physical characteristics. The asteroid itself would be a simple point.

Beyond the main asteroids (Ceres, Vesta, etc.), we are thinking of selecting also asteroids named after persons who marked the history of astronomy in Nice. Some of them do not have an asteroid named after them yet, so we are working on a proposal to the IAU for naming asteroids with adequate orbits after them.

4 Status of the project and perspectives

As this proceeding is written, this is still only a project. The sites are chosen, and the design is ready for the terrestrial planets. The giant planets, being of the scale of the meter (2.2 m for Jupiter) should be made differently and will be designed later. We hope to get authorisations and money to build the inner Solar System (up to the Main Asteroid Belt) in early 2020. This should lead to an official inauguration, and trigger the construction of the giant planets in the following years.

To follow the project, please see `https://www.oca.eu/ssoca/`.
Do not hesitate to contact us[1] and provide feedback (or even a sponsoring offer)!

SSOCA is an Observatoire de la Côte d'Azur project.
The feasibility study by *Le Collectif* and the preliminary work in designing the project have been funded by subsidies from the SF2A, Université Côte d'Azur, and the Provence Alpes Côte d'Azur région.
Many thanks to Roxanne Ligi with whom the idea arose, and to many colleagues whose suggestions and support helped improving the project.

SF2A 2019
P. Di Matteo, O. Creevey, A. Crida, G. Kordopatis, J. Malzac, J.-B. Marquette, M. N'Diaye, O. Venot (eds)

EDUCOSMOS, LA RECHERCHE DANS LA SALLE DE CLASSE

O. Suarez[1], Q. Branchereau[1], L. Abe[2], Ph. Bendjoya[2], J.P. Rivet[2], D. Vernet[1] and A. Marcotto[1,2]

Abstract. EduCosmos is a singular citizen science project that allows high- and medium-school students to participate in scientific research. The classes participating in this program perform astronomical observations remotely, from their schools. They use a 1-meter telescope belonging to the Observatoire de la Cote d'Azur (OCA - Nice, France), located at the Plateau de Calern (alt. 1280m), 70 km away from Nice. Students get involved in the study of asteroids, observing mainly light curves that will be used by the OCA scientists to complete their research. A 2-day teacher-training is proposed to teachers involved in this program, and is carried out in partnership with the local education authorities. Teachers are formed to the scientific project, the observations and the data reduction. During the school year, the participating classes have the opportunity to meet the OCA scientists that will introduce them to the scientific program

Keywords: outreach, education, teaching skills, astronomy activities

1 Introduction

Science transmission to the public and particularly making secondary school students (12−18 years-old) aware of science, is mostly important to build a responsible and educated society. Moreover, students and teachers are one of the pillars where the improvement of the scientific culture of the society can start. In addition, scientific vocations usually start during secondary education. This range of age is the target of the EduCosmos project, that aims to bring science to secondary students thorough the participation in an astronomical research project.

Astronomy is a science that naturally interest general public and young people. It can be an easy way to introduce in the classroom notions that produce usually less excitement from youngsters, as physics or maths. The challenge of EduCosmos is to get students interested in science and to help them to integrate the scientific method used in research. This way they will be armed to fight against obscurantism or fake news, since they will be able to apply the scientific method to be critical with all the information they are receiving.

2 The scientific project

EduCosmos classes perform observations for several scientific projects. The aim is to imply students in a real research work, to increase their interest in science. The main subject is asteroids, since they have several advantages when studied in the classroom: they are solar system objects, and solar system is included in the school curriculum; moreover, it is easy to link asteroids with earth sciences, so the possibility of widening to other subjects than physics is easier; and finally, asteroids are fascinating for students due to the possibility of one of them falling into Earth!

Students usually observe asteroids in photometry, to obtain light curves. They are easy to understand and a simplified data reduction procedure is easy enough for them to perform (see section 3.6)

3 Phases of the project

EduCosmos has several phases that are essential to the project.

[1] Observatoire de la Côte d'Azur, 06304 Nice, France
[2] Université Côte d'Azur, CNRS, Observatoire de la Côte d'Azur, Laboratoire Lagrange, Nice, France

3.1 Teacher training

To ensure the proper functioning of EduCosmos, is it essential to form the teachers to this project. A two-day teacher training session is proposed at the beginning of the school year to all the teachers implied in the program. Teachers are invited to assist in pedagogical teams, to invest students in the project through different subjects.

There are not prerequisites in astronomy to participate to this training that is focused on science (maths, physique, earth sciences) teachers. Two parallel groups are organised concerning the observations, according to the teacher's level. Beginners learn the basics of astronomical observations, while the advanced group focuses in more technical questions. Both groups are reunited to study the astronomical concepts concerning the scientific program the students will work in. The pedagogical part, with the adaptation of the scientific subject to the school curriculum is conducted also with the plenary group.

3.2 Visit of C2PU telescope

The visit of the telescope is important to make students concretize the idea of the telescope they will use. A one-day visit to the site of Calern, of the Observatoire de la Côte d'Azur, is organised each year which each class participating to the program. Students have the opportunity to visit all the instruments of this observation site, located at 1200m altitude that contains several observation facilities.

The C2PU telescope is a 1-m telescope refurbished in 2010 for science and education (`http://c2pu.oca.eu`). It is fully remote-accessible and it has imaging and polarimetry capabilities.

3.3 Astronomy sessions in the classroom

To prepare the students for the participation to the scientific project, several astronomy sessions in the classroom are organised. They have usually a duration of 2h and are organised in two parts: during the first part the astronomical notions are provided in an interactive way by an astronomer. The second part is devoted to games or activities related to the given notions.

These sessions introduce students to astronomy and they allow them to understand the context and the importance of the observations they will perform.

A special session is organised to prepare students to the observations with C2PU. A game conceived by our team is used to fix the different steps needed for a correct observation.

Fig. 1. Left: The C2PU telescope. **Right**: The EduCosmos observing-game.

3.4 First direct sky observation

Even if it is not a part of the astronomical research it is important to let students become familiar with the night sky. Moreover, since the EduCosmos program is often carried out with students from disadvantaged areas, many of them have never gazed at the night sky and this is their first experience under the stars.

We organise a night session in an educational institution, the International Center of Valbonne, where the OCA has installed an amateur 40-cm telescope. Part of this evening is devoted to the visual discovery of the night sky, while during the other part students understand the working of a telescope and they observe through it.

3.5 Remote observation with the C2PU telescope

One remote-observation session is organised with each class participating to EduCosmos. They spend about 3 hours, including the calibrations (pointing and focus) and the scientific observations. Several groups are formed for the observation, each taking care of a particular task.

Two computers are needed at the school, with internet access. They connect to the telescope control software and to the camera control software and allow students to manage the telescope remotely. A webcam has been installed in the telescope dome to follow the movement of the telescope and to make students realize that they are really controlling it. The images taken by the telescope are seen by students in real-time.

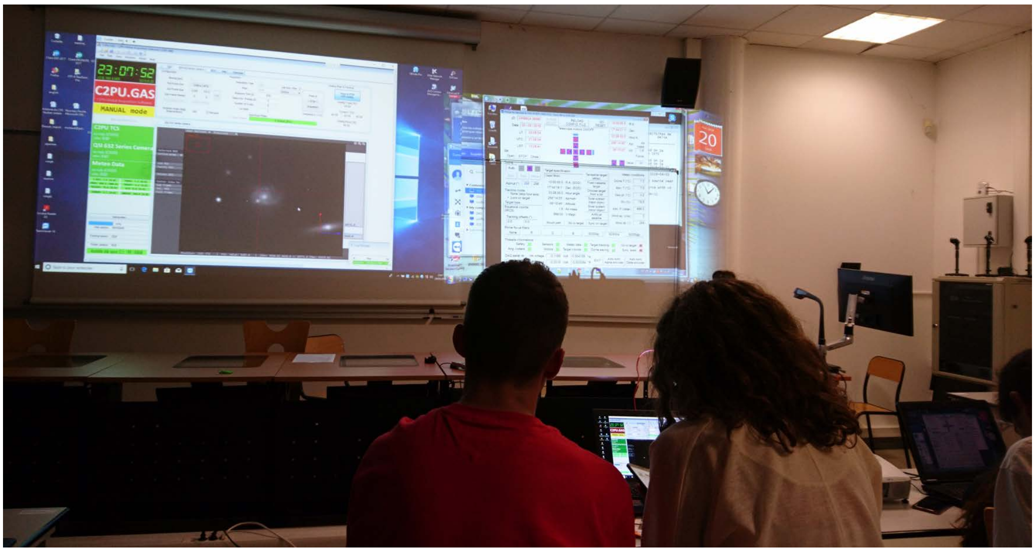

Fig. 2. Observation with the C2PU telescope from the *Lycée Estienne d'Orves* at Nice.

3.6 Data reduction

We train students to perform the data reduction of the light curves they have observed. We have developed a playful activity where students arrange several images of a rotating asteroid (Itokawa's images), and they reconstruct a fictitious light-curve, by measuring the illuminated area in each image. This is useful for them to understand the meaning of a light curve and how it is related to the morphology of the asteroid.

Data reduction continues with real data. We have developed a tutorial to facilitate the use of the image analysis package "AstroImageJ". Without substantial problems, following this tutorial, students get a light curve from the raw images in 30 or 40 minutes.

The goal of making pupils reduce the data is to show them that observational research in astronomy does not consist in looking at the sky, but in understanding the information we can obtain from the different observed objects.

4 Funding and participation

EduCosmos project is supported by the Observatoire de la Côte d'Azur which provides the telescopes and the personal. The participation of classes and additional personal is funded every year with the funds of different

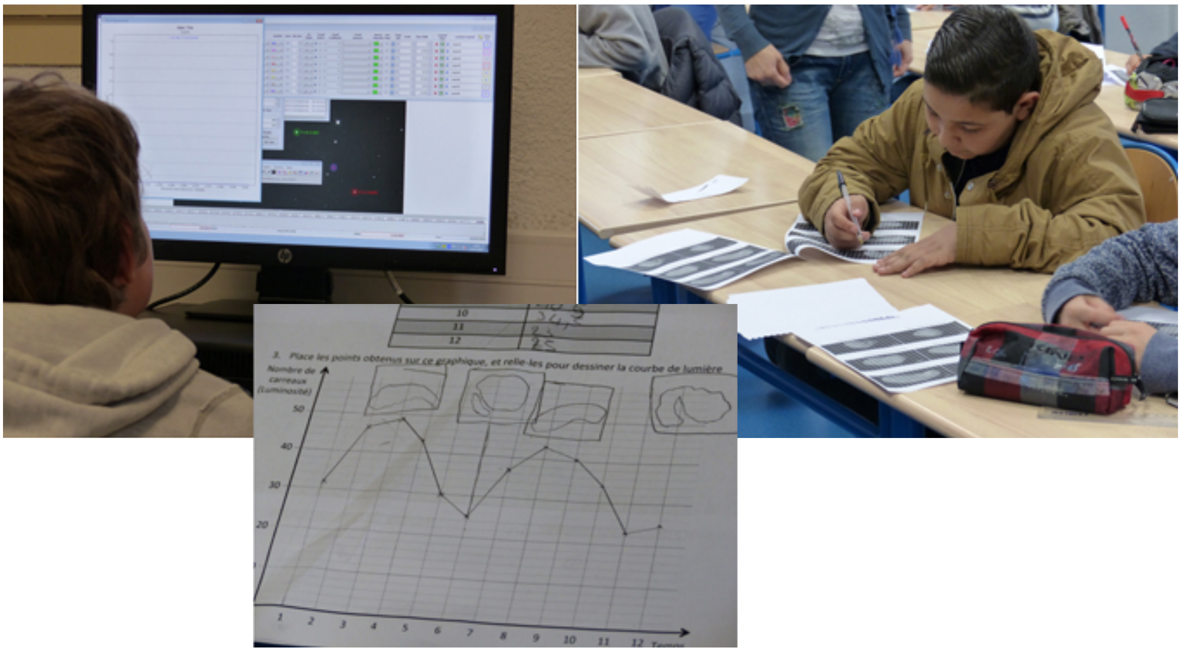

Fig. 3. Data reduction process and exercice.

calls released by the Provence-Côte d'Azur Region (project APERLA), the Alpes Maritimes Departement, or the national project *Cordées de la réussite*. In the past, it has also been funded by the *MEDITES* project, belonging to the French Government program *Investissements d'Avenir*.

Several of these programs are devoted to students in underprivileged areas. The local education authorities (*Rectorat*) help us to select the classes belonging to this population. The capacity of EduCosmos is 10 classes per school year. Over this number it is difficult for us to provide all the different activities related to the program.

The project started in 2012 with a pilot school, and up to know a total of 60 different classes, making some 1500 students have participated.

5 Conclusions

EduCosmos is a project that allow students to participate to a research project by the observations with a professional telescope. This project has several phases that have been detailed here.

A total of 10 classes (∼250) students per year can participate to this project, with about 1500 students having participated from the beginning of the project in 2012.

SF2A 2019
P. Di Matteo, O. Creevey, A. Crida, G. Kordopatis, J. Malzac, J.-B. Marquette, M. N'Diaye, O. Venot (eds)

THE "DE LA PLAGE AUX ÉTOILES" FESTIVAL OF COLLIOURE

M. Sylvestre[1] and M. Montargès[2]

Abstract. From 2011 to 2014, and since 2018, the *De La Plage aux Étoiles* festival of Collioure has invited tourists and inhabitants in Pyrénées-Orientales to discover recent results in astronomy and astrophysics, with exhibitions, conferences and stargazing sessions. After having organised it 5 times and with a sixth festival in preparation in 2019, and as we got a grant from the SF2A in 2018, we wish to present this festival, its evolution, and the feedback from the audience.

Keywords: Outreach

1 Introduction

Fig. 1. A view of Collioure (credit: E. Lagadec).

Collioure (Fig. 1) is a village in the South of France (Pyrénées-Orientales department), 25 km north of Spain. As it is quite far from large cites with astrophysics laboratories (e.g Montpellier is at 140 km), or observatories (the *Pic du Midi* observatory is at 245 km), there were few outreach events or opportunities for the general public to meet researchers. However, we realised that many people have questions about the night sky or celestial bodies, and that they cannot always discriminate genuine information from fake science. Consequently, in 2011, we decided to create *De La Plage aux Étoiles* (From the beach to the stars), an outreach festival about astronomy and astrophysics in Collioure, in order to meet this demand. This is also a great opportunity to show the evolution of our knowledge by talking about the latest scientific results in our field, such as Pluto's

[1] School of Earth Sciences, University of Bristol, Bristol, UK
[2] Institute of Astronomy, KU Leuven, Celestijnenlaan 200D B2401, 3001 Leuven, Belgium

new moons in 2012 or the first black hole image in 2019. Besides, we can explain the activities of French astrophysics laboratories, as the general public often believes that all the research in astrophysics is done at NASA. Here, we present the organisation of this event and what it taught us about the expectations of the general public.

2 Organisation

The *De La Plage aux Étoiles* festival is located at the Cultural Centre of Collioure. It lasts a week and is composed of three types of events:

- An exhibition displayed during the day all the week, for which we offer guided tours to answer questions of the visitors. We also display videos about astronomy and space.

- Conferences on Monday (for the opening of the festival), Friday, Saturday and Sunday evenings from 6 pm to 7 pm.

- Stargazing with telescopes on Friday, Saturday and Sunday evenings from 9 pm to 12 am. We work with local amateur astronomers and we ask the Collioure city council to switch off 5 street lamps around the Cultural Centre, which makes the Milky Way visible.

The festival is entirely free and open to all ages, astronomy enthusiasts or novices.

For the four first festivals (2011-2014), *De La Plage aux Étoiles* was organised without any formal structure and the invoices were paid by the Collioure city council. In 2017, we created an association *loi 1901* (with 7 volunteers to this day) in order to get our own budget. It allowed us to get grants from various organisations (Collioure city council, Pyrénées-Orientales department council, SF2A) and to get more flexibility on our expenses. We were thus able to pay for the travels, meals and accommodation of 3 speakers in 2018, and 2 in 2019, whereas we could only have a single guest per year at the previous festivals. This budget also covers the printing of flyers, posters and a banner. The total cost of a festival is $\sim$ 3000 euro.

Fig. 2. Examples of posters for the *De La Plage aux Étoiles* festival in 2012 (left) and 2018 (right).

We also have sponsors who provide non-financial help such as Paris Observatory and Côte d'Azur Observatory who lend us their exhibitions for free, the local radio France Bleu Roussillon, and the association of retail traders and artisans of Collioure.

The *De La Plage aux Étoiles* festival is advertised by distributing posters (see Fig. 2) and flyers in the village (official displays, visitor center, hotels, shops...), in the official flyer containing the list of all the numerous summer activities in Collioure, on local tourism websites, in astronomy websites and magazines (AFA/Ciel & Espace, SAF/L'Astronomie), and in local media such as the *L'Indépendant* newspaper or the *France Bleu Roussillon* radio. The festival has also its own website`https://www.astrocollioure.fr`.

3 Audience and visitors feedback

We have monitored the number of visitors at the festival year after year (see Fig. 3). In 2018, we welcomed 1009 visitors. The attendance levels at the exhibition are very variable. Conferences are quite successful, as they attract 60 to 100 people each, except the first year of the festival (2011) where the event was less advertised compared to the following years. However, our worst audience at a conference was reached in 2014 on the Saturday, when we proposed a FAQ (Frequently Asked Questions) conference where the audience could ask any astronomy related question to three researchers. Apparently, the audience in Collioure is not ready for this kind of open format (although the people who attended had a really good time as we had a loud timer to limit the length of the answers from the researchers). The stargazing sessions are the most popular element of *De La Plage aux Étoiles*, with a record number of 280 visitors on the last evening in 2018.

These results could be explained by the fact that while the general public is curious about astronomy, there is still a lot of self-censorship. Many people seem to think that even if it is an outreach event, they need to have some prior knowledge to be able to understand its content. Stargazing sessions are perceived as more accessible to the general public, and visitors often like to discuss with the researchers at that time, in a more informal and confidential setting. Our visitors seem to really enjoy the various opportunities to discuss with researchers, and are pleasantly surprised to meet scientists who do not match with the stereotypes (e.g young people, women, French researchers...). After their visit, especially after the stargazing sessions, people realise that our content is totally accessible and many come back to the festival the following days. We also have people who came to our festival on several years.

We noticed that the organisation of *De La Plage aux Étoiles* benefits from its local roots. Indeed, one of the founder of this event and several volunteers of the association come from Collioure, which makes the organisation easier. It is also a valuable asset when we advertise this event.

4 Conclusion

The *De La Plage aux Étoiles* festival in Collioure has been organised 5 times and a 6th edition is currently prepared. With a small budget and a reduced team, we managed to organise a festival with up to 1009 visitors over a week.

M. M. and M. S. would like to thanks the volunteers of the *De La Plage aux Étoiles association*: J.-P. José, R. José-Bigaire, S. Mattei, V. Coudé du Foresto, and R. Boutet. Stargazing sessions are made possible and successful by W. Salies, J.-P. Gélabert, and T. Hervé. We also thank L. Delcroix and A.-M. Rastol from the Cultural Centre as it is always a pleasure to organise this event with them.

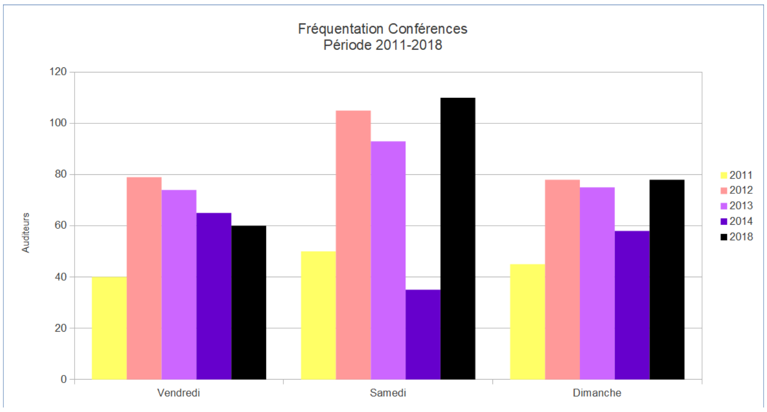

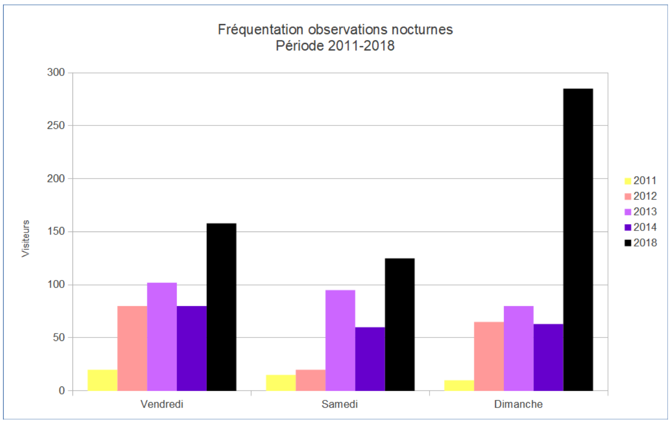

Fig. 3. Attendance levels at the *De La Plage aux Étoiles* festival for the exhibitions (top) and the stargazing sessions (bottom).

Session 15

Atelier général PNPS

SF2A 2019
P. Di Matteo, O. Creevey, A. Crida, G. Kordopatis, J. Malzac, J.-B. Marquette, M. N'Diaye, O. Venot (eds)

DETERMINING SURFACE ROTATION PERIODS OF SOLAR-LIKE STARS OBSERVED BY THE KEPLER MISSION USING MACHINE LEARNING TECHNIQUES

S.N. Breton[1,2], L. Bugnet[1,2], A.R.G. Santos[3], A. Le Saux[1,2], S. Mathur[4,5], P.L. Pallé[4,5] and R.A. García[1,2]

Abstract. For a solar-like star, the surface rotation evolves with time, allowing in principle to estimate the age of a star from its surface rotation period. Here we are interested in measuring surface rotation periods of solar-like stars observed by the NASA mission *Kepler*. Different methods have been developed to track rotation signals in *Kepler* photometric light curves: time-frequency analysis based on wavelet techniques, autocorrelation and composite spectrum. We use the learning abilities of random forest classifiers to take decisions during two crucial steps of the analysis. First, given some input parameters, we discriminate the considered *Kepler* targets between rotating MS stars, non-rotating MS stars, red giants, binaries and pulsators. We then use a second classifier only on the MS rotating targets to decide the best data-analysis treatment.

Keywords: asteroseismology, rotation, solar-like stars, kepler, machine learning, random forest

1 Introduction

Rotation plays an important role in stellar evolution. For cool main-sequence (MS) dwarfs (G, K and M spectral type), age may be determined thanks to gyrochronology (Skumanich 1972): surface rotation evolves roughly as the square root of its age. Even if recent studies suggested that at a given stage of its evolution, the braking of a solar-like star is reduced (van Saders et al. 2016), this relation seems to be verified while the stars remain on the main sequence.

In this work, we use *Kepler* (Borucki et al. 2010) photometric light curves obtained with the KADACS pipeline (*Kepler* Asteroseismic Data Analysis and Calibration Software, García et al. 2011; García et al. 2014). The KADACS pipeline has been specifically designed to correct for *Kepler* light curves from instrumental effects and properly stitch the quarters in an optimized way for asteroseismology studies. We consider different high-pass filters (20, 55, and 80 days) for the processing of the light curves to be sure that rotation period is not filtered out. Rotation period is then extracted thanks to a combination of different methods (Global Wavelet Power Spectrum GWPS, AutoCorrelation Function ACF and Composite Spectrum CS) as described in Mathur et al. (2010), García et al. (2014), Ceillier et al. (2016) and Ceillier et al. (2017). However, the computed rotation period may differ from one KADACS filter to another and from one method to another. Dozens of thousands of stars have to be considered with, until now, no other solution than to use a pre-defined hierarchical decision tree and make a final visual inspection of the conflicting cases. A machine learning algorithm seems the ideal tool to make the decision over the stars of our data set. Before performing this analysis and to avoid any bias, it is nevertheless necessary to distinguish main sequence rotators from other types of targets.

2 Rotators classification

[1] IRFU, CEA, Université Paris-Saclay, 91191 Gif-sur-Yvette, France
[2] AIM, CEA, CNRS, Université Paris-Saclay, Université Paris Diderot, Sorbonne Paris Cité, 91191 Gif-sur-Yvette, France
[3] Space Science Institute, 4750 Walnut Street Suite 205, Boulder, CO 80301, USA
[4] Instituto de Astrofísica de Canarias, 38200 La Laguna, Tenerife, Spain
[5] Universidad de La Laguna, Dpto. de Astrofísica, 38205 La Laguna, Tenerife, Spain

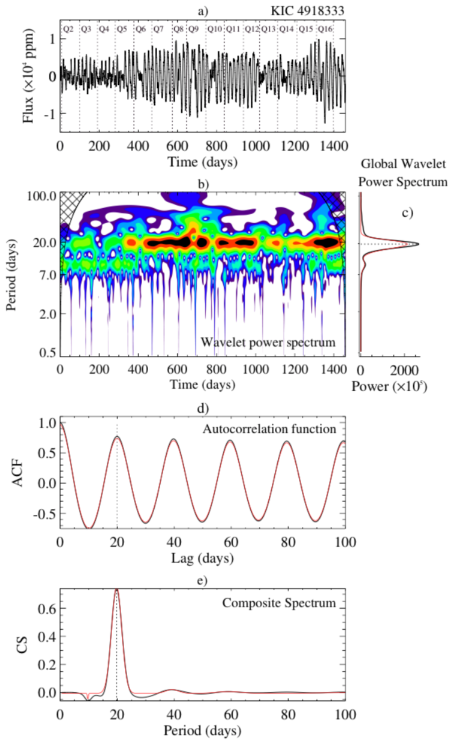

Fig. 1. *From top to bottom* - example of *Kepler* photometric lightcurve analyzed with A2Z pipeline (Mathur et al. 2010), wavelet power spectrum, autocorrelation function and composite spectrum. Extracted from Santos et al. (submitted to ApJ).

Our set of stars consist of 14,441 M and K dwarfs based on the *Kepler* star properties catalog from Mathur et al. (2017), whose rotation periods have been studied by Santos et al. (submitted to ApJ). However, the sample can be polluted by red giants (RG), classical pulsators (CP) or eclipsing binaries. Santos et al. identified these pollutors by visually checking the light curves. Here, we propose to use artificial intelligence methods to automatically detect such pollutions. We train a first random forest algorithm (with the Python package *scikit-learn*, Pedregosa et al. 2011) in order to identify those different targets. The principle of a random forest algorithm is briefly reminded in annex A1. The input parameters are:

- periods computed by each method, $P_{\rm GWPS}$, $P_{\rm ACF}$, $P_{\rm CS}$, and related control values $H_{\rm ACF}$, $G_{\rm ACF}$ and $H_{\rm CS}$ (see Figure 1 and Ceillier et al. 2017 for further explanation);
- photometric activity proxy $\rm S_{ph}$ (García et al. 2010, 2014; Mathur et al. 2014);
- FliPer values (see Bugnet et al. 2018, 2019);
- effective temperature $T_{\rm eff}$ and surface gravity $\log g$ from Mathur et al. (2017).

Those parameters have been chosen because their values are directly related to stellar types and rotation properties. $T_{\rm eff}$ and $\log g$ are good parameters to distinguish between red giants and MS stars. The FliPer metric allows us to help disentangling the proposed classes of stars attending to their power in the PSD. Rotation periods computed by the three methods combined with all the other related parameters ($H_{\rm ACF}$, $G_{\rm ACF}$ and $H_{\rm CS}$) allow

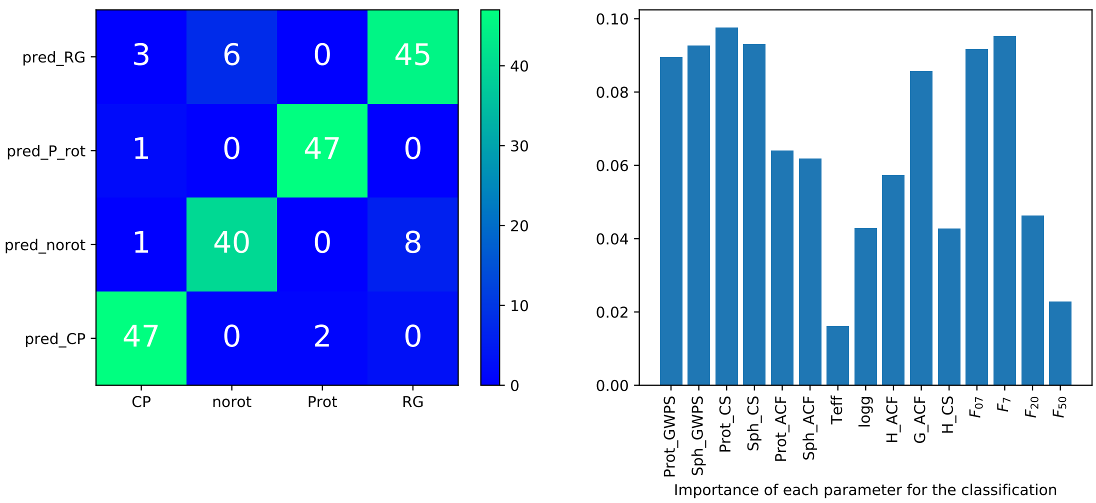

Fig. 2. *Left panel* - classification result for a test set of 200 stars. The algorithm has been trained with 600 stars that were visually classified before-hand. CP stands for classical pulsator, norot for MS non-rotating star, Prot for MS rotating star, RG for red giant. The real class of an element corresponds to its column label, the class assignated by the classifier corresponds to the line label. Accuracy of the classification is 0.895. *Right panel* : relative importance of each parameter used for the classification.

the classifier to decide whether the measured signal corresponds to a rotation period or not. Figure 2 shows the result of the classification of the test set. Stars are globally well classified, except for some non-rotating main-sequence stars and red giants with close $T_{\rm eff}$ and $\log g$. On a $T_{\rm eff}$-$\log g$ diagram, those stars would lay in the subgiants region. Thus, one of the next improvements of the classifier will be to add the possibility for the algorithm to give a label *subgiant*.

3 Period determination

A second random forest classifier is trained to determine the best filter to consider (20, 55, 80 days) to retrieve the most probable rotation period $P_{\rm rot}$. We assume that this $P_{\rm rot}$ will be given by the wavelet method of the correct filter. Comparing the best filter choice and the classifier choice gives us an estimation of the classifier accuracy. Sometimes, even when the classifier choice is not the filter chosen by Santos et al. (submitted to ApJ), the period estimate is approximately the same. If the period differs by less than 10% from the true period labelled on the training set, we consider that the classifier is right and compute what we call the true accuracy (e.g. the true accuracy score is given between the ratio of stars with a retrieved period laying between $\pm 10\%$ error according to the right period over the total number of stars). Our 14,441 stars are distributed between a training set of 12,275 stars (85 %) and a test set of 2,166 stars (15 %). The distribution is randomly chosen. To check whether it could be responsible for a bias in the training, we compute ten trainings of the algorithm with different distributions each time. The average classifier accuracy and true accuracy over those ten runs are respectively 0.936 and 0.979 (see Figure 3 for an example of the training).

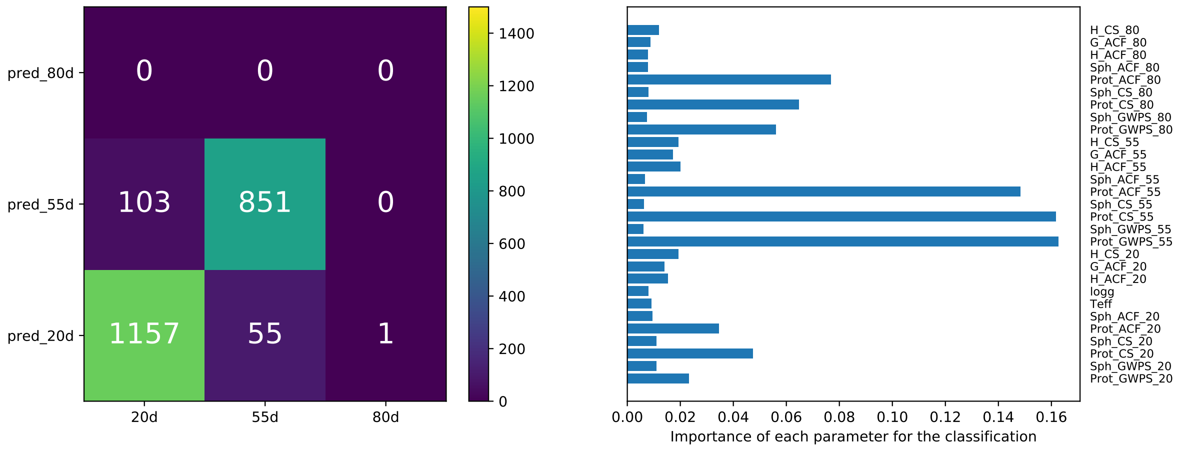

Fig. 3. *Left panel*: filter-choice result for a test set of 2166 rotating MS stars. The algorithm was trained with 12,275 stars. The total number of stars is 14,441. Classifier accuracy is 0.927. The true accuracy on the period is 0.974. *Right panel*: relative importance of each parameter used for the classification. $P_{\rm GWPS}$, $P_{\rm ACF}$, $P_{\rm CS}$, $H_{\rm ACF}$, $G_{\rm ACF}$, $H_{\rm CS}$ and $S_{\rm ph}$ values are considered for each filter (20, 55, 80) and consequently subscripted in the legend of the plot.

4 Conclusions

Random forest classifiers prove themselves to be an excellent tool to study stellar rotation properties and allow us to deal with large datasets. On the two distinct steps of the analysis, we get promising accuracy values of 0.895 for the rotators classification and 0.979 for the retrieval of rotation period. Especially, the classifier seems particularly efficient to retrieve the filter that leads to the rotation period. However, we still need to improve the accuracy of the results in the future, especially by using larger data sets. One of the goal of future work will be to apply the analysis to datasets from other missions like K2 or TESS.

This paper includes data collected by the *Kepler* mission and obtained from the MAST data archive at the Space Telescope Science Institute (STScI). Funding for the *Kepler* mission is provided by the NASA Science Mission Directorate. STScI is operated by the Association of Universities for Research in Astronomy, Inc., under NASA contract NAS 526555. This work has been partially fund by the GOLF and PLATO grants at the CEA. A.R.G.S acknowledges the support from National Aeronautics and Space Administration (NASA) under the grant NNX17AF27G. S.M. acknowledges the support from the Ramon y Cajal fellowship number RYC-2015-17697. S.N.B. thanks all the SSEBE team at the IAC for the all the scientific discussions and support during the internship period at the IAC.

References

Borucki, W. J., Koch, D., Basri, G., et al. 2010, Science, 327, 977
Bugnet, L., García, R. A., Davies, G. R., et al. 2018, A&A, 620, A38
Bugnet, L., García, R. A., Mathur, S., et al. 2019, A&A, 624, A79
Ceillier, T., Tayar, J., Mathur, S., et al. 2017, A&A, 605, A111
Ceillier, T., van Saders, J., García, R. A., et al. 2016, MNRAS, 456, 119
García, R. A., Ballot, J., Mathur, S., Salabert, D., & Regulo, C. 2010, arXiv e-prints, arXiv:1012.0494
García, R. A., Ceillier, T., Salabert, D., et al. 2014, A&A, 572, A34
García, R. A., Hekker, S., Stello, D., et al. 2011, MNRAS, 414, L6
García, R. A., Mathur, S., Pires, S., et al. 2014, A&A, 568, A10
Mathur, S., García, R. A., Ballot, J., et al. 2014, A&A, 562, A124
Mathur, S., García, R. A., Régulo, C., et al. 2010, A&A, 511, A46
Mathur, S., Huber, D., Batalha, N. M., et al. 2017, ApJS, 229, 30
Pedregosa, F., Varoquaux, G., Gramfort, A., et al. 2011, Journal of Machine Learning Research, 12, 2825
Santos, A. R. G., Garca, R. A., Mathur, S., et al. submitted to ApJ, ApJ
Skumanich, A. 1972, ApJ, 171, 565
van Saders, J. L., Ceillier, T., Metcalfe, T. S., et al. 2016, Nature, 529, 181

A1 Random forest classifiers

A random forest algorithm is a useful machine learning tool for classification. Thanks to the training set, the algorithm is able to grow a *forest* of decision trees that will then be used to assign a label to new data. A simple example of decision tree is showed in Figure 4

Decision trees are built with the following principle. The training data set is split from the root of the tree according to the value of one of the parameters of the data. Each resulting node gets a Gini score G :

$$\mathrm{G} = \sum_{k=1}^{\mathrm{N_{classes}}} p_k \times (1 - p_k); \tag{4.1}$$

that quantifies its purity (e.g. the proportion of each class for the data assigned to the node). A Gini score of 0 means that a node is totally pure (i.e. that all the elements assigned to the node have the same class). When the score of a node is low enough, the splitting stops: the node becomes a leaf that assignates to new data the label of the dominant class.

In order to choose a split close to the optimal possibility without consuming too much computation time, a number of possible splits is randomly generated and the best one is chosen over this sample.

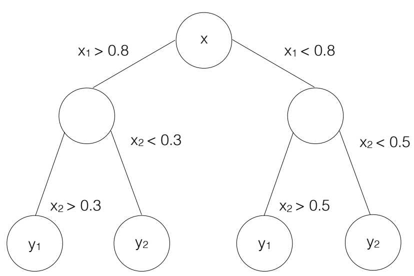

Fig. 4. Example of decision tree designed to classify two-parameters data $\boldsymbol{x} = \{x1, x2\}$ within two classes $\boldsymbol{y}_1$ and $\boldsymbol{y}_2$.

SF2A 2019
P. Di Matteo, O. Creevey, A. Crida, G. Kordopatis, J. Malzac, J.-B. Marquette, M. N'Diaye, O. Venot (eds)

SUN-LIKE OSCILLATIONS IN THE POPULATION II GIANT HD 122563

O. Creevey[1], F. Thévénin[1], F. Grundahl[2], E. Corsaro[3], M. F. Andersen[2], V. Antoci[2], L. Bigot[1], R. Collet[2], P. L. Pallé[4], B. Pichon[1] and D. Salabert[5]

Abstract. We have been monitoring the metal-poor Population II giant, HD 122563, for radial velocity variations since 2016 using the SONG telescope on Tenerife. We have detected the global seismic quantity $\nu_{\rm max}$ which provides information related to the stellar parameters. By combining these data with complementary data, we derive a new precise surface gravity, radius and distance to the star. Our results are corroborated by using the parallax from Gaia DR2. We present these results and some of their implications.

Keywords: asteroseismology, stars: individual: HD 122563, stars: Population II, stars: fundamental parameters

1 Introduction

HD 122563 (V=6.2 mag, $14^{\rm h}02^{\rm m}$ $31.8^{\rm s}$, +09°41′09.95") is a bright metal-poor [M/H] = –2.4 giant star. As such it can be observed using many independent methods. It was first referenced in the literature over 50 years ago (Pagel 1963), however, despite its brightness and interest as a prototype for similar giants in the Galactic halo, today we still debate some of its most fundamental stellar parameters (for example Creevey et al. 2012; Casagrande et al. 2014; Karovicova et al. 2018; Collet et al. 2018, and references therein).

Analyses presented in Creevey et al. (2012) (C12 hereafter, their figure 4) and Creevey et al. (2014) (their figure 3) clearly indicated discrepancies between observations, interpretation and models. The former indicated that standard evolutionary tracks fail to reproduce the observed position of this star in the HR diagramme and unreasonable assumptions in some tunable parameters are needed. The latter showed a comparison of interferometric with spectroscopic analyses of this star's stellar parameters which hinted towards a potential problem in $\log g$.

Given the current discrepancies along with the fact that this star is a benchmark for distant metal-poor giants, we applied to observe this star using the radial velocity instrument on the Hertzsprung telescope in Tenerife in order to detect oscillations and provide a fresh perspective on this star.

In this work we describe the radial velocity observations of this star (Sect. 2), along with an interpretation using the asteroseismic scaling relation for $\log g$ (Sect. 3). We use the most recent data from Gaia DR2 to test our analysis, and after some brief comparisons, we summarise our conclusions in Sect. 4.

2 Observations

2.1 New observations

We obtained time series radial velocity observations with the 1-m Hertzsprung SONG telescope from April 2016 to December 2017. The Hertzsprung telescope is a node of the Stellar Observations Network Group (SONG) located at the Observatorio del Teide. All observations were obtained using an iodine cell for precise wavelength

[1] Université Côte d'Azur, Observatoire de la Côte d'Azur, CNRS, Laboratoire Lagrange, France
[2] Stellar Astrophysics Centre, Department of Physics and Astronomy, Aarhus University, Ny Munkegade 120, 8000 Aarhus C, Denmark
[3] INAF - Osservatorio Astrofisico di Catania, via S. Sofia 78, 95123-I, Catania, Italy
[4] Instituto de Astrofisica de Canarias, 38205 La Laguna, Tenerife, Spain
[5] Previous affil: IRFU, CEA, Universit Paris-Saclay, F-91191, Gif-sur-Yvette, France

	Observations					Derived Parameters				
θ^1	[mas]	0.940	$\pm$	0.011	$\log g$	[dex]	1.39	$\pm$	0.01
$F_{\rm bol}{}^1$	[erg/cm/s]	13.16	$\pm$	0.36	$\log g_{\rm V17}$	[dex]	1.42	$\pm$	0.01
$T_{\rm eff}{}^1$	[K]	4598	$\pm$	41	d	[pc]	305	$\pm$	10
$\nu_{\rm max}$	[μHz]	0.35	$\pm$	0.01	$d_{\rm V17}$	[pc]	296	$\pm$	9
$\pi^2_{\rm GDR2}$	[mass]	3.444	$\pm$	0.063	$d_{\rm GDR2}$	[pc]	290	$\pm$	5

Table 1. Properties derived from this work, except for those from [1]C12 and [2]Gaia Collaboration et al. (2018).

calibration. A spectral resolution of 80 000 and an exposure time of 900s was used throughout. The data were reduced using the standard SONG pipeline (Andersen et al. 2014; Grundahl et al. 2017). The radial velocity (RV) time series of 387 data points is presented in Figure 1, left panel and the typical uncertainty on the RV was found to be in the 11-14m/s range.

We used the Diamonds Bayesian Inference tool (Corsaro & De Ridder 2014) to model the power spectral density (PSD) of the star. The PSD and the best-fit model are shown on the right panel of Fig. 1, and incorporates a flat noise component, two Harvey-like profiles to account for granulation-driven signal, and a Gaussian envelope to model the oscillation power excess (Corsaro et al. 2015). A clear excess of power due to the oscillations is detected at 3 μHz, this is referred to as $\nu_{\rm max}$. We used the marginal distribution of $\nu_{\rm max}$ from this analysis in our subsequent analysis.

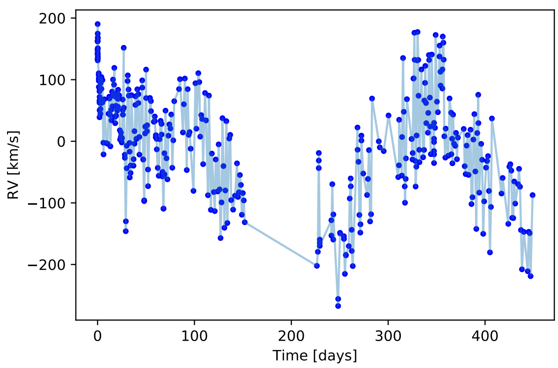

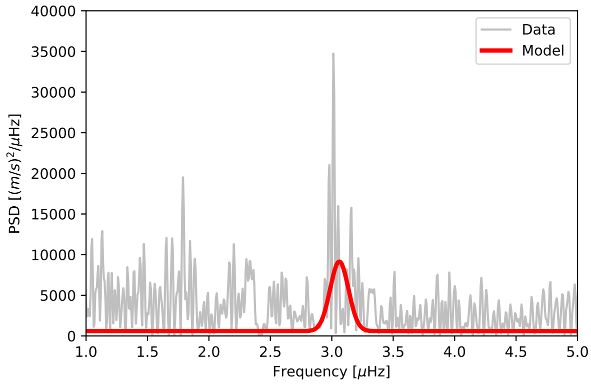

Fig. 1. Left: Time series radial velocities of HD 122563 for the first year of observations. We have subtracted the mean radial velocity and the first observation point is at time T0 = 2457509.38158 Julian days. **Right:** Frequency spectrum of the time series (grey) with a model for the power excess overplotted in red.

2.2 Literature observations

We use the $T_{\rm eff}$ of HD 122563 from C12. This is in agreement with that derived by Karovicova et al. (2018) using independent interferometric measurements, Casagrande et al. (2014) using the infra-red flux menthod, and Heiter et al. (2015) who provide a recommended value based on a compilation of spectroscopic measurements, see Creevey et al. (2019). As we would like to propagate all of the information from the observations, we use the reported bolometric flux $F_{\rm bol}$ and angular diameter θ, where extinction $A_V = 0.01$ mag was assumed.

3 Analysis

3.1 Surface gravity and distance from asteroseismology

The surface gravity of a star can be derived using the so-called *asteroseismic scaling relation* and is given by

$$\frac{\nu_{\rm max}}{\nu_{\rm max\odot}} = f_{\nu_{\rm max}} \frac{g}{g_\odot} \sqrt{\frac{T_{\rm eff\odot}}{T_{\rm eff}}} \tag{3.1}$$

where $f_{\nu_{\max}} = 1$ and $\nu_{\max\odot} = 3050\ \mu$Hz in the classic form (Kjeldsen & Bedding 1995) and $f_{\nu_{\max}} \neq 1$ where corrections are proposed. By using the observational data (θ,$F_{\rm bol}$,$\nu_{\max}$) along with the solar values of $\log g_\odot = 4.438$, $T_{\rm eff\odot} = 5772$ K, we performed Monte-Carlo like simulations to derive the stellar parameters ($\log g$, $T_{\rm eff}$), using the methods described in Creevey et al. (2019). By using a prior on the mass between [0.80,0.90] we additionally derived the radius $R_\star$ and distance d (and consequently the luminosity $L_\star$). In Figure 2 the blue contour lines indicate the density distributions of $\log g$ and d from these results. The green contours show the same results but by setting $f_{\nu_{\max}} = (\mu/\mu_\odot)^{1/2}(\Gamma_1/\Gamma_{1\odot})^{1/2}$, where μ and Γ denote respectively the mean molecular weight and the adiabatic exponent, see Viani et al. (2017) (V17 hereon) and references therein. The derived $L_\star$ and $T_{\rm eff}$ are also shown as the blue error box on the right panel, and for comparison we also show the values from C12 as the grey box. We indicate a vector in blue which represents the relative change in the position if we impose $A_V = 0.08$ mag (Lallement et al. 2014).

3.2 *Distance and surface gravity from Gaia DR2*

We derived d and $\log g$ using the same methodology as above, but by using the set (π, θ) and the mass prior, where π is the parallax from Gaia DR2 (Gaia Collaboration et al. 2018). In Fig. 2 the solution is represented by the black contours (left) and the black box (right).

As can be seen in both figures, similar solutions are obtained using the independent approaches. $\log g$ differs only by $0.02 - 0.04$ dex, and d by less than 1.5σ. Consequently the $L_\star$ agree also to 1σ (1σ error boxes are shown on the right panel). In Fig 1 right panel we also show standard evolutionary tracks from the BASTI models in green (Pietrinferni et al. 2004), and a model from the updated tracks in red (Hidalgo et al. 2018) using solar-scaled canonical models*. Using fine-tuned evolution models from the CESAM evolutionary code (Morel 1997), we could reproduce the observed position but only be reducing the mixing-length parameter by 0.3 from the reference solar value.

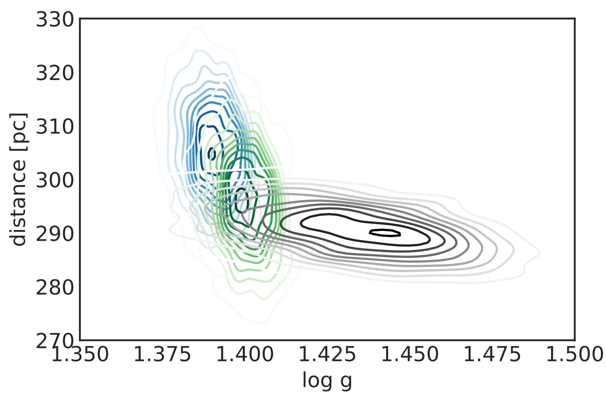

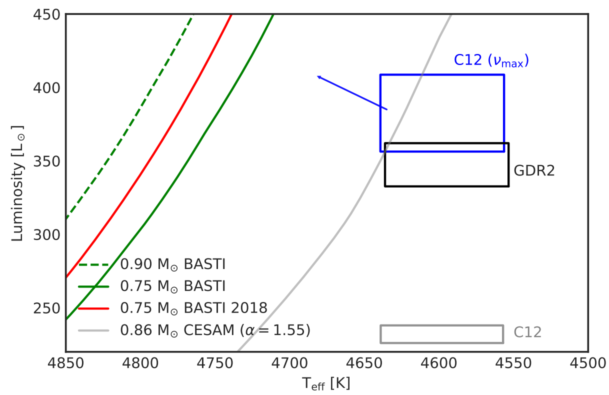

Fig. 2. Left: Density plots of derived distance versus $\log g$ using asteroseismology — without (blue) and with (green) corrections to the seismic relation — and using Gaia DR2 (black) **Right:** HR diagram showing observational position of HD 122563 using different input data (blue, black, and grey), along with standard evolutionary models from BASTI and a tailored CESAM model.

4 Conclusions

- We have detected oscillations in the metal-poor star HD 122563.
- By comparing the distances derived using asteroseismology and that from a parallax from Gaia, we showed that the scaling relations for surface gravity work in the metal-poor and evolved regime.
- We have derived new fundamental parameters for this star using asteroseismology: $\log g = 1.39 \pm 0.01$ and $d = 306 \pm 9$ pc ($d_{\rm GDR2} = 290 \pm 5$ pc).

*α-enhanced tracks from Pietrinferni et al. (2004) are hotter, and those from Hidalgo et al. (2018) are not yet available.

- By applying corrections to the scaling relations for molecular weight and the adiabatic exponent we derived values of $\log g = 1.42 \pm 0.01$ and $d = 296 \pm 9$ pc.
- The new fundamental parameters imply less tension between evolution models although a discrepancy on the order of 150-200 K still exists. This can be remedied by reducing the mixing-length parameter by 0.3 compared to solar, but further studies with more realistic physics in these models should also be addressed.
- Increasing A_V could also alleviate some of the problem.
- The new surface gravity implies less tension with 3D models, see e.g. Collet et al. (2018) who suggest that a lowering of $\log g$ in their analysis to alleviate discrepancies between their molecular- and atomic-species-derived oxygen abundances.
- We continue to collect data from the SONG Hertzsprung telescope. We aim to detect the mean frequency separation, along with individual frequencies, and a more accurate determination of the width of $\nu_{\rm max}$ (see Yu et al. (2018) who indicate a trend of width versus $\nu_{\rm max}$).
- We also aim to understand the long-term trends seen in the time series, see Fig. 1
- The individual frequencies will be very instructive for improving the theoretical models in the metal-poor regime.

We are grateful for the Programme National de Physique Stellaire for financial support for this research project. This work is based on observations made with the Hertzsprung SONG telescope operated on the Spanish Observatorio del Teide on the island of Tenerife by the Aarhus and Copenhagen Universities and by the Instituto de Astrofísica de Canarias. Support for the construction of the Hertzsprung SONG Telescope from the Instituto de Astrofisica de Canarias, the Villum Foundation, the Carlsberg Foundation and the Independent Research Fund Denmark is gratefully acknowledged. E.C. is funded by the European Union's Horizon 2020 research and innovation program under the Marie Sklodowska-Curie grant agreement No. 664931. We also deeply acknowledge the Gaia Data Processing and Analysis Consortium for their huge efforts in bringing us high quality data.

References

Andersen, M. F., Grundahl, F., Christensen-Dalsgaard, J., et al. 2014, in Revista Mexicana de Astronomia y Astrofisica Conference Series, Vol. 45, Revista Mexicana de Astronomia y Astrofisica Conference Series, 83–86

Casagrande, L., Portinari, L., Glass, I. S., et al. 2014, MNRAS, 439, 2060

Collet, R., Nordlund, Å., Asplund, M., Hayek, W., & Trampedach, R. 2018, MNRAS, 475, 3369

Corsaro, E. & De Ridder, J. 2014, A&A, 571, A71

Corsaro, E., De Ridder, J., & García, R. A. 2015, A&A, 579, A83

Creevey, O., Grundahl, F., Thévenin, F., et al. 2019, A&A, 625, A33

Creevey, O., Thévenin, J., Heiter, U., et al. 2014, in SF2A-2014: Proceedings of the Annual meeting of the French Society of Astronomy and Astrophysics, ed. J. Ballet, F. Martins, F. Bournaud, R. Monier, & C. Reylé, 411–415

Creevey, O. L., Thévenin, F., Boyajian, T. S., et al. 2012, A&A, 545, A17

Gaia Collaboration, Brown, A. G. A., Vallenari, A., et al. 2018, A&A, 616, A1

Grundahl, F., Fredslund Andersen, M., Christensen-Dalsgaard, J., et al. 2017, ApJ, 836, 142

Heiter, U., Jofré, P., Gustafsson, B., et al. 2015, A&A, 582, A49

Hidalgo, S. L., Pietrinferni, A., Cassisi, S., et al. 2018, ApJ, 856, 125

Karovicova, I., White, T. R., Nordlander, T., et al. 2018, MNRAS, 475, L81

Kjeldsen, H. & Bedding, T. R. 1995, A&A, 293, 87

Lallement, R., Vergely, J.-L., Valette, B., et al. 2014, A&A, 561, A91

Morel, P. 1997, A&AS, 124, 597

Pagel, B. E. J. 1963, J. Quant. Spec. Radiat. Transf., 3, 139

Pietrinferni, A., Cassisi, S., Salaris, M., & Castelli, F. 2004, ApJ, 612, 168

Viani, L. S., Basu, S., Chaplin, W. J., Davies, G. R., & Elsworth, Y. 2017, ApJ, 843, 11

Yu, J., Huber, D., Bedding, T. R., et al. 2018, ApJS, 236, 42

SF2A 2019
P. Di Matteo, O. Creevey, A. Crida, G. Kordopatis, J. Malzac, J.-B. Marquette, M. N'Diaye, O. Venot (eds)

THE CIRCUMSTELLAR ENVELOPES OF CEPHEIDS AND THEIR IMPACT ON THE PERIOD-LUMINOSITY RELATIONSHIP IN THE JWST AND ELT ERA.

V. Hocdé[1], N. Nardetto[1], E. Lagadec[1], G. Niccolini[1], A. Domiciano de Souza[1], A. Mérand[2], P. Kervella[3] and A. Gallenne[4]

Abstract. Cepheids are the keystone of the extragalactic distance ladder since their pulsation periods correlate directly with their luminosity, through the Period-Luminosity (PL) relation (Leavitt & Pickering 1912). The discovery of the accelerated expansion of the Universe (Riess et al. 1998; 2011 Nobel prize) is largely based on the Cepheid distance ladder. However, the calibration of the PL relation is still suffering from systematics errors of at least 2% and it is the largest contributor on the Hubble constant H0 (Riess et al. 2016). These systematics could be partly due to the CircumStellar Envelopes (CSEs) of Cepheids discovered in the last decade by interferometry. Using Spitzer Space Telescope observations, we reconstruct the spectral energy distribution of 5 Cepheids and we report the observation of an infrared (IR) excess continuum. We show for the first time that the IR excess can be modeled by a free-free emission due to a thin circumstellar shell of ionized gas in the chromospheric region.

Keywords: Techniques : Spectrometry, Photometry – Infrared : CSE, ISM – Stars : Cepheids –

1 Introduction

The extragalactic distance ladder is still largely based on Cepheids PL relations, whose uncertainties on both zero point and slope are today one of the largest contributors to the error on H_0 (Riess et al. 2019). One possible bias could be due to IR excesses from CSEs such as the ones discovered using near- and mid-infrared interferometry around nearby Cepheids (Kervella et al. 2006; Mérand et al. 2006). These studies determined a CSE radius of about 3 stellar radii and a flux contribution in the K band ranging from 2% to 10% of the continuum, for medium- and long-period Cepheids. However, we still do not know how these CSEs are formed, neither their nature, nor their characteristics (density and temperature profiles, chemical composition...). This work aims at understanding the nature of these CSEs by reconstructing and modeling the IR excess of Cepheids.

2 Building the infrared excess using the SPIPS algorithm

SpectroPhoto-Interferometric modeling of Pulsating Stars (SPIPS) is a model-based parallax-of-pulsation code which includes photometric, interferometric, effective temperature and radial velocity measurements in a robust model fit (Mérand et al. 2015). SPIPS uses a grid of ATLAS9 atmospheric models* (Castelli & Kurucz 2003) to compute synthetic photometry to match those from the dataset. While the visible domain up to $\sim 1\mu$m are well described by the pulsational model, an IR excess, increasing with wavelength, is observed (see Fig. 1-left). This IR excess has been modeled by an *ad-hoc* analytic law (see green line in Fig. 1-left):

$$\mathrm{IR_{ex}} = \Delta\mathrm{mag} = m_{\mathrm{obs}} - m_{\mathrm{kurucz}} = \begin{cases} 0, & \text{for } \lambda < 1.2\mu\mathrm{m} \\ \alpha(\lambda - 1.2)^{\beta}, & \text{for } \lambda > 1.2\mu\mathrm{m} \end{cases} \tag{2.1}$$

[1] Université Côte d'Azur, Observatoire de la Côte d'Azur, CNRS, Laboratoire Lagrange, France,
email : vincent.hocde@oca.eu
[2] European Southern Observatory, Karl-Schwarzschild-Str. 2, 85748 Garcing, Germany
[3] LESIA (UMR 8109), Observatoire de Paris, PSL, CNRS, UPMC, Univ. Paris-Diderot, 5 place Jules Janssen, 92195 Meudon, France
[4] European Southern Observatory, Alonso de Córdova 3107, Casilla 19001, Santiago 19, Chile
*http://wwwuser.oats.inaf.it/castelli/grids.html

with two parameters, α and β. In the next section we reconstruct the IR excess up to 30μm owing to *Spitzer* space telescope observations. Our study aims to physically explain the behaviour of this IR excess, which is likely due to CSE.

3 Spitzer data

In order to study the IR excess of Cepheids we selected a sample of Galactic Cepheids with *Spitzer* observations (Werner et al. 2004). The spectroscopic observations were made with the InfraRed Spectrograph IRS (Houck et al. 2004) onboard the *Spitzer* telescope and the full spectra were retrieved from the CASSIS atlas (Lebouteiller et al. 2011).

We derive the IR excess of each star in the sample at the specific phase of *Spitzer* using:

$$\Delta\mathrm{mag} = m_{Spitzer} - m_{\mathrm{kurucz}}[\phi_{Spitzer}] \tag{3.1}$$

where $m_{Spitzer}$ is the magnitude of the *Spitzer* observation and $m_{\mathrm{kurucz}}[\phi_{Spitzer}]$ is the magnitude of the ATLAS9 atmospheric model interpolated at the phase of *Spitzer* observations ($\phi_{Spitzer}$). The $T_{\mathrm{eff}}(\phi)$ and log$g(\phi)$ values of the star at the phase of *Spitzer* are provided by the SPIPS algorithm, while the interpolation is then done in a ATLAS9 grid of models with steps of 250K in effective temperature and 0.5 in log g, respectively. The angular diameter derived by SPIPS is then used to calculate $m_{\mathrm{kurucz}}[\phi_{Spitzer}]$. For V Cen we obtained the IR excess presented in Fig. 1-right. The observed discontinuity at 14μm is due to the different aperture sizes of *Spitzer* short and long wavelengths detectors. We also identify a silicate absorption around 10μm which could obscures a silicate emission from CSE. Therefore it is necessary to correct for the spectra from interstellar silicate absorption for studying the IR excess from CSEs.

4 Correcting for the interstellar silicate absorption in Spitzer data

In order to correct for the Spitzer spectra from interstellar silicate absorption we first derived the visible absorption A_{v} assuming an extinction law $A_{\mathrm{v}} = R_{\mathrm{v}}E(B-V)$ with a ratio of total-to-selective extinction of $R_{\mathrm{v}} = 3.1$, which corresponds to a diffuse ISM along the line of sight (Savage & Mathis 1979). Then we used the relation $A_{\mathrm{v}}/\tau_{9.7} = 18.5$ (Roche & Aitken 1984) which is suited to the diffuse ISM in the solar vicinity, in order to derive $\tau_{9.7}$. We obtain the following equation for the diffuse ISM:

$$A_{9.7}^{\mathrm{ISM}} = 1.086\tau_{9.7} = 1.086\frac{3.1}{18.5}\,E(B-V) = 0.182\,E(B-V), \tag{4.1}$$

Once we derived the specific absorption at 9.7μm, we can use this value to normalize a synthetic silicate absorption model in order to correct the entire *Spitzer* observations. Since we assumed an average ISM temperature of 20K, the dust emission is negligible in the *Spitzer* wavelength range according to Wien's law. Thus, we simply derive the absorption $A_{\lambda}^{\mathrm{ISM}}$ analytically using Mie theory. Hence we adopted the following expression for λ between 5 and $30\mu m$:

$$A_{\lambda}^{\mathrm{ISM}} \propto \kappa_{\lambda} = \int C_{\lambda}^{\mathrm{abs}}(a)\pi a^2 n(a)\mathrm{d}a \tag{4.2}$$

We first derived $C_{\lambda}^{\mathrm{abs}}$ using complex refractive index for silicates from Draine & Lee (1984) (hereafter DL84) assuming an uniform distribution of ellipsoidal shapes given by Bohren & Huffman (1983). Then we derived the absorption coefficient κ_{λ} by taking into account a standard grain size distribution $n(a) \propto a^{-3.5}$ (Mathis et al. 1977). Finally we normalize $A_{\lambda}^{\mathrm{ISM}}$ using its specific value $A_{9.7}^{\mathrm{ISM}}$ at $9.7\mu m$. Correction is presented in Fig. 1.

5 The IR excess from a thin shell of ionized gas

The shape of the mid-IR excess, saturating to a constant flux ratio at large wavelengths (see Fig. 2), suggests an opacity source increasing with wavelength. We used the free-free and bound-free opacities for a pure H shell presenting such behaviour. We consider the emission of a thin gas shell around the star with constant density and temperature for the sake of simplicity. The combined absorption coefficient (in m^{-1}; SI(MKS) unit system) for these two opacities sources is given by (e.g. Rybicki & Lightman 2008)

$$\kappa_{\lambda} = 3.692\times10^{-2}\left[1-\mathrm{e}^{-\frac{hc}{\lambda k T_{\mathrm{s}}}}\right]T_{\mathrm{s}}^{-1/2}\times(\lambda/c)^3(\gamma\rho/m_{\mathrm{H}})^2[g_{\mathrm{ff}}(\lambda,T_{\mathrm{s}})+g_{\mathrm{bf}}(\lambda,T_{\mathrm{s}})] \tag{5.1}$$

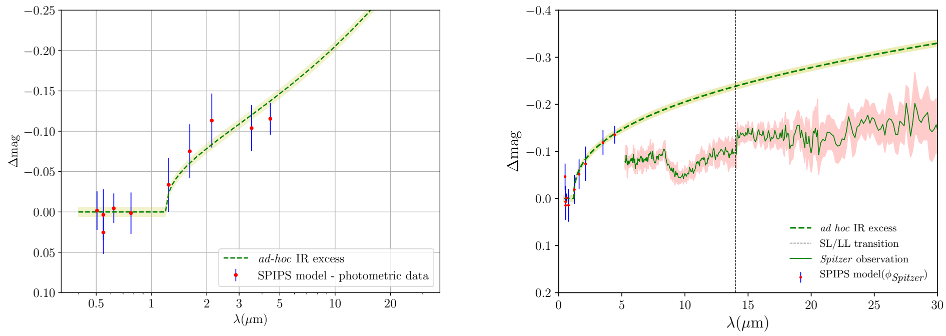

Fig. 1. Left: IR excess analytic law (Eq. 2.1) for V Cen together with the measurements. For each photometric band, red dots with error bars are the mean excess value over the cycle of the Cepheid and the corresponding standard deviation. The green zone is the error on the magnitude obtained using the covariance matrix of SPIPS fitting result. **Right:** *Spitzer* IR excess derived from Eq. 3.1. Red points are SPIPS interpolated IR excesses at the specific Cepheid phase of *Spitzer* observation. The transition between SL and LL detectors is indicated by a dashed line at $\sim 14\mu m$. The cycle-averaged *ad-hoc* analytic laws from SPIPS are represented by a dashed green for comparison only.

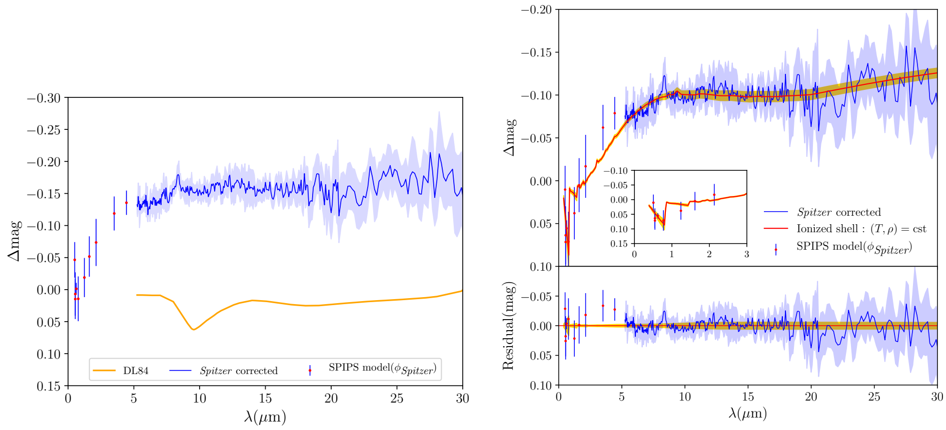

Fig. 2. Left: The IR excess of V Cen is presented, including (1) the interpolated IR excess model from SPIPS, (see Sect. 2), (2) the *Spitzer* observations cleaned from different camera effects and also corrected from the silicate absorption due to the ISM (orange curve see Sect. 4). **Right:** IR excess fitting results of a shell of ionized gas presented with residuals. Yellow region is the error on the magnitude obtained using the covariance matrix of the fitting result.

where h, c, and k have their usual meanings, γ is the degree of ionization (between 0 and 1), $T_{\rm s}$ the temperature of the shell, $m_{\rm H}$ the hydrogen mass and $g_{\rm ff}$ and $g_{\rm bf}$ are the free-free and bound-free Gaunt factors respectively. These factors were computed mainly from approximation formulas given by Brussaard & van de Hulst (1962), Hummer (1988), and references therein. We computed the SED of the star plus the gas shell taking into account the latter absorption coefficient κ_λ. In order to match the SPIPS photometries plus corrected *Spitzer* spectra we performed a χ^2 fitting using the Levenberg-Marquardt method. We fitted three parameters from the gas shell *i.e.* ionized shell mass $\gamma M_{\rm s}$, its temperature $T_{\rm s}$ and radius $R_{\rm s}$. In addition, since the SPIPS fitting assumes that there is no excess in the visible it is necessary to relax this assumption to allow the data to present deficit or excess in the visible depending on the physical behaviour of the ionized shell. We fitted a fourth parameter corresponding to the IR excess offset corresponding to $\mathbf{\Delta m} \neq 0$ for $\lambda < 1.2\mu m$. Results are presented in Fig. 2 in the case of V Cen only. We show that we can reproduce the IR excess with a thin shell of ionized gas with a temperature ranging from 3500 to 4500K depending on the Cepheid considered, with a width of typically $\simeq 15\%$ of the radius of the star. In the case of V Cen, we obtain $T_{\rm shell} = 4353 \pm 106$K, $R_{\rm shell} = 1.156 \pm 0.012\ R_{\rm star}$, $\gamma M_{\rm shell} = 3.61.10^{-9} \pm 2.0.10^{-10}M_\odot$ and Δm=0.057 $\pm$ 0.004.

6 Conclusion and perspectives

For the five Cepheids we studied, we report a continuum IR excess increasing up to $\sim$-0.1/-0.2 magnitudes at 30μm, which cannot be explained by a hot or cold dust model of CSE. We show for the first time that IR excesses of Cepheids can be explained by free-free emission from a thin shell of ionized gas with a thickness of $\simeq$8-17% star radius, an ionized mass of $10^{-9} - 10^{-7}\mathrm{M}_{\odot}$ and a temperature of 3500-4500K. In this simple model, density and temperature have a constant radial distribution.

Interferometric observations have resolved CSEs around Cepheids. These CSEs were modeled with a ring at a distance of 2 to $3R_{\star}$, i.e. close to the star, in a region where the temperature is high enough ($> 2000K$) to prevent dust condensations. Thus, these observations are more likely explained by a shell of partially ionized gas. In parallel, it is interesting to compare Cepheids to very long period Mira stars for which a radiosphere near $2R_{\star}$ due to free-free emission has been reported (Reid & Menten 1997). Also, extensive studies of Hα profiles in the atmosphere of Cepheids have shown that strong increases of turbulence occurs when the atmosphere is compressed during its infalling movement, or because of shock waves dynamics (see for instance Breitfellner & Gillet (1993)). Moreover the analytical work of Neilson & Lester (2008) have shown that mass loss is enhanced by pulsations and shocks in the atmosphere. We suggest this mass loss could be in the form of partially ionized gas. The model of the shell of ionized gas could also be linked to the chromospheric activity of Cepheids. For example, Sasselov & Lester (1994) report HeIλ10830 observation on seven Cepheids providing the evidence of a high temperature plasma and steady material outflow in the highest part of the atmosphere.

However our model does not take into account temperature nor density gradients in the star's atmosphere, and in particular compression and/or shock waves which could also heat up the shell and ionize the gas. Thus, a spatial and chromatic analysis of the shell including interferometric constrains in all available bands with in particular VEGA/CHARA (visible), PIONIER/VLTI (infrared) and MATISSE/VLTI (L, M, N bands) is still necessary to better understand the environment of Cepheids, and eventually, check the impact on the PL relation.

The authors acknowledge the support of the French Agence Nationale de la Recherche (ANR), under grant ANR-15-CE31-0012-01 (project UnlockCepheids).

References

Bohren, C. F. & Huffman, D. R. 1983, Absorption and scattering of light by small particles (New York: Wiley, 1983)

Breitfellner, M. G. & Gillet, D. 1993, A&A, 277, 553

Brussaard, P. J. & van de Hulst, H. C. 1962, Reviews of Modern Physics, 34, 507

Castelli, F. & Kurucz, R. L. 2003, in IAU Symposium, Vol. 210, Modelling of Stellar Atmospheres, ed. N. Piskunov, W. W. Weiss, & D. F. Gray, A20

Draine, B. T. & Lee, H. M. 1984, ApJ, 285, 89

Houck, J. R., Roellig, T. L., van Cleve, J., et al. 2004, ApJS, 154, 18

Hummer, D. G. 1988, ApJ, 327, 477

Kervella, P., Mérand, A., Perrin, G., & Coudé du Foresto, V. 2006, A&A, 448, 623

Lebouteiller, V., Barry, D. J., Spoon, H. W. W., et al. 2011, ApJS, 196, 8

Mathis, J. S., Rumpl, W., & Nordsieck, K. H. 1977, ApJ, 217, 425

Mérand, A., Kervella, P., Breitfelder, J., et al. 2015, A&A, 584, A80

Mérand, A., Kervella, P., Coudé du Foresto, V., et al. 2006, A&A, 453, 155

Neilson, H. R. & Lester, J. B. 2008, ApJ, 684, 569

Reid, M. J. & Menten, K. M. 1997, ApJ, 476, 327

Riess, A. G., Casertano, S., Yuan, W., Macri, L. M., & Scolnic, D. 2019, arXiv e-prints

Roche, P. F. & Aitken, D. K. 1984, MNRAS, 208, 481

Rybicki, G. B. & Lightman, A. P. 2008, Radiative processes in astrophysics (John Wiley & Sons)

Sasselov, D. D. & Lester, J. B. 1994, ApJ, 423, 777

Savage, B. D. & Mathis, J. S. 1979, ARA&A, 17, 73

Werner, M. W., Roellig, T. L., Low, F. J., et al. 2004, ApJS, 154, 1

SF2A 2019
P. Di Matteo, O. Creevey, A. Crida, G. Kordopatis, J. Malzac, J.-B. Marquette, M. N'Diaye, O. Venot (eds)

SHARP VLTI VIEW OF SECOND-GENERATION PROTOPLANETARY DISKS AROUND EVOLVED BINARIES

J. Kluska[1], H. Van Winckel[1], H. Olofsson[2], M. Hillen[1], D. Kamath[3], D.Bollen[3,1], I. Straumit[1], J. Alcolea[4], N. Anugu[5], J.-P. Berger[6], V. Bujarrabal[7], R. Izzard[8], S. Kraus[5], J.-B. Le Bouquin[6,9], M. Min[10] and J.D. Monnier[9]

Abstract. At the end of their life some binary stars (post-AGB binaries) form Keplerian disks of gas and dust from the ejected matter of the primary star at the end of the AGB phase. Those disks are similar to the planet-forming disks around young stars in many aspects. The orbital properties of these evolved binaries are not understood and the circumbinary disks are possibly playing a major role by pumping up the orbital eccentricity via Lindblad resonances. However, the disk structure, evolution and dispersal remain elusive. In this talk we will present the first reconstructed VLTI images of such systems revealing their building blocks: the inner disk rim, the central binary, an unexpected emission from the companion and an over-resolved component. We will also present the key findings of our VLTI snapshot survey pushing the comparison with protoplanetary disks much further. We will end by presenting our recently awarded VLTI large programme that aims to sharpen our view of these exciting objects.

Keywords: stellar evolution, post-AGB stars, binaries, high-angular resolution, infrared interferometry.

1 Introduction

Binarity is present in all kinds of stars (25% of low-mass stars and more than 80% of high-mass stars have at least one companion Duchêne & Kraus 2013). However, binary evolution is complex as it can give birth to diverse phenomena such as thermonuclear novae, supernovae type Ia, sub-luminous supernovae, gravitational waves and objects such as sub-dwarf B-stars, barium stars, cataclysmic variables, and asymmetric planetary nebulae (PNe). Understanding the impact of binarity in stellar evolution is therefore crucial but is, also, still poorly understood.

Here, we focus on the evolution of post-AGB (pAGB) binaries, that are surrounded by a circumbinary disk and that are in fast transition (10^5 years) between the AGB and the PNe stages. These pAGB systems are the remnants of strong binary interactions happening at the end of the AGB phase and, as they have now lost their envelope and are not obscured by a shell anymore, they are perfect to study the consequences of binary interaction.

[1] Instituut voor Sterrenkunde (IvS), KU Leuven, Celestijnenlaan 200D, 3001, Leuven, Belgium.
[2] Department of Space, Earth and Environment, Chalmers University of Technology, Gothenburg, Sweden
[3] Department of Physics and Astronomy, Macquarie University, Sydney, NSW 2100, Australia; Australian Astronomical Observatory, PO Box 915, North Ryde, NSW 1670, Australia
[4] Observatorio Astronómico Nacional (IGN), Alfonso XII, E-28014 Madrid, Spain
[5] University of Exeter, School of Physics and Astronomy, Stocker Road, Exeter, EX4 4QL, UK
[6] Univ. Grenoble Alpes, CNRS, IPAG, 38000, Grenoble, France
[7] Observatorio Astronómico Nacional (OAN-IGN), Ap. 112, E-28803 Alcalá de Henares, Spain
[8] Astrophysics Research Group, Faculty of Engineering and Physical Sciences, University of Surrey, Guildford, Surrey, GU27XH, UK; Institute of Astronomy, University of Cambridge, Madingley Road, Cambridge, CB30HA, UK
[9] University of Michigan, Department of Astronomy, 1085 S. University Ave, West Hall 323, Ann Arbor, MI, 48109, USA)
[10] Astronomical institute Anton Pannekoek, University of Amsterdam, Science Park 904, 1098 XH, Amsterdam, The Netherlands; SRON Netherlands Institute for Space Research, Sorbonnelaan 2, 3584 CA, Utrecht, The Netherlands

Disks around pAGBs were first postulated from the detection of infrared excesses in the spectral energy distributions (SED), that could not be attributed to expanding shells (e.g. de Ruyter et al. 2006). Almost all of the disk sources were then discovered to be binaries through radial velocity measurements (van Winckel 2003; Van Winckel 2007). Those observations led to the conclusion that pAGB disks originate from the evolved star's matter ejections via strong winds that happen at the end of the AGB phase for low- and intermediate-mass stars (0.8 - 8 $M_\odot$). The dynamical interaction between this strong wind and the companion star causes part of the mass loss to be trapped in a circumbinary disk. Millimetre observations of CO lines with the Plateau de Bure interferometer and ALMA showed that these disks appear to be stable, i.e. in Keplerian rotation (Bujarrabal et al. 2013, 2015, 2017, 2018). These observations also revealed a disk-wind component suggesting angular momentum transport in the disk. These disks are dusty with large size dust grains (de Ruyter et al. 2005; Gielen et al. 2011; Hillen et al. 2015) and large crystallinity fraction (Gielen et al. 2008, 2011). Radiative transfer models of protoplanetary disks (PPDs) around young stellar objects (YSOs) are able to reproduce both the SED and infrared interferometric measurements on a few targets (Hillen et al. 2014, 2015, 2017; Kluska et al. 2018). The dust masses found in these disks are of the order of 10^{-4}-10^{-3} $M_\odot$ (Sahai et al. 2011; Hillen et al. 2014). In general, despite very different forming processes, pAGB disks are in many ways (infrared excess, Keplerian rotation, winds, jets, dust mass, dust mineralogy and grain sizes) similar to PPDs around YSOs. As the PPDs are well studied both observationally and theoretically, the very close similarity with the disks around pAGB binaries rises the question of the universality of physical processes in dusty circumstellar disks and more specifically of their planet formation efficiency. Circumbinary disks around pAGBs can therefore be second generation planet forming disks, especially as several planets are candidates of being formed in such disks (e.g. NN Ser Völschow et al. 2014; Marsh et al. 2014).

The period distribution of the post-AGB binaries was predicted to follow a bimodal distribution where short period binaries are post-common envelope systems that spiraled-in and long period binaries are binaries that evolved through wind interaction and have therefore widen their orbits (Nie et al. 2012). However, the observed period distribution falls between the two peaks of the predicted distribution showing that an important element of binary interaction is still not understood in these systems. Moreover, the orbits are predicted to be circular given the circularisation that happen at the common envelope phase. Again the observed orbits can have eccentricities around 0.3 (Oomen et al. 2018). Here, we present high angular observations of these systems that aim to understand the disk-binary interactions and characterise the inner disk parts in these intriguing systems.

2 A VLTI/PIONIER snapshot survey

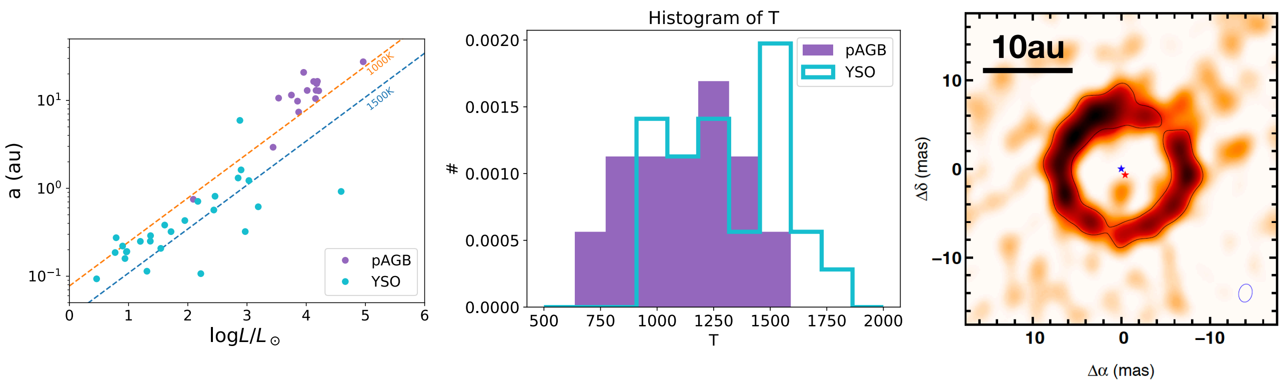

Fig. 1. Left: Near-infrared circumstellar size versus the stellar luminosity for both YSOs and pAGB binaries. The pAGB circumbinary scales with stellar luminosity but the relation is shifted towards larger sizes. **Center:** Histogram of temperatures for the circumstellar (or circumbinary for pAGBs) environments as measured from VLTI/PIONIER data. The environment of pAGB binaries appear to be colder. **Right:** The image reconstruction of the circumbinary environment of IRAS08544-4431 as reconstructed with the SPARCO approach (here the central binary was modelled as two point sources and do not appear in the image reconstruction).

We have conducted a VLTI snapshot survey (Kluska et al. subm.) in the near-infrared with the PIONIER instrument, that is a four beam combiner observing in the H-band (1.55-1.8μm). The aim of this snapshot survey was to uncover the disk morphology (e.g. radius, width, azimuthal brightness distribution), temperature and deduce interesting properties about the physical properties of its inner parts, such as its mineralogy or density. We have observed 23 targets in a snapshot mode, meaning that most of the targets were observed once or twice on two or three configurations. The resulting (u, v)-plane is not optimised for image reconstruction but is enough to recover basic properties of the observed targets. We have therefore fitted different models to the dataset with increasing complexity, starting from a two-parameter model of a point source and a background to a 17 parameters model of a double point source, an azimuthally modulated Gaussian ring and a background. We then have used the Bayesian Information Criterion to select the most likely model that fits the data. From this we could infer that the complexity of the targets is high given that 14 out of 23 targets need to be fitted by models with 11 or more parameters. We could also derive the size of the circumbinary Gaussian ring and place it in a size-luminosity diagram that is used for young stars (Monnier & Millan-Gabet 2002; Monnier et al. 2005; Lazareff et al. 2017). We can see that the sizes of the near-infrared extended emission in pAGB targets (that have a higher luminosity that YSOs) extend the size-luminosity relation that holds for YSOs where the near-infrared size is proportional to the square root of the luminosity. This can be explained by the fact that the near-infrared emission is ruled by dust sublimation physics. There is however a slight off set to higher sizes. We can also see that the distribution of the temperatures of the circumstellar emission in pAGBs is lower that around YSOs. Those two results point towards either the absence of refractory dust grains at the disk inner rim or lower gas density in the dust sublimation region.

Given the complexity of the targets it was difficult to deduce the binary separation and to study in detail the disk morphology and disk/binary interactions. An interferometric imaging survey is needed to reveal the disk complexity and link the disk morphology to the position of the two components of the binary.

3 A first near-infrared image of a post-AGB system

We have also led an interferometric imaging campaign on one post-AGB binary target, IRAS08544-4431. We have obtained a (u, v)-coverage that is suitable for image reconstruction. The visibility has a strong dependency on the observed wavelength channel. This is the so-called chromatic effect that is due to the temperature difference between one unresolved component (here the main star) and its resolve environment (here the circumbinary disk). One needs to take this chromatic effect into account when performing image reconstruction and this is done by using the SPARCO approach (Kluska et al. 2014) that consists in modelling the star and reconstructing its environment only by taking the difference of temperature into account. The first reconstruction have revealed the circumbinary disk but also a point source close to the primary star location (Hillen et al. 2016). This point source is likely the circum-secondary accretion disk (as the main-sequence secondary is too faint to be detected by our observations.) When subtracting this second point source emission the image reconstruction have revealed the complex circumbinary disk morpohology. We have then modelled this dataset (Kluska et al. 2018) with a radiative transfer model of a protoplanetary disk using MCMax (Min et al. 2009). The model treats the vertical disk scale-height self-consistently assuming hydrostatic equilibrium. The dust composition is of interstellar silicates with a power-law distribution of sizes between 0.1μm to 1 mm. The surface density follows a double power-law with radius where in the inner disk index is positive (1.5) and in the outer part it is negative (-1). The inner rim is found to be at 8.25 AU, the outer rim is fixed at 100 AU and the surface density changes at 24.75 AU. We then add a point source to the model to represent the circum-secondary accretion disk. We also found out that the model cannot reproduce the amount of extended flux detected in the interferometric observations. We have therefore add a background component of 8.1%.

This model reproduces well both the SED and the interferometric squared visibilities but is not able to reproduce the closure phases and the azimuthal disk brightness modulations. Those modulations could be due to spirals due to the disk-binary interactions and is a topic of research.

4 INSPIRING: A VLTI Imaging Large Programme

To have a better view of the interaction between the binary and its circumbinary disk we have launched a 250 h long VLTI Large Programme using two near-infrared interferometric instruments (PIONIER and GRAVITY) to observe 11 targets. The programme is entitled INSPIRING (INterferometric Survey of Post-AGB binary Interaction with their RING, PI: Kluska). The aim is to perform image reconstruction (as for IRAS08544-4431) in the continuum with PIONIER and locate any line emission with GRAVITY. The goals are to uncover the complex structure of the circumbinary disk inner rim, look for direct signs of accretion from the circumbinary disk but also for circum-secondary accretion disks and possibly build an evolutionary sequence for these disks.

5 Conclusion

Post-AGB binaries are intriguing objects that are tracing binary evolution and that could be surrounded by second-generation planet forming disks. The brightness and angular size of these targets is ideal to be observed by current infrared interferometric facilities. We have conducted a snapshot survey of these targets using the VLTI/PIONIER instrument and have revealed the complexity of the targets and that the inner disk rims are ruled by dust sublimation physics as it is the case in protoplanetary disks around young stars. The first near-infrared interferometric image of such a system has revealed a prototype of such a system with a post-AGB primary, a main-sequence secondary surrounded by an accretion disk, a circumbinary disk inner rim that has azimuthal brightness modulations probably due to disk-binary interactions and the presence of a strong extended component that is not reproduced by the radiative transfer model. In order to progress on the knowledge of these disks an interferometric imaging survey is needed to study the disk brightness distribution w.r.t. the inner binary. Also observations at larger wavelengths will help to study the disk structure and the disk physical conditions to push the comparison with protoplanetary disks further and look for the possibility of second generation planet formation mechanisms.

We would like to thank the organisers of the S09 session and the LOC for organising this very nice SF2A meeting in Nice. JK and HVW acknowledge support from the Research Council of the KU Leuven under grant number C14/17/082. RM acknowledges support from the Research Council of the KU Leuven under contract GOA/13/012 and the Belgian Science Policy Office under contract BR/143/A2/STARLAB. We used the following internet-based resources: NASA Astrophysics Data System for bibliographic services; Simbad; the VizieR online catalogues operated by CDS.

References

Bujarrabal, V., Alcolea, J., Van Winckel, H., Santander-García, M., & Castro-Carrizo, A. 2013, A&A, 557, A104

Bujarrabal, V., Castro-Carrizo, A., Alcolea, J., & Van Winckel, H. 2015, A&A, 575, L7

Bujarrabal, V., Castro-Carrizo, A., Alcolea, J., et al. 2017, A&A, 597, L5

Bujarrabal, V., Castro-Carrizo, A., Van Winckel, H., et al. 2018, ArXiv e-prints

de Ruyter, S., van Winckel, H., Dominik, C., Waters, L. B. F. M., & Dejonghe, H. 2005, A&A, 435, 161

de Ruyter, S., van Winckel, H., Maas, T., et al. 2006, A&A, 448, 641

Duchêne, G. & Kraus, A. 2013, Annual Review of Astronomy and Astrophysics, 51, 269

Gielen, C., Bouwman, J., van Winckel, H., et al. 2011, A&A, 533, A99

Gielen, C., Van Winckel, H., Min, M., Waters, L. B. F. M., & Lloyd Evans, T. 2008, A&A, 490, 725

Hillen, M., de Vries, B. L., Menu, J., et al. 2015, A&A, 578, A40

Hillen, M., Kluska, J., Le Bouquin, J.-B., et al. 2016, A&A, 588, L1

Hillen, M., Menu, J., Van Winckel, H., et al. 2014, A&A, 568, A12

Hillen, M., Van Winckel, H., Menu, J., et al. 2017, A&A, 599, A41

Kluska, J., Hillen, M., Van Winckel, H., et al. 2018, Astronomy and Astrophysics, 616, A153

Kluska, J., Malbet, F., Berger, J.-P., et al. 2014, A&A, 564, A80

Lazareff, B., Berger, J.-P., Kluska, J., et al. 2017, A&A, 599, A85

Marsh, T. R., Parsons, S. G., Bours, M. C. P., et al. 2014, Monthly Notices of the Royal Astronomical Society, 437, 475

Min, M., Dullemond, C. P., Dominik, C., de Koter, A., & Hovenier, J. W. 2009, A&A, 497, 155

Monnier, J. D. & Millan-Gabet, R. 2002, ApJ, 579, 694

Monnier, J. D., Millan-Gabet, R., Billmeier, R., et al. 2005, ApJ, 624, 832

Nie, J. D., Wood, P. R., & Nicholls, C. P. 2012, MNRAS, 423, 2764

Oomen, G.-M., Van Winckel, H., Pols, O., et al. 2018, A&A, 620, A85

Sahai, R., Claussen, M. J., Schnee, S., Morris, M. R., & Sánchez Contreras, C. 2011, ApJ, 739, L3

van Winckel, H. 2003, ARA&A, 41, 391

Van Winckel, H. 2007, Baltic Astronomy, 16, 112

Völschow, M., Banerjee, R., & Hessman, F. V. 2014, Astronomy and Astrophysics, 562, A19

SF2A 2019
P. Di Matteo, O. Creevey, A. Crida, G. Kordopatis, J. Malzac, J.-B. Marquette, M. N'Diaye, O. Venot (eds)

AUTOMATIC CLASSIFICATION OF K2 PULSATING STARS USING MACHINE LEARNING TECHNIQUES

A. Le Saux[1,2], L. Bugnet[1,2], S. Mathur[3,4], S. N. Breton[1,2] and R. A. García[1,2]

Abstract. The second mission of NASA's *Kepler* satellite, K2, has collected hundreds of thousands of lightcurves for stars close to the ecliptic plane. This new sample could increase the number of known pulsating stars and then improve our understanding of those stars. For the moment only a few stars have been properly classified and published. In this work, we present a method to automaticly classify K2 pulsating stars using a Machine Learning technique called Random Forest. The objective is to sort out the stars in four classes: red giant (RG), main-sequence Solar-like stars (SL), classical pulsators (PULS) and Other. To do this we use the effective temperatures and the luminosities of the stars as well as the FliPer features, that measures the amount of power contained in the power spectral density. The classifier now retrieves the right classification for more than 80% of the stars.

Keywords: asteroseismology - methods: data analysis - thecniques: machine learning - stars: oscillations

1 Introduction

Following the end of the original NASA's *Kepler* mission (Borucki et al. 2010), K2 (Howell et al. 2014) targeted more than 580,000 stars close to the ecliptic between campaign 1 and 20. Today, only a small fraction of these stars are properly classified attending to their pulsation properties. This is why in this project, the objective is to sort this huge amount of pulsating stars with an automatic Random Forest (RF) classifier. The RF classifier is a supervised ML algorithm that consists in an ensemble of decision trees. This method is suitable for star classification because it can deal quickly with a very large amount of data. The difficulty when analyzing K2 data is the special running mode implying a correction of the orbit every six hours that needs to be properly corrected. As a result, the Signal-to-Noise Ratio (SNR) is degraded compared to the *Kepler* main mission. Another issue that had to be faced is related to the Machine Learning (ML) method. Only a few pulsating-stars catalogs are published for the moment, hence it is difficult to form a training set to train the RF classifier in all the parameter space.

2 Methods

2.1 Data

An important part of the work when using ML techniques is to pre-process the data that will be used, particularly with classification algorithms. The objective is to differentiate between types of stars that could be very similar so values of the used features have to be as accurate as possible. In this work, we aim at classifying the stars by using different parameters such as the effective temperature, the luminosity and the amount of power contained in their Power Spectral Density (PSD) because this combination of parameters provide one of the best tools to obtain information about the nature of the pulsating stars. The PSDs are obtained by computing the Fourier transform of the lightcurves.

[1] IRFU, CEA, Universite Paris-Saclay, 91191 Gif-sur-Yvette, France
[2] AIM, CEA, CNRS, Universite Paris-Saclay, Universite Paris Diderot, Sorbonne Paris Cite, 91191 Gif-sur-Yvette, France
[3] Universidad de la Laguna, Dpto. De Astrofísica, 38205 La Laguna, Tenerife, Spain
[4] Instituto de Astrofisica de Canarias, 38200 La Laguna, Tenerife, Spain

Lightcurves used in the project were produced with the EVEREST pipeline developped by Luger et al. (2016, 2018), which aimed at studying exoplanet transit. For stars exhibiting transits, the PSD is dominated by the harmonics of the transiting periods,which could bias the total amount of power. Therefore the stars will be found in the wrong category. Other EVEREST lightcurves show jumps, discontinuities and low-frequency trends that introduce power in the PSD (for more information on those effects see García et al. (2011); García et al. (2014)). To remove those side effects, the available lightcurves were processed with a filtering method inspired by the KASOC filter from Handberg & Lung (2014). This filter was developped to optimize the data for asterosismic analysis by removing instrumental effects and planetary signals. First of all, it was noted that many light curves showed a general increasing or decreasing trend, which affects the calculated values of the PSD. To overcome this, a moving median filter was applied to these timeseries. A light curve is stored digitally as a vector of size N containing N bins. The method used here consists in creating a new vector of the same size N, called $Filter_{median}$. For each component of this vector, the median of the flux is calculated over a time interval, here set at 3 days, which corresponds to a window of a certain number of bins whose size remains fixed throughout the treatment. Then we shift the window by one bin and repeat the operation. The new considered flux, $Flux_{new}$, is calculated from the formula :

$$Flux_{new} = \left(\frac{Flux}{Filter_{median}} - 1 \right) \tag{2.1}$$

Secondly, a threshold was defined in an attempt to remove sharp features due to instrumental effects or transits. Any part of the flux above the threshold is masked.

2.2 Parameters used for classification

The features (input parameters) used for classification are the effective temperature (T_{eff}) and the luminosity (L) from Gaia DR2 (Gaia collaboration et al. 2016, 2018), and the FliPer, a method developed by Bugnet et al. (2018, 2019), which takes into account the total power in a given band of the PSD. FliPer values are computed using the PSD and an estimation of the photon noise level for each star. Here is the definition of the FliPer, F_p, as given by Bugnet et al. (2018):

$$F_p = \overline{PSD} - P_n \tag{2.2}$$

where $\overline{PSD}$ represents the averaged value of the PSD on a given frequency band and P_n is the photon noise. In this study we consider four FliPer parameters corresponding to four frequency ranges that extend from 0.7, 7, 20 and 50 μHz respectively to the Nyquist frequency. Those four FliPer values help to clearly distinguish the shapes of the PSD.

Here the method used to determine the photon noise is different from Bugnet et al. (2018). Indeed, the fact that each campaign points a different part of the sky introduces a different noise level in each of those campaigns. So first, we calibrated the photon noise level of each campaign according to the observed *Kepler* magnitude of the star with a method inspired by Pande et al. (2018). For all the stars we computed the mean of the PSD in the range 150 to 280 μHz in order to avoid the oscillations frequencies. Then we fitted a 3rd order polynomial function of the noise level at the bottom of the dense cloud of points in bins of width 0.5 magnitude. Points (purple star symbols on Fig. 1) that fit the bottom of the cloud of points were adjusted by eye. The white noise level was estimated for stars from campaigns 2 to 8 for now.

2.3 Machine Learning method

Facing the huge amount of data we want to classify, the use of an automatic algorithm seems to be the appropriate solution. We decided to use a Random Forest classifier (Breiman 2001) because of its robustness and its easy implementation. This is a method of supervised learning. That means that the algorithm is trained and validated with a labeled data set. The RF is composed of an ensemble of independent decision trees that gives the most likely class for each star. Each tree is constructed using a random subset of the training set which allows the trees to be independant. To do this the "RandomForestClassifier" function from the Python Sklearn library Pedregosa et al. (2011) was used.

At this point, the training and validation sets can be formed. The objective is to separate the stars in four classes: Classical Pulsators (PULS), Main-sequence Solar-Like stars (SL), Red Giants (RG) and Others. The

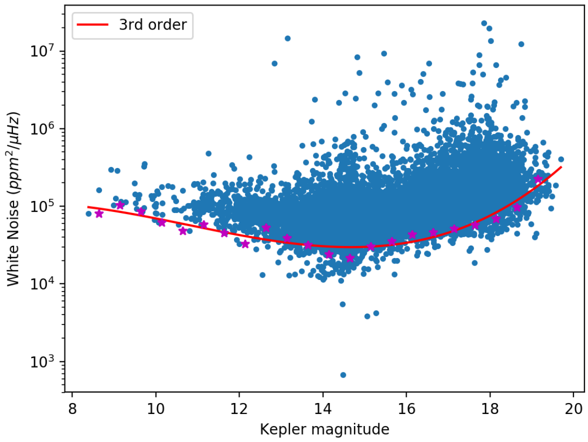

Fig. 1. White noise level for 11,010 stars as a function of their *Kepler* magnitude for Campaign 6. The purple star symbols are an estimation of the bottom of the dense clouds of points and the red line is a 3rd order fit of those purple star symbols.

Others category contains all the stars that the classifier could not classify as SL, RG or PULS, including the Eclipsing Binaries. The data set used to train the RF algorithm was constructed from data published on the NASA's website *K2 approved targets & programs* *. For the training and validation we dispose of 2,186 labeled stars, for wich the class is already known. This includes 340 SL stars from the originial *Kepler* mission and published by Chaplin et al. (2014) because there are only a few SL known among K2 stars. It is possible to add those SL stars from *Kepler* mission because the measurement instruments were the same for both missions. But using stars from *Kepler* is not optimal because of the difference in sensitivity that can appear due to the K2 special running mode. Then we randomly devide this data set in the training set (1,749 stars) and the validation set (379). The *Kepler* stars that were not included in the validation set as they are not stars that we want to classify.

3 Classification results & Perspectives

In this work we present a Random Forest method to perform an automatic classification of K2 pulsating stars. Those preliminary results are very encouraging with an accuracy of 83% on the classification of the validation set wich contain 379 stars. Fig. 2 represents the confusion matrix for a classification test. The confusion matrix compares the prediction made by the model with the actual class of a star. This points out that the main confusion comes from PULS stars that are classified in the Other category (21%). There are also some SL stars that are predicted as classical pulsators (16%). On the other hand, we notice that there is not so much confusion between other classes, less than 9%, and that the RG are very well classified with an accuracy of 98%. In order to improve those results we plan to increase the number of stars in the training set and improve the lightcurves processing.

Perspectives for this work are first of all, classify all K2's campaings and then subdivide the PULS category in 7 sub-classes (RR Lyrae, Slowly Pulsating B-type stars, δ-Scuti, γ- Doradus, β-Cepheid, Cepheid and rapidly oscillating Ap stars). Finally, this study on K2 data provide a better understanding of how the method works for low-resolution PSDs as it does for most of the millions of lightcurves with a 30 minute cadence from the Full Frame Images that will beprovided by TESS (Ricker et al. 2014).

This work was partially fund by PLATO CNES grant. S.M. acknowledges the support from the Ramon y Cajal fellowship number RYC-2015-17697. This paper includes data collected by the K2 mission and obtained from the MAST data archive at the Space Telescope Science Institute (STScI). Funding for the K2 mission is provided by the NASA Science Mission Directorate. STScI is operated by the Association of Universities for Research in Astronomy, Inc., under NASA contract NAS 5-26555.

* https://keplerscience.arc.nasa.gov/k2-approved-programs.html

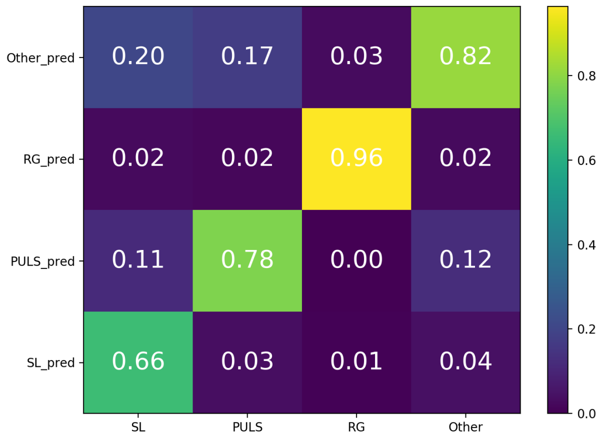

Fig. 2. Confusion matrix resulting from the class estimation of 379 stars from the validation test. The accuracy of the model is 83.0%. On the diagonal there is the percentage of stars that are well classified.

References

Borucki, W. J., Koch, D., Basri, G., et al. 2010, Science, 327, 977

Breiman, L. 2001, Machine Learning, 45, 5

Bugnet, L., García, R. A., Davies, G. R., et al. 2018, A&A, 620, A38

Bugnet, L., García, R. A., Mathur, S., et al. 2019, A&A, 624, A79

Chaplin, W. J., Elsworth, Y., Campantey, T. L., et al. 2014, MNRAS, 445, 946

Gaia collaboration et al. 2016, A&A, 595, A1

Gaia collaboration et al. 2018, A&A, 616, A1

García, R. A., Hekker, S., Stello, D., et al. 2011, MNRAS, 414, L6

García, R. A., Ceillier, T., Salabert, D., et al. 2014, A&A, 572, A34

Handberg, R. & Lung, M. N. 2014, MNRAS, 445, 2698

Howell, S. B., Sobeck, C., Haas, M., et al. 2014, Publications of the Astronomical Society of the Pacific, 126, 398.

Luger, R., Agol, E., Kruse, E., et al. 2016, ApJ, 152, 14 pp.

Luger, R., Kruse, E., Foreman-Mackey, D., Agol, E., & Saunders, N. 2018, ApJ, 156, 21 pp.

Pande, D., Bedding, T., Huber, D., & Kjeldsen, H. 2018, MNRAS, 480, 467

Pedregosa, F., Varoquaux, G., Gramfort, A., et al. 2011, J. Mach. Learn. Res., 12, 2825

Ricker, G. R., Winn, J. N., Vanderspek, R., et al. 2014, in Society of Photo-Optical Instrumentation Engineers (SPIE) Conference Series, Vol. 9143, Proc. SPIE, 914320

SF2A 2019
P. Di Matteo, O. Creevey, A. Crida, G. Kordopatis, J. Malzac, J.-B. Marquette, M. N'Diaye, O. Venot (eds)

FROM THE STAR TO THE TRANSITING EXOPLANETS : CHARACTERISATION OF THE HD 219134 SYSTEM

R. Ligi[1], C. Dorn[2], A. Crida[3,4], Y. Lebreton[5,6], O. Creevey[3], F. Borsa[1], D. Mourard[3], N. Nardetto[3], I. Tallon-Bosc[7], F. Morand[3] and E. Poretti[1]

Abstract.
Exoplanets' properties are directly linked to that of their host star. This is even more true in the case of transiting exoplanets, where the planetary radius cannot be derived if the stellar radius is unknown. Interferometry seems the best technique in this context, as it provides in a quasi-direct way and with exquisite precision the stellar radii. Moreover, the transit light curve can be used to directly obtain the stellar density, and thus the stellar mass.

We apply this technique to the system of HD 219134, which hosts two transiting super-Earths. Using these observational techniques and the correlations between the measured parameters, we directly derive new stellar radius, density and mass : $R_\star = 0.726 \pm 0.014\ R_\odot$, $\rho_\star = 1.82 \pm 0.19\ \rho_\odot$, $M_\star = 0.696 \pm 0.078\ M_\odot$. This yields new planetary parameters, and in particular, we find that the two transiting exoplanets show different densities despite similar masses. This can be explained by three hypothesis, among which one suggests that tides heat the internal part of the innermost planet, leading to a molten mantle with lower density.

Keywords: Stars: fundamental parameters, Stars:individual: HD 219134, Planetary systems, Techniques: interferometric, Methods: numerical, Planets and satellites: fundamental parameters

1 Introduction

After thousands of exoplanets discoveries, we have now entered the era of their characterisation. In this context, transiting exopanets can be considered as the most interesting targets because the knowledge of the stellar radius directly leads to the knowledge of the planetary one. This parameter, along with the mass and density, are the basics to infer exoplanets' internal composition. In a previous work (Crida et al. 2018b,a), we showed that using the transit light curve to measure the stellar density, interferometry to measure the stellar radius, and the combination of both with the computation of the correlation between $M_\star$ and $R_\star$ is a very powerful technique. It was applied to the system of 55 Cnc, for which we provided a radius and mass with 2% and 6.6% precision respectively (Ligi et al. 2016; Crida et al. 2018b). This yielded the characterisation of the transiting exoplanet 55 Cnc *e* and allowed to show that its atmosphere is thinner than previously expected (Crida et al. 2018b,a). The system of HD 219134 hosts two transiting rocky exoplanets and at least two additional exoplanets. We report a new analysis of the star and its transiting exoplanets, which led to a new estimation of their interior, showing than planet *b* could have a molten mantle. The analysis is described in detail in Ligi et al. (2019)

2 Revisiting stellar parameters

2.1 Interferometric observations

We observed HD 219134 with the VEGA/CHARA interferometer (Mourard et al. 2009; Ligi et al. 2013) from 2016 to 2018. We used the baselines S1S2, E1E2, W1W2 and W2E2 (Fig. 1) to insure a wide (u, v) coverage. In total, we collected

[1] INAF-Osservatorio Astronomico di Brera, Via E. Bianchi 46, I-23807 Merate, Italy
[2] University of Zurich, Institut of Computational Sciences, University of Zurich, Winterthurerstrasse 190, CH-8057, Zurich, Switzerland
[3] Université Côte d'Azur, Observatoire de la Côte d'Azur, CNRS, Laboratoire Lagrange, Bd de l'Observatoire, CS 34229, 06304 Nice cedex 4, France
[4] Institut Universitaire de France, 103 Boulevard Saint-Michel, 75005 Paris, France
[5] LESIA, Observatoire de Paris, PSL Research University, CNRS, Université Pierre et Marie Curie, Université Paris Diderot, 92195 Meudon, France
[6] Institut de Physique de Rennes, Universit de Rennes 1, CNRS UMR 6251, 35042 Rennes, France
[7] Univ Lyon, Univ Lyon1, Ens de Lyon, CNRS, Centre de Recherche Astrophysique de Lyon UMR5574, F-69230 Saint-Genis-Laval, France

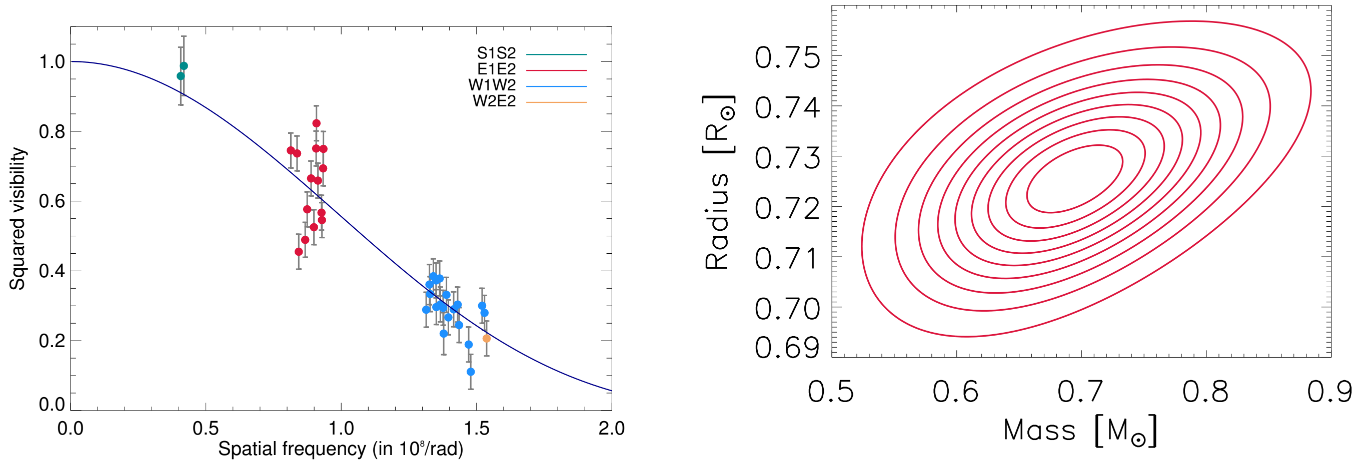

Fig. 1: *Left* : Squared visibilities obtained with VEGA/CHARA for HD 219134. The different colours represent the data points obtained with different baselines. The solid line represents the model of LD diameter. *Right* : Joint likelihood of the radius and mass of the star HD 219134. The nine contour lines separate 10 equal-sized intervals between 0 and the maximum of the joint likelihood of the radius and mass.

36 data points at wavelengths ranging from 685 to 725 nm that led to squared visibilities ranging from 0.111 ± 0.050 to 0.987 ± 0.085 (Ligi et al., subm.). Using the `LITpro` software (Tallon-Bosc et al. 2008), we first fitted our data taking a model of uniform disk to derive a uniform-disk diameter of $\theta_{\rm UD} = 0.980 \pm 0.020$ mas. However, a limb-darkened (LD) diameter is more realistic, and we thus used this representation to derive our final diameter. We used Claret & Bloemen (2011) tables to obtain a limb-darkening coefficient corresponding to $T_{\rm eff,SED} = 4839 \pm 25K$ (the effective temperature derived from the the SED, see Sec. 2.2), gravity $\log(g) = 4.57 \pm 0.14$ dex (average of the $\log(g)$ found in the litterature from 2000), and metallicity [Fe/H] = 0.07 ± 0.1 (idem) in the R and I filters by making interpolations of the surrounding values present in the tables (see Ligi et al., subm. for details). Finally, we obtain a LD diameter of $\theta_{\rm LD} = 1.035 \pm 0.021$ mas.

2.2 Stellar parameters

We applied the method described by Crida et al. (2018b) to compute the probability density function (PDF) of the stellar mass $M_\star$ and radius $R_\star$ (noted $f_{R_\star}$). $f_{R_\star}$ can be expressed as a function of the PDF of $\theta_{\rm LD}$ and the distance d, yielding $R_\star = 0.726 \pm 0.014\ R_\odot$ with $d = 6.533 \pm 0.038$ pc (Gaia Collaboration et al. 2018). In case of a planetary transit, Seager & Mallén-Ornelas (2003) show that the stellar density $\rho_\star$ can be derived from the transit duration, period and depth. Using the transit data from Gillon et al. (2017), we computed the stellar density independently for both transits, and then their average which is $\rho_\star = 1.82 \pm 0.19\ \rho_\odot$. Finally, we computed the joint likelihood of $M_\star$ and $R_\star$, which depends on $f_{R_\star}$, and the PDF of $\rho_\star$. This yields $M_\star = 0.696 \pm 0.078\ M_\odot$, with a correlation between $M_\star$ and $R_\star$ of 0.46. This correlation is clearly seen in Fig. 1 (right) ; we obtain an inclined ellipse in the ($M_\star$, $R_\star$) plane, reducing the possible values of $M_\star$ that relate on $R_\star$ and $\rho_\star$. We note that this value of $M_\star$ is lower than previous estimates from Gillon et al. (2017, $0.81 \pm 0.03 M_\odot$) and Boyajian et al. (2012, $0.763 \pm 0.076 M_\odot$) who used indirect methods to infer it.

To derive the bolometric flux of HD 219134, we used the photometry from the VizieR Photometry tool* while selecting non-redundant points. We fitted our data with the BaSeL empirical library of spectra (Lejeune et al. 1997) with a nonlinear least-squared minimisation algorithm (Levenberg-Marquardt), and perform a Monte-Carlo like simulation on f_λ, E(B-V), $T_{\rm eff}$, $\log(g)$, $[M/H]$ to compute the final $F_{\rm bol}$. We then derived $T_{\rm eff}$ from $F_{\rm bol}$ and $\theta_{\rm LD}$. With $F_{\rm bol} = (19.86 \pm 0.21) \cdot 10^{-8}$ erg s^{-1} cm^{-2}, we obtain $T_{\rm eff} = 4858 \pm 50\ K$, a value close to the effective temperature directly derived from the SED $T_{\rm eff,SED} = 4839 \pm 25\ K$ and to the $T_{\rm eff}$ from Gaia ($4787^{+92}_{-73}\ K$).

*`http://vizier.u-strasbg.fr/vizier/sed/`

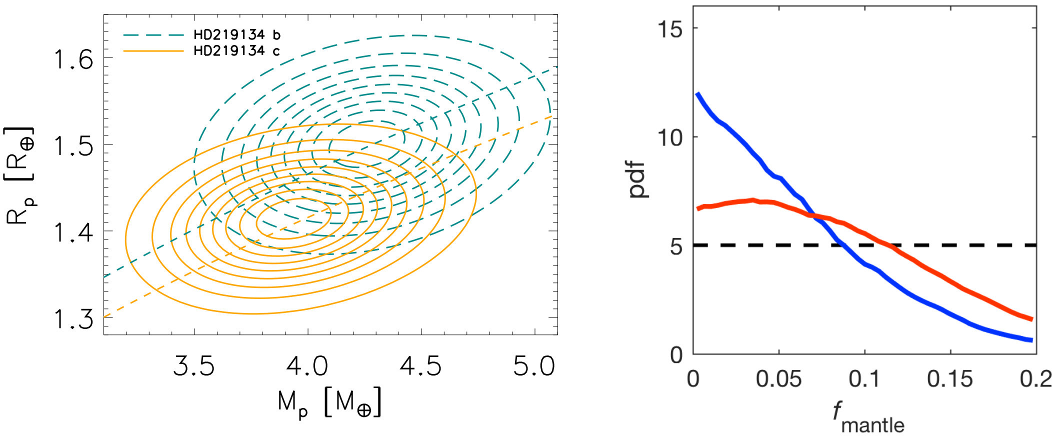

Fig. 2: *Left* : Joint likelihood of the planetary mass and radius for planet *b* (green long-dashed line) and planet *c* (yellow solid line). The dashed lines show the iso-densities corresponding to the mean densities of planets *b* and *c*. The nine contour lines separate 10 equal-sized intervals between 0 and the maximum of the joint likelihood of the radius and mass. *Right* : PDF of the fudge factor for planets *b* (solid red line) and *c* (solid blue line), and the prior (black dashed line).

Table 1: Parameters of the transiting exoplanets of the system HD 219134.

Param.	HD 219134 *b*	HD 219134 *c*
R_p [$R_\oplus$]	1.500 ± 0.057	1.415 ± 0.049
M_p [$M_\oplus$]	4.27 ± 0.34	3.96 ± 0.34
Corr(R_p,M_p)	0.22	0.23
ρ_p [$\rho_\oplus$]	1.27 ± 0.16	1.41 ± 0.17
a [au]	0.037	0.062

3 Properties of the transiting exoplanets HD 219134 b & c

3.1 Radius, mass and density

The system of HD 219134 hosts two transiting exoplanets, HD 219134 *b* & *c*. Since $R_\star$ and $M_\star$ are now well known, we can derive M_p and R_p from the light curves and radial velocity measurements. More precisely, Crida et al. (2018b) showed that for any pair of M_p and $M_\star$, one can derive the associated semi-amplitude K following Kepler's law. Similarly, at any pair of R_p and $R_\star$ can be associated the transit depth ΔF. These values are used to compute the PDF of R_p and M_p (see Crida et al. 2018b, for details and Ligi et al., subm.), which are presented in Tab. 1. Then, the density of each exoplanet is computed from R_p and M_p taking into account the correlation between both parameters (Fig. 2, left). We note that the new determinations of planetary radii are smaller than the previous estimates (for example by Gillon et al. 2017) because of our smaller stellar radius. We point out that these new R_p values clearly locate the two transiting exoplanets in the super-Earths part of the exoplanets radii distribution separated by the Fulton gap (Fulton et al. 2017), which enforce their super-Earth nature. More interestingly, planet *b* has a lower density while a higher mass than planet *c*. Computing the ratio of the planets' densities by using the transit and RV parameters yields $\rho_b/\rho_c = 0.905 \pm 0.131$. This means that there is a 10% difference between both densities with 50% probability, or that there is a 70% chance that the difference be higher than 5%. We investigate in the next section the possible origin of this difference.

3.2 Internal compositions

First, it is worth noticing that the uncertainty in the density ratio also allows for no interior difference between both transiting exoplanets. But if there is a difference, the lower density of planet *b* can be associated to secondary atmospheres or a rock composition that is enriched in very refractory elements (Dorn et al. 2018; Dorn & Heng 2018). Moreover, this difference in density can also be associated to different melt fractions as demonstrated by Bower et al. (2019). To investigate these possibilities, we use the inference scheme developed by Dorn et al. (2017) which calculates the possible interiors and their confidence ranges from the planetary mass, radius, stellar irradiation and abundances. We also consider that the two planets are made of iron-rich cores, silicate mantles, and terrestrial-type atmospheres since they are considered as super-Earths. In addition to the regular interior parameters, we consider a fudge factor that accounts for the decrease in density (see Ligi et al., subm. for details). As a result, we find mantle compositions and core sizes in agreement with bulk densities and stellar abundances constraints. In particular, the core fraction of both planets is close to that of Venus and Earth ($(r_{\rm core}/r_{\rm core+mantle})_{\oplus}$ = 0.53), which again validates their super-Earth nature. More interestingly, planet *b*'s lower density of 10% is attributed to a 10% lower core and a 45% higher fuge factor (Fig. 2, right), meaning that a significantly stronger reduction of mantle density is plausible given the data.

3.3 Dynamical solutions

The possible large molten fraction of planet *b* cannot be explained by its equilibrium temperature (1036K), which is below the melting temperature of silicates. Therefore, we investigate if it could be due to tidal heating caused by an excited eccentricity of the planet. Using the SyMBA N-body code (Duncan et al. 1998), we ran simulations of the planets of the HD 219134 system.

We took the orbital parameters of the four inner planets from Gillon et al. (2017), and found that the system is stable over 1 Gyr and that e_b oscillates from 0. to 0.13 with a period of a few thousand years. However, with initial eccentricities set to 0 for all planets, the system remains stable during 500 Myrs, which is in desagreement with Gillon et al. (2017)'s observations and suggests that the four inner planets may have not acquired their final mass and/or semi-major axes during the proto-planetary disc phase. Adding dissipation, planet *b* drifts inwards and planet *c* as well but less significantly. Both planets cross the 2 : 1 mean motion resonance, kicking their eccentricity. But they are quickly damped and e_c converges to 0.025 while e_b ends up oscillating between 0.005 and 0.037 with a period of $\sim$ 3000 years when it reaches its present semi-major axis. In that case, planet *b* would endure episodes of hundred times more heating per mass unit than Io. In contrast, planet *c* is never heated as musch as the Jovian satellite.

4 Conclusions

We report here a new analysis of the HD 219134 system, which hosts two transiting exoplanets known to date. Using the VEGA/CHARA interferometer, we measured the angular diameter of the star and then its radius using the *Gaia* distance. We used the transit light curve to obtain a direct measurement of the stellar density and then of the stellar mass. We find a radius and mass lower than previous estimates, but an effective temperature consistent with that derived from SED and from *Gaia*. Our new stellar parameters directly impact the properties of the transiting exoplanets. We used (Gillon et al. 2017)'s orbital solutions to compute the PDF of $R_{\rm p}$, $M_{\rm p}$ and $\rho_{\rm p}$, confirming that planets *b* and *c* belong to the super-Earths population. We show that planet *b* has a smaller density while a higher mass than planet *c*. Using an inference scheme, we find that these difference can be due to possible difference in the volatile layer or the rock composition. But this can also come from a different molten fraction. We investigate this possibility using a N-body code simulation, which reveals that a perfectly circular orbit for planets *b* and *c* is unlikely. Planet *b* in particular can experience excentricity of $\sim$ 0.02 with possible large oscillations, that could provoke a large tidal heating causing the melt of the mantle.

Exoplanetary systems are generally complex and need a deep analysis of both stellar and planetary properties. In particular, direct measurements of the stellar parameters and improving the precision of the transit light curves allow a better knowledge and can lead to insights of planetary formation.

R.L. has received funding from the European Union's Horizon 2020 research and innovation program under the Marie Skłodowska-Curie grant agreement n. 664931. C.D. acknowledges support from the Swiss National Science Foundation under grant PZ00P2_174028. This work is based upon observations obtained with the Georgia State University Center for High Angular Resolution Astronomy Array at Mount Wilson Observatory. The CHARA Array is supported by the National Science Foundation under Grants No. AST-1211929 and AST-1411654. This research has made use of the SIMBAD database, operated at CDS, Strasbourg, France. This research has made use of the Jean-Marie Mariotti Center `SearchCal` service † co-developped by LAGRANGE and IPAG, and of CDS Astronomical Databases SIMBAD and VIZIER ‡. This work has made use of data from the European Space Agency (ESA) mission *Gaia* (`https://www.cosmos.esa.int/gaia`), processed by the *Gaia* Data Processing and Analysis Consortium (DPAC, `https://www.cosmos.esa.int/web/gaia/dpac/consortium`). Funding for the DPAC has been provided by national institutions, in particular the institutions participating in the *Gaia* Multilateral Agreement.

† Available at http://www.jmmc.fr/searchcal

‡ Available at http://cdsweb.u-strasbg.fr/

References

Bower, D. J., Kitzmann, D., Wolf, A. S., et al. 2019, arXiv preprint arXiv:1904.08300

Boyajian, T. S., von Braun, K., van Belle, G., et al. 2012, ApJ, 757, 112

Claret, A. & Bloemen, S. 2011, A&A, 529, A75

Crida, A., Ligi, R., Dorn, C., Borsa, F., & Lebreton, Y. 2018a, Research Notes of the American Astronomical Society, 2, 172

Crida, A., Ligi, R., Dorn, C., & Lebreton, Y. 2018b, ApJ, 860, 122

Dorn, C., Harrison, J. H., Bonsor, A., & Hands, T. O. 2018, Monthly Notices of the Royal Astronomical Society, 484, 712

Dorn, C. & Heng, K. 2018, The Astrophysical Journal, 853, 64

Dorn, C., Venturini, J., Khan, A., et al. 2017, Astronomy & Astrophysics, 597, A37

Duncan, M. J., Levison, H. F., & Lee, M. H. 1998, AJ, 116, 2067

Fulton, B. J., Petigura, E. A., Howard, A. W., et al. 2017, AJ, 154, 109

Gaia Collaboration, Brown, A. G. A., Vallenari, A., et al. 2018, ArXiv e-prints

Gillon, M., Demory, B.-O., Van Grootel, V., et al. 2017, Nature Astronomy, 1, 0056

Lejeune, T., Cuisinier, F., & Buser, R. 1997, VizieR Online Data Catalog, 412, 50229

Ligi, R., Creevey, O., Mourard, D., et al. 2016, A&A, 586, A94

Ligi, R., Dorn, C., Crida, A., et al. 2019, A&A, 631, A92

Ligi, R., Mourard, D., Nardetto, N., & Clausse, J.-M. 2013, Journal of Astronomical Instrumentation, 02, 1340003

Mourard, D., Clausse, J. M., Marcotto, A., et al. 2009, A&A, 508, 1073

Seager, S. & Mallén-Ornelas, G. 2003, ApJ, 585, 1038

Tallon-Bosc, I., Tallon, M., Thiébaut, E., et al. 2008, in Society of Photo-Optical Instrumentation Engineers (SPIE) Conference Series, Vol. 7013

SF2A 2019
P. Di Matteo, O. Creevey, A. Crida, G. Kordopatis, J. Malzac, J.-B. Marquette, M. N'Diaye, O. Venot (eds)

TOWARDS ULTRA SPEED UP FOR DUST GROWTH SCHEMES

M. Lombart[1] and G. Laibe [1]

Abstract. Current 3D simulations of dusty protoplanetary discs do not include dust growth and fragmentation comprehensively since the computational cost associated to traditional algorithms is prohibitive. We show that it is possible to overcome this difficulty by using a high-order discontinuous Galerkin solver.

Keywords: Planets and satellites: formation, Dust, extinction, Methods: numerical.

1 Introduction

Recent spatially resolved observations of protoplanetary discs by SPHERE/VLT and ALMA have revealed that structures such as rings, spirals, horseshoes and gaps are ubiquitous (e.g. Avenhaus et al. 2018; Andrews et al. 2018). A novel generation of numerical models including differential dynamics between the gaseous nebula and dust grains has subsequently been developed to interpret these observations (e.g. Dipierro et al. 2015). However, no 3D dust/gas simulation has included dust coagulation and fragmentation comprehensively so far, although 1+1D modelling or 3D simulations with toy models of growth have shown that its effect can not be neglected (e.g. Brauer et al. 2008). This is mainly due to the prohibitive computational cost associated to the resolution of the so-called Smoluchowski equation with existing numerical algorithms. Indeed, any bin added to improve the resolution in size rises up the computational time drastically since one has to pay the cost of the integration of the associated dynamics at every grid point and for each time step. Typically, we aim for $\sim$15 size-bins from 1μm to 1cm with an accuracy of order $\lesssim 0.1\%$ to be consistent with hydro solvers. We show that this challenging difficulty can be overcome by using a well-designed high-order discontinuous Galerkin algorithm.

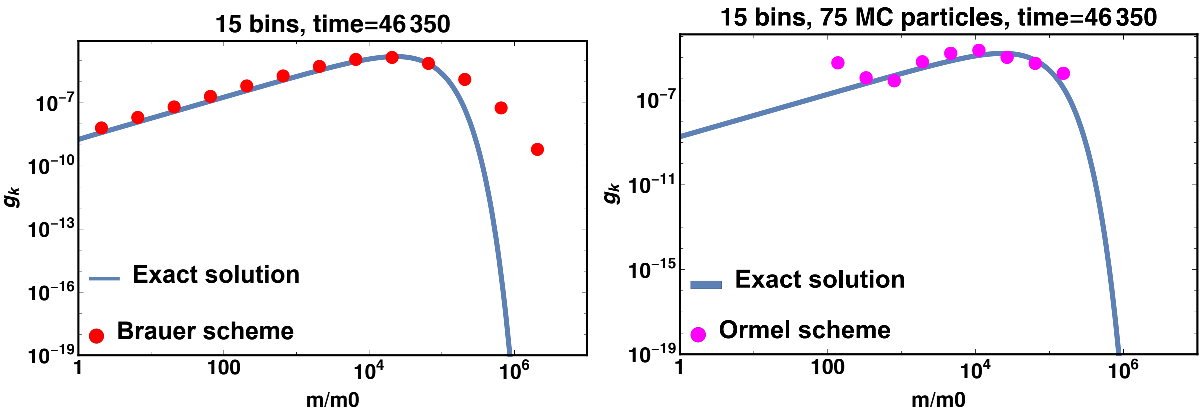

Fig. 1. Numerical solution with a constant kernel $K = 1$ with the algorithms described in Ormel & Cuzzi (2007) (**left**) and in Brauer et al. (2008) (**right**). The desired accuracy of $\lesssim 0.1\%$ is not achieved.

[1] École normale supérieure de Lyon, CRAL, UMR CNRS 5574, Université de Lyon , 46 Allée d'Italie, 69364 Lyon Cedex 07, France

2 Method

Dust coagulation is described by the Smoluchowski equation $\frac{\partial g}{\partial t} + \frac{\partial F[g]}{\partial x} = 0$ where t and x denote time and mass respectively, and g is the mass density of the grain distribution (Tanaka et al. 1996). The mass flux F is a function of the coagulation kernel K that models microscopic growth:

$$F[g](x,t) = \int_0^x \int_{x-u}^{\infty} \frac{K(u,v)}{v} g(u,t)\, g(v,t)\, \mathrm{d}u\mathrm{d}v. \tag{2.1}$$

The key idea consists in approximating the mass distribution on a bin size I_j *not* by a constant function but by a high-order polynomials, separating the variables t and x i.e. $g(x,t) \simeq g_j(x,t) = \sum_{i=0}^{k} c_j^i(t)\phi_i(\xi_j(x))$ – see Fig. 2. Choosing ϕ_i as the Legendre polynomials and projecting Eq. 2.1 onto this basis, one obtains an ordinary system of differential equations for the c_i's. Fluxes are computed using by Gauss Quadrature (Liu et al. 2019).

$$\frac{\mathrm{d}}{\mathrm{d}t}\begin{bmatrix} c_j^0 \\ \ddots \\ c_j^k \end{bmatrix}(t) = \frac{2}{\Delta x_j}\begin{bmatrix} 1/d_0 & & \\ & \ddots & \\ & & 1/d_k \end{bmatrix}\left(\int_{I_j} F[g](x,t)\frac{\mathrm{d}}{\mathrm{d}x}\begin{bmatrix} \phi_0 \\ \ddots \\ \phi_k \end{bmatrix}(\xi_j(x))\,\mathrm{d}x - F[g](x,t)\begin{bmatrix} \phi_0 \\ \ddots \\ \phi_k \end{bmatrix}(\xi_j(x))\,|_{\partial I_j}\right). \tag{2.2}$$

3 Results

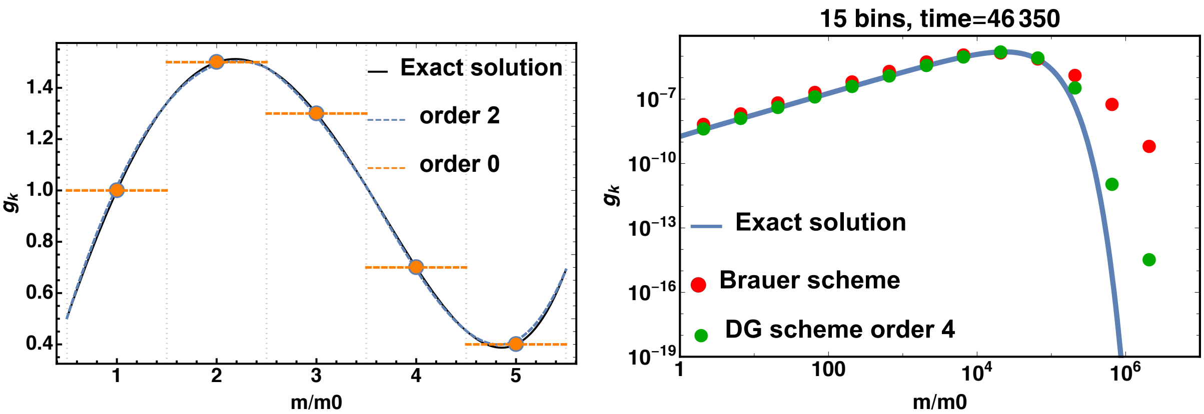

Fig. 2. Left: Low-order *vs.* high-order approximation. **Right:** Numerical solution obtained for an integration of order 4 with a constant kernel $K = 1$ over 15 size bins and 75 degrees of freedom for discontinuous Galerkin algorithm.

For the seminal test with $K = 1$, an error of $\lesssim 0.1\%$ in L_1-norm is achieved under the conditions required by hydrodynamical simulations (Fig. 2). Further refinements of this algorithm have been performed but are not presented here (improved projection basis, refined binning, time stepping, limiter for positivity).

4 Conclusions

We have shown that high-order discontinuous Galerkin algorithms pave the way to include the full dust coagulation equation in realistic 3D dust/gas simulation of protoplanetary discs.

References

Andrews, S. M., Huang, J., Pérez, L. M., et al. 2018, ApJ, 869, L41
Avenhaus, H., Quanz, S. P., Garufi, A., et al. 2018, ApJ, 863, 44
Brauer, F., Dullemond, C. P., & Henning, T. 2008, A&A, 480, 859
Dipierro, G., Price, D., Laibe, G., et al. 2015, MNRAS, 453, L73
Liu, H., Gräpler, R., & Warnecke, G. 2019, SIAM Journal on Scientific Computing, 41, B448
Ormel, C. & Cuzzi, J. 2007, Astronomy & Astrophysics, 466, 413
Tanaka, H., Inaba, S., & Nakazawa, K. 1996, Icarus, 123, 450

SF2A 2019
P. Di Matteo, O. Creevey, A. Crida, G. Kordopatis, J. Malzac, J.-B. Marquette, M. N'Diaye, O. Venot (eds)

3D RECONSTRUCTION OF THE ENVIRONMENT OF THE RED SUPERGIANT μ CEP FROM NOEMA OBSERVATIONS OF THE CO V=0 J=2-1 LINE

M. Montargès[1], W. Homan[1], D. Keller[1], N. Clementel[1], S. Shetye[1,2], L. Decin[1], G. M. Harper[3], P. Royer[1], J. M. Winters[4], T. Le Bertre[5,6] and A. M. S. Richards[7]

Abstract. Red supergiant stars are surrounded by a circumstellar environment containing gas and dust. It is created as the star loses its mantle via an unknown mass-loss process. Refining our knowledge of the morphology and physics of such environments is critical to understanding the processes that drive this mass loss. This mass loss phenomenon is also a key element to determine the fate of the star, as it directly determines the mass of the supernova progenitor and hence of the remaining compact object. We present the result of our observations of the CO $v = 0$ $J = 2 - 1$ emission line of the RSG μ Cep with the NOEMA interferometer at the arcsec angular resolution scale (~ 500 au at the star distance). Using a combination of 3D deprojection and 3D radiative transfer modeling, we show that at least 25% of the mass loss is due to clumps, randomly arranged in space and emitted episodically by the star.

Keywords: circumstellar matter, stars: imaging, stars: individual: μ Cep, stars: mass-loss, supergiants, radio lines: stars

1 Introduction

Cool evolved stars are important contributors to the chemical enrichment of the interstellar medium thanks to their important mass loss (10^{-8} to $10^{-4}\,\mathrm{M}_\odot\ \mathrm{yr}^{-1}$). The elements forged within their cores are transported to their surface via powerful convective motions. Within their stellar winds, these elements are cooling to form molecules and dust grains that will be pristine building blocks for future stellar system and life precursors. Massive stars ($\mathrm{M_{ini}} > 8\,\mathrm{M}_\odot$) evolve into red supergiants (RSG). The mass loss of these stars is not completely understood: the launching mechanism, the dust condensation processes and location, and the role of their chromosphere are still unknown.

2 Observations

We observed the RSG star μ Cep using NOEMA on 2015 December 2 and 2016 March 24 in the 7C (3.4h on source) and 7B (2.6h on source) configurations, respectively. The narrow band backend was used to provide line data in both polarizations with a 160 MHz bandwidth unit. For the CO $J = 2 - 1$ line at 230.538 GHz, this resulted in a spectral resolution of $0.81\,\mathrm{km\ s^{-1}}$ over a range of $\pm 90\,\mathrm{km\ s^{-1}}$. To produce the continuum at 231.276 GHz, we used the Wideband Express (WideX) backend with a 4 GHz bandwidth to select line-free channels. The data were reduced and calibrated using the GILDAS package*. We then performed a self-calibration of the line data in the (u, v) plane using the continuum data. The noise level (σ) was $0.71\,\mathrm{mJy\ beam^{-1}}$ in the continuum map and $2.03 - 4.70\,\mathrm{mJy\ beam^{-1}}$ in the line channel maps. Further details on the data acquisition, reduction and calibration can be found in Montargès et al. (2019, hereafter M19).

[1] Institute of Astronomy, KU Leuven, Celestijnenlaan 200D B2401, 3001 Leuven, Belgium
[2] Institute of Astronomy and Astrophysics, Université libre de Bruxelles, B-1050 Bruxelles, Belgium
[3] Center for Astrophysics and Space Astronomy, University of Colorado, Boulder, CO 80309, USA
[4] Institut de Radioastronomie Millimétrique, 300 rue de la Piscine, 38406, Saint Martin d'Hères, France
[5] LERMA, Observatoire de Paris, PSL Research University, CNRS, UMR 8112, 75014, Paris, France
[6] Sorbonne Universités, UPMC Univ. Paris 06, UMR 8112, LERMA, 75005, Paris, France
[7] Jodrell Bank Centre for Astrophysics, School of Physics and Astronomy, University of Manchester, Manchester M13 9PL, UK
*`http://www.iram.fr/IRAMFR/GILDAS`

3 Data analysis

3.1 Continuum

Figure 1 shows the self-calibrated continuum from the NOEMA data. Only the central source is detected above 3σ, it remains unresolved. Its point flux density is 39.67 ± 7.93 mJy. Using an updated model from Harper et al. (2001), M19 showed that most of the continuum emission comes from the compact free-free emission of the RSG chromosphere.

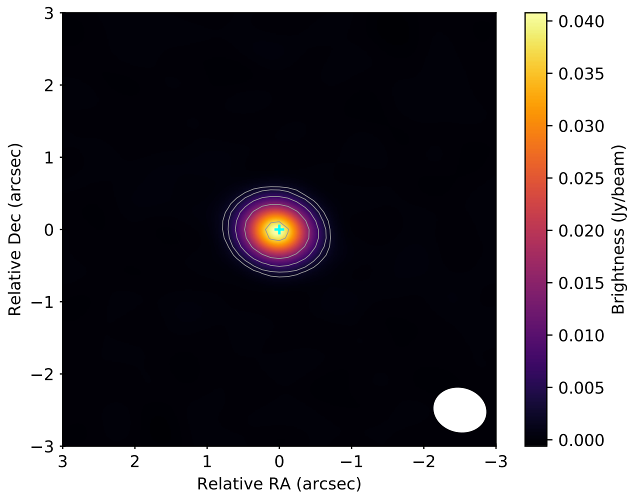

Fig. 1. Self-calibrated continuum map of μ Cep centred at 231.276 GHz. The synthesized beam is represented by the white ellipse at the bottom right corner of the image. The cyan cross marks the position of the star. The contour levels are 3, 5, 10, 20, and 50 times the noise rms (M19).

3.2 Line data

The self-calibrated, continuum subtracted channel maps of the CO v=0, J=2-1 line at 230.538 GHz are represented on Fig. 2. In each map, the gaseous circumstellar environment of the star appears very clumpy. The clumps are identified in detail in M19. In the Local Standard of Rest Kinematic (LSRK) frame the velocity of the star is $v_\star = 32.7 \pm 0.1\,\mathrm{km\ s^{-1}}$. For $v_{\mathrm{LSRK}} > 7.5\,\mathrm{km\ s^{-1}}$, the environment presents a "classical" shape surrounding the star with clumps belonging to a circumstellar envelope or detached from it. However, for $v_{\mathrm{LSRK}} < 7.5\,\mathrm{km\ s^{-1}}$, the environment is dominated by two bright clumps, C1 on the South-West at 1.80 arcsec from the star (1.15 kau at the distance of μ Cep determined to be 641 pc in M19) and C2 roughly centered at the star position.

3.3 3D deprojection and 3D radiative transfer modeling

In order to better understand the characteristics of the circumstellar environment of μ Cep, we used two complementary approaches. First, we deprojected the CO intensity map according to the method used by Guélin et al. (2018). This allows to have a real 3D representation of the material around the star, instead of channel maps. Therefore, it gives access to the full position (x, y, z) of the clumps relative to the star, and to their size. We assumed a constant radial outflow as our beam size of 0.92×0.72 arcsec (590×462 au at 641 pc) resolves only marginally the non-spherical accelerating region (Harper et al. 2001; Höfner et al. 2016). We chose a slow wind velocity of $v_\infty^{\mathrm{slow}} = 25.0\,\mathrm{km\ s^{-1}}$ for the material in channel maps whose velocities are in the interval $v_\star \pm v_\infty^{\mathrm{slow}}$, and a faster wind velocity $v_\infty^{\mathrm{fast}} = 43.0\,\mathrm{km\ s^{-1}}$ otherwise. These velocities are determined from the width of the red and blue line wings of the line respectively. The result of this deprojection is presented in a movie (Fig. 3)

The characteristics of the clumps derived from this deprojection are used as input for a 3D radiative transfer modeling using the code LIME (Brinch & Hogerheijde 2010). The model consists in the different clumps as well as a smooth continuous wind (for more details, see M19). The synthetic emission distribution of the clumps is

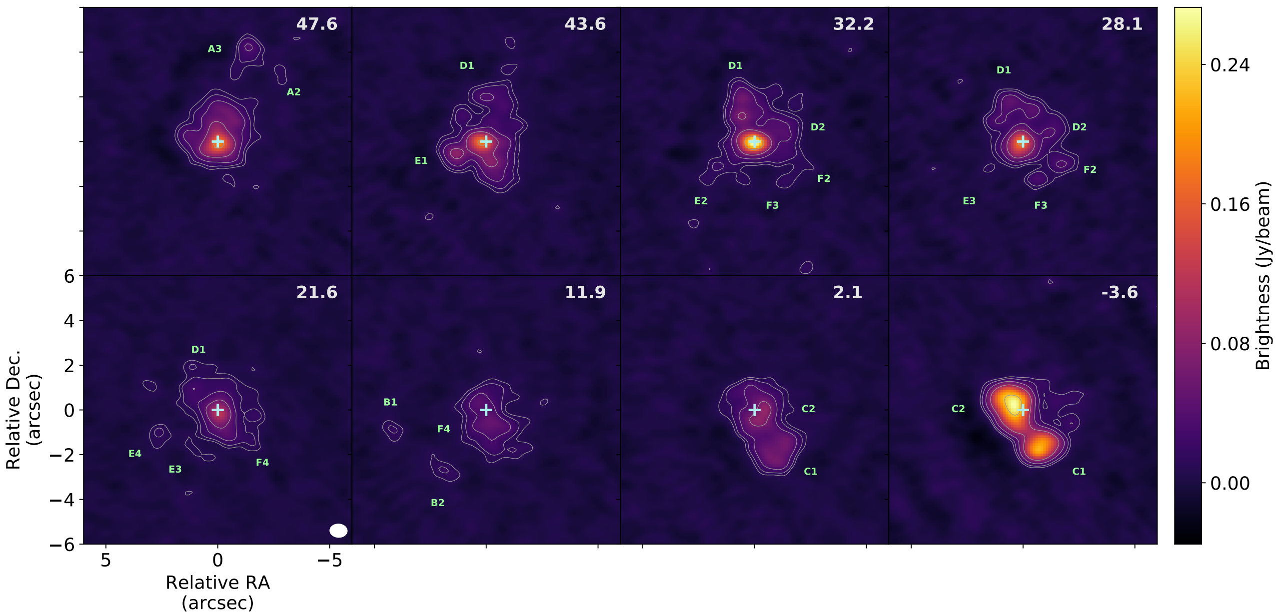

Fig. 2. Sample of the continuum subtracted channel maps of μ Cep obtained with NOEMA and centered at 230.538 GHz. The LSRK (LSR kinematic frame) radial velocity in km s^{-1} is expressed in the top right corner of each map. The LSRK velocity of the star is 32.7 ± 0.1 km s^{-1}. The synthesized beam is represented by the white ellipse at the bottom right corner of the first image of the last row. On each map, the pale blue cross marks the position of the star at the (0, 0) relative coordinates. The contour levels are 3, 5, 10, 20, and 50 times the noise rms of the respective channel. The clumps are identified by the pale green labels. (M19)

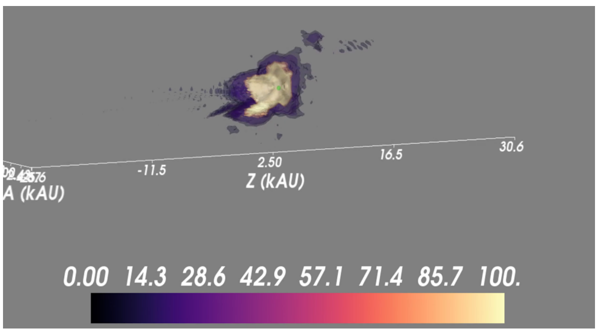

Fig. 3. Three-dimensional rendering of the deprojection of μ Cep's environment in the CO J=2-1 line. A movie is available online at: `https://frama.link/muCep3D`. (M19)

reproducing well the emission from the observed clumps. However, we had difficulties to reproduce the emission located in the central beam area where the smooth outflow component should be dominant, this is particularly the case in the blue wing. This could be due to the presence of unresolved inhomogeneities that cannot be approximated by a smooth outflow. All the clumps except for C1 appear to be optically thin.

The modeling gave us access to the mass of the individual clumps. By using their distance from the central star and the wind speed, we are able to deduce their contribution to the mass loss: $(4.9 \pm 1.0) \times 10^{-7}\,\mathrm{M}_\odot$ yr^{-1}. This value is strongly dependent on the fractional CO abundance we assumed. In particular, according to Huggins et al. (1994) the dominant atomic form of carbon in the circumstellar environment could lead to a CO abundance ten times lower. For the optically thin clumps, this translates in an increase by a factor ten of their mass. For the optically thick C1, if the same process drives the ejection of all the clumps, we can assume that the mass of C1 would also scale inversely to the CO/H_2 ratio. Therefore the mass loss due to the clump would be $(4.9 \pm 1.0) \times 10^{-6}\,\mathrm{M}_\odot$ yr^{-1}. This value is close to the total mass-loss rate determined by Shenoy et al. (2016), meaning that most of the mass loss would then occur through the clumps.

4 Conclusions

We obtained high angular resolution observations of the circumstellar environment of the RSG μ Cep in the CO $J = 2 - 1$ line. The material around the star is distributed in several clumps, two of them being particularly prominent in the blue channels. From a 3D deprojection to properly determine the position and size of the clumps, and a 3D radiative transfer modeling, we were able to determine their mass and therefore their contribution to the mass loss of the star. Depending on the CO fractional abundance, we estimate that at least 25% of the mass loss is contributed by the clumps, the rest being due to a smooth and continuous outflow. However, it is also possible that all the mass loss could be due to the clumps and the smooth spherical outflow non-existent. Mauron (1997) observed the environment of μ Cep from 5 to 60$''$ in the resonant KI lines at 770 nm. He finds evidence of clumps with typical sizes $\sim 2''$. These results agree with ours and suggest that the inhomogeneities that we discovered in the CO line may survive for 10^4 years. The random distribution of the clumps around the star as well as their different distances are arguments in favor of an episodic mechanism launching the mass loss from randomly distributed regions on the photosphere.

This work is based on observations carried out under project number W15BL with the IRAM NOEMA Interferometer. IRAM is supported by INSU/CNRS (France), MPG (Germany) and IGN (Spain). We are grateful to the IRAM/NOEMA staff at the Plateau de Bure observatory for the successful execution of the observations. This project has received funding from the European Union's Horizon 2020 research and innovation program under the Marie Skłodowska-Curie Grant agreement No. 665501 with the research Foundation Flanders (FWO) ([PEGASUS]^2 Marie Curie fellowship 12U2717N awarded to M.M.). LD, WH, DK, and NC acknowledge support from the ERC consolidator grant 646758 AEROSOL. We used the SIMBAD and VIZIER databases at the CDS, Strasbourg (France)[†], and NASA's Astrophysics Data System Bibliographic Services. This research made use of Matplotlib (Hunter 2007), Astropy[‡], a community-developed core Python package for Astronomy (Astropy Collaboration et al. 2013), and Uncertainties[§]: a Python package for calculations with uncertainties.

References

Astropy Collaboration, Robitaille, T. P., Tollerud, E. J., et al. 2013, A&A, 558, A33

Brinch, C. & Hogerheijde, M. R. 2010, A&A, 523, A25

Guélin, M., Patel, N. A., Bremer, M., et al. 2018, A&A, 610, A4

Harper, G. M., Brown, A., & Lim, J. 2001, ApJ, 551, 1073

Höfner, S., Bladh, S., Aringer, B., & Ahuja, R. 2016, A&A, 594, A108

Huggins, P. J., Bachiller, R., Cox, P., & Forveille, T. 1994, ApJ, 424, L127

Hunter, J. D. 2007, Computing In Science & Engineering, 9, 90

Mauron, N. 1997, A&A, 326, 300

Montargès, M., Homan, W., Keller, D., et al. 2019, MNRAS, 485, 2417

Shenoy, D., Humphreys, R. M., Jones, T. J., et al. 2016, AJ, 151, 51

[†] Available at http://cdsweb.u-strasbg.fr/
[‡] Available at http://www.astropy.org/
[§] Available at http://pythonhosted.org/uncertainties/

SF2A 2019
P. Di Matteo, O. Creevey, A. Crida, G. Kordopatis, J. Malzac, J.-B. Marquette, M. N'Diaye, O. Venot (eds)

A SIMPLE TOOL FOR CALCULATING CENTRIFUGAL DEFORMATION STARTING FROM 1D MODELS OF STARS OR PLANETS

P. Houdayer[1], D. R. Reese[1] and T. Guillot[2]

Abstract. We describe a tool which is able to calculate the centrifugal deformation of a rotating star or planet starting from a 1D non-rotating model, for conservative (i.e. cylindrical) rotation profiles. This tool applies an iterative approach based on the Self-Consistent Field (SCF) method while preserving the pressure profile as a function of density. The resultant model is suitable for stellar pulsation calculations, thus making this tool suitable for parametric asteroseismic investigations. It can also be used to calculate the deformation of rapidly rotating planets such as Jupiter and Saturn which contain internal discontinuities.

Keywords: centrifugal deformation, stars, planets, oscillations

1 Introduction

Interferometry has revealed the shortcomings of 1D spherically symmetrical models in describing a number of stars such as Achernar, Vega, or Altair (e.g. Domiciano de Souza et al. 2003; Peterson et al. 2006; Monnier et al. 2007). Likewise, telescope and close-up observations of Jupiter and Saturn have shown that these planets are considerably deformed by the centrifugal acceleration (e.g. Iess et al. 2018; Guillot et al. 2018). Ideally, 2D models which fully take into account the effects of rotation throughout the star's or planet's evolution should be used to model them in a self-consistent way. For instance, the ESTER code is the first to self-consistently take into account centrifugal deformation and baroclinic effects in static rapidly rotating stellar models (e.g. Rieutord et al. 2016). However, such models typically prove to be expensive to calculate and may not currently be the most suitable for a parametric study with, for instance user-defined rotation profiles, or a χ^2 minimisation to fit a set of observations. Furthermore such models do not reach the same degree of realism as 1D models when it comes to modelling stellar or planetary evolution. A solution to this problem is to deform 1D stellar/planetary models using a given rotation profile. Here, we develop a code capable of doing this for conservative (i.e. cylindrical) rotation profiles.

2 Self-Consistent Field method

Our approach is based on the Self-Consistent Field (SCF) method (see Jackson et al. 2005; MacGregor et al. 2007). It consists in calculating the total (gravitational plus centrifugal) potential for a given density distribution and rotation profile, using this to find a new mapping composed of level surfaces, subsequently redistributing density and pressure profiles to this new mapping, and reiterating till convergence. The relation between pressure and density is preserved* by preserving the relation between density and total potential to within an additive constant.

Two variants of this method have been produced:

- a first version which consists in interpolating Poisson's equation onto a spherical grid prior to solving it. Such an approach is computationally fast as Poisson's equation decouples according to different spherical harmonics. However, it is unable to handle discontinuities in the density profile as these line up with level surfaces rather than spherical surfaces.

[1] LESIA, Observatoire de Paris, UniversitÃ© PSL, CNRS, Sorbonne UniversitÃ©, UniversitÃ© de Paris, 5 place Jules Janssen, 92195 Meudon, France
[2] UniversitÃ© CÃ´te d'Azur, Laboratoire Lagrange, Observatorie de la CÃ´te d'Azur, CNRS UMR 7293, 06304 Nice, France

*This turns out to approximate fairly well the more realistic baroclinic models from the ESTER code.

- a second version which solves Poisson's equation directly in a coordinate system based on the level surfaces. Although slower as a result of coupling between the spherical harmonics, this approach is typically more accurate and can handle discontinuous models, which is more appropriate for models of gaseous planets with a solid core, such as Jupiter. The left panel of Fig. 1 illustrate a discontinuous model which has been deformed with this version of the code.

Once such models have been produced, it is possible to study their pulsation modes using the TOP pulsation code (e.g. Reese et al. 2006). The right panel of Fig. 1 illustrates one such mode for a deformed model of Jupiter.

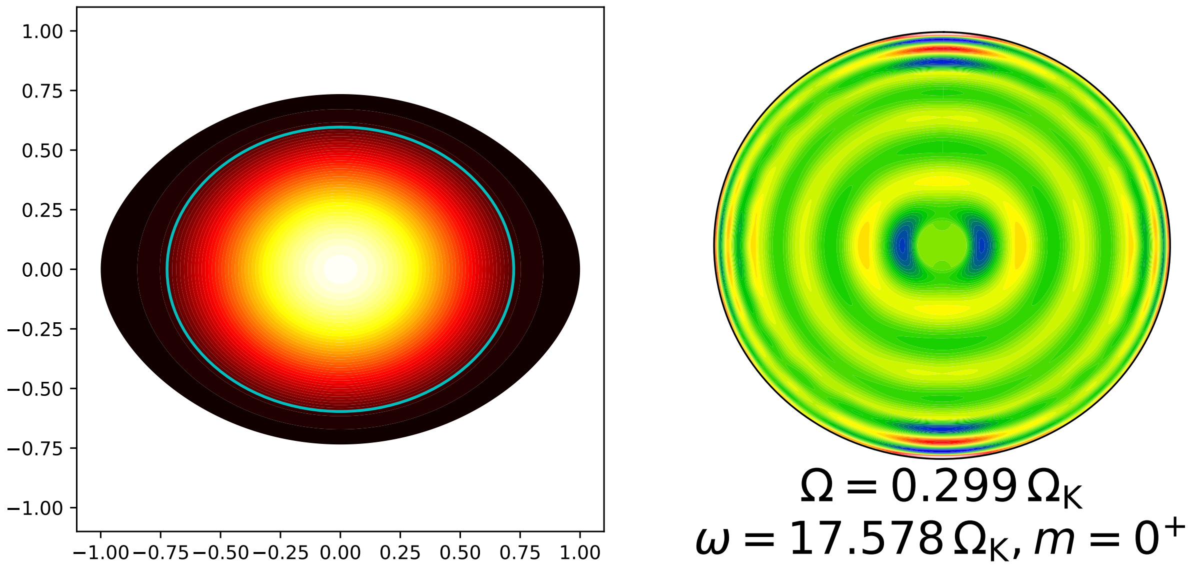

Fig. 1. Left: Deformed $N = 1$ polytropic model with a discontinuity (indicated by the light blue line). **Right:** Pulsation mode in a deformed model of Jupiter.

We gratefully acknowledge the support of the French Agence Nationale de la Recherche (ANR) to the ESRR project under grant ANR-16-CE31-0007 as well as financial support from the Programme National de Physique Stellaire (PNPS) of the CNRS/INSU co-funded by the CEA and the CNES.

References

Domiciano de Souza, A., Kervella, P., Jankov, S., et al. 2003, A&A, 407, L47
Guillot, T., Miguel, Y., Militzer, B., et al. 2018, Nature, 555, 227
Iess, L., Folkner, W. M., Durante, D., et al. 2018, Nature, 555, 220
Jackson, S., MacGregor, K. B., & Skumanich, A. 2005, ApJS, 156, 245
MacGregor, K. B., Jackson, S., Skumanich, A., & Metcalfe, T. S. 2007, ApJ, 663, 560
Monnier, J. D., Zhao, M., Pedretti, E., et al. 2007, Science, 317, 342
Peterson, D. M., Hummel, C. A., Pauls, T. A., et al. 2006, Nature, 440, 896
Reese, D., Lignières, F., & Rieutord, M. 2006, å, 455, 621
Rieutord, M., Espinosa Lara, F., & Putigny, B. 2016, Journal of Computational Physics, 318, 277

SF2A 2019
P. Di Matteo, O. Creevey, A. Crida, G. Kordopatis, J. Malzac, J.-B. Marquette, M. N'Diaye, O. Venot (eds)

A SEISMIC STUDY OF β PICTORIS

D. R. Reese[1], K. Zwintz[2] and C. Neiner[1]

Abstract. The planet-host star β Pictoris has been observed with multiple ground and space-based instruments, especially at the time of the expected transit of the planet's Hill sphere. This has led to a set of pulsation modes detected in up to 5 photometric bands. Using the multi-colour mode amplitudes, we apply a mode identification technique based on a set of $1.8\,\mathrm{M}_\odot$ rapidly rotating stellar models based on the Self-Consistent Field method. We find various solutions and sets of identifications, including near equator-on solutions, as what is expected based on the inclination of the circumstellar disk and planetary orbit. Nonetheless, large discrepancies remain between the observed values of the pulsation frequencies and amplitudes, and the theoretically predicted ones, thus pointing to limitations in the modelling.

Keywords: stars: individual: β Pictoris, stars: oscillations, stars: rotation, stars: interiors

1 Observations

The discovery of an exoplanet orbiting β Pictoris (Lagrange et al. 2010) has sparked considerable interest in this stellar system. Accordingly, this star has been observed by multiple instruments, especially at the time of the expected transit of the planet's Hill sphere thus leading to the detection of 15 pulsation modes in 2 to 5 photometric bands in the frequency range 34 to 55 c/d. Furthermore, this star is rapidly rotating as indicated by its v sin i value of $124 \pm 3\,\mathrm{km\ s}^{-1}$ (Koen et al. 2003), thus pointing to the need to fully include the effects of rotation prior to seismic interpretation.

2 Seismic interpretation

In order to interpret the pulsations of β Pictoris, we applied an MCMC procedure based on the EMCEE package (Foreman-Mackey et al. 2013) in order to fit the pulsation frequencies, amplitude ratios, and a set of classic constraints including the v sin i value, the mass, and the radius. Three free parameters were used in the fitting procedure: the inclination, the rotation rate, and a frequency scale factor (which corresponds to a homologous transformation of the model). The relevant pulsation frequencies and amplitude ratios were obtained by interpolation in a grid of δ Scuti $\ell \leq 3$ pulsation modes obtained for a sequence of $1.8\,\mathrm{M}_\odot$ models based on the Self-Consistent Field method (Jackson et al. 2005; MacGregor et al. 2007) with rotation rates ranging from 0 to 60 % of the critical rotation rate. Pseudo non-adiabatic mode visibilities were derived for inclinations ranging from 0° to 90° using the method described in Reese et al. (2013) and Reese et al. (2017). Instead of using the observational error bars on the frequencies, an adjustable frequency tolerance was used as a trade-off parameter between fitting the pulsation spectrum and fitting the amplitude ratios.

Figure 1 shows scatter plots and histograms of the MCMC solutions in parameter space using only even modes (as expected if the star is close to equator-on in alignment with the planet orbit and circumstellar disk) and a uniform frequency tolerance of 0.1 c/d. The different hatched and coloured regions correspond to solutions with distinct sets of mode identifications. Although the MCMC procedure finds plausible solutions including near-equator ones, discrepancies remain between the observed and theoretical pulsation frequencies and amplitude ratios. Possible ways to improve the agreement include applying full non-adiabatic calculations using ESTER models (Rieutord et al. 2016) and using larger sets of modes, i.e. with $\ell > 3$. A more detailed description of the observations, time series analysis, and seismic study is provided in Zwintz et al. (2019).

[1] LESIA, Observatoire de Paris, Université PSL, CNRS, Sorbonne Université, Université de Paris, 5 place Jules Janssen, 92195 Meudon, France
[2] Institut für Astro- un Teilchenphysik, Universität Innsbruck, Technikerstraße 25, A-6020 Innsbruck, Austria

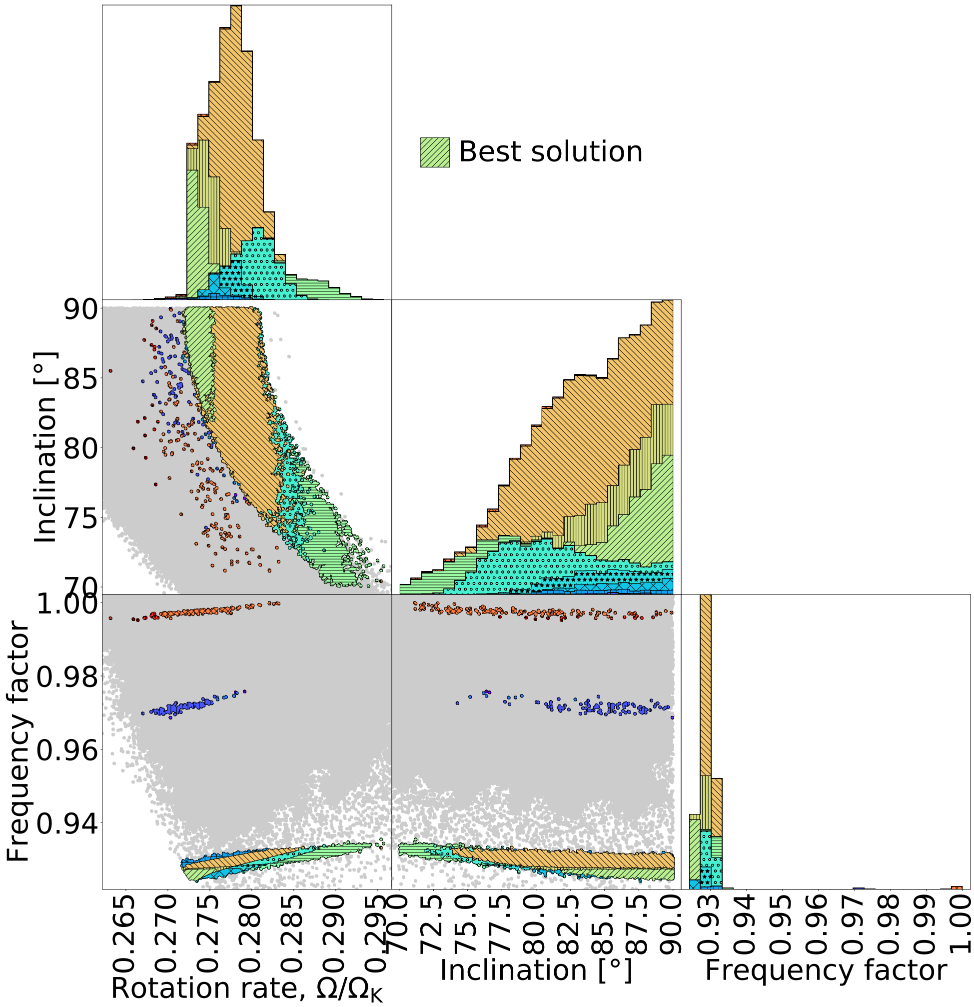

Fig. 1. Scatter plots and histograms depicting the MCMC solutions in parameter space using only even modes and a uniform error tolerance of 0.1 c/d on the frequencies.

DRR acknowledges the support of the French Agence Nationale de la Recherche (ANR) to the ESRR project under grant ANR-16-CE31-0007 as well as financial support from the Programme National de Physique Stellaire (PNPS) of the CNRS/INSU co-funded by the CEA and the CNES. KZ acknowledges support by the Austrian Fonds zur Förderung der wissenschaftlichen Forschung (FWF, project V431-NBL) and the Austrian Space Application Programme (ASAP) of the Austrian Research Pro- motion Agency (FFG).

References

Foreman-Mackey, D., Hogg, D. W., Lang, D., & Goodman, J. 2013, PASP, 125, 306

Jackson, S., MacGregor, K. B., & Skumanich, A. 2005, ApJS, 156, 245

Koen, C., Balona, L. A., Khadaroo, K., et al. 2003, MNRAS, 344, 1250

Lagrange, A. M., Bonnefoy, M., Chauvin, G., et al. 2010, Science, 329, 57

MacGregor, K. B., Jackson, S., Skumanich, A., & Metcalfe, T. S. 2007, ApJ, 663, 560

Reese, D. R., Lignières, F., Ballot, J., et al. 2017, å, 601, A130

Reese, D. R., Prat, V., Barban, C., van 't Veer-Menneret, C., & MacGregor, K. B. 2013, å, 550, A77

Rieutord, M., Espinosa Lara, F., & Putigny, B. 2016, Journal of Computational Physics, 318, 277

Zwintz, K., Reese, D. R., Neiner, C., et al. 2019, A&A, 627, A28

SF2A 2019
P. Di Matteo, O. Creevey, A. Crida, G. Kordopatis, J. Malzac, J.-B. Marquette, M. N'Diaye, O. Venot (eds)

REVISITING THE SURFACE BRIGHTNESS-COLOUR RELATION IN THE CONTEXT OF THE ARAUCARIA PROJECT AND THE PLATO SPACE MISSION

A. Salsi[1], N. Nardetto[1], D. Mourard[1] and O. Creevey[1]

Abstract. The ease of use of Surface Brightness-Colour Relations (SBCRs) is a major advantage in the determination of stellar angular diameters. It currently plays a significant role for the distance determination of eclipsing binaries and also for the characterization of exoplanets host stars. Despite the large number of existing SBCRs, strong discrepancies occur on the outer edges of the surface brightness F_V versus $V-K$ colour diagram. Challouf et al. (2014) reached a precision of 7% on the estimate of the angular diameter for $V-K<0$ mag, while 10% of accuracy only is expected on the other part of the diagram. To overcome these discrepancies, we apply the same methodology to all the angular diameter and photometric estimates available in the literature. We also observe new stars using the CHARA/VEGA and PAVO instruments. We show that the SBCR strongly depends on the spectral type and the luminosity class of stars. An unique SBCR can therefore not be used for any type of star.

Keywords: stars: fundamental parameters – cosmology: distance scale – techniques: interferometric

1 Introduction

Surface Brightness-Colour Relations (SBCRs) are very convenient tools to determine precisely stellar angular diameters. Assuming the star is a black body, the surface brightness (i.e. the flux density per unit angular area) is connected to the angular diameter. Also, the bolometric surface flux $f_{\rm bol}$ is proportional to the effective temperature T_{eff}^4 of the star, and therefore to its colour $m_{\lambda_1}-m_{\lambda_2}$. In this way, the surface brightness can be estimated by the linear relation

$$F_{\lambda_1} = a\,(m_{\lambda_1}-m_{\lambda_2})+b. \tag{1.1}$$

Pietrzyński et al. (2019) have recently constrained the Large Magellanic Cloud distance to 1%, applying SBCRs to 20 eclipsing binaries. The PLATO (PLAnetary Transits and Oscillations of stars) space mission, planned for a launch in 2026, has the aim of characterizing exoplanetary systems, basing on the transit method (Catala & PLATO Team 2006). Knowing the angular diameter of the star very accurately allows to determine the distance of nearby galaxies or the radius of exoplanets. So far, 23 SBCRs have been established in the $V-K$ colour range, covering all spectral types and luminosity classes. We have represented these SBCRs on Fig. 1. Following Nardetto (2018) analysis, we find an agreement of 1-4% (resp. 2-6%) in the PLATO spectral range domain (F5-K7) for stars with classes of IV/V (resp. II/III). For M stars (V-K<5), SBCRs available are precise but inconsistent at the 10% level. For O, B stars (V-K<0), SBCR are unprecise at the 7% level. The major limitation of these SBCRs comes from their inhomogeneous datasets and methodologies.

2 Revisiting the calibration of the SBCRs

2.1 *Early-type stars: the distance of bright eclipsing binaries in nearby galaxies (M31, M33)*

Early-type eclipsing binaries are usually used to determine distances of M31 and M33 (Vilardell et al. 2010; Bonanos et al. 2006). In the course of the Araucaria project (Pietrzyński & Gieren 2002), an observing program with the VEGA instrument on the CHARA array is ongoing. This program, based on the observation of 20 early-type stars, aims at developing a new SBCR that could allow to estimate stellar angular diameters with a precision of about 2%.

[1] Université Côte d'Azur, OCA, CNRS, Laboratoire Lagrange, France

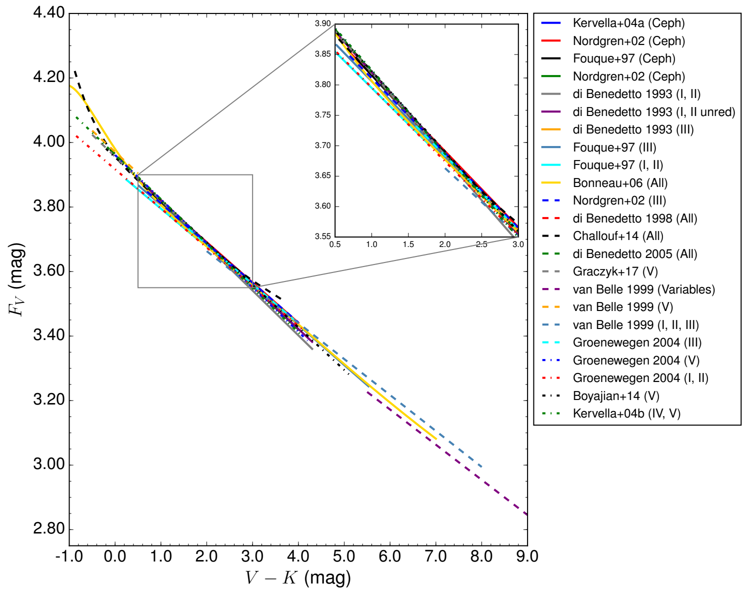

Fig. 1. Comparison of the 23 existing SBCRs in their respective $V-K$ colour domain of application. The square in the upper-right corner shows a zoom in the [0.5;3] mag colour region. See Nardetto (2018) for the references.

2.2 Late-type stars: characterization of exoplanets

On the other hand, late-type stars are stars with F5 to F9, K and M spectral types. Building SBCRs for these cool stars are of primary importance for the PLATO mission. Indeed, SBCRs give stellar angular diameters, that are essential to characterize exoplanetary systems with the transit method. An observation program is dedicated to implement a new SBCR for these types of star. The advantage here is the availability of data from both VEGA and PAVO instruments on the CHARA array. We want first to compare the angular diameters obtained with both instruments, and include them in SBCRs we have developed for late-type stars using existing interferometric data combined with selection criteria we have implemented (Salsi et al. 2020).

3 Conclusions and preliminary results

SBCRs are largely involved in many international projects. However, using one or another relation can lead to significant differences according to the $V-K$ colour of the star. Our works on early-type and late-type stars have therefore the aim to better understand the physics behind the SBCRs and also clarify the effect of stellar activity by revising with a homogeneous approach the whole F_V versus $V-K$ colour diagram. For the very first time, we have implemented criteria to properly select interferometric measurements from the JMMC Measured stellar Diameters Catalog (Chelli et al. 2016) to build strong and accurate SBCRs for late-type stars. This part of the work will be described in Salsi et al. (2020). In this work, we show that considering both the spectral type and the luminosity class of stars is of primary importance to develop accurate SBCRs, since relations for giants are totally inconsistent with those of subgiants and dwarfs.

References

Bonanos, A. Z., Stanek, K. Z., Kudritzki, R. P., et al. 2006, Ap&SS, 304, 207
Catala, C. & PLATO Team. 2006, ESA Special Publication, 1306, 497
Challouf, M., Nardetto, N., Mourard, D., et al. 2014, A&A, 570, A104
Chelli, A., Duvert, G., & Bourgès, L. 2016, A&A, 589, A112
Nardetto, N. 2018, Habilitation Thesis
Pietrzyński, G. & Gieren, W. 2002, AJ, 124, 2633
Pietrzyński, G., Graczyk, D., Gallenne, A., et al. 2019, Nature, 567, 200
Salsi, A., Nardetto, N., Mourard, D., et al. 2020, A&A, in prep.
Vilardell, F., Ribas, I., Jordi, C., Fitzpatrick, E., & Guinan, E. 2010, A&A, 509, 70

SF2A 2019
P. Di Matteo, O. Creevey, A. Crida, G. Kordopatis, J. Malzac, J.-B. Marquette, M. N'Diaye, O. Venot (eds)

3D MAGNETO-HYDRODYNAMIC SIMULATIONS TO COUNTERACT THE CONVECTIVE NOISE SOURCE FOR EXTRASOLAR PLANET DETECTION

S. Sulis[1,2], L. Bigot[2] and D. Mary[2]

Abstract. Convection transports energy from the stellar interior towards the surface in late type stars. Its properties are essential to understand the stellar structure and evolution and can now be reliably inferred by modern 3D magneto-hydrodynamic simulations. Convection is also a significant noise source for detecting extrasolar planets. In this paper, we analyze the potential of 3D MHD simulations in reproducing realistic time series of radial velocity to estimate the statistical properties of this noise source and, in turn, to improve exoplanets' detectability.

Keywords: Sun: granulation, Techniques: radial velocities, Planets and satellites: detection

1 Introduction

Resolved observations of the Sun clearly show moving granular structures that are the manifestation of the convection at the solar photosphere. Present at the surface of all late type stars, convection transports energy from the stellar interior towards the surface and is a key process to understand the stellar structure and evolution. Indeed, the dynamics of the convective cells define the thermal stellar stratification, mix the chemical elements and generate the surface acoustics modes.

Since the 90's, 3D magneto-hydrodynamic simulations (MHD) are developed (Nordlund & Galsgaard 1995) based on radiative compressive hydrodynamics equations (including the wavelength-dependent radiative transfer) as well as on realistic equations-of-state that accounts for ionization, recombination, dissociation (Mihalas et al. 1988) and line opacity (Gustafsson et al. 2008). Generally used for stellar diagnostics (e.g. chemical abundances, limb darkenings, radial velocities), they succeed in reproducing the properties of the stellar convection (granules' size, lifetime, spectral lines shape).

For late-type stars others than the Sun, convection is not resolved but its properties are extracted indirectly from variations of the spectroscopic stellar lines and the photometric variability in integrated starlight (Dravins & Lind 1984). While the study of these different signatures informs a lot on the star, this variability represents a significant noise source hampering the detection of smaller stellar (e.g. acoustic and gravity modes) and planetary signals.

From solar observations, we know that granulation can generate variability with amplitudes up to several tenth of centimeters per second in radial velocities (RV) (Saar & Donahue 1997). This is significant compared to the signal from Earth-like planets : we expect that a Earth orbiting a Sun generate a RV signal of 9 cm.s^{-1} amplitude only (Wright 2018). Thus, the signatures of stellar granulation need to be understood and "statistically controlled" to be able to reliably detect Earth-analogues (Meunier et al. 2015). In Sulis et al. (2017), we demonstrated that using synthetic time series of a granulation noise leads to a better control of the detection tests statistics. We focus in the present paper on the possibility of using MHD simulations to reproduce convection noise of a specific star, the Sun, and we illustrate how the approach can improve the detection of low mass extrasolar planets by the RV technique.

[1] Space Research Institute, Austrian Academy of Sciences, Schmiedlstraße 6, 8042 Graz, Austria
[2] Université Côte d'Azur, Observatoire de la Côte d'Azur, CNRS, Lagrange UMR 7293, CS 34229, 06304, Nice Cedex 4, France

2 Simulations of the solar granulation

Modern MHD codes simulate the surface convection and its stratification over the stellar photosphere in 3D cartesian-box (Nordlund 1985). In this study, we use the STAGGER CODE*, described in Nordlund & Galsgaard (1995) that simulates granulation in a box of size 8000×8000 kms and $+500$ and -3400 km above and below the surface at optical depth $\tau = 1$. The code solves the full set of conservative hydrodynamical equations coupled to an accurate treatment of the radiative transfer. The solar parameters that define our 3D model are $T_{\rm eff} = 5775 \pm 30$ K, $\log g = 4.44$ and a solar chemical composition (Asplund et al. 1999). We impose a traverse magnetic field at the bottom of the simulation's boxes so that the averaged surface field is roughly 100 G, as observed with spectropolarimetry (Trujillo Bueno et al. 2004). The detailed description of this simulation will be published in an article currently in preparation. In total, we generate the evolution of 76 528 snapshots of solar convection corresponding to 53.14 days of physical time (with a temporal sampling of 60 seconds). This is, to our knowledge, the longest simulated time series of granulation ever generated with such a 3D code.

This kind of 3D simulations have already shown their accuracy in resolving observations of the solar surface, see e.g. similarities of the observed structures in continuum intensities (Danilovic et al. 2008) or of the spectrally resolved solar lines width and asymmetries (Asplund et al. 2000). However, their efficiency in retrieving the disk integrated RV properties is still unproved. One reason is that the 3D simulations are too computationally time consuming to simulate what would be the contribution of thousands of convection boxes covering the entire solar disk. In the following subsections, we discuss the influence of the size of the simulated patch as well as its position on the resulting line-of-sight velocities, and present a first comparison of disk-integrated velocities with solar spatial observations.

2.1 3D local simulation patch: velocity dependence on the surface size area

To illustrate the dependence of the observed velocities with the size of the considered surface area, we selected different sizes of solar images taken by the *Helioseismic and Magnetic Imager* (HMI) on board the *Solar Dynamics Observatory* (SDO; Schou et al. (2012)). Fig. 1 shows the RV extracted from these solar images. We see the decrease of the velocity amplitudes with the size of the observed surface of the solar disk. Quantitatively, the velocity root-mean-square (rms) corresponding to a single granule, a set of tenth granules, a single supergranule and a set of tenth supergranules are 247.2, 105.2, 12.3, and 2.3 m.s^{-1}, respectively. This decrease in amplitude is due to a cancellation effect between the contribution of the upflows in the granules' center and the downflows in the intergranular lanes. When comparing this size-dependent observations to the simulated velocity extracted from 3D boxes of similar sizes, we observe a consistent decrease in amplitude. This is shown in the second and last panel of Fig. 1 using 3D simulations of supergranulation (R. Stein, priv. communication) and granulation†.

*`http://www.astro.ku.dk/~kg/Papers/MHDcode.ps.gz`

†In this figure, the granulation velocity has been extracted by considering a subset of the supergranulation 3D box.

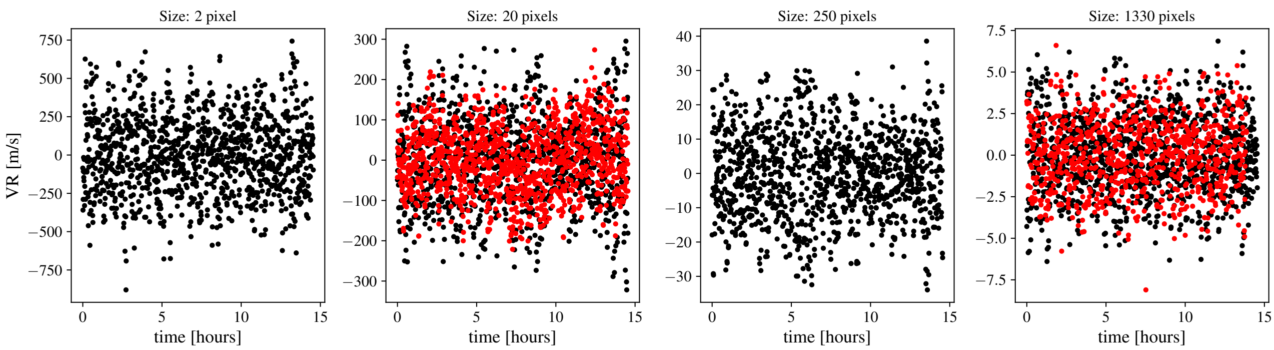

Fig. 1. Sequence of solar radial velocities extracted from HMI/SDO observations (black) for different sizes of the solar surface (in pixel). The size is indicated in the panels' title with 1 pixel corresponding to ≈ 388 km. From left to right the size corresponds roughly to the size of a granule, the size covered by a 3D cartesian-box of granulation, the size of a supergranule and the size covered by a 3D cartesian-box of supergranulation. Synthetic velocities extracted from 3D MHD simulations are compared with observations in the second and last panels (red).

2.2 Inclination of the 3D patch: velocities from center to limb

The line-of-sight projected velocity depends also on the relative distance of the observed surface to the disk center. At a given time, this velocity can be decomposed as a combination of a radial and an horizontal component. The horizontal component, higher in amplitude, is completely cancelled out by projection effect when we look at the center of the solar disk ($\mu = \cos\theta = 1$). At limb, however, the vertical flow vanishes and only the horizontal component contributes to the line-of-sight velocity (Nordlund et al. 2009). The resulting decrease of the velocity amplitudes observed from the limb to the center of the disk is shown in Fig. 2. Hence, the resulting velocities depend critically on the exact region of the solar surface that is observed (Löhner-Böttcher et al. 2018). These amplitudes also depend on the properties of the considered spectral line and on the strength of the local magnetic field as shown in Cegla et al. (2018). Once integrated over the limb angle, the horizontal component is compensated by the radial flows of the disk center. This leads to RV time series of several tenths of cm.s^{-1} in amplitude – which is still enough to mimic/hide RV signatures of small exoplanets.

2.3 Disk-integrated velocities

To compare the simulated velocities with disk-integrated solar observations, we selected observations taken from space by the *Global Oscillation at Low Frequencies* (GOLF) resonant scattering spectrophotometer on board the *Solar and Heliospheric Observatory* (SoHO; Gabriel et al. (1995)). GOLF provides continuous measurements of the sodium doublet lines at $\lambda = 5895.924$ Å and 5889.950 Å . The data, calibrated by Appourchaux et al. (2018), consist in 22 years of almost continuous observations regularly sampled every 20 seconds.
To reproduce these observations, we computed synthetic spectra of the sodium doublet for different μ cosine angles. We then covered the solar surface with simulation patches taken at different time, and we associated to each of them the μ angle corresponding to the patch position on the disk. We integrated the resulting flux to obtain the global disk-integrated velocity at a given time. The detailed description of this procedure will be given in a forthcoming paper.

The final comparison between observed and calibrated disk-integrated synthetic velocities of the solar granulation is shown in panels (a) and (b) of Fig. 3 for the periodograms and velocities, respectively. We observe a good match between the power spectrum density (PSD) estimates over the correlation regime dominated by the granulation noise (i.e., for ν typically in the range $[30, 1000]$ μHz).

3 Design of powerful detection tests

As studied in Sulis et al. (2017), simulations of granulation noise can be exploited to calibrate (or standardize) the periodogram of the observations in order to design more reliable detection tests. In fact, in the case of regularly sampled observations, the distribution of the resulting standardized periodogram ($\widetilde{P}$, see Eq. (8) of Sulis et al. (2017)) is essentially independent of the granulation noise PSD under the null hypothesis $\mathcal{H}_0$ (i.e., when only noise is present in the data). Hence, the false alarm probability (P_{FA}) is *independent of the considered star's granulation.* This is a very interesting feature in practice, which is not present for tests based on the classical periodogram (P). The test threshold can be used to control the P_{FA} in the case of $\widetilde{P}$ but not of P, because in the latter case the distribution of the considered detection test depends on the unknown PSD of the granulation noise.

We now wish to investigate, on a real data set from GOLF, the agreement between our theoretical results

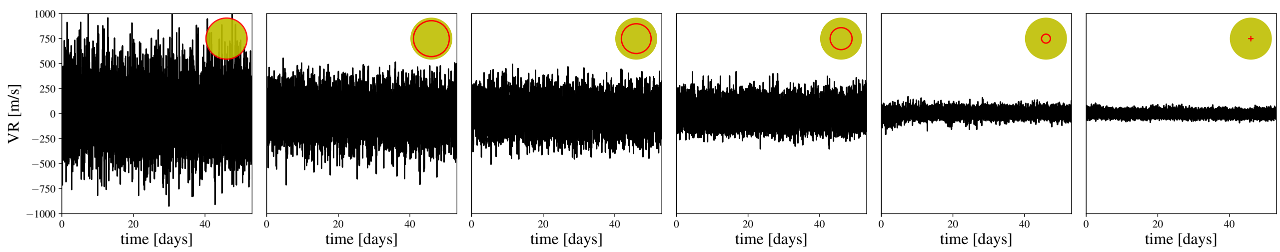

Fig. 2. Simulated velocities for different center to limb cosine angles (μ). From left to right: $\mu = 0.12$, 0.39, 0.60, 0.80, 0.92, 1.00. On each panel, the red circle illustrates the considered μ-isocontour.

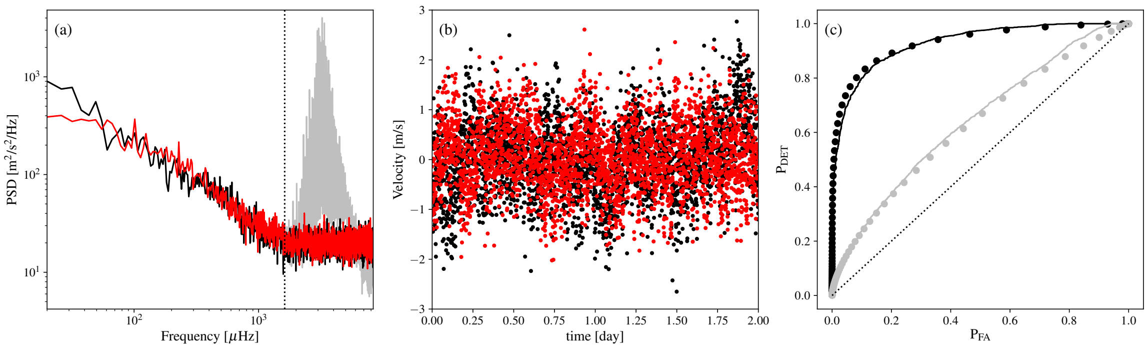

Fig. 3. (a-b) Comparison between GOLF observations (black) and synthetic RV generated using 3D codes (red). Oscillation modes and high frequencies ($\nu_c > 1620$ μHz, see the vertical dotted line in (b)) have been filtered out (in gray : periodogram of synthetic RV with p-modes not filtered out). To restore the flat, high frequency part of GOLF data, we added a white Gaussian noise with variance estimated using GOLF raw periodogram (at frequencies $\nu > \nu_c$). (c) Empirical (solid) and theoretical (dots) ROC curves of tests $T_M(\widetilde{P})$ for planets with mass $\mathrm{M_p} = 0.25\ \mathrm{M_\oplus}$ (black) and $\mathrm{M_p} = 0.15\ \mathrm{M_\oplus}$ (gray) under $\mathcal{H}_1$.

and the actual performances of a particular detection test. The periodogram of GOLF data is here standardized by synthetic velocities coming from our MHD simulations. Consider the test of the maximum periodogram value (see Sulis et al. (2017) for several other interesting tests and their comparison), whose test statistic is defined as $T_M(\widetilde{P}) := \max_{\nu} \widetilde{P}(\nu)$. This test claims a detection if the highest peak of $\widetilde{P}$ is above a predefined threshold. On the theoretical front, analytical expressions for the P_{DET} and the P_{FA} as a function of the number of available noise time series are derived in Chap 3. (Eq. (3.18) and (3.19)) of Sulis (2017). Here, we compare these theoretical expressions with empirical results derived using solar observations. For this comparison, we selected as a data set under $\mathcal{H}_0$ a batch of 1679 sequences of regularly sampled ($dt = 1$ minute) 2-day length solar time series ($N = 2880$ data points for each time series). To build a data set with planetary signals in the considered frequency range[‡], we added to each of these sequences the RV signature of a planet, with 0.25 and 0.15 Earth mass ($M_\oplus$)[§] We then computed the empirical probability of detection (P_{DET}) and the P_{FA} for the test $T_M(\widetilde{P})$ with $\widetilde{P}$ the periodogram of GOLF observations standardized by an averaged periodogram coming from the average of $L = 20$ synthetic RV time series generated through our MHD simulations. The resulting empirical *Receiver Operating Characteristic* (ROC) curves, that represent the P_{DET} as a function of the P_{FA}, are shown in Fig. 3, panel (d). Logically, the performances of both tests increase with the planet's mass. Comparing now the theoretical and empirical ROCs curves of the test for a given mass and a given P_{FA}, we observe a good match of the curves in both cases. This shows that the MHD based approach is successful in controlling, theoretically and in practice, the statistical performance of the test, although the PSD of the granulation noise is partially unknown.

4 Conclusions

Reliably detecting low mass planets whose signatures are buried in the stellar noise is a difficult point. Based on GOLF data, our results show that for Solar-like stars, 3D MHD simulations can be used to generate realistic RV synthetic time series of the granulation noise. These simulations can further be used as training data sets to control accurately the false alarm rate of detection tests in presence of granulation noise.

S. Sulis acknowledges support from the Austrian Research Promotion Agency (FFG) under project 859724 "GRAPPA". We acknowledge financial support from "Programme National de Physique Stellaire" (PNPS) of CNRS/INSU, CEA and CNES, France

[‡]To avoid the influence of other noise sources, we considered only frequencies $\nu \in [30, 1000]$ μHz.
[§]The other Keplerian parameters are fixed: period= 4 hours, inclination and argument of periapsis $= \pi/2$ rad, eccentricity= 0.

References

Appourchaux, T., Boumier, P., Leibacher, J. W., & Corbard, T. 2018, A&A, 617, A108

Asplund, M., Nordlund, Å., Trampedach, R., Allende Prieto, C., & Stein, R. F. 2000, A&A, 359, 729

Asplund, M. et al. 1999, A&A, 346, L17

Cegla, H. M., Watson, C. A., Shelyag, S., et al. 2018, ApJ, 866, 55

Danilovic, S., Gandorfer, A., Lagg, A., et al. 2008, A&A, 484, L17

Dravins, D. & Lind, J. 1984, in Small-Scale Dynamical Processes in Quiet Stellar Atmospheres, ed. S. L. Keil, 414

Gabriel, A. H. et al. 1995, Solar Physics, 162, 61

Gustafsson, B., Edvardsson, B., Eriksson, K., et al. 2008, A&A, 486, 951

Löhner-Böttcher, J., Schmidt, W., Stief, F., Steinmetz, T., & Holzwarth, R. 2018, A&A, 611, A4

Meunier, N. et al. 2015, A&A, 583, A118

Mihalas, D., Dappen, W., & Hummer, D. G. 1988, ApJ, 331, 815

Nordlund, Å. 1985, Solar Physics, 100, 209

Nordlund, Å. & Galsgaard, K. 1995, Technical report, Astronomical Observatory, Copenhagen University,

Nordlund, Å. et al. 2009, Living Reviews in Solar Physics, 6, 2

Saar, S. H. & Donahue, R. A. 1997, The Astrophysical Journal, 485, 319

Schou, J., Scherrer, P. H., Bush, R. I., et al. 2012, Sol. Phys., 275, 229

Sulis, S. 2017, PhD thesis, supervised by par Mary, D. and Bigot, L., Université Côte d'Azur 2017, `http://www.theses.fr/2017AZUR4073/document`

Sulis, S., Mary, D., & Bigot, L. 2017, IEEE TSP, 65, 2136

Trujillo Bueno, J., Shchukina, N., & Asensio Ramos, A. 2004, Nature, 430, 326

Wright, J. T. 2018, Radial Velocities as an Exoplanet Discovery Method, 4

Session 16

Collaborations Amateurs Professionnels

SF2A 2019
P. Di Matteo, O. Creevey, A. Crida, G. Kordopatis, J. Malzac, J.-B. Marquette, M. N'Diaye, O. Venot (eds)

AN EXAMPLE OF AM-PRO COLLABORATION AT THE PIC DU MIDI: THE OATBLS

A. Lekic[1]

Abstract. The objective of the OATBLs is to access the Bernard Lyot Telescope to make observations and thus contribute to the astrophysical studies being conducted on the Pic du Midi site by the statutory observers. The members of the association are called upon in the event of a deficit of the latter, who remain the priority in the planning.

Keywords: OATBL, Pic du Midi, Bernard Lyot, association, am-pro collaboration.

1 Introduction

Like any service observer, the members of the association work with the TBL operations team. They carry out one-week observation missions at the summit of the Pic du Midi and follow the guidelines of the scientific programs established by the supporting astronomers. The observation schedule is established every six months. Three months before the beginning of each semester, it is presented to the OATBLs, who can then fill the places left vacant by the statutory observers. The OATBLs do not only replace the TBL statutory observers. They also have their own amateur research program to which they contribute with discretionary time obtained in collaboration with the OMP. We will first present the instrument and the association. Finally, we will conclude with the preliminary results obtained from observations made during discretionary time.

2 An example of amateur-professional collaboration

2.1 The means of observation: the Bernard Lyot Telescope

Located at an altitude of 2778 m in metropolitan France at the Pic du Midi, the Bernard Lyot telescope is of Cassegrain type. Its mirror has a diameter of 2 m and a focal length of 50 m. The mount is of horseshoe type. The Narval instrument is a spectro-polarimeter with a resolution of R = 65000, installed in 2006. Both spectroscopy and spectro-polarimetry modes are used thanks to Narval. In 2019, Neo-Narval arrived at the Bernard Lyot telescope: it was a stabilisation in radial velocity v of less than 3 m/s of Narval. The study of planetary systems in exoplanetology is the objective of this instrument. The stellar activity of host stars will be studied using the configuration for spectro-polarimetry: the study of the magnetic field of these stars will then be made possible.

2.2 The association and the amateur research program

Since 2016, OATBLs have been filling the schedule of service observers, in addition to the statutory ones. The OATBLs are there to supplement the statutory staff if the schedule cannot be filled. Since 2018, the amateur program has been studying stars with high metallicities. More than 30 target areas have already been recorded. The association involves its members to develop tools and programs to analyze TBL data.

---

[1] OATBL, IPSA, SAF

2.3 First results of the OATBL's amateur research program

Figure 1 correctly details the data to be processed or the data to be understood in the context of the High Metallicity Stars Program. More than 36 spectra have been obtained. Having the study of these spectra already started, we are focusing on the region of the H alpha line.

Emission spectra of VV Cep, and the eclipse of its companion, were obtained by the members of the association during discretionary time. Amateurs attempted to deconvolve the spectra using Gaussian and Lorentzian lines. The understanding of the phenomena is helped by the constant dialogue with the astronomers of the OMP. In addition, there is a great involvement of the members of the association to exploit the data collected: development of python / Matlab programs (especially by student members of OATBLs), data analysis with OATBL2fits. The first idea is that members use existing spectroscopy software to understand the spectra already obtained. Finally, it is also the intergenerational mutual aid that counts: students and young amateurs can work with an older member to share their knowledge.

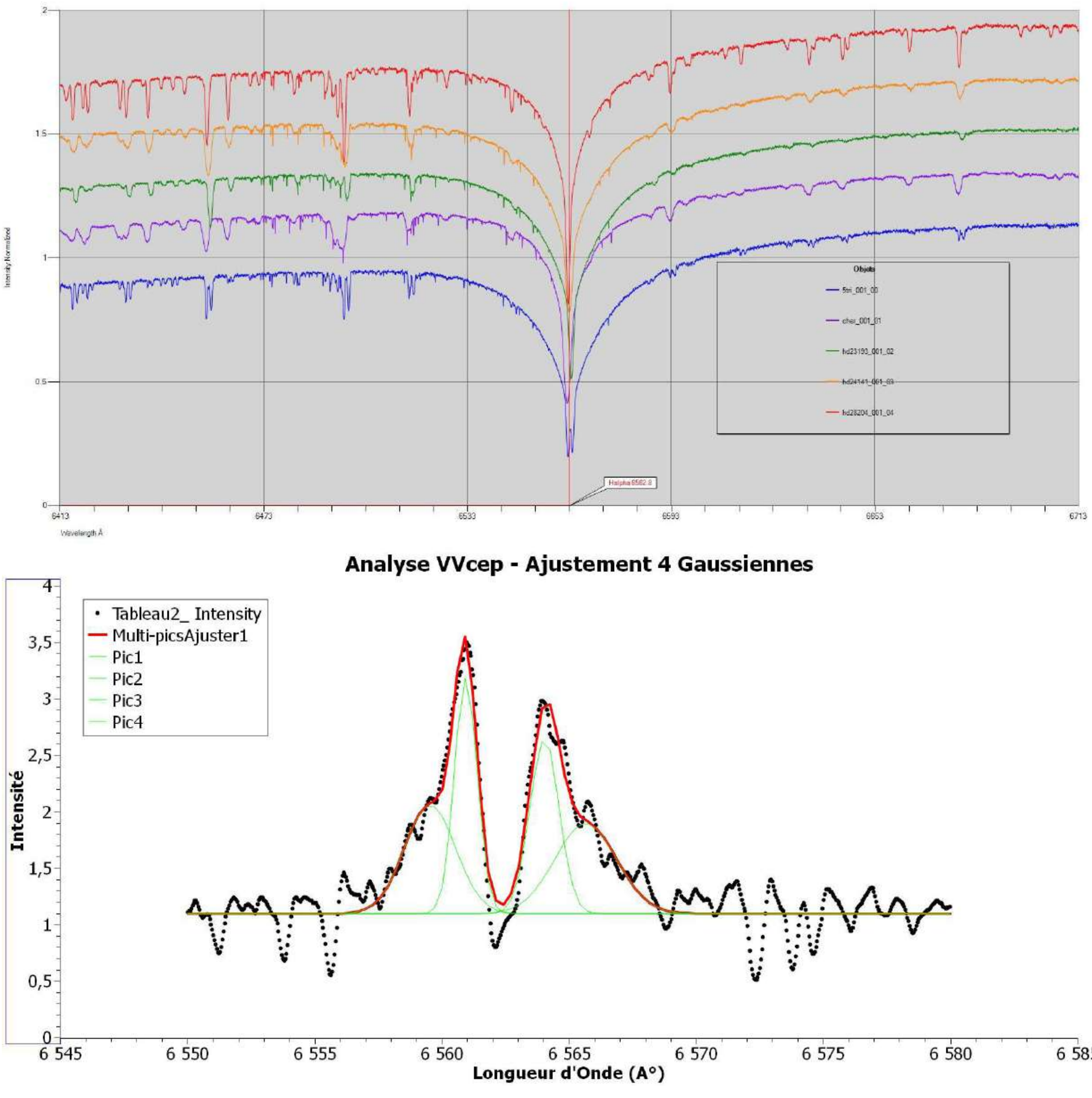

Fig. 1. Top: Data set for 5 stars with high metallicity: alpha balmer line. **Bottom:** Eclipse for VVcep observed by the OATBLs.

3 Conclusions

For the near future, the objective of the OATBL members is as follows: to analyze the spectra of the 36 high metallicity star datasets and deconvolute the spectra correctly while writing in parallel a bibliographic report. A future report will be published and available online on the website of the association.

SF2A 2019
P. Di Matteo, O. Creevey, A. Crida, G. Kordopatis, J. Malzac, J.-B. Marquette, M. N'Diaye, O. Venot (eds)

COLLABORATIVE OBSERVATIONS OF ASYNCHRONOUS BINARY ASTEROIDS

R. Montaigut[1, 2], B. Christmann[1, 3], M. Conjat[4], M. Deldem[5], C. Gillier[1,2], A. Leroy[2, 6], D. Romeuf[7] and P. Sogorb[8]

Abstract. Time-serie photometry of asteroids gives the possibility to discover and study the binary nature of some small bodies of the solar system. In this proceeding, we describe methods and tools developed by a group of French amateur astronomers to make measurements more reliable, characterize the physical properties of asynchronous binary asteroids, and coordinate observations using a collaborative tool.

Keywords: binary asteroids, photometry, lightcurves, collaboration tools

1 Introduction

From differential photometry measurements obtained over many nights, it is possible to determine the rotation period of an asteroid and measure the amplitude of its brightness variation. The shape of the lightcurves provide constrains on the spin orientation and 3D shape of the observed asteroid (Kaasalainen & Torppa 2001; Ďurech et al. 2015).

For the past twenty years, these measurements have been mainly produced by amateur astronomers (see their contribution, in, e.g., Hanuš et al. 2013, 2016). With a small diameter telescope and an entry-level CCD camera, it is indeed possible to obtain valuable photometry (0.01–0.05 mag) on asteroids up to magnitude 16 (Mousis et al. 2014).

The technique of differential photometry is easy to implement and many software used by amateur astronomers make this kind of analysis possible. This method gives the possibility to correct for typical atmospheric effects such as extinction since the target asteroid and the reference stars are in the same field of view. The measurements obtained have a very good fidelity which makes it possible to detect small relative variations in the lightcurve produced.

2 Detection of binary asteroids by photometry

A multi-periodic analysis of differential photometry measurements is a powerful way to detect mutual eclipsing or occulting phenomena on (asynchronous) binary systems. For that, lightcurve caused by the rotation of the primary target upon itself is subtracted from the data to reveal the brightness variation generated by the rotation of the primary asteroid (Pravec et al. 2006; Margot et al. 2015).

Mutual eclipses and occultations can then be characterized, and the orbital period of the system is determined by the repetition of these phenomena. The depth of the secondary occultation provides an estimate of the ratio of the diameters of the two bodies (Pravec et al. 2006; Scheirich & Pravec 2009). The elongation of the secondary body and its rotation period, generally synchronized with the orbital period, can also be detected by this method (Pravec et al. 2016).

[1] Club d'Astronomie de Lyon Ampère (CALA), Place de la Nation, 69120 Vaulx-en-Velin, France
[2] Observatoire OPERA, 33820 Saint Palais, France
[3] Observatoire La Souchère, 69510 Soucieu-en-Jarrest, France
[4] Observatoire de la Côte d'Azur, 06304 Nice, France
[5] Observatoire Les Barres, 13113 Lamanon, France
[6] Uranoscope, Avenue Carnot 7, 77220 Gretz-Armainvilliers, France
[7] Observatoire de Pommier, 63230 Chapdes-Beaufort, France
[8] Observatoire Bastidan, 84240 La Bastide des Jourdans, France

3 Development of methods and tools

To contribute to the discovery and study of binary asteroids, we federated a group of amateur astronomers and developed different tools to master the process of photometric reduction and analyze the data we produce.

A script has been developed in the Prism software* to optimize the aperture photometry technique and to master the color effects by an appropriate selection method and the management of the color indices of the reference stars. The script produces quality indicators and analysis charts to control the representativeness of the measurements. It ensures reproducibility, traceability, and standardization of the results produced.

To analyze the data of the different observers, an Excel™ macro was developed to generate lightcurves and to characterize the physical properties of the objects observed. This tool integrates different features to adjust the offset of each measurements series, to model the lightcurve by a non-parametric regression and to determine the main rotation period of the asteroid by an automatic search of the optimal modeling residue. Multi-periodic analyzes can also be conducted to detect and characterize eclipses and/or occultations of multiple systems. The macro is easy to use and offers many graphical and statistical indicators to check the results. A feature can also generate ephemerides to plan future observations.

The coordination of our group is ensured through a collaborative workspace (Asana™†). Each month, a selection of priority targets to be observed is published and the measurements produced by each member are instantly shared to cross-analyze, compare the results obtained and interpret them. When an observation campaign is conducted on a specific object (binary suspected asteroid for example), the observation resources are prioritized with responsiveness according to weather conditions and availability. The discussions between members and the training sessions provided through this workspace serves multiple purposes: each participant improves his knowledge, understand better the observed phenoma, and the quality of the measurements keeps improving.

4 Conclusion

Since the creation of this group of observers and the setup of the collaborative workspace in 2018, several binary asteroids have been discovered (Conjat et al. 2018; Christmann et al. 2019) and many asteroid rotation periods have been determined. The results obtained are published in Pro-Am collaborative programs like CdR&CdL (Behrend et al. 2006) or BinAstPhotSurvey (Pravec et al. 2006) and contribute to enrich the models explaining the formation and the evolution of these small bodies of the solar system (Pravec et al. 2010; Carry et al. 2015).

We would like to thank Benoit Carry (Université Côte d'Azur, Observatoire de la Côte d'Azur, CNRS, Laboratoire Lagrange, 06304 Nice, France), Raoul Behrend (Geneva Observatory, Sauverny 1290, Switzerland) and Petr Pravec (Astronomical Institute, Academy of Sciences of the Czech Republic, Fricova 1, CZ-25165 Ondrejov, Czech Republic) for their involvement in professional-amateur collaborative programs in the field of asteroid research and their useful support for this work.

References

Behrend, R., Bernasconi, L., Roy, R., et al. 2006, A&A, 446, 1177

Carry, B., Matter, A., Scheirich, P., et al. 2015, Icarus, 248, 516

Christmann, B., Pravec, P., Hornoch, K., Kukova, H., & Kusnirak, P. 2019, CBET, 4634

Conjat, M., Colas, F., Montaigut, R., et al. 2018, CBET, 4566

Ďurech, J., Carry, B., Delbo, M., Kaasalainen, M., & Viikinkoski, M. 2015, Asteroid Models from Multiple Data Sources (Univ. Arizona Press), 183–202

Hanuš, J., Ďurech, J., Brož, M., et al. 2013, A&A, 551, A67

Hanuš, J., Ďurech, J., Oszkiewicz, D. A., et al. 2016, A&A, 586, A108

Kaasalainen, M. & Torppa, J. 2001, Icarus, 153, 24

Margot, J.-L., Pravec, P., Taylor, P., Carry, B., & Jacobson, S. 2015, Asteroid Systems: Binaries, Triples, and Pairs, ed. P. Michel, F. DeMeo, & W. F. Bottke (Univ. Arizona Press), 355–374

Mousis, O., Hueso, R., Beaulieu, J.-P., et al. 2014, Experimental Astronomy, 38, 91

Pravec, P., Scheirich, P., Kušnirák, P., et al. 2006, Icarus, 181, 63

*http://www.prism-astro.com/

†https://asana.com/

Pravec, P., Scheirich, P., Kušnirák, P., et al. 2016, Icarus, 267, 267
Pravec, P., Vokrouhlický, D., Polishook, D., et al. 2010, Nature, 466, 1085
Scheirich, P. & Pravec, P. 2009, Icarus, 200, 531

Session 17

Matière noire à toutes les échelles (atelier PNCG)

SF2A 2019
P. Di Matteo, O. Creevey, A. Crida, G. Kordopatis, J. Malzac, J.-B. Marquette, M. N'Diaye, O. Venot (eds)

DARK MATTER CORE FORMATION FROM OUTFLOW EPISODES

J. Freundlich[1], A. Dekel[1,2] and F. Jiang[1]

Abstract. While cold dark matter numerical simulations predict steep, 'cuspy' density profiles for dark matter halos, observations favor shallower 'cores'. The introduction of baryons alleviates this discrepancy, notably as feedback-driven outflow episodes can expand the dark matter distribution. We present a simple model for the response of a dissipationless spherical system to a sudden gas outflow or inflow from its center. The response is divided into an instantaneous change of potential at constant velocities followed by an energy-conserving relaxation. The model is tested against NIHAO cosmological zoom-in simulations, where it successfully predicts the evolution of the inner dark matter profile between successive snapshots in a large number of cases, failing mainly during mergers. It thus provides a simple understanding of the formation of dark matter halo cores by supernova-driven outflows, which can be extended to other situations such as the formation of ultra-diffuse galaxies.

Keywords: dark matter, galaxies:haloes, galaxies:evolution

1 Introduction

The cold dark matter (CDM) model of structure formation is extremely successful at describing the large scale structure of the universe, but it faces different challenges at galactic scales. In particular, while CDM-only simulations predict steep, 'cuspy' central density profiles for dark matter haloes, observations favour shallower 'cores' (e.g., Oh et al. 2011). The introduction of baryonic processes such as cooling, star formation and feedback resulting from star formation or active galactic nuclei (AGN) in the simulations enables to alleviate this 'cusp-core discrepancy' by reproducing cored density profiles (e.g., Governato et al. 2012; Teyssier et al. 2013). However, complex hydrodynamical simulations do not necessarily specify nor isolate the physical mechanisms through which baryons affect the dark matter distribution. Our main goal here is to propose a theoretical model describing from first principles how episodes of outflows resulting from the different feedback processes can form cores in dark matter haloes.

Since dark matter interacts gravitationally, baryons can affect it through the gravitational potential. When baryons cool and accumulate at the center of a dark matter halo, they steepen the potential well, leading to an adiabatic contraction of the dark matter distribution (Blumenthal et al. 1986). When a clump of gas or a satellite galaxy moves within the halo, it can transfer part of its orbital energy to the dark matter background through dynamical friction (Chandrasekhar 1943). This latter process dynamically 'heats' the dark matter halo and has been shown to contribute to core formation (El-Zant et al. 2001). When stellar winds and supernova explosions generate outflows, they induce mass and potential fluctuations that can also dynamically heat the dark matter and form cores (Pontzen & Governato 2012). We aim here at modelling how a dissipationless dark matter halo react to sudden mass changes resulting from outflows.

The process at stake during dark matter core formation could also explain the formation of ultra-diffuse galaxies (UDGs). These galaxies are characterized by dwarf stellar masses but sizes comparable to that of the Milky Way. They could be failed galaxies that lost their gas after forming their first stars (van Dokkum et al. 2015), dwarf galaxies with particularly high halo spin (Amorisco & Loeb 2016), tidal debris from mergers or tidally disrupted dwarfs (Beasley & Trujillo 2016), or precisely galaxies whose spatial extend is due to episodes of outflows resulting from stellar feedback, as suggested by Di Cintio et al. (2017). In this latter scenario,

[1] Centre for Astrophysics and Planetary Science, Racah Institute of Physics, The Hebrew University, Jerusalem 91904, Israel
[2] Santa Cruz Institute for Particle Physics, University of California, Santa Cruz, CA 95064, USA

gravitational potential fluctuations lead to the expansion of both the dark matter and the stellar distributions. Field UDGs in simulations consistently have typical halo spins, cored dark matter haloes and bursty star formation histories (Jiang et al. 2019, 2020). Since stars can be considered as collisionless particles, the model we propose can be generalized to describe the puffing-up of the stellar distribution of UDGs from outflows.

2 Description of the model

To model the response of a spherical collisionless halo to a sudden mass change m at its center ($m > 0$ for an inflow and $m < 0$ for an outflow), we follow the evolution of spherical shells enclosing given collisionless masses $M(r_i)$, where r_i denotes the initial shell radii. These shells end up at radii r_f when the halo relaxes to a new equilibrium after the mass change.

If the mass change is slow compared to the orbital time at r_i, angular momentum conservation on circular orbits yields

$$\frac{r_f}{r_i} = \frac{M}{M+m} = \frac{1}{1+f} \tag{2.1}$$

with $f = m/M$ the ratio between the mass change and the enclosed mass at r_i. This equation notably applies to adiabatic contraction.

For a sudden mass change, we assume (i) that the gravitational potential adjusts instantaneously while the velocities and hence the kinetic energy are first frozen to their initial values and (ii) that the system subsequently relaxes to a new equilibrium with no dissipation and no energy exchange between shells. If the initial equilibrium state of the halo is described by a density profile $\rho(r; p_i)$ parametrized in terms of p_i allowing an analytical potential $U(r; p_i)$, the initial energy of a shell at r_i can be written as

$$E_i(r_i) = U(r_i; p_i) + K(r_i; p_i), \tag{2.2}$$

where the kinetic energy K is set by the Jeans equation (Binney & Tremaine 2008, Chapter 4). Given our first assumption (i), this energy becomes

$$E_t(r_i) = U(r_i; p_i) - \frac{Gm}{r_i} + K(r_i; p_i) \tag{2.3}$$

right after the mass change. The system is then assumed to relax to a new equilibrium, where the shell that was initially at r_i has moved to r_f. If the mass distribution of this new equilibrium state can be parametrized by the same functional form $\rho(r; p_f)$ with different parameters p_f, the final energy of the shell is

$$E_f(r_f) = U(r_f; p_f) - \frac{Gm}{r_f} + K(r_f; p_f, m), \tag{2.4}$$

where the kinetic energy is again set by the Jeans equation but also depends on the mass m that has been added or removed. The radius r_f can be retrieved from the parameters p_f since the enclosed collisionless mass within each shell is conserved. Our second assumption (ii) means that $E_f(r_f) = E_t(r_i)$ for each shell. Given functional forms $U(r; p)$ and $K(r; p, m)$ for the potential and kinetic energies, this energy conservation equation can be solved numerically to obtain the final parameters p_f. We can thus predict the evolution of the halo density profile when mass is suddenly added or removed at its center. Fig. 1 illustrates the different steps assumed by the model, with the addition of a stellar component.

To describe the transition from cusps to cores, we use a Dekel et al. (2017) parametrisation of the halo density profile where

$$\rho(r) \propto \frac{1}{x^a (1 + x^{1/2})^{2(3.5-a)}} \tag{2.5}$$

depending on parameters a and c with $x = cr/R_{\rm vir}$ ($R_{\rm vir}$ being the virial radius), which has the advantage to have an analytical potential and a free inner slope. This parametrisation was shown to yield excellent fits for haloes in simulations with and without baryons, ranging from steep cusps to flat cores. The associated $U(r; a, c)$ and $K(r; a, c, m)$ can be found in Freundlich et al. (2019) and agree well with simulated potential and kinetic energy profiles.

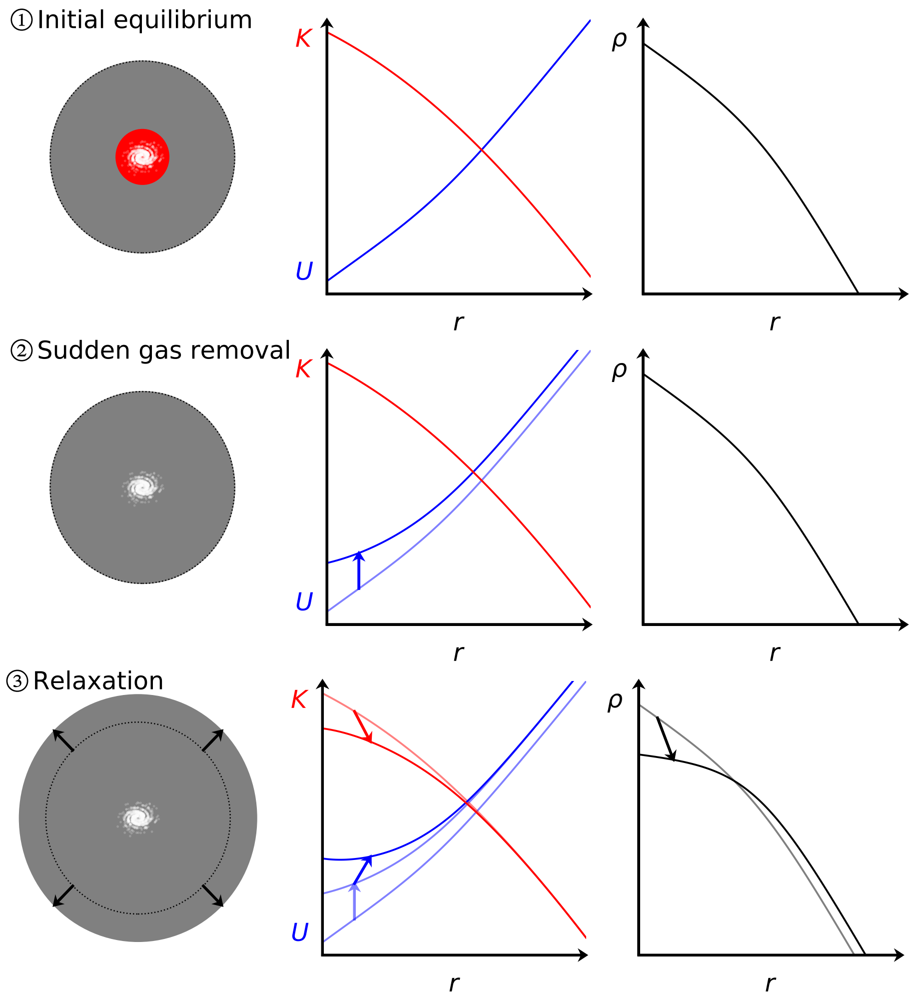

Fig. 1. Schematic representation of the different steps assumed by the model for a gas outflow episode affecting the dark matter distribution: (1) an initial dark matter halo at equilibrium (in gray in the upper left panel), where the dark matter density profile ρ and the associated gravitational potential energy U follow the Dekel et al. (2017) parametrisation while the kinetic energy K stems from the Jeans equation (Eq. 2.2), with gas (in red) and stars (in white) at its center; (2) a sudden gas mass loss with the potential adjusting instantly while the velocities and the kinetic energy remain frozen to their initial values (Eq. 2.3); and (3) a relaxation to a new equilibrium at constant energy $U + K$ (Eq. 2.4) leading to the expansion of the dark matter distribution.

3 Test against the NIHAO simulations

We test the model predictions for the evolution of the dark matter density profile on successive outputs of NIHAO cosmological zoom-in simulations, which are characterized by a relatively strong feedback implementation and a spatial resolution of 1% of the virial radius (Wang et al. 2015). We focus on the 33 galaxies whose stellar mass at $z = 0$ lies in the range $10^7 - 10^9\ M_\odot$ where core formation happens according to Di Cintio et al. (2014), Tollet et al. (2016), and Dutton et al. (2016). For each output, the model prediction is determined from the Dekel et al. (2017) fit to the initial average density profile $\overline{\rho}$ and the mass change m (which is allowed to depend on the shell radii r_i) according to the energy conservation equation. Fig. 2 shows an example of a successful prediction. We find that the model is able to predict the evolution of the inner part of the dark matter density profile and its inner logarithmic slope in about 70% of the cases, although with some scatter. Mergers are found to be the main cause of failure of the model, which we explain by the fact that mergers and fly-bys break the assumed spherical symmetry and lead to processes that are not accounted for in the model such as dynamical friction and tidal interactions. We also test the model predictions over successive outputs, finding that it is able to recover (again with some scatter) the evolution of the inner part of the dark matter density profile up to a few Gyr in the absence of mergers.

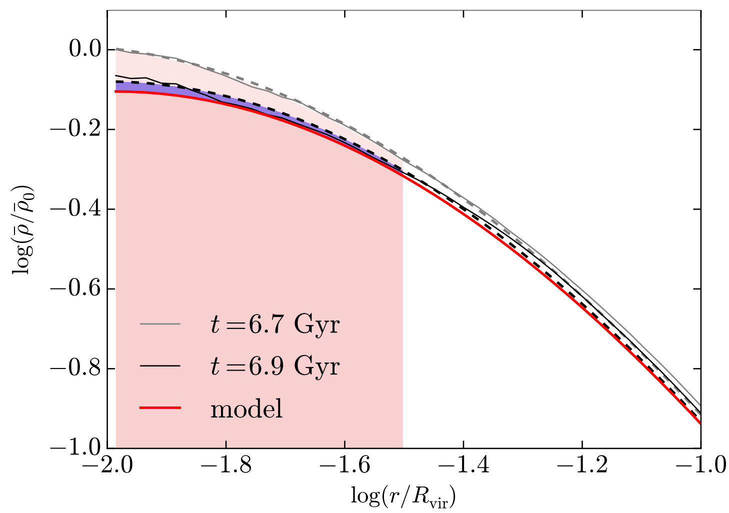

Fig. 2. Evolution of the inner part of the average dark matter density profile between two successive outputs of a NIHAO zoom-in simulation compared to the model prediction. The Dekel et al. (2017) fits are shown as dashed lines.

4 Conclusion

We present a theoretical model providing a simple understanding of the formation of dark matter halo cores from bulk outflows resulting from feedback. This model, which is presented in more detail in Freundlich et al. (2019), can be extended to describe the formation of UDGs. It was successfully tested against NIHAO cosmological zoom-in simulations, where it reproduces well the evolution of the dark matter density profile in the absence of mergers. We nevertheless note that the effect of feedback on dark matter haloes or UDGs can also be modeled as a diffusion process where stochastic density fluctuations induce small 'kicks' to the collisionless particles and progressively deviate them from their initial orbits, as proposed in El-Zant et al. (2016, 2020) and summarized in Freundlich et al. (2016). Both models may be relevent in different situations.

References

Amorisco, N. C. & Loeb, A. 2016, MNRAS, 459, L51
Beasley, M. A. & Trujillo, I. 2016, ApJ, 830, 23
Binney, J. & Tremaine, S. 2008, Galactic Dynamics: Second Edition (Princeton University Press)
Blumenthal, G. R., Faber, S. M., Flores, R., & Primack, J. R. 1986, ApJ, 301, 27
Chandrasekhar, S. 1943, ApJ, 97, 255
Dekel, A., Ishai, G., Dutton, A. A., & Maccio, A. V. 2017, MNRAS, 468, 1005
Di Cintio, A., Brook, C. B., Dutton, A. A., et al. 2017, MNRAS, 466, L1
Di Cintio, A., Brook, C. B., Macciò, A. V., et al. 2014, MNRAS, 437, 415
Dutton, A. A., Macciò, A. V., Dekel, A., et al. 2016, MNRAS, 461, 2658
El-Zant, A., Freundlich, J., Combes, F., & Halle, A. 2020, arXiv:1908.09061
El-Zant, A., Shlosman, I., & Hoffman, Y. 2001, ApJ, 560, 636
El-Zant, A. A., Freundlich, J., & Combes, F. 2016, MNRAS, 461, 1745
Freundlich, J., Dekel, A., Jiang, F., et al. 2019, arXiv:1907.11726
Freundlich, J., El-Zant, A., & Combes, F. 2016, in SF2A Proceedings, 153–156
Governato, F., Zolotov, A., Pontzen, A., et al. 2012, MNRAS, 422, 1231
Jiang, F., Dekel, A., Freundlich, J., et al. 2019, MNRAS, 487, 5272
Jiang, F., Freundlich, J., Dekel, A., et al. 2020, in prep.
Oh, S.-H., de Blok, W. J. G., Brinks, E., Walter, F., & Kennicutt, Jr., R. C. 2011, AJ, 141, 193
Pontzen, A. & Governato, F. 2012, MNRAS, 421, 3464
Teyssier, R., Pontzen, A., Dubois, Y., & Read, J. I. 2013, MNRAS, 429, 3068
Tollet, E., Macciò, A. V., Dutton, A. A., et al. 2016, MNRAS, 456, 3542
van Dokkum, P. G., Abraham, R., Merritt, A., et al. 2015, ApJ, 798, L45
Wang, L., Dutton, A. A., Stinson, G. S., et al. 2015, MNRAS, 454, 83

SF2A 2019
P. Di Matteo, O. Creevey, A. Crida, G. Kordopatis, J. Malzac, J.-B. Marquette, M. N'Diaye, O. Venot (eds)

ARE MILKY-WAY DWARF-SPHEROIDAL GALAXIES DARK-MATTER FREE?

F. Hammer[1], Y. B. Yang[1], J. L. Wang[1 2], F.Arenou[1], C. Babusiaux[3], M. Puech[1] and H. Flores[1]

Abstract. We have found that the high velocity dispersions of dwarf spheroidal galaxies (dSphs) can be well explained by Milky Way (MW) tidal shocks, which reproduce precisely the gravitational acceleration previously attributed to dark matter (DM). Here we summarize the main results of Hammer et al. (2019) who studied the main scaling relations of dSphs and show how dark-matter free galaxies in departure from equilibrium reproduce them well, while they appear to be challenging for the DM model. These results are consistent with our most recent knowledge about dSph past histories, including their orbits, their past star formation history and their progenitors, which are likely tiny dwarf irregular galaxies.

Keywords: cosmology, dark matter, dwarf galaxies, the Milky Way

1 Introduction

DSphs (including ultra-faint dwarfs, UFDs) in the Milky Way halo are by far the smallest galaxies that can be detected and studied. They are believed to contain large amounts of DM, which fraction is generally assumed to increase with decreasing luminosity or stellar mass (Strigari et al. 2008; Walker et al. 2009; Wolf et al. 2010). The existence of DM has been widely accepted since the discovery of the HI-extended and flat rotation curves in giant spirals (Bosma 1978). The extent of the DM paradigm towards the dwarf galaxy regime has been initiated by Aaronson (1983) on the basis of the too large velocity dispersion of the Draco stars. This pioneering result was only based on 3 stars in Draco, though it has been confirmed by major works that have identified new dwarfs, measured their distances, and performed deep photometry and high resolution spectroscopy of their individual stars. During the last 35 years these long term works have provided robust measurements for several tens of MW dSphs (Muñoz et al. 2018; Fritz et al. 2018, and references therein).

The scaling relations between the visible luminosity, the half light radius, the velocity dispersion and the MW distance can be established for 24 dSphs possessing sufficiently robust measurements. Three dSphs (Sagittarius, Crater II and Bootes I) are clearly outliers in these relations, which leads to a sample of 21 dSphs. Analyzing these data, Hammer et al. (2019) demonstrated that the MW gravitation through tidal shocks can fully account for the dSph kinematics. DM estimates (Walker et al. 2009; Wolf et al. 2010) are based on only the projected mass density along the line-of-sight. Hammer et al. (2019, see their Fig. 1) found that this quantity is highly anti-correlated with the MW distance, a property that cannot be reproduced by DM-dominated models. It is however naturally expected if dSphs are tidally shocked during their first passage into the MW halo.

2 DSph progenitors: A first infall of gas-rich dwarfs in the MW?

GAIA DR2 is revolutionizing our knowledge of the MW dSphs orbits in a two-fold way:

1. It has considerably improved our knowledge of the MW mass distribution up to 20-50 kpc, by establishing a more accurate rotation curve (Eilers et al. 2019; Mróz et al. 2019), and by providing better constraints on the Globular Cluster motions (Eadie & Jurić 2019) and on the estimates of the escape velocity (Deason et al. 2019). These studies provide MW masses ranging from 0.7 to 1 $\times 10^{12} M_{\odot}$ (see however Grand et al.

[1] GEPI, Observatoire de Paris, Université PSL, CNRS, Place Jules Janssen 92195, Meudon, France
[2] NAOC, Chinese Academy of Sciences, A20 Datun Road, 100012 Beijing, PR China.
[3] Université de Grenoble-Alpes, CNRS, IPAG, F-38000 Grenoble, France

2019 for a slightly higher value), and all of them seem to exclude larger masses. Fig. 1 shows the different rotation curves and mass distributions of the MW, including the most recent ones (Eilers et al. 2019; Mróz et al. 2019) and the (former) high-mass models (McMillan 2017; Irrgang et al. 2013, with total mass from 1.37 to more than 1.9 $\times 10^{12} M_{\odot}$) adopted by Gaia Collaboration et al. (2018) during the release of dSph proper motions. Top panels of Fig. 1 show that high mass models lead to velocities (red and magenta lines) much higher than that observed (points).

2. The above determined MW mass range allows to calculate accurate orbits that are generally consistent with a first infall for most dSphs. For example 2/3 of them have eccentricities in excess of 0.66 (such as the LMC) and half of them with apocenter larger than 300 kpc (Fritz et al. 2018) when adopting the Bovy (2015) MW mass model that reproduces its kinematics.

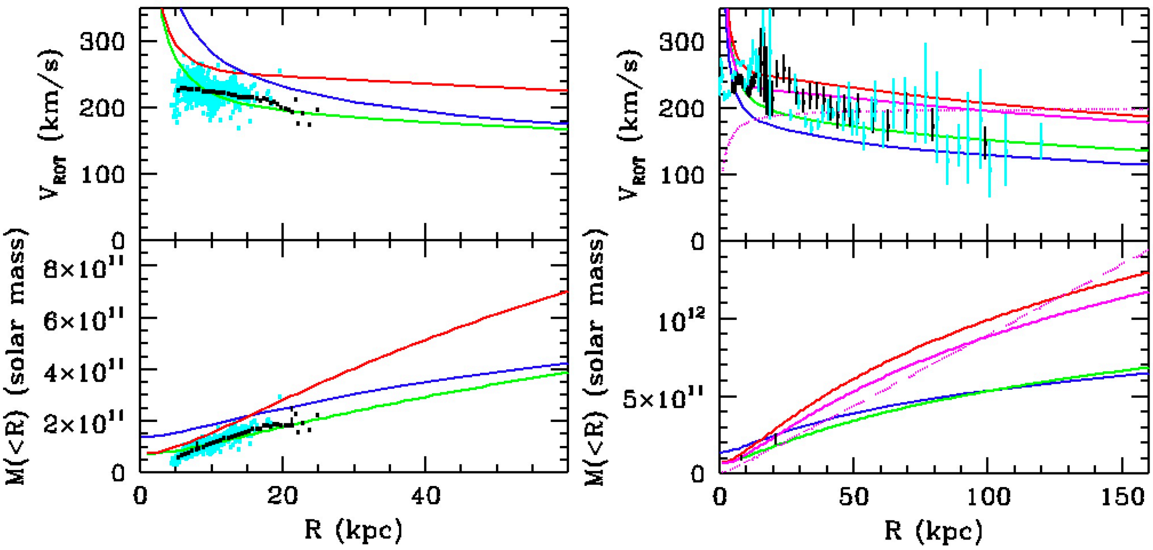

Fig. 1. Top left: Rotation curve of the MW. Black and cyan points represent the new determinations by Eilers et al. (2019) using massive stars, and by Mróz et al. (2019) using cepheids, respectively. The green line shows the Bovy (2015) model, the red line represents the Fritz et al. (2018) model for which they have multiplied the halo mass by 2, and the blue line shows the model of Sofue 2015. **Bottom left:** MW mass profile, same symbols as in the top left panel. **Top right:** Extended rotation curve of the MW. Black and cyan points with error-bars represent compilations from Huang et al. (2016) and Bhattacharjee et al. (2014), respectively. As in the left panels, the green, red and blue lines show the Bovy (2015) model, the Fritz et al. (2018) model for which they have multiplied the halo mass by 2, and the Sofue (2015) model, respectively. The magenta (full and dotted) lines show the models of McMillan 2017 and Irrgang et al. 2013, respectively. **Bottom right:** MW mass profile, same symbols as in the top right panel.

DSph progenitors are likely gas-stripped dwarfs due to the ram-pressure caused by the MW halo gas as it has been proposed by Mayer et al. (2001). Observations support this scenario because all dwarfs (but the Clouds) are gas-rich beyond 300 kpc and gas poor within 300 kpc (Grcevich & Putman 2009). The gas removal by ram-pressure induces a lack of gravity implying that stars are then leaving the system following a spherical geometry. Such a geometry ensures the dominance of tidal shocks over tidal stripping (Binney & Tremaine 2008) explaining the absence of tidal features in most dSphs (Hammer et al. 2019). MW tidal shocks increase the square of the velocity dispersion by $\sigma^2_{\rm MWshocks} = \sqrt{2}\,\alpha_{\rm MW}\; g_{\rm MW}\; r_{\rm half}$ where $g_{\rm MW}$ is the MW gravitational acceleration and $\alpha_{\rm MW} = 1 - \partial log(M_{\rm MW})/\partial log(D_{\rm MW})$ (Hammer et al. 2018). This property reproduces quite precisely the observed dSph velocity dispersions as well as the fundamental relationships established from the observations (see Figs. 1-3 and 5-7 in Hammer et al. 2019).

The role of the gas during the process is essential. First, it would be very unlikely that dSphs progenitors were without gas since such objects are extremely rare in the field. Second, DM-devoid models made by Piatek & Pryor (1995) assumed gas-free progenitors, which implies a strong dominance of tidal stripping. There are similar models (Kroupa et al. 1997; Klessen & Kroupa 1998; Iorio et al. 2019) that also assumed multiple orbits furthermore limiting the possibility that tidal shocks affect the dSph velocity dispersions.

3 Discussion and Conclusion

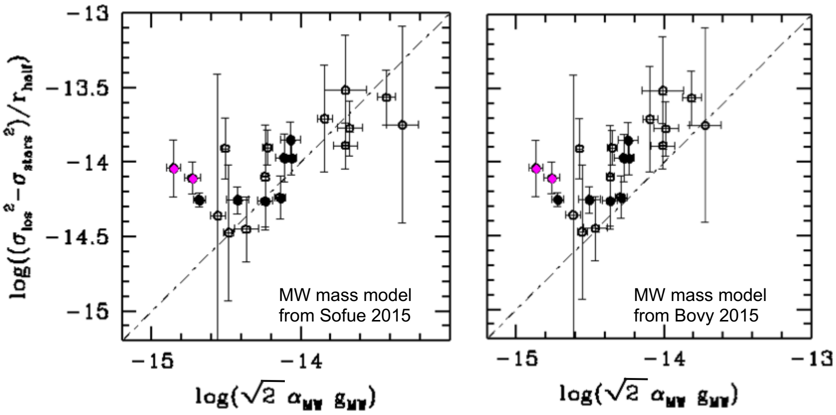

Fig. 2. Self-gravity acceleration $a_{DM} = (\sigma^2_{\rm los} - \sigma^2_{\rm stars}) \times r^{-1}_{\rm half}$ derived from DM estimates in dSphs compared (in logarithmic scale) to that due to MW tidal shocks, $a_{\rm MWshocks} = \sqrt{2}\,\alpha_{\rm MW}\; g_{\rm MW}$. The left and the right panel show the relation for an adopted MW mass profile from Sofue (2015) and from Bovy (2015), respectively. Full (open) dots represent classic (non-classic) dSphs, respectively. Leo I and II are identified by points with magenta color since they do not fully obey the impulse approximation (see Hammer et al. 2019). Their location in the Figure can be well explained if they are affected by tidal stripping in addition to tidal shocks.

The DM content of dSphs derived by Walker et al. (2009) and by Wolf et al. (2010) comes from the measurement of the dSph-DM self-gravity acceleration projected along the line of sight, which is $a_{\rm DM} = GM_{\rm DM} \times r^{-2}_{\rm half} = (\sigma^2_{\rm los} - \sigma^2_{\rm stars}) \times r^{-1}_{\rm half}$. Hammer et al. (2019) showed that over more than a decade, $a_{\rm DM}$ matches very well with the acceleration caused by MW tidal shocks on DM-free dSphs, which is $a_{\rm MWshocks} = \sqrt{2}\alpha_{\rm MW}\; g_{\rm MW}$ (see Fig. 2). Why would the acceleration caused by the DM be precisely what it is expected from MW tidal shocks on DM-free dSphs? Why do MW tidal shocks predict that the DM mass-to-light ratio of Segue 1 is several thousand, while that of Fornax is around ten? The acceleration caused by the DM ($a_{\rm DM}$) also strongly anti-correlates with the dSph distance from the MW (Hammer et al. 2019, see their Fig. 1). The probability that this is just a coincidence is only 3×10^{-4}, which can be conservatively considered as the chance that DM impacts the kinematics of dSphs.

We are aware that the above could seriously affect the paradigm of DM in MW dSphs, and then have an impact on the cosmological models, except if MW dSphs are not representative of the dwarf regime. It is not unexpected that these results would be met with some skepticism. Could this be contradicted by other properties, e.g., of their progenitors that are likely dwarf Irregulars (dIrrs)? The DM content of dIrrs that share a similar stellar mass range than dSphs is still not well constrained. The most massive dSph (e.g., Fornax and maybe Sculptor) progenitors can be found, e.g., in the smallest galaxies of the sample from Lelli et al. (2016), which includes the best studied rotation curves over a large mass range. The DM content of these small galaxies that are all dIrrs has been derived from their rotation curves and varies from none to large values, in particular within a radius similar to the half light radius that is adopted for sampling dSph dynamical properties (Walker et al. 2009; Wolf et al. 2010; Hammer et al. 2019). It appears very hard to assess rotation curves and velocity amplitudes in dwarf galaxies that are too irregular. Trying to identify possible progenitors of smaller dSphs (e.g., UFDs) that constitute the bulk of dSphs leads one to consider extremely small dIrrs, for which establishing their rotation curves can not be seriously attempted (McNichols et al. 2016; Oh et al. 2015; Ott et al. 2012). This is because these tiny objects are far from being represented by a thin disk geometry and also because their velocity amplitudes are similar to that of their dispersion, the latter being mostly associated to star formation and turbulence (Stilp et al. 2013).

Star formation histories of dSphs have been well studied especially for the most massive ones (Weisz et al. 2014). For Fornax (de Boer et al. 2013) it is consistent with a recent gas removal by ram-pressure and then

with the tidal shock scenario. While this also applies to Carina, Leo I and perhaps to Leo II, past histories of Sculptor, Sextans, UMi and Draco (Weisz et al. 2014) are perhaps more problematic. Why did the star formation in the Sculptor progenitor stop about 5 Gyr ago (de Boer et al. 2012) if it was still in isolation at a later time? Only a full hydrodynamical simulation with a well determined orbital history for Sculptor would help us to verify a potential inconsistency. Interestingly, recent simulations (Garrison-Kimmel et al. 2019) have shown that gas-rich dwarfs with Sculptor stellar mass and in isolation may have similar star formation histories than Sculptor, and this also applies to galaxies with smaller masses that form the bulk of the MW dSphs.
The above may lead to a significant change of paradigm in our understanding of the MW dSphs, which could impact the determination of the lower end of the galaxy mass function. Next steps will be to verify if this is consistent with other dSphs of the MW, which total mass can be robustly determined without extrapolations.

References

Aaronson, M. 1983, ApJ, 266, L11
Bhattacharjee, P., Chaudhury, S., & Kundu, S. 2014, ApJ, 785, 63
Binney, J. and Tremaine, S., 1987, Galactic Dynamics, Princeton: Princeton Univ. Press, P. 433.
Binney, J. and Tremaine, S., 2008, Galactic Dynamics: Second Edition, Princeton Univ. Press.
Bosma, A. 1978, Ph.D. Thesis
Bovy, J. 2015, ApJS, 216, 29
Deason, A. J., Fattahi, A., Belokurov, V., et al. 2019, MNRAS, 485, 3514
de Boer, T. J. L., Tolstoy, E., Hill, V., et al. 2012, A&A, 544, A73
de Boer, T. J. L., Tolstoy, E., Saha, A., & Olszewski, E. W. 2013, A&A, 551, A103
Eadie, G., & Jurić, M. 2019, ApJ, 875, 159
Eilers, A.-C., Hogg, D. W., Rix, H.-W., et al. 2019, ApJ, 871, 120
Fritz, T. K., Battaglia, G., Pawlowski, M. S., et al. 2018, A&A, 619, A103
Gaia Collaboration, Helmi, A., van Leeuwen, F., et al. 2018, A&A, 616, A12
Garrison-Kimmel, S., Wetzel, A., Hopkins, P. F., et al. 2019, arXiv e-prints, arXiv:1903.10515
Grand, R. J. J., Deason, A. J., White, S. D. M., et al. 2019, arXiv e-prints, arXiv:1905.09834
Grcevich, J., & Putman, M. E. 2009, ApJ, 696, 385
Hammer F., Yang Y. B., Arenou, F., Babusiaux, C., Puech M., Flores H., 2018, ApJ, 860, 76
Hammer F., Yang Y. B., Arenou, F., Puech M., Flores H., , Babusiaux, C., 2019,ApJ, in press (2018arXiv181210714H)
Huang, Y. , Liu, X.-W., Yuan, H.-B. et al., 2016, MNRAS, 463, 2623.
Iorio, G., Nipoti, C., Battaglia, G., et al. 2019, MNRAS, 1366
Irrgang, A., Wilcox, B., Tucker, E., et al. 2013, A&A, 549, A137
Klessen, R. S., & Kroupa, P. 1998, ApJ, 498, 143
Kroupa, P. 1997, New Astronomy, 2, 139
Lelli, F., McGaugh, S. S., & Schombert, J. M. 2016, AJ, 152, 157
Mayer L., Governato F., Colpi M., Moore B., Quinn T., Wadsley J., Stadel J., Lake G., 2001, ApJ, 559, 754
McMillan, P. J. 2017, MNRAS, 465, 76
McNichols, A. T., Teich, Y. G., Nims, E., et al. 2016, ApJ, 832, 89
Mróz, P., Udalski, A., Skowron, D. M., et al. 2019, ApJ, 870, L10
Muñoz, R. R., Côté, P., Santana, F. A., et al. 2018, ApJ, 860, 66
Oh, S.-H., Hunter, D. A., Brinks, E., et al. 2015, AJ, 149, 180
Ott, J., Stilp, A. M., Warren, S. R., et al. 2012, AJ, 144, 123
Piatek, S., & Pryor, C. 1995, AJ, 109, 1071
Simon, J. D. 2018, ApJ, 863, 89
Sofue, Y. 2015, PASJ, 67, 75
Stilp, A. M., Dalcanton, J. J., Warren, S. R., et al. 2013, ApJ, 765, 136
Strigari L. E., Bullock J. S., Kaplinghat M., Simon J. D., Geha M., Willman B., Walker M. G., 2008, Natur, 454, 1096
Walker M. G., Mateo M., Olszewski E. W., Peñarrubia J., Wyn Evans N., Gilmore G., 2009, ApJ, 704, 1274
Weisz, D. R., Dolphin, A. E., Skillman, E. D., et al. 2014, ApJ, 789, 147
Wolf J., Martinez G. D., Bullock J. S., Kaplinghat M., Geha M., Muñoz R. R., Simon J. D., Avedo F. F., 2010, MNRAS, 406, 1220

SF2A 2019
P. Di Matteo, O. Creevey, A. Crida, G. Kordopatis, J. Malzac, J.-B. Marquette, M. N'Diaye, O. Venot (eds)

DARK MATTER DISTRIBUTION IN CLUSTER GALAXIES

A. Niemiec[1], E. Jullo[2], M. Limousin[2], C. Giocoli[3] and M. Jauzac[4]

Abstract. Galaxy clusters are large structures of the Universe, and they are formed and grow through the accretion of smaller structures such as groups or isolated galaxies. In this scenario, during their infall into the core of a cluster, satellite galaxies are submitted to a number of interactions with their host, both on the level of dark and baryonic matter. In particular, both observations and numerical simulations suggest that part of the dark matter composing their haloes can be stripped by the host tidal forces. We present our weak lensing measurement of the Stellar-to-Halo Mass Relation for satellite galaxies in the redMaPPer clusters, using shear data fro the CS82, CFHTLenS and DES-SV surveys. To help interpret these results we then discuss our analysis of the evolution of subhaloes in the Illustris hydrodynamical simulation.

Keywords: galaxy clusters, galaxy evolution, weak lensing, numerical simulations

1 Introduction

In the ΛCDM model of the Universe, structures are formed in a hierarchical way, which means that small objects, such as galaxies and their dark matter haloes will merge over time to form larger and larger structures. In this scenario, galaxy clusters, which are the largest gravitationally bound structures in the Universe, form and grow through the accretion of individual galaxies or smaller groups.

During this accretion process, when an isolated halo becomes a subhalo of a host, there are different interactions taking place between them, both at the level of baryonic and dark matter. For the baryonic part, different effects such as ram pressure stripping, harassment or mergers will tend to suppress star formation in satellite galaxies and form a population of massive and passive red galaxies. Then, the gravitational interaction between the dark matter in the cluster and in the subhalo creates dynamical friction, which slows down the subhaloes and makes them spiral down towards the centre. Because of this effect, subhaloes that are closer to the centre of their host cluster will on average be the ones that started their accretion earlier. Finally, the gravitational potential of the cluster can exert tidal forces on the subhalo, and these forces may strip part of the dark matter from the subhalo and distribute it into the cluster halo.

In this work we examine how the dark matter of a satellite galaxy is affected during infall. In Sect. 2, we summarize our measurement of the Stellar-to-Halo Mass Relation (hereafter SHMR) for the satellite galaxies of the redMaPPer clusters, using galaxy-galaxy weak lensing. More details can be found in Niemiec et al. (2017) (Paper I). In Sect. 3 we measure the SHMR for central and satellite galaxies in the Illustris simulation, and examine the processes that drive the shift in the SHMR, as described in Niemiec et al. (2019), thereafter referred to as Paper II. The cosmology used throughout is a flat ΛCDM universe consistent with the *Wilkinson Microwave Anisotropy Probe* 9-year data release (WMAP9, Hinshaw et al. 2013, : $\Omega_{\mathrm{m},0} = 0.2726$, $\Omega_{\Lambda,0} = 0.7274$, $\Omega_{\mathrm{b},0} = 0.0456$, $\sigma_8 = 0.809, n_{\mathrm{s}} = 0.963$ and $H_0 = 70.4 \mathrm{km\,s^{-1}}$). The notation log() refers to the base 10 logarithm.

[1] Department of Astronomy, University of Michigan, 1085 South University Ave, Ann Arbor, MI 48109, USA
[2] Aix Marseille Univ, CNRS, CNES, LAM, Marseille, France
[3] Dipartimento di Fisica e Astronomia, Alma Mater Studiorum Università di Bologna, via Gobetti 93/2, I-40129 Bologna, Italy, INFN - Sezione di Bologna, viale Berti Pichat 6/2, I-40127 Bologna, Italy
[4] Centre for Extragalactic Astronomy, Department of Physics, Durham University, Durham DH1 3LE, UK; Institute for Computational Cosmology, Durham University, South Road, Durham DH1 3LE, UK; Astrophysics and Cosmology Research Unit, School of Mathematical Sciences, University of KwaZulu-Natal, Durban 4041, South Africa

2 SHMR for redMaPPer satellite galaxies

To measure the evolution of the dark matter content of cluster galaxies, we first need an observable to describe the stage of accretion of the satellite, as in observations we cannot directly follow the infall of one subhalo. We use the projected distance between the satellite and the centre of the cluster, as it has been shown to correlate on average with the redshift of infall. We split satellite galaxies into two groups: the satellites in the inner part of the clusters, and the one in the outer part, saying that the galaxies close to the centre of the cluster have started their accretion process before the ones in the outskirts. Then, we need to know that we are comparing galaxies that were similar before accretion, and classify them according to their stellar mass, as a proxi for halo mass before infall. And finally we need to know the subhalo mass of the satellite galaxies, and we measure this using gravitational lensing. To summarize, we measure the SHMR for satellite galaxies, and see how this relation evolves between the satellites in the inner part of clusters and the satellites in the outer part.

As the lensing signal produced by a single galaxy has a very low amplitude compared to the intrinsic ellipticity of the background galaxies, it is impossible to significantly measure the lensing profile (and thus the mass) for each cluster galaxy. Stacking the lensing signals produced by a large number of galaxies is therefore necessary to increase the signal-to-noise ratio. To increase our lens galaxy sample, we use the satellite galaxies of many different clusters, and namely the clusters from the redMaPPer catalogue (Rykoff et al. 2014, 2016). We use the part of the catalogue that overlaps with three lensing surveys, CS82 (Moraes et al. 2014), CFHTLenS (Heymans et al. 2012) and DES-SV (Flaugher 2005; Flaugher et al. 2015; Dark Energy Survey Collaboration et al. 2016). We classify the satellite galaxies according to two parameters: the projected distance to the centre of their host, splitting them between the inner part of the clusters ($0.1 < R_s < 0.55\ h^{-1}$Mpc) and the outer part ($0.55 < R_s < 1\ h^{-1}$Mpc); and the stellar mass, splitting galaxies in three bins: $10 < \log(M_\star/M_\odot) < 10.5$, $10.5 < \log(M_\star/M_\odot) < 11$ and $11 < \log(M_\star/M_\odot) < 11.5$.

We measured the stacked lensing signal for each of the 6 satellite galaxy samples thus obtained, and fit a halo model to extract the mean subhalo mass for each sample (see Paper I for details on this procedure). The left panel of Fig. 2 shows the best-fit stellar-to-halo mass relation for the satellite galaxies in the redMaPPer cluster that we measured. The blue points present the galaxies in the inner parts of the clusters, and the red points the galaxies in the outer part. The black solid line is the stellar to halo mass relation computed from abundance matching in Moster et al. (2013) for central or field galaxies. For the galaxies in the outskirts of clusters the SHMR is consistent with the one for centrals, which is what could be expected as these galaxies just started their accretion process and were therefore not much affected by the dense cluster environment. On the contrary, for a given stellar mass, the dark matter mass of galaxies in the inner part of clusters is shifted towards lower value compared the galaxies from the outer part, which is consistent with tidal stripping of the dark matter in the subhaloes.

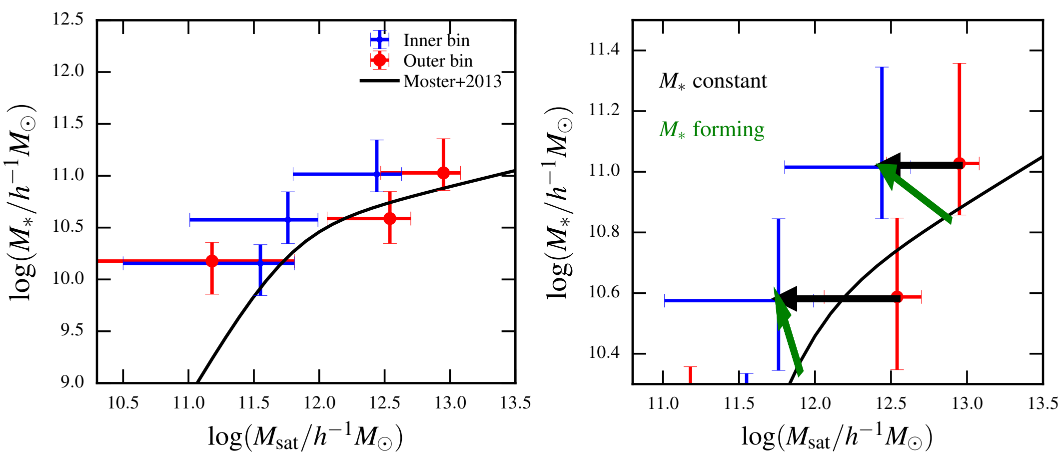

Fig. 1. Left: SHMR for the redMaPPer satellite galaxies, in blue for galaxies in the inner part of clusters, and in red for galaxies in the outer part. **Right:** same as the left panel, but with two extreme evolutionary paths that can explain the SHMR shift between the galaxy in the inner and outer parts of the clusters: the green arrows represent the evolution at constant stellar mass (only dark matter stripping), and the green arrows represent the evolution where the galaxies are forming stars with the same star formation rates as for galaxies in the field. The two figures are adapted from Paper I.

The difference between the SHMR for satellite galaxies in the inner and outer part of clusters can be explained by different evolutionary processes. The first considered scenario is when all the satellite galaxies are quenched: the galaxies then lose part of their dark matter by tidal stripping and keep a constant stellar mass (black arrows in the right panel of Fig. 2). However, it is also possible that at least part of the cluster galaxies continue to form stars during part of their infall. To quantify this scenario, we estimate the amount of stars that could have been formed during accretion, using star formation rates computed in Buat et al. (2008) for central galaxies at the estimated time of accretion for the galaxies that are located in the inner part of their hosts. We then estimate the corresponding subhalo masses before accretion using the SHMR from Moster et al. (2013). This evolutionary path is represented with green arrows in the right panel of Fig. 2, and corresponds to a co-evolution of the dark and baryonic parts of satellite galaxies.

These two scenarios are extreme cases, with either no stellar evolution at all (black arrows), or stellar formation as the same rate as blue star-forming galaxies, and the true evolution should be somewhere between the two. To gain a better understanding of the stellar and dark matter mass evolution of cluster galaxies, we examine the evolution of satellite galaxies in the Illustris simulation, as described in the next section.

3 Subhalo/satellite galaxy evolution in the Illustris simulation

We use the publicly available Illustris simulation* (Vogelsberger et al. 2014a,b), and specifically its most resolved run Illustris-1, where the dark matter particle mass is $m_{\rm DM} = 6.3\times10^6 M_\odot$, and the effective baryonic resolution is $m_{\rm b} = 1.3 \times 10^6 M_\odot$. We select the three most massive haloes at redshift $z = 0$ in the Illustris-1 run, with $M_{200} > 10^{14}h^{-1}M_\odot$ that will represent our sample of "cluster-like" haloes.

We first measure the SHMR for central and satellite galaxies in the simulation. We focus on redshift $z = 0.35$ as it corresponds to the mean redshift of the redMaPPer satellite galaxies that we examined in Sect. 2. The left panel of Fig. 2 present the SHMR for all the central galaxies in the simulation, while the right panel shows the SHMR for the satellite galaxies in the three cluster-like haloes. The blue dots show the the SHMR for each galaxy, while the black crosses represent the median relation in stellar mass bins. We find that at a given stellar, the satellite SHMR is shifter towards lower halo mass compared to the central SHMR, with $M_{\rm sub}(M_\star)/M_{\rm h}(M_\star) \sim 0.3$.

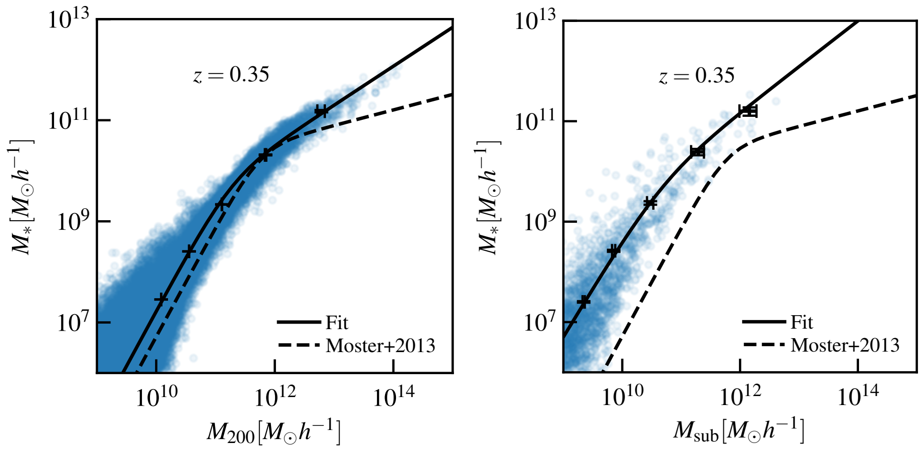

Fig. 2. Left: SHMR for central galaxies at $z = 0.35$. **Right:** SHMR for the satellite galaxies of the 3 cluster-like haloes at $z = 0.35$. The solid black line shows the best-fit relation and the dashed line shows the relation from Moster et al. (2013) as reference. Both figures are adapted from Paper II.

To understand what drives the difference in SHMR between satellite and central galaxies, we then examine the time evolution of different satellite/subhalo properties. We select the satellite galaxies of the three cluster-like haloes that have $M_{\rm sub} > 10^{10}h^{-1}M_\odot$, to ensure that the subhaloes are sufficiently resolved above the mass resolution of the simulation. Using the publicly available merger trees of the simulation, we then follow the

*`http://www.illustris-project.org`

evolution of these galaxies starting from accretion. The accretion time is defined as the time when the satellites enter for the first time the shell of radius $R_{\rm acc} = 2 \times R_{200}$.

Left panel of Fig. 3 shows the evolution of the satellite cluster-centric distance normalized by the virial radius at accretion, the subhalo mass normalized by the mass at accretion, and the satellite stellar mass normalized by its value at accretion, respectively from top to bottom panel. The three columns represent the three cluster-like host haloes. The black lines represent the evolutions for each individual subhaloes, while the red tick and thin lines represent respectively the median evolution and the 16th and 84th percentiles.

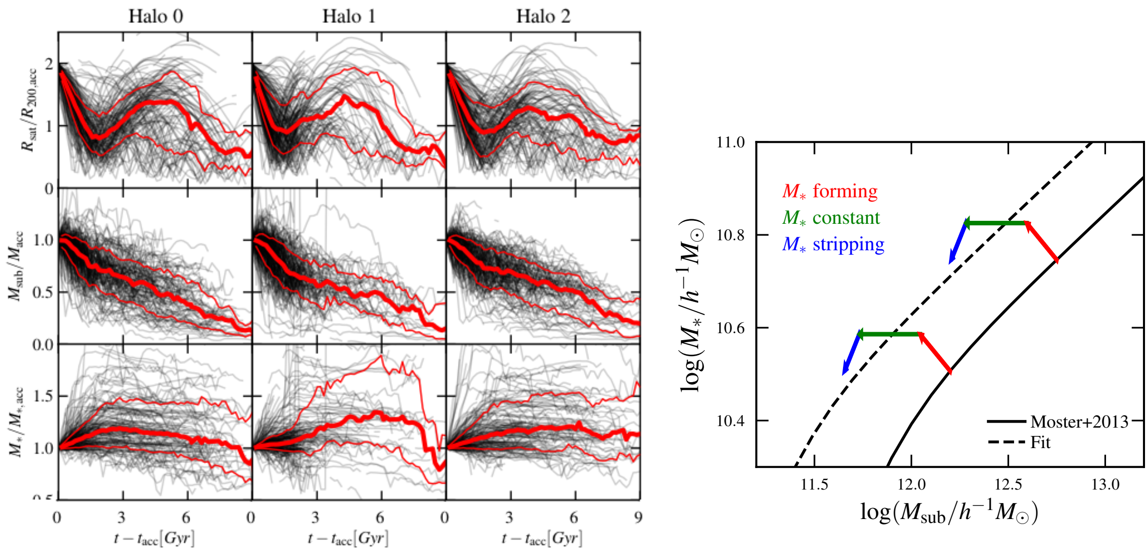

Fig. 3. Left: time evolution of subhalo/satellite galaxy properties since accretion: cluster-centric distance, subhalo mass and stellar mass, from top to bottom. The masses are normalized by their values at the time of accretion. **Right:** summary of the SHMR evolution for satellite galaxies. Three phases can be identified in the process: dark matter stripping + star-formation (red arrows), dark matter stripping at constant stellar mass (green arrows) and dark + stellar matter stripping (blue arrows).

The median evolution of the subhalo mass shows a continuous decrease over time, starting very soon after the subhaloes infall at $2 \times R_{200}$. The mass loss appears to be faster during the first infall into the cluster, with a rate of 20% of the mass at accretion lost per Gyr, and then drops to 6% of the mass at accretion per Gyr. The satellite galaxy stellar mass has a different evolution: it keeps increasing for ~ 2 Gyr after accretion, showing that on average galaxies still have ongoing star formation.

The evolution of the satellite galaxies and their subhaloes can then be summarized as presented on the right panel of Fig. 3: during the first phase, that corresponds roughly to the first infall, the subhaloes start to lose mass by tidal stripping, while the galaxy continues to form stars (red arrows); star-formation is then stopped, and the subhalo mass continue to decrease at fixed stellar mass (green arrows); finally, when only 30% of the initial dark matter mass remains, the galaxy itself can start to be affected by stripping, and the average stellar mass starts to decrease as well (blue arrows). Overall, the total mass evolution is dominated by the subhalo mass loss, and during infall the ratio of stellar to dark matter mass goes from 0.03 to 0.3.

4 Conclusions

We have examined the Stellar-to-Halo mass relation for cluster galaxies. We first measured the SHMR for the satellite galaxies in the redMaPPer clusters, using galaxy-galaxy weak lensing, with shear catalogues coming from the CS82, CFHTLenS and DES-SV surveys. Our measurements suggest that at given stellar mass, the SHMR if shifted towards lower halo masses for galaxies living in the inner parts of their host clusters, which is consistent with tidal stripping of the dark matter. The error bars on the measurements are large, but oncoming large scale surveys such as Euclid will allow to reduce the statistical uncertainties and put tighter observational constraints on the subhalo mass evolution.

We then examined the mechanisms that drive the SHMR shift using the Illustris hydrodynamical simulation. We found that while dark matter stripping is the dominant process that modifies the SHMR, satellite galaxies continue to form stars during infall, and become on average quenched ~ 2 Gyr after accretion. Future work on simulations will allow to determine what systematic errors affect the observational measurements, and measure the expected subhalo lensing signal in different dark matter scenarios.

References

Buat, V., Boissier, S., Burgarella, D., et al. 2008, A&A, 483, 107

Dark Energy Survey Collaboration, Abbott, T., Abdalla, F. B., et al. 2016, MNRAS, 460, 1270

Flaugher, B. 2005, International Journal of Modern Physics A, 20, 3121

Flaugher, B., Diehl, H. T., Honscheid, K., et al. 2015, AJ, 150, 150

Heymans, C., Van Waerbeke, L., Miller, L., et al. 2012, MNRAS, 427, 146

Hinshaw, G., Larson, D., Komatsu, E., et al. 2013, ApJS, 208, 19

Moraes, B., Kneib, J.-P., Leauthaud, A., et al. 2014, in Revista Mexicana de Astronomia y Astrofisica Conference Series, Vol. 44, 202–203

Moster, B. P., Naab, T., & White, S. D. M. 2013, MNRAS, 428, 3121

Niemiec, A., Jullo, E., Giocoli, C., Limousin, M., & Jauzac, M. 2019, MNRAS, 487, 653

Niemiec, A., Jullo, E., Limousin, M., et al. 2017, MNRAS, 471, 1153

Rykoff, E. S., Rozo, E., Busha, M. T., et al. 2014, ApJ, 785, 104

Rykoff, E. S., Rozo, E., Hollowood, D., et al. 2016, ApJS, 224, 1

Vogelsberger, M., Genel, S., Springel, V., et al. 2014a, Nature, 509, 177

Vogelsberger, M., Genel, S., Springel, V., et al. 2014b, MNRAS, 444, 1518

SF2A 2019
P. Di Matteo, O. Creevey, A. Crida, G. Kordopatis, J. Malzac, J.-B. Marquette, M. N'Diaye, O. Venot (eds)

A STELLAR CUSP AT THE HEART OF NGC1068

D. Rouan[1], L. Grosset[1] and D. Gratadour[1]

Abstract. Polaro-imaging observations with SPHERE in the near infrared + adaptive optics of the heart (500 pc) of the type-2 AGN NGC1068 allow to reach a resolution of the order of 2 pc. In addition to an elongated structure on 60 pc, exactly aligned with the molecular torus seen by ALMA, the radial distribution of brightness in H and K corresponds to two power-laws with a high value of the exponent, indicative of a cuspy distribution. Different models are tested to explain both the high value of the exponent and why they are different between H and Ks bands. The most satisfactory is the one combining a stellar cusp with radius 100 pc, together with emission of hot dust directly illuminated by the accretion disk and an unresolved point like central source (1pc) of very hot dust, close to the sublimation temperature. An empirical relationship between brightness and radius of the cusp in the hearts of bright or ultra-bright IR galaxies is also established, from a rather large sample. Cuspy stellar distribution, sculpted or not by dark matter, appear to be an important component of AGN where recent star formation occurred.

Keywords: Galaxies: Seyfert, high angular resolution, near-infrared, cusp

1 Introduction

The cusp/core problem, identified twenty years ago, is the apparent inconsistency between the predicted and observed dark matter density profile at centre of galaxies: cosmological simulations predict a steep power-law (cusp), while observations of low surface brightness disk and gas-rich dwarves rather show a constant density (core). The controversy is still alive with on one hand discussions on mechanisms that could transform cusps into cores such as supernova feedback (Pontzen & Governato 2012 , J. Freundlich in this proceedings), self-interaction and on the other hand identification of bias in data analysis (triaxiality, . . .).

In an active galactic nucleus (AGN), the feeding of the central engine (hereafter CE), i.e. the accretion disc, requires a high accretion rate of matter (0.3 in Seyfert galaxies to 10 M$_{M_\odot}$ yr^{-1}) through a still unclear mechanism for the needed loss of angular momentum at short scale. Hopkins & Quataert (2011)), using the results of their multi-scale hydrodynamical model proposed that lopsided cuspy stellar discs at a scale of $\approx$ 10 pc would be the dominant cause for this angular momentum transport below this scale.

Is there a direct relationship between dark matter and the formation of such a stellar cusp may be a matter of debate, but in any case trying to identify if a cusp is indeed present is important.

The combination of adaptive optics (AO) on large telescopes and imaging in the near-IR (NIR) gives the opportunity to search for such stellar cusp at least on nearby AGNs.

NGC 1068 is one of the closest AGN (14.4 Mac). One consequence is that the nucleus is bright enough to be used as the guide source for the AO system, allowing to obtain images in the NIR at angular resolution of $\approx$ 40 mas, i.e. $\approx$ 3 pc.

A cusp being characterised by a power-law profile, we present here an analysis in terms of radial profile of AO images of NGC 1068 in K_s and H bands obtained with SPHERE on the VLT. The images already showed a polarisation angle map with a clear centro-symmetric pattern, tracing both parts of the ionisation bicone and featured a central non-centro-symmetric pattern approximately 60 pc $\times$ 20 pc wide, with aligned polarisation, that is interpreted as the trace of the outer envelope of the torus, revealed through a double scattering process (Gratadour et al. 2015; Grosset et al. 2018): see Fig.1. Note that there is a fairly good alignment of the elongated pattern with the molecular torus seen by ALMA García-Burillo et al. (in prep.).

[1] LESIA, Observatoire de Paris, PSL Research University, CNRS, Sorbonne Universités, Univ. Paris Diderot, Sorbonne Paris Cité, 5 place Jules Janssen, 92190 Meudon, France

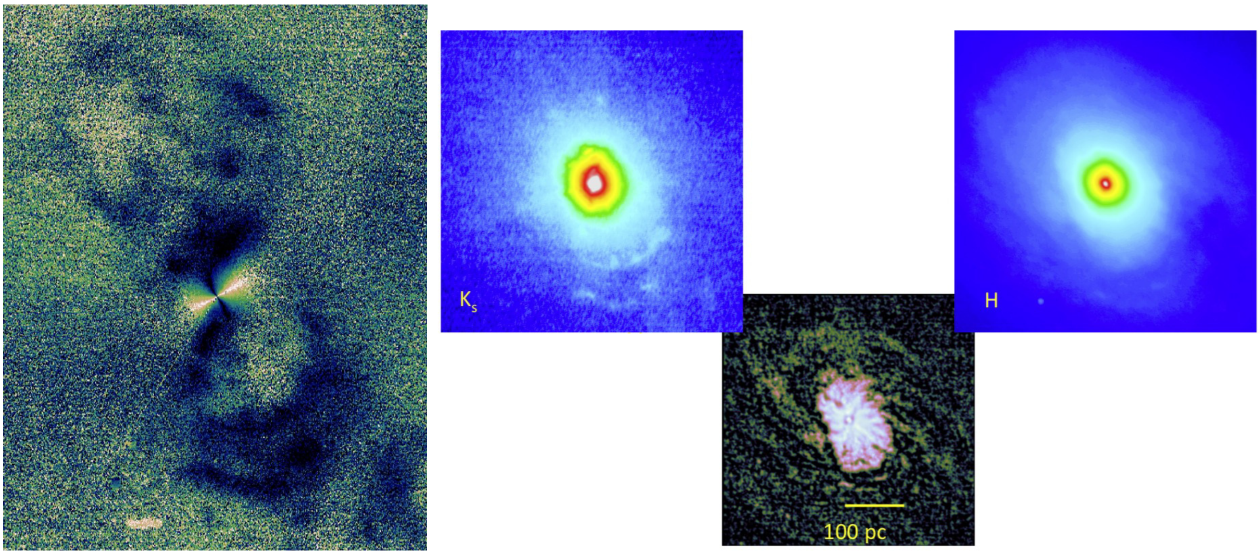

Fig. 1. Left: map of the polarisation angle at 1.65 μm of the central region in NGC1068, revealing both the lobes of the biconical Narrow-Line Region and the central elongated structure tracing the torus (Gratadour et al. 2015). Right top: Ks and H SPHERE images. Right bottom: H images processed to enhance the local contrast and revealing hints of a spiral structure.

2 The median radial brightness profile

We show on Fig.2-left the median radial profiles around the central core deduced from the H and Ks images, together with the PSF profile at K_s measured on a nearby reference star. The H-band profile is almost perfectly fitted by a power law of exponent -1.2, while the K_s-band profile id fitted by a combination of a power-law profile of exponent -2.0 plus the PSF profile properly weighted. In particular, we note that the small bumps on the K_s-band profile, close to the peak, are well fitted by the first and even the second Airy rings of the PSF. The straightforward interpretation is that the K_s-band profile results from the contribution of a central point source and of a smoother distribution that is directly related to the H-band emission. We can safely interpret the point source component as the internal wall of torus heated to dust sublimation temperature around 1400K, as generally admitted.

The two main questions raised by the fit are: a) are we indeed viewing an actual stellar cusp or is it some other source of radiation that mimics a cusp ? b) if yes, why are the exponents of the power-law so different if they trace the same stellar population ?

2.1 Possible nature of the cusp

In the literature, there are at least 3 families of cusp which are identified: *i)* around a massive black hole a cusp forms as the result of 2-bodies interactions that create some segregation between stars and a cusp with exponent between -1.3 and -1.8. However in the case of NGC1068, the relaxation time to reach this state would be too long; *ii)* a compact nuclear cluster, a rather current situation that would be found in 75% of Scd and 70% of E - S0; typical radius and exponent would be R $\approx$ 7pc and -0.6. *iii)* a central starburst cusp, a case found in galaxies forming stars at a high rate; typical radius and exponent would be R $\approx 45 - 2400$ pc and -0.8.

We have examined the catalog of central starburst cusp established by Haan et al. (2013) and found an interesting relation between exponent, radius and luminosity of the cusp: $\gamma = 1.133 \times [log10(L_{cusp}/R_{cusp}) - 6.63]$, as illustrated on Fig. 2-right where the location of NGC1068 is indicated by a star symbol. We conclude that the central cusp in NGC 1068 belongs likely to this class of central starburst cusp.

2.2 A simple radiative transfer model

To tackle the question why are the exponents so different in H and Ks if indeed we are facing a stellar cusp, we have explored different possibilities by developing a simple radiative transfer toy model that can take into

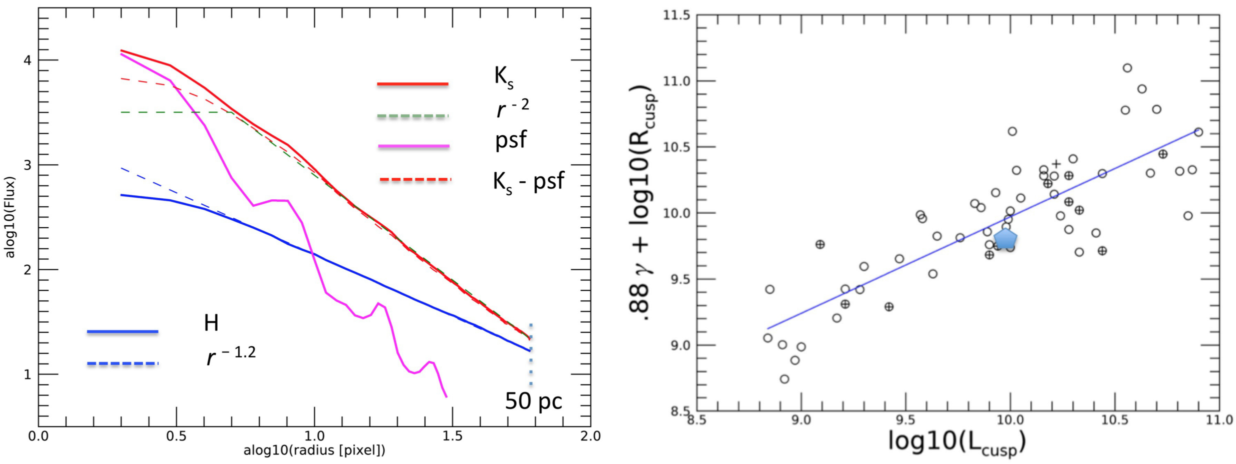

Fig. 2. Left: observed radial profiles in Ks and H (solid red and blue lines) and their fit by a pure power-law in H or by a combination of power-law and point source (magenta) in Ks. Right: cusp luminosity as predicted by the law we found (see text) vs the actual cusp luminosity for the starburst galaxies studied by Haan et al. (2013). The blue line is the linear regression. The star symbol is for NGC 1068.

account different sources of radiation: stellar cusp of profile $r^{-\alpha}$, a point like central engine and hot to warm dust mixed within the stellar cusp. The considered absorber is the same dust, distributed according to some power-law $r^{-\gamma}$. Fig. 3 gives a sketch of the geometry of the model.

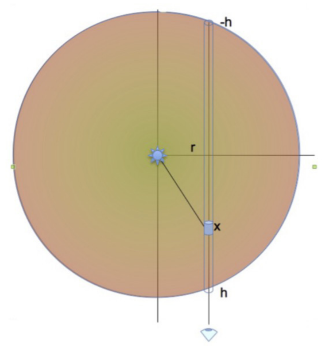

Fig. 3. Sketch of the adopted geometry for the radiative transfer model

We first tested if differential extinction between the H and Ks bands could explain the difference of exponent, if denser dust towards the central region was absorbing more efficiently the shortest wavelength, thus reducing the slope of the brightness with respect to the intrinsic stellar distribution. We could reach an almost satisfying solution, as illustrated on Fig. 4-a, but at the price of an unrealistic exponent of the stellar cusp (r^{-4}) and too large a mass of dust.

An alternative and much more acceptable solution is to consider a mix of stellar cusp and warm dust heated by the central engine. The temperatures reached by the dust mixed with the cusp is high enough to contribute significantly to the emission in the Ks band in the central 15 pc, while the most external region up to 50 pc becomes more and more dominated by the stellar cusp radiation, the combined effect of the two sources mimicking rather precisely a continuous power-law of exponent -2. Of course the same exponent of -1.2 was used for the stellar cusp in both infrared bands. The result of the modelling is illustrated in Fig. 4-b where the green solid line is the result of the observed radial distribution of brightness minus the contribution of the stellar cusp, the later being proportional to the H band profile (solid blue line): we can check that the thermal radiation from warm dust predicted by the model (dotted green line) fit quite well this difference.

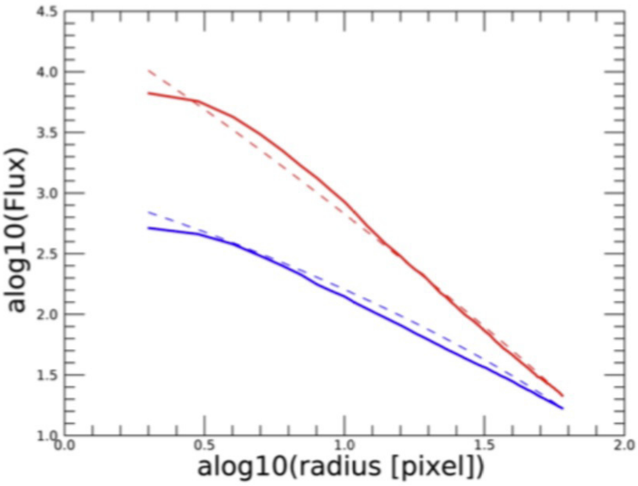

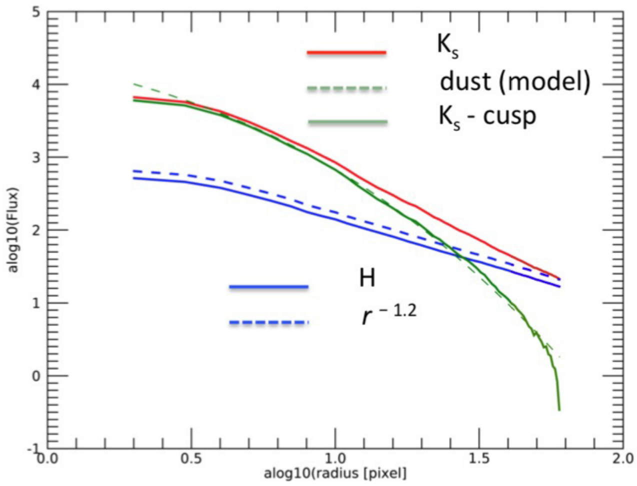

Fig. 4. Left: Effect of differential extinction solely. Red and blue solid lines: observed 2 to 50 pc radial fluxes in K_s and H band; red and blue dashed lines: K_s-band and H-band profiles resulting from the radiative transfer model, when the power law for the stellar and dust radial density have exponents of -4.20 and -1.05, respectively. Right: Preferred solution with warm dust emission. K_s-band (red solid) and H-band (blue solid) radial profiles; green solid line: K_s-band radial profile subtracted with a stellar cusp contribution proportional to the H-band profile; blue dashed line: estimated stellar cusp at K_s; green dashed line: best fit by the model of thermal dust emission (see text).

3 Conclusions

The question of wether a cuspy distribution of stars is actually observed in central region of galaxies, as predicted by dark matter halo simulation, is still a matter of debate.

At least in the case of the Seyfert galaxy NGC1068, the archetype of type 2 AGN, where near-IR images were obtained thanks to high angular resolution observations with VLT-SPHERE, we have shown that indeed a true cusp is observed. There is however the serious problem that the exponents of the power-law fitting the brightness radial profiles, differ notably between the two wavelengths (1.65 μm at H and 2.16 μm at Ks) where observation was done.

We have built a simple model of radiative transfer to try to explain this difference by considering various possibilities mixing stellar emission, dust absorption and dust thermal emission.

We reach the conclusion that at the heart of NGC1068 there are 3 components that explain the profile of the brightness : *i)* a stellar cusp of profile $r^{-1.2}$, with radius $\approx$ 100 pc, and Luminosity = 3.2 10^{10} $L_\odot$, which is a probable remnant of a recent starburst episode; *ii)* warm to hot dust heated by the central engine on $\approx$ 15 pc; *iii)* an unresolved source at $\approx$ 1400 K, likely the internal wall of a thick torus at dust sublimation temperature. Those results are presented in a more detailed way in Rouan et al. (2019).

A question remains: is the pronounced cusp a tracer of a dark matter halo ? This study just brings some elements characterising the cusp that may constrain the problem, but obviously cannot answer the question.

We acknowledge financial support from the Programme National Hautes Energies (PNHE) and from 'Programme National de Cosmologie and Galaxies' (PNCG) funded by CNRS/INSU-IN2P3-INP, CEA, and CNES, France.

References

García-Burillo, S., Combes, F., Ramos Almeida, C., et al. in prep.
Gratadour, D., Rouan, D., Grosset, L., Boccaletti, A., & Clénet, Y. 2015, A&A, 581, L8
Grosset, L., Rouan, D., Gratadour, D., et al. 2018, A&A, 612, A69
Haan, S., Armus, L., Surace, J. A., et al. 2013, MNRAS, 434, 1264
Hopkins, P. F. & Quataert, E. 2011, MNRAS, 415, 1027
Pontzen, A. & Governato, F. 2012, MNRAS, 421, 3464
Rouan, D., Grosset, L., & Gratadour, D. 2019, A&A, 625, A100

SF2A 2019
P. Di Matteo, O. Creevey, A. Crida, G. Kordopatis, J. Malzac, J.-B. Marquette, M. N'Diaye, O. Venot (eds)

THE MILKY WAY'S GRAVITATIONAL ACCELERATION FIELD MEASURED FROM RR LYRAE IN GAIA

C. Wegg[1]

Abstract. From ~16,000 RR Lyrae with proper motions measured by Gaia, we have measured the kinematics of the Milky Way's stellar halo up to 20 kpc from the Galactic centre. By applying the Jeans equations to these kinematic measurements, we have non-parametrically measured the azimuthally averaged gravitational acceleration field. We thereby measure the acceleration field away from the Galactic plane, a region which otherwise has only measurements at the sparsely located stellar streams. By subsequently removing the baryonic contribution from these measurements we have inferred the contribution of dark matter. We find that the gravitational potential of the Milky Way's dark matter appears spherical with flattening $q_\rho = 1.00 \pm 0.09$, slightly more spherical than the average flattening of dark matter halos in simulations of disk galaxies.

Keywords: dark matter, Galaxy:kinematics and dynamics, Galaxy: halo, Galaxy: kinematics and dynamics

1 Introduction

The release of Gaia DR2 in April 2018 has, for the first time, provided us with kinematic information across a wide volume of the Milky Way's halo. This, in principle, provides us with data from which we can extract the gravitational accelerations acting though our halo. Unfortunately Gaia's horizon for accurate parallaxes is confined to a few kpc around the Sun (Figure 1, left side). However, if distances to stars are known then Gaia can provide accurate the proper motions to stars over a much wider volume of the Galaxy (Figure 1, right side).

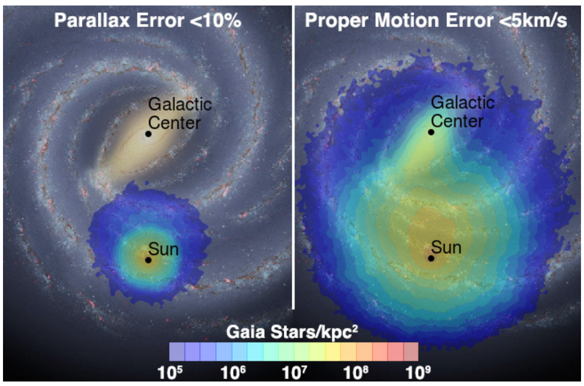

Fig. 1. Simulated Gaia catalog from models in Portail et al. (2017). **Left:** Gaia's horizon for accurate distances limits the volume of the Galaxy that can be directly studied. **Right:** For stars with accurate distances, Gaia proper motions provide accurate transverse velocities over a large volume.

Dynamical modelling of these velocities should allow us over the coming years to build up an accurate map of where both the stellar and dark matter mass lies. In other galaxies we can typically only measure line-of-sight velocities and so such modelling has uncertainties such as the well known mass-anisotropy degeneracy

[1] Laboratoire Lagrange, Université Côte d'Azur, Observatoire de la Côte d'Azur, CNRS, Bd de l'Observatoire, 06304 Nice, France

(e.g. Courteau et al. 2014). However in the Milky Way we can measure kinematics of individual stars in 3D and so these difficulties are circumvented. This allows us to uniquely infer the detailed properties of our own dark matter halo, and by comparison to simulations, understand if dark matter behaves as expected, a process termed near-field cosmology.

2 The Kinematics of the Halo As Traced By RR Lyrae

Motivated by the potential of Gaia's accurate proper motions, we utilised the catalogue of RR Lyrae in Pan-STARRS produced by Sesar et al. (2017). RRab are excellent standard candles and Sesar et al. (2017) estimates the distances in their catalogue to be precise to 3%. We limit the sample to stars at $|b| > 10\,\mathrm{deg}$ from the galactic plane (to avoid regions where extinction hampers RR Lyrae detection) and to stars within 20kpc of the Galactic centre (at which distances Gaia is still able to provide accurate proper motions). Cross matching to Gaia DR2 gives a sample of 16,000 stars with accurate distances and transverse velocities. The sample is centrally concentrated, approximately following a power law with index $\alpha = -2.7$ and flattening $q_{RR} = 0.72$, however the distribution appears too complex to be fully described by a simple parametric form.

Our sample of RR Lyrae have accurate 3D positions and velocities, but their radial velocities are unobserved. These radial velocities will be observed over the coming ~ 5 years by the WEAVE and 4MOST surveys, however, for now we have available 5 of the 6D phase space coordinates. In order to reconstruct the intrinsic kinematics of the halo from this kinematic information we have taken two approaches: (a) assuming that the kinematics are Gaussian and independent of azimuth. (b) a method that recovers the velocity moments of even non-Gaussian velocity distributions, assuming only that the kinematics are independent of azimuth.

For both methods we binned our data into 9 bins logarithmically spaced bins radially, and 5 bins in inclination, which span all azimuthal angles i.e. we make bins in $(\log r, \theta)$ which span all ϕ. Method (a) is more transparent: The 3D velocity ellipsoid is projected onto the sky plane differently at the position of each RR Lyrae, and so from a sample of RR Lyrae at different positions which share the same kinematics we can measure the 3D velocity ellipsoid. Method (b) is more general, but more opaque and less statistically efficient for Normally distributed velocities.

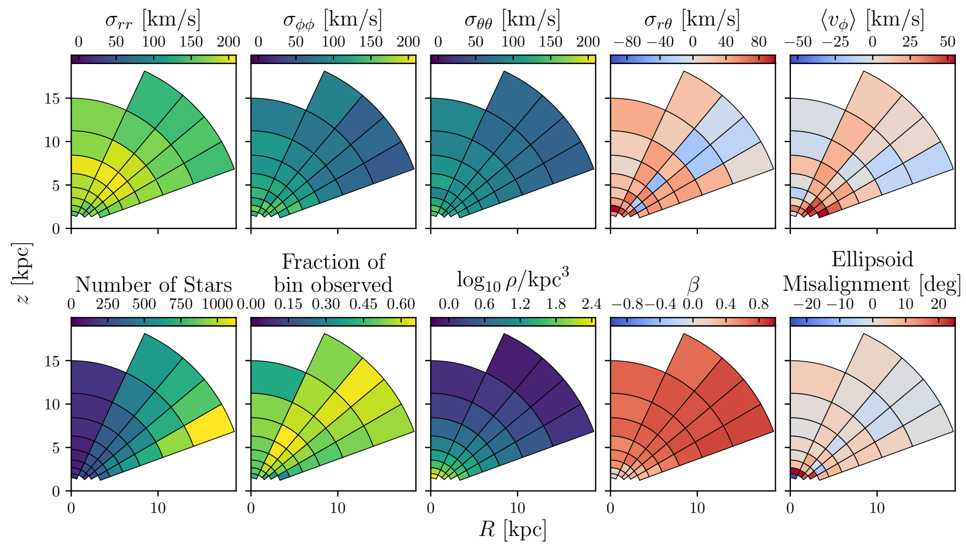

Fig. 2. The azimuthally averaged kinematics of our sample of RR Lyrae. **Upper row:** the elements of the dispersion tensor σ_{rr}, $\sigma_{\phi\phi}$, $\sigma_{\theta\theta}$ and $\sigma_{r\theta}$ and the rotation $\langle v_\phi \rangle$. **Lower row:** the number of stars in each bin and the completeness of each bin. These are combined to compute the azimuthally averaged density in the third plot. The final two plots show the radial anisotropy parameter β and the misalignment of the velocity ellipsoid from spherical.

In Figure 2 we show the results of method (b). However, both methods give the same results: (i) The sample of RR Lyrae is strongly radially anisotropic with anisotropy parameter $\beta \equiv 1 - (\sigma_{\theta\theta} + \sigma_{\phi\phi})/(2sigma_{rr}) \approx 0.8$ over most of the volume with Galactocentric radii < 20kpc. (ii) The velocity ellipsoid is nearly spherically aligned over most of the halo, only near the Galactic plane, or in the innermost regions of the halo does it tilt towards cylindrical alignment. (iii) Most of the volume studied rotates very slowly, or even counter rotates.

However, the inner regions, at < 5kpc from the Galactic center, rotate at up to 50km s^{-1}. This rotation may reflect the early build up of the innermost regions of our stellar halo, but there will also be significant angular momentum transfer from the non-axisymmetric bar at these radii.

3 The Milky Way's Acceleration Field

We have applied the Jean's equations to the kinematics measured in Figure 2. There are two Jeans equations containing F_r and F_θ, the accelerations in the two-dimensional (r, θ)-plane. While the equations are long, they are straightforward, and for the sample of RR Lyrae we have measured all of the required kinematic quantities. Therefore, after discretising the Jeans equations for our bins, we have applied them and the resultant accelerations are plotted in Figure 3.

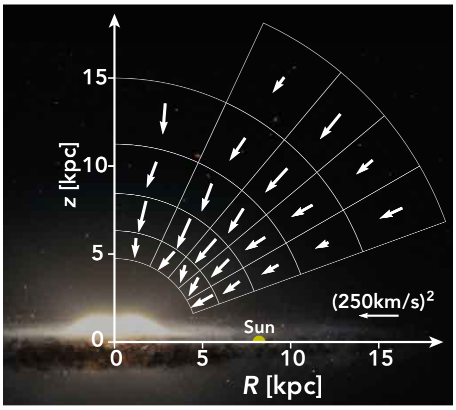

Fig. 3. The Milky Way's acceleration field measured non-parametrically using Gaia data (adapted from Wegg et al. 2019. Artists impression Credit:ESO/NASA/JPL-Caltech/M. Kornmesser/R. Hurt). The resultant velocities have almost equal length, which is the 3D equivalent of the Milky Way's flat rotation curve. To normalise, the forces, in $(\mathrm{km/s})^2/\mathrm{kpc}$, have been multiplied by galactocentric radius: this provides a 3D equivalent of the squared circular velocity.

It is immediately clear from Figure 3 that the forces are mostly radial. To quantify this, and understand the implications for the Milky Way's dark matter distribution, we have subtracted models for the baryonic component. These models consist of the barred models of the inner Galaxy taken from Portail et al. (2017), together with exponential disk models for the stars and gas in the outer Galaxy. Subtracting these models provides us with the forces from the dark matter alone. We have tested the effect of our assumptions on the baryonic distribution, varying for example the stellar disk scale length and normalisation, and find that they are smaller than the statistical errors with our sample size.

Until this point in the modelling all methods have been non-parametric but, after subtracting the baryonic forces, the errors in the dark matter forces are larger, particularly in the baryon dominated inner regions. For this reason we have fit parametric models to the dark matter distribution: either (i) assuming a ellipsoidal dark matter distribution and fitting for the dark matter flattening as a function of radius (ii) fitting the entire dark matter forces to ellipsoidal parametric models of the dark matter such as the NFW and Einsasto profiles.

Both methods give consistent results: using (i) we find that, over the entire $5 - 20$kpc range where we can measure the flattening, the dark matter is consistent with a spherical potential with average flattening $q_\Phi = 1.01 \pm 0.06$. Using (ii) we find that a variety of different profiles fit the dark matter forces equally well, but all agree that the dark matter density is near spherical, with flattening in dark matter density of $q_\rho = 1.00 \pm 0.09$.

4 Tests Using Mock Halos

We have tested that the method is able to recover the kinematics, gravitational accelerations, and dark matter distribution, of two mock halos: (i) A mock halo constructed by disrupting a satellite on a nearly radial orbit in the fixed background potential of `MWPotential2014` taken from GalPy. The system was evolved for 6 Gyr before the particles were observed as mock RR Lyrae. The resultant mock halo demonstrated a similar level of non-axisymmetry to the Milky Way's stellar halo as traced by RR Lyrae, and we would expect it to demonstrate a similar level of phase-mixing. (ii) A mock halo constructed by selectively turning the dark matter particles in the models of Portail et al. (2017) into stars so that the mock stellar halo had similar kinematic properties to the Galaxy's stellar halo. In both mock halos we simulated a larger sample than available and found that the dark matter shape was recovered to within the statistical errors of the real sample size. This demonstrates that the systematic errors of the method (e.g. the finite size of the bin) and the assumptions (e.g. that the kinematics are axisymmetric) are likely to be smaller than the statistical errors.

The results using halo (i) in particular are reassuring because the RR Lyrae at our largest radii are not axisymmetric, and therefore not likely not fully phase mixed. This may reflect their accreted nature by e.g. Gaia-Enceladus/Sausage, and mock halo (i) was designed to test this.

5 Context and Future Prospects

Despite the observational advantage of having 3D velocities of stars, we are yet to reach a consensus on either the profile or shape of the Milky Way's halo. Similar methods to ours have been utilised by Loebman et al. (2014) finding the dark matter to have a flattened potential with $q_\Phi = 0.8 \pm 0.1$ and a corresponding density flattening of $q_\rho = 0.4 \pm 0.1$. However, in contrast using similar data, Bowden et al. (2016) favours a highly prolate dark matter potential with flattening $q_\Phi = 1.5 - 2.0$.

Both these results are in tension with recent work using tidal streams in the halo. For example using GD-1 ($R_{\rm gc} \approx 14$kpc), the flattening of the overall potential has been measured to be $q_\Phi \equiv \langle c/a \rangle_\rho = 0.87^{+0.07}_{-0.04}$ by Koposov et al. (2010), $q_\Phi = 0.90^{+0.05}_{-0.10}$ by Bowden et al. (2015) and $q_\Phi = 0.95 \pm 0.04$ by Bovy et al. (2016). Similarly at the location of Pal-5 ($R_{\rm gc} \approx 18$kpc) the overall potential was measured to be $q_\Phi = 0.95^{+0.05}_{-0.10}$ by Küpper et al. (2015) and $q_\Phi = 0.94 \pm 0.05$ by Bovy et al. (2016). Combining these constraints on the potential with baryonic models results in a dark matter halo with axes ratio $q_\rho = 1.05 \pm 0.14$ (Bovy et al. 2016).

Here we report a measurement using Gaia DR2, which allows us for the first time to apply the Jeans equations to stars over a large region of the Galaxy. In is reassuring that our result of $q_\rho = 1.00 \pm 0.09$ is consistent with those using streams.

In dark matter only CDM simulations, dark matter halos are highly flattened. The introduction of baryons however reduces this to a canonical value of $q_\rho \sim 0.8$ (Debattista et al. 2008, although the recent aurigaia simulations of Grand et al. 2018 appear to be slightly more spherical). Our result of a slightly more spherical halo that these expectations is therefore tantalising.

Spectroscopic surveys like WEAVE, 4MOST will soon begin measuring the kinematics of millions of halo stars. Dynamical modelling of this data, combined with Gaia proper motions, promises to unveil the distribution of dark matter throughout the Milky Way. In combination with modelling of Stellar streams, such as those observed by the S5 survey (Li et al. 2019), we should therefore be able to build a consensus on the dark matter distribution throughout our home Galaxy over the coming 5 years.

This work has made use of data from the European Space Agency (ESA) mission *Gaia*, processed by the *Gaia* Data Processing and Analysis Consortium (DPAC). Funding for the DPAC has been provided by national institutions, in particular the institutions participating in the *Gaia* Multilateral Agreement.

References

Bovy, J., Bahmanyar, A., Fritz, T. K., & Kallivayalil, N. 2016, 833, 31

Bowden, A., Belokurov, V., & Evans, N. W. 2015, 449, 1391

Bowden, A., Evans, N. W., & Williams, A. A. 2016, 460, 329

Courteau, S., Cappellari, M., de Jong, R., et al. 2014, Rev. Mod. Phys., 86, 47

Debattista, V. P., Moore, B., Quinn, T., et al. 2008, 681, 1076

Grand, R. J. J., Helly, J., Fattahi, A., et al. 2018, 481, 1726

Koposov, S. E., Rix, H.-W., & Hogg, D. W. 2010, 712, 260

Küpper, A. H. W., Balbinot, E., Bonaca, A., et al. 2015, 803, 80

Li, T. S., Koposov, S. E., Zucker, D. B., et al. 2019, eprint arXiv:1907.09481

Loebman, S. R., Ivezic, Z., Quinn, T. R., et al. 2014, 794, 151

Portail, M., Gerhard, O., Wegg, C., & Ness, M. 2017, 465, 1621

Sesar, B., Hernitschek, N., Mitrović, S., et al. 2017, 153, 204

Wegg, C., Gerhard, O., & Bieth, M. 2019, 485, 3296

Session 18

Exploration de Ryugu et Bennu par Hayabusa2 (JAXA) et OSIRIS-REx (NASA), atelier PNP

SF2A 2019
P. Di Matteo, O. Creevey, A. Crida, G. Kordopatis, J. Malzac, J.-B. Marquette, M. N'Diaye, O. Venot (eds)

EFFECT OF THE PLANETESIMAL DISK ON THE POSITIONS OF THE SECULAR RESONANCES

D. Baguet[1], J.-M. Petit[1] and A. Morbidelli[2]

Abstract. During the pre-instability period following the disappearance of the protoplanetary gas disk, the giant planets were in a compact multiresonant orbital configuration, before starting to migrate by interacting with the planetesimal disk extending beyond the orbit of Neptune. It is commonly accepted that the planetesimal disk was divided into two parts: a massive disk extending from Neptune to 30 au and a low mass extension of the disk, extending beyond 30 au. We study the effect of the massive part of the disk on the nodal precessions of the giant planets and of the planetesimals in order to find the positions of the nodal secular resonances. The presence of the massive disk removes the degeneracy of the f_5 nodal frequency and allows for a new secular resonance. We show that for some orbital configurations, the f_5 nodal secular resonance is located in the region where the primordial cold classical Kuiper Belt formed.

Keywords: Celestial mechanics, Kuiper Belt, secular resonance

1 Introduction

In order to reproduce the difference between the dynamically hot and cold populations of the Kuiper Belt, current models of dynamical evolution aiming to reproduce their orbital structures consider that the two populations formed from two different regions. The hot population is assumed to be formed from a massive disk (with a mass within the range $\sim 10-60\,M_\oplus$) extending between Neptune and 30 au and the cold population from a light disk extending beyond 30 au. In current numerical integrations aiming to reproduce the cold population, the action of the massive disk on the objects of the light disk is always neglected (e.g. Batygin et al. 2011; Nesvorný 2015), because otherwise the computation would be too heavy. We investigate the effect of this action in the linear secular theory in order to find the locations of the secular resonances, during the period following the dissipation of the protoplanetary gas disk, when the giant planets were in a multiresonant orbital configuration. Because of this multiresonant configuration, we are only able to look at the nodal secular resonances.

2 Method

We compute the gravitational potential caused by the massive disk by using the method developed by Fukushima (2016) and we add its contribution to the secular nodal precessions of the different bodies. Secular resonances occur where the free precession frequency of a small body, represented as a massless particle, equals one of the eigenfrequencies of the planetary system. With the effect of the massive disk, the total angular momentum of the giant planets is not conserved and it allows for the existence of a new secular resonance, called f_5.

3 Results

Fig. 1 shows the positions of the nodal secular resonances, where the free frequency crosses one of the eigenfrequencies, for the multiresonant configuration 3:2, 3:2, 3:2, 3:2. We can see that if the action of the massive disk is included both on the giant planets and on the small body, the f_5 secular resonance is located near 44 au, which is in the region of the current cold population. The f_6 and f_7 secular resonances remain in the region below 20 au. The f_8 and f_9 secular resonances are pushed toward 30 au. Table 1 shows the positions of the f_5 secular resonance in the different multiresonant configurations proposed by Deienno et al. (2017).

[1] Institut UTINAM, UMR 6213, CNRS, Université Bourgogne Franche-Comté, OSU Theta F-25000, Besançon, France
[2] Laboratoire Lagrange, UMR 7293, Université Côte d'Azur, CNRS, Observatoire de la Côte d'Azur, Boulevard de l'Observatoire, 06304 Nice Cedex 4, France

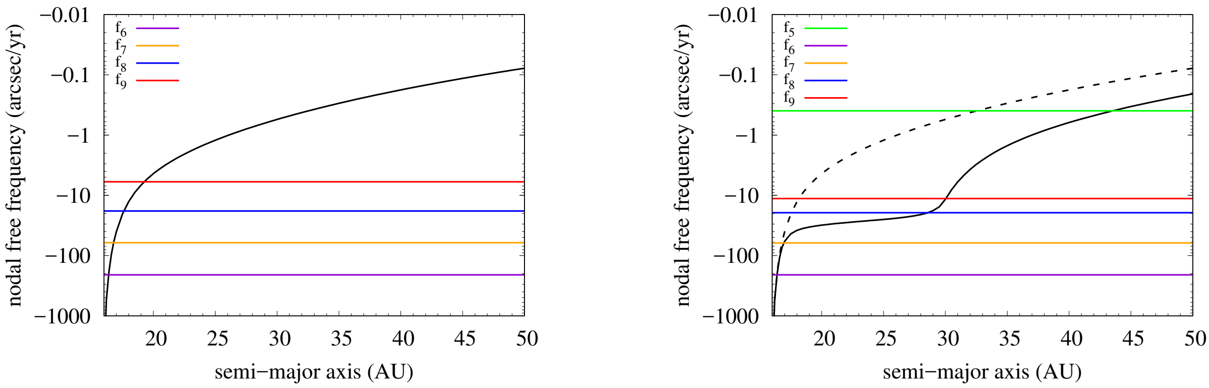

Fig. 1. Nodal free frequency of a small body as a function of its semi-major axis in the configuration 3:2, 3:2, 3:2, 3:2. The horizontal lines are the nodal eigenfrequencies. **Left:** in this model the massive disk is neglected. **Right:** the massive disk is included, with a mass $M_{disk} = 40M_\oplus$. The dashed curve is the nodal free frequency in the case where the action of the massive disk on the particle is neglected and the full black curve is the nodal free frequency but in the case where this action is taken into account.

Table 1. Positions of the f_5 secular resonance for different multiresonant configurations of the giant planets and for three different masses of the massive disk.

Orbital configuration	M_{disk} ($M_\oplus$)	Position of f_5 (au)
3:2, 3:2, 4:3, 4:3	20	42.7
	40	41.0
	60	40.5
3:2, 3:2, 3:2, 3:2	20	45.0
	40	43.5
	60	43.3
3:2, 3:2, 2:1, 3:2	20	48.3
	40	47.5
	60	47.7
3:2, 3:2, 2:1, 2:1	20	55.1
	40	54.7
	60	54.7

4 Conclusions

We have found that if the action of the massive disk, extending from Neptune to 30 au, on the giant planets and on the small bodies of the light disk is not neglected, the f_5 secular resonance could have been located in the region of the current cold population. This resonance can rise the inclinations of the bodies located in it if the angle between the plane orthogonal to the total angular momentum of the giant planets is misaligned with the plane of the massive disk. This effect has always been neglected but futur numerical integrations have to take it into account.

References

Batygin, K., Brown, M. E., & Fraser, W. C. 2011, ApJ, 738, 13

Deienno, R., Morbidelli, A., Gomes, R. S., & Nesvorný, D. 2017, AJ, 153, 153

Fukushima, T. 2016, MNRAS, 462, 2138

Nesvorný, D. 2015, AJ, 150, 68

SF2A 2019
P. Di Matteo, O. Creevey, A. Crida, G. Kordopatis, J. Malzac, J.-B. Marquette, M. N'Diaye, O. Venot (eds)

PREPARING SAMPLE RETURN FROM RYUGU AND BENNU ASTEROIDS WITH MICROMETEORITES FROM THE CONCORDIA COLLECTION

J. Duprat[1], C. Engrand [1], E. Dartois[2], J. Mathurin[3], S. Bernard [4], C. Le Guillou [5], H. Leroux [5], V. Vuitton [6], F.-R. Orthous-Daunay [6], B. Auge [1], B. Guerin [1] and J. Rojas [1]

Abstract. Hayabusa 2 and OSIRIS-REx space missions will give a unique access to the composition of carbonaceous asteroids. A key issue will be the comparison of the organic and mineral compounds from these near-Earth active carbonaceous asteroids with that of carbonaceous chondrites, carbon-rich interplanetary dust particles and cometary samples (81P/Wild2 or in-situ analyses from 67P/CG). The comparison of Ryugu and Bennu samples with chondritic micrometeorites and with extremely carbon-rich interplanetary dust particles such as the Ultra-Carbonaceous MicroMeteorites (UCAMMs) will provide a unique tool to assess their possible links with cometary organics. Analytical methods applied to study micrometeorites from Concordia collection (Antarctica) and the most recent results obtained are summarised. A particular emphasis is put on the dedicated experimental protocols that we developed to analyse micrometeorite fragments and study their mineral-organic association at scales relevant to their intimate association, ranging from tens of nanometers to a few microns.

Keywords: Solar System, space sample return mission, asteroid, micrometeorites, interplanetary organic matter

1 Introduction

Samples from dark asteroids Ryugu and Bennu will be collected and brought back to Earth by Hayabusa 2 and Osiris ReX missions in December 2020 and march 2023 respectively. It is the first-time material from the surface of known carbonaceous asteroids will be available for comparison with the different samples of primitive carbonaceous material. These primitive samples include carbonaceous chondrites, interplanetary dust particles and micrometeorites (MMs). Recent studies on cometary samples (Brownlee et al. 2006; Nakamura et al. 2008) showed that there is no marked difference between the solid phase of icy objects (i.e. comets) and primitive chondritic samples from carbonaceous asteroids. These samples originate from parent bodies that belong to an "Asteroid-Comet continuum". The fact that most of the dust belong to that reservoir strongly suggests that it is representative of most of the Asteroid Belt mass. Dark asteroids such as Bennu and Ryugu could be representative of this "Asteroid-Comet continuum" and, as such, samples from there surface will be of uttermost importance to challenge the relevance of this continuum concept.

The CONCORDIA micrometeorites collection contains one of the best sampling of the interplanetary carbonaceous dust complex encountered by Earth. The majority of the particles in the collection are related to CR and CM chondrites and exhibit both hydrous and anhydrous minerals (Engrand & Maurette 1998). The comparison of Ryugu and Bennu particles with the CONCORDIA collection will provide key constraints on similarities and differences between these samples and the asteroïdal and cometary end-members of interplanetary dust. The techniques developed recently on micrometeorites allow to combine the analysis of both minerals and organics phases at the sub-micron scale. They will be used in the rehearsal of Hayabusa 2 samples analysis.

[1] CSNSM, CNRS-Univ. Paris Sud-Univ. Paris-Saclay, Orsay, France
[2] ISMO CNRS/Univ. Paris Sud, Univ.Paris-Saclay, Orsay, France
[3] LCP, CNRS, Université Paris Sud, Université Paris-Saclay , Orsay, France
[4] IMPMC, CNRS, Sorbonne Université, MNHN, 4 place Jussieu, 75005 Paris, France
[5] Univ. Lille, CNRS, INRA, ENSCL, UMR 8207 - UMET, F-59000 Lille
[6] Univ. Grenoble Alpes, CNRS, CNES, IPAG, 38000 Grenoble, France

2 Micrometeorites from the CONCORDIA Collection

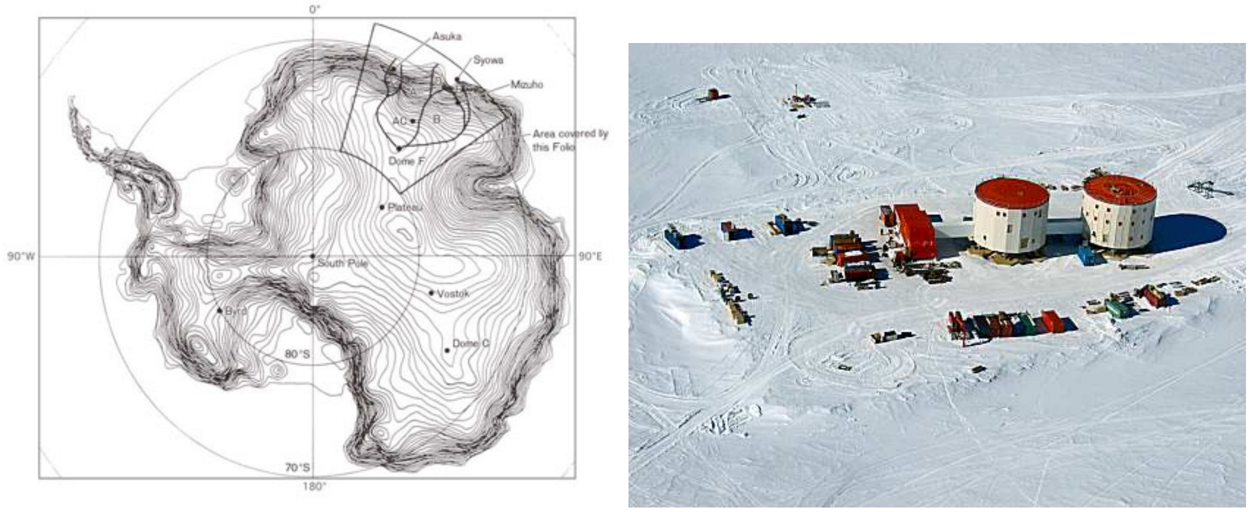

Fig. 1. Left: Dome C location in the central regions of the Antarctic continent. **Right:** CONCORDIA Station (IPEV).

Large collections of interplanetary dust within the 20 μm-1000 μm size range (i.e. micrometeorites) have been recovered from many type of sediments, deep sea floor and polar ice caps.Thanks to the support of the Institut Polaire Français, Paul Emile Victor (IPEV), we collect micrometeorites at the vicinity of the French-Italian polar station CONCORDIA located at Dome C (5° S, 123° E). The location of CONCORDIA station is in the central east regions of the Antarctic continent, at more than 1100 kms from Adélie Land (Figure 1). The surface snow at Dome C is exceptionally preserved from terrestrial dust contamination with the size range of micrometeorites (Duprat et al. 2007). For more than two decades, we recovered manually thousands of particles from ultra-clean snow samples extracted from 4-7 meters deep trenches. The resulting collection contains many unaltered interplanetary dust particles. The micrometeorites from the CONCORDIA collection are well preserved from terrestrial weathering as they were preserved at low temperature (< -40 ° C) within the Antarctic surface snow. The main part of the collection contains micrometeorites typical from the carbonaceous "Asteroid-Comet continuum". Aside from these chondritic micrometeorites, some particles stand apart and exhibit distinctive characteristics of asteroïdal of cometary origins. Some particles exhibit exceptionally high carbon content, with concentrations above 50% of the mass, in the form of organic matter with extreme deuterium enrichments; they are the so-called Ultra-Carbonaceous Antarctic MicroMeteorites (UCAMMs) (Duprat et al. 2010). The mineralogy, the elemental and isotopic composition of these particles clearly indicates that they belong to the cometary reservoir (Dartois et al. 2013). UCAMMs have been identified in both the CONCORDIA and the Japanese collection from Dome Fuji (Nakamura et al. 2005; Yabuta et al. 2017). By contrast, some micrometeorites exhibit clear asteroïdal signature in their mineralogy (Genge et al. 2008; Gounelle et al. 2005) and isotopic composition. As these samples represent somehow the cometary and asteroïdal end-members, the comparison of the Ryugu and Bennu particles to such samples will shed light on primitive carbonaceous material from the solar system protoplanetary disk.

3 Key questions on Ryugu and Bennu minerals and organics

The return of Hayabusa 2 samples will provide for the first-time particles from a known C-type asteroid, 162173 Ryugu (aka 1999 JU3). Together with Secondary Electron Microscopy (SEM) and Transmission Electron Microscopy (TEM) measurements, the infrared spectra will reveal both the mineral and organic content of Ryugu particles. To what extent the Ryugu particles will be similar to chondritic MMs, and will the distribution of their Olivine/Pyroxene ratio be similar to that of MMs? The average amorphous/crystalline ratio of minerals from Ryugu particles will also be of crucial importance, will it be in the classical range of chondritic dust particles (i.e. chondritic MMs)? These measurements will be important to distinguish the interstellar heritage from minerals reprocessed within the carbonaceous asteroïdal reservoir. How extensively will the samples of Ryugu or Bennu exhibit traces of ion irradiation by solar wind and energetic particles like those reported

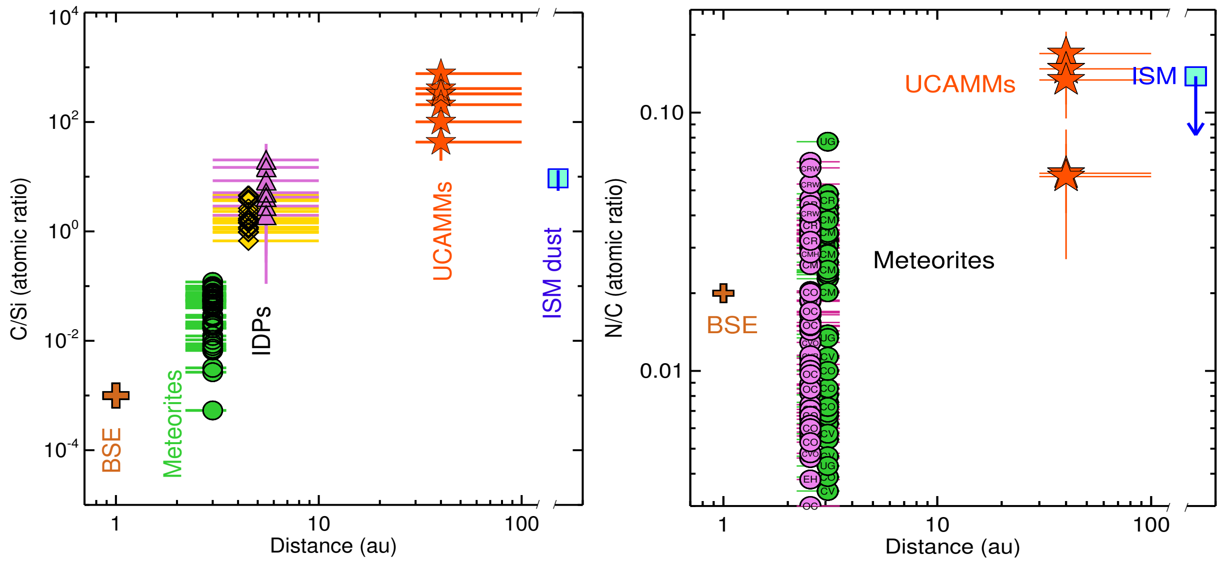

Fig. 2. C/Si **Left:** and N/C **Right:** ratio in different early solar system samples and reservoirs (figure from Dartois et al. 2018)

from Hayabusa I samples? Recently, irradiation tracks and amorphised irradiated rims have been observed in minerals from a UCAMM (Engrand et al. 2019). Measurements will be performed to compare the irradiation history of Ryugu and Bennu surface with that of typical asteroïdal and cometary samples. The C-type asteroïds are expected to be carbon rich and thus their organic/mineral ratio (C/Si) will be of particular interest. Will it be in the range of typical chondritic MMs or higher? Samples from the cometary reservoir tend to exhibit higher concentration in carbonaceous material (see Figure 2), suggesting that an heliocentric (C/Si) gradient was present in the protoplanetary disk. The average value of this ratio will be of crucial importance to better understand the origin of the organic component of carbonaceous asteroïds.

The organic component of meteorites is rich and diverse, most probably reflecting the incorporation of different early solar system organic reservoirs and their subsequent evolution in their parent body. The origin of Ryugu and Bennu organic will provide constraints on the dynamic processes that affected the organics in the protoplanetary disk. A key feature to distinguish between organics produced at different temperatures is their N/C ratio (see Figure 2). The organics from particles of potential cometary origin (such as UCAMMs) exhibit a component with a N/C ratio higher than that usually reported in chondritic material (Dartois et al. 2018). This component was most probably formed by irradiation of ices at the surface of icy parent bodies beyond the nitrogen snow line (Dartois et al. 2013; Augé et al. 2016). Together with the general features of their infrared spectra, the comparison of the distribution of the N/C ratios of the organics in Ryugu and Bennu samples to that reported in MMs will shed light on the various solar system organic components and their different origins.

4 Micrometeorites for rehearsal

The analysis of Ryugu and Bennu samples will face technical issues related to careful handling and preparation of rare samples with sizes ranging from a few tens to a few hundred μm. The different groups working on IDPs and MMs have developed numerous techniques and skills to perform combined measurements on precious samples within this size range. The french micrometeorite collaboration developed expertise to perform mineralogical, elemental, structural and isotopic studies on the same sample. The samples are mounted on dedicated diamond cells allowing SEM, μ- Raman, μ-IR and NanoSIMs measurements on samples with sizes of few tens of microns (Dartois et al. 2013). More recently, thanks to the novel AFMIR technique, the infrared signature of different organic components have been imaged in a UCAMM (see Figure 3, Mathurin et al. 2019) at spatial resolutions lower than a micron (i.e. better than the diffraction limit). The AFMIR analysis of Ryugu and Bennu particles will provide a unique tool to reveal the relation between minerals and organics of carbonaceous asteroids at the sub-micron scale.

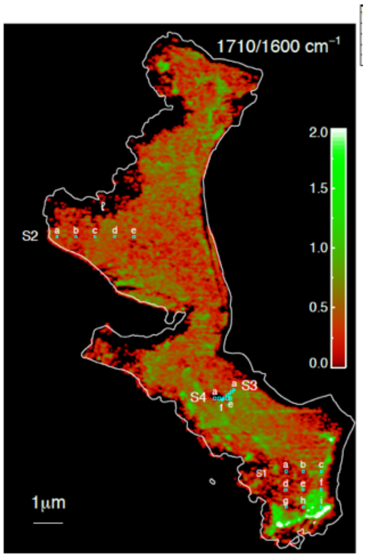

Fig. 3. AFMIR map of a micrometeorites reveals the diversity of organics at the sub- μm scale (figure from Mathurin et al. 2019)

5 Conclusions

The return of Ryugu and Bennu samples provide an opportunity to compare samples from two carbonaceous asteroïds with what we know from asteroïdal and cometary samples. The bulk of micrometeorites consists in chondritic carbonaceous particles that are most probably representative of the matter from the asteroïdal-cometary continuum. The comparison of both minerals and organics returned by Hayabusa 2 and OSIRIS-REx with micrometeorites will shed light on the dynamical evolution of these primitive components prior their incorporation in Ryugu and Bennu asteroïds.

The micrometeorite Concordia collection is supported by the French and Italian polar institutes IPEV and PNRA. This work was supported by the PNP and PCMI programs and by ANR project COMETOR (ANR-18-CE31-0011) and OGRESSE (11-BS56-026-01), DIM-ACAV+ (Région Ile de France), Université Paris-Sud, IN2P3 and the JWST project from the LABEX-P2IO. The NanoIR 2-s microscope was installed on the SMIS3 beam line at SOLEIL Synchrotron.

References

Augé, B., Dartois, E., Engrand, C., et al. 2016, Astronomy and Astrophysics, 592

Brownlee, D., Tsou, P., Aléon, J., et al. 2006, Science, 314, 1711

Dartois, E., Engrand, C., Brunetto, R., et al. 2013, Icarus, 224, 243

Dartois, E., Engrand, C., Duprat, J., et al. 2018, Astronomy and Astrophysics, 609

Duprat, J., Dobrică, E., Engrand, C., et al. 2010, Science, 328, 742

Duprat, J., Engrand, C., Maurette, M., et al. 2007, Adv. Space Res., 39, 605

Engrand, C., Charon, E., Leroux, H., et al. 2019, LPI Contributions, 2157, 6416

Engrand, C. & Maurette, M. 1998, MAPS, 33, 565

Genge, M. J., Engrand, C., Gounelle, M., & Taylor, S. 2008, Meteoritic and Planetary Science, 43, 497

Gounelle, M., Engrand, C., Chaussidon, M., Zolensky, M. E., & Maurette, M. 2005, in 36th Annual Lunar and Planetary Science Conference, ed. S. Mackwell & E. Stansbery, Lunar and Planetary Science Conference, 1655

Mathurin, J., Dartois, E., Pino, T., et al. 2019, Astronomy and Astrophysics, 622

Nakamura, T., Noguchi, T., Ozono, Y., Osawa, T., & Nagao, K. 2005, Meteoritics, 40 Suppl., 5046

Nakamura, T., Noguchi, T., Tsuchiyama, A., et al. 2008, Science, 321, 1664

Yabuta, H., Noguchi, T., Itoh, S., et al. 2017, Geochimica et Cosmochimica Acta, 214, 172

Session 19

Atelier Général PNHE

SF2A 2019
P. Di Matteo, O. Creevey, A. Crida, G. Kordopatis, J. Malzac, J.-B. Marquette, M. N'Diaye, O. Venot (eds)

CHANGING-LOOK SEYFERT GALAXIES WITH OPTICAL LINEAR POLARIZATION MEASUREMENTS

F. Marin[1], D. Hutsemékers[2] and B. Agís González[2]

Abstract. In this lecture note, we make the case for new (spectro)polarimetric measurements of "changing-look" AGNs (CLAGNs), a subclass of the AGN family tree that shows long-term (months to years) large flux variability associated with the appearance or disappearance of optical broad emission lines. We discuss how polarization measurements could help to distinguish which of the several scenarios proposed to explain such variations is/are the most likely. We collected all the past polarization measurements of nearby, Seyfert-like CLAGNs and take stock that almost all polarimetric information we have on those fascinating objects dates from the 80's and 90's. We thus explain how polarization could help us understanding the physical processes happening in the first parsecs of CLAGNs and why new polarization monitoring campaigns are strongly needed.

Keywords: Galaxies: active, galaxies: quasars, galaxies: Seyfert, polarization

1 Introduction

Among active galactic nuclei (AGNs), a new class of object is nowadays recognized. Those specific AGNs have time-dependent spectroscopic signatures that makes them appear as type-1 AGNs for a certain period and then as type-2 AGNs after a while(see, e.g., Khachikian & Weedman 1971; Cohen et al. 1986; Goodrich 1989). Type-1 AGN are characterized by large optical fluxes associated with broad (> 1000 km.s^{-1}) and narrow (≤ 1000 km.s^{-1}) emission lines, while type-2s only shownarrow emission lines and lower optical fluxes. The large Doppler widths result from photo-ionization of an equatorial reservoir of gas composed of many cloudlets that have large Keplerian velocities and densities (Gaskell 2009). Depending on the inclination of the system with respect to the observer, this broad emission line region (BELR) may be hidden by an optically thick, equatorial, circumnuclear layer of dust. This orientation dependence has been used to explain the observational differences between the two AGN types for decades now and is still a very robust interpretation (Antonucci 1993). However, there are rogue AGNs that have shown type transitions on timescales of months to years. Examples of such objects are Mrk 1018, which varied between type-2 and type-1 between 1979 and 1984 (Cohen et al. 1986), NGC 4151 that changed from type-1 to type-2 between 1974 and 1984 (Penston & Perez 1984), or 3C 390.3 that followed the same type transition between 1975 and 1984 (Penston & Perez 1984). From dynamical timescale arguments, it is physically impossible that a parsec-sized object has changed its whole inclination in a human time frame. Then, how can we explain those "rapid" changes of type ? There are several theories involving the appearance or disappearance of optically thick material in front of the observer's line-of-sight (Goodrich 1989; Elitzur 2012), tidal disruptions events (TDEs, Rees 1988; Lawrence et al. 2016) or rapid mass accretion rate drop resulting in the disappearance of the BELR (Noda & Done 2018). In this lecture note, we will expound how (spectro)polarimetric measurements of those "changing-look AGN" (CLAGNs) could help understand the physical processes happening around active supermassive black holes. Here, we will focus on nearby, low-luminosity CLAGNs, and refer to Hutsemékers et al. (2019) for high luminosity objects (quasars).

2 Optical polarization of Seyfert-like CLAGNs

There are at least three scenarios* to explain the dramatic flux variation and spectral change of Seyfert-like CLAGNs. The first one invokes the appearance or disappearance of obscuring material in front of the observer's line of sight. In this case,

[1] Université de Strasbourg, CNRS, Observatoire Astronomique de Strasbourg, UMR 7550, F-67000 Strasbourg, France
[2] Institut d'Astrophysique et de Géophysique, Université de Liège, Allée du 6 Août 19c, 4000 Liège, Belgium

*We also take note of the controversial explanation of large amplitude microlensing by stars in foreground galaxies to explain CLAGNs (Lawrence et al. 2016) a cloud from either the outer BELR or the circumnuclear torus passes in front of the line-of-sight and (partially) obscures the central source, resulting in an opacity-dependent dimming and the apparent disappearance of the broad emission line signatures (Goodrich 1989; Tran et al. 1992). The second scenario explains CLAGNs using unusually luminous TDEs (Lawrence et al. 2016). When a star orbits close enough to the central supermassive black hole of AGNs, it is torn apart by tidal forces and a fraction of the mass is accreted, resulting in a sudden brightening of the black hole. The change in luminosity can easily last for several hundreds of days (Rees 1988). Finally, a third scenario postulates that the CLAGN phenomenon is due to modifications in the source of ionizing radiation, likely a variation in the rate of accretion onto the central supermassive black hole (Penston & Perez 1984; Elitzur et al. 2014; Noda & Done 2018).

Spectroscopic and photometric observations can be explained by one or several of those scenarios, depending on the target. However, their polarization signatures are unique (Marin et al. 2016; Hutsemékers et al. 2017; Marin 2017; Hutsemékers et al. 2019).

- If the central source is intrinsically dimming, at the onset of the flux variation the polarization degree experiences sharp decreases and increases associated with rotations of the polarization angle. Those time-dependent variations are due to lower amounts of direct, unpolarized flux from the central engine and constant amounts of reprocessed (delayed) radiation from the equatorial region. The duration of the high polarization degree peak depends on the distance of the scatterer from the source and can be used to achieve polarized reverberation mapping of the inner CLAGN regions. The polarization degree and polarization position angle then return to a stability period after several years/decades (see Marin & Hutsemékers, A&A, submitted). On the other hand, if the BELR disappears, electron scattering inside the BELR becomes inefficient, the polarization degree decreases and the polarization position angle rotates by 90°. Polarized light echoes are much less bright due to the absence of an electron-filled, nearby scattering target. The duration of the echo is also extended due to the fact that radiation has to scatteronto the parsec-scale torus/winds rather than onto the sub-parsec scale BELR. At the end of the echo, the polarization position angle rotates again by 90°, returning to the initial value at the same time than the polarization degree returns to a stability period. This could, in turn, provide us with an estimation of the inner radius of the torus if the polarized light echo is detectable.
- In the case of cloud obscuration, radiation mainly escapes the central (obscured) region by scattering inside the polar outflows, similarly to what has been postulated for the Unified Scheme of AGNs (Antonucci 1993). This results in much higher polarization degrees (10 – 20%, see e.g., NGC 1068 Antonucci & Miller 1985) and a rotation of the polarization position angle due to the fact that equatorial scattering is no longer visible. The flux and polarization variations are also time-dependent but are likely to be shorter depending on the size and radial distance of the cloud to the central engine (Gaskell & Harrington 2018).

All differences are detailed in Marin (2017) for further details. In any case, it is vital to obtain polarization measurements of CLAGNs, before and after the change of look. We thus compiled the historical spectral type changes and polarization measurements of known changing-look Seyferts (at our best knowledge) in Tab. 1. The spectral types of changing-look Seyferts and the epoch at which they were measured are given in Col. 2. A range of dates indicates that the spectral types measured at these two dates are identical, with no change recorded in between. We emphasize that this does not imply absence of spectral type variations during this period. For some objects, exhaustive monitorings were carried out. In such cases, only some representative types/epochs are reported in Tab. 1. The polarization degrees given in Col. 4 refer to the optical continuum polarization measured in various broad-band filters. For a few objects the polarization was monitored during several years. In such cases, we give three representative values at most in Tab. 1. In total, there are only 23 polarization measurements of Seyfert-like CLAGNs. Among the 23, only 3 observations have been carried out after 2000, which means that our knowledge of the polarization of CLAGNs is based on data that are at least 20 years old. There are only 6 objects (Mrk 6, NGC 1566, NGC 4151, NGC 7603, Fairall 9 and 3C 390.3) that have repeated polarimetric measurements but none of them happened coincidentally with the change of look. At best, we can estimate the past polarization level of CLAGNs before their transition but there is very little we can do about determining the correct physical explanation of the spectral/flux change without new and periodic polarization measurements of those objects.

3 Discussion and conclusions

We have seen that the pool of archival polarimetric measurements of state transitions in CLAGNs is very limited, almost non-existent. This is rather detrimental since polarimetric observational data along with numerical models are a unique tool to determine what are the physical causes of the changes of look, unveiling new frontiers in the AGN physics. New and repeated polarimetric measurements are thus needed as part of a monitoring campaign. There are at least 23 candidates for

Table 1. Changing-look Seyferts with optical linear polarization measurements

Object	Spectral type (year)	References	Polarization degree (year) (%)	References
Mrk 6	2 (1968) → 1.5 (1969-2013)	1,2,3	0.54±0.15 (1976) → 0.90±0.03 (1997) → 0.74±0.17 (2013)	4,5,3
Mrk 372	1.5 (1986) → 1.9 (1990)	6	1.49±0.46 (1976)	4
Mrk 590	1.5 (1973) → 1 (1989-1996) → 1.9 (2006-2014) → 1 (2017)	7,8	0.32±0.30 (1976)	4
Mrk 1018	1.9 (1979) → 1 (1984-2009) → 1.9 (2015)	9,10	0.28±0.05 (1986)	11
NGC 1566	1 (1962) → 1.9 (1969) → 1 (1980) → 1.9 (1985) → 1 (2018)	12,13,14	0.60±0.24 (1980) → 1.33±0.18 (1997)	4,15
NGC 2617	1.8 (1994-2003) → 1 (2013-2016)	16,17,18	0.43±0.15 (1998)	19
NGC 2622	1.8 (1981) → 1 (1985-1987)	11	2.35±0.03 (1986)	11
NGC 3516	1 (1996-1998) → 1 (2007) → 2 (2014-2017)	20	0.15±0.04 (1997)	5
NGC 4151	1 (1974) → 1.9 (1984-1989) → 1.5 (1990-1998) → 1.8 (2001)	21,22,23	0.26±0.08 (1976) → 1.18±0.05 (1992) → 0.32±0.30 (2014)	4,24,25
NGC 7582	2 (1980-1998) → 1 (1998)	26,27	1.03±0.12 (1981)	4
NGC 7603	1 (1974) → 1.8 (1975) → 1 (1976-1998)	28,29	0.32±0.29 (1976) → 0.42±0.03 (1987) → 0.25±0.04 (1997)	4,11,5
Fairall 9	1 (1977-1981) → 1.8 (1984) → 1 (1987)	30,31	0.40±0.11 (1981) → 0.37±0.13 (1997)	4,5
3C 390.3	1 (1975) → 1.9 (1980-1984) → 1 (1985-1988) → 1 (2005-2014)	21,32,33	0.84±0.30 (1976) → 1.30±0.10 (1986) → 1.13±0.18 (2014)	4,34,35

(1) Khachikian & Weedman (1971); (2) Khachikian et al. (2011); (3) Afanasiev et al. (2014); (4) Martin et al. (1983); (5) Smith et al. (2002); (6) Gregory et al. (1991); (7) Denney et al. (2014); (8) Raimundo et al. (2019); (9) Cohen et al. (1986); (10) McElroy et al. (2016); (11) Goodrich (1989); (12) Pastoriza & Gerola (1970); (13) Alloin et al. (1986); (14) Oknyansky et al. (2019); (15) Felton (1999); (16) Moran et al. (1996); (17) Shappee et al. (2014); (18) Oknyansky et al. (2017); (19) Wills et al. (2011); (20) Shapovalova et al. (2019); (21) Penston & Perez (1984); (22) Malkov et al. (1997); (23) Shapovalova et al. (2008); (24) Martel (1998); (25) Afanasiev et al. (2019); (26) Ward et al. (1980); (27) Aretxaga et al. (1999); (28) Tohline & Osterbrock (1976); (29) Kollatschny et al. (2000); (30) Kollatschny & Fricke (1985); (31) Lub & de Ruiter (1992); (32) Veilleux & Zheng (1991); (33) Sergeev et al. (2017); (34) Impey et al. (1991); (35) Afanasiev et al. (2015)

Mrk 6 : Variations in type 1.5 state on short timescales. Equatorial scattering dominated (Smith et al. 2004). Polarization reverberation (Afanasiev et al. 2014). No strong variation of PPA.
Mrk 590 : Variations are likely intrinsic. Candidate for polarization echoes.
Mrk 1018 : Variations are likely intrinsic. Candidate for polarization echoes.
NGC 1566 : Recurrent variations with outbursts from type 1.9/1.8 to type 1.5/1.2 during decades. No strong variation of PPA.
NGC 2617 : Variations are likely intrinsic. Candidate for polarization echoes.
NGC 2622 : Variations are likely due to obscuration. Polar scattering dominated (Smith et al. 2004).
NGC 3516 : Complex variability from 1999 to 2008. Variations are likely due to obscuration.
NGC 4151 : Complex variability on multiple timescales. Equatorial scattering dominated (Smith et al. 2004). Polarization reverberation (Gaskell et al. 2012). No strong variation of PPA.
NGC 7582 : The transition to type 1 was fast, and short.
NGC 7603 : Variations are likely due to obscuration.
3C 390.3 : Complex variability. Radio galaxy. Polarization reverberation (Afanasiev et al. 2015).

a follow up program and a handful more of radio-loud AGNs (Hutsemékers et al. 2019). Ideally, broad-band polarization measurements should be obtained twice a year during typically one or two decades. For the brightest objects (Seyferts) this could be achieved with robotic 1m class telescopes. On the other hand, a follow-up of the polarization of CL quasars as those studied in Hutsemékers et al. (2019) would require 2-4m class telescopes, in particular when the objects are in their faint type-2 phase.

FM would like to thank the Centre national d'études spatiales (CNES) who funded his post-doctoral grant "Probing the geometry and physics of active galactic nuclei with ultraviolet and X-ray polarized radiative transfer". DH is senior research associate F.R.S.-FNRS. BAG acknowledges support provided by the Fonds de la Recherche Scientifique - FNRS, Belgium, under grant No. 4.4501.19.

References

Afanasiev, V. L., Popović, L. Č., & Shapovalova, A. I. 2019, MNRAS, 482, 4985
Afanasiev, V. L., Popović, L. Č., Shapovalova, A. I., Borisov, N. V., & Ilić, D. 2014, MNRAS, 440, 519
Afanasiev, V. L., Shapovalova, A. I., Popović, L. Č., & Borisov, N. V. 2015, MNRAS, 448, 2879
Alloin, D., Pelat, D., Phillips, M. M., Fosbury, R. A. E., & Freeman, K. 1986, ApJ, 308, 23
Antonucci, R. 1993, ARA&A, 31, 473
Antonucci, R. R. J. & Miller, J. S. 1985, ApJ, 297, 621
Aretxaga, I., Joguet, B., Kunth, D., Melnick, J., & Terlevich, R. J. 1999, ApJ, 519, L123
Cohen, R. D., Rudy, R. J., Puetter, R. C., Ake, T. B., & Foltz, C. B. 1986, ApJ, 311, 135
Denney, K. D., De Rosa, G., Croxall, K., et al. 2014, ApJ, 796, 134
Elitzur, M. 2012, ApJ, 747, L33
Elitzur, M., Ho, L. C., & Trump, J. R. 2014, MNRAS, 438, 3340
Felton, M. 1999, Optical polarimetry studies of Seyfert galaxies. Doctoral thesis, Durham University.
Gaskell, C. M. 2009, New A Rev., 53, 140
Gaskell, C. M., Goosmann, R. W., Merkulova, N. I., Shakhovskoy, N. M., & Shoji, M. 2012, ApJ, 749, 148
Gaskell, C. M. & Harrington, P. Z. 2018, MNRAS, 478, 1660
Goodrich, R. W. 1989, ApJ, 340, 190
Gregory, S. A., Tifft, W. G., & Cocke, W. J. 1991, AJ, 102, 1977
Hutsemékers, D., Agís González, B., Marin, F., et al. 2019, A&A, 625, A54
Hutsemékers, D., Agís González, B., Sluse, D., Ramos Almeida, C., & Acosta Pulido, J. A. 2017, A&A, 604, L3
Impey, C. D., Lawrence, C. R., & Tapia, S. 1991, ApJ, 375, 46
Khachikian, E. Y., Asatrian, N. S., & Burenkov, A. N. 2011, Astrophysics, 54, 26
Khachikian, E. Y. & Weedman, D. W. 1971, ApJ, 164, L109
Kollatschny, W., Bischoff, K., & Dietrich, M. 2000, A&A, 361, 901
Kollatschny, W. & Fricke, K. J. 1985, A&A, 146, L11
Lawrence, A., Bruce, A. G., MacLeod, C., et al. 2016, MNRAS, 463, 296
Lub, J. & de Ruiter, H. R. 1992, A&A, 256, 33
Malkov, Y. F., Pronik, V. I., & Sergeev, S. G. 1997, A&A, 324, 904
Marin, F. 2017, A&A, 607, A40
Marin, F., Goosmann, R. W., & Petrucci, P. O. 2016, A&A, 591, A23
Martel, A. R. 1998, ApJ, 508, 657
Martin, P. G., Thompson, I. B., Maza, J., & Angel, J. R. P. 1983, ApJ, 266, 470
McElroy, R. E., Husemann, B., Croom, S. M., et al. 2016, A&A, 593, L8
Moran, E. C., Halpern, J. P., & Helfand, D. J. 1996, ApJS, 106, 341
Noda, H. & Done, C. 2018, MNRAS, 480, 3898
Oknyansky, V. L., Gaskell, C. M., Huseynov, N. A., et al. 2017, MNRAS, 467, 1496
Oknyansky, V. L., Winkler, H., Tsygankov, S. S., et al. 2019, MNRAS, 483, 558
Pastoriza, M. & Gerola, H. 1970, Astrophysical Letters, 6, 155
Penston, M. V. & Perez, E. 1984, MNRAS, 211, 33P
Raimundo, S. I., Vestergaard, M., Koay, J. Y., et al. 2019, MNRAS, 486, 123
Rees, M. J. 1988, Nature, 333, 523
Sergeev, S. G., Nazarov, S. V., & Borman, G. A. 2017, MNRAS, 465, 1898

Shapovalova, A. I., Popović, , L. Č., et al. 2019, MNRAS, 485, 4790
Shapovalova, A. I., Popović, L. Č., Collin, S., et al. 2008, A&A, 486, 99
Shappee, B. J., Prieto, J. L., Grupe, D., et al. 2014, ApJ, 788, 48
Smith, J. E., Robinson, A., Alexander, D. M., et al. 2004, MNRAS, 350, 140
Smith, P. S., Schmidt, G. D., Hines, D. C., Cutri, R. M., & Nelson, B. O. 2002, ApJ, 569, 23
Tohline, J. E. & Osterbrock, D. E. 1976, ApJ, 210, L117
Tran, H. D., Osterbrock, D. E., & Martel, A. 1992, AJ, 104, 2072
Veilleux, S. & Zheng, W. 1991, ApJ, 377, 89
Ward, M., Penston, M. V., Blades, J. C., & Turtle, A. J. 1980, MNRAS, 193, 563
Wills, B. J., Wills, D., & Breger, M. 2011, ApJS, 194, 19

SF2A 2019
P. Di Matteo, O. Creevey, A. Crida, G. Kordopatis, J. Malzac, J.-B. Marquette, M. N'Diaye, O. Venot (eds)

A GLOBAL MODEL OF THE MAGNETOROTATIONAL INSTABILITY IN PROTO-NEUTRON STARS

A. Reboul-Salze[1], J. Guilet[1], R. Raynaud[1] and M. Bugli[1]

Abstract. The magnetorotational instability (MRI) is a promising mechanism to amplify the magnetic field in fast-rotating proto-neutron stars. Many local studies have shown that the magnetic field could be amplified on small scales. However, the efficiency of the MRI at generating a large-scale field similar to the dipolar magnetic field of magnetars ($10^{14} - 10^{15}$ G) is still unknown. We used a three dimensional pseudo-spectral code to develop an idealized global model of the MRI in a proto-neutron star. We show that a dipole field strength consistent with the values of magnetar field intensity can be generated by the MRI, even though it is lower than the small-scale magnetic field. Overall, our results support the ability of the MRI to form magnetar-like dipolar magnetic fields.

Keywords: magnetars, supernovae, magnetohydrodynamics (MHD), instabilities, methods: numerical

1 Introduction

Magnetars are a class of neutron stars which stand out by their emission in gamma-rays or X-rays (Kaspi & Beloborodov 2017, and references therein). A few objects are detected by their pulsar-like radio emission. The observations of these emissions measure the spin-down of the neutron stars. Under the assumption of magnetic braking, a surface dipolar magnetic field of 10^{14}-10^{15} G can be inferred from the spin-down of magnetars.

Several scenarios have been invoked to explain the origin of magnetar magnetic field. It may stem from the field of the progenitor amplified by magnetic flux conservation. However this scenario tends to fall short for the strongest magnetic fields. The other scenarios are the in-situ magnetic field amplification by a turbulent dynamo in the proto-neutron star (PNS), either by a convective dynamo (Thompson & Duncan 1993; Raynaud et al. 2020) or the magnetorotational instability (MRI, Akiyama et al. 2003; Obergaulinger et al. 2009).

The MRI was first discovered in the context of accretion disks by Balbus & Hawley (1991) and its properties have been well studied in this context. However, the physical conditions in proto-neutron stars differ from accretion disks. A strong differential rotation resulting from the core-collapse of the progenitor to a PNS was found in simulations (Akiyama et al. 2003; Ott et al. 2006). The MRI can develop in this strong differential rotation zone. This instability has been mainly studied in the local approximation analytically or by using "shearing box" simulations representing a part of the PNS. For weak magnetic fields (10^{12}-10^{13} G), the wavelength of the MRI is indeed short and difficult to resolve in a global model. The first local simulations in the context of supernovae have shown that an efficient amplification of the magnetic field happens at the small scales (Obergaulinger et al. 2009; Rembiasz et al. 2016). Due to the high density inside the PNS, neutrinos are trapped inside it and their radiation induces a high viscosity, which can limit the growth of the MRI if the initial magnetic field is too low (Guilet et al. 2015).

The impact of the spherical geometry of the full PNS on the MRI turbulence and the ability of the MRI to generate a large-scale field, similar to the observed magnetic field of magnetars, is much less known. Mösta et al. (2015) performed the first simulations describing a quarter of the PNS with a high enough resolution to resolve the MRI wavelength. The model was, however, started with a strong progenitor magnetic dipole and therefore does not represent the scenario in which the MRI generates the magnetar magnetic field.

In this paper, we study the global properties of the MRI in spherical geometry using a different approach, in which the physical setup is reduced to its minimum physical ingredients. This has the advantage to provide a useful reference for our physical understanding. Furthermore, this approach drastically reduces the computational cost and makes the exploration of the parameter space possible.

[1] AIM, CEA, CNRS, Université Paris-Saclay, Université Paris Diderot, Sorbonne Paris Cité, F-91191 Gif-sur-Yvette, France

2 Numerical setup

The simulations performed in this article are designed to represent a fast rotating PNS of $M = 1.3M_\odot$ and a radius of $r_o = 25$ km. In order to simplify the setup, we use the incompressible approximation. Furthermore, we assume that neutrinos are in the diffusive regime and their effect is described by a viscosity $\nu = 7.03 \times 10^{11}$ cm^2 s^{-1}. We choose the physical parameters of the simulations to represent a fast rotating PNS model similar to the study of Guilet et al. (2015). Our model has a density $\rho_0 = 4 \times 10^{13}$ g cm^{-3}. The characteristic angular frequency $\Omega = 10^3$ s^{-1} matches the mean rotation rate. We use a cylindrical rotation profile with a central part that rotates like a solid body and an outer part that follows a power law of r^{-q}, with $q = 1.25$. The resistivity η is expected to be many orders of magnitude smaller than the viscosity, but numerical simulations for realistic values of the resistivity requires a too high resolution. In our study, we use a magnetic Prandtl number $P_m = \nu/\eta = 16$. The initial magnetic field strength is varied from $B_0 = 6.31 \times 10^{14}$ G to $B_0 = 3.36 \times 10^{15}$ G. Spherical harmonics and radial Fourier modes are randomly initialised for a wavelength interval $[L_{min}, L_{max}]$. This intense and small-scale magnetic field can be interpreted as the result of the first amplification described in local models. In order to solve the incompressible MHD equations with explicit diffusivities, we used the pseudo-spectral code MagIC (Wicht 2002; Schaeffer 2013). All the simulaitons presented in this paper were performed using a grid resolution of $(n_r, n_\theta, n_\phi) = (257, 512, 1024)$. For boundary conditions, we assume non-penetrating radial velocity at top and bottom ($v_r = 0$). For the inner boundary, we use standard no-slip boundary ($\vec{v} = 0$) whereas for the outer boundary we force v_ϕ to match the initial rotation profile at all times. For the magnetic field, we compare several conditions: pseudo-vaccuum (normal field), perfect conductor (tangential field), or insulating (matching a potential field outside the domain).

3 A fiducial run

Let us first describe the results from a representative simulation. We initialised the magnetic field as decribed in section 2 with the parameters $B_0 = 8.83 \times 10^{14}$ G, $[L_{min}, L_{max}] = [0.3-0.5]$. We also applied insulating boundary conditions for the magnetic field. The left panel of figure 1 shows the temporal evolution of volume-averaged poloidal, toroidal magnetic energies and turbulent kinetic energy. The axisymmetric differential rotation is not included in the turbulent kinetic energy. After approximately 500 milliseconds, we obtain a quasi-stationary state, where the magnetic field intensity is $B = 2.5 \times 10^{15}$ G. The main contribution is from the toroidal magnetic energy that is 4-5 times stronger than the poloidal magnetic energy. The total magnetic energy is also more than ten times stronger than the turbulent kinetic energy.

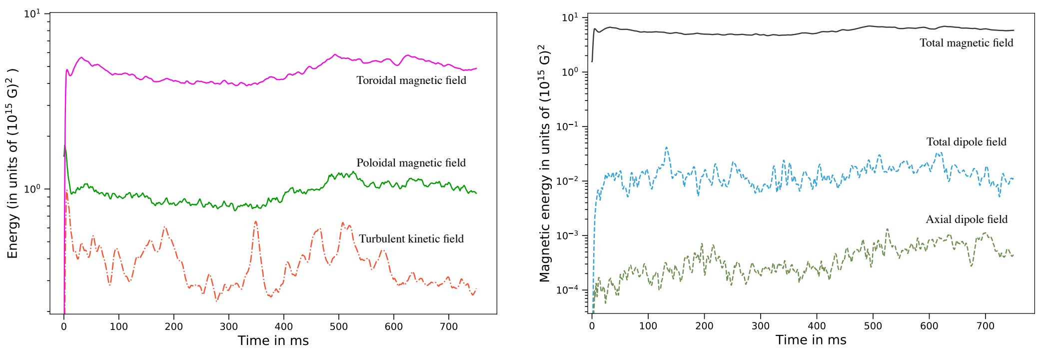

Fig. 1. Left: Temporal evolution of the magnetic and turbulent kinetic energy for $B_0 = 8.83 \times 10^{14}$ G, $[L_{min}, L_{max}] = [0.3-0.5]$. The purple and green lines are the toroidal and poloidal contributions of the magnetic energy, while the dash-dotted orange line is the kinetic turbulent energy (axisymmetric toroidal contribution is removed). **Right**: Temporal evolution of the total magnetic energy and dipolar energy.

To describe more accurately the complex geometry of the magnetic field, it is essential to look at the state of the simulation at a given time. The figure 2 shows a representative snapshot of the quasi-stationary state with a 3D rendering of the magnetic field amplitude (left panel) and the toroidal magnetic field in the meridional plane (right panel). The winding of the magnetic field by the shear is clearly seen in the equatorial plane. The largest visible scales in this snapshot are due to the winding. On the meridional cuts, the magnetic field is more

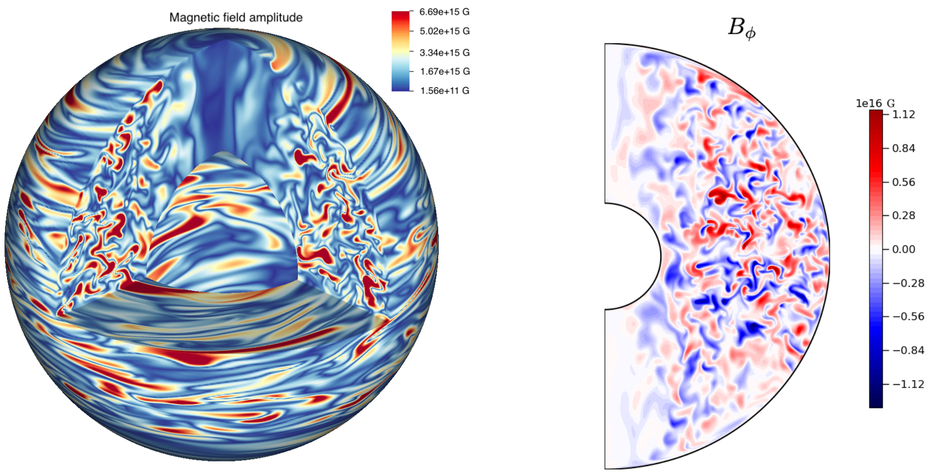

Fig. 2. Left: 3D snapshot of the amplitude of the total magnetic field. The colors represent the magnetic field amplitude from (weak) blue to strong (red). **Right**: Azimuthal magnetic field B_ϕ in the meridional plane for $\phi = 0$.

chaotic at small scale. The meridional slice (right panel) shows that the radial coherence of the initial magnetic field has vanished in favor of small turbulent structures. At the poles, the magnetic field is not very intense due to the solid body rotation for this cylindrical radius. The velocity field presents similar characteristics. The MRI-driven turbulence is present for a cylindrical radius larger than $r \approx 9.4$ km.

Since the magnetar timing parameters only constrain the dipole field strength, we focus in more details on this specific mode. The right panel of figure 1 shows the time evolution of the total magnetic energy (black line), the axial (green line) and total dipole (blue line). The dipole is not the dominant mode in the simulation as its energy is approximately 1000 times smaller than the total magnetic energy. But its strength is equal to $B_{dip} = 1.25 \times 10^{14}$ and could reach 5×10^{14} G with the conservation of the magnetic flux once the PNS cools down and contracts to $r = 12$ km. Therefore we obtain a self-sustained MRI dynamo with a dipole field intensity that matches current observations.

4 Parameter study

The impact of initial conditions and boundary conditions on the magnetic field in the quasi-stationary state needs to be assessed. A small-scale magnetic field may initially lead to a lower intensity because a too incoherent magnetic field may first decay faster than it grows via the MRI in local models (Bhat et al. 2017). However, once the dynamics reaches a quasi-stationary state, we may expect that it is independent of the initial conditions as observed in local models. The initial magnetic field here is controlled by two parameters: the allowed length interval for the Fourier and spherical harmonic modes $[L_{min}, L_{max}]$ and the initial magnetic field amplitude B_0. The left panel of figure 3 shows the time-averaged and volume-averaged magnetic field strength as a function of the initial magnetic field strength B_0. No clear impact of the initial conditions can be seen in the figure. Many models have similar magnetic field strength and different boundary conditions or initial conditions. The magnetic strength varies from 1.8×10^{15} G to 2.7×10^{15} G, which is a 15% difference around the median. A part of this variation can be explained by the stochasticity of the MRI driven dynamos as often found in MHD turbulence. The magnetic field is slightly stronger in the case of perfect conductor boundary conditions but models with other boundaries still occupy the entire intensity range. It shows that the initial conditions and boundary conditions have a small impact on the final quasi-stationary state.

The global properties of the different models are found to be similar. This implies that the small scales and the turbulence do not depend on the boundary conditions. However, the differences should also be checked for the large scales that are constrained by the observations. The right panel of figure 3 shows the dipole amplitude as a function of the total magnetic field strength. It is clear from this figure that the dipole amplitude scales linearly with the total magnetic field. The results on the dipole mode are, thus, robust to both initial and boundary conditions. Our parameter study support the idea that the MRI is a robust mechanism to generate a magnetic field from differential rotation, which could lead to the formation of a magnetar.

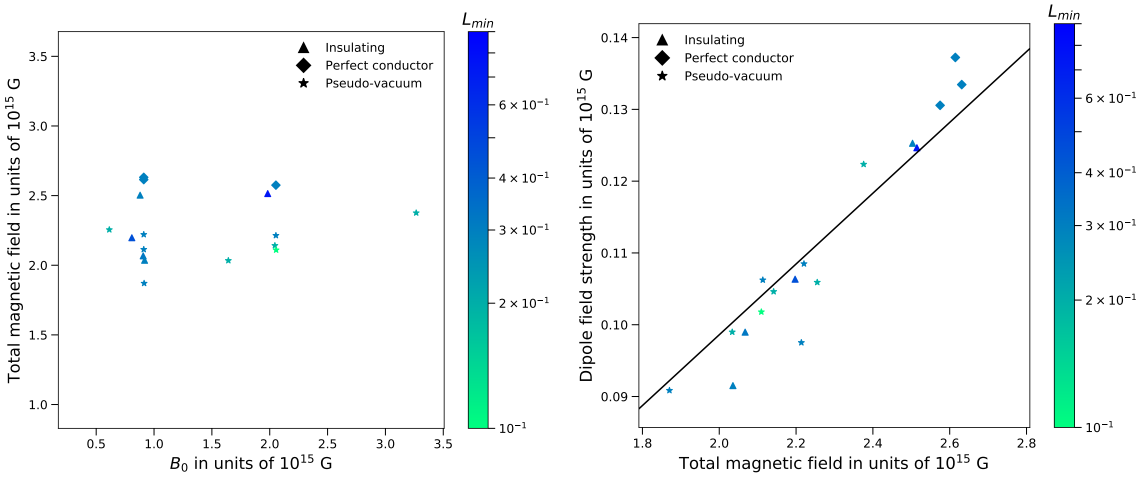

Fig. 3. Left: Total magnetic field strength as a function of the initial magnetic field strength. **Right**: Dipole field strength as a function of the total magnetic field strength. The equation of the linear fit is $y = 0.0493x$. The color indicates the smallest scale L_{min} of the initial magnetic field. The shape of the points represents the magnetic boundary conditions between perfect conductor (diamond), insulating (triangle) and pseudo-vacuum (star).

5 Conclusion

Using numerical simulations of an idealized global model of a proto-neutron star, we have investigated the generation of a large-scale magnetic field by the MRI. In our simulations, the MRI leads to a quasi-stationary state with the following characteristics: it has a strong turbulent magnetic field of $B_{tot} \geq 10^{15}$ G and a non-dominant dipole component $B_{dip} \geq 10^{14}$ G that lies within the lower end of the intensity range for the dipole of magnetars. Such a strong magnetic field could impact the dynamics of the core-collapse and launch jet-driven explosions, even though the complex geometry of our magnetic field may reduce the efficiency of the magnetorotational launching mechanism (Bugli et al. 2020).

We showed that the magnetic field amplification and dipole generation by the MRI is a robust mechanism with respect to the initial conditions and magnetic boundary conditions. Indeed, the turbulent energies and angular momentum transport in the quasi-stationary state does not depend on the initial magnetic field. The dipole strength scales linearly with the total magnetic field strength. These results support the ability of the MRI to generate a strong dipole and may explain the formation of magnetars.

Finally, we know that some limitations may have a quantitative impact on the results of our model (e.g. strength of the magnetic field and its dipolar component, etc.). For instance, taking into account buoyancy effects and the background density gradient may change these results (Guilet & Müller 2015). Our next step will be to implement a realistic interior model using the anelastic approximation to investigate the influence of these limitations.

This research was supported by the European Research Council through the ERC starting grant MagBURST No. 715368. The computations were performed on the CINES supercomputer occigen (applications A0030410317 and A0050410317).

References

Akiyama, S., Wheeler, J. C., Meier, D. L., & Lichtenstadt, I. 2003, ApJ, 584, 954

Balbus, S. A. & Hawley, J. F. 1991, ApJ, 376, 214

Bhat, P., Ebrahimi, F., Blackman, E. G., & Subramanian, K. 2017, MNRAS, 472, 2569

Bugli, M., Guilet, J., Obergaulinger, M., Cerdá-Durán, P., & Aloy, M. A. 2020, MNRAS, 492, 58

Guilet, J. & Müller, E. 2015, MNRAS, 450, 2153

Guilet, J., Müller, E., & Janka, H.-T. 2015, MNRAS, 447, 3992

Kaspi, V. M. & Beloborodov, A. M. 2017, ARA&A, 55, 261

Mösta, P., Ott, C. D., Radice, D., et al. 2015, Nature, 528, 376

Obergaulinger, M., Cerdá-Durán, P., Müller, E., & Aloy, M. A. 2009, A&A, 498, 241

Ott, C. D., Burrows, A., Thompson, T. A., Livne, E., & Walder, R. 2006, ASTROPHYS. J. SUPPL. S., 164, 130
Raynaud, R., Guilet, J., Janka, H.-T., & Gastine, T. 2020, Science Advances, in press
Rembiasz, T., Obergaulinger, M., Cerdá-Durán, P., Müller, E., & Aloy, M. A. 2016, MNRAS, 456, 3782
Schaeffer, N. 2013, Geochemistry, Geophysics, Geosystems, 14, 751
Thompson, C. & Duncan, R. C. 1993, ApJ, 408, 194
Wicht, J. 2002, Physics of the Earth and Planetary Interiors, 132, 281

SF2A 2019
P. Di Matteo, O. Creevey, A. Crida, G. Kordopatis, J. Malzac, J.-B. Marquette, M. N'Diaye, O. Venot (eds)

RWI IN DISK AROUND HIGH SPIN BLACK HOLE: HOW DOES IT IMPACT THE OBSERVABLES

P. Varniere[3,1], F. H. Vincent[2] and F. Casse[1,3]

Abstract. The Rossby-Wave Instability (RWI) has been proposed as the source of the fast, high-frequency quasi-periodic oscillations (HFQPOs) in microquasars. Here we are using NOVAs, our Numerical Observatory of Violent Accreting systems, to follow the evolution of the RWI and obtain observables to compare with X-ray data.

The first aim is to prove the ability of the RWI to modulate the X-ray fluxes in a similar way as is observed. But, thanks to NOVAs we can go further and explore possible imprints of the RWI in other potential observables.

Keywords: microquasars, QPO, spin

1 NOVAs versus Observations

Fig.1 shows succinctly what the building blocks of `NOVAs` are and how they relate to standard observations.

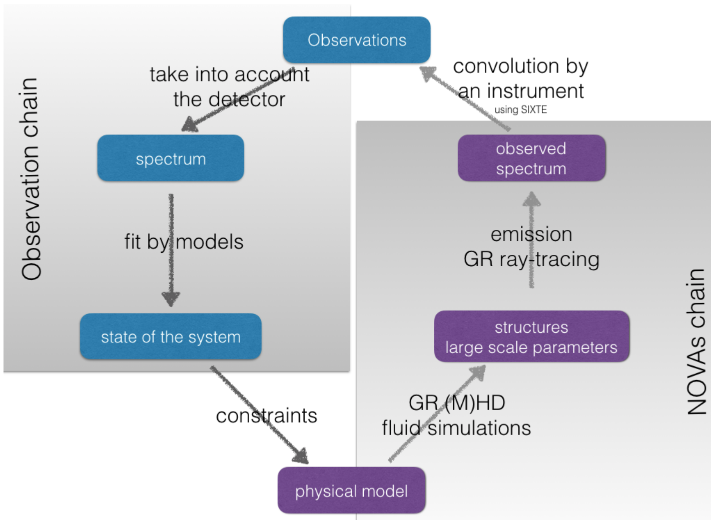

Fig. 1. The different building blocks that compose the `NOVAs` chain and the complementary observation chain.

– All the general relativistic (GR) fluid dynamics are done with the general relativistic version of MPI-AMRVAC: `GRAMRVAC` (Casse et al. 2017; Casse & Varniere 2018)

– For all the GR ray-tracing computations, we use the open-source code `GYOTO` (Vincent et al. 2011)

– In order to add instrumental effects we use the SIXTE package. It allows us to undertake instrument performance analyses and to produce simulated event files for mission and analysis studies.

[1] APC, AstroParticule et Cosmologie, Université Paris Diderot, CNRS/IN2P3, CEA/Irfu, Observatoire de Paris, Sorbonne Paris Cité, 10, rue Alice Domon et Léonie Duquet, 75205 Paris Cedex 13, France

[2] LESIA, Observatoire de Paris, Université PSL, CNRS, Sorbonne Université, Univ. Paris Diderot, Sorbonne Paris Cité, 5 place Jules Janssen, 92195 Meudon, France.

[3] Laboratoire AIM, CEA/IRFU-CNRS/INSU-Université Paris Diderot, CEA DRF/IRFU/DAp, F-91191 Gif-sur-Yvette, France.

2 Time domain ‘observations’ of the RWI

We have performed two types of ‘observations’ related to time domain studies (Varniere et al. 2019). We computed the PDS of several disks with the RWI active. As can be seen on the the left of Fig.2, while a lot of our ‘observations’ have only one detectable peak, some exhibit two peaks in different integer ratios such as 3:2 and 3:4 which are also observed in microquasars (Varniere & Rodriguez 2018).

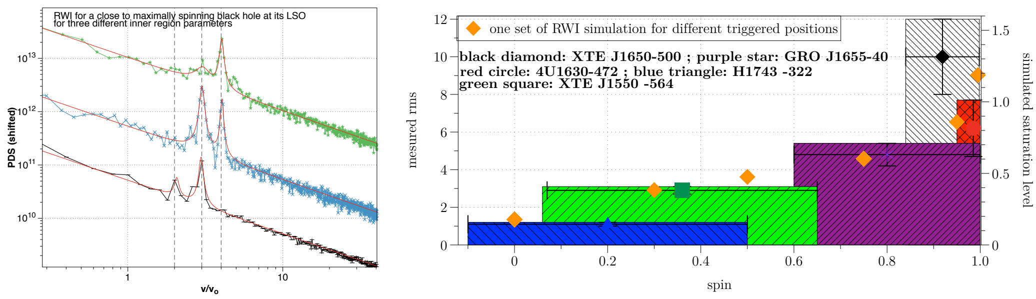

Fig. 2. Two type pf time domain ‘observations’ performed with NOVAs. On the Left three PDS associated with three distinct simulations for the same spin. On the right comparison between the observed rms versus spin behavior and the simulated vaues.

Using `NOVAs` we can follow the RWI in a similar setup while changing the spin. This allows us to see that the higher the spin of the black hole, the higher the rms of the HFQPO can become. Then we can compare with all the observations of HFQPOs in sources with known spins. The right of Fig.2 shows that the predicted behavior is coherent with limited known data.

This shows that the RWI is able to reproduce the time domain observations associated with HFQPOs and even offer other ways to further test the model.

3 Spectral domain ‘observations’ of the RWI

Beyond timing study, the `NOVAs` chain allows us to explore the impact of the RWI on the energy spectrum as well. The aim here is to explore new ways to detect the cause of the HFQPOs. As a first step we compute the energy spectrum of disk with the RWI active at different times along the HFQPO phase.

This allows us to see how much the RWI impacts the energy spectrum of the disk along one full phase. We need to look for good candidates to create energy spectrum binned per phase of the HFQPO. After adding comptonization by a corona, we can process our ‘observations’ through `xspec` and then we can obtain the fitted parameters for the system.

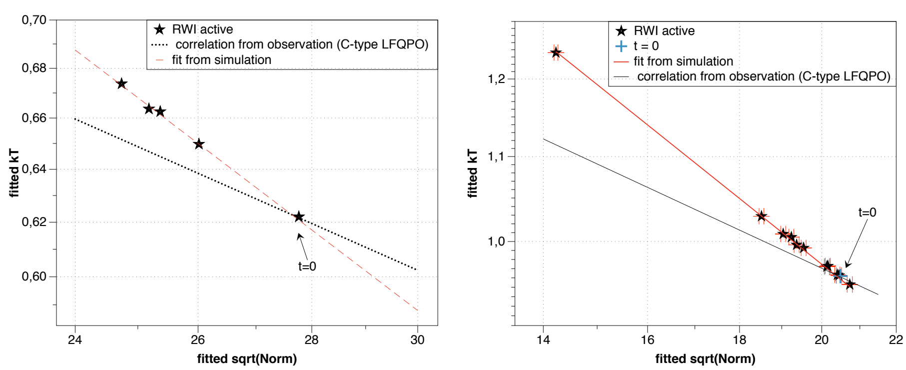

Fig. 3. Correlation between the inner edge position and temperature, as found by the fit when the RWI is active, for spin a=0.9 and a=0.75.

Fig.3 shows, for spin a=0.9 and a=0.75, the correlation between the inner edge position and temperature as found by the fit when the RWI is active.

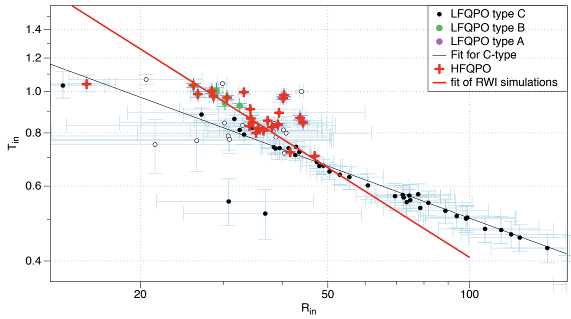

Fig. 4. Correlation between the inner edge position and temperature for XTE J1550-564. The red line represent the fit from the simulated RWI data shown above.

Those can in turn be compared to observations, here the case of XTE J1550-564 with data from both outbursts having known HFQPOs detections. As can be seen on Fig.4, a similar correlation as the one found in the RWI simulations seems to be present in the data when HFQPOs are present.

Those RWI 'numerical observations' are paving the way to further explore archival data as well as triggering new observations.

4 Conclusions

By combining smoothly two GR codes, one providing a full hydrodynamical solution and one providing the ray-tracing of the emission, we now have a fully functional numerical observatory which allows us to obtain spectrums and lightcurves of theoretical models with limited hypotheses.

It is now confirmed that the RWI is triggered at the inner edge of the disk and can modulate the X-ray flux in a similar way as is observed.

The RWI exhibits several sets of peaks in the PDS depending on the local condition in the inner region of the disk.

The impact on the energy spectrum of the RWI has consequences on the fit which is coherent with the observed deviation in presence of HFQPOs.

We now have all the tools necessary to start a more thorough comparison with observations.

We acknowledge the financial support of the UnivEarthS Labex program at Sorbonne Paris Cite (ANR-10-LABX-0023 and ANR-11-IDEX-0005-02).

References

Casse, F. & Varniere, P. 2018, MNRAS, 481, 2736

Casse, F., Varniere, P., & Meliani, Z. 2017, MNRAS, 464, 3704

Varniere, P., Casse, F., & Vincent, F. H. 2019, Astronomy & Astrophysics, 625, 8

Varniere, P. & Rodriguez, J. 2018, ApJ, 865, 113

Vincent, F. H., Paumard, T., Gourgoulhon, E., & Perrin, G. 2011, Classical and Quantum Gravity, 28, 225011

SF2A 2019
P. Di Matteo, O. Creevey, A. Crida, G. Kordopatis, J. Malzac, J.-B. Marquette, M. N'Diaye, O. Venot (eds)

THE GROWTH OF SUPERMASSIVE BLACK HOLES

N. A. Webb[1]

Abstract. Supermassive black holes (10^{6-10} $M_\odot$) are found in the centres of galaxies and appear to have a strong influence over the evolution of their hosts. However, it is not yet clear how these black holes form, nor how they evolve. It is thought that supermassive black holes could form from intermediate mass black holes (10^{2-5} $M_\odot$), but few have been identified observationally. Finding and studying intermediate mass black holes would help us understand how supermassive black holes form and evolve. In this work I will discuss some of the recent observational evidence for intermediate mass black holes and discuss their modes of accretion, as well as methods for searching for a significant population, in order to understand how supermassive black holes grow.

Keywords: Black hole physics, Galaxy: evolution, Galaxies: dwarf, Accretion, accretion disks

1 Introduction

Supermassive ($\sim10^{6-10}$ $M_\odot$) black holes (e.g. Lynden-Bell 1969) like Sgr A* are present in the cores of massive galaxies. These black holes appear to play a major role in the life of the galaxy as the mass of the central black hole has been shown to scale with the galaxy mass (Ferrarese & Merritt 2000; Gültekin et al. 2009). This being said, it is still not clear how supermassive black holes form, nor how they evolve. To understand the relationship with the galaxy mass and understand the role they play in the evolution of galaxies, it is essential to comprehend the origin and growth of supermassive black holes.

It is unlikely that supermassive black holes form from stellar mass black holes, as even continuously accreting at the Eddington limit (the maximum rate for material to be accreted onto the black hole supposing spherical accretion), it is difficult to reach masses as high as $\sim10^9$ $M_\odot$ observed in a massive quasar at z$\sim$7.1 (Mortlock et al. 2011) or the 8×10^8 $M_\odot$ black hole found at z=7.54 (0.69 Gyr, Bañados et al. 2018). There are several theories that discuss how supermassive black holes form. They may form from lower mass black holes, namely intermediate mass black holes (IMBH, 10^{2-5} $M_\odot$), but few of these kinds of objects have been found, making it difficult to validate such theories. There may also be a mechanism to accrete above the Eddington limit, thus allowing supermassive black holes to form more quickly (either from stellar mass or intermediate mass black holes), but the physical mechanism is still unclear. Black hole mergers may also contribute to achieving the masses of the supermassive black holes, or accretion plus mergers may be responsible (see Volonteri 2012; Greene 2012; Mezcua 2017, for reviews). In order to determine which is the true mechanism, it is necessary to find a population of intermediate mass black holes and determine where they are found and how they accrete, and/or determine the mechanism for prolonged super-Eddington accretion.

Finding IMBH is difficult. Originally, Ultra Luminous X-ray (ULX) sources were believed to be the best IMBH candidates (e.g. Makishama et al. 2000). ULXs are bright X-ray sources found outside the nucleus of galaxies, i.e. they are not the SMBHs in the galaxy centres. These sources have luminosities that exceed the Eddington limit for a stellar mass black hole ($\sim10^{39}$ erg s^{-1}), which is why it was originally thought that the black hole masses may be greater than those for stellar mass black holes, i.e. IMBH. However, observing ULXs for the last 30 years has provided evidence that most contain accreting stellar mass black holes or neutron stars (Bachetti et al. 2014, and references therein). Only the very brightest (Lx $> 10^{41}$ erg s^{-1}), known as the hyper luminous X-ray sources, are thought to be IMBH candidates.

However, IMBH are unlikely to be in a configuration where they accrete at high rates, meaning that they are intrinsically faint and thus difficult to find. As the mass of the central black hole has been shown to scale

[1] IRAP, Université de Toulouse, CNRS, CNES, Toulouse, France

with the galaxy mass, they should reside in the lower mass galaxies, so many surveys have focussed on them, but few valid IMBH have been found (see Baldassare et al. 2015, and references therein). IMBH have also been proposed to exist in the centres of globular clusters (e.g. Hut et al. 1992), but so far none have been detected in Galactic globular clusters, although stellar mass black holes have now been discovered in these systems (Strader et al. 2012; Tremou et al. 2018).

To overcome the problem of the sources being faint and difficult to detect, it is possible to wait until they tidally disrupt a passing star. As the star disrupts, approximately half of the matter falls on to the massive black hole (Rees 1988), causing the system to become brighter by several decades in luminosity in X-rays and at other wavelengths before it decays back to the original luminosity over years (e.g. Holoien et al. 2014; Blagorodnova et al. 2017; Cenko et al. 2012; Lin et al. 2011). These tidal disruption events (TDEs) can also go periods of super-Eddington accretion, making them interesting to study to help understand the formation of supermassive black holes. Rates of tidal disruptions are estimated to be $1.7\pm^{+2.85}_{-1.27} \times 10^{-4}$ gal^{-1} yr^{-1} (90% confidence, Hung et al. 2018). Given the number of galaxies known and the fact that the number density of lower mass galaxies dominates over that of the more massive galaxies (see e.g. Torrey et al. 2015), many tidal disruptions should be happening, including those around IMBH. The number of tidal disruption events is even larger for merging galaxies (Arcavi et al. 2014), so searching in the centres of galaxy clusters where minor galaxies frequently merge with major galaxies can enhance the chances of identifying TDEs and thus IMBH.

As both hyperluminous X-ray sources and TDEs are bright in X-ray and it is necessary to survey a large region of sky to identify a new population of IMBH (as described above), the ideal place to search is in X-ray catalogues. *XMM-Newton* is the *European Space Agency's* second cornerstone mission from the *Horizon 2000 programme* (Jansen et al. 2001) and it has the largest effective area of any X-ray satellite (Longinotti 2014), thanks to its three X-ray telescopes observing in the 0.2-12.0 keV domain, each with $\sim$1500 cm^2 of geometric effective area. The field of view (FOV) is 30' meaning that approximately 100 serendipitous sources are discovered in a reasonable length observation (Watson et al. 2009).

The *XMM-Newton Survey Science Centre*[*] (SSC), a consortium of ten European Institutes (Watson et al. 2001) produces catalogues of detections made with the *EPIC* cameras as well as with the OM. The most recent version of the X-ray catalogue is 3XMM-DR8. It was released in May 2018[†]. It contains 775153 X-ray detections, where objects have been detected as many as 59 times over 17 years from Feb. 2000 to Nov. 2017. 332 columns of information are provided for each detection, including coordinates, observation date, time and mode, exposure and background information, counts, fluxes and rates in 7 energy bands, maximum likelihoods of detection, quality and variability flags, as well as multi-band images, lightcurves and spectra. The catalogue is an excellent resource for a wide variety of astrophysical research such as finding new objects and studying homogeneous populations of objects.

2 Intermediate mass black hole candidates

The best studied hyperluminous X-ray source was found in the *XMM-Newton* catalogue (Farrell et al. 2009). 2XMM J011028.1-460421, more commonly known as Hyper Luminous X-ray source 1 (HLX-1, Godet et al. 2009; Webb et al. 2010) has a mass of $\sim 10^4$ $M_\odot$ (Godet et al. 2012). It is highly variable, where the variability comes from periodic accretion from a companion star in a highly elliptical orbit, which is tidally stripped as it approaches periastron (Lasota et al. 2011; Godet et al. 2014; Webb et al. 2014). It is found at 8" from the centre of the galaxy ESO 243-49, which is in the galaxy cluster Abell 2877 (Santiago & Vale 2008). ESO 243-49 is one of the more massive galaxies in the cluster (Hudson et al. 2001). Given its size and proximity to the host cluster centre, ESO 243-49 is expected to have suffered dynamical effects, such as interactions or accretion of other bodies, thus making it probable that HLX-1 stems from a minor merger with its host (Webb et al. 2010; Mapelli et al. 2012; Webb et al. 2017), although no evidence for a recent merger has been found (Musaeva et al. 2015; Webb et al. 2017). Such a merger could be responsible for placing the companion star to the IMBH in its elliptical orbit. As the time between outbursts is becoming progressively longer, it appears that the orbit is becoming unbound, thus making HLX-1 an exceptional system whose lifetime is only tens of years (no outbursts observed in the early 1990s with *Rosat* Webb et al. 2010). This would explain why it appears to be a unique object.

Many TDEs have been identified through exploring *XMM-Newton* data, (e.g. Lin et al. 2011; Saxton et al.

---

[*] `http://xmmssc.irap.omp.eu/`

[†] `http://xmmssc.irap.omp.eu/Catalogue/3XMM-DR8/3XMM_DR8.html`

2015; Lin et al. 2017a; Saxton et al. 2017; Lin et al. 2018). Some of these TDEs show evidence for IMBHs, i.e. the black hole in the centre of the inactive galaxy IC 4765-f01-1504 which underwent a tidal disruption event in 2006. The mass of the black hole has been estimated to be 6×10^4 - 4×10^6 $M_\odot$ (Lin et al. 2011). The massive black hole in a dwarf galaxy orbiting 6dFGS gJ215022.2-055059, also underwent a TDE starting in ∼2005. The mass of this black hole was estimated mass to be $5.3 \times 10^4 < M_{BH} < 1.2\times 10^5$ $M_\odot$ (Lin et al. 2018). Further a TDE showing super-Eddington accretion over more than 10 years was also discovered (Lin et al. 2017b). This supports the idea that it is possible to fuel supermassive black holes at high rates for long periods, although the physical mechanism remains to be elucidated.

3 Finding new intermediate mass black holes

Taking the average length of an *XMM-Newton* observation, the TDE rate and the fact that a TDE involving an IMBH can be detected out to a redshift of ∼1.5 and taking into account the number of galaxies in the field of view, hundreds of TDEs should have been detected with with *XMM-Newton* (Webb 2019). These have not all been identified as a deep X-ray observation of the field in question must exist for the variability to be identified. In 3XMM-DR8, ∼60 objects have varied by more than a factor of 100 in X-ray. Such variability is typical of TDEs, but the signal to noise of these data are insufficient to conclude on the nature of the X-ray source. If the source could be followed up immediately after such extreme variability is identified, it would be possible to identify new TDEs and have sufficient signal to noise in the spectrum to determine the mass through spectral fitting. *XMM-Newton* is expected to fly for another 10 years and so tens of new TDEs could be identified with rapid follow-up (Webb 2019). Amongst these, new IMBH should be identified.

Other new X-ray observatories will also survey the same region of sky repeatedly, such as *eRosita* (Predehl et al. 2011) and *SVOM* (Space-based multi-band astronomical Variable Objects Monitor Cordier et al. 2015; Götz et al. 2014). These should reveal many new transients and notably TDEs and therefore IMBHs.

Alternatively, searching for IMBH in low mass galaxies remains one of the most likely places to investigate. However, scaling relations are often used to infer the mass of the central black hole and these can have quite large error bars, i.e. the black hole fundamental plane (Merloni et al. 2003; Falcke et al. 2004; Plotkin et al. 2012), the black hole mass versus velocity dispersion relation (e.g. Ferrarese & Merritt 2000; Gültekin et al. 2009) or similar mass-luminosity relations (e.g. Graham & Scott 2013), which can lead to black hole masses that are either under- or over-estimated. One way to overcome this problem is to make several observations of each object and use several scaling relationships to provide robust results (e.g. Koliopanos et al. 2017). Alternatively, data mining in wide-field sky surveys and applying dedicated analysis to archival and follow-up optical spectra can provide many new good candidates (Chilingarian et al. 2018).

Many TDEs have been discovered using optical surveys like the Zwicky Transient Facility (Graham et al. 2019) or the All-Sky Automated Survey for Supernovae (ASAS-SN) (e.g. Holoien et al. 2014). The Large Synoptic Survey Telescope (LSST), which will repeatedly survey the same region of sky with excellent sensitivity should therefore discover many more TDEs, which may house IMBHs (Bricman & Gomboc 2018). Moving to other wavelengths, low state/quiescent IMBHs should have steady radio jets. The Square Kilometre Array (SKA) will be able to detect almost any quiescent IMBH in our Galaxy (∼ μJy). Plotting the radio fluxes against quasi-contemporary X-ray fluxes (the fundamental plane of black hole accretion) will demonstrate their IMBH nature (Maccarone 2004). Finally, moving away from the electromagnetic spectrum and to gravitational waves, future facilities, such as *LISA* will also be able to detect IMBH (Barausse et al. 2015).

Over the next twenty years, a significant population of IMBH should be identified, helping us to understand how supermassive black holes form and evolve and therefore shed light on their relationship with their host galaxies.

NW is grateful to the CNES for supporting this research. This research has made use of data obtained from the XMM-Newton serendipitous source catalogue compiled by the 10 institutes of the XMM-Newton Survey Science Centre selected by ESA.

References

Arcavi, I., Gal-Yam, A., Sullivan, M., et al. 2014, ApJ, 793, 38

Bañados, E., Venemans, B. P., Mazzucchelli, C., et al. 2018, Nature, 553, 473

Bachetti, M., Harrison, F. A., Walton, D. J., et al. 2014, Nature, 514, 202

Baldassare, V. F., Reines, A. E., Gallo, E., & Greene, J. E. 2015, ApJ, 809, L14

Barausse, E., Bellovary, J., Berti, E., et al. 2015, in Journal of Physics Conference Series, Vol. 610, Journal of Physics Conference Series, 012001

Blagorodnova, N., Gezari, S., Hung, T., et al. 2017, ApJ, 844, 46

Bricman, K. & Gomboc, A. 2018, arXiv e-prints, arXiv:1812.06054

Cenko, S. B., Krimm, H. A., Horesh, A., et al. 2012, ApJ, 753, 77

Chilingarian, I. V., Katkov, I. Y., Zolotukhin, I. Y., et al. 2018, ApJ, 863, 1

Cordier, B., Wei, J., Atteia, J. L., et al. 2015, arXiv e-prints, arXiv:1512.03323

Falcke, H., Körding, E., & Markoff, S. 2004, A&A, 414, 895

Farrell, S. A., Webb, N. A., Barret, D., Godet, O., & Rodrigues, J. M. 2009, Nature, 460, 73

Ferrarese, L. & Merritt, D. 2000, ApJ, 539, L9

Godet, O., Barret, D., Webb, N. A., Farrell, S. A., & Gehrels, N. 2009, ApJ, 705, L109

Godet, O., Lombardi, J. C., Antonini, F., et al. 2014, ApJ, 793, 105

Godet, O., Plazolles, B., Kawaguchi, T., et al. 2012, ApJ, 752, 34

Götz, D., Osborne, J., Cordier, B., et al. 2014, in Society of Photo-Optical Instrumentation Engineers (SPIE) Conference Series, Vol. 9144, Proc. SPIE, 914423

Graham, A. W. & Scott, N. 2013, ApJ, 764, 151

Graham, M. J., Kulkarni, S. R., Bellm, E. C., et al. 2019, PASP, 131, 078001

Greene, J. E. 2012, Nature Communications, 3, 1304

Gültekin, K., Richstone, D. O., Gebhardt, K., et al. 2009, ApJ, 698, 198

Holoien, T. W.-S., Prieto, J. L., Bersier, D., et al. 2014, MNRAS, 445, 3263

Hudson, M. J., Lucey, J. R., Smith, R. J., Schlegel, D. J., & Davies, R. L. 2001, MNRAS, 327, 265

Hung, T., Gezari, S., Cenko, S. B., et al. 2018, ApJS, 238, 15

Hut, P., McMillan, S., Goodman, J., et al. 1992, PASP, 104, 981

Jansen, F., Lumb, D., Altieri, B., et al. 2001, A&A, 365, L1

Koliopanos, F., Ciambur, B. C., Graham, A. W., et al. 2017, A&A, 601, A20

Lasota, J.-P., Alexander, T., Dubus, G., et al. 2011, ApJ, 735, 89

Lin, D., Carrasco, E. R., Grupe, D., et al. 2011, ApJ, 738, 52

Lin, D., Godet, O., Ho, L. C., et al. 2017a, MNRAS, 468, 783

Lin, D., Guillochon, J., Komossa, S., et al. 2017b, Nature Astronomy, 1, 0033

Lin, D., Strader, J., Carrasco, E. R., et al. 2018, Nature Astronomy

Longinotti, A. L. 2014, XMM-Newton Users Handbook, Tech. Rep. 2.12, ESA: XMM-Newton SOC

Lynden-Bell, D. 1969, Nature, 223, 690

Maccarone, T. J. 2004, MNRAS, 351, 1049

Mapelli, M., Zampieri, L., & Mayer, L. 2012, MNRAS, 423, 1309

Merloni, A., Heinz, S., & di Matteo, T. 2003, MNRAS, 345, 1057

Mezcua, M. 2017, International Journal of Modern Physics D, 26, 1730021

Mortlock, D. J., Warren, S. J., Venemans, B. P., et al. 2011, Nature, 474, 616

Musaeva, A., Koribalski, B. S., Farrell, S. A., et al. 2015, MNRAS, 447, 1951

Plotkin, R. M., Markoff, S., Kelly, B. C., Körding, E., & Anderson, S. F. 2012, MNRAS, 419, 267

Predehl, P., Andritschke, R., Becker, W., et al. 2011, in Proc. SPIE, Vol. 8145, 81450D

Rees, M. J. 1988, Nature, 333, 523

Santiago, B. X. & Vale, T. B. 2008, A&A, 485, 21

Saxton, R. D., Motta, S. E., Komossa, S., & Read, A. M. 2015, MNRAS, 454, 2798

Saxton, R. D., Read, A. M., Komossa, S., et al. 2017, A&A, 598, A29

Strader, J., Chomiuk, L., Maccarone, T. J., Miller-Jones, J. C. A., & Seth, A. C. 2012, Nature, 490, 71

Torrey, P., Wellons, S., Machado, F., et al. 2015, MNRAS, 454, 2770

Tremou, E., Strader, J., Chomiuk, L., et al. 2018, ApJ, 862, 16

Volonteri, M. 2012, Science, 337, 544

Watson, M. G., Auguères, J.-L., Ballet, J., et al. 2001, A&A, 365, L51

Watson, M. G., Schröder, A. C., Fyfe, D., et al. 2009, A&A, 493, 339

Webb, N. A. 2019, Astronomische Nachrichten, 340, 262

Webb, N. A., Barret, D., Godet, O., et al. 2010, ApJ, 712, L107

Webb, N. A., Godet, O., Wiersema, K., et al. 2014, ApJ, 780, L9

Webb, N. A., Guérou, A., Ciambur, B., et al. 2017, A&A, 602, A103

Author Index